Progress in Landslide Research and Technology

Irasema Alcántara-Ayala
Željko Arbanas
Sabatino Cuomo
David Huntley
Kazuo Konagai
Snježana Mihalić Arbanas
Matjaž Mikoš
Kyoji Sassa
Shinji Sassa
Huiming Tang
Binod Tiwari
Editors

Progress in Landslide Research and Technology Volume 2 Issue 1, 2023

OPEN ACCESS

Springer

Progress in Landslide Research and Technology

The Open Access book series of the International Consortium on Landslides (ICL) aims to be the common platform for the publication of recent progress in landslide research and technology for practical applications and the benefit of society contributing to the Kyoto Landslide Commitment 2020, which is expected to continue up to 2030 and even beyond for the global promotion of understanding and reducing landslide disaster risk as well as the 2030 Agenda Sustainable Development Goals. The contributions include original and review articles, case studies, activity reports and teaching tools for the promotion of understanding and reducing landslide disaster risks.

Irasema Alcántara-Ayala • Željko Arbanas •
Sabatino Cuomo • David Huntley •
Kazuo Konagai • Snježana Mihalić Arbanas •
Matjaž Mikoš • Kyoji Sassa • Shinji Sassa
Huiming Tang • Binod Tiwari
Editors

Progress in Landslide Research and Technology, Volume 2 Issue 1, 2023

Springer

ISSN 2731-3794 ISSN 2731-3808 (electronic)
Progress in Landslide Research and Technology
ISBN 978-3-031-39011-1 ISBN 978-3-031-39012-8 (eBook)
https://doi.org/10.1007/978-3-031-39012-8

Cover illustration: Buzulgan landslide occurred in August 2020 and blocked the Gerkhozhan-Su River valley in Northern Causasus of Russia. (Photograph provided by Oleg V. Zerkal)

This Springer imprint is published by the registered company Springer Nature Switzerland AG
The registered company address is: Gewerbestrasse 11, 6330 Cham, Switzerland

Editorial Board of the Book Series

Qunli Han, Co-chair of the Global Promotion Committee of the International Programme on Landslides and Kyoto Landslide Commitment 2020
Nicola Casagli, President of the International Consortium on Landslides
Peter Bobrowsky, Immediate past President of the International Consortium on Landslides

Advisory Members for KLC2020
Abou Amani, Director, Division of Water Sciences, Secretary, Intergovernmental Hydrological Programme (IHP), UNESCO
Soichiro Yasukawa, Programme specialist, Coordinator for Disaster Risk Reduction and Resilience, UNESCO
Daniel Lebel, Director General, Geological Survey of Canada, Natural Resources Canada, Canada
John Ludden, President of the International Union of Geological Sciences (IUGS)
John LaBrecque, Chair of IUGG GeoRisk Commission, Center for Space Research, University of Texas at Austin, USA
Rafig Azzam, President of the International Association for the Engineering Geology and the Environment (IAEG)
Paolo Canuti, past President of the International Consortium on Landslides (ICL), Italy
Sàlvano Briceño, First chair of the Global Promotion Committee of the International Programme on Landslides
Badaoui Rouhban, Chair of the KLC2020 Launching Session and Moderator of ISDR-ICL Sendai Landslide Partnerships 2015–2025 Session of 3rd WCDRR in 2015

KLC2020 Official Promoters

Host Organization
International Consortium on Landslides (ICL)/Nicola Casagli

Public Sectors: KLC2020 Official Promoters-Public

International Unions/Associations, Governmental Organizations, Universities and Research Institutes
The International Union of Geological Sciences (IUGS)/John Ludden
The International Union of Geodesy and Geophysics (IUGG)/Kathy Whaler
The International Association for the Engineering Geology and the Environment/Rafig Azzam
International Geosynthetics Society (IGS)/John Kraus
Geological Survey of Canada, Natural Resources Canada, Canada/Daniel Lebel
Faculty of Civil and Geodetic Engineering, University of Ljubljana, Slovenia/Matjaž Mikoš
China University of Geosciences, Wuhan, China/Huiming Tang
Department of Civil Engineering, National Taiwan University, Chinese Taipei/Shang-Hsien Hsien
Institute of Rock Structure and Mechanics, the Czech Academy of Sciences/Josef Stemberk
Institute of Cold Regions Science and Engineering, Northeast Forestry University, China/Wei Shan

Private Sectors: KLC2020 Official Promoters-Private

Companies and Corporation

Marui & Co. Ltd, Japan Nippon Koei Co., Ltd, Japan Ellegi srl, Italy
IDS GeoRadar s.r.l., Italy
Chuo Kaihatsu Corporation, Japan Godai Corporation, Japan

Global Promotion Committee of the International Programme on Landslides and Kyoto Landslide Commitment 2020

A Commitment to the Sendai Framework and the Sustainable Development Goals

Chair

Matjaž Mikoš (Faculty of Civil and Geodetic Engineering, University of Ljubljana)

Co-chairs

Qunli Han (Integrated Research on Disaster Risk, IRDR)
Soichiro Yasukawa (Programme Specialist on Disaster Risk Reduction, UNESCO, Paris)
Hiroshi Kitazato (Treasurer of IUGS)
John LaBrecque (Chair of IUGG GeoRisk Commission)

Secretary

Kyoji Sassa (IPL World Centre, Director)

Members of the IPL-KLC Global Promotion Committee

ICL Full Members

Geotechnical Engineering Office, Hong Kong, China; UNESCO Chair for the Prevention and the Sustainable Management of Geo-hydrological Hazards—University of Florence, Italy; Faculty of Civil and Geodetic Engineering, University of Ljubljana (ULFGG), Slovenia; and other members (total 61 members from 30 countries/regions).

ICL Supporting Organizations

UNESCO, UNDRR, WMO, FAO, UNU, ISC, WFEO, IUGS, IUGG, Government of Japan (CAO, MEXT, MAFF, MLIT)

KLC2020 Official Promoters

Host Organization

International Consortium on Landslides (ICL)/Nicola Casagli

Public Sectors: KLC2020 Official Promoters—Public

- The International Union of Geological Sciences (IUGS)/John Ludden
- The International Union of Geodesy and Geophysics (IUGG)/Kathy Whaler
- The International Association for the Engineering Geology and the Environment (IAEG)/Rafig Azzam
- International Geosynthetics Society (IGS)/John Kraus
- Geological Survey of Canada, Natural Resources Canada, Canada/Daniel Lebel
- Faculty of Civil and Geodetic Engineering, University of Ljubljana, Slovenia/Matjaž Mikoš

- China University of Geosciences, Wuhan, China/Huiming Tang
- Department of Civil Engineering, National Taiwan University, Chinese Taipei/Shang-Hsien Hsien
- Institute of Rock Structure and Mechanics, the Czech Academy of Sciences/Josef Stemberk
- Institute of Cold Regions Science and Engineering, Northeast Forestry University, China/Wei Shan

Private Sectors: KLC2020 Official Promoters—Private

- Marui & Co. Ltd, Japan
- Nippon Koei Co., Ltd, Japan
- Ellegi srl, Italy
- IDS GeoRadar s.r.l., Italy
- Chuo Kaihatsu Corporation, Japan
- Godai Corporation, Japan
- Kiso-Jiban Consultants Co., Ltd, Japan
- Kokusai Kogyo Co., Ltd., Japan
- OSASI Technos, Inc., Japan

IPL World Centre

IPL World Centre (IWC) was established in 2006 by the Tokyo Action Plan to serve, as it does, as the secretariat of IPL, GPC/IPL as well as of UNITWIN UNESCO-KU-ICL Programme. IWC also serves as the secretariat of KLC2020. IWC is a part of the legal body (NPO-ICL registered in Kyoto, Japan) of ICL. The Council of the IWC consists of advisors from Ministry of Education, Sports, Science and Technology, Ministry of Agriculture, Forestry and Fisheries, Ministry of Land, Infrastructure and Tourism of the Government of Japan, UNESCO, and of members from ICL Headquarters, chairs of GPC/IPL-KLC, presidents and officers of ICL.

Secretariat of GPC/IPL-KLC

Secretary

Kyoji Sassa
International Consortium on Landslides
138-1 Tanaka-Asukai cho, Sakyo-ku, Kyoto 606-8226, Japan
Tel: +81 (75) 723 0640
Fax: +81 (75) 950 0910
E-mail: klc2020@iclhq.org
URL: https://www.landslides.org/

Contents

The Second-Year Publication of the Open Access Book Series "Progress in Landslide Research and Technology"

Kyoji Sassa

Abstract

The ICL new open-access book series "Progress in Landslide Research and Technology" was launched in 2022, and the founding issues, Vol.1, No.1 and No.2 2022 were successfully published by active authors, KLC2020 official promoters as well as voluntary volume editors. The starting point of this new book series is the publication of the journal "Landslides" of the ICL in 2004. Based on the experience and the assets of good editors and enthusiastic authors through these 18 years, the ICL and journal editors have been challenged to launch the Open Access Book Series "Progress in Landslide Research and Technology" in 2022.

The book series provides a joint platform for the publication of recent progress in landslide research and technology for practical applications and the benefit for the society contributing to the Kyoto Landslide Commitment 2020, which is expected to continue until 2030 and beyond to globally promote the understanding and reduction of landslide disaster risk, as well as to address and help implementing the UN 2030 Agenda Sustainable Development Goals.

This short article states firstly the financial management (Book Processing Charge: BPC), which is the most important for the sustainability of publishing an open access book series, and the selection of cover photo and the issue editors on the front cover. Number of issue editors were changed from 5 for Volume 1 Issue 1, to 9 for Volume 1 Issue 2 and 11 for Volume 2 Issue 1. Secondly, the creation of a new Award related to this book series, and the support of the core activities of the International Programme on Landslides (IPL): *A Programme of the ICL for Landslide Disaster Risk Reduction* through this book series are explained.

The countries of the authors, and the number of pages and articles of eight categories were compared in the founding two issues and the first issue of the second year. Finally, the oral presentation opportunity on their results for the authors of P-RLT in 2023 is introduced. We had the first oral presentation opportunity at the ICL 20th Anniversary and IPL-KLC Symposium in November 2022. Authors obtained something different merits from printed publication as from oral presentation. We have a plan to offer the next opportunity for orally presenting the results in June and November, 2023.

Keywords

Open Access Book Series · Kyoto Landslide Commitment 2020 · ICL Book Article Award · IPL-KLC Award for Success

1 Management of P-LRT

Book processing charge

The total number of printed pages of an article is flexible in the book series up to 100 pages. The page number of one article is within three ranges, 4–10 pages, 11–20 pages, and more than 20 pages. The book processing charge (BPC) is different in these three ranges. BPC is different reflecting the financial and practical contributions to P-LRT as shown in Table 1

- BPC for Regular authors are USD50 per page for 4–20 pages, and USD40 per page for an additional page (from 21 to 100 pages).
- BPC for ICL Associates, ICL Supporters, and Working editors for P-LRT are USD25 per page from 4 to 10 pages, USD50 per page from 11 to 20 pages, and USD40 per page for an additional page (from 21 to 100 pages).
- BPC for ICL full members and KLC Official promoters are USD0 per page until 10 pages and USD50 per page for

K. Sassa (✉)
International Consortium on Landslides, Kyoto, Japan
e-mail: secretariat@iclhq.org

I. Alcántara-Ayala et al. (eds.), *Progress in Landslide Research and Technology, Volume 2 Issue 1, 2023*,
Progress in Landslide Research and Technology, https://doi.org/10.1007/978-3-031-39012-8_1

Table 1 Book Processing Charge (BPC) in the four categories

Book Processing Charge (BPC)			
Type of authors	BPC: up to 10 pages	BPC: 11–20 pages	BPC: additional pages
Regular	USD50 per page		USD40 per page
ICL associates, supporters, working editors	USD25 per page	USD50 per page	USD40 per page
ICL full members, KLC official promoters	USD0 per page	USD50 per page	USD40 per page
Note 1	The reduced BPC (USD25 per page and USD0 per page up to 10 pages) for ICL Full members, KLC Official promoters, ICL Associates, ICL Supporters and editors is applicable for one article from each organization in each volume.		
Note 2	Full members which have selected one rank lower category of membership fee are classified to Type of ICL Associate.		
Note 3	Editor is an editor working for each volume.		
Note 4	The invoice will be sent after the acceptance/publication		

11 to 20 pages, and USD40 per page for an additional page (from 21 to 100 pages).

Additional Explanation

- USD0 or reduced BPC up to 10 pages is applicable for one article for each of ICL organization in each volume (NOT each issue). Membership fee payment for each organization of ICL is once a year.
- ICL membership fee is decided in proportion to GNI/PC published annually by the World Bank for each country.
- Each full member can select one rank lower category of membership fee. Those members are classified as ICL associates.
- Invoice of BPC will be sent after acceptance and formatting of an article by the publisher.

The publisher will format each article in its editorial role. Printed figure size and layout will be different from the submitted article. Often the final page number is different. BPC is charged to the printed page number and not submitted one.

Design of the book cover

Design of the book cover as well as the assignment of the handling editor for each submitted article is decided by the all editors meeting by Zoom crossing three continents (America, Europe and Asia). We organized such Book Editorial Meetings eight times in 2022.

Figure 1 presents the cover of Vol. 1, Issue 1 and Issue 2. Each photo was selected from the published articles in each book. Photo of Vol. 1, Issue 1 is the 2016 Rain-induced rapid and long-travelling landslide with 127 fatalities in Aranayake, Sri Lanka. Photo of Vol. 1, Issue 2 is the 2016 Earthquake-induced rapid triggered by 2016 Kumamoto Earthquake in Aso, Japan. The Aso-Ohashi Bridge was destroyed and disappeared. Figure 2 presents the proposing cover design of Vol. 2, Issue 1. The final design is decided by the publisher. The photo is the 2020 reactivated slow moving (0.4–0.5 m/day) landslide in Buzulgan, Northern Caucasus, Russia.

Editors on the front cover of Vol. 1, Issue 1 was five editors with Editor-in-Chief role in the WEB editorial manager "EquinOCS." However, editors on the front cover of Vol. 1, Issue 2 were additionally four active authors writing more than two articles in the previous and the coming issues, as well as the five EIC in OCS. Editors on the front cover of Vol. 2, Issue 1 are selected six active authors as well as five EIC in OCS in the same principle. For the success of this book series, contributions as writing authors, book series editors and KLC2020 official promoters are equally important.

New Awards and Free BPC as an award

The founding two issues of the new ICL Book Series "Progress in Landslide Research and Technology" were published. Based on the publication of this new book series to promote the Kyoto Landslide Commitment 2020, the ICL has launched two new awards, A: ICL Book Article Award, and B: IPL-KLC Award for Success as below.

A: ICL Book Article Award

- Award is a free Book Processing Charge (BPC) for 20 pages.
- The effective period for a book article submission is 1 year after the decision of the award.
- The number of annual awards is 1–3 in different article categories.

(1) Award candidate nomination committee members (around 10) is from EIC members (5) of OCS-web and a few editors (1–3), who read almost all the articles.
(2) Nomination of Award (2–3) is voted by the editors of P-LRT who attend the periodical (around 2–4 times for one issue) editorial meeting of the Book.

Fig. 1 Published cover of Volume 1, Issue 1 and Volume 1, Issue 2 of the P-LRT

B: IPL-KLC Award for Success

- Award is USD3000 in cash.
- The number of awards for each World Landslide Forum is 1–3 in different article categories (similar to the previous IPL Award for Success).

(1) Candidates are authors of ICL open access book series (prerequisite condition) and Journal "Landslides" to have reported IPL-KLC activities.
(2) The first nomination is around 10 candidates from EIC members (5) of P-LRT and the screening editors of Journal Landslides who monthly read submitted articles.
(3) The approval is by the IPL-KLC Global Promotion Committee.

Both awards are expected to contribute to the success of the Kyoto Landslide Commitment 2020 as well as the new book series. BPC can be a supplementary award for ICL awards.

- 20 pages free BPC is awarded to the recipient of annual Varnes medal as a supplementary award. He/she needs to contribute one article within a year.
- 10 pages free BPC is awarded to the recipient of annual Oldrich Hungr award. He/she needs to contribute one article within a year.
- 10 pages free BPC is awarded to the recipient of the triennial Hiroshi Fukuoka IPL Award. He/she is requested to contribute one article within a year.
- 20 pages free BPC is awarded to the recipient of the Landslides-best paper award.
  The effective period is 1 year.

World Centres of Excellence and IPL Projects

The World Centers of Excellence on Landslide Risk Reduction (WCOE) 2020–2023 was nominated in 2020. And WCOE 2023–2026 will be nominated in 2023 by the application and the evaluation procedure.

The applicating organization for a WCoE 2023–2026 should have published or contributed to P-LRT [Vol. 1, Issue 1 and Issue 2 in 2022, Vol. 2, Issue 1 and Issue 2 in 2023 or Vol. 3, 1. Candidates of WCOE 2023–2026 which have neither published nor contributed for 2½ years (five issues) are not eligible to be evaluated, even if they submitted an application.

Fig. 2 Book cover for Volume 2, Issue 1

The International Programme on Landslides (IPL) is a programme of the ICL for landslide disaster risk reduction. IPL projects are a core activity of IPL. The IPL project leaders published simple annual reports to the IPL web. The ICL has now the new open access book series, which are accessed and downloaded free of charge. Leaders of the ongoing IPL projects can contribute an article to the open access book series "Progress in Landslide Research and Technology" and disseminate their results worldwide.

2 Comparisons of Vol. 1-1, Vol. 1-2, and Vol. 2-1

At the begging of the second year of P-LRT, we have compared three issues to evaluate the initial state of this new publication.

Authors for each issue.

- Vol. 1, Issue 1: The number of contributing authors is highest in Italy and Japan (both with 20 authors). And the number of countries/regions/United Nation and International organizations are highest (26) within three issues.
- Vol. 1, Issue 2 issue: The number of contributing authors is highest in Japan, and the second was Vietnam.
- Vol. 2, Issues 1: the number of contributing authors is more than 10 in 6 countries: 21 Vietnam, 15 Italy, 14 Croatia, 13 Japan, 12 Mexico, 11 Russia.

Table 2: Number of articles and the number of pages in each article category.

- Vol. 1, Issue 1: Three forewords with video from ICL President, IUGS President, IUGG Presidents, and three greetings (greeting for the Fifth World Landslide Forum) from the United Nations Special Representative of the Secretary-General for Disaster Risk Reduction, the United Nations Under-Secretary General (Rector of the United Nations University) and the Assistant Director-General for Natural Sciences of the UNESCO were published.
  The following three editorials were published as the basic information of this book series; (1) Aim and outline of the new book series, (2) the International Consortium on Landslides, (3) the International Programme on Landslides.
  10 articles, 118 pages for IPL/WCoE/KLC activities are highest in the three issues.
- Vol. 1, Issue 2: 13 articles, 161 pages for original articles are the highest in the three issues.
- Vol. 2, Issue 1: 2 articles and 124 pages for ICL Landslide lesson. This category presents lessons by global and emerging experts with distinguished achievements in one of the specific aspects in understanding and reducing landslide disaster risk. Landslide lesson is a characteristic category of this book series for practitioners and the benefit for the society contributing to the Kyoto Landslide Commitment 2020.

Figure 3: Shares of the article number and the page number of each category.

Trend of the categories for 3 years is clearly presented in Fig. 3. Original articles (blue) and IPL/WCoE/KLC articles (purple) are two big categories through 3 years. ICL Landslide lesson (Vol. 2, Issue 1) and World Landslide Report (Vol. 1, Issue 2) is 1 year only. Articles for ICL two articles in the category of Landslide lesson are expected to contribute to Vol. 2, Issue 2. The World Landslide Report are reports from less funded authors from landslide-prone developing countries. Reports of landslides less published regions/countries are invited to contribute to this category. No BPC for articles in this category. Maximum 40 pages per issue. Review articles are 76 pages in Vol. 1, Issue 2. However, no

Table 2 Number of articles and the number of pages in each article category

	Vol. 1, Issue 1		Vol. 1, Issue 2		Vol. 2, Issue 1	
Breakdown	Number of articles	Number of pages	Number of articles	Number of pages	Number of articles	Number of pages
Front matters	3	9	3	8	3	7
Forewords/greetings	6	12	0	0	0	0
Table of contents	1	4	1	4	1	4
Editorial (ICL history, IPL overview and others)	3	60	1	8	1	7
ICL Landslide Lesson	0	0	0	0	2	124
Original articles	11	135	13	161	9	113
Review articles	1	5	6	76	0	0
IPL/WCOE/KLC activities	10	118	4	61	5	79
Teaching Tools	1	64	2	44	2	26
Technical Notes and Case studies	1	8	1	9	3	32
World Landslide Reports	0	0	3	37	0	0
Official Promoters	16	46	16	46	16	46
Back matters	1	3	1	3	1	2
Total	54	464	51	457	43	440

review articles are published in Vol. 2, Issue 1. However, two review articles (one is long) are planned to contribute to Vol. 2, Issue 2.

Teaching tools with video tutorials are the characteristic of this book series for practitioners and the benefit for the society contributing to KLC2020. Every issue includes teaching tools with video tutorials.

3 Oral Presentation Invitation for the Authors of P-RLT Articles

(Vol. 1, Issue 1 and Issue 2, Vol. 2, Issue 1 and Issue 2, Vol. 3, Issue 1)

All articles of P-LRT are available worldwide free of charge. The oral presentation face-to-face with an opportunity for discussion with colleagues in the community of landslide disaster risk reduction and the KLC2020 has a different meaning from written contributions.

2023 IPL-KLC WEB Symposium on Landslides

Invited speakers will include: Authors of the Open Access Book (P-LRT) Vol. 2, Issue 1 and Vol. 2, Issue 2 (Submission deadline: 30 March 2023), Proposers of the WCoE 2023–2026 (submission deadline is 30 March 2023), and proposers of 2023 IPL projects (Submission deadline is 30 May 2023).

Time and date:

Time domain (PDT) 9:30–12:00 PM on 22–23 June 2023
Time domain (CEST) 6:30–9:00 AM on 23–24 June 2023
Time domain (JST) 1:30–4:00 PM on 23–24 June 2023

6th World Landslide Forum on 14–17 November 2023 in Florence, Italy

The Open Access Book (P-LRT) was launched to promote the Kyoto Landslide Commitment 2020.

The following sessions of the Theme 1 Kyoto Landslide Commitment for sustainable development invite the authors of P-LRT from Vol. 1, Issue 1 and Issue 2 in 2022, Vol. 2, Issue 1 and Issue 2, in 2023, and Vol. 3, Issue 1 in 2024 to join the Forum sessions.

Theme 1: Kyoto Landslide Commitment for sustainable development

Coordinators: Kyoji Sassa, Matjaž Mikoš, Shinji Sassa, Khang Dang

Session 1.1 International Programme on Landslides

Conveners: Kyoji Sassa, Matjaž Mikoš, Irasema Alcantara-Ayala

Session 1.2 Global and International activities for KLC2020

Conveners: Qunli Han, Kazuo Konagai, Claudio Margottini, Snježana Mihalić Arbanas

Session 1.3 Cascading multi-hazard risks: Submarine landslides, tsunamis, and impacts on infrastructures

Conveners: Shinji Sassa, David Tappin, Finn Løvholt

Session 1.4 Landslides and Society: Open and citizen science for capacity development and education

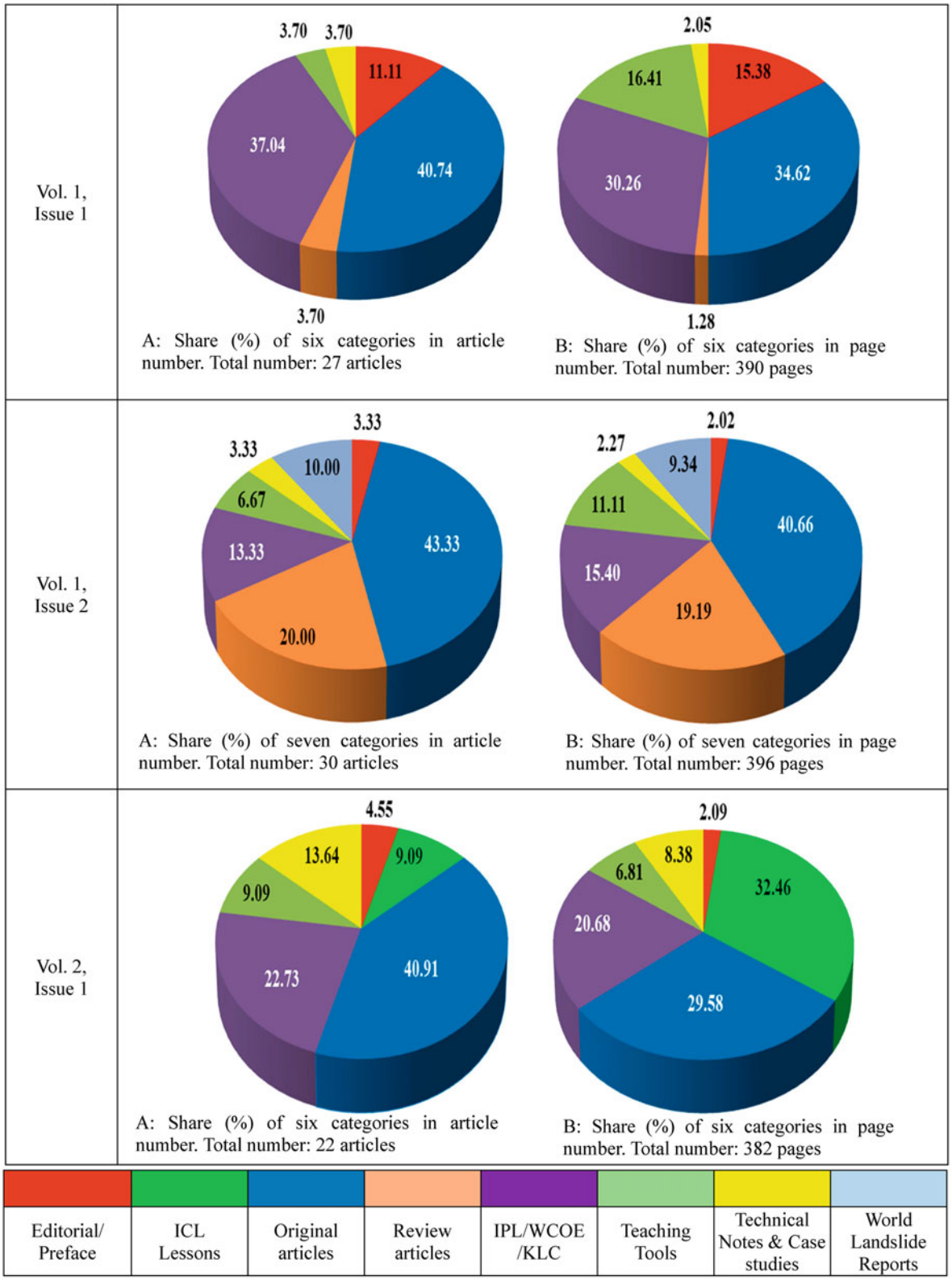

Fig. 3 Share (%) of categories in Vol.1, Issue 1, Vol.1, Issue 2 and Vol.2, Issue 1

Conveners: Matjaž Mikoš, Irasema Alcántara-Ayala, Beena Ajmera

Call for Contribution and KLC2020 Official Promoters

Editors as well as the KLC2020 secretariat sincerely request any further contribution of articles and further expansion of the number of KLC2020 official promoters in order to sustain global understanding and reducing landslide disaster risk. The success of the open access book series deeply depends on the contribution of good articles and strong support from the KLC2020 official promoters.

Those who are willing to contribute articles and promote this initiative as KLC2020 official promoters are requested to inform the KLC2020 Secretariat:

Kyoji Sassa
Secretary General of the Kyoto Landslide Commitment 2020 and the ICL
Editor-in-Chief, ICL Open Access Book Series
"Progress in Landslide Research and Technology"
e-mail: klc2020@iclhq.org
Kyoto, Japan, date: 25 January 2023

Part I

ICL Landslide Lesson

Sliding-Surface Liquefaction and Undrained Steady-State Shear-Strength

Kyoji Sassa, Loi Doan, Khang Dang, and Pham Tien

Abstract

The sliding-surface liquefaction (SSL) is one of the most important concepts to understand and reduce rapid landslide disaster risk. SSL occurs even in dense sandy layers. SSL is caused by a series of phenomena, 1) grain-crushing due to shearing under overburden pressure in the shear zone, 2) volume reduction in the shear zone, 3) generation of high pore-water pressure in the shear zone, and 4) liquefaction of the shear zone material.

After SSL, a mass of soil layer above the liquified sliding surface moves at high speed. Motion of sandy layer above the liquified sliding-surface was physically simulated under the corresponding normal stress by the undrained stress-control ring-shear apparatus. The shear stress acting on the sliding-surface and the generated pore pressure near the sliding surface are monitored. After failure, shear strength mobilized on the shear zone decreases by the effects of increased pore-water pressure, then, the shear strength working on the shear surface together with the generated pore pressure reaches a certain constant value which is the undrained steady-state shear-strength (USS). After reaching to USS, only shear displacement is increased without any change of shear stress and pore pressure. It is a common feature of rapid and long-travelling landslides which poses a high risk to people living in/near slopes.

K. Sassa (✉) · L. Doan
International Consortium on Landslides, Kyoto, Japan

K. Dang
International Consortium on Landslides, Kyoto, Japan

VNU University of Science, Hanoi, Vietnam

P. Tien
Institute of Geological Sciences, Vietnam Academy of Science and Technology, Hanoi, Vietnam

Keywords

Landslides · Sliding-surface liquefaction · Undrained steady-state shear strength

1 Introduction

A new Open Access Book Series "Progress in Landslide Science and Technology (P-LRT)" was launched for the platform to implement the Kyoto Landslide Commitment 2020 in 2022. P-LRT has a new category of ICL landslide lessons. This article is the first ICL landslide lesson in P-LRT. This article consists of the following four parts.

Background information of SSL in the context of landslide risk reduction

- Concept of the sliding-surface liquefaction
- Initiation mechanism of landslides and Types of landslides based on the stress path

Tools to support SSL and USS

- Physical landslide simulator: Formation of sliding surface and post failure motion
- Development of undrained dynamic loading ring shear apparatus
- Development of LS-RAPID to simulate long travel distance using the post failure strength reduction and the USS

Original test results for this article

- Experiment of standard sand "Silica sand No.6"
- Experiment of natural soils (example of Volcanic debris taken from Unzen)

Different case studies of sliding-surface liquefaction from previous research

- 2006 Mega-slide in Leyte, Philippines, triggered by a small earthquake after long rainfall.
- Large-scale landslides triggered by the 2004 Mid-Niigata earthquake, Japan

I. Alcántara-Ayala et al. (eds.), *Progress in Landslide Research and Technology, Volume 2 Issue 1, 2023*,
Progress in Landslide Research and Technology, https://doi.org/10.1007/978-3-031-39012-8_2

- Hypothetical submarine landslides in Suruga Bay, Japan
- Large-scale landslides triggered by the 2011 typhoon "Talas" in Kii Peninsula, Japan
- 1792 Historical mega-slide in Unzen, Japan.

2 Background Information of Significance of Sliding-Surface Liquefaction

2.1 Background

Landslide disasters are classified in the following two types,

1. Disasters give damages to roads, railways, brides, dams mining pits, and other engineering facilities. This type of landslide disasters have studied with funds to maintain the social infrastructure.
2. Human disasters by rapid and often long-travelling fatal landslides. Funding of research on fatal landslides is not always easy.

The International Consortium on Landslides (ICL) together with the landslide community has made efforts to obtain support from the United Nations, International and national stake holders. Supports from the United Nations and International organizations to the ICL and the landslide communities are realized the establishment of the International Programme on Landslides (IPL) in 2006, the Landslide Sendai Partnerships 2015–2025 in 2015, and the recent framework is the Kyoto Landslide Commitment 2020 for global promotion of understanding and reducing landslide disaster risk.

The founding of this new open access book series is owed to the Kyoto Landslide Commitment 2020 and the KLC2020 official promoters. The sliding-surface liquefaction is one of key to understand the fatal rapid landsides. Before entering in to technical contents, we wish to outline the framework which has enabled to launch the IPL, the Sendai landslide Partnerships, and the Kyoto Landslide Commitment 2020 with thanks for all supporting organizations as below.

2.2 Kyoto Landslide Commitment 2020

Kyoto 2020 Commitment for Global Promotion of Understanding and Reducing Landslide Disaster Risk (Kyoto Landslide Commitment 2020: KLC2020): A Commitment to the ISDR-ICL Sendai Partnerships 2015–2025, the Sendai Framework for Disaster Risk Reduction 2015–2030, the 2030 United Nations Agenda Sustainable Development Goals, the New Urban Agenda and the Paris Climate Agreement was launched in Kyoto, Japan on 5 November 2020 (Sassa 2021).

Fig. 1 Logos of the ICL and the Kyoto Landslide Commitment 2020

Figure 1 is the logo of the ICL (left) and the Kyoto Landslide Commitment 2020 (right). The Kyoto Landslide Commitment 2020 was established based on the ICL and its scientific programme IPL. The ICL was founded in 2002, the IPL was launched in 2006 with the MoU between the ICL and each of the following five United Nations Organizations and two global stakeholders.

- United Nations Educational, Scientific and Cultural Organization (UNESCO)
- United Nations Office for Disaster Risk Reduction (UNDRR)
- World Meteorological Organization (WMO)
- Food and Agriculture Organization (FAO)
- United Nations University (UNU)
- International Science Council (ISC)
- World Federation of Engineering Organizations (WFEO)

Based on the IPL and the 2015 Sendai Landslide partnerships (Sassa 2016), the Kyoto Landslide Commitment 2020 has been launched in 2020. This framework is expected to continue to 2030 and beyond. Blue arrow symbolizes this process (Sassa et al. 2022).

The Kyoto Landslide Commitment 2020 was signed by 90 United Nations, Global, International, and national organizations by 5 November 2020. Representatives from all 90 organizations are invited to join these launching sessions. Under the participation of all KLC2020 partners and greetings from major organizations, the Kyoto Landslide Commitment 2020 was established by the 2020 Kyoto Declaration "Launching of Kyoto Landslide Commitment 2020." All 90 partners and participants of this launching session are reported in Landslides, Vol.18, No.1 issue (Sassa 2021).

The ICL is a host organization of KLC2020 and also the Open Access Book Series "Progress in Landslide Research and Technology" for KLC2020. The IPL and also Kyoto Landslide Commitment 2020 is a global and long-standing cooperation framework as long as landslide disaster risk threatens people's lives worldwide and the society.

2.3 The Sliding-Surface Liquefaction in Landslides

A landslide is a downslope movement of rock or soil, or both. The movement velocity can be very different. Cruden and Varnes (1996) classified the velocity of landslides in the following seven classes (Table 1).

Class 1 to Class 5 are slower than 3 m/min. Though these landslides may damage infrastructure, but the risk to human lives are not serious. However, landslides at the velocity class No.6 (50 mm/s to 5 m/s) are dangerous. Especially, Velocity class No.7 (faster than 5 m/s) landslides are very rapid and fatal.

Landslides as a result of the sliding-surface liquefaction move very fast, similar to skiing or sliding on snow or skating on ice. Snow under rapidly moving skiing and sled or ice under skating blade changes from snow/ice to water by rapid loading. When water entering speed under skiing, sliding or skating blades is greater than the velocity of water drain under skiing or sled or skating blades, undrained loading state is formed. Namely water (liquid) exists under skiing or skating.

Let us examine what is the mechanism of rapid motion of the skater (non-liquefied mass) on the ice using the Fig. 2. When a skater stands on a skating blade and moves on the ice by kicking another skating blade, the surface of the ice is liquefied to water by loading and shearing by the moving skating metal edge. The water generated under the metal edge laterally drains to both sides of the metal edge as well as forward and backward. At a slower speed than a critical value, water drainage is faster than the water generation speed. In this case, water cannot exist between the skating edge and the ice. Frictional resistance is that of contact between the metal edge and the ice. Whereas, in the case of faster speed than a critical value, a water layer remains between the ice and the metal edge. As such, frictional resistance is close to the value of water. The skater can slide very fast on the liquefied ice layer. The sliding-surface liquefaction beneath the skating blade is the reason for the rapid motion of the skater. The mechanism of the sliding-surface liquefaction in landslides is analogous to that of the ice skating. Only difference is in the skater and the moving landslide mass on the sliding-surface liquefaction layer. The ice corresponds to the saturated soil layer. The ice melts by loading and shearing. The saturated soil layer is liquefied by grain crushing due to shearing.

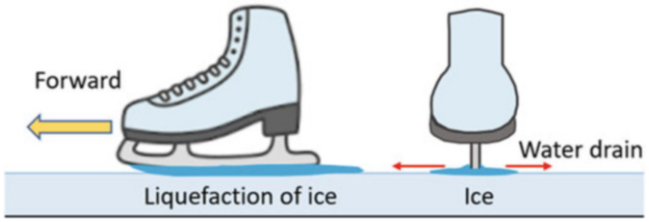

Fig. 2 Sliding-surface liquefaction in ice-skating

Sassa et al. investigated the landslide in Leyte Island in Philippines in 2006 which was triggered by a very small earthquake after a long rainfall. The landslide was rapid and the travel distance was long and wide. It destroyed one village and killed around 1000 people. We investigated this landslide and took samples and conducted the ring shear test seismic loading using the monitored earthquake record (Sassa et al. 2010). The mechanism was investigated using the undrained dynamic-loading ring-shear apparatus which was developed by K. Sassa and colleagues of Kyoto University. It is explained in Tools to support the concepts of the sliding-surface liquefaction (SSL) and the undrained steady-state shear-strength (USS) in more detail. This ICL Landslide Lesson introduces sliding-surface liquefaction and undrained steady-state shear-strength. We will explain, with the illustration of grain-crushing, volume-reduction and pore-pressure increase, the instance of the sliding-surface liquefaction and steady-state shear strength triggered by a very small earthquake—using Fig. 3.

Figure 3b shows a time series data of undrained dynamic loading ring shear test for the sample taken from the Leyte Landslide. The lines indicate monitored normal stress (black line), monitored shear stress acting on the shear surface (red line), the pore pressure monitored near the sliding zone (blue line), the shear displacement at the center of the inner ring and the outer ring of the apparatus (green line), respectively. T1 shows the start of seismic loading, T2 shows the start of shear displacement when pore pressure started to develop by grain-crushing due to shearing. T3 shows the start of the steady-state shearing, in which normal stress, shear stress, and pore pressure were constant, but only shear displacement proceeded.

Table 1 Seven velocity class of landslides

1	2	3	4	5	6	7
Extremely slow	Very slow	Slow	Moderate	Rapid	Very Rapid	Extremely Rapid
Slower than 5×10^{-7} (mm/s)	Slower than 5×10^{-5} (mm/s)	Slower than 5×10^{-3} (mm/s)	Slower than 5×10^{-1} (mm/s)	Slower than 5×10^{1} (mm/s)	Slower than 5×10^{3} (mm/s)	Faster than 5×10^{3} (mm/s)
Slower than 16 mm/year	Slower than 1.6 m/year	Slower than 13 m/months	Slower than 1.8 m/h	Slower than 3 m/min	Slower than 5 m/s	Faster than 5 m/s

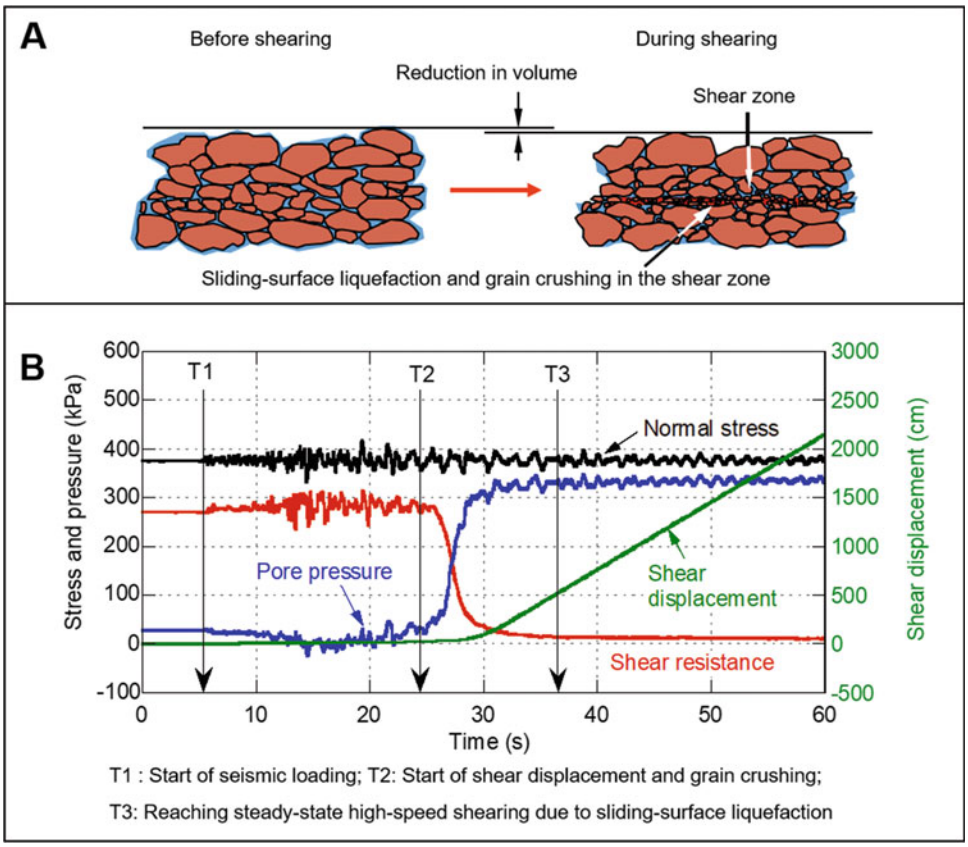

Fig. 3 Illustration and experimental data for the Sliding-surface liquefaction

Figure 3a is an illustration of grain-crushing of volcanic debris due to shearing. The left figure illustrates before applying the seismic loading at, or before T1. The right figure illustrates the situation at the steady-state shearing at i.e. after T3. Angular volcanic grains are crushed due to shearing under a high-normal stress. Then, volume reduction proceeds. The shear box is fully saturated and shearing is maintained under undrained condition.

The situation explained above demonstrate that the pore pressure should rise due to the tendency of volume reduction. In the case of drained condition, a greater volume reduction will occur, but pore pressure does not build up. Due to the tendency of volume reduction and the resulting pore pressure increase, liquefaction occurs in a narrow shear zone. It is different from liquefaction of saturated and loose sand mass during an earthquake. Like in the case of skating, often, the whole landslide mass above the sliding surface is not always liquefied.

2.4 Landslide Initiation Mechanism and Landslide Types by Shearing Mechanism

The landslide initiation mechanism from the stress path at the sliding surface is explained using Fig. 4. The upper figure of Fig. 4 shows a section of slope and one vertical column element and its working force elements. A mass of the column (m) x gravity (g) is working on the soil column. The stresses acting on the bottom of the column, namely sliding surface, are 1) normal stress: $mg \cdot \cos\theta$. 2) shear stress: $mg \cdot \sin\theta$.

The lower figure of Fig. 4 is a graph between normal stress and shear stress. Initial stress without pore water pressure is Point I ($\sigma 0$, $\tau 0$). The length of the line from the origin (0) to Point I is mg in the case of no porewater pressure acting on the sliding plane. When ground water level increases by rainfalls, the stress point I will move to the left. When the stress point will reach the failure line, landslide will be initiated. Deep landslide needs a large increase of pore-water pressure until failure. Shallow landslides are generated by a smaller pore-water pressure increase. But the failure line is the same. Mechanism of rain-induced landslide are the same. The stress path is also changed under earthquake wave. In this case, stress path is Not the straight line like the Fig. 4. If pore water pressure is high, and the initial stress point is near the failure line before an earthquake, a small earthquake triggers a landslide. The Leyte landslide case (Fig. 3) is the case. Earthquake shaking is the last push to the failure.

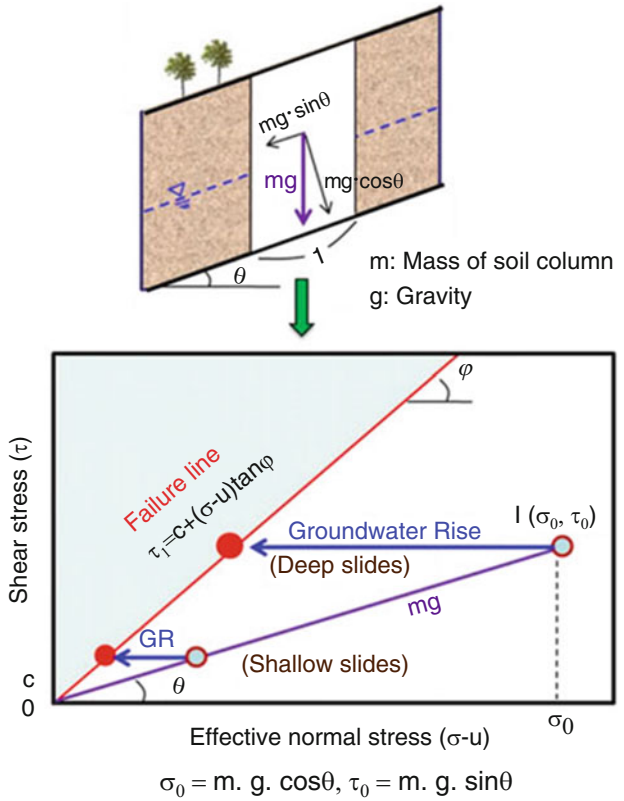

Fig. 4 Landslide initiation mechanism by pore pressure increase

2.4.1 Shearing Types of Landslides in Stress Path

Sassa published the Geotechnical Classification of Landslides (Sassa 1985, 1989), the sliding surface liquefaction was explained in his further publication (Sassa 1999). The extremely slow moving "Creep" is a geomorphic process, but not the target of landslide risk reduction.

It is important to understand the mechanism of the landslide initiation and the post-failure motion for understanding and reducing landslide disaster risk, focused by the KLC2020. Four types of shearing of landslides are classified in the stress path which shows the shift of the stress on the sliding surface from a stable state to failure, and from the failure to the steady state motion in the domain of shear stress (vertical axis) and normal stress (horizontal axis).

Type I: Peak strength slide

This type is called as "Slope Failure" in Japan and others. This type of landslides occurs in steep and stiff slopes at the inclination steeper than the failure line during motion. Most cases are the fist-time slide (virginal slide) on the slope. After failure, the stress pass drops to the failure line during motion. The gravity force by the stress reduction from the peak to the stress during motion is spent for the acceleration of the landslide mass. Therefore, the speed is fast. If the sliding surface is saturated, and shearing causes volume reduction generating high-water pressure, it is classified as Type IV-sliding surface liquefaction.

Type II: Residual state slide

This type of landslide repeatedly moves. The soil layer on the sliding surface is in a residual state, no stress reduction takes place at failure. So, no acceleration will occur. Slow and very small distance of movement occurs, but soon stops due to the increase of stability by the movement onto a flatter slope. The movement is very limited and the ground surface is gentle, and often the soils are fertile and wet (water rich). Those residual state landslide areas are used for paddy field to product rice and pasture for grazing cattle. The movement is gentle and poses no/less risk to cattle and working farmers, although those areas are not always suitable to construct houses and buildings. Due to rainfall and ground water rise during rainy season, the stress will move leftward due to pore-water pressure increase, and may reach the failure line at residual state and start movement. However, it will stop after a limited movement.

Type III: Mass liquefaction

In saturated coastal areas consisting of a loose sand deposit, sometimes landslides occur during earthquakes.

Earthquake shaking causes liquefaction of loose sand deposit. A liquefied sand layer starts to move even in a gentle slope. In the mountain slopes, sometimes those mass liquefactions will occur. Along a concave slope such as extension of torrent, surface water caused by rainfall will penetrates into the ground and flow into the underground of the concave slopes. A long-time ground water flow gradually erodes fine particles within the sandy layer. Then, a loose structure of sand layer is produced. During earthquakes or during heavy rainfalls, such a loose structure may be failed, and volume reduction occurs. The mass liquefaction occurs in the loose-structure part of the sand layer. The upper soil layer will start to move on the liquefied sand mass. After earthquakes or heavy rainfall, a new valley is formed, suddenly.

It is a phenomenon similar to if a snake went out from the slope or a valley deposit went out. This phenomenon is called as Snake-off or Valley-off in Japan (Fig. 5).

Type IV: Sliding-Surface-Liquefaction

This type of landslide occurs without having loose structure of sands. The soils in the shear zone must be saturated, and the soil grains can be crushed during shearing under the given overburden pressure. Strong grains can be crushed during shearing at a greater overburden pressure. This type of landslides occurs in deep slopes as well as shallow slopes. The effective stress will move during rainfalls or/and earthquakes from the initial stress point to the failure line at

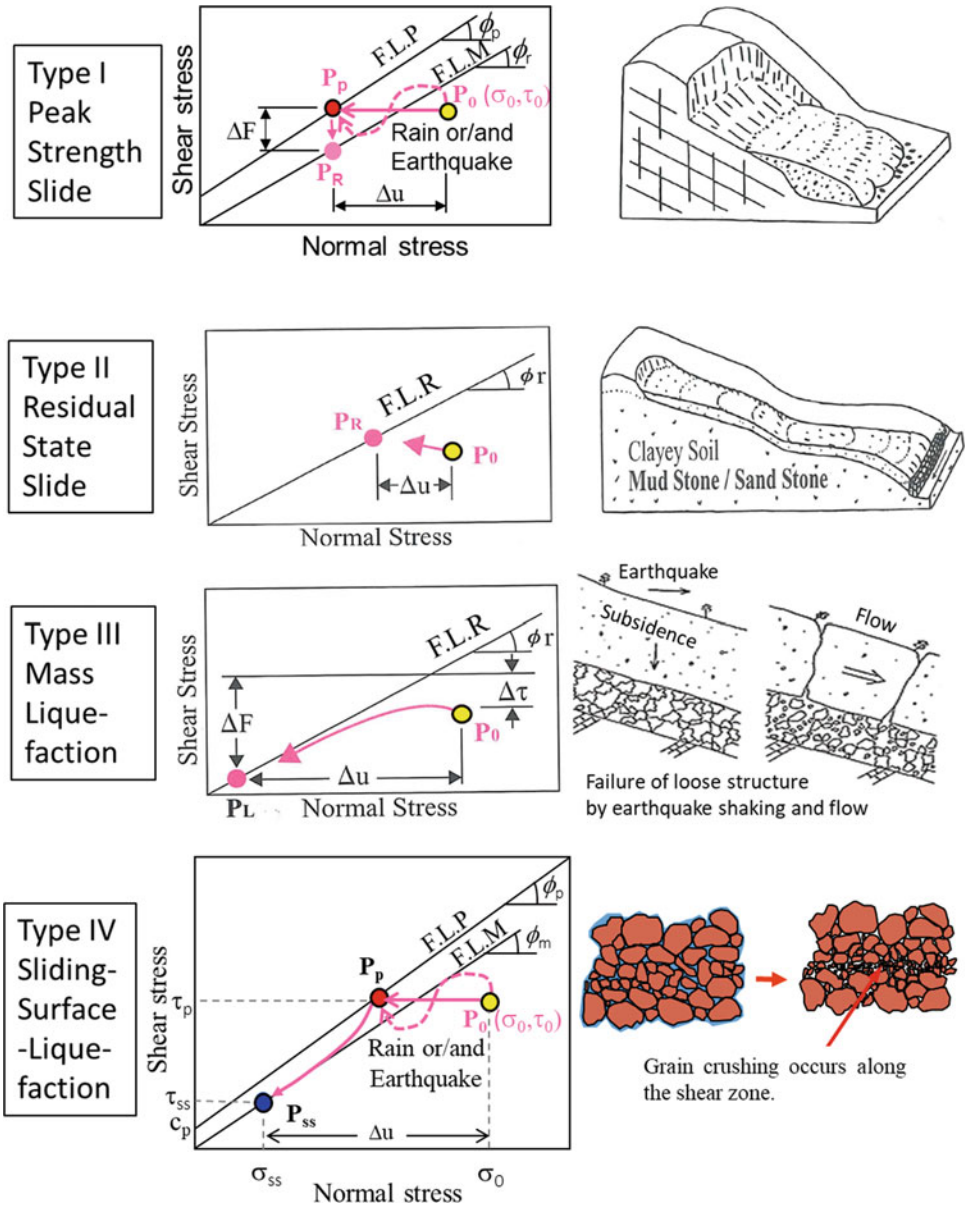

Fig. 5 Shearing types of Landslides. *F.L.P* failure line at peak strength, *F.L.M* failure line during motion, *F.L.R* failure line at residual state

peak. Failure occurs when the stress point reaches the failure line at peak. When sand/gravel grains are subjected to grain-crushing by shearing, volume reduction of the sand/gravel grains should occur. If the soil layer is saturated, a high-pore-water pressure is generated. Namely the sliding-surface liquefaction occurs in the shear zone. Thereafter the soil layer above the liquified sliding surface will move rapidly. During this rapid motion of landslides, sometimes the soil layer is kept with standing stress; sometimes the whole mass is liquefied by shaking during the motion or collision to Sabo dams (check dams), natural steps, sharp curves, or sharp change of the width of the valley route and others. When the whole moving mass is liquefied, it is called debris flow.

3 Tools to Support SSL and USS

The study of the sliding-surface liquefaction (SSL) required a development of the testing apparatus to reproduce the sliding-surface liquefaction within the apparatus. The study of the undrained steady-state shear strength (USS), the key parameter controlling the post-failure motion required an apparatus to reproduce the long-range shear displacement reaching to a steady state.

To assess the landslide disaster risk due to SSL and USS, an integrated computer simulation model for the initiation and motion using the SSL and USS parameter is needed. A

difficulty of landslide simulation is how to model the transient phase from the stability analysis of the stable slope before motion to the dynamics of a moving landslide mass including solid (sand) and liquid (water).

This section devotes to the concept of a landside ring-shear simulator, development of a series of undrained dynamic-loading ring-shear apparatus and development of an integrated landslide simulation model using the landslide dynamics parameters measured or estimated by the developed undrained dynamic-loading ring-shear apparatus (UDRA).

3.1 Physical Landslide Simulator—Formation of Sliding-Surface and Post-Failure Motion

The concept for the development of the undrained dynamic-loading ring-shear apparatus is to physically re-produce the formation of sliding surface and post failure motion within an apparatus.

Image is shown in Fig. 6. Sample is taken from the shear zone in the slope and/or the shear zone which will be formed within a soil deposit by a rapid (undrained) loading due to the moving landslide mass.

When the landslide mass initiated from the steep slope reaches onto an alluvial deposit, saturated at a certain depth, a high-water pressure will be generated within the ground water level, and a soil layer will be sheared. To estimate the landslide dynamics, parameters of landslide dynamics are measured by reproducing this process.

Samples taken from the landslide sites (potential sliding surface) are set up in the ring-shear box. They are saturated and consolidated under the in-situ overburden pressure. Then, normal stress, shear stress and pore-water pressure in the site are loaded on the sample.

- To investigate rain-induced landslides, porewater pressure is increased to reproduce the initiation of sliding surface and post failure motion of the rain-induced landslides.
- To investigate earthquake-induced landslides, seismic stresses are loaded on the initial stresses before landslides.
- To investigate landslides triggered by an earthquake after rainfalls (typical example is the 2006 Leyte landslide in Philippines), initially the pore pressure within the shear box is increased, seismic stress due to earthquake is loaded on the sample within the shear box, and the resulting behavior (mobilized shear stress on the sliding surface, generated pore water pressure near the shear zone, post-failure motion-shear displacement) are monitored.

Landslide velocity after failure is important for the study. The landslide velocity is controlled by pore-water pressure generated in the shear zone. The key element to physically reproduce the post-failure motion is how to reproduce the pore pressure in the shear zone, and how to monitor the generated pore pressure under moving rings. The objectives of developing the undrained dynamic-loading ring shear test

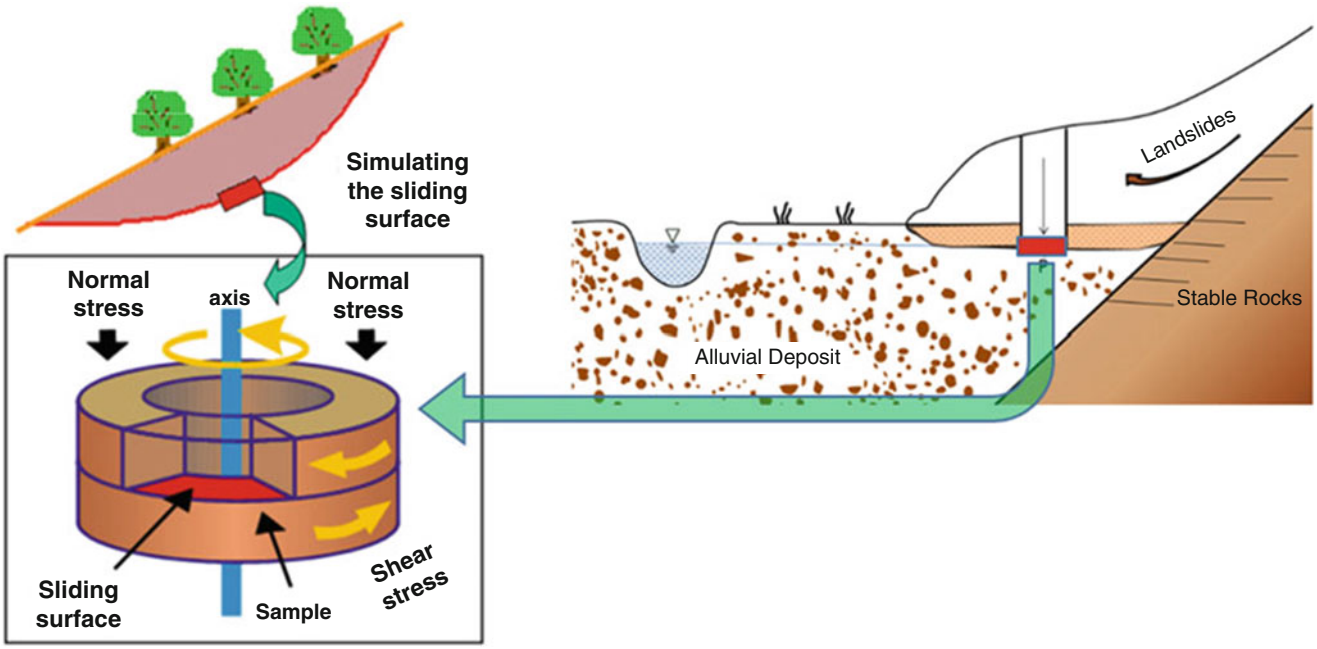

Fig. 6 Concept of Landslide Ring-shear Simulator

were how to keep undrained state of the ring shear box in a better way and how to monitor the pore-pressure near the shear zone.

The undrained dynamic-loading ring-shear apparatus was successfully developed. The undrained ring-shear testing reproduces the sliding-surface liquefaction and the steady-state shear strength which are the results of undrained shearing, pore-water pressure generation by grain crushing, which are not always understood. It is very important to coin the term "sliding surface liquefaction", the key of rapid and fatal landslides; then, developing the apparatus in DPRI, Kyoto University. Sassa et al. (2004) developed the undrained transparent shear box for DPRI-7 model, focusing on demonstration to the community.

DPRI-7 has a normal stainless-steal shear box for research and a transparent shear box for demonstrating to the community. Let us show the test result of a transparent shear box using Fig. 7 and the video on the initiation, failure, acceleration and steady state motion. It is a visual example to present the capability and performance of the undrained dynamic loading ring-shear apparatus.

Photo (a) of Fig. 7 shows the transparent shear box. A stainless-steel metal edge is attached at the bottom of the upper shear box. A rubber edge is attached on the top of the lower shear box. To keep undrained condition, two metal edges and rubber edges must be parallel, both the inside and the outside shear boxes in the lower shear boxes as well as the upper shear boxes. To ensure this condition, the rubber edge attached to the inner and the outer shear boxes of the lower shear box was processed by the lathe. The distance of the upper shear box and the lower shear box is always adjusted by the servo-control piston with precise monitoring of the distance by a gap sensor (GS) with a precision of 1/1000 mm. The plastic shear box is easily deformed by temperature change. We could not successfully perform the undrained test of transparent shear box for many times. It is not the practical test.

Used sample was silica sand No.1. It is coarse sand, and easy to observe grains and the grain crushing. Test was shear speed control test. Shear speed was increased from 0 cm/s to 200 cm/s for 5 s. It was programmed to stop shearing when the shear displacement reaches 30 m. The normal stress was kept constant at 200 kPa.

Photo (b) presents the motion of lower shear box. The grains along the shear zone are crushed due to shearing under 200 kPa normal stress. Photo (c) presents muddy water going upward and downward due to high pore-water pressure. Photo (d) presents steady state shearing.

Monitored data during the test are shown in the right column.

(a) Present time series data of normal stress in the black color, and shear stress mobilized at the shear surface in the red color, and the pore water pressure in the blue color.
(b) The shear displacement is shown in the black color and the shearing speed is shown in the red color.

Comparing two figures (a) and (b), the peak shear strength appeared at the 0.154 cm shear displacement, whereas 0.154 shear displacement is not visible in Fig. (b). The servo-control normal stress is not kept this instant at failure (a). At around 10 cm shear displacement, pore-water pressure suddenly stated to increase which should be the result of grain crushing and volume reduction in the shear zone. Excess pore-water pressure is generated and increased at 10 cm to 1000 cm shear displacement. Then, the value of pore-water pressure became constant, namely steady-state of shearing was created and continued until the end of the test (3000 cm). (c) in the right column presents the stress path of this test.

When the shear displacement is started, the shear stress is jumped to the failure line at peak at 0.154 cm shear displacement. The stress path drops to the failure line during motion at 1 cm shear displacement. Thereafter, the stress point goes down along the failure line during motion; then stops at 3000 cm shear displacement. The apparent friction angle at the final value was 3.3 degrees. It is very small compared to the peak friction angle and the friction angle during motion. A rapid landslide occurs and the movement continues until 3.3-degree slope.

Figure 8 presents the grain size distribution. The black line shows that of the original sample, namely sample before shearing. The red line presents the grain size distribution in the lower shear box. The finer grains increased because the finer grains produced in shear zone are falling in the lower shear box as seen in (c) and (d).

Please click the link to Video. You can observe this process from (a) to (d), and 200 cm/s speed undrained shearing.

3.2 Development of Undrained Dynamic-Loading Ring-Shear Apparatus

The development of untrained dynamic-loading ring shear test was aimed on how to better keep undrained state of the ring shear box and how to monitor the pore pressure near the shear zone (Table 2).

3.2.1 An Overview of a Series of the Undrained Dynamic-Loading Ring-Shear Apparatus in the Chronological Order

1. *Preparation stage*: **DPRI-1** before the undrained condition

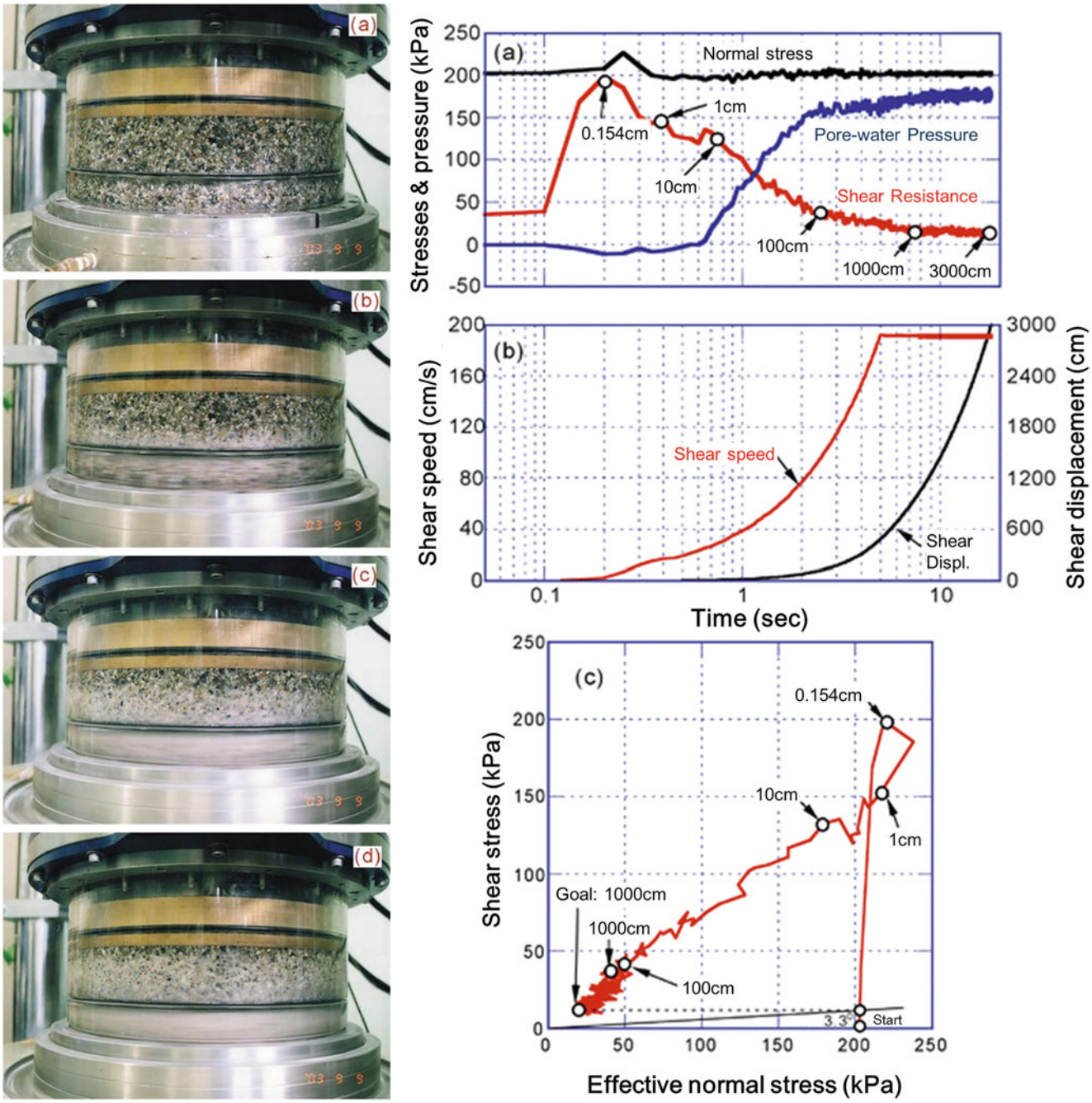

Fig. 7 Test result of undrained speed control shear test by DPRI-7 (Sassa et al. 2004). Sample: Silica sand No.1, Normal stress: 200 kPa, Maximum shear displacement: 30 m, Speed control: 0–200 m/s within 0–5 s. Video link: https://us06web.zoom.us/rec/share/DQdfHQhL-F6QhvAJvAe8GUERe%2D%2DIdXdGpfpYA8djeMjTq1-WtsuwvFzGmWo3i5At.8E-DdvJWe1KVIt_X

K. Sassa developed the first ring shear apparatus (termed as DPRI-1). It was reported in Sassa (1984) in 4th ISL in Toronto, Canada and Sassa (1988) in 5th ISL in Lausanne. The outline features are presented below.

- Aim: to reproduce debris-flow motion under a certain normal stress within a rotational channel.
- Target: Debris flows frequently occurred in Volcano Usu, Volcano Sakurajima and others in Japan
- Shear box: 300–480 mm in diameter and transparent acrylic shear box for eye-monitoring flow of debris

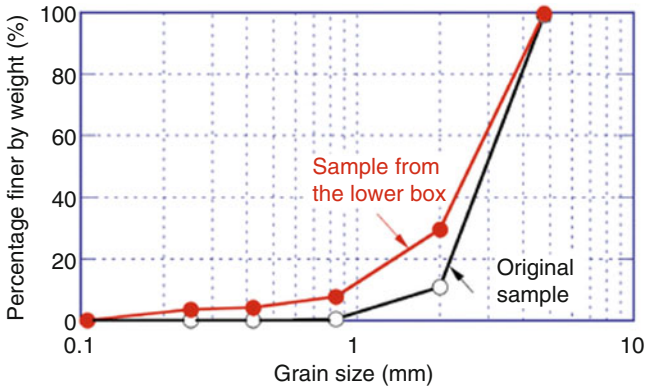

Fig. 8 Grain size distribution of the original sample (Silica sand No.1) before shearing, and the sample taken from the lower shear box (fine crushed particles fell down from the shear zone to the lower shear box)

- Maximum normal stress: 40 kPa
- Loading system: Rubber tube by air compressor and regulator which was installed between the loading plate and the top cap of the upper shear box
- Loading system: Speed-control motor
- Maximum shear speed in the center of shear box: 100 cm/s
- Gap control system: Manual gap control by measuring the position change of the upper loading plate
- Sealing of sample leakage: Silicon rubber
- Undrained condition: Not possible. No pore pressure monitoring.

2. *Transient stage:* **DPRI-3** from drained ring-shear apparatus to the undrained ring-shear apparatus. It was reported in Sassa et al. (1992) in 6th ISL in Christchurch, and in Sassa (1996) in 7th ISL in Trondheim.

- Aim: to reproduce earthquake-induced landslides.
- Target: Ontake landslide triggered by the 1984 Naganoken-Seibu earthquake in Japan.
- Maximum normal stress: 500 kPa
- Loading system: Loading piston with air servo-valve, compressor and loading frame to support piston
- Monitoring: two load cells, one for loading pressure, another for side friction within the shear box
- Shear box: 210–310 mm in size with a transparent acrylic outer ring
- Loading system: Stress-control and speed-control motor
- Maximum shear speed in the center of shear box: 37 cm/s
- Gap control, undrained condition, and pore-pressure monitoring
- Sealing of water leakage: Polychloroprene (®Neoprene) rubber edge attached on the lower ring (Rubber hardness Index, 45_JIS)
- Gap control: Servo-gap control system by measuring the position change of the upper loading plate and adjusting by servo-motor
- Undrained condition and pore-water pressure monitoring: It was improved from 6th ISL in Christchurch, 1992 to 7th ISL in Trondheim,1994 Successful undrained condition: 400 kPa
- Pore pressure was monitored by a needle inserted close to the shear zone in 1992. It was monitored from the gutter (4 _ 4 mm) along the whole circumference of the upper-outer shear box 2 mm above the gap in 1994
- Major reports: Sassa et al. (1992) in 6th ISL and 7th ICL in 1996

3. *Undrained ring-shear apparatus:* **DPRI-6.** It was reported in Sassa et al., Vol.1, No.1 of *Landslides* in 2004.

1995 Hyogo-ken Nanbu earthquake caused a big disaster in Kobe, Japan. It occurred in very dry season. In the condition of no rainfall, a rapid landslide triggered in the densely populated urban area killed 34 people. We received a budget to study earthquake-induced landslides. Then, DPRI-5 and DPRI-6 was developed. The size of shear box is different. But other features are similar.

- Aim: to develop landslide ring-shear simulator for earthquake-induced landslides.
- Maximum normal stress: designed for 3000 kPa. However, normal stress servo-control system does not function

Table 2 A series of dynamic-loading ring-shear apparatuses developed by Sassa and colleagues

Features and parameters	DPRI-3 (1992)	DPRI-4 (1996)	DPRI-5 (1997)	DPRI-6 (1997)	DPRI-7 (2004)	ICL-1 (2011)	ICL-2 (2012)	ICL-2CS (2021)
Inner diameter (cm)	21.0	21.0	12.0	25.0	27.0	10.0	10	10
Outer diameter (cm)	31.0	29.0	18.0	35.0	35.0	14.0	14.2	14.2
Max. height of sample (cm)	9.0	9.5	11.5	15.0	11.5	5.2	5.2	5.2
Shear area (cm^2)	408.41	314.16	141.37	471.24	389.56	75.36	79.79	79.79
Max. normal stress (kPa)	500	3000	2000	3000	500	1000	3000	1000
Max. pore pressure (kPa)	N/A	490	400–600	400–600	400–600	1000	3000	1000
Max. shear speed (cm/s)	30.0	18.0	10.0	224	300	5.4	50	50

well. Tests were conducted upto 750 kPa by changing the normal stress load cell.
- Normal stress loading system: Loading piston by oil servo-valve and oil-pressure pump and loading frame to support piston
- Monitoring: two load cells: one for loading pressure, the other for side friction within the shear box
- Shear box: 250–350 mm in size with non-transparent outer and inner rings of stainless steel. Maximum shear speed in the center of shear box: 224 cm/s
- Rubber edge in the gap: Polychloroprene rubber with Rubber hardness Index, 45_ JIS
- Gap control: Piston with oil servo-valve and oil pressure pump by measuring the position change of the upper loading plate. To observe the effect of extension of central axis, a displacement guide was installed within the central axis
- Successful undrained condition: 550 kPa
- Pore pressure is monitored along the entire circumference of the upper-outer shear box 2 mm above the gap (same with DPRI-3)

4. *Undrained dynamic-loading apparatus for megaslide (3 mega pascal)*: **ICL-2.** It was reported by Sassa et al. in Vol.11, No.5 of Landslides in 2014, and Sassa & Dang in Landslide Dynamics, 2018.

- Aim: to develop a landslide ring-shear simulator for mega-slides (3 MPa normal stress) and able to be maintained in a developing country
- Targets: 1792 Unzen Mayuyama landslide killing 14,528 people
- Maximum normal stress: 3 MPa
- Normal-stress loading system: Loading piston by oil servo-valve and oil pressure pump which is retained by the central axis (no loading frame)
- Monitoring: One load cell with automatic side-friction canceling
- Shear box: 100–142 mm in diameter with non-transparent outer and inner rings of stainless steel
- Shear speed in the center of shear box: up to 50 cm/s
- Rubber edge in the gap: Polychloroprene rubber with Rubber hardness Index, 90_JIS
- Gap control: Mechanical jack driven by a servo-control motor with feed-back signal of gap sensor for the position change of the upper loading plate. (To avoid the effect of extension of central axis, a displacement guide is installed within the central axis). Successful undrained condition: 3 MPa
- Pore pressure is monitored through three-layer metal and felt cloth filter along the whole circumference of the upper-outer shear box 2 mm above the gap.

5. *ICL-2 with a reduced loading stress (1000 kPa).*

ICL-2 apparatus is used in countries other than Japan. Most users do not need normal stress more than 1000 kPa.

ICL-2 CS is the version of reduced normal stress (1000 kPa). To protect possible damage between the bottom of the upper shear box and the lower shear box due to reducing the height of the rubber edge for long use, a Teflon holder pressed the rubber edge in ICL-2. Instead of Teflon holder, Teflon O-ring was installed in the inner ring, and it protects the contact between the bottom of the upper shear box and the top of the lower shear box. The rubber edge holder is only stainless-steel holder which supports the rubber edge from the inside to resist the horizontal force from the soil sample to the rubber edge.

ICL-2CS is a slightly modified version from ICL-2. The vertical load cell was replaced by 1/3 capacity version. And the structure of sealing rubber edge was modified.

3.2.2 Difference of Loading Structures Between DPRI-6 and ICL-2 Which Enabled the Undrained Test Under a High Normal Stress (3000 kPa)

We targeted to shear soil under 3000 kPa normal stress for DPRI-6. The mechanical structure of DPRI-6 is shown in Fig. 9.

The oil pump and the oil piston (OP1) and oil-servo valve (SV), Normal stress monitoring load cell (N1), Side-friction monitoring load cell (N2), and the oil piston (OP2) and oil-servo valve were ready. To shear samples under the high-normal stress, two torque and speed-control servo-motors (Servo Mother No.1 and No.2) are installed. However, both DPRI-5 and DPRI-6 failed to test the undrained condition at more than 400–600 kPa. Servo-control of the normal stress loading was not possible. The cause of servo-control of normal stress was the elastic deformation of the beam to support the loading normal stress, and also the elastic extension and compression of two long shafts to support the horizontal beam. The elastic response is faster than the servo-control. Vibration occurs and the gap between the upper shear box and the lower shear box is also affected. The gap is controlled to be a constant—to keep contact pressure at the rubber edge and the bottom of the upper ring shear boxes more than pore water pressure inside the sample box. When the pore-pressure generated in the sample exceeds the contact pressure, pore-water dissipates out of the sample box. Namely undrained condition is not kept.

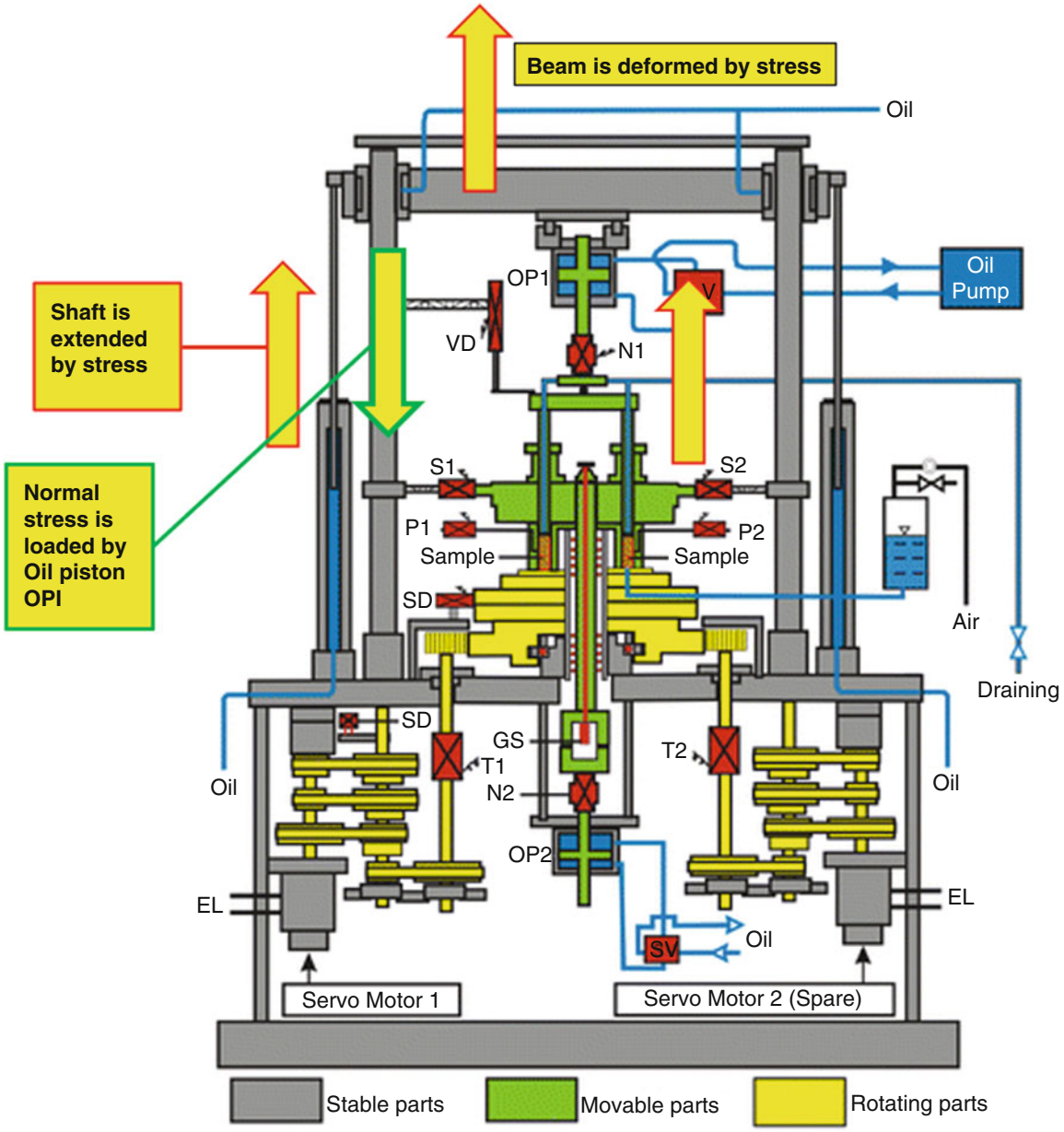

N1, N2: Load cell for normal stress; S1, S2: Load cell for shear resistance:
P1, P2: Pore-pressure transducer; GS: Gap sensor: OP1 , OP2: Oil piston:
VD: Vertical displacement transducer; SD: Shear displacement transducer:
T1, T2: Load cell for torque; EL: Electricity line.

Fig. 9 Mechanical structure of DPRI-6

In order to enable to do undrained ring shear test up to 3000 kPa, we replaced the loading frame which consisted of one horizontal beam and two vertical shafts with the central axis that is pulled by one oil piston, three vertical loading rods (two rods are seen in Fig. 10, really three rods), which gives normal stress on the sample. This system has two merits.

1. It does not include a long deformable horizontal beam and two long shafts.
2. DPRI-6 needs two load pistons and two loading cells (one for loading normal stress another for side friction in the shear box. ICL-2 needs only one piston and one load cell. Namely side friction is automatically cancelled out.
3. Instead of oil pump and oil-servo valve, the same sized another oil piston is used for normal stress control. The stress was controlled by the servo-control motor. This system is very quiet, whereas oil pumps in DPRI-3-6 were noisy.

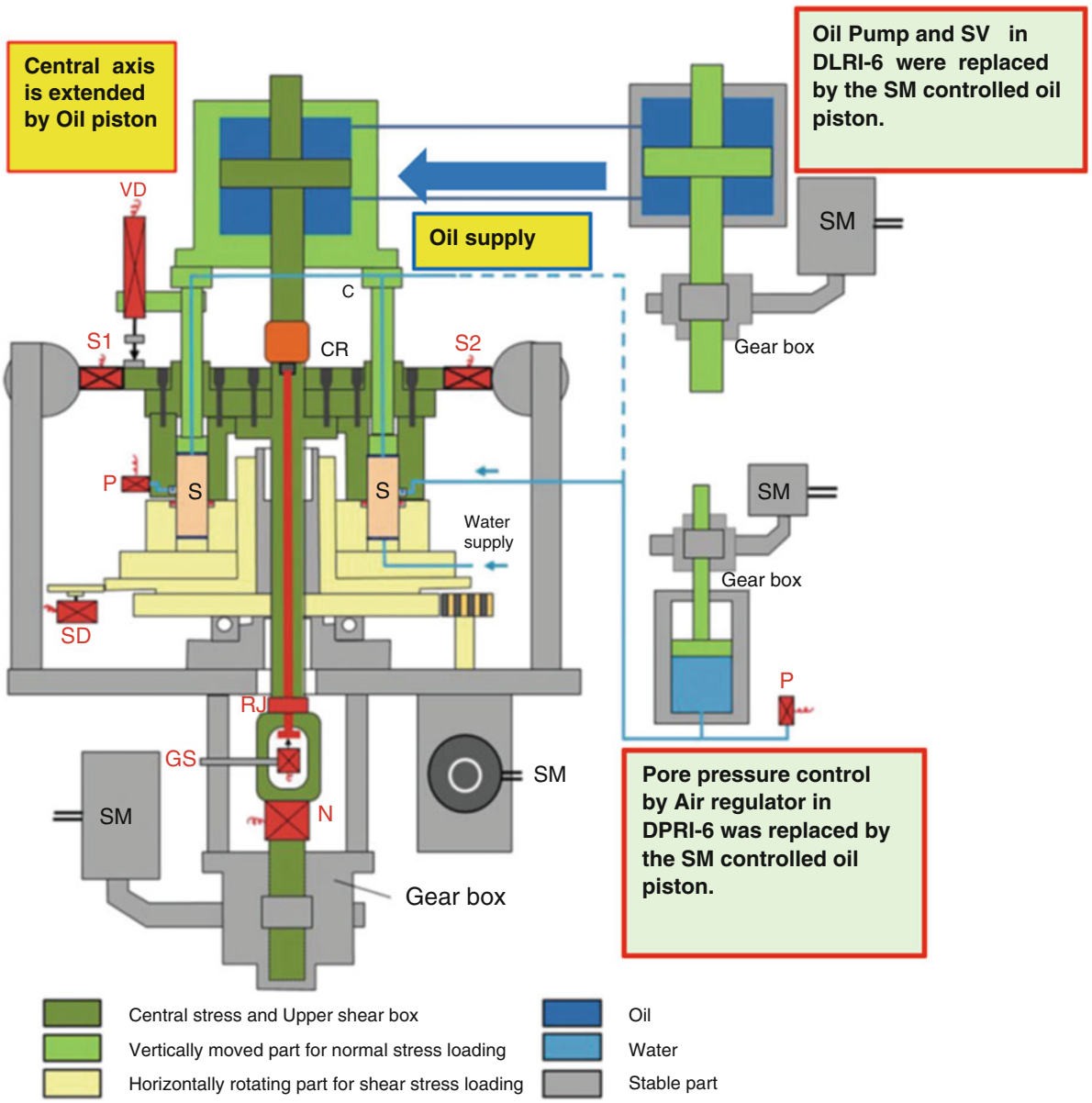

Fig. 10 Mechanical structure of ICL-2

The loading system in ICL-2 is explained by Fig. 11 (left). The normal stress working on the sliding surface gives upward force. This upward force is balanced by the downward force acting at the central axis. DPRI-6 needed two load cells (one for normal stress, another for side friction). In this system, the side friction is automatically canceled out. Then, one load cell is enough.

Rubber edge keeps contacts to the upper shear box. This contact force is necessary to keep the undrained state of the shear box. As we can see in the figure, the normal stress measured by the load cell N is the sum of the normal stresses acting on the sample and the rubber edge contact force. The real normal stress must be modified from the measured normal stress.

It was investigated in the following way. The sample was consolidated by a normal stress. Then, pore water pressure gradually increased. The water pressure when the instant of lifting of the loading plate (namely a water film or a thin water layer is formed) should be the same with the normal stress working on the shear zone. Table 3 shows the relationship between the measured normal stress, the water pressure at the instant of lifting the loading plate, and its ratio (α).

α = measured water pressure u (equal to the actual normal stress on the sliding surface)/measured stress by N. The ratio

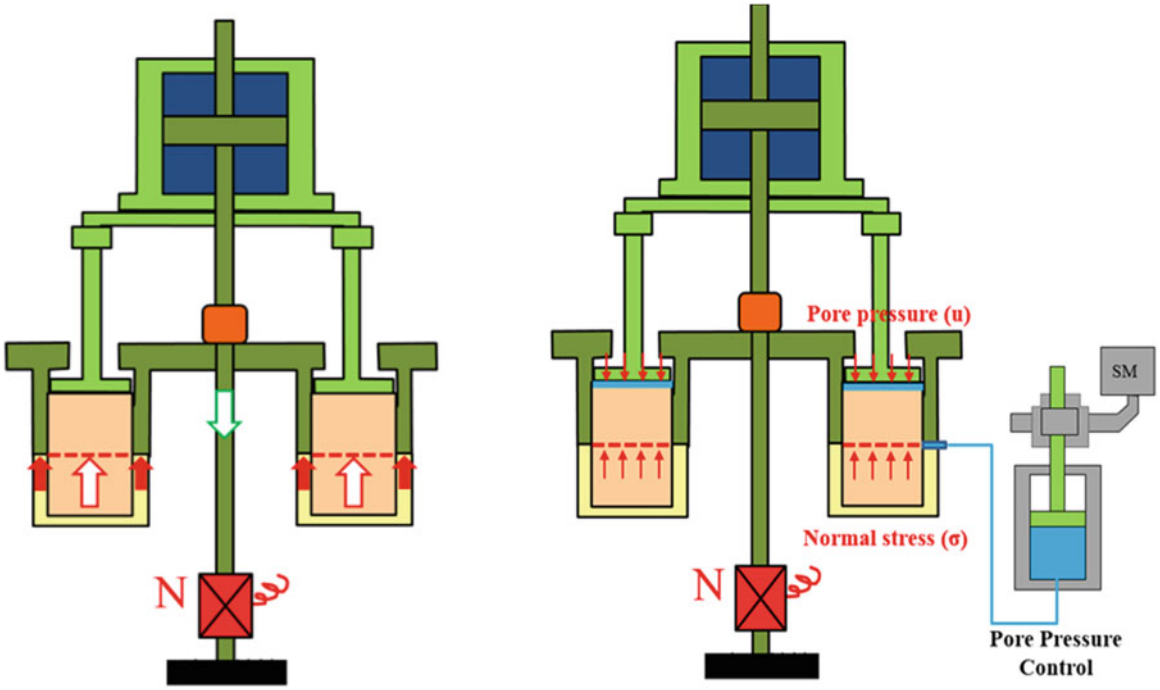

Fig. 11 Simple structure to see the forces in ICL-2 (left) and how to measure the stress working on the shear surface (right)

changes by the value of normal stress from 0.85 to 0.96. The undrained test needs the sealing rubber edge. The effect must be corrected by rubber edge correction factor (α) (Fig. 12).

3.2.3 Electronic Servo-control System of ICL-2 for Undrained State of Shearing, and Seismic-Loading Test, and Pore-Pressure Control Test

Figure 13 presents the servo-control system of ICL-2.

1. Gap servo-control: the position of the upper shear box must be controlled very precisely to keep the rubber edge contact force greater than the generated pore-pressure. The position is adjusted by the control signal (CS) from the computer through serve amp (SA). The precise location is measured by the gap sensor (1/1000 mm precision). To avoid the extension and compression of central axis, a hole is made in the center of the central axis. A narrow bar (orange color) keeps touching the gap sensor through the hole in the center of the central axis. The current precise location is informed by the servo-amp as feedback signal (FS). If CS and FS is not the same,

Table 3 Measured normal stress, the pore water pressure equal to the real normal stress, and ratio (α)

Measured normal stress (kPa)	Pore-water pressure (kPa)	α (u/σ_m)
100	96	0.960
200	182	0.910
300	268	0.893
400	352	0.880
500	437	0.874
600	520	0.867
700	606	0.866
800	689	0.861
900	769	0.854
1000	850	0.850

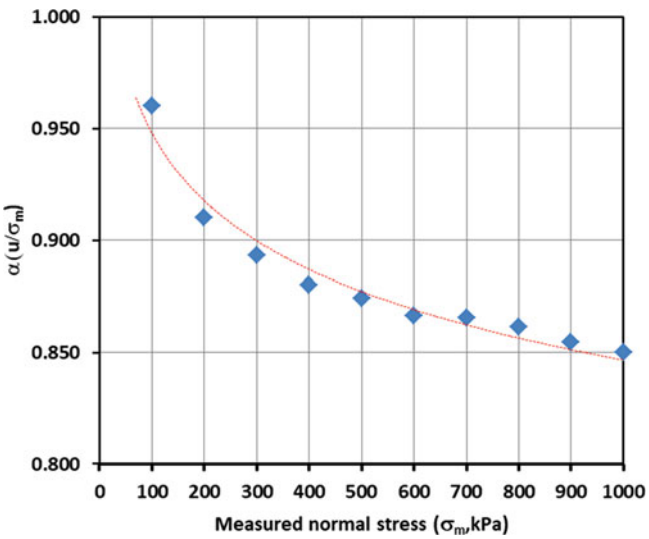

Fig. 12 Relationship between the measure normal stress and the correction factor (α). Real normal stress = α × (normal stress measured by the load cell (N))

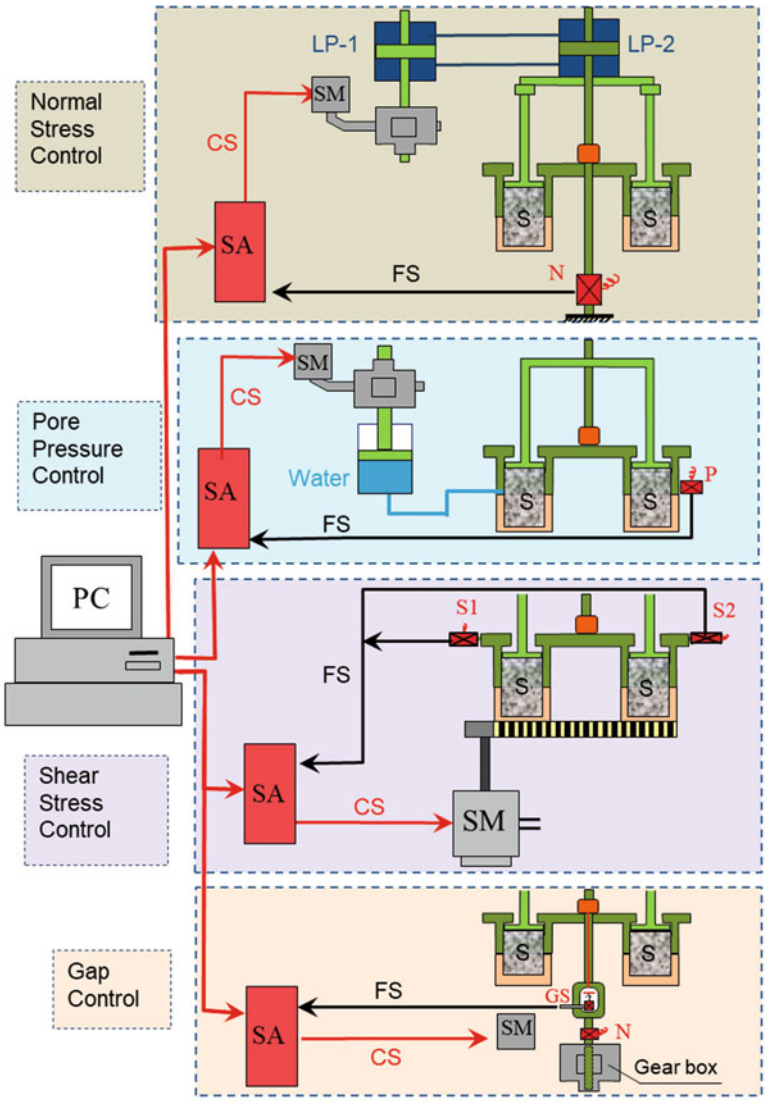

Control System of ICL-2 apparatus
PC- Computer system; S- Sample; N- Load cell for Normal Stress; S1, S2- Load cell for shear resistance; GS- Gap sensor; FS- Feedback signal; CS- Control signal; PC- Computer; SM- Servo-motor; LP- Loading Piston; SA- Servo-amplifier

Fig. 13 Electronic servo-control System of ICL-2

servo-amp sends the further CS to servo-motor to adjust the location. Then, the gap, namely the contact force of the rubber edge is kept constant even during seismic loading.

2. Shear stress servo-control: in the case of cyclic loading test or seismic loading test, the computer sends CS to shear stress loading Servo-motor. Shear stress acting on the shear surface is monitored by shear load cell (S1 and S2), and the monitored shear stress is informed to the shear stress servo-amp as the feedback signal (FS). If FS is not the same value with the CS, further modified CS will be sent until reaching CS=FS. S1 and S2 shear load cells retain the rotation of the upper shear box against the rotational force transferred from the sliding surface. Thus, the value corresponds to the shear stress acting on the shear surface.
3. Normal stress control: Control signal is sent from the computer to the servo-amp and the normal stress loading servomotor. The oil pressure is changed within the loading piston (LP-1). LP-1 pressure is transferred to LP-2. LP-2 loading is given to the sample on the shear box. Normal stress loading on the shear surface is retained by the vertical load cell (N). The value of N is sent to the servo-amp as the feedback signal (FS). If FS is not the same with CS, further CS is sent to Servo-motor and continues until the FS=CS.
4. Pore-pressure control test: to reproduce the rain-induced landslide, pore pressure is increased by the control signal from the computer to the Servo-amp and to the servo-motor to create a pore-water pressure. The increased pore pressure is monitored by a pore pressure gauge

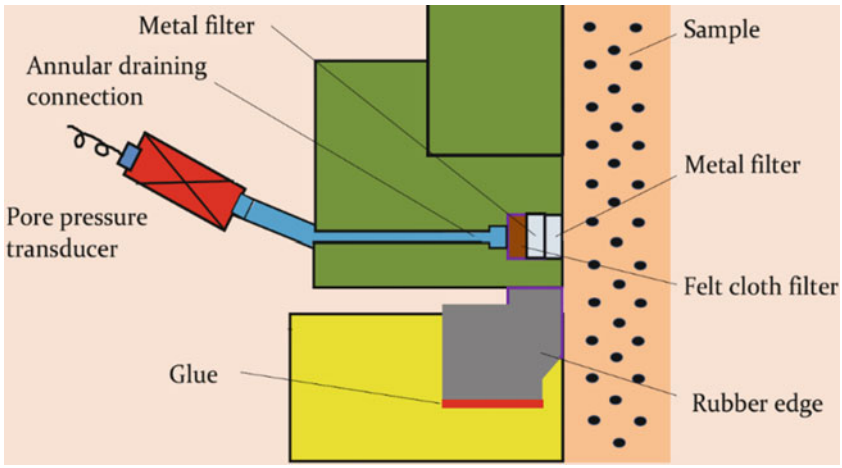

Fig. 14 DPRI-3 Final: Stair shape of the polychloroprene rubber edge (Rubber Hardness Index is 45_JIS) attached onto the lower ring.
• Successful undrained condition up to 400 kPa under 0.1 Hz cyclic test.
• Successful pore-pressure measuring through the gutter along the entire circumference in the upper ring

installed in the shear box near the sliding surface. The monitored value is sent to SA as a feedback signal. When CS-FS is different, further CS will be sent and continues until FS=CS.

3.2.4 Development of a Series of Rubber Edge Structure for Undrained Water Sealing

Water sealing and pore pressure measurement near the sliding surface have progressed from DPRI-3. Many trial types of water sealing and pore pressure monitoring were examined in DPRI-3. Figure 14 presents the most successful version DPRI-3 final. The stair shape of rubber edge was attached on the lower ring by Acryl Glue. The thickness of Acryls glue cannot be constant. Then, top surface of the rubber edges of inner ring and outer ring was processed by lathe post attachment.

The three layers filter (two metal filters and one felt cloth filter) were set in the inlet of pore water in the sample. Pore-pressure was monitored by a pore pressure transducer with a small-scale sensitive diaphragm. Water is collected through the metal filters filled in the gutter along the whole circumference in the upper ring. The lower ring of DPRI-3 was an acryl transparent shear box.

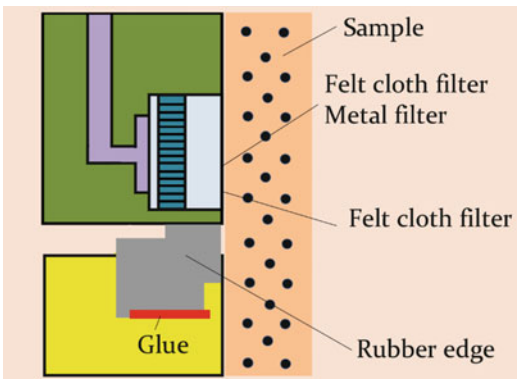

Fig. 15 DPRI-6: Stair shape of the polychloroprene rubber edge (Rubber Hardness Index is 45_JIS) attached onto the lower ring

Figure 15 presents the structure of water sealing used in DPRI-6. Basic structure was the same with DPRI-3. The shape of filters is greater to collect more water. The undrained condition is better kept for seismic loading.

After the rubber edge is attached, the upper surfaces of inner and outer rubber edges need to be processed by a lathe or file to ensure that the rubber surface is at the same height everywhere. Successful undrained condition up to 550 kPa under realistic seismic wave loading. Successful pore-pressure measuring through the gutter along the entire circumference in the upper ring.

Figure 16 presents the structure of ICL-2. Processing by lathe or file after attaching the rubber edge is troublesome. And it cannot be maintained in developing countries. In ICL-2, lath or file is not needed. Rubber edge is simply placed in the lower ring. Then, the rubber edge is pressed by Teflon holder, and the Teflon holder is pressed by stainless steel holder.

ICL2 tests soil at 3000 kPa normal stress. In this case, lateral pressure acts from the soils to the rubber edge. The force deforms/bends the rubber edge to the outside. Then, water leakage occurs. As such, support to prevent the outer deformation of the rubber edge was necessary. Then, Teflon and steel holder support the rubber edge. However, the distance between the holder and the bottom of the upper ring was very close. Therefore, rubber edge height is gradually decreased by wear during rotation. The direct contact between the stainless holder and stainless upper ring may damage the bottom of the upper ring. Teflon holder is installed between the rubber edge and stainless-steel holder to prevent this.

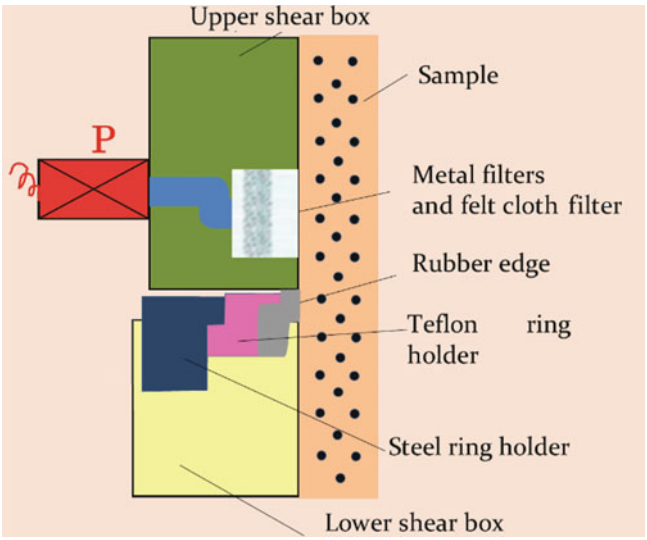

Fig. 16 ICL-2 The polychloroprene rubber edge (grey) (Rubber Hardness Index is 90_JIS) was pressed by a polytetrafluoroethylene (Teflon) ring holder (pink) which was pressed by a stainless-steel ring holder (dark blue). No glue was used. The rubber edge was simply placed and pressed. Glue to attach the rubber edge is not used. No need for the process of rubber edge surface by a lathe or file after rubber edge setting. A great progress in the maintenance of the apparatus! Successful undrained condition—up to 3000 kPa. Successful pore-pressure measurement—up to 3000 kPa

Figure 17 shows the latest rubber edge water sealing structure. The Teflon holder in the ICL-2 was replaced by the Teflon O-ring in the inner ring. It protects the direct contact between the stainless-steel holder and the upper ring. The rubber edge is supported directly by the stainless holder. It is more effective to protect the rubber edge deformation by strong lateral pressure caused by 3000 kPa normal stress.

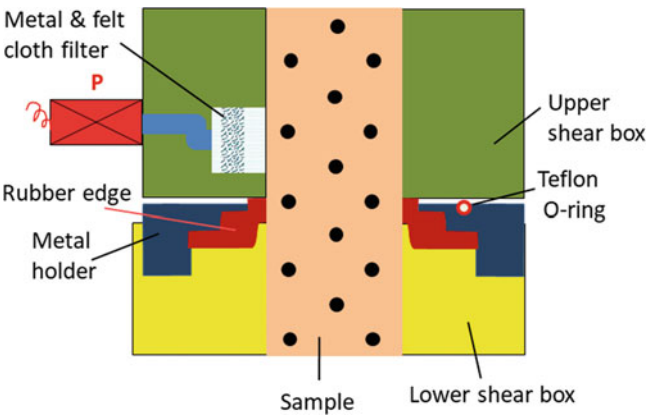

Fig. 17 ICL-2 CM. This is the latest version of sealing. To protect the damage contacting of the bottom of upper shear box to the top of the lower shear box, a Teflon O-ring (red circle) was placed in the inside part around the central axis. Then, the metal holder (without the Teflon holder) directly supports the back side of rubber edge which is pushed from sample

3.3 Development of an Integrated Landslide-Simulation Model for Rapid Landslides (LS-RAPID)

LS-RAPID is an integrated simulation model capable of capturing the entire landslide process starting from a state of stability to landslide initiation and movement to the mass deposition. This section provides an overview of the use of LS-RAPID to simulate landslide case histories around the world, provides a manual for readers to begin using the program for simulations, and describes the use of the program for several models. Detailed explanation and how to use LS-RAPID with video tutorials is published as LS-RAPID Manual with Video Tutorials in the category of Teaching Tools of Vol.1, No.1 of "*Progress in Landslide Research and Technology (P-LRT)*".

Shear resistance mobilized during motion is not as simple as static slope stability analysis, because it will be mostly determined by pore-water pressure generation in the shear zone during shearing. The undrained dynamic-loading ring-shear test can simulate various cases of landslide initiation and motion, and measure the pore-water pressure generation and resulting shear resistance mobilized at the sliding surface. However, a hazard assessment needs the areal distribution of a landslide mass. The areal distribution of the landslide mass is estimated though numerical simulation by inputting the key measured or estimated parameters obtained from the undrained dynamic-loading ring-shear apparatus.

Sassa (1988) initially proposed a numerical simulation model for the motion of landslides. However, the landslide dynamic parameters were not directly measured by the ring-shear apparatus. Sassa et al. (2010) proposed a model simulating both landslide initiation and motion within the same model using the landslide dynamics parameters measured by the well-developed undrained dynamic-loading ring-shear apparatus. A computer programming company has modified it to include user-friendly input and output systems. This version of the model is called LS-RAPID and is commercially available to any user.

The basic concept of this simulation is explained using Fig. 18. A vertical imaginary column is considered within a moving landslide mass. The forces acting on the column are (1) self-weight of column (W), (2) Seismic forces (vertical seismic force Fv, horizontal x–y direction seismic forces Fx and Fy), (3) lateral pressure acting on the side walls (P), (4) shear resistance acting on the bottom (R), (5) the normal stress acting on the bottom (N) given from the stable ground as a reaction of normal component of the self-weight, (6) pore pressure acting on the bottom (U).

The landslide mass (m) will be accelerated by an acceleration (a) given by the sum of these forces: driving force (Self-weight + Seismic forces) + lateral pressure + shear resistance. The relation is expressed by Eq. (1). Here, R includes the

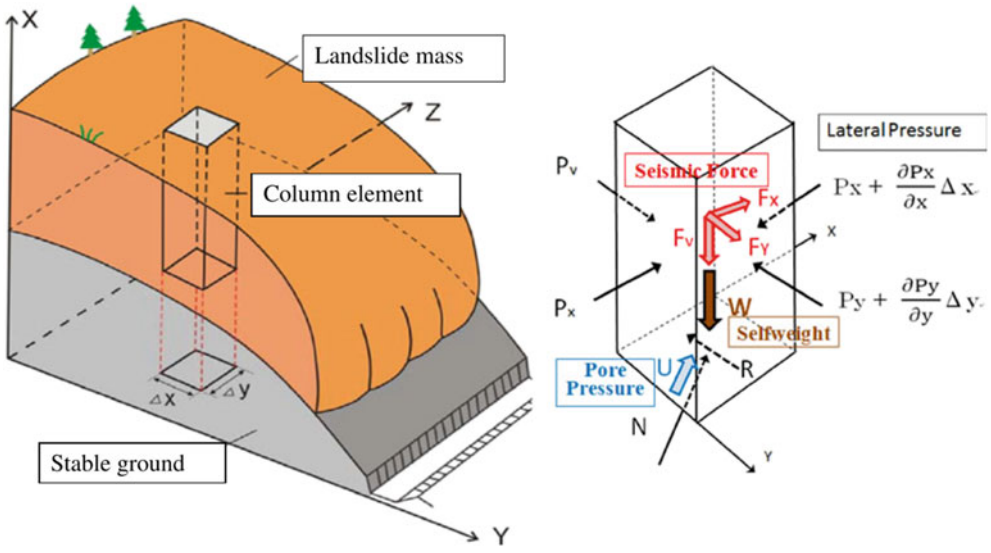

Fig. 18 Concept of LS-RAPID

effects of forces of N and U, and works in the upward direction of the maximum slope line before the motion and in the opposite direction of landslide movement during the motion.

$$am = (W + Fv + Fx + Fy) + \left(\frac{\partial P_x}{\partial x}\Delta x + \frac{\partial P_y}{\partial y}\Delta y\right) + R \quad (1)$$

Equation (1) can be expressed into x and y directions (Sassa et al. 2010) as shown in Eqs. (2) and (3). The assumption that the sum of landslide mass that flows into a column (M, N) is the same with the change or increase of height of the soil column, will give the relationship presented in Eq. (4). The used symbols and parameters in Equations are explained in Table 4. Further related explanation is referred to Sassa and Dang (2018).

$$\begin{aligned}&\frac{\partial M}{\partial t} + \frac{\partial}{\partial x}(u_o M) + \frac{\partial}{\partial y}(v_o M) \\ &\quad g\ h\left\{\frac{\tan\alpha}{q+1}(1+Kv) + Kx\ \cos^2\alpha\right\} \\ &= -(1+Kv)k\ g\ h\frac{\partial h}{\partial x} \\ &\quad - \frac{g}{(q+1)^{1/2}} \\ &\quad \cdot \frac{u_o}{\left(u_o^2 + v_o^2 + w_o^2\right)^{1/2}}\left\{h_c(q+1) + (1-r_u)h\ \tan\varphi_a\right\}\end{aligned} \quad (2)$$

Table 4 Symbols and parameters of the LS RAPID model equations

Symbol/parameters	Description
h	Height of soil column within a mesh (depth of the moving mass)
g	Gravity (acceleration)
α, β	Angles of the ground surface to x-z plain and y-z plain
uo, vo, wo	Velocity of a soil column to x, y, z directions (Velocity distribution in z direction is neglected, regarded to be a constant)
M, N	Discharge of soil per unit width in x, y directions, respectively (M = uo h, N = vo h)
k	Lateral pressure ratio (ratio of lateral pressure and vertical pressure)
tan φa	Apparent friction coefficient mobilized at the sliding surface of landslide
hc	Cohesion c expressed in the unit of height (c = ρ g hc, ρ: density of soil)
q	$\tan^2\alpha + \tan^2\beta$
wo	− (uo tan α + vo tan β)
Kv, Kx, Ky	Seismic coefficients to the vertical, x and y directions
ru	Pore pressure ratio (u/σ)

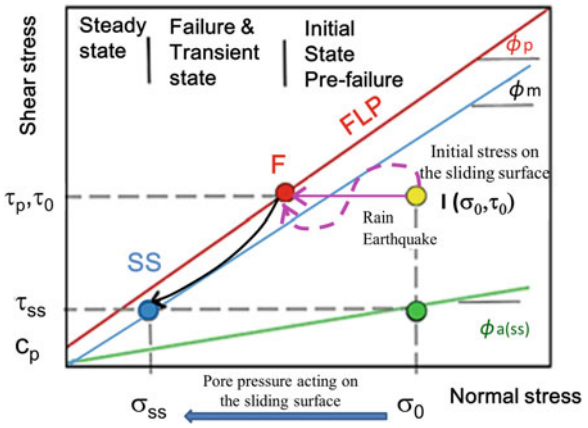

Fig. 19 Stress path from the landslide initiation to the steady state motion

$$\frac{\partial N}{\partial t}+\frac{\partial}{\partial x}(u_o N)+\frac{\partial}{\partial y}(v_o N) = g\ h\left\{\frac{\tan\beta}{q+1}(1+Kv)+Ky\ \cos^2\beta\right\} - (1+Kv)k\ g\ h\frac{\partial h}{\partial y} = -\frac{g}{(q+1)^{1/2}} \cdot \frac{v_o}{\left(u_o^2+v_o^2+w_o^2\right)^{1/2}}\{h_c(q+1)+(1-r_u)h\ \tan\varphi_a\} \tag{3}$$

$$\frac{\partial h}{\partial t}+\frac{\partial M}{\partial x}+\frac{\partial N}{\partial y}=0 \tag{4}$$

Landslide initiation is a matter of the stability analysis and the landslide motion is a matter of dynamics at a certain friction during motion. The transient state between the stability and the dynamics is most important. The initiation, the transient state, and the steady state of motion of landslides are illustrated in Fig. 19 in the stress path.

I: Initial state on the sliding surface. Rainfalls move the stress point by the increasing pore-water pressure; earthquakes move the stress point by additional seismic stress. When the stress reaches the failure line (FLP) at the peak strength state (point F), shear failure will occur. When the shearing causes the volume reduction of the soil layer, excess pore-water pressure will be generated. Then, the stress point moves to the failure line during motion. Thereafter, the stress path goes down and reach the steady state (point SS).

Figure 20 shows a series of undrained loading ring shear test results on the Osaka formation (deposits of weathered granite in Osaka area) where a rapid landslide occurred in Nikawa area of the Nishinomiya city and 34 people were killed by the 1995 Hyogo-ken Nanbu Earthquake. Seven undrained speed control tests were conducted at different normal stresses. Granit is composed of three different minerals. Granitic sands are easy to be crushed due to shearing. Stress paths of seven different tests converge to a steady state shear strength at a certain normal stress. It means that grain crushing was continued until a certain normal stress, namely normal stress at the steady state (σss). The mobilized shear stress is the steady-state shear-stress (strength) (τss). We tested many samples other than Osaka formation. Some soils at greater normal stresses can be crushed out during shearing and may not reach the same steady-state stress mobilized at a lower normal stress. In order to investigate this, a least crushable sample (a single mineral hard-sand: Silica sand) and a crushable volcanic sand were tested and described in Sect. 4.

In the case of real landslides, the initial stress is not zero shear stress. Figure 21 shows the cyclic loading test result of the Higashi Takezawa landslide triggered by the 2004 Mid-Niigata Prefecture earthquake.

Figure 21a presents the stress path, Fig. 21b presents the time series data, and Fig. 21c presents the shear stress and shear displacement relationship. Shear stress starts to decrease at DL (lower shear displacement and shear stress reaches the steady state at (DU) modelling the transient state

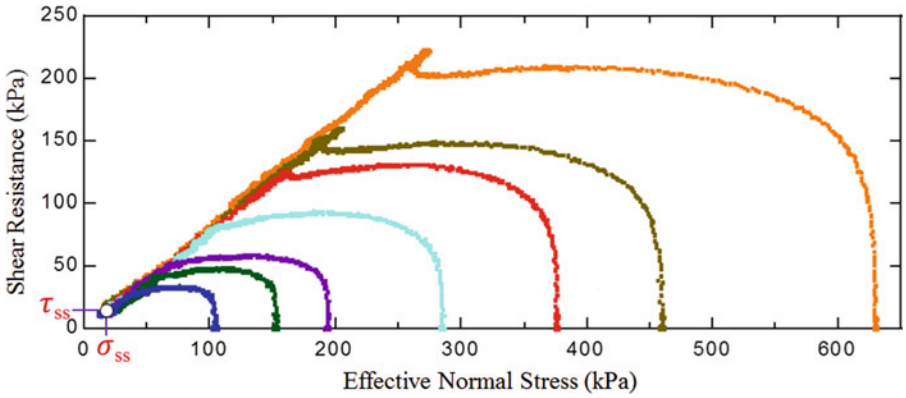

Fig. 20 Test results of undrained speed-control tests of the Osaka Formation sample (Sassa et al. 2014a, b; Okada et al. 2000)

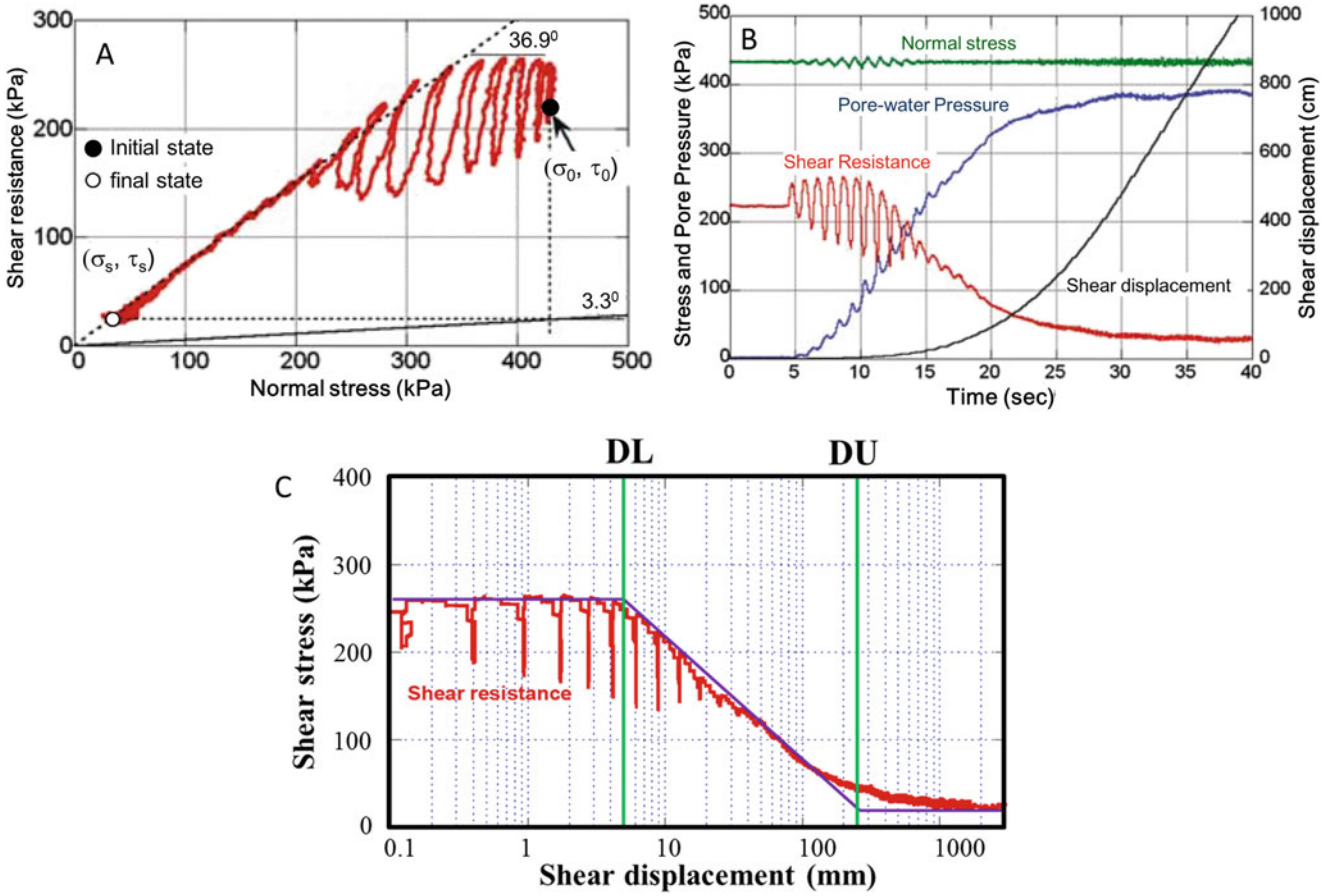

Fig. 21 Relationship of Shear stress and shear displacement in the saturated undrained shearing. Samples taken from the Higashi-Takezawa landslide triggered by the 2004 Mid-Niigata Prefecture earthquake

by a linier function. Figure 22 demonstrates another example of shear stress and shear displacement relationship. The transient state can be modeled by a liner relationship between DL (5 mm) and DU (110 mm).

Materials in Figs. 21 and 22 are different, one for tertiary sand from the Higashi-Takezawa landslide, Niigata (DL = 5 mm and DU = 110 mm), another is volcanic debris in Unzen volcano. Nagasaki (DL = 6 mm, DU = 100 mm). However, the values and shapes are similar.

Modeling of the transient state from peak to Steady state

Based on the result of Figs. 21 and 22, the transient state of sear stress is approximately expressed by the following Eq. (5).

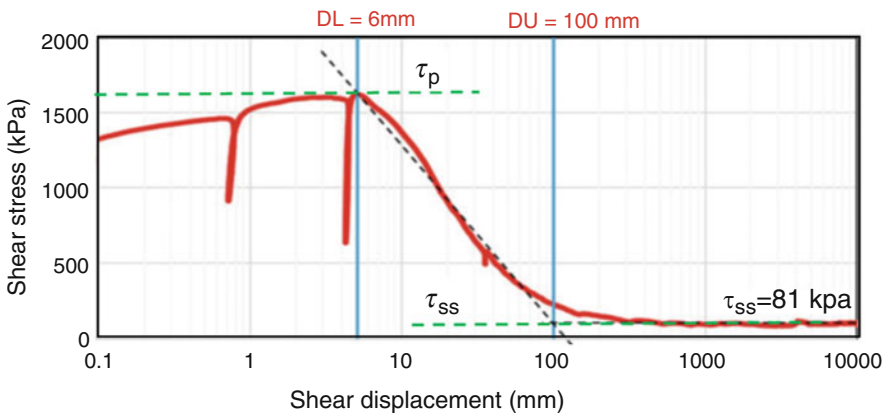

Fig. 22 Test data for the Unzen Landslide soil—modeling of the transient state from peak to the steady state

$$\tau_D = \tau_P - \frac{log\,D - log\,DL}{log\,DU - log\,DL} \cdot (\tau_p - \tau_{SS}) \qquad (5)$$

The concept of Eq. (5) is that the shear resistance (τD) at shear displacement between DL and DU is estimated by shear resistance at peak (τp) and shear resistance at steady state (τss). This is the practical and simple method.

In the past, Sassa et al. (2010) and Sassa and Dang (2018) expressed the shear resistance in the transient stage using tan φa, cohesion c and pore pressure ratio ru in the Eq. (6).

$$DL \le D \le DU :$$

$$tan\,\varphi_a = tan\,\varphi_p - \frac{log_{\,D} - log_{\,DL}}{log_{\,DU} - log_{\,DL}} \times \left(tan\,\varphi_p - tan\,\varphi_{a(ss)}\right)$$

$$c = c_p\left(1 - \frac{log_{\,D} - log_{\,DL}}{log_{\,DU} - log_{\,DL}}\right)$$

$$\gamma_u = \gamma_u \frac{log_{\,DU} - log_{\,D}}{log_{\,DU} - log_{\,DL}} \qquad (6)$$

However, τss is the steady state shear resistance obtained from the undrained ring shear test. It is not calculated by friction angle, cohesion and pore pressure ratio. Grain shape and grain size distribution can be dramatically changed by grain crushing and pore water pressure can also change. The shear stress in the transient state is not possible to be calculated from c, φ. It is reasonable to decide it based on the experiment using Eq. (5). Then, the programme was changed from (6) to (5). Concept is different, but no practical change occurred. Then, we have decided to use the relationship of Eq. (5).

Landslide depth and the apparent friction angle at the steady state

In the case of undrained steady state, shear resistance (τss) is almost constant, the excess pore pressure (Us) in deep landslides (A) is high, whereas in the medium-depth landslides (B), the excess pore pressure is moderate. Very shallow landslides (C) do not generate any excess pore pressure. The landside mobility corresponds to the apparent friction angle (φa). Here, tan (φa) = steady state shear strength/initial normal stress. Thus, in the same soil, deeper landslides show great mobility. The medium landslides show moderate mobility. Figure 23 illustrates the landslide depth and the apparent friction angle at the steady state.

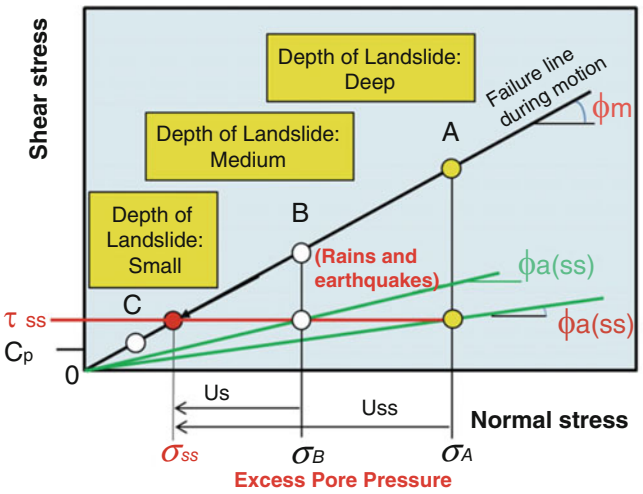

Fig. 23 Landslide depth and the apparent friction angle at the steady state

Pore pressure ratio Bss

One of key parameters of the mobility used in LS-RAPID is pore pressure ratio Bss.

Figure 24 presents the relationship between the pore pressure rate (Bss) and the steady state shear resistance:

Fully saturated state Bss = 1.0 Dry state Bss = 0

Partially saturated state Bss = between 0 and 1.0

Pore pressure rate Bss is B value at the steady state. It is similar to the pore pressure parameter B value.

B-value was measured for different degrees of saturation for the 1984 Ontake debris flow study. Figure 25 presents the relationship between the B-Value and the Degree of Saturation using the Triaxial test results. The pore-pressure parameter B is 0.2 for 95% degree of saturation, 0.5 for 96–97% degree of saturation. Bss = 1.0 for the test result of fully saturated ring shear test (B = 0.95 or more). As seen in

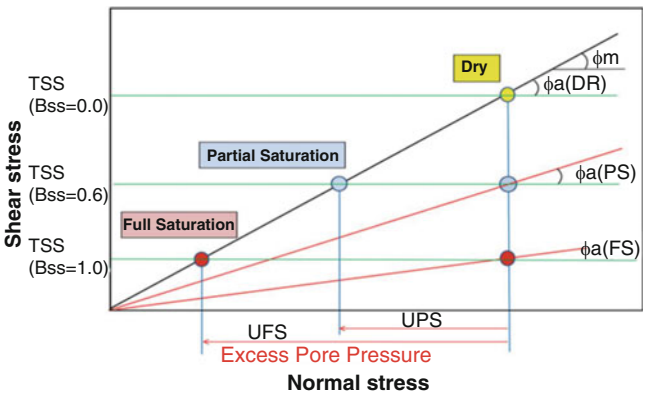

Fig. 24 Pore pressure rate (Bss) and the steady state shear resistance

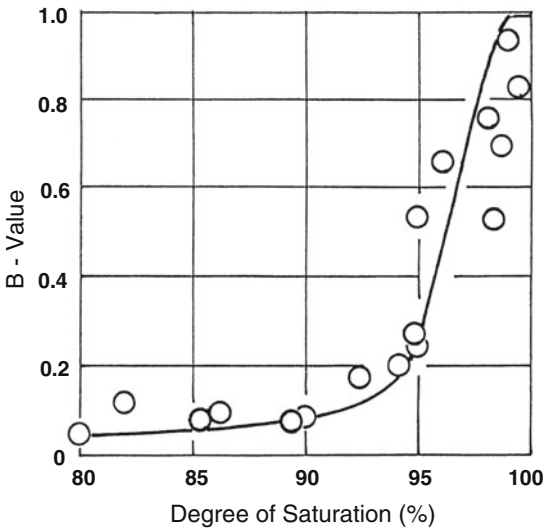

Fig. 25 Effect of saturation on the pore pressure parameter B-Value (Ratio of the generated pore pressure for confining pressure increment by the undrained triaxial test (Sassa 1988)

Fig. 25, B value higher than 0.95 could not be produced. Bss = 1.0 is around B = 0.95. During the grain crushing, water volume will not change, but void in the sand structure in the shear zone will decrease. So, the degree of saturation in the shear zone at the steady state may be increased from the initial stage before the motion.

3.3.1 Video of the Initiation and Motion of Rain-Induced Landslides and Earthquake-Induced Landslides in LS-RAPID

Figure 26 shows LS-RAPID rain-induced landslide on a simple slope. The used rainfall record is 2016 Aranayake landslide in Sri Lanka (front cover of Vol.1, No.1 of P-LRT).

Figure 27 shows LS-RAPID for an earthquake-induced landslides on a simple slope. The used earthquake record is 2008 Iwate-Miyagi Earthquake Record.

The upper figure of Fig. 26 LS-RAPID rain-induced landslide presents the instant of initial local failure at the top of a slope which is circled by a red color line (Maximum velocity at this local failure = 0.2 m/s. The whole landslide area is shown in the blue color line. The lower figure shows the landslide mass after deposition (velocity = 0 m/s).

Clicking the video link, you can see the whole movement from the initiation to motion and the deposition.

The upper figure of Fig. 27 LS-RAPID for an earthquake induced landslides presents the state when the initial landslide mass has been created by the progress of local failures such as the upper figure of Fig. 26.

Both cases can be seen by video. LS-RAPID can reproduce a local failure at a weak point in the slope. When a part moves more than DL (usually a few mm), a failure occurs. After DL, the shear resistance is reduced to the steady state shear strength. When shear resistance is reduced in a part, the adjacent elements may move more than DL. Another failure will occur. Such a progressive failure can be seen. Then, the whole landslide body is formed and starts to move as a landslide body onto the downslope. In case where the downslope layer or the layer in the flat area is saturated, the undrained loading causes the pore pressure generation within the saturated soil layer. The landslide mass moves together with a scraped soils above the shear surface. However, when downslope layer is dry or less saturated, the shear surface will be formed within the moving landslide mass which moves leaving a soil mass below the shear surface and stop shortly. Figure 28 illustrates three cases for the initiated landslide mass moving over the downslope.

3.3.2 Three Cases for the Initiated Landslide Movement over the Downslope

Sassa (1988) proposed three cases for downslope movement of a landslide mass as seen in Fig. 28.

Case A: It is the case where a landslide mass moves on a concrete channel or a bed rock. Pore-water within the landslide mass does not dissipate. The movement will continue without leaving soil or scraping soils.

Case B: It is the case where a landslide moves on a saturated soil layer (such as torrent deposit or alluvial deposit seen in Fig. 6—Concept of Landslide Ring-shear Simulator). Pore pressure is generated due to the undrained loading within the saturated deposit. In this case, a sliding surface is created within the soil layer (around ground water surface). Then, the soil layer above the sliding surface is included in the landslide mass. So, the landslide mass is increased during motion. Sometimes the landslide mass around the top of torrent is increased to 5–10 times of initial landslide mass.

Case C: It is the case which a landslide mass moves on less saturated or dry soil layer. In this case, pore water of the moving landslide mass dissipates to the dry or less saturated ground. The shear surface is formed within the moving landslide mass. Then, the landslide mass moves downslope leaving a soil mass below the sliding surface, and gradually terminates its motion and stabilize.

Bss is a very important parameter to control the motion of landslides. In the relation of Fig. 24 Pore pressure rate (Bss) and the steady state shear resistance, the value of the steady state shear resistance τ_{ss} are much affected. Bss = 0, τ_{ss} is close to the shear strength at the failure line during motion.

4 Original Test Results for This Article

During the course of writing the ICL landslide lesson on sliding-surface liquefaction (SSL) and undrained steady-state shear strength (USS), we conducted original tests

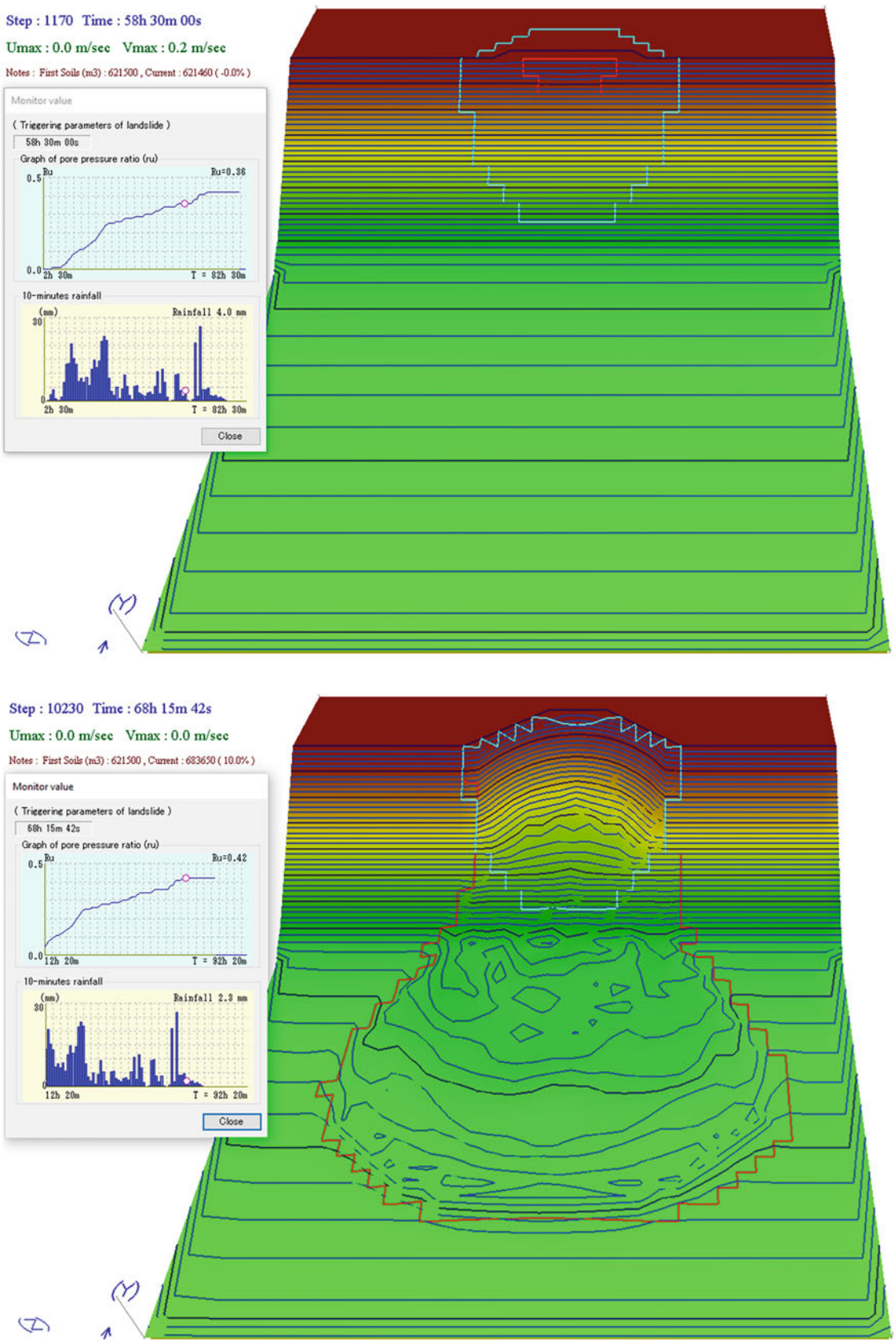

Fig. 26 LS-RAPID rain-induced landslide on a simple slope. **Video Link:** https://us06web.zoom.us/rec/play/V190Nvu9TPzmwIerczFBkGBWsewvKxJX_f_tnSFfpnZPyH5LAE9NmIkVVKsAs5RIjKDhr3xAMnwyGnWy.9ONvy5uiiohjS7qq?continueMode=true

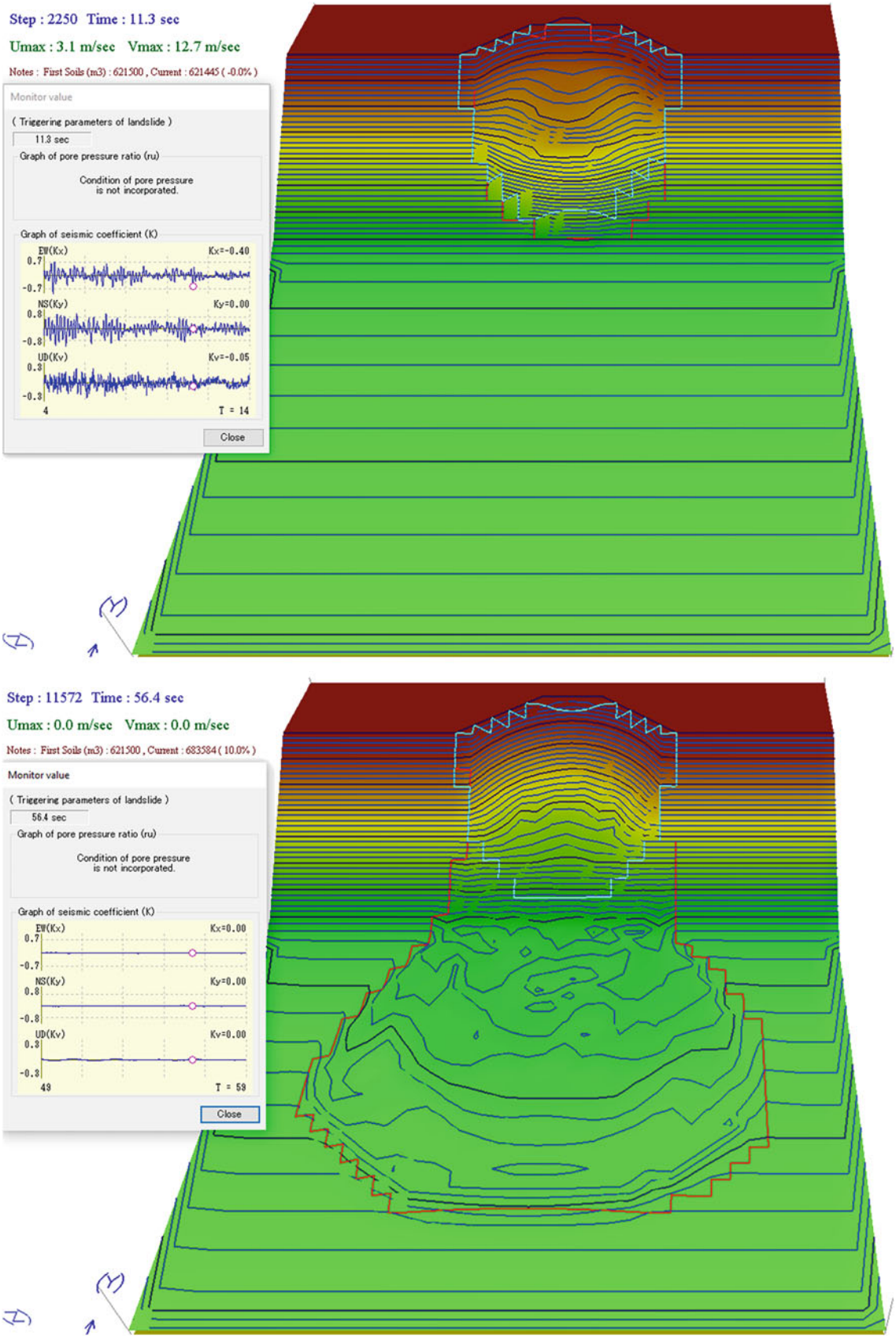

Fig. 27 LS-RAPID for an earthquake induced landslides on a Simple slope. **Video Link**: https://us06web.zoom.us/rec/share/Vjdll3lzRLHWykSmUKNJI5qsh0o90uEdRtJTeohG5X7sL1R7I0nM2RjdSAQHSOjA._40ADQ-lCyhgOimq

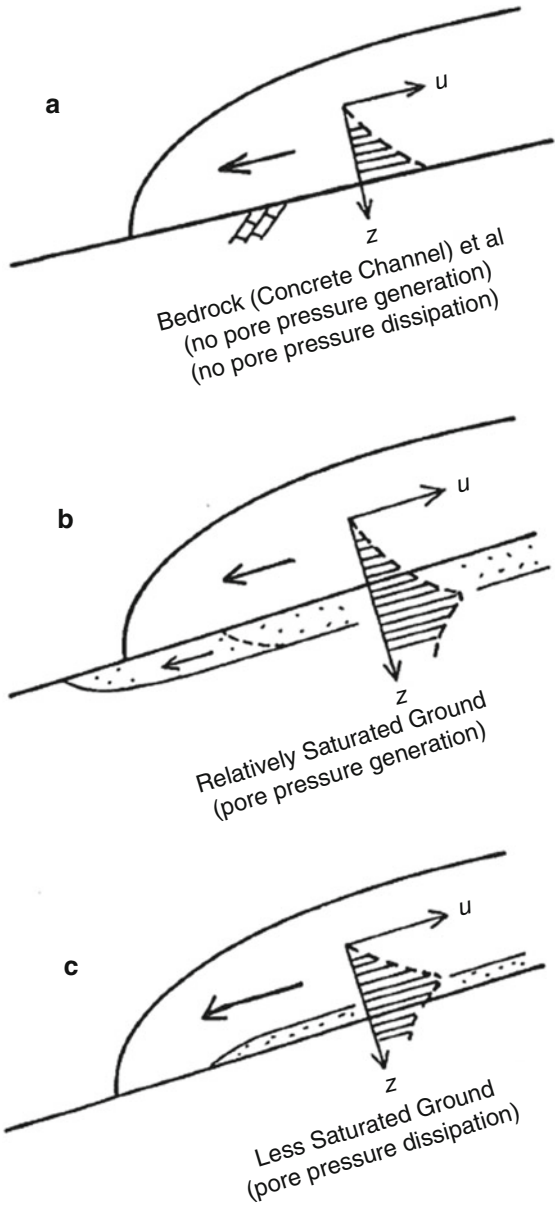

Fig. 28 Three cases for the initiated landslide movement over the downslope (Sassa 1988)

focusing on SSL and USS for one standard sand (silica sand No.6) and a natural sand causing the sliding-surface liquefaction.

As an example of natural sands, we went to the Unzen volcano and took a sample from the 1792 Unzen landslide site (around 15,000 fatalities). The 2006 Leyte landslide (around 1000 fatalities) occurred in a volcanic deposit. The grain size distributions of both samples are shown in Fig. 29. Silica sand is a hard quartz sand. The Unzen sand is volcanic andesitic fragile sand.

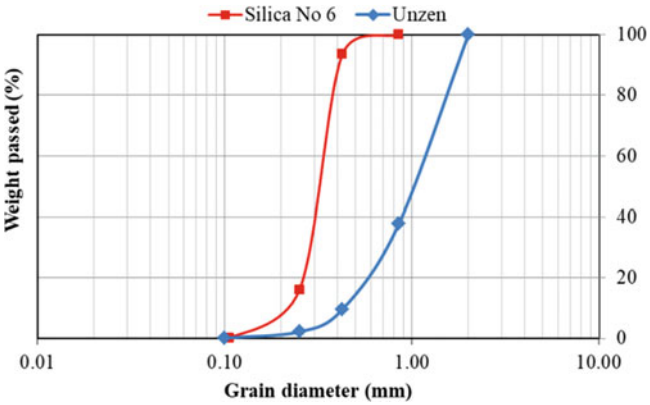

Fig. 29 Grain size Distribution of Silica sands and the Unzen sands

4.1 Experiment of Standard Sand "Silica Sand No.6"

Sliding-surface liquefaction occurs only in the undrained condition. All measured parameters are affected by pore pressure values measured in the undrained state. Under the condition of no pore-water pressure, namely in the drained state, we estimated the failure line during motion and measured the friction angle during motion of both samples.

Figure 30 presents the results of a test measuring the failure line in the drained state and the friction angle during motion. Firstly, normal stress of 1000 kPa was applied. Then, the sample was sheared at a constant speed (1 mm/s). The shear stress reached the failure line during motion. Then, normal stress was decreased to zero at the rate of 0.2 kPa/s for 5000 s.

Shear stress reached the failure line during motion due to the initial 1000 s of shearing, namely 1000 mm shearing.

Then, normal stress decreased at a rate of 0.2 kPa/s. The time series data of normal stress, shear stress, shear displacement, and pore water pressure (0) are shown in the left figure, and the stress path from the initial stress point (normal stress = 1000 kPa, and shear stress = 0) to the failure line during motion, then, gradually decreasing to zero stress. The friction angle during motion was 35.2 degrees.

Three undrained speed-control tests and two undrained stress-control tests were conducted on the Silica sand as presented in Table 5.

Figure 31 shows the test result of Test number 1 of silica sand. After saturation and consolidation at 250 kPa, a constant speed of shearing (1 mm/s) started in the undrained state. Figure 31a presents the stress path. The black line represents the stress path of the total stress. The stress point moved up until failure, then, went down to the shear stress at the steady state shear strength.

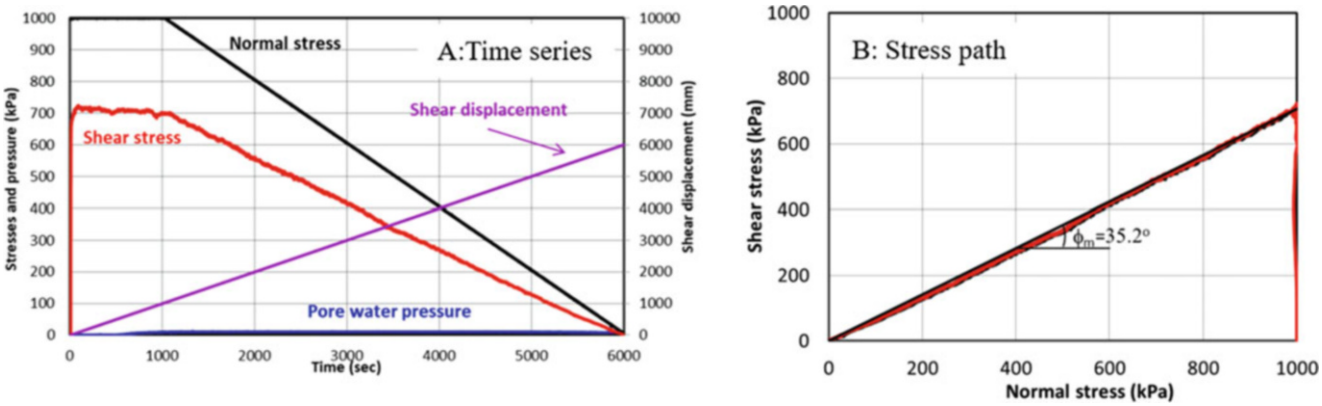

Fig. 30 Results of the saturated constant-speed drained shear test. Sample: Silica sand, Shear speed: 1 mm/s, Normal stress decreasing rate: 0.2 kPa/s. (**a**) Time series data. (**b**) Stress path data

The red line represents effective stress path. When shearing started, pore water pressure was generated with the progress of shear displacement due to volume reduction by gradual deformation of sand structure. Then, the stress point reached the failure line at peak (36.9 degrees). Once dilatancy occurred, namely the sand volume tended to increase, then the stress point moved to the right direction to the failure line at peak. Grain crushing started in the shearing zone. Excess pore pressure was generated and the stress point went down along the failure line during the motion (35.2 degrees). No further grain-crushing state, namely steady state was reached at the shear stress of 40 kPa.

Figure 31b presents the time series data of normal stress (black), shear stress (red), pore pressure measured near the shear zone (blue), and the shear displacement (purple). One can find that pore pressure generation started at the progress of shear displacement and reached its maximum value around 2000–4000 s, namely at 2–4 m shear displacement. Grains of Silica sands are very hard comparing to the Unzen volcanic sands and granitic sands. However, quartz sands were gradually crushed and caused volume reduction, and the effective normal stress working on sand grains were reduced at the progress of grain crushing. Then, grain crushing was terminated and the steady state was reached. Namely, shearing was continued without any changes in stress.

Figure 31c presents the relationship between shear stress and the shear displacement. Shear speed line is added.

This graph presents the peak strength (τp) at which shear stress reduction started, and the steady state shear strength (τss), and the shear displacement at the peak (DL), the shear displacement at the start of the steady state (DU) can be seen.

In the LS-RAPID, the experimental curve from DL to DU is replaced by a line connecting two points at DL and DU. This transient state between the peak failure point and the steady state shear state is very difficult to analyze from theoretical analysis. During the state, many factors of grain size, grain shape, the grain size distribution, and pore water pressure change. The experimental estimation based on the peak strength (τp) and the steady state shear strength (τss), shear displacement (DL and DU) and the current shear displacement (D) in the Eq. (5) are described in Sect. 3.

$$\tau_D = \tau_P - \frac{log\, D - log\, DL}{log\, DU - log\, DL} \cdot \left(\tau_p - \tau_{SS}\right) \tag{5}$$

Figure 32 (Normal stress = 500 kPa), Fig. 33 (Normal stress = 1000 kPa) show the test results of Test number 2 and the results of Test number 3 are presented in a set of three graphs, (a) Stress path, (b) Time series data, (c) Shear stress–shear displacement relationship.

Number 1 (250 kPa) and Number 2 (500 kPa) show very similar steady state shear strengths 40 kPa and 46 kPa. DL are 10 mm and 8 mm, respectively. DU are 1300 mm and 1100 mm.

Table 5 A series of tests on Silica sand

Test number	Fig. number	Normal stress	Shear mode	Shear speed	Shear stress increment
1	Fig. 31	250 kPa	Speed control	1 mm/s	
2	Fig. 32	500 kPa	Speed control	1 mm/s	
3	Fig. 33	1000 kPa	Speed control	1 mm/s	
4	Fig. 34	500 kPa	Stress control		0.5 kPa/s
5	Fig. 35	1000 kPa	Stress control		0.5 kPa/s

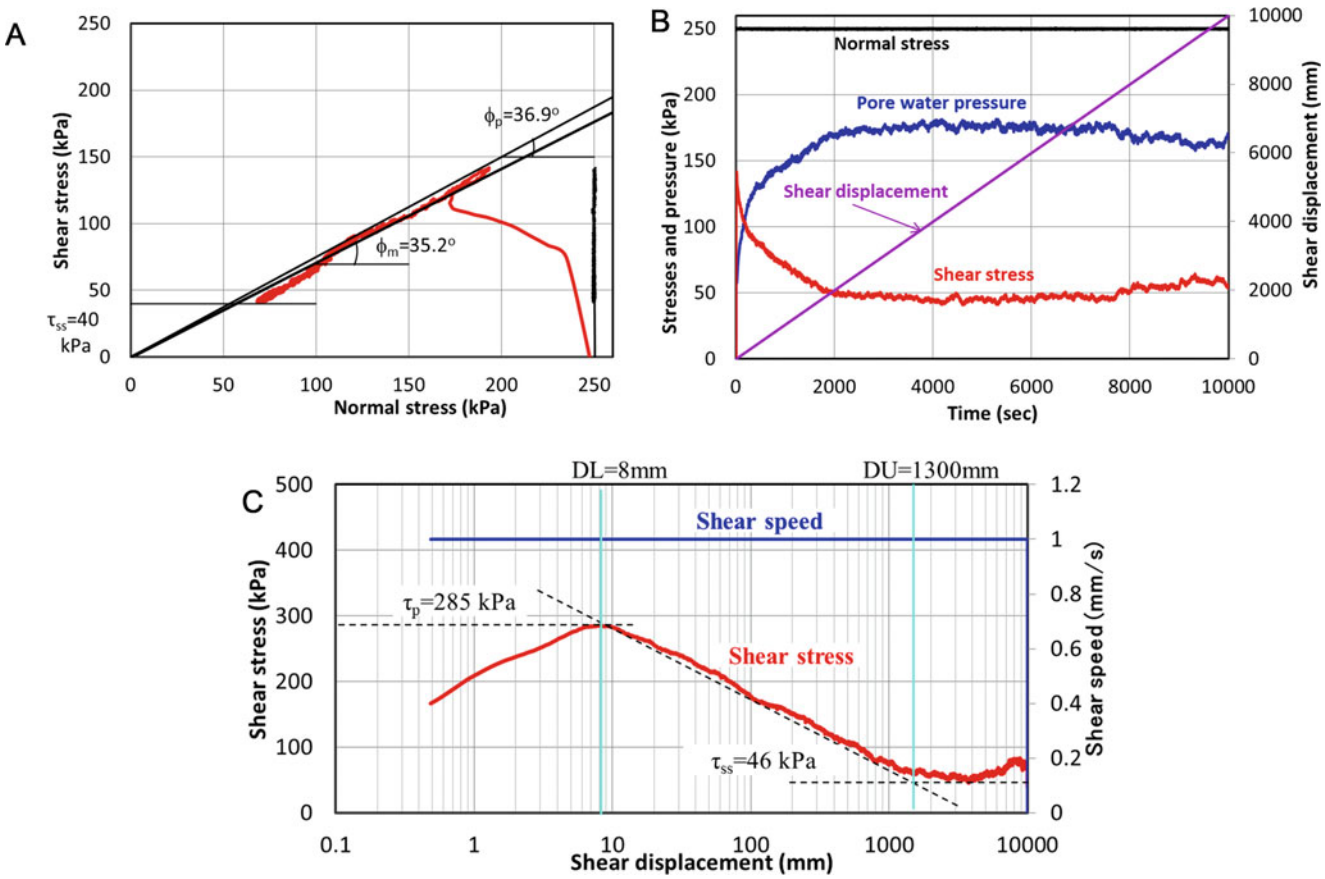

Fig. 31 Saturated and undrained speed control test for Silica sand No.6. Normal stress = 250 kPa, BD = 0.95, Shear speed = 1 mm/s. (**a**) Stress path, (**b**) Time series data, (**c**) Shear stress–shear displacement relationship

However, Test number 3 (Normal stress = 1000 kPa) showed a higher steady state shear strength (145 kPa) in Fig. 33. Probably all crushable grains crushed in this high normal stress. Figure 20 for Osaka formation presents the same steady state between 100 and 630 kPa. Stress range was less than 1000 kPa.

Figure 34 shows the test result of shear-stress control test under the normal stress (500 kPa). It uses the torque control mode of servo-motor. After saturation and consolidation, shear stress was increased at the speed of 0.5 kPa/s.

Figure 34a presents the stress path. The black line shows the stress path of the total stress. The stress point moved up until failure, then, went down to the shear stress at the steady state shear strength.

The red line shows the effective stress path. When shear stress was increased at 0.5 kPa/s, the effective stress path almost vertically moved up to the failure line at peak. Pore pressure generation is minimum until failure. After the failure at the failure line at peak (37.8 degrees), pore pressure started to increase due to the progress of grain crushing. Then, the stress path shifted to the failure line during motion, then reached the steady state (τss = 70 kPa). The friction angle of the failure line during motion was 35.2 degrees.

Figure 34b graph showed the time series data of the normal stress (black), the shear stress (red), the pore pressure (blue) and the shear displacement (purple). The shear displacement acceleratedly increased after failure. A rapid increase of the pore pressure was found at the same time of shear displacement increase.

Figure 34c graph presents the relationship between shear stress and the shear displacement. Shear speed curve (it was increased from 0 to around 120 mm/s during the test) is added. This graph presents the peak strength (τp = 375 kPa) at which shear stress reduction started, and the steady state shear strength (τss = 70 kPa), and the shear displacement at the peak (DL = 5 mm), the shear displacement at the start of the steady state (DU = 2300 mm) are well seen.

Figure 35 shows the test result of shear-stress controlled test under the normal stress (1000 kPa). After saturation and consolidation, shear stress was increased at the speed of 0.5 kPa/s.

Figure 35a presents the stress path. The black line is the stress path of the total stress. The stress point moved up until failure, then, went down to the shear stress at the steady state shear strength.

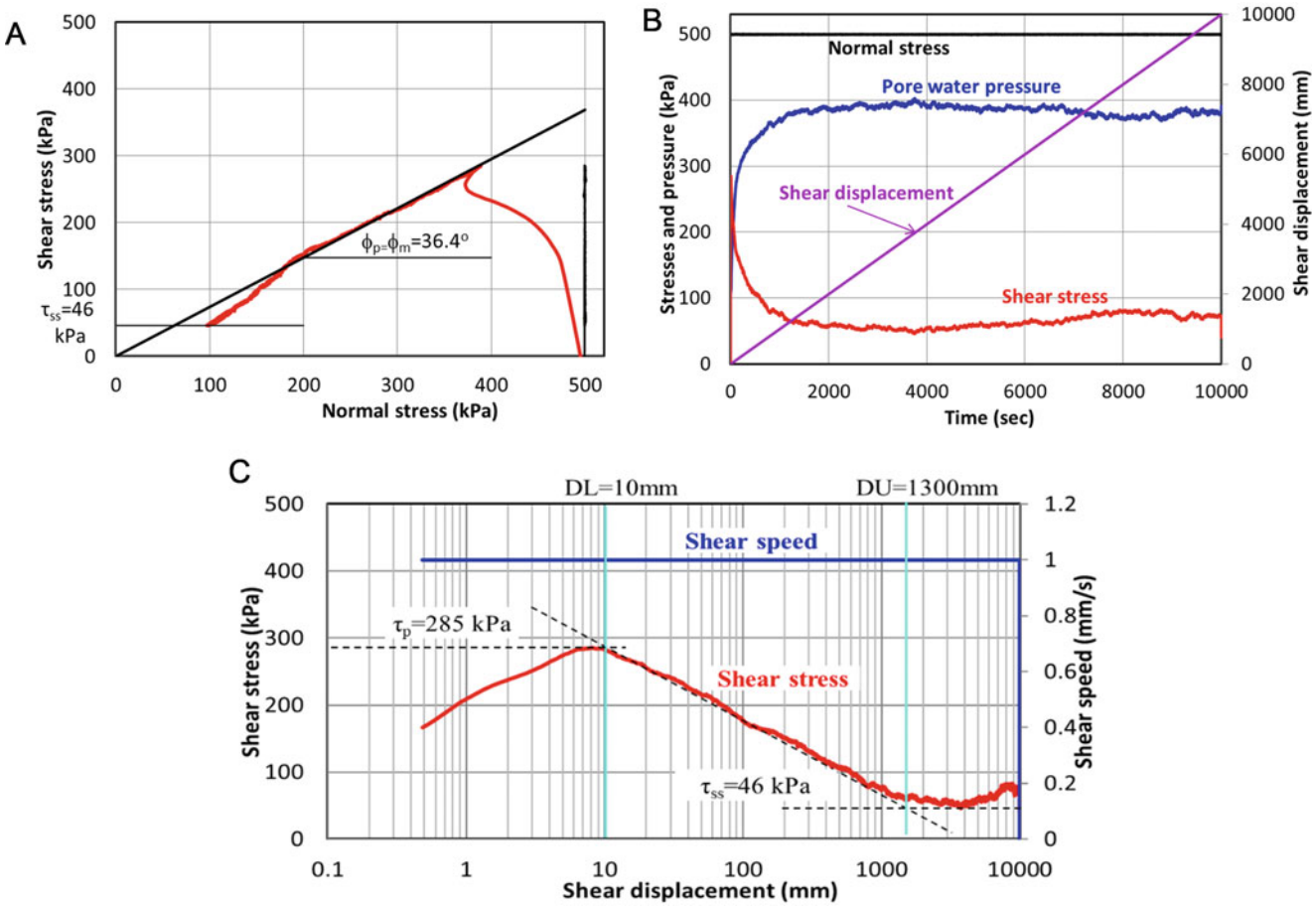

Fig. 32 Saturated and undrained speed control test for Silica sand No.6. Normal stress = 500 kPa, BD = 0.96, Shear speed = 1 mm/s. (**a**) Stress path, (**b**) Time series data, (**c**) Shear stress–shear displacement relationship

The red line shows the effective stress path. When shear stress was increased at 0.5 kPa/s, the effective stress path almost vertically moved up to the failure line at peak. Pore pressure generation is minimum until failure. After the failure at the failure line at peak and during motion (35.8 degrees). Pore pressure started to increase due to the progress of grain crushing, the stress points went down along the failure line and reached the steady state (τss = 65 kPa).

Figure 35b graph showed the time series data of the normal stress (black), the shear stress (red), the pore pressure (blue) and the shear displacement (purple). The shear displacement rapidly increased and reached 10 m. A rapid increase of the pore pressure was found at the same time of shear displacement increase.

Figure 35c graph presents the relationship between shear stress and the shear displacement. Shear speed curve (it was increased from 0 to around 150 mm/s during the test) is added. This graph presents the peak strength (τp = 655 kPa) at which shear stress reduction started, and the steady state shear strength (τss = 65 kPa), and the shear displacement at the peak was DL = 3 mm, the shear displacement at the start of the steady state was DU = 1000 mm.

The results of three shear-speed-control tests and two shear-stress-control tests are plotted in a combined stress path graph in Fig. 36. All stress paths of five tests reached the same failure line during motion at 35.0 degrees.

As explained in Fig. 30, we conducted a saturated constant-speed **Drained test** to investigate the friction angle during motion. No pore pressure existed through the whole drained test. The failure line during motion was manifested by decreasing normal stress (0.2 kPa/s) at the constant speed of shearing (1 mm/s). The friction angle during motion obtained by this test was 35.2 degrees. The value of undrained shear tests of Fig. 36 was almost the same at 35.0 degrees.

The results of three shear-speed-control tests and two shear-stress-control tests are plotted in a combined shear stress–shear displacement relationship in Fig. 37. All five DL (shear displacement which shear strength reduction started) are 3–8 mm. All four DU are 1000–2000 mm.

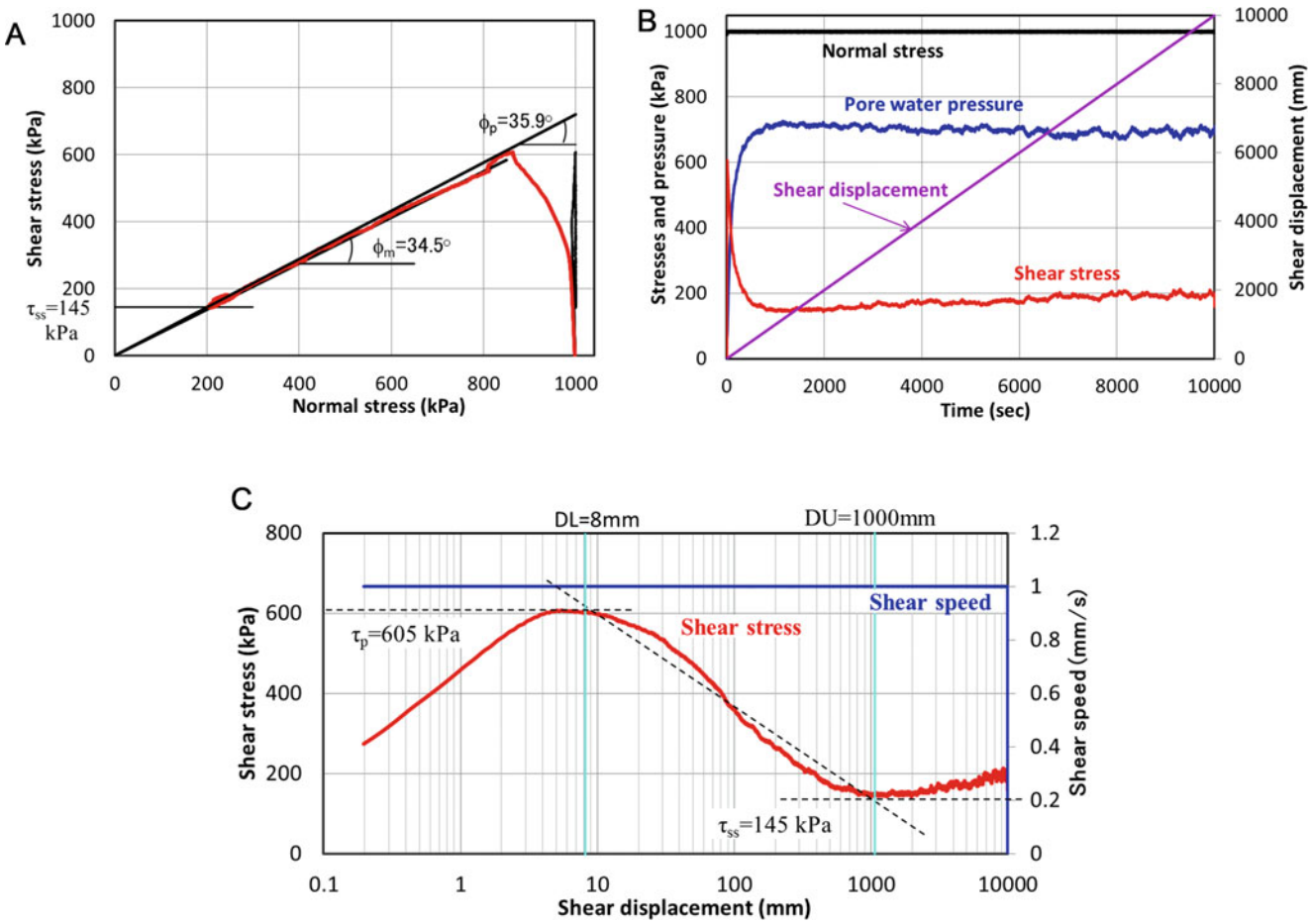

Fig. 33 Saturated and undrained speed control test for Silica sand No.6. Normal stress = 1000 kPa, BD = 0.95, Shear speed = 1 mm/s. (**a**) Stress path, (**b**) Time series data, (**c**) Shear stress–shear displacement relationship

The steady state τss in the speed controlled tests are 40–70 kPa for normal stress of 250–500 kPa in Figs. 31 and 32. However, the steady state τss in the speed controlled tests was 145 kPa for the normal stress of 1000 kPa in Fig. 33. Probably all crushable grains crushed out before reaching the steady state. In contrast, the steady state τss in the stress-controlled test for the normal stress of 1000 kPa was 65 kPa in Fig. 35 which was the same with 250–500 kPa tests. This large difference of both tests is in shear speed. Shear speed in the speed controlled test was 1 mm/s, and the shear speed of the stress controlled test was at maximum of 150 mm/s. The steady-state shear strength can be affected by shear speed. Natural phenomena are under the stress-controlled condition. So, for the reproduction of natural phenomenon, the stress controlled test is suitable. By contrast, constant speed test is suitable to precisely monitor pore-water pressure during motion. Both tests have different suitability.

4.2 Experiment of Natural Soils (Example of Volcanic Debris Taken from Unzen)

We went to the Unzen landslide which caused a very rapid and long-travelling landslides. The moving mass entered into the Ariake sea and caused a big Tsunamis which killed around 5000 people on the opposite bank (Kumamoto Prefecture) and islands around the Ariake sea. Figure 38 presents the total view of the Unzen Landslide. Red arrows show the head scarp of the landslide. Weathered debris were falling from the head scarp and entered into torrents. The torrent deposits are the weathered materials which remained on the slope after the landslide. They are same materials which caused the landslide.

We went to the central torrent and took samples at the point of No.1 with yellow mark in the Fig. 38. The lower photo shows a part of the torrent. Large boulders are also included in the torrent deposit, but those are not suitable to

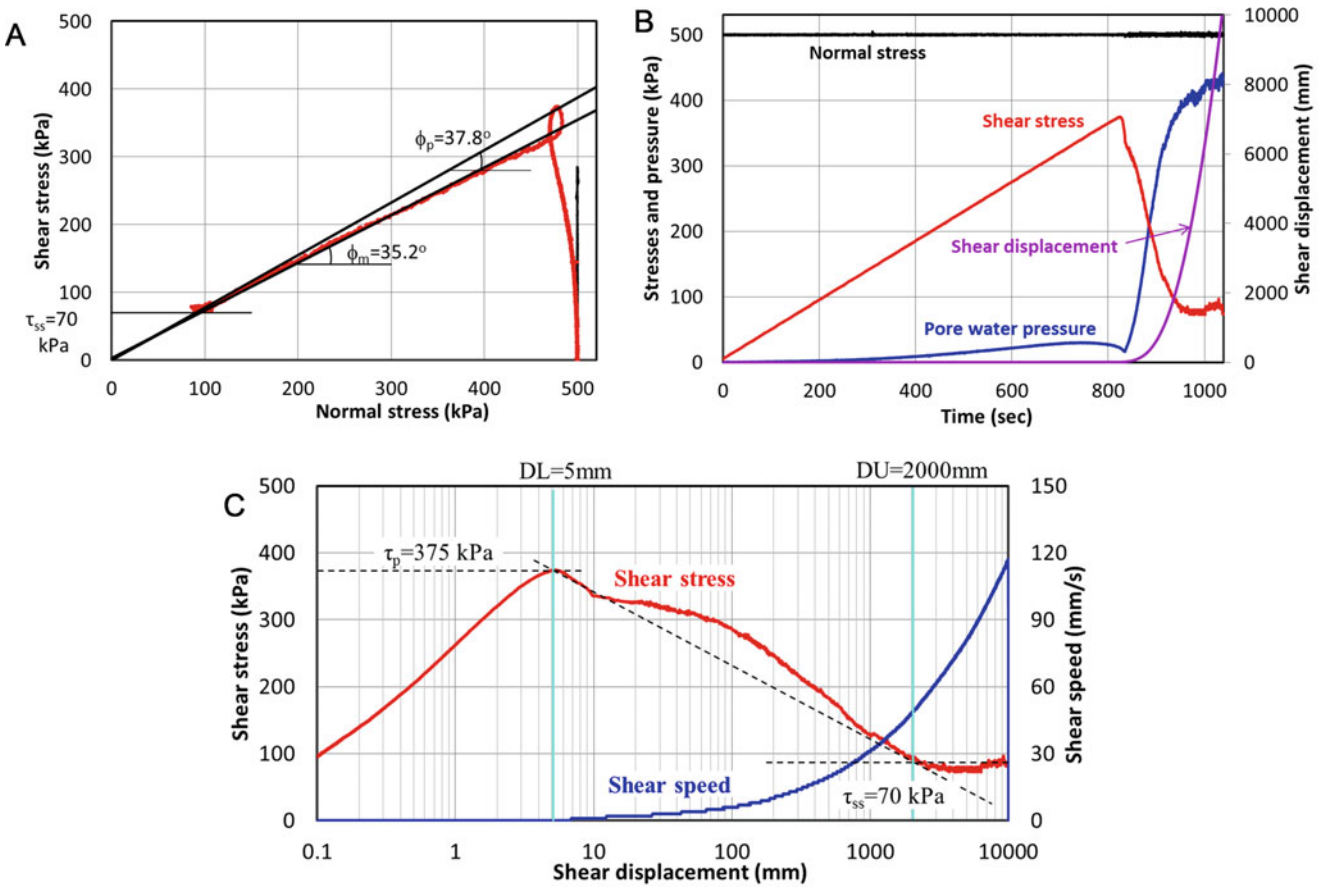

Fig. 34 Saturated and undrained stress control test for Silica sand No.6. Normal stress = 500 kPa, BD = 0.95, Shear stress increment = 0.5 kPa/s. (**a**) Stress path, (**b**) Time series data, (**c**) Shear stress–shear displacement relationship

the ring shear testing. We took volcanic sand deposits near the torrent wall. The lower right photo is the close up of the sample. As a test sample, less than 2 mm grains were used.

Figure 39 presents a test measuring the failure line in the drained state and the friction angle during motion. Firstly, normal stress of 1000 kPa was loaded. Then, the sample was sheared at a constant speed (1 mm/s). The shear stress reached the failure line during motion. Then, normal stress was decreased to zero at the rate of 0.2 kPa/s for 5000 s. The whole test was conducted in the drained condition. No pore water pressure existed in the shear zone. Namely, the failure line during motion was manifested in the drained state. The friction angle during motion of the Unzen sand was 38.6 degrees. It is much higher than the silica sand which is 35.2 degrees.

Three stress controlled tests and three speed controlled tests as shown in Table 6 were conducted on the Unzen sand to investigate the sliding-surface liquefaction and the undrained steady-state shear resistance.

Figure 40 shows the test result of Test number 1 of the Unzen sand. After saturation and consolidation at 250 kPa, a constant rate of shear stress (0.5 kPa/s) was loaded in the undrained state. Figure 40a presents the stress path. The black line shows the stress path of the total stress. The stress point moved up until failure; then, it vertically went down to the shear stress at the steady state shear strength. The red line shows the effective stress path. When shear stress was increased at the rate of 0.5 kPa/s, pore water pressure was generated and the stress path moved to the left direction. However, the stress point reached the failure line during motion (38.3 degrees), pore pressure decreased due to dilatancy and the stress path moved to the right direction. The peak shear strength was mobilized on the failure line at peak (42.2 degrees). After peak, pore pressure was generated and the stress path moved to the failure line during moion (38.3 degrees). In the progress of shearing, further pore pressure increase continued until the steady state shear strength of τ_{ss} = 14 kPa.

Figure 40b presents the time series data of normal stress (black), shear stress (red), pore pressure measured near the shear zone (blue), and the shear displacement (purple). One can find that pore pressure generation started at the progress of shear stress and reached a small peak at around 53 kPa,

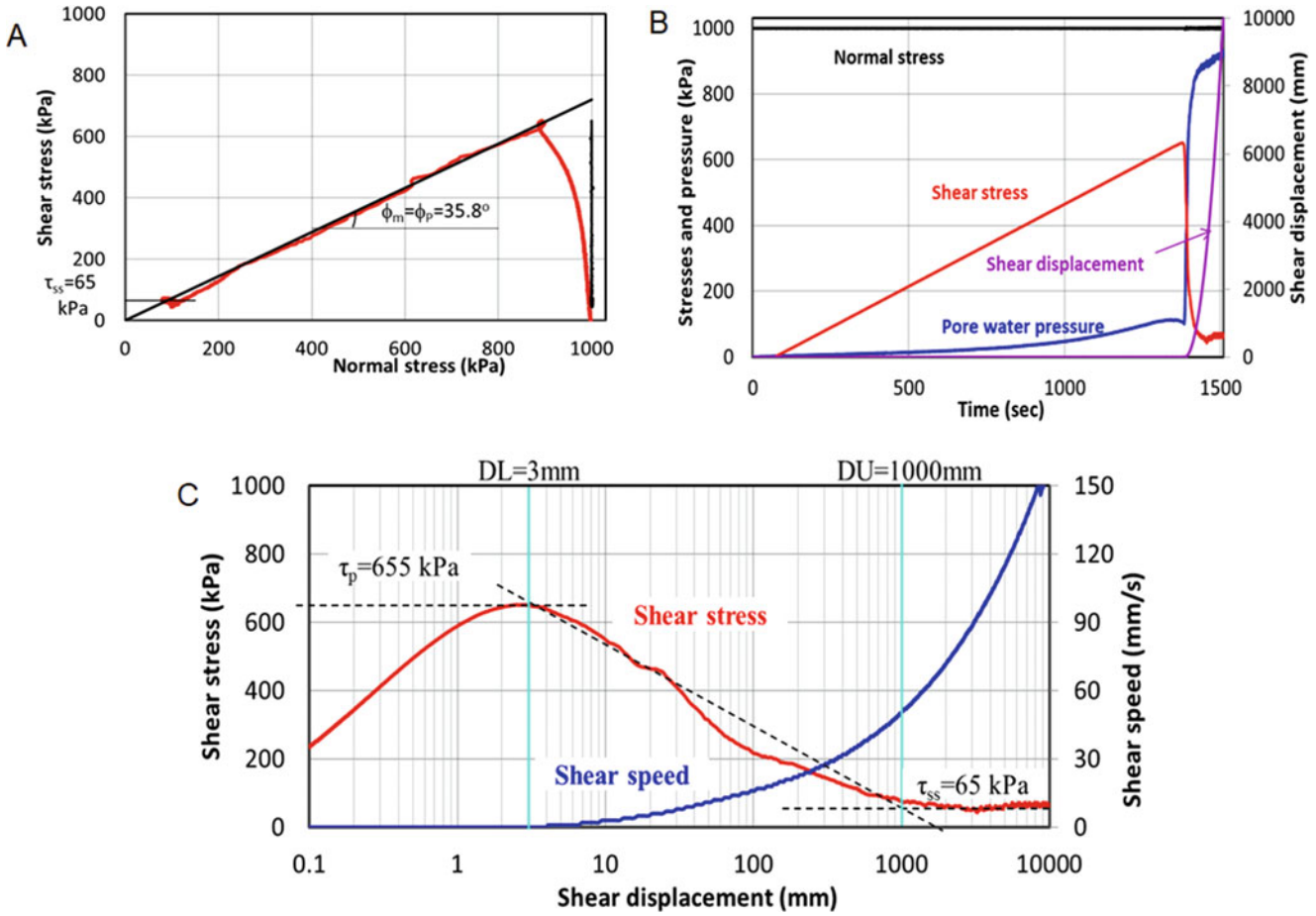

Fig. 35 Saturated and undrained stress control test for Silica sand No.6. Normal stress = 1000 kPa, BD = 0.94, Shear stress increment = 0.5 kPa/s. (**a**) Stress path, (**b**) Time series data, (**c**) Shear stress–shear displacement relationship

then, once pore pressure was decreased. However, at the same time of the start of the shear displacement, a rapid pore pressure due to grain crushing was generated. Pore pressure value was close to the normal stress. Hence, the typical sliding-surface liquefaction occurred. The shear displacement acceleratedly increased.

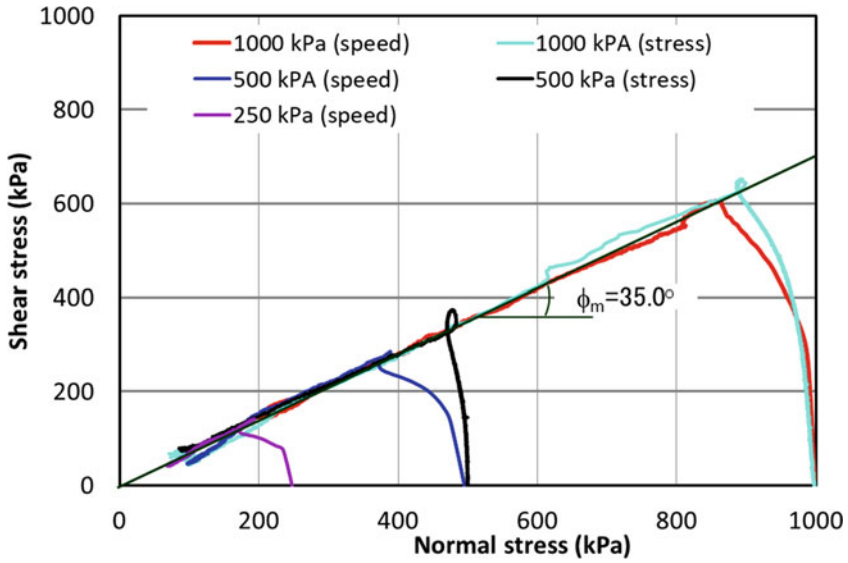

Fig. 36 Stress path of three speed controlled tests (250 kPa, 500 kPa, 1000 kPa) and a stress controlled test (500 kPa, 1000 kPa) for Silica sand No.6

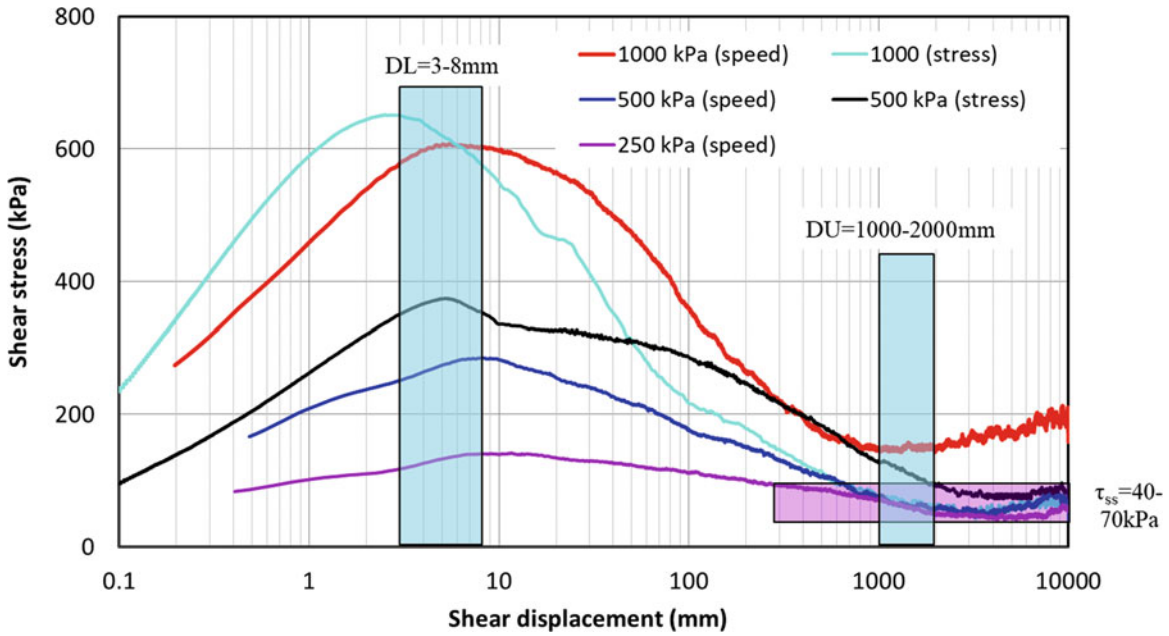

Fig. 37 Shear stress–shear displacement of three speed controlled tests (250 kPa, 500 kPa, 1000 kPa) and a stress controlled test (500 kPa, 1000 kPa) for Silica sand No.6

Figure 40c presents the relationship between shear stress and the shear displacement. Shear speed line is added.

This graph presents the peak strength ($\tau p = 211$ kPa) at DL = 7 mm from which shear stress started to decrease until the steady state shear stress ($\tau ss = 14$ kPa).

Figure 41 presents the test result of saturated and undrained stress contolled test for Unzen sample. Normal stress was 750 kPa, Shear stress increment was the same at 0.5 kPa/s. The friction angle at peak was 41.8 degrees, the friction angle during motion was 38.0 degrees. The peak shear strength was 473 ka, and the steady state shear strength was 15 kPa. Approximating the stress reduction curve in Log-scale by two lines, the start of steady state motion (DU) was around 80 mm.

Figure 42 presents the test result of saturated and undrained speed-controlled test for Unzen sample. Normal stress was 250 kPa, Shear speed was 1 mm/s. The friction angle at peak and the friction angle during motion were the same at 36.1 degrees. The peak shear strength was 137 kPa. The steady state shear strength was 18 kPa which was almost the same for the previous three stress controlled tests.

The shear stress reduction curve is not smooth. For the range from shear displacement of 100–700 mm, shear stress reduction was minimum. After that, the shear strength reduction rate was the same with that during 8–100 mm shear displacement. Because of this irregular state, the DU (the shear displacement between two lines approximating the shear displacement curve was around 1000 mm).

Figure 43 presents the test result of saturated and undrained speed-contolled test for Unzen sample. Normal stress was 500 kPa, Shear speed was 1 mm/s. The friction angle at peak and the friction angle during motion was the same at 36.3 degrees. The peak shear strength was 214 kPa. The steady state shear strength was 18 kPa which was the same with Fig. 43.

The shear stress reduction curve is also not smooth. For the range from shear displacement of 100–700 mm, shear stress reduction was minimum. After that, the shear strength reduction rate was same with that during 7–100 mm shear displacement. Such irregular shape did not appear in Silica sand. The Unzen volcanic sand seems to be not homogeneous.

Figure 44 presents the test result of saturated and undrained speed-controlled test for Unzen sample. Normal stress was 1000 kPa, Shear speed was 1 mm/s. This sample also did not show the friction angle at peak. The friction angle during motion was 42.0 degrees. The peak shear strength was 502 kPa. The steady state shear strength was 66 kPa which was the largest. However, DU = 100 mm, and the shear stress reduction curve was smooth.

The test results from Fig. 40 to Fig. 45 are somehow similar and also different. To view the general shear behavior, all six undrained test results are combined in the stress path (Fig. 45) and also in the shear stress–shear displacement relationship (Fig. 46).

Figure 45 presents the combined stress paths of all six undrained shear tests; three shear-stress controlled tests and three constant shear-speed controlled tests. The friction angle during motion was 38.7 degrees. This value was almost same with 38.6 degrees in the Fig. 39 which was measured by the

Fig. 38 Sampling of Unzen sands in Shimabara, Japan and the photo of Sample No.1 (Unzen-1). Upper photo: General view of Unzen landslide. Lower photo (Left): Sampling site within the central gulley. Lower photo (right): Close up photo of samples in the field

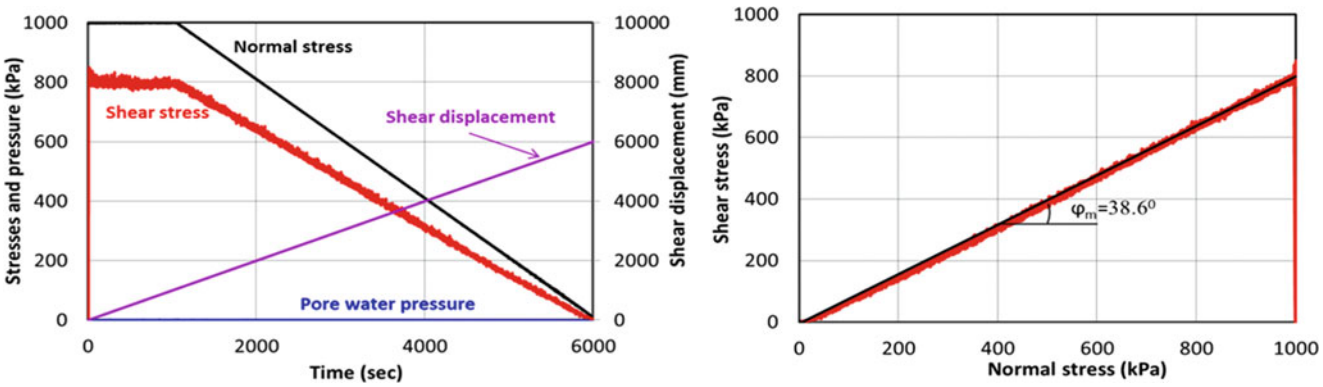

Fig. 39 Results of the saturated constant-speed drained shear test. Sample: Unzen volcanic sand, Shear speed: 1 mm/s, Normal stress decreasing rate: 0.2 kPa/s. (**a**) Time series data. (**b**) Stress path data

Table 6 A series of tests on Unzen sand

Test number	Fig. number	Normal stress	Shear mode	Shear speed	Shear stress increment
1	Fig. 40	250 kPa	Stress control		0.5 kPa/s
2	Fig. 41	750 kPa	Stress control		0.5 kPa/s
3	Fig. 42	941 kPa	Stress control		0.5 kPa/s
4	Fig. 43	250 kPa	Speed control	1 mm/s	
5	Fig. 44	489 kPa	Speed control	1 mm/s	
6	Fig. 45	1000 kPa	Speed control	1 mm/s	

drained normal-stress decreasing test independent of any pore water pressure.

Figure 46 presents the combined shear-stress and shear-displacement curves of all five undrained shear tests; three shear-stress control tests and three constant shear-speed controlled tests. The shear displacements DL, which started shear stress reduction, namely at the peak shear strength, were 5–8 mm. The steady state shear strengths were 14–18 kPa (except 1 kPa data). The start of the steady state to be used in LS-RAPID is 80–200 mm. Some test results suggested DU = 400 mm (Figs. 40 and 43). However, DU = 100–200-mm seems to be practical from Fig. 46. It is 10% of Silica sand (DU = 1000–2000 mm). When DU is short, the materials are brittle. A local failure within the slope expands to progressive failure, and create the landslide block. It often becomes rapid landslides.

5 Case Studies of Sliding-Surface Liquefaction from Previous Research

Section 5 of this landslide lesson are devoted to introduce various types of landslides which are rapid landslides affected by sliding-surface liquefaction.

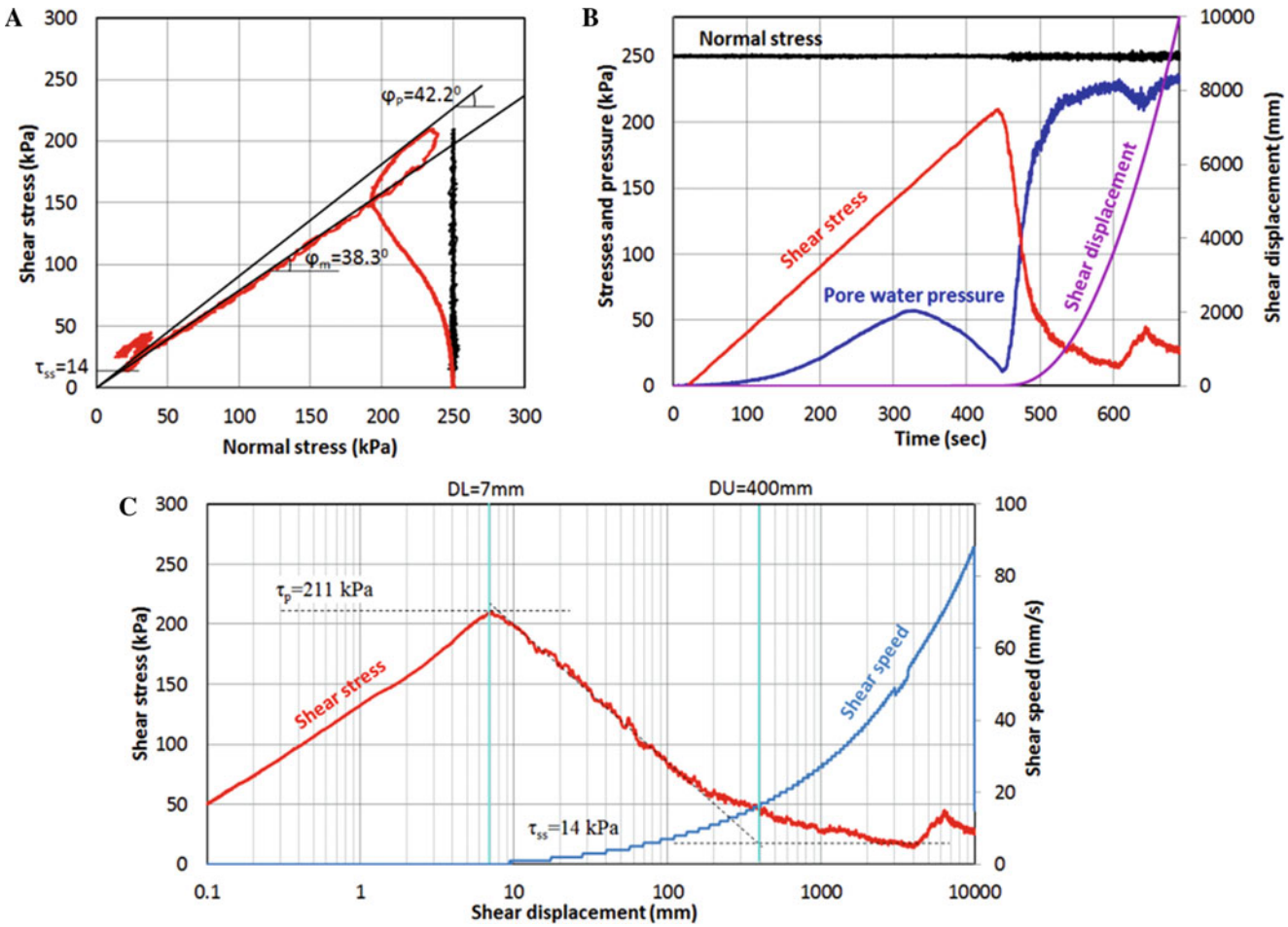

Fig. 40 Saturated and undrained stress-control test for Unzen sample. Normal stress 250 kPa, B_D = 0.94, alpha = 0.9, Shear stress increment = 0.5 kPa/s. (**a**) Stress path, (**b**) Time series data, (**c**) Shear stress–shear displacement

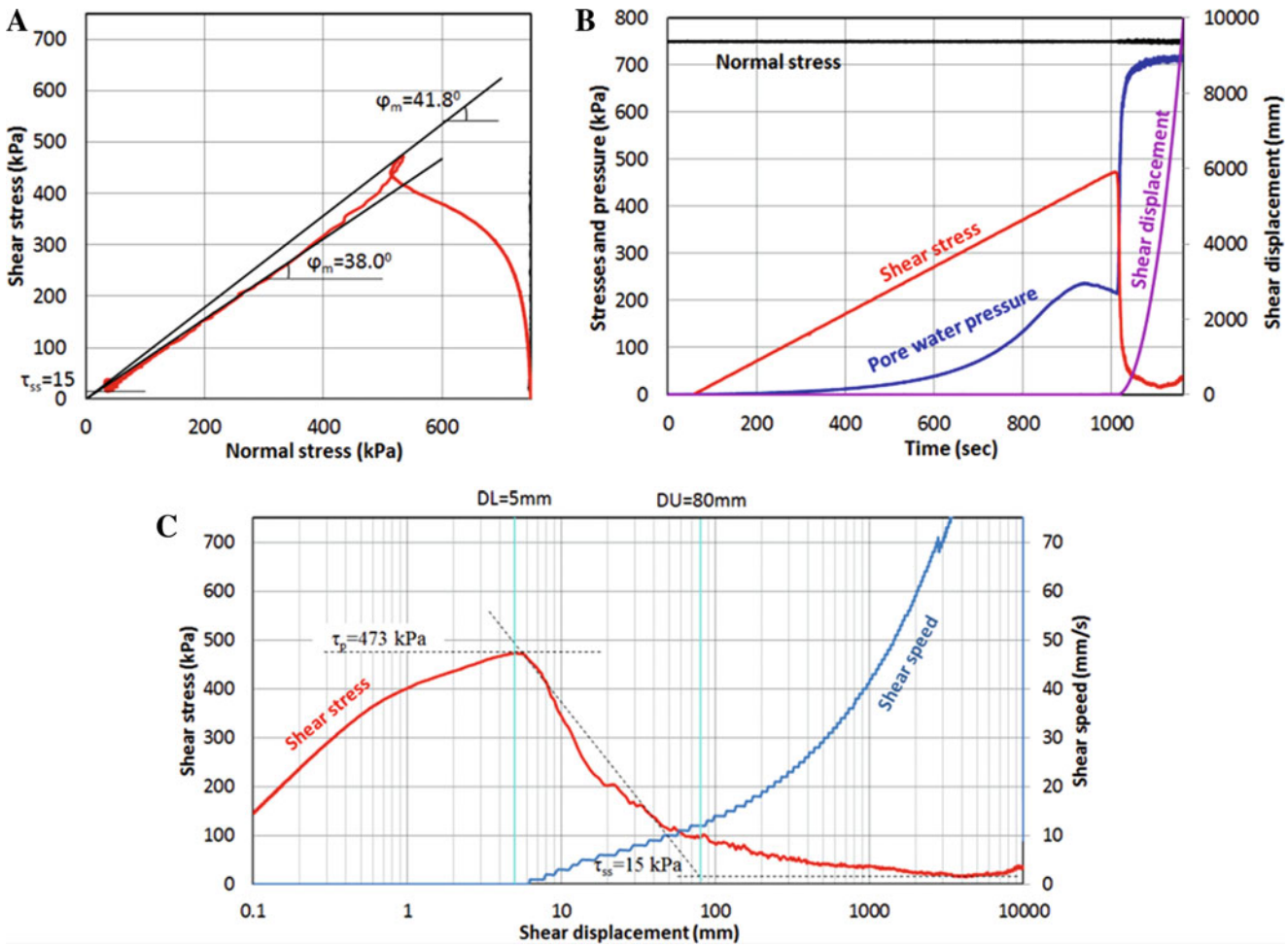

Fig. 41 Saturated and undrained stress control test for Unzen sample. Normal stress 750 kPa, BD = 1.0, Shear stress increment = 0.5 kPa/s. (**a**) Stress path, (**b**) Time series data, (**c**) Shear stress–shear displacement

The examples include the five cases including the 2006 Mega-slide in Leyte Philippines which was first application of a new integrated landslide simulation model "LS-RAPID", the 1792 historical landslide causing the largest landslide disaster and the largest volcanic disaster and the largest landslide-induced tsunami in Japan, large-scale landslides triggered by 2004 Mid-Niigata earthquake, in which the undrained ring shear testing proved that the sliding surface of rapid landslide was formed by the sliding surface liquefaction at the bottom of sand layer, a hypothetical submarine landslide with sampling from 300 m below the sea floor near the Suruga trough (a part of Nankai trough) by an IODP (Integrated Ocean Drilling Progamme) drilling, and large-scale landslides induced by 2011 typhoon "Talas". These are typical landslides caused by pore-water-increase. Those five cases are introduced from our previous articles published in journal "Landslides" and some others.

4.1 2006 Mega-slide in Leyte, Philippines, triggered by a small earthquake after long rainfall.
4.2 Large-scale landslides triggered by the 2004 Mid-Niigata earthquake, Japan
4.3 Hypothetical submarine landslides in Suruga bay, Japan
4.4 Large-scale landslides triggered by the 2011 Typhoon "Talas" in Kii Peninsula, Japan
4.5 1792 Historical mega-slide in Unzen, Japan.

5.1 2006 Mega-Slide in Leyte, Philippines, Triggered by a Small Earthquake After Long Rainfall

This landslide and its analysis of the initiation and the motion by the undrained ring-shear testing using the sample from the landslide and the integrated landslide simulation model (LS-RAPID) is introduced from the following paper.

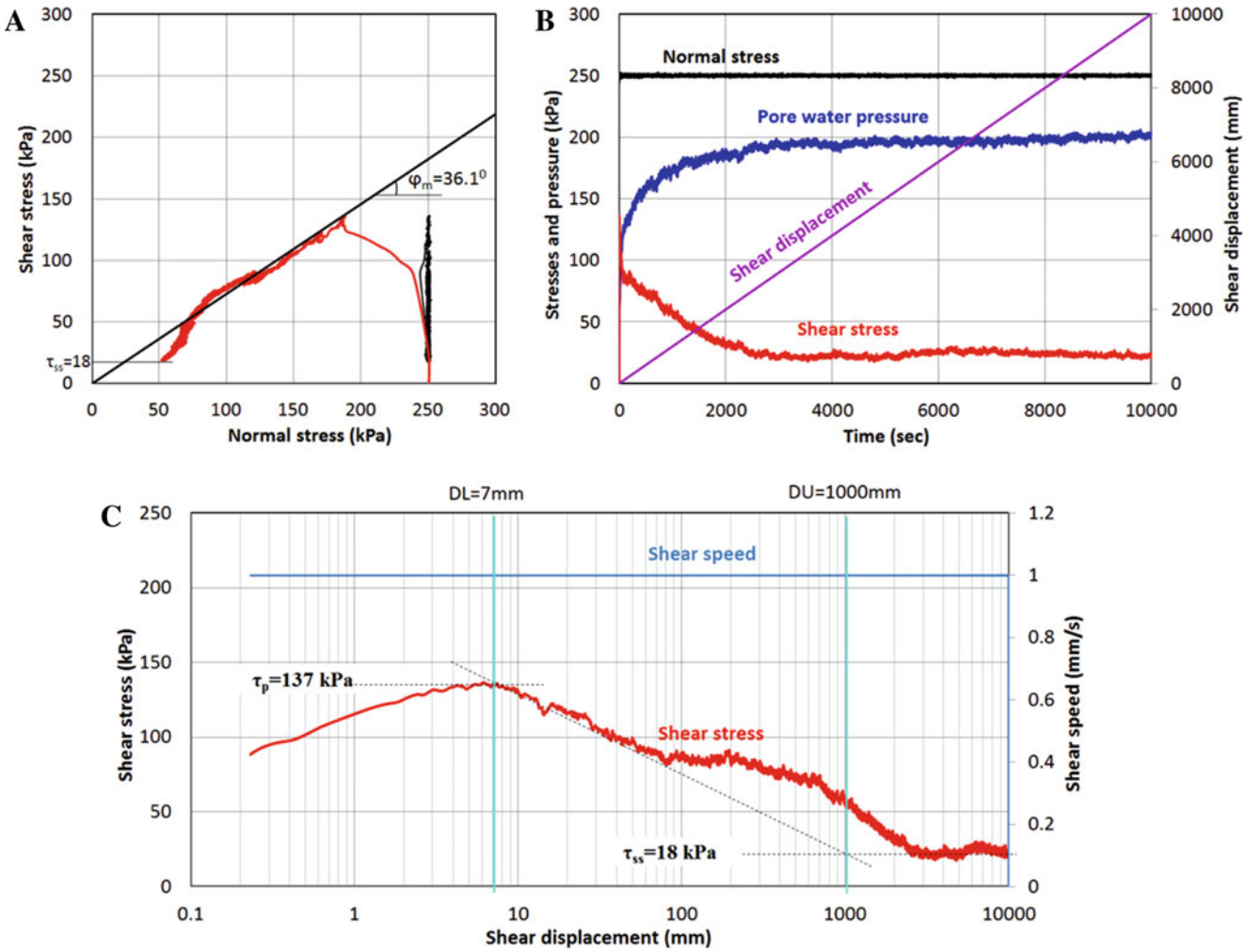

Fig. 42 Saturated and undrained speed control test for Unzen sample. Normal stress 250 kPa, BD = 0.9, Shear speed = 1 mm/s. (**a**) Stress path, (**b**) Time series data, (**c**) Shear stress–shear displacement relationship

"*Sassa K, Nagai O. Solidum R, Yamazaki Y, Ohta H (2010) An integrated model simulating the initiation and motion of earthquake and rain induced rapid landslides and its application to the 2006 Leyte landslide. Landslides 7:219-236*".

5.1.1 Landslide Field Investigation

A rapid and long-traveling landslide occurred in the Leyte Island, Philippines on 17 February 2006 in the southern part of Leyte Island, Philippines. The landslide caused 154 confirmed fatalities and 990 people missing in the debris. The International Consortium on Landslides (ICL) and the Philippine Institute of Volcanology and Seismology (PHIVOLCS) organized investigation with a joint Japanese and Philippine team of 22 scientists and engineers. The team investigated the landslide from the ground and from a chartered helicopter. The landslide volume was 20 million m^3 (Catane et al. 2007). Figure 47 presents the location of landslide in Philippines and a front view of the landslide source area (upper photo) and the total landslide moving area (lower photo) taken from a helicopter chattered by the joint investigation team.

A planer hard rock is outcropped at the left side of the head scarp. Other parts of the slope seem to be weathered volcanoclastic rocks or debris. The landslide mass moved from the slope and deposited on the flat area. Many flow-mounds or hummocky structure were found.

Figure 48 presents the central section of this landslide and the sampling point (landslide flow mound S in the upper photo of Fig. 47). The section of the central line of the landslide was surveyed by a non-mirror total station and a ground-based laser scanner in the field and compared with a SRTM (Shuttle Radar Topography Mission) map before the landslide. The red-color part shows the initial landslide mass while the blue-color part presents the displaced landslide debris after deposition. The length of landslide from the head scar to the toe of the deposition is around 4 km. The inclination connecting the top of the initial landslide and the

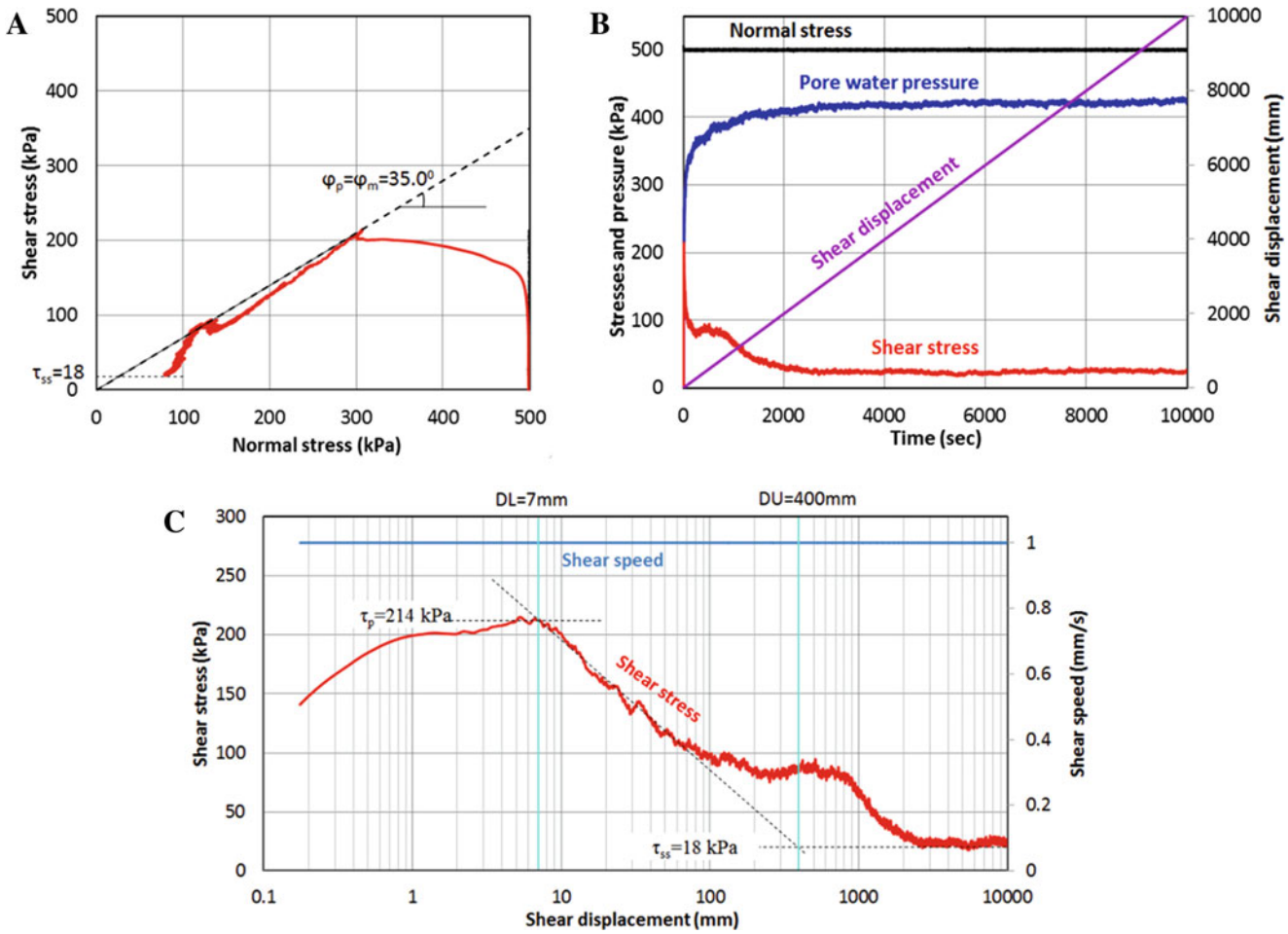

Fig. 43 Saturated and undrained speed control test for Unzen sample. Normal stress 500 kPa, $B_D = 0.95$, Shear speed = 1 mm/s. (**a**) Stress path, (**b**) Time series data, (**c**) Shear stress–shear displacement relationship

toe of the displaced landslide deposit is approximately 10°, which indicates the average apparent friction angle mobilized during the whole travel distance. The value is much smaller than the usual friction angle of debris (sandy gravel) of 30–40°. Therefore, it suggests that high excess pore-water pressure was generated during motion, namely the sliding-surface liquefaction.

The material of the flow mound is volcanoclastic debris, including sand and gravel. We observed the material in the source area by eye observation from the surface and by hand scoop excavation in the valley-side slope after the landslide. It consisted of volcanoclastic debris or strongly weathered volcanoclastic rocks. It is regarded to be the same material (either disturbed or intact) observed in the flow mound shown in Fig. 48. Therefore, we took a sample of about 100 kg from the base of the flow mound shown in the point "S" in the section of Fig. 47) and the photo of Fig. 48b. The location is in the center of travel course and just below the source area. Then, we transported the material to Japan and subjected it to the undrained dynamic-loading ring-shear test.

5.1.2 Triggering Factors of the Landslide

We examined the triggering factors of the Leyte landslide. A small earthquake occurred near the site at the time of occurrence of the landslide, and the location of the hypocenter of this earthquake was estimated by the US Geological Survey (USGS) and the PHIVOLCS. According to PHIVOLCS, the earthquake occurred at a location (10.30 N, 124.90 E) 22 km west of the source area of the landslide, 6 km deep, with magnitude Ms 2.6, at 10:36 hours on 17 February 2006. The seismic record at Maasin is shown in Fig. 49b. E-W component (blue color) was the major direction of seismic shaking, other two components are around a half magnitude. Using the standard attenuation function between peak ground acceleration and hypocentral distance (Fukushima and Tanaka 1990), the peak ground acceleration at the landslide site was estimated at 10 gal for this magnitude. We then estimated the expected peak acceleration at the bottom of the landslide mass as about 60–200 gal from the following consideration. (1) Three to five times amplification of ground accelerations at the sliding surface due to the difference in the compression

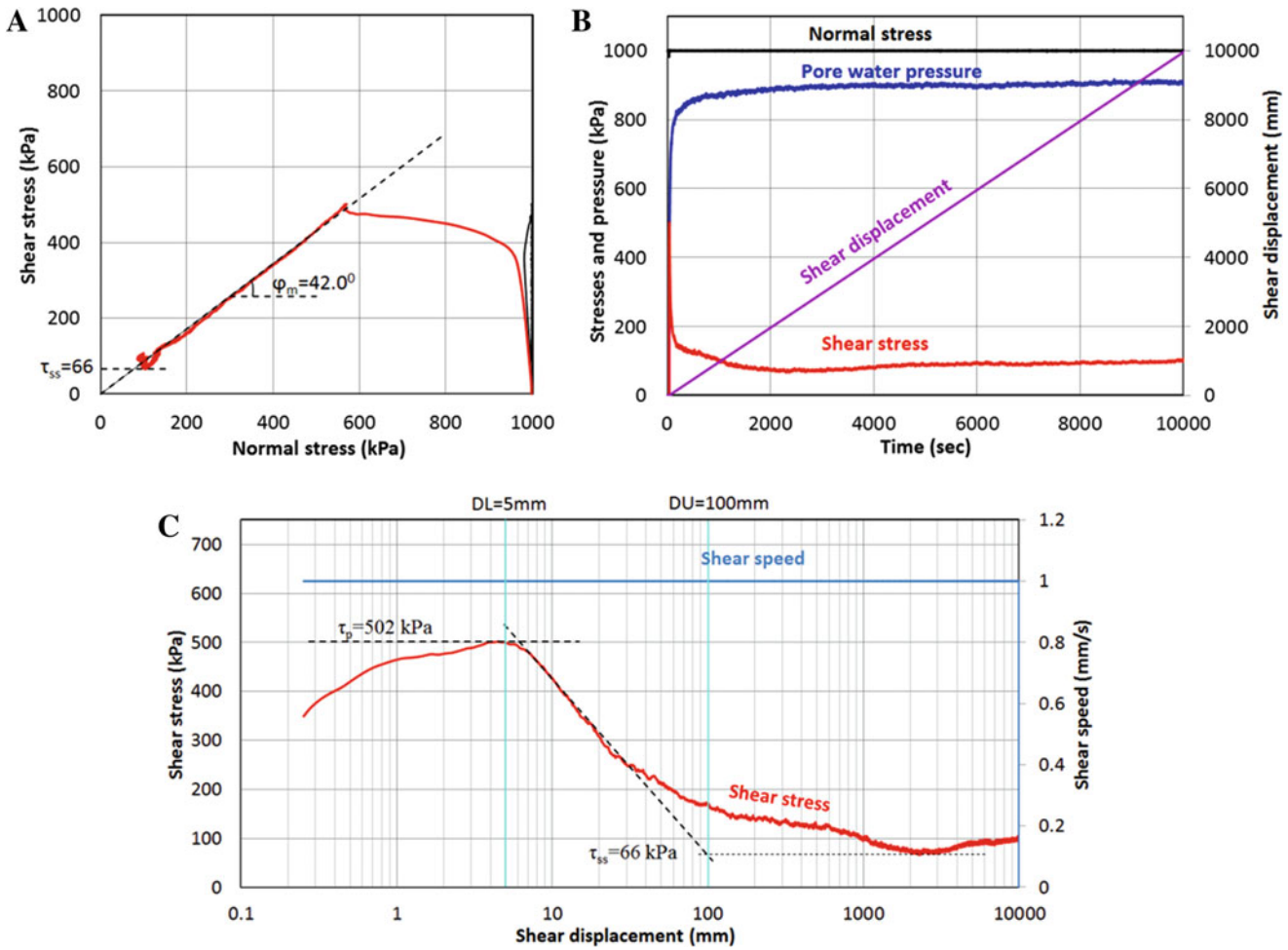

Fig. 44 Saturated and undrained speed control test for Unzen sample. Normal stress 1000 kPa, $B_D = 0.99$, Shear speed = 1 mm/s. (**a**) Stress path, (**b**) Time series data, (**c**) Shear stress–shear displacement relationship

(P) wave speeds between soft volcanoclastic debris (Vp = 0.5–1.5 km/s) and hard volcanic bed rock (Vp = 2.5–5- km/s) that outcropped in the head scarp, because the amplification level is proportional to the velocity contrast between two layers. Though the shear (S) wave speeds of the volcanoclastic debris and the bed rock are unclear, similar level of velocity contrast to the P wave is expected at the sediment/bed rock interface. (2) An additional magnification of 2–4 times is expected in the landslide site due to the focusing of seismic waves onto the mountain ridge. Namely the total magnification of this site will be 6–20 times.

Heavy rainfall (459.2 mm for 3 days on 10–12 February and 571.2 mm for 5 days on 8–12 February 2006) occurred in this area before the day of the landslide as shown in Fig. 49a. This rainfall should have increased the ground-water level and pore-water pressure inside the slope. However, the peak ground-water level had likely depleted before the occurrence of the landslide on 17 February because the rainfall on 13–-17 February was small (total 99.0 mm for 5 days). We simulated the ground-water level using a tank model that had been developed to simulate the ground-water level in the Zentoku landslide, Japan (Hong et al. 2005), which had a depth and inclination similar to that of the Leyte landslide. When inputting 10 days' precipitation records at the nearest monitoring station in Otikon (about 7 km west of the landslide) on 8–17 February, the peak ground-water level occurred on 13 February 2006. Because the peak ground-water level had already passed when the landslide occurred on 17 February, we deduced that a small earthquake was the final trigger of the landslide.

5.1.3 Undrained Dynamic-Loading Ring-Shear Test

Based on this consideration, a dynamic-loading ring-shear test on the sample taken from the landslide was conducted as follows:

The sample was set in the shear box (250 mm inside diameter, 350 mm outside diameter) of DPRI-6, and fully saturated (BD = 0.98). The stress acting on the sliding surface of the deepest part (around 120–200 m) is very

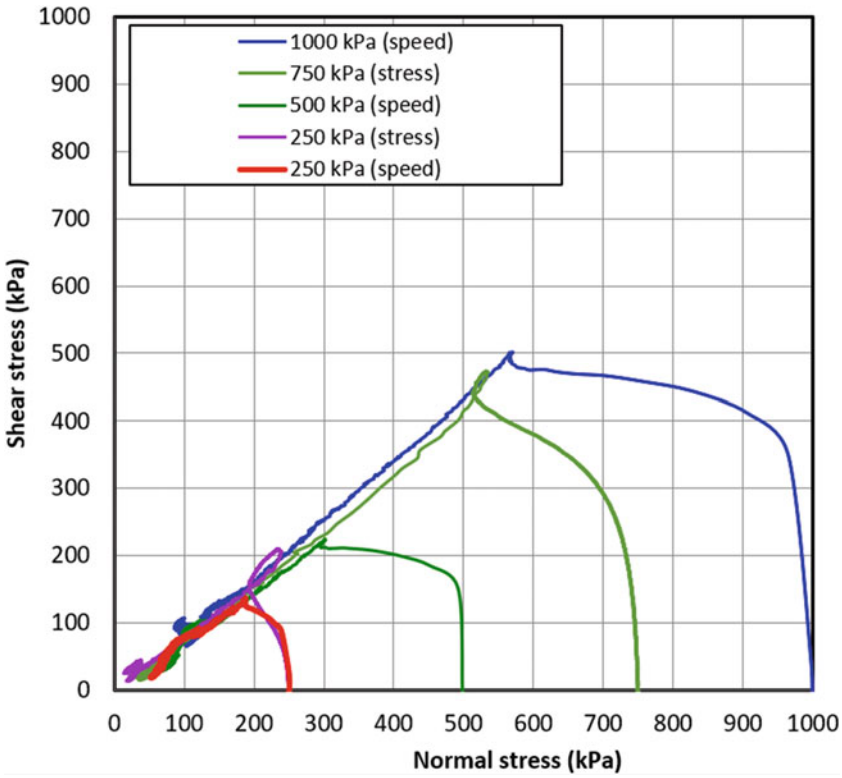

Fig. 45 Stress path of three speed control tests (250, 500, 1000 kPa) and two stress control tests (250, 750 kPa) for Unzen sample

high. However, because of the capacity of this apparatus: the sliding surface was assumed for the test to be 35 m deep and at an inclination of 25°. The unit weight of the soil was assumed to be 20 kN/m^3. In the preliminary test to increase pore-water pressure until failure, the failure line of this material was obtained. It was 39.4° in the friction angle and almost zero cohesion. In the simulation test of a rain- and earthquake-induced landslide, the normal stress corresponding to that of 5 m lower than the critical ground-water level (i.e., further 5 m rise of ground-water level shall

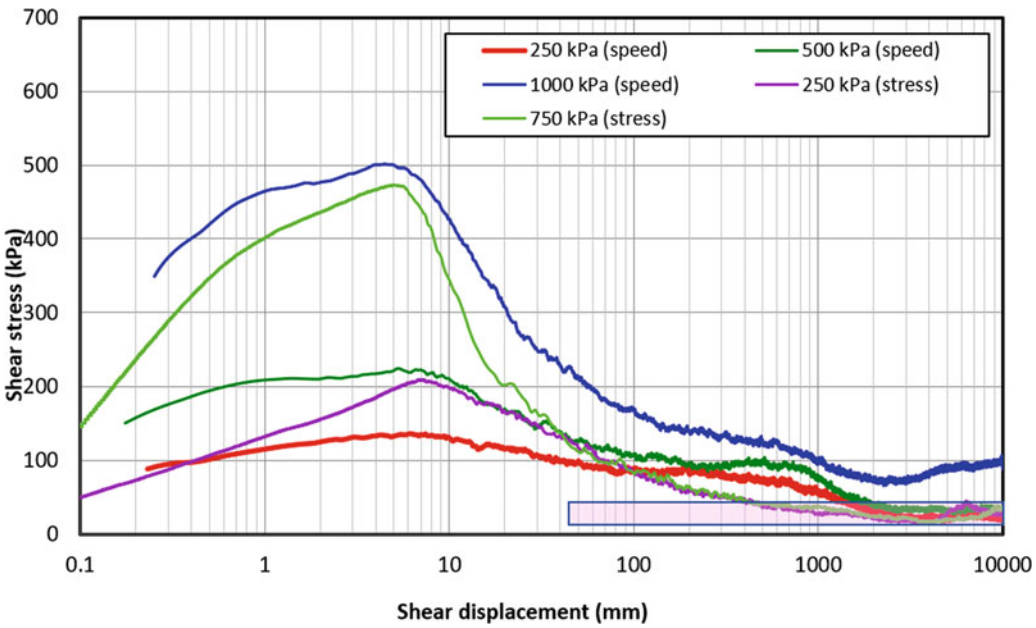

Fig. 46 Shear stress–shear displacement of three speed control tests (250, 500, 1000 kPa) and two stress-control tests (250, 750 kPa) for Unzen sample

Fig. 47 Photo of the 2006 Leyte landslide. Left: The location of the Leyte landslide in Philippines. Photo of the landslide source area. S: Sampling point in the landslide flow mounds which traveled from the source area and deposited in the flat alluvial deposit. Bottom: A widely spread landslide mass which destroyed the whole village including a school, a church and many houses, and residents of around 1000 people

trigger the landslide) was first loaded on the sample. Then, the shear stress due to the self-weight of the soil layer was loaded. It is the stress point shown by the white circle in Fig. 50a. Using three components of seismic record observed at Massin (PHIVOLCS, Code number: MSLP, Latitude:10.1340, Longitude: 124.8590, Elevation: 50.0), normal stress and shear stress acting on the shear surface of 35 m deep with 25° inclination on the direction of the Leyte

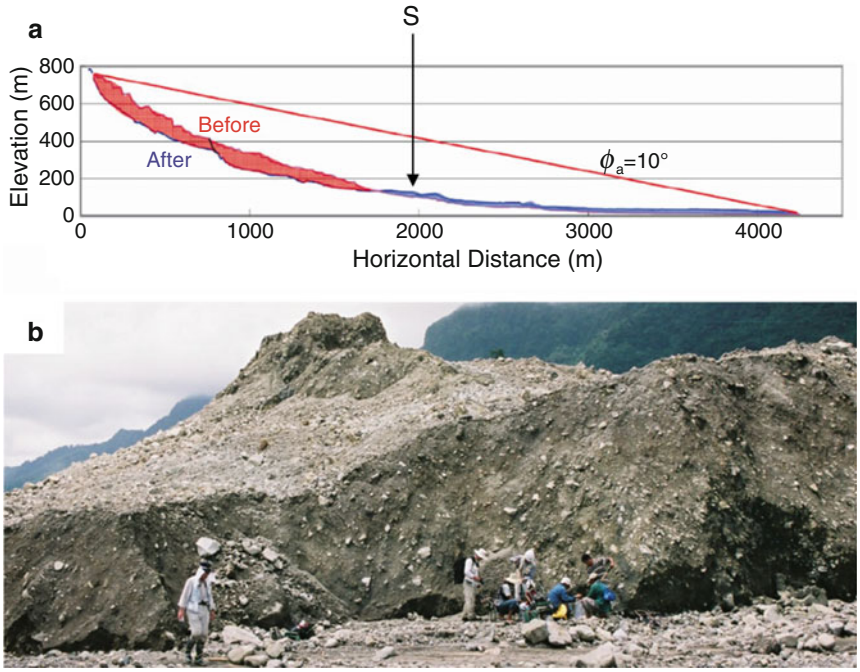

Fig. 48 Central section of the landslide from the top to the toe (**a**). The landslide flow mound and the sampling from the bottom of the flow mound (**b**)

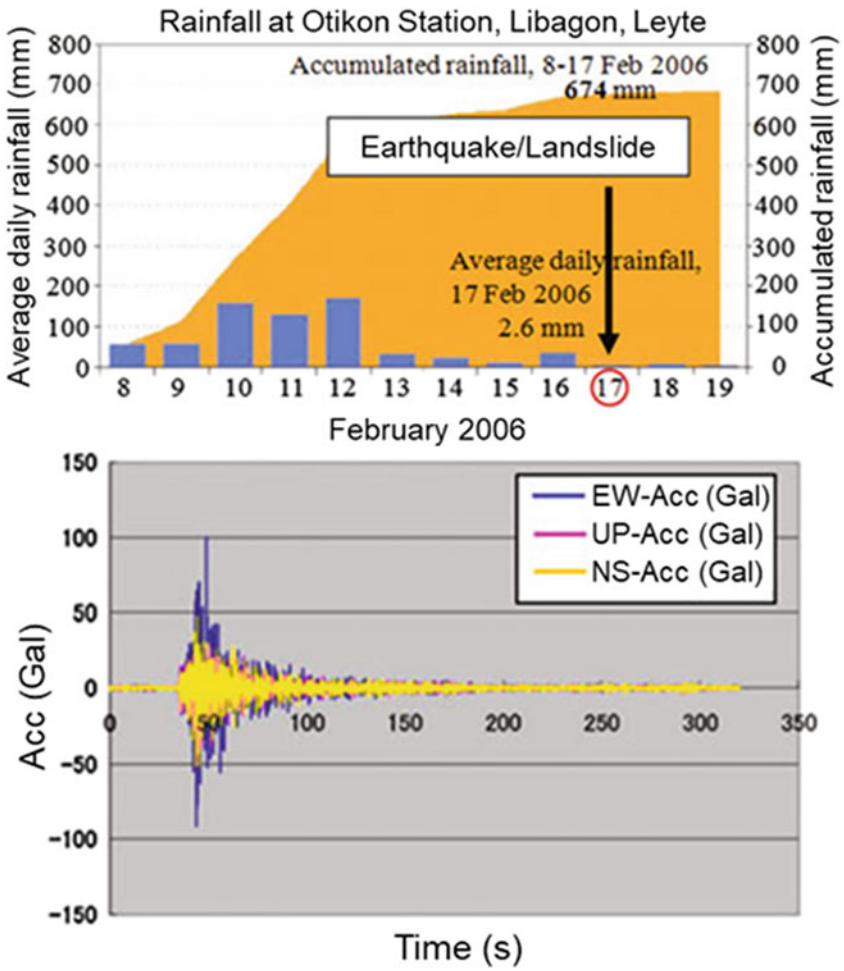

Fig. 49 Triggering factors of the Leyte landslide. (**a**) Daily rainfalls and accumulated rainfalls from 8 to 18 February 2006. (**b**) An earthquake (Ms = 2.6) monitored at Maasin, Leyte, located 22 km from the landslide

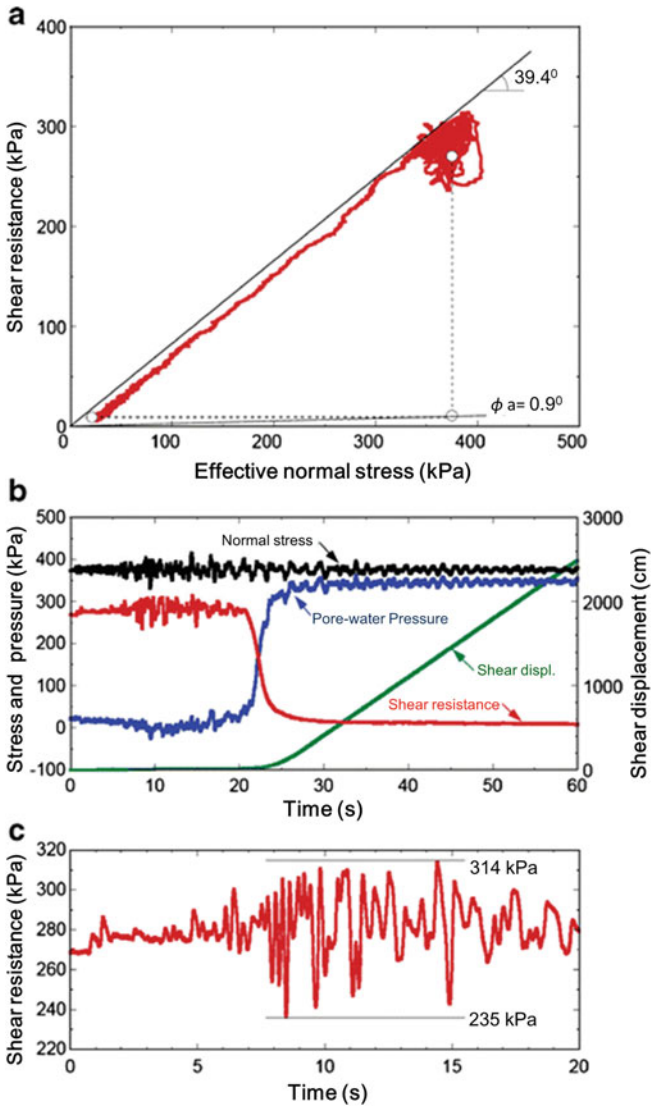

Fig. 50 Undrained seismic loading ring shear test. (a) Effective stress path. (b) Time series data of normal stress, shear stress, pore pressure and shear displacement. (c) Mobilized shear-stress in the ring shear testing, The maximum = 314 kPa, the minimum = 235 kPa

landslide were calculated so that the peak seismic stress may correspond to the range of seismic acceleration of 60–200 gal, but as low as possible to avoid failure before seismic loading.

The test results are presented in Fig. 50a–c. Figure 50a presents the stress path of the test. The effective stress path showed a complicate stress path like a cloud. The stress path reached the failure line repeatedly. Therefore, this small seismic stress failed the soil and gave a repeated shear displacement during the period of stress reaching the failure line. It generated a pore water pressure (blue color line) due to grain crushing and volume reduction, and it was accelerated in progress of shear displacement (green color line). Namely the sliding-surface liquefaction phenomenon occurred. The value reached a very small steady state stress (red color line). This process is presented in the time series data around the failure in Fig. 50b. The mobilized apparent friction coefficient defined by steady-state shear resistance divided by the total normal stress was 0.016 (0.9°). The loaded seismic stress is so small, the control was not easy.

The monitored shear resistance is shown in Fig. 50c. When the stress reaches failure line, the balance of shear stress and shear resistance is manifested as acceleration. As seen in the figure, the magnitude of increment of shear resistance seems to be slightly smaller than the decrement. The level of seismic stress is around 40 kPa, the shear stress due to gravity is around 275 kPa. The ratio is 0.145. Namely the seismic coefficient K = 0.145. The estimated magnitude of stress is to load 60–200 gal, namely K = 0.06–0.20. This level will be around the filed condition. It was the minimum possible value to avoid failure before seismic loading in some trial test because of stability of initial shear stress loading. This geotechnical simulation test could physically reproduce the rapid landslide motion triggered by a small seismic shaking in a high pore pressure state due to rain falls. Thus, the combined effect of rainfall and earthquake was confirmed and it was examined in the new integrated computer simulation LS-RAPID.

5.1.4 LS-RAPID Simulation for the Leyte Landslide

The most important parameter is the steady-state shear resistance (τss). The steady-state shear strength is very low as less than 10 kPa in Fig. 50. The testing condition is 100% saturation and the loading stress corresponding to 35 m deep much shallower than the real landslide: 120–200 m). DPRI-6 planned to test normal stress and pore pressure of 3000 kPa. However, the maximum testing normal stress in undrained state was 400–600 kPa. Therefore, testing was conducted below 400 kPa. 3000 kPa test can be conducted by ICL-2 by changing the normal stress loading system from the loading frame type such as triaxial apparatus to a new loading structure without the loading frame which is explained in 3.2.2 and Figs. 9 and 10.

Because the testing condition (35 m) is much shallower than the real landslide and the used sample may be more weathered than that in this deep landslide body, we selected τss = 40 kPa as a practical value for this landslide.

Various combinations of values of factors can be considered. It is not easy, but we assumed the followings: The landslide is deep and the material seems to be intact in the source area as seen in Fig. 47. Then, we estimated that the peak friction and peak cohesion before motion in the source area should be high (tan ϕp = 0.9, cp = 100–300 kPa); the part of head scarp shown in Fig. 47 would be not saturated because it is close to the ridge, probably there is less ground water to generate excess pore water pressure. Then,

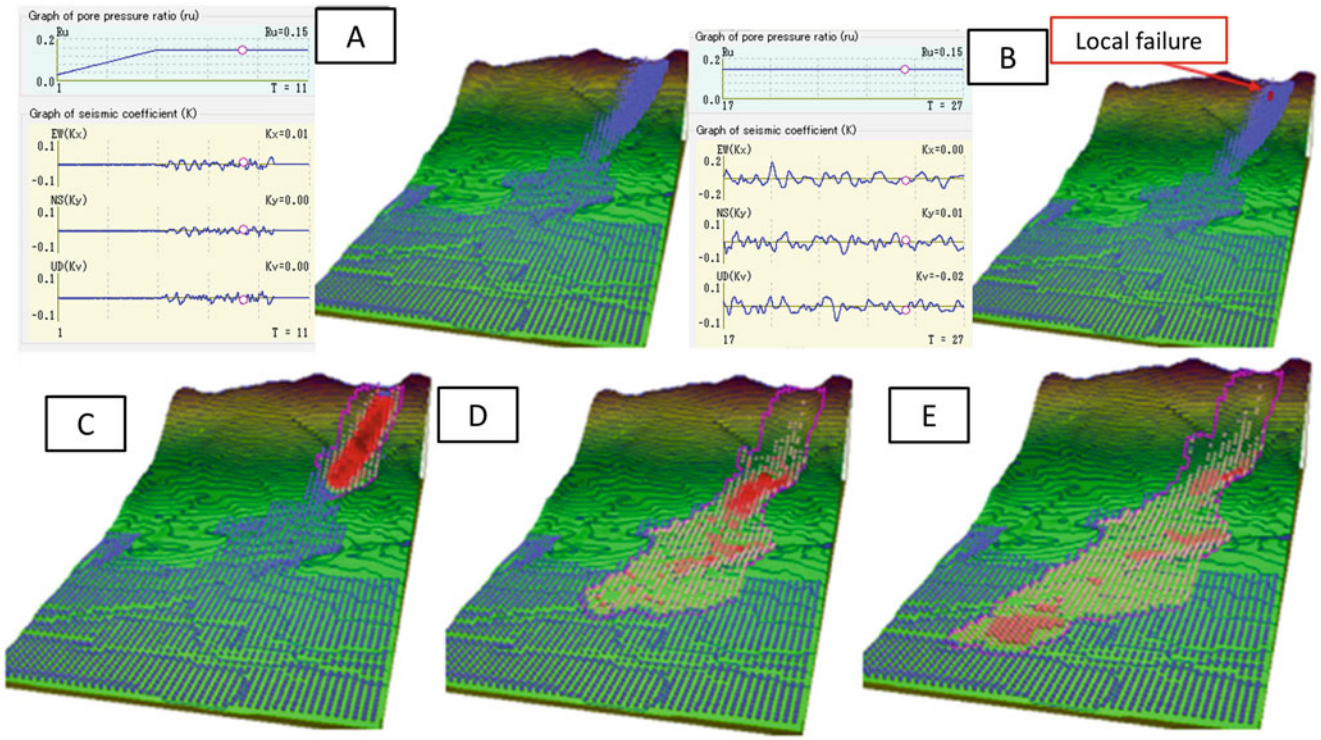

Fig. 51 Simulation result of the initiation and the motion of the Leyte landslide by LS-RAPID. 1 Mesh, 40 m; Area, 1960×3760 m; Contour line, 20 m; 3 m unstable deposits in the alluvial deposit area (blue balls)

Bss = 0.1–0.2 was given in this area, and the middle part was probably more saturated (Bss = 0.4–0.6) and the lower part in the paddy field on the flat area was probably well saturated (Bss = 0.9–0.97); The landslide body was stiff in the top, and moderate in the middle and much disturbed in the lower part and on the flat area (lateral pressure ratio k = 0.2–0.7).

Various magnitude of seismic shaking using the wave forms of EW, NS, and UD recorded at Maasin, Leyte were given in addition to pore pressure ratio of 0.15. The border to create a rapid landslide existed between seismic coefficient $K_{EW} = 0.11$ and 0.12. Then, we gave $K_{EW} = 0.12$. We used the ratio of magnitudes of seismic records of EW, NS and UD, $K_{NS} = K_{UD} = 0.061$. The seismic shaking of three directions of EW, NS and UD were given in this simulation. A 3 m unstable deposit was assumed in the alluvial deposit area. Blue balls shown in Fig. 51a–e are the unstable soil deposits (initial landslide body) in the source area and also unstable deposits in the alluvial flat area. The critical height ($\Delta hcr = 0.5$ m) to reduce shear strength from peak to the steady state was given.

A series of motion (a–e) was presented in the case of $K_{EW} = 0.12$, $K_{NS} = K_{UD} = 0.061$, $r_u = 0.15$ in Fig. 51.

a: ru rises to 0.15 and earthquake will start but no motion.
b: Continued earthquake loading triggers a local failure within the source area as presented in red color mesh
c: An entire landslide block (red color block) is formed and moving
d: The top of landslide mass goes on to alluvial deposits
e: Termination of the landslide motion

The air photo taken from the chartered helicopter and the simulation results presented in 3D view from a similar angle are presented in Fig. 52. The travel distance and the major part of landslide distribution were well reproduced by LS-RAPID using landslide dynamics parameters which were measured by the undrained dynamic-loading ring-shear apparatus.

5.2 Large-Scale Landslides Triggered by the 2004 Mid-Niigata Earthquake, Japan

This landslide and its analysis of the initiation and the motion by the undrained ring-shear testing using the sample from the landslide and the integrated landslide simulation model (LS-RAPID) is introduced from the following paper.

This case study is a typical earthquake induced landslides. The sliding surface of this landslide was located between the sandy layer and a silt layer below it. Dynamic-loading ring-shear tests were conducted on soils taken from both sand layer and silt layer. Initially people thought that the sliding

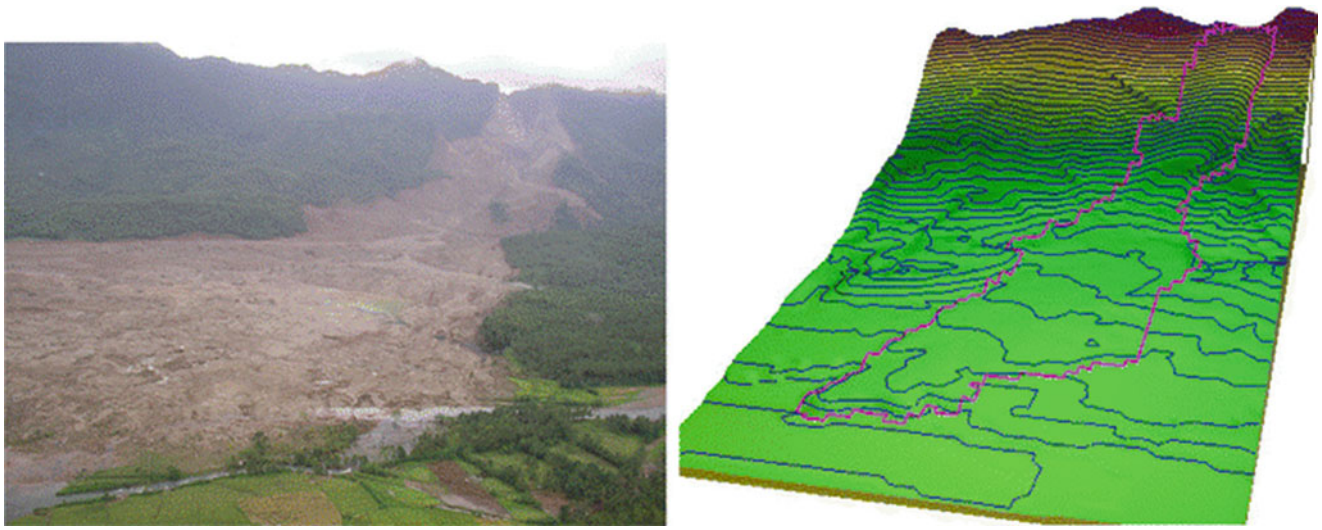

Fig. 52 Landslide moving area (photo-left and simulation result-right)

surface was formed in the outcropped silt layer after the landslide. However, the undrained cyclic and seismic loading tests revealed that silt layer is very strong against earthquake loading. The sliding surface was formed within the sand layer where the sliding-surface liquefaction occurred. This case study is introduced from the following paper.

Sassa K, Fukuoka H, Wang f, Wang G (2005) Dynamic properties of earthquake-induced large-scale rapid landslides within past landslide masses. Landslides 2:125-134

5.2.1 Outline of the Higashi-Takezawa Landslide

The 2004 Mid-Niigata Prefecture earthquake (M6.8) triggered 362 landslides more than 50 m wide, and 12 large-scale landslides of more than 1 million cubic meters, and the total volume of all landslides was about 100 million cubic meters. The area is the Tertiary landslide area in Niigata Prefecture. So many landslides exist in the Tertiary weathered mudstone (silt) area (Sato et al. (2004)). The behavior of the Tertiary landslides through the snowy period in Niigata Prefecture, Japan was reported by Niigata prefecture. https://www.jstage.jst.go.jp/article/jls2003/41/1/41_1_37/_pdf/-char/en

Those landslides were triggered by the snow melting water in the snowy area. The permeability of silt was very low. The slow and long-term water supply caused the landslide movement. By contrast, short-term strong rainfalls caused shallow landslide and debris flow.

Landslides triggered by the Mid-Niigata Prefecture were reactivation of past large-scale landslide masses. Two major landslides of the Higashi Takezawa landslide and its neighboring Terano landslide occurred within the previous landslide mass. As explained in this section, the sliding surface of this earthquake-induced-landslide was formed in the sand layer.

Figure 53 presents the view of the Higashi-Takezawa landslide. It created the largest landslide dam that has posed the risk of debris flow disaster by dam failure. The head scarp of the current landslide is shown on the figure by red arrows, and the head scarp of the previous landslide is shown by a curved line with red arrows. The building in the foreground was an elementary school. This landslide mass rapidly moved around 100 m, and hit the opposite bank of Imokawa River. A part of landslide mass spread cross the road and hit the school. We investigated the head scarp of this landslide. A very straight, gently-dipping (around 20 degrees) stiff silt (stone) layer outcropped as shown in Fig. 53. This layer seemed to be a part of the sliding surface of this landslide. It is relatively impermeable and groundwater flowed over this stiff silt layer. The sand layer over this stiff silt layer was soft. It was probably a part of previously moved landslide mass.

The central section of the Higashi-Takezawa landslide is presented in Fig. 54a. The black line presents the ground surface before the landslide, and the green line shows the ground surface after the landslide. The mass A (red dots) and the mass B (black dots) are the unstable mass before the current landslide movement.

The initial average slope angle between P1 and P2 was around 14.6 degrees, and the average slope angle between P1 and P3 was around 13.5 degrees. The mobilized energy line between P1 and P4 (highest point) was around 7.5 degrees. Hence, this rapid landslide occurred in a gentle slope less than 15 degrees, and the mobilized average apparent friction angle during motion was 7.5 degrees. The large difference between the energy line and the center of gravity of the moving mass suggests a rapid motion. Block A initially

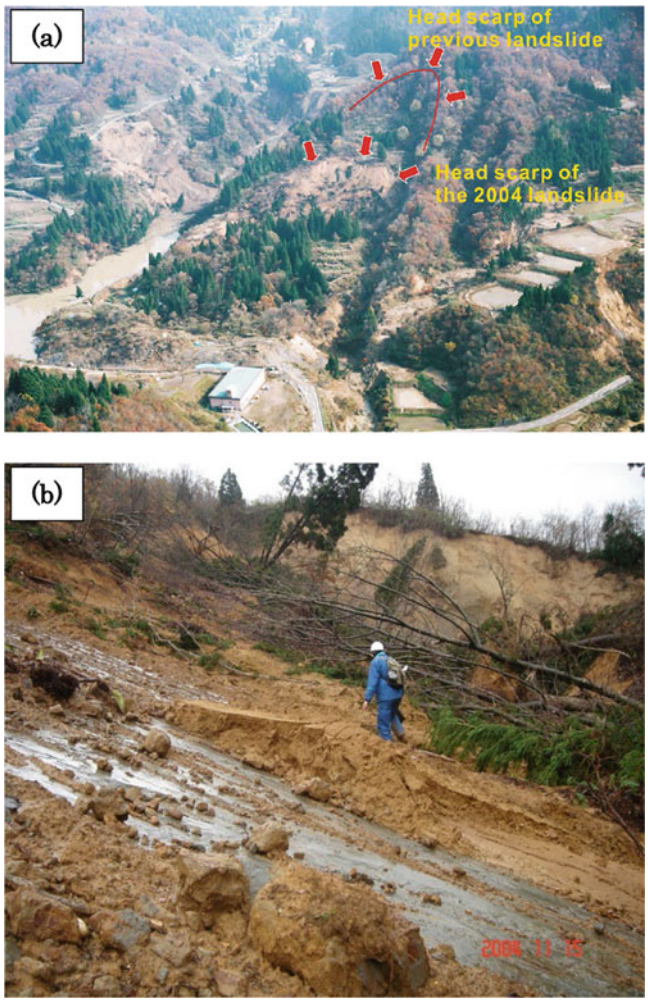

Fig. 53 Photos of the Higashi-Takezawa landslide triggered by 2004 Niigata-ken Chuetsu Earthquake. (**a**) A Photo of the general view of the landslide taken from the chartered helicopter (K. Sassa). The earthquake-induced landslide occurred within the previous landslide. (**b**) Photo of the exposed silt stone layer under the sand layer in the source area. The slope is gentle. And the silt-stone layer was hard to take sample. The undrained ring shear test was conducted on the silt taken from the nearby Terano landslide

started to move due to seismic loading and resulted in excess pore pressure generation. Thus, the movement of block A imposed an undrained loading to block B. This undrained loading effect can be greater than earthquake loading for the Block B. Then, the block B started to move with the block A and crossed the Imokawa River and hit the opposite bank. Mud found on the wall of elementary school was jumped from the landslide mass due to the strong impact between the rapid landslide mass and the river embankment. Figure 54b shows the section of the Terano landslide.

The main body of the landslide block at the toe was composed of sands (T1) that seem to be similar to the samples of H1 and H2 of the Higashi-Takezawa landslide. The head scarp of this landslide was also investigated, and in contrast to the Higashi Takezawa landslide, the silt sample (T2) taken from the head scarp was well weathered and soft. The head scarp and sample T2 was inside the previously moved landslide mass as suggested by the section of Fig. 54b.

The grain size distributions of samples T1, T2 and H2 are shown in Fig. 55. Samples H2 and T1 are rather similar though sample T1 includes a slightly greater portion of finer grains. While silt sample T2 is quite different from samples T1 and H2, it is much finer than those sands.

Using the samples from the Higashi-Takezawa landslides (H2) and from the Terano landslide (Terano sand T1 and Terano silt T2), 1) a seismic-loading test was conducted on the H2 sample using the monitored earthquake record at the monitoring site NIG019 in K-NET (NIED), and 2) cyclic loading tests were conducted on the Terano sand and the Terano silt to investigate their undrained dynamic properties.

5.2.2 Seismic Loading Test on Sands from the Higashi-Takezawa Landslide

Seismic loading test was performed to simulate the initiation of the Higashi Takezawa landslide using the real monitoring record of the Mid-Niigata earthquake in the closest site. The monitored record was obtained from one observation station of K-NET (Kyoshi Net), which is the strong earthquake motion monitoring network by the National Research Institute for Earth Science and Disaster Prevention (NIED). K-NET is a system which sends strong-motion data on the Internet. The data are obtained from 1000 observatories (25 km mesh) deployed all over Japan. The nearest monitoring site to the Higashi Takezawa landslide is the observation station of NIG019 at Ojiya, around 10 km west of the Higashi Takezawa landslide, and WNW 7 km from the epicenter of the main shock. The Higashi Takezawa landslide is ENE 3.6 km from the Epicenter. The location of the epicenter is between the NIG019 and the Higashi Takezawa landslides, but closer to the landslide.

The real acceleration and its wave form that affected the Higashi Takezawa landslide cannot be known in detail as it is complex due to inter alia topography, geology, underground structure, and distance from the fault and the epicenter. Therefore, the monitored earthquake record in NIG019 was applied as the first approximation of input acceleration to the sliding surface. Using three components of acceleration records, normal stress component and shear stress component on the bottom of landslide were calculated based on the section of the Higashi Takezawa landslide.

Figure 56 presents the result of the undrained real-earthquake-wave loading test on the Higashi-Takezawa sand (H2).

The result of seismic loading of the sample was presented as the time series monitoring result of loaded normal stress, mobilized shear resistance (not the same with the applied shear stress because failure occurred in the sliding surface

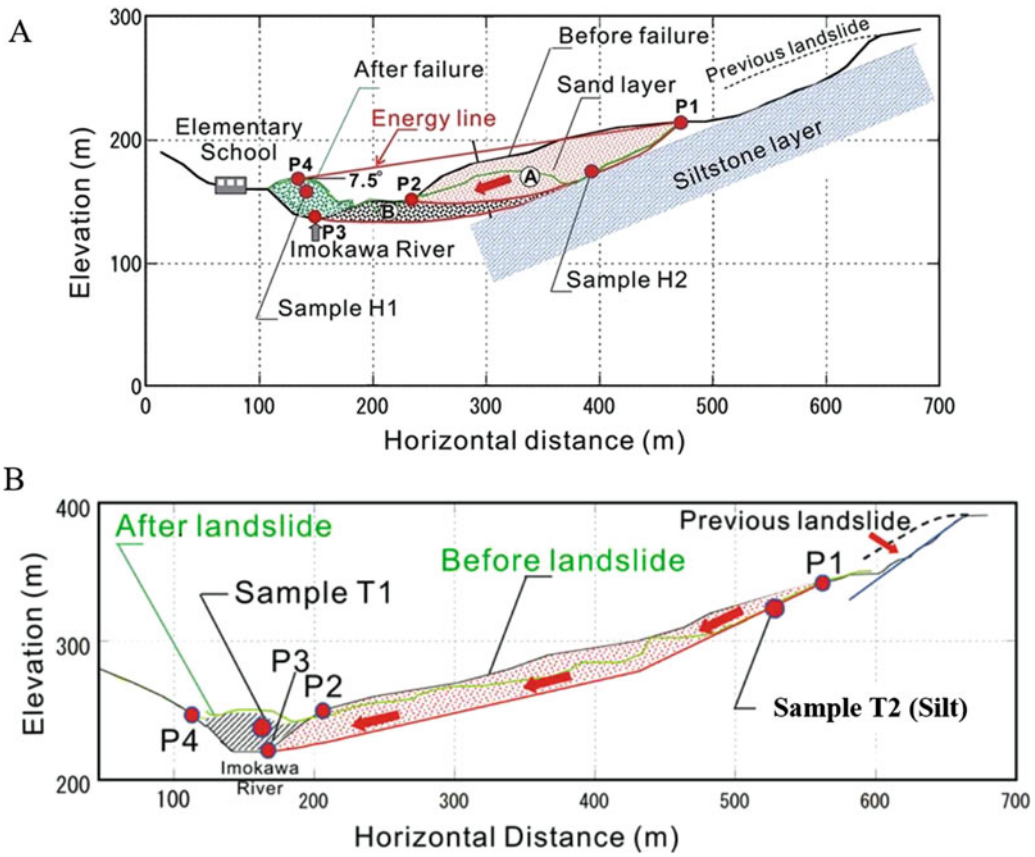

Fig. 54 Central sections of the Higashi Takezawa landslide (**a**) and the Terano landslide (**b**)

at the failure line), generated pore pressure and the resulting shear displacement as seen in Fig. 56a. Due to seismic shaking, pore water pressure was generated, then shear failure occurred and shear displacement started. As shear displacement progressed, a typical sliding surface liquefaction phenomenon occurred, namely grain crushing along the shear zone proceeded and a higher pore pressure was generated with progress of shear displacement. The sand was originally a marine deposit and much stronger than volcanic deposits such as pyroclastic flow deposits and pumice, and also weathered granitic sands. However, the shearing stress under 40 m overburden pressure was high enough to cause grain crushing and resulting volume reduction. It caused sliding surface liquefaction. The mobilized apparent friction angle was only 2.5 degrees at the steady state.

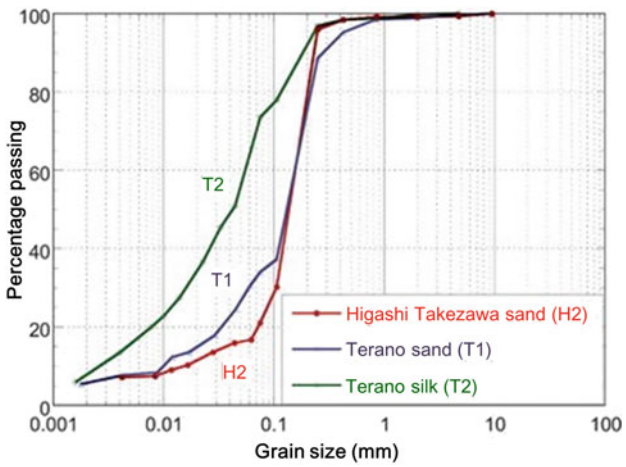

Fig. 55 Grain size distribution of the tested soils

The stress path of the test is shown in Fig. 56b (in which a red color stress path shows the effective stress path and a green color stress path presents the total stress path). The apparent friction angle was obtained from the ratio of mobilized steady state shear resistance divided by the initial normal stress. The effective friction angle mobilized in the post failure process is not so clear in Fig. 56b because seismic stress was reproduced by the undrained ring-shear test, but pore water pressure monitoring was delayed due to the permeability of soils. Therefore, instead of real seismic loading, cyclic loading test (1 Hz: 1 cycle/s) was conducted on the same sample. In this test, normal stress was kept constant. The effect of the loaded normal stress was cancelled by the generated pore water pressure at the undrained state. The cyclic shear stress was loaded. The test result is presented

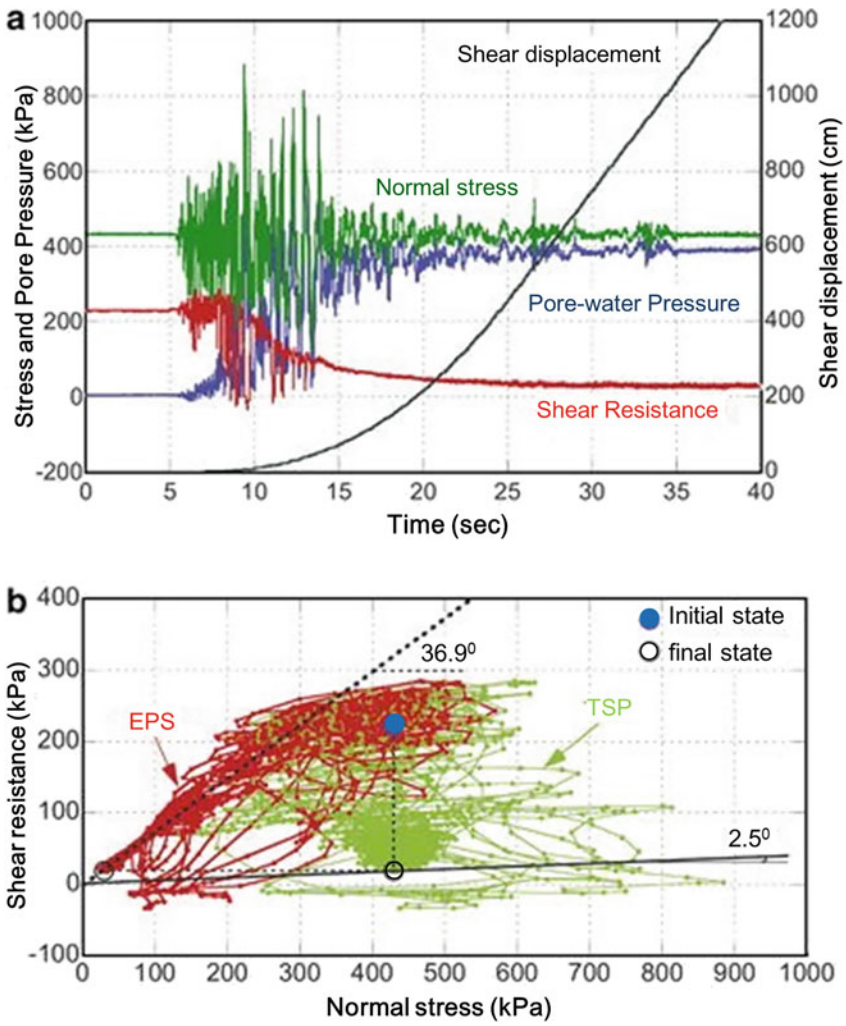

Fig. 56 Undrained real-earthquake-wave loading test on the Higashi-Takezawa sand (H2) (BD = 0.98). (**a**) Time series data, and (**b**) Stress path

in Fig. 57. In this 1 Hz test, pore-pressure monitoring can follow the shear stress change. 1 Hz cyclic shear stress can be seen in Fig. 57a time series data and also in Fig. 57b stress path data. From the stress path data, we can know that the friction angle during motion of this sample was 36.9 degrees.

5.2.3 Cyclic Loading Tests for the Sand (T1) and Silt (T2) of the Terano Landslide

In order to investigate the landside dynamics behavior of the sand layer and the silt layer, we took sample from the sand layer (T1) and the silt layer (T2) in the same Terano landslides. Sample position is shown in Fig. 54 Central sections of the Terano landslide (b). The grain size distributions of both samples are shown in Fig. 55.

Test results are presented in Fig. 58 for the sand sample (T1) and in Fig. 59 for the silt sample.

During the test, normal stress was kept constant, and shear stress of sine curve of 1 Hz loading frequency was applied. The shear stress was increased step by step until 15 cycles. All test conditions were the same for T1 sand and T2 silt.

The peak friction angle of the sand sample was 38.4 degrees, and the friction angle during motion was 35.7 degrees.

In the test of T2, no pore pressure was generated through the test. The stress path only vertically moved. The peak friction angle was 33.3 degrees.

The shear displacement in the sand acceleratedly increased after failure and even after the termination of cyclic loading. The apparent friction angle in the steady state was 3.8 degrees. By contrast, the shear displacement increased step by step during the cyclic loading test, but the movement stopped after cyclic loading. Shear resistances before loading and after loading were the same (around 100 kPa).

From these two tests, the following is estimated.

In the snowy period, pore pressure gradually increased. When the stress path reached the peak failure line of 33.3 degrees, landslide motion was initiated. The peak failure line

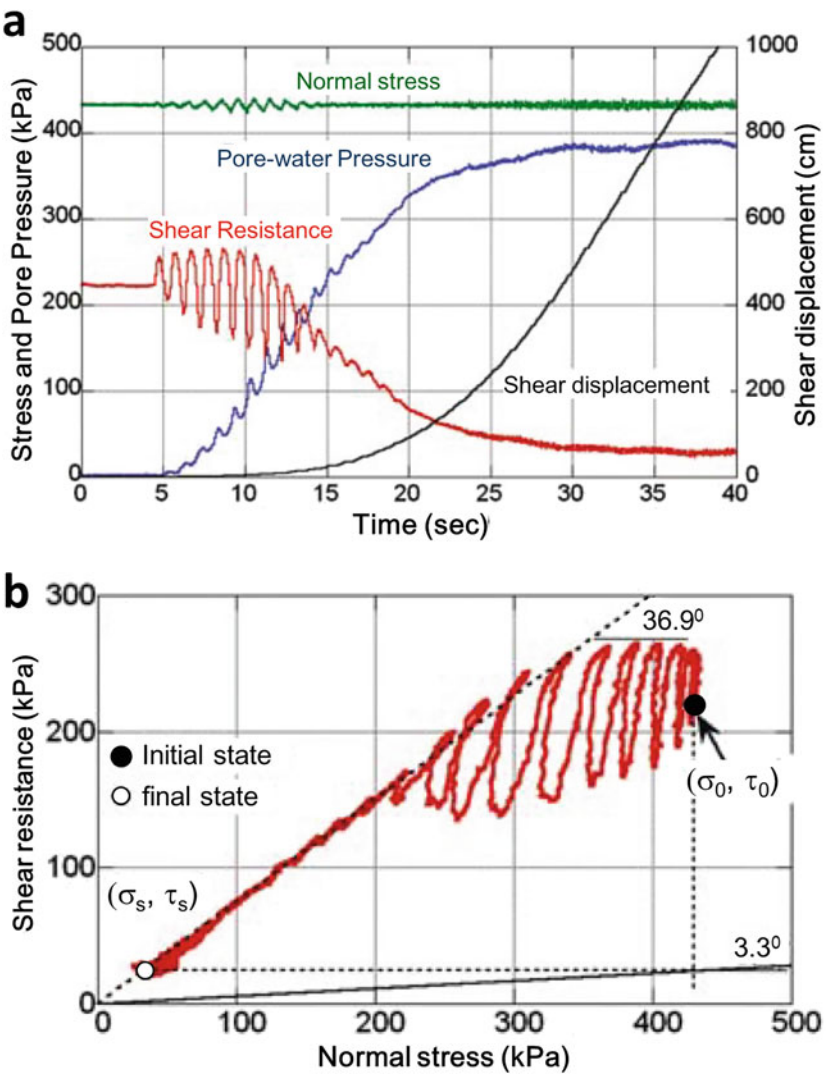

Fig. 57 Undrained cyclic loading test of the Higashi Takezawa sand (H2) ($B_D = 0.98$). (**a**) Time series data, and (**b**) Stress path

of the sand layer was 38.4 degrees. This layer was stable during those pore pressure increases. In the tertiary mudstone area, sand layer and silt layers alternated.

During the earthquake loading, sand layer generated excess pore pressure due to grain crushing by seismic shaking. However, no excess pore pressure was generated in the silty layer. Then, the layer was stable during the earthquake.

Figure 54 presents the central section of the Higashi-Takezawa landslide and the Terano landslides. Landslide debris (mass) produced by snow-melting or rain triggered landslides moved by earthquake loading. The sliding surface was formed possibly in the border of sand and silt as seen in Fig. 53 (lower photo). But from a mechanical point of view, the sliding surface of this earthquake-induced landslides was formed in the sand layer (such as the bottom of the sand layer), and the sliding surface of the water-induced landslide was formed in the silt layer (such as the top of the silt layer).

5.3 Findings by the Investigation of Two Landslides

1. Two rapid major landslides triggered by the 2004 Mid-Niigata earthquake were investigated. Both created landslide dams on the Imokawa River.
2. Cyclic loading ring shear test on sands from the Higashi Takezawa landslide and the Terano landslide proved that both sands can be liquefied by the sliding surface liquefaction under 20–40 m over burden pressure. Since silt taken from the Terano landslide proved that the silt was not subjected to excess-pore-water-pressure generation by seismic/cyclic loading, and the shear displacement was only limited when the shear stress reached or exceeded the failure line, the movement stopped at the end of cyclic loading.
3. A dynamic loading ring shear test to simulate the HigashiTakezawa landslide using the monitored seismic record in Ojiya (NIG019) on the sand collected from the

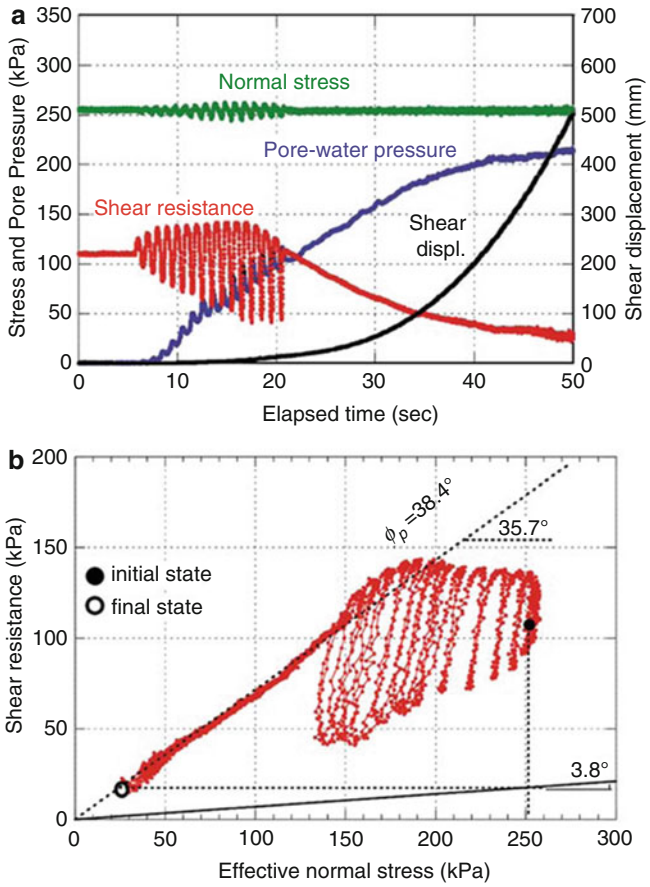

Fig. 58 Undrained cyclic loading test on the Terano sand (T1) (BD = 0.98). (**a**) Time series data, and (**b**) Stress path

head scarp of the landslide reproduced the initiation of rapid landslide resulting from the sliding-surface liquefaction. The mobilized friction angle at the steady state was only 2.5 degrees.

5.4 Hypothetical Submarine Landslides in Suruga Bay, Japan

The 2011 off the Pacific coast of Tohoku Earthquake so called the 2011 Tohoku earthquake (Mw 9.0) occurred. The magnitude of this earthquake was Mw 9.0; it was the largest in the Japanese earthquake monitoring history. This earthquake induced an enormous tsunami which caused major disasters along the north-eastern coast of Japan. Another big earthquake was concerned along the plate boundaries such as the Nankai Trough. This section is devoted to possible contribution from landslide scientists to this type of mega-disaster. The paper was published in the following.

1) Sassa K, He B, Miyagi T, Strasser M, Konagai K, Ostric M, Setiawan H, Takara K, Nagai O, Yamashiki Y, Tutumi S (2012) A hypothesis of the Senoumi submarine megaslide in Suruga Bay in Japan—based on the undrained dynamic-loading ring shear tests and computer simulation. Landslides 9:439–455

Coastal and submarine landslides can cause tsunami. The submarine landslides in Suruga Bay should have caused big tsunami and also may cause big tsunami in the future. It was presented on the World Tsunami Awareness Day Special Event on 5th November 2021 at the Fifth World Landslide Forum in Kyoto, Japan. It was published in the following paper by Springer Nature in 2021

2) Doan Huy Loi, Kyoji Sassa, Khang Dang, and Toyohiko Miyagi (2021) Simulation of Tsunami Waves Induced by Coastal and Submarine Landslides in Japan. Understanding and Reducing Landslide Disaster Risk. Vol.1 (edts: Sassa K, Mikos M, Sassa S, Bobrowsky P, Takara K, Dang K): 295–327.

5.4.1 Area of Investigation

The Nankai Trough (Fig. 60) is characterized by destructive earthquakes that recur along the plate boundary megathrust where the Philippine Sea Plate subducts under SW Japan. The authors examined 250 m mesh bathymetry of the sea floor along the Nankai Trough from Kii Peninsula to Izu Peninsula. Many submarine slope deformation features are seen there. Some are similar scale with the Senoumi feature (shown in Fig. 61). However, the social significance is the highest in the Senoumi case because the head scarp is located at the coast of densely populated Yaizu city which Japanese transportation arteries (the Shinkansen and the Tokyo–Nagoya highway) pass through.

White circles in Fig. 60 mark gullies identified due to their distinctive shape. The Senoumi forms a step on the western side of the Suruga Bay with a gully (Fig. 61). The section A-A′ passing through this gulley is shown in the right-side figure of Fig. 61. The slopes in the steep parts of the head scarp and toe in the section A-A′ are 8–12°. The Senoumi Megaslide hypothesis was made from the following consideration of this feature.

The shape of the Senoumi feature differs from those of most landslides: the exit to the Suruga Trough is very narrow, relative to the width of Senoumi depression. If it would be formed by a blockslide, its mass could not move out through this narrow exit. However, when a large strength reduction occurs within the soil mass after failure, this type of feature can be created (such as quick clay landslide in Norway: Photo is shown in Sassa et al. 2012). This shape is possible to occur when landslide mass is almost liquefied after failure and move/flow downward with a very small shear resistance while the landslide expands upward retrogressively. This

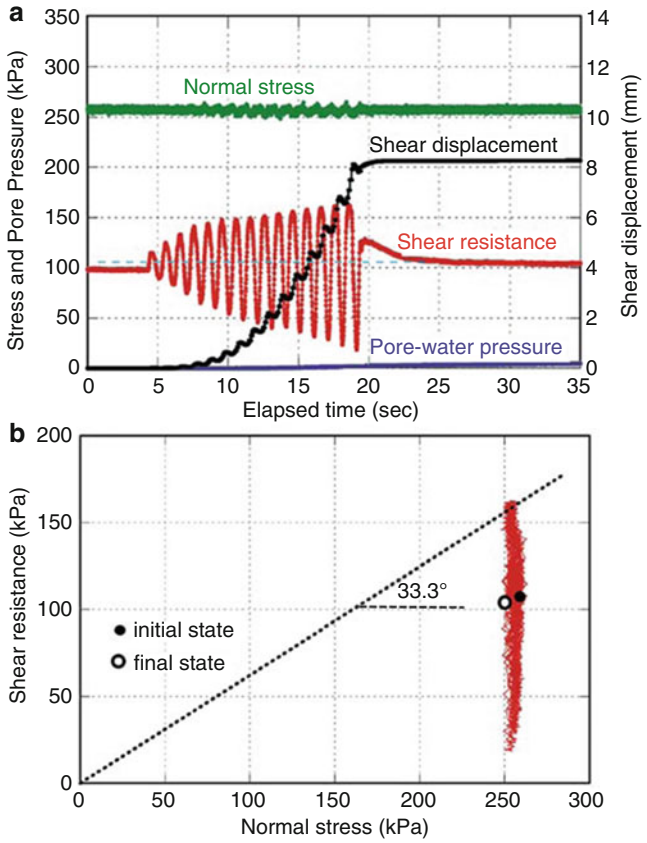

Fig. 59 Undrained cyclic loading test on the Terano silt (T2) ($B_D = 0.98$) (**a**) Time series data, and (**b**) Stress path

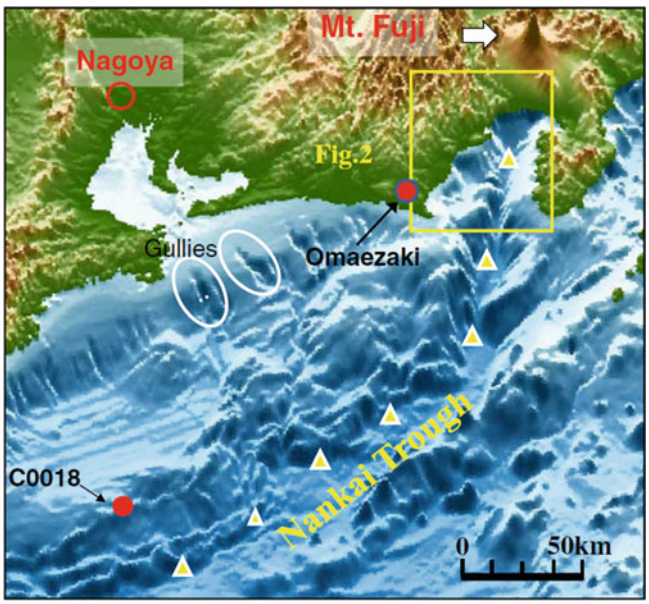

Fig. 60 Location of investigation area and drill sites. Empty triangle: Nankai Trough, yellow square the target area of Suruga Bay, red circles two sampling points (C0018 drilling site of the IODP-Expedition 333 and the Omaezaki hill)

area must have been disturbed by tectonic movements and shear bands must develop near the border (Nankai trough-Suruga trough) between the Eurasian Plate and the Philippine plate. Many mega-landslides as well as mega-earthquakes often occur near the borders of plates, because the fractures of rocks and soil layers reduce strength of the layer and the ground water flow through the fractures may provide excess pore water pressure and promote weathering of the layer.

Both sides of Suruga Trough (Omaezaki hill and Izu peninsulas) are composed of the Neogene layers. The base of the Senoumi area is likely formed by Neogene layers. The soil layer of the Senoumi area before landslide can be deposits transported by the Oi River. We sampled and tested Neogene soils taken from Omaezaki hill. The deposits may include Neogene deposits and also the volcanic ash. Then, we tested samples from Omaezaki shown in Fig. 62 and also volcanic ash taken from IODP drilling C0018 in Fig. 60.

Figure 62 presents the location of the Suruga Trough, the extension of Nankai Trough shown as the white line with a line of white triangles. This is the plate border. Because of high-stress, shear bands and fold structures parallel to the Suruga trough such as Izu Peninsula. The shear bands are often created in a set of two (parallel and perpendicular directions) directions. Oi River and the Gully along A-A' will be one of shear bands perpendicular directions of the Suruga Trough. The shear bands are crushed, therefore, those part are week and also pore-water pressure through shear band system from the higher elevation (Fig. 6 schematic figure of excess pore-pressure in continental shelf, in Sassa et al. 2012). Many similar gullies are found within the continental shelf in Fig. 60.

5.4.2 Sampling from Volcanic Ash by IODP Drilling

The depth of Senomi landslide is between 200 and 600 m. We plan to use a sample taken from a few hundred meters before the sea floor. Such a deep drilling in the sea floor is conducted by the Integrated Ocean Drilling (IODP). And drilled cores of IODP around Japan are stored in the Kochi Institute for Core Sample Research of JAMSTEC (Japan Agency for Marine Earth-Science and Technology). Sassa visited the Kochi Institute and searched the cores. One of the nearest IODP drilling site was C0018. The sampling way from a drilling ship and the drilling core and its geology. The pink color part at the bottom of MTD is volcanic ash. The photo of this volcanic ash layer, its grain size distribution and the microscopic photo are shown in Fig. 63.

This volcanic ash layer correlates to the "Pink" volcanic ash sourced from Kyushu Island, Japan and is dated to 0.99–1.05 Ma (Hayashida et al. 1996). Comparable volcanic ash layer as cored at IODP C0018 drill site are likely to have been deposited also in Suruga Bay, where no deep-drill hole is available yet. We therefore used a sample taken from this

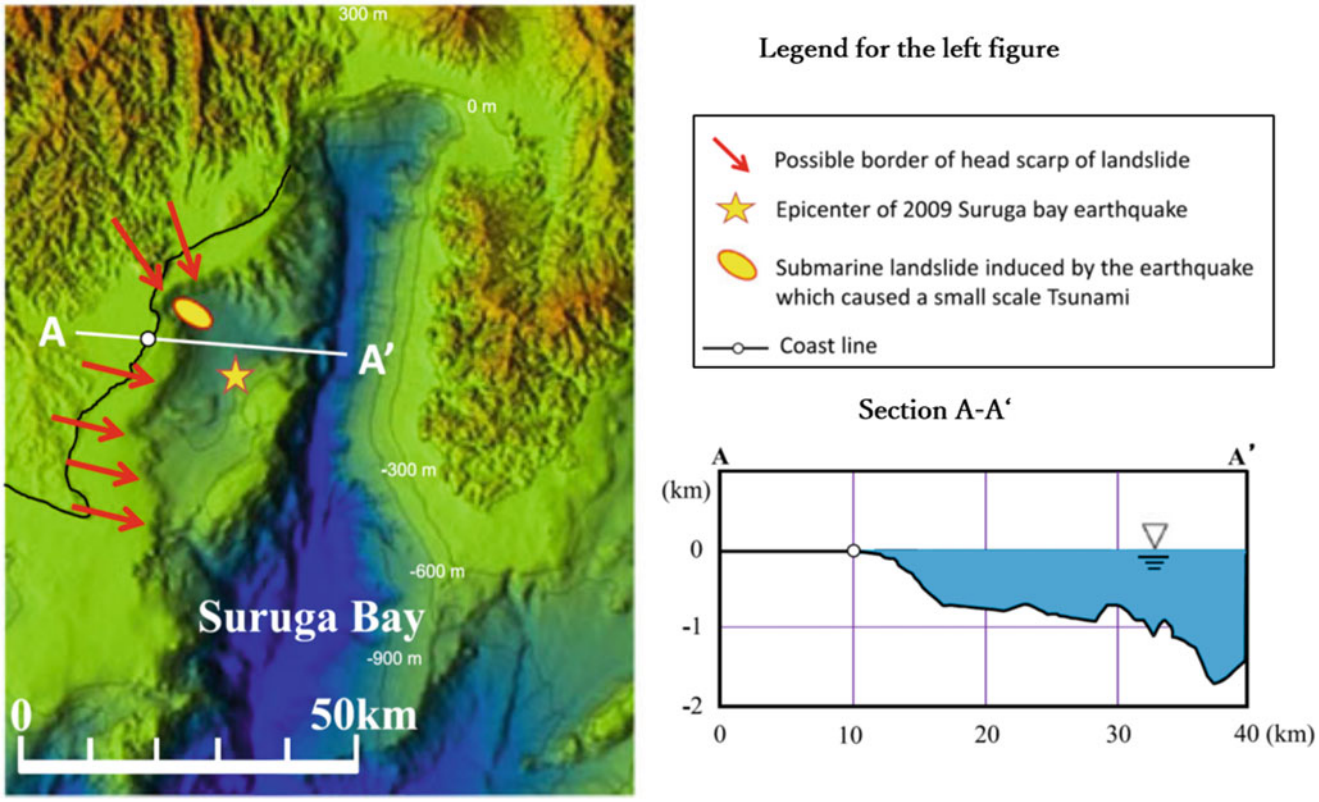

Fig. 61 A hypothetic mega-slide (the area called as Senoumi) in Suruga Bay. A characteristic bathymetric feature called as Senoumi-stone flower sea which is delineated by red arrows. This feature was possibly created by a submarine megaslide. Possible border of the head scarp of landslide, Epicenter of 2009 Suruga Bay earthquake, small submarine landslide induced by this earthquake, and the coast line are found in the left figure. The section of the A-A' crossing the hypothetic landslide the Suruga trough which is an extension of the Nankai trough

fine-grained volcanic ash layer at the base of landslides (MTD) drilled at IODP Site C0018 as analog material for potential Suruga Bay sliding surfaces and tested it by the undrained ring-shear apparatus. ICL-2 which can test 3 MPa was not yet developed. So, we tested this sample by ICL-1 which was developed in 2011 and is able to test until 1 Mega normal stress in the undrained cyclic-loading and seismic-loading condition.

We tested the Omaezaki silt and the Omaezaki sandy silt which were sampled from the Omaezaki hill in Fig. 62. The grain size distribution of three samples is shown in Fig. 64. The Omaezaki silty sand and the IODP volcanic ash are very similar in its grain size.

5.4.3 Undrained Basic Cyclic—Loading Tests

Cyclic-loading tests were conducted on IODP volcanic ash and Omaezaki sand and Omaezaki silt. Frequency is 0.1 Hz. Figure 65 presents the test result of cyclic-loading ring-shear tests of three samples: (a)—IODP volcanic ash, (b)—Omaezaki sand, (c)—Omaezaki silt. As the initial stress, we used the normal stress = 1000 kPa, the initial shear stress = 160 kPa. This is 160/1000 = 0.16. It is the slope angle = 9.09°. This angle corresponds to the slope of the central section of A-A' of the Senoumi hypothetic landslide (8–12°).

The shear stress was increased step by step in 10 cycles until 400 kPa increment (large enough to cause failure). Shear stress was gradually increased in 10 cycles. Then, a certain cycle of loading was kept constant to confirm pore pressure generation and decreased step by step. This procedure was decided by the preliminary tests to confirm to study shear failure, and post-failure strength reduction due to pore pressure generation until the steady state. When soils are fully saturated, effective normal stress should be constant in the undrained condition. Soils were regarded as in the undrained condition during earthquake loading because loading is very quick to dissipate generated pore pressure. Therefore, only shear stress was loaded, while normal stress was kept constant by means of automatic servo-control system.

The left column figures of Fig. 65 show the time series data. In this figure, the black color line shows normal stress, the red color line presents mobilized shear resistance, the blue line shows the generated pore water pressure, the purple line presents the resulted shear-displacement, and the green line shows the control signal to stress servo-control motor (stress control motor) by pre-decided computer program. The shear

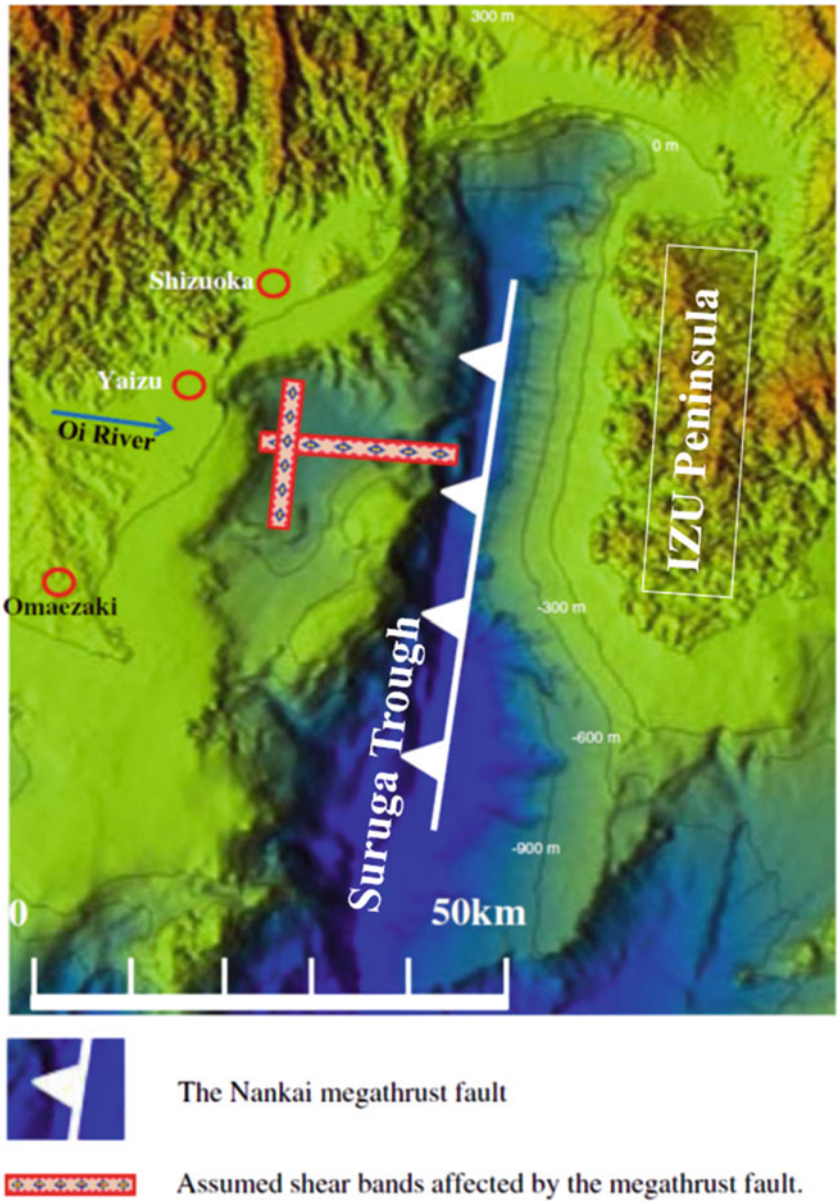

Fig. 62 Assumption of fracture zones in Senoumi. The deep-sea floor in the blue color is called as Suruga Trough which is a part of Nankai Trough

stress motor is to load the ordered stress. The control signal and mobilized shear resistance is the same until failure. However, after failure, power provided by servo-control motor is spent for frictional energy consumption and acceleration. The mobilized shear resistance after failure gets smaller than the control signal.

The right column figures show the stress path of total stress (blue line) and the effective stress (red line). The total normal stress is kept constant, while the effective normal stress is shifted by the generated pore water pressure. When the stress path reached the peak failure line, failure occurred. The following findings are obtained from these test results.

1. IODP volcanic sand generated a high pore-water pressure during cyclic loading, and strength reduction was the largest. The shear speed was accelerated to the maximum speed of ICL-1 (5.4 cm/s) and the planned 3–5 m shear displacement was reached. Then, shearing was stopped to avoid ablation of rubber edge. The mobilized steady-state shear strength was 72 kPa (shear displacement curve is seen in Fig. 66). Pore pressure ratio reached 0.8 (normal stress = 1000 kPa, pore-water pressure = 800 kPa). The peak friction angel was 36.2°.
2. Neogene silty–sand also generated a high pore-water pressure. The shear speed was accelerated after failure, but it decelerated after the stop of cyclic loading. The control-signal corresponding to 160 kPa (shear stress due to the self-weight of soil layer) was close to the steady-state shear resistance. The difference between stress and shear resistance will create acceleration. Therefore, no

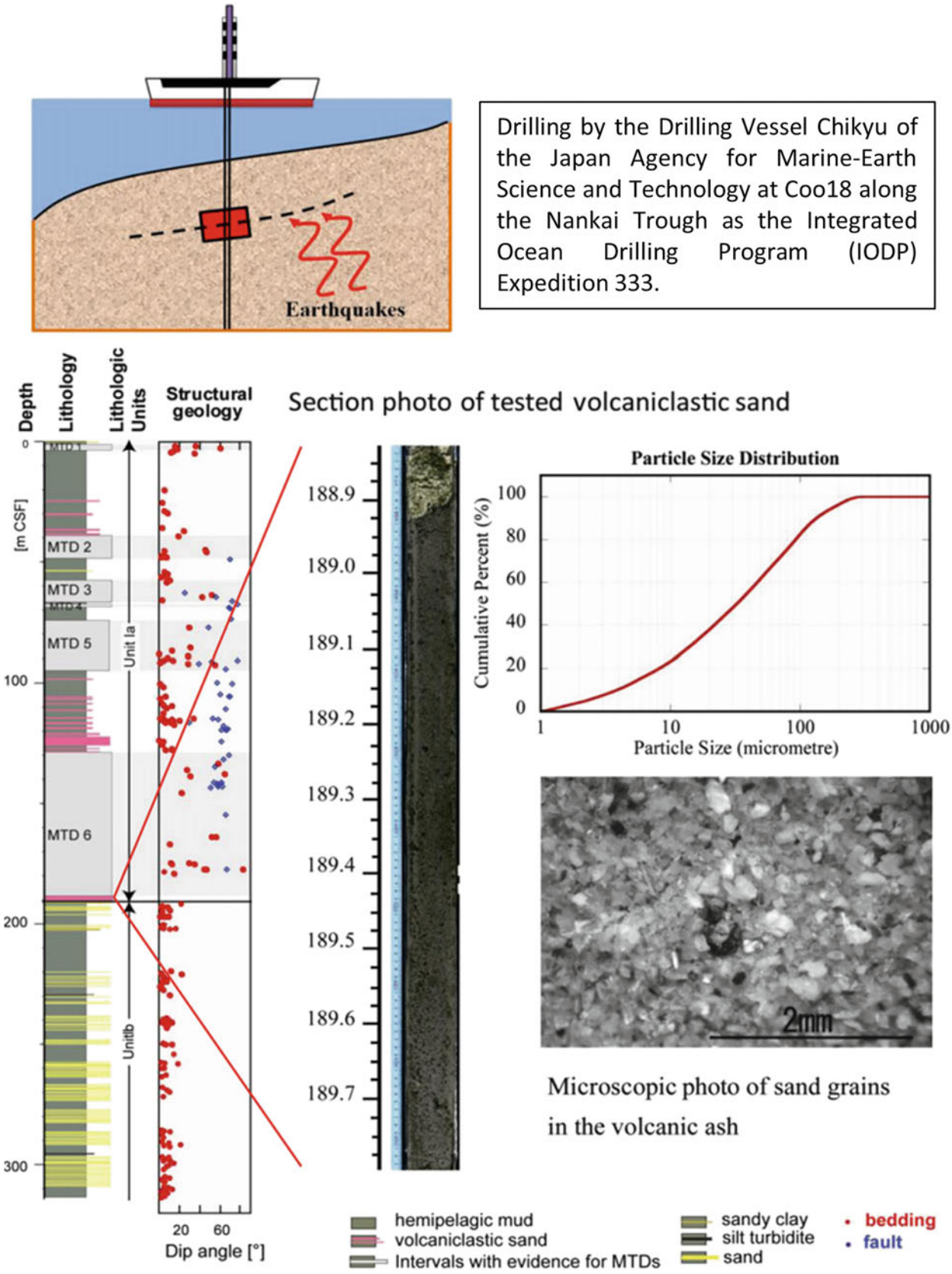

Fig. 63 IODP drilling and the core of sample of the volcanic ash in around 189 m in which a sliding surface was formed

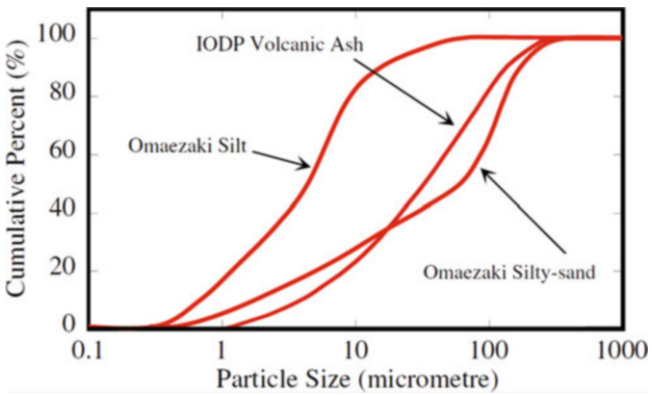

Fig. 64 Grain size distribution of IODP volcanic ash, Omaezaki silt, and Omaezaki Silty-sand

acceleration occurred after the stop of cyclic loading. The peak friction angle was 39.5°. It is the greatest value in these three soil samples.

3. Neogene silt failed at a lower peak shear resistance comparing to two other samples. Pore pressure generation during cyclic loading was small. Shear displacement occurred step by step during cyclic loading after failure, but it stopped in the decreasing cycles at around 600 mm. The peak friction angle was 36.8°.

5.4.4 Seismic-Loading Tests Using the 2011 Tohoku Earthquake Wave Record

We planned to investigate the landslide dynamic characteristics of the IODP sample subjected to the strong earthquake of the 2011 Tohoku Earthquake record by the undrained dynamic loading ring shear apparatus.

Figure 67 shows three components of seismic record of 2011 Tohoku Earthquake. The largest measured earthquake acceleration 2933 gal as the resultant acceleration of EW, NS, and UD components and 2699 gal as a single component were recorded at station MYG004 at Tsukidate in Miyagi Prefecture which is 176 km west from the epicenter. Since mega earthquakes similar to the 2011 Tohoku earthquake occurred in the past and, likely, will occur in the future. The seismic record of NS component of MYG004 was used for the ring shear simulation test as an example of mega earthquake loading.

Examination of loading shear stress

We examined the testing plan of seismic loading ring shear test based on the result of cyclic loading test of Fig. 65a, b. Initial normal stress and shear stress were decided to be the same with those of the cyclic loading test, namely 1000 and 160 kPa, which represented the normal stress and shear stress due to gravity on a slope of 9.09° which corresponds to the slope angle of A-A' section in Fig. 61. According to the test of Fig. 65, additional 400 kPa of shear stress may fail the sample. So, we used 0.3 times of MYG004 (2699 gal in NS component wave), namely the maximum acceleration 810 gal in this ring shear simulation test. The same value was recorded in FKS009 in Ono of Fukushima Prefecture (217 km from the epicenter).

Examination of loading duration

The test of Fig. 65 was conducted at 0.1 Hz. The servo-shear stress control motor (400 W) of ICL-1 (we did not yet produce the powerful ICL-2) cannot reproduce the high-frequency loading using the recorded data (Fig. 67). Preliminary tests were conducted to investigate the time required to reproduce the seismic wave form of MYG004 by increasing the shaking time by factors of 10, 20, and 30. We found that a 30-fold increase in time scale could reproduce shear stress changes similar to the recorded wave form. The ring shear test was conducted under the undrained condition. Pore pressure value was not affected by time because any of pore pressure dissipation did not occur. The same stress path would be obtained in 30 times longer test with that in the real time test. The comparison of the monotonic (corresponding to 0.0 Hz) undrained shear stress loading test and 0.2, 0.4, and 1.0 Hz cyclic undrained shear stress loading test presented almost the same relationship between stress and shear displacement and also almost the same stress path between the curve of monotonic loading test and the curve connecting peak values of cyclic loading test (Trandafir and Sassa 2005). Then, the test was conducted in the 30 times longer time period.

Results of undrained dynamic-loading ring-shear tests using the 2011 Tohoku earthquake wave form

Figure 68 presents both of seismic loading test results, the left figure for IODP volcanic ash and the right figure for Omaezaki Neogene sand. The IODP ash generated a high pore-water pressure in the first main shock. The large shear displacement started in the second main shock and an accelerating motion was created. Namely, this ring-shear simulation test visualized that a rapid landslide would be triggered on 9.09° slope, while the Neogene sand generated a smaller pore water pressure during the first main shock. A large pore water pressure was generated at the second main shock and a rapid motion was started. But when the level of seismic loading got smaller, the movement was decelerated. It is similar to cyclic loading test of Neogene sand (Fig. 65). The Neogene sand has a greater peak friction angle (39.5°) than that of IODP volcanic ash (36.2°). The Neogene sand did not fail during the first main shock; therefore, the soil mobilized the same value of shear resistance with the loaded shear stress. As seen in Fig. 68b, the green line (control

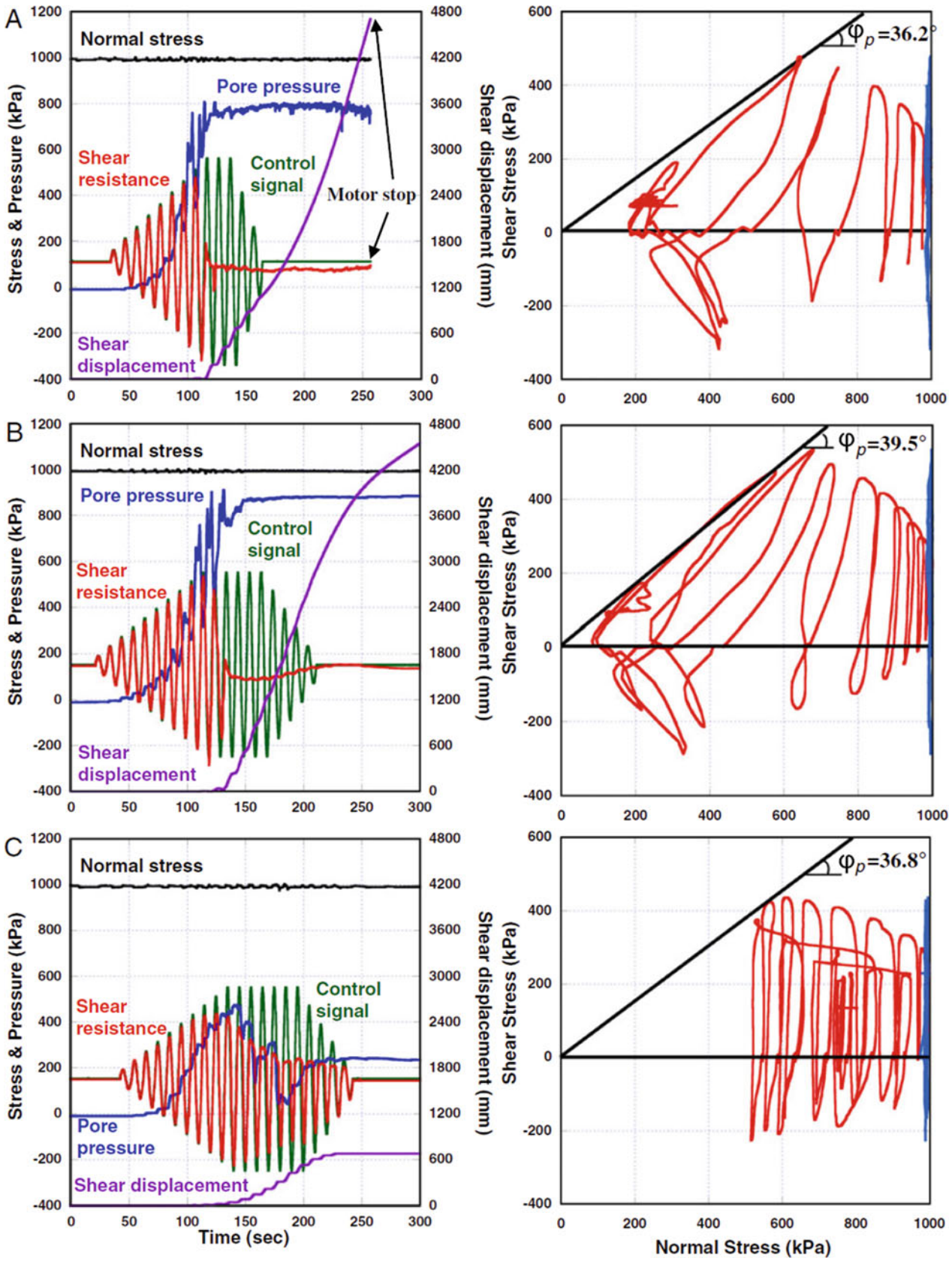

Fig. 65 Result of undrained cyclic loading tests. (**a**) IODP volcanic ash, (**b**) Omaezaki Neogene sand, (**c**) Omaezki Neogene silt

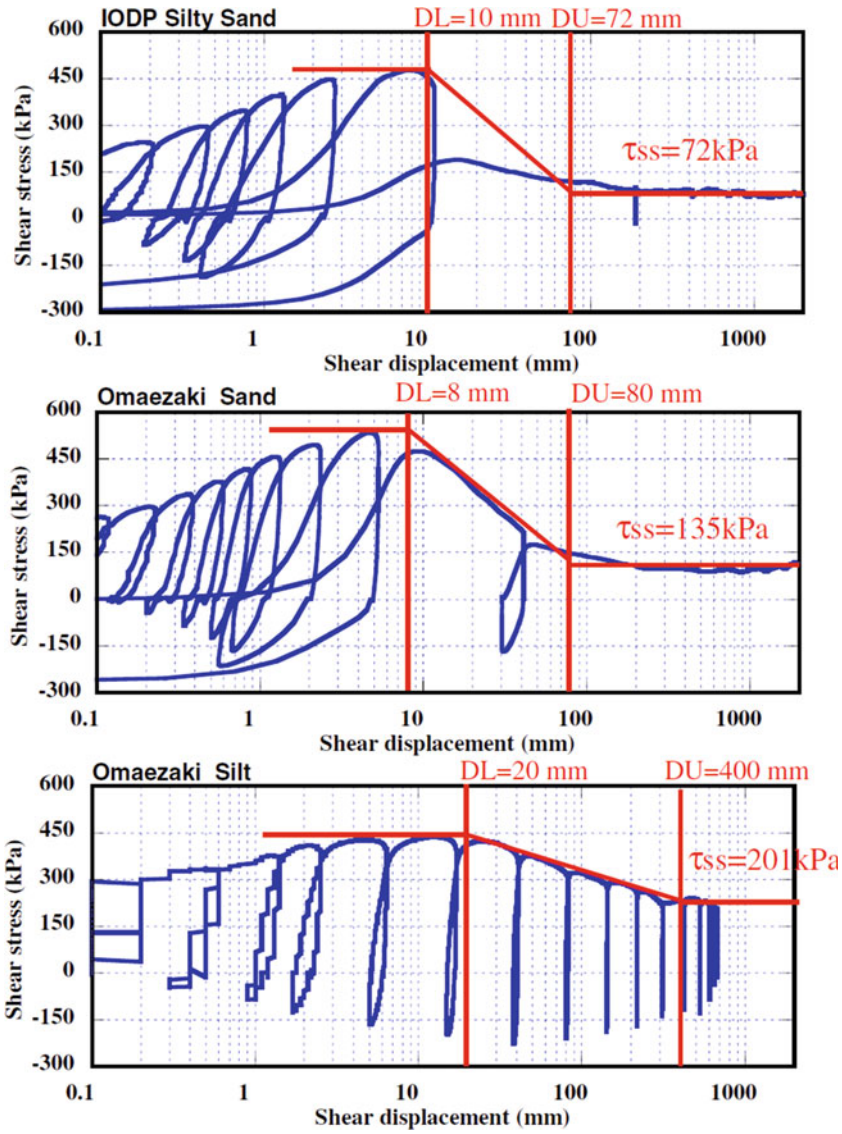

Fig. 66 Shear stress–shear displacement curves of the cyclic-loading ring shear tests on IODP silty sand (ash), Omaezaki sand, and Omaezaki silt

signal) and the red line (mobilized shear resistance) are overlapped until the second main shock. From this ring shear test, slopes with the same or greater angle than 9.09° will fail by 810 gal of earthquake having the same wave form as that of MYG004. Neogene sand will move by this seismic loading, but the movement will stop after seismic loading. The relationship is very similar to the cyclic loading test in Fig. 65.

5.4.5 Reproduction of the Movement of the Hypothetical Senoumi Landslide by LS-RAPID

We have prepared Fig. 69 to implement LS-RAPID.

(a) Firstly, we estimated the ground surface before the landslide
(b) Current elevation of the ground and the sea floor. Red zone was the estimated initial landslide mass caused by pore-pressure supplied through T-shape shear bands (Fig. 62, red colored cross shape part)
(c) The difference of both elevations, namely landslide mass.

Figure 70 presents LS-RAPID simulation result. Blue colored cells are no motion. Red colored cells are moved parts.

(a) A red color block MJ (major landslide) moved at the fist shock. (b) The initial landslide block (MJ) progressively expanded to the south (downward) and the landslide started to enter into Suruga trough. (c) Flowed out landslide mass moved downward along the Suruga trough. (d) Landslide debris moved out to Suruga trough.

The simulation result for IODP volcanic ash using 1.0×MYG004 seismic record is shown in Fig. 70. Blue balls represent soil columns stable or less than 0.5 m/s moving

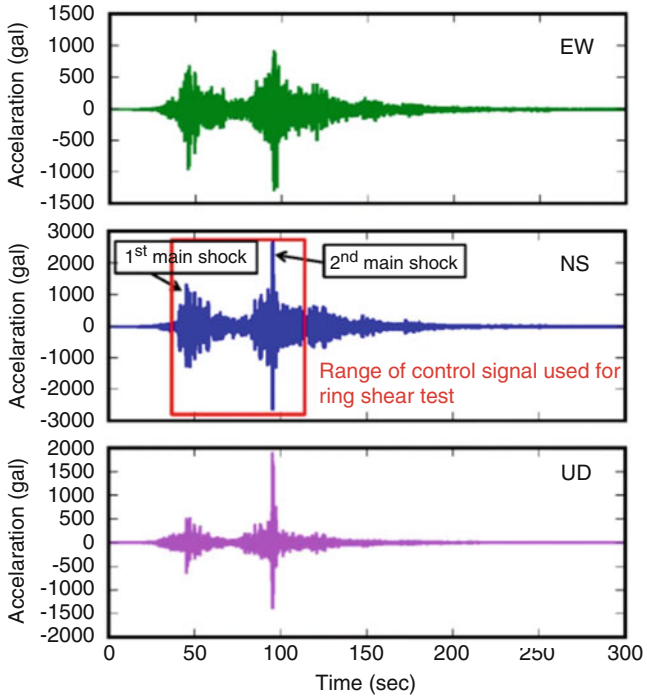

Fig. 67 2011 Tohoku earthquake record (MYG004)

velocity. Red balls show columns with values greater than 0.5 m/s velocity. Figure 70a is the situation soon after the first shock. The first shock moved the excess pore pressure acting area (major landslide block, MJ) and failed a part of bottom-left red-colored area (minor landslide block, MN). The left figure of Fig. 70a presents the pore pressure ratio (upper graph) and loaded acceleration (lower graph). Figure 70b shows the landslide moving area soon after the second main shock. All columns in the whole simulation area were subjected to movement with the velocity more than 0.5 m/s. Figure 70c is the instant of 400 s. Landslide mass is flowing down along the Suruga trough from north to south (see the vertical white arrow), while the part of bottom of the simulation area is moving to the Suruga trough (see the horizontal white arrow). Figure 70d shows the termination of movement at 4463 s (1.2 h) from the initiation.

Further application of this undrained ring-shear testing on the Senoumi hypothetic landslide

Based on the landslide simulation (LS-RAPID), we implemented the LS-Tsunami analysis (Sassa et al. 2016). The concept of LS-Tsunami is introduced in Fig. 100 of this article. The result was published in Loi et al. (2021). Figure 71 is a result of LS-Tsunami analysis by this Senoumi hypothetic landslide.

Figure 71a–h presents the propagation of the tsunami caused by the Senoumi landslide based on the ring shear test result (Fig. 65a) of the IODP Volcanic ash sample and the 1.0× Tohoku earthquake record (Fig. 67).

Figure 71a at 30 s shows the tsunami soon after the first shock. It appears to be only a local tsunami occurring in Suruga Bay. Figure 71b at 80 s shows the tsunami soon after the second shock. The negative tsunami heights are shown in blue and positive tsunami heights are in red. Tsunami waves expanded onto the opposite bank (Figure 71c). Figure 71d illustrates that the tsunami wave will hit the Fuji area, which is the third largest city in terms of population in Shizuoka Prefecture. Omeazaki area was attacked by tsunami

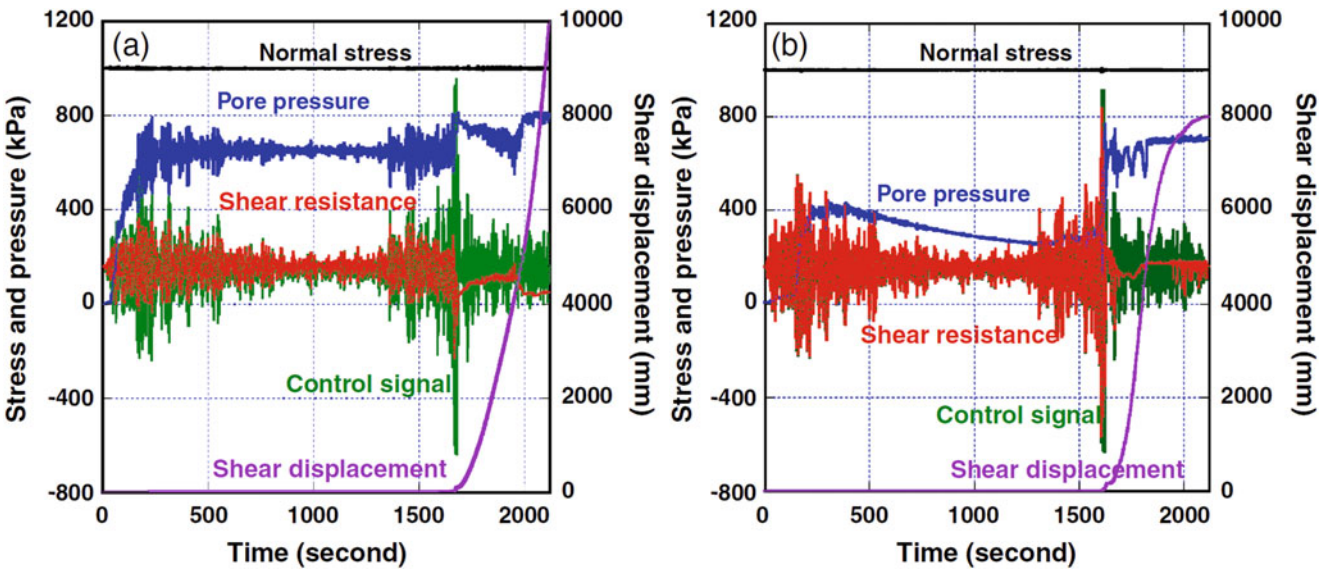

Fig. 68 Undrained seismic-loading ring-shear test using the 2011 Tohoku earthquake record wave form. Left (**a**): IODP Volcanic ash; Right (**b**): Omaezaki Neogene sand

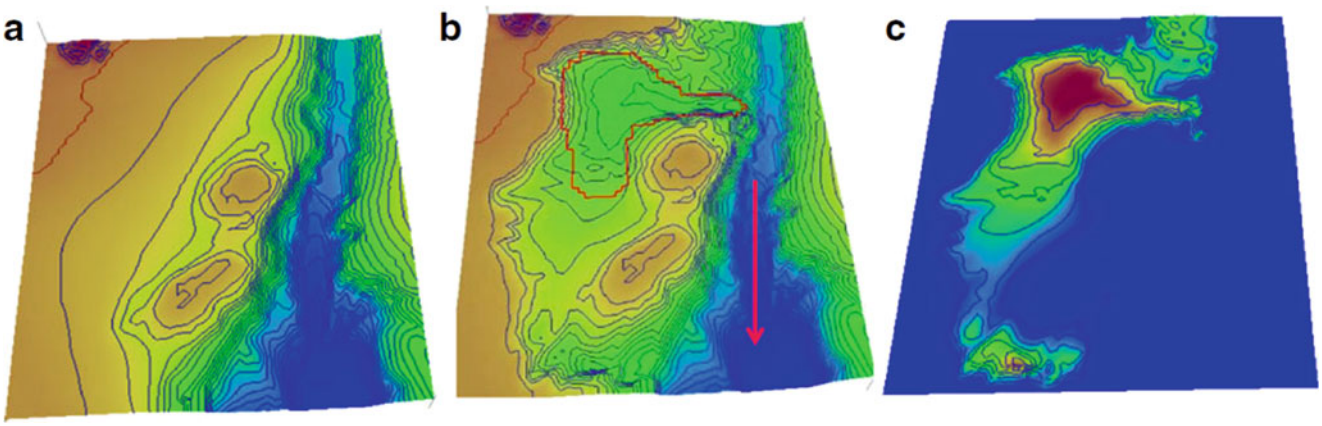

Fig. 69 Reproduction of the topography before the Senoumi landslide for LS-RAPID. (**a**) Elevation of the ground before the landslide. (**b**) Current elevation after the landslide. Red zone was the initial landslide mass caused by pore-pressure supplied through T-shape shear bands (Fig. 62). (**c**) Depth distribution of unstable mass (different between **a** and **b**)

wave at 860 s (Figure 71e). Figure 71f shows that tsunami reached the Ota River. Along the Ota River, four tsunami deposit layers were found in the excavation site (Fujiwara et al. 2019). The right figure on the bottom (Fig. 71h) at 5550 s shows the tsunami wave when the landslide stopped moving.

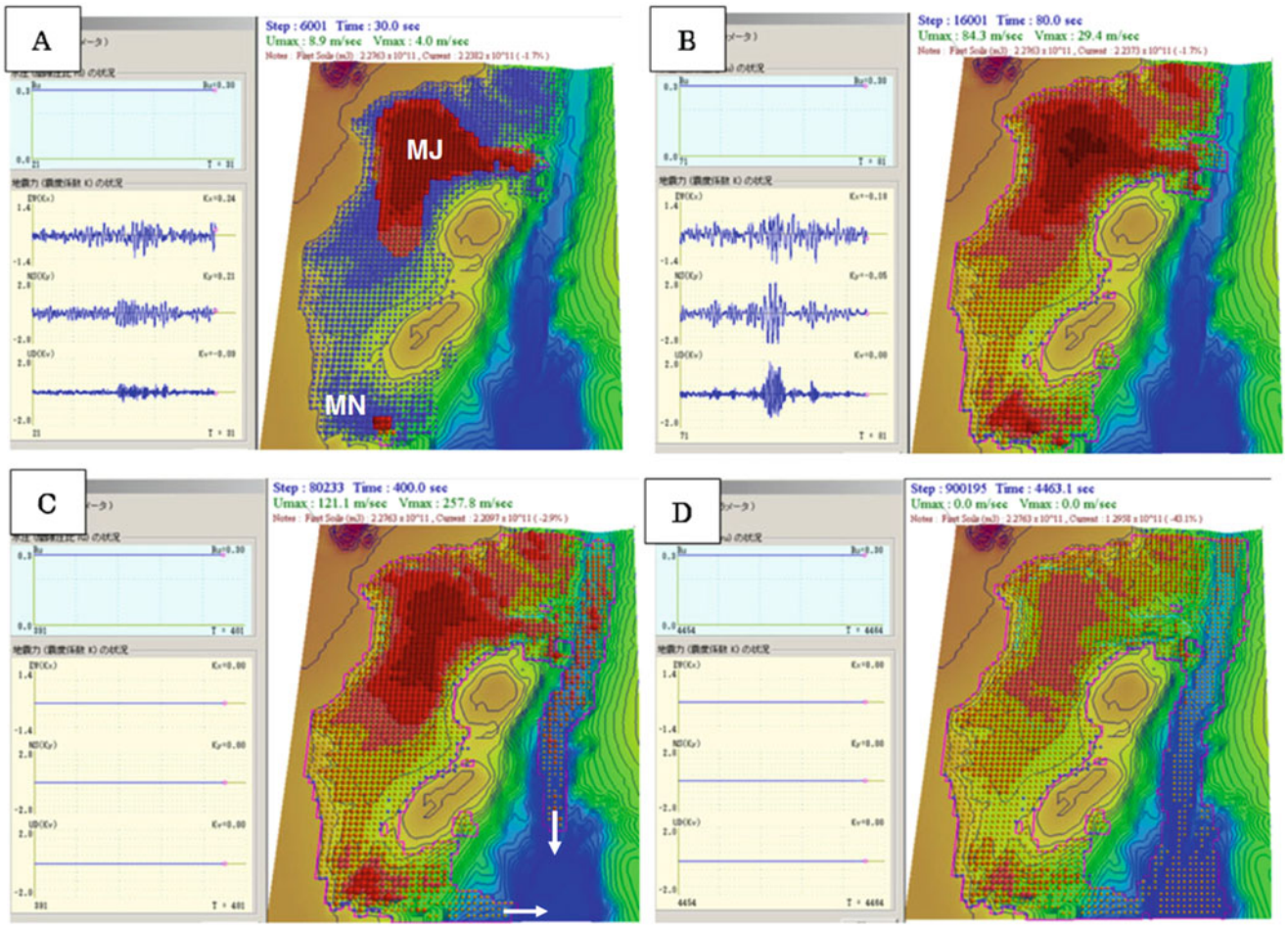

Fig. 70 Landslide simulation result for IODP volcanic ash by the 1.0× Tohoku earthquake record (MYG004)

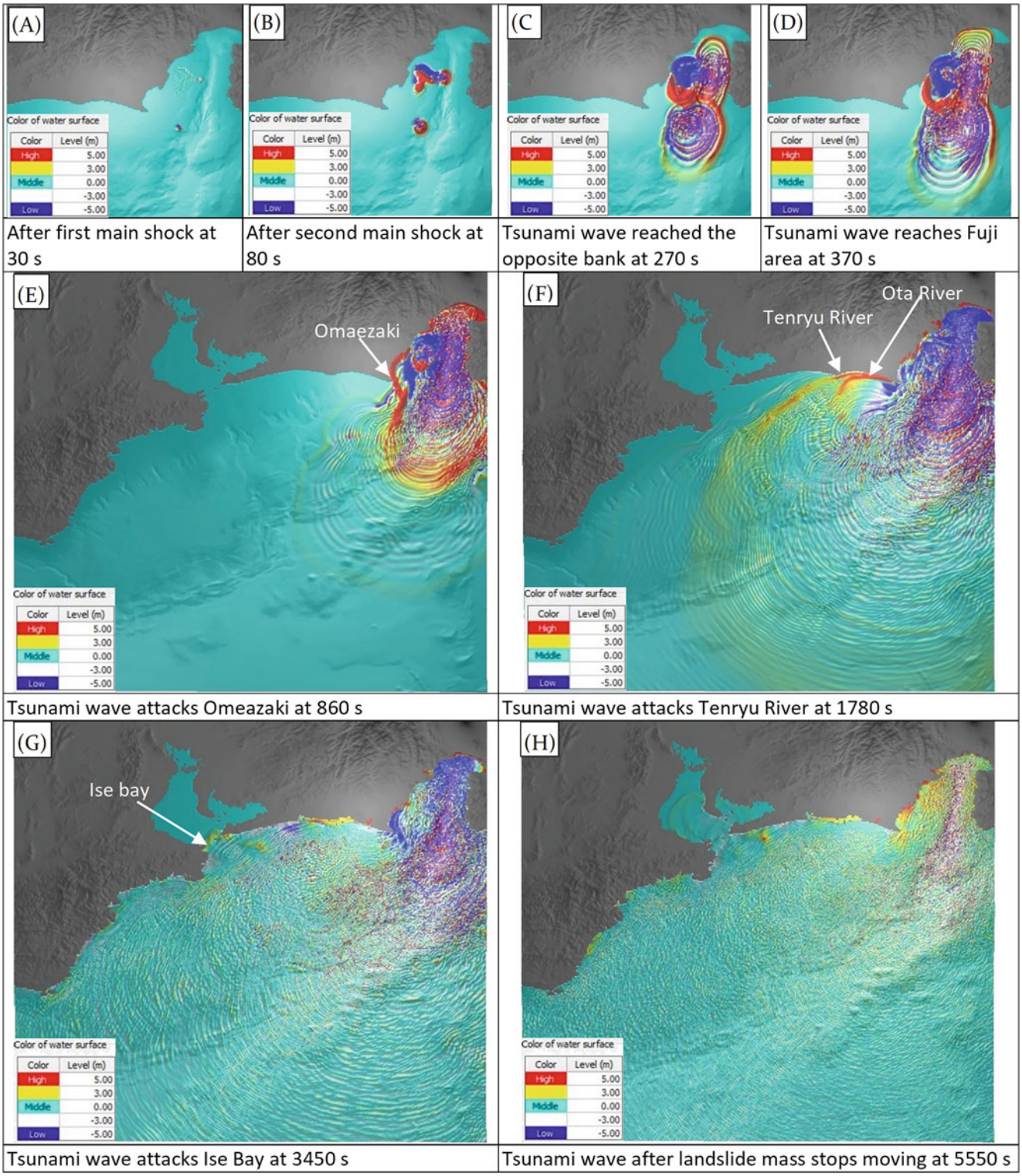

Fig. 71 LS-Tsunami simulation results when considering the hypothetical Senoumi landslide in the IODP volcanic ash triggered during the 1.0 Tohoku earthquake record (MYG004). In this figure, the red, yellow, light blue, white and dark blue represent the wave heights corresponding to more than 5 m, 3–5 m, 3 to −3 m, −3 to −5 m and less than −5 m, respectively

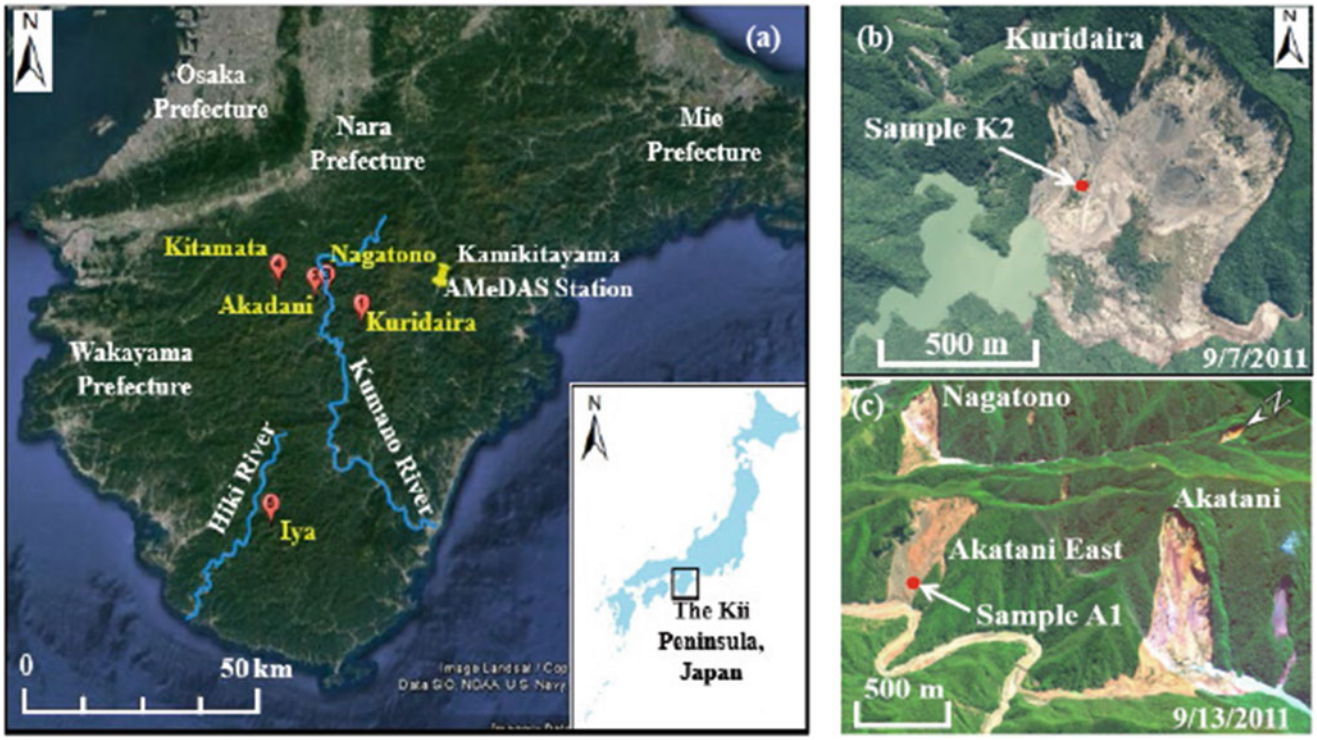

Fig. 72 (**a**) Location of the Kii Peninsula, (**b**) the Kuridaira landslide (modified from an aerial photograph taken by the Kii Mountain District Sabo Office), and (**c**) Google Earth image showing the Akatani landslide area

5.5 Landslides Triggered by the 2011 Typhoon "Talas" in the Kii Peninsula, Japan

5.5.1 Case Studies of the Kuridaira and Akatani Landslides in Kii Peninsula

The Kii Peninsula (Fig. 72a), located in the southeast of Japan, is known as one of the regions frequently prone to deep-seated catastrophic landslides due to its complex climatic condition and geological and morphological settings in fault and fracture zones of Cretaceous to Neogene Shimanto accretional complex (Hayashi et al. 2013; Tien et al. 2018). The area has suffered the most destructive landslide disasters in the years of 1889, 1953 and 2011. In August 1889, the worst storm associated heavy rainfalls triggered more than 1000 large landslides and 33 landslide dams with a total volume up to 200 million m^3 were formed in the peninsula. The fatal disasters of landslides, flooding and dam breach killed 1492 lives and forced 2500 people to move out of the Totsukawa village to a new place in Hokkaido (Tabata et al. 2001; Inoue and Doshida 2012; Chigira et al. 2013). In 1953, the Arida-Kawa disasters of flood and landslide dam breach that were induced by heavy rainfall caused 1064 deaths (Tabata et al. 2001). In contrast, the second most severe sediment-related disasters that were triggered by the 2011 record historical rainfall claimed 98 people, completely destroyed 379 houses and partially damaged to 3159 houses (FDMA 2012). In the latest event, about 100 million m^3 of landslide sediments was produced from more than 3000 landslides. Among them, large deep-seated landslides exceeding an area of 10,000 m^2 were formed in 72 locations with a total of 17 huge landslide dams. Five largest landslide dams (namely Kuridaira, Akatani, Nagatono, Kitamata, Iya as shown in Fig. 72a) have been put under urgent countermeasures by Ministry of Land, Infrastructure, Transport and Tourism (MLIT) due to high risks from overflow, debris flow, erosion and dam breach (Hayashi et al. 2013; SABO 2013).

Case studies of this research are the two largest deep-seated landslide dams in Kuridaira and Akatani valleys upstream of the Kumano River in the Totsukawa village, Yoshino District, Nara Prefecture, Kii Peninsula (Fig. 72b, c). The two landslide cases were selected because of not only the biggest size and the highest risk to potential hazards resulting from river blocking, but also the typical features in term of geology, topography, trigger and failure characteristics. The Kuridaira landslide was about 100 m deep, 750 m long and 600 m wide, with the largest volume of 23.0 million m^3. The Akatani landslide had the second biggest volume of 10.2 million m^3 with 67 m in depth, 900 m in length and a width ranging from 300 m at the head and to 500 m at the toe (Tien 2018). The Kuridaira landslide created the highest dam on the left bank of the Kuridaira River and on the right tributary of the Taki River joining to the Kumano

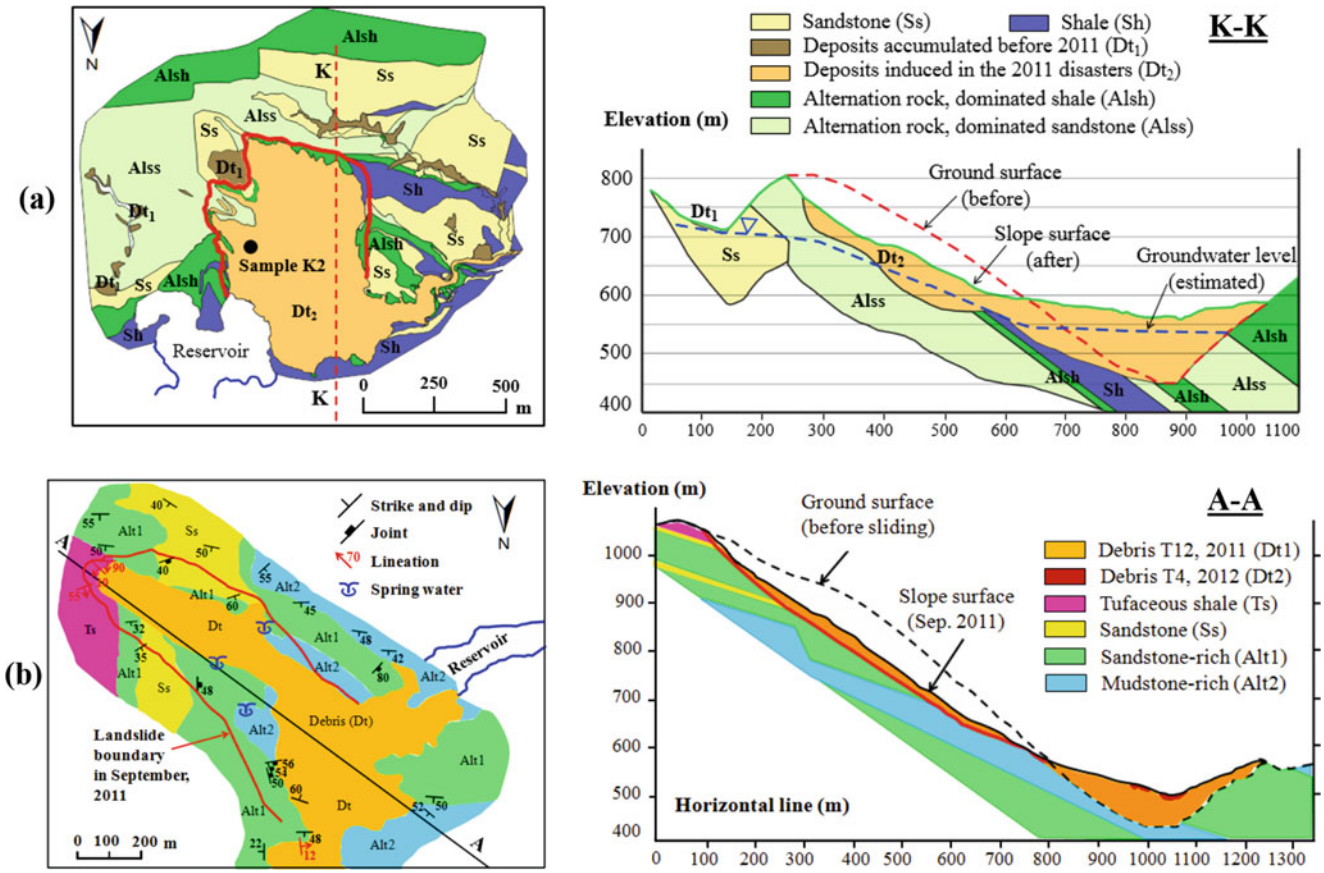

Fig. 73 Geological plan (left) and a cross section (right) of the landslides: (**a**) Kuridaira and (**b**) Akatani (redrawn and modified from the figures created by Kii Mountain District Sabo Office)

River. The Akatani landslide-dammed lake is formed on the right-bank tributary of the Kawarabi River joining to the Kumano River. The mass movement of Kuridaira and Akatani landslides blocked the valley courses and formed natural dams up to 100 m high a catchment area of 8.7 km^2 and 85 m high in a catchment of 13.2 km^2, respectively (SABO 2013). The storage capacity is of 7.5 and 5.5 million m^3 for the Kuridaira and Akatani natural lake, respectively. Although two natural lakes were created by the river blockage in the Akatani valley, the Akatani East landslide dam is about 1.5 km downstream of the Akatani dam was breached just after its formation. The Fig. 72c also presents the Nagatono landslide dam that is behind and and on a nearby slope of the Akatani landslide.

The landslide areas are characterized by broken formations and mixed rocks of Hidakagawa Group in the Shimanto Belt (Tien 2018). The geological map and the cross-section of these two landslides created by Kii Mountain District Sabo Office are denoted in Fig. 73. The Kuridaira and Akatani landslides are characterized by the structure of mixed rocks, broken formations and fractured wedge-shaped discontinuities that are favorable conditions for the build-up of groundwater table (Chigira et al. 2013; Tien et al. 2018). The Kuridaira slope composes debris materials produced from fractured shale and sandstone-dominated rock masses (Fig. 73a). The Akatani slopes is mainly characterized by interbedded sandstone- and mudstone-rich material layers (Fig. 73b). The sliding surfaces of the landslides were mainly formed along the North-West dip direction of the strata on the planes of weakness, such as faults or bedding planes. The sliding plane of the Kuridaira slope was formed in interbedded sandstone and shale layers while it was existed along the interbedded layers of sandstone and mudstone rocks for the Akatani slope. As can be seen in Fig. 73, there existed an abundant condition of groundwater in the study areas with a high level of groundwater table in the Kuridaira slope.

The Kii Peninsula landslides were induced by a record-breaking accumulative precipitation exceeding 1800 mm during the 2011 Typhoon Talas. Rainfall data recorded between August 31 and September 4 at Kamikitayama AMeDAS Station 17 km northeast from the Kuridaira slope is presented

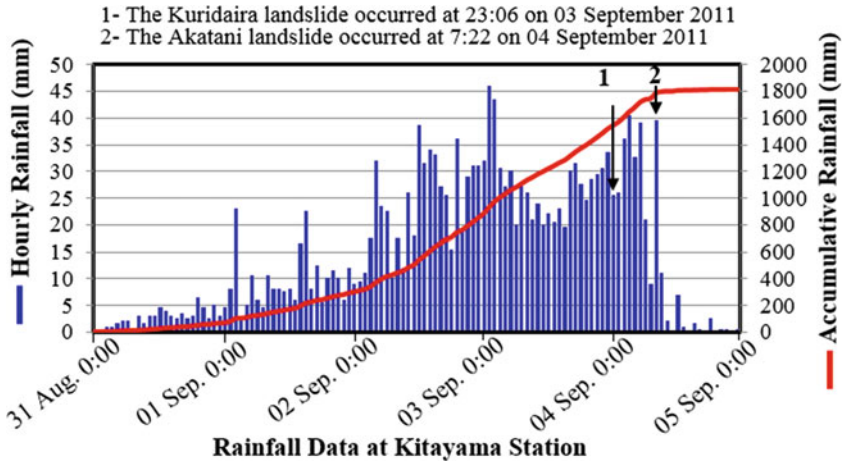

Fig. 74 Rainfall Data at Kitayama Station during the Typhoon Talas in Sep. 2011 (Tien et al. 2018)

in Fig. 72a. The maximum 72-h rainfall was 1650.5 mm and the maximum daily rainfall reached 661 mm on September 3. The accumulative precipitation triggering the Kuridaira and Akatani mass movements were 1516.5 mm and 1746 mm, respectively (Fig. 74). These high cumulative values of rainfall not only caused a saturation of slope materials, but also brought about a high pore water pressure to trigger the slides (Tien et al. 2018). Seismic recordings of the landslides revealed that the Kuridaira landslide occurred at 23:06:13 on September 3 in duration of 100 s while the Akatani landslide took place at 7:22:00 on September 4 during 70 s (Yamada et al. 2012). The average speed of slope movements was about tens of meters per second, in which, the maximum velocity of the movement of the Akatani landslide was calculated to be 80–100 km/h (Chigira et al. 2013).

Various researches have investigated the geological, topographical and morphological features of the 2011 Kii landslides, there has been still a lack of the understanding of the physical mechanism of the deep-seated landslides in the Kii Peninsula (Tien 2018; Tien et al. 2018). This study aims to clarify physical failure mechanisms of the two rainfall-induced landslides and particularly to investigate the liquefaction behaviour of sliding-surface samples that govern the rapid travel of the landslides. For these objectives, a series of laboratory experiments on collected samples was carried out by using the undrained high-stress dynamic-loading ring shear apparatus. The study will not only be helpful for understanding the sliding mechanisms of the Kuridaira and Akatani landslides, but the findings may be employed for the landslide hazard assessment of slopes with the similarity of geology and geomorphology such as in the Kii Peninsula (Tien et al. 2018). Understanding failure mechanism and computer modeling of landslides are indispensable for taking countermeasures in mitigation and preparedness phases against the future landslide disasters.

5.5.2 Soil Sampling and Laboratory Experiment Setting

Because the Akatani landslide has been continuously posing high risks from debris flows and rock failures, the access to the Akatani landslide area was not allowed in the site surveys. Site investigation and soil sampling were carried out in the Akatani East landslide area that were very similar to geological, topographical and morphological features of the Akatani landslide. Based on geological features of the sliding surface, four soil samples, including samples K1 (sandstone-dominated material) and K2 (fractured shale) of the Kuridaira landslide and samples A1 (mudstone-rich material) and A2 (sandstone) in Akatani slope area were collected for ring shear tests (Tien 2018; Tien et al. 2018). Sample K1 contains both coarse-grained clastic rocks and clay-size materials in brown color. Sample K2 comprises small grain-size angular fragments of broken shale in black greenish color and is very brittle to break with hands. Sample A1 is light-gray sandstone-rich materials while sample A2 contains landslide debris of dark-gray mudstone-rich materials. For the above-mentioned objectives, this paper only presents test results and its detailed analysis for shear behaviours of sample K2 and A1. The locations of soil sampling for studying the Kuridaira and Akatani landslides are respectively denoted in Fig. 72b, c, while the photographs of the sampling are shown in Fig. 75. Soil samples were passed through a 2 mm size sieve before ring shear testing. The grain-size distribution of these samples (K2 and A1) are presented in Fig. 76. The unit weight of sample K2 and A1 are 19.5 and 20.2 kN/m^3.

The ring shear simulator with a high undrained capability of 3.0 MPa was employed to investigate the failure mechanisms, changing process of pore water pressure, mobilized shear strength and possible liquefaction for large displacement at steady state (Sassa et al. 2014a, b). In this

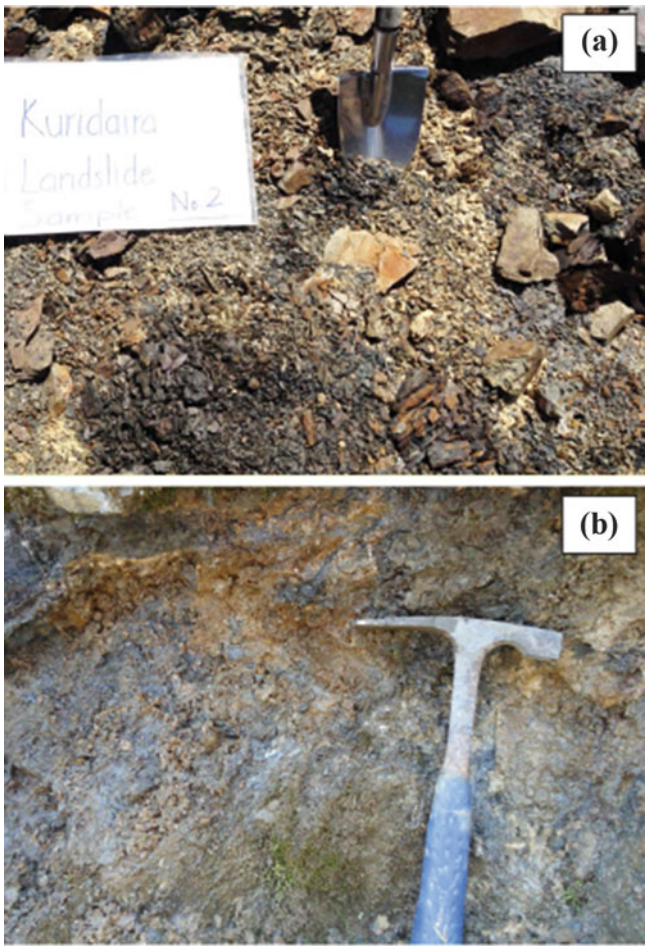

Fig. 75 Photos of soil sampling on the sliding surface of Kuridaira (**a**) and Akatani-East (**b**) landslides

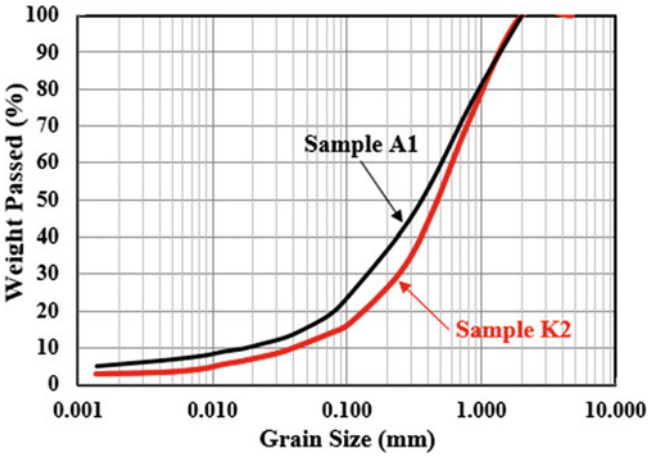

Fig. 76 Grain-size distribution of tested soil samples

study, ring shear tests were then performed up to 1500 kPa and 1000 kPa of normal stresses that correspond to over 100 m and near 70 m depth of the sliding surface, respectively. The initial stress conditions were calculated as the depth by slope inclination and soil weight. All of tests were conducted on fully saturated samples with $B_D \geq 0.95$.

First, the samples were consolidated at the initial stress state of normal stress and shear stress simulating forces acting on the soil mass at the sliding surface under drained condition. The sample was then sheared in different modes of shearing including undrained shear stress controlled tests and drained pore water pressure controlled tests. The pore water pressure simulating the buildup of groundwater table was increased by using a backpressure control device with a servo-motor. Mobilized shear resistance, pore water pressure change, deformation and displacement of the samples were monitored during the shearing. The analysis of test results is presented in the following section.

5.5.3 Ring Shear Test Results

(a) ***Undrained shear-stress control tests for sample K2***

Undrained shear stress controlled tests (SSC) were conducted on sample K2 under three different normal stresses (σ) of 500, 1000 and 1500 kPa. For each test the samples were first consolidated at the designed normal stresses in the drained condition. Shear stress was then loaded gradually at a given rate (Δτ/s) of 1–2 kPa/s until the failure in SSC tests. The stress path (a), time series (b), and shear stress–shear displacement curves are presented in Figs. 77, 78 and 79. The tests indicated the failure occurred as the effective stress path reached the failure line. After the failures, the shear strength reduced quickly in progress with an acceleration of shear displacement due to excess pore water pressure generation. The shear stress continued moving along the failure line to certain values of the steady-state shear resistance. All stress paths almost had the same friction angle at peak, namely 44.1° (Figs. 77a and 78a) and 43.8° (Fig. 79a). The friction angle during motion for sample K2 were 42.3° (Fig. 77a). The test at higher normal stress shows the higher mobilized shear resistance at peak and higher steady-state shear resistance. Values of the mobilized shear resistance at peak (τp) were 276, 459, 756 kPa whereas the steady state shear resistance (τss) were 25; 37 and 95 kPa for the 500, 1000 and 1500 kPa tests. The rapid motions were observed when the samples stayed at steady state with low values of residual strength, which indicate the rapid landslide motion. The maximum shear speed reached to about 175 mm/s (Fig. 79c). Test results indicate the occurrence of liquefaction phenomena within the sliding surface due to undrained high-speed shearing condition.

The undrained test results for three different normal stresses, ranging from 500 kPa to 1500 kPa, are plotted in

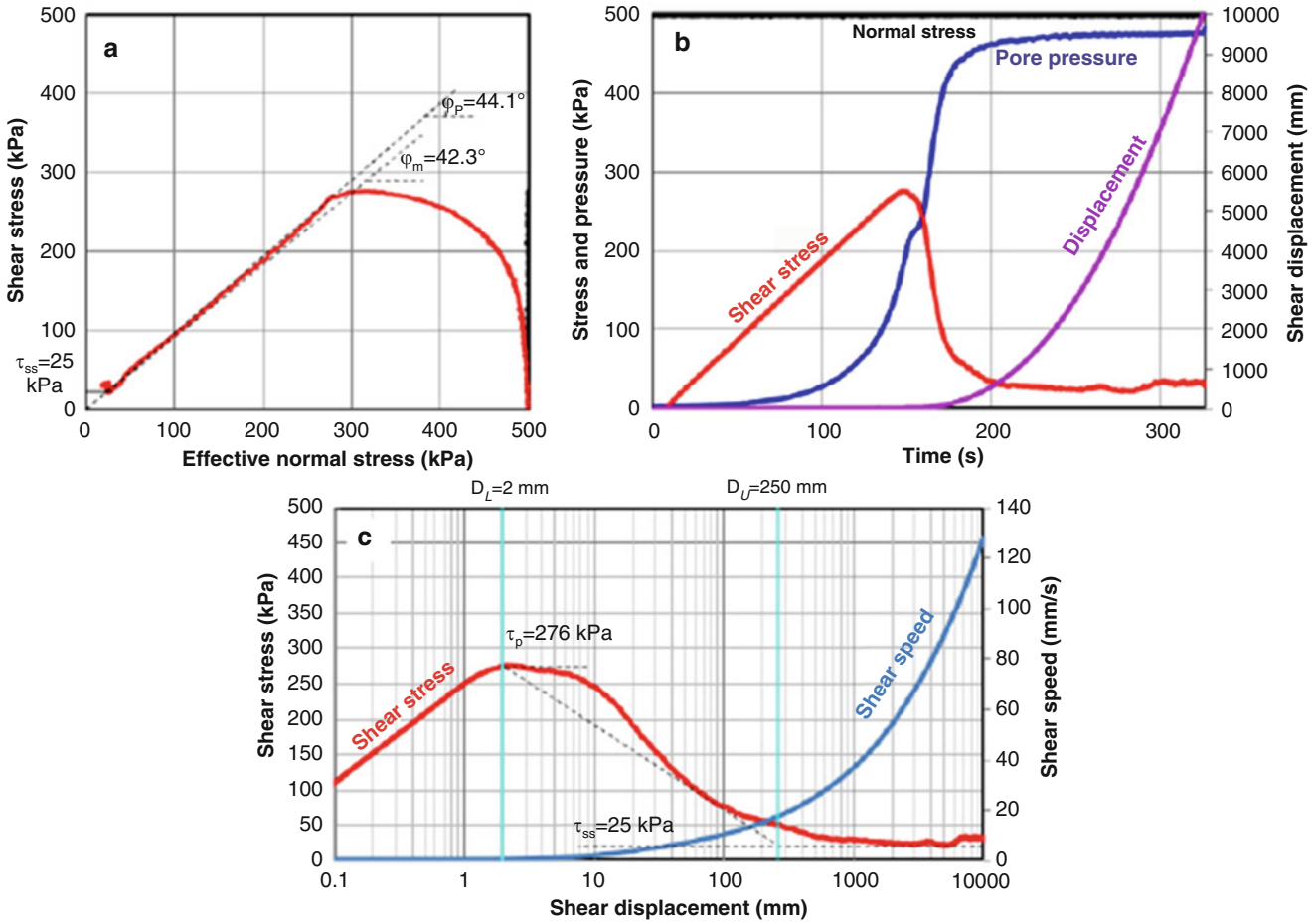

Fig. 77 Saturated and undrained stress-controlled test for Kuridaira sample (stress path (**a**) and time series (**b**), Shear stress–shear displacement (**c**)), normal stress 500 kPa, BD = 0.95, Shear stress increment = 2 kPa/s

Fig. 80. Although there is a small difference in the values of steady-state shear resistance, all the effective stress paths reached the failure line. The sliding surface liquefaction took place as the failure line approached the steady state stress point. The tests show slight negative excess pore pressure generation at the steady state. The reason might be because of a low permeability and dense clay-sized grain materials created by grain crushing within the shear zone. The relation of the shear strength reduction and the progress of shear displacement is presented in Fig. 81. The failure of all soil samples exhibited three main periods including pre-failure, transient state and steady state that were separated by the values of DU and DL (Sassa et al. 2010).

The DU value defines the shear displacement at the starting point of shear strength reduction (at peak strength) and the DL value indicates the shear displacement at the ending point of shear strength reduction (the shear strength for the initiation of steady-state shear resistance). The values were DU = 2 mm and DL = 150 250 mm for Kuridaira sample 2.

(b) ***Pore-water-pressure controlled tests***

The rainfall-induced landslides in Kuridaira and Akatani slopes were reproduced in the drained pore water pressure controlled tests. The designed initial stress conditions were estimated from a representative sliding plane depth of about 70 m for the two landslides. Thus, the saturated samples were first consolidated to 1000 kPa normal stress. Under the drained condition, the initial shear stresses were then reproduced at 600 kPa and 620 kPa for Kuridaira and Akatani landslides, respectively. The ratios of shear stress and normal stress were 0.60 and 0.62 that correspond to the natural slope angles of 31 degrees for Kuridaira slope and 34 degrees for Akatani slope, respectively. The simulation of the increment of groundwater level due to rainfall was implemented by using a back pressure control device. Pore water pressure increment simulating rainfall-induced landslide was maintained at a constant rate of 1.0 kPa/s for sample K2 and 0.5 kPa/s for sample A1 (Figs. 82 and 83). The failure of sample K2 and sample A1 initiated as the controlled pore pressure values were about 360 and 340 kPa, respectively. It

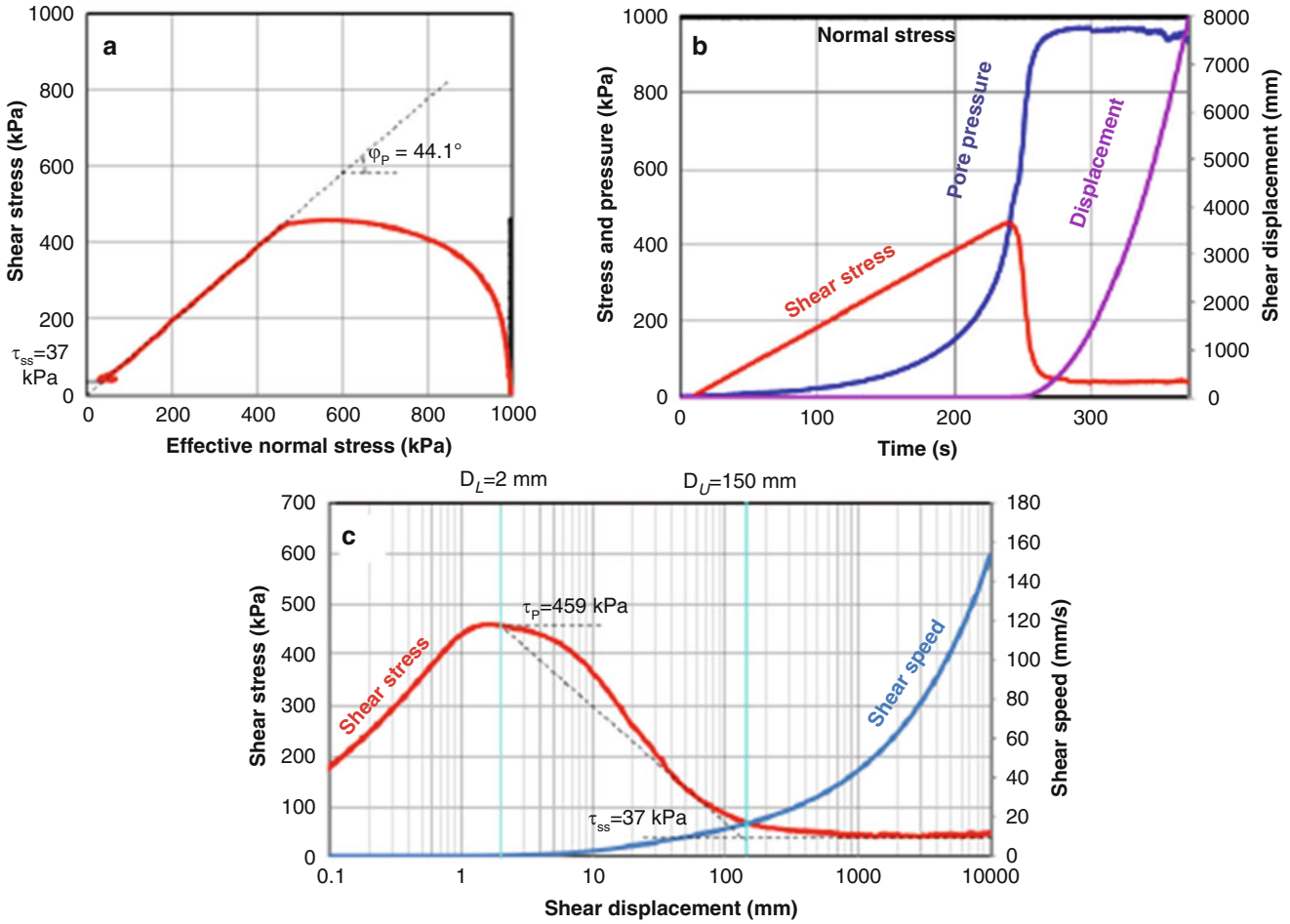

Fig. 78 Saturated and undrained stress controlled test for Kuridaira sample (stress path (**a**) and time series (**b**), Shear stress–shear displacement (**c**)), normal stress 1000 kPa, BD = 0.96, Shear stress increment = 2 kPa/s

indicates that the critical pore water pressure ratios (ru) triggering the failures were 0.36 for sample K2 and 0.34 for sample A1, whereas the friction angles at peak were 42.7° for sample K2 and 42.4° for sample A1, respectively. After the failure, both samples remained at small values of apparent friction angle of 3.4° and 5.5°. The steady state shear resistances were 60 and 94.5 kPa for sample K2 and A1, respectively. Both tested samples indicate a high level of landslide mobility because of a great loss of shear resistance under shearing. In the tests, the exact values of excess pore pressure generation were not completely monitored due to the drained condition during shearing. The excess pore pressures were monitored because the generation rate due to grain crushing was larger than the dissipation rate. In addition, it was observed that pore pressure slightly fluctuated due to both generation of positive and negative pore pressures at a large shear displacement in the post-failure moving stage.

The shear stress–shear displacement curves of pore water pressure controlled tests are presented in Figs. 82c and 83c. The values of DU and DL were 4 and 1500 mm for sample K2 while they are 5 and 1500 mm for sample A1. Before the end of shearing at the prescribed shear displacements, the maximum values of shear velocity reached 115 and 140 mm/s, respectively. The simulation demonstrates the groundwater contribution resulting in high pore water pressure that triggered the rapid landslides.

5.5.4 Sliding-Surface Liquefaction Behavior

The results from undrained shear-stress controlled tests on sample K2 indicate that liquefaction phenomena within the sliding surface resulted from much grain-crushing and excess pore water pressure generation, causing the significant drop of its shear strength at a large displacement (Figs. 77, 78 and 79). In the drained pore water pressure controlled test, the SSL took place at steady state as the shear strength reduced from peak of 42.7° to residual friction angle of 3.4° for sample K2 and from 42.1° to 5.5° for sample A1. The evidences of SSL in the ring shear tests for sample K2 are presented in Figs. 13a and 13b, in which the soil samples

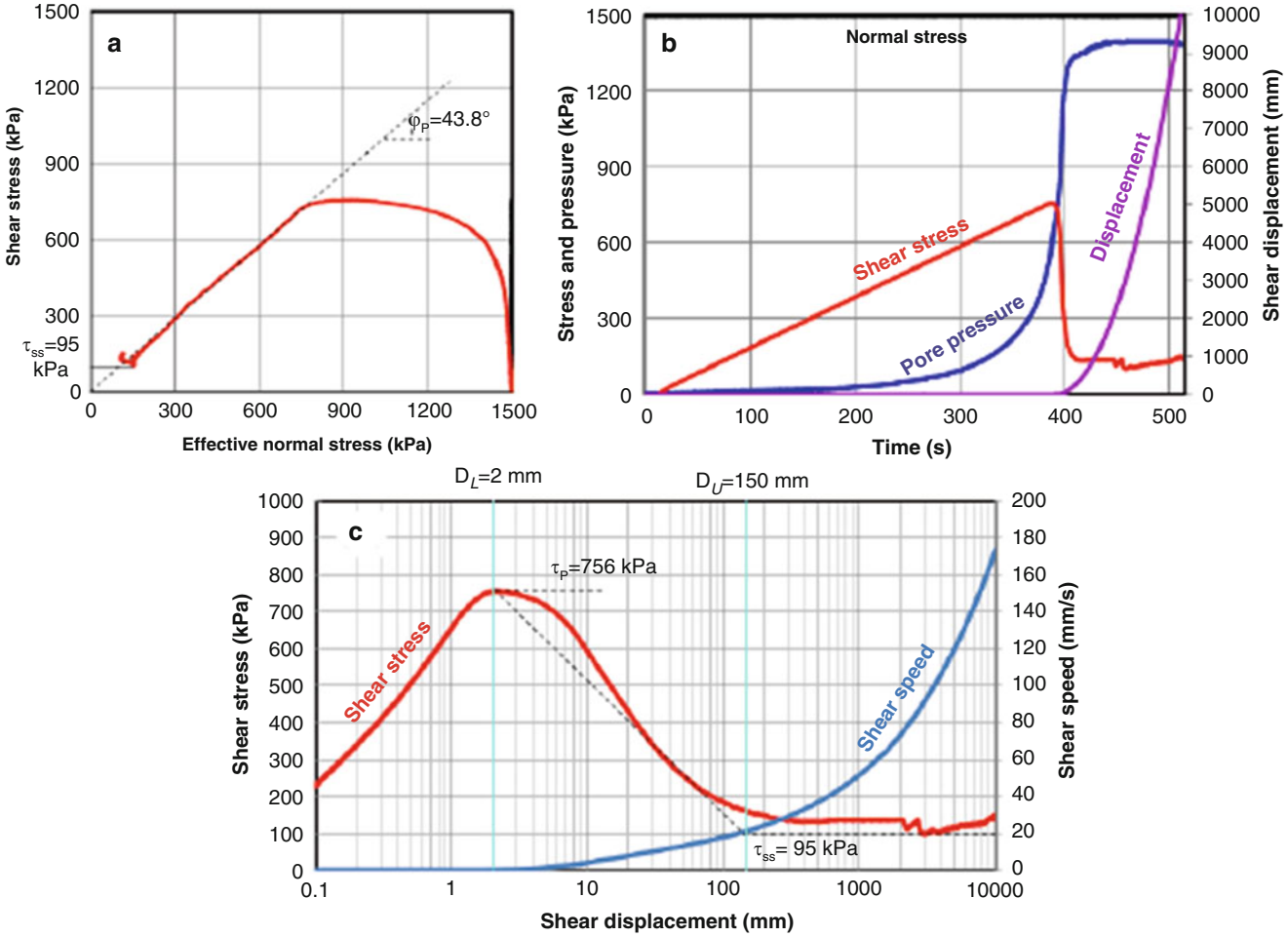

Fig. 79 Saturated and undrained stress controlled test for Kuridaira sample (stress path (**a**) and time series (**b**), Shear stress–shear displacement (**c**)), normal stress 1500 kPa, BD = 0.96, Shear stress increment = 2 kPa/s

were mostly crushed and liquefied to be finer grained particles. The liquefied materials within the shear zone indicate much grain crushing during a high-speed shearing. The sliding surface liquefaction highly agrees with the onsite observations of liquefied materials within the sliding plane of the Kuridaira landslide (Figs. 84c, d). The SSL behavior of sample K2 and A1 was the main reason for the rapid motion of the landslides. This behavior of sliding-surface liquefaction is helpful for the understanding of the rapid moving and long run-out landslides in the Kii Peninsula.

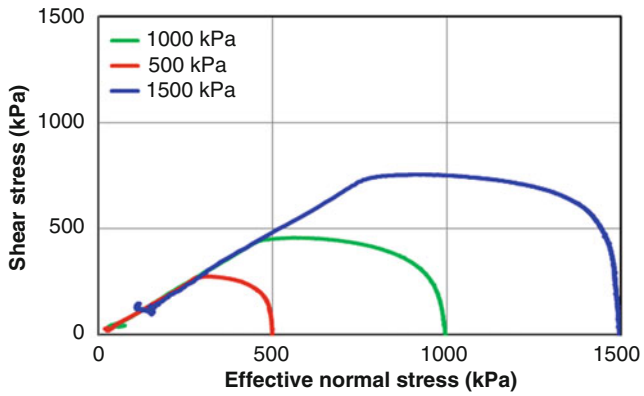

Fig. 80 Combined stress path of three shear stress controlled tests (500, 1000, 1500 kPa) for Kuridaira sample K2

5.6 1792 Historical Mega-Slide in Unzen, Japan

The 1792 Mayuyama landslide in the Unzen volcano is a very rapid mega-slide in Japan that caused the largest landslide disaster, the largest volcanic disaster, and the landslide induced tsunami disaster in Japan. The landslide and the landslide induced tsunami reportedly killed a total of 15,153 people. 10,139 people were killed in the Shimabara area. Many other people were killed on the opposite banks by the landslide-induced tsunami wave; 4653 people in the Kumamoto Prefecture, 343 people in Amakusa Island and 18 people in other areas (Usami 1996).

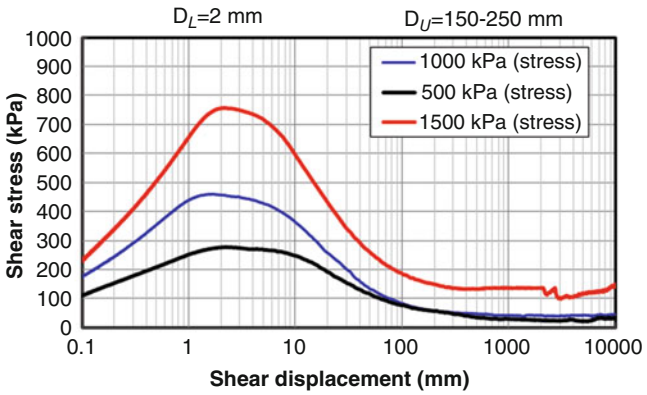

Fig. 81 Shear stress–shear displacement of three stress controlled tests (500, 1000, 1500 kPa) for Kuridaira sample K2

Though this event occurred 230 years ago, the events were well documented. The objective of the development of the high-stress undrained ring shear apparatus (ICL-2) which can test 3 MPa normal stress test is to study the Mayuyama Mega-slide killing 15,153 people. As stated in Table 2, we tried to develop the undrained high-normal stress apparatus (2 mega (DPRI-5) and 3 mega (DPRI-6)). However, we could not succeed in the undrained test more than 400–600 kPa. To succeed in 3 MPa undrained ring shear test, we were able to develop ICL-2 which can test 3 MPa undrained ring-shear test by changing the loading structure from Fig. 9 (DPRI-6) to Fig. 10 (ICL-2) which was published in Sassa et al. (2014a, b).

The Unzen-Mayuyama landslide caused a big tsunami and killed around 5000 people in the opposite bank. To make an assessment of the landslide induced tsunami hazard, we have developed a new landslide-induced tsunami simulation model (LS-Tsunami) which was reported in Sassa et al. (2016).

The organizing committee of the Fifth World Landslide Forum planned a field trip to the Unzen-Mayuyama landslides, Hiroshima urban landslides, earthquake-induced landslides in Aso volcano area. The field trip was cancelled

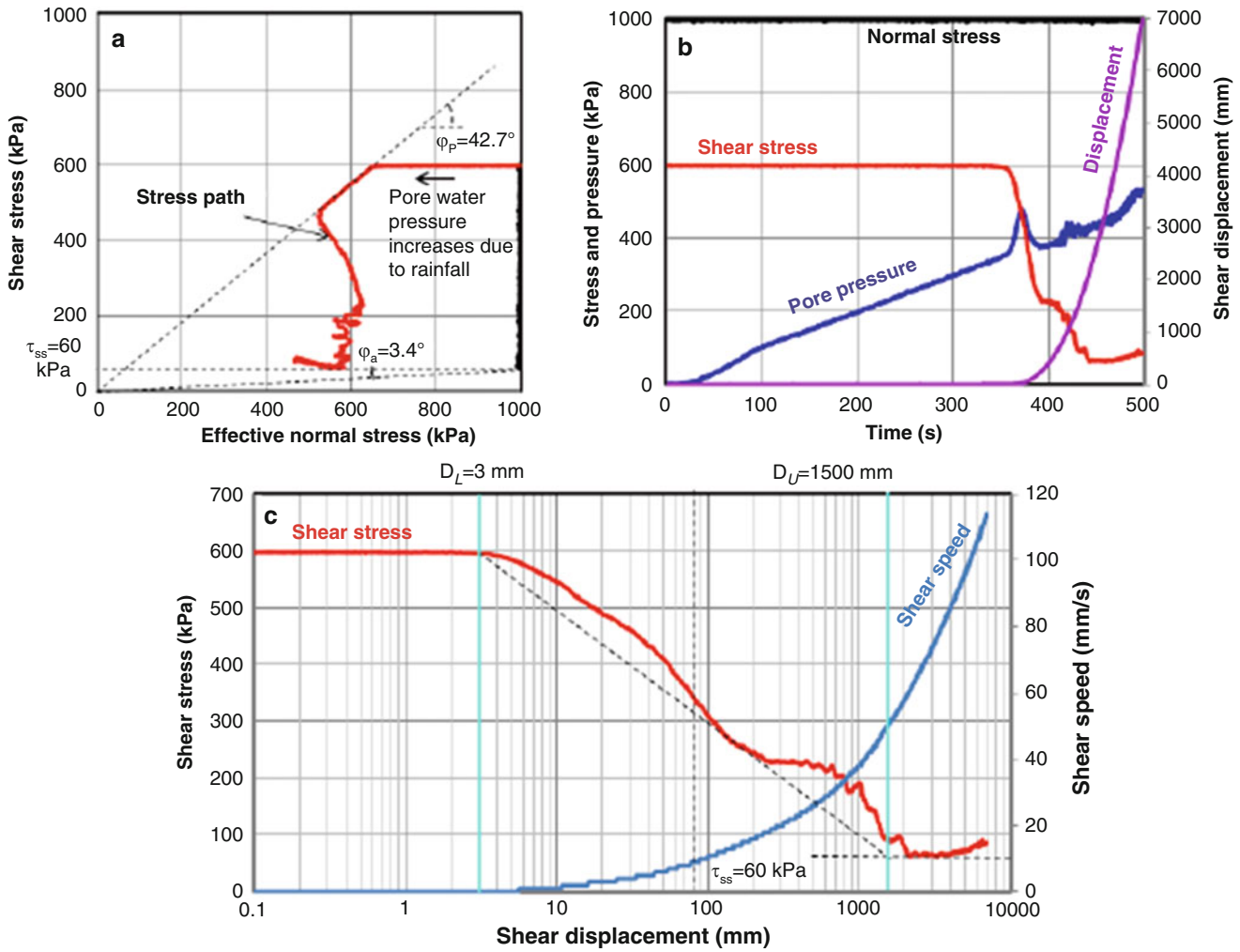

Fig. 82 Saturated and pore water pressure controlled test for K2 sample (stress path (**a**) and time series (**b**), Shear stress–shear displacement (**c**)), normal stress 1000 kPa, shear stress 600 kPa, BD = 0.96, Pore water increment = 1.0 kPa/s

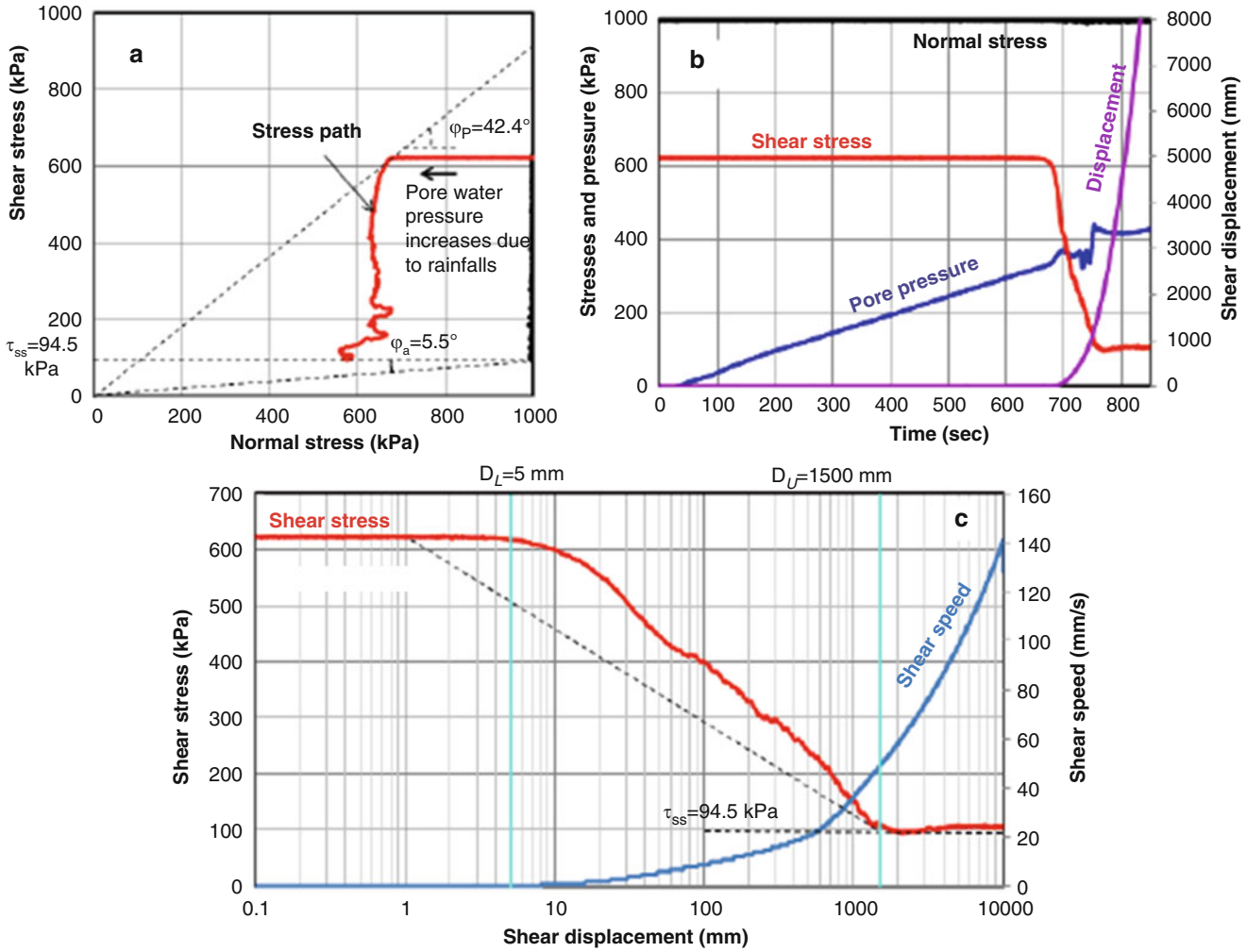

Fig. 83 Saturated and pore water pressure controlled test for A1 (stress path (**a**) and time series (**b**), Shear stress–shear displacement (**c**)), normal stress 1000 kPa, shear stress 620 kPa, BD = 0.95, Pore water increment = 0.5 kPa/s

due to COVID-19, but the content of the field trip was contributed to Vol.1, No.2 of the Progress in Landslide Research and Technology which is published. Reviewing those three papers, Sect. 5.6 was written as the final chapter of the ICL Landslide lesson: Sliding-surface liquefaction and undrained steady-state shear strength.

1. Kyoji Sassa, Khang Dang, Bin He, Kaoru Takara, Kimio Inoue, Osamu Nagai (2014) A new high-stress undrained ring-shear apparatus and its application to the 1792 Unzen–Mayuyama megaslide in Japan, Landslides 11: 827–842.
2. Kyoji Sassa, Khang Dang, Hideaki Yanagisawa, Bin He (2016) A and its application to the 1792 Unzen-Mayuyama landslide-and-tsunami disaster. Landslides 13: 1405–1419.
3. Daisuke Higaki, Kiyoharu Hirota, Khang Dang, Shinji Nakai, Masahiro Kaibori, Satoshi Matsumoto, Masataka Yamada, Satoshi Tsuchiya (2022) Landslides and Countermeasures in Western Japan: Historical Largest Landslide in Unzen and Earthquake-induced Landslides in Aso, and Rain-induced Landslides in Hiroshima. Progress in Landslide Research and Technology, Vol.1, No.2 (in print).

5.6.1 Outline of the Unzen-Mayuyama Landslide

Figure 85 presents the image of the Unzen-Mayuyama landslide (from Google Earth) in the Shimabara city of Nagasaki Prefecture. S1 is the sampling point for the landslide source area. S2 location was selected outside of the landslide moving area to eliminate the effect of the displaced landslide mass.

Within Fig. 85, one may find many islands in the Ariake Sea which were parts of the Unzen-Mayuyama landslide. Initially much greater number of islands were formed. However, most of them disappeared by sea erosion after the event. But some landslide mounds still exist as islands as seen in the photo.

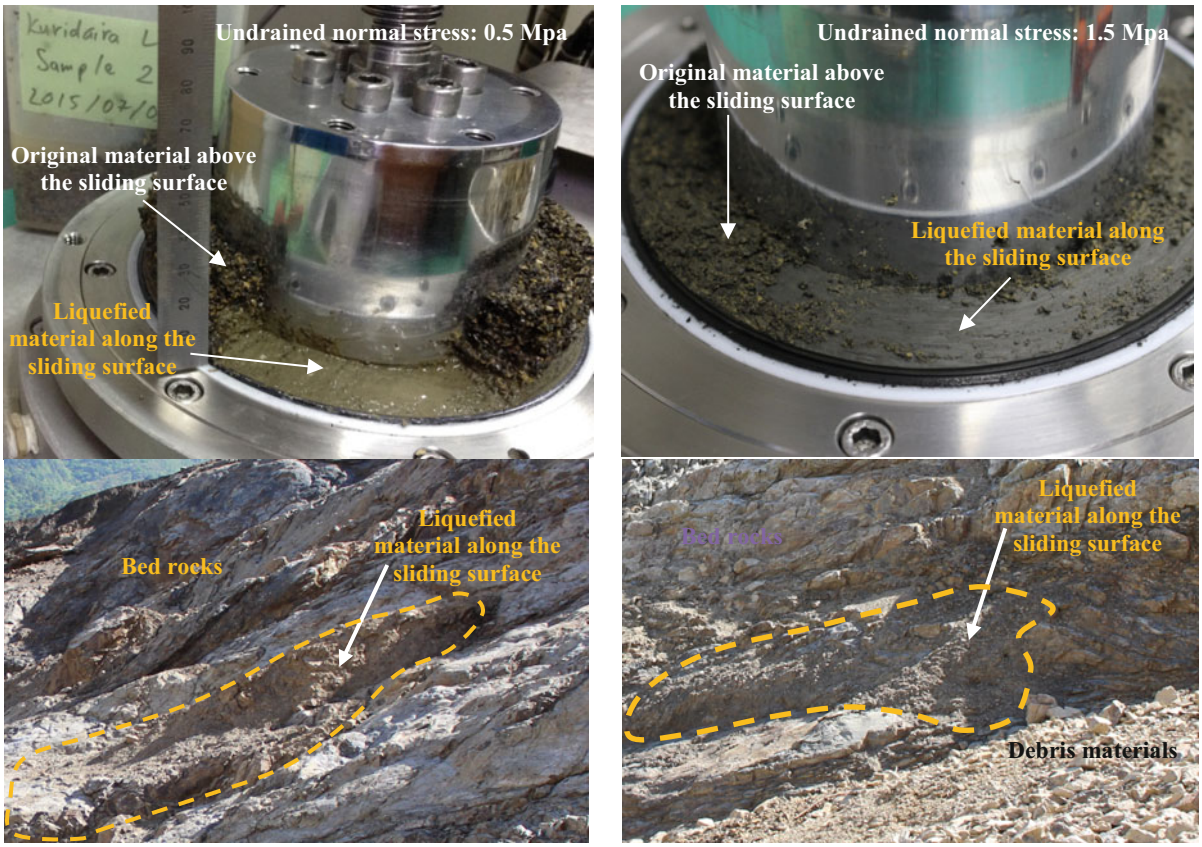

Fig. 84 Sliding surface liquefaction behavior of shale samples under different normal stresses in ring shear tests

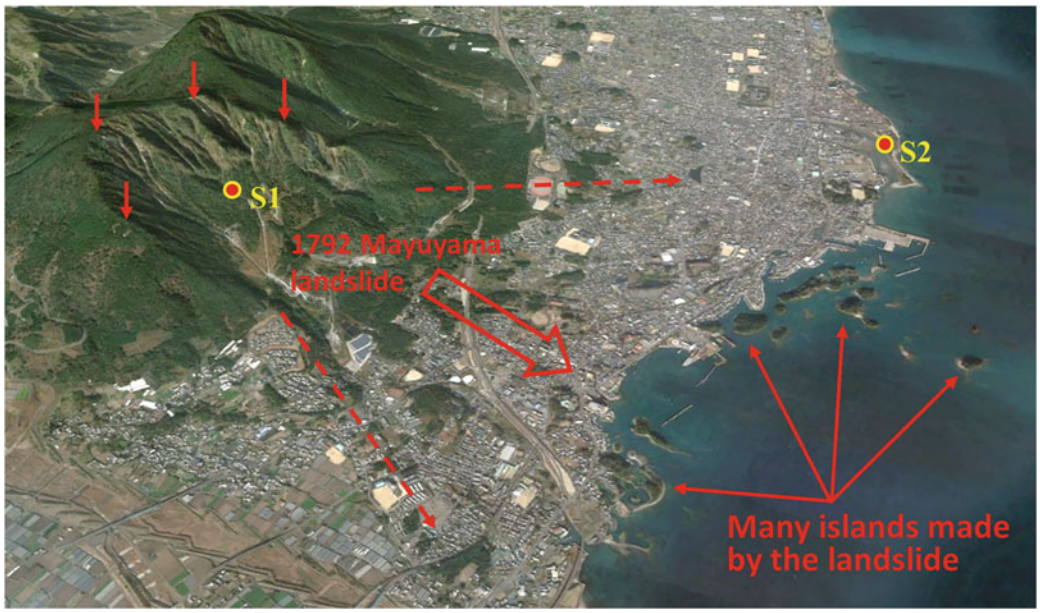

Fig. 85 1792 Mayuyama landslide in the Unzen Volcano and sampling points

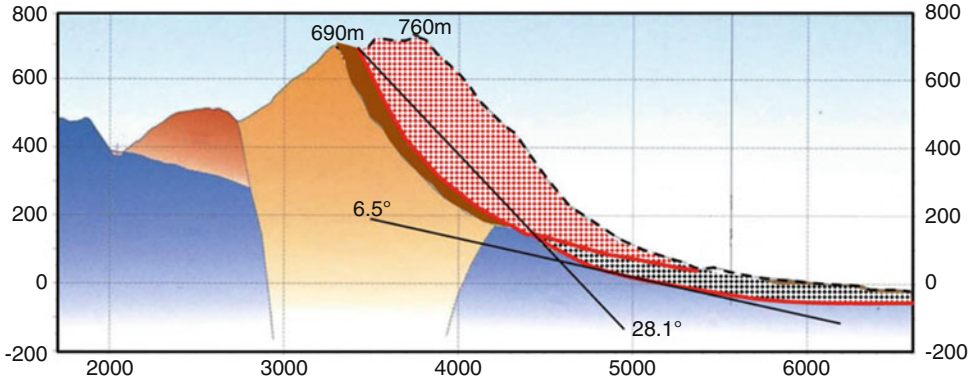

Fig. 86 The central section of the Mayuyama landslide before/after failure

Figure 86 presents the section of this landslide which was revised from Inoue (1999) and the MLIT Unzen Restoration Office (2002). The Unzen-Mayuyama mountain consists of volcanic lava rock and unconsolidated eruption products (sand and debris). The section of the initial main landslide block is shown by a red dotted mass, and the secondary sliding block pushed forward by the motion of the initial landslide mass is shown by a black dotted soil layer. The main sliding block and the secondary sliding block were interpreted by the authors. The lines of slope angle of 6.5° and the 28.1° were drawn for the undrained dynamic-loading ring shear test to physically simulate the initiation of the landslide (red dotted area) and the movement of the secondary sliding block (black dotted area) continued to the coast due to the undrained loading from the moving landslide mass.

This megaslide moved very rapidly and entered into the Ariake sea, then caused a very big tsunami wave. Landslide mass and the landslide-induced tsunami cased an enormous landslide and tsunami disaster in Shimabara city and Kumamoto prefecture. Figure 87 is the map showing this big disaster around Ariake sea which was modified from the Unzen Restauration Office (2003).

The total number of deaths was 15,153 people. The size of circles is proportional to the number of human fatalities in the area. The legend for the number of deaths is shown in the right-top corner (B). (C) The greatest deaths are Shimabara town around the castle (5251 people). (D) The second largest deaths are the southern part of Shimabara Peninsula (around 3500 people). (E), (F), (G) Tsunami-Dome-Ishi (a stone showing the tsunami reaching point, was set to record the tsunami by the community in Kyodomari (E), Umedo (F), and Otao (G) of the Higo (Kumamoto) Han area. The tsunami-Dome-Ishi in Kyodomari was moved for the construction of a road, but its former location is marked on the road retaining wall (by the regional education committee). The Tsunami-Dome-Ishi is limited in Higo (Kumamoto) Han area. These tsunami records are reliable. (H), (I) Stone pillars for memorial service for deaths by Tsunami in Futsu (H) and Mie (I) in Shimabara Han area. Tsunami reaching points recorded by Tsunami-dome stones were: Kyodomari: 9.6 m, Umedo: 14.9 m, Ohtao: 22.5 m, Futsu: 57 m (probably this is too high), Mie: 7.7 m.

This value was compared with the Tsunami simulation model (LS-Tsunami) based on the landslide movement estimated by the landslide simulation model (LS-Rapid) in Fig. 99.

5.6.2 Sampling from the Unzen-Mayuyama Landslide

We took two samples from the landslide site. Sample S1 was taken from the landslide source area and sample S2 was taken from the coastal area outside the landslide area to represent a soil overridden by the landslide.

Sample S1 was taken from a sand layer exposed along a torrent gully in the source area of the landslide. The close-up photo of the sampling site with a hammer. The large debris covered the fine volcanic debris. We took the fine and homogeneous sands for testing. Grainsize is different. Both are the same material. The grain-size distribution of Sample S1 and Sample S2 is shown in Fig. 88b. Sample 1 is finer than Sample 2.

5.6.3 Undrained Monotonic Stress-Control Ring-Shear Tests on Sample S1

A new ICL-2 undrained ring-shear apparatus was used to test samples taken from the Unzen. This apparatus was developed to investigate landslides with 100–300 m depth. The shear motor of ICL-2 is 11 kW, which is almost 30 times larger than the 400 W motor of the ICL-1. Loading method is the shear-stress increasing test with a constant stress increment ($\Delta\tau$ = 1–2 kPa/s). Loaded normal stresses are from 0.3 to 3.0 Mpa. Four tests were conducted with different normal stresses. The test results are presented in Figs. 89, 90, 91 and 92.

Figure 89 presents the stress paths and time-series data for 375 kPa normal stress test. The loaded shear stress is increased at the rate of 1 kPa/s. Stress path went up and leftward initially. The stress path moved vertical, then

rightward due to negative pore pressure, and it reached the peak shear resistance on the failure line at peak (39.8°). After peak, the stress path shifted to the failure line during motion (38.5°) and went down along the line and reached the steady state shear resistance (τss = 20 kPa). Time series data (b) visualized the negative pore-water pressure due to dilatancy near the peak, a rapid pore pressure increase at the same time of the start of shear displacement. Shear displacement crushed grains in the shear zone, then, a minimal volume reduction generated a high pore-water pressure. Shear speed in the shear stress–shear displacement relationship (c) showed the accelerated motion after failure at 273 kPa. After failure at DL = 7 mm, shear stress was reduced rapidly and reached to the steady state shearing at 20 kPa. These three set of graphs demonstrated a typical sliding surface liquefaction.

Figure 90 presents the test result for 1030 kPa normal stress. The stress path is similar to Fig. 89, but there was no negative pore pressure, although a constant (no increase, and no decrease) pore pressure was measured just before failure. The peak shear strength was 697 kPa, and the steady state shear strength was 45 kPa. The post failure stress drop was very large. Thus, the shear speed acceleratedly increased after failure. This is very similar to Fig. 89.

Figure 91 presents the test result for 1970 kPa normal stress test. The failure line at peak and the failure line during motion were almost the same (40.7° and 39.8°). The peak

Fig. 87 Disasters caused by the Mayuyama landslide

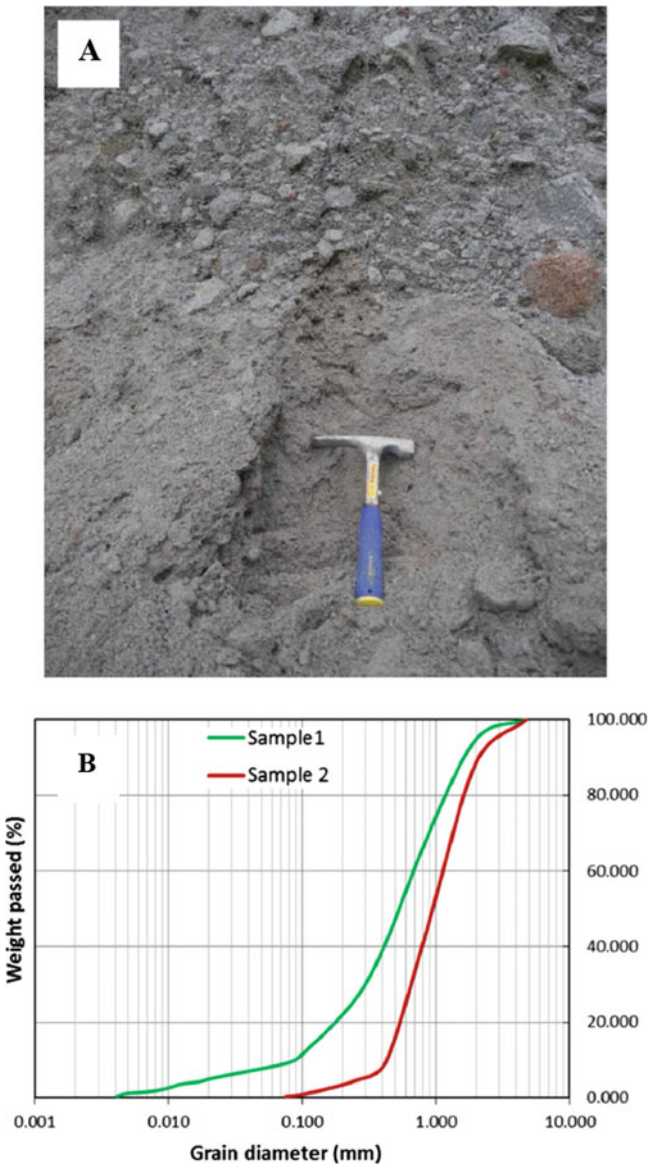

Fig. 88 Photo of Sample 1 in the source area of the Mayuyama Landslide (**a**) and grain size distribution of Sample 1 and Sample 2 (**b**)

shear strength was 1472 kPa, and the steady-state shear resistance was 80 kPa.

Shear resistance decreased to only 5%. Shear speed is the fastest of 25 cm/s due to rapid stress drop.

Figure 92 presents the test result of 2900 kPa, close to 3 MPa. It is very large normal stress, but still a complete undrained state was kept during the rotation of the lower ring at the speed of 18 cm/s. The peak failure line and the failure line during motion is almost same (40.3°). The peak shear strength was 1571 kPa and the steady-state shear resistance was 120 kPa. The steady state shear resistance was 7.6% of the peak strength. This is also the typical sliding surface liquefaction.

All stress paths are plotted in the same figure in Fig. 93. As shown, the four tests overlapped along the failure line during motion at 39.8°.

All shear stress–Shear displacement curves are plotted in the same figure in Fig. 94.

The peak shear strengths are much different in the four normal stress tests from 375 kPa to 2900 kPa. However, the steady-state shear resistances were much closer. In the case of Unzen volcanic sands, the undrained shear behaviors are classified as the sliding surface liquefaction. These test results verified the mechanism of rapid landslide motion of the Unzen-Mayuyama Megaslide causing a big tsunami wave. The total number of deaths was more than 15,000, which were the largest landslide disaster and the largest volcanic disaster in Japan.

5.6.4 Initiation Mechanism of Landslides

Three types of initiation process were examined for the Unzen case on Sample 1 and Sample 2

1. Landslide initiation by pore-pressure increase.
   Pore-pressure control test was conducted as the basic information.
2. Landslide initiation by volcanic seismic shaking.
   From the historical review, the volcanic earthquake ($M = 6.4 \pm 0.2$) occurred in Shimabara city and it was the trigger of the landslide.
3. Initiation of the motion of deposits downslope and alluvial deposits by the moving landslide mass (such as Fig. 6).

5.7 Case for the Landslide Initiation Mechanism by Pore-Pressure Increase (Fig. 95)

The first basic test for this landslide (Fig. 95) was to trigger landslide failure by increasing only the pore-water pressure.

Firstly, the sample was saturated (BD value, 0.98), then consolidated to 3.0 MPa normal stress and 1.5 MPa shear stress in a drained condition. This preparatory stage was to reproduce the initial stress in the slope, and is shown as a black line in Fig. 95. This initial stress corresponded to a slope of arctan (1.5/3.0) = 26.5°. This is a similar slope to the landslide block in Fig. 86. Then, in order to simulate the pore-pressure-induced landslide process, the pore-water pressure was gradually increased at a rate of $\Delta\sigma = 5$ kPa/s. Failure occurred at a pore-water pressure of 1.2 MPa (a porewater pressure ratio ru = 1.2/3.0 = 0.4). The friction angle at failure was 39.4°.

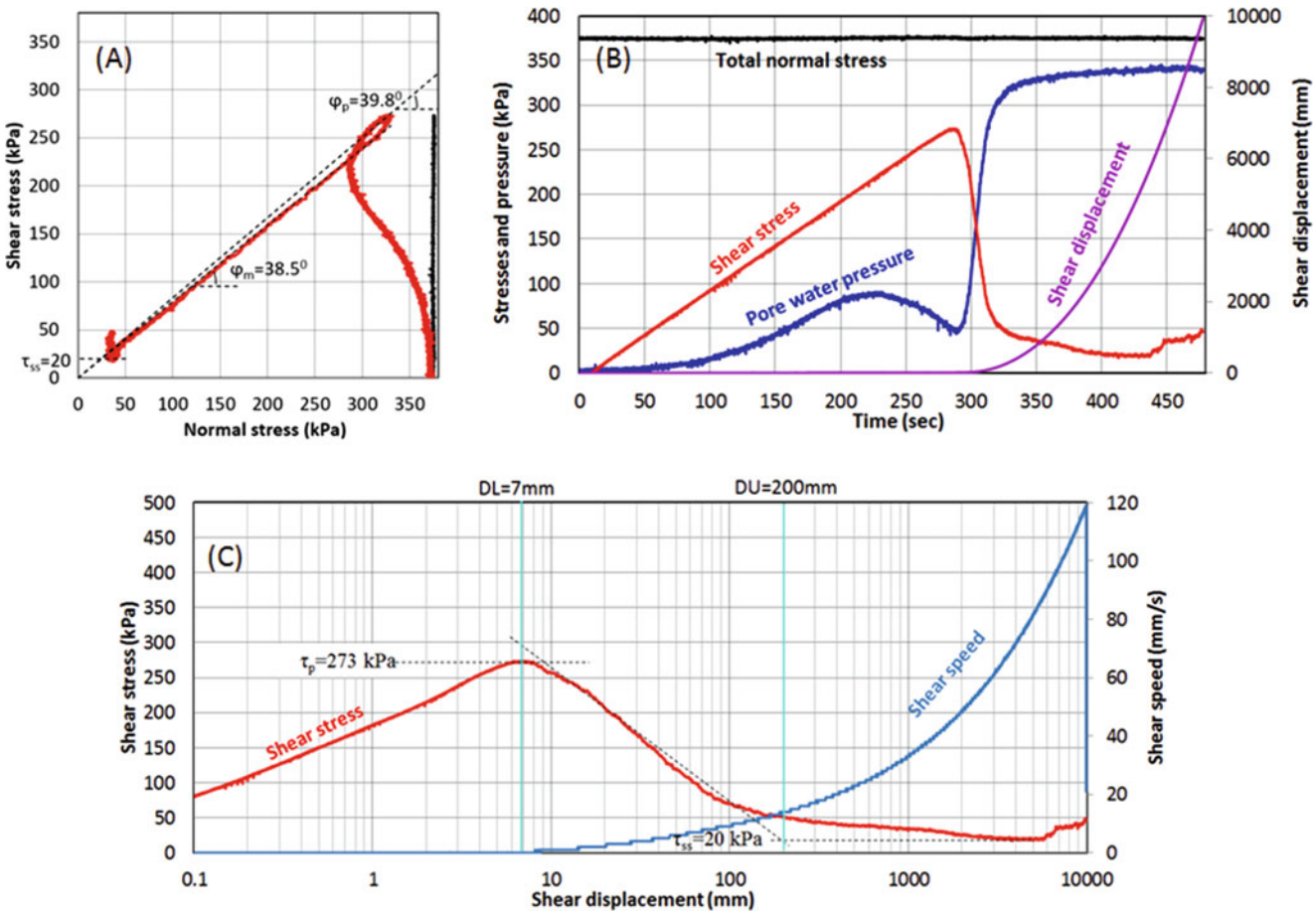

Fig. 89 Saturated and undrained stress controlled test for Unzen sample S1. Normal stress 375 kPa, BD = 0.93, Shear stress increment = 1 kPa/s. (**a**) Stress path, (**b**) Time series data, (**c**) Shear stress–shear displacement relationship

5.8 Case for the Landslide Initiation by Volcanic Seismic Shaking (Fig. 96)

The third test (Fig. 96) was a seismic-loading ring-shear test to simulate the landslide initiation of the Mayuyama Landslide by the combined effect of pore-water pressure and earthquake shaking. Initially, the sample (S1) was saturated (BD = 0.94) and consolidated to 3 MPa in normal stress and 1.5 MPa in shear stress (the corresponding slope angle was arctan (1.5/3.0 = 26.6°). Then porewater pressure was increased up to 800 kPa, (a pore-water pressure ratio ru = 800/3000 = 0.27) as the initial slope condition. An exact value remains unknown, but it must have been smaller than 0.4. A preparatory test (Fig. 95) showed that ru = 1.2/3.0 = 0.4 was a critical pore-water pressure which could cause a landslide without an earthquake. The earthquake which triggered the 1792 Unzen–Mayuyama Landslide was estimated to be magnitude M = 6.4 ± 0.2, with a seismic intensity of VII during the earthquake; in the Japanese standard, this corresponds to a seismic acceleration of more than 400 cm/s^2, as explained above.

The maximum recorded seismic acceleration in the 2008 Iwate–Miyagi earthquake was 739.9 cm/s^2, which caused the Aratozawa Landslide. We loaded the N–S component of the 2008 Iwate–Miyagi earthquake record (maximum acceleration is 739.9 cm/s^2) at MYG004 as the additional shear stress. For precise pore-pressure monitoring, as well as to maintain servo-stress control, a five times slower rate was used in applying the recorded seismic acceleration. The test result is shown in Fig. 96.

The green line indicates the control signal. The maximum value is 2469 kPa (1500 + 969 kPa) and the minimum value is 369 kPa (1500−1131). The loaded acceleration (a) is calculated from the ratio of seismic acceleration and gravitational acceleration: a/g = 969/1500 or a/g = 1131/1500, because ma = 969 kPa and mg = 1500 kPa, expressing the landslide mass at unit area as m. The acceleration corresponds to +633 and −739 cm/s^2. Therefore, the control signal for shear stress sent to the ring-shear apparatus exactly corresponded to the monitored acceleration record. As Fig. 96 shows, failure occurred around 1825 kPa, namely, a/g = (1825−1500)/1500 = 0.22; the necessary acceleration

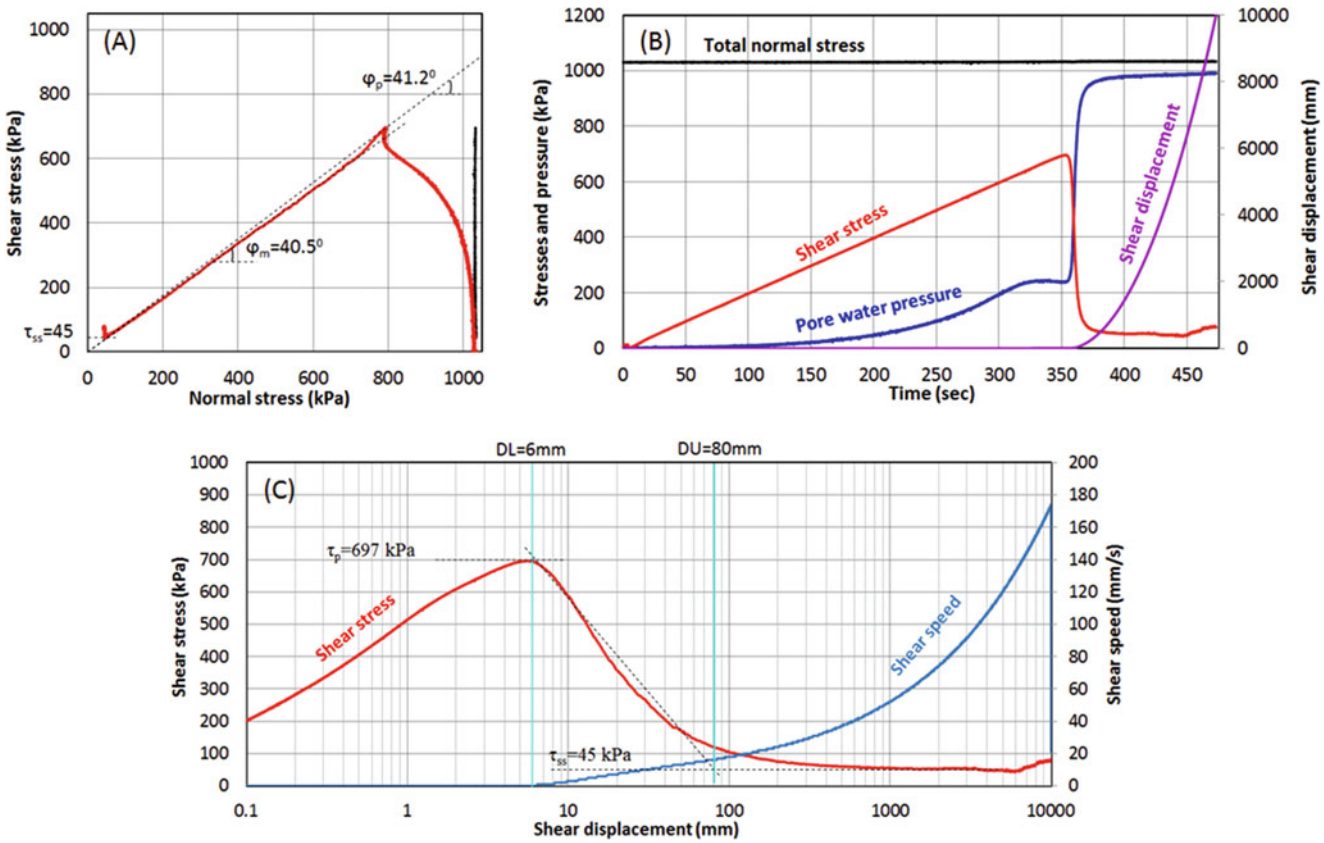

Fig. 90 Saturated and undrained stress controlled test for Unzen sample S1. Normal stress 1030 = kPa, BD = 0.95, Shear stress increment = 2 kPa/s. (**a**) Stress path, (**b**) Time series data, (**c**) Shear stress–shear displacement relationship

to failure was 216 cm/s^2. This test result suggested that a lesser earthquake shaking (of around 216/633 = 0.34) than occurred in the Iwate–Miyagi earthquake could have caused failure under a slope condition with a pore-pressure ratio of 0.27. The steady-state shear strength was 157 kPa.

5.9 Case for the Initiation of the Motion of Deposits Downslope/Alluvial Deposits by the Moving Landslide Mass (Fig. 97)

ICL-2 was used to simulate undrained loading on the black-dot layer in the lower slope continued to the coast (Fig. 86) using the displaced mass from the upper slope (red-dot block). Figure 97 presents the test result of an undrained dynamic loading test simulating this scenario. Firstly, the initial normal stress and the initial shear stress (σ_0 = 1000 kPa, τ_0 = 150 kPa, corresponding to an 8.5° slope) were loaded in the drained condition to reproduce the initial stress state at the bottom of the black-dot layer. The normal stress was increased to 2790 kPa (which is close to the 3 MPa capacity of the apparatus) as the undrained load, although a 400-m-deep initial landslide will result in a greater normal stress. If the lower slope mass can resist the undrained load from the upper slope without raised porewater pressure, it may resist around 2374 kPa (2790×tan (40.4°)) in this dynamic loading. However, as seen in Fig. 97, a high porewater pressure was generated in the undrained loading. The sample failed at 720 kPa and its steady-state stress was 80 kPa. The landslide mass from the upper slope should scrape off a layer of the lower slope and move together as a combined greater mass toward the sea. This scenario was proven to be possible by this landslide simulation test using ICL-2.

5.9.1 Observation of the Shear Zone State Between Undrained Test and the Drained Test (Fig. 98)

Sample S2 was taken from Volcanic debris. The grain shape is angular. We compared the shear zone after shearing under the high normal stress of 3 MPa.

The left photo shows the shear zone of S2 after the undrained stress control test (Fig. 92), the right photo shows the shear zone of pore-pressure control test (Fig. 95). Pore-pressure control test was conducted under the drained condition. Pressure of pore-water was controlled, while pore-water moved from/to the shear box through the pore water control system (Fig. 10). Shearing proceeded in almost

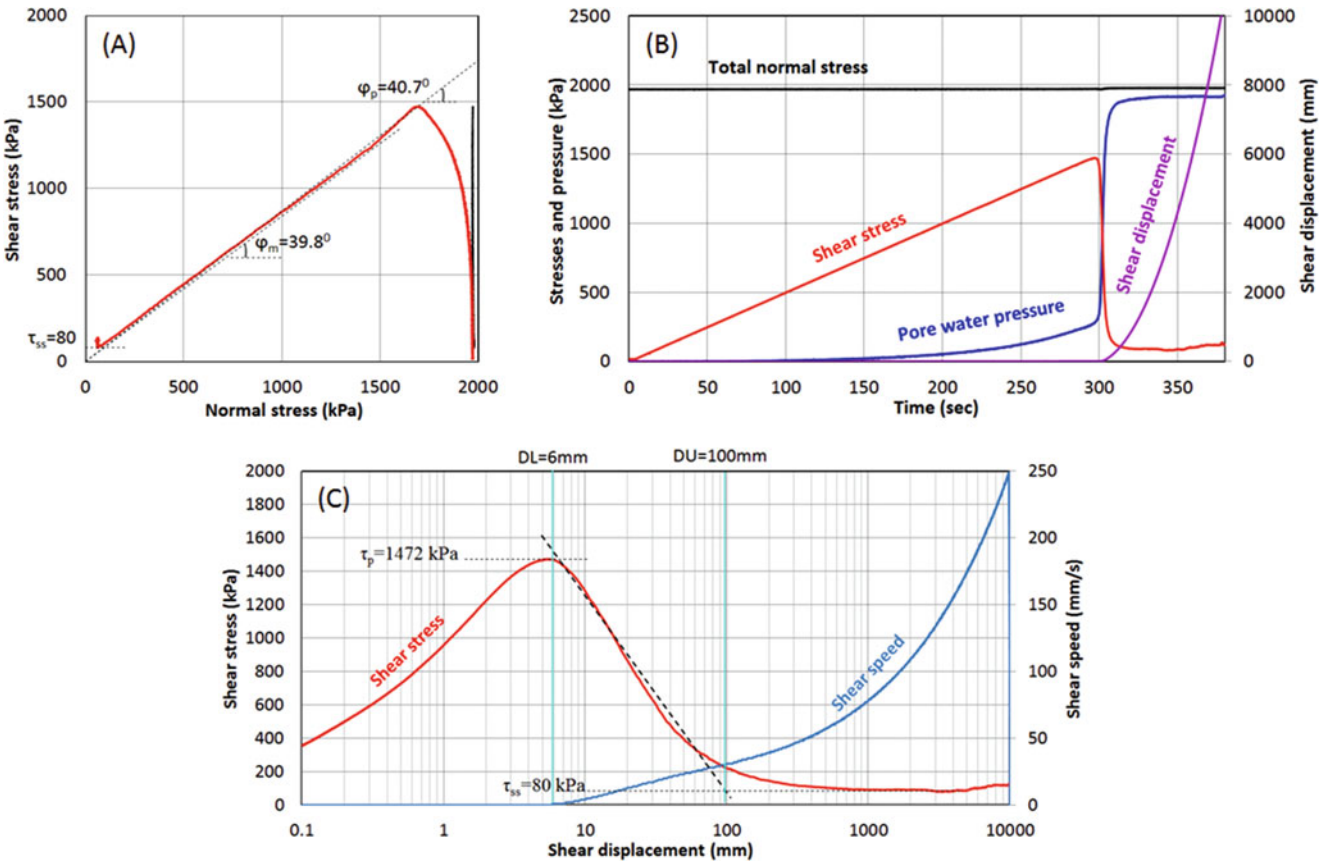

Fig. 91 Saturated and undrained stress controlled test for Unzen sample S1. Normal stress 1970 kPa, BD = 0.96, Shear stress increment = 2 kPa/s. (**a**) Stress path, (**b**) Time series data, (**c**) Shear stress–shear displacement relationship

liquefied state in the undrained test (Figs. 92 and 96), whereas shearing in the pore pressure control (drained test) proceeded not in the liquefied state. So, grain crushing under the pore-pressure control test should be greater than that of the undrained shear test. The right photo visualized a silty shear zone which was formed by grain crushing of the sample. We could not find the shear surface in the left photo. The steady state was reached at 10–20 cm shear displacement. During the steady state, effective normal stress, pore pressure and shear stress were constant. Only shear displacement progressed without further grain crushing.

5.9.2 LS-RAPID Simulation (Fig. 99)

We applied LS-RAPID to estimate the motion of the 1792 Unzen-Mayuyama Landslide.

Triggering factors used were pore-water pressure + earthquake shaking which represent the case for the landslide initiation by volcanic seismic shaking (Fig. 96). The parameters used in the computer simulation are listed in Table 7.

The simulation result is presented in Fig. 99.

Red color balls represent the moving mass, while blue balls represent the stable mass.

At 11 s, the pore-water pressure reached 0.21 and the earthquake started, but no motion occurred.

At 17 s, the main shock of earthquake struck the area and failure occurred within the slope. Failure began from the middle of the slope.

At 26 s, the earthquake has almost terminated. The whole landslide mass was formed during the earthquake shaking.

At 64 s, the landslide mass continued to move after the earthquake ended and entered into the sea

At 226 s, the landslide mass stopped moving and was deposited.

In Fig. 99, the simulated deposition area was compared with the map made by the Unzen Restoration Office of the Ministry of Land, Infrastructure and Transport of Japan (2002) based on topographic survey (right-bottom of the figure). To compare both landslide motions, the section of line A in the right-bottom figure and the E–W section (almost the same as line A) of the computer simulation were compared. Both movements were very similar. The travel distances from the head scarp of the initial landslide to the toe of the displaced landslide mass were around 6 km. The travel distance in the

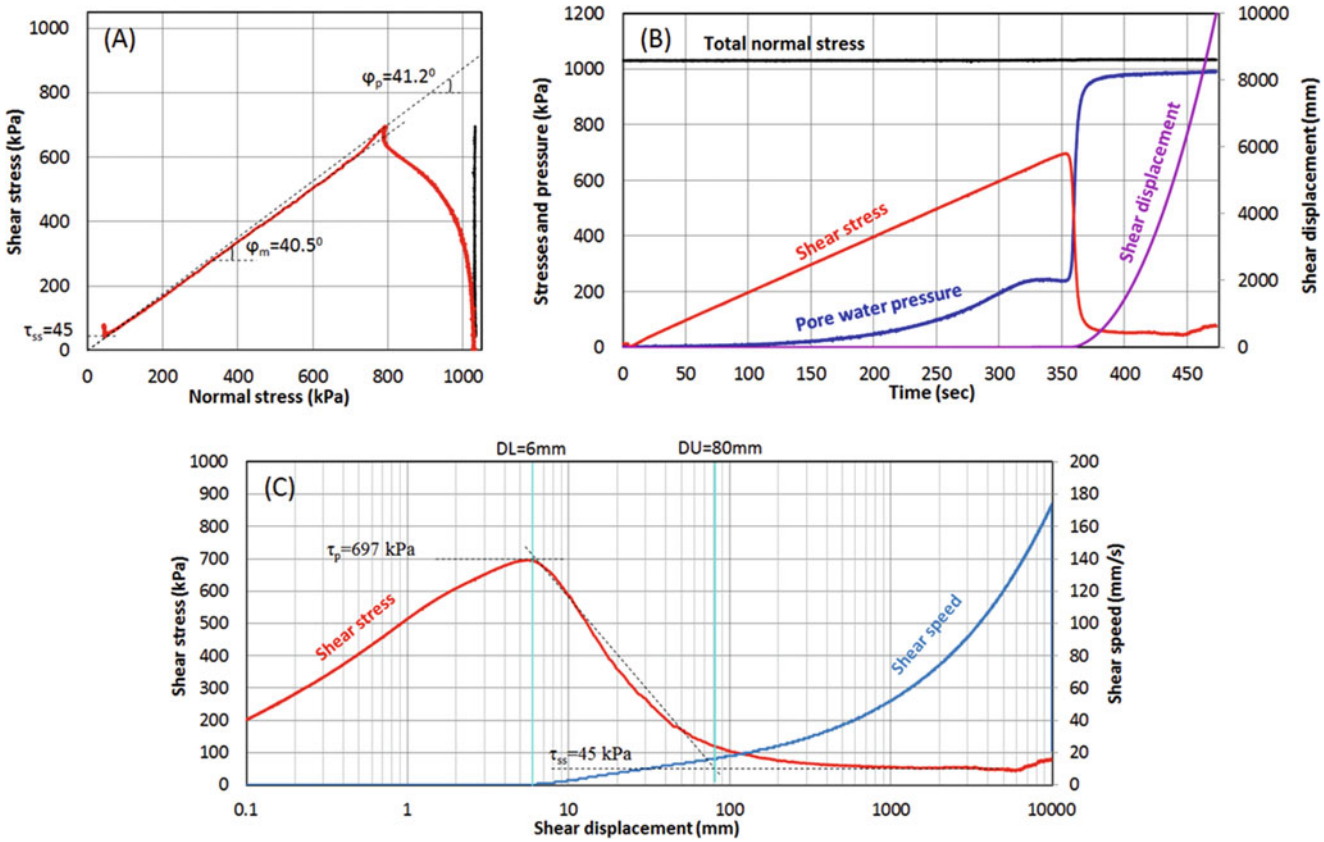

Fig. 92 Saturated and undrained stress controlled test for Unzen sample S1. Normal stress 2900 kPa, BD = 0.96, Shear stress increment = 2 kPa/s. (**a**) Stress path, (**b**) Time series data, (**c**) Shear stress–shear displacement relationship

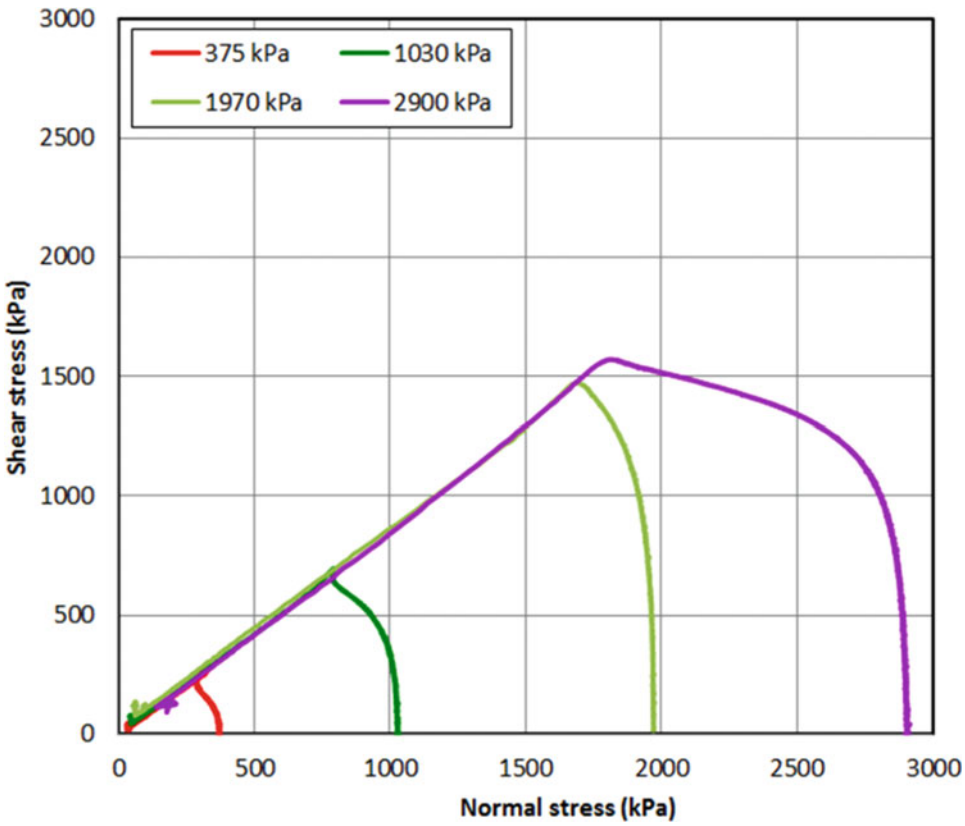

Fig. 93 Combined stress paths of saturated and undrained stress controlled tests for Unzen sample S1

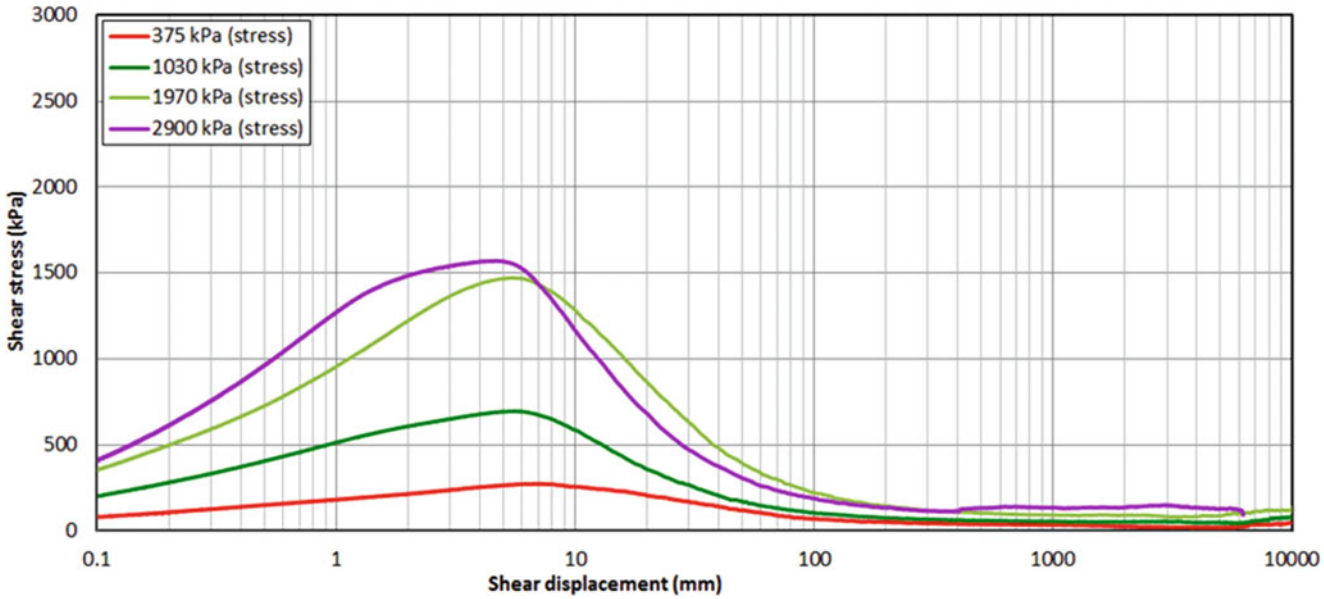

Fig. 94 Combined shear stress and shear displacement relationship of the undrained stress controlled tests for Unzen sample S1

computer simulation was 6.6 km, while the distance based on the field investigation of the deposits was 5.9 km.

5.9.3 LS-Tsunami Simulation (Fig. 100)

Figure 100a presents the basic principle of the landslide-induced tsunami simulation model and Fig. 100b presents the tsunami wave calculated by LS-Tsunami (Sassa et al. 2016).

The basic principle of the landslide-induced tsunami model (Fig. 100a)

The left part of Fig. 100a is the same as the principle of the integrated landslide simulation model (LS-RAPID) of Sassa et al. (2010). The only difference here is that the landslide mass is located beneath a water surface. The right part of Fig. 100a illustrates the elevated water mass (which causes a tsunami wave) by the upward displacement of the interface between the landslide and the water due to the movement of the landslide mass over the sea floor.

When the landslide mass enters or travels across the sea floor, the elevation of the submarine ground surface (which is the interface of landslide mass and submarine water) will be

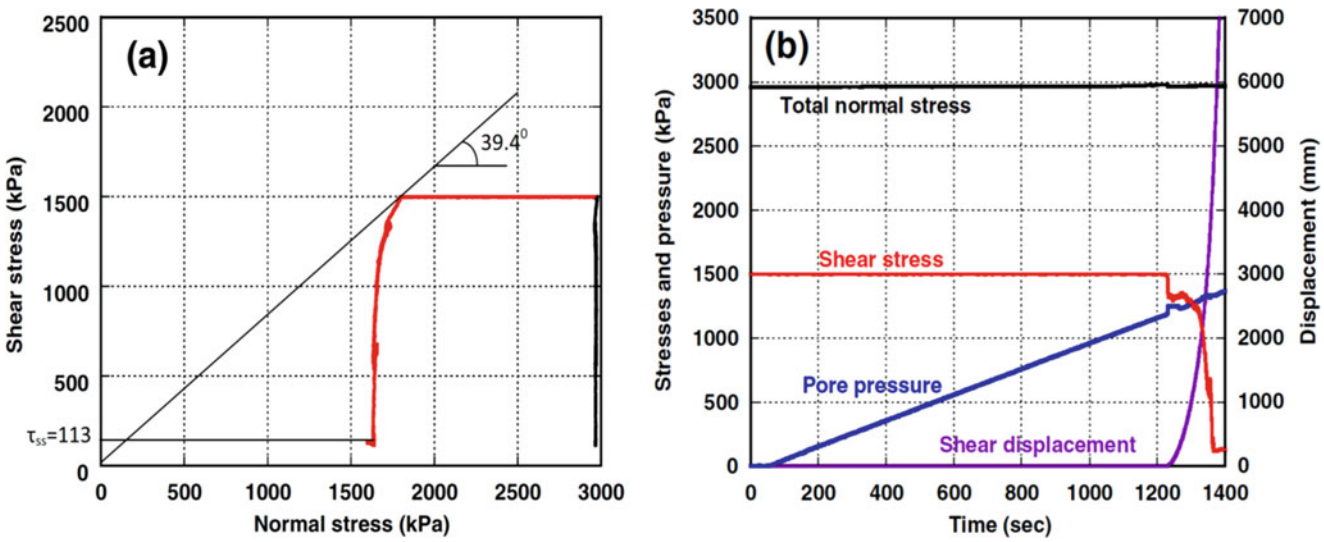

Fig. 95 Pore-pressure-controlled test on the Unzen sample S1 to simulate a rain-induced landslide

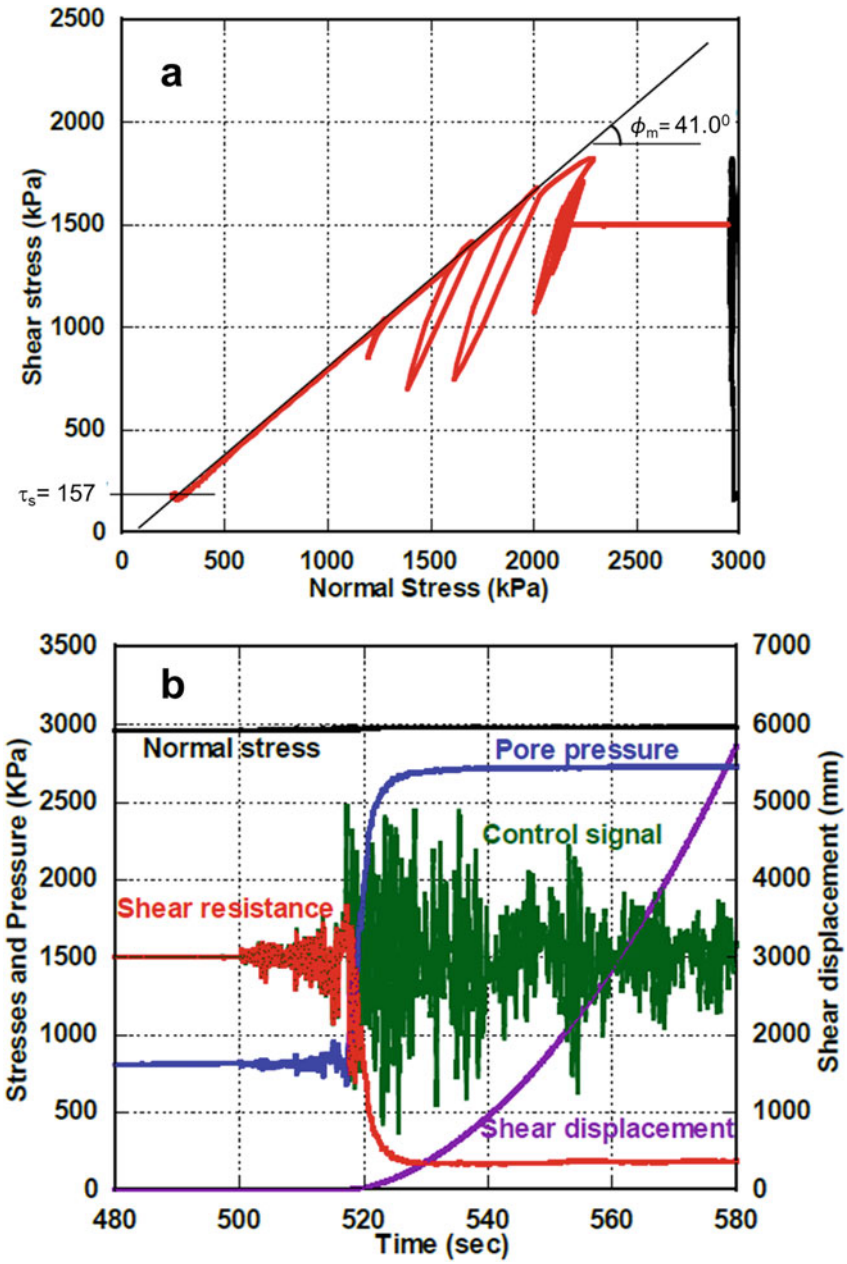

Fig. 96 Seismic-loading ring-shear test on the Unzen sample S1. (**a**) Stress path, (**b**) Time series data

increased. The submarine ground surface elevated by the landslide mass will raise the water mass above the landslide-water interface by an amount, Δh, in a unit time, Δt. The shear resistance (τ_{sw}) between soil and water at this interface should be much smaller than the shear resistance within the soil. Hence, this resistance, τ_{sw}, was ignored in the simulation. The effective stress acting on the surface between the bottom of the soil column and the top of the sea floor was regarded as being unaffected by the increase in water height for the following two reasons: (1) The surficial deposit on the sea floor is unconsolidated and hence is expected to be permeable enough to transmit the water pressure change due to water height change to the bottom of the soil column above the sea floor; and (2) the soil column of the moving mass is both unconsolidated and water saturated, and hence the transmission of water-pressure change from the top of soil column to the bottom of the soil column is fast (elastic wave velocity of water is around 1.5 km/s) and can be regarded as instantaneous.

When a landslide mass enters into water, the buoyant force by water will act on the soil mass. Namely, the unit weight of soil mass (γ_t) on land will change to the buoyant unit weight of soil mass, the difference between γ_t and γ_w (unit weight of seawater) under water. In the case of partial submersion, the buoyant force by water will act only on the part of soil mass below the water surface. No tangential force between soil and

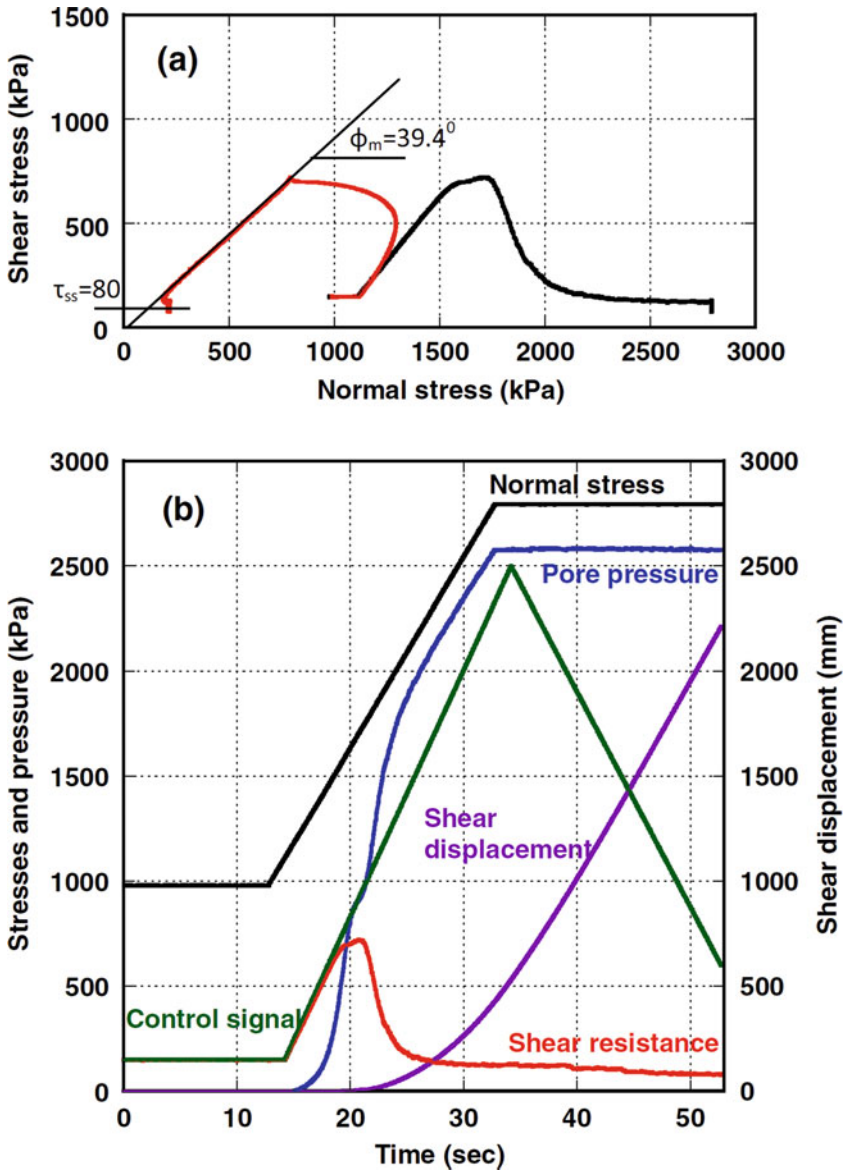

Fig. 97 Undrained dynamic loading test on Sample 2 $B_D = 0.97$. Initial stress (Normal stress = 1000 kPa, Shear stress = 150 kPa). (**a**) Stress path, (**b**) Time series data

water is considered because the tangential force by water will be negligible compared to the shear resistance mobilized in the shear surface of large-scale landslides.

There are many parameters to regulate landslide motion on land and submarine landslide motion. The values of such landslide dynamics parameters were mostly measured by the undrained ring shear testing on the samples taken from the landslide source area and its moving area. The parameters used in tsunami simulation (LS-Tsunami) are the unit weight of seawater and Manning's roughness coefficient for basal resistance between water and ground.

The Result of LS-Tsunami-Propagation of Tsunami Wave from the Landslide to the Opposite Bank (Fig. 100b)

Figure 100b presents the contour of the maximum tsunami height at each mesh with the tsunami height records in the Kumamoto side coast and in the Shimabara side coast. The coastline is shown in red where the tsunami wave moved up to the land. Table 8 presented the reported and simulated tsunami heights at five sites along the Kumamoto and the Shimabara coasts. Differences between the computer simulation and the historical records for the five specific points were

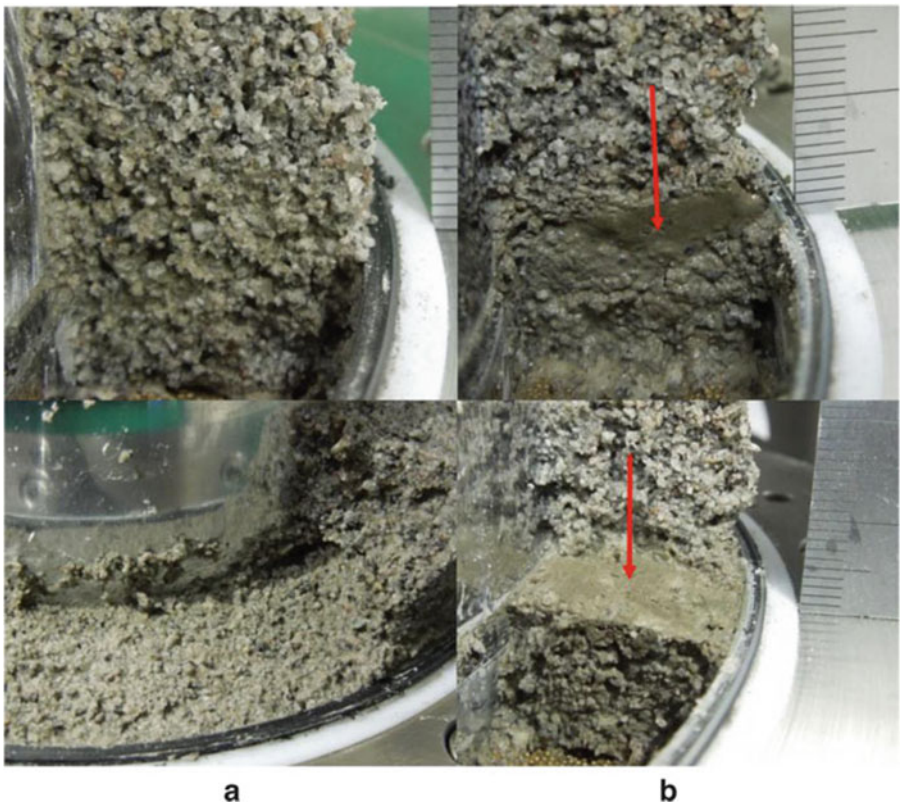

Fig. 98 Samples after shearing. Left: undrained test. Right: Drained test (pore-pressure control test)

less than 5.7 m for Manning's coefficient 0.025 $m^{-1/3}/s$, 4.6 m for Manning's coefficient, 0.020 $m^{-1/3}/s$, and 5.2 m for Manning's coefficient 0.015 $m^{-1/3}/s$ except the case at Futsu. Futsu is a special case where the first direct tsunami wave from the source of tsunami hits the cliff of the Futsu terrace and probably amplified due to the gulf-shaped coast line.

The simulation of LS-Tsunami used 100 m mesh data. It cannot include the effect of local amplification of tsunami height due to the sharp topography in this part of the coast. LS-Tsunami uses the average elevation for each 100-m mesh. The elevation of Tsunami-Dome-Ishi on the slope is not always close to the average height of calculated mesh. In the case of 15–20° slope, 25-m (one fourth of one mesh) difference in horizontal distance cause 6.7–9.1-m elevation difference. The maximum 5.7-m difference in Table 8 is within the elevation difference on the slope. Considering these conditions, the estimated area of tsunami and the tsunami heights along the coast by LS-Tsunami matches with the historical record. It can be understood that the result of this trial test on the Unzen-Mayuyama Landslide-and-tsunami disaster presented a reasonable extent of reliability and a meaningful extent of precision within the variation of Manning's coefficient and the resolution of ground elevation. Carefully examining the value difference in different Manning's coefficient, the effect of the coefficient is greater in the long travel distance of tsunami and gives closer tsunami heights in Kyodamari and Umedo.

Table 7 Parameters used in computer simulation (LS-RAPID and LS-Tsunami) of the Unzen-Mayuyama landslide

Parameters used in simulation	Value	Source
Parameters of soils in the source area (deeper area)		
Steady state shear resistance (τ_{ss})	120 kPa	Test data
Lateral Pressure ratio ($k = \sigma_h/\sigma_v$)	0.7–0.8	Estimation (see text)
Friction angle at peak (ϕ_p)	42.0°	Test data
Cohesion at peak (c)	10 kPa	Assuming small
Friction angle during motion (ϕ_m)	40.0°	Test data
Shear displacement at the start of strength reduction (D_L)	6 mm	Test data
Shear displacement at the start of steady slate (D_U)	90 mm	Test data
Pore pressure generation rate (B_{ss})*	0.7–0.9	Estimated
Total unit weight of the mass (γ_t)	19.5 kN/m^3	From the test
Parameters of soils in the moving area (shallower area)		
Steady state shear resistance (τ_{ss})	30–80 kPa	Test data
Lateral Pressure ratio ($k = \sigma_h/\sigma_v$)	0.8–0.9	Estimated
Friction angle at peak (ϕ_p)	40.0°	Test data
Cohesion at peak (c)	10 kPa	Assuming small
Friction angle during motion (ϕ_m)	40.0°	Test data
Shear displacement at the start of strength reduction (D_L)	6 mm	Test data
Shear displacement at the end of strength reduction (D_U)	90 mm	Test data
Pore pressure generation rate (B_{ss})	0.7–0.9	Estimated
Total unit weight of the mass (γ_t)	19.5 kN/m^3	From the test
Triggering factor		
Excess pore pressure ratio in the fractured zone (r_u)	0.21	Assumption
0.5 times of the 2008 Iwate–Miyagi earthquake	Max:370 cm/s^2	Wave form of the Ground motion record at MYG004
Parameters of the function for non-frictional energy consumption		
Coefficient for non-frictional energy consumption	1.0	Data (Sassa et al. 2010)
Threshold value of velocity	100 m/s	A few times greater than maximum reported speed
Threshold value of soil height	400 m	Maximum depth of the initial source area
Other factors		
Steady state shear resistance under sea	10 kPa	Data (Sassa et al. 2004)
Unit weight of sea water	10.1 kN/m^3	Average sea water density

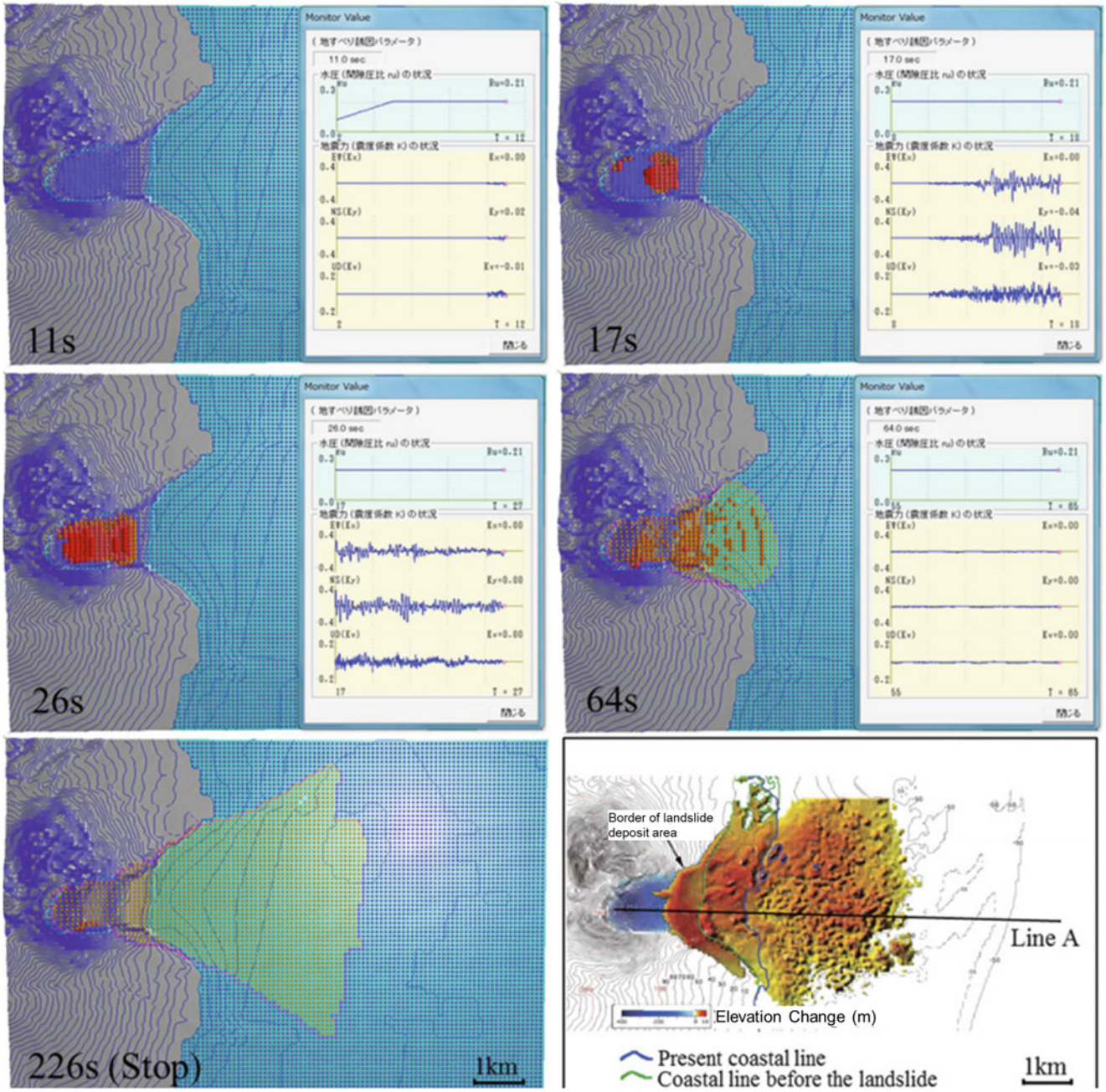

Fig. 99 Movement of the Mayuyama landslide estimated by LS-RAPID simulation

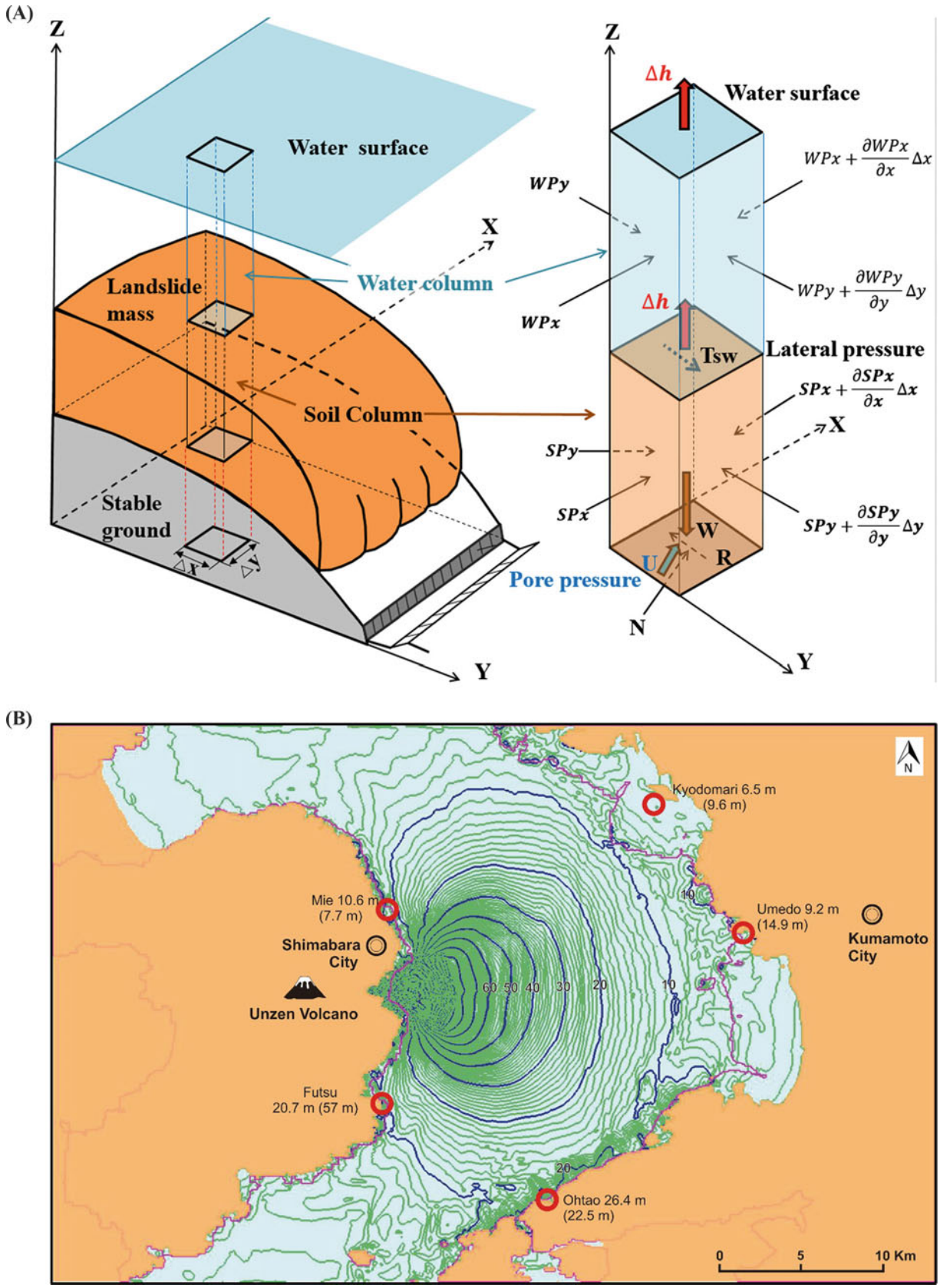

Fig. 100 Landslide-induced tsunami simulation model (LS-Tsunami) (**a**) and its application for the Tsunami wave induced by the Mayuyama Landslide (**b**)

Table 8 Comparison of tsunami heights between the simulation result and the historical record

Location		Tsunami heights from Tsunami-Dome-Ishi and memorial stone pillars	Tsunami heights by LS-Tsunami Manning's coefficient = 0.025 ($m^{-1/3}$. s)	Tsunami heights by LS-Tsunami Manning's coefficient = 0.020 ($m^{-1/3}$. s)	Tsunami heights by LS-Tsunami Manning's coefficient = 0.015 ($m^{-1/3}$. s)
Kumamoto coast	Kyodomari	9.6 m	6.5 m	7.7 m	9.7 m
	Umedo	14.9 m	9.2 m	11.2 m	13.2 m
	Ohtao	22.5 m	26.4 m	27.1 m	27.7 m
Shimabara coast	Futsu	57 m	20.7 m	21.0 m	21.3 m
	Mie	7.7 m	10.6 m	10.9 m	11.0 m

Acknowledgements The authors acknowledge the International Consortium on Landslides (the host organization of KLC2020) and the official (public and private) promoters of the KLC2020 as well as all 90 signatory organizations of KLC2020 for creating an opportunity to publish this lesson in an Open Access media.

The authors wrote this landslide lesson as a Commitment to the Sendai Landslide Partnerships 2015-2025 and the Kyoto Landslide Commitment 2020.

One of targets of this landslide lesson is to create a teaching tool for capacity development in Sri Lanka and other countries suffering from rapid and long-travelling landslides. The ICL and the National Building Research Organisation (NBRO) in Sri Lanka jointly applied for and obtained budget from a SATREPS "Science and Technology Research Partnership for Sustainable Development" programme under the title of "Development of Early Warning Technology of Rain-Induced Rapid and Long Travelling Landslides" from 2019 to 2025.

References

Catane SG, Cabria HB, Tomarong CP, Saturay RM, Zarco MA, Pioquinto WC (2007) Catastrophic rockslide-debris avalanche at St. Bernard, Southern Leyte, Philippines. Landslides 4(1):85–90

Chigira M, Tsou C-Y, Matsushi Y, Hiraishi N, Matsuzawa M (2013) Topographic precursors and geological structures of deep-seated catastrophic landslides caused by Typhoon Talas. Geomorphology 201:479–493

Cruden DM, Varnes DJ (1996) Landslides: investigation and mitigation. Chapter 3 Landslide Types and Processes. Transportation Research Board Special Report, 247

FDMA (2012) Report No. 20 released by the Fire and Disaster Management Agency on 28 September 2012, 10 pages (in Japanese)

Fukushima Y, Tanaka T (1990) A new attenuation relation for peak horizontal acceleration of strong earthquake ground motion in Japan. Bull Seismol Soc Am 84:757–783

Fujiwara O, Aoshima A, Irizuki T, Ono E, Obrochta S, Sampei Y, Sato Y, Takahashi A (2019) Tsunami deposits refine great earthquake rupture extent and recurrence over the past 1300 years along the Nankai and Tokai fault segments of the Nankai Trough, Japan. Quat Sci Rev

Hayashi S, Uchida T, Okamoto A, Ishizuka T, Yamakoshi T, Morita K (2013) Countermeasures against landslide dams caused by Typhoon Talas 2011. Asia-Pacific Tech Monitor 30(1):20–26

Hayashida A, Kamata H, Danhara T (1996) Correlation of widespread tephra deposits based on paleomagnetic directions: link between a volcanic field and sedimentary sequences in Japan. Quat Int 34–36: 89–98

Hong Y, Hiura H, Shino K, Sassa K, Fukuoka H (2005) Quantitative assessment on the influence of heavy rainfall on the crystalline schist aldnslide by monitoirng system—case study on Zentoku landslide in Japan. Landslides 2(1):31–41

Inoue K (1999) Shimabara–Shigatusaku Earthquake and topographic changes by Shimabara catastrophe. J Jpn Soc Erosion Control Eng 52(4):45–54

Inoue K, Doshida S (2012) Comparison of Distribution of Disasters Occurring in 1889 and 2011 on Kii Peninsula. J Japan Soc Erosion Control Eng 65(302):42–46

Loi DH, Sassa K, Dang K, Miyagi T (2021) Simulation of tsunami waves induced by coastal and submarine landslides in Japan. In: Sassa K, Mikoš M, Sassa S, Bobrowsky PT, Takara K, Dang K (eds) Understanding and reducing landslide disaster risk: volume 1 Sendai Landslide Partnerships and Kyoto Landslide Commitment. Part III Landslide-induced Tsunamis. Springer Nature, pp 295–327

Okada Y, Sassa K, Fukuoka H (2000) Liqefacton and the steady state of wethered granitic sands obtained by undrained ring shear tests: a fundamental study of the mechanism of liquidized landslides. J Nat Disaster Sci 22(2):75–85

SABO (2013) A pamphlet released in October, 2013 on Overview of the 2011 disaster induced by Typhoon No. 12, Implementation of an urgent investigation and countermeasures to disaster areas. The Kii Mountain District SABO Office, Kinki Regional Development Bureau. The Ministry of Land, Infrastructure, Transport and Tourism. http://www.kkr.mlit.go.jp/kiisanchi/outline/, 24 pages (in Japanese)

Sassa K (1984) The mechanism starting liquefied landslides and debris flows. In: Proceedings of 4th international symposium on landslides, vol 2, pp 349–354

Sassa K (1985) Geotechnical classification of landslides. In: Proceedings of the 4th International Conference and Field Workshop on Landslides. pp 31–40

Sassa K (1988) Special Lecture "Geotechnical model for the motion of landslides". In: Proceedings of the 5th International Symposium on Landslides, Lausanne, Landslides, Balkema, vol 1, pp 37–56

Sassa K (1989) Geotechnical classification of landslides. Landslide News 3:21–24

Sassa K (1996) Prediction of earthquake induced landslides. In: Special Lecture for 7th International Symposium on Landslides. "Landslides", vol 1. Balkema Co. Ltd., pp 115–132

Sassa K (1999) Introduction of landslides of the world. In: Sassa K (ed) Japan Landslide Society. Kyoto University Press, pp 3–18

Sassa K, Fukuoka H, Lee CH and Zhang D (1992) Measurement of the apparent friction angle during rapid loading by the high-speed high-stress ring shear apparatus. Interpretation of the relationship between landslide volume and the apparent friction during motion, Landslides, Balkema/Rotterdam, vol 1, pp 545-552

Sato H, Shiraishi S, Ito T (2004) The behavior of the Tertiary landslides through the snowy period in Niigata Prefecture, Central Japan. J Japan Landslide Soc 41(1):37–42. https://www.jstage.jst.go.jp/article/jls2003/41/1/41_1_3_7/_pdf/-char/en

Sassa K, Dang K (2018) TXT-tool 0.081-1.1: Landslide dynamics for risk assessment. Landslide dynamics: ISDR-ICL Landslide interactive teaching tools. In: Sassa K, Guzzetti F, Yamagishi H, Arbanas Z, Casagli N, McSaveney M, Dang K (eds) Fundamental, mapping and monitoring, vol 1. Springer, pp 1–79

Sassa K, Fukuoka H, Wang G, Ishikawa N (2004) Undrained dynamic-loading ring-shear apparatus and its application to landslide dynamics. Landslides 1:7–19

Sassa K, Nagai O, Solidum R, Yamazaki Y, Ohta H (2010) An integrated model simulating the initiation and motion of earthquake and rain induced rapid landslides and its application to the 2006 Leyte landslide. Landslides 7:219–236

Sassa K, He B, Miyagi T, Strasser M, Konagai K, Ostric M, Setiawan H, Takara K, Nagai O, Yamashiki Y, Tutumi S (2012) A hypothesis of the Senoumi submarine megaslide in Suruga Bay in Japan—based on the undrained dynamic-loading ring shear tests and computer simulation. Landslides 9:439–455

Sassa K, Dang K, He B, Takara K, Inoue K, Nagai O (2014a) A new high-stress undrained ring-shear apparatus and its application to the 1792 Unzen–Mayuyama megaslide in Japan. Landslides 11:827–842

Sassa K, He B, Dang K, Nagai O, Takara K (2014b) Plenary: progress in landslide dynamics. Landslide Sci Safer Geoenviron 1:37–67

Sassa K, Dang K, Yanagisawa H, He B (2016) A new landslide-induced tsunami simulation model and its application to the 1792 Unzen-Mayuyama landslide-and-tsunami disaster. Landslides 13:1405–1419

Sassa K (2016) Implementation of the ISDR-ICL Sendai Partnerships 2015–2025 for global promotion of understanding and reducing landslide disaster risk. Landslides 13:211–214

Sassa K (2021) The Kyoto Landslide Commitment 2020: launched. Landslides 18:5–20

Sassa K, Canuti P, Bobrowsky P, Casagli N (2022) International Consortium on Landslides from IDNDR, IGCP, WCDRR2+3, to Kyoto Landslide Commitment 2020. P-LRT 1(1) (in press)

Tabata S, Inoue K, Hayakawa T, Sano S (2001) Study of formation and collapse of many landslide dams caused by heavy rain- Totsukawa Hazard (1889) and Aridakawa Hazard (1953). Japan Soc Erosion Control Eng 53(6):66–76

Tien PV (2018) Mechanisms and hazard assessment of rainfall-induced landslide dams. Ph.D. Thesis, Kyoto University

Tien PV, Sassa K, Takara K, Fukuoka H, Dang K, Shibasaki T, Ha ND, Setiawan H, Loi DH (2018) Formation process of two massive dams following rainfall-induced deep-seated rapid landslide failures in the Kii Peninsula of Japan. Landslides 5:1761–1778

Trandafir A, Sassa K (2005) Seismic triggering of catastrophic failures on shear surfaces in saturated cohesionless soils. Can Geotech J 42:229–251

Unzen Restoration Office of the Ministry of Land, Infrastructure and Transport of Japan (2002) The Catastrophe in Shimabara—1791–92 eruption of Unzen–Fugendake and the sector collapse of Mayu-Yama. An English leaflet (23 pages)

Unzen Restoration Office of the Ministry of Land, Infrastructure and Transport of Japan (2003) The Catastrophe in Shimabara—1791–92 eruption of Unzen–Fugendake and the sector collapse of Mayu-Yama. A Japanese leaflet (44 pages)

Usami T (1996) Materials for comprehensive list of destructive earthquakes in Japan. University of Tokyo Press, Tokyo

Yamada M, Matsushi Y, Chigira M, Mori J (2012) Seismic recordings of landslides caused by Typhoon Talas (2011), Japan. Geophys Res Lett 39:L13301

Identification and Mitigation of Reservoir Landslides: Cases Studied in the Three Gorges Reservoir Area of China

Huiming Tang

Abstract

Reservoir landslides are one of the most common types of geohazards in reservoir areas. It is of great theoretical significance and engineering application value to carry out the identification and mitigation research of them. In the Three Gorges Reservoir area (TGRA), a series of studies were conducted on the reservoir landslides in aspects of their characteristics, evolution mechanisms, prevention and control, and forecasting by means of field investigation, monitoring and in-situ experiment, etc. Massive corpora of these research work are summarized and presented here in five aspects, with the goal of gaining insights into the effective prevention and mitigation of them: (1) the characteristics of the reservoir landslides located in the TGRA were summarized; (2) the stability evaluation methods of reservoir landslide include qualitative, limit equilibrium methods, numerical simulation methods and probabilistic methods were introduced; (3) the in-situ experiment on slipping zone soil of reservoir landslides carried out on the Huangtupo landslide was described; (4) the research progresses in reservoir landslide prevention and control was introduced; (5) the prospects of reservoir landslides forecasting based on physical-mechanical mechanism was elaborated. Based on the overview, suggests topics for future research are given to address the remaining challenges of reservoir landslides.

Keywords

Reservoir landslide · Characteristics · Assessment · In-situ experiment · Prevention and control · Forecasting

H. Tang (✉)
Faculty of Engineering, China University of Geosciences, Wuhan, Hubei, China

Badong National Observation and Research Station of Geohazards, China University of Geosciences, Wuhan, China
e-mail: tanghm@cug.edu.cn

1 Introduction

Landslides caused by the impoundment and drawdown of reservoir are called reservoir landslides. They're widespread throughout the globe, posing a threat to the safety of residential areas, roads, and water transportation in the reservoir area. Once it occurs, on the one hand, the impact of the sliding mass can produce huge surges, which causes flood when crossing the dam and rushing to the downstream; On the other hand, the sliding mass can block the river and form a natural dam, causing upstream backwater and potential threats of debris flow or flooding. The 1963 Vajont landslide is a typical reservoir landslide in Italy. The sliding mass glides down as a whole at a maximum speed of 30 m/s, causing a surge of 250 m high that demolished the Longarone town and caused over 2000 deaths (Paronuzzi and Bolla 2012). Reservoir landslides is a serious natural disaster that must attract attention.

The influencing factors of reservoir landslides are various, including geological environment, rainfall, reservoir water level fluctuations, and engineering excavation, etc. (Huang and Gu 2017; Wen et al. 2017; Froude and Petley 2018). Water is a key factor in all of these. Through the affection of hydrostatic pressure, buoyancy force, hydrodynamic pressure, the sliding zone is developed and the physical-mechanical properties of the sliding mass are changed, which eventually lead to the landslide. Therefore, figure out how to reduce the impact of water has always been the top research priority in the mitigate of reservoir landslides. Although hundreds of billions of RMB have been invested in the study and treatment of these reservoir landslides, many of them remain in a state of continuous deformation, with cumulative displacements of several meters now documented at the Huangtupo Landslide (Tang et al. 2015a; Zou et al. 2020; Dumperth et al. 2016), Outang (Yin et al. 2016), and Baishuihe (Li et al. 2010; Du et al. 2013).

The identification and mitigation study of reservoir landslides has attracted wide attention globally, as a great

I. Alcántara-Ayala et al. (eds.), *Progress in Landslide Research and Technology, Volume 2 Issue 1, 2023*,
Progress in Landslide Research and Technology, https://doi.org/10.1007/978-3-031-39012-8_3

deal of scientific research has been undertaken on them over the past decades. Statistical data show that, among the 969 papers on the theme of reservoir landslides from 1999 to 2018 included in the Web of Science (WOS), only a few were published annually before the completion of the Three Gorges Dam (TGD) in 2003. Then, the number of papers related to reservoir landslides and the number of citations increased rapidly at an annual rate of 20–40% (Li et al. 2020). The construction of the TGD in China has greatly enriched the study of reservoir landslides.

The VOS viewer's examination results of the abstracts and titles of 969 papers aforementioned are displayed in Fig. 1. Each ball's size denotes the frequency with which that term appears, the line thickness between balls represents the degree of link between two high-frequency terms, and the balls' colors represent the many topics to which those terms pertain. Results show that research on reservoir landslides over the past 20 years has primarily focused on the three topics as shown by the distribution of high frequency terms related to reservoir landslides in Fig. 1. These topics are "deformation, stability, seepage" (red ball), "prediction, landslide hazard, network" (blue ball), and "sediment, erosion, deposit" (green ball). Density plots of these frequently-used terms reveal that "China," "Gorges Reservoir," "deformation," and "stability" are the most-used and most-related terms, suggesting that the stability of the reservoir landslide in the Three Gorges Reservoir area (hereafter referred to as TGRA) is the primary focus of reservoir landslide study.

To make a comprehensive entirety introduction of the reservoir landslides, the study of reservoir landslides in the TGRA was summarized here from the following five aspects: (1) characterizing TGRA reservoir landslides; (2) evaluating reservoir landslides' stability; (3) conducting of reservoir landslides in-situ experiment; (4) designing of reservoir landslides prevention and control measures; and (5) elaborating the potential for reservoir landslide forecasting based on physical-mechanical mechanisms. Suggestions for future research toward the goal of disaster reduction and discusses difficulties engineering geologists face in the prevention and mitigation of TGRA reservoir landslides were also given (Tang et al. 2019).

2 Characteristic of Reservoir Landslides in the TGRA

2.1 Spatiotemporal Distribution

Along the Yangtze River, the distribution density of landslides shows clearly distinct regional differences. The landslides tend to concentrate along the Yangtze River and some of its tributaries but are most common to the east of Wanzhou in the TGRA, (Fig. 2a). In terms of quantity, landslides and rock avalanches are especially common in Zigui and Badong counties (Fig. 3). Considering the tributary rivers, landslides are most frequent in the catchments of Xiangxi, Guizhou, Qinggan, Caotang, Meixi, and Wujiang Rivers, accounting for 44.3% of the total number of landslides and collapses present along the Yangtze River tributaries.

The evolution process determines the complexity and diversity of reservoir landslide, and also determines the boundary conditions and spatiotemporal development law of landslide. For instance, it is found that the occurrence time and front elevation of landslide have close relationships with the neotectonic movements in different periods of the Yangtze River and the elevation of river terraces (Fig. 2). The formation of slip zone is controlled by multi-stage crack expansion and connectivity, revealing the multi-scale spatial distribution law of reservoir landslide.

The landslides in the TGRA generally have significant regularity in the elevation distribution. The elevations of the front edges of reservoir landslides that occur along the Yangtze River are shown in Fig. 2b. Among them, 93% of their front edges' elevations are concentrated between the elevation segment of 100–175 m, which was the water level fluctuation zone after the construction of the TGD. This indicates that the reservoir landslides are closely related to the effects of the fluvial erosion of the slope toe. The river water erodes the side part of riverbed or the slope toe, gradually forming better free space conditions, which makes the upper sliding mass lose sufficient support and leads to shear failure. Overall, the reservoir landslides are concentrated in the first and second terraces as well as reservoir water level fluctuation zones, while only a small amount of them are developed in the third terrace. The number of reservoir landslides decreases with increasing elevation. This is due to the relatively late formation of reservoir landslides in the first and second terraces, while those that formed earlier in the third terrace were gradually denuded or even disappeared during their evolution process under the influence of reservoir (Li et al. 2018).

2.2 Slide-Prone Strata

Lithology is a primary determinant of reservoir landslides distribution in the TGRA (Li et al. 2018). The sandstone, mudstone, and interbedded sandstone/mudstone layers of the Triassic Badong Formation and the Jurassic strata are known as the most slide-prone strata, producing numerous landslides. The reservoir landslides identified in these strata account for 91.1% of the total landslide volume in the TGRA.

The Badong formation strata are distributed widely in the TGRA, in which large-size landslides and deep-reaching loosely consolidated formations are likely to occur. The

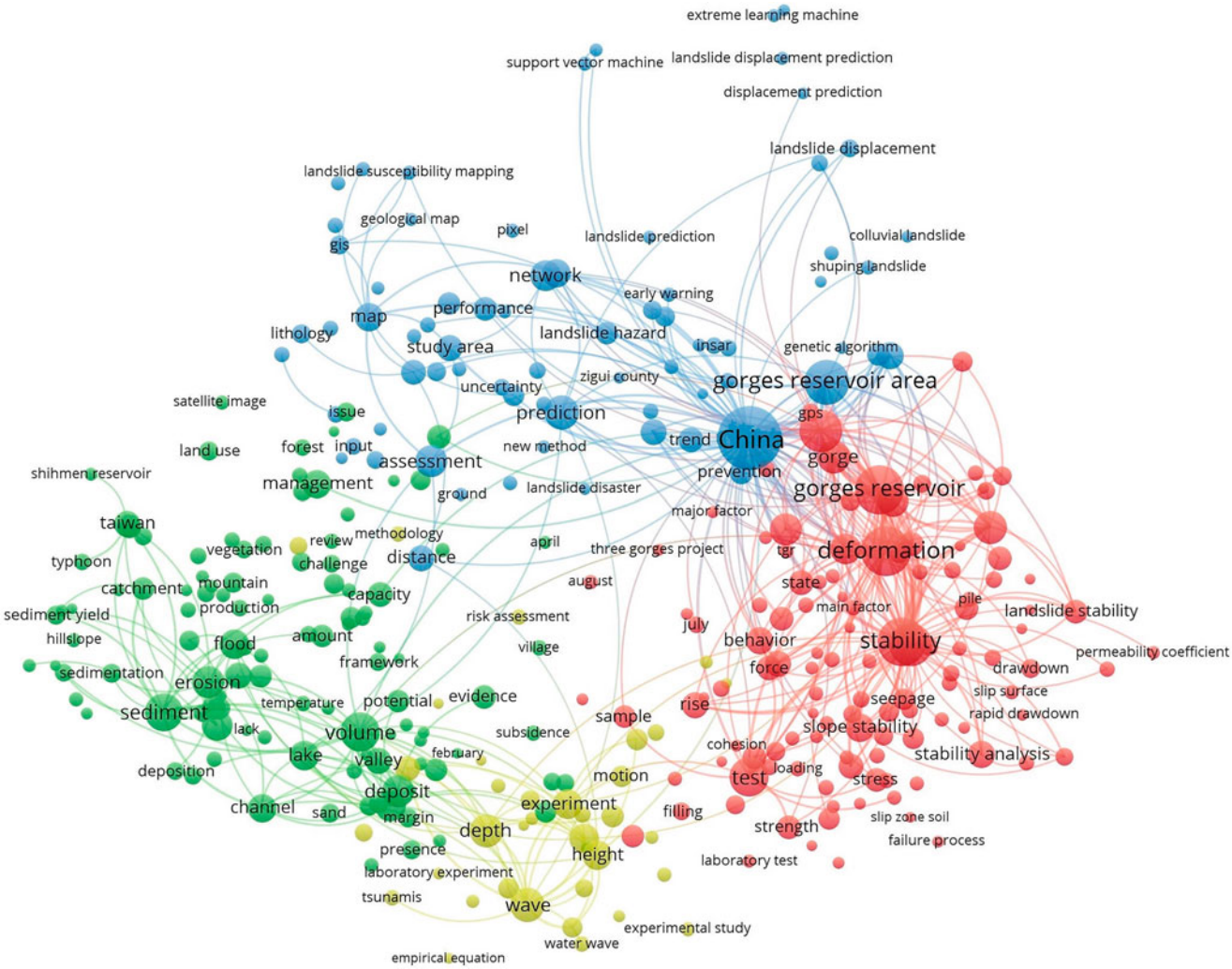

Fig. 1 High frequency terms in title and abstract from 1999 to 2018 (after Li et al. 2020)

TGRA's Badong formation strata can be divided into five sections (from T^2b^1 to T^2b^5), with lithology combinations characterized by sandwich of soft and hard strata. The lithology and lithological combinations exhibit a unique spatial law of variation. The strata of the Badong formation are characterized by rich variation, an outcome of long-term slope deformation as well as all-important evidence for understanding the triggers and mechanism of landslide formation.

Figure 4 shows the histogram of strata measured. Generally, and it is characterized by thick stratum in the east and thin stratum in the west. The horizontal stratum thickness of the Badong formation is unstable and subject to great variation. The spatial differences of stratum thickness of the Badong formation are attributed to three factors: different thickness of deposition, uneven denudation, and impact of subsequent structural deformation.

No large landslides are associated with Precambrian magmatic and metamorphic rocks, and only small slumps occurred in the weathered materials near the dam. Additionally, slope instabilities are relatively infrequent in the carbonate rock area that hosts the famous Three Gorges. Less than 8% of the total volume of identified landslides is associated with these rocks.

2.3 Influence of Geologic Structure

In the TGRA, landslides are most likely to occur where strata drop at moderate angles toward rivers, specifically on the flanks of anticlines and cores of synclines. These settings are suitable for the formation of large consequent bedding landslides. Two notable examples are the Qianjiangping and Huangtupo landslides, which originated in the Zigui and Guandukou synclines, respectively (Fig. 2a). Reservoir landslides in the TGRA can be attributed to six main evolutionary models as is shown in Fig. 5, in which, the geologic structural and evolution characteristics are stand out a mile.

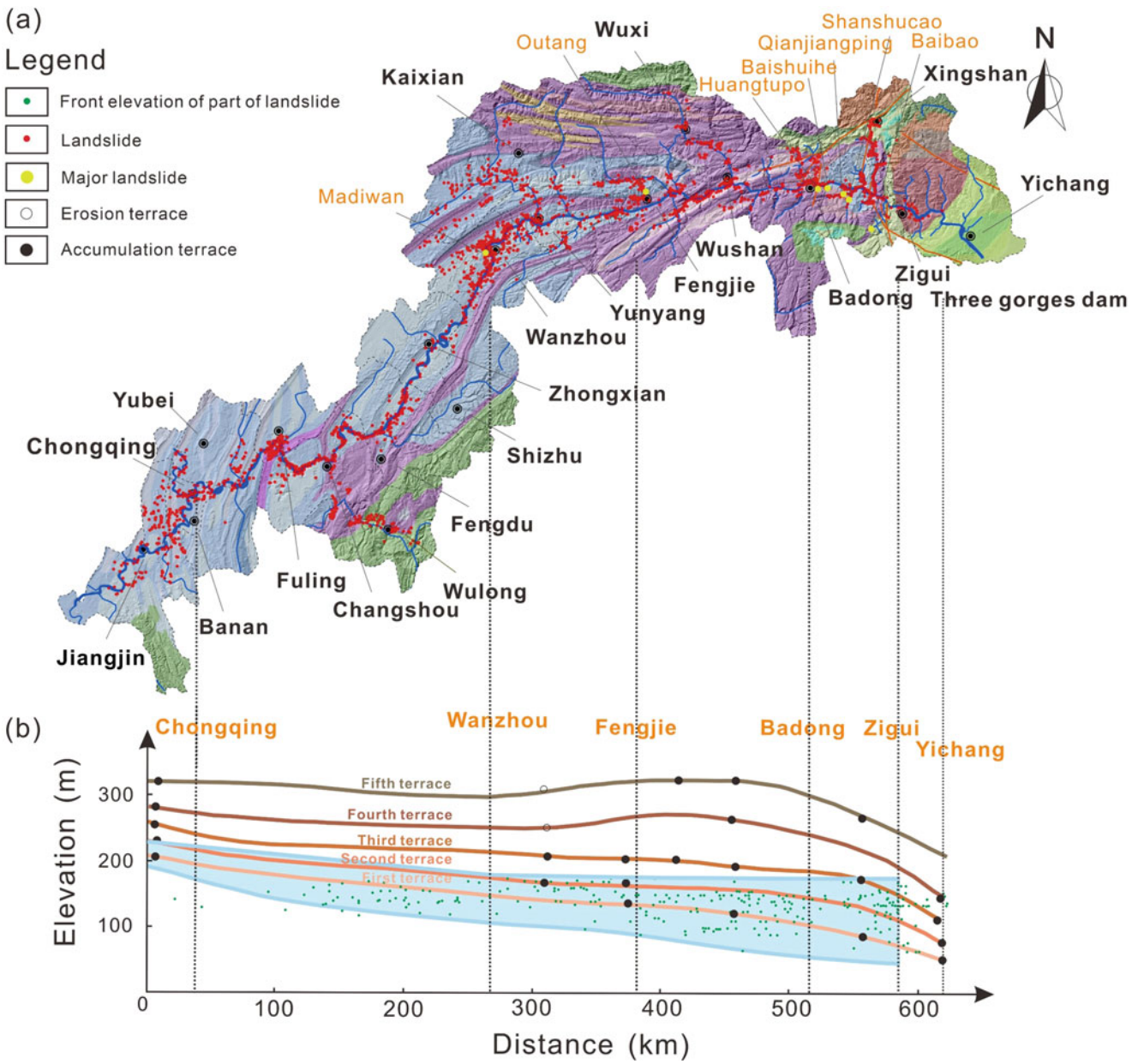

Fig. 2 The corresponding relationship between the river terrace elevation and the occurrence of the landslide (after Tang 2015; Tang et al. 2019; Tian et al. 1996)

2.4 Dynamic Characteristics of Reservoir Landslide Evolution

(1) *Deformation process of landslides*

The deformation and failure processes of reservoir landslides were studied via site surveys, monitoring, physical model tests and numerical simulations. Many TGRA landslides were affected by periodic variations in water level and rainfall. Some landslides deform intermittently and show step-like cumulative displacement curves, such as the Baishuihe landslide (Li et al. 2010), Shuping landslide (Wu et al. 2019) and Outang landslide (Yin et al. 2016). Other TGRA landslides deformed continuously and had linear-like curves of cumulative displacement, such as the Majiagou landslide (Ma et al. 2017).

Researchers have utilized a variety of techniques in studying and reconstructing the evolution process and deformation mechanism of reservoir landslides, such as physical model experiments and numerical simulations. Others adopted finite element analysis to examine the coupling effect of precipitation and reservoir water levels variation. (Jiang et al. 2011;

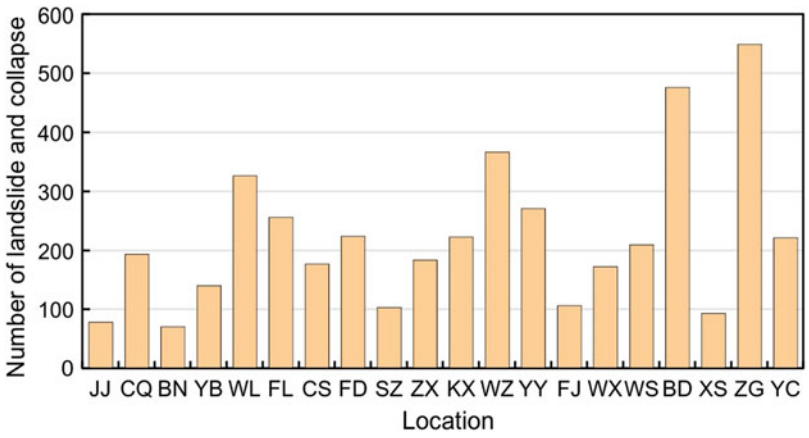

Fig. 3 Number of landslides and collapses along the impounded reach of the Yangtze River starting from the westernmost area of Jiangjin (JJ) to the easternmost area of Yichang (YC). (See Fig. 2 for location) (after Tang et al. 2019)

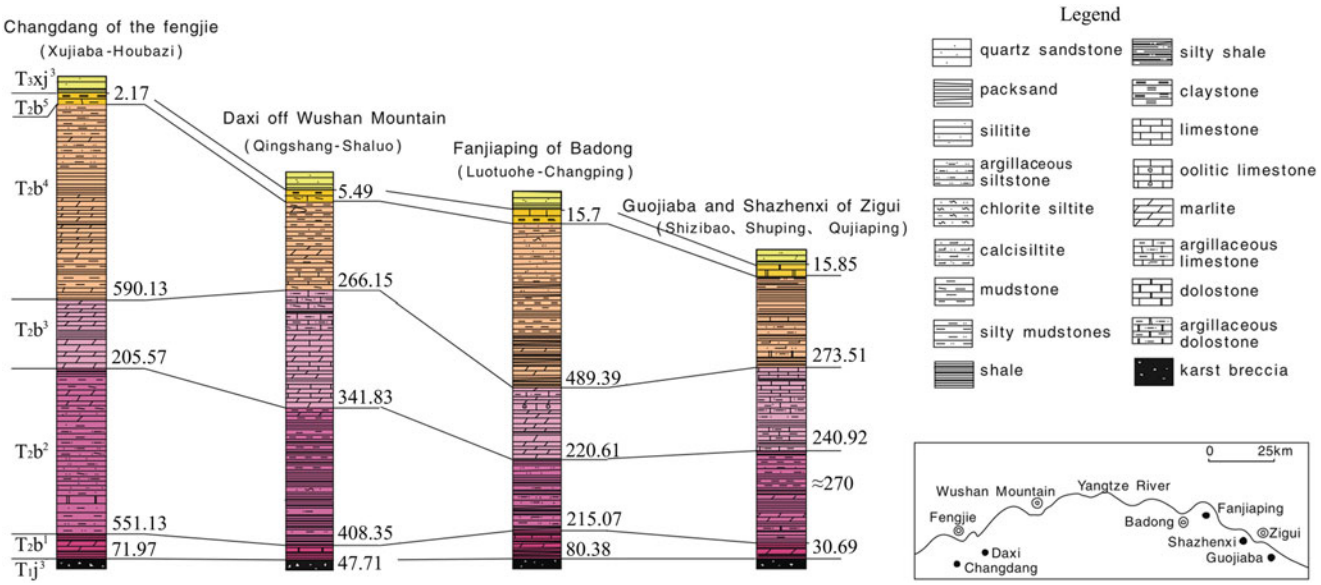

Fig. 4 Histogram for comparison of the strata measured in Fengjie–Wushan Mountain–Badong–Zigui of the Badong formation

Zhao et al. 2017). The Anlesi landslide mechanism was studied using a rheology model (Jian et al. 2009). The effects of rainfall and water level fluctuations on the behavior of the Quchi landslides were investigated using a universal discrete code (Huang and Gu 2017).

(2) *Mechanical characteristics of reservoir landslides*

The stability of the landslides affected by the reservoir water mainly via hydrostatic pressure, buoyancy force, and hydrodynamic pressure, etc. Based on the different affection way of water in the reservoir landslides' deformation, the mechanical characteristics of reservoir landslides could be classed as seepage-induced or buoyancy-induced. In seepage-induced landslides, deformation occurs mostly when reservoir water level decreases (Fig. 6a), but in buoyancy-induced landslides, deformation occurs primarily when reservoir water level is high (Fig. 6b). Landslides triggered by seepage are more likely to occur in sliding material with low permeability. When the reservoir water level drops abruptly, it is difficult for pore water pressure to dissipate, resulting in outward seepage force that tends to destabilize the landslide. Buoyancy-induced landslides are more likely to arise in sliding masses with a high permeability. The reservoir water penetrating the sliding material as the water level rises softens the sliding zone and lightens the sliding mass, reducing the landslide's stability. These two forms of mechanical characteristics are exemplified by the Baishuihe and Muyubao landslides as is shown in Fig. 6c, d. Two typical reservoir landslides of these two types, Shuping landslide and Qianjiangping landslide, are detailed described in Sects. 2.6 and 2.7.

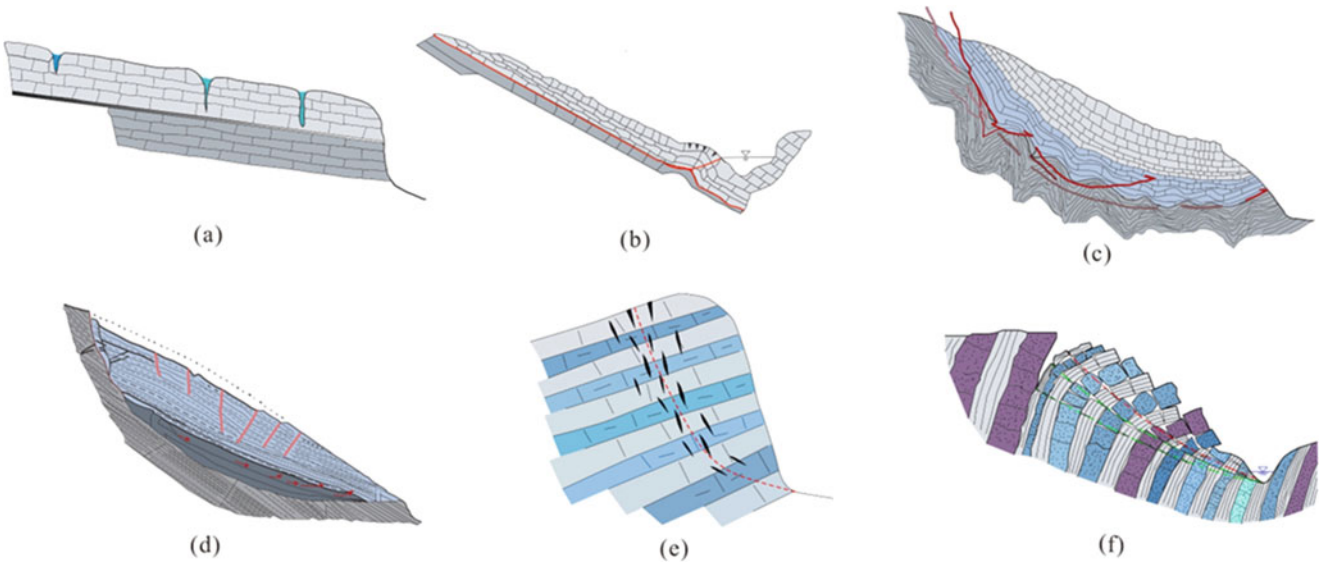

Fig. 5 Evolution modes of reservoir landslides. (**a**) Progressive slip along gentle-dip layer; (**b**) Bucking failure along steep-dip layer; (**c**) Creep slip along deep layer; (**d**) Plastic flow slip of weak interlayer; (**e**) Breakthrough abrupt slip in inclined cross-cutting layer; (**f**) Bending slip in steep anti-dip layer

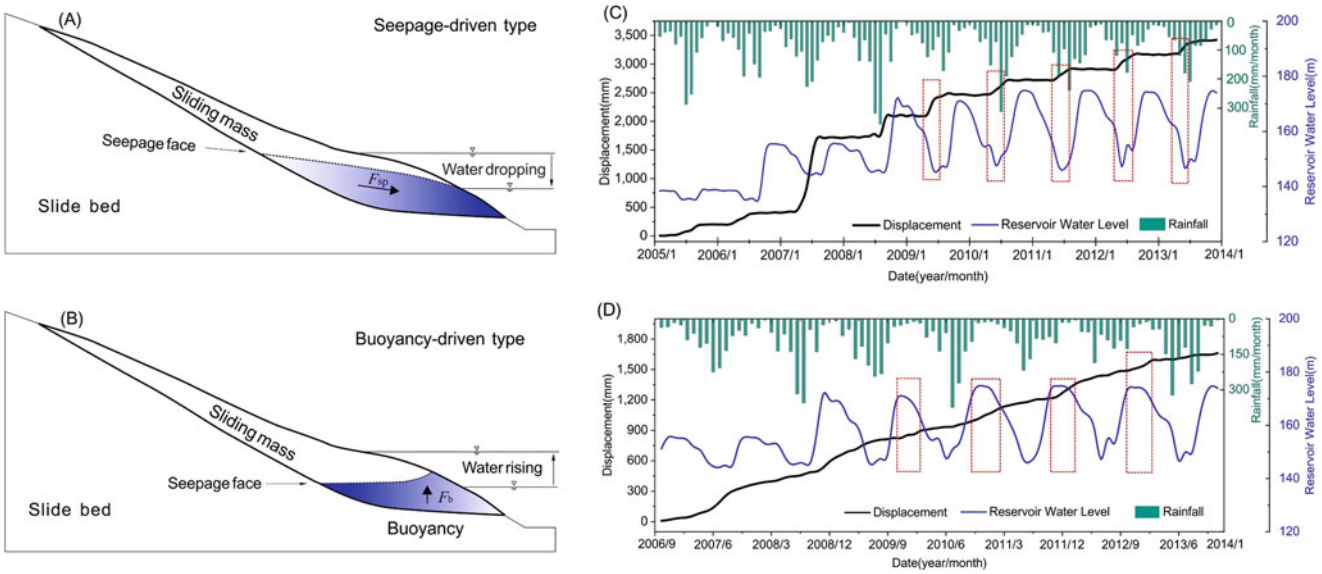

Fig. 6 Landslide deformation can accelerate by either rising or falling reservoir water level, depending on whether seepage forces (parts **a**, **c**) or buoyancy forces (parts **b**, **d**) are predominant. The differences between the seepage-driven Baishuihe landslide (**c**) and the buoyancy-driven Muyubao landslide (**d**) are observed through the corresponding periods of faster movement (red boxes) (after Tang et al. 2019)

2.5 Influence of Rainfall and Fluctuating Water Level

Reservoir landslide's occurrence is usually triggered by the interaction of external factors and specific regional geological conditions. Rainfall and reservoir water level fluctuations are considered to be the two major external influencing factors of reservoir landslides (Tang et al. 2019).

(1) *Influence of rainfall*

Seasonal rainfall is a significant factor that affects reservoir landslides (Wang et al. 2021a). For example, the rainfall in the TGRA is heavy during the annual low water level period. Rainwater infiltrates the sliding mass, increasing its weight and raising the groundwater level, which reduces the effective stress of the slide zone and causes the landslide to be

unstable. It has also been noted that rainfall at the rear of large reservoir landslides significantly raises its groundwater level, increases the head difference between the leading and trailing edges of sliding mass, significantly increases the hydraulic gradient, and is extremely detrimental to the stability of landslides (Zhang et al. 2021a).

The study of how the rainfall affects the reservoir landslides in TGRA varies. Water infiltration mechanisms and rainfall's impact on slope stability were studied by multiple researchers with field monitoring. Observation wells were constructed in typical colluvial landslides (Tang et al. 2015b) and decomposed granite slope (Zhang et al. 2000). The rainfall infiltration process was studied using the monitoring data on suction and temporary pore pressure variations during the rainfall. Additionally, the influence of rainfall characteristics (amount, intensity, distribution pattern) on slope stability was studied (Yang et al. 2017; Liu et al. 2018).

(2) *Influence of reservoir water level fluctuation*

Reservoir impoundment has clearly increased the frequency of reservoir landslides in the TGRA. Most significant was the reactivation of large landslides, whose newly submerged toes became subject to fluctuating hydrologic conditions (Song et al. 2018).

Seepage, in the form of hydrodynamic pressure, is considered to be the primary reactivation mechanism of most (70%) landslides, whereas 15% of the landslides were affected by buoyancy in the TGRA (Yan et al. 2010). When the reservoir water level drops rapidly, the water level drawdown inside the landslide lags behind due to the poor permeability, which causes hydrodynamic pressure and seepage-induced landslides to form under these circumstances. When the reservoir water level rises and remains at a certain height, the weight of the foot-of-slope rocks diminishes under the effect of the buoyancy force, the passive forces decrease, and the stability is disturbed (Lindenmaier and Zehe 2005). Buoyancy-induced reservoir landslides generally occur under this condition.

The first storage of the reservoir is considered to be the most hazardous. During the initial storage period of the TGRA, the effect of reservoir water was strong and long-lasting, e.g., the number of newly formed landslides has been at a high level for 3 years after 135 m of storage. This effect has since diminished year by year; for example, the number of newly formed landslides has dropped rapidly to a very small value after 1 year of 175 m storage.

The periodic TGRA water level fluctuation can alter the seepage field, the stress field and the material properties, resulting in a change in slope stability. Such findings were reported by Hu et al. (2012), Zhang et al. (2014a) and Zhao et al. (2017). The effect of rising and falling water levels was also studied through model tests or numerical simulations considering different rates of water level variation (e.g., Sun et al. 2017a, b). In addition, Liao et al. (2005) demonstrated that slope stability was closely related to the variation in the permeability coefficient of rocks.

(3) *Combined effect of rainfall and water level fluctuation*

In many instances, the development of reservoir landslides depends on the combined effect of rainfall and water level fluctuation. Numerical simulations were used to study the characteristics of the seepage field based on saturated-unsaturated theory (Miao et al. 2018). Many TGRA landslides have been continuously monitored. Based on the monitoring data, the influence of rainfall and water level fluctuation on the landslide deformation was analyzed (Li et al. 2010; Tang et al. 2015a; Wang et al. 2017). In addition, data mining methods, such as gray relational grade analysis, two-step cluster analysis and Apriori algorithm analysis, were applied to examine and quantify the influence of rainfall and water level variation on landslide deformation (Ma et al. 2017; Tan et al. 2018a).

For a better understanding of the combined effect of rainfall and water level fluctuation on landslide's deformation, a correlation analysis between displacement velocity at G1 of Shiliushubao landslide and its rainfall, rate of reservoir level change, and reservoir level are shown in Fig. 7. The size of the bubbles represents the deformation velocity. The larger bubbles tend to plot where the rainfall is higher. Meanwhile, the large bubbles are mainly concentrated where the reservoir level is between 140 and 150 m and are located where the reservoir level fluctuates slowly (between −4.4 and 9.0 m/month). This indicates that reservoir level fluctuations mainly trigger accelerated landslide movements when the reservoir level is low. The maximum size bubble appears where the rainfall is about 325 mm/month, and the water level rises between 4.5 and 9.0 m/month. The combined effect of heavy rainfall and rising reservoir level on landslide deformation is more significant than low rainfall combined with reservoir level drawdown.

2.6 Seepage-Induced Reservoir Landslide

The Shuping landslide is a typical seepage-induced reservoir landslide. It is located in Shazhenxi Town, Zigui County, Hubei Province, 47 km upstream from the TGD, and on the southern bank of the Yangtze River (Fig. 8). After the first impoundment of the reservoir in 2003, significant deformation was observed, endangering 580 residents and Yangtze River navigation. Therefore, multiple monitoring techniques were utilized to assess the deformation characteristics and stability of the landslide, as well as to observe the interactions between the various landslide segments (Fig. 9).

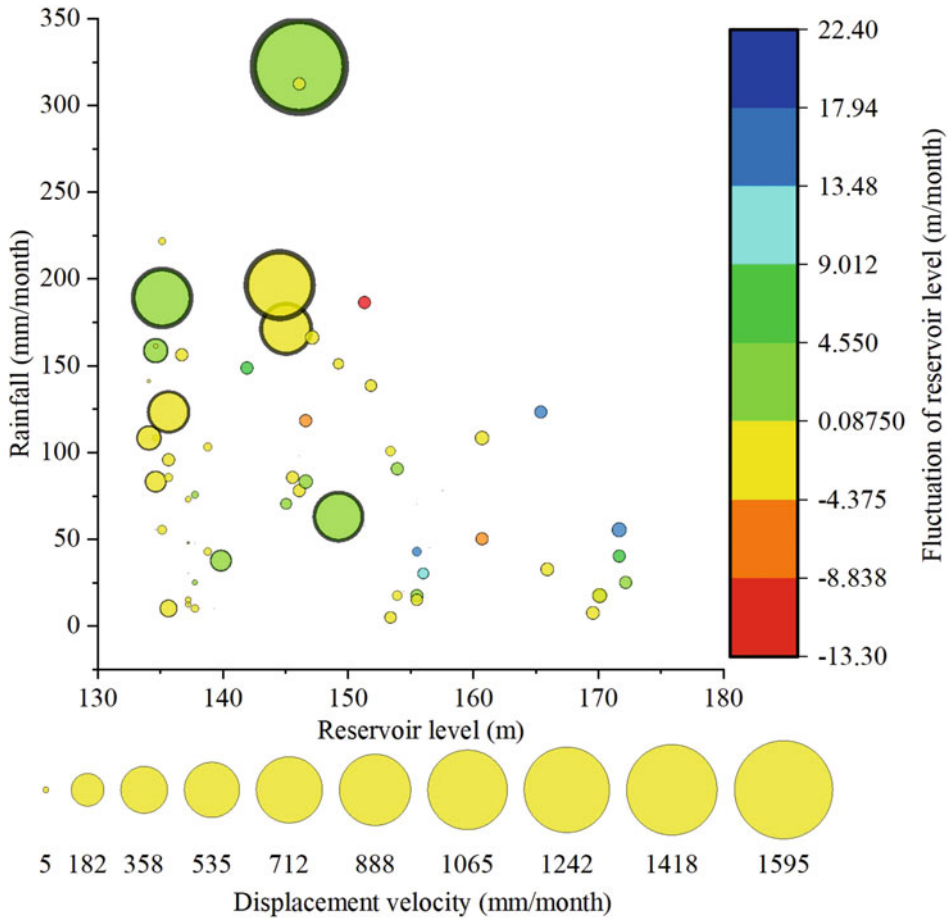

Fig. 7 Correlation between displacement velocity, reservoir level, rainfall, and fluctuation of reservoir level at Shiliushubao landslide (after Zhang et al. 2021b)

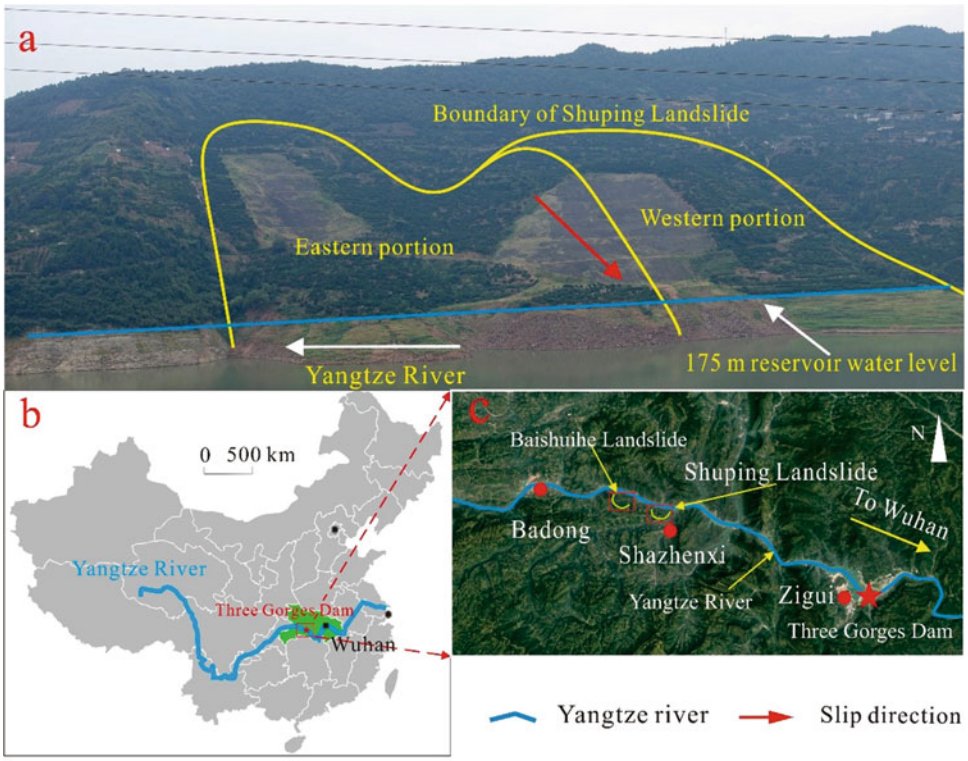

Fig. 8 Location and photograph of the Shuping landslide (after Zhang et al. 2020)

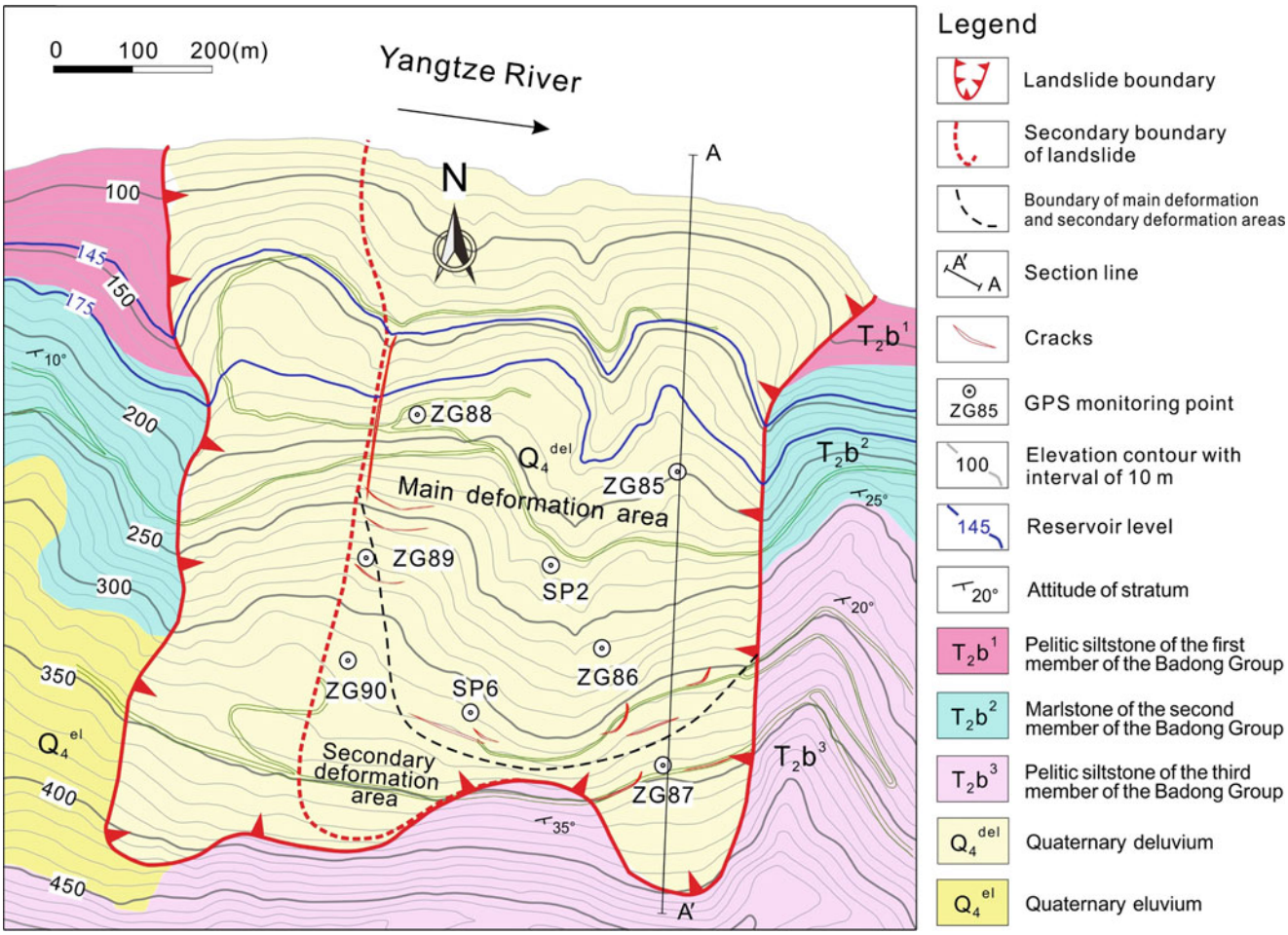

Fig. 9 Monitoring arrangement of the Shuping landslide (after Zou et al. 2021)

Professional monitoring of surface displacement commenced in June 2003, with seven GPS monitoring points (SP2, ZG85, ZG86, ZG87, ZG88, ZG89, and ZG90) (Fig. 10). The system was upgraded to automatic, real-time monitoring in June 2012, and all GPS monitoring points were surveyed every half month. The daily rainfall and daily reservoir level are recorded by Meteorological Station near the Shuping landslide and China Three Gorges Corporation, respectively.

(1) *Overall deformation feature*

The results of monitoring indicate that the evolution of the Shuping landslide consists of four stages that related to human activity, which are 139-m above-sea-level (ASL) trial reservoir impoundment (from April 2003 to September 2006), the 156 m ASL trial reservoir impoundment (from September 2006 to September 2008), the 175 m ASL trial reservoir impoundment and deformation control engineering project of the Shuping landslide conducted between September 2014 and June 2015 (Fig. 10).

The GPS monitoring system and field investigations revealed the deformation features (Figs. 10 and 11). The main sliding mass can be divided into a main deformation area and a secondary deformation area (Fig. 9). As measured at sites ZG85, ZG86, ZG88, SP2 and SP6, the main deformation area underlies most of the area with the cumulative displacement up to 4–5 m. Throughout the 13-year monitoring period, point SP2 experienced the greatest cumulative displacement (5.168 m), followed by ZG86 and ZG88, which recorded 5.039 m and 4.919 m, respectively. Deformations at the monitoring sites were essentially synchronous, as evidenced by the similar shape of their cumulative displacement curves, which typically exhibit steady rises in the first impoundment stage, step-like trends in the second and third impoundment stages, and flat trends after the engineering treatment. In the secondary deformation area, deformations were smaller and more stable, as indicated by the gentle

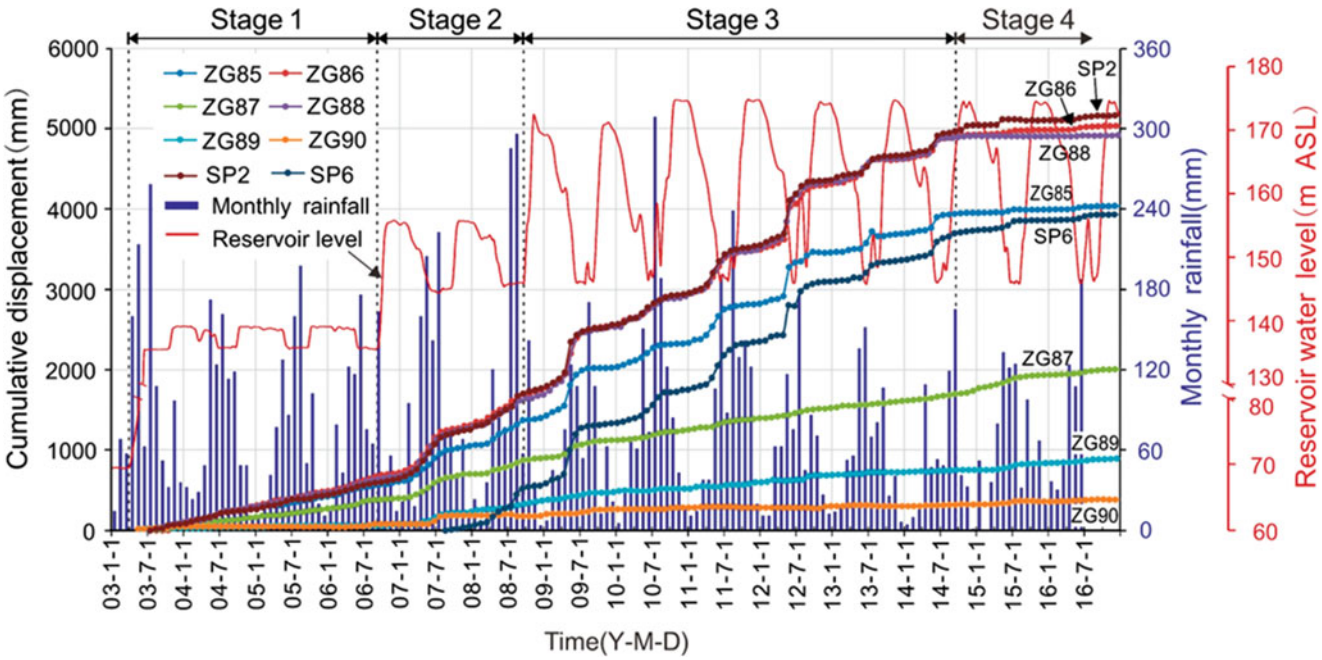

Fig. 10 Monitoring data for Shuping landslide from 2003 to 2016 (after Zou et al. 2021)

cumulative displacement curves at ZG89, ZG90, and ZG87, which recorded cumulative displacements of 0.5–2 m from 2003 to 2016.

(2) *Deformation feature in different stages*

After the reservoir level rose to 135 m ASL for the first time in June 2003, the main deformation area deformed at an average rate of 15.6 mm/month until September 2006, with each site recording relatively steady displacement curves whose small or nonexistent steps correspond to the annual variations in reservoir level. During Stage 1, there was no obvious deformation at ZG89 and ZG90 in the secondary deformation area.

When the reservoir level first rose to 156 m ASL during the first 2 months of Stage 2 (September and October 2006), displacement velocities of the main deformation area decreased to 13.4 and 9.7 mm/month, respectively, indicating an improvement in sliding mass stability. During the subsequent 2 months, the velocity increased to 11.5 and 14.3 mm/month while the reservoir level remained unchanged at 156 m ASL. During the subsequent drawdown period, the displacement velocity increased to a maximum of approximately 100 mm/month when the reservoir level dropped to 145 m ASL in 2007 (Fig. 12), resulting in an average "jump" of 458 mm in the cumulative displacement curve, which then flattened while the reservoir level remained at 145 m ASL (Fig. 10).

During the beginning of Stage 3, when the reservoir first rose to nearly 175 m in October 2008, the displacement velocity of the main deformation area decreased to 12.7 mm/month compared to 65, 74, and 32 mm/month in the previous 3 months. Shortly after the reservoir rose to its highest level, the level underwent a gradual decline, and the displacement velocity increased steadily. The maximum displacement velocity reached 378.6 mm/month at ZG88 in May 2009 when the water level declined rapidly, a rate almost four times higher than when the reservoir dropped from 156 to 145 m ASL in 2007. After the water level was steady at 145 m ASL, the displacement velocity decreased to a relatively low value (Fig. 11b).

During the next 6 years of Stage 3, the reservoir level underwent a series of similar annual fluctuations, and the sliding mass responded with a series of "jumps" in deformation. During these cycles, the displacement velocity decreased as the reservoir level rose, remained low speed when the reservoir level remained high, increased as drawdown began, and reached a maximum of 165 mm/month during rapid drawdown. As the reservoir was maintained at a low level of 145 m ASL, the corresponding cumulative displacement curves flattened considerably. These results clearly demonstrate that displacement velocity is high during reservoir drawdown and low during reservoir rise.

After the engineering treatment was completed in June 2015, the cumulative displacement curves became extremely flat and the "jumps" disappeared (Fig. 11). In the main

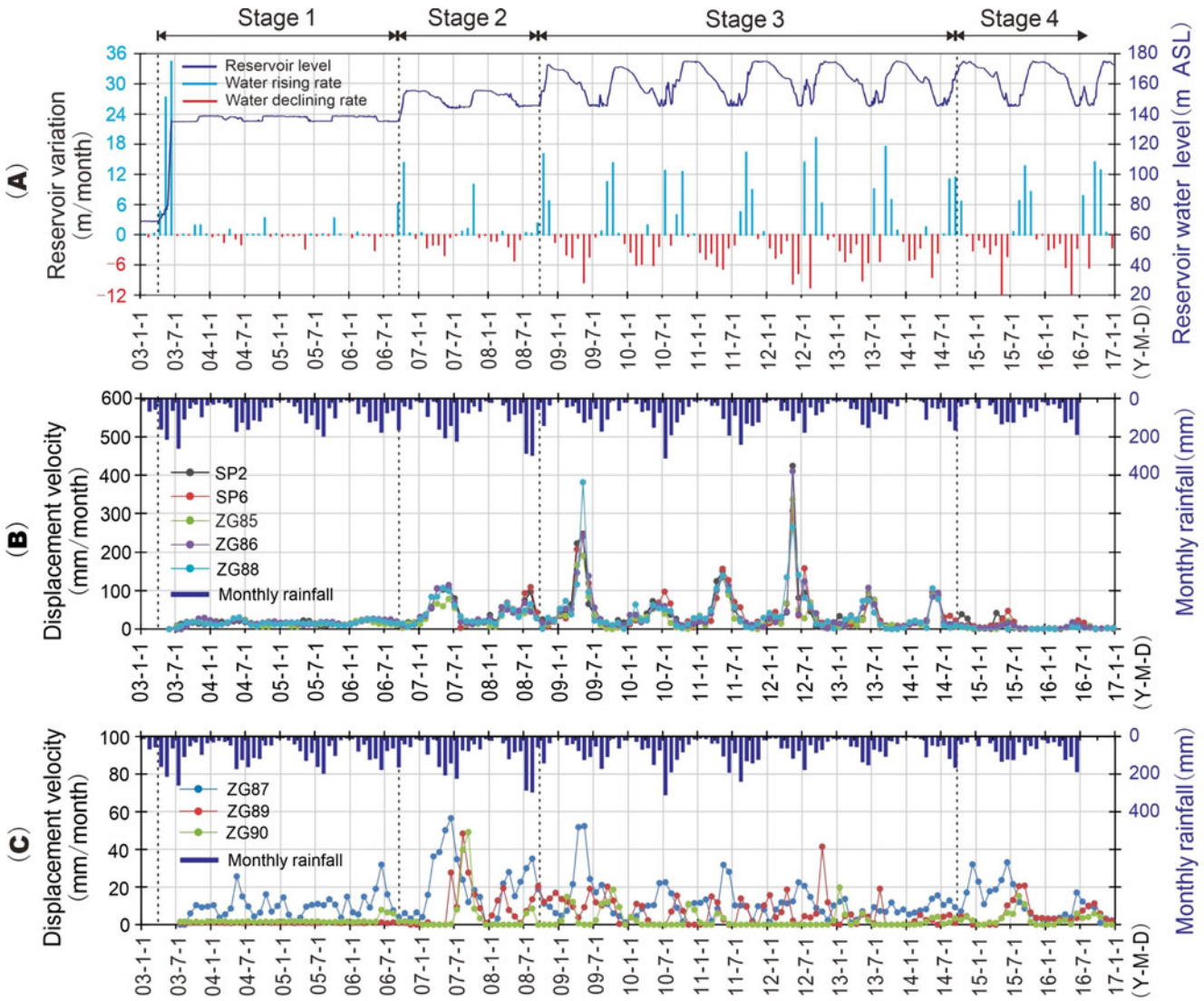

Fig. 11 Time series of reservoir level, rainfall and landslide displacement from 2003 to 2016. (**a**) Reservoir water levels and variation rates (positive for level rise, negative for level drop); (**b**) Displacement velocity of the GPS points in the main deformation area and monthly rainfall; (**c**) Displacement velocity of the GPS points in secondary deformation area and monthly rainfall (after Zou et al. 2021)

deformation area, the deformation was reduced to a low level of 4.1 mm/month, demonstrating effective treatment.

(3) *Effect of water-level fluctuation and rainfall on the deformation of Shuping landslide*

The largest "jump" in the cumulative displacement curves occurred in May to June of 2012 with an average of 479 mm and the second largest "jump" of 458 mm in May to June of 2009. These periods corresponded to the two highest monthly drawdown rates of 9.67 and 9.38 m, respectively (Fig. 11a). During these 2 years, the highest monthly precipitation amounts were 180 mm/month in 2009 and 190 mm/month in 2012 (Fig. 11). These data demonstrated conclusively that the deformation of the Shuping landslide is driven primarily by reservoir level fluctuations and not by precipitation. Low displacement velocities and flat cumulative displacement curves during the peak of the rainy season in July and August, when the reservoir is at its lowest level, also confirm this relationship.

The influence of reservoir level and rainfall on landslide deformation is illustrated in Fig. 12. The reservoir level fell at an average rate of 0.041 m/day in December 2013, and the corresponding velocity of displacement was 0.22 mm/day. In the subsequent 3 months, the rate of drawdown of the reservoir level increased to 0.147 m/day and the velocity of displacement increased to 0.54 mm/day. In March 2014, the displacement velocity decreased as the water level rose, despite the fact that heavy rainfall (up to 27.5 mm/day) was recorded during this time. During the subsequent rapid

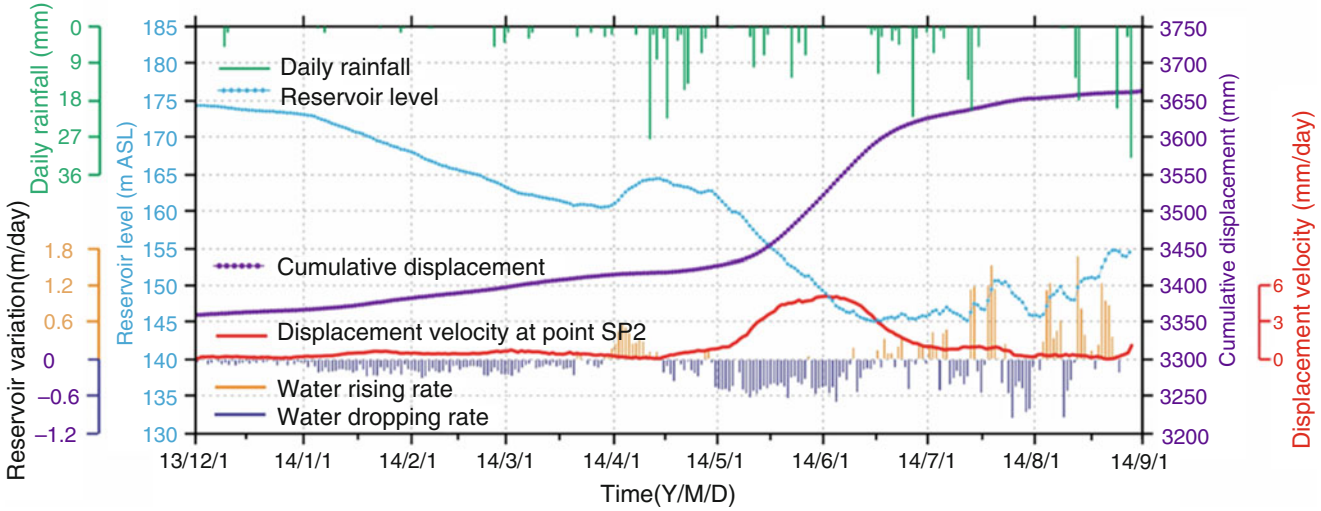

Fig. 12 Monitoring data of GPS point SP2 on the middle part of the Shuping landlide, from December 2013 to September 2014 (after Zou et al. 2021)

drawdown period (0.419 m/day) from May to June, the velocity of displacement increased to approximately 5 mm/day. Subsequently, the velocity of displacement decreased to less than 1.2 mm/day as the water level remained low despite abundant precipitation. These facts demonstrate that the Shuping landslide's displacement velocity is positively correlated with the reservoir's drop rate, while rainfall has little effect.

In contrast to the flat displacement curves and low displacement velocity observed in other years when the reservoir level was stable at its lowest annual level in July and August, displacement velocities were large in 2008 and 2010 (65.0 and 73.8 mm/month in July and August 2008; 58.4 mm/month in July 2010, approximately half of the average highest monthly displacement velocity, 165 mm/month, during rapid draw down period). During those periods, up to 300 millimeters (mm) of rainfall per month was recorded, which is heavy. However, August 2011 had the next heaviest rainfall of 250 mm/month, yet the cumulative displacement curve remained flat, and the displacement velocity was low (22.2 mm/month). These data illustrate that heavy rainfall can decrease landslide stability and accelerate deformation however it was a secondary factor. The difference in the displacement velocity between the months with the highest (2008, 2010) and the second highest (2011) levels of rainfall suggests that a threshold exists, with rainfall exceeding this value having a significant effect but with less having little significance. This threshold appeared to be approximately 250–300 mm/month.

2.7 Buoyancy-Induced Reservoir Landslide

The Qianjiangping landslide is a typical buoyancy-induced reservoir landslide. It is located in Shazhenxi Town, Zigui County, Hubei Province, on the western side of Qinggan River (a tributary of the Yangtze), 50 km upstream from the TGD (Tang et al. 2017). The Qianjiangping landslide formed along weak bedding planes in Jurassic strata that generally dip approximately 30 degrees to the southeast, downslope and toward the river. This mass has a length of 1150 m, a width of 600 m, and an average thickness of 30 m (Fig. 13). The total area is greater than 0.69 km^2 and the volume is $21 \times 106\ m^3$. Maximum elevation of the main scarp is 450 m, but it extends to river level (Fig. 14, red dotted line). On July 14, 2003, the sliding mass moved approximately 250 m toward S45°E, all within a period of 1~5 min. The slide mass is thinner in the main body and thicker at the toe. The dip angle of the lower rupture surface is mostly coincident with bedding in the upper part, however it becomes nearly horizontal at the toe of the landslide. Case histories show that slope failure in this region is common where the Jurassic strata have steep, downslope dips toward major rivers.

The landslide is bordered on the east, south, and west by a prominent incised meander in the Qinggan River (Fig. 13). The water level of the Qinggan River rose from 95 m to 135 m in June 2003, immediately after the impoundment of the TGRA, which is just a few weeks prior to the landslide event.

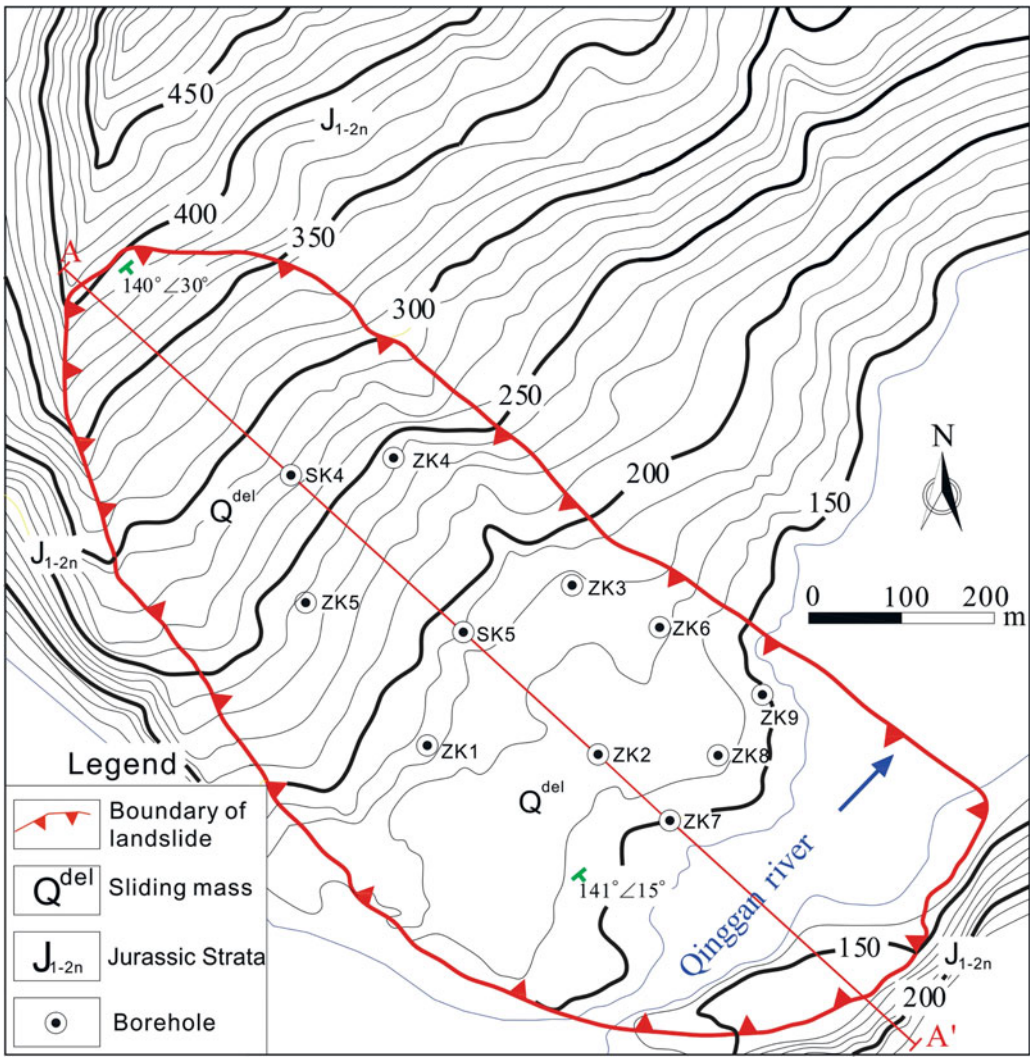

Fig. 13 Topography of the Qianjiangping landslide after 2003 (after Tang et al. 2017)

(1) *Geology and structure of the landslide*

The Qianjiangping landslide is a bedding-controlled landslide. The local stratigraphic section is, from top to bottom, alluvium, clay and gravel of Quaternary age, feldspathic quartz sandstone of Upper Jurassic–Cretaceous age, and fine sandstone with carbonaceous shale, siltstone with mudstone, and silty mudstone of the Middle to Lower Jurassic Niejiashan formation ($J_{1–2n}$). The sandstone is interbedded with weak silty mudstone and shale layers. The greater region is structurally complex and tectonically active. The rapid incision of the Yangtze River, thought to have occurred in response to Quaternary tectonic uplift (Li et al. 2001), has produced unstable slopes along its banks in numerous places. Field investigations show that fractures and discontinuities are abundant in the slightly weathered bedrock. The dip direction of the strata is reversed near the Qinggan River.

(2) *Hydrology and Hydrogeology*

The Qinggan River has numerous tributaries and ravines. The gullies are usually dry, but carry significant intermittent flows during the rainy season. The north bank of the Qinggan River is a consequent slope with a dip angle between 20° and 30°, while the south bank slope is an obsequent topographic surface.

Near the landslide, data of groundwater are hard to obtained. The data obtained from the boreholes on the landslide indicate that the phreatic zone within the slope material is in a very deep place. Along planes of discontinuities and contacts between the dipping sandstone and mudstone units, artesian contact springs were observed. Groundwater recharge and levels are primarily determined by the amount of rainfall, the infiltration rate and the level of reservoir water. Additionally, boring revealed that a highly fractured, 1–2 m

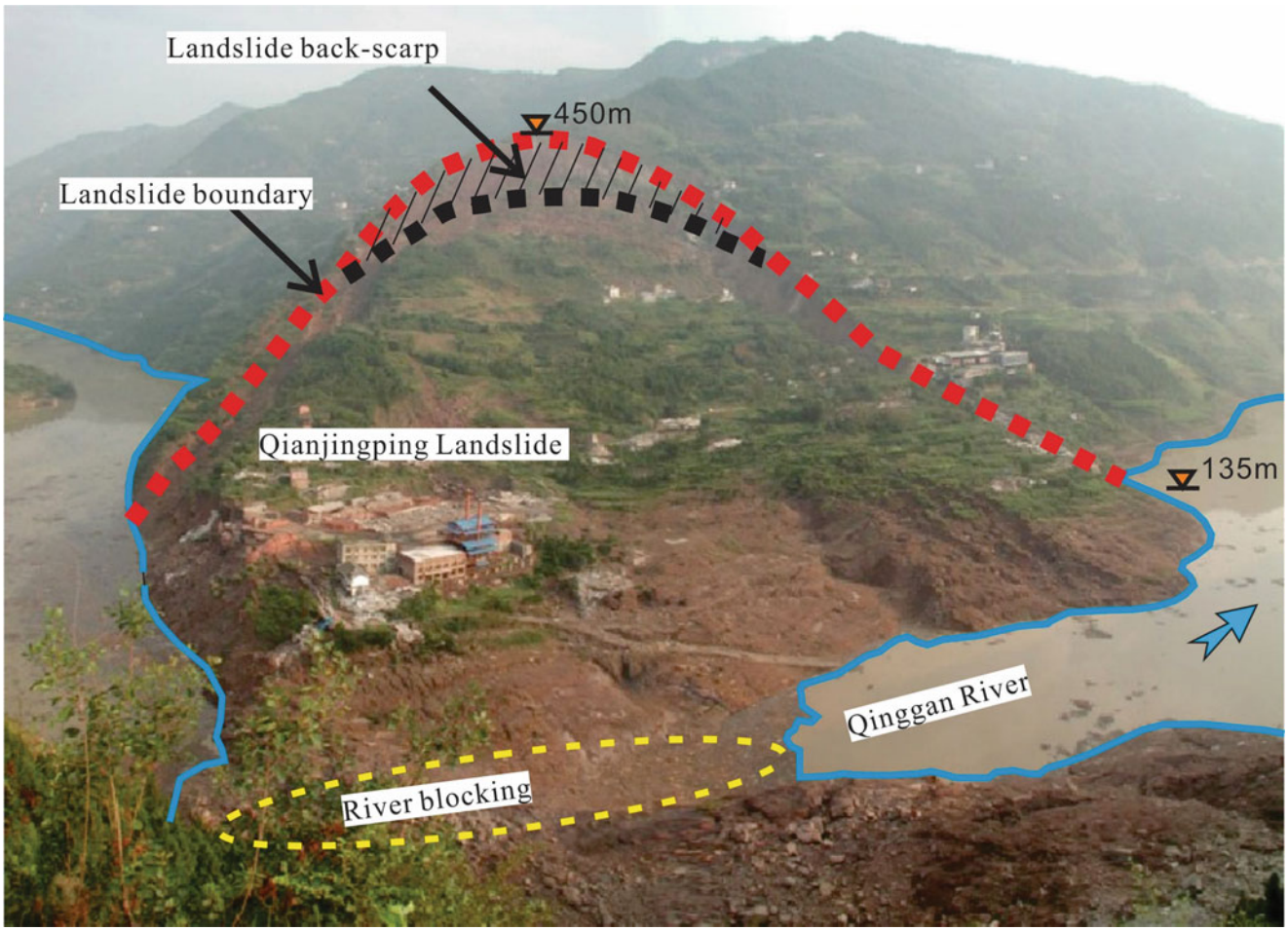

Fig. 14 Front view of the landslide, looking NW (after Tang et al. 2017)

thick zone of bedrock immediately underlies the main slip zone, while the deeper bedrock was only slightly fractured. This indicates that the bedrock immediately below the slip zone has good permeability.

(3) *Inducing factors of the landslide*

The monitoring report shows that, the Qianjiangping landslide occurred immediately after a nearly continuous period of rainfall from June 21 to July 11, 2003. In addition, the water level of the Qinggan River rose rapidly from 95 m to 135 m ASL shortly after the Three Gorges reservoir was impounded on June 1, 2003. Studies indicate that this landslide was caused by the combined effect of this reservoir's water level rise and heavy rainfall (Jian et al. 2014). Groundwater data for the area surrounding the Qianjiangping landslide and its environs are limited, but it is evident that the rapid increase in the reservoir level affected the groundwater level near this landslide's toe, which further contributed to the mass' destabilization. The erosion at the slope toe caused by the river also decreased the slope's stability.

Overall, the Qianjiangping landslide was caused by both internal and external factors. Internal factors include the loose accumulation of the slide mass, significant geomorphic features, and weak bedding surfaces. External factors include the precipitous rise in the reservoir's water level in June 2003, which coincided with the season of heavy rainfall.

(4) *Mechanism analysis of Qiangjiangping landslide*

Buoyancy played a vital role in the evolution of Qiangjiangping landslide. With the effect of rising reservoir water level and the rainfall, water gradually seeped from the slope surface into the interior of the sliding mass, and the water capacity within the slope varied in different reservoir filling stages. Cao and Luo (2007) and Li et al. (2013) found that the shear strength and deformation properties of slip zone soils of the Qianjiangping landslide were highly influenced

by the variations in soil moisture through laboratory investigations. The reservoir impoundment affected the toe of the Qianjiangping landslide mainly, and the effect of shear strength reduction at the foot of the sliding mass was the most important factor in the landslide initiation. It was determined that the shear strength weakening of the slip zone in the lower layers of this landslide had the greatest effect on its stability (Wen et al. 2008). Specifically, the lower layers were gradually saturated with water as the reservoir was filled. As a result of the saturation and softening effects of water, the strength of the slide mass and the sliding zone would decrease proportionally, reducing the slope's stability. In addition, as the water level rose, the buoyant force in the lower layers decreased the slope-resistance toe's force (Wang et al. 2008). Variations in resistance force altered the mechanical equilibrium of the mass of the slide, resulting in the failure of the slope along bedding planes of weak rocks. Thus, the Qianjiangping landslide was caused by the combined effects of Three Gorges reservoir impoundment and persistent rainfall.

3 Assessment of Reservoir Landslides Stability

Stability assessment is an important aspect in the study of reservoir landslides. In terms of the TGRA, the water level fluctuation can greatly change the hydrogeological conditions of the sliding mass. The landslides in TGRA have experienced the long-term evolution process since its formation and have tended to be stable. Therefore, although strong precipitation and earthquakes have a certain effect on the stability of landslides, a single rainstorm and earthquake will not cause the overall re-instability and failure of the landslide in normal circumstances. However, when reservoir water level fluctuates between 175 and 145 m, the generated dynamic water pressure acts on the slopes, and the softening effect of water reduces the physical-mechanical properties of the sliding mass and rupture surface, thereby reducing the stability of the slope. When evaluating the stability of landslides induced by strong precipitation and rapid drawdown of reservoir water level, the following problems need to be considered and solved:

Firstly, when taking the water table in reservoir areas into account, the concept of sudden drawdown cannot be applied to all the cases. The so-called sudden drawdown means that the decline of the groundwater level in the slope lags behind the decline of the reservoir water level, so that the excess pore water pressure generated in the slope is difficult to dissipate momentarily, and no significant amount of water is drained from the soil body during the descending process. If the permeability coefficient of the slope is large enough, the groundwater level will decrease with the reservoir water level rapidly, and the potential difference between seepage and infiltration curves will be small, in which case the sudden drawdown will not occur. At present, there is no theoretical basis for the seepage and infiltration curve formed by the reservoir water level declination, and there is no support from the measured data, resulting in too conservative landslide stability evaluation and reinforcement scheme of high slopes in the reservoir area.

Secondly, the empirical method only uses the permeability coefficient of the landslide body to estimate the stagnation height of the infiltration curve when the reservoir water level drawdown. There is a lack of research on the mechanical model of groundwater acting on the landslide, so it is difficult to fully explain the mechanism of landslides induced by reservoir water level rapid drawdown and rainstorm.

Thirdly, when calculating the pore water pressure, sometimes the lateral water pressure of the soil strip is omitted, and only the water pressure on the sliding surface at the bottom of the soil strip is calculated; Besides, some simulations are made to decide different soil weight, such as using saturated bulk density to describe the soil below the infiltration curve and above the reservoir water level, and using the floating bulk density to describe the soil below the reservoir water level, etc. Such a statement does not clearly explain the conversion relationship between the surrounding water pressure and the seepage force, which leads some people to consider both the hydrostatic pressure and the seepage force in the stability analysis, resulting in repeated calculations of the hydrostatic pressure. In fact, the penetration force is a pair of balance forces with the in the soil strip and the surrounding hydrostatic force. Considering the hydrostatic pressures as a whole is helpful to analyze the influence of seepage force on landslide stability. Therefore, how to consider the impact of the sudden drawdown of the reservoir water level on the stability of the landslide is a difficult problem encountered in the prevention and control of landslides in the reservoir area.

Based on the above understanding, according to the TGRA water level regulation scheme and the reservoir landslides groundwater action mechanics model, the transient seepage field of the landslide when the reservoir water level declines is analyzed, and the conditions for the formation of the rapid drawdown of the reservoir water level are obtained. Determination of the infiltration curve when reservoir water level drawdown and different stability evaluation methods are introduced below, and the stability of the reservoir landslides during the TGD operation are introduced subsequently.

3.1 Determination of the Infiltration Curve When Reservoir Water Level Drawdown

(1) *Saturated and unsaturated seepage models*

According to the water level control scheme in the TGRA, the reservoir water level fluctuates between 175 m and 145 m. When the reservoir water level drawdown, the sliding mass above the reservoir water level is unsaturated, and the landslide mass below the reservoir water level is in a saturated state. Simultaneously, the pore water pressure gradually dissipates, and the soil changes from saturated to unsaturated state. The movement of soil water in the unsaturated area and the movement of water in the saturated area are interrelated, and the discussion unifying these two movements is the so-called as saturation-unsaturated problem (Wu et al. 2009).

When the water head h is used as the dependent variable of the governing equation, the governing equation for anisotropic two-dimensional saturated-unsaturated seepage is:

$$\frac{\partial}{\partial x}\left(k_x \frac{\partial h}{\partial x}\right) + \frac{\partial}{\partial y}\left(k_y \frac{\partial h}{\partial y}\right) = m_w \rho_w g \frac{\partial h}{\partial t} \tag{1}$$

where: k_x, k_y are the saturation permeability coefficients in the horizontal and vertical directions respectively; ρ_w is the density of water; g is the acceleration of gravity; m_w is the specific water capacity, which defined as the negative value of the partial derivative of the volumetric water content θ_w to the matric suction $(u_a - u_w)$:

$$m_w = -\frac{\partial \theta_w}{\partial (u_a - u_w)} \tag{2}$$

The seepage boundary conditions are:

① Water head boundary

$$k\frac{\partial h}{\partial n}\bigg|_{\Gamma_1} = h(x, y, t) \tag{3}$$

② Flow boundary

$$k\frac{\partial h}{\partial n}\bigg|_{\Gamma_2} = q(x, y, t) \tag{4}$$

By using the two-dimensional finite element analysis program SEEP/W to simulate the steady and transient saturated and unsaturated flow, the Eq. (1) can be solved, and the seepage infiltration curve when the reservoir water level drawdown can be obtained.

(2) *Mechanical model of groundwater effects on landslides in TGRA*

Compared to the seepage condition of earth dams, the seepage of landslides when the reservoir water level drawdown suddenly has more complex seepage conditions. Due to the different geological formation age of each landslide, the structural and hydrogeological conditions of the landslides are very different. Therefore, the hydrological response of each landslide is also very different when the reservoir water level rapidly drawdown. According to different hydrogeological conditions, the mechanical mechanism of groundwater acting on landslides can be summarized into the following two modes.

① Phreatic—aquifer mode

Pore phreatic water, founded in the alluvial-pluvial deposit, landslide accumulation layer and colluvial deposit that consists of Quaternary loose sediments, are mainly distributed in Wushan, Fengjie, Mudong, Lidu, etc. The groundwater in the landslide is mainly recharged by atmospheric precipitation and pore water. Since the permeability of rock and soil below the slip surface is relatively poor, the slip surface can be considered as confining boundary, or so-called zero flow boundary. The stability of the landslide mainly depends on the sudden drawdown of the reservoir water level. Besides, the rainstorm infiltration can increase the weight of the sliding mass above the infiltration curve and reduces the strength of the soil in sliding zone, and most of the loose accumulation landslides in the reservoir area belong to this category. In addition, if the groundwater level is buried deeply, rainstorm infiltration is difficult to raise the groundwater level.

② Confined water—aquifer mode

In terms of large-medium pore- or fissure-phreatic water, which is founded in the landslides such as Fanjiaping, Guling, Baota-Jipazi, Jiuxianping, etc., the bedrock is mostly disintegrated into rock blocks or even a mixture of soil and rock. The bedrock is severely weathered and broken, containing pore-fissure water or karst fissure water, and the groundwater is influenced significantly by rainfall, gullies and reservoir river water level fluctuations. At this time, the sliding surface of the landslide seepage boundary is the pressure or flow boundary. In this type of groundwater

mechanics, the stability of the landslide is greatly affected by the sudden drop of groundwater level and reservoir water level. The rainstorm infiltration will raise the groundwater level, and the reservoir bank landslide is prone to occur under the effect of the sudden drawdown of the reservoir water level and the rainstorm infiltration.

3.2 Stability Evaluation Methods

Considering the variety and complexity of reservoir landslides' characteristics in TGRA, different kinds of methods are used in the relevant stability evaluation. The methods include both qualitative and quantitative approaches, concomitantly taking the deterministic and probabilistic methods into account.

(1) *Qualitative methods*

The qualitative analysis method is mainly used to analyze the various factors affecting the landslide stability, the mechanical mechanism of instability, the possible deformation and failure modes, the cause of the landslide and the evolution history, aiming at giving the quantitative description of possible trends of the evaluated landslide in terms of its stability and characteristics. The qualitative method can quickly evaluate and predict the stability of the landslide. However, the disadvantage is that this method is highly empirical and has no quantitative limit. When analyzing the landslides in TGRA, the following qualitative approaches are commonly used:

Historical cause analysis method, or so-called geological analysis method, is mainly used to deduce the whole process of the historical evolution of the landslide. This method is conducted by analyzing the geological tectonic environment (such as topography, geological conditions, etc.) and the signs of slope deformation and damage.

Graphical method is commonly used in the preliminary evaluation of landslide stability. This method generally includes stereographic projection, solid proportional projection, double-sided projection, joint pole diagram and contour diagram method, etc. If combined with the strength conditions of the structural plane and the engineering force, this method can also support the quantitative calculation of the slope stability.

Engineering geological analogy method applies the analysis experience of landslides that have been studied to the landslides with similar conditions that need to be evaluated. The landslide database, expert system and case-based reasoning evaluation method are also an extension of this method in essence. The expert system method is a computer program analysis method, which completes the analysis of landslide stability at the expert level, and combines a large amount of practical knowledge of landslide stability analysis with the problem-solving strategy of simulating human beings (Zhu et al. 2014). Moreover, studies based on database management system (DBMS) and geological information system (GIS) were employed to evaluate the reservoir areas (Bai et al. 2009). For instance, the remotely sensed graphical data can be used to produce a landslide hazard map, that indicates the relationship between the land instability and human activities (Fourniadis et al. 2007).

(2) *Limit equilibrium methods*

The limit equilibrium methods investigate the equilibrium of soil mass tending to slide down under the driving and resisting forces. At present, the unbalanced thrust method (also known as the residual thrust method) is often used in the stability calculation of landslides in the TGRA, in which case the sliding mass is considered as the composition of vertical slices. In term of the stability evaluation of landslides in reservoir area, taking the seepage force generated from reservoir water level fluctuation into account is a crucial part. As shown in Fig. 15, the water force induced by the change of reservoir water level can be quantified by either the ambient pore-water pressure or by the seepage and buoyancy force (Lambe and Whitman 2018).

The seepage force F_{sp} caused by the frictional drag of water flowing through the voids can be expressed as:

$$F_{sp} = \gamma_w iV = \gamma_w \sin(\beta)V \tag{5}$$

Where γ_w is the unit weight of water, i is the hydraulic gradient, β is the slope angle of the phreatic surface, and V is the submerged volume of the analyzed soil slice, which is expressed as the area of trapezoid *bcde* in Fig. 15.

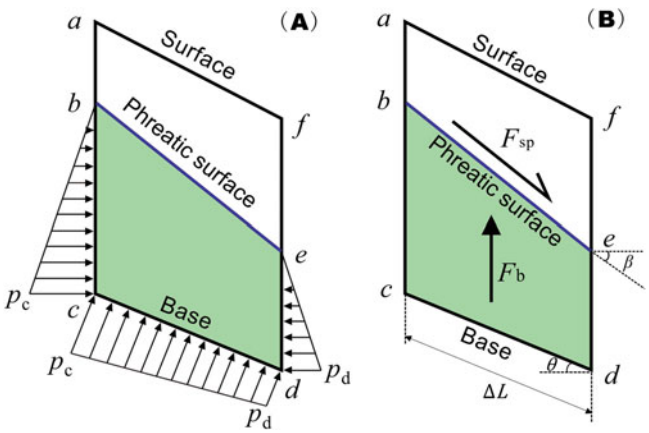

Fig. 15 Water force acting on a sliding mass expressed by: (**a**) ambient pore water pressure; (**b**) seepage force F_{sp} and buoyancy force F_b (after Zou et al. 2021)

The buoyancy force F_b in the submerged part of the soil slice can be expressed as:

$$F_b = \gamma_w V \tag{6}$$

The landslide stability can be quantified by the factor of safety (*Fos*), which is defined as the ratio of shear resistance along the potential failure surface to the sliding force. If Mohr-Coulomb failure criterion is considered (Wang et al. 2014), *Fos* can be defined as:

$$Fos = \frac{F_r}{F_s} = \frac{\sum_{j=1}^{n} \left[c\Delta L_j + N_j \tan\varphi\right]}{\sum_{j=1}^{n} w_j \sin\theta_j} \tag{7}$$

Where n is the total number of the slices, N is the normal force on the base of each slice, θ is the slope angle of the slice base (referring to the slope of sliding surface), ΔL is the length of the slice base, c is the cohesion of soil and φ is the internal friction angle of soil.

In addition to the unbalanced thrust method, the limit equilibrium methods used in the landslide stability evaluation includes Janbu method, Modified bishop method, Spencer's method, Sarma method, Morgenstern-Price, etc. When studying the slopes and reservoir landslides TGRA, some of these methods were further modified based on specific boundary conditions and/or additional assumptions. For instance, the rock mass above the failure surface was simplified as an entire sliding block (Yong et al. 2016), and the assumptions of water level and rainfall infiltration conditions were made to proceed the equilibrium analysis (Tang et al. 2017). Besides, the influence of water level fluctuation and rainfall could be quantified in the equilibrium evaluation by introducing the time interval into the equations (Sun et al. 2016). Furthermore, the two-dimensional limited equilibrium method was extended to three-dimensional limited equilibrium method (Wang and Xu 2013).

(3) *Numerical simulation methods*

Considering the complexity of stability conditions and deformation mechanism, numerical models were commonly established for the TGRA landslide cases. The finite element method (FEM) fully satisfies the statically admissible condition, strain compatibility, and the constitutive relationship between stress and strain, which is a more rigorous method for the theoretical system. Meanwhile, because the numerical analysis method can break through the limitation of the material inhomogeneity and the inconsistency of the slope geometry, it can be an ideal approach to analyzing the stress-deformation and stability conditions of landslides (Liu et al. 2007).

The recent studies use the traditional method of reducing strength index, considering the state that elastoplastic finite element calculation fails to fulfil the convergence conditions as the criterion for slope instability. Griffiths and Lane (2001) made a useful exploration in this regard. The basic principle of the slope stability analysis based on the strength reduction FE analysis is to divide the strength parameters of the slope, cohesion c' and friction angle ϕ', by a reduction factor F. Afterwards, new values of c' and ϕ' are obtained and be considered as the new soil strength parameters, which are used in the following trial calculation. When the calculation results do not converge, the corresponding F is called the minimum safety factor of the slope. At this time, the slope reaches the limit state, shear failure occurs, and the critical slip surface can be obtained.

The elastic-plastic FEM based on the strength reduction method can simulate complex geometric boundary shapes and variations of soil properties, including changes in water level and pore pressure. Generally, an ideal elastic-plastic model that satisfies the Mohr-Coulomb failure criterion is used. The elastic model is assumed to be used in the beginning of the numerical calculation, normal and shear stresses are generated at all Gaussian points within the mesh of the soil model, and these stresses are then compared to the Mohr-Coulomb failure criterion. If the stress at a particular Gaussian point locates within the Mohr-Coulomb failure circle, the point remains in the elastic state; if it is on or outside the circle, the point is yielding, and the yield stress will be redistributed in the mesh. When a sufficient number of Gaussian points yield, leading to a change of soil mechanism, the global shear failure is considered to have occurred.

When performing the FE stability analysis for landslides in TGRA, the effect from water needs to be considered. For instance, the FEM-based strength reduction method was combined with the saturated-unsaturated theory to analyze the stability of the Bazimen landslide (Zhang and Cheng 2011), in which case the effect of rainfall intensity can be evaluated. Additionally, the effects of dry-wet cycles on the sliding mass soil in a reservoir zone was investigated by conducting the hydro-mechanical couples' simulation in the numerical modeling (Yang et al. 2022).

Furthermore, water-induced deterioration on rocks needs to be considered for the rock landslides in TGRA, since the dry-wet cycles induced by the water level fluctuation in reservoir areas reduce the rock strength and the deformation parameters. In the relevant FE analysis, the rock damage constitutive model needs to be improved by the progressive failure mechanism of rock under water-rock interaction. In addition to the rock damage evolution equation considering

the initial damage, multi-parameter comprehensive evaluation of the cumulative damage effect of rock physical and mechanical properties under different water-rock interactions is conducted, and parameters based on energy theory are proposed to characterize the deterioration law of physical-mechanical properties under the action of different water and rock. Then the rock damage effect under different water-rock interaction is coupled to the damage constitutive model to perform the numerical stability analysis.

(4) *Probabilistic analysis methods considering uncertainties*

The geological model, mechanical properties and external factors that are required in the stability analysis of landslides can be complex and may not be characterized with certainty. Therefore, failure probability analysis characterized by Monte Carlo simulation analysis can be applied to evaluate the landslide stability. Generally, the values of cohesion c and friction angle φ of the sliding zone are taken as random variables obeying normal distribution, and the safety factor (F) being a certain function of c and φ is also a random variable. Using Monte Carlo analysis, a series of c and φ values are produced by simulation, and then the values are applied to the limit equilibrium method to obtain the factor of safety (F). Hence the probability of $F < 1$ (the failure probability) is taken as the index of the stability judgment.

As a supplement to the failure probability analysis, sensitivity analysis can be used in the stability investigation of the reservoir landslides. This analysis is the study of sensitivity of a given parameter to the factor of safety by changing the one and keeping the other invariant in the stability calculation, which can ascertain the controlling factors of the landslides' stability. Sensitivity analysis investigates the relation between the factor of safety with the different reservoir water level, ground water level, seismic intensity and sudden drawing down of the reservoir water level to flood control limitation level, and so on. Considering the factors based on the mother rock properties, the granular composition and the water content variation of the sliding zone can also be included in the analysis. Then the variation range of the shear strength parameters (c and φ) are evaluated, and the stability of landslides under various constitution of conditions can be investigated.

For examples, in the sensitivity analysis of landslides stability in TGRA, Wang et al. (2020a) considered the rainfall effects on the reservoir landslides and constructed a probability model integrating landslide susceptibility index and rainfall process when assessing the landslide hazard. In addition, Gong et al. (2020) promoted an approach of stratigraphic uncertainty modelling with random field. As explained in the paper, the spatial correlation of the stratum existence between different subsurface elements was characterized by an autocorrelation function, and the probability of the existence of a particular stratum in the non-borehole element could be determined according to the derived spatial correlations. By applying this approach to Majiazhou landslide for a probabilistic stability analysis, the influences of the stratigraphic uncertainty on the stability of this landslide and the location of the slip surface were revealed.

3.3 Stability of the Reservoir Landslides During the TGD Operation

The impoundment of the TGR altered the environmental conditions of the reservoir landslides, which had a significant impact on their stability.

(1) *Reservoir landslides stability during the trial impoundment*

During the June 2003 reservoir trial impoundment, the reservoir water level rose approximately 70 m to 135 m ASL and keeps. Monitoring revealed that between 2003 and 2006, 177 landslides occurred in the TGRA after this trial impoundment. The movement of these landslides caused local cracking and destruction of houses and roads, which leads to the relocation of over 6900 people.

(2) *Reservoir landslides stability during the 156 m ASL impoundment*

The water level fluctuated between 145 m and 156 m ASL during the period of the impoundment aimed at 156 m ASL, which lasted from September 2006 to September 2008. In the entire TGRA, a total of 152 landslides and significant deformations occurred, resulting in the cracking of households and roads. During this period of impoundment, approximately 3000 people were relocated, and emergency investigation, monitoring, and rescue operations were conducted with approximately 180 emergency disposals in the reservoir area.

(3) *Reservoir landslides stability during the 175 m ASL impoundment*

The 175 m ASL impoundment of TGRA was conducted after the 2008 rainy season. The impoundment of the reservoir began on September, 2008, and ceased on October 8, 2008, when the water level reached 156 m ASL. Then, the reservoir impoundment restarted on October 17, and the water level reached 172 m ASL on November 14. After that, the water level of the reservoir slowly declined. By the end of March 2009, the water level had fallen back to 159 m ASL, then to 155 m ASL at the end of May and to 145 m ASL on 10 June

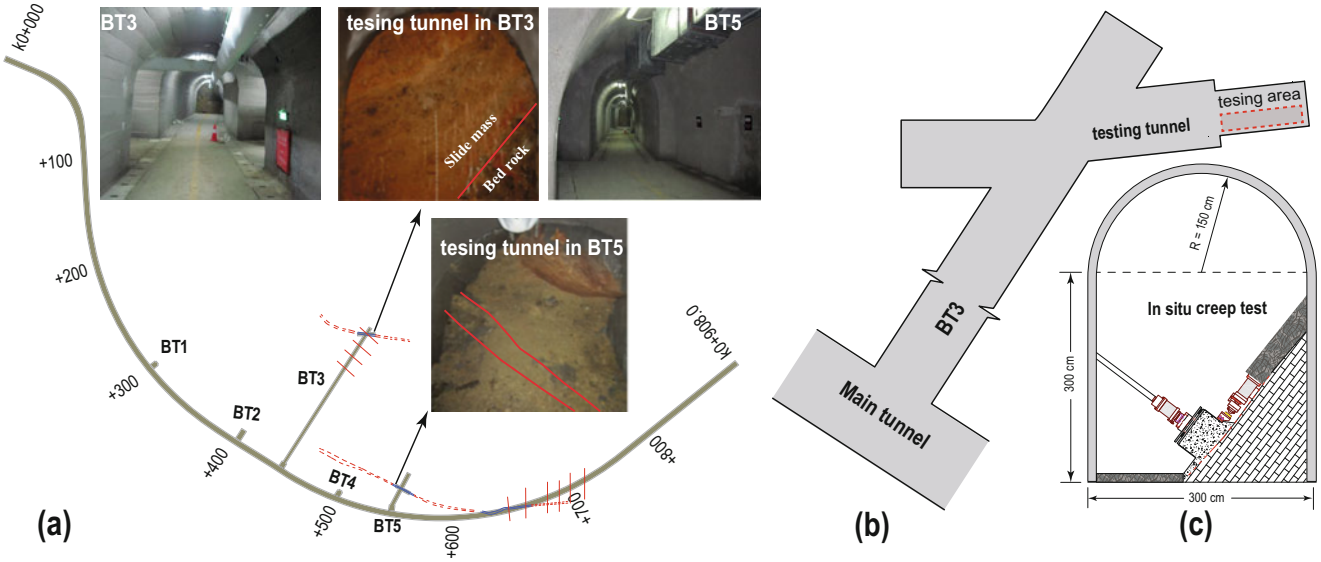

Fig. 16 (**a**) The tunnels in the Huangtupo landslide, (**b**) creep test area in the testing tunnel in BT3, and (**c**) the direct shear device fixed on the shear surface (after Wang et al. 2020b)

2009. During this period, 196 landslides and reservoir bank deformation events occurred in the TGRA. The former included the November 2008 North Nierwan landslide in Zigui County, the April 2009 Liangshuijing landslide in Yunyang County and the October 2009 Taping landslides in Wushan. Overall, the landslides and bank deformation caused the cracking of buildings and roadways on the reservoir banks, threated 24,000 residents, and posed a threat to Yangtze River shipping.

4 In-Situ Experiment on Slipping Zone Soil of Reservoir Landslides

4.1 In-Situ Direct Shear Creep Test

As the shear zone in BT3 is much thicker than that in BT5 and the hydrological condition in BT3 is more suitable for the in situ test, the testing tunnel in BT3 was selected as the in situ creep test site, as shown in Fig. 16b. Several samples were prepared in the east direction of the testing tunnel in BT3. To this end, the left side of the testing tunnel was excavated, leaving a platform with shear-zone soil above the shear surface. The shear-zone soil was then prepared to block samples for the in situ creep tests. To mimic the landslide movement as realistically as possible, in situ creep shearing was conducted parallel to the shear surface, as shown in Fig. 16c. A direct shear apparatus was designed for the purpose of long-term reliable in situ creep testing at the field site.

Through the in situ direct shear creep test carried out at the Badong field test site, the creep properties of the clastic soil within the shear zone were examined over various shear stress ranges. Additionally, some laboratory ring shear creep tests were carried out with the same soil. With the comparison of the test results and those obtained by triaxial creep tests reported in the literature, the following discoveries were drawn: The in situ direct shear creep test yields a failure stress of approximately 0.95 of the peak shear strength. Compared to the ring shear creep test, a much larger rate of creep displacement was obtained due to shearing along the landslide direction. The tested sample in the in situ direct shear creep test exhibits very low compressibility during creep due to the high content of coarse particles (25 and 50 wt%) and over consolidation. In the ring shear creep tests, the critical creep stress was approximately 0.98 of the peak shear strength at the prepeak state. However, at the residual state, the critical creep stress was equal to the residual strength of the soil. The shear-zone soil is prone to failure under shear conditions rather than triaxial compression conditions. Nonattenuating creep responses were obtained in both the in situ direct shear and the laboratory ring-shear creep tests, while no accelerated failure was observed in either the laboratory or the in situ triaxial creep tests.

4.2 In-Situ Triaxial Creep Test

To investigate the characteristics of the in situ sliding zone soil, which is distinguished by a high rock content and high

degree of compression, an in situ triaxial creep test was performed in BT3 as well. A subdivision of the Huangtupo landslide called Riverside Slump #1 is where the examined sample was found (Fig. 17). The test took 191 days to complete, after which the results were examined.

The test results showed that only decaying creep occurs without abrupt failure. A constitutive equation with both linear and nonlinear viscoplastic terms was deduced to accurately fit the test data. The surface with an orientation of 35° presents anisotropic traits in terms of displacement, possibly due to cracks that have formed over time; and the sliding zone exhibits low compressibility due to the high rock content (54.3%) and long-time consolidation by the overlying soil mass. The sliding zone soil behavior resembles the behavior of a landslide when a stress magnitude similar to that of the in situ stress environment is applied to the sample. The deformation and characteristics of the sample, taken together with the test results, suggest that the Huangtupo 1# landslide will continue to creep.

5 Prevention and Control of Reservoir Landslides

Due to the non-negligible effect of water, the most important measures to prevent or control reservoir landslides is drainage, combined with slope reprofiling and unloading, construction of stabilizing piles, prestressed anchor cables, anchors, lattice beams shore protection works, dynamic monitoring and composite retaining structures, etc. (Zhang et al. 2014b). The prevention and control of reservoir landslide should be based on its type, scale, stability, and combined with the regional engineering geological conditions, hazard objects and construction season and other conditions, and the comprehensive use of a variety of forementioned management forms. Studies in aspect of stabilizing piles, anchoring, and practical treatment projects of reservoir landslides are described as below.

5.1 Stabilizing Piles

In reservoir areas, stabilizing piles was one of the most common and effective methods for preventing and mitigating landslides. Numerous studies have focused on the theory and analysis of stabilizing piles in the past decades. The landslide thrust, interaction mechanism between stabilizing piles and landslides, and design optimization were investigated using numerical simulation techniques, laboratory, and in-situ tests (Dai 2002; Tang et al. 2016). In the landslide thrust analysis, the landslide evolution process that accounts for water fluctuations was also considered (Jia et al. 2009; Tang et al. 2014).

The interaction mechanisms between the stabilizing pile and landslide include those between the stabilizing pile and sliding mass (pile–soil interaction) and those between the

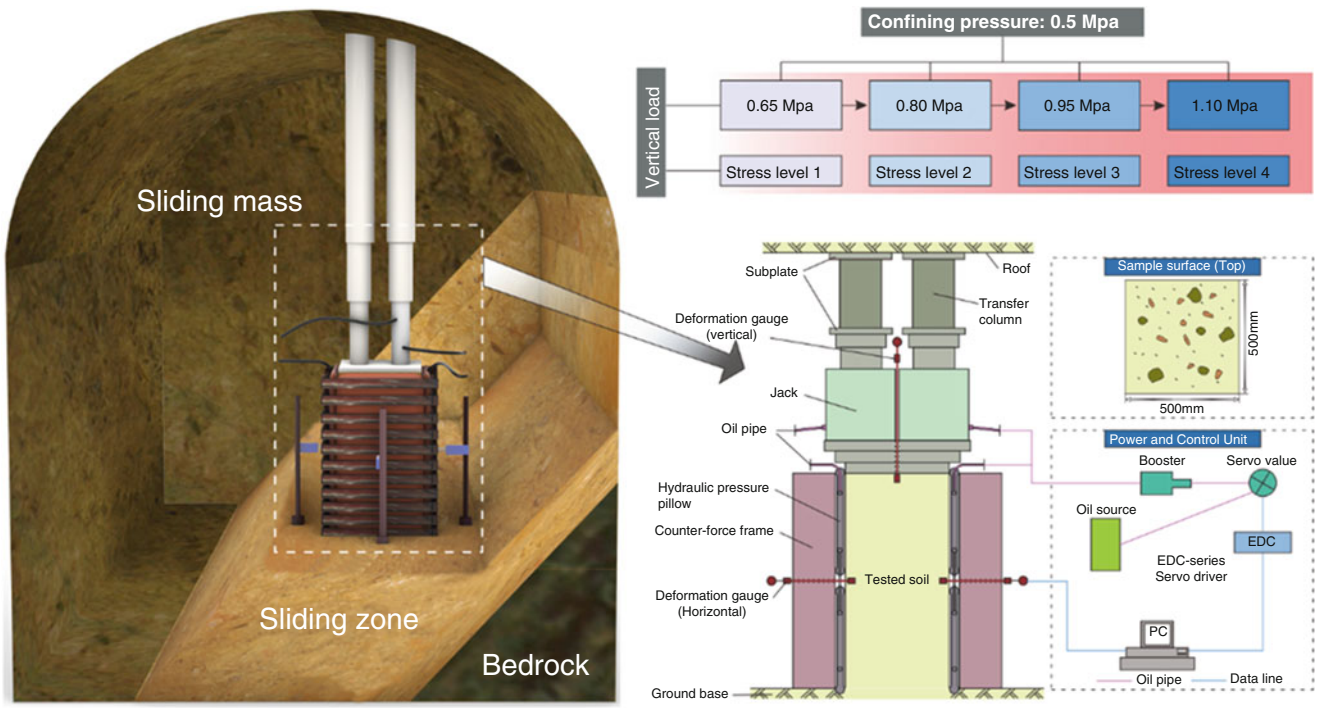

Fig. 17 In-situ triaxial creep test on sliding zone soil of the Huangtupo landslide (after Tan et al. 2018b)

stabilizing pile and bedrock (pile–rock interaction). Both are essential for the optimal design of stabilizing piles. In the study of pile-soil interaction mechanism, the effect of soil arching was considered (Tang et al. 2014; Zhang et al. 2018). In terms of pile-rock interactions, physical model tests and numerical studies were frequently utilized. Li et al. (2016) studied the behavior of stabilizing piles with different embedded lengths in bedrock with a strong upper layer and a weak lower layer using physical model tests.

Design optimization is a crucial component of stabilizing pile design. Theoretical and numerical methods based on soil arching effects were frequently employed to optimize the cross-section size and piles' spacing (Li et al. 2016; Wu et al. 2017). A deformation control principle was developed based on the multilayer subgrade coefficient method and physical model tests to determine the optimal pile length (Li et al. 2019). Theoretical and numerical methods that consider the safety requirement, the critical slip surface, and the stress and deformation of the stabilizing piles were used to determine the optimal pile location (Li et al. 2017).

5.2 Anchors

Due to the advantages of low cost, high efficiency and easy operation, anchors have been widely used in TGRA landslides. However, theoretical research on anchorages has been lag behind in some aspects already. The engineering analogy method and the semitheoretical and semiempirical methods are still commonly used in engineering practice (Liu et al. 2018). The design of the anchoring system requires constant optimization.

The study of interaction mechanism between anchor and rock mass (soil) is of great significance. The pullout characteristics of anchorage, which include the stress transfer between the anchor, mortar and surrounding rock, should be the most critical point. The variety of strata leads to complicated stress distribution. For instance, considering the nonuniform stress of the horizontally layered rock mass along anchors, the load transfer characteristics of anchors in the rock mass with weak interlayers were investigated. It was found that due to the existence of weak interlayers, the shear stress mutates at the weak and hard rock interface, and the axial force appears to "rebound" at the bottom of the anchored section (Wang et al. 2021b). Song et al. (2022) revealed that the shear stress distribution and the axial stress distribution were characterized by negative exponential attenuation, and the time-history variation law of the prestress was explored. The prediction formula was verified in Maya High Slope at the Shuibuya Hydropower station.

In addition, as the anchors pass through the sliding zone, they are subjected to a strong shearing when there is relative displacement between the sliding mass and sliding bed; hence, there is a growing body of literature that recognises the importance of anchor shearing. In laboratory tests, the stress of external environment (Zheng et al. 2021a), the properties of rock masses and discontinuities, for instance, JRC of rock joints (Wang et al. 2022), and the anchorage parameters and modes (Zheng et al. 2021b), can be significant factors for the effectiveness of anchor support and the stability of landslides. In theoretical aspect, considering the relationship between the dilation effect and the bolt deformation and the influence of joint surface abrasion on the attenuation of the internal friction angle, Zheng et al. (2021c) proposed an analytical model for predicting the shear behavior of bolted rough joints, which successfully predicted the shear load-shear displacement curve of the anchoring joint and the change curve of the anchor shaft force.

In terms of the design optimization of anchor, the direction angle should be of particular importance. An et al. (2020) proposed a new method to calculate the optimal anchorage direction angle, for case of the reinforcement direction perpendicular to the strike direction of the slope, derivative method was used, and when the reinforcement direction has no restrictions, the fmincon function was adopted to optimize the anchorage direction angle. The proposed method can further improve the anchoring effects and reduce the total usage of slope supporting costs.

The reservoir landslides may lead to anchor shearing (Fig. 18). However, modeling the shear mechanical behaviors of bolted rock joints is very complicated due to the complex factors that affect the axial and shear forces on the bolts. In the process of shearing, the rough surface of the joint undergoes a dilation effect and morphological abrasion, which is very common in reservoir landslides, were highlighted in our model (Zheng et al. 2021b).

The key steps of the model are as follows: the contribution of the bolt to the shear strength is a combination of the axial and shear forces (Fig. 19), based on the Mohr-Coulomb criterion, the following formula can be applied to compute the shear loads of the bolted rock joints:

$$T_{bj} = (R_c + \Delta R_{c_b}) + (\Delta R_{\sigma_{nb}} + R_{\sigma_n}) \tan \phi_j \tag{8}$$

$$\Delta R_{c_b} = (N_{\mathrm{O}} \sin \omega_{\mathrm{O}} + Q_{\mathrm{O}} \cos \omega_{\mathrm{O}}) \tag{9}$$

$$\Delta R_{\sigma_{nb}} = (N_{\mathrm{O}} \cos \omega_{\mathrm{O}} - Q_{\mathrm{O}} \sin \omega_{\mathrm{O}}) \tag{10}$$

Where T_{bj} is the shear load of the bolted rock joint; R_c is the shear load provided by the cohesion of the joint surface; ΔR_{c_b} is the shear load provided by the additional cohesion of the bolt; $\Delta R_{\sigma_{nb}}$ is the additional normal load provided by the bolt on the joint surface; R_{σ_n} is the initial normal load of the joint

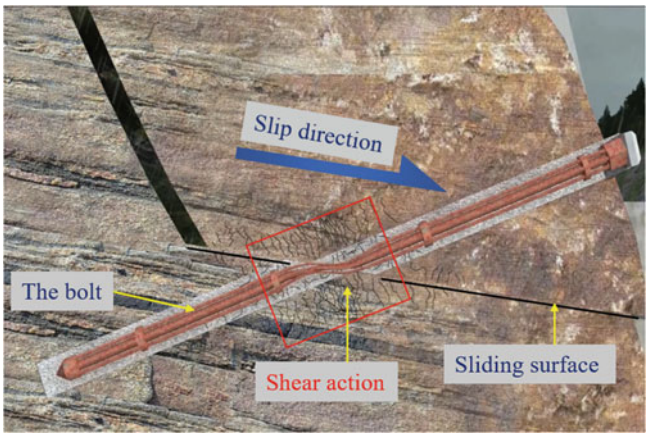

Fig. 18 Schematic diagram of anchor under shearing

surface; ϕ_j is the joint friction angle; and ω_o is the rotation angle of Point O.

The internal friction angle is not a constant (Fig. 20), and the evolution process of the internal friction angle can be described by following functions:

$$\phi_e = \begin{cases} H_1\delta_v{}^2 + H_2\delta_v + H_3 & \delta_v \in [0, \delta_d) \\ H_4\delta_v{}^2 + H_5\delta_v + H_6 & \delta_v \in [\delta_d, \delta_e) \\ H_7 & \delta_v > \delta_e \end{cases} \tag{11}$$

where H_1, H_2, H_3, H_4, H_5, H_6 and H_7 are undetermined coefficients and δ_v is the shear displacement.

In this model, a bolt is regarded as a semi-infinite beam on the elastic foundation, and the elastic foundation beam theory is used to calculate the shear force:

$$Q_O = \begin{cases} \dfrac{110\sigma_c{}^{0.85} v_o}{\lambda} & , DI \le 0.02 \\ \dfrac{110\sigma_c{}^{0.85} v_o}{\lambda\left(1 + 3\left(\frac{v_o}{D_b} - 0.02\right)^{0.8}\right)^4} & , DI > 0.02 \end{cases} \tag{12}$$

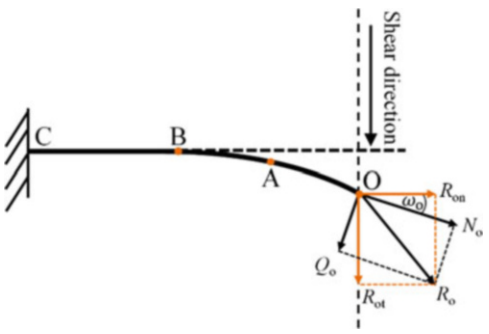

Fig. 19 Force of the bolt under shear action

where σ_c is the compressive strength of grouting concrete; v_o is the transversal displacement of the bolt (i.e., bolt deflection); D_b is the bolt diameter; λ is bedding coefficient; DI is a dimensionless damage coefficient.

Considering the dilation effect and the influence of normal stress (Fig. 21), the calculation formula of the axial force of the bolt at joint is shown in function (13), Where ε_L is the strain of AO; A_b is the cross-sectional area of the bolt; ε_e is the strain corresponding to the yield strength of the material; k is the modulus of the elastic foundation (i.e., spring stiffness); E is the elastic modulus, E_p is the plastic modulus; ω_{op} is the is the plastic rotation angle of Point O.

$$N_C = \begin{cases} \varepsilon_L A_b E\cos(\omega_o) - \dfrac{kv_O}{2\lambda}\sin(\omega_o) + \dfrac{3kv_O}{4\lambda}\sin\left(\dfrac{11}{18}\omega_o\right) & \varepsilon_L < \varepsilon_e \\ (\varepsilon_e A_b E + (\varepsilon_L - \varepsilon_e)A_b E_p)\cos(\omega_{op}) - \dfrac{kv_O}{2\lambda}\sin(\omega_{op}) + \dfrac{3kv_O}{4\lambda}\sin\left(\dfrac{11}{18}\omega_{op}\right) & \varepsilon_L > \varepsilon_e \end{cases} \tag{13}$$

The tensile-shear failure mode of the bolt adopts the Tresca strength criterion:

$$\left(\frac{N_o}{N_p}\right)^2 + \left(\frac{Q_o}{Q_p}\right)^2 = 1 \tag{14}$$

where N_p and Q_p represent the corresponding ultimate axial force and shear force, respectively, under noninteractive force conditions; $N_p = A_b\sigma_p$; $Q_p = A_b\sigma_p/2$; and σ_p is the ultimate axial stress at failure.

Through the above steps, the shear load-shear displacement curves of bolted rock joints can be obtained, we verified the model by conducting laboratory tests. Figure 22 shows the analysis models of the roughness of five different joint surfaces and the results of the direct shear tests. The analysis model shows agreement with the experimental results, which verified the validity of the model. The model reveals that it is necessary to consider the dilation effect and morphological abrasion of rock joint when the bolt is subjected to shear action in reservoir landslides.

5.3 Case Studies

To examine the effectiveness of the proposed method for the determination of stabilizing piles location in the reservoir landslides with interbedding of hard and soft bedrock, the Yanguan landslide located in Yichang city, China, was taken as an example (Fig. 23). With the proposed method, it was found that the location of the hard layer in bedrock has a significant effect on the pile deformation. The impact of hard bedrock layer on piles relies on its location coefficient. The optimal pile location corresponds to a region with both hard top and bottom layers in bedrock. The optimal location of

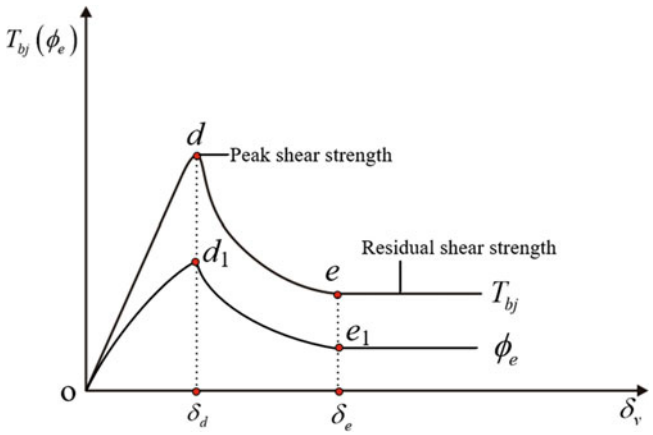

Fig. 20 Calling process of the friction angle with shear displacement

stabilizing piles should be located in the hard top and bottom bedrock layers, with a considerable decrease in both the displacement and internal force of stabilizing piles.

Drainage, a straightforward but frequently effective method for preventing landslides, was frequently utilized in some larger and deeper reservoir landslides with significant movement. The Huanglashi landslide in Badong County is a successful example of hazard control by drainage. The volume of the landslide is 18 million m^3, and its hydrogeological and engineering geological conditions are complex (Guo et al. 1999). The variation of groundwater was found to have a significant effect on the stability of the Huanglashi landslide. Thus, a drainage system was implemented to stabilize and prevent further landslide development (Fig. 24). The following control schemes were implemented: On the central portion of the Huanglashi landslide, a row of evenly spaced wells was installed initially. It contained 33 drainage wells of 20–30 m deep with distances ranging from 5 to 10 m between them. Then, an adit was installed to collect water beneath the sliding zone. Water entered the adit via drainage wells and then flowed into surface ditches. Based on the monitoring and observations (giving dates or periods), it

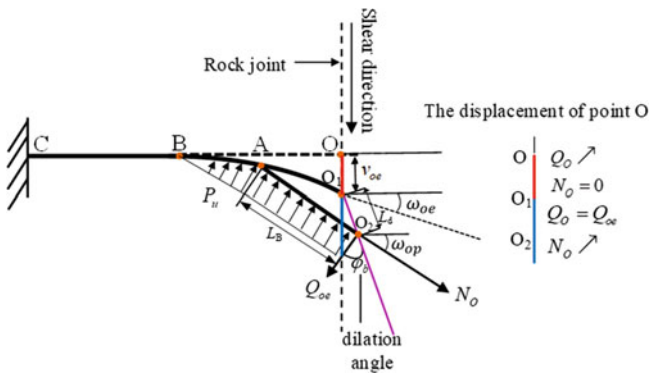

Fig. 21 Shear deformation process of the bolt

was found that the implemented control measures were quite effective.

6 Forecasting of Reservoir Landslides

6.1 Forecast Model of Reservoir Landslides

In the field of geohazard prevention and control, reservoir landslides forecasting, especially temporal forecasting, is a long-standing challenge that has received considerable attention. The primary objective of reservoir landslides short-term forecasting is to determine the critical sliding time, whereas long-term forecasting focuses on predicting long-term deformation based on displacement-time series under the influence of multiple external and internal factors. The forecast methods can be classified into four categories: physical-mechanical forecast methods, traditional nonintelligent methods, intelligent methods, and probabilistic forecast methods.

Since the proposal of the Satio model, the physical-mechanical forecast model was established based on the analysis of large-scale laboratory experiments and field monitoring data, which are suitable for short-term forecasting. In consideration of the complexity, time consumption, and cost of experiments, physical-mechanical forecast models have strict research and application restrictions, and research has gradually slowed down in recent decades. Based on creep theory, these models describe the deformation of landslides mainly in the forms of rheological functions. In the reservoir landslides long-term forecasting, traditional nonintelligent methods, intelligent methods, and statistical forecasting methods are primarily used nowadays. For traditional non-intelligent methods, prediction models are often developed from algorithms such as Wavelet transform, grey theory, time series, Kalman filter, etc. to forecast the behavior of reservoir landslides in the TGRA (Xu et al. 2011). As the artificial intelligence algorithms rapid developed recently, intelligent methods such as artificial neural network (ANN) and supporting vector machine (SVM) have become more prevalent in the long-term prediction of reservoir landslides (Bai et al. 2009; Du et al. 2013; Ma et al. 2017). Intelligent methods are effective at handling complex problems associated with landslide forecasting, and the effect of uncertainty in these methods has raises widely attentions as probabilistic models that can explicitly consider the uncertainty have been developed in the recent years (Ma et al. 2018).

In order to mitigate the reservoir landslides effectively, an early warning criterion that issues timely alarms is also vital.

Typically, the early-warning criteria for reservoir landslides in TGRA are based on macroscopic precursors, stability indices, displacement data, and environmental conditions. Examples of macroscopic precursors include the

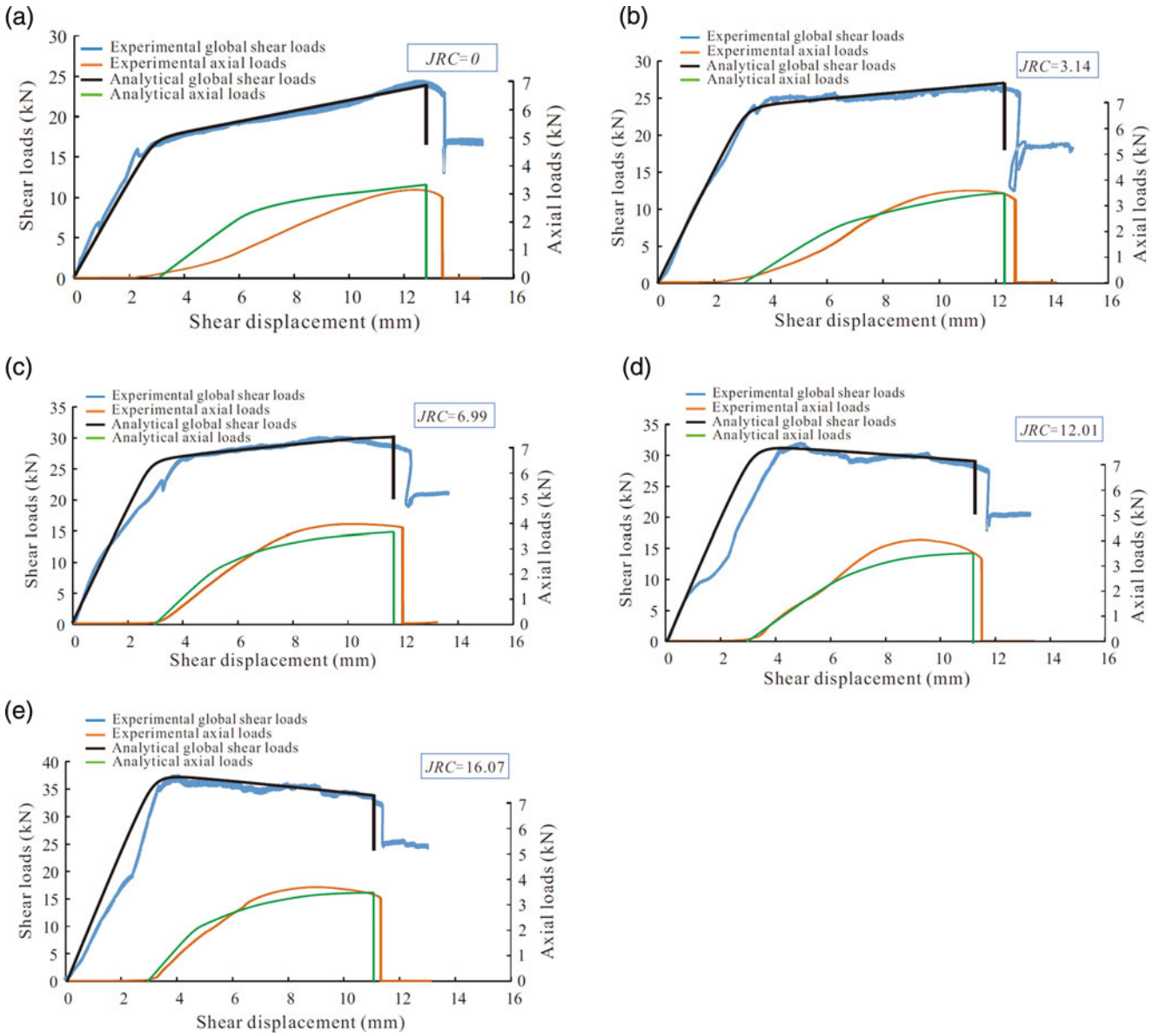

Fig. 22 Comparison between the calculated value and experimental value: (**a**) JRC = 0; (**b**) JRC = 3.14; (**c**) JRC = 6.99; (**d**) JRC = 12.01; and (**e**) JRC = 16.07

significant deformation of the ground surface and buildings, the collapse of the landslide toe, and the sudden variation of subsurface water table. During the critical sliding stage, these phenomena are distinct and generally detectable by native residents. The stability indices are based on the of safety factor and the reliability index, which are derived from deterministic and probabilistic analyses, respectively (Hu et al. 1996). Displacement data represent the most direct and accessible information obtained through landslide monitoring. Consequently, many criteria, such as displacement rate and acceleration (Yuan et al. 2015) and displacement vector angle, have been proposed based on displacement data (He et al. 2003). Criteria based on the environmental conditions are mainly related to rainfall and TGR water level fluctuation. Maximum 24-h rainfall intensity and reservoir water level decline rate are effective indicators for early warning of TGRA landslides (Ni et al. 2013).

Except for the physical-mechanical forecast model, universal and accurate prediction of the aforementioned methods is a bottleneck problem, as they concentrate on the characteristics of landslide behavior and external dynamic factors. To overcome this difficulty, the development of a

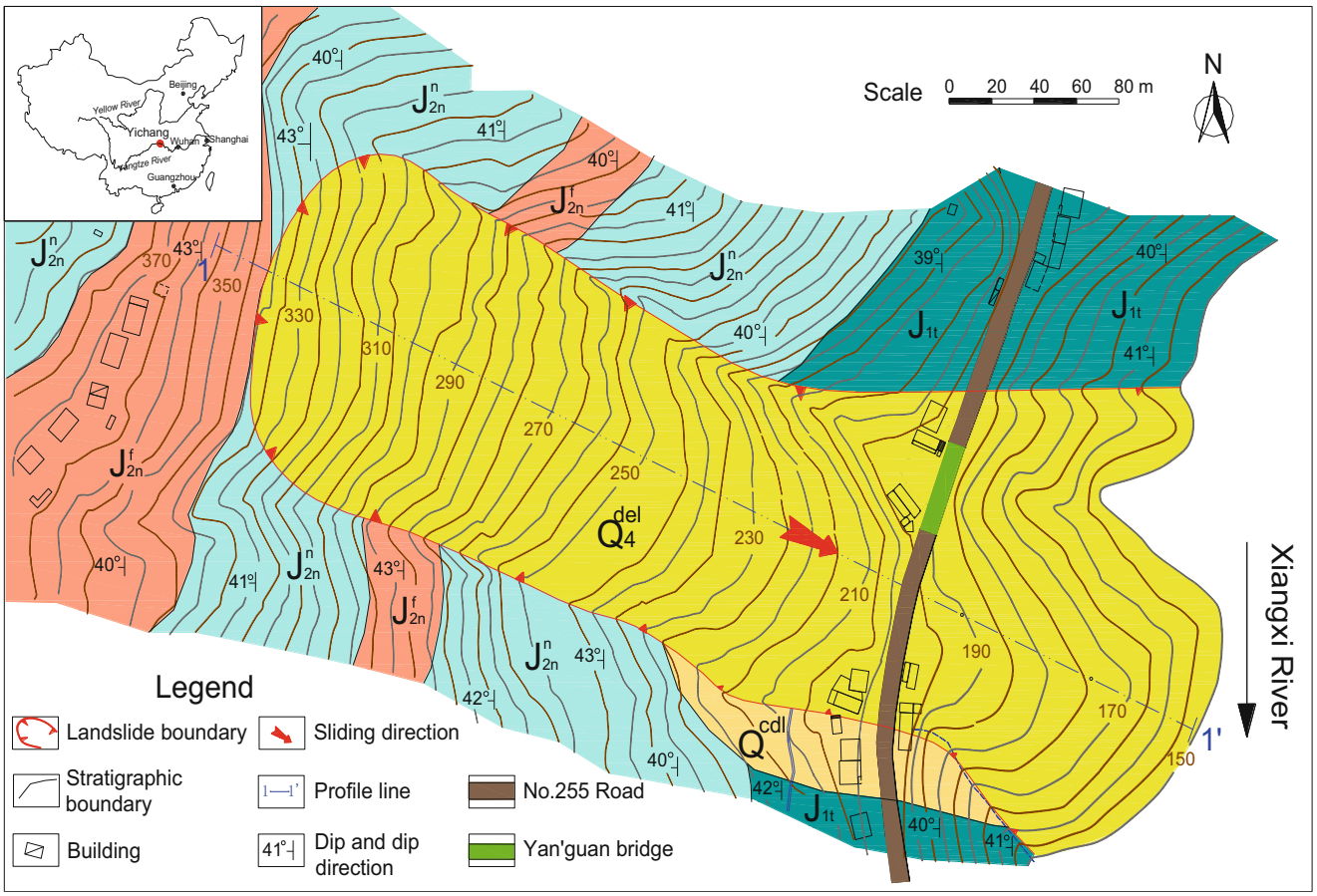

Fig. 23 Engineering geology plane of the Yanguan landslide (after Li et al. 2017)

reservoir landslide forecast model based on its physical-mechanical mechanism should become a priority research topic.

6.2 Framework of Physical-Mechanical Forecast Model

To develop the reservoir landslides prediction model based on physical-mechanical mechanism, works has been done in three aspects: (1) development of comprehensive multi-field spatiotemporal correlation monitoring system; (2) development of multi-source monitoring data fusion method; (3) numerical prediction model. The fusion of the above studies can finally realize the construction of the reservoir landslides real-time prediction platform based on the physical-mechanical model.

(1) *Comprehensive multi-field spatiotemporal correlation monitoring system*

The first step in developing physical-mechanical forecast model for reservoir landslides is to build a 3D comprehensive monitoring system of reservoir landslides that includes multi-field spatiotemporal correlated monitoring technology. The developed monitoring system allows for the real-time and effective acquisition of key parameters of prediction geological criteria and initiation criterion. The Huangtupo landslide in the TGRA has been chosen, and a 3D comprehensive monitoring system was built on it (Fig. 25).

At various latitudes, surface displacement and meteorological data were monitored by space-air-ground technology. Through interferometric synthetic aperture radar (InSAR) and multi/hyperspectral remote sensing satellites, the landform and displacement distribution of the entire landslide and its surrounding area was obtained, and the sensitive area of landslide dynamic evolution can be quickly identified. Distributed monitoring of local sensitive areas of landslide was carried out by using technologies and methods such as drone laser scanner (DLS), unmanned aerial vehicle (UAV), ground-based InSAR, etc., from which only a few representative feature sites were selected for further monitoring. Global navigation satellite system (GNSS), borehole monitoring, and other methods were used to monitor these representative feature sites to obtain aging effective characteristic parameters that accurately reflect the landslide evolution

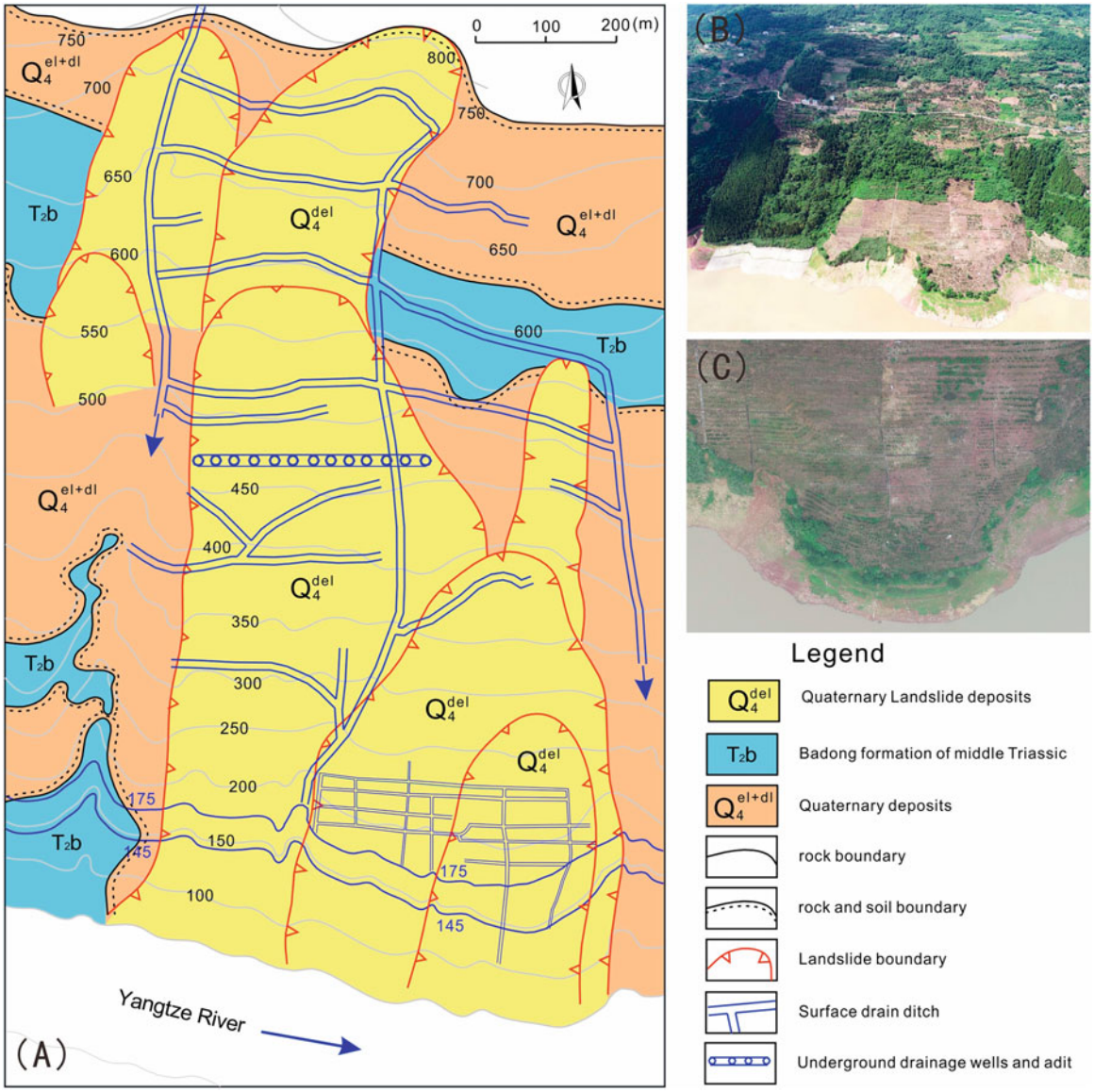

Fig. 24 (**a**) Drainage system used to stabilize the Huanglashi landslide, whose toe is affected by TGR water level fluctuations (note the 145 m and 175 m contours); (**b**) Full view of the Huanglashi landslide; (**c**) Aerial photo showing surface drainage system

state. To achieve continuous monitoring of reservoir landslide multi-field under large deformation, a multi-point distributed flexible inclinometer and deformation coupled pipeline trajectory inertial measurement were developed. On this basis, a multi-field spatiotemporal correlated monitoring technology integrating deep displacement, groundwater level, earth pressure was developed. The obtained monitoring parameters of various types have a high degree of spatiotemporal consistency and correlation, which can effectively improve data information density and prediction value.

(2) *Multi-source monitoring data fusion of reservoir landslides*

Aiming at the defects that the fusion of reservoir landslides multi-source monitoring data and their evolution process and physical-mechanical mechanism are disconnected, the structural form and features of landslide multi-source monitoring data were analyzed first (Fig. 26). Then, the classification and coding specification of multi-source monitoring data of landslide was established, and the standardized processing method of multi-source heterogeneous monitoring data was

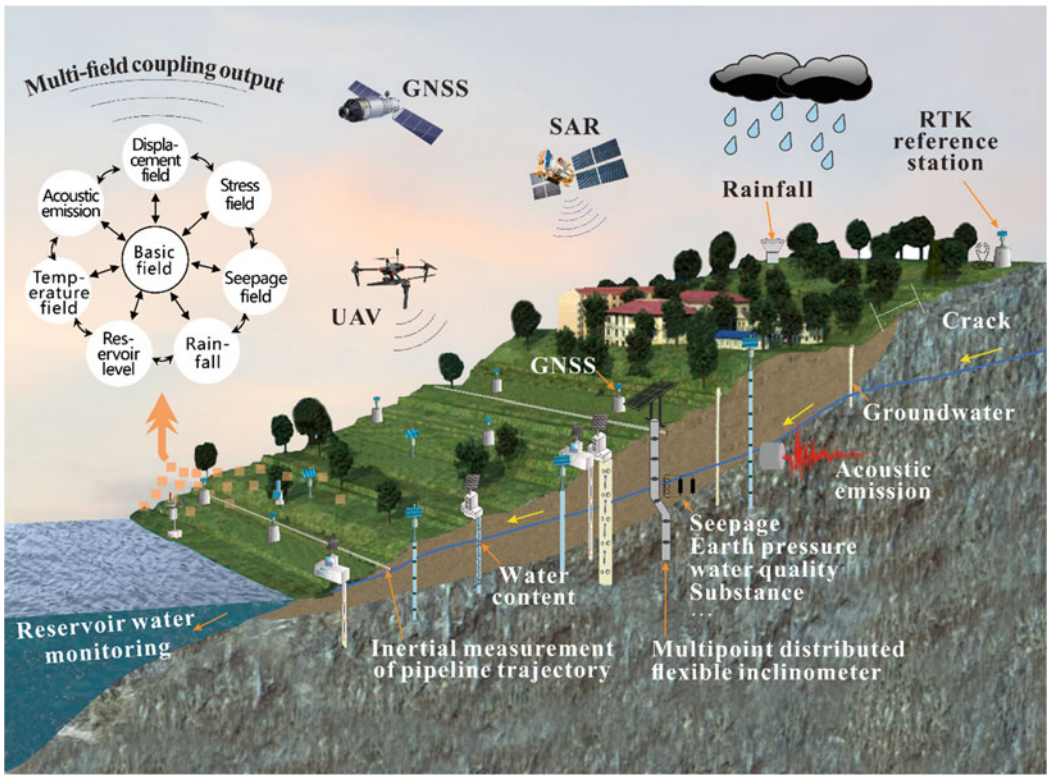

Fig. 25 3D comprehensive monitoring system in Huangtupo landslide

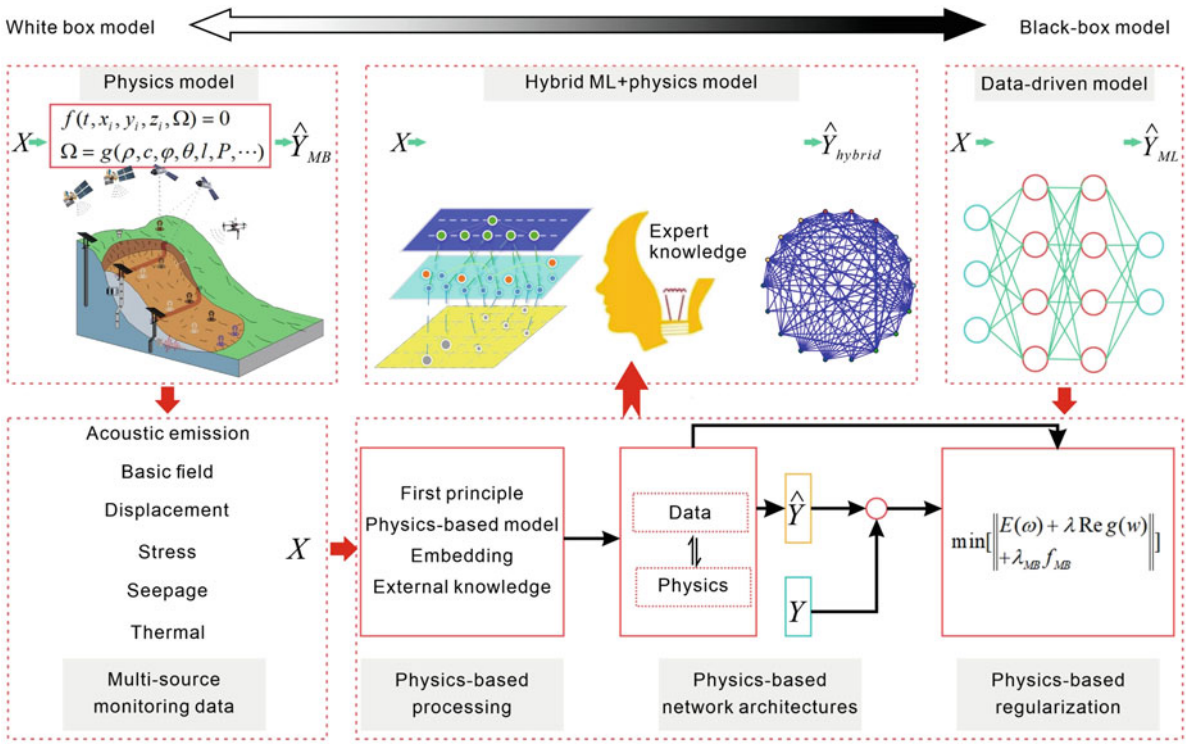

Fig. 26 Multi-source monitoring data fusion technology

proposed to realize the establishment of a priori model of nonlinear system of landslide evolution process. Study on the time-series correlation of multi-source monitoring information during landslide evolution process is carried out to reveal the self-consistent rules between the nonlinear priori model of landslide and multi-source monitoring information. A time-domain fusion method of landslide multi-source monitoring data driven by a mixture of geological processes and data was proposed so that the key field characteristic attributes of landslide evolution and the logical co-occurrence structure of multiple fields can be extracted. After the sequence pattern of landslide multi-field correlation monitoring data was identified, the critical characteristics of evolution state transition was mined and the landslide evolution state transition equation was established, the geological mathematical analysis method of landslide multi-source monitoring information can be developed eventually.

(3) *Numerical prediction model of reservoir landslides*

Based on the initiation mechanism and mechanical model of reservoir landslides, a generalized intrinsic evolution model of reservoir landslides was developed by characterizing the mechanical process under the constraints of the dominating structures of geo-material, as well as complex and volatile hydraulic forces. Then, the physical-mechanical evolution model of reservoir landslide was established based on the multimap between the spatial-temporal varying pivotal characteristic parameters of the reservoir landslide (e.g., displacement, velocity, acceleration, stress, pore pressure, etc.) and the constitutional model of the critical geo-material (e.g., slip zone, weak intercalation in the rock mass, soil-bedrock interface, etc.). Meanwhile, the probabilistic characterization and modeling methodology of the field-scale geological model and external dynamic factors in terms of fluctuating reservoir water level and rainfall were proposed, and a probabilistic prediction model of landslide initiation based on physical-mechanical process was established. It enables real-time ensemble modeling of the landslide evolution process based on variable geological elements, initial conditions, and external hydraulic forces. These variable factors can be inversed dynamically based on Bayesian theory and multi-field monitoring data in real time. The updated factors was employed to predict the forward evolution behavior of landslides, thus enabling real-time inversion and dynamic updating. Therefore, a numerical landslide forecasting (NLF) mode was established by integrating probabilistic characterization of the geological model and external dynamic forces, probabilistic forecasting of landslide initiation, and real-time dynamic update of landslide evolution processes, as shown in Fig. 27.

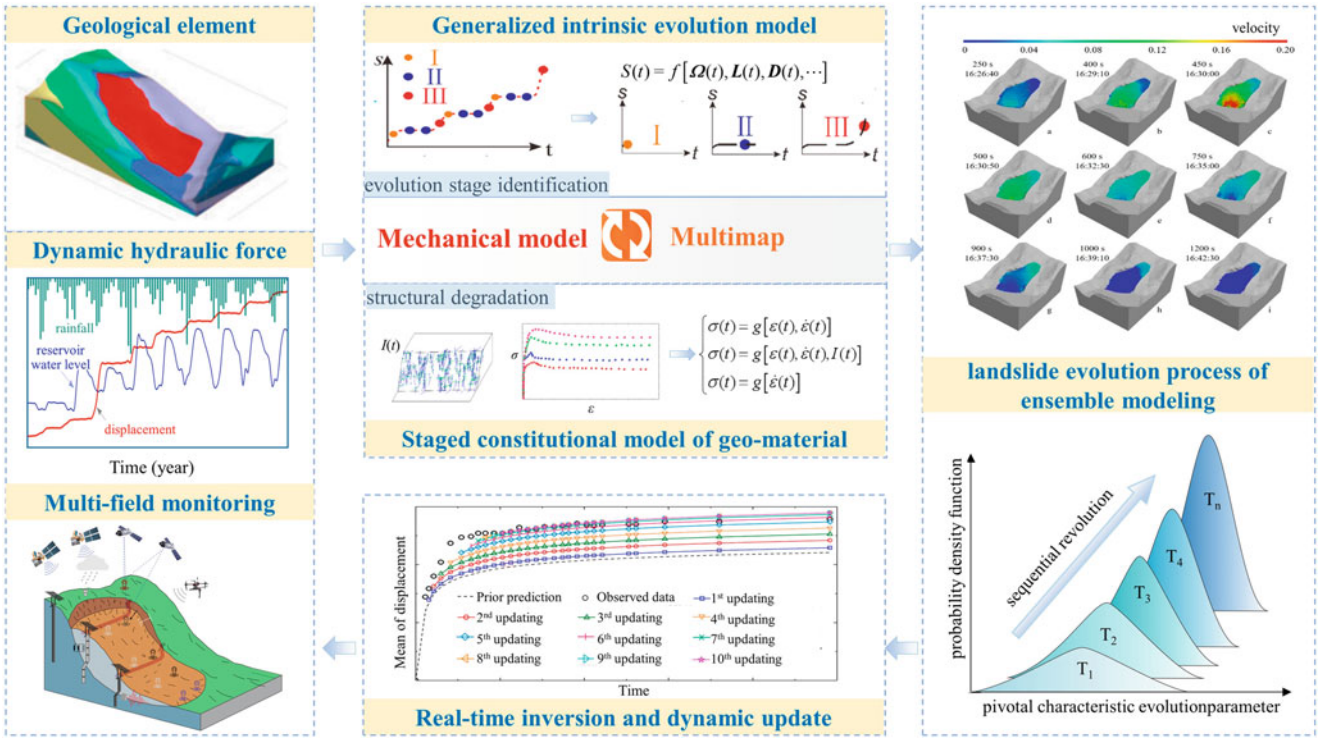

Fig. 27 Schema of reservoir landslides numerical prediction

6.3 Real-Time Prediction Platform

NLF is a radically different paradigm for landslide prediction with two aspects of requirements. First, the physical-mechanical model, the core of the mode, should be as sophisticated as possible. It is required not only to identify the progressive evolution of landslides based on the evolution phase, but also to characterize the evolution process employing the stress-strain-strength-time correlation of the key geo-material corresponding to the actual stress traits to the greatest extent possible. Moreover, the multi-field correlated monitoring of landslides should capture the variations of the most critical evolutionary parameters as much as possible.

On this basis, establishing a real-time prediction platform is an effective way to achieve NLF. Comparing the current geohazard and meteorological real-time prediction platforms, it is proven feasible to build a clouding platform. The main functions of the platform include four parts: storage and recall of background data of landslide, real-time acquisition and transmission of multi-field monitoring data, real-time pre-processing of multi-source data, numerical forecast and further information distribution, as shown in Fig. 28.

The landslide background data system covers a series of basic geological data, including landslide formative background, fundamental geological data, engineering geological data, hydrogeological data, remote sensing data, etc. Based on the research and development of multi-field correlation monitoring technology, a space-air-ground-underground integrated monitoring network can be constructed through the Internet of Things (IoT) and other information transmission technologies to obtain landslide monitoring data in real time. The multi-source monitoring data fusion technology can be employed to implement clouding data pre-processing and computing, thus synchronizing the display of monitoring data on the client side and the cloud. Subsequently, the ensemble modeling of the landslide evolution process can be implemented based on uncertainty theory with the geological elements, initial and boundary conditions as variable inputs. Bayesian networks and Markov theory are then adopted to calibrate and update the physical-mechanical model and inputs with multi-field monitoring data in real time, and derivate the entire evolution process of landslide and implement dynamic prediction based on the updated boundary conditions and parameters in the cloud. It is similar, but not identical, to data assimilation. Data assimilation is essentially the process of incorporating new observations into the dynamic operation of a numerical model to bring the predicted values closer to the true values. In contrast, the process of dynamic inversion in NFL is essentially a process of correcting the inputs of the model with observations to achieve dynamic prediction. The computed landslide process and probabilistic forecasting information of landslide initiation are then submitted to the PC terminal for backup storage and dynamic display. Depending on the initiation criteria and threshold, the landslide evolution and initiation probabilistic forecasting information can be further distributed and alerted to particular users.

7 Challenges and Suggestions

The reservoir landslide research conducted over the past several decades has generated a vast amount of valuable scientific and technical literature. These works have enhanced our comprehension and capacity to prevent and mitigate their effects. Although significant achievements have been made, numerous challenges remain. To overcome these challenges, future research must invest significantly more time and resources. The following list of challenges and suggested topics is intended to stimulate further research.

(1) *3D fine geological modeling of reservoir landslides*

The macroscopic geomechanical model of reservoir landslides is vital in the assessment of reservoir landslides and their evolution mechanisms. The consideration of the combined action of multiple fields, phases and factors needs to be further deepened in the traditional reservoir landslide geomechanical modeling method. Modern noncontact investigation techniques, such as small unmanned aerial vehicles (UAV), remote sensing, 3D laser scanners and LiDAR, should be adopted and systematically integrated in reservoir landslide field investigations. Combined with the detailed field investigation, the refined modeling of the three-dimensional geological model of landslides in complex strata in the reservoir area can be realized.

(2) *Long-term stability assessment of reservoir landslides*

Prior research concentrated primarily on the rheology and residual strength properties of the sliding mass and the slip surface. Nevertheless, the reservoir landslides involve a process of dynamic stress change and deformation caused by external factors. These dynamic changes must be taken into account and explicitly incorporated into the long-term stability assessment of reservoir landslides. More research is required to evaluate the long-term stability of reservoir landslides stabilized by engineering structures.

(3) *Construction of in-situ experimental station of reservoir landslides*

The comprehensive platform for landslide in situ testing is an important means to study the formation and evolution mechanism of reservoir landslides. By constructing the field in situ

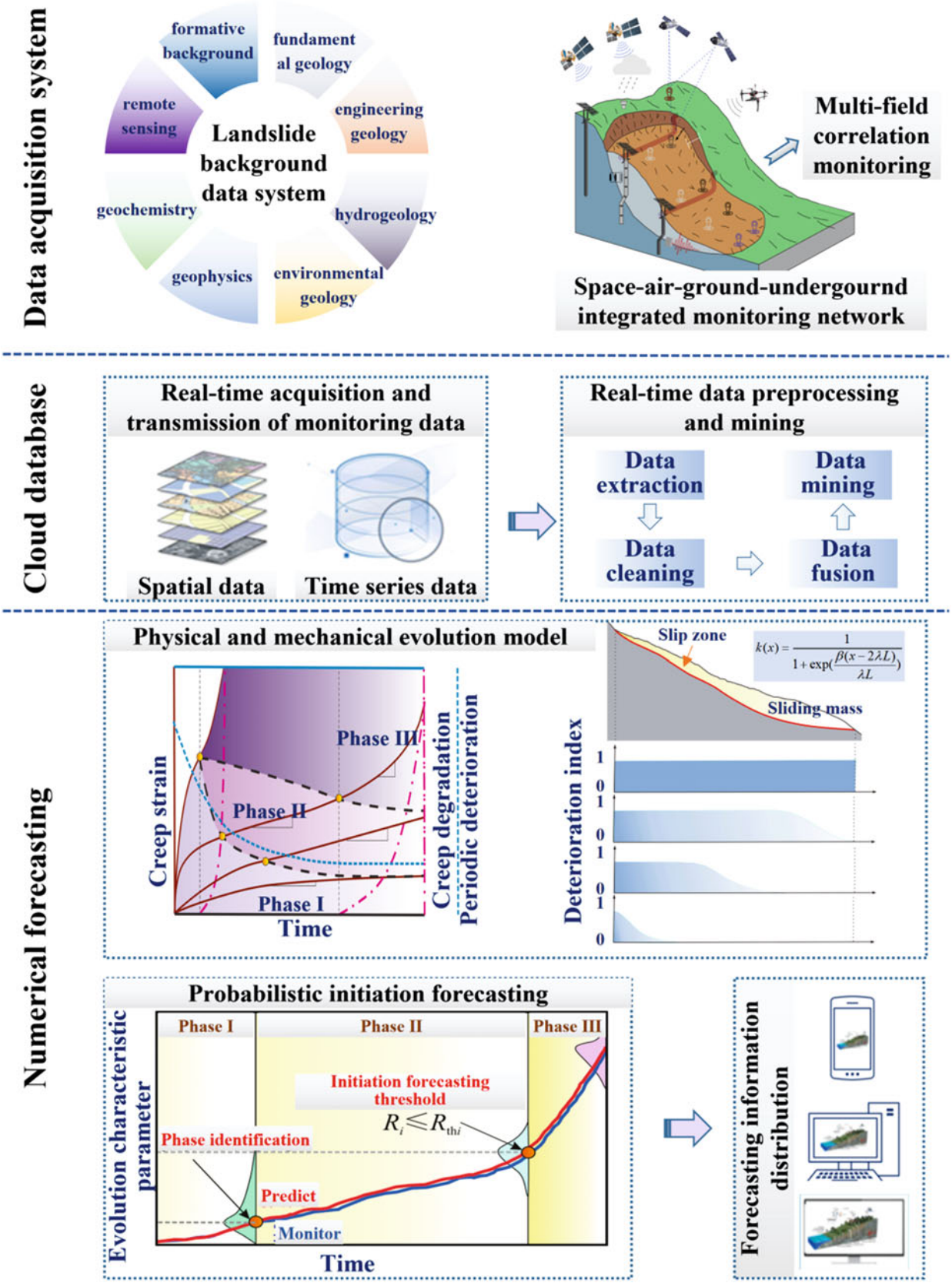

Fig. 28 Schema of reservoir landslides real-time prediction platform

test station of reservoir landslides and carrying out the in situ mechanical test and comprehensive monitoring demonstration project, valuable first-hand test and monitoring data can be obtained to further confirm the results of theoretical and numerical analyses, which is conducive to promoting research on the long-term evolution evaluation of reservoir landslides under complex conditions (such as reservoir water fluctuation and rainfall conditions).

(4) *Multi-parameter integrated monitoring system for reservoir landslides*

The evolution process of reservoir landslides can be more accurately revealed through the integrated acquisition of multi-parameter data that may be cross-correlated. However, the current monitoring systems was usually in the form of the randomly combination of different monitoring devices, which collect the data independently. Thus, an integrated monitoring system of multi-parameter is urgently needed. The integrated and correlated information regarding the evolution of various fields inside reservoir landslides, such as reservoir seepage, stress, and surface/subsurface displacement, provides a more solid foundation for more accurate landslides analysis. Research of integrated monitoring technology, as well as new algorithms for effectively utilize the multi-parameter correlated information in the rapid assessment of landslide stability and deformation is required (Tang et al. 2019).

(5) *Control countermeasures for huge reservoir landslides*

In TGRA, over 30 enormous landslides (volume >10 million m^3) have been identified. Many of these landslides, such as the Huangtupo and Baishuihe landslides, are still active and pose a significant threat to Yangtze River navigation with cumulative displacements of several meters per year. Due to the size of these landslides, however, traditional control methods such as anti-slide piles and anchor cables are difficult to implement. The creation of efficient preventative measures to manage and control these massive landslides is urgently needed.

(6) *Combination of prediction model and physical-mechanical mechanisms for reservoir landslides*

The numerical models used to predict reservoir landslides are based on mathematical methods and statistical theories that are unrelated to the landslide evolution process and physical-mechanical mechanism. These models' forecasting universality and success rate have always been an unavoidable issue. Thus, if forecasting models are not fully integrated with reservoir landslide physical-mechanical mechanisms, the theoretical and technical bottlenecks of landslide prediction and forecasting will never be broken.

8 Conclusions

The study of reservoir landslides has been a major focus of the engineering geology research, and received special attention in the construction of the TGD in China in the past few decades. These efforts have led to better knowledge and practice in the identification and mitigation of reservoir landslides. A comprehensive introduction of the reservoir landslides related articles and research developments in the TGRA are presented here. First, the studies of characteristics of reservoir landslide in TGRA in aspect of spatiotemporal distribution, slide-prone strata, influence of geologic structure, dynamic characteristics, influence of rainfall and fluctuating water level was summarized. Typical seepage-induced reservoir landslide and buoyancy-induced reservoir landslide from TGRA are introduced and analyzed, respectively. Then, the assessment methods for reservoir landslides in the past few decades was examined. After that, large-scale in-situ experiments, including in-situ direct shear creep test and in-situ triaxial creep test, conducted inside the Huangtupo landslide was described, which offered a unique research opportunity for a better understand of sliding zone soil's properties. Hereafter, research progress in aspect of stabilizing piles, anchoring, and practical treatment projects were described. Finally, the prospects of reservoir landslide forecasting based on physical-mechanical mechanisms were elaborated.

Despite the major advances in the research and development, challenges still exist in the identification and mitigation of reservoir landslides. These include issues such as the 3D fine geological modeling of reservoir landslides, long-term stability assessment of reservoir landslides, construction of in-situ experimental station for reservoir landslides, multi-parameter integrated monitoring system for reservoir landslides, control countermeasures for huge reservoir landslides and the combination of prediction model and physical mechanics mechanism for reservoir landslides. These challenges represent real opportunities for the engineering geologists in their pursuit of reservoir landslides-related hazards reduction and mitigation.

Acknowledgements The authors would like to express their sincere gratitude to the National Key Research and Development Program of China (Grant No. 2017YFC1501305), and National Major Scientific Instruments and Equipment Development Projects of China (Grant No. 41827808) for supporting this work.

References

An C, Liang Y, Wang L, Deng S, Sun Z, Fan B, Zheng L (2020) Three-dimensional optimization design for the direction angle of anchor cable reinforcement in wedge rock slope. Rock Soil Mech 41(08): 2765–2772. (in Chinese)

Bai SB, Wang JZ, Lu GN, Zhou PG, Hou SS, Xu SN (2009) GIS-based and data-driven bivariate landslide-susceptibility mapping in the Three Gorges area, China. Pedosphere 19(1):14–20

Cao L, Luo XQ (2007) Experimental study of dry-wet circulation of Qianjiangping Landslide's unsaturated soil. Rock Soil Mech 28:93–97. (in Chinese)

Dai ZH (2002) Study on distribution laws of landslide-thrust and resistance of sliding mass acting on anti-slide piles. Chin J Rock Mech Eng 21(4):517–521. (in Chinese)

Du J, Yin K, Lacasse S (2013) Displacement prediction in colluvial landslides, three Gorges reservoir China. Landslides 10:203–218

Dumperth C, Rohn J, Fleer A, Xiang W (2016) Local-scale assessment of the displacement pattern of a densely populated landslide, utilizing finite element software and terrestrial radar interferometry: a case study on Huangtupo landslide (PR China). Environ Earth Sci 75:880

Fourniadis IG, Liu JG, Mason PJ (2007) Regional assessment of landslide impact in the Three Gorges area, China, using ASTER data: Wushan-Zigui. Landslides 4(3):267–278

Froude MJ, Petley DN (2018) Global fatal landslide occurrence from 2004 to 2016. Nat Hazard Earth Syst Sci 18:2161–2181

Gong WP, Zhao C, Juang CH, Tang HM, Wang H, Hu XL (2020) Stratigraphic uncertainty modelling with random field approach. Comput Geotech 125:103681

Griffiths D, Lane PA (2001) Slope stability analysis by finite elements. Géotechnique 51:653–654

Guo XZ, Huang XB, Xu KX, Chen WM, Li HW, Tao WH (1999) The control works of Lianziya dangerous rock mass and Huanglashi landslide in the Three Gorges of Yangtze river. Chin J Geol Hazard Control 10(4):15–34. (in Chinese)

He KQ, Yang JB, Wang SJ (2003) Displacement vector angle of colluvial slope and its significance. Chin J Rock Mech Eng 22(12): 1976–1983. (in Chinese)

Hu GS, Men YM, Liu YH, Wang SQ (1996) The criterion of Xintan landslide forecasting. Chin J Geol Hazard Control S1:67–72. (in Chinese)

Hu XL, Tang HM, Li CD, Sun RX (2012) Stability of Huangtupo riverside slumping mass II# under water level fluctuation of Three Gorges Reservoir. J Earth Sci 23(3):326–334

Huang D, Gu DM (2017) Influence of filling-drawdown cycles of the three Gorges Reservoir on deformation and failure behaviors of anticlinal rock slopes in the Wu Gorge. Geomorphology 295:489–506

Jia GW, Zhan TLT, Chen YM, Fredlund DG (2009) Performance of a large-scale slope model subjected to rising and lowering water levels. Eng Geol 106:92–103

Jian WX, Wang ZJ, Yin KL (2009) Mechanism of the Anlesi landslide in the Three Gorges Reservoir, China. Eng Geol 108(1–2):86–95

Jian WX, Xu Q, Yang HF, Wang FW (2014) Mechanism and failure process of Qianjiangping landslide in the Three Gorges Reservoir, China. Environ Earth Sci 72(8):2999–3013

Jiang JW, Ehret D, Xiang W, Rohn J, Huang L, Yan SJ, Bi RN (2011) Numerical simulation of Qiaotou Landslide deformation caused by drawdown of the three Gorges Reservoir, China. Environ Earth Sci 62(2):411–419

Lambe TW, Whitman RV (2018) Soil mechanics SI version. Wiley

Li CD, Long JJ, Jiang XH, Fu ZY (2020) Advance and prospect of formation mechanism for reservoir landslides. Bull Eng Geol Environ 39(1):67–77

Li CD, Wang XY, Tang HM, Lei GP, Yan JF, Zhang YQ (2017) A preliminary study on the location of the stabilizing piles for colluvial landslides with interbedding hard and soft bedrocks. Eng Geol 224: 15–28

Li CD, Wu JJ, Tang HM, Hu XL, Liu XW, Wang CQ, Liu T, Zhang YQ (2016) Model testing of the response of stabilizing piles in landslides with upper hard and lower weak bedrock. Eng Geol 204:65–76

Li CD, Yan JF, Wu JJ, Lei GP, Wang LQ, Zhang YQ (2019) Determination of the embedded length of stabilizing piles in colluvial landslides with upper hard and lower weak bedrock based on the deformation control principle. Bull Eng Geol Environ 78(2): 1189–1208

Li DY, Yin KL, Leo C (2010) Analysis of Baishuihe landslide influenced by the effects of reservoir water and rainfall. Environ Earth Sci 60(4):677–687

Li JJ, Xie SY, Kuang MS (2001) Geomorphic evolution of the Yangtze Gorges and the time of their formation. Geomorphology 41:125–135

Li SL, Xu Q, Tang MG, Lqbal J, Liu J, Zhu X, Liu FZ, Zhu DX (2018) Characterizing the spatial distribution and fundamental controls of landslides in the Three Gorges Reservoir area, China. Bull Eng Geol Environ 78(6):4275–4290

Li YR, Wen BP, Aydin A, Ju NP (2013) Ring shear tests on slip zone soil zone soils of the three giant landslides in the Three Gorges Project area. Eng Geol 154:106–115

Liao HJ, Sheng Q, Gao SH, Xu ZP (2005) Influence of drawdown of reservoir water level on landslide stability. Chin J Rock Mech Eng 24(19):3454–3454. (in Chinese)

Lindenmaier F, Zehe E (2005) Process identification at a slow-moving landslide in the Vorarlberg Alps. Hydrol Process 19:1635–1651

Liu JQ, Tang HM, Li Q, Su AJ, Liu QH, Zhong C (2018) Multi-sensor fusion of data for monitoring of Huangtupo landslide in the three Gorges Reservoir, China. Geomat Nat Haz Risk 9(1):881–891

Liu YH, Liu CZ, Li TF, Lian JF (2007) Numerical simulation for deformation mechanism and stability study of Badong large slope system in the Three Gorges Reservoir. Hydrogeol Eng Geol 2007(1): 47–52. (in Chinese)

Ma JW, Tang HM, Hu XL, Bobet A, Zhang M, Zhu TW, Song YJ, Eldin MAME (2017) Identification of causal factors for the Majiagou landslide using modern data mining methods. Landslides 14(1): 311–322

Ma JW, Tang HM, Liu X, Wen T, Zhang JR, Tan QW, Fan ZQ (2018) Probabilistic forecasting of landslide displacement accounting for epistemic uncertainty: a case study in the Three Gorges Reservoir area, China. Landslides 15(6):1145–1153

Miao FS, Wu YP, Li LW, Tang HM, Li YN (2018) Centrifuge model test on the retrogressive landslide subjected to reservoir water level fluctuation. Eng Geol 245:169–179

Ni WD, Tang HM, Hu XL, Wu YP, Su AJ (2013) Research on deformation and stability evolution law of Huangtupo riverside slump-mass No. 1. Rock Soil Mech 34(10):2961–2970. (in Chinese)

Paronuzzi P, Bolla A (2012) The prehistoric Vajont rockslide: an updated geological model. Geomorphology 169:165–191

Song K, Wang FW, Yi QL, Lu SQ (2018) Landslide deformation behavior influenced by water level fluctuations of the Three Gorges Reservoir (China). Eng Geol 247:58–68

Song M, Xiang X, Zhang G, Yang X, Wen L (2022) Study on the mechanical characteristics and prestress loss of slope-anchored structure. Chin J Rock Mech Eng 41(S1):2791–2800. (in Chinese)

Sun GH, Yang YT, Cheng SG, Zheng H (2017a) Phreatic line calculation and stability analysis of slopes under the combined effect of reservoir water level fluctuations and rainfall. Can Geotech J 54(5): 631–645

Sun GH, Yang YT, Jiang W, Zheng H (2017b) Effects of an increase in reservoir drawdown rate on bank slope stability: a case study at the Three Gorges Reservoir, China. Eng Geol 221:61–69

Sun GH, Zheng H, Tang HM, Dai FC (2016) Huangtupo landslide stability under water level fluctuations of the Three Gorges reservoir. Landslides 13:1167–1179

Tan FL, Hu XL, He CC, Zhang YM, Zhang H, Zhou C, Wang Q (2018a) Identifying the main control factors for different deformation stages of landslide. Geotech Geol Eng 36(1):469–482

Tan QW, Tang HM, Fan L, Xiong CR, Fan ZQ, Zhao M, Li C, Wang DJ, Zou ZX (2018b) In situ triaxial creep test for investigating deformational properties of gravelly slip zone soils: example of the Huangtupo 1# landslide, China. Landslides 15(12):2499–2508

Tang HM (2015) Engineering geology research on prediction and prevention of slope geological hazards. Science Press, Beijing

Tang HM, Hu XL, Xu C, Li CD, Yong R, Wang LQ (2014) A novel approach for determining landslide pushing force based on landslide-pile interactions. Eng Geol 182:15–24

Tang HM, Li CD, Hu XL, Wang LQ, Criss RE, Su AJ, Wu YP, Xiong CR (2015a) Deformation response of the Huangtupo landslide to rainfall and the changing levels of the Three Gorges Reservoir. Bull Eng Geol Environ 74(3):933–942

Tang HM, Li CD, Hu XL, Su AJ, Wang LQ, Wu YP, Criss RE, Xiong CR, Li YA (2015b) Evolution characteristics of the Huangtupo landslide based on in situ tunneling and monitoring. Landslides 12: 511–521

Tang HM, Zhang YQ, Li CD, Liu XW, Wu JJ, Chen F, Wang XY, Yan JF (2016) Development and application of in situ plate-loading test apparatus for landslide-stabilizing pile holes. Geotech Test J 39(5): 757–768

Tang HM, Wasowski J, Juang CH (2019) Geohazards in the three Gorges Reservoir Area, China – Lessons learned from decades of research. Eng Geol 261:105267

Tang HM, Yong R, Eldin MAME (2017) Stability analysis of stratified rock slopes with spatially variable strength parameters: the case of Qianjiangping landslide. Bull Eng Geol Environ 76:839–853

Tian LJ, Li PZ, Luo Y (1996) Development history of the Three Gorges Valley of the Yangtze River [M]. Southwest Jiaotong University Press, Chengdu

Wang DJ, Tang HM, Zhang YH, Li CD, Huang L (2017) An improved approach for evaluating the time-dependent stability of colluvial landslides during intense rainfall. Environ Earth Sci 76(8):321

Wang FW, Zhang YM, Huo ZT, Peng XM, Wang SM, Yamasaki S (2008) Mechanism for the rapid motion of the Qianjiangping landslide during reactivation by the first impoundment of the Three Gorges Dam reservoir, China. Landslides 5(4):379–386

Wang HL, Xu WY (2013) Stability of Liangshuijing landslide under variation water levels of Three Gorges Reservoir. Eur J Environ Civ Eng 17(Suppl 1):s158–s177

Wang J, Schweizer D, Liu Q, Su A, Hu X, Blum P (2021a) Three-dimensional landslide evolution model at the Yangtze River. Eng Geol 292:106275

Wang JE, Xiang W, Lu N (2014) Landsliding triggered by reservoir operation: a general conceptual model with a case study at Three Gorges Reservoir. Acta Geotech 9:771–788

Wang L, Zhu L, Zheng L, Fan B, Sun Z, Chen H (2021b) Shear test of bolted joint rock masses considering joint roughness. Chin J Highw Transp 34(06):38–47. (in Chinese)

Wang S, Wang J, Wu W, Cui D, Su A, Xiang W (2020b) Creep properties of clastic soil in a reactivated slow-moving landslide in the Three Gorges Reservoir Region, China. Eng Geol 267:105493

Wang Y, Xiang X, Li C, Zhu G, Song C, Xian J, Zhang J (2022) Load transfer laws of tensile anchors in rock masses with weak interlayers based on a shear-slipping updating model. J Mount Sci 19(3): 812–825

Wang Z, Wang D, Guo Q, Wang D (2020a) Regional landslide hazard assessment through integrating susceptibility index and rainfall process. Nat Hazards 104:2153–2173

Wen B, Shen J, Tan J (2008) The influence of water on the occurrence of Qianjiangping landslide. Hydrogeol Eng Geol 3:3–18

Wen T, Tang HM, Wang YK, Lin CY, Xiong CR (2017) Landslide displacement prediction using the GA-LSSVM model and time series analysis: a case study of Three Gorges Reservoir, China. Nat Hazard Earth Syst Sci 17:2181–2198

Wu JJ, Li CD, Liu QT, Fan FS (2017) Optimal isosceles trapezoid cross section of laterally loaded piles based on friction soil arching. KSCE J Civ Eng 21(7):2655–2664

Wu Q, Tang HM, Ma XH, Wu YP, Hu XL, Wang LQ, Criss RE, Yuan Y, Xu YJ (2019) Identification of movement characteristics and causal factors of the Shuping landslide based on monitored displacements. Bull Eng Geol Environ 78(3):2093–2106

Wu Q, Tang HM, Wang LQ, Lin ZH (2009) Analytic solutions for phreatic line in reservoir slope with inclined impervious bed under rainfall and reservoir water level fluctuation. Rock Soil Mech 30(10):3025–3031. (in Chinese)

Xu F, Wang Y, Du J, Ye J (2011) Study of displacement prediction model of landslide based on time series analysis. Chin J Rock Mech Eng 30(4):746–751. (in Chinese)

Yan ZL, Wang JJ, Chai HJ (2010) Influence of water level fluctuation on phreatic line in silty soil model slope. Eng Geol 113:90–98

Yang X, Fasheng M, Yiping W, Daniel D (2022) Dynamic stability assessment of reservoir colluvial landslide using a hypoplastic clay constitutive model considering the effects of drying-wetting cycles on the hydro-fluctuation belt. Eng Geol 307:106791

Yang BB, Yin KL, Xiao T, Chen LX, Du J (2017) Annual variation of landslide stability under the effect of water level fluctuation and rainfall in the three Gorges Reservoir, China. Environ Earth Sci 76(564)

Yin Y, Huang B, Wang W, Wei Y, Ma X, Ma F, Zhao C (2016) Reservoir-induced landslides and risk control in Three Gorges Project on Yangtze River, China. J Rock Mech Geotech Eng 8:577–595

Yong R, Li CD, Ye J, Huang M, Du SG (2016) Modified limiting equilibrium method for stability analysis of stratified rock slopes. Math Probl Eng 2016:8381021

Yuan Y, Ma XH, Li QY, Du Q, Lv JH (2015) A study of landslide inducing factors and early warning criterion by analyzing the automatic monitoring curves of the Shuping Landslide. Hydrogeol Eng Geol 42(5):115–122. (in Chinese)

Zhang CY, Yin YP, Yan H, Li H, Zhang N (2021a) Reactivation characteristics and hydrological inducing factors of a massive ancient landslide in the three Gorges Reservoir, China. Eng Geol 292(1):106273

Zhang GR, Cheng W (2011) Stability prediction for Bazimen landslide of Zigui County under the associative action of reservoir water level fluctuations and rainfall infiltration. Rock Soil Mech 32(Supp.1): 476–482. (in Chinese)

Zhang J, Jiao JJ, Yang J (2000) In situ rainfall infiltration studies at a hillside in Hubei Province, China. Eng Geol 57(1):31–38

Zhang J, Tang H, Tannant DD, Lin C, Xia D, Wang Y, Wang Q (2021b) A novel model for landslide displacement prediction based on EDR selection and multi-swarm intelligence optimization algorithm. Sensors 21(24):8352

Zhang JR, Tang HM, Wen T, Ma JW, Tan QW, Xia D, Zhang Y (2020) A hybrid landslide displacement prediction method based on CEEMD and DTW-ACO-SVR—Cases studied in the three gorges reservoir area. Sensors 20(15):4287

Zhang L, Yang DX, Liu YW, Che YT, Qin DJ (2014a) Impact of impoundment on groundwater seepage in the Three Gorges Dam in China based on CFCs and stable isotopes. Environ Earth Sci 72(11): 4491–4500

Zhang Y, Shi SW, Song J, Cheng YJ (2014b) Evaluation on effect for the prevention and control against the landslide disasters in the Three Gorges Reservoir area. In: Landslide science for a safer geoenvironment. Springer, Cham, pp 407–414

Zhang YM, Hu XL, Tannant DD, Zhang GC, Tan FL (2018) Field monitoring and deformation characteristics of a landslide with piles in the Three Gorges Reservoir area. Landslides 15(3):581–592

Zhao NH, Hu B, Yi QL, Yao WM, Ma C (2017) The coupling effect of rainfall and reservoir water level decline on the Baijiabao landslide in the three Gorges Reservoir Area, China. Geofluids:1–12

Zheng L, Wang L, Zhu L (2021a) Experimental study on the effect of locking mode on shear characteristics of bolted rock joint. Rock Soil Mech 42(04):1056–1064. (in Chinese)

Zheng L, Wang L, Zhu L (2021c) Analytical model of shear mechanical behaviour of bolted rock joints considering influence of normal stress on bolt guide rail effect. J Cent South Univ 28(05):1505–1518

Zheng L, Wang L, Zhu L, Fan B, Dong M, Sun Z, An C (2021b) Analytical model of the shear behaviors of bolted rough joints based on the dilation effect and surface abrasion. Eng Geol 294: 106339

Zhu AX, Wang RX, Qiao JP, Qin CZ, Chen YB, Liu J, Du F, Lin Y, Zhu TX (2014) An expert knowledge-based approach to landslide susceptibility mapping using GIS and fuzzy logic. Geomorphology 214: 128–138

Zou Z, Yan J, Tang H, Wang S, Xiong C, Hu XL (2020) A shear constitutive model for describing the full process of the deformation and failure of slip zone soil. Eng Geol:105766

Zou ZX, Tang HM, Criss RE, Hu XL, Xiong CR, Wu Q, Yuan Y (2021) A model for interpreting the deformation mechanism of reservoir landslides in the Three Gorges Reservoir area, China. Nat Hazards Earth Syst Sci 21(2):517–532

Part II

Original Articles

Impact of Input Data on the Quality of the Landslide Susceptibility Large-Scale Maps: A Case Study from NW Croatia

Martin Krkač, Sanja Bernat Gazibara, Marko Sinčić, Hrvoje Lukačić, Gabrijela Šarić, and Snježana Mihalić Arbanas

Abstract

The study presents analyses of input data impact on the quality of the landslide susceptibility large-scale maps. For comparison, two input data sets were used to produce two landslide susceptibility maps. The first input data set included free-available, small-scale data with low spatial accuracy, while the second set included high-resolution remote sensing data. The same nine types of landslide causal factors were derived and used for susceptibility analyses. Furthermore, LiDAR-based landslide inventory and bivariate statistical method, i.e. Information Value method, were used for susceptibility modelling. The resulting landslide susceptibility maps were compared with ROC curves. Success and prediction rates showed that the landslide susceptibility model based on causal factors derived from high-resolution remote sensing data is approximately 10% more accurate than the model based on causal factors derived from small-scale input data. Furthermore, based on the conducted research, it can be concluded that susceptibility modelling based on small-scale data and LiDAR-based inventories enables reliable landslide susceptibility assessments at the regional level.

Keywords

Landslide susceptibility · LiDAR landslide inventory · Input data · Causal factor maps · Resolution · Spatial accuracy

M. Krkač (✉) · S. Bernat Gazibara · M. Sinčić · H. Lukačić · G. Šarić · S. Mihalić Arbanas
University of Zagreb, Faculty of Mining, Geology and Petroleum Engineering, Zagreb, Croatia
e-mail: mkrkac@rgn.hr; sbernat@rgn.hr; msincic@rgn.hr; hlukacic@rgn.hr; gsaric@rgn.hr; smihalic@rgn.hr

1 Introduction

One of the first prerequisites for risk reduction measures and mitigation of landslide consequences is creating prognostic maps, such as landslide susceptibility maps. Reliable susceptibility maps on a large scale (≤1:5000) require good quality input data, i.e., detailed and complete landslide inventories (Glade 2001; van Westen et al. 2008) and appropriate resolution and spatial accuracy of geo-environmental and triggering factors (Guzzetti et al. 1999; van Westen et al. 2006). Reichenbach et al. (2018) pointed out that nowadays, landslide investigators are more interested in experimenting with different modelling techniques than acquiring good-quality input data and they often use landslide and geo-environmental information captured at different (in cases very different) cartographic scales even for the same study area.

The most usual mapping techniques for preparing large-scale landslide inventories are the interpretation of aerial and satellite images, interpretation of digital elevation models, and field mapping (Eeckhaut et al. 2007; Fiorucci et al. 2011; Bernat Gazibara 2019). The advantage of the LiDAR (Light Detection and Ranging) technique and data derived by ALS (Airborne Lidar Scanning) compared to other remote sensing techniques is ground detection in forested terrain and the possibility of creation of high-resolution bare-earth digital elevation models (DEMs), which enables the identification and mapping of small and shallow landslides in densely vegetated areas (Chigira et al. 2004; Eeckhaut et al. 2007; Razak et al. 2011; Đomlija 2018; Bernat Gazibara et al. 2019a, b).

For large-scale landslide susceptibility analyses, researchers mainly use geomorphological, hydrological, geological and land use data (Reichenbach et al. 2018). Geomorphological (i.e. slope, aspect, elevation) and some hydrological data (i.e. drainage network, wetness) can be derived from digital elevation models, which are generated from different input data in various scales, for example, from

I. Alcántara-Ayala et al. (eds.), *Progress in Landslide Research and Technology, Volume 2 Issue 1, 2023*,
Progress in Landslide Research and Technology, https://doi.org/10.1007/978-3-031-39012-8_4

topographic maps (Pellicani et al. 2014; Roşca et al. 2015; Zêzere et al. 2017; Vojteková and Vojtek 2020), aerial photographs, LiDAR data (Petschko et al. 2014; Yusof et al. 2015; Gaidzik and Ramírez-Herrera 2021), and satellite images in resolution ranged from 25 cm (Vojteková and Vojtek 2020) up to 15 or 30 m (Xing et al. 2021). Geological data, such as lithology or geological contacts, are usually available on smaller-scale maps, from 1:25,000 (Lee and Min 2001; Pellicani et al. 2014; Zêzere et al. 2017) to 1:100,000 (Pellicani et al. 2014; Sinčić et al. 2022a). Land use data used in susceptibility analysis can be derived from satellite images, aerial photos, or official land use plans (Zêzere et al. 2017).

The objective of the paper is to analyse the impact of input data on the quality of landslide susceptibility large-scale maps. Therefore, two susceptibility maps were prepared based on the same thematic type of information but derived from input data which differ in spatial accuracy, resolution and scale. Furthermore, with conducted research, we wanted to address that the adequate scale of input data will minimise deviations from actual environmental conditions on final landslide susceptibility maps. The landslide inventory used for modelling and validating susceptibility maps is LiDAR-based (Krkač et al. 2022).

2 Study Area

The study area comprises 20.22 km^2 of hilly terrain, located in the Hrvatsko Zagorje region, NW Croatia (Fig. 1). Approximately 88% of the study area has slope angles greater than 5°, and approximately 57% of the area has slope angles between 12° and 32°, which makes the study area prone to sliding. In addition, the elevation ranges between 222 and 682 m a.s.l., whereas most of the study area (66%) is placed at elevations below 300 m a.s.l.

The lithological units of the study area are composed of Miocene (78%), Quaternary (14%) and Triassic sediments (7%). The Triassic sediments, located in the northeastern part of the study area, are composed of sandstones, shales, dolomites, limestones and dolomitised breccias (Šimunić et al. 1982). The Miocene sediments are composed of sandstones, marls, calcareous marls, biogenic and marly limestones, sands and tuffs. The Quaternary sediments, located in the valleys around streams and rivers, are composed of sands, silts and gravels.

According to the Corine Land Cover land use data (URL-1) the area is covered by forests (63%), agricultural areas (36%) and artificial areas (1%). According to official

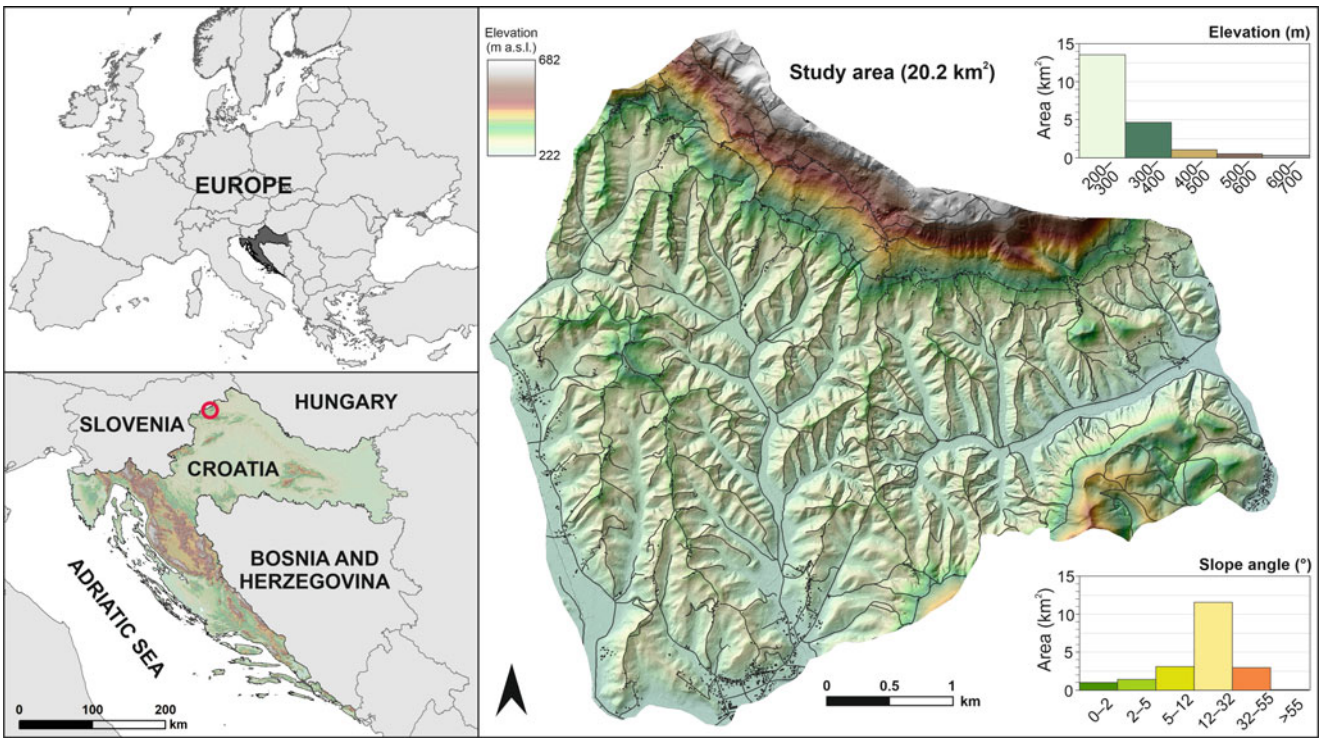

Fig. 1 Geomorphological conditions and location of the study area (NW Croatia)

spatial planning maps of the local municipalities (URL-2 and URL-3), 52% of the area is covered by forests, 40% by agricultural areas and pastures and 8% by artificial areas (Sinčić et al. 2022b).

Generally, precipitations and human activities are the primary triggers of landslides in NW Croatia (Bernat et al. 2014). The climate of the study area is continental, with a mild maritime influence. The mean annual precipitation for 1949–2020 is 873.7 mm (Zaninović et al. 2008), according to the data from the nearest meteorological station (30 km to the east).

3 Materials and Methods

3.1 Landslide Inventory

The landsides were interpreted from the detailed LiDAR digital terrain model (DTM) derivatives based on the recognition of landslide features (Krkač et al. 2022). The LiDAR DTM derivatives used to interpret the landslide morphology were hillshade maps, slope maps and contour lines. The mapping was performed on a large scale (1:100–1:500) to ensure the correct delineation of the landslide boundaries. In addition, orthophoto images from 2014 to 2016 were used to check the morphological forms along roads and houses, such as artificial fills and cuts, similar to landslides on DTM derivatives.

Totally, 912 landslides were mapped, with a total area of 0.408 km^2, or 2.02% of the study area. The mean landslide density is 45.1 slope failures per square kilometre. The size of the recorded landslides ranges from a minimum value of 3.3 m^2 to a maximum of 13,779 m^2, whereas the average area is 448 m^2 (median = 173 m^2, std. dev. = 880 m^2). The small size of the landslides is probably the result of geological conditions (mainly Miocene marls covered with residual soils) and geomorphological conditions, where the differences between the valley bottoms and the top of the hills are rarely higher than 100 m (Krkač et al. 2022). The prevailing dominant types of landslides are shallow soil slides.

3.2 Input Data and Landslide Causal Factors

Several input data sources were used to acquire landslide causal factors (Table 1), considering the scale, the purpose of the study and availability. The input data for the geomorphological and hydrological causal factors were EU Digital Elevation Model (URL-1) and the LiDAR data. The EU Digital Elevation Model (EU-DEM) is available on a regional scale as a part of the Copernicus Land Monitoring Service (CLMS), providing elevation data in 25 m resolution. The average spacing of the LiDAR ground points, obtained by scanning the study area, was 0.28 m, providing sufficient density to create a DTM up to a 0.3 m resolution.

The input data for geological causal factor maps was Basic Geological Map (Šimunić et al. 1982; Aničić and Juriša 1984) on a scale of 1:100,000, which presents the only available source of geological information for the study area. Anthropogenic landslide input data were obtained from publicly available Corine Land Cover (CLC) (URL-1) and Open Street Map (OSM). CLC for the 2018 period was derived dominantly from Sentinel-2 satellite data and Landsat-8 for gap filling. OSM is a community-driven initiative providing map data for various applications about traffic infrastructure, buildings and other spatial information. Additional input data used to derive causal factor maps on a more detailed scale were digital orthophoto maps on a scale 1:5000.

3.3 Information Value Method

The landslide susceptibility of the study area was assessed by the Information Value Method (IVM). IVM is a bivariate statistical approach based on the calculation of weights of landslide causal factors (Yin and Yan 1988; Jade and Sarkar

Table 1 Input data used for derivation of landslide causal factors

Data	TYPE OF DATA	Scale
EU-DEM	DTM	25 m resolution
LiDAR point cloud		5 m resolution
Croatian Basic Geological Map	Geological	1:100,000
Corine Land Cover	Land use	1:100,000
Open Street Map	Traffic infrastructure	Large
Digital Orthophoto Map	Orthophoto	1:5000

1993; Sarkar et al. 2013). In this method, landslide occurrence is considered a dependent variable, and each causal parameter is considered an independent variable (Farooq and Akram 2021).

The information value I_i of each variable i is given by Yin and Yan (1988):

$$I_i = log \frac{S_i/N_i}{S/N} \quad (1)$$

where S_i is the number of grid cells involving the parameter i and containing a landslide, N_i is the number of grid cells involving the parameter i, S is the number of grid cells with a landslide, and N is the total number of data points (grid cells). Negative values of I_i mean that the presence of the variable is not relevant in landslide development (Zêzere et al. 2017). Positive values of I_i indicate a relevant relationship between the presence of the variable and landslide development, whereas the higher value indicates a stronger relationship.

The total information value I_j for a grid cell j is given by the equation (Yin and Yan 1988):

$$I_j = \sum_{i=1}^{m} X_{ji} I_i \quad (2)$$

where m is the number of variables, X_{ji} is either 0 if the variable is not present in the grid cell j, or 1 if the variable is present. The obtained values are directly proportional to the susceptibility.

3.4 Validation of Landslide Susceptibility Maps

The performance of landslide susceptibility maps was evaluated by Receiver Operator Characteristic (ROC) curves (Lobo et al. 2008), i.e. a graphical representation of sensitivity to 1-specificity (false positive rate). ROC curves are one of the most used methods to describe the landslide susceptibility model performance (Rossi and Reichenbach 2016). The model's accuracy is considered higher if the ROC curve is closer to the upper left corner and lower if it is closer to the diagonal, representing a random test. If the ROC curve is derived from the set of landslides used for susceptibility modelling, it represents the success rate of the landslide susceptibility map. Likewise, the ROC curve derived with landslide inventory for model validation shows the prediction rate of the landslide susceptibility map. Out of 912 landslides in the LiDAR-based inventory, for the study area of 20.22 km^2, approximately 50% of the landslides were selected for landslide susceptibility analyses, while the remaining landslides were used to verify the results.

4 Landslide Causal Factors

From the available input data, two sets of nine landslide causal factors maps were derived for susceptibility assessment and to analyse the impact of input data on the quality of landslide susceptibility large-scale maps. The first set of causal factor maps, used in Scenario 1, is derived from less detailed input data, such as EU-DEM or CLC. This group of causal factor maps is derived in a raster resolution of 25 m. The second set of causal factor maps, used in Scenario 2, is derived from more detailed input data, such as LiDAR point cloud or digital orthophoto. This group of causal factor maps is derived in 5 m resolution. A list of landslide causal factor maps and input data is presented in Table 2, while the comparison of factor class area distributions is presented in Fig. 2.

The geomorphological factor maps derived from EU-DEM and LiDAR point clouds are elevation, slope and aspect. The elevation is a frequently used parameter in landslide susceptibility studies because landslides may form in specific relief ranges (Lee et al. 2001). Factor maps were created by reclassifying the elevations into classes of 50 m. The slope gradient is often considered to be the most important geomorphometric parameter used to analyse and describe relief (van Westen et al. 2008). Factor maps were created by reclassifying the slopes into classes of 5°. The aspect causal factor maps were classified into ten main classes (N, NE, E, SE, S, SW, W, NW and flat surface).

The hydrological factor maps, derived from EU-DEM and LiDAR DTM, were drainage network and topographic wetness. A drainage network is a set of all drainage systems in an area, i.e. a set of natural canals through which water constantly or temporarily flows and which are connected into a single stream and represent the smallest independent geomorphological component (Marković 1983). The drainage networks were derived with several tools in the Spatial Analyst (Hydrology Toolbox) in ArcGIS 10.8.1. Topographic wetness is a steady-state wetness index, and it is commonly used to quantify topographic control on hydrological processes (Sinčić et al. 2022b). The topographic wetness maps are derived by the Compound Topographic Index (CTI) tool in Geomorphometry and Gradient Metrics Toolbox (Evans et al. 2014). Lower values of CTI indicate lower wetness (hill tops), and higher CTI values indicate higher terrain wetness (plain areas).

Geological factor maps were obtained by digitising a geological map on a scale of 1:100,000, resulting in two causal factor maps, a stratigraphic unit map, and a distance to geological (lithological) contact map. However, field

Table 2 Landslide causal factors maps, derived from different input data, used in different susceptibility scenarios

		Input data	
Data type	Causal factor	Scenario 1	Scenario 2
Geomorphological	Elevation	EU-DEM	LiDAR point cloud
	Slope		
	Aspect		
Hydrological	Distance from the drainage network		
	Topographic wetness		
Geological	Lithology	Basic Geological Map	LiDAR DTM mapping, Basic Geological Map
	Distance from the geological contact		
Anthropogenic	Land use	Corine Land Cover	Digital orthophoto maps, LiDAR point cloud and DTM
	Distance from road	Open Street Map	

verification of Basic Geological Map showed significant deviations in the position of the geological contacts (Sinčić et al. 2022b). To obtain more precise data for Scenario 2, stratigraphic units (corresponding to engineering geological formations) were additionally mapped (by modifying the geological contacts and adding one more unit, i.e. superficial slope-wash and talus sediments) using LiDAR DTM derivatives according to the suggestions by Jagodnik et al. (2020a, b).

Land use causal factor map for Scenario 1 was derived from CLC. Considering large-scale landslide hazard assessment, all classification levels showed little difference regarding land use classes in the study area (Sinčić et al. 2022b). Therefore, the first hierarchy level was selected for a representative land use factor map. A more detailed land use map, for Scenario 2, was the most demanding to derive as required different input data sets (LiDAR data and digital orthophoto maps) and different processing methods. A detailed explanation of the land use map derivation can be found in Sinčić et al. (2022b). Distance from roads causal factor map was derived from OSM for Scenario 1 and by combining LiDAR data and digital orthophoto maps for a more detailed causal factor map in Scenario 2. The total length of all roads in Scenario 1 is 54 km and the total length of roads in Scenario 2 is 165 km.

5 Results

The GIS-based landslide susceptibility assessment for the study area in NW Croatia, for two scenarios, comprises the following steps: (1) the pairwise correlation analysis of input variables; (2) the calculation of information values for each class of each factor map based on landslide modelling set; (3) the calculation of total information values, i.e. calculation of susceptibility; (4) calculation of success rate based on landslide modelling set; (5) calculation of prediction rate based on the landslide validation set; (6) reclassification of susceptibility maps. The landslides used in the calculation of information values and for the calculation of success and prediction rates are firstly converted from polygons to points (centroids) and then to raster (25 m resolution in Scenario 1, and 5 m resolution in Scenario 2). In the process, some of the small landslides in Scenario 1, located near each other, were converted to the same pixel, resulting in a different number of landslide pixels in both scenarios (Table 3).

Before performing landslide susceptibility analysis of the study area, the pairwise conditional independence test of the input landslide causal factors was done using Pairwise correlation analysis in the LAND-SUITE V1.0 (Rossi and Reichenbach 2016; Rossi et al. 2021) i.e. LAND-SVA: LANDslide-Susceptibility Variable Analysis, which includes Pairwise correlation analysis and Multicollinearity test. Inspection of the correlation results confirmed no correlations within nine landslide causal factors of both scenarios, assuming a Pearsons' R absolute value of 0.5 as the threshold for detecting correlations.

The information values for each class of each factor map, for both scenarios, are presented in Table 3. According to the analyses of factor maps in Scenario 1, the highest influence on landslide development have slope classes with angles between 20 and 30° and aspect class with azimuth towards NE, while elevation and lithology do not influence landslide development. The analyses of factor maps in Scenario 2 show that the highest influence on landslide development have slope classes with angles between 30 and 45°, while elevation and lithology practically do not influence on landslide development.

The landslide susceptibility maps were derived by the calculation of the total information values according to the Eq. (2). Susceptibility maps for scenarios 1 and 2 are presented in Fig. 3. Figure 3 also shows details of reclassified susceptibility maps, classified by the quantile method. The performance of the IVM was evaluated using the ROC curve, i.e. the area under the curve (AUC). The success rate of the susceptibility model in Scenario 1, calculated on the training set, is AUC = 70.8%, and the predictive rate, based on the validation set, is AUC = 69.8% (Fig. 4a). The success rate of the susceptibility model in Scenario 2 is AUC = 80.3%, and the predictive rate is AUC = 78.8% (Fig. 4b).

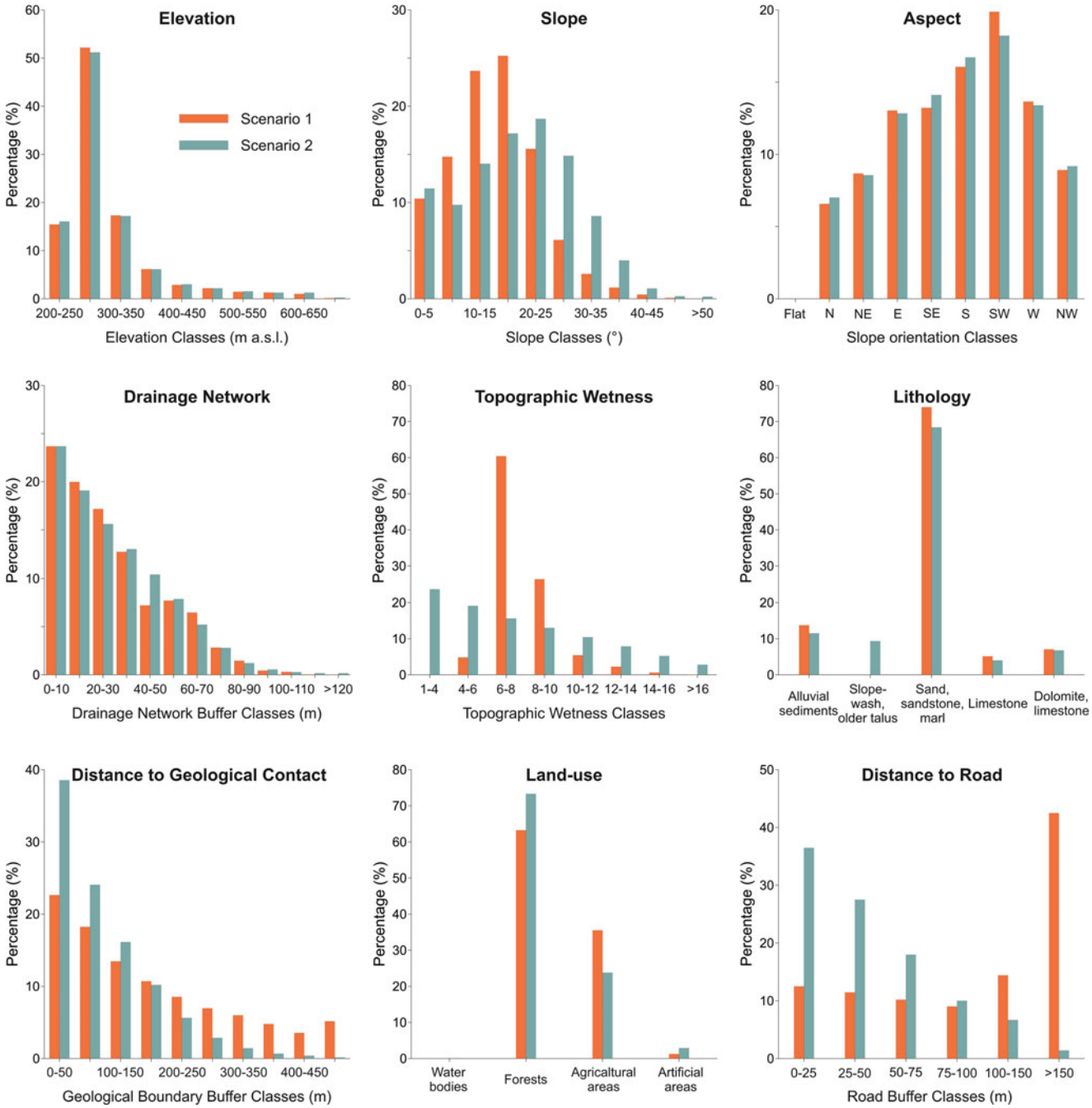

Fig. 2 Comparison of landslide causal factor classes derived from different types of input data

6 Discussion and Conclusions

Statistically-based susceptibility models are dependable on the type, abundance, quality and relevance of the available landslide and the geo-environmental information. In the presented research, we analysed the influence of input data quality and scale on the accuracy of landslide susceptibility models assessment on a large scale. For landslide susceptibility analysis, we chose the most commonly used thematic and environmental causal factors, i.e. elevation, slope, aspect, drainage network, topographic wetness, lithology, distance to geological contact, land use and distance to roads. For comparison, two different input data sets, i.e. scenarios, were used to derive landslide causal factor maps, while the landslide data used for susceptibility analysis was LiDAR-based inventory. Scenario 1 included free-available input data sets with a lower resolution and lover

Table 3 Calculated information values for landslide causal factors based on the Information Value Method

Causal factor map		Scenario 1				Scenario 2			
		Class description	Class (Npix)	Landslide (Npix)	IV	Class description	Class (Npix)	Landslide (Npix)	IV
Geomorphological landslide causal factors	Elevation m a.s.l.	200–250	4885	33	–0.3095	200–250	129,204	34	–0.3328
		250–300	16,514	309	0.1329	250–300	412,139	330	0.1504
		300–350	5475	71	–0.0262	300–350	138,447	68	–0.0618
		350–400	1954	10	–0.4300	350–400	49,249	11	–0.4040
		400–450	907	6	–0.3186	400–450	24,056	6	–0.3561
		450–500	690	4	–0.3759	450–500	17,346	2	–0.6912
		500–550	464	1	–0.8056	500–550	12,522	3	–0.3736
		550–600	404	1	–0.7455	550–600	10,249	1	–0.7637
		600–650	314	1	–0.6360	600–650	10,196	1	–0.7615
		650–700	39	0		650–700	1857	0	
		SUM	**31,646**	**436**		**SUM**	**805,265**	**456**	
	Slope angle (°)	0–5	3293	6	–0.8786	0–5	92,135	0	
		5–10	4670	41	–0.1957	5–10	78,518	13	–0.5341
		10–15	7488	84	–0.0892	10–15	112,905	38	–0.2260
		15–20	7983	141	0.10788	15–20	138,299	38	–0.3141
		20–25	4927	116	0.23270	20–25	150,428	69	–0.0915
		25–30	1936	41	0.18671	25–30	119,568	87	0.1089
		30–35	817	5	–0.3524	30–35	69,143	101	0.4115
		35–40	365	2	–0.4004	35–40	32,020	79	0.6392
		40–45	137	0		40–45	8562	29	0.7768
		45–50	28	0		45–50	2064	2	0.2333
		>50	2	0		>50	1623	0	
		SUM	**31,646**	**436**		**SUM**	**805,265**	**456**	
	Slope orientation	Flat terrain	2	0		Flat terrain	0	0	
		N	2077	42	0.1666	N	56,402	41	0.1085
		NE	2745	64	0.2284	NE	68,863	69	0.2478
		E	4127	71	0.0964	E	103,371	65	0.0455
		SE	4184	36	–0.2045	SE	113,655	40	–0.2066
		S	5082	46	–0.1824	S	134,594	46	–0.2193
		SW	6288	56	–0.1894	SW	146,682	64	–0.1132
		W	4320	71	0.07660	W	107,815	69	0.0531
		NW	2821	50	0.10939	NW	73,883	62	0.1708
		SUM	**31,646**	**436**		**SUM**	**805,265**	**456**	
Hydrological landslide causal factors	Proximity to the drainage network (m)	0–10	7493	129	0.0968	0–10	190,658	157	0.1626
		10–20	6320	102	0.0687	10–20	153,701	130	0.1742
		20–30	5433	95	0.1035	20–30	125,635	77	0.0344
		30–40	4024	44	–0.1004	30–40	104,686	48	–0.0917
		40–50	2282	29	–0.0351	40–50	83,849	31	–0.1852
		50–60	2440	17	–0.2961	50–60	63,336	3	–1.0776
		60–70	2048	15	–0.2744	60–70	41,879	6	–0.5969
		70–80	894	2	–0.7895	70–80	22,499	2	–0.8042
		80–90	466	1	–0.8076	80–90	9708	1	–0.7402
		90–100	138	1	–0.2790	90–100	4414	0	
		100–110	95	0		100–110	2260	0	
		110–120	8	1	0.9577	110–120	1282	0	
		>120	5	0		>120	1358	1	0.1141
		SUM	**31,646**	**436**		**SUM**	**805,265**	**456**	
	Topographic wetness					1–4	80,088	50	0.0424
		4–6	1522	12	–0.2424	4–6	432,300	256	0.0194
		6–8	19,113	267	0.0060	6–8	202,915	115	0.0004
		8–10	8382	124	0.0309	8–10	58,028	25	–0.1187

(continued)

Table 3 (continued)

Causal factor map		Scenario 1				Scenario 2			
		Class description	Class (Npix)	Landslide (Npix)	IV	Class description	Class (Npix)	Landslide (Npix)	IV
		10–12	1712	26	0.0423	10–12	19,900	6	–0.2737
		12–14	712	6	–0.2135	12–14	8439	2	–0.3783
		14–16	190	1	–0.4179	14–16	2892	2	0.0868
		>16	15	0		>16	703	0	
		SUM	**31,646**	**436**		**SUM**	**805,265**	**456**	
Geological landslide causal factors	Lithology	Q_2	4335	25	–0.3782	M, S, Gal	92,563	1	–1.7195
		M_2^2	1615	8	–0.4443	MS, Cb_d	75,261	42	–0.0063
		M_1^2	23,125	393	0.0911	S, Ss, Ms	550,716	407	0.1156
		Θ	290	3	–0.1244	Ls	32,231	1	–1.2613
		E_3	45	0		D, Ls	54,494	5	–0.7904
		T_2	1839	5	–0.7048				
		T_1	397	2	–0.4369				
		SUM	**31,646**	**436**		**SUM**	**805,265**	**456**	
	Proximity to the geological contact (m)	0–50	7162	90	–0.0400	0–50	310,330	177	0.0031
		50–100	5770	73	–0.0370	50–100	193,700	130	0.0738
		100–150	4259	58	–0.0050	100–150	129,881	83	0.0525
		150–200	3387	56	0.0792	150–200	82,099	29	–0.2050
		200–250	2698	38	0.0096	200–250	45,286	19	–0.1302
		250–300	2206	31	0.0086	250–300	22,988	10	–0.1145
		300–350	1898	25	–0.0195	300–350	11,361	5	–0.1095
		350–400	1512	30	0.1584	350–400	5298	3	0.0000
		400–450	1124	20	0.1111	400–450	3184	0	
		>450	1630	15	–0.1753	>450	1138	0	
		SUM	**31,646**	**436**		**SUM**	**805,265**	**456**	
Anthropogenic landslide causal factors	Land cover	Forest	20,015	320	0.0646	Forest	590,194	425	0.1044
		Agricultural	11,235	116	–0.1253	Agricultural	191,383	28	–0.5878
		Artificial	396	0		Artificial	23,039	2	–0.8145
						Water bodies	649	1	0.4347
		SUM	**31,646**	**436**		**SUM**	**805,265**	**456**	
	Proximity to roads (m)	0–25	3958	26	–0.3217	0–25	293,600	128	–0.1136
		15–50	3621	50	0.0010	15–50	221,333	155	0.0923
		50–75	3222	53	0.0770	50–75	144,854	105	0.1072
		75–100	2847	42	0.0297	75–100	80,428	47	0.0137
		100–150	4556	61	–0.0124	100–150	53,707	20	–0.1820
		>150	13,442	204	0.0420	>150	11,343	1	–0.8078
		SUM	**31,646**	**436**		**SUM**	**805,265**	**456**	

spatial accuracy, such as EU-DEM or Corine Land Cover. In contrast, Scenario 2 included a more detailed input data set, such as high-resolution remote sensing data, i.e. LiDAR point cloud and digital orthophoto imagery in resolution 0.5 m.

The difference between the causal factor maps derived from different input data sets is visible from the class area distribution (Fig. 2). The highest distinction in the class area distribution of geomorphological and hydrological factor maps is among slope maps and topographic wetness maps. Slope map derived from LiDAR DTM generally have higher total area values in classes with a lower slope angle than slope maps derived from EU-DEM. This observation is similar to previous research, such as Grohmann (2015), who concluded that the slope parameter is prone to changes as the resolution is coarsened, with a strong decrease in maximum values, mean values and standard deviation. Therefore, it can be concluded that high-resolution LiDAR DTM enables a more accurate presentation of environmental conditions in the case of slope and topographic wetness. Contrarily, the differences in the class area distribution of elevation, aspect and drainage network maps derived from EU-DEM and LiDAR DTM are generally low.

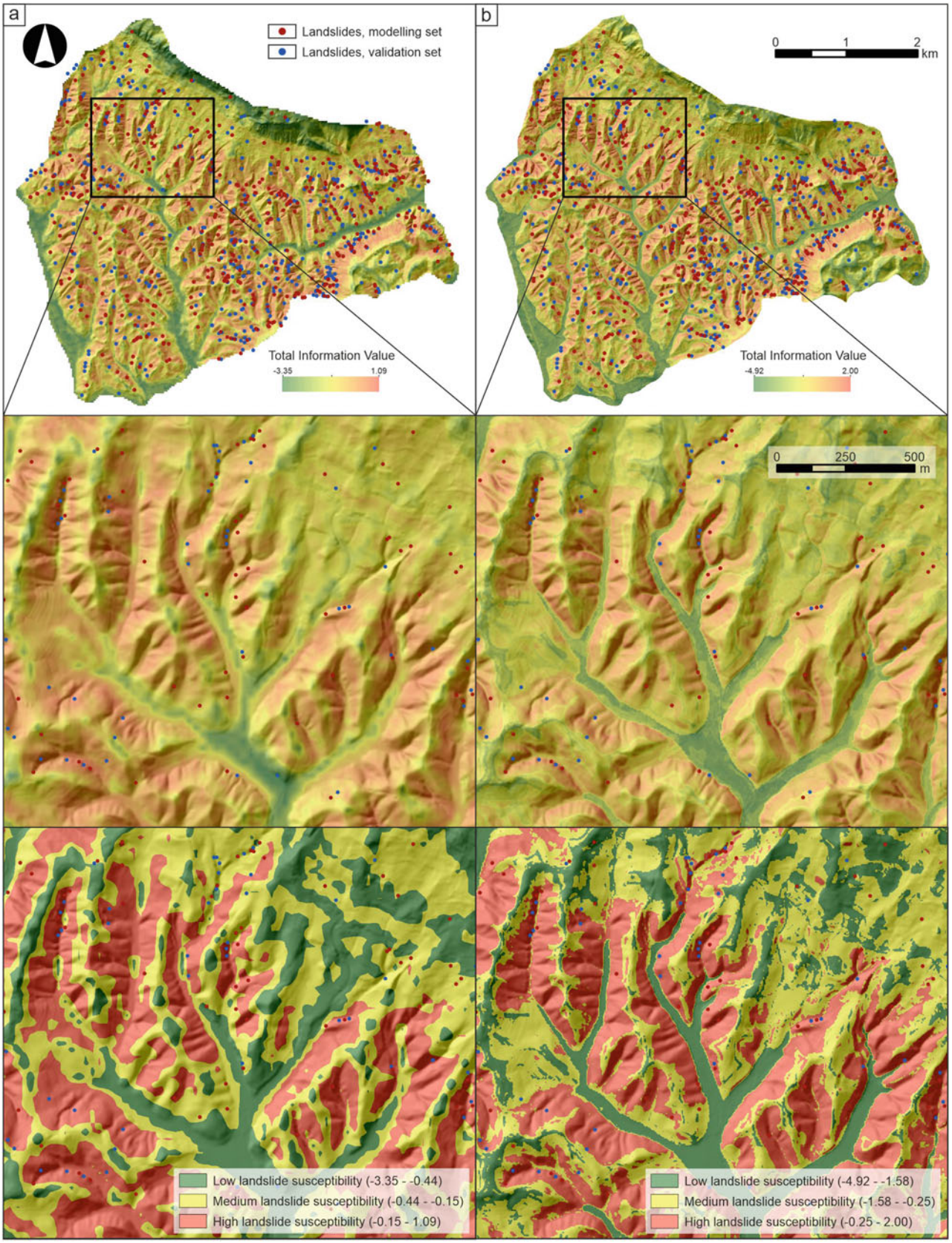

Fig. 3 Comparison of landslide susceptibility map classes derived from different types of input data: (**a**) Scenario 1; (**b**) Scenario 2

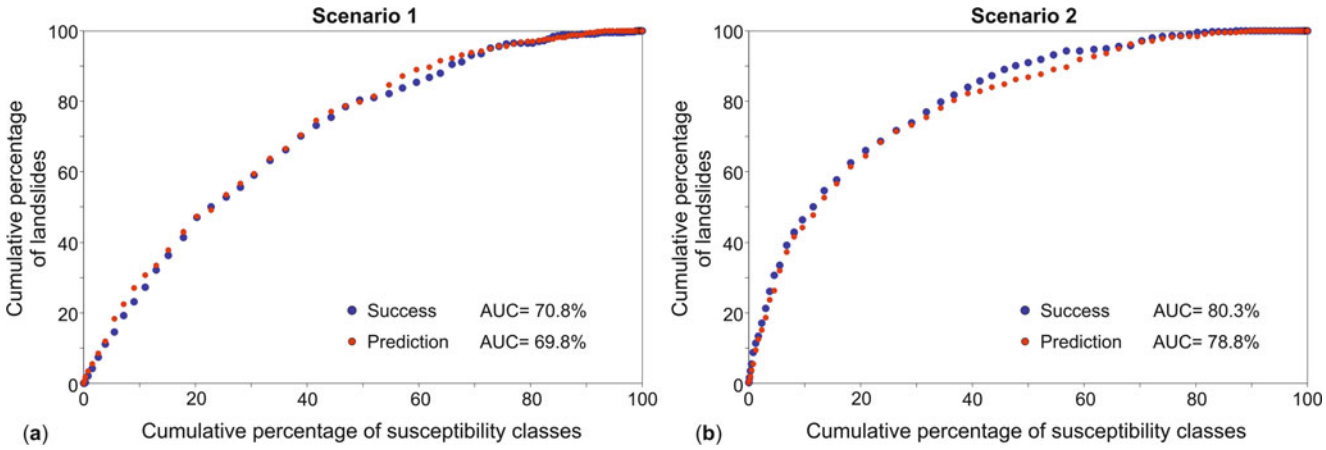

Fig. 4 ROC curve results for the rate of success and the rate of prediction for the landslide susceptibility maps

The lithological factor map for Scenario 1, derived from the Basic Geological Map in scale 1:100,000, has a similar distribution of lithological units as the engineering geological unit map interpreted based on LiDAR DTM derivatives. An exception is the presence of an additional engineering geological unit interpreted on LiDAR DTM derivatives, i.e. slopewash and older talus, which significantly affected the class area distribution of distance to the geological contact map in Scenario 2 compared to the class area distribution of factor map derived from Basic Geological Map 1:100,000 in Scenario 1.

The land use map for Scenario 1, derived from Corine Land Cover, has similar class area distribution as the land use map derived based on the automatic classification of high-resolution orthophoto imagery in Scenario 2. However, the spatial distribution of the land use classes between the scenarios is significant (Sinčić et al. 2022b), i.e. degree of cartographic matching between the two land use maps would be low and probably have a significant impact on the accuracy of the final landslide susceptibility maps. For example, the distance to roads map in Scenario 2, derived based on high-resolution remote sensing data, resulted in the total length of roads for almost 300% more than the length of roads derived only from the OSM input data in Scenario 1, and consequently, a significantly higher area percentage of the class 0–75 m in Scenario 2.

Generally, landslide susceptibility analysis and information values showed that the same factor classes in both scenarios showed an influence on landslide occurrence. Only factor classes in topographic wetness and proximity to geological contact maps have the opposite effect on landslide susceptibility. The most significant factor classes for the landslide occurrence are slope class 20–25° and aspect class NE for Scenario 1, and slope classes 35–45° for Scenario 2. Furthermore, the most significant factor classes in Scenario 2 have 2–3 times higher information values than the most significant factor classes in Scenario 1. High information values in Scenario 2 resulted in different ranges of total susceptibility values in the two landslide susceptibility maps.

The resulting large-scale landslide susceptibility maps were compared with ROC curves, i.e. the success and predictive rates of AUC values for Scenario 1 (derived based on available small-scale input data) and Scenario 2 (derived based on high-resolution remote sensing data). The success and predictive rates for Scenario 1 are approximately 10% lower than the AUC values for Scenario 2. On first look, unclassified landslide susceptibility maps may look relatively similar, although the most significant difference between the two scenarios is the percentage of low landslide susceptibility values in valleys. Considering the stated, the landslide susceptibility map based on causal factors derived from high-resolution remote sensing data (Scenario 2) has minor deviations from actual environmental conditions. i.e. spatial accuracy of resulting susceptibility assessment is higher. However, after the classification of landslide susceptibility maps into three classes based on the quantile method, on the Scenario 1 map, it is possible to observe that the low susceptibility class is spread from the flat valleys to the hilly slopes. Contrary, on the Scenario 2 map, the low susceptibility class is confined only to flat areas. In the end, it can be concluded that different input data resolutions and scales can provide similar information regarding large-scale landslide susceptibility assessment, although high-resolution input data provide more spatially accurate information. Also, large-scale landslide susceptibility modelling based on small-scale input data would show significantly different results if we did not use sustainable complete, LiDAR-based landslide inventory in the analysis. Furthermore, it follows that it is possible to conduct regional landslide susceptibility assessment in small pilot areas (10–30 km^2) with high-resolution remote sensing data sets and apply them to larger research areas (>100 km^2) with similar geomorphological and geological conditions and only small-scale available input data.

Acknowledgments This research has been fully supported by the Croatian Science Foundation under the project methodology development for landslide susceptibility assessment for and use planning based on LiDAR technology, LandSlidePlan (HRZZ IP-2019-04-9900, HRZZ DOK-2020-01-2432).

References

Aničić B, Juriša M (1984) Basic geological map, scale 1:100,000, Rogatec, Sheet 33-68

Bernat Gazibara S (2019) Methodology for landslide mapping using high resolution digital elevation model in the Podsljeme area (City of Zagreb). Doctoral Thesis, Faculty of Mining, Geology and Petroleum Engineering, University of Zagreb

Bernat Gazibara S, Krkač M, Mihalić Arbanas S (2019a) Verification of historical landslide inventory maps for the Podsljeme area in the City of Zagreb using LiDAR-based landslide inventory. Rudarsko-geološko-naftni zbornik 34(1):45–48. https://doi.org/10.17794/rgn.2019.1.5

Bernat Gazibara S, Krkač M, Mihalić Arbanas S (2019b) Landslide inventory mapping using LiDAR data in the City of Zagreb (Croatia). Journal of Maps 15:773–779. https://doi.org/10.1080/17445647.2019.1671906

Bernat S, Mihalić Arbanas S, Krkač M (2014) Inventory of precipitation triggered landslides in the winter of 2013 in Zagreb (Croatia, Europe). In: Sassa K, Canuti P, Yin Y (eds) Landslide science for a safer geoenvironment. Springer International, Cham, pp 829–835

Chigira M, Duan F, Yagi H, Furuya T (2004) Using an airborne laser scanner for the identification of shallow landslides and susceptibility assessment in an area of ignimbrite overlain by permeable pyroclastics. Landslides 1:203–209. https://doi.org/10.1007/s10346-004-0029-x

Đomlija P (2018) Identification and classification of landslides and erosion phenomena using the visual interpretation of the Vinodol Valley digital elevation model. Doctoral Thesis, Faculty of Mining, Geology and Petroleum Engineering, University of Zagreb

Eeckhaut MVD, Poesen J, Verstraeten G, Vanacker V, Nyssen J, Moeyersons J, van Beek LPH, Vandekerckhove L (2007) Use of LIDAR-derived images for mapping old landslides under forest. Earth Surf Process Landforms 32:754–769. https://doi.org/10.1002/esp.1417

Evans JS, Oakleaf J, Cushman SA, Theobald D (2014) An ArcGIS toolbox for surface gradient and geomorphometric modeling, version 2.0-0

Farooq S, Akram MS (2021) Landslide susceptibility mapping using information value method in Jhelum Valley of the Himalayas. Arab J Geosci 14:824. https://doi.org/10.1007/s12517-021-07147-7

Fiorucci F, Cardinali M, Carlà R, Rossi M, Mondini AC, Santurri L, Ardizzone F, Guzzetti F (2011) Seasonal landslide mapping and estimation of landslide mobilisation rates using aerial and satellite images. Geomorphology 129:59–70. https://doi.org/10.1016/j.geomorph.2011.01.013

Gaidzik K, Ramírez-Herrera MT (2021) The importance of input data on landslide susceptibility mapping. Sci Rep 11:19334. https://doi.org/10.1038/s41598-021-98830-y

Glade T (2001) Landslide hazard assessment and historical landslide data — an inseparable couple. In: Glade T, Albini P, Francés F (eds) The use of historical data in natural hazard assessments. Springer, Dordrecht, pp 153–168

Grohmann CH (2015) Effects of spatial resolution on slope and aspect derivation for regional-scale analysis. Comput Geosci 77:111–117. https://doi.org/10.1016/j.cageo.2015.02.003

Guzzetti F, Carrara A, Cardinali M, Reichenbach P (1999) Landslide hazard evaluation: a review of current techniques and their application in a multi-scale study, Central Italy. Geomorphology 31:181–216. https://doi.org/10.1016/S0169-555X(99)00078-1

Jade S, Sarkar S (1993) Statistical models for slope instability classification. Eng Geol 36:91–98. https://doi.org/10.1016/0013-7952(93)90021-4

Jagodnik P, Bernat Gazibara S, Arbanas Ž, Mihalić Arbanas S (2020a) Engineering geological mapping using airborne LiDAR datasets – an example from the Vinodol Valley, Croatia. J Maps 16:855–866. https://doi.org/10.1080/17445647.2020.1831980

Jagodnik P, Bernat Gazibara S, Jagodnik V (2020b) Types and distribution of quaternary deposits originating from carbonate rock slopes in the Vinodol valley, Croatia – new insight using airborne lidar data. Mgpb 35:57–77. https://doi.org/10.17794/rgn.2020.4.6

Krkač M, Bernat Gazibara S, Sinčić M, Lukačić H, Mihalić Arbanas S (2022) Landslide inventory mapping based on LiDAR data: a case study from Hrvatsko Zagorje (Croatia). In: Proceedings of the 5th Regional Symposium on Landslides in the Adriatic – Balkan Region. Faculty of Civil Engineering, University of Rijeka and Faculty of Mining, Geology and Petroleum Engineering, University of Zagreb, pp 81–86

Lee S, Min K (2001) Statistical analysis of landslide susceptibility at Yongin, Korea. Environ Geol 40:1095–1113. https://doi.org/10.1007/s002540100310

Lee CF, Li J, Xu ZW, Dai FC (2001) Assessment of landslide susceptibility on the natural terrain of Lantau Island, Hong Kong. Environ Geol 40:381–391. https://doi.org/10.1007/s002540000163

Lobo JM, Jiménez-Valverde A, Real R (2008) AUC: a misleading measure of the performance of predictive distribution models. Global Ecol Biogeogr 17:145–151. https://doi.org/10.1111/j.1466-8238.2007.00358.x

Marković M (1983) Osnove primjenjene geomorfologije (Basics of applied geomorphology). Geoinstitut, Beograd

Pellicani R, Van Westen CJ, Spilotro G (2014) Assessing landslide exposure in areas with limited landslide information. Landslides 11:463–480. https://doi.org/10.1007/s10346-013-0386-4

Petschko H, Brenning A, Bell R, Goetz J, Glade T (2014) Assessing the quality of landslide susceptibility maps – case study Lower Austria. Nat Hazards Earth Syst Sci 14:95–118. https://doi.org/10.5194/nhess-14-95-2014

Razak KA, Straatsma MW, van Westen CJ, Malet J-P, de Jong SM (2011) Airborne laser scanning of forested landslides characterisation: terrain model quality and visualisation. Geomorphology 126:186–200. https://doi.org/10.1016/j.geomorph.2010.11.003

Reichenbach P, Rossi M, Malamud BD, Mihir M, Guzzetti F (2018) A review of statistically-based landslide susceptibility models. Earth-Sci Rev 180:60–91. https://doi.org/10.1016/j.earscirev.2018.03.001

Roşca S, Bilaşco Ş, Petrea D, Fodorean I, Vescan I, Filip S, Magut F-L (2015) Large scale landslide susceptibility assessment using the statistical methods of logistic regression and BSA – study case: the sub-basin of the small Niraj (Transylvania Depression, Romania). Landslides and Debris Flows Hazards

Rossi M, Reichenbach P (2016) LAND-SE: a software for statistically based landslide susceptibility zonation, version 1.0. Geosci Model Dev 9:3533–3543. https://doi.org/10.5194/gmd-9-3533-2016

Rossi M, Bornaetxea T, Reichenbach P (2021) LAND-SUITE V1.0: a suite of tools for statistically-based landslide susceptibility zonation. Earth and space science informatics

Sarkar S, Roy AK, Martha TR (2013) Landslide susceptibility assessment using Information Value Method in parts of the Darjeeling Himalayas. J Geol Soc India 82:351–362. https://doi.org/10.1007/s12594-013-0162-z

Šimunić A, Pikija M, Hečimović I (1982) Basic geological map, scale 1:100,000, Varaždin, Sheet 33-69

Sinčić M, Bernat Gazibara S, Krkač M, Mihalić Arbanas S (2022a) Landslide susceptibility assessment of the City of Karlovac using the

bivariate statistical analysis. Rudarsko-geološko-naftni zbornik 34(1):45–48. https://doi.org/10.17794/rgn.2022.2.13

Sinčić M, Bernat Gazibara S, Krkač M, Lukačić H, Mihalić Arbanas S (2022b) The use of high-resolution remote sensing data in preparation of input data for large-scale landslide hazard assessments. Land 11:1360. https://doi.org/10.3390/land11081360

URL-1: Https://Land.Copernicus.Eu/Pan-European/Corine-Land-Cover/Clc2018?Tab=download (CLC2018_CLC2012_V2018 12_20b2.Gdb). Accessed 15 June 2022

URL-2: Http://Arhiva.Vzz.Hr/Images/Stories/Prostorni-Plan/LEPOGLAVA_ID/LEPOGLAVA_ID2/K1_KORISTENJE_I_NAMJENA_POVRSINA_HTRS.Pdf. Accessed 15 June 2022

URL-3: Http://Arhiva.Vzz.Hr/Images/Stories/Prostorni-Plan/BEDNJA/2-ID-PPUO-Bednja-05-2017/K1_KORISTENJE_I NAMJENA_POVRSINA_ID2.Pdf. Accessed 15 June 2022

van Westen CJ, van Asch TWJ, Soeters R (2006) Landslide hazard and risk zonation—why is it still so difficult? Bull Eng Geol Environ 65: 167–184. https://doi.org/10.1007/s10064-005-0023-0

van Westen CJ, Castellanos E, Kuriakose SL (2008) Spatial data for landslide susceptibility, hazard, and vulnerability assessment: an overview. Eng Geol 102:112–131. https://doi.org/10.1016/j.enggeo.2008.03.010

Vojteková J, Vojtek M (2020) Assessment of landslide susceptibility at a local spatial scale applying the multi-criteria analysis and GIS: a case study from Slovakia. Geomatics Nat Hazards Risk 11:131–148. https://doi.org/10.1080/19475705.2020.1713233

Xing Y, Yue J, Guo Z et al (2021) Large-scale landslide susceptibility mapping using an integrated machine learning model: a case study in the Lvliang Mountains of China. Front Earth Sci 9:722491. https://doi.org/10.3389/feart.2021.722491

Yin KL, Yan TZ (1988) Statistical prediction model for slope instability of methamorphosed rocks. In: Proceedings of Fifth International Symposium on Landslides. Lausanne, pp 1269–1272

Yusof NM, Pradhan B, Shafri HZM, Jebur MN, Yusof Z (2015) Spatial landslide hazard assessment along the Jelapang Corridor of the North-South Expressway in Malaysia using high resolution airborne LiDAR data. Arab J Geosci 8:9789–9800. https://doi.org/10.1007/s12517-015-1937-x

Zaninović K, Gajić-Čapka M, Perčec Tadić M, Vučetić M, Milković J, Bajić A, Cindrić K, Cindrić L, Katušin Z, Kaučić D (2008) Climate atlas of Croatia 1961. – 1990., 1971. – 2000.

Zêzere JL, Pereira S, Melo R et al (2017) Mapping landslide susceptibility using data-driven methods. Science of The Total Environment 589:250–267. https://doi.org/10.1016/j.scitotenv.2017.02.188

Landslide Warning Systems in High-Income Countries: Past Accomplishments and Expected Endeavours

Irasema Alcántara-Ayala and Ricardo J. Garnica-Peña

Abstract

Special emphasis has been given to the role Early Warning Systems (EWSs) can play as mechanisms for disaster risk reduction (DRR) around the globe. Along this line, the International Consortium on Landslides (ICL) has promoted several efforts to create regional and global network initiatives that include, among other relevant activities, landslides early warning systems (LEWSs). This task has actively involved the ICL community in supporting the implementation of the Sendai Framework for Disaster Risk Reduction (SFDRR) in all the nations included as members.

Despite the advances in the development of LEWSs, their successful implementation worldwide remains a challenge to be addressed. Building on earlier efforts, an overview of the diverse dimensions of LEWSs in High-Income Countries (HICs) is provided in this chapter.

Insights derived from a systematic literature review, are included in this document and organized into five sections. The introductory part focuses on the relevance of LEWSs in HICs and outlines the structure of the chapter. It is followed by a general reflection on hazard knowledge-based LEWSs. Details on the methodology used for this analysis are provided in the third section. The outcomes of the literature review are presented in the fourth section, while key messages are included at the end of the chapter.

Technology development for potential LEWSs, hazard analysis for LEWSs, and models and prototypes for LEWSs are the main thematic focus of research in the analyzed publications.

Keywords

Landslide Early Warning Systems · high-income countries · implementation · disaster risk reduction

I. Alcántara-Ayala (✉) · R. J. Garnica-Peña
Institute of Geography, National Autonomous University of Mexico (UNAM), Mexico City, Mexico
e-mail: ialcantara@geografia.unam.mx; garnica@geografia.unam.mx

1 Introduction

The use of Early Warning Systems (EWSs) has increased since the establishment of the Sendai Framework for Disaster Risk Reduction (UNISDR 2015) as a fundamental mechanism to reduce disaster risk. The design, validation, and implementation of Landslide Early Warning Systems (LEWSs) have been strongly promoted by the International Consortium for Landslides (ICL) through an extensive array of collaboration and synergies among networks, Centres of Excellence, along with global strategies (Sassa 2015, 2016) and commitments (Alcántara-Ayala and Sassa 2021).

The Kyoto Landslide Commitment 2020 (KLC2020) is of particular relevance to this task. An effort that seeks to promote larger awareness of the need to implement people-centered early warning based on high accuracy and reliable prediction technology for landslides considering the context and challenges of a changing climate (Sassa 2019, 2020).

Just like any other type of EWSs, the development of LEWSs has been initiated in countries where human and financial capacities for the progress of science are not hindered by economic or political factors. Nonetheless, international scientific associations such as ICL have helped to enhance the dissemination of EWS around the world for the benefit of society.

In earlier works, insights regarding the application of LEWSs in low- and lower-middle-income countries (LICs and MICs) (Alcántara-Ayala and Garnica-Peña 2023a) and Upper Middle-Income Countries (UMICs) (Alcántara-Ayala and Garnica-Peña 2023b), from 1991 to 2021, have been presented. Building on these works, this chapter aims to offer a review of the implementation of LEWSs in High-Income Countries (HICs), during the same period. Excluding the introduction, this chapter comprises four sections: a brief account concerning the architecture of EWSs, the methodology, and results, and a final consideration of past accomplishments and expected endeavours.

I. Alcántara-Ayala et al. (eds.), *Progress in Landslide Research and Technology, Volume 2 Issue 1, 2023*,
Progress in Landslide Research and Technology, https://doi.org/10.1007/978-3-031-39012-8_5

2 Hazard Knowledge-Based Landslide Early Warning Systems

More than a decade ago, initial efforts took place to build people-centered EWSs (ISDR-PPEW 2005). Nonetheless, a very high percentage of EWSs are based on merely hazard perspectives. Instead of the balance tilting towards the role of the EWS being to guide practices for the formulation of policies that guarantee risk reduction, they have a highly technical nature that responds to humanitarian actions (Alcántara-Ayala and Oliver-Smith 2017, 2019).

Although it is essential to have hazard assessments that are as precise as possible, up to now elements of risk knowledge of the population exposed to the potential impact of landslides have not been incorporated.

LEWSs in HICs also show a clear tendency for their structure to focus on the landslide hazard dynamics. This includes rigorous scientific instrumentation, monitoring, and modeling and diverse methodologies that seek to estimate failure thresholds. Likewise, communication protocols are determined along with the dissemination of warnings to the population. Civil protection entities oversee providing access to the warning, action protocols, and response (Fig. 1).

There is no doubt that the increase in intensity and frequency of precipitation due to global warming will play an even greater role in landslide occurrence in the coming years (IPCC 2014; Cardona Arboleda et al. 2020; Adler et al. 2022). Therefore, additional efforts must consider moving from landslide hazard-based EWSs to integrated landslide disaster risk management (Alcántara-Ayala 2021). This will encourage strengthening alliances between the science and technology community and policy making.

3 Methodology

A systematic review of the literature was performed. The ISI Web of Science database data was used as the only source to conduct the analysis. This included the definition of the review scope, literature search, literature analysis, and synthesis. Past accomplishments and expected endeavours of LEWSs were also further explored.

In the same manner, as the analyses undertaken for low- and lower-middle-income countries (LICs and MICs) (Alcántara-Ayala and Garnica-Peña 2023a) and Upper Middle-Income Countries (UMICs) (Alcántara-Ayala and Garnica-Peña 2023b), the words "landslide", "warning system", and "early warning" in the title and abstract of the articles were considered in the search criteria and keywords for this study. The initial literature search for all countries was conducted between January and February 2022, and the analysis for HICs was performed in September 2022.

Fig. 1 The hazard knowledge-based nature of LEWSs

The years 1991–2021 were chosen as the publication period of analysis to avoid the incorporation of work in progress in 2022. A total of 1762 papers were included as search outputs (Fig. 2).

A filtering process was performed to exclude publications that did not have the full abstract available, were published in languages other than English, and were focused on LICs and MICs, and UMICs. The number of publications was reduced to 1159.

After removing publications that did not correspond to the objective of the literature review, as well as retracted publications, editorial material, and letters, the number of publications was reduced to 1009.

The last filter applied concerned the identification of publications in which LEWs were involved. Therefore, the number of documents included in this analysis was 584 (Fig. 2).

Like in the previous book chapters regarding LICs and MICs and UMICs, the examination and synthesis of the literature consisted of geographical analysis, timeframe of publications, institutions involved, research areas, methodological typology, and perspectives (Fig. 2). After the final selection of publications, exchanges, and discussion of perspectives by two researchers to confirm the relevance of

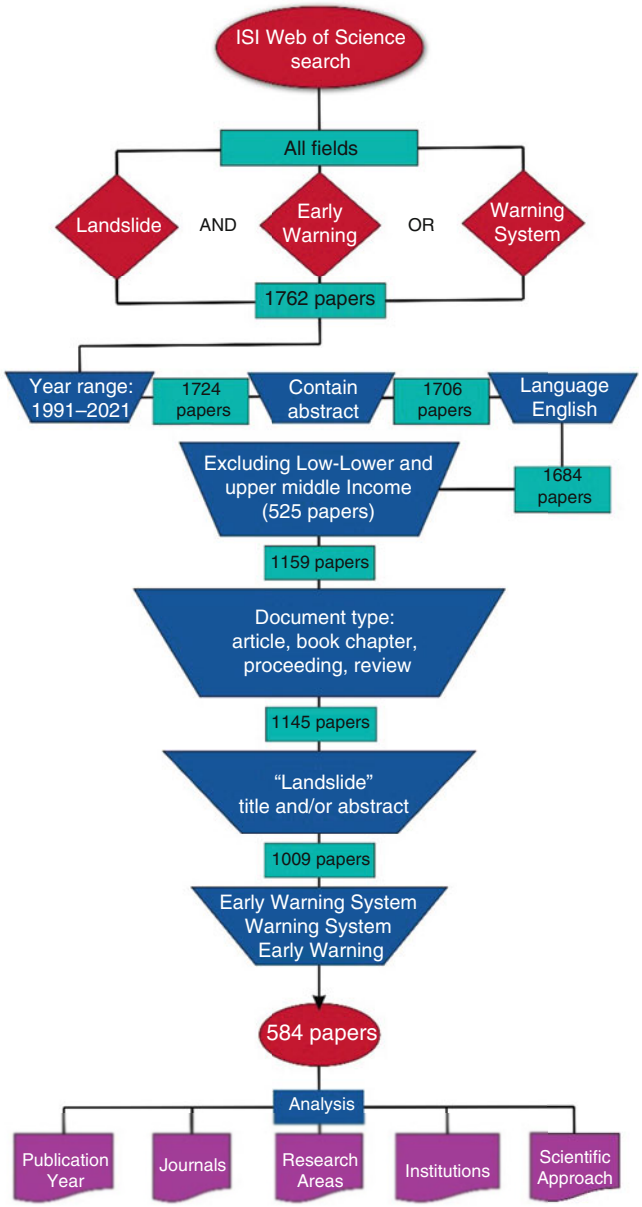

Fig. 2 Search strategy for systematic review

selected publications to the goal of the analysis was carried out.

Data were managed and analyzed by using Excel and HistCite. Past accomplishments and expected endeavours of LEWS in High-income countries (HICs) were shaped based on the insights derived from the analysis and the practical knowledge of the authors.

4 Results

Countries including Italy, the United States of America, Taiwan, Switzerland, the United Kingdom, Germany, Japan, Austria, Canada, France, Norway, Spain, the Republic of Korea, Netherlands, Croatia, Poland, Slovenia, Australia, and the Czech Republic are the HICs where 96% of the total publications considered in the present literature review were developed.

The first two publications concerning LEWS included in ISI Web of Science were available in 1991, and they corresponded to publications generated in two of the HICs. Thus, the period of analysis considered in this chapter is 1991–2021 (Fig. 3).

Although there has been a growing tendency in the number of publications on LEWSs in HICs since 1991, 2003 was the first year when this increase was noted with the publication of eight papers. In 2010, there was a much clearer rise as 29 articles were published. Likewise, quite clearly, since the year 2015, when the Sendai Framework for Disaster Risk Reduction commenced, the temporal distribution of publications showed a marked surge. 2017 was the year with the highest number of publications produced by academicians working in HICs so far, which was in the order of 63 papers (Fig. 3).

The type of publications analyzed comprised articles (N = 399), conference proceedings (N = 155), book chapters (N = 9), and reviews (N = 21).

The publications focused on various fields of research in the diverse topic areas associated with landslides. Of the total publications, 23% was concentrated in the areas of engineering and geology (N = 135), followed by geology, meteorology, and water resources (N = 79), engineering (N = 57), and geology (N = 47). Additional relevant areas are physical geography and geology (N = 21), geochemistry and geophysics (N = 18), environmental science and ecology and water resources (N = 13), engineering, geology, and water resources (N = 10) environmental sciences and ecology and geology (N = 10) and geology and water resources (Fig. 4). Not a single publication produced by researchers in HICs was included in social sciences. Therefore, the total predominance of a technical perspective was documented.

The top four journals in which most of the papers were published included the Landslides Journal (N = 79), followed by Natural Hazards and Earth System Sciences (N = 47), Natural Hazards (N = 22), and Engineering Geology (N = 19). Additional articles were issued in publications such as Advancing the Culture of Living with Landslides (N = 12), Geomorphology (N = 12), Engineering Geology for Society and Territory (N = 11), Geophysical Research Letters (N = 11), Water (N = 11) Journal of Hydrology (N = 10) and Remote Sensing (N = 10) (Fig. 5).

Experts from 160 research institutions from HICs participated as contributors to more than one publication. The top institutions regarding participation in the largest number of publications were the University of Florence (N = 51), the National Research Council (CNR) of Italy (N = 41), the US Geological Survey (N = 22), University of Naples Federico II (N = 21), and the Swiss Federal

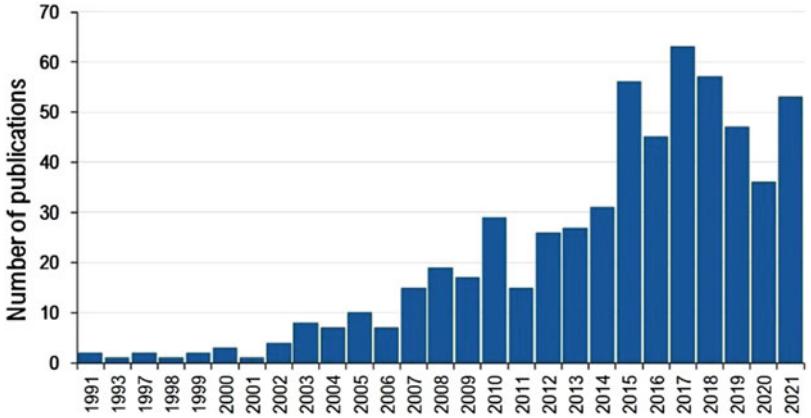

Fig. 3 Time analysis: number of publications analyzed concerning LEWSs in HICs

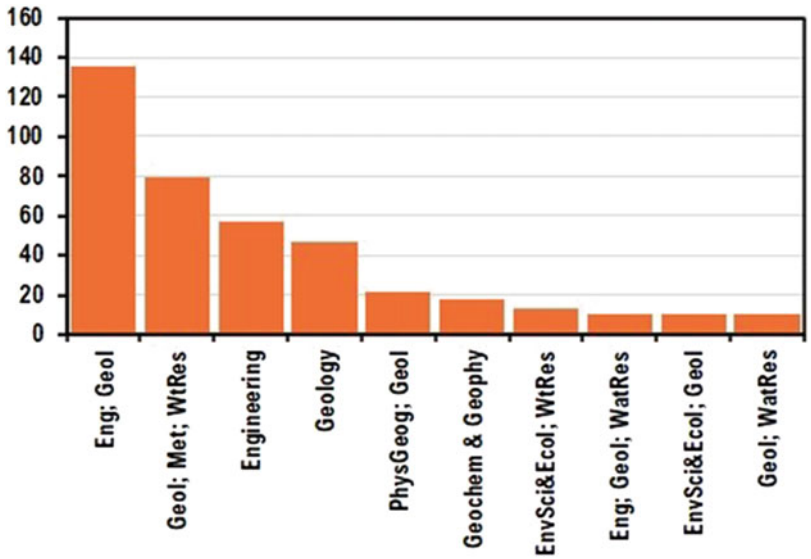

Fig. 4 Research areas concerning the publications analyzed on LEWSs HICs

Institute of Technology (N = 20) (Fig. 6). Quite clearly, through the work developed by the University of Florence and the National Research Council (CNR), Italy is at the top of the global production of papers on LEWSs.

Other institutions comprised at the top were the National Taiwan University (N = 16), University of Calabria (N = 16), University of Salerno (N = 16), National Institute of Geophysics and Volcanology (Istituto Nazionale di Geofisica e Vulcanologia, Italy) (N = 12), University of Roma La Sapienza (N = 12), University of Padua (N = 10), National Chiao Tung University (Taiwan) (N = 9), Norwegian Geotechnical Institute (N = 9), University of Perugia (N = 9) and University of Tokyo (N = 9) (Fig. 6).

The investigations included in the analyzed publications were concentrated on three main thematic lines of research. The highest percentage of publications was focused on diverse topics associated with technology development for potential LEWSs (N = 202, 34.5%). This was followed by hazard analysis for LEWSs (N = 194, 33.2%). The third category included models and prototypes for LEWSs (N = 118, 20.2%) (Fig. 7).

The second group of themes comprised the actual implementation of LEWSs (N = 18, 33.2%), while the need to implement LEWSs (N = 14, 33.2%) and various aspects of landslide risk management (N = 11, 33.2%) followed (Fig. 7).

Further topics comprised surveys (N = 7, 1.1%), reviews (N = 5, 0.85%), ICL initiatives (N = 4, 0.68%), manual, guidelines and standards (N = 4, 0.68%), international efforts (N = 2, 0.34%), education (N = 3, 0.51%), barriers for implementation (N = 1, 0.17%), and technological and institutional capabilities (N = 1, 0.17%) (Fig. 7).

The research focused on the development and improvement of LEWSs in HICs has been extensive (Fig. 8).

Italy concentrates the largest number of study cases reported in the analyzed publications, followed by Taiwan and Switzerland (Fig. 9).

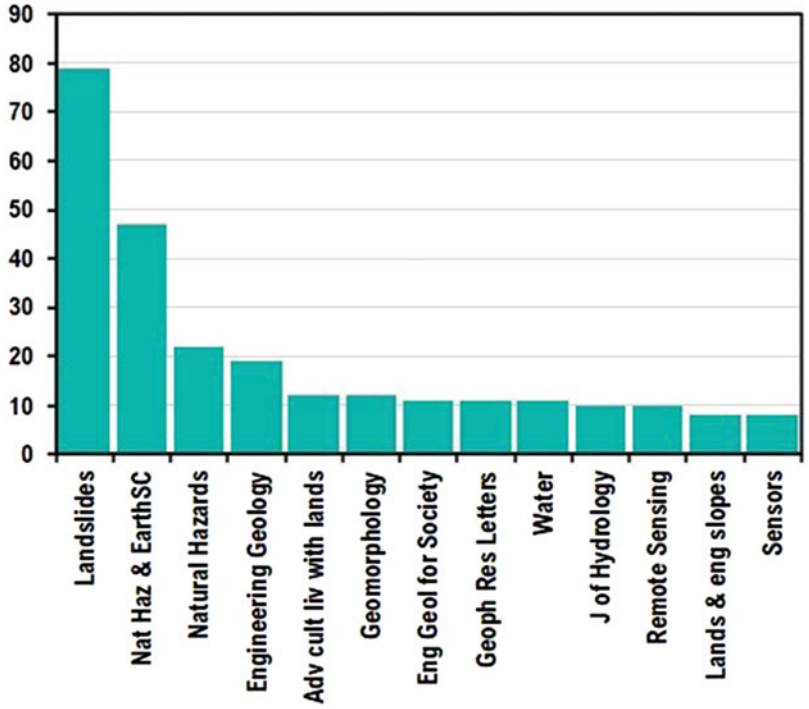

Fig. 5 Journals of publications regarding LEWSs in HICs

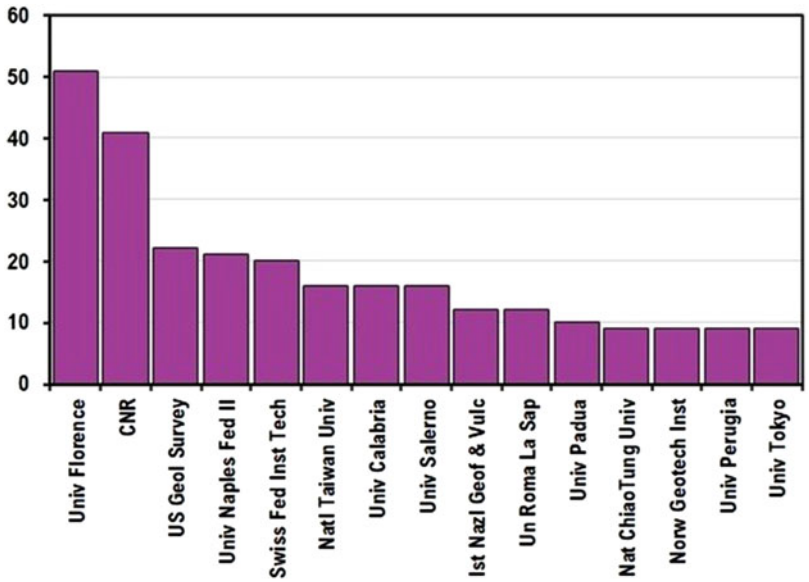

Fig. 6 Research and academic institutions to which the authors of the analyzed publications are affiliated

4.1 Technical Developments for Potential LEWSs

Quite clearly, due to the availability of resources and specific interest in improving EWSs, research in HICs is highly focused on technical developments for potential LEWSs. This includes to a major extent near-real-time monitoring of surface displacements, experimental application of distributed optical fiber sensors, techniques of optical remote sensing, acoustic sensing technology, geoelectrical, and seismic geophysical surveys, and three-dimensional experiments and modeling. A common feature is the use of a real-time GPS network, a ground-based interferometric linear synthetic aperture radar, LIDAR, and automated topographic monitoring systems.

Emphasis was also given to the use of low-cost ad hoc wireless sensor networks and flexible spatial web service technology, sensor networks for debris-flow monitoring and warning, time domain reflectometry for the continuous capture of dynamics and locations of shear deformations with

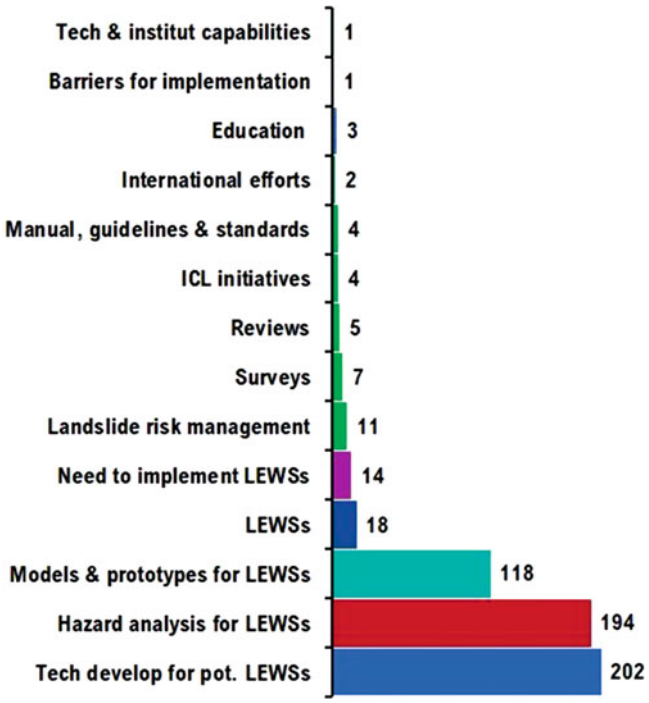

Fig. 7 Thematic lines of research associated with LEWSs in HICs, based on the systematic literature review

high temporal and spatial coverages, artificial intelligence camera prototypes, measurement of deformations by using Time Domain Reflectometry, Reflectorless Video Tacheometry, and Low-Cost Global Navigation Satellite System, among others.

4.2 Hazard Analysis for LEWSs

Diverse characterizations of landslide hazards were also reported. A large amount of research was concentrated on the analysis of localized rainfall intensity, antecedent precipitation index, rainfall intensity-duration thresholds, and topography that affected the hydrologic processes.

Likewise, a wide diversity type of techniques and methodologies to understand the various aspects linked to the dynamics of landslides were used. This included numerical modeling, physics-based hydrology, slope stability models, multiple regression analysis, combined finite discrete element methods, the weight of evidence, analytic hierarchy process, fuzzy logic methods, multitemporal interferometry, optical Landsat TM images, Sentinel-1 SAR images, multisatellite precipitation analysis, high-resolution three-dimensional laser scanning monitoring, Monte Carlo simulations, predictive models with machine-learning approaches, monitoring of slope displacements, dendrochronological based analysis of slope movements, and others.

Results from landslide hazard characterization dynamic were produced in terms of landslide rainfall thresholds, characterization of soil properties, hazard indexes, landslide susceptibility models, insights into the understanding of

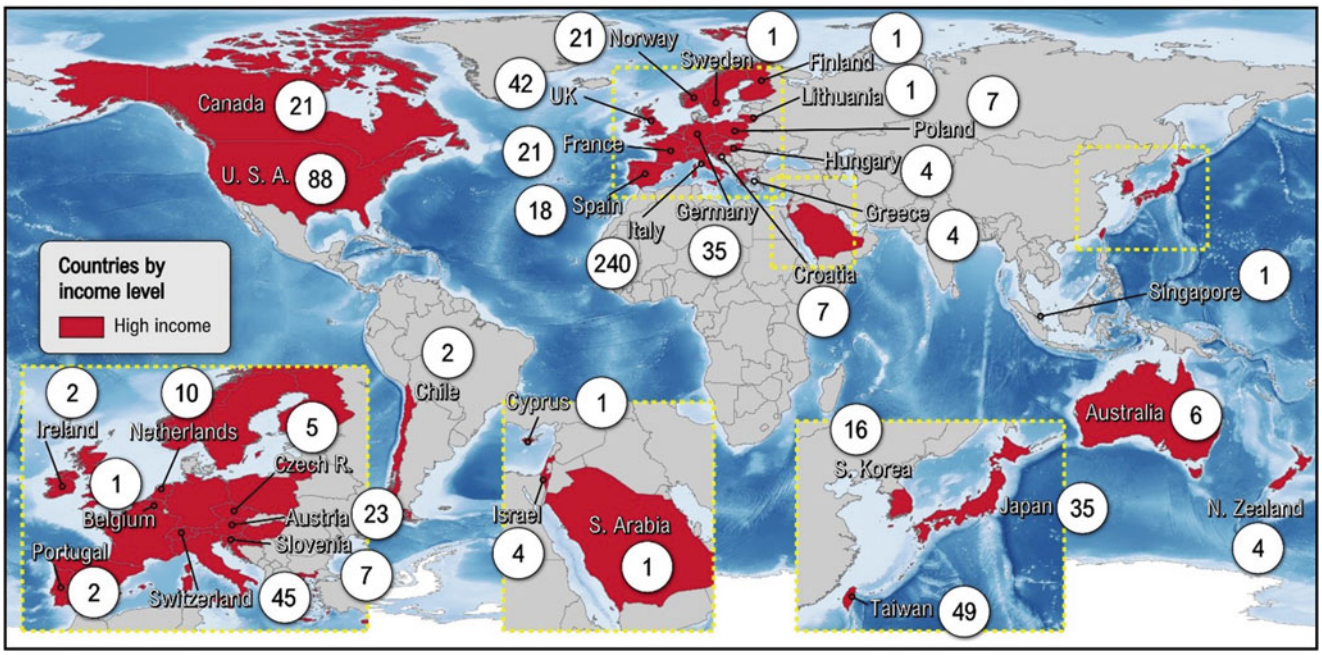

Fig. 8 Countries of the research and academic institutions to which the authors of the analyzed publications are affiliated. The number inside the circle represents the number of publications per country

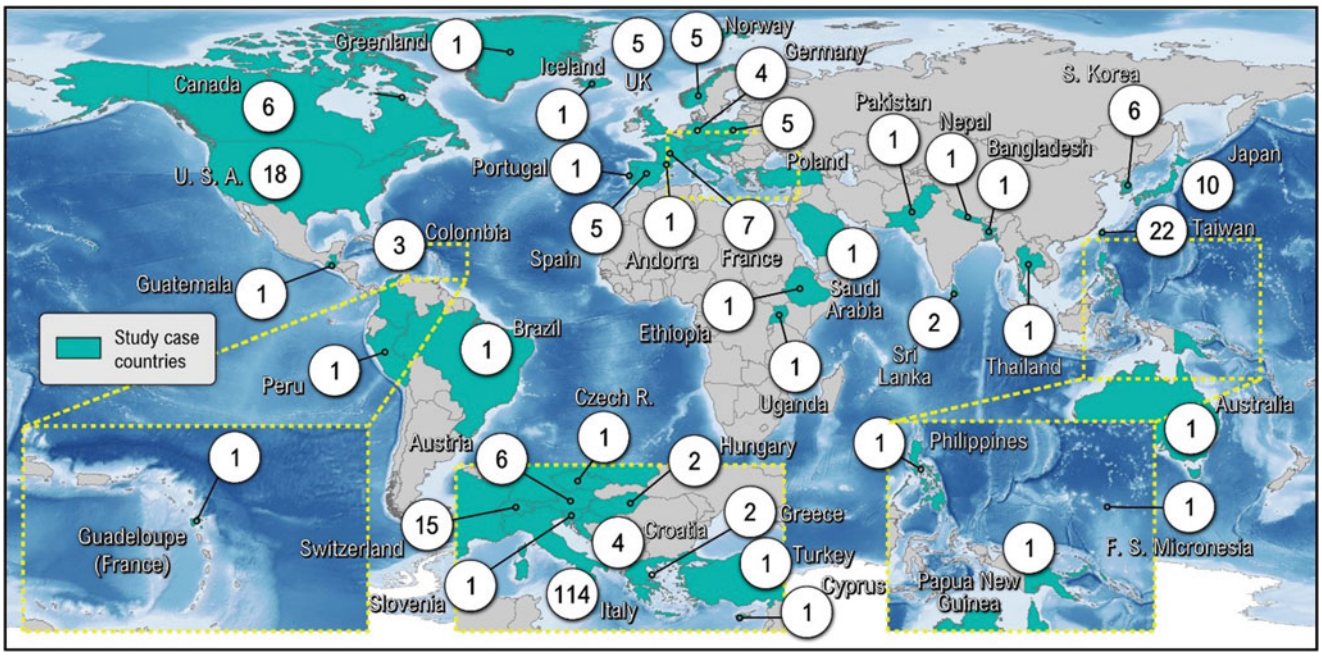

Fig. 9 Study case countries reported in the analyzed publications. The number inside the circle represents the number of study cases per country, including those which are not categorized as HICs

hydrological processes at slope scale, the evolution of surface deformation, the extent to which vegetation enhances slope stability, landslide potential maps, landslide-generated tsunami scenarios, and so forth.

4.3 Models and Prototypes

A series of models and prototypes have been developed in diverse institutions situated in HICs. Although it is not possible to make a follow-up on the implementation of those models and prototypes, its potential operation is higher than in other countries where resources are scarcer.

Some of these models include hydrological models such as the Forecasting of Landslides Induced by Rainfall (FLaIR), which is applicable for forecasting recurrent landslides and is based on the identification of a mobility function (Capparelli and Tiranti 2010; Capparelli and Versace 2011).

Likewise, mathematical models for LEWS have included different processes to provide rainfall and the occurrence evaluation of landslides (De Luca et al. 2010). The use of stochastic real-time predictors of rainfall-induced landslides has also helped to increase the time for successfully triggering risk mitigation procedures (Greco et al. 2013).

4.4 Operational LEWSs from Publications in HICs

The implementation of LEWs in diverse countries was reported in 18 publications, out of which 5 were from Italy, 2 from Canada, Norway, Switzerland, and the USA, and 1 from the Republic of Korea, Japan, Taiwan, Germany, and New Zealand.

Based on intensity-duration rainfall thresholds, a LEWS was established in the Tuscany region in Italy to provide alert levels for 25 distinct alert zones, for which specific thresholds were calculated (Segoni et al. 2015). Dei Cas et al. (2018) reported the monitoring undertaken in the Gallivaggio rock cliff in the San Giacomo Filippo district, thanks to which it was possible to successfully alert the Civil Protection Unit and the Municipality.

In 2005, after the Chichi Earthquake, a LEWS was created in Taiwan. It is based on the identification of rainfall threshold values derived from information produced by local weather stations and it is adapted according to specific geomorphologic context. The implementation of this LEWS has helped to reduce the casualties associated with landslide disasters (Chen and Huang 2010).

The Norwegian national LEWS initiated operations in 2013. It relays on rainfall thresholds, hydrometeorological

and real-time landslide observations, along with landslide inventory and susceptibility maps. The performance of this LEWS was recently evaluated and results indicate that the definition of the density criterion is a fundamental issue that system managers need to consider to be able to provide an idea of the expected number of landslides for every warning level in each warning zone (Piciullo et al. 2017).

A regional LEWS was put into operation by the government of Busan, the second-largest city in South Korea. Based on time-varying rainfall data, alerts are constructed through statistical, physically based, and geomorphological calculations. Analysis carried out to evaluate the LEWS revealed that close collaboration and feedback between researchers and operating authorities and clear divisions of legal responsibility are critical for its successful implementation and sustainable operation (Park et al. 2020).

Owing to the frequent impact of debris flows in the Swiss Alps, in the Canton of Valais, since the year 2000, a LEWS was in place. The system comprises community organizational planning, detection and alerting of events, geomorphological catchment observation, and development of an early warning system based on weather forecasting. According to an evaluation of its performance, out of the 20 automated alerts that have been issued, there was only 1 false alarm (Badoux et al. 2009).

References were also made to the need of implementing LEWS in different parts of the world. For example, in UNESCO cultural and natural World Heritage sites (Monteleone et al. 2016), flanks of active volcanoes, the Swiss Alpine region, and Croatia (Krkač et al. 2015), among others.

An important issue identified through the literature review was landslide disaster management. Thematic interests in this matter included the need to improve community resilience, the need to revise modes of risk governance, urban planning, and landslide insurance, and the need to develop and share new and best practices in the technical-scientific and regulation fields (Plagiara et al. 2017).

4.5 Additional Topics of Concern Related to LEWSs in UMICs

Further to the four lines of research mentioned earlier, the publications addressed topics of huge relevance for society.

When analyzing multi-risk governance for natural hazards, comprising landslides, in Naples and Guadeloupe, Scolobig et al. (2014) concluded that the main weaknesses were focused on the interagency communication and cooperation, and the use and dissemination of scientific knowledge at the time of the development of policies and practices. Nonetheless, warning systems and the assessment of hazards and exposure were considered major strengths.

In the same vein, within the context of mainstreaming multi-risk approaches into Policy, which included LEWS, Scolobig et al. (2017) identified that warning systems provide innovative and effective information, but also involve specific challenges to policymakers and practitioners associated with their transversal disciplinary aspects.

Regarding education, after the experience derived from the induced rainfall debris flow that occurred near Casita volcano, in Nicaragua, in 1998, where around 2000 people died, the term Education for Self-Warning and Evacuation was proposed as part of the mitigation measures (Scott 2000). Similarly, international efforts have been directed to encourage networking among members from specialized institutions and experts of EWS and LEWS. This includes diverse activities of ICL members (Bozzano et al. 2010; Zvelebil et al. 2010; Mikoš 2012; Tofani et al. 2017).

Inspired by a review and their own experience in the design, implementation, management, and verification of geographical LEWSs in Italy, Guzzetti et al. (2020) provided 30 recommendations to further develop and improve such systems and to enhance their reliability and credibility.

By undertaking semi-structured interviews, Lin and Chang (2020) found that local knowledge can improve early warning and build their capacities to respond to disasters. They suggested that local knowledge must be integrated into governmental scientific-based knowledge as a primordial insight for disaster risk management.

As a result of a survey applied in some countries of Europe and Asia, concerning the application and reliability of techniques for landslide site investigation, monitoring, and early warning, it was possible to identify that precipitation amount, pore-water pressure, and displacement monitored by wire extensometers, GPS, and total stations, accompanied by air temperature and EM-emissions monitoring and displacement monitored by crack gauges were considered the most promising parameters for early warning (Baroň and Supper 2013).

LEWS could be traditional when warnings are issued by watchful attendants or based on sophisticated electronic devices. Nonetheless, it is critical that all of them are applied by experts, regional and local authorities, and the population in the understanding that the alert should be transmitted to the people at risk, at the right time and provided accurate planning of emergency measures (Kienholz 2003).

4.6 Scientific International Collaborations

According to the literature review, a total of 725 collaborations were identified among HICs. Italy, the United States of America, and Taiwan are the HICs with the highest number of collaborations with 240, 88, and 49, correspondingly. In these three countries, 52% of the

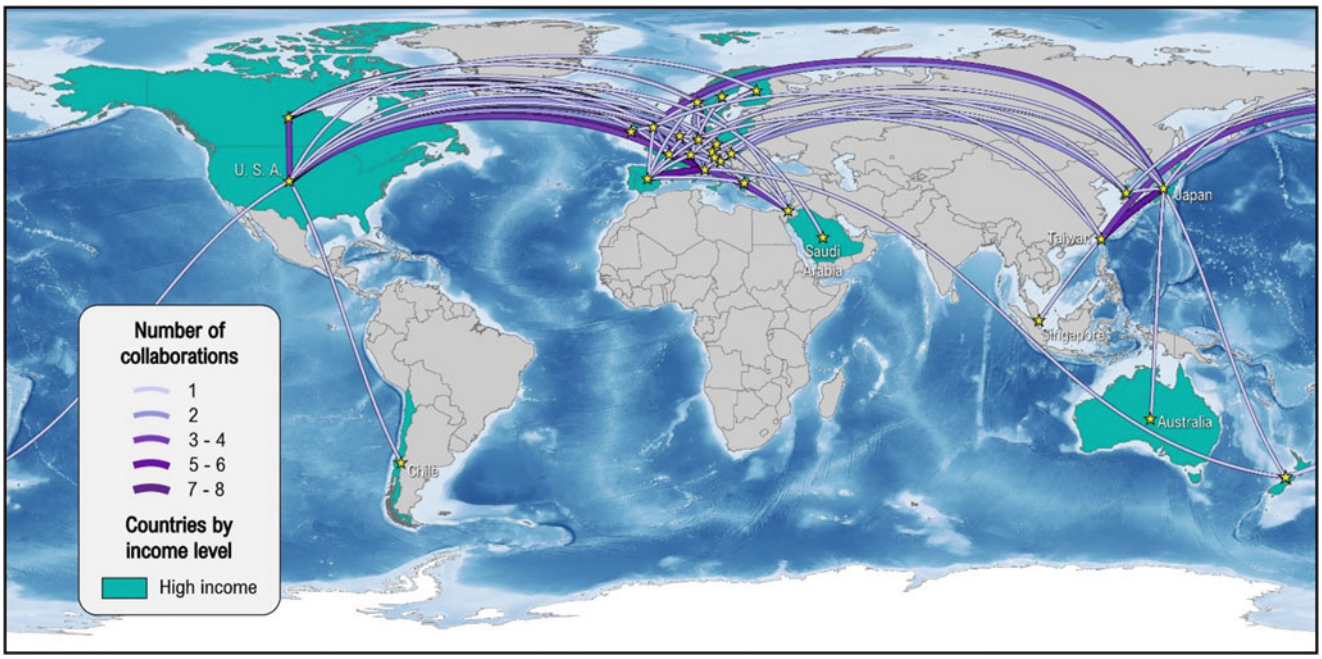

Fig. 10 Regional and international collaborations among HICs and other countries

total collaboration registered is concentrated. They are followed by Switzerland with 45, the United Kingdom with 42, and Germany and Japan with 35 each (Fig. 10).

A third group is formed by Austria (N = 21), Canada (N = 21), France (N = 21), Norway (N = 21), Spain (N = 18), and the Republic of Korea (N = 16). Netherlands (N = 10), Croatia (N = 7), Poland (N = 7), Slovenia (N = 7), Australia (N = 6), and the Czech Republic (N = 5) came after. Other countries also reported a minor number of collaborations (Fig. 10).

Italy and Norway have been collaborating through national and regional forecasting services for rainfall-induced landslides. These services use a combination of quantitative thresholds and daily rainfall forecasts and qualitative expert analysis to provide landslide hazard assessments. This type of collaboration is of significant relevance all the time, particularly when large low-pressure systems affect entire regions (Devoli et al. 2018).

The ICL Landslide Monitoring and Warning Thematic Network represents a productive collaboration among ICL member organizations and ICL supporters from eight countries. The main activity is sharing experiences and practices on monitoring and LEWSs (Mikoš 2012).

An ambitious collaboration reported an attempt to develop a global LEWS induced by rainfall and/or earthquakes. Beyond high-standard scientific models, its implementation will require wide interdisciplinary efforts and multi-agency collaboration (Hong and Adler 2007).

5 Discussion

The role of LEWS in strategies aimed at reducing risk around the world has been more evident in recent years, particularly in HICs.

A series of investigations have been devoted to characterizing the dynamics of landslide hazards, along with the development of new technologies, models, and prototypes to improve the accuracy of the understanding of landslide mechanisms and spatial-temporal predictions.

Key questions to be addressed as expected endeavours for the future concern varied components of implementation. When will the governments support the systematic implementation of LEWSs? How can the current technical dominant architecture of LEWSs be articulated with disaster risk knowledge and the diverse vulnerability dimensions of people at risk? How will the formulation of alliances and partnerships enhance the successful use of LEWSs in areas at risk? Will it be possible to have regional and global LEWSs that can be accessed by all people in the future? How can we strengthen the linkages between LEWSs and education? How can effective LEWS implementation go hand in hand with disaster risk governance?

These key questions are fundamental to advancing the relevance and usefulness of LEWSs as one of the components of Integrated Landslide Disaster Risk Management (ILDRIM) (Alcántara-Ayala 2021).

To accomplish such endeavours, stronger collaboration among disciplines along with wider interaction among the relevant disaster risk reduction stakeholders is necessary. In the same vein, sound strategies for ILDRIM call for multi-sectoral and multi-scale approaches and partnerships.

Future research on LEWSs would also benefit from integrating social and natural science approaches into mixed-method designs. This will allow us to build a holistic understanding of landslide disaster risk and implement LEWS based on risk scenarios, and not just hazard characterization.

6 Concluding Remarks

According to the systematic literature review presented here, there are a series of accomplishments made in the field of LEWSs in HICs.

Innumerable efforts have been made regarding technology development for potential LEWSs, hazard analysis for LEWSs, and models and prototypes for LEWSs. Likewise, implementation of LEWSs has increased and although the number of them is not as high as needed, current efforts show a positive tendency towards their enforcement.

A growing area of research concerning topics associated with the delineation and implementation of LEWS involves perspectives in the medium and short terms to strengthen desired successful warning outcomes for the benefit of societies.

After conducting a literature review of research related to LEWSs we came to three conclusions about the future expected endeavours that can be assigned to the implementation of LEWSs. First, we suggest that LEWSs need to be understood as a component of ILDRIM, but not as its replacement. Second, it is imperative that, at the same time as progress is made in understanding landslide hazards, there is also progress in integrating vulnerability concerns. Third, there is a complex relationship between the implementation of LEWSs and disaster risk governance.

Therefore, while one of the main functions of integrated disaster risk research is to support transdisciplinary processes, the implementation of LEWS requires a strong commitment from the scientific and technological community interested in reducing the risk of slope instability-related disasters to build transdisciplinary alliances and bridges aiming at the co-production of knowledge and mainstreaming integrated disaster risk management into local governments (Kirsch-Wood et al. 2022).

In highlighting research opportunities on the role of LEWSs in disaster risk management, the challenge posed by the Sendai Framework to move from managing disasters to managing disaster risk (UNISDR 2015) from an integrated perspective can be supported.

Acknowledgments Our sincere gratitude to DGAPA-UNAM, who kindly provided financial support to carry out landslide risk research through Project PAPIIT IN300823. We also thank the anonymous reviewers of the manuscript.

References

Adler C, Bhatt I, Huggel C, Muccione V, Prakash A, Alcántara-Ayala I et al (2022) Cross-Chapter Paper 5: Mountains. In: Pörtner HO, Roberts DC, Tignor M et al (eds) IPCC [Intergovernmental Panel on Climate Change]. Climate Change 2022: Impacts, Adaptation, and Vulnerability. Contribution of Working Group II to the Sixth Assessment Report of the Intergovernmental Panel on Climate Change. Cambridge University Press, Cambridge

Alcántara-Ayala I (2021) Integrated Landslide Disaster Risk Management (ILDRiM): the challenge to avoid the construction of new disaster risk. Environ Hazards 20(3):1–22

Alcántara-Ayala I, Garnica-Peña RJ (2023a) Landslide warning systems in low- and lower-middle-income countries: future challenges and societal impact. In: Progress in landslide research and technology, vol 1, issue 1, Book Series of the International Consortium on Landslides. Springer Nature Switzerland

Alcántara-Ayala I, Garnica-Peña RJ (2023b) Landslide warning systems in upper-middle-income countries: current insights and new perspectives. In: Progress in landslide research and technology, vol 1, issue 2, Book Series of the International Consortium on Landslides. Springer Nature Switzerland

Alcántara-Ayala I, Oliver-Smith A (2017) The necessity of early warning articulated systems (EWASs): critical issues beyond response. In: Sudmeier-Rieux K, Fernández M, Penna IM, Jaboyedoff M, Gaillard JC (eds) Identifying emerging issues in disaster risk reduction, migration, climate change and sustainable development. Springer, Cham, Switzerland, pp 101–124

Alcántara-Ayala I, Oliver-Smith A (2019) Early warning systems: lost in translation or late by definition? A FORIN approach. Int J Disaster Risk Sci 10:317–331

Alcántara-Ayala I, Sassa K (2021) Contribution of the international consortium on landslides to the implementation of the Sendai framework for disaster risk reduction: engraining to the science and technology roadmap. Landslides 18:21–29

Badoux A, Graf C, Rhyner J, Kuntner R, McArdell BW (2009) A debris-flow alarm system for the Alpine Illgraben catchment: design and performance. Nat Hazards 49(3):517–539

Baroň I, Supper R (2013) Application and reliability of techniques for landslide site investigation, monitoring and early warning–outcomes from a questionnaire study. Nat Hazards Earth Syst Sci 13(12): 3157–3168

Bozzano F, Mazzanti P, Prestininzi A, Scarascia Mugnozza G (2010) Research and development of advanced technologies for landslide hazard analysis in Italy. Landslides 7(3):381–385

Capparelli G, Tiranti D (2010) Application of the MoniFLaIR early warning system for rainfall-induced landslides in Piedmont region (Italy). Landslides 7(4):401–410

Capparelli G, Versace P (2011) FLaIR and SUSHI: two mathematical models for early warning of landslides induced by rainfall. Landslides 8(1):67–79

Cardona Arboleda OD, Carreño Tibaduiza ML, Mendes Arraiol KC, Alcántara-Ayala I, Midori SS (2020) Slope instability and landslides. In: Moreno JM, Laguna-Defior C, Barros V, Buendía EC, Marengo JA, Spring UO (eds) Adaptation to Climate Change Risks in Ibero-American Countries — RIOCCADAPT Report. McGraw Hill, Madrid, pp 397–434. ISBN: 9788448621667

Chen SC, Huang BT (2010) Non-structural mitigation programs for sediment-related disasters after the Chichi Earthquake in Taiwan. J Mountain Sci 7(3):291–300
Dei Cas L, Pastore ML, Rivolta C (2018) Gallivaggio landslide: the geological monitoring, of a rock cliff, for the early warning system. Ital J Eng Geol Environ 18:41–55
De Luca DL, Biondi D, Capparelli G, Galasso L, Versace P (2010) Mathematical models for early warning systems. IAHS-AISH Publ 340:485–495
Devoli G, Tiranti D, Cremonini R, Sund M, Boje S (2018) Comparison of landslide forecasting services in Piedmont (Italy) and Norway, illustrated by events in late spring 2013. Nat Hazards Earth Syst Sci 18(5):1351–1372
Greco R, Giorgio G, Capparelli G, Versace P (2013) Early warning of rainfall-induced landslides based on empirical mobility function predictor. Eng Geol 153:68–79
Guzzetti F, Gariano SL, Peruccacci S, Brunetti MT, Marchesini I, Rossi M, Melillo M (2020) Geographical landslide early warning systems. Earth-Sci Rev 200:102973
Hong Y, Adler RF (2007) Towards an early-warning system for global landslides triggered by rainfall and earthquake. Int J Remote Sens 28(16):3713–3719
IPCC (Intergovernmental Panel on Climate Change Climate Change) (2014) Synthesis Report. Contribution of Working Groups I, II and III to the Fifth Assessment Report of the Intergovernmental Panel on Climate Change, Geneva, Switzerland, 151 pp
ISDR-PPEW (2005) International Early Warning Programme (IEWP). Brochure, 4 pp, ISDR Platform for the Promotion of Early Warning (PPEW), Bonn
Kienholz H (2003) Early warning systems related to mountain hazards. In: Early warning systems for natural disaster reduction. Springer, Berlin, pp 555–564
Kirsch-Wood J, Katsanakis R, Hieber Girardet L, Kumar A, Mena R, Cook R, Delpech F, Elsworth J, Langella F, Alcántara-Ayala I et al (2022) Global Assessment Report 2022. United Nations Office for Disaster Risk Reduction, Geneva
Krkač M, Arbanas SM, Arbanas Ž, Bernat S, Špehar K (2015) The Kostanjek landslide in the City of Zagreb: forecasting and protective monitoring. In: Engineering geology for society and territory, vol 5. Springer, Cham, pp 715–719
Lin PSS, Chang KM (2020) Metamorphosis from local knowledge to involuted disaster knowledge for disaster governance in a landslide-prone tribal community in Taiwan. Int J Disaster Risk Reduct 42: 101339
Mikoš M (2012) The ICL landslide monitoring and warning thematic network. Landslides 9(4):565–569
Monteleone A, Dore N, Giovagnoli A, Cacace C (2016) VIDEOR: cultural heritage risk assessment and monitoring on the Web. In: Fourth International Conference on Remote Sensing and Geoinformation of the Environment, vol 9688, pp 269–283
Plagiara P, Onori R, Sorrenti A (2017) Understanding and reducing landslide disaster risk: challenges and opportunities for Italian civil protection. In: Sassa K, Mikoš M, Yin Y (eds) Advancing culture of living with landslides. WLF 2017. Springer, Cham
Park JY, Lee SR, Kim YT, Kang S, Lee DH (2020) A regional-scale landslide early warning system based on the sequential evaluation method: development and performance analysis. Appl Sci 10(17): 5788
Piciullo L, Dahl MP, Devoli G, Colleuille H, Calvello M (2017) Adapting the EDuMaP method to test the performance of the Norwegian early warning system for weather-induced landslides. Nat Hazards Earth Syst Sci 17(6):817–831
Sassa K (2015) ISDR-ICL Sendai partnerships 2015-2025 for global promotion of understanding and reducing landslide. Landslides 12(4):631–640
Sassa K (2016) Implementation of the ISDR-ICL Sendai Partnerships 2015–2025 for global promotion of understanding and reducing landslide disaster risk. Landslides 13(2):211–214
Sassa K (2019) The Fifth World Landslide Forum and the final draft of the Kyoto 2020 Commitment. Landslides 16(2):201–211
Sassa K (2020) Launching session of the Kyoto Landslide Commitment 2020. Landslides 17(8):1743–1744
Scolobig A, Komendantova N, Patt A, Vinchon C, Monfort-Climent D, Begoubou-Valerius M et al (2014) Multi-risk governance for natural hazards in Naples and Guadeloupe. Nat Hazards 73(3):1523–1545
Scolobig A, Komendantova N, Mignan A (2017) Mainstreaming multi-risk approaches into policy. Geosciences 7(4):129
Scott KM (2000) Precipitation-triggered debris-flow at Casita Volcano, Nicaragua: implications for mitigation strategies in volcanic and tectonically active steeplands. In: Debris-flow hazards mitigation: mechanics, prediction and assessment, pp 3–13
Segoni S, Battistini A, Rossi G, Rosi A, Lagomarsino D, Catani F et al (2015) An operational landslide early warning system at regional scale based on space–time-variable rainfall thresholds. Nat Hazards Earth Syst Sci 15(4):853–861
Tofani V, Bicocchi G, Rossi G, Segoni S, D'Ambrosio M, Casagli N, Catani F (2017) Soil characterization for shallow landslides modeling: a case study in the Northern Apennines (Central Italy). Landslides 14(2):755–770
UNISDR (United Nations International Strategy for Disaster Reduction) (2015) Sendai framework for disaster risk reduction 2015–2030. UNISDR, Geneva
Zvelebil J, Šíma J, Vilímek V (2010) Geo-risk management for developing countries—vulnerability to mass wasting in the Jemma River Basin, Ethiopia. Landslides 7(1):99–103

Modelling of Landslide-Structure Interaction (LSI) Through Material Point Method (MPM)

Angela Di Perna, Sabatino Cuomo, and Mario Martinelli

Abstract

A novel numerical approach, namely Material Point Method (MPM), is applied to analyze the build-up of pore water pressure inside the landslide body during the impact against different types of structures. To this aim, the landslide soil is schematized as a two-phase elasto-plastic material, while the structural materials are assumed as one-phase elasto-plastic bodies. The complex Landslide-Structure Interaction (LSI) is simulated for different landslide scenarios, including the formation of "dead-zones" behind the structures and/or the run-up mechanisms, even including in some cases unacceptable displacements or the complete disruption of the impacted structure. Independent on site-specific conditions, it is shown that landslide pore water pressures undergo significant tempo-spatial evolution during a dynamic impact, meaning that a hydro-mechanical coupled approach is fully needed for an adequate LSI analysis.

Keywords

Structure · Impact · Pore-water pressure · MPM · Flow

1 Introduction

The impact of debris flows against rigid walls, obstacles, barriers, and similar types of protection structures, has been attracting the interest of practitioners and scientists since decades. There is in fact the practical challenge to adequately design such structures. In doing that, the inner complexity of flow-like landslides must be considered.

A. Di Perna · S. Cuomo (✉)
Department of Civil Engineering, Geotechnical Engineering Group (GEG), University of Salerno, Fisciano, SA, Italy
e-mail: adiperna@unisa.it; scuomo@unisa.it

M. Martinelli
Deltares, Delft, Netherlands
e-mail: mario.martinelli@deltares.nl

It is indeed a multi-scale and multi-phase problem.

i) Multiscale problem: It is well known that shallow landslides may occur at several locations during a rainstorm. Thus, the so-called territorial (also named regional, or large-area) approaches are needed to assess the observed landslide source areas (back-analysis) or to forecast the potential landslide failure zones (forward-analysis). Regarding that, it is worth mentioning some pioneering works (Dietrich et al. 1998; SHALSTAB model), paving the way to enhanced approaches including unsaturated soil (Baum et al. 2008; Cuomo and Iervolino 2016; TRIGRS model), failure probability (Tofani et al. 2017; Cuomo et al. 2021a; HIRESSS model), soil liquefaction (Lizárraga et al. 2017). The propagation (even along large distances) of the flows is another demanding issue to be analyzed basically, because detailed and large Digital Terrain Model (DTM) must be used as input data to achieve realistic simulations of the field behavior. In addition (and related) to that, it is a significant computational effort needed, which has favored the fluorescence of many different (continuum-, discrete-, or combined) approaches. The interested readers can find details about Smooth Particle Hydrodynamics (Pastor et al. 2009; Cuomo et al. 2015), Discrete Element Method (Chen and Song 2021), Material Point Method (Yerro 2015; Cuomo et al. 2021b), and other methods in the scientific literature. For instance, Cuomo (2020) reviewed the engineering analysis methods applicable to detect the potential landslide source areas and the following propagation zones.

ii) Multi-phase problem: Especially the propagation of flow-like landslides is affected by excess pore water pressures. Despite this feature, empirical propagation methods based on slope morphology, or more elaborated (still simplified) approaches have been used for years. The concept of apparent friction angle is useful in case of granular/debris landslide materials, allowing to analyze the landslide motion and the governing equations in terms of total stresses. It is a way to by-pass the computation of pore

I. Alcántara-Ayala et al. (eds.), *Progress in Landslide Research and Technology, Volume 2 Issue 1, 2023*,
Progress in Landslide Research and Technology, https://doi.org/10.1007/978-3-031-39012-8_6

water pressure, if moderate changes happen during the process. A significant novelty was introduced by the so-called landslide propagation-consolidation model proposed by Hutchnison (1986), later enriched by Pastor and co-workers in the early 2000s. Nowadays, several hydro-mechanical coupled approaches exist for both landslide initiation and propagation modelling (Cuomo 2020).

2 Approaches for LSI Modelling

The landslide impact, more in general, the Landslide-Structure Interaction (LSI) is governed by the multi-scale and multi-phase features discussed before.

However, while practitioners have preferred (i) empirical approaches and they are looking forward to having available (ii) analytical approaches, researchers have also developed (iii) physical models and (iv) numerical approaches.

i) Empirical approach: These approaches provide an estimation of the maximum impact pressure (or force). Some (hydro-static) methods require only the flow unit weight and thickness (Scotton and Deganutti 1997; Scheidl et al. 2013); other (hydro-dynamic) methods use as input the flow density and the square velocity of the flow (Bugnion et al. 2012; Canelli et al. 2012); other (mixed) methods consider both the static and the dynamic components of the flow (Arattano and Franzi 2003; Cui et al. 2015). None of them allow assessing the evolution of the impact force over the time. Recent research tried to overcome these limitations. Di Perna et al. (2022) proposed an enhanced empirical method, firstly calibrated via numerical analyses, then validated referring to a large dataset of real debris flows from China (Hong et al. 2015). This method allows estimating the impact duration (not only the peak impact pressure), which regulates the deformation of the protection barrier.

ii) Analytical approach: Yong et al. (2019) proposed an analytical solution for estimating the sliding of a barrier under the impact of a boulder, both assumed as rigid, with the impact studied through the elastic collision principles. Li et al. (2021) proposed an analytical model to estimate the peak impact pressure that a debris flow exerts on a rigid barrier. Song et al. (2021) obtained an analytical model for evaluating the deflection of a flexible barrier (a net fixed to the ground) through the validation against experimental results of centrifuge tests. Ng et al. (2021a) proposed an analytical impact equation for the design of multiple rigid barriers, stressing that the height of the first barrier governs the impact dynamics of debris flow on the next barrier in a channel. Cuomo et al. (2022) casted an analytical method to simulate the inelastic collision of the impacting landslide and the protection barrier. From there, the landslide energy release and the deformation plus the eventual displacement of the barrier is determined.

iii) Physical model: Flume experiments are a powerful, although expensive, tool to observe into details complex soil-structure behaviors. Bugnion et al. (2012), in their 41 m long experiments of hillslope debris flows, stated that pressures depend primarily on the flow speed, which in turn appears to depend on the grain-size and water content. Experiences from Hong Kong highlighted that a large flume model is needed to study the impact mechanisms of two-phase flows, as observed in a 28 m long flume (Ng et al. 2019, 2021b).
Reduced-scale laboratory tests have been used to derive and validate the most common empirical formulations (Hübl et al. 2009; Scheidl et al. 2013).

iv) Numerical approach: LSI has been studied through Eulerian methods (e.g., Moriguchi et al. 2009), Smoothed-Particle Hydrodynamics (SPH) (Bui and Fukagawa 2013) or Discrete Element Method (DEM) (Leonardi et al. 2016; Calvetti et al. 2017; Shen et al. 2018). Cuomo et al. (2021c, 2022) applied an advanced numerical code based on Material Point Method (MPM), i.e., the Anura 3D code (with recent enhancements developed by Deltares), to entirely reproduce the LSI including the mutual actions between the landslide and the barrier as well as the landslide propagation during the LSI, i.e., the eventual barrier overtopping of some part of the landslide volume.

For those structures behaving as "rigid" during the LSI, any of those approaches is useful. Whereas, if the impacted structure may undergo significant damage, numerical models are preferable, but they need careful calibration.

3 Damage and Protection

Within a framework of landslide risk mitigation, we may assume that an impacted structure can undergo: i) limited damage to non-structural elements, ii) damage to the structure (with eventual partial destruction), iii) collapse.

Examples of the cases (i) and (ii) are respectively provided in Figs. 1 and 2. The features of the flow-like landslides have been reviewed before.

Here it is worth point out that the structures impacted are typically constituted by bricks or concrete elements eventually reinforced with steel bars. It entails that complex 3D structural configurations should be analyzed, where linear and planar structural elements interact to develop proper resisting mechanisms. Nevertheless, the analysis of

Fig. 1 Example of damage to non-structural elements caused by the impact of flow-like landslides in the Sarno area, Campania, southern Italy, 1998 (from Mavrouli et al. 2014)

combined materials such bricks and mortar, or concrete and steel, requires a sound structural scheme to be defined, where the geometrical items (e.g., pillars, beams) and connections (hinges, joints) are modelled.

The occurrence of any damage scenario and its severity is the outcome of different factors combined. The type of urbanization (dense or sparse), the construction features (type, materials, age, etc.), the exposure (direct or limited) to the impact, the type of impact (frontal or lateral), and other site- or case-specific features. Thus, the assessment of potential damage to a structure requires analyses and zoning at detailed scale.

Reinforcing the structures against flow-like landslides impact is difficult to be pursued. The main limitation is that structures are conceived to bring their self-weight and the external loads, which are predominantly vertically oriented. Thus, providing additional resisting mechanisms against horizontal (or quasi-) actions is doable in practice only for special cases or for limited size/extension of the structure.

Fig. 2 Example of a building partially destroyed by a flow-like landslide occurred in the Cervinara area, Campania, southern Italy, 1999 (from Cascini et al. 2011)

More often, the endangered structures are protected by means of concrete walls, blocks, or combinations of rigid-like vertical elements like baffles.

Reinforced Concrete (RC) walls are commonly used as protection measures in hilly areas to contain falling boulders and landslide debris, and the sliding displacement of these barriers is a key design issue when space is limited. RC walls are usually made as slab concrete dams, that can be reinforced with counterfort. For such slender constructions, the flow impact dynamics must be carefully evaluated, as the wall must retain the flowing material without tilting or without showing excessive displacements. For these reasons, the foundations of these structures are particularly large. In bedrock, the foundations are usually made by steel tension anchors (ribbed bars), while in loose deposits, the ground must sustain the weight of the concrete construction together with the loads generating from the impact (Barbolini et al. 2009). An example is provided in Fig. 3.

An alternative can be a Mechanically Stabilized Earth (MSE) wall. In the context of landslide protection, they are also called Deformable Geosynthetics-Reinforced Barrier (DGRB), as they are composed of granular soil and geosynthetics reinforcement elements, such as high tenacity polyester (PET) geogrids (Cuomo et al. 2020a). These geostructures have been formerly investigated (Gioffrè et al. 2017; Cuomo et al. 2019) to reduce the runout (and the potential damage) of flow-like landslides, while they are typically used as deformable barriers against snow avalanches or rockfalls (Fig. 4).

The stability of a DGRB is derived by the interaction of coarse material with the reinforcements, involving friction and tension resistances. The facing is relatively thin, with the primary function of preventing erosion of the structural backfill. The result is a massive structure that is flexible and can withstand various loads combinations. DGRB is an appropriate protection structure when a medium to very high kinetic energy event is expected, i.e., from a few hundred kilojoules to tens of megajoules (Descoeudres 1997). The other advantages are the low maintenance costs and the reduced visual impact since DGBR are greened (Brunet et al. 2009). Nevertheless, they are not appropriate on steeper slopes and their construction generally requires extensive space and accessibility for heavy vehicles.

The optimal location of the barriers (RC or MSE walls) is an issue. In fact, to minimize the height and length of the barrier (hence the cost), they must be located at the distal part of the propagation path so that flow velocity has reduced before; however, the barrier should be not so close to the structures to be protected.

What is really challenging is to find a mathematical framework to properly describe the so different materials and

Fig. 3 Example of Reinforced Concrete (RC) wall used as diverting dam against snow avalanches at Odda, Norway (Barbolini et al. 2009)

behavior of both (i) the flow-like landslide and (ii) the impacted structure.

One relatively new method, namely Material Point Method (MPM), allows simulating large deformations and displacements (with no restriction), that are typical features of both a flow-like landslide and a building structure under severe external loads such an impulsive impact.

4 Remarks on Material Point Method (MPM)

4.1 Framework

MPM can be considered a modification of the well-known FEM, and it is particularly suited for large deformations (Sulsky et al. 1995). The continuum body is schematized by a set of Lagrangian points, called material points (MPs). Large deformations are modelled by a set of MPs moving through a background mesh, which also covers the domain where the material is expected to move. The MPs carry all the

Fig. 4 Example of MSE walls used as protection structures (Barbolini et al. 2009)

physical properties of the continuum such as stress, strain, density, momentum, material parameters, and other state parameters, whereas the background mesh is used to solve the governing equations without storing any permanent information.

The interaction between phases (solid and liquid in a saturated soil) can be tracked through the "two-phase single-point" formulation (Jassim et al. 2013; Ceccato et al. 2018), where the liquid and the solid acceleration fields are the primary unknowns (Fern et al. 2019).

On the other hand, the so-called "one-phase single-point" formulation can be opportunely adopted for dry soils or for saturated soil in the simplified hypothesis that the ratio of pore water pressure divided by total stress is constant inside the deforming body and throughout the whole deformation process.

The contact between different bodies (flow-base, flow-barrier) is handled with a frictional contact algorithm. An improved contact algorithm, proposed by Martinelli and Galavi (2022), was used, being the velocity of the liquid phase corrected to prevent both inflow and outflow.

Moreover, the computational scheme proposed by Martinelli and Galavi (2022) is adopted to compute accurate reaction forces along contact surfaces, especially between non-porous structures and soils with high liquid pressures. The contact algorithm cannot be applied along the impacted sides of the barrier, therefore the interface flow-barrier is perfectly rough and permeable.

4.2 One-Phase Formulation

The conservation of mass is reported in Eq. (1) and is automatically satisfied as the solid mass remains constant in each MP during deformation.

$$\frac{d\rho}{dt} + \rho \nabla \cdot \mathbf{v} = \mathbf{0} \tag{1}$$

The conservation of momentum includes the conservation of both linear and angular momentum. The former is represented by the equation of motion, even known as Newton's second law (Eq. 2), while the conservation of angular momentum refers to the symmetry condition of the stress matrix ($\boldsymbol{\sigma} = \boldsymbol{\sigma}^T$).

$$\rho \frac{d\mathbf{v}}{dt} = \nabla \boldsymbol{\sigma}^T + \rho \boldsymbol{g} \tag{2}$$

Finally, the constitutive equation needs to be expressed to include the stress-strain dependency (Eq. 3). The term $\mathbf{D}$ is the stiffness matrix; $\boldsymbol{\sigma}'$ and $\dot{\varepsilon}$ are the stress and strain rate tensors of the solid phase, respectively. Ω is the spin tensor and $\dot{\varepsilon}_{vol}$ is the volumetric strain increment. To simulate large deformations (Eq. 3 is derived) the Jaumann's stress rate of Kirchhoff stress can be considered; on the other hand, the Cauchy one which is limited to small strain rate (Martinelli and Galavi 2022).

$$\dot{\boldsymbol{\sigma}}' = \mathbf{D}\dot{\varepsilon} + \Omega\boldsymbol{\sigma}' - \boldsymbol{\sigma}'\Omega - \dot{\varepsilon}_{vol}\boldsymbol{\sigma}' \tag{3}$$

In undrained conditions, the stress state can be described in terms of effective stresses. The excess pore pressures can be computed by means of the so-called Effective Stress Analysis (Eq. 4), which assumes strain compatibility between the solid skeleton and the interstitial liquid.

$$\Delta p_L = \mathrm{K}_L \Delta \varepsilon_{vol} \tag{4}$$

The time integration scheme considered in MPM is explicit, since most of the dynamic problems, including wave or shock propagation, cannot be treated properly by an implicit integration which tends to smooth the solution (Fern et al. 2019).

Let's consider the critical time step Δt_{cr} as the time increment during which a wave with speed c crosses the smallest element length d (Eq. 5).

$$\Delta t_{cr} = \frac{d}{c} = \frac{d}{\sqrt{E/\rho}} \tag{5}$$

The critical time step defines the biggest time increment which can be used for a stable calculation, but often it can't be estimated in case of non-linear problems. For this reason, the critical time step is multiplied by an additional factor C_{NB} (namely Courant number) to reach stability. The Courant number has values between 0 and 1. Generally, the smaller the Courant number and the smaller the time step, improving the accuracy of the numerical results.

4.3 Two-Phase Formulation

A saturated porous medium is schematized as a solid phase which represents the solid skeleton, whereas the liquid phase fills the voids among the grains. Each MP represents a volume of the mixture V, given by the sum of the solid V_S and liquid V_L phases volumes. The behaviour of a saturated porous medium is here described using only one set of

MPs, in which the information about both the solid and liquid constituents is stored.

The velocity field of solid and liquid phases are both used, but the material points move throughout the mesh with the kinematics of the solid skeleton. The equations to be solved concern the balance of dynamic momentum of solid and liquid phases, the mass balances, and the constitutive relationships of solid and liquid phases. The accelerations of the two phases are the primary unknowns: the solid acceleration $\mathbf{a}_S$, which is calculated from the dynamic momentum balance of the solid phase (Eq. 6), and the liquid acceleration $\mathbf{a}_L$, which is obtained by solving the dynamic momentum balance of the liquid phase (Eq. 7). The interaction force between solid and liquid phases is governed by Darcy's law (Eq. 8). Numerically, these equations are solved at grid nodes considering the Galerkin method (Luo et al. 2008) with standard nodal shape functions and their solutions are used to update the MPs velocities and momentum of each phase. The strain rate $\dot{\boldsymbol{\varepsilon}}$ of MPs is computed from the nodal velocities obtained from the nodal momentum.

$$n_S \rho_S \mathbf{a}_S = \nabla \cdot (\sigma - n p_L \mathbf{I}) + (\rho_m - n\rho_L)\mathbf{b} + \mathbf{f}_d \tag{6}$$

$$\rho_L \mathbf{a}_L = \nabla p_L - \mathbf{f}_d \tag{7}$$

$$\mathbf{f}_d = \frac{n\mu_L}{k}(\mathbf{v}_L - \mathbf{v}_S) \tag{8}$$

The resolution of solid and liquid constitutive laws (Eqs. 9 and 10) allows calculating the increment of effective stress $d\boldsymbol{\sigma}'$ and excess pore pressure dp_L, respectively. The mass balance equation of the solid skeleton is then used to update the porosity of each MP (Eq. 11), while the total mass balance serves to compute the volumetric strain rate of the liquid phase (Eq. 12) since fluxes due to spatial variations of liquid mass are neglected ($\nabla n\rho_L = 0$).

$$\mathrm{d}\boldsymbol{\sigma}' = \mathbf{D} \cdot \mathrm{d}\boldsymbol{\varepsilon} \tag{9}$$

$$\mathrm{d}p_L = \mathbf{K}_L \cdot \mathrm{d}\varepsilon_{vol} \tag{10}$$

$$\frac{Dn}{Dt} = n_S \nabla \cdot \mathbf{v}_S = \mathbf{0} \tag{11}$$

$$\frac{D\varepsilon_{vol}}{Dt} = \frac{n_S}{n}\nabla \cdot \mathbf{v}_S + \nabla \cdot \mathbf{v}_L \tag{12}$$

In the two-phase single-point formulation the liquid mass, and consequently the mass of the mixture, is not constant in each material point but can vary depending on porosity changes. Fluxes due to spatial variations of liquid mass are neglected and Darcy's law is used to model solid-liquid interaction forces. For this reason, this formulation is generally used in problems with small gradients of porosity, and laminar and stationary flow in slow velocity regime. However, this formulation proves to be suitable for studying flow-structured-interaction (Cuomo et al. 2021c). The water is assumed linearly compressible via the bulk modulus of the fluid $\mathbf{K}_L$ and shear stresses in the liquid phase are neglected.

The current MPM code uses three-node elements which suffer kinematic locking, which consists in the build-up of fictitious stiffness due to the inability to reproduce the correct deformation field (Mast et al. 2012). A technique used to mitigate volumetric locking is the strain smoothening technique, which consists of smoothing the volumetric strains over neighbouring cells. The reader can refer to Al-Kafaji (2013) for a detailed description.

Regarding the critical time step, the influence of permeability and liquid bulk modulus must be considered as well (Mieremet et al. 2016). In particular, the time step required for numerical stability is smaller in soil with lower permeability (Eq. 13).

$$\Delta t_{cr} = min\left(\frac{d}{\sqrt{(E + \mathbf{K}_L/n)/\rho_m}}; \frac{2(\rho_m + (1/n - 2)\rho_L)k_{sat}}{\rho_L \boldsymbol{g}}\right) \tag{13}$$

The sliding modelling of the flowing mass on the rigid material is handled by a frictional Mohr-Coulomb strength criterion. The contact formulation was used to ensure that no interpenetration occurs, and the tangential forces are compatible with the shear strength along the contact. The reaction force acting on the structure at node j was calculated as in Eq. (14).

$$F_j(t) = m_{j,S}\Delta a_{S,contact} + m_{j,L}\Delta a_{L,contact} \tag{14}$$

The terms $\Delta a_{S,\ contact}$ and $\Delta a_{L,\ contact}$ are the change in acceleration induced by the contact formulation, for both solid and liquid phase, and $m_{i,\ S}$ and $m_{i,\ L}$ are the corresponding nodal masses. The total reaction force is the integral of the nodal reaction forces along the barrier.

5 Modelling the Damage of an Infill Wall

5.1 Input Scheme

To analyse the complex mechanisms of a flow-like landslide impact against a RC framed building with URM infill walls, the numerical modelling of a single URM wall is firstly conducted.

Here, the experimental tests of Vaculik (2012) on URM wall are modelled. The wall is made of two components: standard Australian clay bricks with nominal dimensions 230 mm × 110 mm × 76 mm, perforated with two rows of five holes and mortar joints with standard thickness of 10 mm using a composition of 1:2:9 (portland cement, lime and sand). The dimensions of the wall are h = 2494 mm and B = 4080 mm, with the lateral boundary confined in embedded return wall, each 480 mm long (Fig. 5).

Some mechanical properties taken from literature for both bricks and mortar-joint are reported in Table 1. The MPM computational domain has been set both in 3D and 2D for different purposes. The 3D scheme (Fig. 6a) is used to reproduce the mechanical response of the wall under OOP pressure. In such model all the boundary conditions can be considered, either as the fixities or as mortar joints. Conversely, a 2D simplified model (Fig. 6b) must be validated for later extensive applications to design-oriented analyses.

The URM wall is schematized as an equivalent uniform continuous frictional-cohesive material, with the mechanical parameters (Table 2), selected as follows. The density ($\rho = 1936$ kg/m^3) and the Poisson ratio ($\nu = 0.2$) are those measured for the wall by Vaculik (2012). The Young's modulus (E) is taken from the experimental evidence reported by Vaculik (2012) for combo p2 (E = 2240 kPa) or assumed as equal to that of the mortar for combo p1 (E = 442 kPa). The cohesion of the wall material is varied to get numerical results similar to the experimental ones. The internal friction angle (φ') is set equal to the average value reported by Vaculik (2012) and Graziotti et al. (2019) for the mortar bed-joints. The K0 value is determined as 1-senφ' using the friction angle of the brick since it is plausible that the horizontal and vertical stress distribution is like that of a brick column. The tensile strength (f_t) of the wall is simply obtained as the ratio between cohesion (c') and friction angle (tanφ'), assuming that the friction angle is the same in both compressive and tensile stress (Table 2).

5.2 Numerical Results

The 3D computational mesh is 1.00 m × 4.08 m × 3.00 m large and made of 116,325 tetrahedral (four-noded) elements with average size of about 0.1 m inside and outside the wall (Fig. 8a). In 2D conditions, the domain is 3.50 m × 3.00 m and made of 2605 three-noded triangular elements, ranging from 0.08 m (inside the wall) to 0.50 m (Fig. 8b). The wall is fixed at top and bottom sides. Several simulations were performed assessing the combos p1 and p2 of Table 2 as the best-fitting set of parameters for simulating the experiments of Vaculik (2012) in 3D and 2D conditions, respectively.

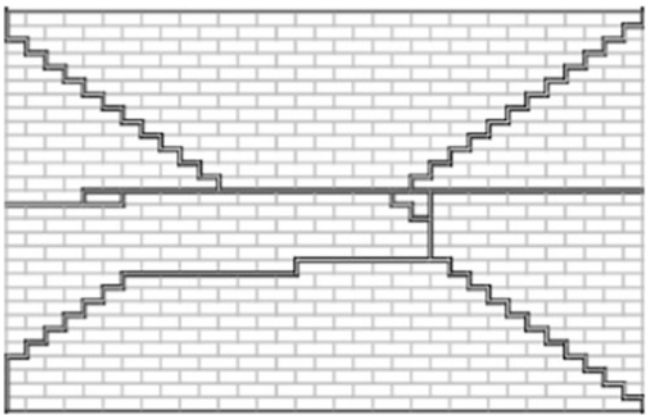

Fig. 5 Cracks of the interior face of the wall resulting from the experiment of Vaculik (2012)

A selection of results is reported in Fig. 9, with reference to the deviatoric strain defined as $\varepsilon_d = \frac{2}{3}\sqrt{(\varepsilon_x - \varepsilon_y)^2 + (\varepsilon_y - \varepsilon_z)^2 + (\varepsilon_z - \varepsilon_x)^2}$.

The load capacity of unreinforced masonry wall depends on: dimensions and support conditions, amount of compressive and tensile strength of the masonry. Particularly, the crack patterns and the load-displacement curve depend on different kinds of wall supports.

For numerical modelling, all the boundaries of the wall are fixed, thus yielding deformations occur as follows: (i) first at the top of the wall, (ii) then at the bottom of the wall, (iii) at the side boundaries of the wall. From now on, yielding zones enlarged along the boundaries where they appeared but (iv) a plastic hinge forms at the mid-height of the wall, and (v) yielding also appears along the diagonal directions (Fig. 7a). This is in accordance with the experiment of Vaculik (2012), as reported in Fig. 5, showing that 3D simulations allow a better understanding of how plastic deformations develop during the OOP loading.

Figure 7b reports the development of plastic deformations in the 2D barycentric vertical cross-section of the wall. Firstly, two plastic hinges appear along the extremities of the wall (F = 30.5 kN), then for F = 34.5 kN the mid-height of the wall starts to yield due to excessive bending, and finally the plastic deformations increase and spread over the central zone of wall for F = 40.3 kN (Fig. 7b). Such results are consistent with 3D simulation results, demonstrating that also a 2D simplified model scheme could be used in real applications.

A quantitative comparison between numerical and experimental outcomes in terms of horizontal displacements of the wall is provided in Fig. 8, showing that both 3D and 2D modelling clearly well reproduce the failure mechanism of the wall. Moreover, it is possible to derive the load-displacement curve from both 2D and 3D simulations and compare it with that obtained from the experimental test

Table 1 Some material properties from literature

Material	E[a] (MPa)	ν[a]	c' (kPa)	φ' (°)	f_t (kPa)
Brick	52,700	0.2	1500[b]	15[b]	686[c]
Mortar bed joints	442	0.2	180[d] 81 ÷ 206[c]	30[a] ÷ 32[d]	110÷140[e] 170÷500[f]

[a]Vaculik (2012); [b]Hulse et al. (1982); [c]Magenes and Calvi (1992); [d]Graziotti et al. (2019); [e]Varela-Rivera et al. (2012); [f]Wei and Stewart (2010)

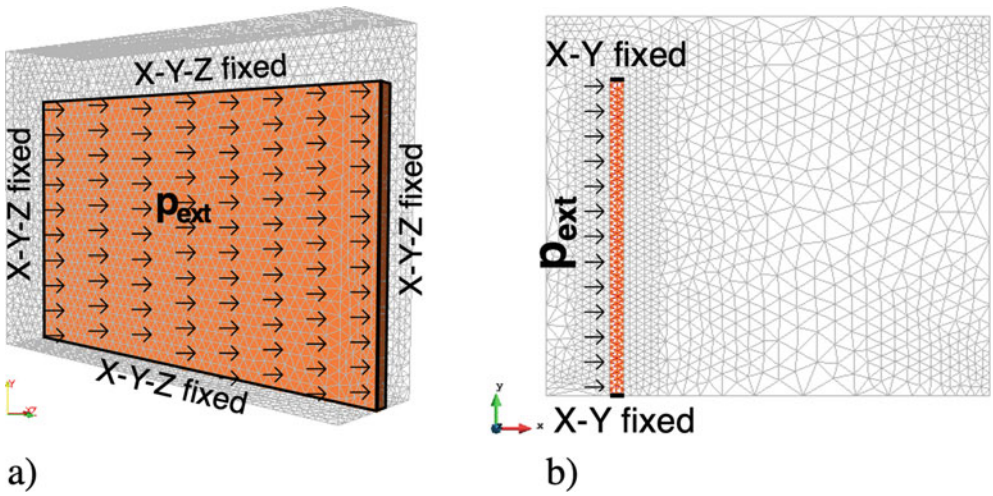

Fig. 6 Computational domain used to simulate the experiments of Vaculik (2012): (**a**) 3D model; (**b**) 2D model (barycentric vertical cross-section of the wall)

(Cuomo et al. 2020b). The experimental curve shows a different trend after reaching a horizontal displacement of about 18 mm due to the decreasing of the external load, with a maximum displacement of 30 mm and a final recovery of about 15 mm. This recovery path is neglected for the numerical modelling. However, the F-Δ plot in the loading phase is well captured by 3D and 2D simulations (i.e., for $\Delta = 0$–18 mm).

6 Modelling Landslides Impacting a Two-Storey Building

6.1 Input Scheme

The 2D modelling of the URM wall proved sufficient compared to 3D, with remarkably reduced computational time. A 2D modelling is here used to simulate the interaction between a flow landslide and a two-storey RC framed building.

For the modelling of the building, the bearing frame is assumed rigid and fixed in space, while the non-structural external and internal URM walls can be deformed and eventually destroyed following the impact of the landslide. Such modelling aims to highlight that even the collapse of non-structural elements can pose serious risks to people.

The geometric schematization of the building is reported in Fig. 9. The external walls are 0.3 m thick, with two panels 0.1 m thick separated by a 0.1 m internal cavity. The height of the walls excluding the thickness of the exposed beam (0.60 m) is equal to 2.5 m. The computational mesh and material points distribution for both the building and the landslide are reported in Fig. 10a, b, respectively. The overall computational domain (Fig. 11) is characterized by 12,279 triangular elements with average size of 0.1 m for the smaller structural elements and of 0.5 m elsewhere.

Figure 11 even highlights the considerable size of the landslide compared to that of the building.

The flow and the wall are modelled through the single-point MPM formulation, respectively with two-phase and one-phase.

All the walls are modelled with the same constitutive law of the previous section and the mechanical properties are those of the combo p2 (Table 2), which proved to be the best-fitting set in the 2D modelling of the URM wall. Regarding the constraints: the extremity of each wall is fixed in x-direction, so the wall can be considered pinned-pinned.

Table 2 Sets of material properties used for modelling the URM wall

Combo	ρ^a (kg/m^3)	ν^a	E^a (MPa)	c' (kPa)	φ' (°)	K_0	f_t (kPa)
p1 (3D)	1936	0.2	442	80	31	0.74	133
p2 (2D)	1936	0.2	2240	115	31	0.74	191

[a]Vaculik (2012)

Another issue is the modelling of the landslide. The height of the impacting mass has been assumed equal to the first-floor height, as deducted from in-situ investigations (Faella and Nigro 2003), that is equal to 3 m in this example, while the length is set to 21 m (i.e., seven times the height).

It is worth noting that the Landslide-Structure Interaction is referred to the site scale. Due to high computational time of the simulations, it is difficult to reproduce the entire landslide dynamics also including the triggering and propagation stages of the landslide. Hence, the attention is focused on the moment before the impact, considering a simplified initial configuration of the landslide with a 45°-inclined front and a prolonged tail. Moreover, two landslides with different initial velocity (5 and 10 m/s) are considered.

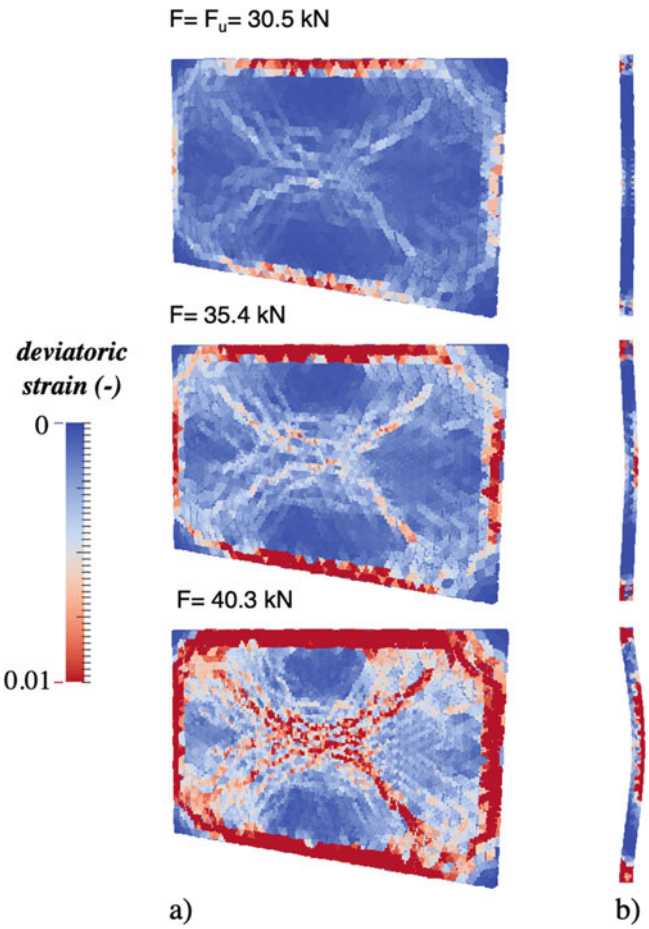

Fig. 7 Deviatoric strain computed for different external force: (**a**) 3D modelling; (**b**) 2D modelling (barycentric vertical cross-section)

The landslide material is assumed as a saturated mixture with linear distribution of initial pore-water pressure and an elasto-plastic behaviour at failure. The contact along the base is assumed to be smooth to avoid reduction in velocity due to friction. The initial stress distribution is set through gravity loading. Based on literature values and other related researches (Cuomo et al. 2020a), the mechanical properties are selected as follows: density of the mixture (ρ_m) equal to 1800 kg/m^3, Poisson ratio (ν) of 0.25, Young's modulus (E) equal to 2000 kPa, nil cohesion (c'), internal friction angle (φ') is 20°, nil dilatancy angle, hydraulic conductivity (k) equal to 10^{-3} m/s, liquid viscosity (μ_L) of 10^{-3} Pa·s, liquid bulk modulus (K_L) of 30 MPa. Moreover, two initial landslide velocity (5 and 10 m/s) are considered.

6.2 Numerical Results

The impact of the landslide with initial velocity of 5 m/s against the RC building is firstly investigated with reference to some snapshots reported in Fig. 12. Specifically, the distribution of landslide pore-water pressure and deviatoric strain inside the infill walls is shown.

At the impact stage, the front of the landslide is compressed against the external wall (t = 0.50 s), showing the increase in pore-water pressure (up to 226 kPa) and consequent increment of total earth pressure on the wall, which of course fails with no chance to withstand to such large external action. In the following moments, the flow continues to propagate dragging all the walls of the ground floor, without showing signs of stopping and therefore also the pore-water pressure is not reduced.

Worse is the case of a landslide with higher initial velocity (v_0 = 10 m/s), reported in Fig. 13. Interestingly, the pore-water pressure at impact (t = 0.50 s) is much higher and the deformations inside the walls are larger than the previous case of Fig. 15. After the impact, the landslide material runs up along the structure, causing the damage and the final collapse of the first-floor wall (t > 1.50 s). This means that people behind that wall would be seriously injured. In the meantime, large part of the flow continues to propagate and destroy the URM walls at the ground. This type of impact mechanism is named "run-up" mechanism, which consists in the formation of a vertical jet with high speed that overruns the structure. Such behaviour of the flow mostly depends on flow velocity (or related quantities), soil mechanical behaviour and geometry of the impacted structure.

Nevertheless, the structural elements (especially RC columns) of the ground floor are almost certainly overloaded laterally from the flow. Therefore, a 3D modelling of the entire structure would be advisable even if a proper schematization of the mechanical behaviour of the bearing frame would be mandatory.

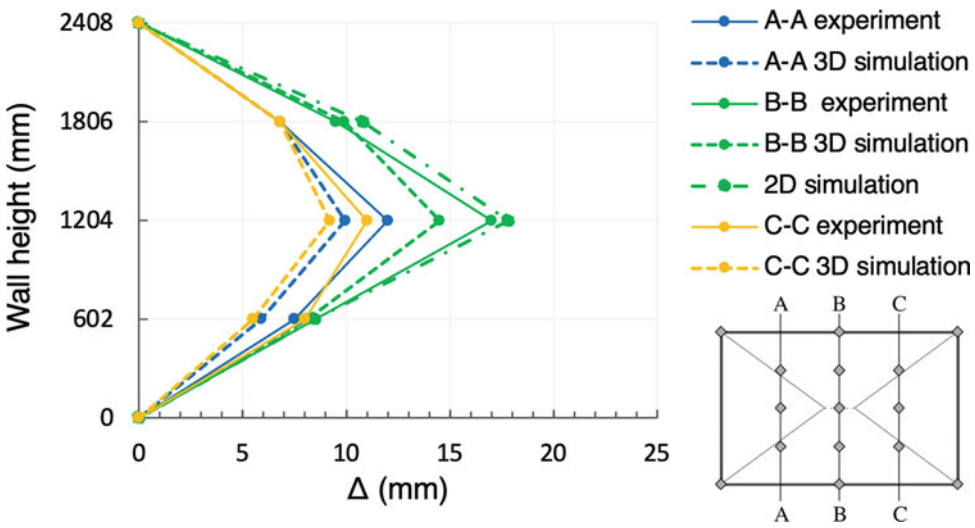

Fig. 8 Horizontal displacements computed through 3D and 2D MPM modelling compared to those measured at the ultimate strength of the wall (Fu = 30.5 kN) by Vaculik (2012)

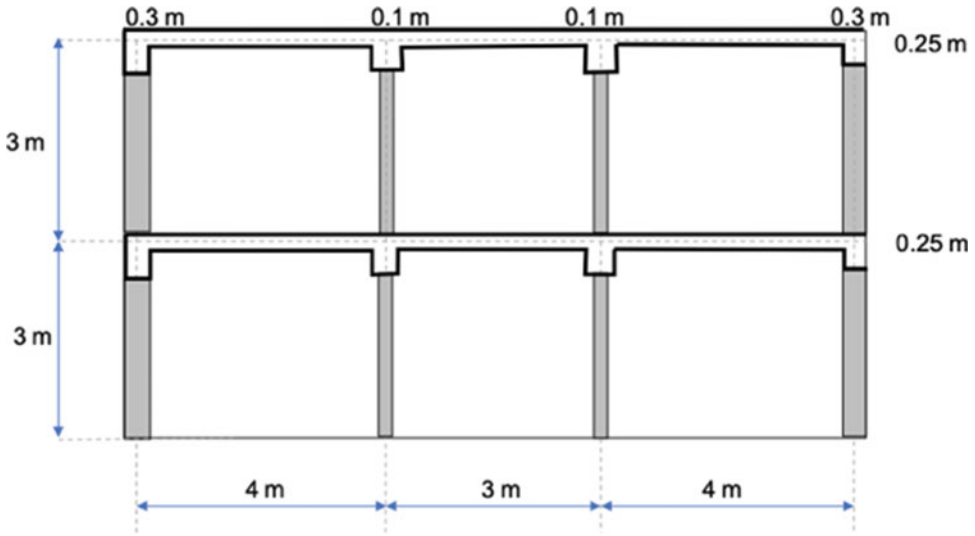

Fig. 9 Geometric schematization of the RC framed building with URM infill walls

However, it is worth remarking that the topic here is referred to landslides still catastrophic but not able to destroy the whole building. Hence, the present model may help for a preventive assessment inside the zones of the urban areas where building collapses are not expected while damage to non-structural elements may happen.

In such scenario, the type and the amount of damage must be properly evaluated to direct the actions for the emergency phase and to design the correct mitigation options for reinforcement and protection of the buildings.

7 Modelling Landslides Impacting a RC Wall

7.1 Input Scheme

This section investigates the failure mechanisms of a RC protection wall under the impact of a flow-like landslide (Fig. 14). The geometric configuration, the mechanical properties, smooth contact at the base, initial velocity and pore-water pressure of the landslide are the same proposed in the previous section.

The RC wall is schematized as a homogeneous material, with frictional contact at base and elasto-plastic behaviour. The wall is 6 m high with a foundation platform of 11 m (see Table 3 and Fig. 14 for dimensions details). The material properties used in the study were determined by Ardiaca (2009) from design regulations, considering the type of concrete with a characteristic compressive strength of 25 MPa. The base-concrete interface is handled with a frictional contact, imposing a coefficient equal to 0.67 (Ilori et al. 2017). The mechanical properties of the RC wall are: barrier density (ρ_b) equal to 2500 kg/m^3; effective friction angle (φ') of 35°; cohesion (c') as 510 kPa; Young's modulus (E) = 30,000 MPa; Poisson's ratio (ν) equal to 0.25; tensile strength (f_t) of 750 kPa and frictional coefficient ($\tan\delta_b$) equal to 0.24.

The computational unstructured mesh (Fig. 15) is made of 17,267 triangular elements with dimensions ranging from

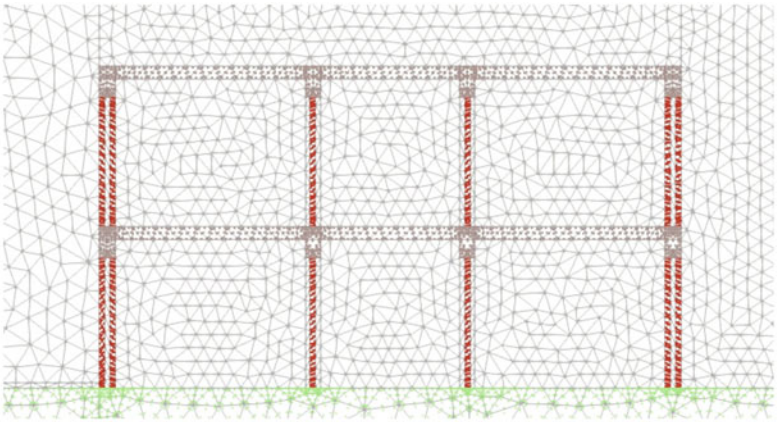

(a)

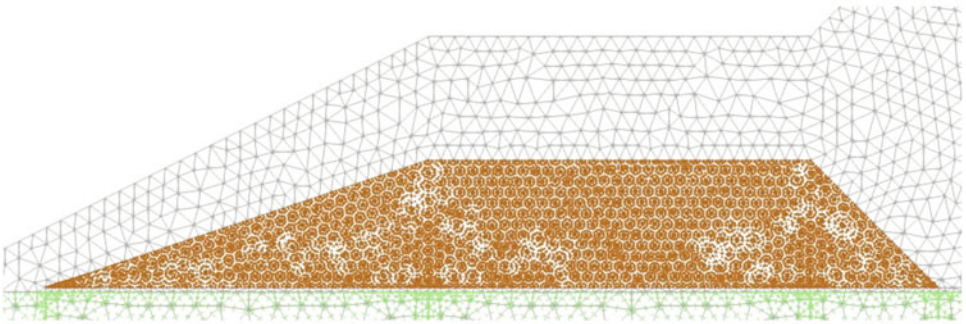

(b)

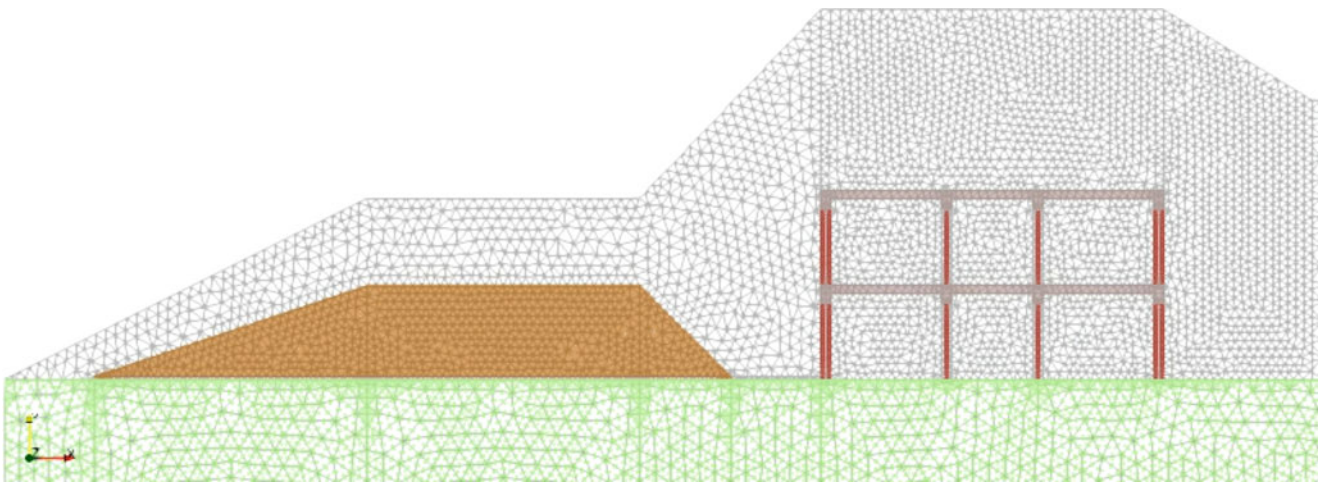

Fig. 10 Computational mesh of building (**a**) and landslide (**b**)

Fig. 11 Overall computational domain for the 2D modelling of the landslide and the two-storey building

0.10 (in the proximity of the wall and the impact area) to 0.50 m (elsewhere). The flow and the RC wall are modelled through the two-phase and one-phase single-point MPM formulation, respectively. Also here, the build-up of excess pore-pressure during the impact is considered as well as the hydromechanical coupling and the elasto-plastic failure criterion of the flow.

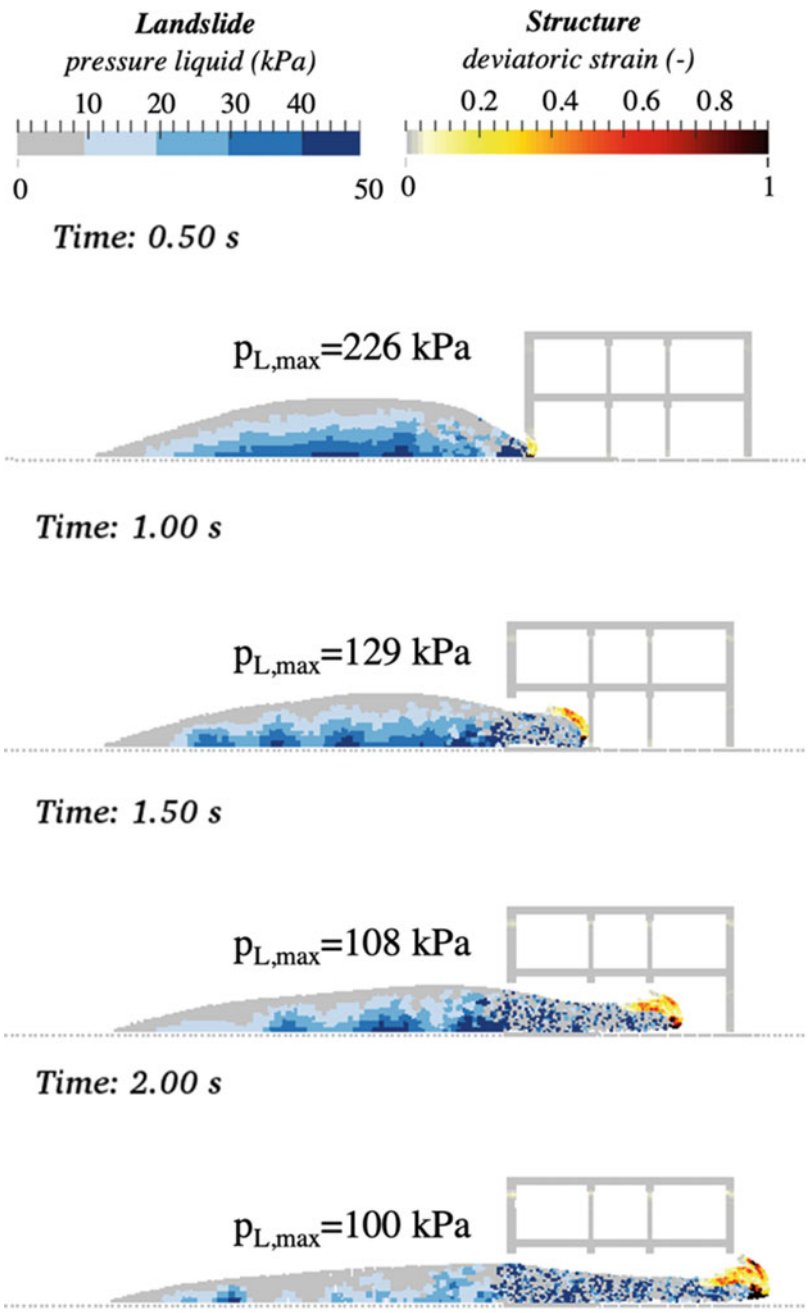

Fig. 12 Pore-water pressure (landslide) and deviatoric strain (infill walls) distribution during impact ($v_0 = 5$ m/s)

7.2 Numerical Results

Selected results are shown as the spatial distribution of pore-water pressure within the flow mass and the appearance of deviatoric deformations inside the structure. Firstly, the flow with initial velocity equal to 5 m/s is considered (Fig. 16).

At impact (t = 1.00 s) the pore-water pressure increases up to 288 kPa, then diminishes (t = 1.50 s) due to the beginning of wall mobilization and increases again (t = 2.00 s) due to the rising of the flow along the vertical column. After that, the liquid pressure is mostly decreasing, indicating that the landslide is losing kinetic energy. The internal shear deformations of the wall are practically nil; thus, the wall is subjected to a rigid translation with a final displacement equal to 0.90 m.

In the case of a faster flow (Fig. 17), the pore-water pressure at impact (t = 0.50–1.00 s) reaches higher values than before (up to 515 kPa), but in the following time lapse the values diminish drastically. Also here, there is a rigid translation of the wall exhibiting an excessive final displacement (12 m). However, deformations are relevant, causing a slight bensing of the column. A correct design of the barrier requires the coexistence of two mechanisms (shifting and bending) in a way that the barrier does not move too far, and the vertical wall does not bend too much. However, the structure seems to completely stop the entire propagating mass, since the amount of flow material that exceed the barrier is very few, therefore the effectiveness of preventing the overtopping of the barrier is very high.

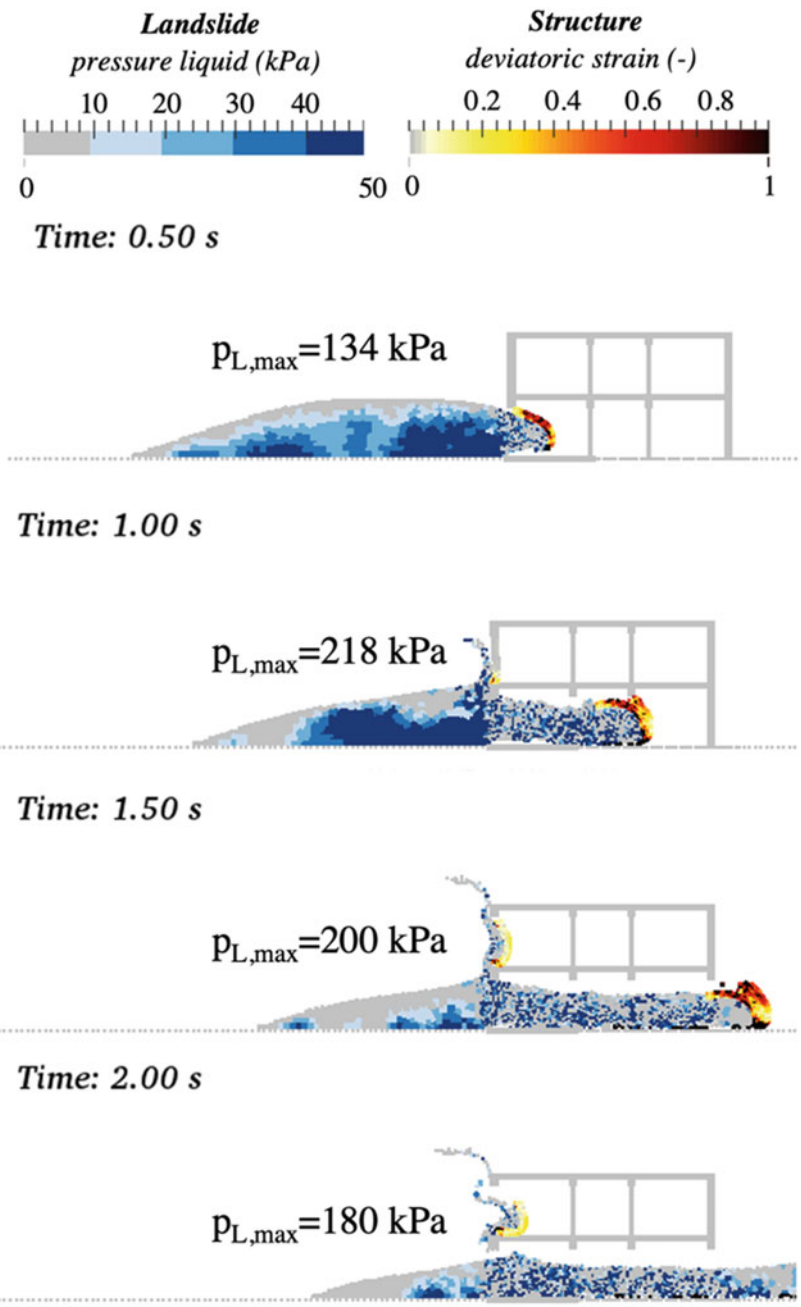

Fig. 13 Pore-water pressure (landslide) and deviatoric strain (infill walls) distribution during impact ($v_0 = 10$ m/s)

8 Modelling Landslides Impacting a Deformable Barrier

8.1 Input Scheme

The interaction between the landslide and a Deformable Geosynthetics-Reinforced Barrier (DGRB) is analysed (Fig. 18), with the same mechanical and geometric features of the flow used before.

A full numerical analysis of the geosynthetics-reinforced soil structure is quite complex since modelling each component and their interactions is challenging. Thus, an equivalent approach is here employed to analyse the DGRB. A composite reinforced soil properties is considered and with less input parameters needed. However, localized failures cannot be reproduced, as the individual material properties are not considered and the interaction between the soil and the reinforcement cannot be studied independently.

The assessment of the elasto-plastic parameters to set for the equivalent approach is carried out considering the internal friction angle (φ'), Young's modulus (E) and Poisson's ratio (ν) of the equivalent material equal to those typically

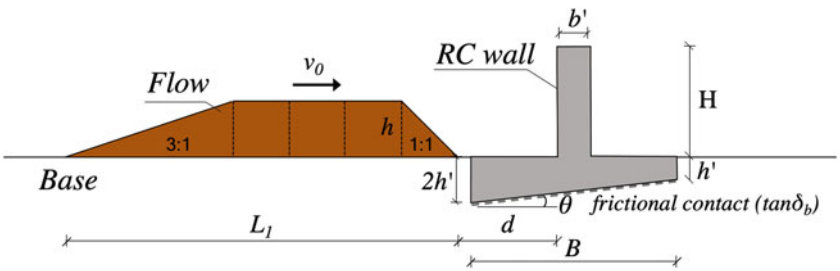

Fig. 14 Geometric schematization for the LSI numerical simulations with RC walls

Table 3 Geometric features of the RC wall

$\theta_{found.}$ (°)	d (m)	B (m)	b' (m)	H (m)	h' (m)	V (m^3/m)
0	3	11	1.80	6	1.20	24

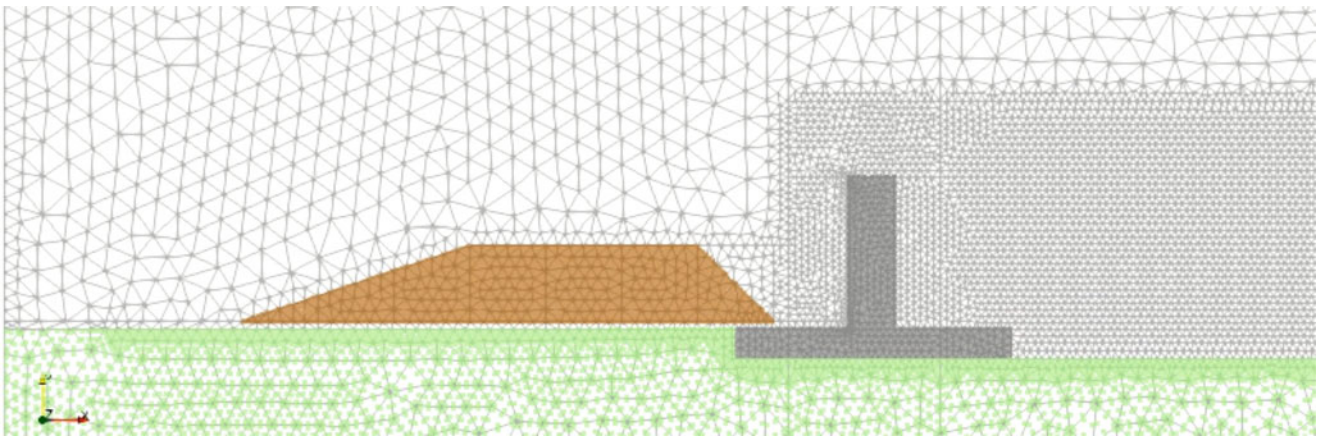

Fig. 15 Computational domain for the 2D MPM modelling of the landslide and the RC wall

employed for the backfill soil for practical applications. In addition, a tensile strength equal to the ultimate shear resistance of the geosynthetics reinforcement is imposed for this equivalent material. What is the most difficult to determine is the cohesion value. In such equivalent approach, the cohesion in the reinforced zone is increased using pseudo cohesion or anisotropic cohesion approach which states that the additional strength of the reinforced soil can be imparted by an apparent anisotropic cohesion (Nguyen et al. 2021; Maji et al. 2016). In this study, the value of cohesion was found by making sure that the Factor of Safety (FS) under gravity load obtained for the composite structure is the same than in the equivalent model.

The barrier is 6 m high, 11 m wide and the inclination of the impacted side is 70° (Table 4). The failure behaviour is non-associative (zero dilatancy) elasto-plastic criterion.

The mechanical properties chosen for the barrier are: the barrier density (ρ_b) equal to 2000 kg/m^3; effective friction angle (φ') of 38°; cohesion (c') as 58 kPa; Young's modulus (E) equal to 15 MPa; Poisson's ratio (ν) equal to 0.25; tensile strength (f_t) of 100 kPa and frictional coefficient ($\tan\delta_b$) equal to 0.29. The frictional resistance along the base is set equal to the 80% of the strength properties of the base material (Cuomo et al. 2019).

The homogeneous barrier with the achieved cohesion equal to 58 kPa represents a composite structure with FS = 3.73 under gravity load. The factor of safety is calculated through LEM analysis, with Morgenstern-Price method.

The flow and barrier are modelled through the single-point MPM formulation, respectively with two-phase and one-phase. The computational unstructured mesh is made of 16,356 triangular elements with dimensions ranging from 0.10 (to refine the impact zone) to 0.50 m (Fig. 19).

Also in this case, the landslide is assumed as approaching the barrier with a fixed geometric configuration and constant velocity (5 and 10 m/s), until LSI begins.

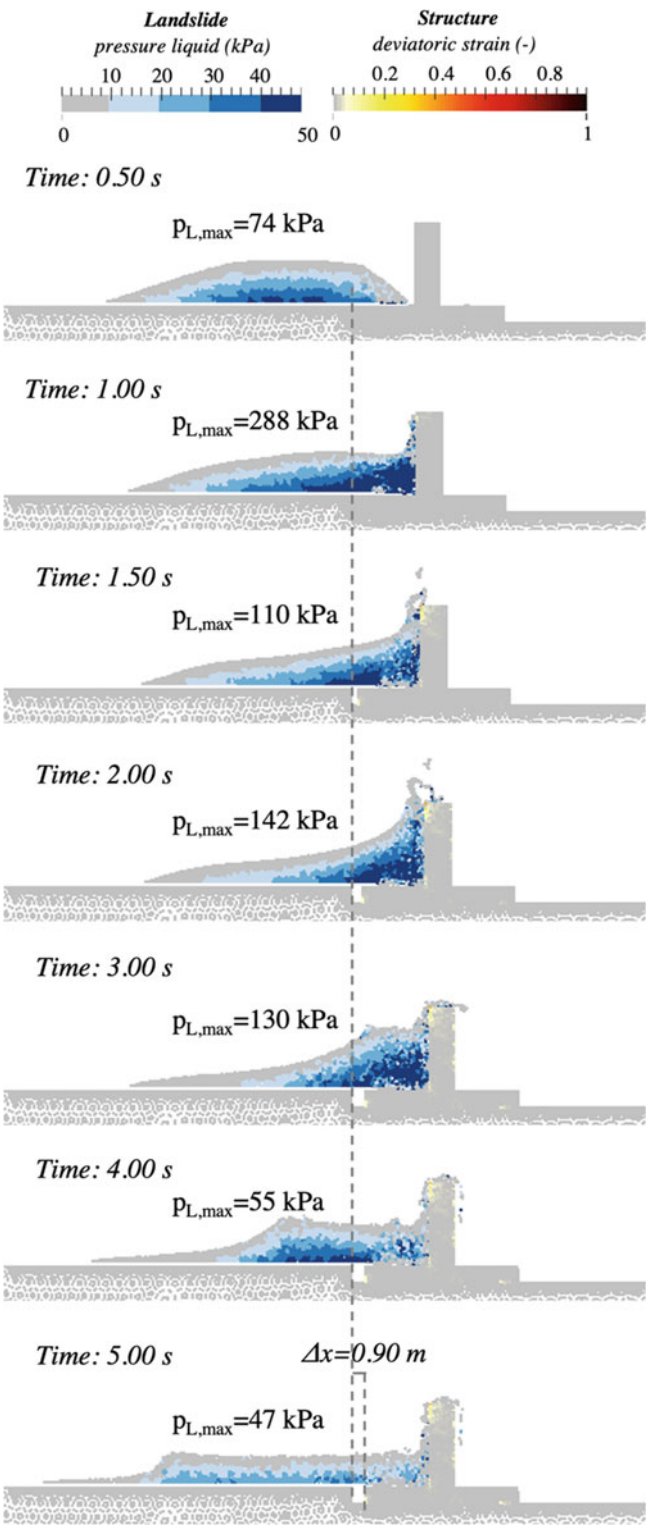

Fig. 16 Pore-water pressure (landslide) and deviatoric strain (RC wall) distribution during impact ($v_0 = 5$ m/s)

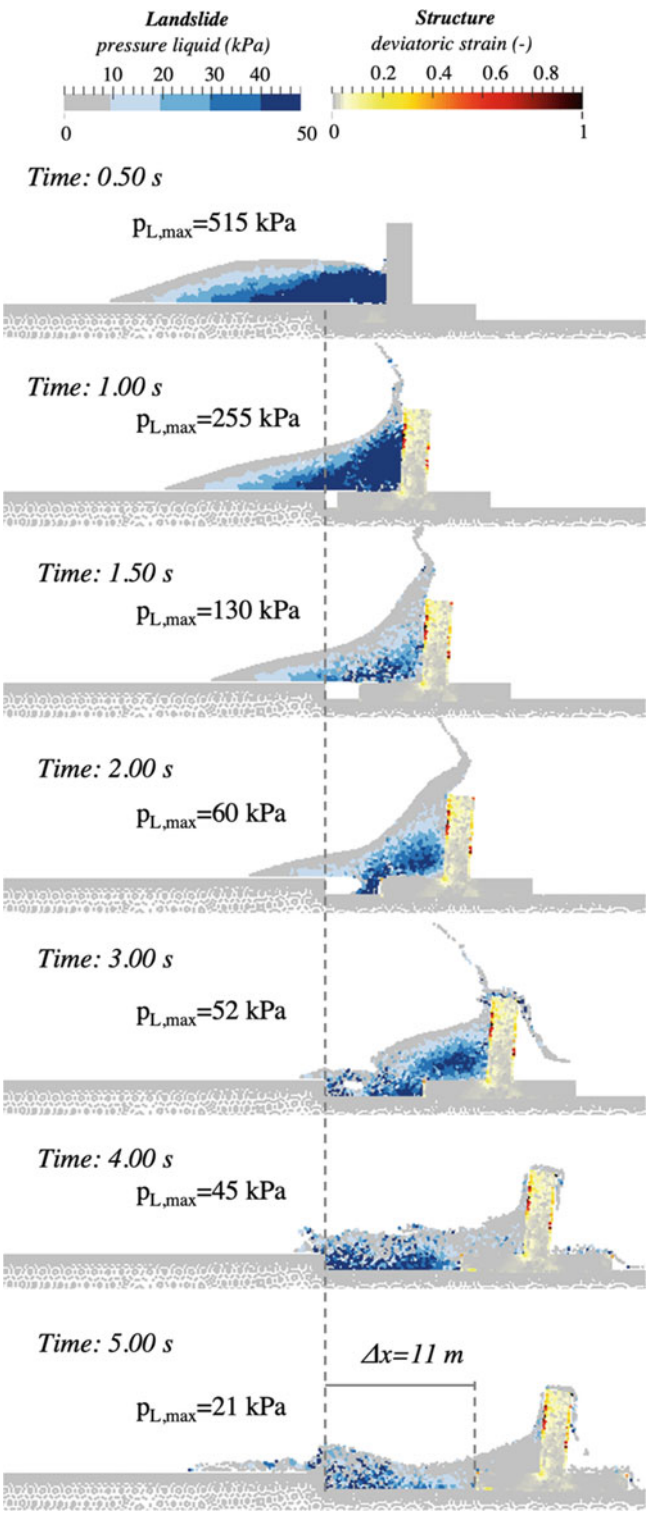

Fig. 17 Pore-water pressure (landslide) and deviatoric strain (RC wall) distribution during impact ($v_0 = 10$ m/s)

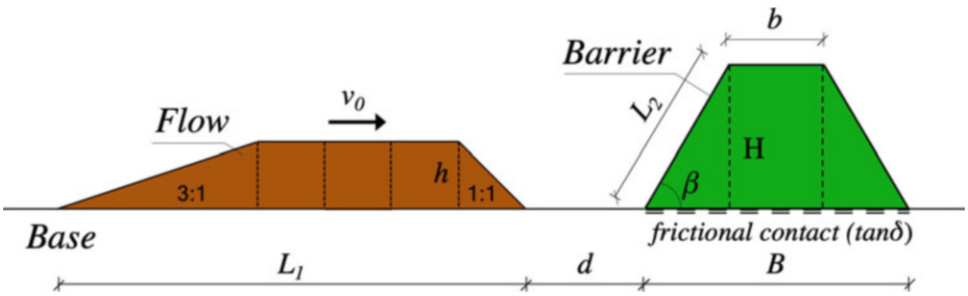

Fig. 18 Geometric schematization for the LSI numerical simulations with deformable barrier

Table 4 Geometric features of the barrier

β (°)	d (m)	L_2 (m)	B (m)	b (m)	H (m)	V (m^3/m)
70	3	6.39	11	6.63	6	52.89

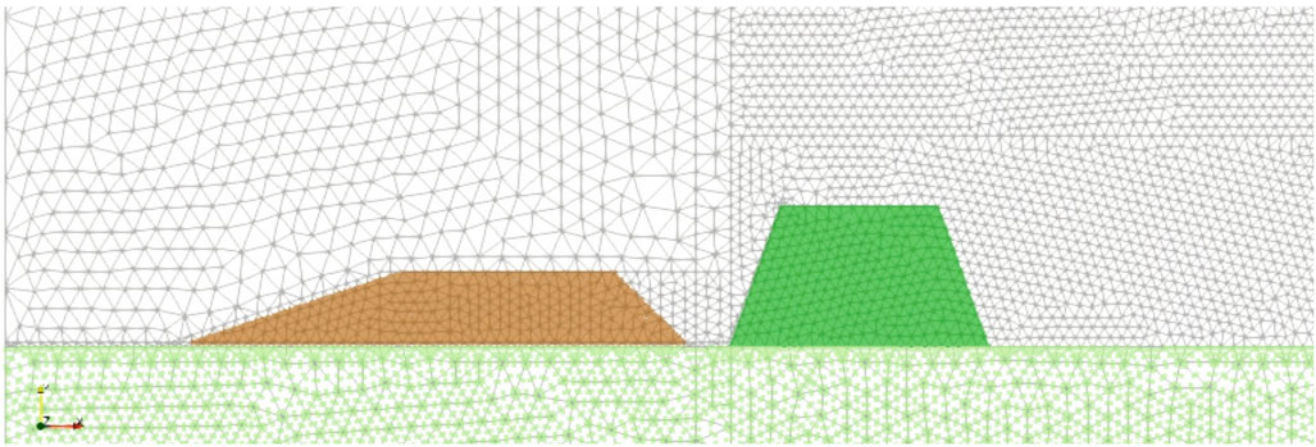

Fig. 19 Computational domain for the 2D MPM modelling of the landslide and the deformable barrier

8.2 Numerical Results

The results of pore-water pressure (landslide) and deviatoric strain (barrier) are reported first for the flow with low initial velocity (Fig. 20). In particular, the liquid pressure reaches the maximum value of 153 kPa after some instants from impact (t = 1.00 s). This is probably related to the increase of the impacted area. Simultaneously, the shear deformations along the impacted side are growing.

For t > 1.50 s, the kinetic energy of the flow decreases and this is well understandable from the lower values of $p_{L,max}$ and from the unchanging deformations inside the barrier. Moreover, the barrier does not show any horizontal displacement and all the flow is completely block by the barrier.

In the case of a faster flow (Fig. 21) the results are quite different, since the maximum value of $p_{L,max}$ is higher than before (386 kPa) and it is reached at t = 0.50 s. The deviatoric strains inside the impacted zone are larger than Fig. 20.

At t = 1.00 s, the barrier begins to move and thus the pore-water pressure drastically decreases. Then the run-up of the landslide along the barrier side generates some compression and therefore the liquid pressure increases again (t = 1.50 s). At the same time, the deviatoric plastic deformations begin widespread in the upper zone of the barrier due to the impact of the downward flow. After that, the landslide dissipates more and more kinetic energy and therefore pore-water pressure diminishes and the deviatoric strains inside the structure remain unchanged.

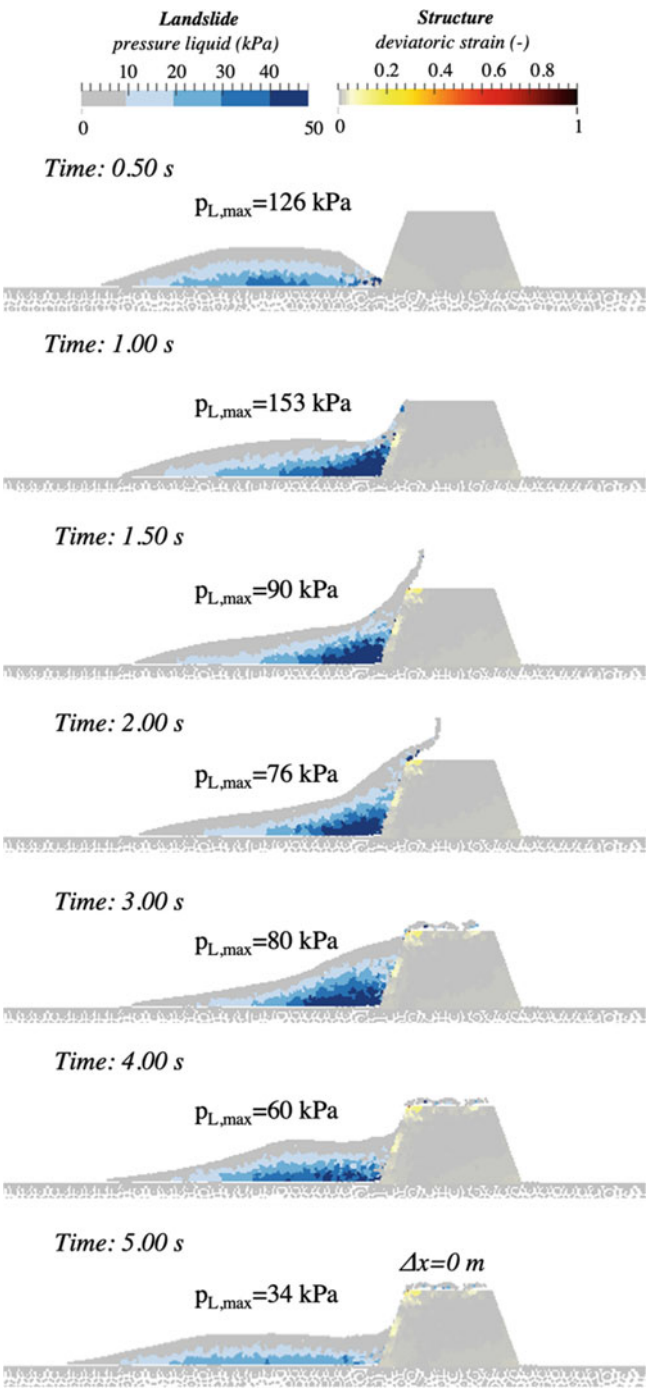

Fig. 20 Pore-water pressure (landslide) and deviatoric strain (barrier) distribution during impact ($v_0 = 5$ m/s)

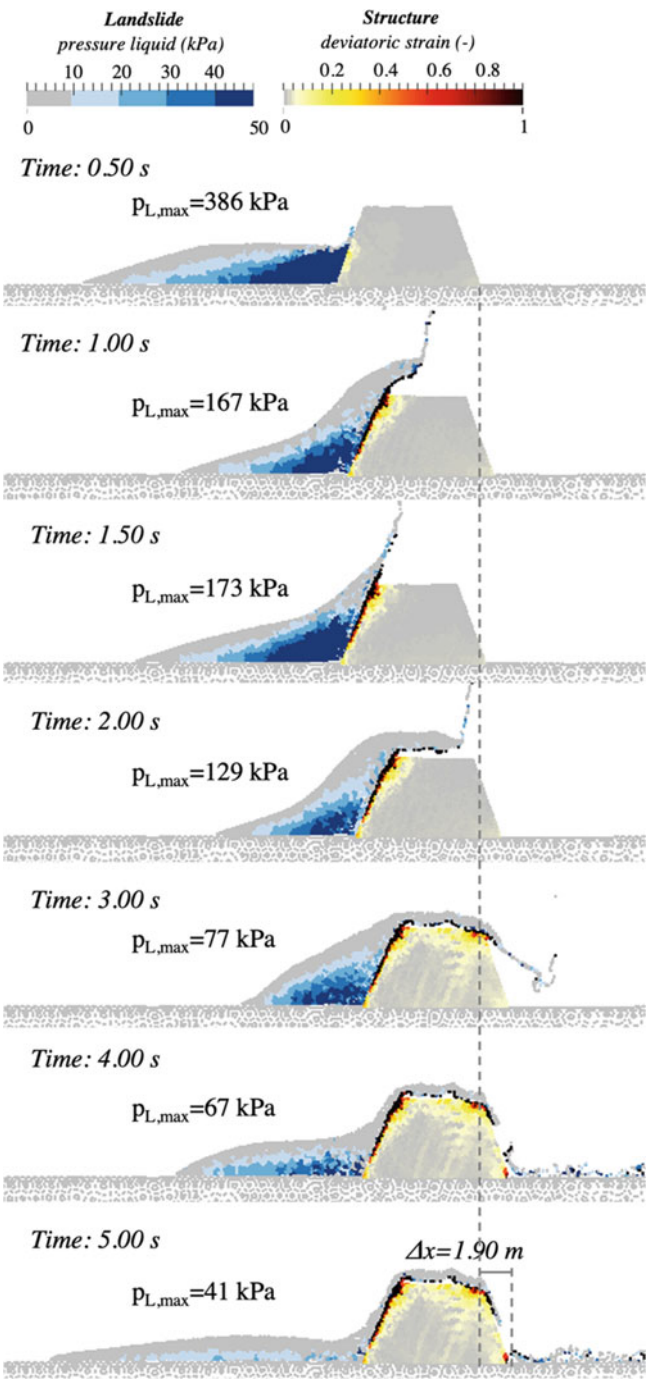

Fig. 21 Pore-water pressure (landslide) and deviatoric strain (barrier) distribution during impact ($v_0 = 10$ m/s)

The deformable barrier with these geometric characteristics can withstand the potential of the flow, showing a plausible displacement of 1.90 m and retaining a large amount of flow volume. However, the acceptability threshold of the barrier final displacement must be evaluated from site to site.

9 Concluding Remarks

The paper proposed a comparative numerical modelling, based on Material Point Method (MPM), relative to the impact of flow-like landslides against different types of structures like a two-strorey building, a Reinforced Concrete

Table 5 Maximum pore water pressure (liquid pressure, $p_{L,max}$) inside the landslide body at different time lapses, and maximum horizontal displacement (Dx) of the structure during the Landslide-Structure Interaction (LSI)

	$p_{L,max}$ (kPa)					
	v = 5 m/s			v = 10 m/s		
t (s)	Building	RC wall	DGRB	Building	RC wall	DGRB
0	0	0	0	0	0	0
0.5	226	74	126	134	515	386
1	129	288	153	218	255	167
1.5	108	110	90	200	130	173
2	100	142	76	180	60	129
3	–	130	80	–	52	77
4	–	55	60	–	45	67
5	–	47	34	–	21	41
LSI, Dx (m)	Failure	0.9	0	Failure	11.0	1.90

(RC) protection wall, and a Deformable Geosynthetics-Reinforced Barrier (DGRB).

The numerical MPM-based modelling of LSI for those different types of structures outlined that landslide pore water pressure largely increase in the early stages of the impact ($t < 1$ s), while reducing later dependent on landslide deformation plus propagation (Table 5) and related also to the displacement plus deformation of the protection structure.

The excess pore water pressure generated during the Landslide-Structure Interaction (LSI) is modelled, and it is proved as an important mechanism contributing to landslide run-up, overtopping and structure displacement or disruption until failure or unserviceability condition.

Acknowledgments The research was developed also within the framework of Industrial Partnership PhD Course (POR Campania FSE 2014/2020). All the MPM simulations were performed using a version of Anura3D code developed by Deltares.

References

Al-Kafaji I (2013) Formulation of a dynamic material point method (MPM) for geomechanical problems. Ph.D. thesis, University of Stuttgart

Arattano M, Franzi LJNH (2003) On the evaluation of debris flows dynamics by means of mathematical models. Nat Hazards Earth Syst Sci 3(6):539–544

Ardiaca DH (2009) Mohr-Coulomb parameters for modelling of concrete structures. Plaxis Bull 25:12–15

Barbolini M, Domaas U, Faug T, Gauer P, Hákonardóttir KM, Harbitz CB, Rammer L (2009) The design of avalanche protection dams recent practical and theoretical developments

Baum RL, Savage WZ, Godt JW (2008) TRIGRS: a Fortran program for transient rainfall infiltration and grid-based regional slope-stability analysis, version 2.0. US Geol. Survey, Reston, VA, pp 2008–1159

Brunet G, Giacchetti G, Bertolo P, Peila D (2009) Protection from high energy rockfall impacts using Terramesh embankment: design and experiences. Proceedings of the 60th Highway Geology Symposium, Buffalo, NY, pp 107–124

Bugnion L, McArdell BW, Bartelt P, Wendeler C (2012) Measurements of hillslope debris flow impact pressure on obstacles. Landslides 9(2):179–187

Bui HH, Fukagawa R (2013) An improved SPH method for saturated soils and its application to investigate the mechanisms of embankment failure: case of hydrostatic pore-water pressure. Int J Numer Anal Methods Geomech 37(1):31–50

Calvetti F, Di Prisco CG, Vairaktaris E (2017) DEM assessment of impact forces of dry granular masses on rigid barriers. Acta Geotech 12(1):129–144

Canelli L, Ferrero AM, Migliazza M, Segalini A (2012) Debris flow risk mitigation by the means of rigid and flexible barriers–experimental tests and impact analysis. Nat Hazards Earth Syst Sci 12(5):1693–1699

Cascini L, Cuomo S, De Santis A (2011) Numerical modelling of the December 1999 Cervinara flow-like mass movements (Southern Italy). Ital J Eng Geol Environ 635644

Ceccato F, Yerro A, Martinelli M (2018) Modelling soil-water interaction with the Material Point Method. Evaluation of single-point and double-point formulations. NUMGE, 25–29 June. Porto, Portugal

Chen Z, Song D (2021) Numerical investigation of the recent Chenhecun landslide (Gansu, China) using the discrete element method. Nat Hazards 105(1):717–733

Cui P, Zeng C, Lei Y (2015) Experimental analysis on the impact force of viscous debris flow. Earth Surf Process Landf 40(12):1644–1655

Cuomo S (2020) Modelling of flowslides and debris avalanches in natural and engineered slopes: a review. Geoenviron Disasters 7(1):1–25

Cuomo S, Calvello M, Villari V (2015) Inverse analysis for rheology calibration in SPH analysis of landslide run-out. In: Engineering geology for society and territory, vol 2. Springer, Cham, pp 1635–1639

Cuomo S, Iervolino A (2016) Investigating the role of stratigraphy in large-area physically-based analysis of December 1999 Cervinara shallow landslides. J Mt Sci 13(1):104–115

Cuomo S, Moretti S, Aversa S (2019) Effects of artificial barriers on the propagation of debris avalanches. Landslides 16(6):1077–1087

Cuomo S, Moretti S, Frigo L, Aversa S (2020a) Deformation mechanisms of deformable geosynthetics-reinforced barriers (DGRB) impacted by debris avalanches. Bull Eng Geol Environ 79:659–672

Cuomo S, Di Perna A, Martinelli M (2020b) MPM modelling of buildings impacted by landslides. In: Workshop on world landslide forum. Springer, Cham, pp 245–266

Cuomo S, Masi EB, Tofani V, Moscariello M, Rossi G, Matano F (2021a) Multiseasonal probabilistic slope stability analysis of a large area of unsaturated pyroclastic soils. Landslides 18(4): 1259–1274

Cuomo S, Di Perna A, Martinelli M (2021b) Modelling the spatio-temporal evolution of a rainfall-induced retrogressive landslide in an unsaturated slope. Eng Geol 294:106371

Cuomo S, Di Perna A, Martinelli M (2021c) MPM hydro-mechanical modelling of flows impacting rigid walls. Can Geotech J 58(11): 1730–1743

Cuomo S, Di Perna A, Martinelli M (2022) Analytical and numerical models of debris flow impact. Eng Geol 308:106818

Descoeudres F (1997) Aspects géomécaniques des instabilités de falaises rocheuses et des chutes de blocs. Publications De La Société Suisse De Mécanique Des Sols et Des Roches 135:3–11

Di Perna A, Cuomo S, Martinelli M (2022) Empirical formulation for debris flow impact and energy release. Geoenviron Disaster 9(1): 1–17

Dietrich WE, de Asua RR, Coyle J, Orr B, Trso M (1998) A validation study of the shallow slope stability model, SHALSTAB, in forested lands of Northern California. Stillwater Ecosystem, Watershed & Riverine Sciences. Berkeley, CA

Faella C, Nigro E (2003) Dynamic impact of the debris flows on the constructions during the hydrogeological disaster in Campania-1998: description and Analysis of the Damages. In: Proceedings of International Conference on Fast Slope Movements-Prediction and Prevention for Risk Mitigation (FSM2003), Napoli (Italy), pp 11–13

Fern E, Rohe A, Soga K, Alonso E (2019) The material point method for geotechnical engineering: a practical guide. CRC Press

Gioffrè D, Mandaglio MC, di Prisco C, Moraci N (2017) Evaluation of rapid landslide impact forces against sheltering structures. Rivista Italiana Geotecnica 3:79–91

Graziotti F, Tomassetti U, Sharma S, Grottoli L, Magenes G (2019) Experimental response of URM single leaf and cavity walls in out-of-plane two-way bending generated by seismic excitation. Constr Build Mater 195:650–670

Hong Y, Wang JP, Li DQ, Cao ZJ, Ng CWW, Cui P (2015) Statistical and probabilistic analyses of impact pressure and discharge of debris flow from 139 events during 1961 and 2000 at Jiangjia Ravine, China. Eng Geol 187:122–134

Hübl J, Suda J, Proske D, Kaitna R, Scheidl C (2009) Debris flow impact estimation. In: Proceedings of the 11th international symposium on water management and hydraulic engineering, Ohrid, Macedonia, vol 1, pp 1–5

Hulse R, Ambrose RJ, Lumbard P (1982) The shear strength of bricks and brickwork. In: 6th International Brick/Block Masonry Conference, pp 16–32

Hutchinson JN (1986) A sliding–consolidation model for flow slides. Can Geotech J 23(2):115–126

Ilori AO, Udoh NE, Umenge JI (2017) Determination of soil shear properties on a soil to concrete interface using a direct shear box apparatus. Int J Geo-eng 8(1):1–14

Jassim I, Stolle D, Vermeer P (2013) Two-phase dynamic analysis by material point method. Int J Numer Anal Methods Geomech 37(15): 2502–2522

Leonardi A, Wittel FK, Mendoza M, Vetter R, Herrmann HJ (2016) Particle-fluid-structure interaction for debris flow impact on flexible barriers. Comput Aided Civ Inf Eng 31(5):323–333

Li X, Zhao J, Soga K (2021) A new physically based impact model for debris flow. Géotechnique 71(8):674–685

Lizárraga JJ, Frattini P, Crosta GB, Buscarnera G (2017) Regional-scale modelling of shallow landslides with different initiation mechanisms: sliding versus liquefaction. Eng Geol 228:346–356

Luo H, Baum JD, Löhner R (2008) A discontinuous Galerkin method based on a Taylor basis for the compressible flows on arbitrary grids. J Comput Phys 227(20):8875–8893

Magenes G, Calvi GM (1992) Cyclic behaviour of brick masonry walls. In: Proceedings of the 10th world conference on earthquake engineering, pp 3517–3522

Maji VB, Sowmiyaa VS, Robinson RG (2016) A simple analysis of reinforced soil using equivalent approach. Int J Geosynthetics Ground Eng 2(2):1–12

Martinelli M, Galavi V (2022) An explicit coupled MPM formulation to simulate penetration problems in soils using quadrilateral elements. Comput Geotech 145:104697

Mast CM, Mackenzie-Helnwein P, Arduino P, Miller GR, Shin W (2012) Mitigating kinematic locking in the material point method. J Comput Phys 231(16):5351–5373

Mavrouli O, Fotopoulou S, Pitilakis K, Zuccaro G, Corominas J, Santo A et al (2014) Vulnerability assessment for reinforced concrete buildings exposed to landslides. Bull Eng Geol Environ 73(2): 265–289

Mieremet MMJ, Stolle DF, Ceccato F, Vuik C (2016) Numerical stability for modelling of dynamic two-phase interaction. Int J Numer Anal Methods Geomech 40(9):1284–1294

Moriguchi S, Borja RI, Yashima A, Sawada K (2009) Estimating the impact force generated by granular flow on a rigid obstruction. Acta Geotech 4(1):57–71

Ng CW, Choi CE, Majeed U, Poudyal S, De Silva WARK (2019) Fundamental framework to design multiple rigid barriers for resisting debris flows. In: Proceedings of the 16th Asian regional conference on soil mechanics and geotechnical engineering, 14–18 October

Ng CWW, Majeed U, Choi CE, De Silva WARK (2021a) New impact equation using barrier Froude number for the design of dual rigid barriers against debris flows. Landslides 18(6):2309–2321

Ng CW, Liu H, Choi CE, Kwan JS, Pun WK (2021b) Impact dynamics of boulder-enriched debris flow on a rigid barrier. J Geotech Geoenviron 147(3):04021004

Nguyen TS, Yang KH, Ho CC, Huang FC (2021) Postfailure characterization of shallow landslides using the material point method. Geofluids 2021

Pastor M, Haddad B, Sorbino G, Cuomo S, Drempetic V (2009) A depth-integrated, coupled SPH model for flow-like landslides and related phenomena. Int J Numer Anal Methods Geomech 33(2): 143–172

Scheidl C, Chiari M, Kaitna R, Müllegger M, Krawtschuk A, Zimmermann T, Proske D (2013) Analysing debris-flow impact models, based on a small scale modelling approach. Surv Geophys 34(1):121–140

Scotton P, Deganutti AM (1997) Phreatic line and dynamic impact in laboratory debris flow experiments. In: Debris-flow hazards mitigation: mechanics, prediction, and assessment. ASCE, pp 777–786

Shen W, Zhao T, Zhao J, Dai F, Zhou GG (2018) Quantifying the impact of dry debris flow against a rigid barrier by DEM analyses. Eng Geol 241:86–96

Song D, Zhou GG, Chen XQ, Li J, Wang A, Peng P, Xue KX (2021) General equations for landslide-debris impact and their application to debris-flow flexible barrier. Eng Geol 288:106154

Sulsky D, Zhou SJ, Schreyer HL (1995) Application of a particle-in-cell method to solid mechanics. Comput Phys Commun 87(1–2): 236–252

Tofani V, Bicocchi G, Rossi G, Segoni S, D'Ambrosio M, Casagli N, Catani F (2017) Soil characterization for shallow landslides modeling: a case study in the Northern Apennines (Central Italy). Landslides 14(2):755–770

Vaculik J (2012) Unreinforced masonry walls subjected to out-of-plane seismic actions (Doctoral dissertation)

Varela-Rivera J, Moreno-Herrera J, Lopez-Gutierrez I, Fernandez-Baqueiro L (2012) Out-of-plane strength of confined masonry walls. J Struct Eng 138(11):1331–1341

Wei X, Stewart MG (2010) Model validation and parametric study on the blast response of unreinforced brick masonry walls. Int J Impact Eng 37(11):1150–1159

Yerro A (2015) MPM modelling of landslides in brittle and unsaturated soils. PhD Dissertation, UPC, Spain

Yong AC, Lam C, Lam NT, Perera JS, Kwan JS (2019) Analytical solution for estimating sliding displacement of rigid barriers subjected to boulder impact. J Eng Mech 145(3):04019006

Landslide Research and Technology in International Standards

Matjaž Mikoš

Abstract

Science, Technology, and Innovation play a pivotal role in the Sendai Framework for Disaster Risk Reduction 2015–2030 (SF DRR). The International Consortium on Landslides (ICL) initiated the Sendai Landslide Partnerships 2015–2025 as a voluntary commitment to SF DRR. In 2020, the ICL launched the Kyoto 2020 Commitment for Global Promotion of Understanding and Reducing Landslide Disaster Risk (KLC2020) as a follow-up of the Sendai Landslide Partnerships 2015–2025.

Landslide-related scientific articles discussing methodologies were extracted from the Web of Science and SCOPUS, using different search terms in the article titles, abstracts, and keywords. SCOPUS yielded a somewhat higher number of extracted articles, especially when using article abstracts. The extracted articles were mainly related to assessment, hazard, and risk, and less to vulnerability or damage.

A list of 22 international standards containing landslide-related terms (landslide, debris flow, rock fall) was prepared using the Online Browsing Platform by the International Organization for Standardization (ISO). This is a rather small fraction of over 22,000 ISO standards published so far. Next, two ISO standards are discussed in a more detailed way. Additionally, a set of Austrian standards in the field of torrent control are mentioned.

The International Consortium on Landslides with its global membership may contribute more to the field of standardization for landslide disaster risk reduction.

Keywords

Disaster risk reduction · Early warning systems · International standards · Landslides · Sustainable development goals

1 Introduction

Landslide risk assessment, landslide mitigation strategies and technologies should to some extent be harmonized and based on some standardized procedures or standardized engineering mitigation works, if we want to estimate a global situation and make comparisons between regions and/or countries; or even transfer good practices from one part of the world into another one.

For example, recognition of landslides through the visual analysis of stereoscopic aerial photography is an empirical and uncertain technique, and standards for it do not exist (Guzzetti et al. 2012). The authors stated that there is a need for standardized landslide maps. Furthermore, the United States Geological Survey report from 2000 about the national landslide hazards mitigation strategy (USGS 2000) stated that in general, there are no standards for landslide hazard mapping and assessments in the USA. But spatial data used for risk assessment (i. e. spatial data infrastructure), also in the field of landslide disaster risk assessment, need to be harmonized to make it possible interoperability for any international collaboration or comparison/exchange (Núñez-Andrés et al. 2022). Any inventory data for modelling of natural hazards should be kept in harmonized databases based on internationally recognized standards so that such data can be shared (Wirtz et al. 2014). The European directive INSPIRE (Infrastructure for Spatial Information in the European Community) (Directive 2007) is based on the International Organization for Standardization (ISO) standards (ISO 2006) required harmonization of EU databases to obtain interoperable services to access to the databases. For natural risk zones, there are technical

M. Mikoš (✉)
University of Ljubljana, UNESCO Chair on Water-Related Disaster Risk Reduction & Faculty of Civil and Geodetic Engineering, Ljubljana, Slovenia
e-mail: matjaz.mikos@fgg.uni-lj.si

I. Alcántara-Ayala et al. (eds.), *Progress in Landslide Research and Technology, Volume 2 Issue 1, 2023*,
Progress in Landslide Research and Technology, https://doi.org/10.1007/978-3-031-39012-8_7

guidelines for data specification on natural risk zones (INSPIRE 2013). European geological surveys are nowadays using the INSPIRE directive to harmonize their landslide databases (Herrera et al. 2018). The INSPIRE directive is also useful for development of multi-risk databases, which is the way to go to support multi-hazard risk assessment.

A landslide zoning methodology for Tasmania was developed by Mazengarb and Stevenson (2010) following the Guideline for landslide susceptibility, hazard and risk zoning for land use planning, produced by the Australian Geomechanics Society (AGS 2007a, b).

Choi and Cheung (2013), when discussing man-made slopes in Hong Kong susceptible to landsliding during periods of high seasonal rainfall, reported that prior to 1977, this situation was exacerbated by the lack of proper engineering standards in their design and construction.

Ortigao and Sayao (2004) in the Handbook on Slope Stabilization is mentioning standards, looking into the Subject Index, only in case of drilling and standard drilling diameter. Bobrowsky (2013) in Encyclopedia on Natural Hazards as the major reference work is mentioning standards, looking into the Subject Index, only when referring to building codes and standards. Bobrowsky and Marker (2018) in the Encyclopedia of Engineering Geology as the major reference work has only a few mentions of ISO standards, mainly in the context of diverse laboratory and field testing. In this encyclopedia, Van Westen (2018) wrote a contribution on Risk Mapping, stating that ISO 31000:2009 (revised as ISO 31000:2018) defines risk assessment as a process made up of three processes: risk identification, risk analysis, and risk evaluation.

The Indian National Landslide Risk Management strategy (NDMA 2019), based on wide spread property loss during recent landslides stated that most of the construction plans are ill-conceived and do not follow standard norms for landslide safety. Therefore, it recommends that the existing bylaws and regulations at local body or state level in India should be incorporated in the National Landslide Mitigation Policy and the National Landslide Mitigation Strategy.

Genevois et al. (2022) recognized the importance of standardization for the design of remediation works for mitigation and prevention against geological hazards: "*The choice of the most appropriate and cost-effective intervention must consider the type of hazard and environmental issues, and selects, wherever possible, naturalistic engineering operations that are consequently implemented according to the environmental regulations or the design and specification standards imposed by the competent public administrations*".

1.1 The Focus of This Study

A wide topic of landslide guidelines was recently covered e.g. by Flentje et al. (2007), Fell et al. (2008), and later Wang et al. (2013), who found in their review paper more than 30 such guidelines from around the globe. Landslide guidelines and best practices for professional engineers and geoscientists were also studied by Bobrowsky et al. (2014). Corominas et al. (2014) published recommendations for the quantitative analysis of landslide risk.

Some methodologies or guidelines are further developed and approved as international standards. The aim of this paper was focused on international standards. In this paper, the following research questions were the starting point for the study:

- Is standardization mentioned in important landslide-related international documents, such as the Sendai Framework for Disaster Risk Reduction, and the United Nations 2030 Agenda for Sustainable Development.
- Are there in the International Organization for Standardization (ISO) database with international standards documents related to landslide research, practice and technological applications for landslide disaster risk reduction.

2 Materials and Methods

2.1 Landslide Disaster Risk Reduction and the Sendai Framework for Disaster Risk Reduction 2015–2030

The Sendai Framework was adopted at the Third UN World Conference on Disaster Risk Reduction in Sendai, Japan in 2015. It outlines seven targets and four priorities for action to prevent new and reduce existing disaster risks (SF DRR 2015).

The methodologies and models for risk assessment is mentioned in the SF DRR text under Priority 1: Understanding disaster risk, namely at national and local levels: "*24 (j) To strengthen technical and scientific capacity to capitalize on and consolidate existing knowledge and to develop and apply methodologies and models to assess disaster risks, vulnerabilities and exposure to all hazards.*"

The development of standards is mentioned in the SF DRR under:

i) Priority 2: Strengthening disaster risk governance to manage disaster risk, namely at national and local levels: "*27 (j) To promote the development of quality standards, such as certifications and awards for disaster risk management, with the participation of the private sector, civil society, professional associations, scientific organizations and the United Nations.*", and
ii) Priority 3: Investing in disaster risk reduction for resilience, namely at national and local levels, it is important: "*30(h) To encourage the revision of existing or the development of new building codes and standards and rehabilitation and reconstruction practices at the national or local levels, as appropriate, with the aim of making them more applicable within the local context, particularly in informal and marginal human settlements, and reinforce the capacity to implement, survey and enforce such codes through an appropriate approach, with a view to fostering disaster-resistant structures."*
iii) Priority 4: Enhancing disaster preparedness for effective response and to "Build Back Better" in recovery, rehabilitation and reconstruction, namely at national and local levels, it is important: "*33(j) To promote the incorporation of disaster risk management into post-disaster recovery and rehabilitation processes, facilitate the link between relief, rehabilitation and development, use opportunities during the recovery phase to develop capacities that reduce disaster risk in the short, medium and long term, including through the development of measures such as land-use planning, structural standards improvement and the sharing of expertise, knowledge, post-disaster reviews and lessons learned and integrate post-disaster reconstruction into the economic and social sustainable development of affected areas. This should also apply to temporary settlements for persons displaced by disasters.*" and "*33(k) To develop guidance for preparedness for disaster reconstruction, such as on land-use planning and structural standards improvement, including by learning from the recovery and reconstruction programmes over the decade since the adoption of the Hyogo Framework for Action, and exchanging experiences, knowledge and lessons learned.*"
iv) Furthermore, technical standards are mentioned in the section V. Role of stakeholders in the manner that States should encourage actions such as: "*36(c) Business, professional associations and private sector financial institutions, including financial regulators and accounting bodies, as well as philanthropic foundations, … actively participate, as appropriate and under the guidance of the public sector, in the development of normative frameworks and technical standards that incorporate disaster risk management.*"
v) Also support from international organizations is covered by: "*48(c) The United Nations Office for Disaster Risk Reduction, in particular, to support the implementation, follow-up and review of the present Framework by: … reinforcing a culture of prevention among relevant stakeholders through supporting development of standards by experts and technical organizations, advocacy initiatives and dissemination of disaster risk information, policies and practices, as well as by providing education and training on disaster risk reduction through affiliated organizations …*"

2.2 Landslide Disaster Risk Reduction and the United Nations 2030 Agenda for Sustainable Development

The General Assembly of the United Nations adopted in 2015 a resolution on the 2030 Agenda for Sustainable Development (UN 2015) and declared 17 Sustainable Development Goals (SDGs). Today, the Division for Sustainable Development Goals (DSDG) in the United Nations Department of Economic and Social Affairs (UNDESA) provides substantive support and capacity-building for the SDGs and their related thematic issues. The implementation of the 2030 Agenda for Sustainable Development and it 17 Sustainable Development Goals is supported by:

- A list of 169 targets of the 17 SDGs;
- A global indicator framework as contained in the UN resolution (UN 2017)—as of June 2022, it includes 231 unique indicators;
- The Global SDG Indicator Data Platform (https://unstats.un.org/sdgs/dataportal/)
- The annual SDG reports—as of June 2022, an advance unedited version of the SDG Progress Report 2022 is already available.

Strongly natural-hazard-related SDGs are:

- SDG9 Industry, Innovation and Infrastructure: "Build resilient infrastructure, promote inclusive and sustainable industrialization and foster innovation" with 8 targets, among them:
  - Target 9.1: Develop quality, reliable, sustainable and resilient infrastructure, including regional and transborder infrastructure, to support economic development and human well-being, with a focus on affordable and equitable access for all.
- SDG11 Sustainable Cities and Communities: "Make cities and human settlements inclusive, safe, resilient and sustainable" with 10 targets, among them:

  - Target 11.4: Strengthen efforts to protect and safeguard the world's cultural and natural heritage.
  - Target 11.5: By 2030, significantly reduce the number of deaths and the number of people affected and substantially decrease the direct economic losses relative to global gross domestic product caused by disasters, including water-related disasters, with a focus on protecting the poor and people in vulnerable situations.
  - Target 11.b: By 2020, substantially increase the number of cities and human settlements adopting and implementing integrated policies and plans towards inclusion, resource efficiency, mitigation and adaptation to climate change, resilience to disasters, and develop and implement, in line with the Sendai Framework for Disaster Risk Reduction 2015–2030, holistic disaster risk management at all levels.
- SDG13 Climate Action: "Take urgent action to combat climate change and its impacts" with its 5 targets, among them:
  - Target 13.1: Strengthen resilience and adaptive capacity to climate-related hazards and natural disasters in all countries.
  - Target 13.3: Improve education, awareness-raising and human and institutional capacity on climate change mitigation, adaptation, impact reduction and early warning.
- SDG15 Life on Land: "Protect, restore and promote sustainable use of terrestrial ecosystems, sustainably manage forests, combat desertification, and halt and reverse land degradation and halt biodiversity loss" with its 12 targets, among them:
  - Target 15.2: By 2020, promote the implementation of sustainable management of all types of forests, halt deforestation, restore degraded forests and substantially increase afforestation and reforestation globally.

Looking at the global indicator framework for SDGs, landslides are not mentioned in SDG indicators at all, they are covered by the more general term "disaster(s)".

In 2020, the Making Cities Resilient 2030 (UNDRR 2022) initiative was launched, supporting especially SDG11. ISO has supported these efforts by recently issuing three ISO standards on sustainable cities and communities in order for a city to recognize its level of resilience. The Intergovernmental Panel on Climate Change (IPCC 2012, p. 5) defines resilience as "the ability of a system and its component parts to anticipate, absorb, accommodate, or recover from the effects of a hazardous event in a timely and efficient manner, including through ensuring the preservation, restoration, or improvement of its essential basic structures and functions".

2.3 The International Organization for Standardization (ISO) and the United Nations 2030 Agenda for Sustainable Development Goals

A practical guide how the practical experience of regulatory authorities, governments and local administrations, as well as regional groups of countries are using standards towards sustainable development and the implementation of the Agenda 2030 was prepared by the United Nations Economic Commission for Europe (UNECE 2018).

The implementation of the UN SDGs is supported also by the International Organization for Standardization (ISO) and their over 22,000 standards (ISO 2018). A special web platform (ISO 2022b) was developed for stakeholders to search for any ISO standards that correspond to each of the 17 SDGs. Using ISO Advanced Search for Standards web page, for each of the SDGs, relevant ISO standards can be searched for, using keywords or phrases.

2.4 Landslide Definitions in International Standards

Hungr et al. (2014) have defined the variety of landslide forms, and described their visible signs to be recognized in the field as well as their peculiarities. Such a system to distinguish between different landslide forms is mainly used to systemize various landslide processes. When looking at international standards, such a fine-tuned system on landslide classification is not used at all, and the definitions are much more rudimentary.

The International Organization for Standardization (ISO) has launched a new Online Browsing Platform (OBP). With this search engine it is possible to access the most up-to-date contents in ISO standards, graphical symbols, codes or terms and definitions.

Using Online Browsing Platform (ISO 2022a) for looking for terms in ISO standard database, the terms are defined:

i) the term »landslides« is defined as:

- »wide variety of processes that result in the downward and outward movement of slope-forming materials including rock, soil, artificial fill or a combination of these« in two standards: ISO 22300:2021(en) and ISO 22327:2018(en)
- »phenomenon of rock mass, earth mass or debris moving down a slope under gravity" in one technical guidelines IWA 33-1:2019(en) 5.8;

ii) the term »debris flow« and "mudflow" is defined as:

– "sudden flood carrying a lot of solid matter like sediment and rocks, which takes place in a mountainous area, in most cases due to a rainstorm or intense melting of ice and snow" in one technical guidelines IWA 33-1:2019 (en) 5.12—the definition is given jointly for "debris flow" and "mudflow", no distinction is made;

iii) the term »rockfall« is defined as:

– "phenomenon of rock falling abruptly down a steep slope" in one technical guidelines IWA 33-1:2019(en) 5.9.

3 Results and Discussion

3.1 Methodologies for Landslide Disaster Risk Reduction

The two databases: Web of Science Core Collection (WoS) by Clarivate Analytics, and SCOPUS by Elsevier were used to look at the total number of landslide-related articles published in these two databases that discuss methodologies. For the WoS we used the following search term: "landslide* AND methodology*" in Title, Author keywords, Abstract, and Topic (title, abstract, author keywords, and Keywords Plus). For the SCOPUS we used the same search term: "landslide* AND methodology*" in Article Title (TITLE), Keywords (KEY), Abstract (ABS), and in Article title & Abstract & Keywords (TITLE-ABS-KEY).

The same approach was applied also for the terms "debris flow*", "mud flow*", "rockfall*" and "rock fall*", respectively. The total number of landslide-related articles in these two databases is shown in Table 1. Generally, as expected, more articles were found in SCOPUS than in Web of Science Core Collection (Clarivate 2022); especially when looking at article abstracts. Each of the collected groups of articles were further sub-categorized with respect whether they also contain one of the six landslide-related terms: susceptibility, hazard, vulnerability, damage, risk, and assessment. The most abundant were landslide-related articles containing also the terms hazard, risk, and assessment. Much less abundant were articles containing the terms susceptibility, vulnerability and damage (see Table 1 for details). The landslide-related articles about methodologies are rather general, covering hazard, risk, and hazard and risk assessment, and much less about methodologies for susceptibility, vulnerability and damage. From process point of view, the largest number of collected articles were related to landslide(s), followed by debris-flow(s)-related and rockfall-related articles; the least articles were found to be related to mud flow(s). We should remember that all collected articles were about methodologies.

A step in the direction of standardization in the field of landslide disaster risk reduction is also to develop (joint) methodologies for assessing different parameters relevant for landslide DRR. Klose et al. (2014, 2015) proposed a methodological approach to landslide cost modeling for transportation infrastructures.

3.2 Graphical Symbols for Landslides

There are only two registered landslide-related graphical symbols defined in ISO standard for graphical symbols ISO 7010:2019(en), namely sign W076 for warning of a "debris flow zone", and W078 for warning of a "Landslide zone", respectively:

– the former is used to warn of a zone where large debris flow or flash flooding can occur with the intention to understand the warning by: "*taking care in the vicinity of zones susceptible to flash flooding or debris flow following torrential or persistent heavy rainfall*", and
– the latter is used to warn of landslide or unstable slopes with the intention to understand the warning by: "*taking care in the vicinity of zones susceptible to landslides or unstable slopes following earthquake, heavy rain or stormy weather*".

A reference to these warning signs is given in ISO 22578: 2022(en).

A good overview of natural disaster safety way guidance system ISO/DIS 22578 is given on the web (Sanwa Sanko 2022).

3.3 Landslide-Related International Standards (ISO)

In Table 2 shown international standards are mentioning landslide-related terms to a different extent—it is more clearly related to landslides if the used term is mentioned in the section "1 Scope" of the standard.

There are though a few more specific international standards related to landslides. We will show two case studies in this regard on the basis of ISO standards. The third case study will be dedicated to the Austrian standards in the field of torrent control that cover broad field of landslide phenomena in mountain areas, including debris flows and rock falls.

Table 1 The total number of landslide-related articles discussing methodologies from Web of Science Core Collection and SCOPUS databases (as of the end of July 2022)

Web of Science Core Collection						
Total number	. . . article further related to:					
	Susceptibility	Hazard	Vulnerability	Damage	Risk	Assessment
*Landslide**						
Title: 84	18	12	3	2	13	15
Author keywords: 17	4	6	2	0	2	4
Abstract: 1443	353	523	137	243	476	460
Topic: 1900	596	953	219	316	732	786
*Debris flow**						
Title: 9	0	3	1	0	1	1
Author keywords: 4	1	1	1	0	1	0
Abstract: 349	39	119	29	66	99	99
Topic: 554	93	229	51	96	166	210
*Mud flow**						
Title: 0	0	0	0	0	0	0
Author keywords: 0	0	0	0	0	0	0
Abstract: 92	2	7	1	12	6	8
Topic: 115	5	9	2	13	11	15
Rockfall OR Rock fall**						
Title: 19	0	9	1	0	4	9
Author keywords: 3	1	2	1	0	1	0
Abstract: 293	29	113	21	44	91	87
Topic: 361	61	175	29	58	138	136
SCOPUS						
*Landslide**						
Article title: 115	20	17	3	2	22	20
Keywords: 247	49	86	23	16	70	101
Abstract: 2088	437	783	219	332	711	635
Article title, Abstract, Keywords: 2389	493	1,017	278	378	891	1,091
*Debris flow**						
Article title: 15	0	5	1	0	3	3
Keywords: 59	2	15	3	6	12	19
Abstract: 544	47	199	47	97	167	150
Article title, Abstract, Keywords: 824	58	247	56	124	210	274
*Mud flow**						
Article title: 1	0	0	0	1	0	0
Keywords: 7	0	0	0	0	0	0
Abstract: 271	4	14	2	37	25	20
Article title, Abstract, Keywords: 324	4	23	2	47	40	36
Rockfall OR Rock fall**						
Article title: 6	0	4	0	0	2	3
Keywords: 6	0	3	0	0	2	2
Abstract: 290	15	71	16	31	81	60
Article title, Abstract, Keywords: 365	16	101	18	39	104	117

Note: An article can be related to several categories

Table 2 An overview of international standards containing landslide-related terms (debris flow, landslide, rock fall) as found in the Online Browsing Platform (ISO 2022a). The standards are given in a numerical order

Standard	Mention in the standard text
ISO 2394:2015(en)	1 Scope This International Standard constitutes a risk- and reliability-informed foundation for decision making concerning design and assessment of structures both for the purpose of code making and in the context of specific projects. The principles presented in this International Standard cover the majority of buildings, infrastructure, and civil engineering works, whatever the nature of their application and use or combination of the materials used 6.2.2.2 Classification . . . Geotechnical actions from soil or rock, including earth pressures, earth slides and earthquakes, sub-soil vibrations, settlements . . .
ISO 6421:2012(en)	1 Scope This International Standard describes methods for the measurement of temporal and spatial changes in reservoir capacities due to sediment deposition. 4.1 Origin of the sediment deposited in the reservoir . . . to the rock type and slope of the drainage basin. In addition, ***landslides*** produce ***debris flows***. Sediment is delivered to the reservoir both as suspended sediment load and as bed ...
ISO 7010:2019(en)	1 Scope This International Standard prescribes safety signs for the purposes of accident prevention, fire protection, health hazard information and emergency evacuation. Amendment 117: Safety sign W076: Warning; ***Debris flow*** zone. Amendment 119: Safety sign W078: Warning; ***Landslide*** zone.
ISO 10252:2020(en)	1 Scope This International Standards provides requirements and guidelines for the design and assessment of structures in relation to the possible occurrence of accidental actions induced by human activities. Fire and man-made earthquake, however, are not included. 5.1 Types of accidental actions Accidental actions due to human activities shall be considered in the design and assessment of buildings and other civil engineering structures. These actions include but are not limited to: – Impact from vehicles, trains and tramways, ships, aircrafts, helicopters, forklift trucks, falling materials (***rockfall***, ***debris flow***, dropped objects from cranes), machine related impacts like toppling cranes, wind turbines, parts detached from a rotary machine, blades detached from turbines, etc.; . . .
ISO 13628-15:2011 (en)	1 Scope This part of ISO 13628 addresses recommendations for subsea structures and manifolds, within the frameworks set forth by recognized and accepted industry specifications and standards. It covers subsea manifolds and templates utilized for pressure control in both subsea production of oil and gas, and subsea injection services. 5.5.1 General . . . subsurface obstacles such as boulders, as well as drilling aspects such as mud pressure, ***mudflow***, washout, etc., as part of the selection criteria. In order to design ...
ISO 14055-1:2017 (en)	5.3.1.1 Soil erosion by water ... of deep incisions, down into the subsoil, due to concentrated runoff; —***landslides***, ***mudflows*** or mass movements of soil that occur locally and often cause widespread serious damage; ... A.5.2 Volcanic eruptions . . . Hazards associated with volcanic eruptions include lava flows, falling ash and projectiles, ***mudflows***, and toxic gases. Volcanic activity may also trigger other natural hazardous events . . .
ISO 16063-42:2014 (en)	1 Scope This part of ISO 16063 specifies the instrumentation and procedure to be used for the accurate calibration of seismometer sensitivity using local gravitational acceleration (local Earth's gravitation; local value for the acceleration due to the Earth's gravity) as a reference value. The intended end-usage of the seismometer to be applied is as follows: a) measurement and observation for the earth science including geophysics usage; b) measurement and observation for disaster prevention, such as detecting the precursor of a ***land slide***; . . .
ISO 17745:2016(en)	1 Scope This International Standard specifies the characteristics of steel wire ring net panel for retaining of unstable slopes controlling and preventing ***rockfalls*** and loose ***debris flow*** along roads, highways and railway, urban areas, mines and quarries, and for snow avalanche protection produced from metallic-coated steel wire or advanced metallic coating. It is not applicable to anchors or soil nails for fixing of steel mesh to an unstable slope.
ISO 17746:2016(en)	1 Scope This International Standard specifies the characteristics of steel wire rope net panels and rolls for retaining of unstable slopes controlling and preventing ***rockfalls*** and loose ***debris flow*** along roads, highways and railway, urban areas, mines and quarries, and for snow avalanche protection.
ISO 19901-2:2017 (en)	1 Scope This International Standard contains requirements for defining the seismic design procedures and criteria for offshore

(continued)

Table 2 (continued)

Standard	Mention in the standard text
	structures; guidance on the requirements is included in Annex A. The requirements focus on fixed steel offshore structures and fixed concrete offshore structures. The effects of seismic events on floating structures and partially buoyant structures are briefly discussed. 5 Earthquake hazards . . . the design and, when warranted, should be addressed by special studies (e. g. ***mudflow*** loading, seabed deformation) . . .
ISO 19901-8:2014 (en)	1 Scope This part of ISO 19901 specifies requirements, and provides recommendations and guidelines for marine soil investigations. A.1 Scope of work . . . description and dating of turbidites, of soil in a deposition area of previous ***debris flows***. In some cases, specialized combinations of shallow geophysical investigation and marine soil ...
ISO 19901-10:2021 (en)	1 Scope This part of 19901 provides requirements and guidelines for marine geophysical investigations. A.10.6 Investigation of geohazards . . . the resulting mass-transport deposits (stacked or rafted blocks, slides, slumps, ***debris flows***, ***mudflows***, creep features, turbidites, meta-stable slopes, loose sands, etc.) . . .
ISO 20074:2019(en)	1 Scope This International Standard specifies requirements and gives recommendations on the management of geohazards risks during the pipeline design, construction and operational periods. This standard is applicable to all reasonable and credible natural hazards induced by natural forces and hazards induced by human activity that manifest similarly to natural hazards collectively referred to as "geological hazards" or "geohazards", or through industry as attributed to "natural forces". Geohazards covered by this standard include, but are not limited to: – Mass wasting processes, including ***landslides***, lateral spreads, ***rockfalls***, ***debris flows***, avalanches, and similar processes whether naturally occurring or anthropogenic; . . .
ISO 22327:2018(en)	1 Scope This International Standard gives guidelines for a ***landslide*** early warning system. It provides a definition, aims to improve understanding, describes methods and procedures to be implemented, and gives examples of types of activities. It is applicable to communities vulnerable to ***landslides***, without taking secondary effects into consideration. It recognizes population behaviour response planning as a key part of the preparedness. It takes into account the approach of ISO 22315:2014(en) and provides additional specifications for ***landslides***.
ISO 22328-1:2020 (en)	Introduction Disasters such as earthquakes, tsunamis, volcanic eruptions, high river flows (e. g. floods, low river flows, sudden flash floods), ***landslides***, storm surges and hurricanes as well as slow-onset events such as drought, extreme temperatures, heat waves or soil erosion can have devastating impacts. 1 Scope This International Standard gives guidelines for the implementation of a community-based disaster early warning system (EWS). It describes the methods and procedures to be implemented and provides examples. This document is applicable to communities vulnerable to disasters, without taking secondary/indirect effects into consideration.
ISO 31000:2018(en)	1 Scope This International Standard provides guidelines on managing risk faced by organizations. The application of these guidelines can be customized to any organization and its context. This document provides a common approach to managing any type of risk and is not industry or sector specific.
ISO 37120:2018(en)	1 Scope This International Standard specifies and establishes definitions and methodologies for a set of indicators for smart cities. As accelerating improvements in city services and quality of life is fundamental to the definition of a smart city, this standard, in conjunction with ISO 37120, is intended to provide a complete set of indicators to measure progress towards a smart city. 3 Terms and definitions 3.7 Natural hazard Geological or meteorological phenomena that can cause damage to physical infrastructure or loss of life in cities
ISO 37122:2019(en)	1 Scope This International Standard specifies and establishes definitions and methodologies for a set of indicators for smart cities. As accelerating improvements in city services and quality of life is fundamental to the definition of a smart city, this standard, in conjunction with ISO 37120, is intended to provide a complete set of indicators to measure progress towards a smart city.
ISO 37123:2019(en)	1 Scope This International Standard defines and establishes definitions and methodologies for a set of indicators on resilience in cities. This standard is applicable to any city, municipality or local government that undertakes to measure its performance in a comparable and verifiable manner, irrespective of size or location. Maintaining, enhancing and accelerating progress towards improved city services and quality of life is fundamental to the definition of a resilient city,

(continued)

Table 2 (continued)

Standard	Mention in the standard text
	so this standard is intended to be implemented in conjunction with ISO 37120. This standard follows the principles set out in ISO 37101, and can be used in conjunction with this and other strategic frameworks. 3 Terms and definitions 3.3 Hazard . . . Geological or geophysical hazards originate from internal earth processes (e.g. earthquakes, volcanic activity, ***landslides***, ***rockslides***, ***mud flows***). Hydro-meteorological hazards are of atmospheric, hydrological or oceanographic origin (e.g. cyclones, typhoons, hurricanes, floods, drought, heatwaves, cold spells, coastal storm surges). Hydro-meteorological conditions can also be a factor in other hazards such as ***landslides***, wildland fires and epidemics. . . . 3.4 Hazard map Map developed to illuminate areas that are affected or vulnerable to a particular hazard (e.g. earthquakes, ***landslides***, ***rockslides***).
ISO/DIS 22328-2	1 Scope This standard under development gives guidelines for a landslide early warning system. It provides a definition, aims to improve understanding, describes methods and procedures to be implemented, and gives examples of types of activities. It is applicable to communities vulnerable to landslides, without taking secondary effects into consideration. It recognizes population behaviour response planning as a key part of the preparedness. It takes into account the approach of ISO 22315 and provides additional specifications for landslides.
ISO/DIS 22328-3(en)	1 Scope This standard complements the generic guidelines in ISO 22328-1 by giving additional information related to tsunamis. It provides definitions, understanding, method, procedure, implementation, and activities specifically related to tsunamis.
ISO/TS 21219-19: 2016(en)	1 Scope This part of ISO/TS 21219 defines the TPEG Weather (WEA) application for reporting weather information for travellers. It provides general weather-related information to all travellers and is not limited to a specific mode of transportation. 9.27 wea110:HazardElements . . . Flooding 2 Localized flooding 3 Risk of flash floods 4 Storm surge 5 ***Landslides*** 6 ***Mudflows*** 7 Smoke 8 Smog 9 Ash cloud 10 Dust 11 Sand 12 Dust whirls . . .

3.4 Case Study 1: Standardization Efforts for Landslide Early Warning Systems (LEWS)

The implementation of a community-based disaster EWS is consistent with the Sendai Framework for Disaster Risk Reduction of 2015–2030 (SF DRR 2015), specifically target g) of the seven global targets: "*Substantially increase the availability of and access to multi-hazard early warning systems and disaster risk information and assessments to people by 2030*". Based on the fourth priority of the framework, the improvement of preparedness is the basis for the capability to respond effectively to a disaster. Improvement of preparedness can be achieved by implementing an EWS, in addition to improving the dissemination and communication of knowledge about the early warning of disasters at local, national, regional and international levels.

Also the Kyoto 2020 Commitment for Global Promotion of Understanding and Reducing Landslide Disaster Risk KLC2020 (Sassa 2021) recognizes the importance of EWS: the Priority action no. 1 "People centered early warning", and the Priority action no. 3 "Technologies for monitoring, testing & early warning".

An Early Warning System (EWS) was recognized by the Sendai Framework for Disaster Risk Reduction (SF DRR 2015) as an important contribution to the improvement of preparedness as a part of disaster risk reduction—also for landslide disaster risk. A community-based warning system is defined in ISO 22315:2014(en) as "*a method to communicate information to the public through established networks*".

A new proposal of a standard for community-based landslide early warning systems has been promoted to the International Organization for Standardization (ISO) by Universitas Gadjah Mada (Fathani et al. 2016, 2017, 2022; Fathani and Karnawati 2018), in corporation with the Indonesian Standardization Agency and the National Agency for Disaster Management (BNPB). The Indonesian proposal was accepted and published as ISO 22327:2018 Guidelines for implementation of a community-based landslide early warning system—a first international ISO standard coming from a developing country (Fathani et al. 2022). The work was led by the ISO Technical Committee 292 Security and resilience (ISO/TC 292), established in 2015 and currently with 47 participating members and 22 observing members (National Standards Bodies).

In 2020, LandAware as a new international network of landslide early warning systems was established. Among the network goals there is also a statement that its members are committed to: "producing common standards and terminology, guidelines, recommendations, opinion papers and white papers (Calvello et al. 2020).

3.5 Case Study 2: Standardization Efforts for Sustainable Cities and Communities

Since the world population in urban environments has overtaken the one in non-urban, rural areas, the importance of SDG11 on Sustainable Cities and Communities is obvious. The International Organization on Standardization (ISO) via its technical committee ISO/TC 268 has published three ISO standards on sustainable cities and communities defining indicators for: city services and quality of life (ISO 37120:2018), smart cities (ISO 37122:2019), and resilient cities (ISO 37123:2019). The term natural hazard in the first standard on city services and quality of life covers geological and meteorological phenomena that can cause damage to physical infrastructure or loss of life in cities (see Table 2). As one of the ten safety indicators in this standard, "Number of natural-hazard-related death per 100,000 population" is a core indicator. The term hazard used in the standard on resilient cities covers flooding and also landslides, rockslides and mud flows (see Table 2); and a resilient city should be able to thrive regardless of the hazards, shocks and stresses it faces. Among city indicators, many are disaster-related or natural-hazard-related, among others the following ones:

- Historical disaster losses and average annual disaster loss as a percentage of city product.
- Percentage of population trained in emergency preparedness and disaster risk reduction.
- Frequency with which disaster-management plans are updated.
- Percentage of buildings structurally vulnerable to high-risk hazards.
- Percentage of damaged infrastructure that was "built back better" after a disaster.
- Percentage of population at high risk from natural hazards.
- Annual percentage of the city population directly affected by natural hazards.
- Percentage of city population covered by multi-hazard early warning system.
- Percentage of city area covered by publicly available hazard maps.

3.6 Case Study 3: Standardization in the Field of Torrent Control in Austria

In Austria, there is a long tradition in the torrent control activities (Hübl and Nagl 2019). Therefore, different approaches for designing and numerous types of protection structures on different condition levels exist. A set on national standard rules as technical regulative acts were prepared by a national interdisciplinary working group in order to achieve a standardization of the load models, design, construction, and life cycle assessment of technical structures as protection works for torrent control founded on the Eurocode, encompassing: i) torrential processes, ii) snow avalanches, and iii) rock fall.

The new standardization for torrential processes in Austria encompasses the following rules:

- Protection works for torrent control—Definition and classification (ONR 24800:2009).
- Protection works for torrent control—Action on structures (ONR 24801:2013).
- Protection works for torrent control—Design of structures (ONR 24802:2011).
- Protection works for torrent control—Operation, monitoring and maintenance (ONR 24803:2008)

that would include among others also protection works against debris flows, especially debris-flow dams, their planning, design, and implementation.

The new standardization for rockfall processes in Austria encompasses the following rule:

- Technical protection against rockfall—Terms and definitions, effects of actions, design, monitoring and maintenance (ONR 24810:2021)

that applies to primary measures such as anchorage and nailing and also secondary measures (e. g. nets, dams). Static and dynamic load assumptions are described as well as proof of evidence for actions and materials. In addition, this ONR 24810:2021 specifies current surveillance of construction and acceptance of the measures implemented, maintenance and repair as well as durability of the measures taken.

These above mentioned national technical rules were published in German language, and are presented in details in professional literature (ASI 2014).

4 Conclusions and Further Work

This article is a companion paper to the original article on landslide research and technology in patent documents (Mikoš 2022). Taking both articles into consideration, further such studies are needed to enlighten the present state-of-the-art status of landslide research and technology around the world from this rarely used perspective (patents & standards).

It is true that landslide risk mitigation is in many respects location-impacted problem to be solved each in an original way, taking into account local conditions and triggering mechanisms as well as its own landslide dynamics, bringing in also "engineering judgement". But standardization in the field of landslide research and technology may nevertheless help to improve the overall success of landslide hazard and

risk prevention and mitigation. The standardization is at the top of a pinnacle, composed of best available technologies (BAT), best practice case studies, Lessons Learned, white papers, opinion papers, methodologies, recommendations, guidelines etc. The existing landslide-related international standards are concentrated to landslide prevention on one side, and on the other side to field and laboratory methods for soil and rock investigations and technologies to design and execute mitigation measures, and on supporting building codes. Many more options are open to work on new standards to support landslide disaster risk reduction, locally and globally.

The International Consortium on Landslides with its global membership may take a more active role in this regard in future as a part of its voluntary contribution to the Sendai Framework for Disaster Risk Reduction 2015–2030 within the activities of the Kyoto 2020 Commitment for Global Promotion of Understanding and Reducing Landslide Disaster Risk.

Acknowledgments The author would like to acknowledge the financial support of Slovenian Research and Innovation Agency by core funding P2-0180, and of the University of Ljubljana from the Development Fund for the activities of the UNESCO Chair on Water-related Disaster Risk Reduction (WRDRR).

References

AGS (2007a) Guideline for landslide susceptibility, hazard and risk zoning for land use planning. Aust Geomech 42(1):13–36

AGS (2007b) Commentary on guideline for landslide susceptibility, hazard and risk zoning for land use planning. Aust Geomech 42(1):37–62

ASI (2014) Normensammlung Schutz vor Naturgefahren: Die Normenreihe ONR 24800 über Wildbach-, Lawinen- und Steinschlagschutzbauwerke. Austrian Standards Institute, Vienna, Austria. 512p. ISBN 978-3-85402-290-9. https://shop.austrian-standards.at/action/de/public/details/515135/Austrian_Standards_Institute__Hrsg____Normensammlung_Schutz_vor_Naturgefahren_-_Die_Normenreihe_ONR_24800_ueber_Wildbach-__Lawinen-_und_Steinschlagschutzbauwerke_____ISBN_978-3-85402-290-9

Bobrowsky PT (ed) (2013) Encyclopedia of natural hazards. Springer Dordrecht, 1133 p. https://doi.org/10.1007/978-1-4020-4399-4

Bobrowsky PT, Marker B (eds) (2018) Encyclopedia of engineering geology. Springer International Publishing, Cham, 978 p. https://doi.org/10.1007/978-3-319-73568-9

Bobrowsky P, VanDine D, Couture R (2014) Landslide guidelines and best practices for professional engineers and geoscientists. In: Lollino G, Arattano M, Giardino M, Oliveira R, Peppoloni S (eds) Engineering geology for society and territory, vol 7. Springer, Cham. https://doi.org/10.1007/978-3-319-09303-1_45

Calvello M, Devoli G, Freeborough K, Gariano SL, Guzzetti F, Kirschbaum D, Nakaya H, Robbins J, Staehli M (2020) LandAware: a new international network on Landslide Early Warning Systems. Landslides 17(10):2699–2702. https://doi.org/10.1007/s10346-020-01548-7

Choi KY, Cheung RWM (2013) Landslide disaster prevention and mitigation through works in Hong Kong. J Rock Mech Geotech Eng 5(5):354–365. https://doi.org/10.1016/j.jrmge.2013.07.007

Clarivate (2022) Web of Science Core Collection Cited References Search. Clarivate Analytics, Philadelphia, PA. https://www.webofscience.com/wos/woscc/cited-reference-search. Accessed 23 Apr 2022

Corominas J, van Westen C, Frattini P, Cascini L, Malet J-P, Fotopoulou S, Catani F, Van Den Eeckhaut M, Mavrouli O, Agliradi F, Pitilakis K, Winter MG, Pastor M, Ferlisi S, Tofani V, Hervas J, Smith JT (2014) Recommendations for the quantitative analysis of landslide risk. Bull Eng Geol Environ 73:209–263. https://doi.org/10.1007/s10064-013-0538-8

Directive (2007) Directive 2007/2/EC of the European Parliament and of the Council of 14 March 2007 establishing an Infrastructure for Spatial Information in the European Community (INSPIRE). Off J Eur Union, L 108/1–108/14. https://eur-lex.europa.eu/legal-content/EN/ALL/?uri=CELEX%3A32007L0002. Accessed 16 Jul 2022

Fathani TF, Karnawati D, Wilopo W (2016) An integrated methodology to develop a standard for landslide early warning systems. Nat Hazards Earth Syst Sci 16:2123–2135. https://doi.org/10.5194/nhess-16-2123-2016

Fathani TF, Karnawati D, Wilopo W (2017) Promoting a global standard for community-based landslide early warning systems (WCoE 2014–2017, IPL-158, IPL-165). In: Sassa K, Mikoš M, Yin Y (Eds.): Advancing culture of living with landslides. 1 ISDR-ICL Partnerships 2015-2025. Springer, Cham 355–361.

Fathani TF, Karnawati D (2018) TXT-tool 2.062-1.1: A landslide monitoring and early warning system. In: Sassa K et al (eds) Landslide dynamics: ISDR-ICL landslide interactive teaching tools, Fundamentals, mapping and monitoring, vol 1. Springer, Cham, pp 297–308. https://doi.org/10.1007/978-3-319-57774-6_21

Fathani TF, Karnawati D, Wilopo W, Setiawan H (2022) Strengthening the resilience by implementing a standard for landslide early warning system. In: Sassa K et al (eds) Progress in landslide research and technology, vol 1, No. 1. Springer, Cham. (in print)

Fell R, Corominas J, Bonnard C, Cascini L, Leroi E, Savage WZ (2008) Guidelines for landslide susceptibility, hazard and risk zoning for land use planning. Eng Geol 102:85–98. https://doi.org/10.1016/j.enggeo.2008.03.022

Flentje PN, Miner A, Whitt G, Fell R (2007) Guidelines for landslide susceptibility, hazard and risk zoning for land use planning. Aust Geomech 42(1):13–26. https://ro.uow.edu.au/engpapers/2823

Genevois R, Tecca PR, Genevois C (2022) Mitigation measures of debris flow and landslide risk carried out in two mountain areas of North-Eastern Italy. J Mt Sci 19(6):1808–1822. https://doi.org/10.1007/s11629-021-7212-6

Guzzetti F, Mondini AC, Cardinally M, Fiorucci F, Santangelo M, Chang K-T (2012) Landslide inventory maps: new tools for an old problem. Earth Sci Rev 112:42–66. https://doi.org/10.1016/j.earscirev.2012.02.001

Herrera G, Mateos RM, García-Davalillo JC et al (2018) Landslide databases in the geological surveys of Europe. Landslides 15:359–379. https://doi.org/10.1007/s10346-017-0902-z

Hungr O, Leroueil S, Picarelli L (2014) The Varnes classification of landslide types, an update. Landslides 11(2):167–194. https://doi.org/10.1007/s10346-013-0436-y

Hübl J, Nagl G (2019) From practical experience to national guidelines for debris-flow mitigation measures in Austria. In: Kean JW, Coe JA, Santi PM, Guillen BK (eds) debris flow hazards mitigation: mechanics, monitoring, modeling and assessment. Proceedings of the Seventh International Conference on Debris-Flow Hazards Mitigation, Golden, Colorado, USA, June 10–13, 2019. Association of Environmental and Engineering Geologists, Special Publication 28. pp 981–987. https://repository.mines.edu/bitstream/handle/11124/173051/Engineering_and_Mitigation.pdf. Accessed 10 Aug 2022

INSPIRE (2013) D2.8.III.12 INSPIRE Data Specification on Natural Risk Zones – Technical Guidelines Version 3.0. European Commission Joint Research Centre. 135 p. https://inspire.ec.europa.eu/id/document/tg/nz. Accessed 16 July 2022

IPCC (2012) Managing the risks of extreme events and disasters to advance climate change adaptation. A special report of Working Groups I and II of the Intergovernmental Panel on Climate Change. In: Field CB, Barros V, Stocker TF, Qin D, Dokken DJ, Ebi KL, Mastrandrea MD, Mach KJ, Plattner G-K, Allen SK, Tignor M, Midgley PM (eds) Cambridge University Press, Cambridge, 582 pp. https://www.ipcc.ch/site/assets/uploads/2018/03/SREX_Full_Report-1.pdf. Accessed 31 Jul 2022

ISO (2006) ISO/TC 211. Geographic information/geomatics. International Standard Organization, Geneva. http://www.isotc211.org. Accessed 16 Jul 2022

ISO (2018) Contributing to the UN Sustainable Development Goals with ISO standards. International Organization for Standardization, Geneva. 42 p. https://www.iso.org/files/live/sites/isoorg/files/store/en/PUB100429.pdf. Accessed 21 Jul 2022

ISO (2022a) Online Browsing Platform (OBP) Version 4.19.0. International Organization for Standardization, Geneva. https://www.iso.org/obp/ui/#home. Accessed 5 Jun 2022

ISO (2022b) Standards – Sustainable Development Goals. International Organization for Standardization, Geneva. https://www.iso.org/sdgs.html. Accessed 21 Jul 2022

ISO 2394:2015(en) General principles on reliability for structures. International Organization for Standardization, Geneva. https://www.iso.org/obp/ui#iso:std:iso:2394:ed-4:v1:en. Accessed 8 Jun 2022

ISO 6421:2012(en) Hydrometry – Methods for assessment of reservoir sedimentation. International Organization for Standardization, Geneva. https://www.iso.org/obp/ui/#iso:std:iso:6421:ed-1:v1:en. Accessed 5 Jun 2022

ISO 7010:2019(en) Graphical symbols – Safety colours and safety signs – Registered safety signs. International Organization for Standardization, Geneva. https://www.iso.org/obp/ui/#iso:std:iso:7010:ed-3:v2:en. Accessed 5 Jun 2022

ISO 10252:2020(en) Bases for design of structures – Accidental actions. International Organization for Standardization, Geneva. https://www.iso.org/obp/ui/#iso:std:iso:10252:ed-1:v1:en. Accessed 5 Jun 2022

ISO 16063-42:2014(en) Methods for the calibration of vibration and shock transducers — Part 42: Calibration of seismometers with high accuracy using acceleration of gravity. International Organization for Standardization, Geneva. https://www.iso.org/obp/ui/#iso:std:iso:19901:-8:ed-1:v1:en. Accessed 8 Jun 2022

ISO 17745:2016(en) Steel wire ring net panels – Definitions and specifications. International Organization for Standardization, Geneva. https://www.iso.org/obp/ui#iso:std:iso:17745:ed-1:v1:en. Accessed 3 Aug 2022

ISO 17746:2016(en) Steel wire rope net panels and rolls – Definitions and specifications. International Organization for Standardization, Geneva. https://www.iso.org/obp/ui#iso:std:iso:17746:ed-1:v1:en. Accessed 3 Aug 2022

ISO 19901-8:2014(en) Petroleum and natural gas industries – Specific requirements for offshore structures – Part 8: Marine soil investigations. International Organization for Standardization, Geneva. https://www.iso.org/obp/ui/#iso:std:iso:19901:-8:ed-1:v1:en. Accessed 6 Jun 2022

ISO 19901-10:2021(en) Petroleum and natural gas industries – Specific requirements for offshore structures – Part 10: Marine geophysical investigations. International Organization for Standardization, Geneva. https://www.iso.org/obp/ui/#iso:std:iso:19901:-10:ed-1:v1:en. Accessed 6 Jun 2022

ISO 22300:2021(en) Security and resilience – Vocabulary. International Organization for Standardization, Geneva. https://www.iso.org/obp/ui#iso:std:iso:22300. Accessed 5 Jun 2022

ISO 22315:2014(en) Societal security – Mass evacuation – Guidelines for planning. International Organization for Standardization, Geneva. https://www.iso.org/obp/ui#iso:std:iso:22315:ed-1:v1:en. Accessed 8 Jun 2022

ISO 22327:2018(en) Security and resilience – Emergency management – Guidelines for implementation of a community-based landslide early warning system. International Organization for Standardization, Geneva. https://www.iso.org/obp/ui#iso:std:iso:22327:ed-1:v1:en. Accessed 8 Jun 2022

ISO 22328-1:2020(en) Security and resilience – Emergency management – Part 1: General guidelines for the implementation of a community-based disaster early warning system. International Organization for Standardization, Geneva. https://www.iso.org/obp/ui#iso:std:iso:22328:-1:ed-1:v1:en. Accessed 8 Jun 2022

ISO 22578:2022(en) Graphical symbols – Safety colours and safety signs – Natural disaster safety way guidance system. International Organization for Standardization, Geneva. https://www.iso.org/obp/ui/#iso:std:iso:22578:ed-1:v1:en. Accessed 5 Jun 2022

ISO 31000:2018(en) Risk management – Guidelines. International Organization for Standardization, Geneva. https://www.iso.org/obp/ui#iso:std:iso:31000:ed-2:v1:en. Accessed 4 Sept 2022

ISO 37120:2018(en) Sustainable cities and communities — Indicators for city services and quality of life. International Organization for Standardization, Geneva. https://www.iso.org/obp/ui#iso:std:iso:37120:ed-2:v1:en. Accessed 12 Jun 2022

ISO 37122:2019(en) Sustainable cities and communities — Indicators for smart cities. International Organization for Standardization. Geneva, Switzerland. https://www.iso.org/obp/ui#iso:std:iso:37122:ed-1:v1:en. Accessed 12 Jun 2022

ISO 37123:2019(en) Sustainable cities and communities – Indicators for resilient cities. International Organization for Standardization, Geneva. https://www.iso.org/obp/ui#iso:std:iso:37123:ed-1:v1:en:sec:12.2.1. Accessed 12 Jun 2022

ISO/DIS 22328-2 Security and resilience – Emergency management – Part 2: Guidelines for the implementation of a community-based landslide early warning system. International Organization for Standardization, Geneva. https://www.iso.org/standard/83417.html. Accessed 21 Jul 2022

ISO/DIS 22328-3(en) Security and resilience – Emergency management – Part 3: Guidelines for the implementation of a community-based tsunami early warning system. International Organization for Standardization, Geneva. https://www.iso.org/obp/ui/#iso:std:iso:22328:-3:dis:ed-1:v1:en. Accessed 5 Jun 2022

ISO/TC 292 International Organization for Standardization Technical Committee 292 Security and Resilience. Participation. International Organization for Standardization, Geneva. https://www.iso.org/committee/5259148.html?view=participation. Accessed 3 Aug 2022

ISO/TS 21219-19:2016(en) Intelligent transport systems – Traffic and travel information (TTI) via transport protocol experts group, generation 2 (TPEG2) – Part 19: Weather information (TPEG2-WEA). International Organization for Standardization, Geneva. https://www.iso.org/obp/ui#iso:std:iso:ts:21219:-19:ed-1:v1:en. Accessed 8 Jun 2022

IWA 33-1:2019(en) Technical guidelines for the development of small hydropower plants — Part 1: Vocabulary. International Organization for Standardization, Geneva. https://www.iso.org/obp/ui/#iso:std:iso:iwa:33:-1:ed-1:v1:en. Accessed 5 Jun 2022

Klose M, Highland L, Damm B, Terhorst B (2014) Estimation of direct landslide costs in industrialized countries: challenges, concepts, and case study. In: Sassa K, Canuti P, Yin Y (eds) Landslide science for a safer geoenvironment, Methods of landslide studies, vol 2. Springer, Berlin, pp 661–667

Klose M, Damm B, Terhorst B (2015) Landslide cost modeling for transportation infrastructures: a methodological approach.

Landslides 12(2):321–334. https://doi.org/10.1007/s10346-014-0481-1
Mazengarb C, Stevenson MD (2010) Tasmanian Landslide Map Series: User guide and technical methodology Record Geological Survey Tasmania 2010/01. https://www.mrt.tas.gov.au/mrtdoc/dominfo/download/UR2010_01/UR2010_01.pdf. Accessed 4 Sept 2022
Mikoš M (2022) Landslide research and technology in patent documents. In: Sassa K et al (eds) Progress in landslide research and technology, vol 1, no 2 (in print)
NDMA (2019) National Landslide Risk Management Strategy. National Disaster Management Authority, Ministry of Home Affairs, Government of India, New Delhi, India. https://nidm.gov.in/PDF/pubs/NDMA/26.pdf. Accessed 4 Sept 2022
Núñez-Andrés MA, Lantada Zarzosa N, Martínez-Llario J (2022) Spatial data infrastructure (SDI) for inventory rockfalls with fragmentation information. Nat Hazards 112(3):2649–2672. https://doi.org/10.1007/s11069-022-05282-2
ONR 24800:2009 Protection works for torrent control – Terms and their definitions as well as classification. Austrian Standard Rule. Austrian Institute for Standardisation, Vienna. 75p. (in German)
ONR 24801:2013 Protection works for torrent control – Static and dynamic actions on structures. Austrian Standard Rule. Austrian Institute for Standardisation, Vienna. 31p. (in German)
ONR 24802:2011 Protection works for torrent control – Design of structures. Austrian Standard Rule. Austrian Institute for Standardisation, Vienna. 95p. (in German)
ONR 24803:2008 Protection works for torrent control – Operation, monitoring, maintenance. Austrian Standard Rule. Austrian Institute for Standardisation, Vienna. 38p. (in German)
ONR 24810:2021 Technical protection against rockfall – Terms and definitions, effects of actions, design, monitoring and maintenance. Austrian Institute for Standardisation, Vienna. 107p. (in German)
Ortigao JAR, Sayao ASFJ (eds) (2004) Handbook of slope stabilisation. Springer, Berlin, 483 p. https://doi.org/10.1007/978-3-662-07680-4
Sanwa Sanko (2022) Natural disaster safety way guidance system ISO/DIS 22578. Sanwa Sanko Co., LTD. Tokyo. https://www.sanwa-sanko.co.jp/en/legal/jis-out/. Accessed 5 Jun 2022
Sassa K (2021) The Kyoto Landslide Commitment 2020: launched. Landslides 18(1):5–20. https://doi.org/10.1007/s10346-020-01575-4
SFDRR (2015) Sendai Framework for Disaster Risk Reduction 2015–2030. https://www.preventionweb.net/files/43291_sendaiframeworkfordrren.pdf. Accessed 12 Jun 2022
UN (2015) Resolution adopted by the General Assembly on 25 September 2015 – 70/1. Transforming our world: the 2030 Agenda for Sustainable Development. UN A/RES/70/1. 35 p. http://www.un.org/ga/search/view_doc.asp?symbol=A/RES/70/1&Lang=E. Accessed 12 Jun 2022
UN (2017) Resolution adopted by the General Assembly on 6 July 2017 – 71/313. Work of the Statistical Commission pertaining to the 2030 Agenda for Sustainable Development. UN A/RES/71/313. 25 p. https://digitallibrary.un.org/record/1291226/files/A_RES_71_313-EN.pdf. Accessed 12 Jun 2022
UNDRR (2022) My city is getting ready. Is yours? United Nations Office for Disaster Risk Reduction. Geneva. https://mcr2030.undrr.org/. Accessed 12 Jun 2022
UNECE (2018) Standards for the Sustainable Development Goals. United Nations Economic Commission for Europe, Geneva, Switzerland. 82 p. https://unece.org/sites/default/files/2021-03/ECE_TRADE_444.pdf. Accessed 21 Jul 2022
USGS (2000) National Landslide Hazards Mitigation Strategy – a framework for loss reduction. Open-File Report 00-450. U.-S. Geological Survey, Department of the Interior, Reston, VA. 49 p. https://pubs.usgs.gov/of/2000/ofr-00-0450/ofr-00-0450.pdf. Accessed 13 Jul 2022
van Westen C (2018) Risk mapping. In: Bobrowsky PB, Marker B (eds) Encyclopedia of engineering geology. Springer, Cham, pp 761–769
Wang B, Ruel M, Couture R, VanDine D, Bobrowsky P, Blais-Stevens A (2013) Current status of landslide guidelines around the world. In: Margottini C, Canuti P, Sassa K (eds) Landslide science and practice. Springer, Berlin. https://doi.org/10.1007/978-3-642-31313-4_35
Wirtz A, Kron W, Löw P, Steuer M (2014) The need for data: natural disasters and the challenges of database management. Nat Hazards 70(1):135–157. https://doi.org/10.1007/s11069-012-0312-4

Mathematical and Numerical Modeling of Slope Stability for the Mong Sen Landslide Event in the Trung Chai Commune, Sapa, Vietnam

Binh Van Duong, Igor K. Fomenko, Lan Chau Nguyen, Kien Trung Nguyen, Tuan-Nghia Do, Denis N. Gorobtsov, Oleg V. Zerkal, and Hien The Dinh

Abstract

The northern mountainous region of Vietnam is particularly susceptible to sediment-related disasters, such as landslides, during the rainy season. This paper presents slope stability modeling results for a landslide event triggered by heavy rainfall in Trung Chai commune, Sapa, Vietnam. Stability simulations were conducted using input data, including 1-m DEM, the distribution and characteristics of slope materials, and the change of pore pressure ratio. The behavior of slopes under the impact of rainfall was analyzed using the limit equilibrium method and the finite element method, which are integrated into the programs of Rocscience Inc. In addition, since the Trung Chai commune is located in a seismically active region, single earthquakes or the combination of earthquakes and rainfall may trigger landslides. As a result, the study determined the relationship between seismic loading and pore water pressure for the studied slope. The study results showed that both limit equilibrium and the finite element methods have high efficacy in modeling slope stability in this study. Therefore, this study recommended that these methods may be employed for slope stability studies in other regions of Vietnam or other regions of the world with similar geological conditions.

Keywords

Rainfall-induced landslide · Slope stability · Seismic loading · Limit equilibrium method · Finite element method · Mong Sen · Sapa

B. Van Duong (✉)
Department of Engineering Geology, Ordzhonikidze Russian State Geological Prospecting University, Moscow, Russia

Department of Engineering Geology, Hanoi University of Mining and Geology, Hanoi, Vietnam
e-mail: duongvanbinh@humg.edu.vn

I. K. Fomenko · D. N. Gorobtsov
Department of Engineering Geology, Ordzhonikidze Russian State Geological Prospecting University, Moscow, Russia

L. C. Nguyen
University of Transport and Communications, Civil Engineering Faculty, Hanoi, Vietnam
e-mail: nguyenchaulan@utc.edu.vn

K. T. Nguyen
Vietnam Academy of Science and Technology, Department of Hydrogeology and Engineering Geology, Institute of Geological Sciences, Hanoi, Vietnam

T.-N. Do
Thuyloi University, Civil Engineering Faculty, Hanoi, Vietnam
e-mail: dotuannghia@tlu.edu.vn

O. V. Zerkal
Department of Dynamic Geology, Lomonosov Moscow State University, Moscow, Russia

H. T. Dinh
Department of Engineering Geology, Hanoi University of Civil Engineering, Hanoi, Vietnam

1 Introduction

Loss of life and property may be caused by landslides in mountainous areas, particularly during or after prolonged periods of heavy rainfall. Understanding the factors that trigger and contribute to landslide occurrences and the subsequent debris transport distance is critical for landslide hazard assessment (Dai et al. 2003). Large residential communities are nevertheless frequently affected by the mass instability of soil slopes in regions of steep topography and experience prolonged hot and dry periods followed by extreme weather events (heavy rainfall, rainstorms). Although slope failures may originate because of human-induced factors such as slope-top loading or the removal of the toe of a natural slope for construction activities, numerous natural slopes become unstable simply because of the impact of rainwater penetrating the slope material layers (Collins Brian and Znidarcic 2004).

The interactions between landslide triggering and causative factors and the environment around them lead to the establishment and development of the landslide processes in

I. Alcántara-Ayala et al. (eds.), *Progress in Landslide Research and Technology, Volume 2 Issue 1, 2023*,
Progress in Landslide Research and Technology, https://doi.org/10.1007/978-3-031-39012-8_8

the given area. Therefore, new insights into the prevention and mitigation of landslides may be gained through a better knowledge of the differences in landslide processes and the features of landslide movement (Yang et al. 2021). For this purpose, several studies on different landslide science aspects have been conducted, including case studies in numerous areas and their failure scenarios (Alimohammadlou et al. 2013).

This article presents the results of the slope stability analysis conducted in connection with a landslide event triggered by heavy rainfall in the Trung Chai commune, Sapa district, Vietnam. The stability of the analyzed slope was evaluated using finite element (FEM) and limit equilibrium (LEM) methods. By conducting deterministic and probabilistic analyses, this study determined the relationship between pore water pressure and the stability of the examined slope. In addition, the obtained relationship between the two primary landslide triggers (rainfall and seismic loading) is also a significant result of this study.

2 Study Area

Located in the northwest of Lao Cai Province, the Sapa district, which covers an area of 675.8 km^2 and has an elevation of 150 m to more than 3000 m, is well-known as a famous tourist destination in Vietnam. In recent years, Sapa has experienced an increase in the frequency and magnitude of landslides due to rapid urbanization, construction, and agriculture. Most landslide incidents in the area were triggered by precipitation (Dang et al. 2018; Tien Bui et al. 2017).

Trung Chai commune is located in the northeastern Sapa district, where the 4D national road connects Laocai city and the Sapa district. Trung Chai (14 landslides), Ta Van (16 landslides), and Ban Ho (27 landslides) are the three communes in Sapa that reported the highest number of landslides (Binh Van Duong et al. 2022). The combination of mountainous terrain and agricultural and construction activity has triggered numerous landslide events in this area. The sliding mass in this study (Fig. 1) was investigated during the construction of the Mong Sen Bridge, which connects the Sapa district and the Hanoi-Laocai expressway. This landslide event was triggered by a heavy rain event, which caused the displacement of slope materials and the formation of cracks on the surface of the sliding body.

3 Evaluation of Slope Stability for the Mong Sen Landslide

3.1 Methods

Both the factor of safety (FS) and the probability of failure (PF) are significant factors to determine when assessing slope stability. The quality of topographic and geotechnical data plays a critical role in establishing a simulation model of slope behavior to achieve highly accurate analysis results (Azizi et al. 2020). It is widely accepted that the ratio between the available shear strength (s) and the equilibrium shear stress (τ) (shear stress along the sliding surface required to maintain the stability of the slope) is defined as the factor of safety value (Duncan et al. 2014):

$$FS = \frac{s}{\tau} \tag{1}$$

Slope stability is frequently quantified in geotechnical engineering using a factor of safety (FS) as the resulting value. Considered an indicator to define the likelihood of slope failures caused by a landslide, the FS value is used to predict the occurrence of landslide-related slope deformations (Fomenko et al. 2019; Fomenko and Zerkal 2017). By assuming that the values of all model input parameters are accurately known, the deterministic analysis produces a single value of FS. However, materials on slopes are frequently heterogeneous, with variations in spatial distribution and properties depending on the slope's location and surrounding environment. Therefore, probabilistic analyses are especially helpful in slope stability studies because it allows the determination of the impact of uncertainty or variability in input parameters on the slope stability analysis results (Nagendran et al. 2019). Generally, statistical distributions can be assigned to the input parameters when conducting probabilistic analyses. Samples may be taken an unlimited number of times for each calculation, and combinations of these samples are used to determine the factor of safety (FS). The probability of failure (PF) for the slope may be defined as follows (Cami et al. 2021), according to the Eq. (2):

$$PF(\%) = \frac{Number\ simulations\ with\ FS < 1}{Total\ number\ of\ simulations} \tag{2}$$

In addition, a probabilistic analysis may also be conducted to determine the reliability index (RI), which is defined as the capacity of a system to perform necessary tasks under given circumstances for a predetermined amount of time (Wang and Constantino 2009). In a slope stability analysis, the safety of the slope is quantified by the reliability index based on the number of standard deviations that separate the best estimate of FS from the defined failure value of 1.0 (Christian John et al. 1994). Along with the factor of safety value, the reliability index determined in probabilistic analysis, which corresponds to the probability of failure, is also the indicator used to measure the stability of the slope. It has been determined that the greater the dependability index, the lower the probability of failure (Cheng and He 2020). Consequently, the definition of an acceptable level of safety, i.e., the highest failure probability value without structural collapse, is one of the most challenging aspects of reliability

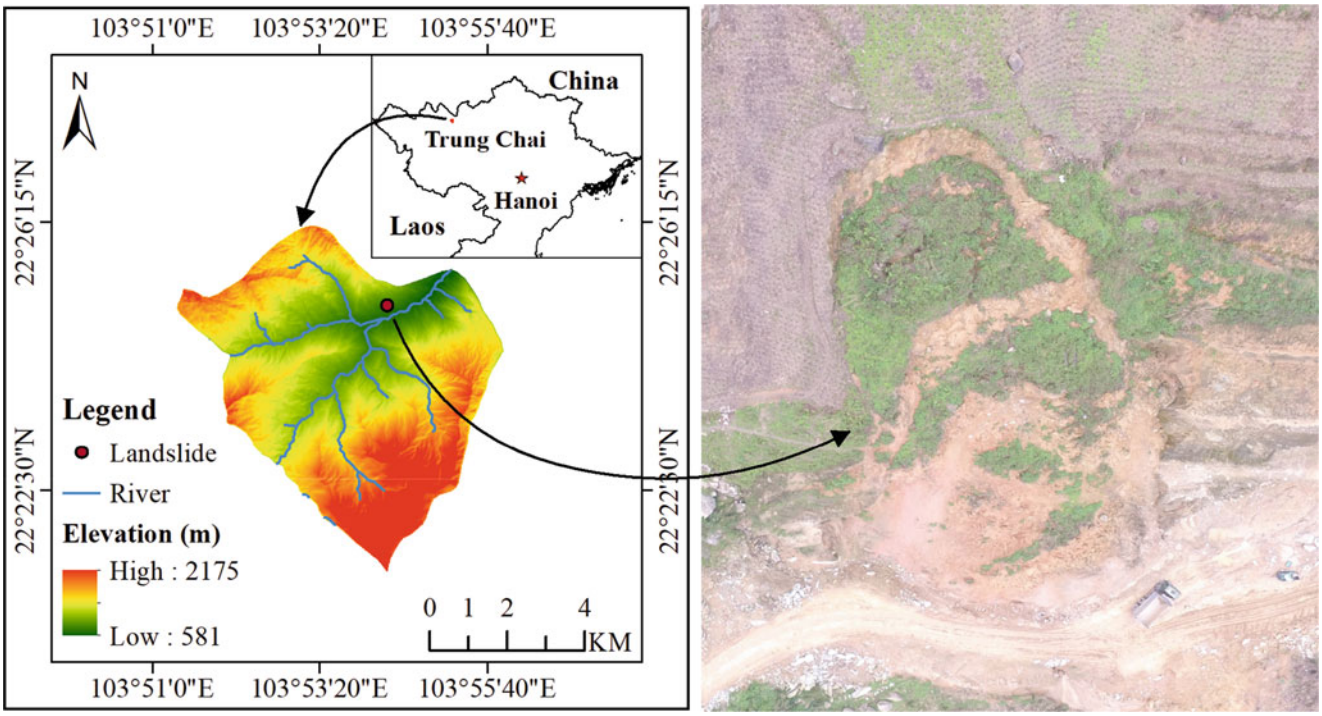

Fig. 1 Location of landslide site

analysis. However, there are currently different proposals on this issue (Douglas J. Kamien 1997; Withiam et al. 1998). In geotechnical design, it is frequently required to have a reliability index value greater than 3.0 (i.e., PF equal to 0.001) to achieve performance that is better than "above average" (Abdulai and Sharifzadeh 2021).

3.2 Strength of Slope Materials

When conducting a slope stability analysis, the slope materials and their strength properties must be well-defined to improve the performance of the slope behavior model. In stability analysis models, the strength of slope materials may be determined using various failure criteria. In limit equilibrium analyses, the Mohr-Coulomb Failure Criterion and the Infinite Strength Failure Criterion were employed to determine the strength parameters of the upper soil and intact rock layers, respectively. Meanwhile, the Mohr-Coulomb Failure Criterion was used in the analyses that utilized the finite element method.

The soil samples were taken in the field survey during the dry and rainy seasons. Afterward, the physico-mechanical properties of the soil layer were determined using laboratory tests to provide input data for modeling. The direct shear test was conducted to determine the strength parameters of the Mohr-Coulomb criterion, including the friction angle and cohesion. The physico-mechanical properties of the soil layer are shown in Table 1.

For modeling the behavior of slopes in stability studies, the pore water pressure ratio (r_u) has been widely used to describe the pore water pressure condition. As a result of the absence of PWP data in this study, the pore water pressure at any position may be best described using the pore water pressure ratio proposed by Bishop and Morgenstern (1960):

$$r_u = \frac{u}{\gamma h} \tag{3}$$

where h denotes the depth of the point in the soil mass below the soil surface, and γ denotes the soil unit weight.

The general solutions are based on the assumption of a constant pore water pressure ratio (r_u) throughout the cross-section, also known as a homogeneous pore water pressure distribution. However, the necessity for a single constant value is a significant drawback of the r_u approach. The only circumstance in which the r_u value is constant is when the piezometric line is at the ground surface, a scenario that occurs in nature relatively seldom.

In this study, the SLIDE model (Liao et al. 2010) was used to evaluate the variation in pore water pressure ratio based on rainfall data gathered during a heavy rainfall event from 22:00 h on May 30 to 24:00 h on May 31, 2020. At 15:00 h on May 31, the maximum r_u value was 0.286. The relationship between pore water pressure ratio and rainfall intensity is shown in Fig. 2.

Table 1 Parameters of soil layer

Parameter	Unit	Sampling season	
		Dry season	Rainy season
Unit weight (γ)	kN/m^3	18.9	19.3
Cohesion (c)	kPa	22.0	20.0
Friction angle (φ)	(°)	16.3	15.1

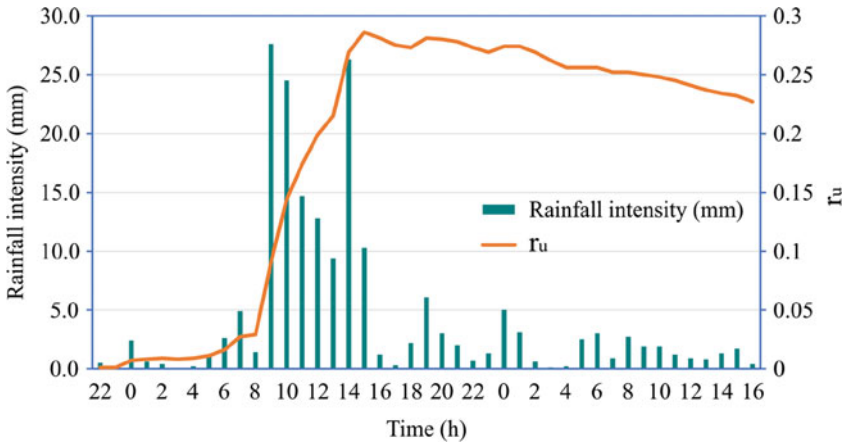

Fig. 2 Relationship between rainfall intensity and r_u

3.3 Model Calibration

The models in this study were calibrated by comparing simulation results with actual slope failure data. Until recently, slope stability and risk assessments based on deformation analysis had been conducted by various geotechnical engineers. With the introduction of 3D methods into computations for slope stability, it has become possible to solve these problems (Bar et al. 2021). However, while performing slope stability assessments, various challenges remain unsolved. They are primarily due to uncertainties in the calculation of slope stability, such as inaccuracies in determining the strength parameters of the slope materials, the selection of methods for solving the problem, algorithms for optimizing the sliding surface (using GLE limit equilibrium methods), and inaccuracies in the establishment of the geometric model (Fig. 3).

Despite minor inconsistencies between the calculation result and the actual data on the position of the landslide body, the authors considered the results produced using the Yanbu simplified method to be the most acceptable for evaluating landslide stability (Figs. 4 and 5).

3.4 Results of the Slope Stability Analysis Using LEM

After configuring the Slide3 model's input parameters, deterministic and probabilistic analyses were performed to determine the slope stability associated with changes in the pore water pressure caused by actual rainfall. These simulations were performed in the dry season and during periods of heavy rain, which increased the pore water pressure in the soil layer.

The analysis results indicated that the stability of the studied slope is maintained in the dry season. In simulations conducted during the dry season, the factor of safety (FS) value determined by probabilistic and deterministic analyses is 1.258 and 1.178, respectively. The probability of failure (PF) is 3.2%, which indicates that 3.2% of 1000 samples evaluated had a factor of safety value of less than 1 (Fig. 4).

The penetration of rainwater into the soil layer led to an increase in the pore water pressure ratio, which in turn resulted in a reduction in the slope stability or factor-of-safety value. The pore water pressure ratio increased from 0 in the absence of rain to 0.286 at 15:00 h on May 31. In probabilistic analysis, the FS value reduced from 1.258 to 0.901, whereas in deterministic analysis, it decreased from 1.178 to 0.895 (Table 2). When the pore water pressure ratio reached its maximum value, the probability of failure increased from 3.2% to 80.6%. In addition, the analysis results revealed that the studied slope became unstable around 10:00 h on May 31 when the FS value was less than one (Fig. 5).

Figures 6 and 7 show the relationship between the variation of the FS and PF values and the change in the pore water pressure ratio of the soil layer on the slope, as determined by the probabilistic analysis conducted in Slide3. Simultaneously, the analysis results performed by Slide3 also indicated a relationship between the probability of failure (PF) and the reliability index (RI) (Fig. 8).

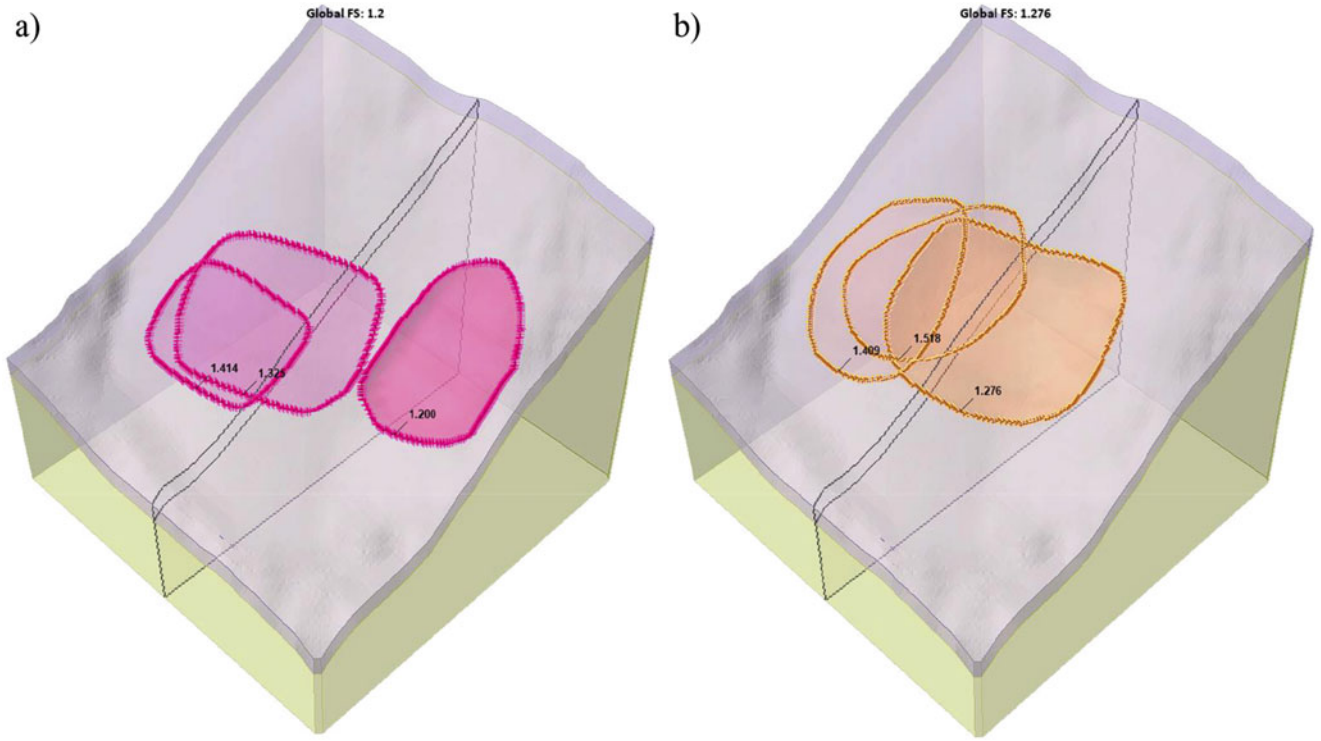

Fig. 3 Multimodal particle swarm optimization, Bishop's method (**a**) and Spencer's method (**b**)

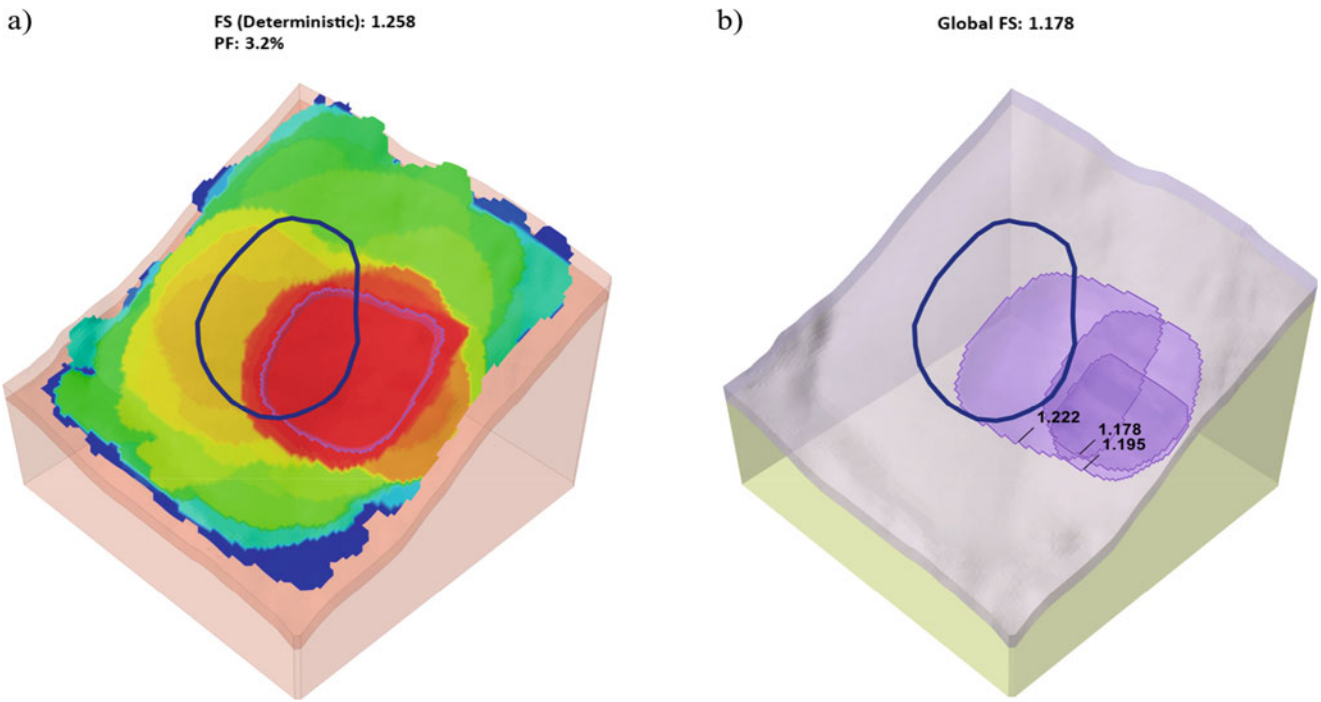

Fig. 4 The result of slope stability analysis using Slide3 in the dry season

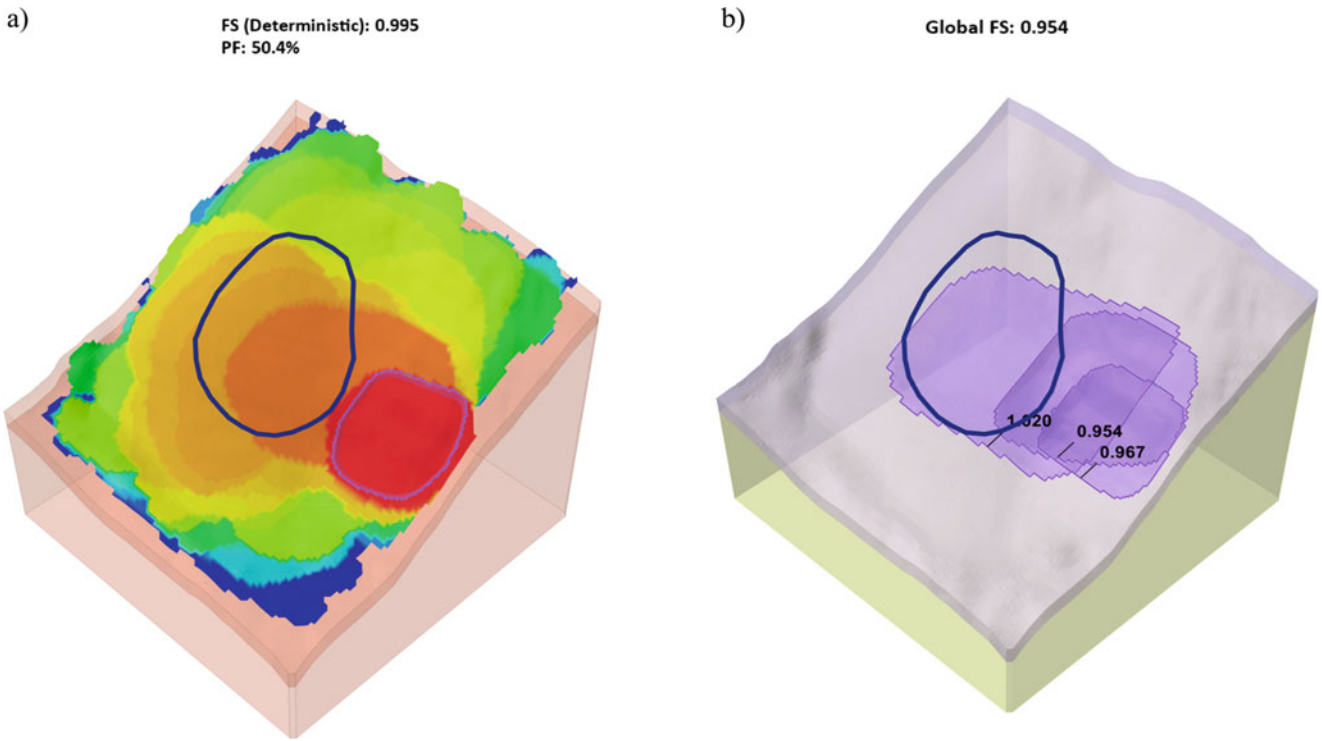

Fig. 5 The result of slope stability analysis using Slide3 at 10:00 h, May 31

Table 2 Results of slope stability analysis using LEM

Step	Time (h)	r_u	Slide3				Slide2
			Probabilistic analysis			Deterministic analysis	
			FS	PF (%)	RI	FS	
1		0	1.258	3.2	1.85	1.178	1.164
2	22	0.001	1.113	20.1	0.848	1.051	1.08
3	23	0.001	1.113	20.1	0.848	1.051	1.08
4	0	0.007	1.115	19.6	0.87	1.112	1.081
5	1	0.008	1.098	23	0.754	1.076	1.073
6	2	0.009	1.1	22.1	0.77	1.081	1.08
7	3	0.008	1.098	23	0.754	1.076	1.073
8	4	0.009	1.1	22.1	0.77	1.081	1.08
9	5	0.011	1.069	28.6	0.555	1.082	1.075
10	6	0.016	1.097	22.9	0.749	1.087	1.073
11	7	0.027	1.103	22	0.784	1.057	1.062
12	8	0.029	1.081	25.6	0.643	1.074	1.06
13	9	0.091	1.054	32.7	0.431	1.038	1.025
14	10	0.144	0.995	50.4	−0.014	0.954	0.986
15	11	0.174	0.97	58.6	−0.225	0.946	0.972
16	12	0.199	0.94	68.9	−0.504	0.941	0.929
17	13	0.215	1.039	37.9	0.309	0.944	0.941
18	14	0.269	0.983	55.6	−0.13	0.949	0.914
19	15	0.286	0.901	80.6	−0.891	0.895	0.902

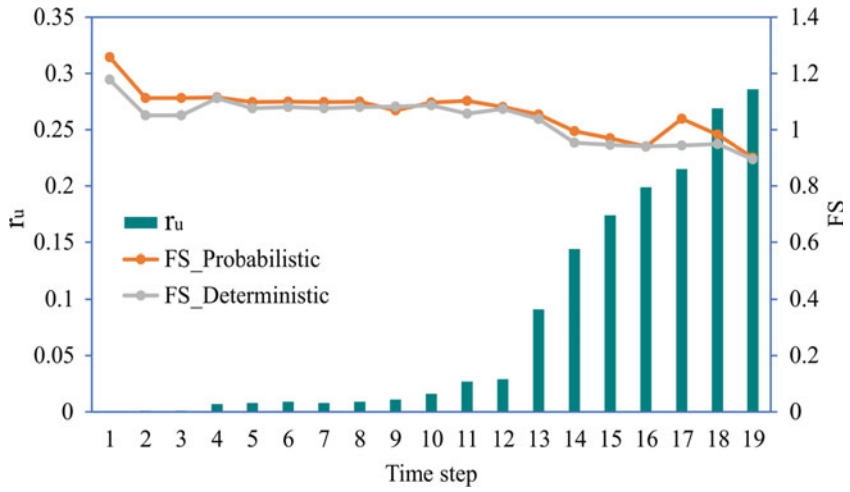

Fig. 6 Relationship between FS and r_u by probabilistic and deterministic analysis in Slide3

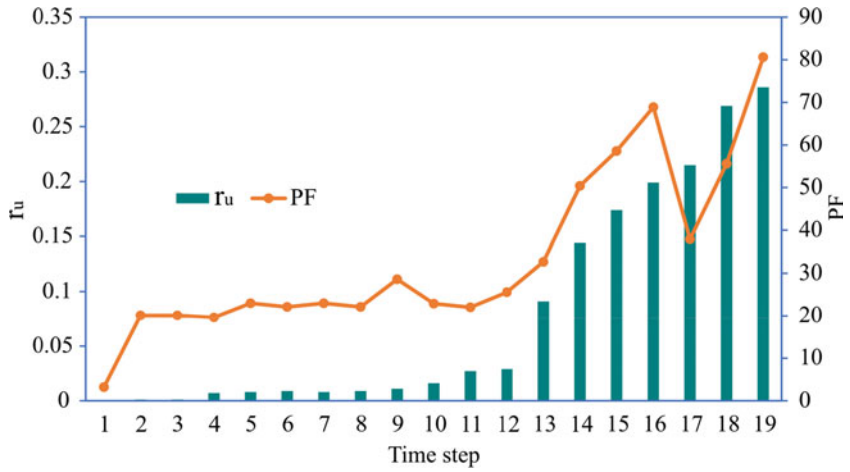

Fig. 7 Relationship between PF and r_u by probabilistic analysis in Slide3

Meanwhile, a correlation between the factor of safety (FS) and the pore water pressure ratio was also determined using the deterministic analysis in Slide3 (Fig. 6). The higher the pore water pressure ratio in the soil layer, the lower the FS value and the higher the PF value.

Using the "section creator" function in Slide3, a cross-section was generated for stability analysis in Slide2 based on the three-dimensional slope analysis model in Slide3. Afterward, slope stability assessments utilizing the same precipitation scenario as in Slide3 were performed in Slide2.

The outcomes of slope stability simulations during the dry season (a) and at the failure time of slope (b) are shown in Fig. 9. The position of the sliding surface is in the middle of the examined slope, which is relatively compatible with the sliding surface position determined by Slide3 and the actual sliding mass position. According to the 2D analysis results, the slope is stable throughout the dry season, as shown by the factor of safety (FS) value of 1.164. The pore water pressure ratio has increased because of rainwater penetration into the soil layer, resulting in a decrease in the factor of safety value. As the pore water pressure ratio increased from 0 to 0.286, the FS value reduced from 1.164 to 0.902 (Fig. 10). In addition, the analysis performed in Slide2 indicated that the slope became unstable on May 31, around 10:00 h, when the r_u value reached 0.144, which is equivalent to the simulation result in Slide3.

Table 2 summarizes the stability analysis results for the examined slope at each analysis step. As a result, we have determined that the factor of safety and probability of failure are the functions of the pore water pressure ratio. As seen in Table 2 and graphs, an increase in pore water pressure reduces the factor of safety value and increases the probability of failure value. However, steps 17 and 18 of our research produced several unexpected results in Table 2. This issue can be explained as follows:

1) The pore water pressure ratio is used to characterize pore-water conditions in slope stability analyses. However, the necessity for a single constant value is a significant drawback of the r_u method. It is well-known that the r_u value is

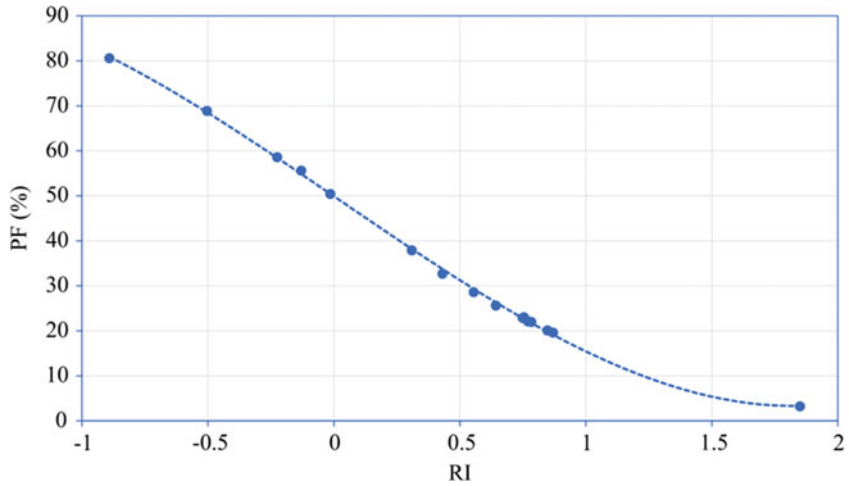

Fig. 8 Relationship between PF and RI by probabilistic analysis in Slide3

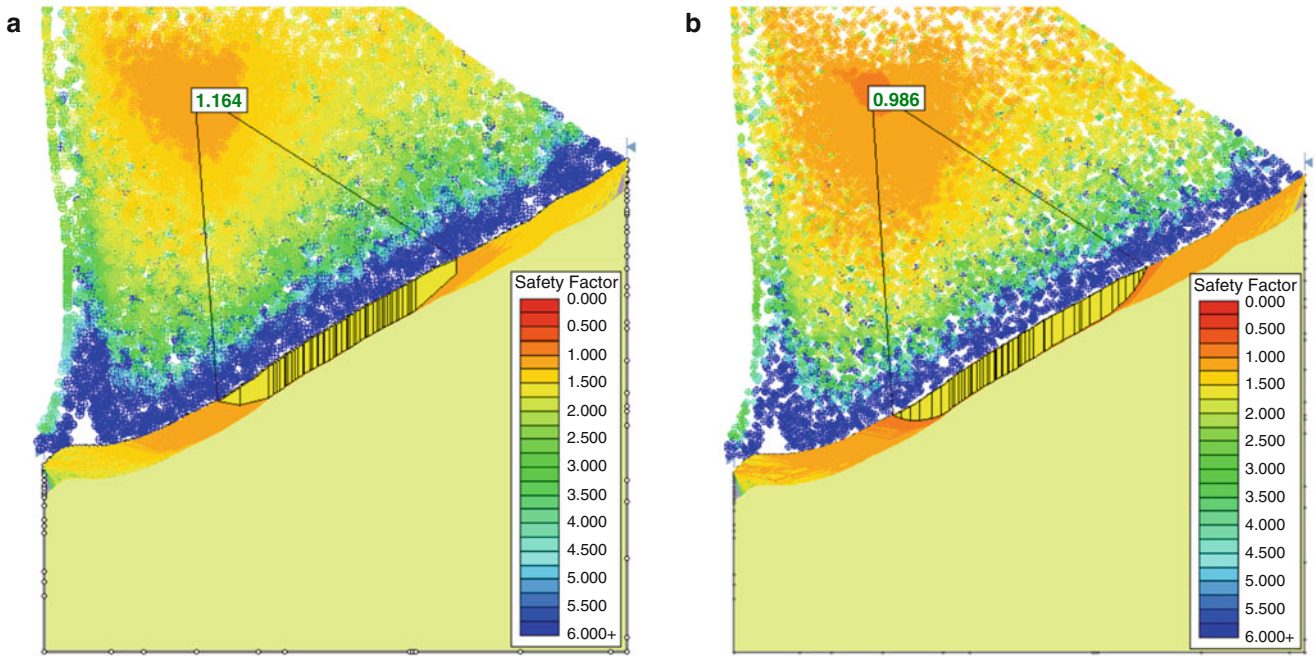

Fig. 9 The result of slope stability analysis using Slide2 in the dry season (**a**) and at 10:00 h, May 31 (**b**)

a constant only when the piezometric line is at the ground surface, which rarely occurs in nature. Therefore, it is not an ideal method to simulate actual groundwater conditions in all circumstances because the presence of any negative pore-water pressures is omitted when conducting simulations. Although the factor-of-safety results are acceptable, the analysis is based on the imperfect prediction of pore water pressure conditions.

2) These unexpected results may be caused by the sampling technique, the number of samples, the type of analysis, or the parameters used to set the sliding surface search method when performing simulations. However, increasing the number of analyzed samples and modifying the initial parameters will result in a considerable increase in analysis time and a significant increase in the demands on computational resources. Because the failure time of the slope has been determined, these anomalies have been accepted in this study.

Along with the factor of safety and probability of failure, the reliability index (RI) is a critical outcome for evaluating slope stability. The relationship between the probability of failure and the reliability index is shown in Fig. 8. As indicated by the computed maximum reliability index of 1.85 $<$ 3, it is necessary to implement protection measures to prevent this slope from becoming unstable. In addition, the analysis

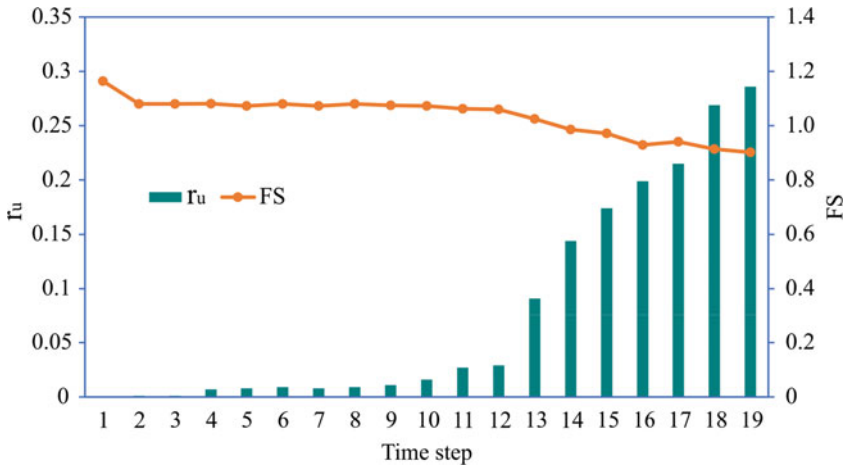

Fig. 10 Relationship between FS and r_u using Slide2

results demonstrated that the analyzed slope becomes unstable rapidly under the impact of rainfall.

3.5 Results of the Slope Stability Analysis Using FEM

Using the same input parameters as limit equilibrium analyses, two- and three-dimensional slope stability evaluations were conducted using the finite element method. As indicated by three-dimensional analysis using RS3, the slope is stable in the dry season with a critical strength reduction factor (SRF) of 1.32 (Fig. 11a). The penetration of rainwater into the soil caused an increase in pore water pressure in the sliding mass on the examined slope, resulting in a decrease in the critical strength reduction factor. The SRF value decreased from 1.32 to 0.96, corresponding to the pore pressure ratio increasing from 0 to 0.286 (Table 3). Additionally, the analysis results indicated that the studied slope became unstable around 14:00 h on May 31, when the SRF reached 0.98 (Fig. 11b).

An assessment result of the relationship between the critical strength reduction factor (SSR) as determined by the shear strength reduction method (SSR) integrated into RS3 and the pore water pressure ratio in the soil layer on the examined slope is shown in Fig. 12.

Generally, FS values determined by finite element analysis are higher than those calculated by limit equilibrium analysis. The FS values determined by RS3 are, on average, 1.06 times greater than those obtained by Slide3. The distribution of the instability zone predicted by finite element analysis corresponds to the results of limit equilibrium analysis.

For 2D slope stability analyses, the cross-section in RS2 was built up in the same way as in Slide2. The computed cross-sections were then set up using a uniform finite element mesh consisting of three-noded triangular elements. Simultaneously, this study investigated the influence of element mesh selection on the outcomes of stability analyses using meshes with 5000 (Fig. 13), 10,000 (Fig. 14), and 20,000 elements (Fig. 15). The SRF values obtained from the 5000 and 10,000 element meshes are higher than the SRF values obtained from RS3, whereas the SRF values obtained from the 20,000-element mesh are lower than those obtained from RS3. For simulations with grids of 5000 and 10,000 elements, the slope maintains a stable state with minimum strength reduction factors of 1.07 and 1.01, respectively. Meanwhile, the examined slope became unstable at about 14:00 h on May 31 when the strength reduction factor was 0.99, according to the stability analysis utilizing a 20,000-element mesh.

Similar to RS3, the results of slope stability analysis by RS2 revealed the relationship between the strength reduction factor (SRF) and the pore water pressure ratio. Figure 16 shows the relationship between the strength reduction factor and the pore water pressure ratio using different element meshes. In addition, the relationship between the number of mesh elements and the strength reduction factor is shown in Fig. 17. As shown in the figures, the higher the number of mesh elements, the lower the calculated strength reduction factor.

When the slope is affected by precipitation, the shear strength decreases, and the weight of the soil mass increases, causing a reduction in SRF. In addition, a quasi-linear relationship between these two variables was also determined. The study indicated that the appropriate selection of a finite element mesh is a crucial factor that directly influences the simulation results and slope stability assessment. The slope stability analysis results for each step are detailed in Table 3.

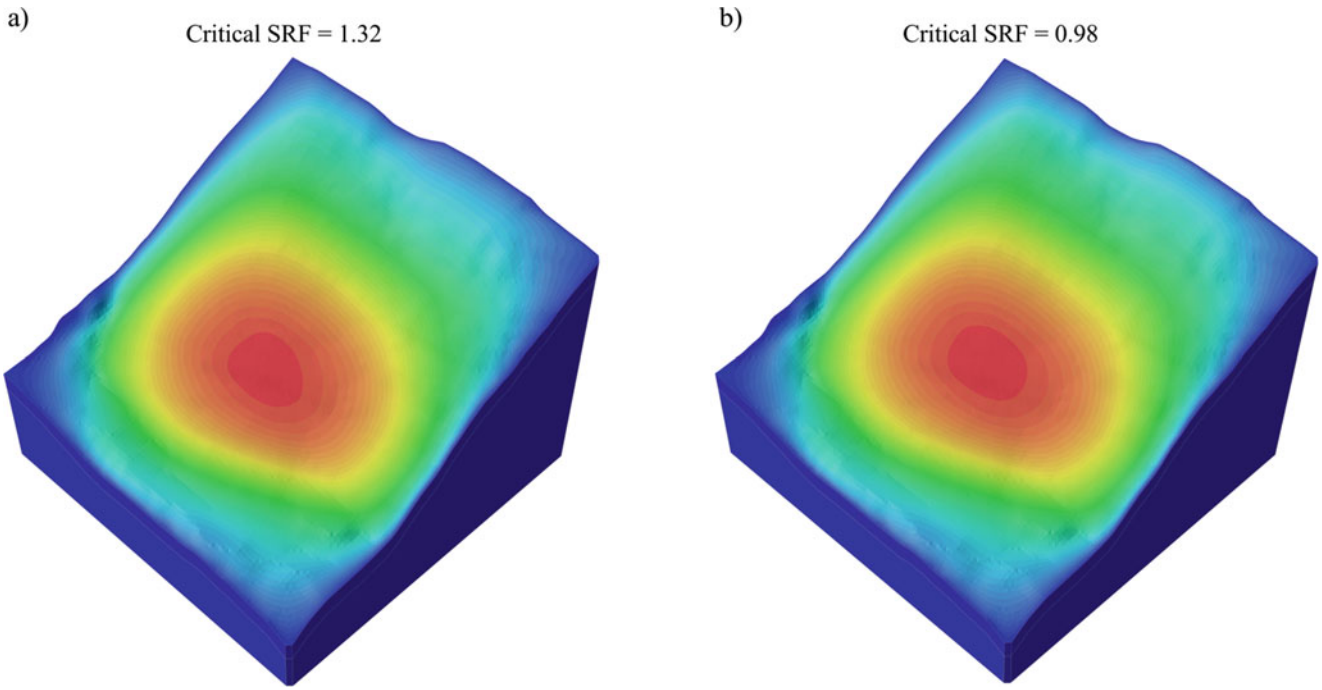

Fig. 11 The result of the slope stability analysis using RS3 in the dry season (**a**) and at 14:00 h, May 31 (**b**)

Table 3 Results of slope stability analysis using FEM

			RS2			
			5000-element mesh	10,000-element mesh	20,000-element mesh	RS3
Step	Time (h)	r_u	SRF	SRF	SRF	SRF
1		0	1.43	1.35	1.3	1.32
2	22	0.001	1.29	1.21	1.17	1.19
3	23	0.001	1.29	1.21	1.17	1.19
4	0	0.007	1.28	1.21	1.17	1.18
5	1	0.008	1.28	1.21	1.17	1.18
6	2	0.009	1.28	1.21	1.17	1.18
7	3	0.008	1.28	1.21	1.17	1.18
8	4	0.009	1.28	1.21	1.17	1.18
9	5	0.011	1.28	1.21	1.17	1.18
10	6	0.016	1.27	1.2	1.16	1.18
11	7	0.027	1.27	1.2	1.15	1.17
12	8	0.029	1.27	1.19	1.15	1.17
13	9	0.091	1.22	1.15	1.11	1.12
14	10	0.144	1.18	1.11	1.07	1.08
15	11	0.174	1.16	1.09	1.05	1.05
16	12	0.199	1.14	1.08	1.04	1.03
17	13	0.215	1.13	1.06	1.02	1.02
18	14	0.269	1.08	1.03	0.99	0.98
19	15	0.286	1.07	1.01	0.98	0.96

3.6 Comparison of the Slope Stability Analysis Results Using LEM and FEM

All the results of calculating the change in FS values of the examined slope are shown in Fig. 18 to compare the difference in FS values between LEM and FEM stability analyses (Table 4).

The study results revealed that the decreasing trend of the factor-of-safety graphs established by the two methods corresponds to the increase in the pore water pressure ratio.

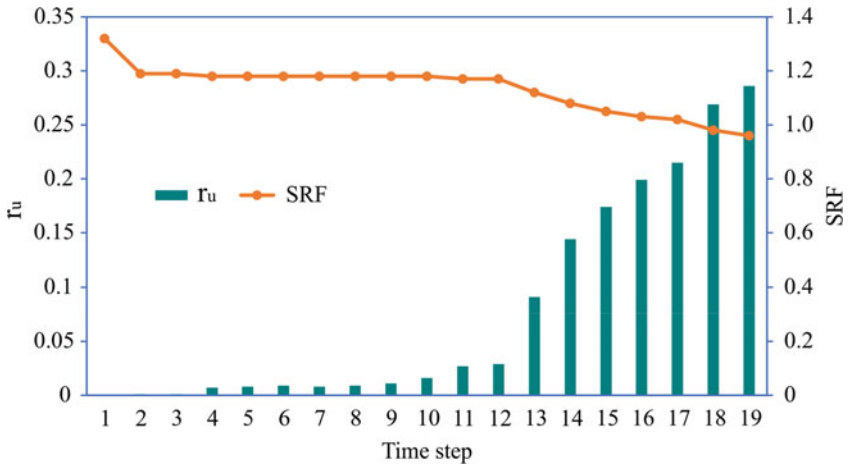

Fig. 12 Relationship between SRF and r_u using RS3

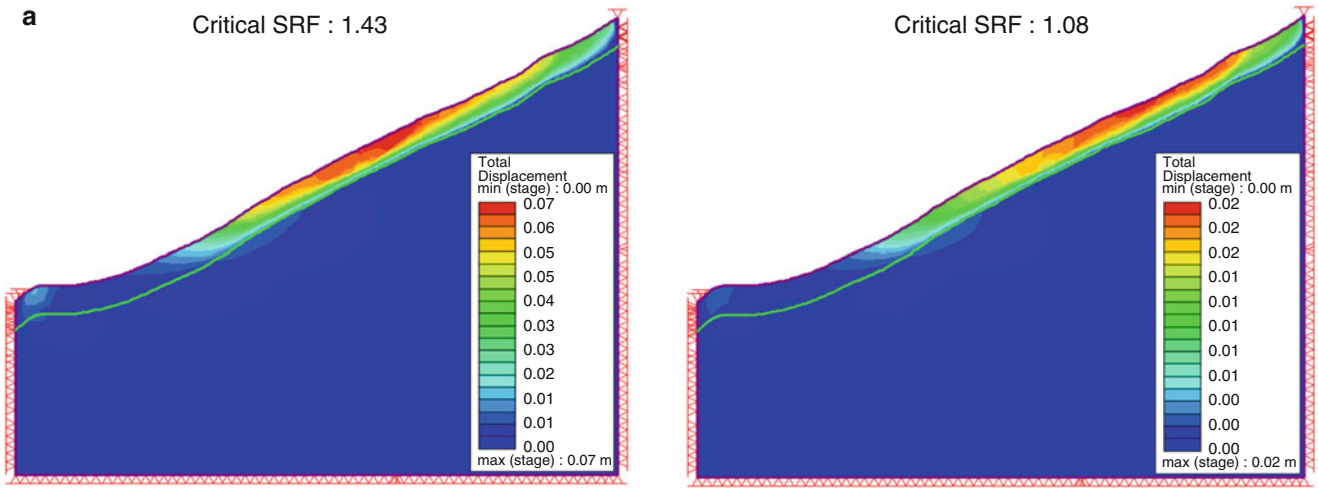

Fig. 13 The result of the stability analysis using RS2 in the dry season (**a**) and at 14:00 h, May 31 (**b**) (5000-element mesh)

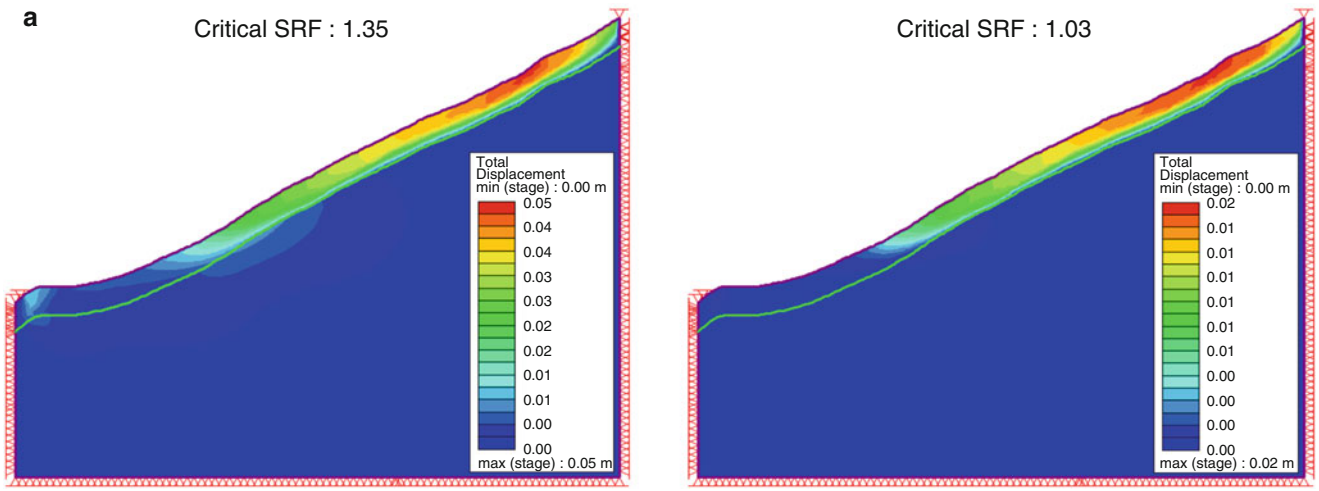

Fig. 14 The result of the stability analysis using RS2 in the dry season (**a**) and at 14:00 h, May 31 (**b**) (10,000-element mesh)

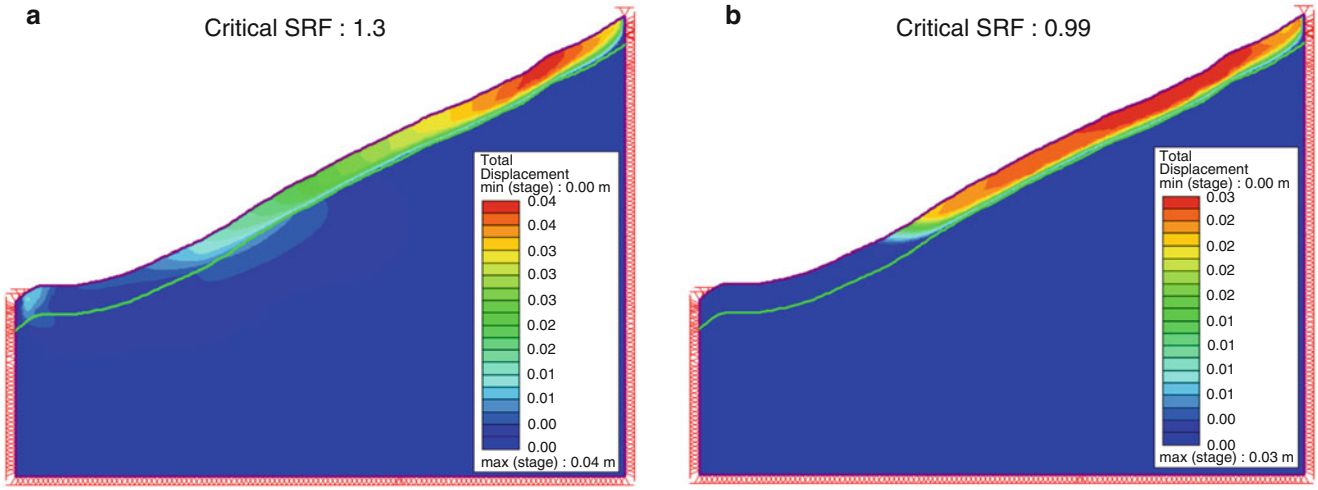

Fig. 15 The result of the stability analysis using RS2 in the dry season (**a**) and at 14:00 h, May 31 (**b**) (20,000-element mesh)

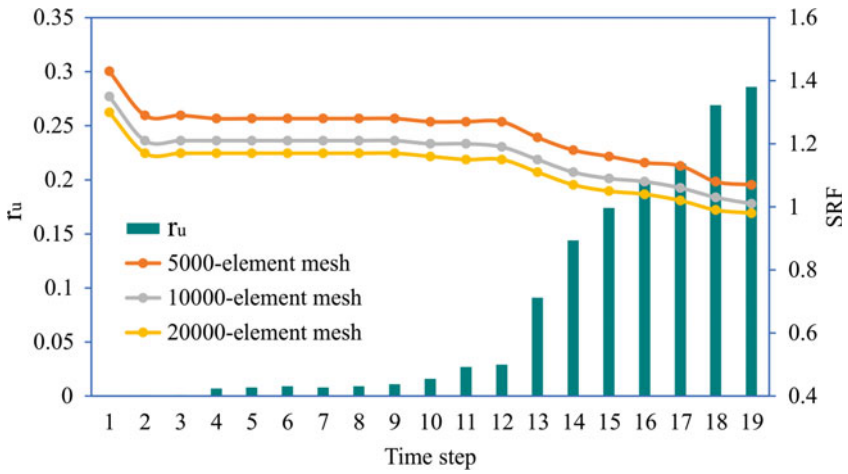

Fig. 16 Relationship between SRF and r_u using RS2

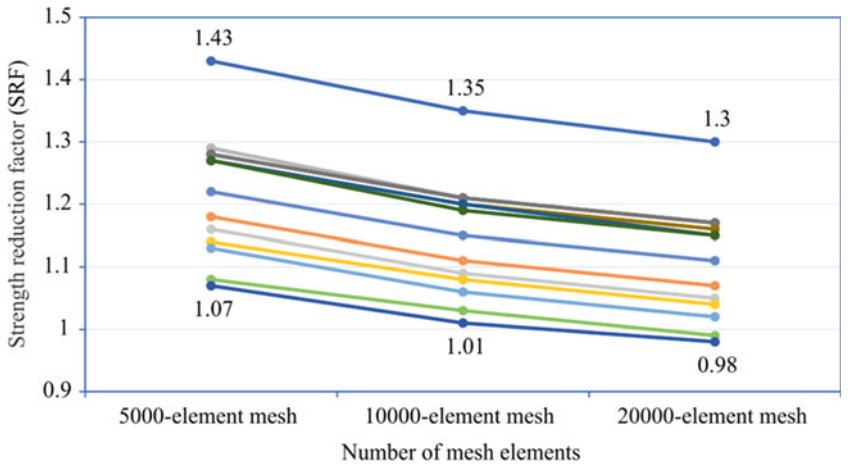

Fig. 17 Relationship between SRF and element mesh

Nonetheless, analyses indicated that the finite element method yields greater FS values than those from the limit equilibrium method. In 3D simulations, the mean difference between the finite element method and the limit equilibrium method for calculating the FS values is only 6.03% (probabilistic) and 8.59% (deterministic). Meanwhile, in 2D analyses,

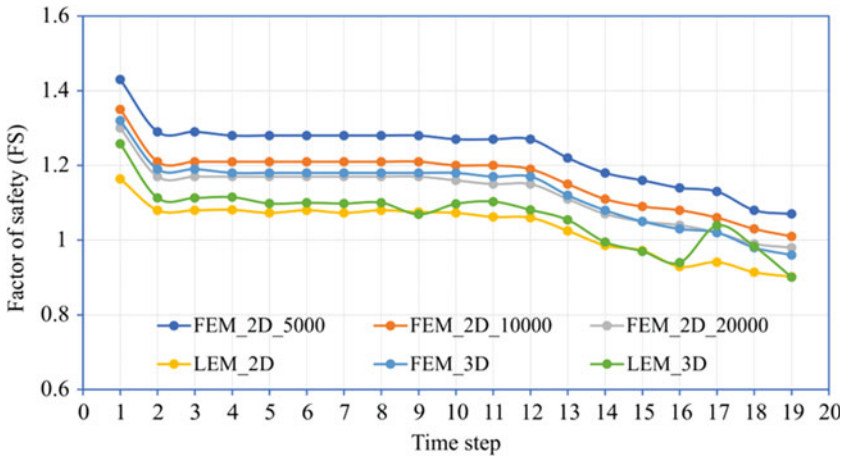

Fig. 18 Results of stability analysis using FEM and LEM

Table 4 Difference between FS values

Analysis method	Mean difference between FS values (%)	Min-max difference between FS values (%)
FEM 3D and LEM 3D	6.03	−1.86 to 9.41
	8.59	3.16 to 11.68
FEM 2D (5000-element mesh) and LEM 2D	16.3	15.37 to 18.6
FEM 2D (10,000-element mesh) and LEM 2D	11.28	10.58 to 13.78
FEM 2D (20,000-element mesh) and LEM 2D	8.08	7.43 to 10.67
FEM 2D (5000-element mesh) and FEM 3D	8.31	7.09 to 10.28
FEM 2D (10,000-element mesh) and FEM 3D	2.81	1.65 to 4.95
FEM 2D (20,000-element mesh) and FEM 3D	−0.69	−1.74 to 2.04
LEM 3D and LEM 2D	2.78	−0.56 to 9.43
	0.09	−3.35 to 3.69

the mean difference between the finite element method and the limit equilibrium method for the value of FS is 16.3 (5000-element mesh), 11.28 (10,000-element mesh), and 8.08% (20,000-element mesh), respectively. According to the simulation results, 3D analyses show a lower difference in FS values than 2D analyses. When comparing the outcomes of 2D and 3D finite element analyses, the mean difference in the FS values is 8.31 (5000-element mesh), 2.81 (10,000-element mesh), and −0.69% (20,000-element mesh), respectively. The simulation results revealed that 2D analysis with the 20,000-element grid provides the most comparable results to 3D analysis. The mean difference in the FS values between the 2D and 3D simulations using the limit equilibrium method is 2.78% (probabilistic) and 0.09% (deterministic). The FS values obtained from the 3D limit equilibrium analyses compared to the 2D analyses are consistent with the slope stability studies of numerous other authors.

3.7 Relationship Between Pore Water Pressure Ratio and Seismic Coefficient

Landslides may be triggered by a single earthquake in the Sapa area since the district is located in a seismically active zone of Vietnam. In addition, earthquakes that occur during rainy periods may increase the probability and scale of landslides, therefore increasing the potential damage. As a result, a relationship between pore water pressure and earthquake loading has been established in this study for examined sliding mass (Fig. 19). The area above the trendline indicates instability, whereas the area under this trendline indicates slope stability. When the r_u value is high, as shown in Fig. 19, even a minor earthquake might cause slope failures. Destabilization of the studied slope might occur because of individual earthquakes with a seismic coefficient of approximately 0.08 or rainfall with a r_u value of more than 0.19. When considering the combined effects of the two triggers, the equation shown in Fig. 19 may be employed. This relationship may be established for any natural or artificial slope in the study area to provide the most comprehensive evaluation of slope instability hazards.

4 Conclusions

The slope stability assessment has a critical role, especially given the increasing development of urban areas in Vietnam's mountainous provinces. The assessment quality has a significant impact on the selection of the worksite and the most

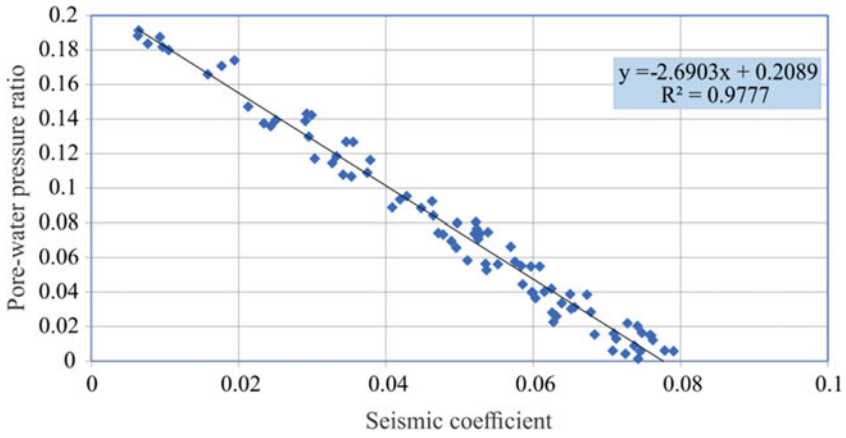

Fig. 19 Relationship between pore water pressure ratio and seismic coefficient

suitable solutions for preventing slope failures. Based on the above idea, a slope stability analysis has been conducted for a landslide in Trung Chai commune, Sapa district, Lao Cai province.

The change in pore water pressure caused by rainfall was simulated using the pore water pressure ratio. Slope stability models may be established in two- and three-dimensions using input data obtained by field survey, including the digital elevation model of the sliding mass, the boundary between soil and rock layers, and their related physico-mechanical parameters. The Slide2, Slide3, and RS2, RS3 models were used to assess two-dimensional and three-dimensional slope stability utilizing the limit equilibrium and finite element methods, two of the most frequently employed methods in slope stability analysis. The variation in slope stability was investigated using probabilistic and deterministic analyses simultaneously. The study outcomes were utilized to establish correlations between slope stability (i.e., the factor of safety and probability of failure) and the change in PWP condition and to identify the slope failure moment. Comparing the 2D and 3D analysis results, the 2D FEM analyses provide a higher FS value than the 3D FEM analyses, whereas the 2D LEM analyses yield a lower FS value than the 3D LEM analyses. A comparison of the results between the FEM simulations and the LEM simulations reveals that the 2D and 3D FEM simulations provide higher FS values.

Despite some unexpected outcomes, the study investigated the behavior of slopes under the effect of precipitation and determined the moment of slope collapse. These results are consistent with the actual landslide occurrence, demonstrating the reliability of the simulation models. In Vietnam, the safety factor is currently the most significant parameter for evaluating slope stability. As a result, there is some subjective evaluation when studying slope stability, implying future risks. According to the research team, slope stability analysis reports should include additional values for the probability of failure and the reliability index. Additionally, it is necessary to establish a specific standard for the reliability index, which will be used to assess the probability of failure for various types of projects.

Acknowledgments We would like to express our gratitude to the Institute of Geological Sciences, Vietnam Academy of Science and Technology, and the national science and technology project under grant number ĐTĐL.CN-81/21 for supplying simulation data, as well as the Rocscience company for granting an academic software license (the Department of Engineering Geology of MGRI is a participant in the Rocscience Academic Bundle program).

References

Abdulai M, Sharifzadeh M (2021) Probability methods for stability design of open pit rock slopes: an overview. Geosciences 11(8). https://doi.org/10.3390/geosciences11080319

Alimohammadlou Y, Najafi A, Yalcin A (2013) Landslide process and impacts: a proposed classification method. CATENA 104:219–232. https://doi.org/10.1016/j.catena.2012.11.013

Azizi MA, Marwanza I, Ghifari MK, Anugrahadi A (2020) Three dimensional slope stability analysis of open pit mine. In: Kanlı AI (ed) Slope engineering. IntechOpen, London. https://doi.org/10.5772/intechopen.94088. ISBN: 978-1-83962-946-4

Bar N, Arrieta M, Espino A, Diaz C, Mosquea L, Mojica B, McQuillan A, Baldeon G, Falorni G (2021) Back-analysis of ductile slope failure mechanisms and validation with aerial photogrammetry, InSAR and GbRAR to proactively manage economic risks to protect the mine plan. In: Hammah RE, Yacoub TE, McQuillan A, Curran J (eds) The evolution of geotech – 25 years of innovation. CRC Press, London, pp 512–526. https://doi.org/10.1201/9781003188339-25. ISBN: 978-1-003-18833-9

Bishop AW, Morgenstern N (1960) Stability coefficients for earth slopes. Géotechnique 10(4):129–153. https://doi.org/10.1680/geot.1960.10.4.129

Cami B, Ma T, Yacoub T, Javankhoshdel S (2021) Considering multiple failure modes: a comparison of probabilistic analysis and multi-modal optimization for a 3D slope stability case study. In: Hammah RE, Yacoub TE, McQuillan A, Curran J (eds) The evolution of geotech – 25 years of innovation. CRC Press, London, pp 189–195. https://doi.org/10.1201/9781003188339-25. ISBN: 978-1-003-18833-9

Cheng Y, He D (2020) Slope reliability analysis considering variability of shear strength parameters. Geotech Geol Eng 38(4):4361–4368. https://doi.org/10.1007/s10706-020-01266-w

Christian John T, Ladd Charles C, Baecher Gregory B (1994) Reliability applied to slope stability analysis. J Geotech Eng 120(12): 2180–2207. https://doi.org/10.1061/(ASCE)0733-9410(1994)120:12(2180)

Collins Brian D, Znidarcic D (2004) Stability analyses of rainfall induced landslides. J Geotech Geoenviron Eng 130(4):362–372. https://doi.org/10.1061/(ASCE)1090-0241(2004)130:4(362)

Dai FC, Lee CF, Wang SJ (2003) Characterization of rainfall-induced landslides. Int J Remote Sens 24(23):4817–4834. https://doi.org/10.1080/01431160131000082424

Dang KB, Burkhard B, Müller F, Dang VB (2018) Modelling and mapping natural hazard regulating ecosystem services in Sapa, Lao Cai province, Vietnam. Paddy Water Environ 16(4):767–781. https://doi.org/10.1007/s10333-018-0667-6

Duncan JM, Wright SG, Brandon TL (2014) Soil strength and slope stability. Wiley, Hoboken, NJ. ISBN: 9781118917954. 336p

Fomenko IK, Zerkal OV (2017) The application of anisotropy of soil properties in the probabilistic analysis of landslides activity. Proc Eng 189:886–892. https://doi.org/10.1016/j.proeng.2017.05.138

Fomenko I, Zerkal O, Kurguzov C, Shubina DD (2019) Probabilistic analysis of slope stability and landslide risk assessment. Disaster Dev 8(1 and 2):1–9

Kamien DJ (1997) Engineering and design: introduction to probability and reliability methods for use in geotechnical engineering. United States Army Corps of Engineers, Washington, DC

Liao Z, Hong Y, Wang J, Fukuoka H, Sassa K, Karnawati D, Fathani F (2010) Prototyping an experimental early warning system for rainfall-induced landslides in Indonesia using satellite remote sensing and geospatial datasets. Landslides 7(3):317–324. https://doi.org/10.1007/s10346-010-0219-7

Nagendran S, Ismail M, Wen Y (2019) 2D and 3D rock slope stability assessment using Limit Equilibrium Method incorporating photogrammetry technique. Bull Geol Soc Malay 68:133–139. https://doi.org/10.7186/bgsm68201913

Tien Bui D, Tuan TA, Hoang N-D, Thanh NQ, Nguyen DB, Van Liem N, Pradhan B (2017) Spatial prediction of rainfall-induced landslides for the Lao Cai area (Vietnam) using a hybrid intelligent approach of least squares support vector machines inference model and artificial bee colony optimization. Landslides 14(2):447–458. https://doi.org/10.1007/s10346-016-0711-9

Van Duong B, Fomenko IK, Nguyen KT, Vi LHT, Zerkal OV, Dang Hong V (2022) Application of GIS-based bivariate statistical methods for landslide potential assessment in Sapa, Vietnam (in Rus). Bull Tomsk Polytechnic Univ. Geo Assets Eng 333(4): 126–140. https://doi.org/10.18799/24131830/2022/4/3473

Wang W, Constantino C (2009) Reliability analysis of slope stability at nuclear power plant site. Proceedings of 20th International Conference on Structural Mechanics in Reactor Technology (SMiRT 20), Espoo, Finland, 9–14 August 2009

Withiam J, Voytko E, Barker R, Duncan M, Kelly B, Musser S, Elias V (1998) Load and resistance factor design (LRFD) for highway bridge substructures. Federal Highway Administration, Washington, DC

Yang D, Qiu H, Zhu Y, Liu Z, Pei Y, Ma S, Du C, Sun H, Liu Y, Cao M (2021) Landslide characteristics and evolution: what we can learn from three adjacent landslides. Remote Sens 13(22). https://doi.org/10.3390/rs13224579

Landslide Early Warning System Based on the Empirical Approach: Case Study in Ha Long City (Vietnam)

Nguyen Duc Ha, Nguyen Huy Duong, Nguyen Quoc Khanh, Tran The Viet, Do Van Vung, Nguyen Thi Hai Van, and Nguyen Hoang Ninh

Abstract

Landslides refer to a common type of natural disaster in the mountainous areas in Vietnam, potentially causing detrimental impacts on humans, property, and the environment. In light of the emerging damage pertaining to this type of natural disaster in recent years, the construction of an effective landslide early warning system appears to be more critically urgent than ever.

This study proposes a landslide early warning system based on a landslide susceptibility map and a rainfall threshold for Ha Long City (capital of Quang Ninh Province). Due to the difference in the collected data, the Spatial Multi-Criteria Evaluation (SMCE) method was used to create a landslide susceptibility map at a scale of 1:50,000 for Quang Ninh Province, while the empirical method was used to establish the landslide rainfall threshold for Ha Long City, using data from 2005 to 2016 on rainfall and landslides.

The results, which were verified with the inventory map (for the landslide susceptibility map) and with the landslide and rainfall data in the 2017–2021 period (for the rainfall threshold), showed the reliability of predicting the spatial and temporal occurrences of landslides.

Following that, the landslide susceptibility map and rainfall threshold can be added to a WebGIS-based landslide early warning system along with information from automatic weather stations and rainfall forecasts. This will help authorities and local people in the study area get landslide warnings effectively.

Keywords

Natural disaster · Landslide early warning · SMCE · Rainfall threshold · Ha Long City

1 Introduction

Landslides are one of the deadliest natural catastrophes with the potential for serious socioeconomic devastation, including loss of life and damage of property. Landslides occur in a diversity of landscapes around the world and rainfall is often the most prevalent trigger (Crosta and Frattini 2008; Tran et al. 2021). For example, the heavy rain caused by Hurricane Mitch in October and November 1998 induced thousands of landslides in Honduras, El Salvador, Guatemala, and Nicaragua (Bucknam et al. 2001). About 147 slope failures and 33 debris flows were recorded around Umyeon mountain in South Korea in July 27, 2011 due to heavy rainfall (Viet et al. 2016).

In general, efficient planning and management might significantly lessen the damage caused by landslides (Sultana and Tan 2021). To mitigate the landslide disaster, especially human casualties and injuries, the most effective method is probably the early identification of the locations and time of landslide occurrence. Brabb (1991) concluded that more than 90% of the damages could be avoided if landslides could be warned early.

Cetina and Nadim (2008) defined a landslide early warning system as "monitoring devices designed to avoid, or at least to minimize the impact imposed by a threat on humans". Establishing an early warning system for landslide occurrence (location and time) plays a vital role in managing, preventing, and mitigating probable hazards and damages. There are several systems that integrated landslide susceptibility maps, rainfall thresholds, real-time and forecasted rainfall data with WebGIS (Zhang et al. 2011; Ahmed et al. 2018). While physically-based models are usually appropriate for small areas (a single slope or a small catchment), the

N. D. Ha (✉) · N. H. Duong · N. Q. Khanh · N. T. H. Van · N. H. Ninh
Vietnam Institute of Geosciences and Mineral Resources, Hanoi, Vietnam

T. T. Viet · D. Van Vung
Thuyloi University, Hanoi, Vietnam

I. Alcántara-Ayala et al. (eds.), *Progress in Landslide Research and Technology, Volume 2 Issue 1, 2023*,
Progress in Landslide Research and Technology, https://doi.org/10.1007/978-3-031-39012-8_9

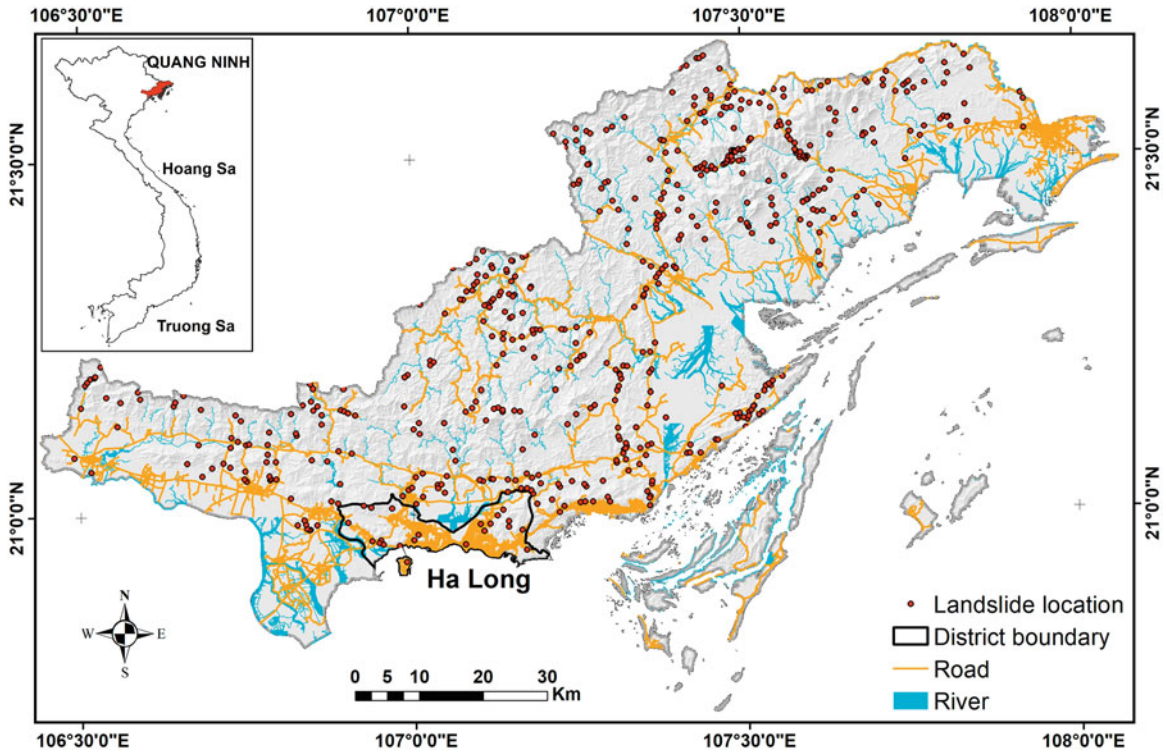

Fig. 1 Landslide locations in Ha Long City and Quang Ninh Province

empirical approach can be applied to much larger areas (city, province, country) if the historical data are available (Guzzetti et al. 2020).

Vietnam is one of the nations that have been deeply affected by natural hazards and climate change (Le et al. 2021). Principally, mountainous areas often suffer from abnormal weather phenomena causing many extreme rainfall events and accelerating the process of natural disasters. This trend results in the urgent requirement for effective effort in order to prevent and mitigate damage. However, one of the barriers to researching and developing a landslide early warning system in Vietnam is the heterogeneity and difficulty in data collection, especially data on historic landslide events (Hung et al. 2017).

To develop a landslide early warning system for Ha Long City, the landslide susceptibility map and rainfall thresholds triggering landslides need to be achieved. To perform these tasks, information on landslide locations (for landslide susceptibility mapping) and landslide occurrence times (for identifying rainfall thresholds) needs to be collected. However, the rapid urbanization in Ha Long City renders it more difficult to determine the locations of landslide occurrences. According to the survey results of the State-Funded Landslide Project (SFLP): "Investigation, assessment, and warning zonation for landslides in the mountainous regions of Vietnam" in 2015, only 20 landslide locations inside Ha Long City can be identified and surveyed. In contrast, numerous landslide spots (494 in total) may still be reliably found in other regions of Quang Ninh Province (Fig. 1). The time of occurrence is critical for determining the rainfall threshold triggering landslides (at least the date of landslide occurrence). However, most landslide sites in Vietnam are only properly statisticized and recorded if they result in severe damages such as human deaths, building collapses, and traffic bottlenecks on key and essential roads. As a result, the occurrence time of landslides may only be gathered if they occur in densely populated residential regions such as Ha Long City.

Because of this discrepancy, the authors had to create a landslide susceptibility map for the whole of Quang Ninh province (Ha Long City included) and establish a dedicated rainfall threshold for Ha Long City.

2 Study Area

Being a province situated in the northeast of Vietnam, Quang Ninh features quite a diverse topography with types of coastal plains and swamps, midland hills, and mountains. The province has a typical tropical climate with a hot, rainy, and humid summer (from May to October) and cold, dry winter (from November to April). The province receives an average of 1995 mm of precipitation every year, the majority of which falls during the summer (80–85% of the total annual

precipitation). Due to the influence of several natural, environmental, and societal variables, the mountainous region of Quang Ninh province is prone to numerous natural catastrophes, particularly landslides.

Ha Long is the capital city of Quang Ninh Province. With the benefit of coal resources and a favorable location for tourism, and trade, Ha Long City has recently had the fastest growth and urbanization in Vietnam. The topography of Ha Long City is also quite diverse and complex, including mountains, delta, coastal, and island. The hilly and mountainous areas are mainly in the north and northwest and account for about 70% of the land area. According to the Quang Ninh Department of Construction assessment, many households in Ha Long City live in landslide-prone areas (DOC 2016). Therefore, developing a system for landslide early warning in Ha Long City is very urgent.

3 Methodology and Results

3.1 Landslide Susceptibility Map by Spatial Multi-criteria Evaluation (SMCE) Method

The SMCE method is a semi-quantitative evaluation technique that is often used to determine the landslide susceptibility index (LSI). This method was developed from the analytical hierarchical process (AHP), and it can support users in performing multi-criteria assessment in a spatial model.

Technically, the SMCE method overcomes the limitations of quantitative assessment methods which require a large amount of accessible and comprehensive data. The method is heavily reliant on expert opinion, since each landslide causal component is employed as a mapping parameter, and each of those mapping parameters is assessed based on the subjective experience of experts (Castellanos 2008). The difference between semi-quantitative and qualitative methods is the association of the weight under certain criteria. In fact, the semi-quantitative technique has an advantage when the timing of occurrence of landslides cannot be determined and the available numeric data is restricted (Castellanos Abella and Van Westen 2007).

Input maps of the SMCE method are used as representative spatial criteria, which are grouped, normalized, and weighted in a "criteria tree". The output of the SMCE method consists of one or more "composite index maps" that show the results of simulations (Castellanos Abella and van Westen 2007).

The SMCE can be represented, as a matrix as depicted in the diagram in Fig. 2, whereas:

- Matrix A includes criteria (factors that influent the landslide initiation) represented on an axis (C1 to Cn) and a list of possible alternatives (to establish a hierarchy, score, assign weights, etc.). The decision is made from the set of criteria (the result of matrix A) showing a different axis (A1 to Am).
- Each cell in the matrix (aij) represents performing a specific alternative for each specific criterion. The value of each cell in the matrix is the product of the multiplication of the value (normalized to values between 0 and 1) of each criterion for a particular alternative and the weight corresponding to each criterion (W1 to Wn).
- As long as the cells in the matrix have been filled (all criteria have been evaluated), the final value equals the sum of all the cell values of the different criteria for each particular alternative (for example sum of the values of cells a11 to a1n for alternative A1).

The process of landslide susceptibility mapping for Quang Ninh Province follows 08 main steps as below:

(1) Collect available information, data, and spatial factor maps for the study area

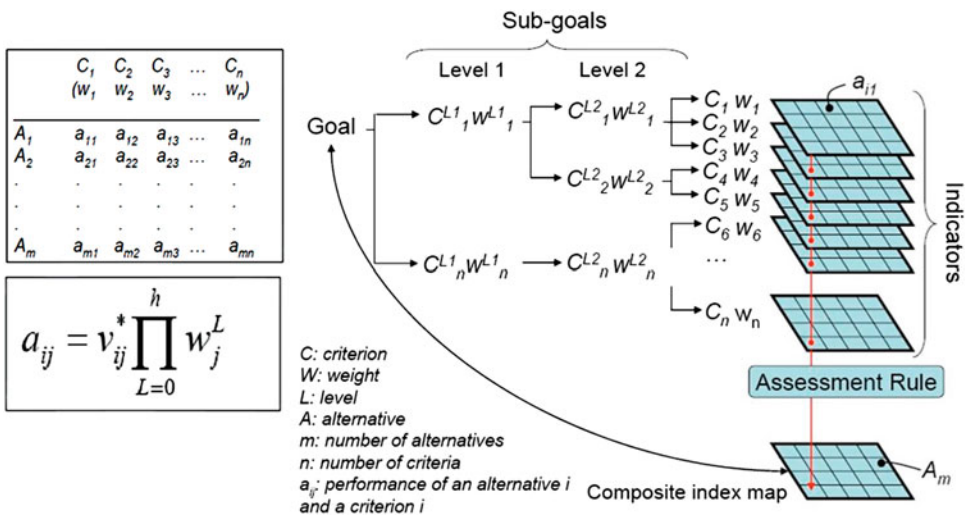

Fig. 2 Schematic procedure of the Spatial Multi-Criteria Evaluation (SMCE) method (Castellanos Abella and Van Westen 2007)

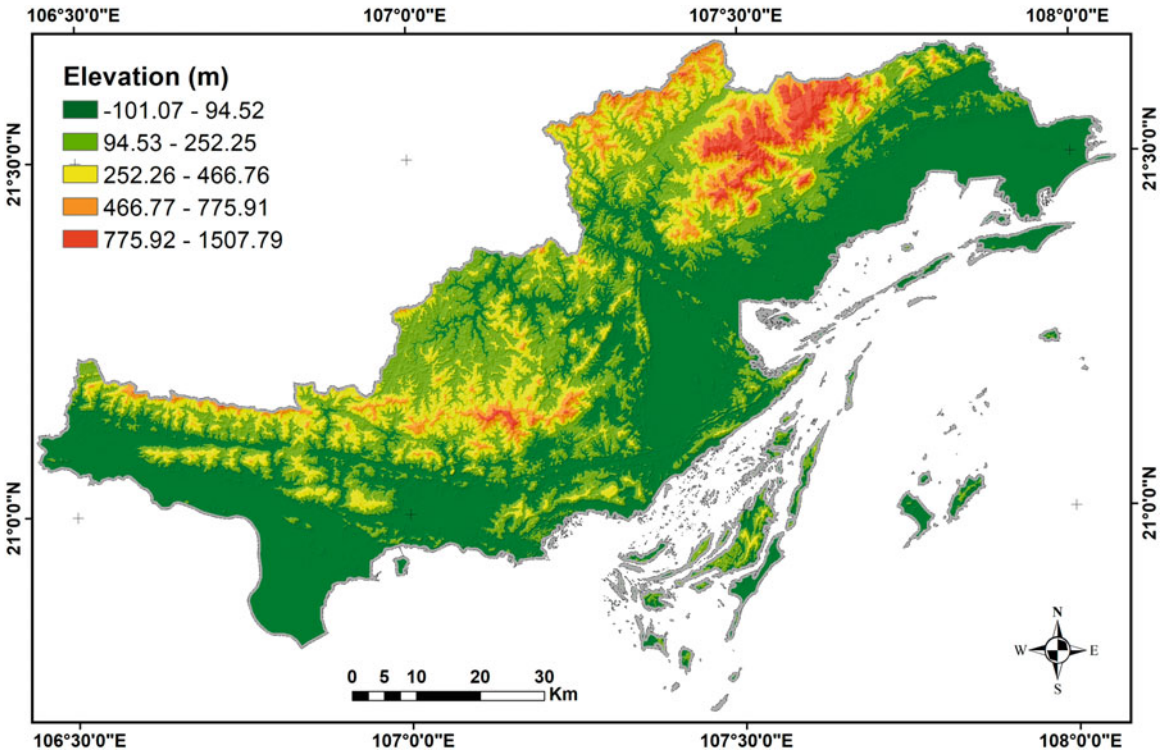

Fig. 3 Landslide factor map: Elevation

(2) Compile and normalize all selected spatial factor maps and their attributes
(3) Rasterize factor maps and divide them into different groups of criteria
(4) Structure the problem into a criteria tree by assigning the spatial data that is relevant for each of the criteria
(5) Standardize factor maps and design value functions using SMCE model in which the map or column values are converted to values between 0 and 1
(6) Determine the weights of the criteria within one group and among groups using SMCE tools such as direct weights, pairwise comparison and rank ordering
(7) Calculate and evaluate the output map as Landslide Susceptibility Index (LSI) map
(8) Classify the results to generate the final map as the landslide susceptibility map

From the results of document collection and synthesis, and on the basis of the completeness of the factor maps in terms of data structure and attributes, nine landslide factor maps were selected as the main input data for landslide susceptibility assessment by the SMCE method. These factors are: Elevation, slope, land cover, amplitude of relief, lineament density, drainage density, groundwater availability, and weathering crust type. The maps of these factors were collected from the SFLP project at 1:10,000 and 1:50,000 scales and applied to the SMCE module using ArcGIS software with the exact resolution of 20 m (Figs. 3, 4, 5, 6, 7, 8, 9, 10 and 11).

The role of nine selected factors susceptible to landslides in Quang Ninh Province has been analyzed and evaluated based on summarizing the assessment opinions of 02 groups of experts: field survey staff and professional research staff. The assessment of the influential role of the input factors for the SMCE model in the Quang Ninh area is summarized in the "criteria tree" presented in Fig. 12. The map layers are considered as the "main criteria", and the attributes of each map layer are considered as "sub-criteria". The susceptibility of each criterion to the landslide is expressed by the weight W. The values of weight W are calculated by the Analytic Hierarchy Process AHP (Saaty 1977, 2000), on the basis of pairwise comparisons between the "main criteria" and between the "sub-criteria" of each "main criteria".

Based on the natural distribution of susceptibility values, four thresholds of susceptibility index to landslide have been determined to classify the LSI map (output of SMCE module) into five susceptibility classes: Very low, low, moderate, high, and very high (Table 1). The landslide susceptibility maps of Quang Ninh Province and Ha Long City were generated, as shown in Figs. 13 and 14.

The landslide locations (identified through field survey and aerial image interpretation) (Fig. 1) were employed to validate the accuracy of the landslide susceptibility map. The

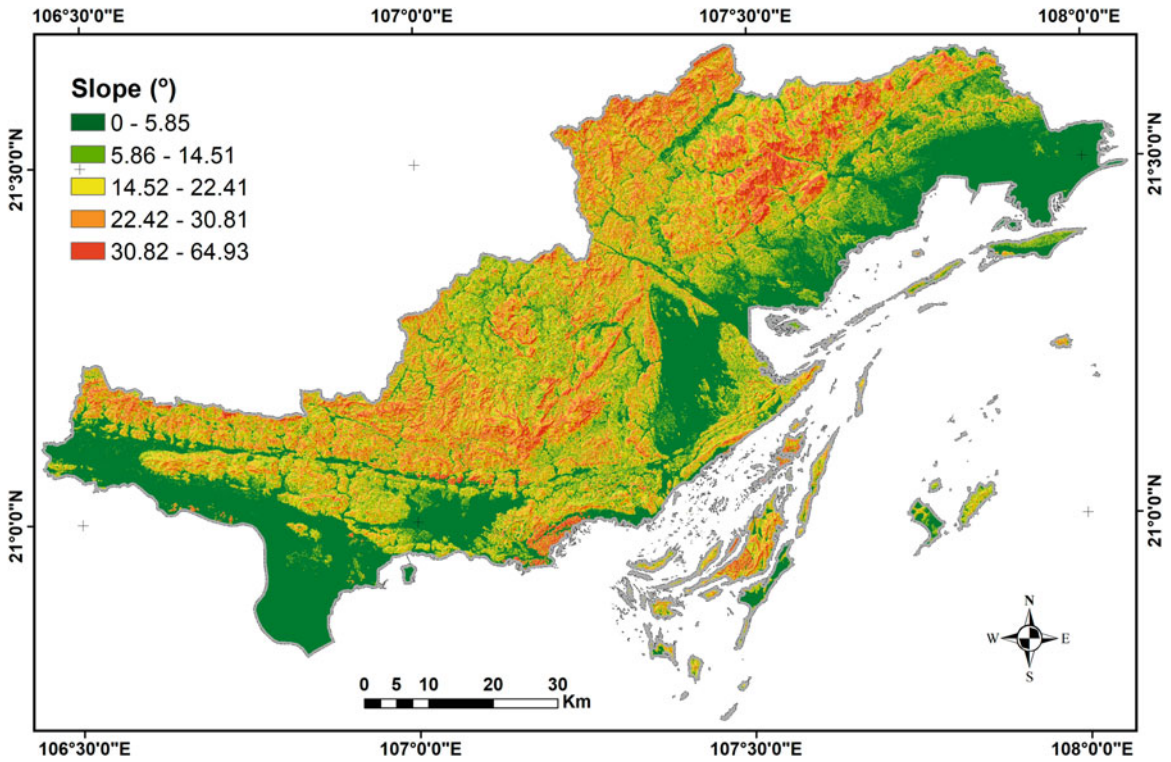

Fig. 4 Landslide factor map: Slope

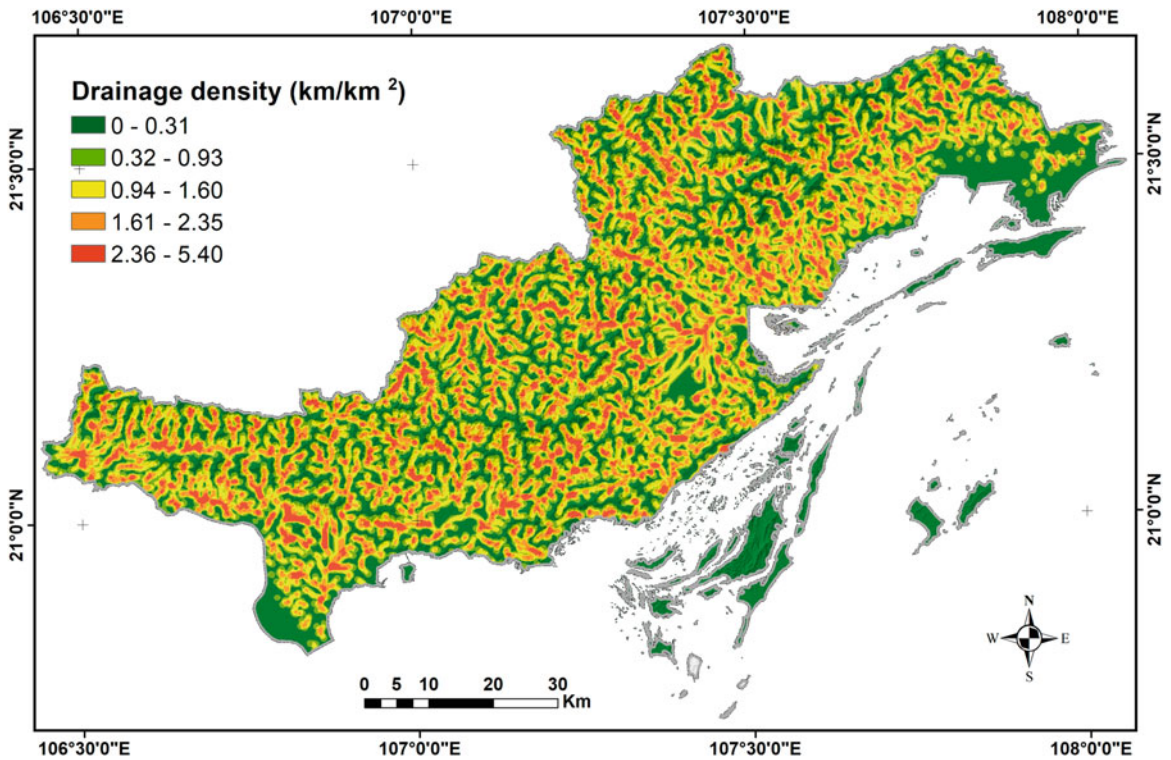

Fig. 5 Landslide factor map: Drainage density

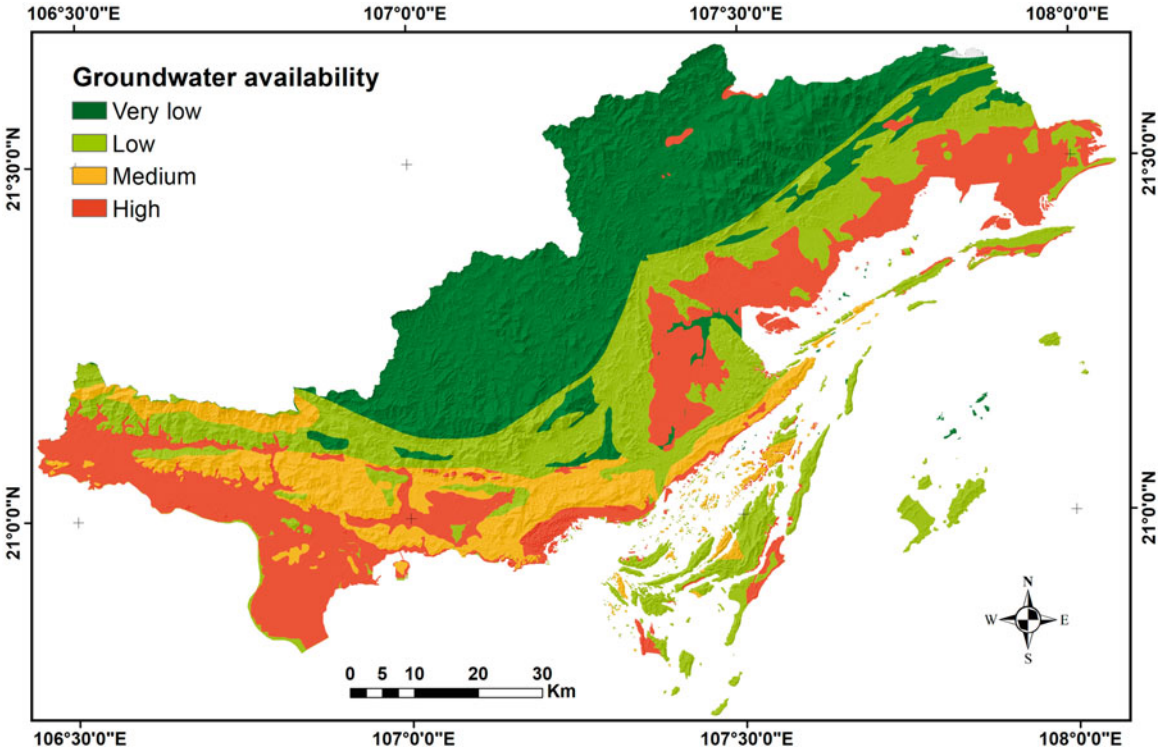

Fig. 6 Landslide factor map: Groundwater availability

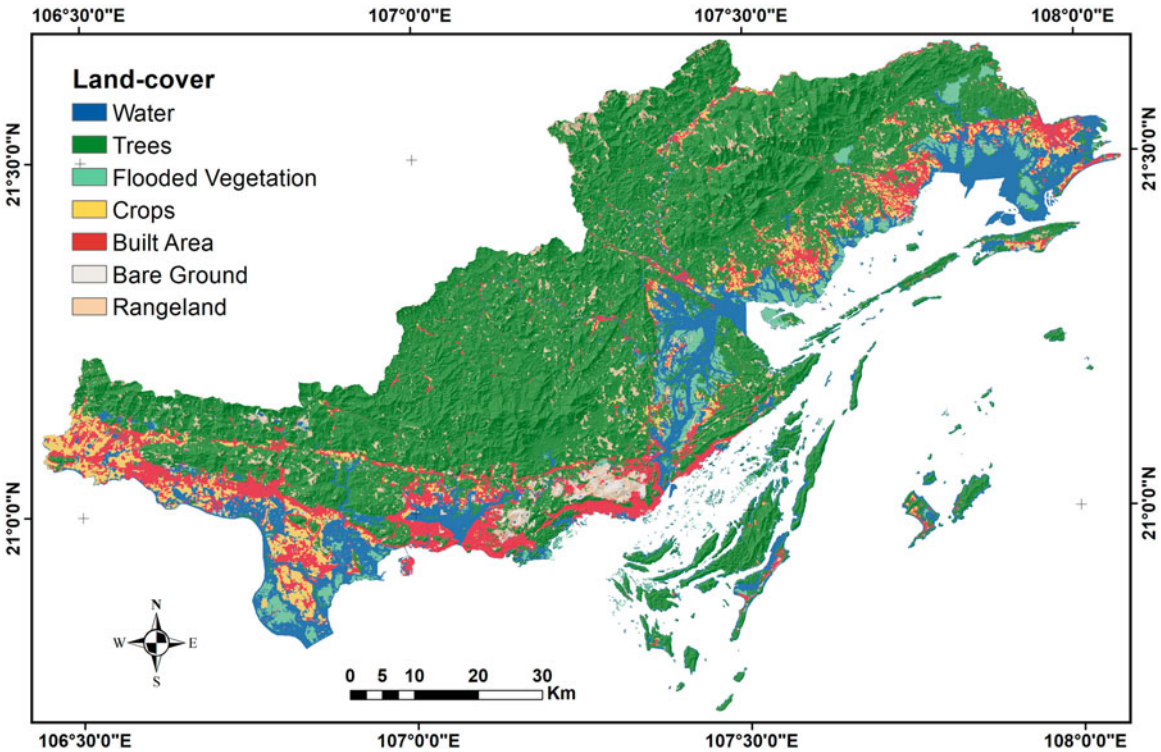

Fig. 7 Landslide factor map: Land cover

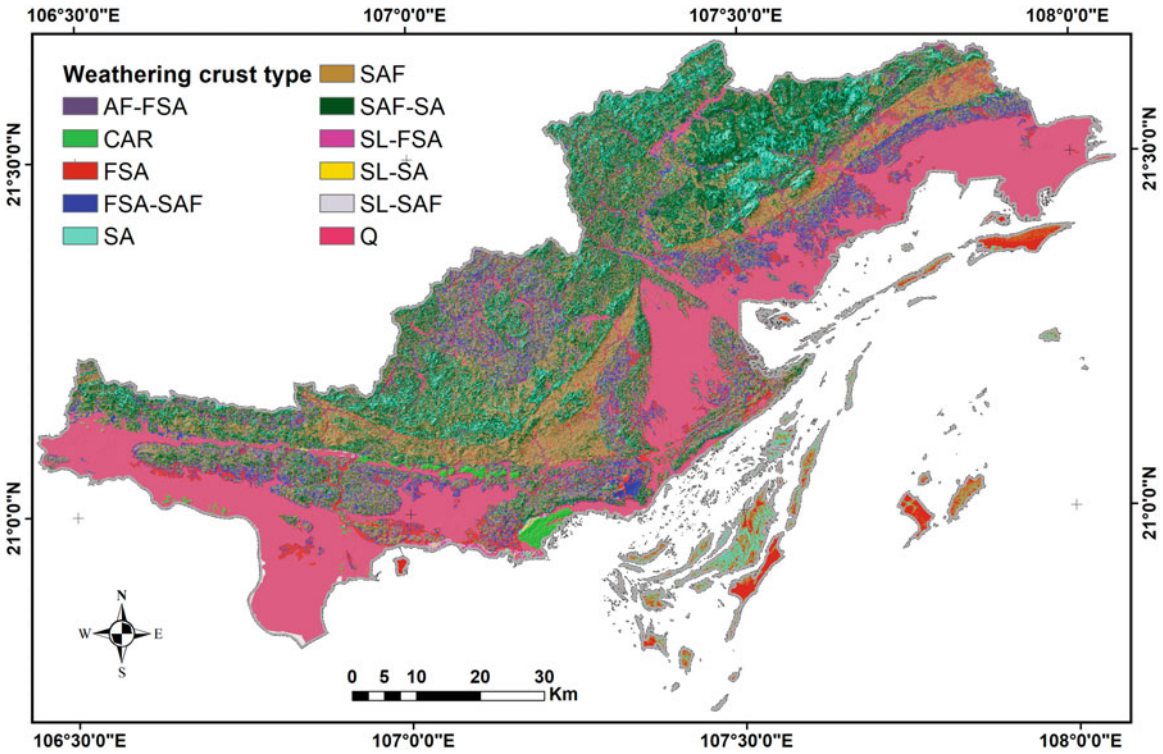

Fig. 8 Landslide factor map: Weathering crust type

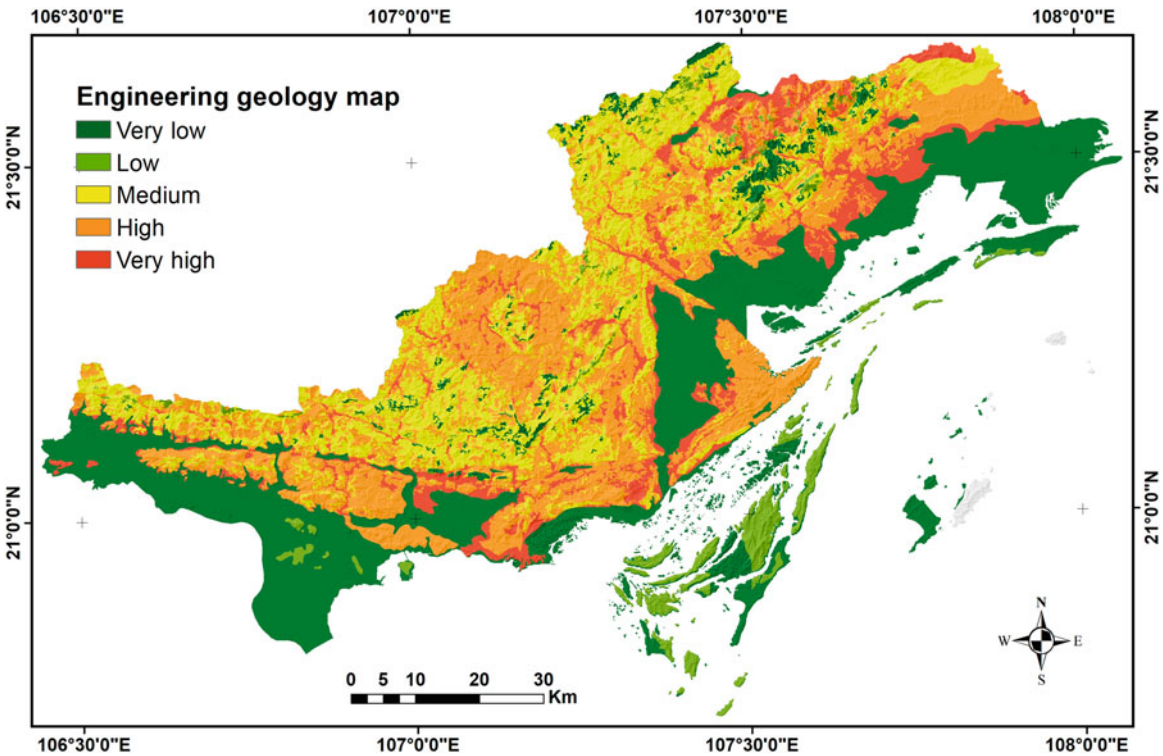

Fig. 9 Landslide factor map: Engineering geology

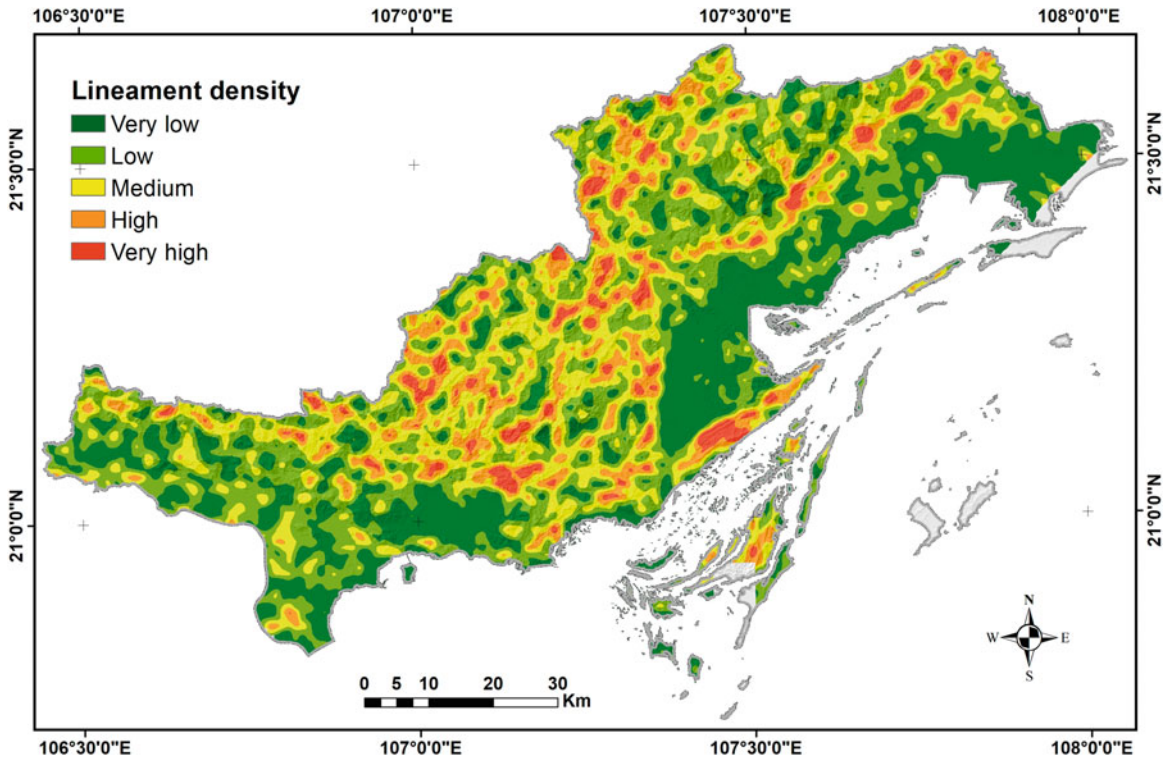

Fig. 10 Landslide factor map: Lineament density

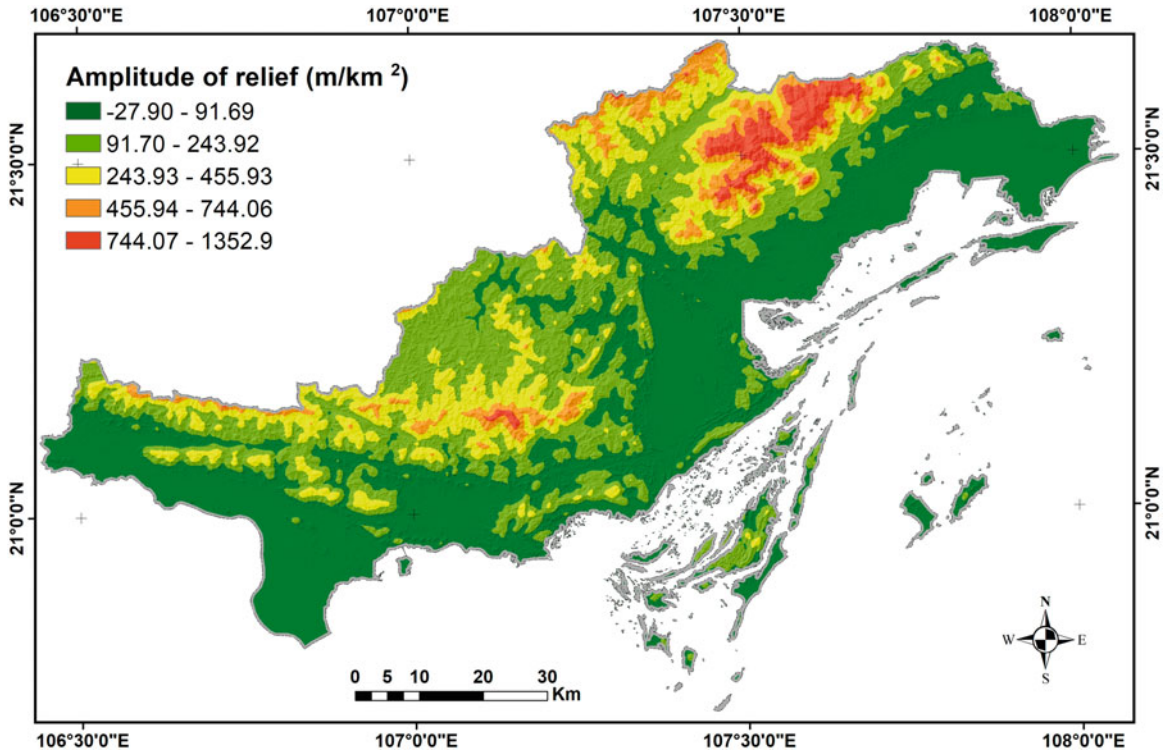

Fig. 11 Landslide factor map: Amplitude of relief

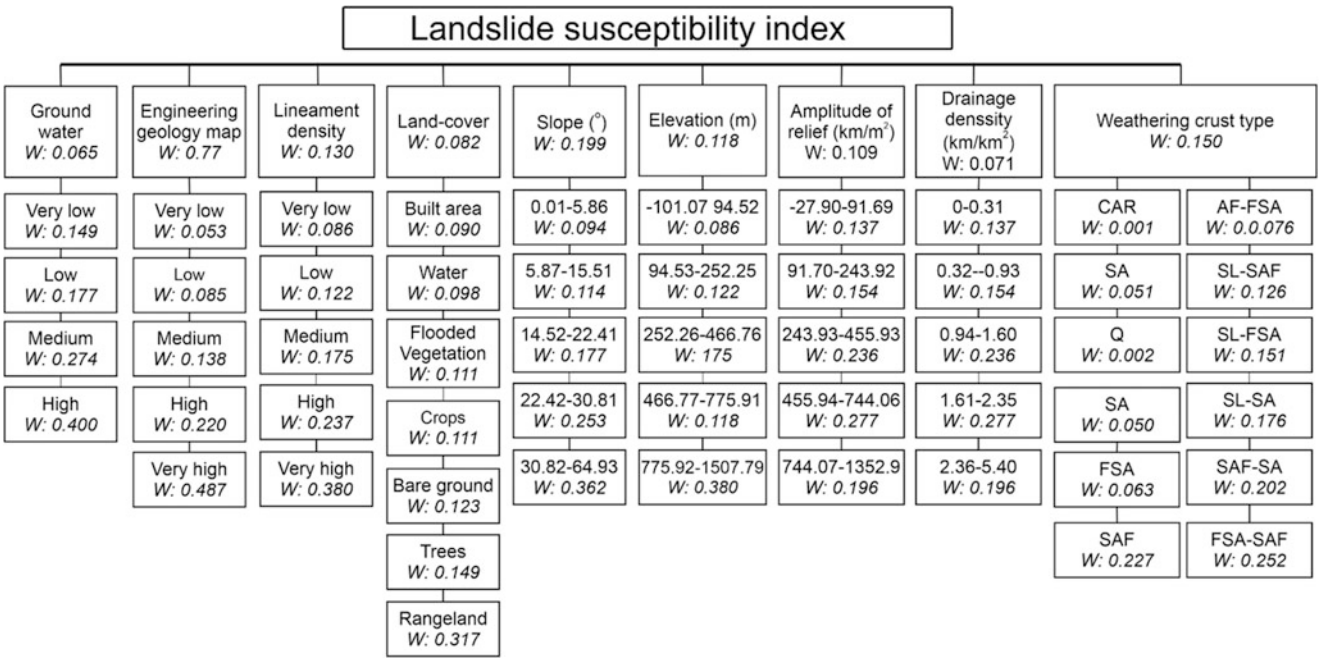

Fig. 12 Criteria tree for criteria weight (W), showing the influence on landslide occurrence of 09 factors

Table 1 LSI thresholds for generating landslide susceptibility map in Quang Ninh Province

Susceptibility index (LSI)	Landslide susceptibility class
0–0.1181	Very low
0.1182–0.1502	Low
0.1503–0.1765	Moderate
0.1766–0.2017	High
0.2018–0.2923	very high

distributions of the predicted landslide susceptibility classes (very low, low, moderate, high, and very high) in the susceptibility map compared with the observed landslides in Quang Ninh Province and Ha Long City were summarized in Tables 2 and 3 respectively. The result shows that 323 landslide events (63% of the recorded landslides) occurred in the zones with high and very high susceptibility, although these zones account for only 29% of the total area of Quang Ninh Province. Only 18 landslide events (4%) occurred in low susceptibility areas covering around 2916 km^2 (48%) of the province area. Considering Ha Long City only, 40% (8/20) of observed landslides are distributed in the two most susceptibility zones that cover 8% of the city area.

In the comparison tables for both Quang Ninh Province and Ha Long City, the largest proportions of landslides are located in the moderate susceptibility zones (34% in Quang Ninh Province and 50% in Ha Long City). However, it is worth noting that most of these landslide locations are on excavated slopes (for road and house constructions).

These results are consistent with the actual situation of the landslide occurring in Quang Ninh Province and Ha Long City. It shows that the landslide susceptibility map for Quang Ninh Province has high reliability to be applied in the early warning system for Ha Long City.

3.2 Empirical Rainfall Threshold

The empirical approach is applied to identify rainfall thresholds by analyzing historical rainfall events that triggered and did not trigger landslides. The main principle of this approach involves the assumption about the past relationship representing the rainfall-initiated landslides that will also induce landslide events in the future (Gioia 2013).

The method to identify landslide rainfall threshold includes three main steps as follows:

Step 1) Collect and process data:

- Collect information related to landslides in Ha Long City from mass media, field investigation, and previous studies.
- Collect rainfall data in the past. The rainfall data (hourly and daily) in rainy seasons (May–October) from 2005 to

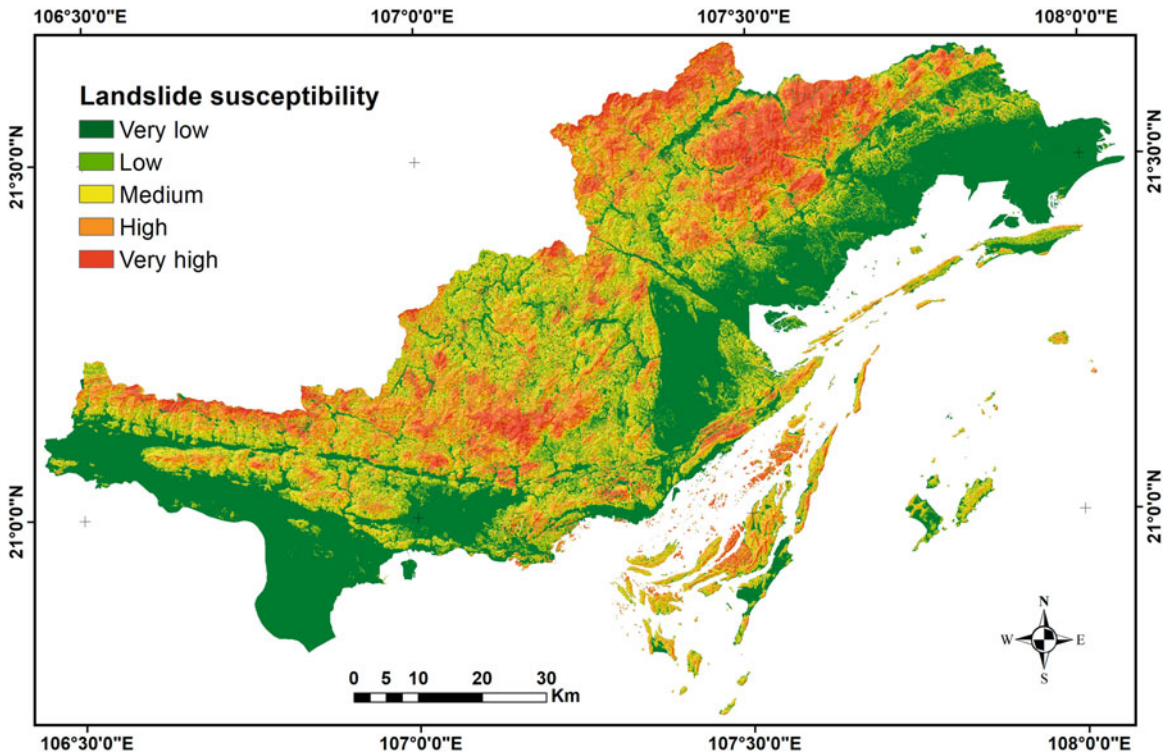

Fig. 13 Landslide susceptibility map of Quang Ninh Province

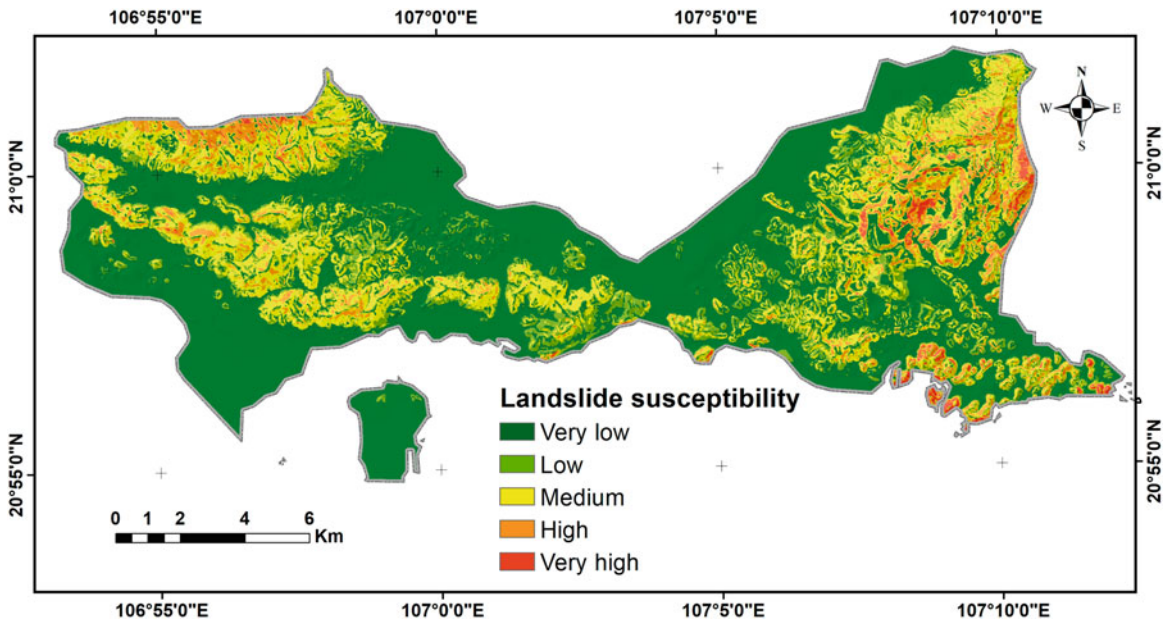

Fig. 14 Landslide susceptibility map of Ha Long City

2021 was used in this study. It comes from the Bai Chay National Hydro-meteorological station in Ha Long City's center.

Step 2) Examine the correlation between rainfall data and landslide events in the study area from 2005 to 2016.

- Collecting hourly and daily rainfall data during and before the dates of landslide occurrences.
- Determining the relationship between the daily rainfall (on the dates of landslide occurrence) and the antecedent rainfall values (from 1 to 60 days).

Table 2 The distribution of the predicted landslide susceptibility classes and compared with the landslide inventory map in Quang Ninh Province

	Predicted landslide susceptibility classes		Observed landslides	
Landslide susceptibility class	Area (km^2)	Percentage (%)	Number	Percentage (%)
Very low	2413.77	40	4	1
Low	501.69	8	14	3
Moderate	1310.72	22	173	34
High	1150.13	19	165	32
Very high	613.75	10	158	31

Table 3 The distribution of the predicted landslide susceptibility classes and compared with the landslide inventory map in Ha Long City

	Predicted landslide susceptibility classes		Observed landslides	
Landslide susceptibility class	Area (km^2)	Percentage (%)	Number	Percentage (%)
Very low	120.40	58	0	0
Low	28.88	14	2	10
Moderate	42.47	20	10	50
High	14.83	7	5	25
Very high	2.82	1	3	15

- Determining the relationship between maximum hourly and daily rainfall and cumulative rainfall event.
- Generating the rainfall thresholds for the initiation of landslides based on the relationship between rainfall data.

Step 3) Evaluate the accuracy of the rainfall thresholds generated.

- Based on rainfall data and landslide events in the 2017–2021 period, the appropriateness of the rainfall thresholds determined in Step 2 will be verified.

In Ha Long City, 26 rainfall-triggered landslide incidents could be accurately dated between 2005 and 2021 (refer to Table 4 for details). These occurrences all took place during the rainy season, and each downpour is deemed as having ended if there is no rain after 24 consecutive hours. The values of rainfall events (whether triggering or not specified to induce landslides) such as daily rainfall (R), maximum hourly rainfall (Ihmax), maximum daily rainfall (Idmax), rainfall duration (D), cumulative event rainfall (E) and antecedent rainfall for different durations (1–60 days) were extracted and analyzed.

The data in the rainy season of the 2005–2016 period will be used to identify rainfall thresholds. During this period, 418 rainfall events were recorded at Bai Chay national hydro-meteorological station, of which 16 events were identified as triggering landslides. The correlations of maximum daily/hourly rainfall (Idmax/Ihmax) and cumulative event rainfall (E) with landslides are shown quite clearly in Figs. 15 and 16. Information on landslide events (occurrence date, maximum hourly rainfall (Ihmax), maximum daily rainfall (Idmax), cumulative event rainfall (E) is presented in Table 4.

These landslide-related rainfall events mostly had significantly higher maximum daily/hourly rainfall and cumulative event rainfall than other events. This trend is consistent with the findings from Onodera et al. (1974), Canon et al. (2001) and the fact that heavy or prolonged rainfall is the most important trigger. Following earlier research which adopted a regression model to manually draw the thresholds (Marques et al. 2008; Elias et al. 2020), the threshold Td (based on Idmax and E) and the threshold Th (based on Ihmax and E) were proposed for Ha Long City:

$$\text{Threshold Td}: \text{Idmax} = -0.47^{*}\,\text{E} + 177 \quad (1)$$

$$\text{Threshold Th}: \text{Ihmax} = -0.23^{*}\,\text{E} + 70 \quad (2)$$

Parameters of the threshold Eqs. (1) and (2) were estimated based on lines delimited manually in the scatter plots in Figs. 15 and 16, respectively. In general, depending on the priority given to the accuracy of predicting non-landslide or landslide occurrences, empirical thresholds could be slightly adjusted to be closer to the part of the non-triggering rainfall events or to the part of triggering ones. Nevertheless, too low thresholds will lead to too many fail alarms, while too high will result in additional damage (Staley et al. 2012). For Ha Long City, due to the limitation of collected landslide data and for safety purposes, thresholds were fitted to the region of non-triggering rainfall events.

Among 23 rainfall events from 2005 to 2016 in Ha Long city exceeding the threshold Td, 14/16 landslide events (87.5%) could be correctly warned, and only 09 rain events (39.1%) did not trigger landslides in the vicinity. Even so, two rainfall events (Nos. 8 and 14) were reported as causing landslides in reality, although their (E, Idmax) data points remain considerably below the Td threshold.

Table 4 Landslide events and related rainfall data (from 2005 to 2021)

ID	Date of landslide occurrence (mm/dd/yyyy)	Ihmax (mm)	Idmax (mm)	E (mm)
1	06/09/2005	49.9	120.3	212.9
2	07/31/2006	67.0	186.5	301.8
3	08/07/2006	51.2	131.1	265.5
4	08/18/2006	48.6	119.2	266.5
5	07/01/2007	67.9	230.6	302.6
6	08/09/2008	60.0	124.3	234.9
7	08/17/2010	41.7	99.8	202.7
8	07/08/2011	66.7	74.6	74.6
9	05/25/2012	70.7	178.9	242.1
10	10/28/2012	45.3	179.7	215.4
11	07/23/2013	48.8	108.8	436.1
12	07/28/2013	56.4	125.2	645.6
13	08/08/2013	39.6	171.3	355.8
14	06/06/2014	54.3	77.5	92.0
15	07/26/2015	74.9	243.2	282.3
16	07/05/2016	54.0	284.6	321.4
17	07/13/2017	104.0	386.2	66.1
18	08/17/2017	62.8	176.5	31.3
19	10/07/2017	187.1	286.9	37.6
20	06/27/2018	112.4	154.9	35.8
21	07/21/2018	164.6	434.6	42.1
22	08/02/2018	135.0	330.1	36.7
23	05/29/2019	70.5	73.6	60.4
24	08/02/2020	182.0	409.9	32.8
25	07/17/2020	173.8	414.9	59.0
26	08/12/2021	92.9	212.8	22.8

Among 35 rainfall occurrences surpassing the threshold Th between 2005 and 2016, 100% (16/16) of landslide events could be reliably predicted, but 54.3% (19/35) of rainfall events could not be defined as connected to landslide dangers. The maximum daily rainfall and cumulative event rainfall of the two rainy events Nos. 8 and 14 were not really high (less than 100 mm). However, because to the height of maximum hourly rainfall, they could be properly projected with the threshold Th.

Data of 190 rainfall events in the rainy seasons from 2017 to 2021 were used in combination with ten landslide events to validate identified rainfall thresholds Td and Th. These data are shown and compared with thresholds Td (Fig. 17) and Th (Fig. 18).

Among a total of 190 rainfall events during the test period, 17 events surpassed the threshold Td, including 9 events (52.9%) that were not identified to be connected with landslides. Meanwhile, using the Td threshold, 8/10 rain-induced landslide incidents (80%) may be appropriately warned. When the threshold Th was applied to these rainfall and landslide events, the percentage of over-threshold but unidentified occurrences related with landslides climbed to 56.5% (13/23 events). The use of threshold Th in the warning system, on the other hand, yields a safer outcome, with 100% of rainfall-triggered landslide occurrences being able to be notified in advance.

Four possible cases of outcomes or contingencies (Staley et al. 2012) when a rain threshold is applied: a true positive (TP) is an event where the data point is above the rainfall threshold, and at least 01 landslide was recorded; a true negative (TN) is a rain event with data point is below the rainfall threshold, and no landslides were induced; a false positive (FP) is an event where the data point exceeds the rainfall threshold but did not trigger a landslide; a false negative (FN) is an event where the data point is below the rainfall threshold, yet a landslide was recorded.

To evaluate the accuracy of two rain thresholds Td and Th, based on common methods used to assess accuracy (Segoni et al. 2018; Staley et al. 2012), four skill scores are determined: (1) the probability of detection (POD = TP/(TP +FN)); (2) the probability of false detection (POFD = FP/(FP+TN)); (3) the probability of false alarm (POFA) and (4) The Hanssen and Kuipers (1965) skill score which calculates the accuracy of predicting events with and without landslides (HK = POD − POFD).

Contingencies and skill scores calculated for rainfall thresholds Td and Th are present in Tables 5 and 6. It can be seen that the POFD and POFA skill scores for thresholds

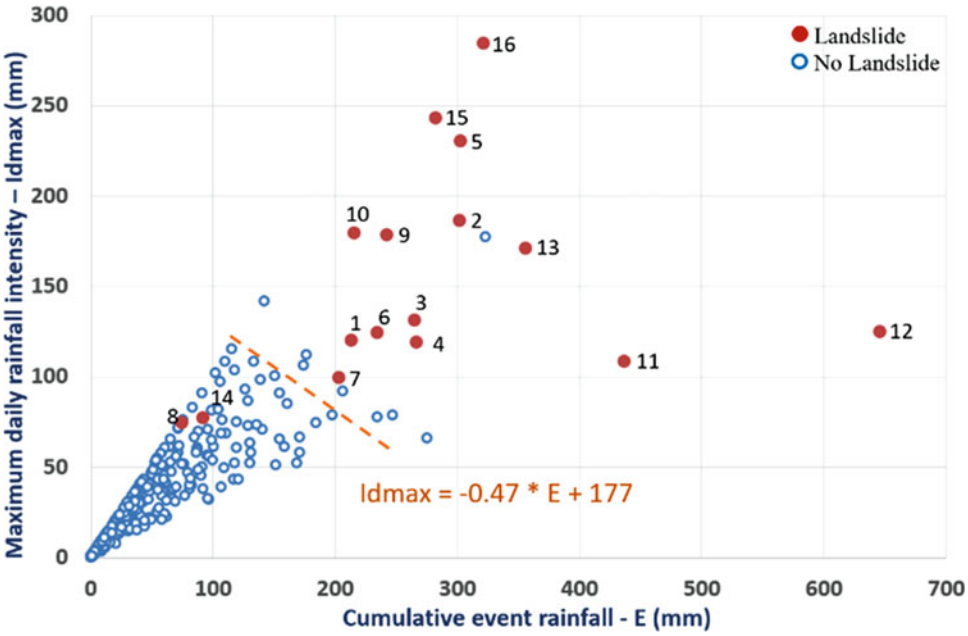

Fig. 15 Relationship between maximum daily rainfall intensity (Idmax) and cumulative event rainfall (E) (Landslide and rainfall data from 2005 to 2016)

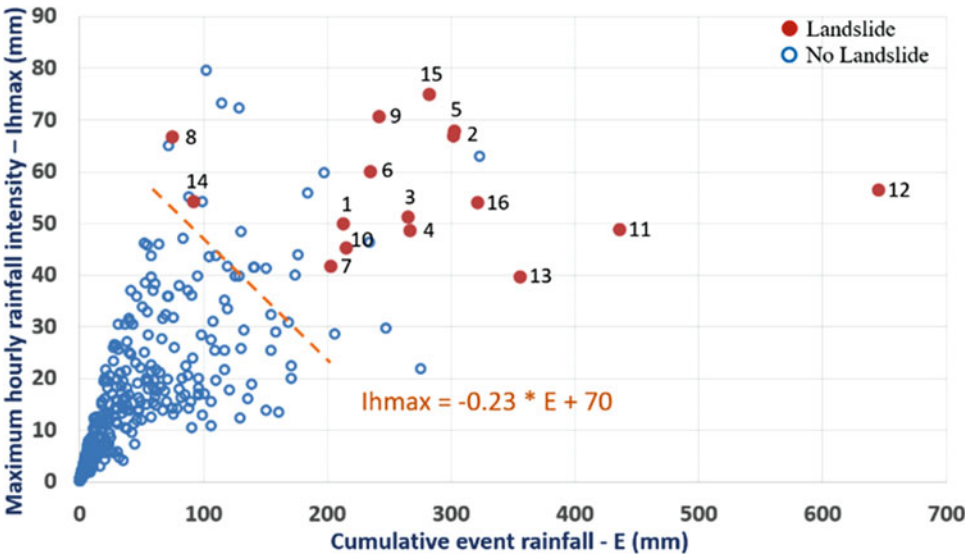

Fig. 16 Relationship between maximum hourly rainfall intensity (Ihmax) and cumulative event rainfall (E) (Landslide and rainfall data from 2005 to 2016)

Td and Th are quite similar. However, the POD and HK skill scores applied with the threshold Th are significantly higher than these scores with the threshold Td. Therefore, to be employed in the early warning system for Ha Long City, the rainfall threshold Th should be prioritized.

3.3 Proposed Landslide Early Warning System

WebGIS is a product that combines geographic information systems (GIS) and internet technologies (Miao and Yuan 2013). WebGIS is a tool for representing and analyzing geographical data over the internet environment. With the rapid development of Web and internet technologies, exchanging geographic information and transmitting urgent decisions through the WebGIS system is regarded as one of the fastest and most efficient methods (Zhang et al. 2011; Chen et al. 2016; Mamai et al. 2017). As a result, the WebGIS system may play an essential and effective role in the prevention and mitigation of natural catastrophe damage (Martinelli and Meletti 2008; Pessina and Meroni 2009).

In many areas, the landslide susceptibility map is mainly used for land-use planning and the development of measures to minimize the damage caused by landslides. Furthermore, when the susceptibility map is co-related with rainfall

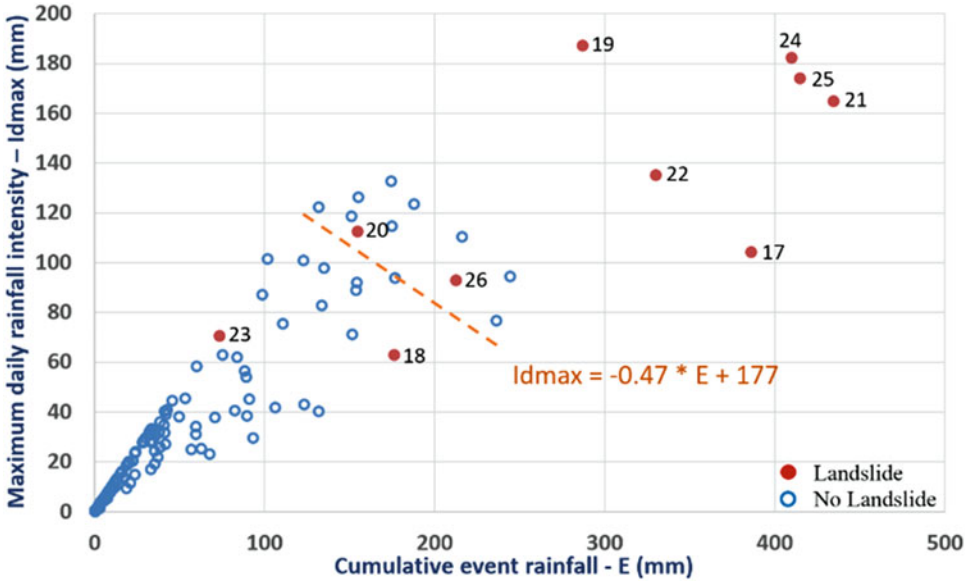

Fig. 17 Relationship between maximum daily rainfall intensity (Idmax) and cumulative event rainfall (E) (Landslide and rainfall data from 2017 to 2021)

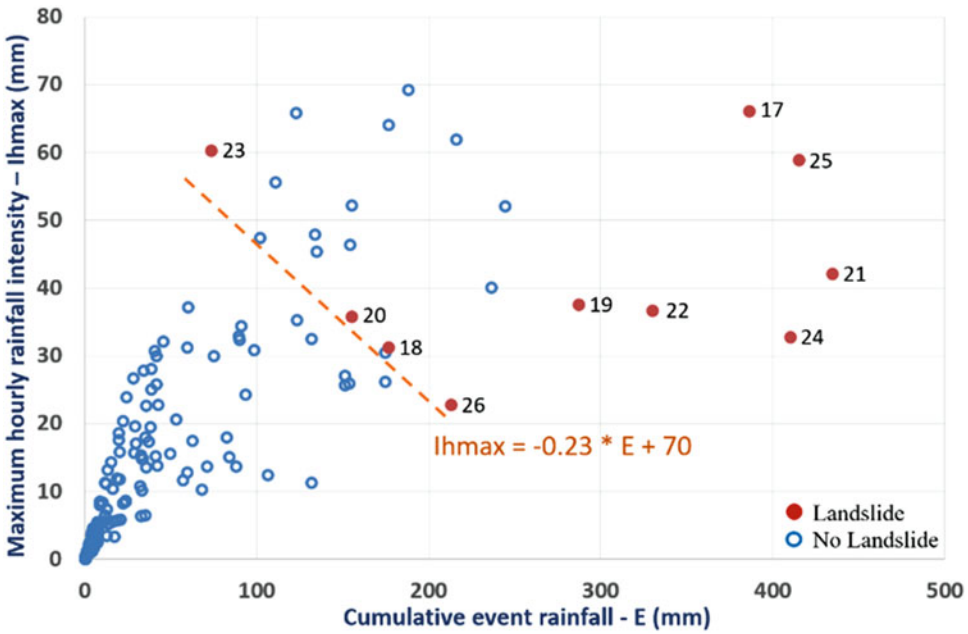

Fig. 18 Relationship between maximum hourly rainfall intensity (Ihmax) and cumulative event rainfall (E) (Landslide and rainfall data from 2017 to 2021)

thresholds, the hazard map will be formed to figure out when landslides are likely to happen, and where people should be ready to take precautions or leave.

Within the framework of the SFLP project, a WebGIS system has been developed with free and open-source software. The WebGIS system has a three-tier structure, including: (1) the data tier uses the Database Management System PostgreSQL; (2) the server tier employs an HTTP web server—Apache and a map server—GeoServer; (3) the interface tier uses OpenLayers to visualize and manipulate maps and geographic objects on Web browsers. Some members of the author team have succeeded in developing tools to help the WebGIS system of SFLP automatically collect real-time rainfall data from two meteorological monitoring stations (installed in Ha Long city) and rainfall forecast data from the National Centers for Environmental Prediction (NCEP) system—USA. The structure and method of developing a WebGIS system integrated real-time rainfall data collection and forecasted rainfall data collection tools could be referred to in detail in Ha et al. (2021).

In order to effectively use the landslide susceptibility map and triggering rainfall threshold, these are required to be added to the WebGIS system along with automatic meteorological monitoring stations and rainfall forecasting systems.

Table 5 Contingencies calculated for thresholds Td and Th

ID	Contingency	Td	Th
1	TP	8	10
2	TN	9	13
3	FP	2	0
4	FN	171	167

Table 6 Skill scores calculated for thresholds Td and Th (best scores are shown in bold)

ID	Skill score	Optimal value	Td	Th
1	POD	1	0.80	**1.00**
2	POFD	0	**0.05**	0.07
3	POFA	0	**0.53**	0.57
4	HK	1	0.75	**0.93**

Rainfall thresholds need to be evaluated on a regular basis with real-time and anticipated rainfall data to identify the occurrence time of a high-risk landslide. The landslide susceptibility of Ha Long City's predefined zones will be able to assist local authorities in focusing on warnings and organizing evacuations for high-risk areas, hence limiting landslide damage.

4 Discussion and Conclusion

The Spatial Multi-Criteria Evaluation (SMCE) technique is chosen with the benefit of being able to leverage expert knowledge to perform a landslide susceptibility map at a scale of 1:50,000 for the region of Quang Ninh Province. In this work, the input data for the SMCE model includes nine attribute map layers indicating nine component characteristics influencing the landslide phenomena in the region. The generated susceptibility map showed high consistency with the inventory map when more than 60% of landslide locations occurred in high and very high susceptibility areas. A significant amount of landslides occurred along the main roads and fell within the moderate susceptibility zone. This issue may come from two main reasons: the influence of human activities (house and road construction) and the limitations of input maps (terrain changes were not updated, and the spatial resolution is not high enough to represent small slopes). The influence of human activities should be considered if survey data can be collected in more detail.

The ratio of triggered and non-triggered over-threshold occurrences is an essential consideration when using the triggering rainfall threshold. If the non-triggered landslide rate is high, the warning's efficacy will be reduced owing to people's lack of faith upon getting wrong warning information (no geohazard occurrences). When compared to the use of threshold Th with threshold Td, it is clear that threshold Th is more reliable in assessing the risk of landslide occurrence. Despite the greater risk, using a threshold Td may assist in reducing the number of warnings for over-threshold rainfall events without triggering landslides.

Although empirical methods cannot pinpoint exactly each landslide site, they may assist local authorities and the public in anticipating high-risk landslide areas and periods throughout the rainy season. The use of empiric approaches is primarily reliant on experience, expert knowledge, and data from previous catastrophes. However, this strategy may avoid many problems associated with data heterogeneity. If information and attributes of landslide occurrences in Ha Long City are regularly updated, the accuracy of susceptibility zonation and rainfall thresholds for the initiation of landslides may be steadily improved over time.

In this research, the WebGIS system for landslide early warning was proposed. Real-time rainfall data (from a municipal meteorological monitoring station) and forecast rainfall data (from systems such as NCEP) may be linked and gathered into the system. The measurements are computed continually inside the system and compared to rainfall thresholds to anticipate the onset of landslides. Before and during severe rainfall events with the potential to surpass the threshold, landslide warnings can be issued through the WebGIS system.

It seems impossible to eliminate landslide occurrences in mountainous areas. Therefore, preparation and prevention are imperative to reduce the loss of life and property. Based on the empirical approach, this paper suggests the WebGIS system for early warning. However, implementing such a system is not easy, given the requirements of close collaboration among landslide specialists, local governments, and the general public in collaboratively designing countermeasure strategies, sharing information, and conducting prompt reaction plans.

Acknowledgments This work is a part of the Project "Designing and establishing a unified interdisciplinary big data system for early warning of landslides, debris flows, flash floods" (TNMT.2021.04.07). The data used in the research was supported by the State-Funded Landslide Project "Investigation, assessment and warning zonation for landslides in the mountainous regions of Vietnam".

Special thanks go to colleagues from the Vietnam Institute of Geosciences and Mineral Resources for their support and comments on this study.
The authors are grateful to the anonymous reviewer for insightful comments and suggestions that improved this paper.

References

Ahmed B, Rahman MS, Islam R, Sammonds P, Zhou C, Uddin K, Al-Hussaini TM (2018) Developing a dynamic web-GIS based landslide early warning system for the Chittagong Metropolitan Area, Bangladesh. ISPRS Int J Geo-Inf 7(12):485. https://doi.org/10.3390/ijgi7120485

Brabb EE (1991) The world landslide problem. Episodes 14(1):52–61

Bucknam RC, Coe JA, Chavarria MM, Godt JW, Tarr AC, Bradley LA, Rafferty SA, Hancock D, Dart RL, Johnson ML (2001) Landslides triggered by Hurricane Mitch in Guatemala – inventory and discussion, USGS Numbered Series 2001-443. https://doi.org/10.3133/ofr01443

Cannon SH, Bigio ER, Mine E (2001) A process for fire-related debris-flow initiation, Cerro Grande Fire, New Mexico. Hydrol Process 15(15):3011–3023

Castellanos Abella EA, Westen CJ (2007) Generation of a landslide risk index map for Cuba using spatial multi-criteria evaluation. Landslides 4(2007):311–325

Castellanos EA (2008) Multi-scale landslide risk assessment in Cuba. PhD Dissertation, ITC and University of Utrecht

Cetina ZM, Nadim F (2008) Stochastic design of an early warning system. Georisk: Assess Manage Risk Eng Syst Geohazards 2(4):223–236. https://doi.org/10.1080/17499510802086777

Chen W, He B, Zhang L, Nover D (2016) Developing an integrated 2D and 3D WebGIS-based platform for effective landslide hazard management. Int J Disaster Risk Reduct 20:26–38. https://doi.org/10.1016/j.ijdrr.2016.10.003

Crosta GB, Frattini P (2008) Rainfall-induced landslides and debris flows. Hydrol Process 22(4):473–477. https://doi.org/10.1002/hyp.6885

DOC (2016) Report on the migration plan to mitigate landslide and flood disasters for Quang Ninh province from 2016 to 2020 with orientations to 2025. Department of Construction, Quang Ninh Provincial People's Committee, the Socialist Republic of Vietnam (In Vietnamese)

Elias EC, Olga CM, Janneke E, Cees JW, Agus SM, Akhyar M (2020) Satellite-derived rainfall thresholds for landslide early warning in Bogowonto Catchment, Central Java, Indonesia. Int J Appl Earth Observ Geoinf. https://doi.org/10.1016/j.jag.2020.102093

Gioia E (2013) Landslide forecast: empirical and physical predictive models applied to the Marche region (central Italy). PhD thesis, Universita' Politecnica Delle Marche, Universita' Politecnica Delle Marche

Guzzetti F, Gariano SL, Peruccacci S, Brunetti MT, Marchesini I, Rossi M, Melillo M (2020) Geographical landslide early warning systems. Earth-Sci Rev. https://doi.org/10.1016/j.earscirev.2019.102973

Ha ND, Hung LQ, Sayama T, Sassa K, Takara K, Dang K (2021) An integrated WebGIS system for shallow landslide hazard early warning. In: Casagli N, Tofani V, Sassa K, Bobrowsky PT, Takara K (eds) Understanding and reducing landslide disaster risk. WLF 2020. ICL Contribution to Landslide Disaster Risk Reduction. Springer, Cham. https://doi.org/10.1007/978-3-030-60311-3_22

Hanssen AW, Kuipers WJA (1965) On the relationship between the frequency of rain and various meteorological parameters. Koninklijk Nederlands Meteorologisch Institut, Meded. Verhand, pp 2–15

Hung LQ, Van NTH, Son PV, Ninh NH, Tam N, Huyen NT (2017) Landslide inventory mapping in the fourteen northern provinces of Vietnam: achievements and difficulties. Advancing culture of living with landslides. Springer International, Cham, pp 501–510. https://doi.org/10.1007/978-3-319-59469-9_44

Le TTT, Tran TV, Hoang VH, Bui VT, Bui TKT, Nguyen HP (2021) Developing a landslide susceptibility map using the analytic hierarchical process in Ta Van and Hau Thao Communes, Sapa, Vietnam. J Disaster Res 16(4):529–538

Mamai L, Gachari M, Makokha G (2017) Developing a web-based water distribution geospatial information system for Nairobi northern region. J Geogr Inf Syst 9:34–46. https://doi.org/10.4236/jgis.2017.91003

Martinelli F, Meletti C (2008) A WebGIS application for rendering seismic hazard data in Italy. Seismol Res Lett 79(1):68–78. https://doi.org/10.1785/gssrl.79.1.68

Marques R, Zezere J, Trigo R, Gaspar J, Trigo I (2008) Rainfall patterns and critical values associated with landslides in Povoação County (São Miguel Island, Azores): relationships with the North Atlantic Oscillation. Hydrol Process 22:478–494. https://doi.org/10.1002/hyp.6879

Miao F, Yuan Q (2013) A WebGIS-based information system for monitoring and warning of geological disasters for Lanzhou City, China. Adv Meteorol. Article ID 769270. https://doi.org/10.1155/2013/769270

Onodera T, Yoshinaka R, Kazama H (1974) Slope failures caused by heavy rainfall in Japan. In: Proceedings of the 2nd International Congress of the International Association of Engineering Geology. Sao Paulo, Brazil, vol 11. pp 1–10

Pessina V, Meroni F (2009) A WebGis tool for seismic hazard scenarios and risk analysis. Soil Dyn Earthquake Eng 29(9):1274–1281. https://doi.org/10.1016/j.soildyn.2009.03.001

Saaty TL (1977) A scaling method for priorities in hierarchical structures. J Math Psychol 15:234–281. https://doi.org/10.1016/0022-2496(77)90033-5

Saaty TL (2000) Fundamentals of decision making and priority theory with the Analytic Hierarchy Process. RWS Publications, Pittsburg, PA

Segoni S, Piciullo L, Gariano SL (2018) A review of the recent literature on rainfall thresholds for landslide occurrence. Landslides 15:1483–1501. https://doi.org/10.1007/s10346-018-0966-4

Staley DM, Kean JW, Cannon SH (2012) Objective definition of rainfall intensity–duration thresholds for the initiation of post-fire debris flows in southern California. Landslides 10:547–562. https://doi.org/10.1007/s10346-012-0341-9

Sultana N, Tan S (2021) Landslide mitigation strategies in southeast Bangladesh: lessons learned from the institutional responses. Int J Disaster Risk Reduct 62:1–18

Tran TV, Hoang VH, Pham HD, Go S, Vu HH (2021) A non-linear, time-variant approach to simulate the rainfall-induced slope failure of an unsaturated soil slope: a case study in Sapa, Vietnam. J Disaster Res 16(4):512–520

Viet TT, Lee G, Thu TM, An HU (2016) Effect of digital elevation model resolution on shallow landslide modeling using TRIGRS. Nat Hazards Rev 18(2):1–12

Zhang G, Chen L, Dong Z (2011) Real-time warning system of regional landslides supported by WEBGIS and its application in Zhejiang Province, China. Proc Earth Planet Sci 2:247–254. https://doi.org/10.1016/j.proeps.2011.09.040

The Modern Activity of the Buzulgan Landslide and Its Influence on the Debris Flow Hazard for the Tyrnyauz Town (Northern Caucasus, Russia)

Oleg V. Zerkal, Sergey S. Chernomorets, Viktoriia A. Iudina (Kurovskaia), Mikhail D. Dokukin, Inna N. Krylenko, Elena A. Savernyuk, Tatiana A. Vinogradova, and Eduard V. Zaporozhchenko

Abstract

The valley of the Gerkhozhan-Su River (a tributary of the Baksan River) in the Norther Caucasus is one of the most debris flow-prone areas in Russia. Large-scale debris flows here have occurred in 1937, 1960, 1961, 1962, 1977, 1999, 2000, 2002, 2011, 2017. The Tyrnyauz town is located in the impact zone of the debris flows. A significant impact on the debris flow hazard in the Gerkhozhan-Su River valley is exerted by the Buzulgan landslide, which was formed on the right side of the valley with a height of about 350 m and an average steepness of 23–25°. The area where the Buzulgan landslide was formed is located within the Pshekish-Tyrnyauz suture zone, which is a 2–3 km wide belt of the intensive tectonic fragmentation. The modern landslide activity began in March 2020. The main phase of the landslide displacement occurred in August 2020. The total volume of the landslide is estimated as 7.0–7.2 × 10^6 m^3. It formed a dam that blocked the Gerkhozhan-Su River valley. No large lake was impounded upstream, as the river has eroded a new channel near the left side of the valley in a short time. A landslide dam, composed of disintegrated deposits, increases the debris flow hazard. The occurrence of debris flows in the river valleys upstream the dam site will rise the landslide-damned lake level, which rapid breakthrough may cause a catastrophic debris flow surge downstream. In this study the influence of Buzulgan landslide on the debris flows passage was identified. The method of complex modeling was applied: the transport-shift model (the FLOVI program) for the zone of the potential debris flow—landslide interaction and the FLO-2D hydrodynamic model for the valley zoning. Modeling of the alluvial fan inundation was carried out for the case of the channel blockage at the Tyrnyauz bridge by debris flow deposits or bridge collapse. The difference between inundation zones using the various rheological parameters was ~10%. The distinction between inundation zones for this case and in the absence of the bridge blockage was about 26%. Residential buildings, buildings of the Elbrus district administration, several schools, and a kindergarten are located in the flood prone zone.

Keywords

Caucasus · Buzulgan landslide · Gerkhozhan-Su River · Tyrnyauz town · Debris flow hazard

O. V. Zerkal (✉)
Geological Department, Lomonosov Moscow State University, Moscow, Russia
e-mail: zerkalov@geol.msu.ru

S. S. Chernomorets · V. A. Iudina (Kurovskaia) · I. N. Krylenko · E. A. Savernyuk
Faculty of Geography, Lomonosov Moscow State University, Moscow, Russia
e-mail: sc@geogr.msu.ru

M. D. Dokukin
High-Mountain Geophysical Institute, Nalchik, Russia

T. A. Vinogradova
Gidrotechproject, Saint-Petersburg, Russia

E. V. Zaporozhchenko
Debris Flow Association, Pyatigorsk, Russia

1 Introduction

The Greater Caucasus form the north-eastern sector of the Alpine-Mediterranean belt (Fig. 1), bounding the Eurasian Plate from the south and formed by continental collision of interacting Eurasian and Arab Plates (Khain 1998).

The Gerkhozhan-Su River valley is located in the Northern Caucasus and is one of the most debris flow-prone territories in Russia. Catastrophic debris flows have repeatedly occurred in the basin of the Gerkhozhan-Su river. They caused significant damage to the Tyrnyauz town. Large-scale debris flows took place here in 1937, 1960, 1961, 1962, 1977, 1999, 2000, 2002, 2011, 2017 (Chernomorets 2005; Baranovsky 2004; Gerasimov 1980; Zaporozhchenko 2002;

I. Alcántara-Ayala et al. (eds.), *Progress in Landslide Research and Technology, Volume 2 Issue 1, 2023*,
Progress in Landslide Research and Technology, https://doi.org/10.1007/978-3-031-39012-8_10

Fig. 1 Position of the study site in the Greater Caucasus

Seinova et al. 2003). One of the factors that increase the level of debris flow hazard in the Gerkhozhan-Su River basin is the river damming cased by the Buzulgan landslide movements. In this case, the debris flows acquire additional material and impulse. The role of the Buzulgan landslide is described by an eyewitness of the July 19, 2000 debris flow Mr. S.-D. Dzhubuev: "*The main wave of the debris flow caught up with us ..., which destroyed a 9-storey building before our eyes... There was no water in the riverbed before the wave of the debris flow... Apparently, there was a jam in the area of the landslide, after which there was a breakthrough, which is why a wave was formed.*" (Chernomorets 2005).

2 Natural Conditions

The research site is located 38 km east of the central part of volcano Elbrus, the highest peak in Europe (the western cone is 5642.7 m, the eastern cone is 5620 m). According to radiocarbon dating, the last volcanic eruptions occurred 1330 ± 80 and 990 ± 60 years ago (Laverov 2005).

2.1 Geomorphological Conditions

The Buzulgan landslide formed on the right-bank slope of the 4 km long Gerkhozhan-Su River valley—a right tributary of the Baksan River. The Tyrnyauz town is located at their confluence (Fig. 2).

Fig. 2 Central part of the Tyrnyauz town

The Gerkhozhan-Su River is formed by the confluence of the Kayarty-Su and the Sakashili-Su Rivers sourced from the glaciers of the Main Caucasian Ridge located at altitudes of more than 4000 m. The Buzulgan landslide was formed almost immediately downstream from their confluence. The average annual water flow in the Gerkhozhan-Su River is 1.1 m^3/s, but in summer the flow rate increases up to 5 m^3/s (Chernomorets 2005).

The relief of the area is of the alpine type. The Gerkhozhan-Su River valley is V-shaped. The width of the valley at the watershed level (at elevations ~ 2000 m) is about 1.5 km, while that of the valley floor is less than 100 m. The height of the right west-facing slope of the valley at the Buzulgan landslide site is about 350 m with an average steepness of 23–25°.

2.2 Geological and Tectonic Conditions

The area where the Buzulgan landslide occurred is located within the Pshekish-Tyrnyauz suture zone (Fig. 3)—a narrow (2–3 km wide) tectonic zone affected by a fault system, traceable for more than 150 km. Within the Pshekish-Tyrnyauz suture zone, almost all geological boundaries have a tectonic nature. This zone started forming in the Early Variscan tectonic subepoch and was rejuvenated in the Alpine-Himalayan tectonic epoch. South of Tyrnyauz town, the neointrusive granite massif of the Tyrnyauzsky complex ($\gamma N_2 tr_2$) is confined to the Pshekish-Tyrnyauz suture zone.

Currently, the Pshekish-Tyrnyauz suture zone separates the northern limb of the Northern Caucasus megaanticlinorium (tectonic block) from the horst-anticlinorium (tectonic block) of the Main Caucasus ridge. The geological map is shown in Fig. 3. Tectonic wedges and tectonic slabs trace Paleozoic thrust faults.

In the modern relief, the Pshekish-Tyrnyauz suture zone is expressed by a system of sublatitudinal faults separating the blocks with different altitude. Currently, the tectonic structures of the Pshekish-Tyrnyauz suture are deformed by the Sakashil-Kordonsky right strike-slip fault traced south of the Buzulgan landslide site.

The territory of the Caucasus is seismically active. The possible intensity of earthquakes in the area of the Pshekish-Tyrnyauz suture is estimated to be up to 10 points (Seismic 2018), though no one historical earthquake reported in this part of the Greater Caucasus had so high intensity.

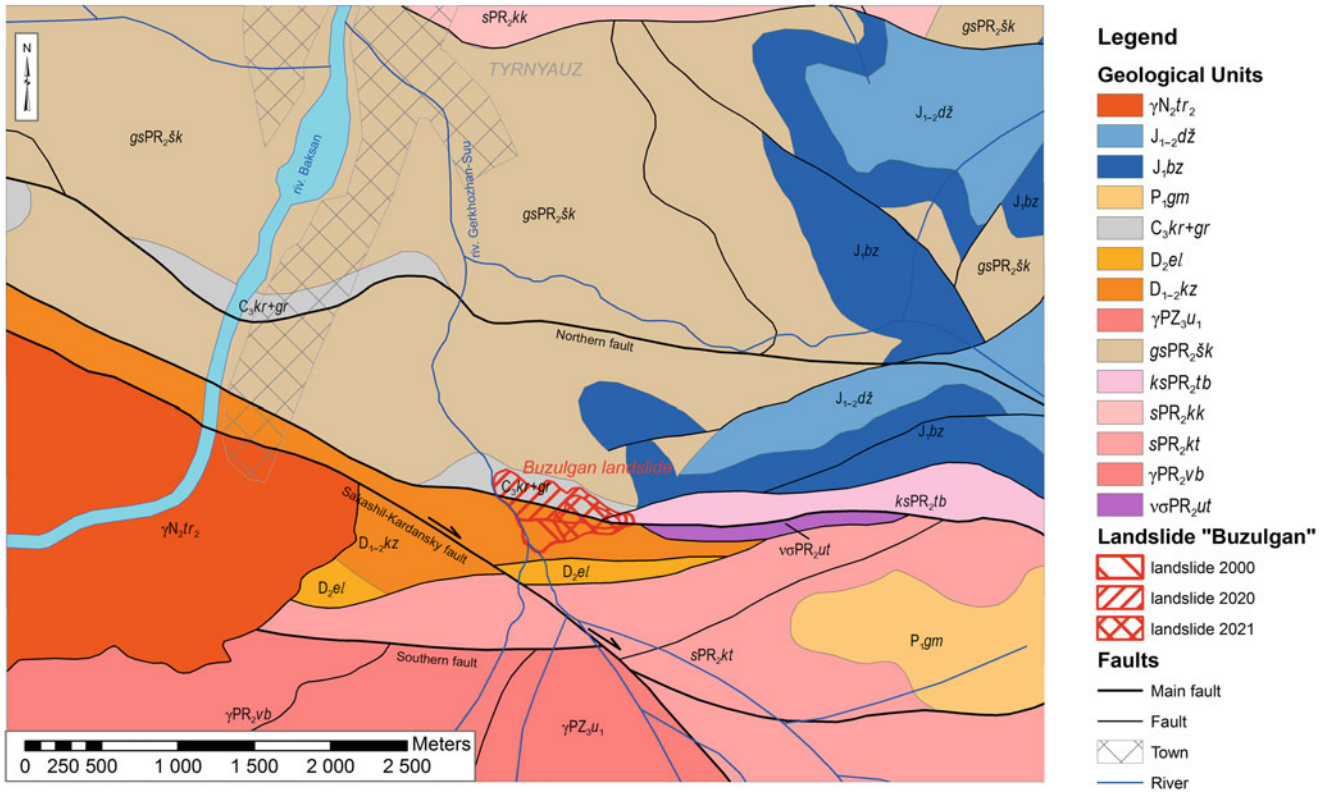

Fig. 3 A detailed fragment of the State Geological Map (sheet K-38-I, VII) (by Pysmenny et al. 2013, with modified). Geological Units: $\gamma N_2 tr_2$—tyrnyauzsky complex (leucocratic granites); $J_{1\text{-}2}dž$—dzhigiatskaya formation (sandstones, aleurolites, argillites); J_1bz—bezengijskaya formation (conglomerates, sandstones, aleurolites); P_1gm—gimaldykskaya formation (conglomerates, sandstones, aleurolites, argillites, tuffites); C_3kr+gr—karadzhelmasskaya and gremuchinskaya formations (interbedding sandstones, aleurolites, argillites with coaly interbed); D_2el—elmeztjubinskaya formation (tuff conglomerates, tuffstones, phyllite-like argillites); $D_{1\text{-}2}kz$—kyzylkolskaya formation (interbedding tuff conglomerates, tuffstones, spilites, phyllite-like argillites with jasper); γPZ_3u_1—ullukamsky complex (granites); $gsPR_2šk$—shaukolsky complex (gneiss, crystalline schists); $ksPR_2tb$—tuballykulakskycomplex (quartzites, crystalline schists); sPR_2kk—kamyksky complex (crystalline schists); sPR_2kt—ktiteberdinsky complex (crystalline schists); γPR_2vb—verhnebalkarsky complex (migmatite-granites); $v\sigma PR_2ut$—ullutallykolsky ultrabasite complex (pyroxenites)

3 The Buzulgan Landslide

3.1 History of Study

The Buzulgan landslide is located on the right bank of the Gerkhozhan-Su River valley (Figs. 3 and 4). Though the exact time of the landslide formation is unknown, its influence on debris flow activity in the Gerkhozhan-Su River valley has been repeatedly noted when describing debris flows that occurred in 1937, 1960–1962, 1978, 1999, 2000, 2011 and 2017 (Gerasimov 1967, 1980; Zolotarev et al. 1979; Seinova et al. 2003; Chernomorets 2005; Dokukin et al. 2012; Dokukin et al. 2018; Bekkiev et al. 2020). The Buzulgan landslide partially dammed and displace the riverbed of the Gerkhozhan-Su River.

It caused the congestion during the passage of debris flows and the formation of catastrophic debris flow surges. The main reason for the activation of the Buzulgan landslide is usually considered due to the erosive activity of debris flows that undercut the frontal part of the landslide. However, the activation of the Buzulgan landslide in August 2020 was not caused by such effect.

Before 1999–2000, slope deformations occurred in the lower part of the slope. Devonian deposits of the Kyzylkolskaya formation ($D_{1\text{-}2}kz$), distributed south of the fault crossing the slope (Fig. 3), were involved in the displacement. According to the geodetic observations, the maximum velocity of the lower part of the landslide in 1965 was 0.75 m/day, and in 1977 was 0.5 m/day (Zolotarev et al. 1979; Gerasimov 1980). The greatest total shift of the riverbed (20–25 m) during the movement of the landslide, previously estimated by the results of the analysis of multi-time remote sensing data, occurred after the 1977 debris flow (Bekkiev et al. 2020). A comparable displacement of the Gerkhozhan-Su riverbed was also observed during debris flows in 1999 and 2000 (Chernomorets 2005). However, after them slope deformations were detected in the middle

Fig. 4 General view on the Buzulgan landslide (2020) (Photo of O.V. Zerkal)

part of the slope. During the debris flows of 2011 and 2017, the banks of the Gerkhozhan-Su River remained almost unchanged. In 2019, signs of landslide activity were recorded in the upper part of the slope (Bekkiev et al. 2020).

3.2 Method for Assessing the Current Landslide Activity

To assess the current state of the Buzulgan landslide, a field description of landslide activity was carried out and a survey of the slope deformations development area and the adjacent territory was carried out using the MavicPro Platinum quadcopter equipped with an FC220 camera. As a result of the survey, an orthophotoplan and a DEM were obtained that were analyzed later, along with field observation data.

3.3 Modern Activity of the Buzulgan Landslide

Destabilization of the slope massif—local rock falls in the frontal part of the old (2000) landslide—began to be noted from March 2020 (Bekkiev et al. 2020). According to M.D. Dokukin's observations, the first stage of landslide displacements occurred from the end of May to the beginning of August 2020. During this period, the movement of the landslide was about 35 m at an average speed of 0.4–0.5 m/day. The main phase of the landslide displacement occurred from 07.08.2020 to 14.08.2020 (Bekkiev et al. 2020). The peak activity of the landslide was on 12–14.08.2020. During this time, the movement in the frontal part of the landslide was up to 120 m at an average speed of 40 m/day (~1.67 m/h). The movement in the upper part of the landslide during this time was 290 m at an average speed of up to 97 m/day (~4 m/h). In total, the upper part of the landslide (V landslide phase) shifted by ~430 m from 07.08.2020 to 14.08.2020. Unlike earlier displacements, the main slope deformations in 2020 involved not Devonian ($D_{1\text{-}2}kz$), but Carboniferous deposits (C_3kr+gr) that outcrops north of the fault crossing the slope (Figs. 3 and 5). As a result of active slope displacements, a landslide array of complex structure was formed (Figs. 4 and 5). At present, Buzulgan landslide body can be divided into several parts.

The oldest part of the Buzulgan landslide (that was activated last time in 1999–2000) is the deformation zone in

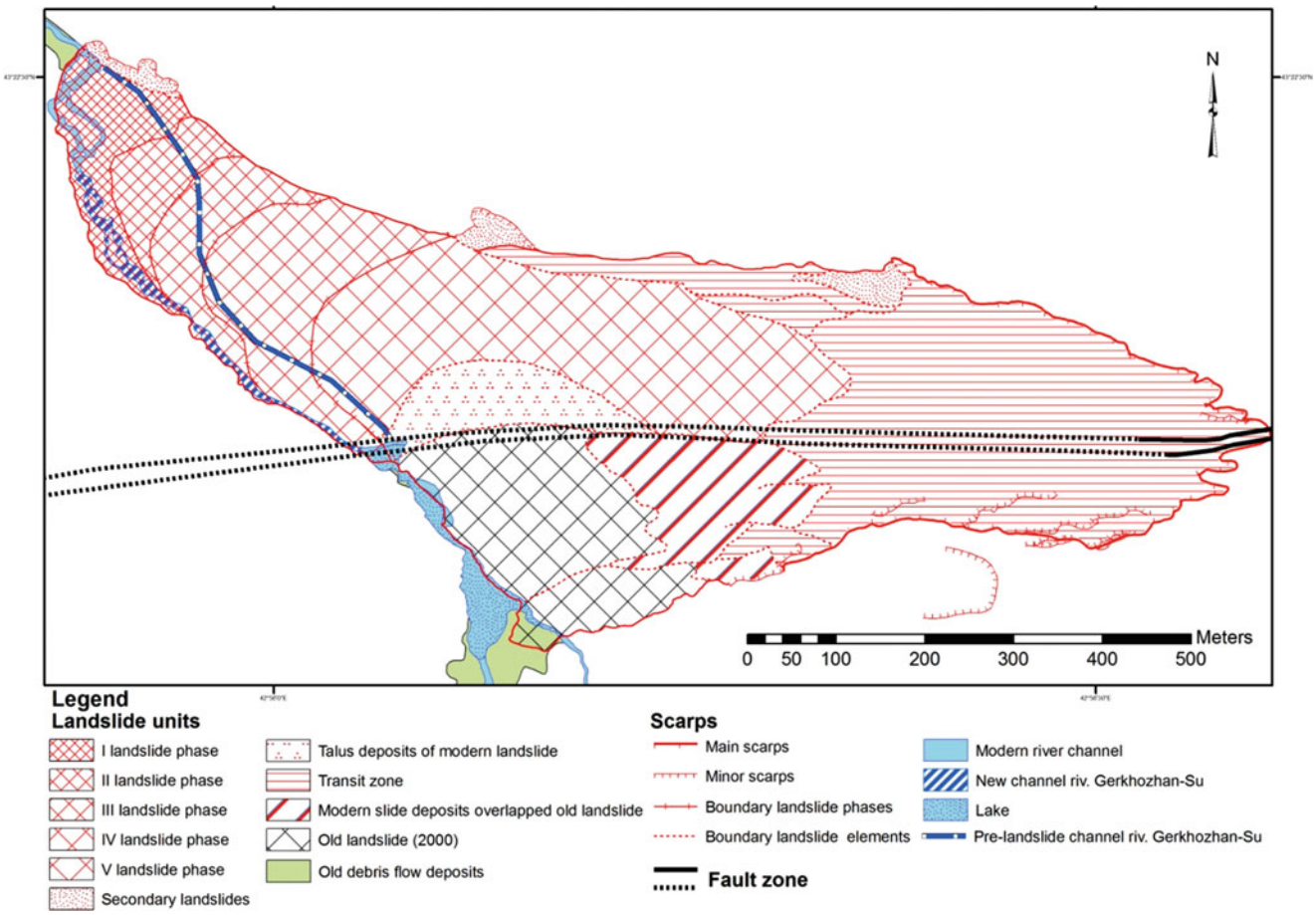

Fig. 5 Map of a structure of Buzulgan landslide (2020) (made by O.V. Zerkal)

the lower and middle parts of the slope located south of the fault (the southeastern part of the landslide massif). The total length of this one is about 290–300 m with a width of the sliding surface up to 250 m. The excess over the riverbed of the Gerkhozhan-Su River is ~160 m (H/L = 0.55, $\alpha \approx 33.5^{o}$). The volume of displaced masses is estimated at 1.2–1.5 mln m^3. The tuffstones, spilites, phyllite-like argillites of the kyzylkolskaya formation ($D_{1\text{-}2}kz$) were involved in the displacement. The lower part of this "old landslide" experienced some reactivation in 2020. Local rock falls were observed here. The upper part of the "old landslide" was overlaid by the material of the 2020 landslide when a significant expansion of the area of slope deformations took place.

In 2020 the sandstones, aleurolites, argillites with coal interbed of the karadzhelmasskaya and gremuchinskaya formations (C_3kr+gr) of Carboniferous age were involved in the displacements. These formations lie to the north of the fault crossing the slope. The total length of the 2020 landslide deformation zone is about 1160 m, including 270 m in the segment along the riverbed. Width of the sliding surface is up to 200 m. The excess over the riverbed of the Gerkhozhan-Su River is ~320 m (H/L = 0.36, $\alpha \approx 21^{o}$). The length of the transit zone within the landslide headscarp is ~400 m. The total length of displaced masses is about 780 m, and their volume is estimated at 5.8–5.9 mln m^3.

The displacement of the landslide in 2020 occurred in five phases, which deposits consistently overlapped the landslide masses of earlier phases, forming ramparts and steps on the landslide surface (Figs. 5 and 6). In the lower part, the landslide reached the bed of the Gerkhozhan-Su River, where it turned and continued moving down the valley floor at a distance of up to 480 m. However, the river quickly eroded a new channel in a landslide dam composed of disintegrated deposits (Fig. 7). As a result, a large-scale landslide-dammed lake was not formed (Fig. 8). The new riverbed was shifted 95–100 m towards the left side of the valley.

Currently, the total width of the Buzulgan landslide headscarp is 350 m. In the upper part of the slope it narrows up to 200–250 m. In the axial part of the headscarp there is a fault that is a part of the system of the Pshekish-Tyrnyauz

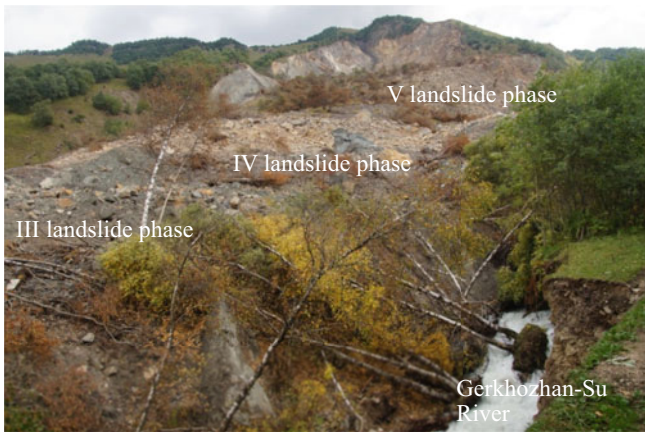

Fig. 6 The central part of the Buzulgan landslide (Photo of O.V. Zerkal)

suture. The total volume of the Buzulgan landslide is estimated at 7.0–7.2 mln m^3.

Thus, the modern Buzulgan landslide is an active polyphase retrogressing landslide (Varnes 1978; Cruden and Varnes 1996; WP/WLI, 1993a, b; Hungr et al. 2014). J.N. Hutchinson defined landslides of this type as multiple rotation slides (Hutchinson 1988).

4 Debris Flows Activity and Hazard

Since the dynamics of the Buzulgan landslide directly affect the debris flow passing along the Gerkhozhan-Su River, we performed a simulation to assess the hazard for buildings and structures in the Tyrnyauz town.

4.1 Materials and Methods

In this study, the method of complex modeling was applied: the transport-shift model (the FLOVI program) for the zone

Fig. 7 New Gerkhozhan-Su River channel (Photo of O.V. Zerkal)

Fig. 8 The upstream part of the landslide dam formed in 2020 (Photo of O.V. Zerkal)

of potential debris flow origination site in this case and the FLO-2D hydrodynamic model for the valley zoning. Modeling on the alluvial fan inundation was carried out for the case of the channel blockage in the bridge area by debris flow deposits or as a result of the bridge collapse (Fig. 9).

4.2 Transport–Shift Model (FLOVI)

The FLOVI computer program was applied to calculate the debris flow characteristics at the Buzulgan landslide site where significant entrainment takes place. The program is based on the equations of the transport-shift model of debris flow formation (Vinogradov 1980; Vinogradov and Vinogradova 2010). This model took into the account the measurements obtained during the Chemolgan experiments (Vinogradova and Vinogradov 2017). The calculated and observed values were also compared, the difference was from 9 to 38%. It is assumed that the increment in the solid flow while crossing the landslide body is directly proportional to the instability coefficient of the PDFB (potential debris flow body), the elementary potential flow capacity and the index of debris flow mass mobility (Vinogradova and Vinogradov 2017). Previously, the model was improved and used to simulate both debris flows and outburst floods (Kurovskaia et al. 2022).

The area of potential debris flow increment was identified where it crosses the landslide body. The total length was 332 m, the average slope was 12.4°. The input discharge before the landslide was assumed to be 700 m^3/s, which is equal to that of the 2017 debris flow. The parameters of a potential debris flow massif, such as initial moisture content, internal friction angle, and density were selected based on measurement data (Zaporozhchenko 2002). Thus, the internal friction angle was set as 32°, and the density of the massif was assumed to be 2500 kg/m^3.

Fig. 9 The road bridge on the Gerkhozhan-Su River alluvial fan. Photo by S.S. Chernomorets (2020)

Due to the fact that there are a large number of springs in the landslide, the maximum value of the initial moisture content was increased to 0.4, which was obtained during measurements (Zaporozhchenko 2002). The simulation results were the debris flow mass increment, the change in density and the debris flow wave hydrograph along the entire length of the valley section where it crosses the landslide.

4.3 Hydrodynamic Model FLO-2D

The hydrodynamic model FLO-2D (O'Brien et al. 1993) was applied to calculate the flow transformation in the valley. The model is based on the solution of the Saint-Venant equations, in which the flow characteristics are averaged over depth (the so-called "shallow water" equations) (Cunge et al. 1980). The motion of debris flow in FLO-2D model is simulated under the assumption that it moves as Bingham (viscoplastic) liquid (O'Brien et al. 1993). If the detail rheological analysis of debris flow and deposits cannot be made, the authors of the model propose the following parameters from Table 1.

For identification of the Buzulgan rockslide dynamics, route surveys have been carried out since 2020, a month after the movement. The relief data was obtained using a UAV DJI Mavic Pro Platinum. The average spatial resolution of the surveys was 12.2 cm/pixel. The images were processed using the Agisoft Metashape program software [https://www.geoscan.aero/ru/software/agisoft/metashape_pro]. In areas where a large number of trees were identified, automatic classification was performed for a dense point cloud for the "high vegetation" class. Carrying out this operation made it possible to avoid the creation of a "false dam" in forested areas. Thus, a high-resolution digital surface model (DSM) was created, which took into account the location of the tray and buildings. After correction, all relief data were interpolated into the 3 × 3 m computational grid of the model.

4.4 Results and Discussion

The discharge of a possible debris flow at the outlet of the landslide site according to UAV data from 2020 was 1019 m^3/s, with an input of 700 m^3/s. At the top of the alluvial fan, the flow discharges vary approximately from 1 to 18% depending on the parameters set of the rheological block in the FLO-2D model (Table 2).

The maximum flow velocities on the alluvial fan were observed in the channel of the Gerkhozhan-Su River and changed for different variants of rheological parameters: a) −9.3 m/s, b) −10.7 m/s, c) −11.5 m/s, d) −10.7 m/s. The obtained values turned out to be slightly lower than the values if there was no blockage of the channel at the road bridge site (Kurovskaia et al. 2022).

The flow velocity on the fan itself varied from 1.5 to 5 m/s and higher. The flow depth at the alluvial fan, on average, for all variants of rheological parameters changed from 1 to 9 m, which was higher than for the modeling without the channel blockage by debris flows (Kurovskaia et al. 2022). The average inundation zone on the alluvial fan was 0.385 km^2. The largest zone was obtained using the variant of parameters a), the smallest—c), the difference between them was about 10%. The distinction between inundation zones for this case and in the absence of blockage of the bridge was about 26%. At the same time, the debris flow covered both along the left bank of the Gerkhozhan-Su River and along the right bank. According to the simulation results, residential buildings, buildings of the of the Elbrus region administration, several schools, and a kindergarten were

Table 1 Parameters for calculating the stress of plastic flow and viscosity as a function of sediment concentration (O'Brien and Julien 1988)

		Parameters for calculating plastic friction stress		Parameters for calculating flow viscosity	
Calculation variant	Slide deposit sample	α_2	β_2	α_1	β_1
a)	ANS	0.152	18.7	0.00136	28.4
b)	G1	0.0345	20.1	0.00283	23.0
c)	G2	0.0765	16.9	0.0648	6.20
d)	G3	0.000707	29.8	0.00632	19.9

Note: *G* Glenwood, *ANS* Aspen natural soil

Table 2 Debris flow modeling results

Variants of parameters for FLO-2D model calculations	a)	b)	c)	d)
Debris flow discharge at the top of the alluvial fan, m^3/s	992	1192	1203	1092

located in the flood prone zone, despite the debris flow observed in August 2022 passed exclusively through the flume. In 2021, the flume was cleared; therefore, the inundation hazard was reduced for some time. However, after debris flow in August 2022, the flume was partially filled with deposits again. Thus, the simulation reproduced the worst situation (Fig. 10).

5 Conclusion

The valley of the Gerkhozhan-Su River (a tributary of the Baksan River) in the Northern Caucasus is one of the most debris flow-prone areas in Russia. One of the factors of catastrophic debris flows in the valley of the river Gerkhozhan-Su is the Buzulgan ladslide. Earlier, as a result of the landslide movement, the debris flows entrained additional solid material and impulse.

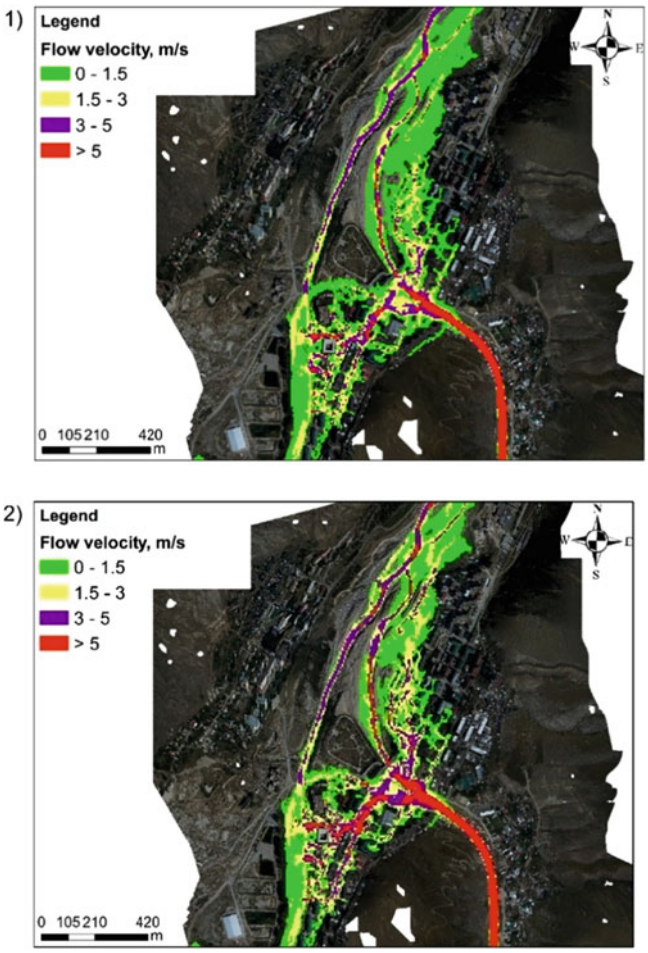

Fig. 10 Planar distribution of debris flow velocities on the alluvial fan of the Gerkhozhan-Su River using the FLO-2D model 1) calculation variant a), 2) calculation variant c)

The Buzulgan landslide was formed within the Pshekish-Tyrnyauzskaya suture, which is a narrow (2–3 km) tectonic zone affected by derives of faults.

The modern destabilization of the slope massif has been observed since March 2020. The peak of the landslide activity was in August 2020. At this time, the movement in the frontal part of the landslide was up to 120 m at an average speed of 40 m/day (~1.67 m/h). The movement in the upper part of the landslide during this time was 290 m at an average speed of up to 97 m/day (~4 m/h). In total, the upper part of the landslide shifted by ~430 m from 07.08.2020 to 14.08.2020. The total volume of the Buzulgan landslide is estimated at 7.0–7.2 mln m^3.

As a result of the movement of the landslide in August 2020, the bed of the Gerkhozhan-Su River was blocked for 480 m. However, the river quickly eroded a new channel in a landslide dam, composed of disintegrated debris. As a result, no large-scale landslide-dammed lake was formed in 2020. The new river channel was shifted 95–100 m towards the left side of the valley.

Currently, the role of the Buzulgan landslide in increasing the debris flow hazard is the possible formation of a new landslide-dammed lake when a debris flow originate sup stream in the valley. The subsequent breakthrough of such a landslide-dammed lake may be accompanied by the formation of a high debris flow surge. Such a scenario could be catastrophic for the Tyrnyauz town, which is located just 2 km down the valley. Thus, the continuation of the study of the Buzulgan landslide and organization of monitoring at this site are critically important.

The paper presents the results of modeling based on the FLOVI and FLO-2D PRO software package. The FLOVI program, which is based on the equations of the transport-shift model, was used to calculate the flow characteristics at the site where debris flow crosses the Busulgan landslide. Modeling of flow transformation in the valley was performed using a two-dimensional hydrodynamic model FLO-2D. The sensitivity of the hydrodynamic model to the rheological parameters was shown, so the difference in debris flow discharges at the alluvial fan varied from 1 to 18%, the difference of inundation zone was about 10%. Modeling on the cone itself was carried out for the case of the channel blockage in the bridge area by debris flow deposits or because of the collapse of the bridge. In this case, the area of the flood

zone is 26% larger. The results obtained show the effectiveness of the applied complex of models.

References

Baranovsky AF (2004) Debris flows of 2000 in the Gerkhozhan-Su basin. Proceedings of the confenence "Protection of economic facilities from the impact of debris flows", vol 2. Sevkavgiprovodkhoz, Pyatigorsk, pp 90–96. (in Russian)

Bekkiev MY, Anaev MA, Dokukin MD, Kalov RK, Malneva IV, Khadzhiev MM (2020) Anomalous movement of Buzulgan landslide in the valley Gerkhozhan-Su River (Central Caucasus) in 2020. Georisk 14(4):44–54. (in Russian)

Chernomorets SS (2005) Origination sites of debris flow disasters: before and after. Scientific World Press, Moscow. 184 p. (in Russian)

Cruden D, Varnes DJ (1996) Landslide types and processes. In: Turner AK, Schuster RLE (eds) Landslides: investigation and mitigation: Transportation Research Board. Special Report 247. National Academy Press, Washington, pp 36–75

Cunge GA, Holly FM, Verwey A (1980) Practical aspects of computational river hydraulics, London

Dokukin MD, Bekkiev MY, Bogachenko EM, Kalov RK, Savernyuk EA, Khadzhiev MM (2018) Debris flows on August 14-15, 2017 in the river basin Gerkhozhan-Su (Central Caucasus): conditions and causes of formation, dynamics, consequences. Georisk 3:82–94. (in Russian)

Dokukin MD, Savernyuk EA, Bogachenko EM, Ivanov GI (2012) Debris flows on August 3, 2011 in the Gerkhozhan-Su river basin: causes, dynamics and possible consequences. Georisk 2:48–56. (in Russian)

Gerasimov VA (1967) Debris flows in the area of Tyrnyauz 1/VIII 1960, 14/VIII 1961 and 31/VII 1962. Proceedings of High Mountain Geophysical Institute. Nalchik. 6:198–205. (in Russian)

Gerasimov VA (1980) Debris flows on August 10 and 11, 1977 in the Gerkhozhan-Su river basin (North Caucasus) and the conditions of their formation. Debris Flows 4:68–76. (in Russian)

Hungr O, Leroueil S, Picarelli L (2014) The Varnes classification of landslide types, an update. Landslides 11(2):167–194. https://doi.org/10.1007/s10346-013-0436-y

Hutchinson JN (1988) General Report: Morphological and geotechnical parameters of landslides in relation to geology and hydrogeology. In: Bonnard C (ed) Proceedings of the 5th International Symposium on Landslides, vol 1. Balkema, Rotterdam, pp 3–35

International Geotechnical Society's UNESCO Working Party on World Landslide Inventory (WP/WLI) (1993a) A suggested method for describing the activity of a landslide. Bull Intern Assoc Eng Geol 47:53–57

International Geotechnical Society's UNESCO Working Party on World Landslide Inventory (WP/WLI) (1993b) A multi-lingual landslide glossary. Bitech Publishers, Vancouver. 59 p

Khain VE (1998) The Pyrenees-Alps-Carpathians-Caucasus: experience of comparative analysis. Tectonics and geodynamics: General and regional aspects. Proc XXXI Tectonic Conf Geos Moscow 2:241–243. (in Russian)

Kurovskaia VA, Chernomorets SS, Krylenko IN, Vinogradova TA, Dokukin MD, Zaporozhchenko EV (2022) Buzulgan rockslide: simulation of debris flows along Gerkhozhan-su river and scenarios of their impact on Tyrnyauz town after changes in 2020. Water Resour 49(1):58–68. https://doi.org/10.31857/S0321059622010114

Laverov NP (ed) (2005) Modern and holocene volcanism in Russia. Nauka, Moscow. 604 p (in Russian)

O'Brien JS, Julien PY (1988) Laboratory analysis of mudflow properties. J Hydraulic Eng CXIV(8):877–887

O'Brien JS, Julien PY, Fullerton WT (1993) Two-dimensional water flood and mudflow simulation. J Hydraulic Eng CXIX(2):244–261

Pysmenny AN, Pyhudjkov AN, Zarubina MA, Gorbachev SA et al (2013) The State Geological Map of the Russian Federation. Scale 1:200000. Sheet K-38-I, VII. Moscow. MB VSEGEI

Seinova IB, Popovnin VV, YeA Z (2003) Intensification of glacial debris flows in the Gerkhozhan Basin, Caucasus, in the late 20th century. Landsl News 14(15):39–43

Seismic building design code. SP (Building rules) 14.13330.2018. (2018). Moscow (in Russian)

Varnes DJ (1978) Slope movement types and processes. In: Schuster RL, Krizek RJ (eds) Landslides, analysis and control: Transportation Research Board. Special Report 176. National Academy of Sciences, Washington, pp 11–33

Vinogradova TA, Vinogradov AY (2017) The experimental debris flows in the Chemolgan river basin. Nat Hazards LXXXVIII:189–198. https://doi.org/10.1007/s11069-017-2853-z

Vinogradov YB (1980) Etudes about debris flows. Gidrometeoizdat, Leningrad. 160 p (in Russian)

Vinogradov YB, Vinogradova TA (2010) Mathematical modeling in hydrology. Academia, Moscow. 304 p (in Russian)

Zolotarev EA, Kirpichenkov SY, Seinova IB (1979) The results of observations of landslide source zone in the lower part of debris flow-prone rivers using the photogrammetric method. Debris flows in mountainous regions of the USSR. Moscow University Press, Moscow, pp 84–87. (in Russian)

Zaporozhchenko EV (2002) Flows of the Gerkhozhan-Su river basin: history of manifestation, conditions of formation, energy characteristics. Sevkavgiprovodkhoz. Pyatigorsk 15:80–148. (in Russian)

A Risk Evaluation Method of Unstable Slopes Using Multipoint Tilting Sensors

Makoto Fukuhara, Lin Wang, Shangning Tao, Zhijun Tang, Wenjian Tang, Linyao Dong, and Zhongjie Fan

Abstract

Slope monitoring and early warning systems (EWS) are a promising approach toward mitigating landslide-induced disasters. Many large-scale sediment disasters result in the destruction of infrastructure and loss of human life. The mitigation of vulnerability to slope and landslide hazards will benefit significantly from early warning alerts. The authors have been developing monitoring technology that uses a Micro Electro Mechanical Systems (MEMS) tilt sensor array that detects the precursory movement of vulnerable slopes and informs the issuance of emergency caution and warning alerts. In this regard, the determination of alarm thresholds is very important. Although previous studies have investigated the recording of threshold values by an extensometer which installation at appropriate sites is rather difficult. The authors prefer tilt sensors and have proposed a novel threshold for the tilt angle, which was validated in this study. This threshold has an interesting similarity to the previously reported values using viscous models. Additionally, multi-point monitoring has recently emerged and allows for many sensors to be deployed at vulnerable slopes without disregarding the slope's precursory local behavior. With this new technology, the detailed spatial and temporal variation of the behavior of vulnerable slopes can be determined as the displacement proceeds toward failure.

Keywords

Disaster mitigation · Early warning · Risk evaluation · Slope failure · Warning threshold

M. Fukuhara · L. Wang (✉) · S. Tao · Z. Tang
Chuo Kaihatsu Corporation, Technology Center, Tokyo, Japan
e-mail: fukuhara@ckcnet.co.jp; wang@ckcnet.co.jp; tao.s@ckcnet.co.jp; tang@ckcnet.co.jp

W. Tang · L. Dong · Z. Fan
Changjiang River Scientific Research Institute, Changjiang Water Resource Commission, Wuhan, China
e-mail: wjtang@mwr.gov.cn

1 Introduction

Slope instability is a natural hazard that exerts a profound influence on the operation and reliability of infrastructure. Unlike engineered structures, natural slopes are not designed for safe performance. As a consequence of natural processes, slopes have heterogeneous material properties. Moreover, slopes are prone to erosion, and their gradient changes with time. Underground hydrology is hardly captured in practical engineering. Therefore, quantitatively assessing the extent of slope stability is very difficult in practical situations. Although the movement of landslide masses, which has been slow in conventional studies, is already a major threat to human activities, rapid and unpredictable slope failure triggered by gravity or heavy rain is more hazardous because it may instantaneously result in an enormous loss of human life and the destruction of infrastructure. However, predicting the abrupt failure of slopes to avoid damage is still difficult. Communities in mountain regions are particularly prone to this type of damage. The situation is more serious for transportation infrastructure because its function can be entirely disrupted by a single slope failure (Lee et al. 2013; Sartori et al. 2003). Ongoing global climate change increases the likelihood of heavy and concentrated rainfall, which results in more rainfall-induced slope failures.

As stated above, the mitigation of landslide disasters is difficult and the available funding for conducting elaborate site investigations is far too little. Practitioners have been trying to improve safety by developing slope monitoring and early warning system (EWS) technologies with the objective of predicting slope failure in advance based on the observed slope behavior and mitigating the extent of damage (Medina-Cetina and Nadim 2008). The United Nations International Strategy for Disaster Reduction (UN-ISDR 2006) advocates that EWS should "empower individuals and communities threatened by hazards to act within sufficient time and in an appropriate manner to reduce the possibility of

I. Alcántara-Ayala et al. (eds.), *Progress in Landslide Research and Technology, Volume 2 Issue 1, 2023*,
Progress in Landslide Research and Technology, https://doi.org/10.1007/978-3-031-39012-8_11

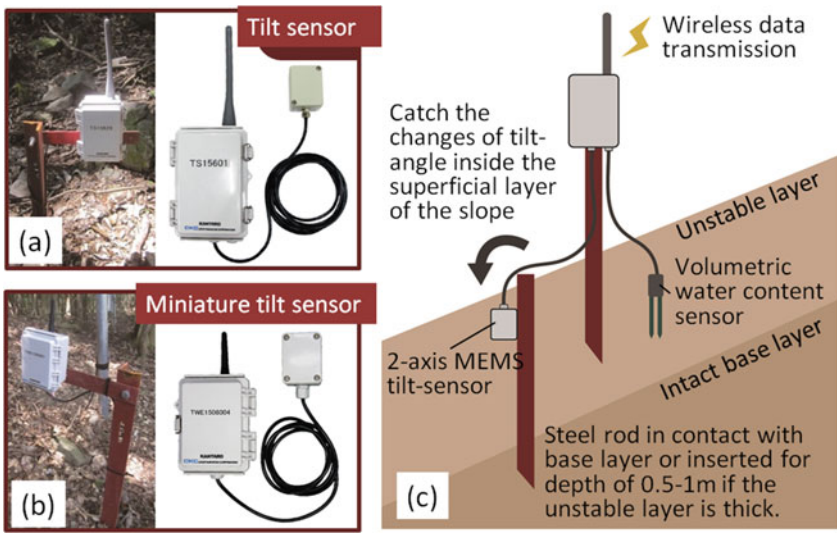

Fig. 1 Schematic illustration of MEMS tiltometer sensor for early warning (Wang et al. 2017)

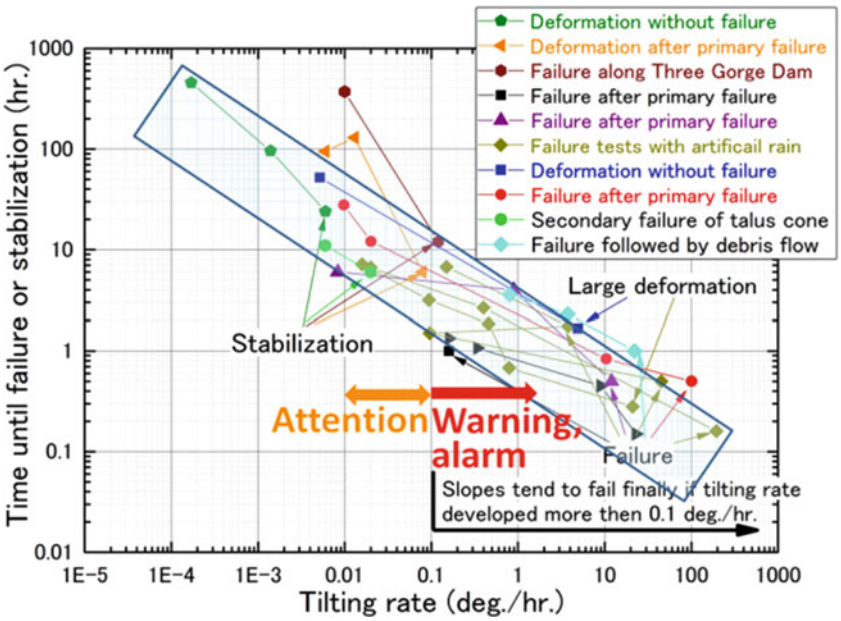

Fig. 2 Graphic illustration of the tilting rate as a function of time before slope failure (or stabilization) for several case studies (Uchimura et al. 2015)

personal injury, loss of life, and damage to property and the environment" (from the UN-ISDR web site).

There is a long history of prevention and mitigation of rainfall and/or scouring-induced landslides. Mechanical countermeasures to prevent slope failure have been widely used, including retaining walls and ground anchors. However, these methods can be expensive and are not always realistically applicable to all slopes of varying scales and potential risk factors. Therefore, careful monitoring of slope behavior and consequent early warning of failure provides a reasonable and slope-specific alternative.

In this paper, an early warning system for slope failure is proposed and its development is described (Fig. 1) (Wang et al. 2017). The system consists of a minimum number of low-cost sensors strategically placed on a slope, with monitoring data that are collected being transmitted via a wireless network. It is anticipated that this low-cost and simple system will provide at residents risk with access to accurate and timely precautions or warnings of slope failure.

Uchimura et al. (2015) summarized case studies of slope tilting rates during pre-failure stages obtained on several natural slope sites under natural or artificial heavy rainfall. Figure 2 presents an example of the typical monitoring data obtained, in which the tilting rate (X-axis) can be related with the time elapsed until slope failure or slope stabilization (Y-axis). Figure 3 shows the definition of the tilting rate and the time in Fig. 2, in which Ti is the time until failure or stabilization, and Ri is tilting rate.

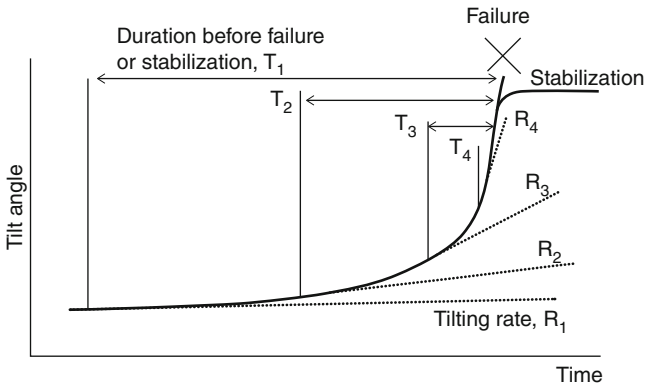

Fig. 3 Definition of the tilting rate and the durations (Uchimura et al. 2015)

In cases where the slope failed at the position of the tilt sensor, the elapsed time is measured from the time when tilting accelerated to the time of failure. In cases where the slope did not fail but instead stabilized, the time is measured from when tilting decelerated to the time when the slope stabilized.

According to Fig. 2, the order of tilting rate observed with slope deformation varied widely, from 0.0001°/h to 10°/h depending on several factors. The tilting rate tends to increase towards failure with a relatively short time until failure, when a higher tilting rate is observed. The observed tilting rate was >0.01°/h for all the cases in which the slope failed or nearly hour was observed before failure for a tilting rate of 0.1°/h.

Based on the past case studies, it is proposed that when the tilting rate exceeds 0.1°/h a warning of slope failure should be issued, and a precaution issued at a tilting rate of 0.01°/h, taking safety into account. Additionally, this paper explores efforts by the current authors to improve the applicability of the monitoring and early warning system. The miniature tilt sensors are modified from that currently available to be more cost-effective, smaller in size and weight, and simpler to install, maintain and operate. As a result, it is possible to install a larger number of sensors on a given slope, thereby providing greater coverage and higher data density.

Figure 4 illustrates the typical arrangement of two types of proposed sensors, with data transfer pathways also shown. Despite the advantages described above, the new type of miniature tilt sensors has relatively short radio transmission distances (~30 m in non-ideal conditions). They are arranged densely on high-risk areas of a slope, with one conventional tilt sensor unit collecting all the data of each area. The data are transmitted over greater distances (300–600 m) and uploaded to an internet server.

2 Field Validation of Tilt Sensor for Slope Monitoring

Previously, MEMS tilt sensors have been used at more than 100 sites with slope instability in worldwide. Most of these slopes did not fail, but several of these slopes have failed with and without rainfall and provided important data. Based on these data, the warning threshold has been determined as 0.1°/h. In this section, various cases that have not been reported are discussed.

2.1 Prevention of Secondary Disaster During Restoration of Failed Slope–Fukuoka Pref., Japan

An EWS was successfully used in 2015 in Fukuoka Prefecture, Japan. When this region received heavy rainfall during

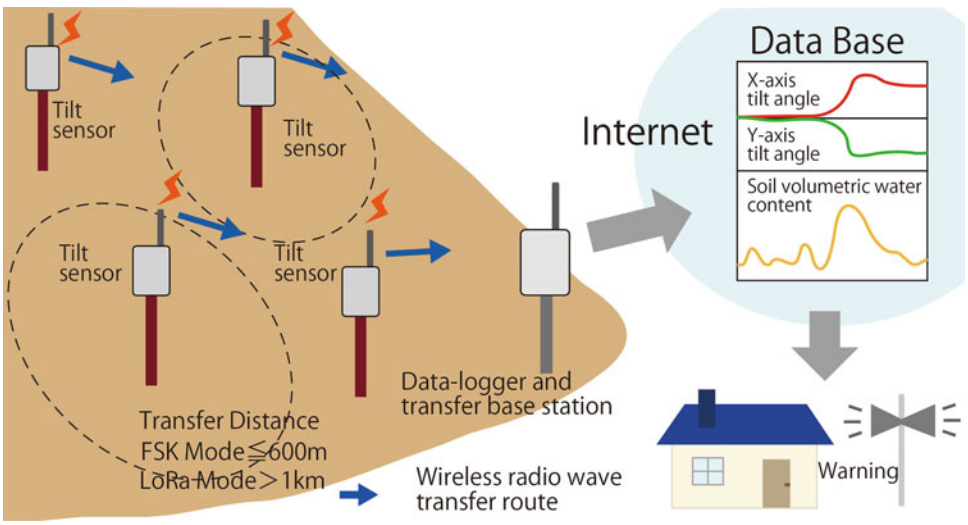

Fig. 4 An early warning system of slope failure by multi-point tilt and volumetric water content (Wang et al. 2017)

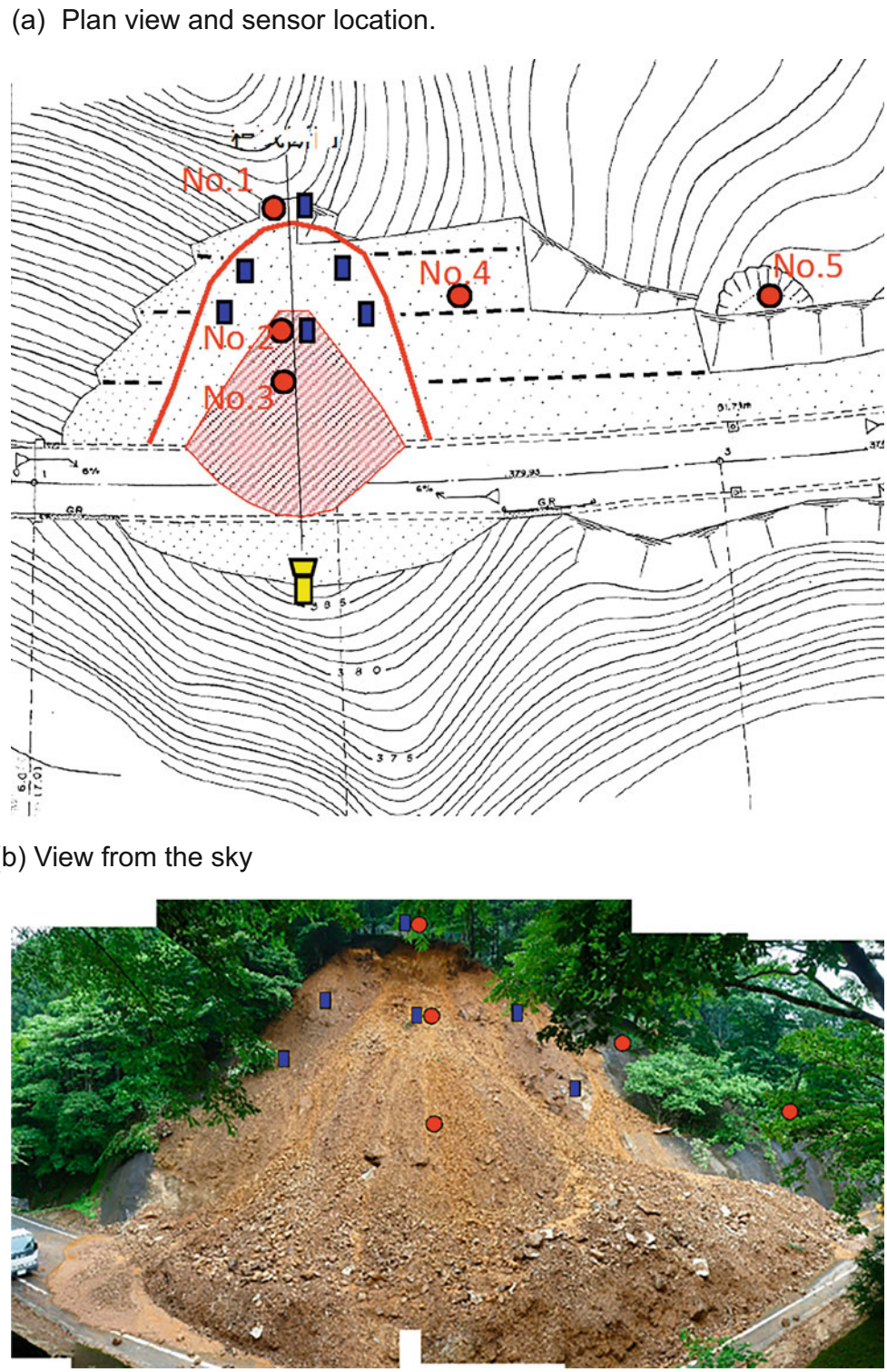

Fig. 5 Monitored slope in Fukuoka

typhoon No. 11 "Nangka" on July 17 and 18, the slope collapsed and the local road was closed for traffic (Fig. 5). This slope comprises Funi volcanic rock of andesite karst, tuff breccia, and tuff. To safely keep one lane open for traffic during slope restoration, the slope movement was monitored by a set of tilt sensors as shown in Fig. 6. The traffic was intended to stop if the tilt sensor detected an excessive tilting rate during the slope restoration works.

Figure 6 shows the plot of the tilt angle and the rainfall data on July 21st and 22nd, shortly after the main slope

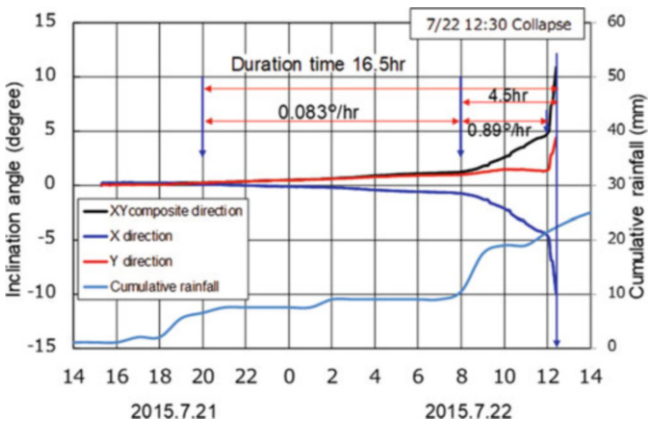

Fig. 6 Time histories of monitored data at Fukuoka site

collapse. The slope was considered to be prone to further failures during the restoration works. From 4 PM to 8 PM on July 21st, that is, immediately after the tilt sensor installation, the tilting rate of 0.083°/h was recorded and continued until 8 AM on July 22nd. Thereafter, the tilting rate accelerated to 0.89°/h, possibly owing to rainfall amounting to approximately 10 mm from 8 AM to 9 AM. Furthermore, owing to further rainfall after 11 AM, the tilting rate sharply increased to 12°/h after 12 PM and the slope finally collapsed at 12: 30 PM. Thus, the field monitoring helped control the traffic during the critical period and ensured the safety of human life.

Based on practical experiences at many sites with and without failure, the authors (2015) recommend that a warning and evacuation order should be issued at this tilting rate. Moreover, precautions may be issued at a tilting rate of 0.01°/h to ensure safety, because the time left until failure will be several hours or longer.

In the typical case wherein the surface soil thickness is 150 cm (Fig. 1) in Japan, the 0.01°/h and 0.1°/h tilting rates correspond to the displacement rates of 150 × tan (0.01°) or 150 × tan (0.1°), that is, 0.026 cm/h or 0.26 cm/h, respectively. Hence, it is extremely difficult for GPS, LIDAR, and InSAR to continuously monitor this small movement during heavy rainfall. Therefore, the authors prefer using tilt sensors. The following sections discuss the practical experience acquired at other slope-monitoring sites and used to validate the warning principle described above.

2.2 Practical Tilt Sensor Monitoring in Tokyo

Because of the heavy rain associated with Typhoon No. 21 "Jebi" on October 23, 2018, a part of industrial waste landfill collapsed in Tokyo. Consequently, a part of the collapsed sediment flowed and reached the prefectural road below the slope (Fig. 7).

Accordingly, a temporary protective fence and large sandbags were placed along the road, but drastic measures against the landfill collapse were not implemented. However, it was highly likely that slope failure would reoccur during the rainy season in 2019. Hence, the Environment Bureau of the Tokyo Metropolitan Government installed three extensometers at the edge of the landfill for monitoring. Moreover, three tilt sensors were installed for research purposes.

Figure 8 shows the monitored time history of the cumulative rainfall and the tilt angles. When the rainfall, which cumulatively amounted to 38 mm, occurred before 8 PM on June 15, there was no significant change in the records of tilt sensors K-1 and K-2. Thus, the situation remained relatively stable. A few hours later, in the early morning of June

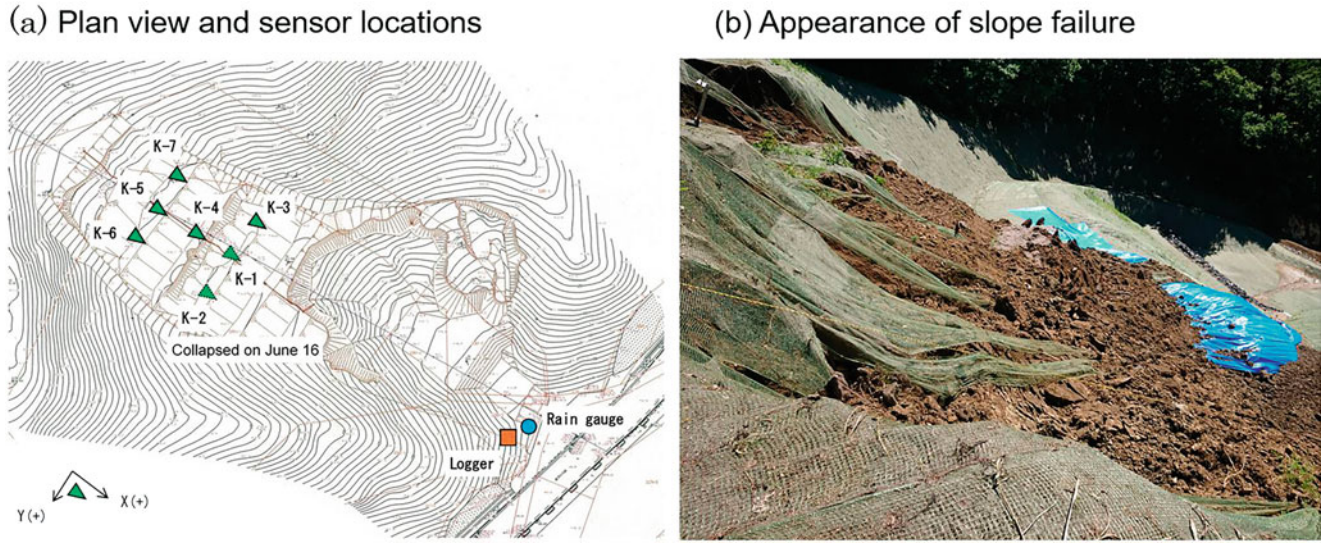

Fig. 7 Monitoring at landfill slope in Tokyo. (**a**) Plan view and tilt sensor locations. (**b**) Appearance of slope failure

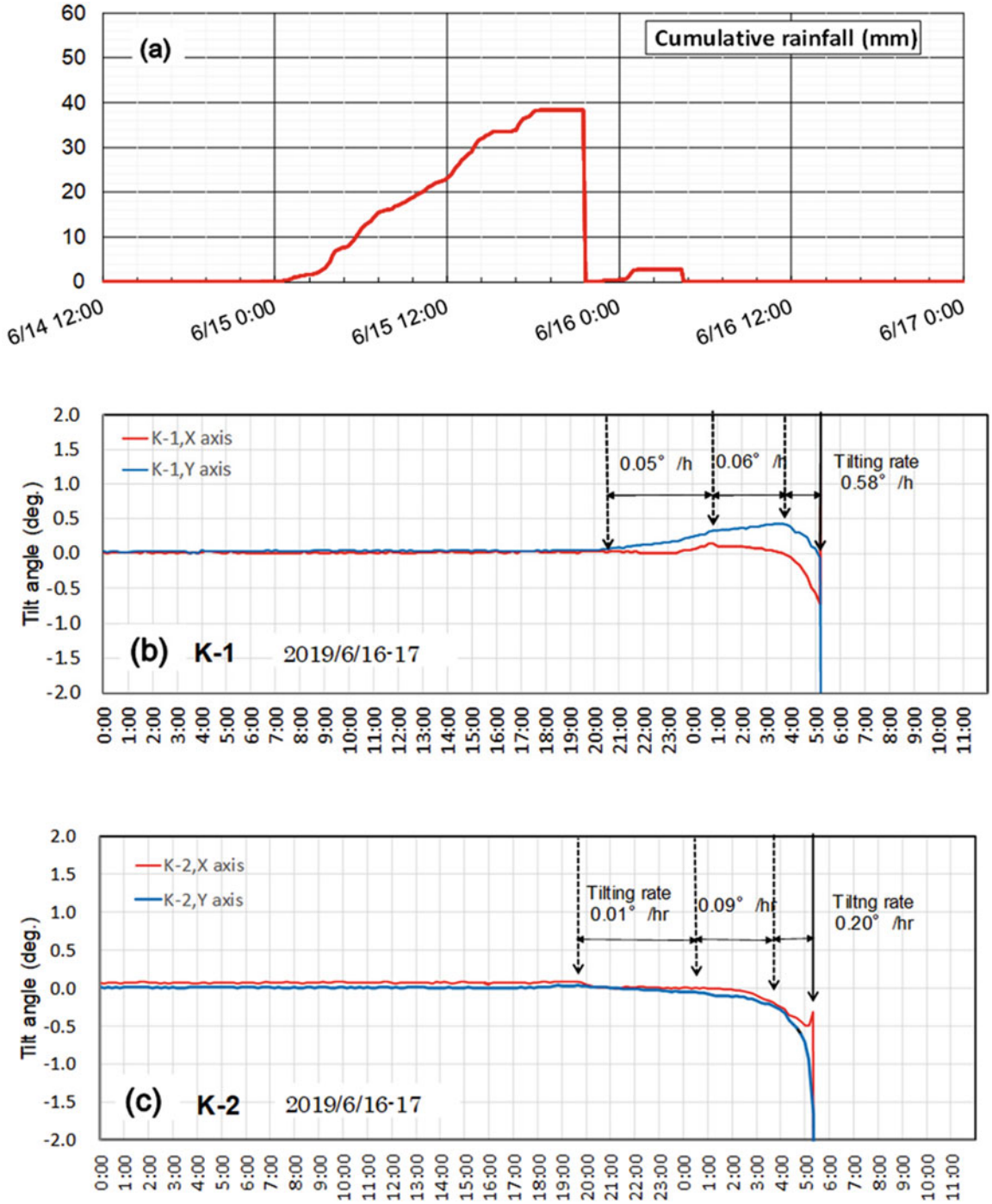

Fig. 8 Recorded cumulative rainfall and tilt angles at sensor K-1 and K-2 at the site shown in Fig. 7 (June 15th and 16th)

16, the tilt angles started to increase toward infinity at 5: 10 AM (slope collapse). The tilting rate of sensor K-1 reached 0.58°/h (X axis of slope direction) at 4 AM on June 16, and sensor K-2 reached 0.20°/h (X axis of slope direction) at 3:30 AM on the same day. Because the record of the tiltmeters accumulated in the negative direction of the X axis (toward the top of the slope), it is believed that the slope failure mechanism was associated with a circular slip (rotation).

2.3 Monitoring Slope Failure at Manzawa, Yamanashi, Japan

The Manzawa area in the Yamanashi Prefecture of Japan contains a large-scale reactivation of old slope failures featuring rockfalls that involve the detachment and rapid downward movement of rock.

Because most traditional slope monitoring methods are expensive, difficult to control and may not be suitable for application in this civilian area, the simple and low-cost monitoring system was deployed on a test slope to validate field performance. It should be noted that the research is supported by the Japanese Government during 2014–2017, and the following result that is reported in this paper.

Figure 9 shows the scale of Manzawa slope failure site, and Fig. 10 shows the arrangement of the multi-point tilt sensors and locations, where two types of tilt sensor were used. The arrangement interval of the sensor is designed to 5 m. A total of 66 sets of sensors were deployed.

The 66 sensor units are divided into three groups, left/middle/right zone, and one data receiver unit and one logger/gateway unit for internet to collect all the data from respective group as shown in Fig. 10. There were eight heavy rainfall events during summer of 2015 shown in Fig. 11, and the tilting rate averaged during each rainfall event is shown in Fig. 12. Distribution of tilting behaviors of two tears result was figured out by multi-point monitoring in Fig. 13 during 2015–2017.

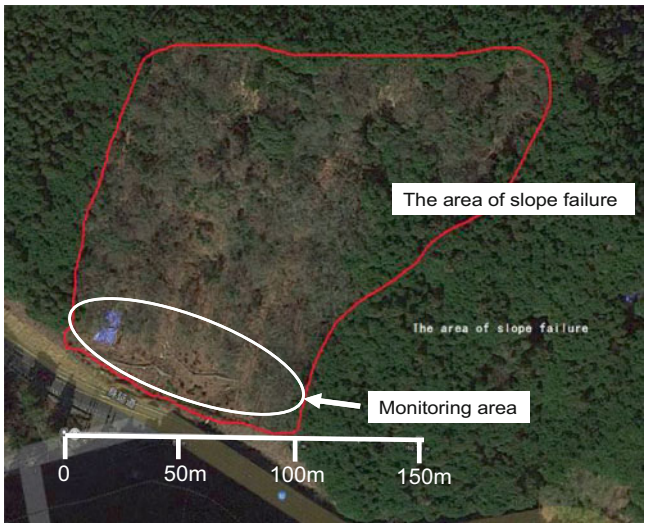

Fig. 9 Area of slope failure at Manzawa site, Japan

2.4 Early Warning by Using Multi-point Monitoring

Wang et al. (2017) proposed an early warning method based on single-sensor monitoring. Recently, the authors have extended the scope of slope monitoring to multi-point monitoring, which can capture both the spatial and temporal behavior of the entire slope. Additionally, multi-point monitoring can avoid erroneous warnings caused by very local

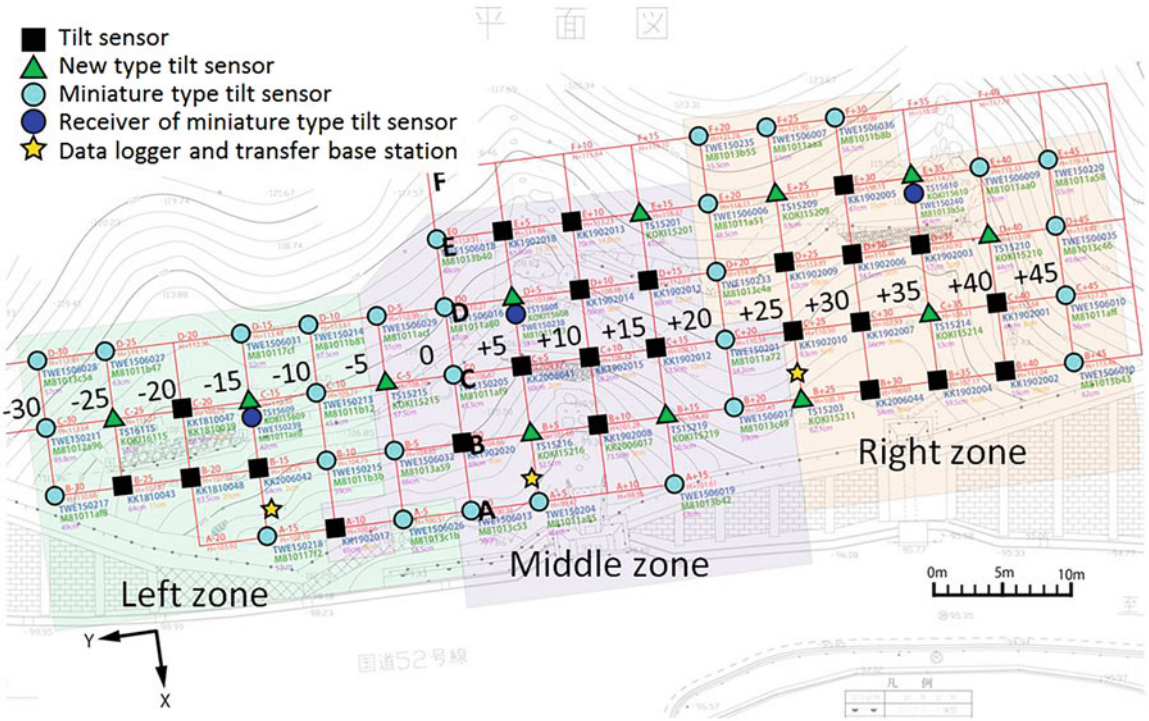

Fig. 10 Arrangement of the multi-point tilt sensors

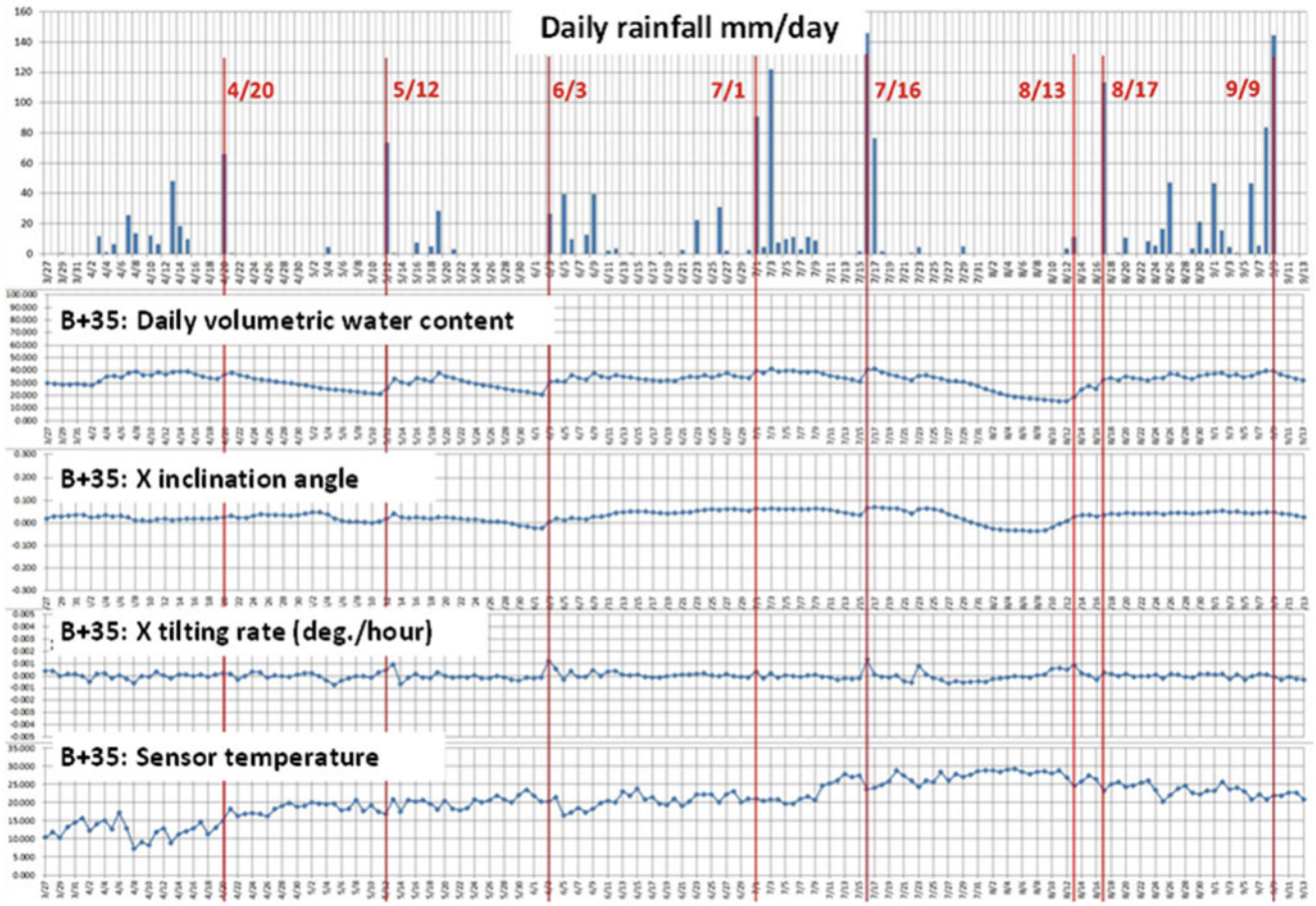

Fig. 11 Time histories of movements in rainy days during summer of 2015

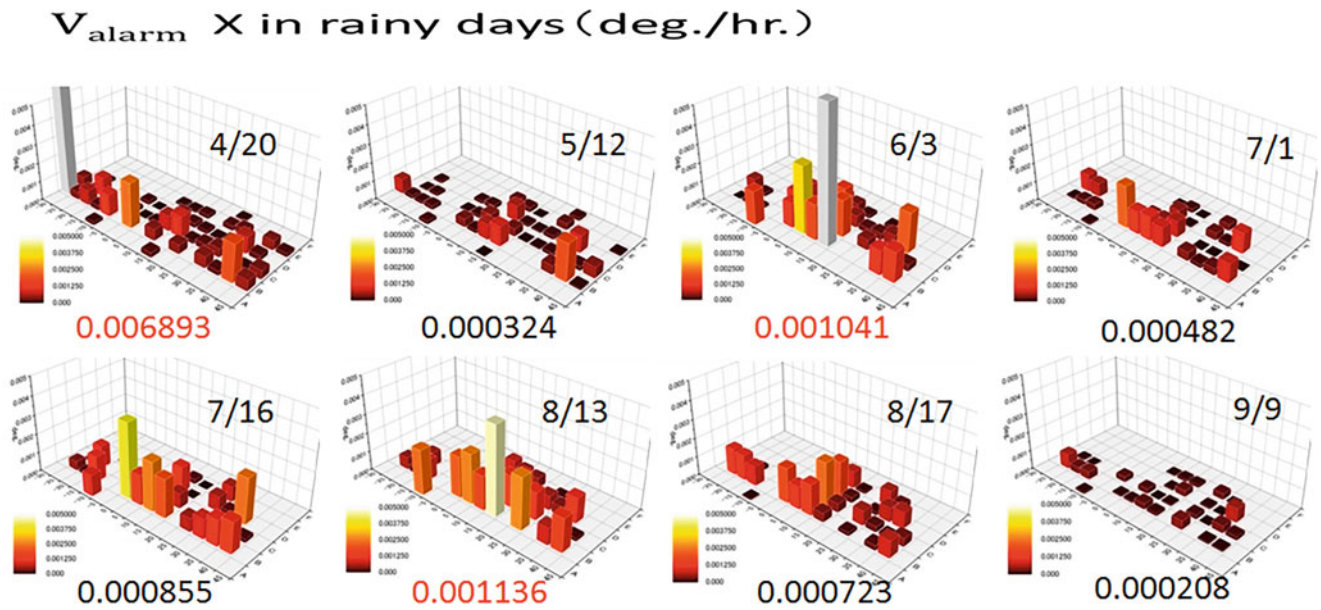

Fig. 12 Distribution of tilting rates during each rain day during summer of 2015

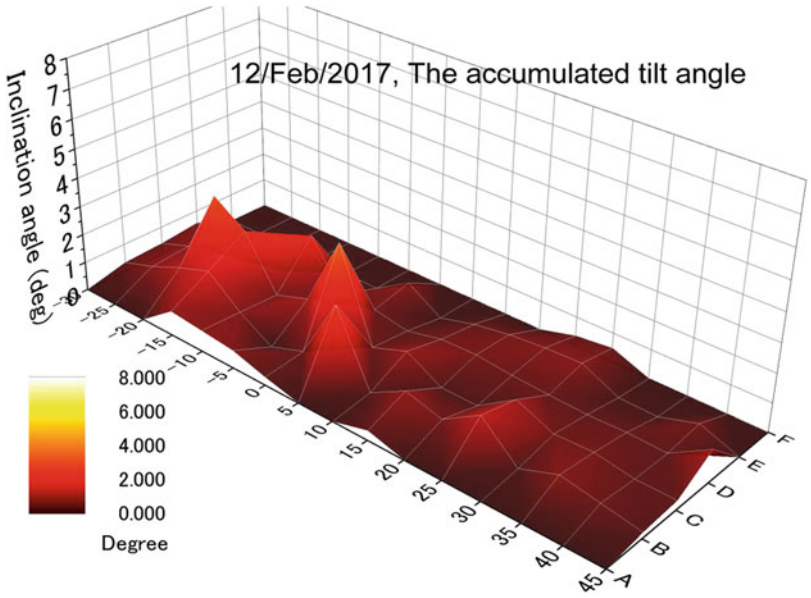

Fig. 13 Distribution of accumulated inclination angle during 2015–2017

slope movement and animal contact, among other causes of error. Thus, the reliability of early warning is improved.

The spacing between multiple sensors must be kept within a reasonable limit (a few meters to a few tens of meters, as in the practical cases discussed in this paper), and a new index of slope movement must be proposed in place of a single sensor's tilting rate, as in past practical cases.

Certainly, the new index must handle data at all monitoring points. Presently, the new index is assumed to be expressed as follows:

$$V_{alarm} = \sum_{n=1}^{n} \left(|Vn| * \frac{An^*}{A0} \partial n \right) \quad (1)$$

where n is the total number of tilt sensors; V_i is the tilting rate (otherwise denoted as dα/dt) in the slope direction of the ith sensor (°/h); A_i is the area covered by the ith sensor; A_0 is the area covered by the entire sensor array; ∂_i is the coefficient determined by the geology, geography, soil type, and vegetation conditions at the installation points. Moreover, the ∂_i coefficients regard the field conditions, and their values are determined based on the results of geomaterial experiments and the assessment of geologists. Although this issue requires further investigation, $\partial_i = 1$ is currently used in practical situations.

3 Conclusion

The authors have been developing slope failure monitoring and early warning technology. This technology is characterized using MEMS tilt sensors. In earlier versions, monitoring was conducted using a single sensor. However, a multi-sensor approach was implemented in recent development. This paper introduces the most recent development of the authors' EWS based on data obtained from several sites and their interpretation. The following conclusions were drawn from this study:

(1) In the previous version of the technology, a caution alert was issued when the tilting rate exceeded 0.01°/h, while a warning associated with an evacuation order was issued when the rate exceeded 0.1°/h. These threshold values are based on practical experience and have been validated by recently obtained monitoring results.
(2) In this paper, various monitoring cases are summarized. The linear relationship between the logarithm of the rate of the tilting angle of the sensors and the logarithm of the time remaining until slope failure was demonstrated. This relationship has an interesting similarity to the relationships suggested by the Monkman-Grant model (Monkman and Grant 1956) and Saito's rheological interpretation of laboratory soil tests (Saito and Uezawa 1961; Saito 1965).
(3) The recent extension of monitoring to multi-point practice enables a more detailed interpretation of slope behavior in the transient stage and up to the final failure.

As the actual plans, the authors are currently undertaking the National key R&D project of Sino-Japan "Development and demonstration of monitoring and warning technology for the rainstorm induced mountain torrent disaster chain", which takes the rainstorm-flood-landslide-debris flow disaster chain as the research object and is carrying out through international cooperation and joint research. By using the strength of

the Japanese participating units in the field of disaster mechanism research and sensing technology and bring into play the advanced level of the Chinese participating units in communication technology and platform development, the results such as deeply exploring the occurrence and evolution mechanism and developing the key technologies for precise monitoring and dynamic warning of the rainstorm-induced mountain flood disaster chain are expected to be obtained. The project aims to provide scientific and technological support for the mountain flood disaster chain prevention and control, and effectively improve the theoretical and technological level of disaster prevention and reduction research between China and Japan.

Acknowledgments This research was supported by Council for Science, Technology and Innovation, "Cross-ministerial Strategic Innovation Promotion Program (SIP), Infrastructure Maintenance, Renovation, and Management". (Funding agency: NEDO) of Japan. The National Key R&D Program of China (Grant number 2021YFE0111900), and the National Natural Science Foundation of China (Grant No. 41977171, 41902300).

References

Lee WF, Liao HJ, Wang CH (2013) Failure analysis of a highway dip slope slide. 4th International Seminar on Forensic Geotechnical Engineering, Bangalore. pp 325–338

Medina-Cetina Z, Nadim F (2008) Stochastic design of an early warning system. Georisk Assess Manage Risk Eng Syst Geohazards 2:223–236. https://doi.org/10.1080/17499510802086777

Monkman FC, Grant NJ (1956) An empirical relationship between rupture life and minimum creep rate in creep rupture tests. Proc Am Soc Test Mater 56(1956):593–620

Saito M, Uezawa H (1961) Failure of soil due to creep. Proceedings of the 5th International Conference on Soil mechanics and Foundation Engineering, vol 1. pp 315–318 (Paris). https://www.issmge.org/uploads/publications/1/40/1961_01_0054.pdf

Saito M (1965) Forecasting the time of occurrence of a slope failure. Proceedings of the 6th International Conference on Soil Mechanics and Foundation Engineering, vol 2. pp 537–541 (Montréal). https://www.issmge.org/uploads/publications/1/39/1965_02_0116.pdf

Sartori M, Baillifard F, Jaboyedoff M, Rouiller JD (2003) Kinematics of the 1991 Randa rockslides (Valais, Switzerland). Nat Hazards Earth Syst Sci, Copernicus Publications on behalf of the European Geosciences Union 3(5):423–433. https://doi.org/10.5194/nhess-3-423-2003

Uchimura T, Towhata I, Wang L, Nishie S, Yamaguchi H, Seko I, Qiao JP (2015) Precaution and early warning of surface failure of slopes by using tilt sensors. Soils Found 55(5):1086–1099. https://doi.org/10.1016/j.sandf.2015.09.010

UN-ISDR (2006) Developing early warning systems, a checklist: Third international conference on early warning (EWC III), Bonn, Germany, 27–29 March 2006. UNISDR. https://www.unisdr.org/2006/ppew/info-resources/ewc3/checklist/English.pdf

Wang L, Nishie S, Su L, Uchimura T, Tao S, Towhata I (2017) Proposed early warning system of slope failure by monitoring inclination changes in multipoint tilt sensors. 19th International conference on soil mechanics and geotechnical engineering, Seoul, South Korea, pp 2215–2218

Part III

IPL Projects, World Centres of Excellence on Landslide Risk Reduction, and Kyoto Landslide Commitment 2020

Community Level Slope Disaster Risk Reduction Program through Multi-Scale Mapping by Mountain Ethnic Group in Northern Vietnam: Project Study by JICA/Lao Cai DARD/ITST

Nguyen Kim Thanh, Toyohiko Miyagi, Ta Cong Huy, Eisaku Hamasaki, Dinh Van Tien, and Yasuhiro Kasuya

Abstract

Recent advances in remote sensing have been remarkable, not only in terms of technology but also in terms of operability and price. Ethnic minorities in the mountains have historically barely survived repeated disasters. As a result, they are still living in an environment with a high risk of landslide disasters. Although the economic conditions of these residents deter their efforts to find engineering solutions to mitigate potential landslide disasters, they can adequately assess the regional conditions daily. By combining their abundant but fragmental knowledge of landslide disasters with our "Site Prediction Technology of Mapping," we are trying to develop a local community that can avoid disasters and ensures their safety.

This project focuses on mountainous areas in northern Vietnam and is a collaborative effort among Vietnamese and Japanese engineers, local governments, and international organizations. We have begun to present ALOS World 3D (AW3D) data and data acquired by Unmanned Aerial Vehicles (UAV) to residents and use them for disaster prevention and evacuation drills. This mapping process is called Communication Based Evacuation Mapping (CBEM). Despite Japan's long history of using maps to prevent disasters, it is rare for residents to use them actively, as having an engineer make and publish a map will not lead to its use by the residents. This paper introduces a series of measures taken from the creation of maps to the engagement of residents in slope disaster risk reduction.

Keywords

Community level · Communication Based Evacuation Mapping (CBEM) · Multi-scale mapping · Slope disaster · Mountain ethnic group · Vietnam

1 Introduction: Necessity of Mountainous Slope Disaster Prevention in Mountainous Areas of Vietnam

Vietnam is located in the northern part of Southeast Asia, on the central coastal region of the Indochina Peninsula. It is long in the north-to-south direction, from 8 degrees north latitude to 23.5 degrees north latitude. The Annan Mountains run parallel to the coast. Southern China and Laos border northwestern to the central part of the country. The border area is steep and mountainous, with an average altitude of more than 2000 m. The mountainous region has a tropical monsoon climate and is influenced by northeast trade winds and typhoons. It receives a large amount of precipitation during the rainy season, with the annual rainfall reaching 4000 mm in some areas. From the Annan Mountains, the backbone of the Indochina Peninsula, to China in the north and west to Myanmar, the geology of the Mesozoic to Paleozoic Erases is widely distributed. The Paleozoic zone suffers from large-scale fold deformation (Nam 1995). Many ethnic groups live in these mountainous areas of Vietnam. Ethnic minorities generally retain their traditional lifestyles, and many make their living by farming in mountainous areas. While income levels appear typically low, the survey sites often provide glimpses of self-sufficient living styles. Survey

N. K. Thanh (✉)
Institute of Transport Science and Technology, Hanoi, Vietnam

Tohoku Gakuin University, Sendai, Japan

T. Miyagi · E. Hamasaki
Advantechnology Co., Ltd, Chiyoda, Japan
e-mail: c1934009@mail.tohoku-gakuin.ac.jp; hamasaki@advantechnology.co.jp

T. C. Huy
LaoCai DARD, Lao Cai, Vietnam

D. Van Tien
Institute of Transport Science and Technology, Hanoi, Vietnam

Y. Kasuya
JICA Vietnam, Hanoi, Vietnam
e-mail: Kasuya.Yasuhiro@jica.go.jp

I. Alcántara-Ayala et al. (eds.), *Progress in Landslide Research and Technology, Volume 2 Issue 1, 2023*,
Progress in Landslide Research and Technology, https://doi.org/10.1007/978-3-031-39012-8_12

sites indicate that basic infrastructure, such as roads and electric power, are often inadequately developed, and the living and working conditions are poor.

In recent years, there has been concern that natural disasters caused by global warming and climate change are becoming increasingly severe, associated with heavy rainfalls, particularly in mountainous areas of Vietnam (MONRE 2021). The study areas have a long geological history of folding and faults. Moreover, chemical weathering during tropical rain has strongly affected the areas.

According to data on the risk of global disaster fatalities compiled by UNDRR (2009), South and Southeast Asia, from India and Nepal to the Philippines and Indonesia, are considered the world's largest high-risk regions.

2 Regional Overview and Vietnam's Disaster Prevention System

2.1 Slope Disaster Risk in Northwestern Vietnam's Mountain Region

A sizable tectonic region (Red River Fault) runs from northwest to southeast through the central part, along which flows the Red River. The area has elevations over 1000 m above sea level, containing Phan Xi Pang (3143 m above sea level), Vietnam's highest peak, which rises on the border of Lao Cai Province and Lai Chau Province. In these mountainous areas, unstable slopes are widespread, with active sediment movement associated with landslides and debris flows. There were 946 landslides in 15 northern provinces between 2001 and 2019, according to the Ministry of Agriculture and Rural Development (MARD) (2020). There have been 590 flash floods. These disasters resulted in the deaths of 748 residents and damaged 52,000 homes. One of the most striking aspects is that nearly 4000 houses were relocated due to the disasters.

In our preliminary survey, we noted that the mass relocation in villages was an early sign of the occurrence of landslides. Although relocations were in progress in other villages, some families reportedly returned to their old homes. Residents of North Vietnam are generally well aware of the high risk posed by landslides due to the prevalence of factors such as topography, geology, and climate conditions. It can be inferred that such awareness was a driving force behind the Vietnamese government-sponsored relocation program.

2.2 Disaster Risk Characteristics from the Humanities and Living Environment Perspectives

The area around the northern mountain provinces serves as the residence of various hill minorities. Although the life and land use tendencies of each ethnic group are diverse, the Thai, Tay, Hmong, and Dao tribes have a population greater than 1 million (Dang 2002). Generally, they make a living by cultivating rice terraces on the slopes, paddy fields, and pastoring buffaloes. Rice terraces are an excellent way to use the landscape in this area, but this requires that the natural forests be cut down. Thus, there are concerns that the risk of slope collapses and debris flows will increase during heavy rains. We believe it is necessary to understand the relationship between the risk of slope disaster occurrences and land use. However, quantitative assessments of the relationship between the two have not been examined.

2.3 Vietnamese Government's Disaster Risk Reduction Policy and Regional Disaster Risk Reduction Policy Initiatives and Challenges

Efforts to tackle slope disasters in Vietnam began with the enactment of the Disaster Prevention Law (Vietnam's National Assembly 2013). Tachi, a JICA expert from the Ministry of Agriculture and Rural Development (MARD), and Sakai, a JICA expert from the National Research Institute, took further steps (Tachi and Sakai 2019). Based on these references, we submitted a proposal for a slope project outlined by Disaster Risk Reduction. We will outline slope disaster prevention in particular.

Government Policy The Disaster Prevention Law sets out five basic principles for preventing and managing natural disasters. These are: (1) In extreme weather, the Vietnamese government must make proactive plans for the prevention and timely response to take prompt and effective corrective measures. (2) The prevention and control of natural disasters is the responsibility of the State, organizations, and individuals. The State plays a leading role, organizations, and individuals take the initiative, and local communities help each other. The prevention and control of natural disasters are carried out according to four maxims on the spot: command the local army for the organization of households or individuals in an area at risk of the natural disaster/s, vehicles and materials, and onsite logistics. (3) Natural disaster prevention and management content should be integrated into national and local socio-economic development master plans. Sectoral development master plans must ensure humanity, fairness, transparency, and gender equality. (4) For to prevent and control natural disasters, actions taken by the State must be based on science. Combine traditional experiences with the progress made through science and technology. A combination of structural and non-structural solutions; environmental protection, ecosystems, and adaptation to climate change. (5) Prevention and control of natural disasters will be decentralized with close

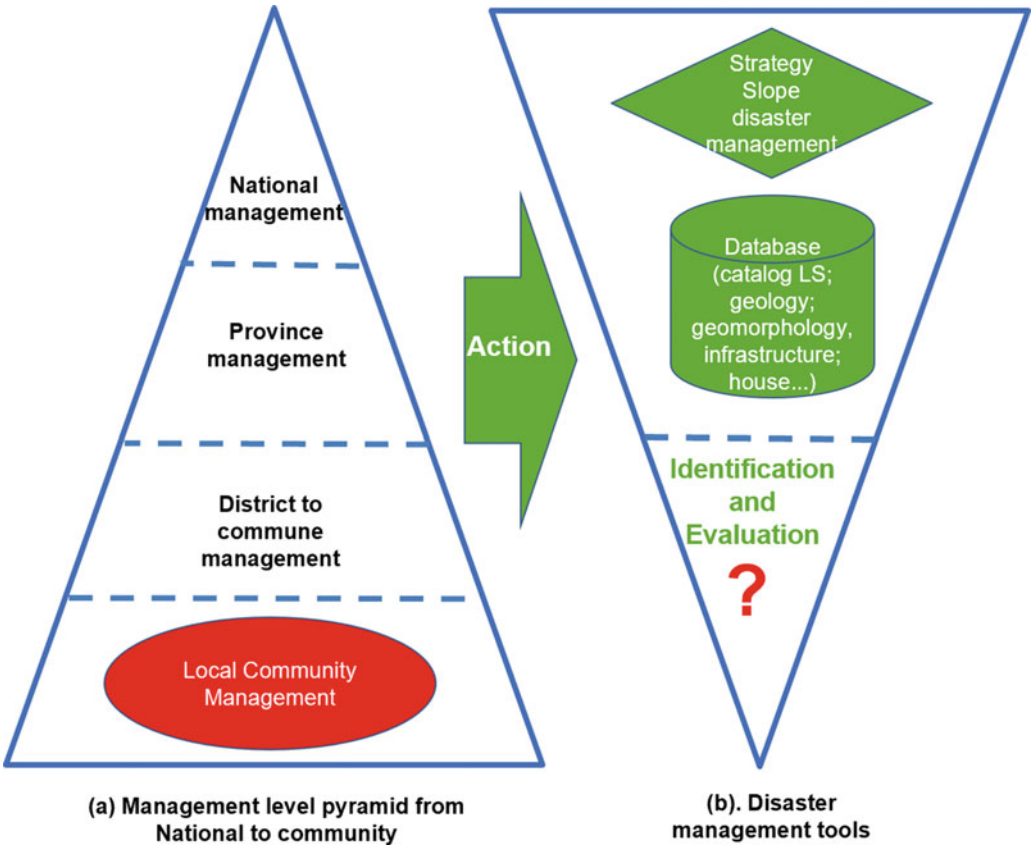

Fig. 1 Diagram shows the relationship between slope disasters, objects, and management tools. (**a**) Management level pyramid from National to community. (**b**) Disaster management tools

coordination between armed forces and natural disaster risk levels (National Assembly of Vietnam 2013). An organizational chart of disaster prevention measures to be constructed at the local people's committees level is also presented. It clearly states that this mechanism assists with disaster prevention through the cooperation of each organization in the region.

Needless to say, natural disasters in Vietnam may also be related to social factors. In Southeast Asia, such as Vietnam, paddy field cultivation and slash-and-burn cultivation using slopes have been practiced since ancient times. This practice suggests that many people live on mountainous slopes, with a high possibility of landslide disasters and soil erosion due to land use. In a social environment where mountain slopes are both a place of land use and a residence, it suggests the necessity of measures to mitigate disasters (Fig. 1).

Especially in areas with moist tropical mountains, such as Vietnam, slope disasters are repeatedly disrupting the lives of residents. However, residents in mountainous areas lack the practical knowledge and skills to avoid disasters. Although government officials are concerned about this, adequate measures are not easy to take. Disaster prevention organizations are established at all levels, from the center to the local level, including the provincial, district, and communal levels. The ability to understand landslides at the actual administrative level varies from program to program, plan, or project. At the regional level, and in villages, it is necessary to formulate appropriate response plans, taking into account the level of knowledge related to individuals involved the disaster prevention.

We need to educate the residents to raise awareness of landslides, such as what they are, what their causes are, when they occur, and pointing out landslides and safe locations. Maintaining a map with appropriate accuracy will be necessary to satisfy the above requirements. Examples include (1) an integrated map of landslide risk assessment, (2) a landslide distribution map at an appropriate scale, and (3) a map that can help locals identify the extent of the landslide area and the features associated with the topography in the area in which they reside.

At the national level, the Ministry of Natural Resources and the Environment has prepared a slope-disaster risk assessment map at a scale of 1:50,000 for use in community-scale development (Hung et al. 2017). However,

this is not easy to apply to the scale of local communities such as communes and houses. For their benefit, further creation of applicable disaster prevention maps is required.

3 Significance and Framework of the Project Outline and Aim of the Technical Support Project

3.1 Background to Building Relations and Identifying Issues Between Vietnam and Japan

In the past, the project "Development of Landslide Risk Assessment Technology along Transport Arteries in Vietnam" (Project leader: Kyoji Sassa, Academic Representative of the International Consortium on Landslide, ICL) was implemented as a project of the joint JICA/JST Planning Project (SATREPS) between 2011 and 2016 (Tien et al. 2017). As part of this project, "Extraction of Landslide Danger Slopes by Wide-Area Landslide Mapping" was established, and the authors of this paper (Miyagi, Hamasaki, DV. Tien, N.K. Thanh, etc.) are core members, leading to the cultivation of important technology, knowledge, and relationships. These elements proved to be foundational to the subsequent project. In 2017–2018, a science program was adopted as one of the JST's Sakura Science Programs, which allowed the authors to invite young engineers from Vietnam to introduce the current situation of landslide disasters and response measures in various parts of Japan. In 2018, an international symposium entitled "The Reality of Slope Disasters Caused by Earthquakes and Ways to Overcome Them" was held in Kurihara City. This event commemorated the tenth anniversary of the Iwate Miyagi Inland Earthquake, which caused the largest known landslide in Japan, the Aratozawa Landslide. Five years later, the Kurikoma Geopark was established in the wake of the landslide disaster. Kurihara City was the proposed municipality for this project but has had a history of academic exchange between Japan and Vietnam since 2011.

This project is implemented as JICA's grassroots technical cooperation. The project is organized into two parts. The Japanese side consists of Kurihara City as the implementing body of the proposed municipality and Advantechnology Co., Ltd., and the Vietnamese counterpart Department of Agriculture Rural and Development (DARD) of Lao Cai Province. ITST of the Ministry of Transport (MOT) is a support organization.

In 2015, the Third United Nations World Conference on Disaster Risk Reduction was held in Sendai. Here, the natural disaster response policy from 2015 to 2030 was adopted as the Sendai Framework for Disaster Risk Reduction 2015–2030 (UNDRR 2015). In 2015, the Third United Nations World Conference on Disaster Risk Reduction was held in Sendai. The natural disaster response policy from 2015 to 2030 was adopted as the Sendai Framework for Disaster Risk Reduction 2015–2030 (UNDRR 2015). Four of the seven action guidelines presented in the Sendai Framework focused on communities and residents relating to establishing early warning measures.

3.2 Outline of Technical Support Project

Based on the background described above, this project aims to expand the experience and mitigation technology in Vietnam (cultivated over more than ten years) to the residential areas of hill tribes, which are considered to be one of the most challenging areas to reach and yet the most in need of such assistance. The intention is stated in the project title, "Capacity Building of local Community for Slope Disaster Risk Reduction - **SLOPE DRR.**"

The overall goal of this project is for residents to work together to grasp disaster risks better and build disaster-resilient communities. The immediate goal is for residents to take the lead in formulating and implementing disaster prevention, mitigation, and evacuation plans. To that end, (1) It will be necessary to grasp the characteristics and disaster risks in the community areas. (2) On the Japanese side, administrative authorities and regional disaster prevention officials will work together to implement an awareness program focused on understanding disaster risks and evacuation. (3) Community-level organizations will formulate evacuation plans autonomously based on the materials and experience cultivated in (1) and (2). (4) Through pioneering activities, we will foster disaster avoidance capabilities in local communities. As already stated, it is challenging to establish regional disaster prevention works in which residents take the lead. However, it is also true that in recent years, the development of various notable technologies and social systems in sensing has progressed. We are consciously utilizing UAV, AW3D data, and Google Earth. In this project, as a mechanism to foster a common understanding between engineers and residents through visualization and exchange of opinions, we are using technologies such as UAVs that can easily acquire images of the region at a low cost to construct precise maps using digital information through research. With the help of UAV-related technology, it is possible to assess a site with residents immediately after a disaster. This approach may have been different in conventional disaster research and disaster prevention planning. Residents can be victims of a disaster, in essence. We feel that the use of UAVs has the potential to foster collaboration among these individuals. In addition, using AW3D can pave the way for the region and the government to understand the

disaster potential by developing regional topographic landslide distribution maps. Data can be created on digital topographic maps of wide areas that can supply much useful information regarding geography and geomorphology at a much lower cost than aerial photographs and the like. The AW3D JAXA/RESTEC/NTT DATA uses four million photos acquired by the Japanese satellite Daichi. This developed technology can build Digital Surface Model (DSM) data with a 2.5 ~ 5 m resolution anywhere in the world.

In parallel with developing high-precision local land information using advanced technologies, we will conduct a questionnaire survey of residents. Although the questionnaire is simple in terms of disasters and the necessity of disaster prevention, it will be possible to grasp the level of awareness of the residents themselves and the necessity of preparing basic materials for disaster prevention in the region. Some specific questions include: (1) To what extent do you grasp the status of disasters occurring in the region? (2) How much basic knowledge do you have about disasters in general? (3) How strong is the awareness of promoting regional disaster prevention? We believe that combining the local land information and the survey results will lead to constructing a technical and organizational system that contributes to regional disaster prevention.

In this project, three communes of two districts of Sapa and Baxat Districts in Lao Cai Province have been selected as pilot communes. In these areas, we collaborate with residents and the local government to promote initiatives that contribute to mapping, regional surveys, disaster avoidance, etc. In the following section, we report on the status of initiatives in Trung Chai Commune, Sapa District, Lao Cai Province, where progress is clear at this time.

4 Various Initiatives for Mapping in Trung Chai Commune, Lao Cai Province

4.1 Hypothesis of Communication Base Evacuation/Risk Mapping

Main Premise The importance and difficulty of regional disaster prevention is the development of an evacuation map among community residents. Disaster mitigation must formulate a disaster response map that balances disaster risk and regional safety and has been improved over and over for decades in Japan. This need is also clearly stated in the Natural Disaster Prevention Law enacted in Vietnam in 2013 (Vietnam Government 2013). The Red Dao ethnic group resides in the pilot area of the Trung Chai commune. According to interviews conducted in this study, their awareness of disaster prevention is very high (detailed interview survey in Sect. 4.5 in this paper). This study focuses on the necessity and possibility of creating a "communication-based evacuation map to realize slope disaster prevention."

Two hypotheses have been established, as explained in the following two sections. We propose to select three local communities to serve as pilot communes. The goal is to create a more disaster-resilient commune by developing disaster prevention measures through interactive evacuation maps. Why is it necessary to "conduct two-way communication between engineers and residents and jointly create disaster prevention and evacuation maps" mentioned above?

Hypothesis 1: Using hazard maps can reduce disasters.

In reality, hazard maps are not currently utilized by residents. There are four main reasons for the lack of utilization of such maps, the first being that residents feel there is no prospect of a disaster. Every time a disaster occurs, a common sentiment from victims is that they never thought it would happen to them. This mentality is based on their assumption that since they were not affected by previous disasters, they will remain unharmed. The second reason is that residents do not put forth the effort to use hazard maps. If a person knew to read such maps, disaster response would be fast. Another reason hazard maps are not implemented is that the responsibility is often left to a government entity. Lastly, it's hard to predict how and where a disaster will occur, leaving evacuation maps obsolete. To summarize, reasons for hazard maps to be effectively useless are low awareness, shifting of the responsibility of implementation, the unpredictability of disasters, and a general sense of apathy.

Incompleteness Among the Hazard Map Maker A Hazard Map Maker wants to make an advanced map. It is developed with this specific use in mind. Hazard maps are often created mainly through contracts between the government and the contractor. Inevitably, the map is made considering the administration's thinking and budget. On the other hand, the target areas have extremely individual circumstances leaving a wide range of aspects for which the disaster prevention maps created are difficult for residents to utilize.

Hypothesis 2: If you make it yourself, you want to use it daily.

In general, residents have a vague sense of uneasiness about the possibility of disasters in the area, whether they make a map or not. With the following factors in mind, communities can use hazard maps: (1) Give subjectivity to maps created. (2) Since the community makes this map, it is more personal and will accommodate their interests and needs. (3) Learn

from examples of disasters in surrounding areas, and use that to inform how to avoid similar problems, and evacuate effectively. (4) In addition to disaster prevention, it can also be used to understand the regions' characteristics.

Past Examples and Cartographers' Perspectives The above hypothesis is based on one of the authors' experiences with the effects of tsunami evacuation plans during the Great East Japan Earthquake in 2011 (Miyagi 2016). Since 2006, the author has been engaged in initiatives to evacuate residents in the event of a tsunami in some areas of Miyagi Prefecture in Japan. The region had already anticipated a significant earthquake and tsunami during the short earthquake. To this end, we have been conducting evacuation-related field checks and making maps. This work was carried out so that "the authors and residents exchanged opinions" (Miyagi 2016). The region's conditions, related knowledge, and information change over time. For this reason, updating the map almost every year was necessary. There were two ways to create maps: My Evacuation Map for family members to evacuate and Community Evacuation Map to manage the area. Three months after the sixth upgrade was made and the version distributed to all households, the M.9.0 East Japan Earthquake occurred, and a massive tsunami with a maximum wave height of 10 m struck the area. It was on a scale far beyond expectations.

As soon as the earthquake struck, most residents fled to evacuation sites according to plan. However, we realized that the evacuation site could not be safe. Based on the mutual agreement of the evacuees, we made a second evacuation to a higher place. As a result, the number of victims in the community that had previously prepared evacuation maps was overwhelmingly small compared to others.

Here, we realized the greatest role of hazard maps. The residents learned the importance of cultivating disaster response skills through map-making. A resident said, "The tsunami did not come as you said. But I was studying, so I was saved by the second evacuation." To summarize this experience, the authors set the concept of cartography as follows.

"Communication Base Evacuation Mapping (CBEM)".

Integration of hypotheses: The two hypotheses above suggest that a hazard map will more likely be used when residents make it voluntarily.

4.2 Mapping Steps

We have been working on mapping actual information in three communities to create a two-way slope disaster prevention map as a **Communication Base Evacuation Map (CBEM)** and figure out how to utilize it effectively. The steps for this map are as follows:

Step 1: Development and improvement of the printing version AW3D and site map.
Step 2: Listen to residents' experiences of natural disasters, unwritten rules, etc.
Step 3: Hold workshops with residents.
Step 4: Recognize trends in spatial perception.

The above steps will be implemented for each community. By repeating these four steps, the disaster prevention capabilities of the region will gradually improve.

The target area belongs to an ethnic minority called the Red Dao. Since these people have distinct characteristics peculiar to the region (Dang 2002), discretion is necessary. As assumed here, the Dao people in the mountainous areas surveyed have yet to see an accurate map. Part of them may not speak Vietnamese. The illiteracy rate also seems to be high. On the other hand, many locals have recently mastered using smartphones despite many difficulties. With a smartphone, they can use open-source images like Google Earth. The current situation allows us to feel that there is a potential to dispel many of the concerns mentioned at the beginning of this article.

4.3 Disaster Experiences of Residents

According to statistics for the past ten years (2010 to 2020) in Lao Cai Province (Table 1), many damage cases have been recorded, including 128 deaths and missing persons, 179 injuries, and damages to 3464 houses. As shown in Table 2, 103 people were recorded dead or missing in the flash flood in 2008.

There are 13 provinces in the northern mountainous region, not limited to Lao Cai Province. In addition, various slope disasters and flood damage occur in the mountainous provinces of central China almost every year (Lao Cai DARD 2021).

Case Study of Slope Disaster at Trung Chai Commune The commune is located halfway between Lao Cai City and Sapa City. The Mong Sen River flows south of the area and is paralleled by National Road 4D. The construction of expressways is currently ongoing. The Mong Sen area can be cited as a major landslide-disaster-prone area (Fig. 2). Landslides have been recorded in the Mong Sen region during heavy rains in 1998, 2002, and 2004. On May 9, 2004, a series of disasters occurred, including a large-scale landslide near the Mong Sen Bridge, frequent debris flow throughout the surrounding area, and large-scale debris flows blocking the Mong Sen River (Yem et al. 2006; Duan

Table 1 Natural disasters result in Lao Cai Province Vietnam 2010 to 2020 (Lao Cai DARD 2021)

TT	Damage list	Total	2010	2011	2012	2013	2014	2015	2016	2017	2018	2019	2020
I	**Population**												
1	Dead	120	12	7	17	25	7	4	26	5	4	4	9
2	Missing	8							8				
3	Injured	179	38	10	2	81	7	4	16	6	0	4	11
4	House collapses, drifts	3,464	66	27	27	166	15	11	131	396	754		1,871
5	House is affected	44,573	6,901	741	3,193	16,183	2,279	296	3,126	3,596	832	2.812	4,614
II	**Agriculture**	0											
1	Damaged rice and crops	53,061	564	517	971	3,249	15,046	2,580	23,027	2,574	1,766	78	2,688
2	Dead cattle	22,626	68	14,320	210	480	700	203	3,974	476	1.918	164	113
III	**Infrastructure damage**	0											
1	Damaged traffic works	493	12	11	10	13			49	89	236		73
2	Mass of landslide	1,809,504	167,162	390,000	127,250	60,000	164,524	161,159	339,983	60,517	144,031	52	194,826
3	Irrigation works, embankments damaged	21,963	9		33	9	54	30	78	51	65	21,575	59
4	Volume of channel damage	18,914	998	1,567	12,000					1,215	1,798	19	1,317
5	Other damage to the construction	1,837	24	18	18	31	98	44	18	19	12	1,537	18
IV	**Economic loss (billion VND)**	4,242	54	72	225	635	340	273	768	657	699	102	417

Table 2 Major natural disasters and the damage from 2008 to 2020 in Lao Cai Province, Vietnam (Lao Cai DARD 2021)

Year	Natural disasters	Damage
2008	Flash floods, landslides	Killed and missing 103 people, 314 households had to move, 904 houses collapsed, drifted. Losses over VND 1,024 billion;
2012	Flash floods, landslides	Dead and missing 17; collapsed 84 houses, damaged 3,193 houses, Losses over VND 225 billion;
2013	Hail, tornadoes, flash floods	Killing 25 people and wounding 81; collapsed, drifted 166 houses and damaged 16,183 houses; Losses of VND 635 billion;
2016	flash Floods, landslides	Killing, missing 34 people, wounding 16, collapsing 160 homes and damaging 3,126 homes; Losses over VND 768 billion;
2019	Naturel disaster include flash floods, landslides	Natural disasters have left 4 people dead and 4 injured: Harm over VND 102 billion
2020	Naturel disaster include flash floods, landslides	More than 32 natural disasters killed 9 people and injured 11

et al. 2011). In the region, surface landslides and debris flows have repeatedly occurred. Our visits confirmed micro features of secondary landslide deformation in Posingai and Mong Sen villages, which are part of a significant landslide topography. Many residents seem to have a grasp of where these disasters are located and the signs of disasters. They were also confirmed in a joint survey conducted by Vietnamese and Japanese engineers and residents, as shown in Fig. 6.

4.4 Difficulty of Community Disaster Prevention

The provincial disaster prevention authorities (Lao Cai DARD), in charge of regional disaster risk management, have faced various difficulties unique to the field. According to the impression of community-level disaster prevention officers, efforts at disaster risk reduction on the community level seem to face various difficulties (Fig. 3). Specifically, more concrete measures are needed to improve the capabilities of people in charge of disaster management in a community. Experience in assessing disaster risks, the response to the risks, examples of what it means to have expertise in disaster management, and improvements to the abilities of the personnel in charge can occur immediately. Vietnam's community disaster prevention policy was recently launched (Vietnam's National Assembly 2013). However, organized guidelines on the importance and purpose of reducing disaster risks through the voluntary actions of residents and specific means have yet to be developed.

Each region is unique, with diverse disaster characteristics, infrastructure, and land use. Even if a national government or other super-authority sets uniform guidelines, it will be accompanied by difficulties applying them to the region mechanically. Furthermore, in the Vietnamese general society, the custom of using maps as essential information to accurately grasp the region seems limited. In addition, there are difficulties, such as not speaking Vietnamese and having a high illiteracy rate among ethnic minorities.

To summarize, the following five points should be improved. (1) Poor systematic knowledge of the disaster itself. Disaster prevention personnel at the regional level need to be equipped with the skills to assess the disasters experienced by the region and to examine the disaster

Fig. 2 Landslide and debris flow at Mong Sen Bridge, SaPa district Lao Cai in September 2004 (Left, Yem et al. 2006); Recent Mong Sen Aeras (Right, Thanh N.K., on March first, 2020)

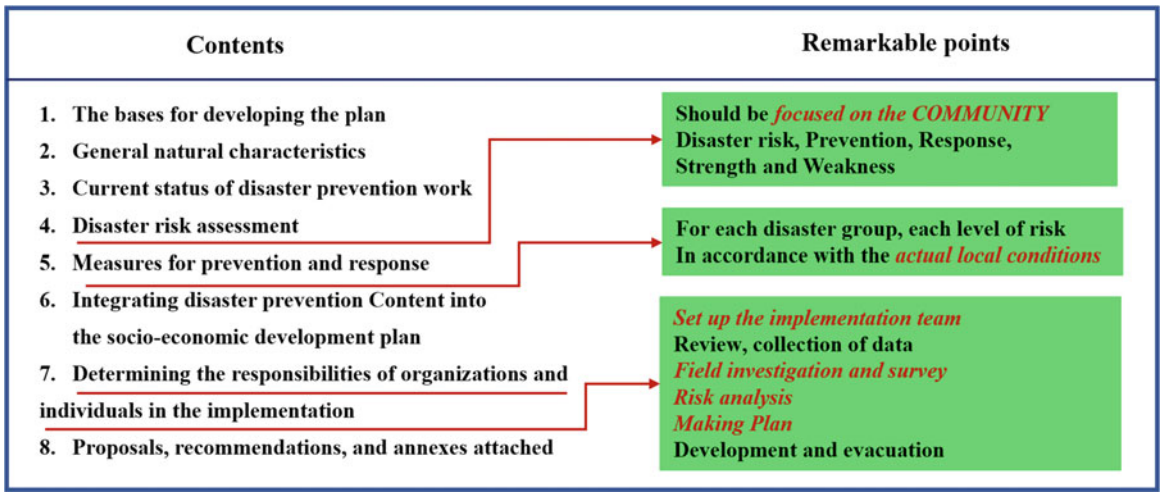

Fig. 3 Difficulties in disaster prevention at the community level

prevention measures. (2) More concrete disaster prevention and disaster prevention scenarios must be implemented. Specifically, more than precipitation information that is thought to lead to the prediction of disasters is required. (3) Insufficient development of voluntary disaster prevention organizations has occurred. Organizations to tackle disaster prevention and mitigation are being developed in the region. However, the role that the members of these organizations should play needs to be clarified. In addition, the development of voluntary disaster prevention organizations with on-site response capabilities to address the issues in the individual local communities is an issue for the future. (4) More human resources are necessary. Both community and planning personnel are few. The number of trained people is further limited. (5) Extreme weather and disaster forecasting in recent years have been complex. The complexity of these projections makes the previous four efforts difficult.

4.5 Interview Survey on the Necessity of Slope DRR

Characteristics of Residents in the Pilot Interview The interviews were conducted in Posingai Village in Trung Chai Commune and Lao Vang Village in Phin Ngan Commune, where the risk of landslide disasters is high. The inhabitants of the villages are ethnic minorities known as the "Red Dao." They have a history of seeing natural disasters that occur in their region in a day in 2016. After several days of heavy rains, the risk of landslides and debris flows increased, they thought. In light of this situation, the residents decided to relocate to an upstream land about 1 km away. In cooperation with the local government, they moved and settled there. Residents and the local government worked together to develop various infrastructures such as the maintenance road, schools, cultural facilities, and electrical machinery. However, to maintain their daily routines, they have to continue using their original farming fields, which are susceptible to landslides and debris flows.

Perception of the Current State of Slope DRR in Local Communities Local Communities: The interview was intended to increase the local people's awareness about slope disasters' impacts. This interview is believed to be a pivotal component of the direct approach to preventing slope disasters. Here, direct sensing is a technology that visually interprets land information acquired through a sensing tool. A typical example of this is aerial photo interpretation. In particular, UAVs can engage residents in work processes such as data acquisition, imaging, and three-dimensional processing. The data and interpretation results obtained in this process are expected to be independent natural sources for a common understanding. We can consider the significance of visual interpretation together with residents as highly significant. The UAV initiative is an attempt based on our hypothesis that the situation in which the residents are involved in the creation of materials will be directly linked to the revitalization of the use of data. From there, we can make an image from which it is feasible to evaluate the challenges to overcome in the short and long term and examine the feasibility of building a society that understands the most appropriate response solutions.

This study has five to six questions about the basic knowledge of slope disasters, involvement with local communities, and experience with disasters. These questions and the result are summarized in Tables 3 and 4.

Table 3 Results of the interview study related to the basic knowledge of slope disasters in the Trung Chai Commune and Phin Ngan Commune, Lao Cai Province, Vietnam

Basic knowledge of slope disasters	Result interview local residents Po Si Ngai Village – Trung Chai – Sapa and Lao Vang village – Phin Ngan Bat Xat						
	Ans	RF	%	Ans	RF	%	Evaluation of reporter
The language "slope disaster" has been heard.	Y	78/200	39%	N	122/200	61%	Due to the difference in language, and identification slople disaster of local resident in the next period, it will be improved with image and icon recognition
Has many slopes and flood disasters where you live	Y	200/200	100%	N	0/200	0%	High consensus rate due to High-risk areas
Climate has changed recently.	Y	200/200	100%	N	0/200	0%	Local residents recognize climate changes such as more rain, hotter temperatures and extreme climate events
The local government has a solution for disaster prevention	Y	200/200	100%	N	0/200	0%	The local government has evacuated people to the resettlement village area
Know the difference of prevention and reduction	Y	56/200	28%	N	144/200	72%	Future improvement through training

The response from the residents in the surveys indicated a need to reduce the risk of landslide disasters. They are often direct victims of disasters. In recent years, slope disasters have occurred frequently in the pilot area from 2016 to 2020, and large-scale slope disasters occurred in 2002 and 2004. Experience history proves that disaster prevention measures alone cannot protect the local communities and people's lives. Therefore, residents must formulate voluntary disaster mitigation measures to reduce slope disasters. To realize the residents' understanding of regional disaster risks, we will build a communication-based disaster prevention map that residents and engineers jointly implement.

4.6 Arrangement of the Base Maps and Validity

Data Mapping in Trung Chai Commune (AW3D and Layer Structure Contour lines generated from the AW3D 2.5 m DSM data covering the Trung Chai area can be used to understand the primary land conditions of the area. In addition, land cover, roads, and building system information could be obtained from Google Earth. This information can be superimposed on AW3D maps by simple ortho-processing (Figs. 4, 5, 6, and 7). This data will be the basis for creating a communication-based evacuation map

Table 4 Result of the interview study related to residents' basic knowledge of the community in the Trung Chai Commune and Phin Ngan Commune, Lao Cai Province, Vietnam

Basic knowredge of the community	Result interview local residents Po Si Ngai Village – Trung Chai — Sapa and Lao Vang village – Phin Ngan Bat Xat						
	Ans	RF	%	Ans	RF	%	Evaluation of reporter
Are you responsible for keeping the community safe (eg, do not cut wood indiscriminately, notify everyone if there arc signs of disaster happens)	Y	103/200	51.5%	N	97/200	48.5%	People with functions in the community, men answered yes Due to customs as well as expanding production, some people dig fishponds, so the consensus rate is not high.
The community has the slope disaster risk (Debris flow, flush flood etc.)	Y	200/200	100%	N	0/200	0%	The community has frequent landslides in recent years such as 2016-2020
I have experiences of slope disaster yet.	Y	176/200	88.0%	N	24/200	12%	Depending on the age of the respondents, young and middle-aged people usually answer yes, children and women say no.
Evacuation is the most important for disaster risk management.	Y	199/200	99.5%	N	1/200	0.5%	Most agree because people have been resettled from dangerous areas
I like to show the strength when the community need.	Y	125/200	62.5%	N	75/200	37.5%	Depending on the subject: men, local dignitaries answer yes; women and children often say no because they don't have the skills
I remember the Mong Sen Landslide disaster in Trung Chai and the Sung Hoang Landslide Disaster in Phin Ngan Bat Xat.	Y	139/200	65.5%	N	61/200	30.5%	Depending on the age of the respondents, young and middle-aged people usually answer yes, children and female say no.

Note: Ans: is the answer, yes or no; RF is a rating based on votes; % is the percentage of answer votes

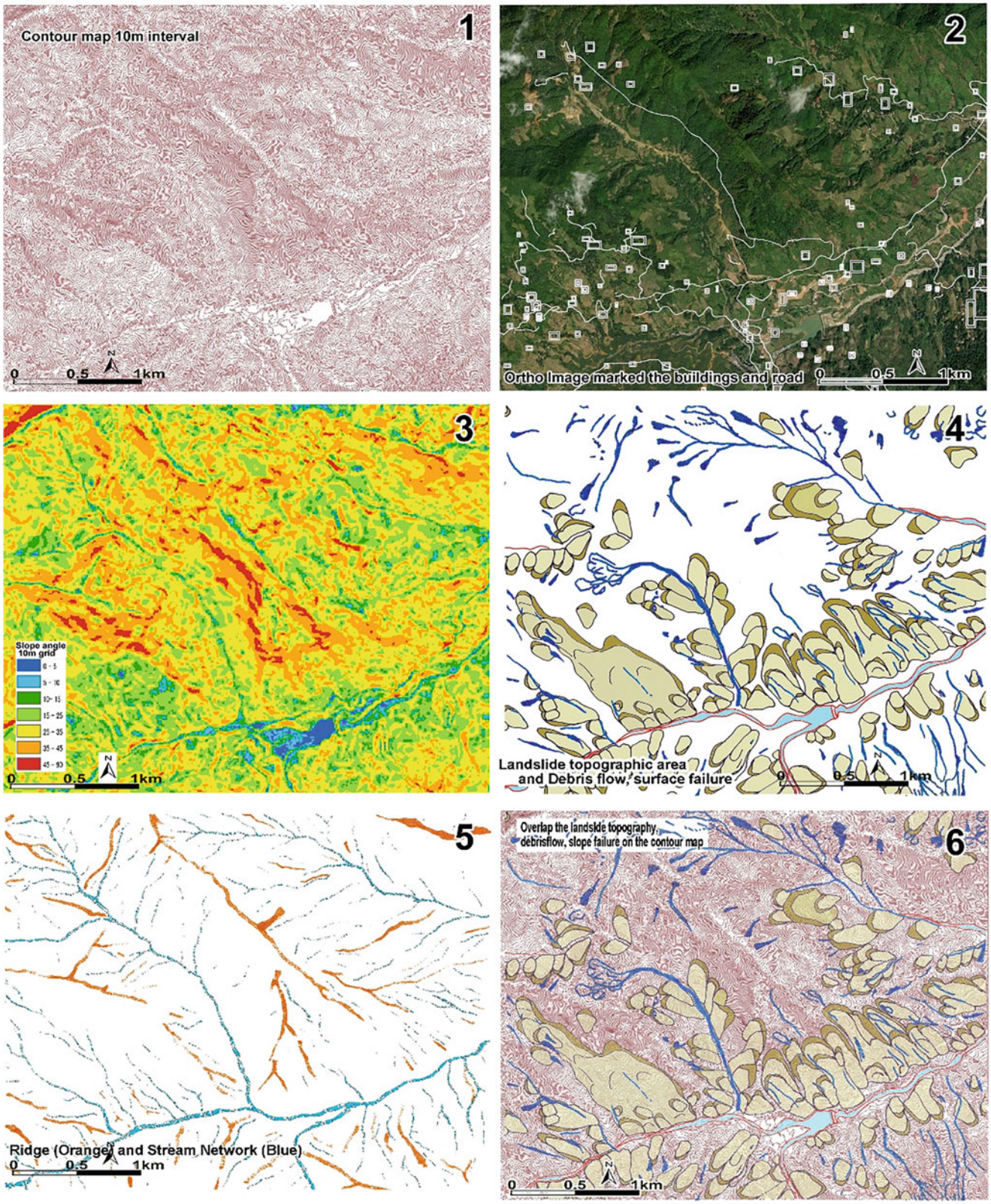

Fig. 4 Series of maps of a portion of the Trung Chai Commune, Lao Cai Province, Vietnam. Based on the 2.5 m DSM, and 5 m DSM from AW3D (ALOS World 3 Digital Data: created by JAXA, RESTEC, and NTT Data). (1) Contour map at a 10 m interval. (2) Ortho-image for the section in 1. Houses, colonies, and roads are overlain to direct identify within the image. (3) Slope angle classification map created by GIS. Landslide topographic area developing the slope angle primarily between 15° and 35°. Surface failure primarily developed on 25° to 40° slopes. (4) Main scarp and the body of the landslide topographic area are marked based on visual identification. The debris flow and slope failure are also marked in blue as identified from the ortho and Google Earth images. (5) Ridge system and stream network system identified by the contour patterns. (6) Overlapping of the slope disaster results on the contour map

Fig. 5 Variety of the autochthonous rock facies compared with landslide materials at Trung Chai Commune, Lao Cai Province, Vietnam. (1) Fresh rock identified as "Granitic gneiss." (2) Fresh hard rock facies exposed at channel and waterfall. (3) Slightly weathered rock with joint systems. (4) Deeply weathered rock mostly changed to a clayey texture with an identifiable grain pattern structure

(CBRM) that can be edited to be easy for local people to use. It is also necessary for the residents to understand the engineers' intentions to prevent regional disasters.

To put it simply, as mentioned previously, no matter how precise a map for disaster response is created and provided, it will only be meaningful if the residents can understand and use it. More is needed to provide and visualize information. Instead, engineers will also need to deepen their understanding of the region through the exchange of opinion and be required to have the flexibility to make corrections for a more user-friendly map.

4.7 Verification of the Landslide Topographic Area Distribution Maps

In this research, contour lines are formed from AW3D DSM data acquired with a grid size of 2.5 m to 5 m as primary data for the mapping, including the landslide topography. Therefore, the accuracy of the terrain information is controlled by the grid size of the data. Also, since it is a DSM, it does not reproduce the terrain but often reproduces the surface of the vegetation cover layers. It seems unreasonable to use this as a source for topographic classification. However, if the contour line data generated from DSM is observed based on its accuracy, it is possible to grasp the topographic characteristics. From this viewpoint, reading the pattern of contour lines does not make any difference from conventional aerial photo interpretation. From the generated contour lines, it is not possible to grasp small-scale terrain features such as surface failures. On the other hand, it is possible to decipher the morphological characteristics of large-scale landslide phenomena on a spatial scale exceeding several hectares.

AW3D data is used as the source material to grasp the disaster risk in the area to prepare the landslide topographic

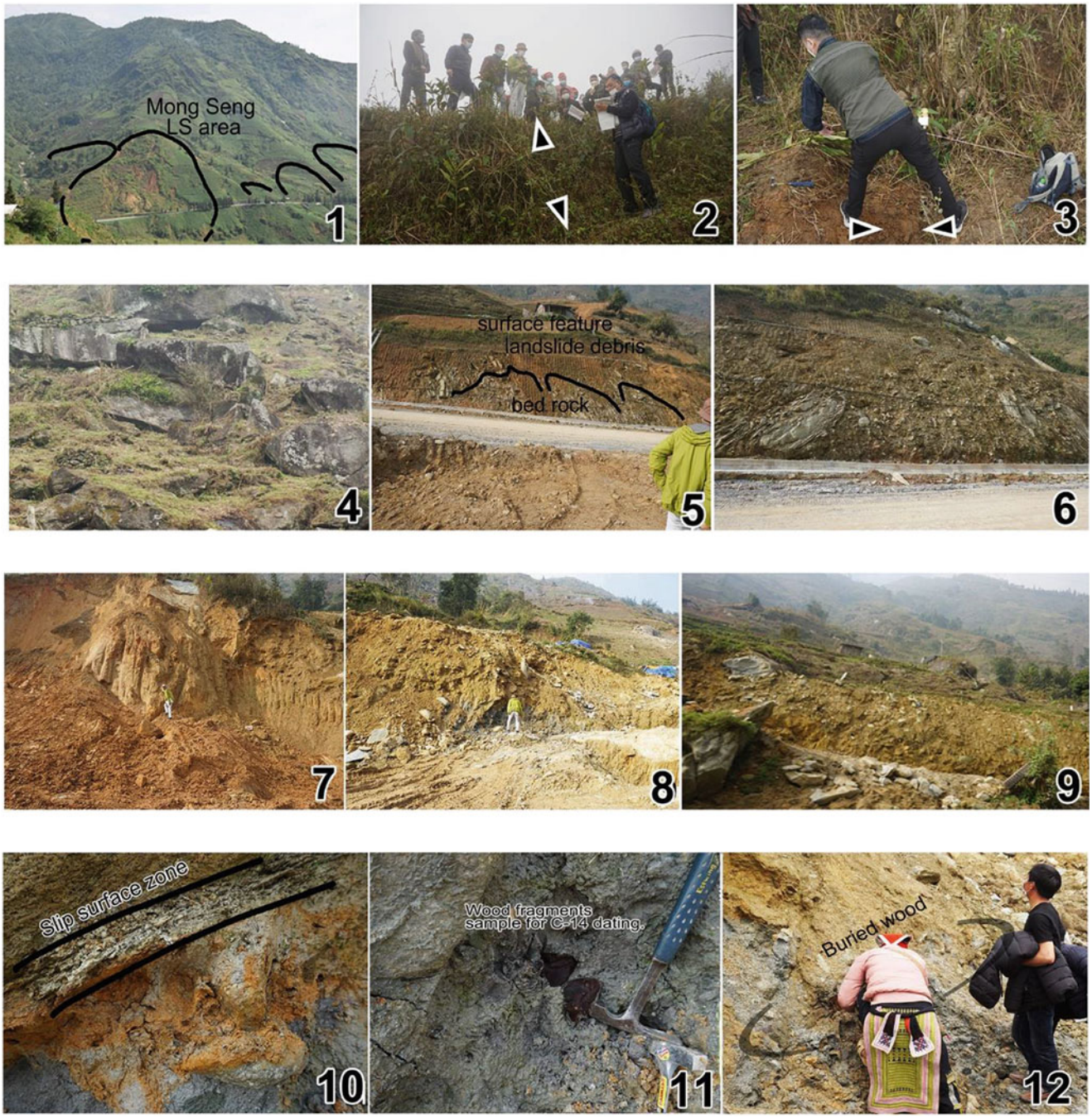

Fig. 6 Field evidence based on the collaborative investigation with community residents at Trung Chai Commune, Lao Cai Province, Vietnam. (1) Recent overview of the Mong Seng Landslide (Taken on 28th Feb. 2022). The same landslide was mentioned in Fig. 2. (2): Vertical dislocation observed (between the two arrows) one year ago by the resident. It is located at the top of Mong Sen Landslide. (3) The large crack stretching near the step (No. 6) that is getting wider annually. We suggest placing a marker set. (4) Exposed huge boulder and accumulated at the landslide body. (5, 6, 7, 8, and 9) There are apparent differences between landslide materials and bedrock. The landslide body consists of deeply weathered clayey soil and crushed angular to subrounded gravel. Huge boulders are also present. (10) The slip surface of a part of the landslide material. The surface is about 7 cm thick and consists of clay to sandy loam with a thin foliated structure. (11) Buried wood fragments under the slip surface (No. 10) subject to C-14 dating in a laboratory. 12: A large wood stem (4 m long, 30 cm in width) is exposed nearby the images in No. 10 and 11

distribution map. At the same time, we used high-resolution image information such as ortho and Google Earth images to identify superficial and small-scale disaster phenomena such as surface slope failure and debris flow. The disaster risk is obtained by superimposing both pieces of information in a particular area.

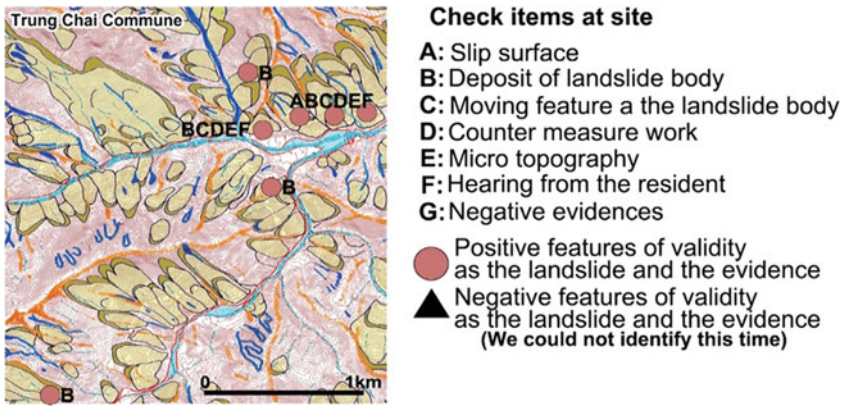

Fig. 7 Landslide topography and the field evidence collection sites at Trung Chai commune

There is a slight gap in the understanding of slope disasters between the authors and the administrative authorities. It is necessary to devise ways to reconcile this understanding. Tachi and Sakai (2019) highlighted the following regarding recognizing slope disasters in Vietnam. Vietnam's Disaster Prevention Law (2013) defines slope disasters differently from Japan. Two categories of landslides and debris flows are defined in the broad classification. "Landslides" are a combination of landslide topography and surface landslides, as depicted in this paper. On the other hand, "debris flows" collectively cover everything from surface landslides to debris flows. It is unrealistic for large-scale phenomena like landslides to be categorized together with surface landslides. In addition, categorizing debris flows and surface landslides together as debris flows is also very different from the classification used in Japan and is controversial.

Field Evidence and Mapping Validity In this research, a distribution map of landslide topography is created using only contour information. Landslide topographic distribution maps have traditionally been created by interpreting aerial photographs. From aerial photographs, it is possible to decipher the morphological characteristics and related information such as vegetation, land use, small steps, and cracks in the ground. Aerial photo interpretation engineers have also considered this relevant information to determine the landslide terrain area. Based on this point, it was judged that when mapping using only contour lines, it would be necessary to evaluate the validity of the interpretation results through confirmation through field surveys.

We clarify the validity of landslide topographic mapping. In general, it is known that variations in landslide properties produce several characteristic shapes and material structures. Among these characteristics, the geology of the landslides, the microtopography, the sediment characteristics of the landslide body, etc., were confirmed. At the same time, on-site interviews were also conducted (Fig. 6).

Geology The study area comprises granite gneiss of the Ordovician period of the Paleozoic Era. However, the study site is located in the humid tropics, suffers strong chemical weathering, and is expected to have significant weathering and viscous soiling. The stratigraphic phase of sediments disturbed by landslide action may be similar to that of weathered rocks. Here, to distinguish the determination of landslides from the rocks, the characteristics of the rocks were confirmed in the rock phase series from fresh rocks to strongly weathered rocks (Fig. 5). Even weathered primordial rocks often show crystalline particle structure and quartz veins. Using this as a clue, we checked to see if a landslide was deforming the mapped area.

Landslide Body Properties The landslide body that constitutes the area for the landslide terrain differs from the rock phase of the original position described above and is composed of disturbed and crushed sediment (Figs. 6, 7, 8, 9). In rare cases, the slip surface and typical landslide sediments can also be confirmed (Figs. 6, 7, 8, 9, 10). Even today, it fluctuates slowly, and buried wood was found in the mobile body of the landslide when anchoring was installed (Figs. 6, 7, 8, 9, 10, 11, 12). The Japan Accelerator Measurement Laboratory collected and commissioned a portion of this to the C-14 date using the AMS method. An age of IAAA-212510 40,204;/−284 cal. BP. (Calendar year correction) was obtained. In addition, huge boulders with diameters exceeding several meters in many landslide areas are also noteworthy (Fig. 6). In landslide movement, thick, fragile, viscous weathered soil layers also cause fluctuations in fresh rocks and deeply weathered core stones during landslides. Megaliths that are resistant to surface erosion are selectively left.

Microtopography Indicating Landslide Variation Steep horseshoe-shaped slopes dominate typical landslide terrain through a distinct slope transformation line with the

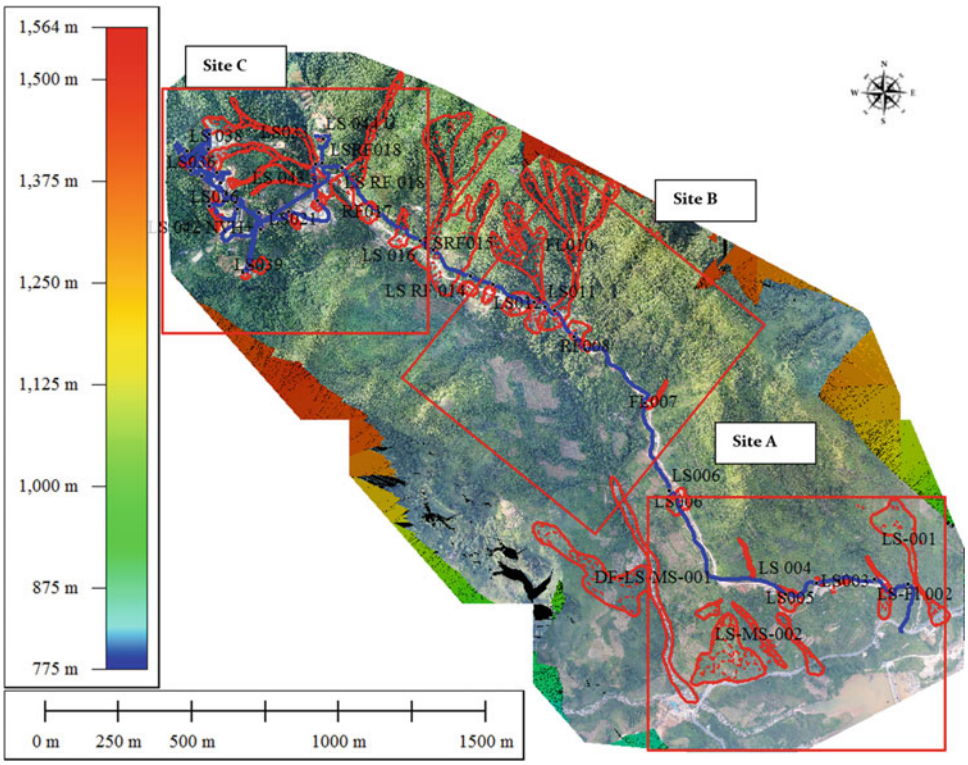

Fig. 8 The simple mapping with UAV data (All data has been reported by Thanh et al. 2021)

surrounding non-landslide slopes. This forward-expanding mobile body forms a gentle slope. If such a topographic composition can be observed at the site, it can be judged as a landslide terrain. In addition, if a small deformation such as a step or a crack can be confirmed in part of the terrain, and the deformation is harmonious with the assumed change in landslide movement, it can be judged as a sign of a landslide (Figs. 3 and 6).

Resident Information Red Dao, whose residents live in the area, has been cultivating paddy fields for hundreds of years. The landscape of the rice terraces has cultural and tourist value. The residents have agreed to an evident division of land ownership, and once landslide features develop, they work together to address them. Therefore, the landslide movement might be remembered for several decades. For example, the Monsen landslide introduced earlier seems to have repeatedly been moving over the past few decades (Fig. 6).

Figure 7 shows the distribution of landslide topography drawn through contour interpretation, overlaid with evidence of landslide variation confirmed at the site. The distribution map of the landslide terrain drawn from the contour lines and the confirmation at the site are generally harmonious.

4.8 UAV Data Collection Study for Site Map and the Validity at Trung Chai Commune

4.8.1 Overview of UAV Data Acquisition and Mapping

Many image data sets were acquired using UAV and converted into a three-dimensional digital information model using SfM's technique, resulting in multi-viewpoint photogrammetry. From image acquisition to generation and analysis of contour information, we worked together with residents. This collaborative work will significantly deepen the residents' understanding of the map and give impetus to understanding disaster risks and formulating evacuation plans. The technology to visualize dimensionally is the Structure from motion (SfM) (Westby et al. 2012; Saito et al. 2018). This technology is used in various fields. Paradoxically, various small local changes can be captured by repeatedly acquiring images. At the same time, the operation skill of the UAVs will be deepened.

UAVs are capable of responding to the needs of small-scale study areas, especially within a limited budget, and are easy to use. These characteristics will be a powerful weapon to pave the way for the mitigation of slope disasters by understanding the living conditions of the residents in

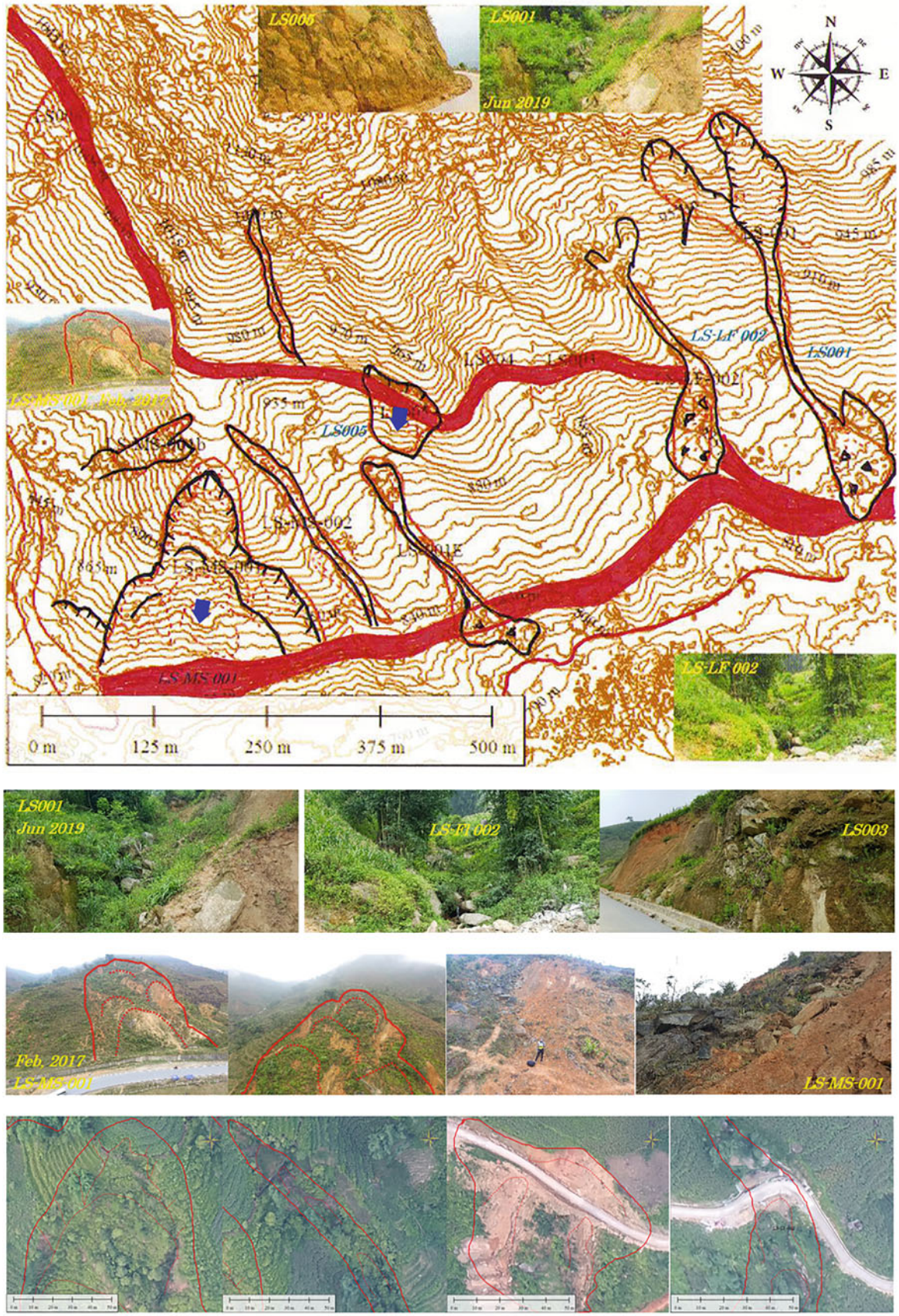

Fig. 9 Landslide recognition using UAV data for Site A (Thanh et al. 2021)

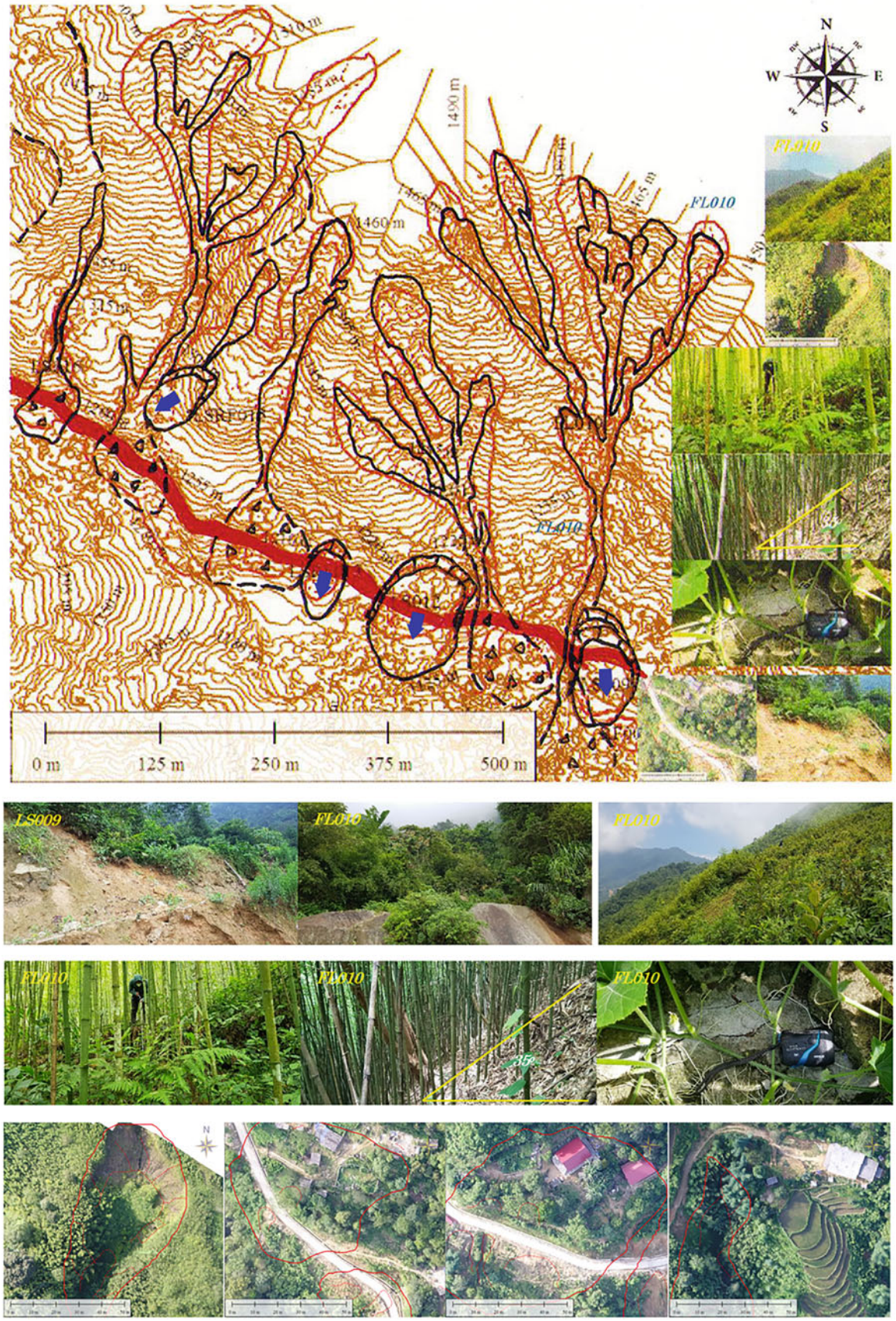

Fig. 10 Landslide recognition using UAV data for Site B (Thanh et al. 2021)

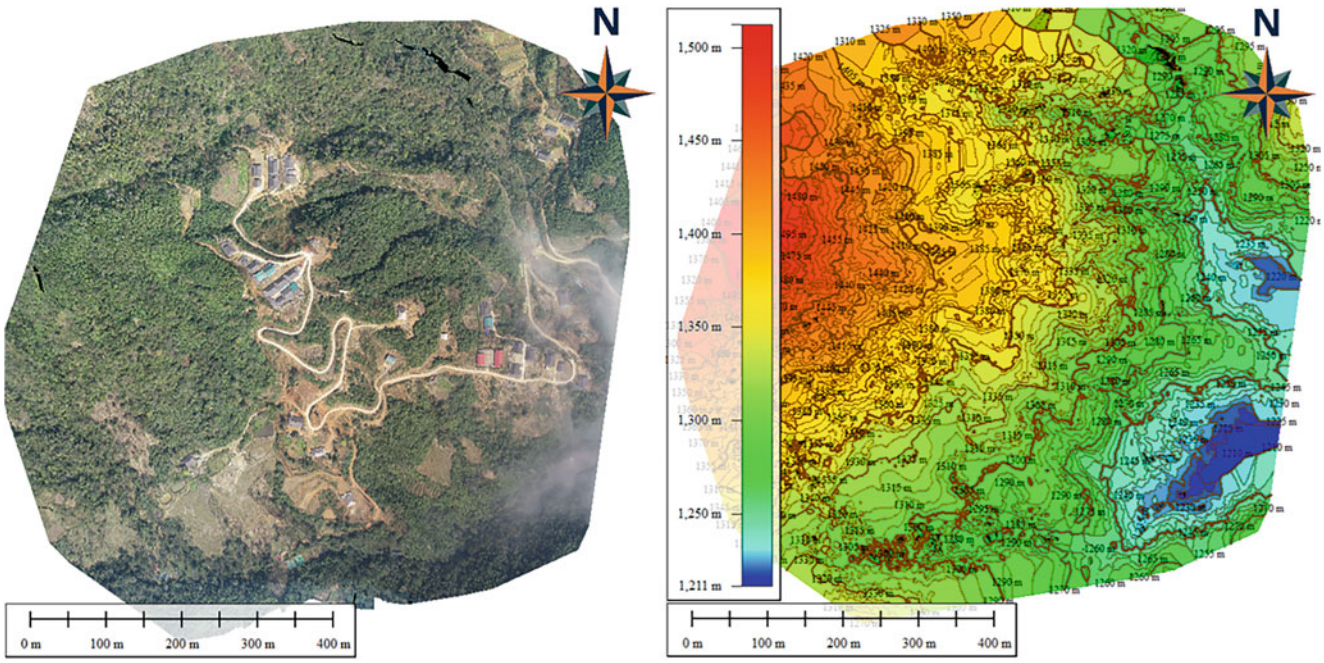

Fig. 11 UAV Mapping at Site C (New Posingai Village) in March 2022 (by Thanh N.K)

tropical mountainous regions, expanding disaster prevention knowledge, and understanding disaster risk.

Data Collection and Mapping by UAV in Trung Chai Commune UAV data collection and detailed mapping have been carried out in Posingai Village, Trung Chai Commune, Sapa Town, Lao Cai Province. The first flight area of 3.6 square kilometers was flown in 2019 using DJI Phantom-4 Pro equipment. A series of photo images were analyzed automatically using Pix4D Mapper software with the output Ortho-mosaic images and DSMs. The simple map of this area is presented in Fig. 12. We worked with the

Fig. 12 Explain the Slope DRR and CBEM. (1) A Lao Cai DARD officer representative presents the significance of promoting community-based disaster risk reduction (Trung Chai Commune). (2) Explain the meaning and contents of this activity (Trung Chai Commune). (3) Discussion with the village leader at Posingai (Trung Chai Commune). (4) Presentation of the significance (Thanh Binh Commune). (5) Luncheon meeting at the resident's house (Thanh Binh Commune). (6) Explanation of a mapping sample (Phin Ngan Commune)

residents to check and confirm the landslides and debris flows in the field. A topographic map with 5 m contours was built (Fig. 4). Landslide identification (Miyagi 2013; Hamasaki and Miyagi 2013a, 2013b) was implemented to identify and transfer an inventory map using the UAV data.

Within a 5 km long stretch of National Road No. 4 and its branch line running through the part of Posingai Village, 40 slope disasters were identified. They varied in size and type. Landslides, slope failures, debris flows, rockfalls, etc., could be identified. In addition, we also found places that showed unstable rocks.

From Fig. 12, we created a detailed site map for three places that we judged particularly noteworthy.

Site A (Monsen Landslide Site): A massive landslide hits Route 4 and has been plagued repeatedly for years.

Site B (formerly Posingai Village): Formerly the center of the village. In 2016, a large-scale debris flow occurred. In 2017, residents gave up on living in the area and relocated. Currently, only two households are in this area.

Site C (New Posingai Village Relocation Site): This is a new area for the relocation from Site B, where roads have been improved, and many houses have been relocated. This area is a district that expects to conduct evacuation drills.

This map shows the Mong Sen Area - a typical landslide with a width of 250 m and a height of 200 m. Referring to LS-MS 001, the slip surface depth is estimated to be about 10–20 m deep. The landslide body has been moved and changed into multiple landslide blocks. In pictures nos. 1, 2, 3, and 4, a field check was carried out, and the marked landslide sites were recorded in March 2022.

Figure 10 shows the details of site B, where in August 2016, a debris flow appeared on the natural slopes from the impact of typhoon No. 2. The initial appearance of gullies on the weathered granite surface of the natural slope is shown. The depth of the gullies is from 1 m to 3 m. According to the terrain's natural Slope, the gullies gradually expanded and gathered to form a fan shape. The main scarps of debris flows are visible on the ortho-mosaic, for example, at the LF 010 location.

Recent UAV data of Site C (New Posingai Village), in March 2022 It was foggy when we flew a UAV to shoot the area, a common feature in the Sapa Lao Cai, but we could finish the flight. Using just about 20 minutes of automatic flight at an altitude of 300 m over a flight area of 400 m by 400 m, UAV imaging data at the center of Posingai village was collected. The accuracy results from quick data analyses with an average ground sampling distance (GSD) equal to 11.1 cm/pixel were carried out shortly afterward. The contour map from DSM makes it easy to recognize the slope stability. The created DSM and ortho-mosaic resolution data are useful for situations that need data quickly, such as training local people to evacuate.

5 Discussion of Map Adaptability and the Validity for Community-Level Slope DRR

5.1 Community-Level Disaster Prevention and Evacuation Map

A map identifies a study area and appropriately visualizes the facts in that range. The purpose of this study is to use maps for community-level disaster prevention. The community can be broken down into several scales. In addition, each community is unique. The following viewpoints are set: (1) A map to help residents implement the evacuation plans appropriately, and (2) A map to visualize the area's characteristics, a place of daily use. To achieve these viewpoints, it was necessary to identify a suitable scale, the range to examine, and the methods of expression, among other factors. However, many different stakeholders are involved in a community-level disaster prevention program. There are several hierarchies, such as the ministry, which has jurisdiction over disaster prevention; the county, which oversees disaster prevention of the region; the commune, which will confront the disaster, the village, the home, and the individual. The contents represented on the maps should be decided with their needs in mind.

On the other hand, the cost of creation and technical difficulty should also be considered. In this study, the landslide map at a scale of 1/25,000 had already been developed. When the slope disaster danger at the province level and the county was depicted, an exchange of opinions was undertaken to find a suitable scale. The scale was agreed to be between 1/5000 and 1/10,000 for specific areas (ex., Trung Chai, Phin Ngan, and Thanh Binh Commune). A map of commune-level disaster management was also prepared. For these maps, we used 5 m DEM and 2.5 m DSM data from AW3D, which covers the entire world at a lower cost when compared with aerial photography. It may also target a specific village like Trung Chai and other communities. UAV data was taken and used for this section. The maps created by UAVs are named "**Site maps**." For concrete mapping, it is necessary to consider the purpose and means of the stakeholders' intentions. Here, we considered the ideal way for the appropriate maintenance of maps, mainly in Trung Chai Commune Posingai Village, where the most information was collected as an example.

5.2 Case Study of Site Mapping at Posingai Village in Trung Chai Commune

Trung Chai Commune is a county with an area of about 30 km^2 and consists of four villages. Therefore, we mapped about 25 km^2 using the AW3D as the base map (Fig. 4).

Although the evacuation plan of Posingai village was made in that, Posingai village is about one-third of the area of the mapped region. The densely populated area is a much smaller part of the map. The current main settlement of the village is located on more complex mountain slopes. There is a history that all houses were consulted several years ago and moved to a place that was assumed to be safer because signs of a landslide appeared in the old village. Specifically, dozens of houses were moved to an area with several narrow ridges and valleys in about 20 ha only.

Based on the two viewpoints outlined at the beginning of this section, we proposed an effective map communicating the evacuation plan for Posingai Village. Suppose a community-based disaster management map is to be produced on a village-by-village basis. In that case, it will be necessary to show the main portions of the village and the relevant adjacent areas in one figure. On the other hand, it is necessary to understand and visualize the situation in further detail, such as areas with the population scattered in the village and places with high disaster risk. With this in mind, a photographic map was prepared based on images taken with a UAV. In addition, we tried to express the slope characteristics and locations of villages, including those relocated on a three-dimensional map, to make it easier to understand.

In this paragraph, we discuss the effectiveness of UAV-based mapping. The site map data obtained by flying a UAV has significant advantages and some limitations. There are limits to the range of maps. Suppose the area over which data is acquired is large. In that case, it will take a considerably long time and technical skills in various points of the acquisition time, data processing, and representation as figures. It becomes complicated even if corresponding figures are created. As a result, it is extremely difficult for an end user, such as the residents, to understand the map. The UAV data is a point to map the necessary range. When the community realizes the necessity by themself, sometimes the resident and the engineer call the data collection and develop the map together.

The initial site maps (acquired in 2019), which were created for Posingai Village, are a brief indication of the regional conditions immediately after the disaster that occurred in 2016. The effectiveness of the site map is further increased by combining it with photographic evidence on site. In addition, we introduced the site map acquired in March 2022. It provided the state of the whole village three years after the site map was acquired. The Structure of the village has almost become clear. Based on this map, the villager exchanges opinions on selecting evacuation sites and routes during heavy rains. A site map can show the disaster risk and strengths of each house block in a village, with a tentative name like “Disaster strengths and weaknesses around us. With this map, it might be possible to maintain a medical record to prevent disasters in each house. Figure 17 shows a possible example.

As mentioned above, creating and presenting disaster prevention maps according to the actual regional conditions on multiple scales over different ranges with accuracy and periodic improvements with the assistance of residents will lead to improvements in the effectiveness of disaster prevention.

5.3 Workshop for Creating the Communication Base Evacuation Map “CBEM”

To succeed in CBEM, a mutual understanding between the engineers and the residents is necessary. We already described the steps to develop a CBEM. Next, we will consider the actions that can be taken.

Explain the Slope DRR and CBEM As introduced, the Vietnamese government’s policy promotes community-level disaster prevention. Therefore, the region carried out a series of activities described below. First, a person in charge of The Laocai Department of Agriculture and Rural Development (Laocai DARD) of the local government, which is the promotion base, will explain the purpose, set the goals, and points to emphasize for regional disaster prevention promotion to the management sector through the community officer. Next, we explain the importance of materializing CBEM and the associated creation procedure. The project has three pilot communes: Trung Chai, Thanh Binh, and Phin Ngan. We carried out the work in the same way in each commune, as shown in Fig. 16.

Initiate the Interest (Case study/Picture Story Show) Residents need to understand the significance of disaster prevention and mapping to ensure that the effectiveness of community-level disaster prevention, primarily evacuation actions, can be guaranteed, as described earlier in this paper. Above all, the inhabitants of this area are ethnic minorities called the Dao people.

Various difficulties hamper community-level disaster prevention efforts. For example, in Vietnam, which is a multi-ethnic nation, mountain minorities do not necessarily understand Vietnamese. It is not necessarily understood that disaster prevention is accompanied by concrete action. In other words, there is currently a common sentiment that this topic is viewed and heard through public relations from the administrative authorities. However, as detailed in part 4.5, residents seem to believe that merely recognizing the need for disaster prevention is enough. Community-level disaster prevention begins when residents understand their significance and the specifics of disaster prevention and evacuation. If the

Fig. 13 Workshop communication, explaining the Slope DRR and CBEM in Trung Chai Commune. (1) Explain the outline of the base map and related Images in the commune. (2) Explain the enlarged base map on the blackboard. (3) Group leader reports their recognition and their description to others. (4) Write while talking the knowledge through the engineer. (5, 6) Write through the advice

residents are conscious of the significance of implementing the specifics independently, the actual prevention and evacuation may be attained. Thus, it is naturally necessary to emphasize the importance of disaster prevention and evacuation and to arouse interest. We introduced the case of Japan as an approach to attention. Next, we performed a disaster-prevention picture story show, "Kamishibai," based on the community characteristics of the Dao people.

Base Map Present and Workshop for Developing CBEM We explained the base maps developed using AW3D data for community-level disaster prevention management. These maps will become the materials for the foundation of CBEM. We also created a UAV-based site map. At the workshops, the district-disaster-prevention infrastructure map was introduced to the residents. Next, a map is distributed to each resident, and individual data, such as names, roads, residential zones, etc., are filled in. Through these processes, it was possible to make clear the community images and disaster risks among the residents. The maps were assumed to be the first experience for ethnic minorities in Vietnam to see detailed and systematic community-level maps. In addition, developing a map based on the actual understanding of the residents is an essential step to completing CBEM. Many community-level disaster prevention personnel and district residents participated in the workshops. There was no extreme bias in the age groups or genders of the participants. To widely grasp the ideal way of map understanding, which presents each district by changing the description items and the description range little by little, it was more rational for all stakeholders (Fig. 13).

5.4 Data Analysis of the Spatial Cognition of the Residents

Results and Suggestions for Easy Use in the Community Through CBEM Creating a disaster prevention map that the residents want to use is essential for disaster risk management. We applied the method of making CBEM, which Miyagi (2016) successfully implemented in Japan, to the mountainous ethnic groups in Vietnam. In CBEM, a mutual understanding was the starting point for establishing a dialogue. As a result, CBEM proposed to create a map that clearly describes the main characteristics of the region, primarily using AW3D data. The important buildings related to the social environment, especially educational facilities, and life-related information are to be shown. They include the people's committee hall, school, hospital, and other social environments; topographical water system; disaster-related information such as landslide topography and debris flows; and life-related information such as roads and dwellings.

The Dao Ethnic Group area is too sparse to identify a specific location. The sphere of the daily life of the resident is limited to the village. Fellow villagers can identify the individuals and houses concerned. On the other hand, interest in neighboring villages was extremely scarce. It was realistic to prepare a regional disaster prevention management map based on this background. The above basic information was posted on the CBEM, but some blank items were always included in the legend for personal necessity. For adding the necessary information, the proposed regional disaster prevention management map had a column describing agreed-upon essential places in the region. They include

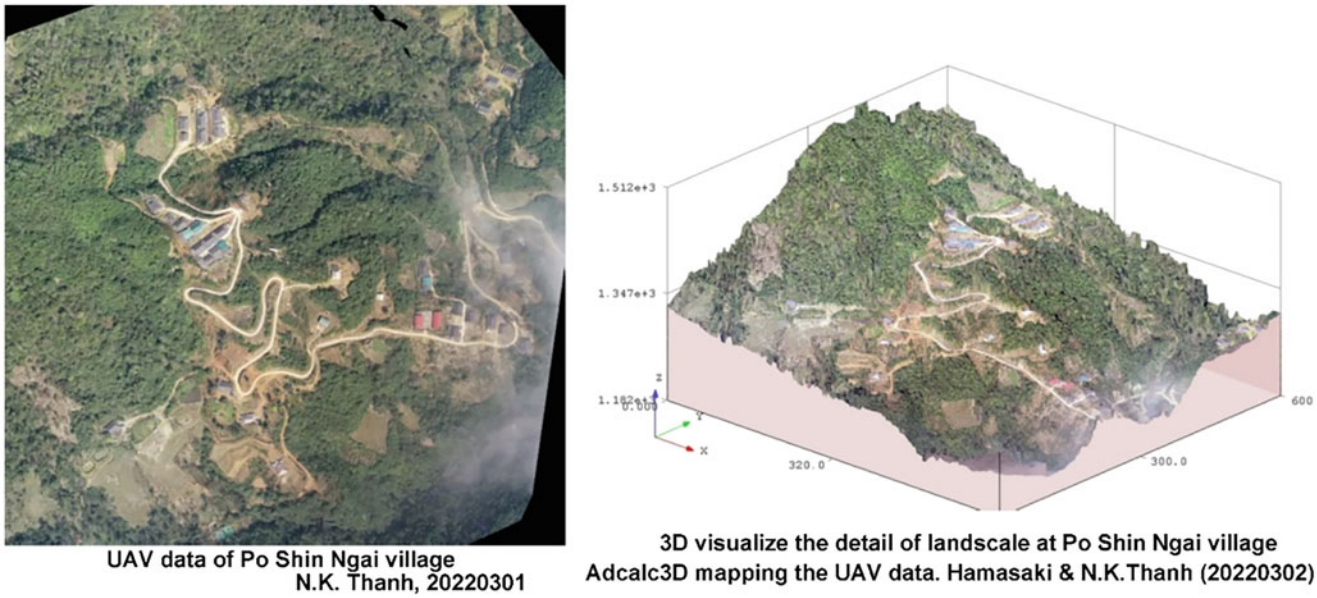

Fig. 14 UAV data of Posingai village Trung Chai Commune and 3D image extracted using ADCALC 3D

temporary evacuation sites, evacuation facilities, expected secondary evacuation routes, individual houses, and neighbors' homes with close relationships. By marking this while discussing with the family, the residents will be able to complete their own customized CBEM. On the other hand, more detailed map information was also required for the region.

The process of making the map called for the residents to use their experiences. To develop an easy-to-use map, it was necessary to include such information. The presentation of the photo map and the images from UAVs showing traces of past natural disasters was indispensable for regional understanding and disaster prevention. In addition, 3D information extracted from UAV photographs using Adcalc3D is also presented. Some actual residents, for example, routinely viewed open-source image data, such as Google Earth. Future developments in the residents' understanding of open-source image data are expected (Fig. 14).

5.5 Discussion with the Residents for More Understanding of the Evacuation Drill Planning at Posingai Village, Trung Chai Commune

For the evacuation drill plans, maps usually have a suitable scale for the purpose. The mapping by AW3D was suitable the set up the general orientation of evaluation. UAV mapping was effective in direct and exact site imaging among the residents. These maps were suitable for identifying the exact locations. Residents need to recognize their homes on the series of maps.

Given our previous experiences at Posingai Village in 2021, when using UAV maps, the ability to see residents' houses and the surrounding features was much easier. With a trial UAV map, almost every resident could confirm the location of their home and nearby features along the evacuation route. A discussion on the evacuation drill plans at Posingai Village, Trung Chai Commune, was conducted in April 2022 between us and the experienced residents of the village, the former village chief, and reputable people in the community. The steps of the discussion process are shown in Figs. 15 and 17.

These figures showed the final result of the discussion. The five locations (A to E) in Fig. 16 were considered safer by the people. They decided on an evacuation shelter at a higher place deemed relatively stable. The remaining four locations are areas with high, smooth, and flat shapes and sufficiently stable to save each person. However, the areas risk isolation when debris flow and surface failure occur along the road.

Since the date and conditions at the occurrence of a disaster can not be selected, evacuation plans should be made for multiple conditions. For example, in the case of Posingai Village, the location of the inhabitants is completely different during the daytime versus the night. The presence of elderly, disabled family members, and pregnant women also change over time. It is also necessary to develop a new system to respond to such situations and promptly advance discussions on what conditions make this district the most

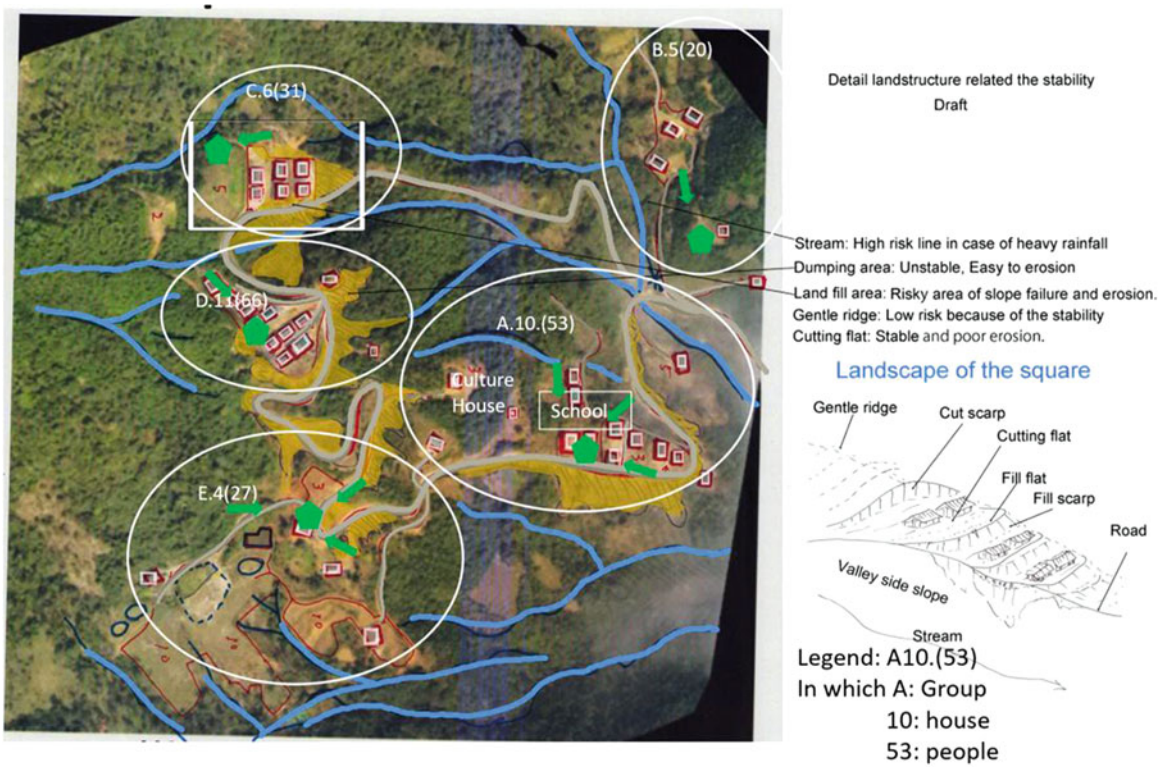

Fig. 15 UAV site map after discussion with the community residents at Site C: Posingai Village, Trung Chai Commune

vulnerable to disasters. We summarized the steps of the scenario of the evacuation drill in Fig. 17.

The most important things are evaluation meetings for the next. Assessment of safety after a landslide occurs through people's observations of the area's topography after the landslide. This assessment is the first step when discussing using maps and evacuation drills with residents.

5.6 The Evacuation Drill at Posingai Village, Trung Chai Commune

The evacuation drill was carried out between the people of Posingai Village in Trung Chai Commune in June 2022 and us. With nearly 100 participants, five locations assessed as safe by residents were identified for evacuation drill purposes, as discussed in part 5.5. It was raining during the evacuation drill, which is a realistic simulation condition for when a natural disaster might occur. The evacuation drill is divided into two phases. The first phase is to get the locals used to the alarm signal. When the alarm sound is triggered, people move quickly from the village hall (point O) to the elementary school area (point A) in Fig. 18. The request is that people move quickly, support volunteer forces and the elderly, and leave heavy properties such as corn bags, rice bags, etc. As a result, three minutes were required to move all people to a safe location with a travel distance of 300 m.

The second phase of the evacuation drill is carried out when people are in their houses under the assumption that a slope disaster divides the residential areas. When the warning sounded, people from clusters of houses moved to five safe areas (A, B, C, D, and E) in Fig. 18. The head of each residential cluster was responsible for guiding people to move along the route defined on the maps. During the exercise, UAV was used to re-record the entire process. People were moved to safe areas within about five minutes.

6 Remark: How about Realizing Autonomous Disaster Risk Reduction in the Community by Aiming for a Usable Slope Disaster Prevention Map?

To reduce slope disaster risks for ethnic groups living in mountainous provinces of northern Vietnam, we prepared maps and improved them through dialogues with local organizations trying to utilize their experiences for disaster risk reduction and evacuation drills. Three pilot communes in Lao Cai Province were designated, and the implementation status of the program was reported.

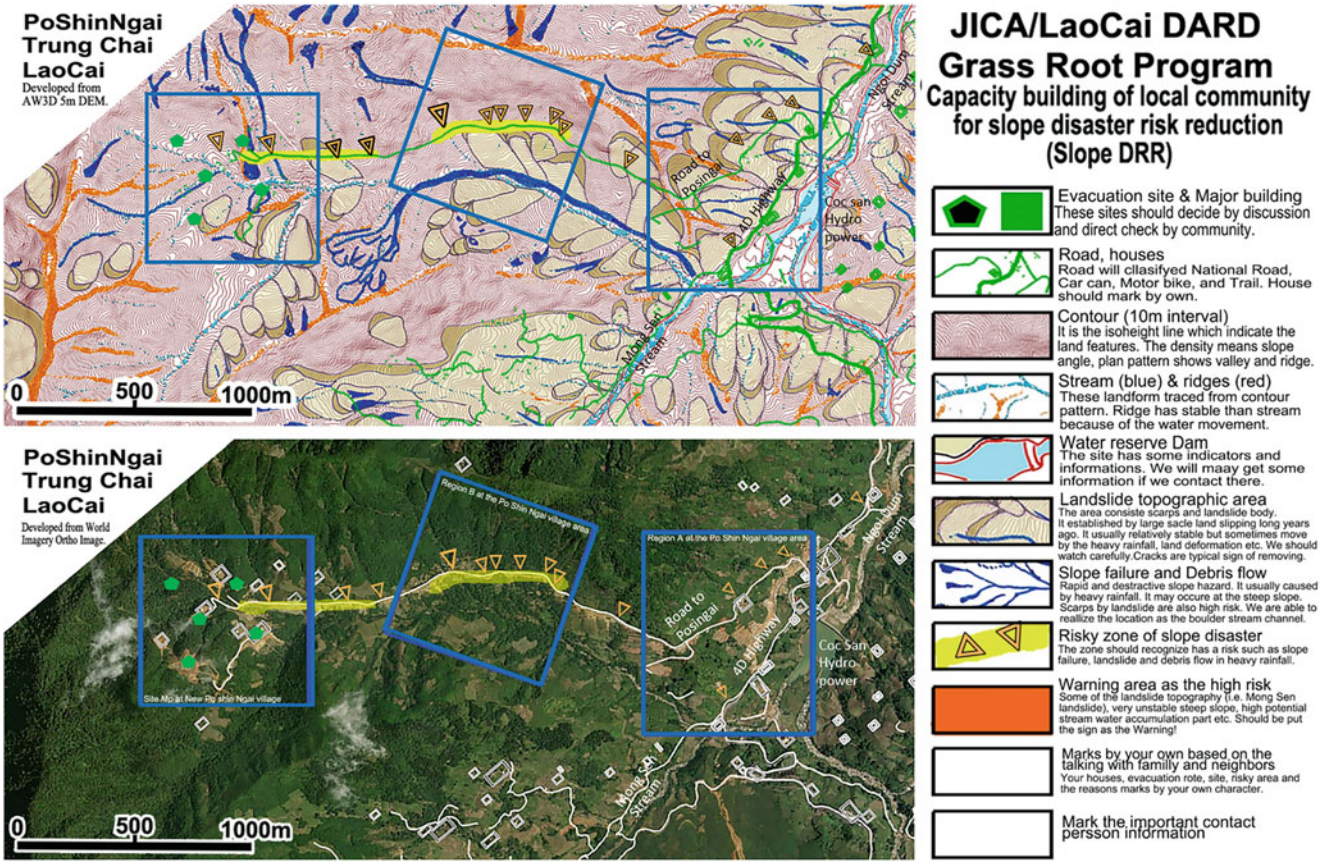

Fig. 16 Modified Village SLOPE DRR Management Map based on discussion with residents and engineer

Fig. 17 Flow chart for the discussions with residents

Fig. 18 Evacuation Drill at Posingai Village, Trung Chai Commune, Laocai Province on June 2022

In the last decade, the progress of sensing tools and technology has been remarkable. In addition, the expansion of open-source images and GIS data has also been remarkable, along with discussions on the environment and disaster prevention. This project is aimed at the living areas of mountain minority ethnic groups that are generally considered to be far from investment in technology and limited in the budget to alleviate disasters. These groups live in poverty and remote areas where infrastructure development is still inadequate and traditional lifestyle habits are present. Because of this, we thought that utilizing the latest sensing, which is now considered easy, would open the way to free efforts in regional disaster prevention. Mountain minorities do not usually speak Vietnamese. However, most residents use a smartphone. Initially, we imagined that the project would be challenging. However, in actuality, we, the engineering side, and the residents understood each other the contour lines on the map as an image, and we understood the difference between a large-scale landslide and a surface landslide. In their daily life, the residents had a rough grasp of the topography, the local space, and the risk of disasters. The mapping of regional information is now easy to understand for residents. What was once considered difficult to read and not worthwhile has now been organized into an easy-to-read map. Based on this experience, we may be able to reconsider the use of Communication Base Evacuation Mapping (CBEM).

Acknowledgments This paper is a reconstruction, addition, and correction of a part of the dissertation titled "Development of the Direct Sensing Technology for Slope Disaster Risk Reduction with the Special References of Local Community Management in the Humid Tropical Mountains, Vietnam" application submitted to Tohoku-Gakuin University in 2022 by the first author, Nguyen Kim Thanh.

References

Dang NV (2002) Ethnic minorities in Vietnam. The Gioi Publishers, Hanoi, p 203

Duan NB et al (2011) Studied to determine the causes of the landslide in the area of the Mong Sen bridge, Lao Cai province. Vietnam J Earth Sci* 33:164–174

Hamasaki E, Miyagi T (2013a) TXT-tool 1.081-2.3 abstracting unstable slopes (landslide topography) using aerial photos and topographic maps: concept and frameworks. In: Sassa K, He B, McSanency M, Nagai O (eds) ICL landslide teaching tools. Springer, Cham, pp 22–35. ISBN: 978-4-9903382-2-0

Hamasaki E, Miyagi T (2013b) TXT-tool 1.081-2.4 risk evaluation using the Analytic Hierarchy Process (AHP) – introduction to the process concept. In: Sassa K, He B, McSanency M, Nagai O (eds) ICL landslide teaching tools. Springer, Cham, pp 36–49

Hung NQ et al (2017) Landslide inventory mapping in the fourteen northern provinces of Vietnam: achievements and difficulties. In: WLF4. Springer, Ljubljana Slovenia EU, pp 501–510

Laocai DARD (2021) Report for kick-off meeting for project "Capacity building for resident disaster risk reduction in Lao Cai"*

MARD (2020)* lessons learned to respond to typical flash floods and landslides from 2000-2019

Miyagi T (2013) TXT-tool 1.081-2.1 landslide topography mapping through aerial photo interpretation. In: Sassa K, He B, McSanency M, Nagai O (eds) ICL landslide teaching tools. Springer, Cham, pp 1–10

Miyagi T (2016) Drill of hazard mapping as the practice of physical geography and disaster prevention study in the East Japan great Earthquake201, "create disaster reduction and the academic/education society", Japan Scientific Council Series No.22, 8. in Japanese

MONRE (2021)* Vietnam's climate change scenario

Nam TN (1995) The geology of Vietnam, A summary and problems. Shizuoka, Japan

Saito H et al (2018) Landslides triggered by an earthquake and heavy rainfall at Aso volcano, Japan, detected by UAS and SfM-MVS photogrammetry. Prog Earth Planet Sci 5:15

Kenichiro Tachi and Yusuke Sakai (2019) The current status and the future of the landslide disaster in Vietnam. Erosion control and management, No 250. p. 60–66. (In Japanese)

Thanh NK, Miyagi T, Isurugi S, Tien DV, Luong LH (2021) Developing recognition and simple mapping by UAV for a resident in a mountainous area in Vietnam – a case study in Po xi Ngai community, Laocai province. Workshop on world landslide forum 5th (WLF-5), understanding and reducing landslide disaster risk, pp 103–109. Online ISBN 978-3-030-60227-7; Print ISBN 978-3030-60226-0: Springer, WLF 5th

Tien DV, Khang NX, Sassa K (2017) Results of a Technical Cooperation Project to Develop Landslide Risk Assessment Technology along Transport Arteries in Vietnam (IPL-175). Retrieved 4 6, 2020, from https://link.springer.com/chapter/10.1007/978-3-319-59469-9_36

UNDRR (2009) Disaster risk management programs for priority countries, global facility for disaster reduction and recovery. Chapter Two, Global disaster risk patterns trend and drivers. p. 18–57

UNDRR (2015) Sendai framework for disaster risk reduction 2015-2030

Vietnam's National Assembly (2013)* Law on natural disaster prevention and control. Law No. 33/2013/QH13 of the National Assembly

Westby MJ, Brasington J, Glasser NF, Hambrey MJ, Reynolds JM (2012) "Structure-from-motion" photogrammetry: a low cost, effective tool for geoscience applications. Geomorphology 179:300–314

Yem NT et al (2006) Assessment of landslides and debris flows at some prone mountainous areas Vietnam and recommendation of remedial measures. Phase I: a study of the east side of the Hoang Lien son mountainous area of Vietnam. Institute of Geological Survey Vietnam, Hanoi

Note (year) * published in Vietnam.[1]

[1] Note: Year of publication in Vietnam has been indicated with Asterisk.

Landslide Risk Assessment in the Tropical Zone of Vietnam as a Contribution to the Mitigation of Natural Disaster Vulnerability

Dinh Van Tien, Nguyen Kim Thanh, Lam Huu Quang, Do Ngoc Ha, Kyoji Sassa, Toyohiko Miyagi, and Shinro Abe

Abstract

Landslide risk assessment is considered an important objective in minimizing damage caused by this extreme event. The biggest challenge of assessing landslide risk is predicting the likelihood of a catastrophic event. To evaluate this possibility, studies have focused on building integrated maps of assessment, using predictive models such as testings, scale models, numerical models, and actual field observations. This article summarizes the research achievements and applications achieved in the past ten years of the Institute of Transport Science and Technology in the landslide risk assessment in Vietnam.

Keywords

Landslide · Risk assessment · Potential · Susceptibility · Reactive · Testing · Ring shear apparatus · Monitoring · Early warning

D. Van Tien (✉) · L. H. Quang
Institute of Transport Science and Technology, Hanoi, Vietnam

N. K. Thanh
Institute of Transport Science and Technology, Hanoi, Vietnam

Tohoku Gakuin University, Sendai, Japan

D. N. Ha
VNU Vietnam Japan University, Hanoi, Vietnam
e-mail: dn.ha@vju.ac.vn

K. Sassa
International Consortium on Landslides, Kyoto, Japan

T. Miyagi
Advantechnology Co., Ltd, Chiyoda, Japan
e-mail: c1934009@mail.tohoku-gakuin.ac.jp

S. Abe
Okuyama Boring Co., Ltd, Yokote, Japan

1 Introduction

Vietnam is located on the Indochinese peninsula in Southeast Asia, with a population of over 90 million people. The average annual rainfall from 1400 to 2400 mm receipt in most places of the country, with some places reaching over 4000 mm Vietnam regularly suffer from 7 to 10 tropical storms accompanied by floods and landslides. Over the past two decades, natural disasters in Vietnam have caused more than 13,000 casualties and over US$6.4 billion in property damage, of which landslides are considered the most catastrophic natural disasters.

Vietnamese Government Strategy for landslide reduction to mountainous areas and central highlands is "proactively prevent natural disasters", for which landslide risk evaluation is one of the key solutions. The Institute of Transport Science and Transportation (ITST) under the MOT was established in 1956 as an institution for science and technology research and application for the transport sector. For more than 35 years ITST has been involved in the landslide field and proposed several solutions for scientific research and new technology application in disaster prevention, response, and mitigation to specific strategy mentioned above. Since the ODA Project named "Development of Landslide Risk Assessment Technology along Transport Arteries in Vietnam" began in November 2011, the development of new landslide risk assessment technology and its application to forecasting, monitoring, and disaster preparedness of landslides in Vietnam has been raised to a new level and contributed to geo-disaster reduction along main transport arteries and on residential areas. This paper is a summary of the achievements in Landslide Risk Assessment in the tropical zone of Vietnam that contributes to the mitigation of natural disaster vulnerability over the last 10 years.

I. Alcántara-Ayala et al. (eds.), *Progress in Landslide Research and Technology, Volume 2 Issue 1, 2023*,
Progress in Landslide Research and Technology, https://doi.org/10.1007/978-3-031-39012-8_13

2 Concept of Landslide Risk Assessment

The term "risk" combines the concepts of threat to life, difficulty and danger of evacuating people and property in the event of a disaster, potential structural damage and house value housing, social disruption, crop loss, and destruction of public facilities.

In the framework of this paper, the concept of risk is determined from the point of view of the International Center for Geohazards (ICG) of the Norwegian Geotechnical Institute (Uzielli 2009) as follows: R = HxVxE (1) Where: R (Risk) is the possibility of loss due to the accident occurring. H (Hazard) is the likelihood of a catastrophic event occurring. The value of H will be determined between 0 and 1, where H = 0, corresponds to no events occurring, and H = 1 corresponds to certain events. H has no units. V (Vulnerability): When an accident occurs, injuries may be caused to people, their production, and daily life. V is understood as people's ability and material, social, economic, environmental, cultural, institutional, and political assets to be damaged due to disasters. V has no units and ranges from 0 to 1, where V = 0 corresponds to no injury and V = 1 corresponds to complete injury. E (Value of Vulnerable Elements): Vulnerable elements include people, assets (houses, traffic structures, vehicles, crops, livestock. . .), livelihood activities, and the environment. E is defined in monetary units (for economic damage assessments) or person units (for human damage assessments).

Along with the concept, risk assessment methods are also increasingly diverse. These methods can be grouped in two directions of assessment: direct—qualitative and indirect—quantitative (through a set of indicators), specifically: sociological investigation method, integrated cartographic method, etc. combination and index method. Each assessment method has its advantages and disadvantages.

For the field of landslides, due to the diverse nature of scale, type, and large distribution space, when considering the concept of risk, most scientists focus on assessing the probability of occurrence of hazard event (H) on an area scale and evaluate the risk for specific landslides.

Assessing the overall landslide risk for an area involves answering the questions of what "types of landslides occur", "where they did occur", "where is landslide susceptibility area", and "how likely they are to reactivate". The best tool to assess landslide risk for an area is the development of integrated landslide maps related such as landslide distribution maps, landslide classification maps, landslide susceptibility assessment maps, or reactive assessments of landslides that have occurred. Based on integrated maps, the planning, land use, response, and damage reduction of the phenomenon are determined. Due to a large number of occurrences, the assessment of the probability of occurrence of each landslide in an area is usually not covered. However, risk assessment for the specific landslide case is mentioned for landslides with special significance such as large scale, important located places. Models for prediction at different levels such as laboratory tests, small-scale simulation models, numerical models, and monitoring and evaluation of characteristic parameters on Real models are used to study and evaluate the shifting mechanism through the expression of related parameters. Based on result predictions from these models, the mitigation measures are determined.

3 Achievements in Landslide Risk Assessment

3.1 Landslide Identification and Integrated Landslide Mapping

3.1.1 Landslide Identification and Landslide Topographic Area Mapping

As mentioned above, the first input when assessing landslide risk is to recognize the type and location in which they are distributed. When a landslide occurs, it will change the topography of the area and leave easily recognizable and distinguishable signs on the land surface from the surrounding environment. Most of these signs are related to changes landform of the topography of the area. To identify the phenomenon of landslides, it is necessary to have a view from above and the surrounding area of the overall slope failure to identify the features and interpret the changing process of these features over time. In the recognition and interpretation of aeronautical images, a three-dimensional view of the deformation of a slope can be established through stereoscopic observations of pairs of aerial images for aeronautical interpretation. Through this stereoscopic image, an overall picture of the land can be observed; Landform classification, land cover classification, and vegetation classification can be determined; The area of land deformed by the landslide can be cleared (Miyagi 2013).

Based on knowledge of geomorphology, characteristics of vegetation cover, drainage conditions, signs of surface displacement in the form of landslides such as scarps; irregular or hummocky topography below scarps, at the body; bare linear tracks oriented downslope; fresh rock exposure; fresh rock accumulation at the slope base; disordered vegetation and disarranged drainage. . . are realized.

These signs are analyzed and compared with an identification catalog of characteristics of landslide types such as Rotational slide, Translational slide, Compound slide, Debris slide, Debris Flow, complex slide, etc., from which the type, features, and evolution of the past displacement process can be determined, interpreted and recognized. However, the aerial photograph is a similar image. The interpretation of

topographic information from vegetation images was used as a method of information collection. Depending on the image quality and scale, some positions or features within the slider block are not clearly defined. In such cases, it is necessary to conduct an actual field survey. The information on landslide features is recorded as a landslide identification information layer. The landslide distribution topographic map is created by the combination between the landslide identification information layer and the topographic information layer.

The method of building topography maps by aerial photo interpretation in Vietnam has been applied since early. However, the landslide inventory maps have only been carried out and published after 2000. A typical example of Landslide identification and mapping is a landslide inventory map along HCM road (Central region of Vietnam), which has been carried out and published in 2016.

Figure 1 is the landslide distribution map of the Kham Duc area, in Viet Nam—one of the 6 first sheets of landslide inventory maps. Based on the analysis of more than 100 black and white aerial photographs on a scale of 1/33,000, ninety-six landslides were recognized, with 5 types of landslides including (1) Rotational sliding; (2) (Translational sliding; (3) Complex; (4) Debris sliding; (5) Debris flow. Of the five types, the first three are identified by topographic and topographic form characteristics; the other two types are identified by the topographical features of the sliding body.

Currently, remote sensing image technology is being increasingly developed and provides better quality land surface images for analysis, but landslide identification based on interpretation of images taken from aircraft is still considered the basis for landslide identification, which has been carried out in Vietnam.

3.1.2 Application of Landslide Identification Using Unmanned Aerial Vehicles (UAV) in National Road Survey of Vietnam

Remote sensing imaging technology using unmanned aerial vehicles (UAVs) for landslide terrain recognition has become common in the field of landslide disaster prevention in many countries, but its application for survey and design of prevention and mitigation works in Vietnam has not been popularized. Research and application of remote sensing imaging technology using unmanned aerial vehicles (UAV) in landslide surveys of roads in Vietnam is a requirement set by the Ministry of Transport (MOT) to ITST the research team.

The experiment was conducted at the road connecting Lao Cai-Sapa, National Highway 4D, Highway 7-Nghe An Province, and Ha Long City—Quang Ninh Province using a UAV Phantom IV. The images were taken from the UAV with a larger than 70% overlap area. Classifying of photos, and handling blurry and noisy images were carried out with specialized software. The overall image of the target area was built by combining coordinates of UAV photos in the same GIS geographic coordinate system and correcting through the coordinates of the ground control point (GCP). The orthogonal image model and Digital surface model (DSM) were built from cloud point technology and automatically recognize similar points. Photograph of the area and contour maps, which were constructed from DSM-assisted landslide identification. Figure 2 depicts the development of a landslide topographic map of the section KM 119-Km121, National Highway 4D, Vietnam.

Through the study and evaluation of the type of UAV, the method of photography and interpretation analysis, the advantages and disadvantages of the method compared with conventional survey and images taken by UAV equipment, developing the landslide occurred map was considered feasible.

The advantages of this method are low cost, short implementation time, and high access capacity to hazardous locations where landslides are occurring. For the preliminary landslide survey, the 1:1000 scale landslide topographic map is suitable. The detail of the GSD ground image is proportional to the flight height, (the lower the flight height, the higher the detail image we can get). To build the landslide topographic map with a scale of 1/500 to 1/1000, UAVs fly heights within 50 to 150 m are suitable. To identify the microfeature of the sliding block such as cracks, scrap, etc., a GSD of at cm/pixel is required. However, the biggest drawback of this method is the uneven vegetation cover on the soil surface. In such areas, the Digital Elevation Model (DEM) will be built from the DSM after removing the vegetation cover elevation or comparing it with the available topographic elevation documents.

Although there are still limitations, this topographic survey method still has undeniable outstanding advantages of creating a panoramic view of the landslide object and short implementation time. This method is also safe for operators, and especially suitable for emergency response when a new landslide occurs.

3.1.3 Landslide Mapping through Alos World 3D Mapping (AW3D) and Google Earth

Landslide identification through stereo pair aerial photograph interpretation is considered a primitive technology for the construction of landslide distribution maps. However, in Vietnam, this source of air photo data is limited in quantity, image scale as well as shooting time. With the rapid development of remote sensing imaging technology, taking pictures of the entire surface of the earth has become common and available. Digital images with three-dimensional coordinate information of the land surface in various scale formats through services such as NASA's SRTM can be used as an

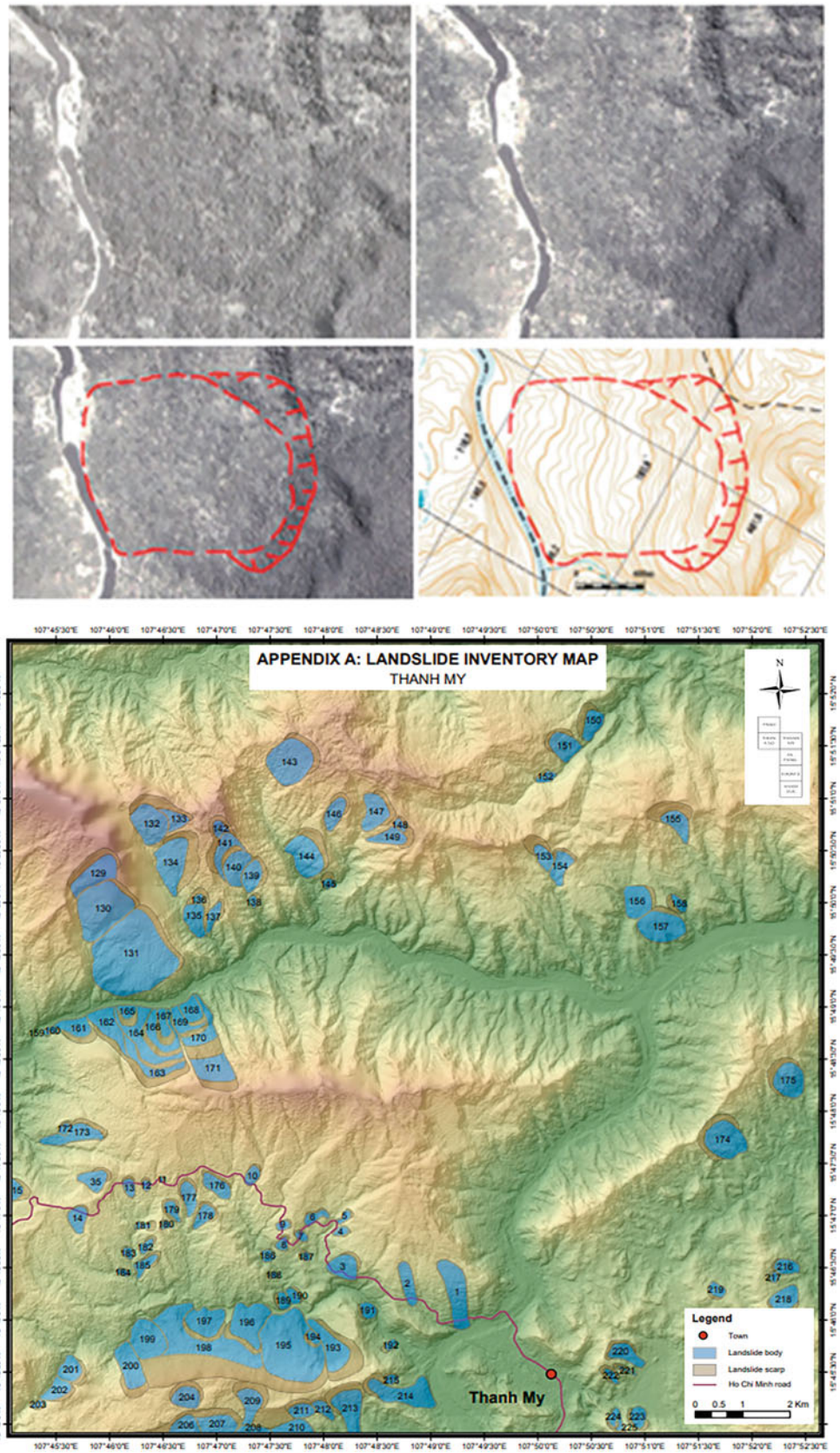

Fig. 1 Illustrates a rotational slide interpreted from pair of aerial photographs (D2-99-05-168 & 169) (above) and the landslide distribution map of the Kham Duc area—in Viet Nam (below) (Luong et al. 2016)

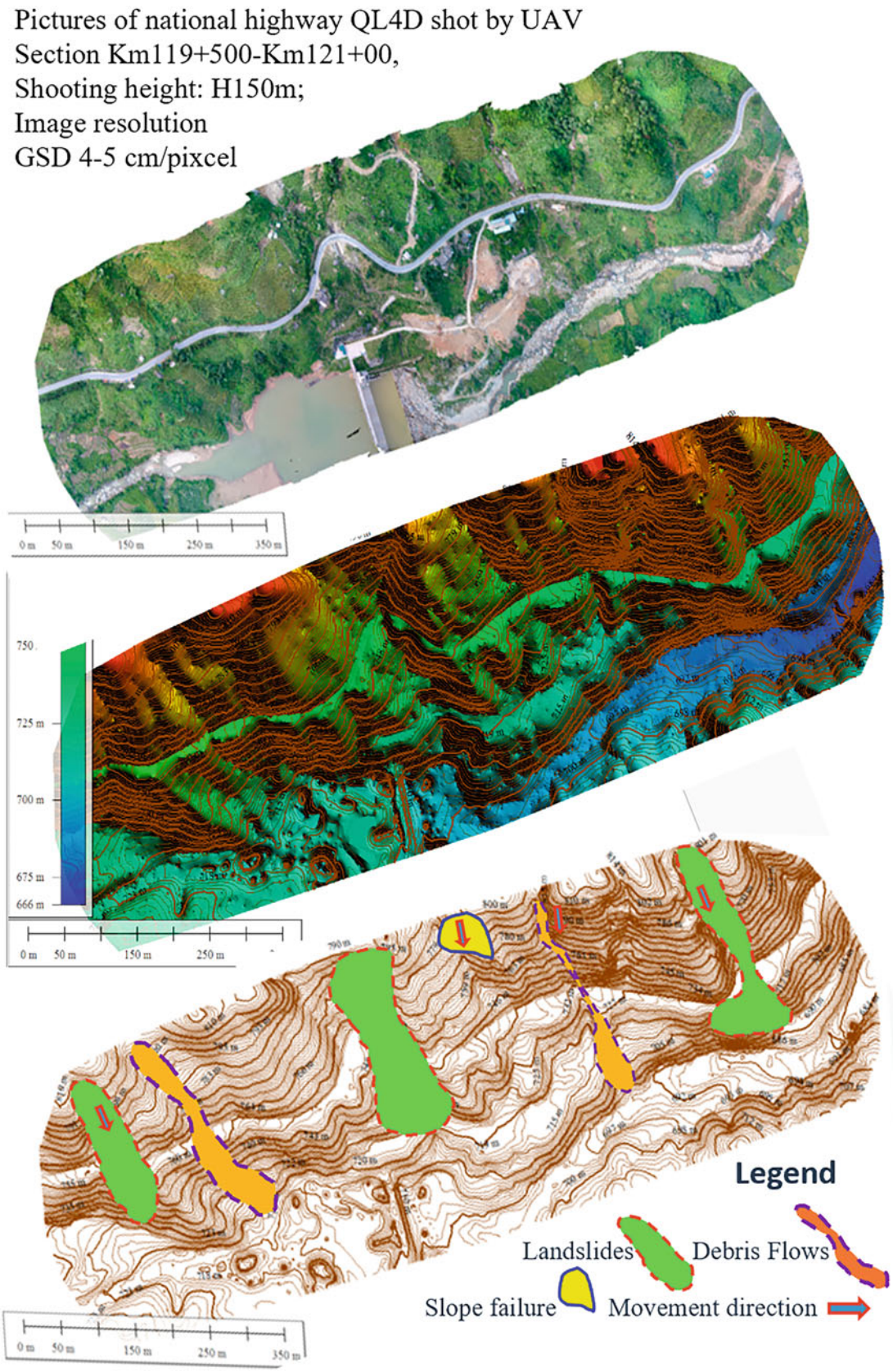

Fig. 2 Developing landslide topographic map of the section KM 119-Km121, National Highway 4D, Vietnam using UAV (Thanh et al. 2020)

alternative to stereo pair aerial photographs by traditional technology in building stereoscopic images.

The landslide identification map of 70 km along National Highway 7—Nghe An Area—Vietnam was conducted to set up a test based on the above idea. Experimentation with 3 representative locations was conducted from AW3D data with 10 m contour generation. The comparison of the landslide interpretation results of the sliding block such as landslide boundary, main scarp, and landslide body with the actual ones of the landslide through the field survey showed similarities.

The AW3D data with a 5 m grid size, has almost the same level of detail as the 1/2000 scale aerial photograph used. Topographic maps with contours generated from the above DSM data combined with visualizations from Google Earth are used for analysis and identification of landslides along the route. Different viewing angles to Google Earth and Landform from topographic maps with contour lines from 5 to 10 m have helped identify small to medium-scale landslides with a width of 50–200 m (Fig. 3).

Landslide mapping through Digital 3D World map (AW3D) and Google Earth offers many advantages over traditional aerial analysis, but it still has its weaknesses due to the use of DSM for analysis. In some areas, "fake" main scrap may be identified where there is a sudden change in vegetation cover with high height.

3.1.4 Assessing Landslide Reactivation Potential and Risk Evaluation Mapping for Occurring Landslides

The next issue with assessing landslide risk for an area after the landslides are identified is to compare their susceptibility to reactivation. The ability to reactivate a landslide depends on 3-factor groups including Trigger factors (rain phenomena, earthquakes), Characteristics of the sliding mass (type of motion, and geometrical and geomorphological features), and Internal factors (geology, hydrology). The trigger factor group is a passive factor and the sensitivity to the landslide reactivation is proportional to the magnitude and frequency of the phenomenon that their potential did not study in this research. Excluding the trigger factors, when assessing the risk and building the risk assessment map for humid tropical areas like Vietnam, 2 group factors landslide characteristics and internal factors have been considered.

The groups of feature elements of the landslide are considered from the perspective of geomorphology and divided into sub-groups according to the point of view of Miyagi et al. 2004 including (1)The micro landforms of the soil body as an aspect of the characteristics of movement; (2) The boundary of major landslide components as an aspect of the time process and (3)The landslide topography and the adjoining environment as an index of geomorphic setting. In each sub-group, the related geomorphological member factors that affect the reactive ability of the sliding block were mentioned and classified by a score (Fig. 4).

As for the internal factors, the geological factors mentioned include geologic age, bedrock lithology and structure, surficial geology, and level of weathering. Each geological factor is classified into different features or levels that describe the susceptibility to landslide reactivation and are characterized by a certain number of scores (Fig. 5).

Based on the discussion, the assessment of each factor affecting the reactivity is divided into different levels which are specified by a certain weight score value using the AHP model. The susceptibility of different landslide sites to reactivation depends on the total AHP score, in which geomorphology will account for 44.44% and geology will account for 55.56%.

Figure 6 depicts a landslide risk map in the area of Thanh My—one of 6 landslide risk maps, which were developed based on the identification map and risk assessment method which is mentioned above. For these maps, the landslide reactivation potential is divided into 4 levels AA: very high, A high, B medium, and C low. This landslide risk assessment map is one of the first and most important ones in Vietnam for evaluation of the landslide reactive susceptibility to occurring landslides.

3.1.5 Landslide Potential Assessment and Landslide Susceptibility Mapping

For Landslide Risk Evaluation on natural slopes where landslides have not occurred, an assessment of the sensitivity to vulnerability of the slope by sliding was carried out.

The basic principle for evaluation is based on "past and present are the keys to the future" (Vaners 1984; Carrara et al. 1991). Under this hypothesis, future landslides are likely to occur under the same geological, geomorphological, and hydrogeological conditions as having occurred with previous landslides. The conditions that led to the landslide can be used to identify possible landslides in similar areas in the future.

On that basis, surveys and statistics on the occurrence of landslide phenomenon were conducted for the study area. The Landslide distribution map was developed for the target area. The main causative factors related to the occurrence of sliding block displacements such as slope angle (geomorphology), type of rock, fault density (geology), distance to the road, land used (human being), and precipitation (climate) are selected for assessment. The affection of causative factors to each occurred landslide was discussed and recorded.

Figure 7 is a score comparison matrix of causative factors and the classes within each factor, as required by the AHP method.

The causative factor maps were developed on the same scale from available data, in which each one was classified for assessment. The number and density of occurred

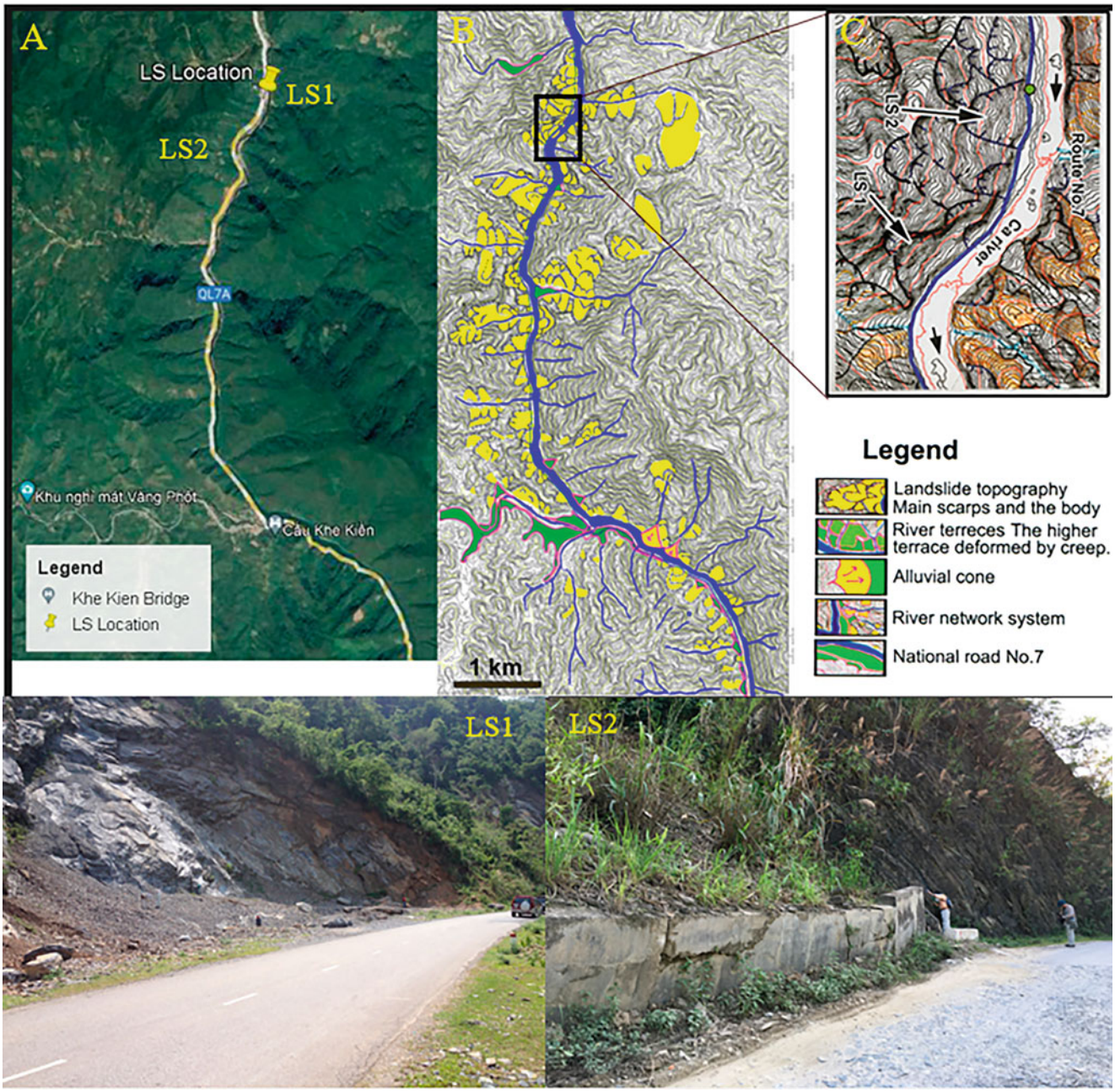

Fig. 3 Depicts an interpretation of landslide mapping through World Digital 3D (AW3D) and Google Earth maps of part of a 70 km mountain area along National Highway 7 of Vietnam. (**a**) image is taken from Google Earth, (**b**) landslide identification map on AW3D background. (**c**) LS1 and LS2 location identification details. LS1 and LS2: detailed images of 2 locations (Dung et al. 2016)

landslides for each class are estimated by superimposing the landslide distribution map with the causative factors map in the GIS system. The sensitivity to a landslide of each class zone of causative factor maps is calculated and evaluated through the value of the number and density of occurred landslide. The weight value point was given to each causative factors map depending on their sensitiveness and their classes then an analytical hierarchical process (AHP) is used to combine these maps for landslide susceptibility mapping.

The landslide distribution map and Landslide susceptibility map of the corridor area, along HCM road from Quang Tri to Kontum in the center of Viet Nam are created from overlap landslide causative factors maps with calculated Eigenvectors from the AHP model.

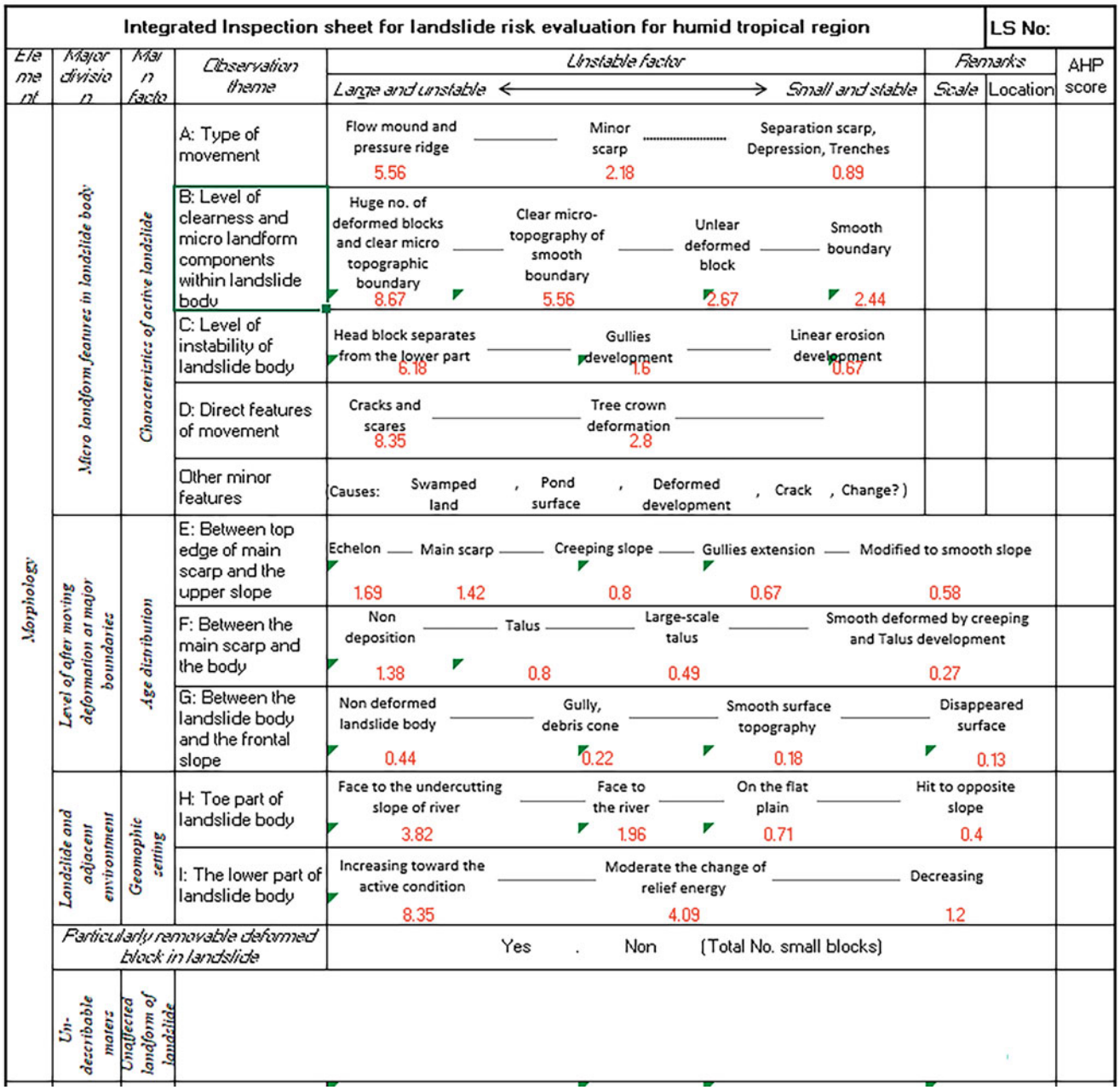

Fig. 4 Geomorphological integrated inspection sheet for landslide risk evaluation for the tropical region (Miyagi et al. 2004)

According to the Landslide susceptibility map presented in Fig. 8, susceptibility to land sliding was divided into 4 classes very high, high, moderate, and low. The calculation showed that 82.66% of over 600 occurred landslides in the distribution map fall in the high and very high susceptible zone.

For each study area, the accuracy of the Landslide susceptibility map depends on the data and basic parameters selected to calculate and assess the risk of landslide hazards presented in the form of maps in the GIS system. The selection of input map data to calculate landslide hazard risk depends on three main factors, namely "relevance", "availability", and "scale" of the map." Relevance" shows the close relationship of the main factors related to landslides in the study area. "Availability" refers to the available data and the data likely to be obtained in the study. And "scale" of the input map refers to the map scale of the factors affecting the landslide process that will be used to calculate the risk of landslide hazard for the study area. The accuracy of the map

Geology	Geoloy age	Geoloy age	Primary geologic unit (Rock type)	Mesozoic (Triassic to the Jurassic sedimentay rock: Conglomerate, Gritstone, 4.39	Quarternary (River soil sediment) 3.97	Precambrian (Schist and Granit gneiss) 1.93	Paleozoic (Schist, Quazt-sericite Schist, ...) 1.23	
	Bedrock Lithology and Structure	Bedrock Lithology and Structure	Attitude of beds	Beds of rock that parallel or dip in the same direction as the slope 4.76			Beds that dip into the slope 1.59	
			Presence and degree of fractures, joints, and foliation	Numerous (distance between fractures, joints, and foliation less than 20cm) 22.57	Few (distance between fractures, joints, and foliation ranging from 20cm to 50cm) 12.42		Very few (distance between fractures, joints, and foliation greater than 50cm) 6.84	
			Tratigraphy (Sensitive key layer)	Hard beds overlaying softer rock (coal..) 5.72	Hard beds overlaying softer rock (mudstone..) 5.57		Massive 1.63	
	Level of weather	Level of weather	Degree of weathering	Completely weathered 18.12	Highly weathered 8.46	Moderately weathered 3.42	Slightly weathered 1.96	
Risk of landslide occurrence base on your experience				Large → Middle → Small			Total points of AHP assessment: ..... scores	
Comment and view of each selection							Score by own inspector: ..... scores	

Fig. 5 Geological integrated inspection sheet for landslide risk evaluation for the tropical region (Luong et al. 2016)

is characterized by the number of landslides occurring over a highly susceptible zone.

3.1.6 Digital Database Structure on Topography, Geology, Hydrology, and Landslide Identification for Landslide Mitigation in Survey and Design Work

Based on researching and applying digital databases for the management of landslides and disaster prevention in the world, an orientation to create and apply a database for storing, managing, and proposing landslide mitigation solutions is created. The built-in landslide data layer is considered a separate layer in the structure of many different data layers in the same geographic coordinate system GIS, which is known as Big Data. The research objective is to build a database structure on landslides including the information on topography, geology, and hydrology relating to landslide identification for landslide response and mitigation for traffic in the mountain zone. The data structure consists of two parts including Assessing the level of risk and Countermeasure selection.

3.1.7 Assess the Level of Risk

Besides spatial and temporal parameters as well as time and type of movement, relevant factors are divided into groups such as the Topographic group (length, height, natural slope gradient angle on the upper slope, distance from the foot of the slope to the road, and a number of steps on the slope), Geology group (slope materials, degree of weathering, the depth and strike of the material layer, cracks; and Hydrogeological and hydrogeological groups (daily rainfall intensity and signs of groundwater). The survey sheet for landslide collecting data is presented in Fig. 9. Each factor is again assigned a certain weight depending on its importance to the degree of susceptibility to displacement.

The weighted model (AHP) is then used for the classification and evaluation of landslides inbuilt stores, in which The total score (maximum 100) of the risk factors for each landslide site is divided into 5 levels Very High Risk, High Risk, Medium Risk, Low Risk, Low Risk, Very Low Risk with scores as 100–80, 80–60, 60–40, 40–20 and 20–1, respectively. (Thanh et al. 2020).

Three special factors of sliding blocks mentioned as Direction of discontinuity, Wethearing, and Groundwater are used to evaluate the level hazard of sliding blocks. Depending on the presence of these factors during the survey, the hazard level was divided into five levels, with the level increasing gradually. Table 1 presents the principles of assessing the hazard level of Landslides.

3.1.8 Countermeasure Selection

Based on assessing the level of risk and level of Hazard, the response and mitigation solutions are considered and selected. A detailed survey of the selected locations is conducted for further evaluation and countermeasures selection. Three groups of countermeasures include the impact mitigation Control works; Prevention works and monitoring and early warning work are given and recommended for

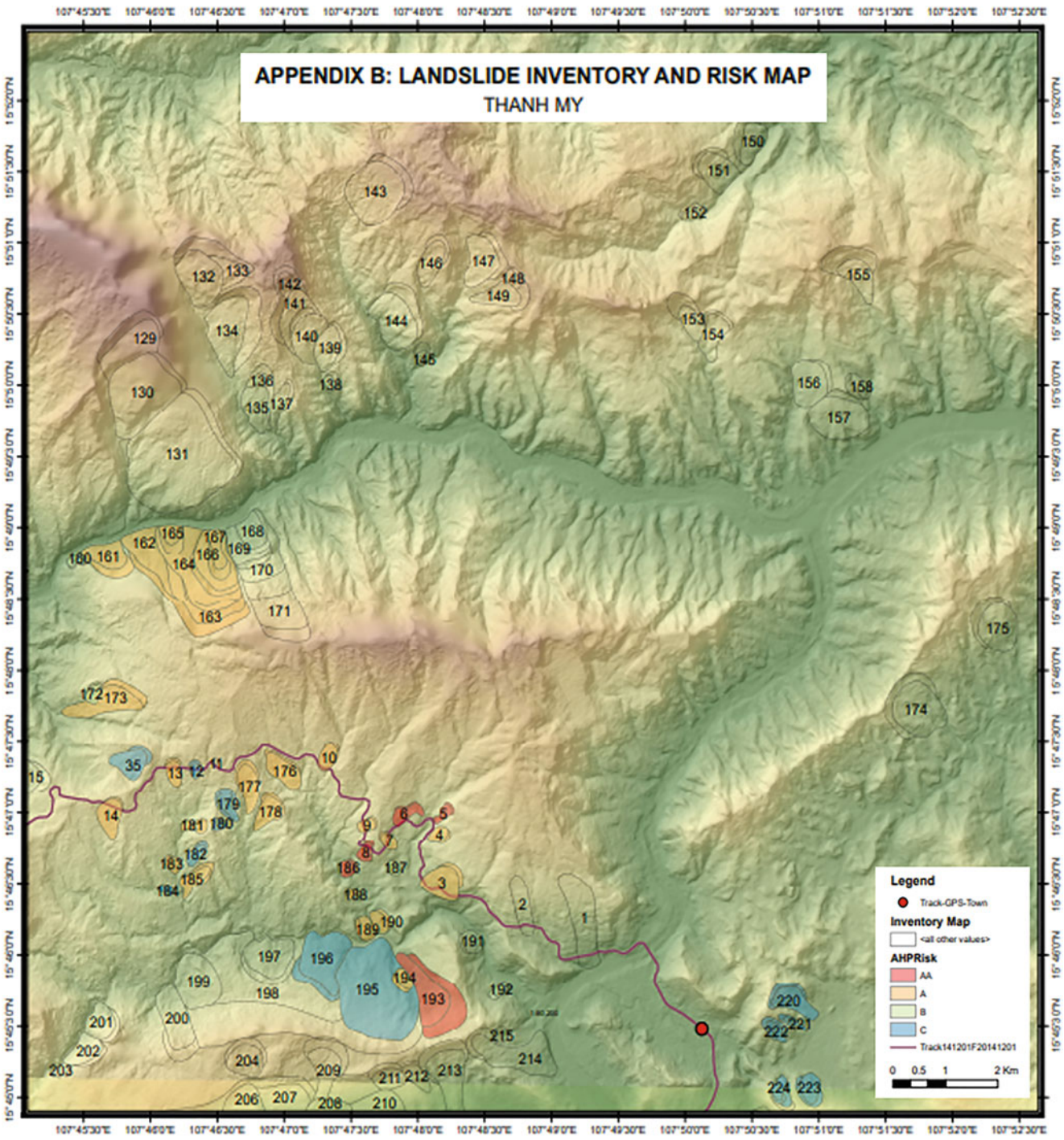

Fig. 6 Landslide risk assessment map of Thanh Mỹ -Vietnam (Luong et al. 2017)

applicability according to characteristics and recommended levels of danger. Depending on the actual situation of each landslide, suitable solutions will be selected.

The successful application of research results for building a database for National Highway NH4D, NH 6, and NH 7 in Vietnam is the first step for applying Big data in managing landslides along the roads.

3.2 Landslide Simulation and Testing

3.2.1 Development of Untrained Dynamic-Loading Ring Shear Apparatus

The dynamic-loading ring shear apparatus is Prof. Sassa's Invention in 1992(DPRI-3). ICL 2 is the sixth generation

AHP modal for landslide causative factors and the classes

Causative Factor	[1]	[2]	[3]	[4]	[5]	[6]	[7]	Eigenvectors
[1] Fault density	1							0.0287
[2] Distance to the road	2	1						0.04
[3] Rock type	5	3	1					0.0752
[4] Land use	7	5	3	1				0.1292
[5] Precipitation	8	7	4	3	1			0.2875
[6] Slope angle	9	9	5	4	2	1		0.4395
CR = 0.0578								
Sub-Table1-Slope angle								
[1] Flat-gentle slope (> 3°)	1							0.0287
[2] Fair slope (3–8°)	2	1						0.04
[3] Moderate slope (8–15°)	5	3	1					0.0752
[4] Fairly moderate slope (15–30°)	7	5	3	1				0.1292
[5] Steep slope (30–45°)	8	7	4	3	1			0.2875
[6] Very steep slope (>45°)	9	9	5	4	2	1		0.4395
CR = 0.0578								
Table 5-Land use								
[1] Special use forest land.	1							0.3192
[2] Agricultural land	2	1						0.0888
[3] Production forest land	3	2	1					0.1759
[4] Protection forest land	5	4	3	1				0.2731
[5] Special and defense forest	9	7	6	5	1			0.4303
CR = 0.0488								

Causative Factor	[1]	[2]	[3]	[4]	[5]	[6]	[7]	Eigenvectors
Sub-Table 3-Rock type								
[1] Limestone	1							0.0238
[2] Igneous rocks	3	1						0.0452
[3] Mesozoic sedimentary rock	3	1	1					0.0452
[4] Sedimentary with coal and	5	3	3	1				0.0955
[5] Metamorphic+sedimentary	7	5	5	3	1			0.1962
[6] Metamorphic rocks	7	5	5	3	1	1		0.1962
[7] Quaternary sediment rock	9	7	7	5	3	3	1	0.3979
CR =0.0474								
Sub- Table 4-Total annual								
[1] <2300 mm/year	1							0.0333
[2] 2300–2600 mm/year	3	1						0.0633
[3] 2600–2900 mm/ year	5	3	1					0.129
[4] 2900–3200 mm/ year	7	5	3	1				0.2615
[5] >3200 mm/ year	9	7	5	3	1			0.5128
CR =0.0593								
Sub-Table 2-Fault density								
[1] <=150 m/km2	1							0.0438
[2] 150–300 m/km2	4	1						0.0885
[3] 300–4500 m/km2	7	4	1					0.2431
[4] >=450 m/km2	9	6	3	1				0.6246
CR =0.060								
Sub-Table 6-Distance to the								
[3] >=100 m	1							0.1095
[2] 50–100 m	3	1						0.309
[1] <= 50 m	5	3	1					0.8516
CR =0.0018								

Fig. 7 AHP modal for landslide causative factors and the classes (Tien et al. 2016)

device that was developed to donate it to Vietnam together with the technological transfer.

Like other shearing apparatus, ICL 2 was designed for the Physical simulation of landslides. It can reproduce stress on the potential sliding surface within a slope during rainfall,

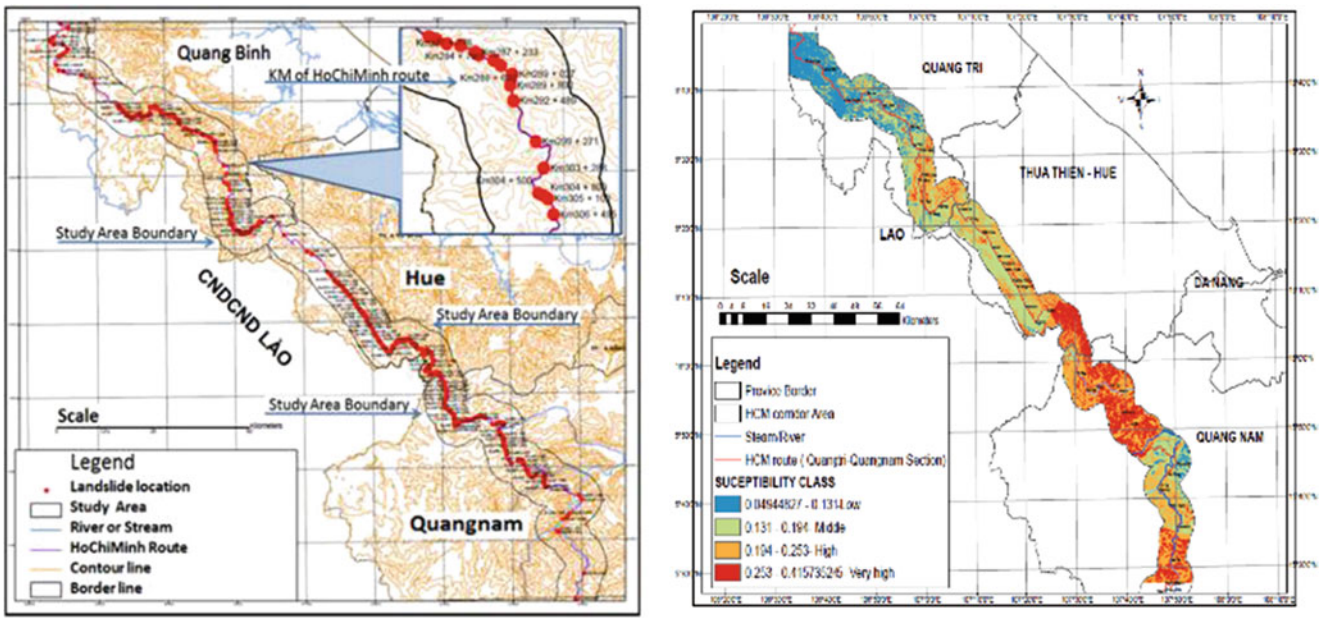

Fig. 8 Landslide distribution map and Landslide susceptibility map of the corridor area, along HCM road from Quang Tri to Kontum in the center of Vietnam (Tien et al. 2016)

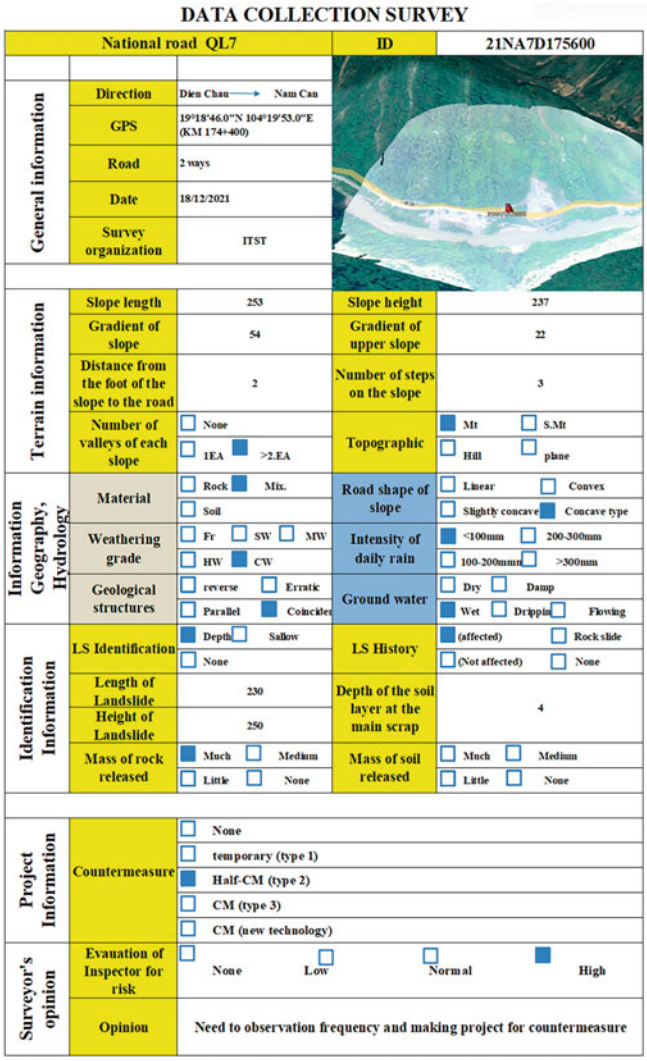

DATA COLLECTION SURVEY

National road QL7			ID	21NA7D175600
General information	Direction	Dien Chau → Nam Can		
	GPS	19°18'46.0"N 104°19'53.0"E (KM 174+400)		
	Road	2 ways		
	Date	18/12/2021		
	Survey organization	ITST		
Terrain information	Slope length	253	Slope height	237
	Gradient of slope	54	Gradient of upper slope	22
	Distance from the foot of the slope to the road	2	Number of steps on the slope	3
	Number of valleys of each slope	☐ None ☐ 1EA ■ >2.EA	Topographic	■ Mt ☐ S.Mt ☐ Hill ☐ plane
Information Geography, Hydrology	Material	☐ Rock ■ Mix. ☐ Soil	Road shape of slope	☐ Linear ☐ Convex ☐ Slightly concave ■ Concave type
	Weathering grade	☐ Fr ☐ SW ☐ MW ☐ HW ■ CW	Intensity of daily rain	■ <100mm ☐ 200-300mm ☐ 100-200mm ☐ >300mm
	Geological structures	☐ reverse ☐ Erratic ☐ Parallel ■ Coincider	Ground water	☐ Dry ☐ Damp ■ Wet ☐ Drippin ☐ Flowing
Identification Information	LS Identification	■ Depth ☐ Sallow ☐ None	LS History	■ (affected) ☐ Rock slide ☐ (Not affected) ☐ None
	Length of Landslide	230	Depth of the soil layer at the main scrap	4
	Height of Landslide	250		
	Mass of rock released	■ Much ☐ Medium ☐ Little ☐ None	Mass of soil released	☐ Much ☐ Medium ☐ Little ☐ None
Project Information	Countermeasure	☐ None ☐ temporary (type 1) ■ Half-CM (type 2) ☐ CM (type 3) ☐ CM (new technology)		
Surveyor's opinion	Evaluation of Inspector for risk	☐ None ☐ Low ☐ Normal ■ High		
	Opinion	Need to observation frequency and making project for countermeasure		

Item & Score					
Slope length		<100m	100~200m	200~300m	≥300m
Score					
Slope height		<10m	10~20m	20~50m	≥50m
Score		1	2	3	4
Gradient of slope		<45°	45°~55°	55°~63°	≥63°
Score		2	3	4	5
Gradient of upper slope	reverse	0~10°	10°~20°	20°~30°	≥30°
Score	0	2	3	4	5
Distance to the road	≥4m	3~4m	2~3m	1~2m	<1m
Score	0	1	2	3	4
Number of steps on the slope	Yes	No			
Score	0	3			
Road shape of slope	Convex	Linear	Slightly concave type	Concave type	
Score	0	2	3	4	
Number of valleys of each slope	0	1EA.	≥2EA		
Score	0	1	3		
Material		Rock	Mix	Soil	
Score		1	2	4	
Weathering grade	Fresh	Slightly weathered (SW)	Moderately weathered (MW)	Highly weathered (HW)	Completely weathered (CW)
Score	0	3	5	7	9
Geological structures	reverse	Erratic	Parallel	Coincident	
Score	0	2	3	5	
Ground water	Dry	Damp	Wet	Dripping	Flowing
Score	0	1	2	5	8
Intensity of daily rain	None	<100mmm	100~200mm	200~300mm	≥300mm
Score	0	3	5	7	8
LS Identification	None	Sallow	Depth (rock)	Depth (soil)	
Score	0	2	5	5	
Length of Landslide		<20m	20~50m	50~100m	≥100m
Score		1	2	3	4
Height of Landslide		<10m	10~20m	20~50m	≥50m
Score		1	2	3	4
Depth of the soil layer at the main scrap	<0.5m	0.5~1.0m	1.0~2.0m	2.0~3.0m	≥3.0m
Score	0	2	3	4	5
Mass of rock released	None	Little	Medium	Much	
Score	0	2	4	5	
LS History	None	Rock slide	Landslide (Not affected)	Landslide (affected)	
Score	0	3	5	7	
Countermeasure (CM)	CM (new technology)	CM (type 3)	Half-CM (type 2)	temporary (type 1)	None
Score	0	1	3	4	5
Evaluation of Inspector	None	Low	Normal	High	
Score	0	1	2	3	

Fig. 9 Survey sheet for landslide collecting data and item and score of relative factors for landslide risk assessment. (left) and the matrix of score evaluation of causative classes. (right)

earthquakes, and both. It can also measure the shear displacement and pore pressure, as well as the mobilized shear resistance during shearing (Figs. 10 and 11).

The ICL-2 has six main components, including (1) Computer control system, (2) Main control unit for control and monitoring, (3) Instrument box, (4) Power supply box, (5) Pore-water pressure control unit with backpressure unit, and (6) de-aired water and vacuum system. The overview of ICL-2 is shown in Fig. 10.

The important improvement of ICL 2 compared to previous models is the sample box with 100 mm inner diameter, 142 mm outside diameter, and the largest sample height of 52 mm to create a shearing area of 79.79 cm^2 and Max. shear speed (cm/s) of 50 cm/s and the Max. Pore water pressure and the Max. normal stress up to 3000 Kpa. ICL2 is capable of simulating undrained shear state, pore-water pressure control state, and monitoring earthquake state.

After ICL-2 donated version has been completed, it has been tested by Vietnamese long-term and short-term trainees for around two years. All trouble sources were solved, and all trainees had the confidence to use ICL-2. Manuals via video

Table 1 The principles of assessing the hazard level of Landslides

Hazard level-Features	Hazard level							
Features	V	IV	IV	III	III	III	II	I
Discontinuity Direction	X	X	X	X				
Wethering	X		X		X			
Groundwater	X	X				X		

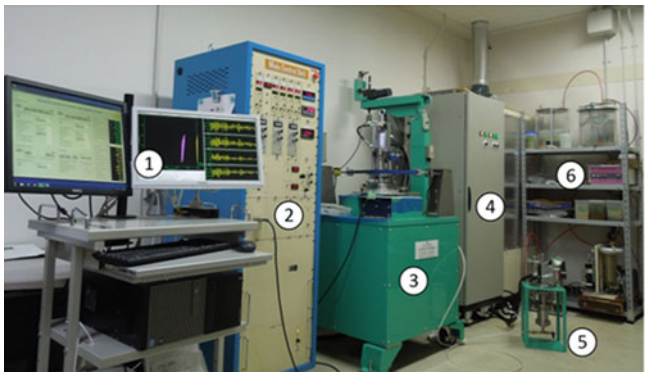

Fig. 10 Undrained dynamic loading ring shear apparatus ICL-2

and written materials were developed for use by future trainees. The video manual made by ITST is included in Landslide Dynamics: ISDR-ICL Landslide Interactive Teaching Tools.

3.2.2 Mastering the Use of the ICL2 and Applying it to Study Rapid Landslides in Vietnam

The ICL2 ring shear apparatus is single-piece production equipment that is relatively complex and highly costly. To efficiently operate the device and apply it to study rapid landslides in Vietnam, understanding its structure, comparing its performance with other devices, conducting practical tests, and building operating instructions were required by the MOT.

After 2 years of experience on the ICL2 device, long-term and short-term Vietnamese trainees made some comparative comments on the improvement of ICL compared to previous devices as following (Fig. 12).

The new high-pressure undrained ring shear apparatus (ICL-2) is used to simulate the undrained shear behavior of soil under all kinds of loads such as minimum normal stress: 300 kPa (corresponding to a depth of 15 m) to a maximum of 3000 kPa (corresponding to a sliding surface depth of 100–200 m), at the maximum shear speed of 50 cm/s. It can create a large shear displacement (such as 5–20 m shear displacement) necessary to measure the shear strength during the motion of landslides. It is quite different from the direct shear test and the triaxial test with shear displacement being less than a few centimeters to 10 centimeters.

Another advantage is ICL 2's ability to create pore pressure and monitor up to the Undrained test. High-speed landslides are the result of high-pore water pressure mobilized during motion. To measure pore water pressure during movement, a prerequisite is the ability to hold the pore pressure generated in the shear box/cell. This feature cannot apply to Direct shear, Triaxial tester, and conventional ring shear tester.

The new high-pressure undrained ring shear apparatus (ICL-2) with more advanced features than the old ones. The normal stress loading system is the biggest improvement of the ICL-2 device compared to the DPRI devices. The normal stress loaded from a long frame above the shear box in DPRI devices is replaced by pulling the center axis of the shear box on the ICL-2. The deformations of the preload during stress changes are very small on ICl-2, giving better resistance to drainage. The next difference in the ICL and DPRI series of machines is the waterproof rubber ring. The rubber ring of all DPRI devices is firmly attached to the cutter box. The thickness of the adhesive layer must be uniform and the height of the rubber ring top faces of the inner and outer rings should be equal to maintain the undrained condition. They must have an extremely smooth surface, which requires high technology to be manufactured. In the ICl series, the rubber ring is compressed by a Teflon ring and held in place by a metal ring with screws attached. It is therefore not necessary to be as smooth as the rubber rings used in the DPRI series of machines.

The difference between the ICL-1 and ICL-2 devices is the normal stress and shear speed. The maximum shear speed of the ICL-1 device is 5.4 cm/s and the maximum shear speed of the ICL-2 device is 50 cm/s. The maximum normal stress and resistance to drainage of ICl-1 are 1 MPa while that of ICL-2 is 3 MPa.

Currently, for other common tests, it is not possible to determine the residual shear resistance value of the soil. So when it is only necessary to test the soil in a non-destructive state, other common tests such as Direct shear, Triaxial tester as well as Conventional ring shear tester can be used. After failure, it is necessary to determine the parameters of the soil using the ring shear test.

ICL2 ring shear apparatus plus LS-RAPID simulation software are effective tools to study the mechanism of movement and assess the risk of large-scale landslides.

3.2.3 Elucidation of the Initiation Mechanism of the Landslide

ICL2 was applied by Lam Huu QUANG and other Vietnamese engineers to test the samples taken from drilling in the Hai van Station and succeeded to test those samples. This is the world's first successful application of the undrained dynamic-loading ring-shear apparatus to test samples taken from the potential sliding surface found from the drilled cores in the precursor stage of Landslides.

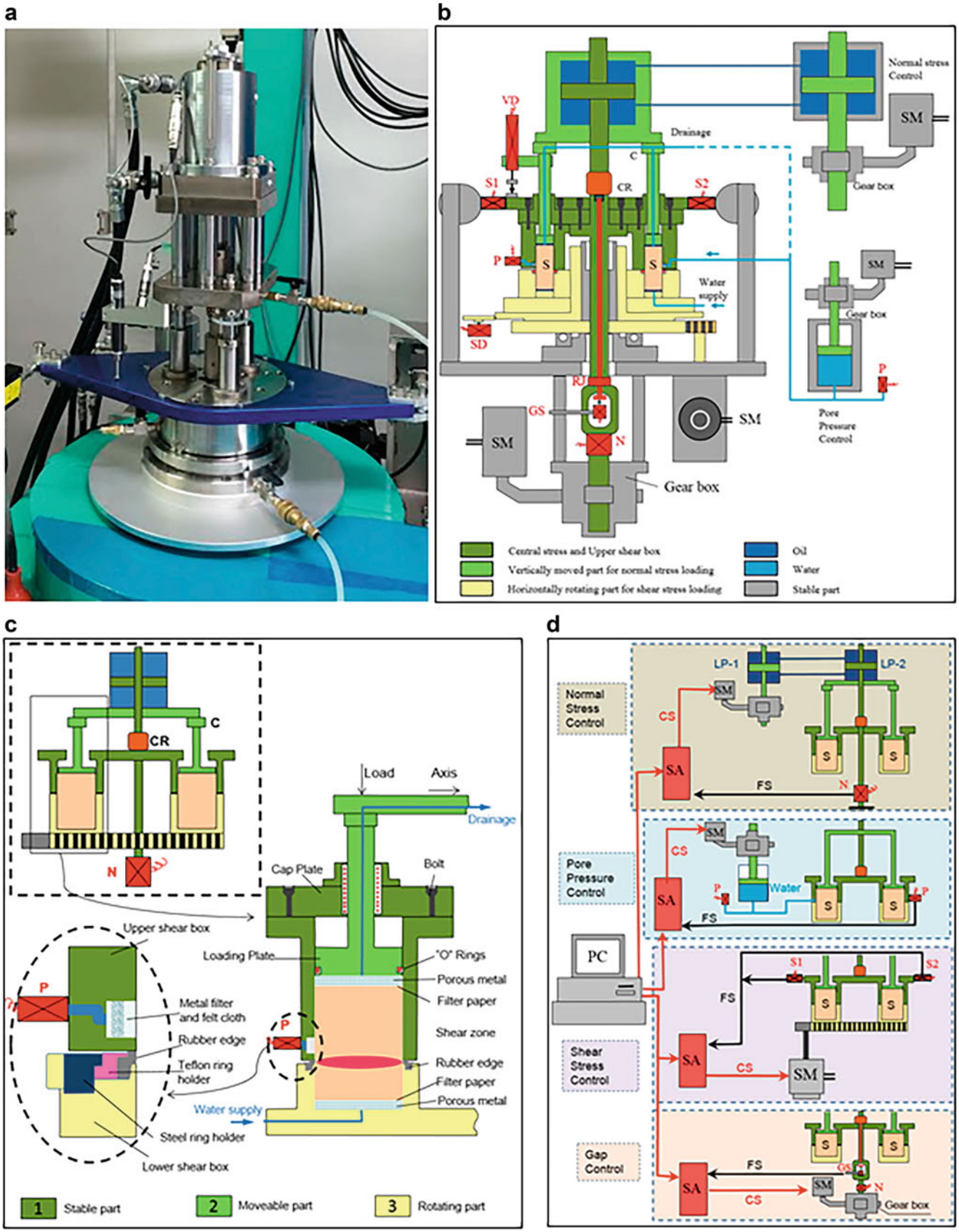

Fig. 11 The design and construction of RSA (ICL-2). (**a**) Photo of the main apparatus. (**b**) Mechanical structure. (**c**) Close-up view of the shear box and sealing. (**d**) Servo-control system for Normal stress, shear stress, pore pressure, and gap. Red arrow: control signal. Black arrow: feedback signal. The blue line is for water control

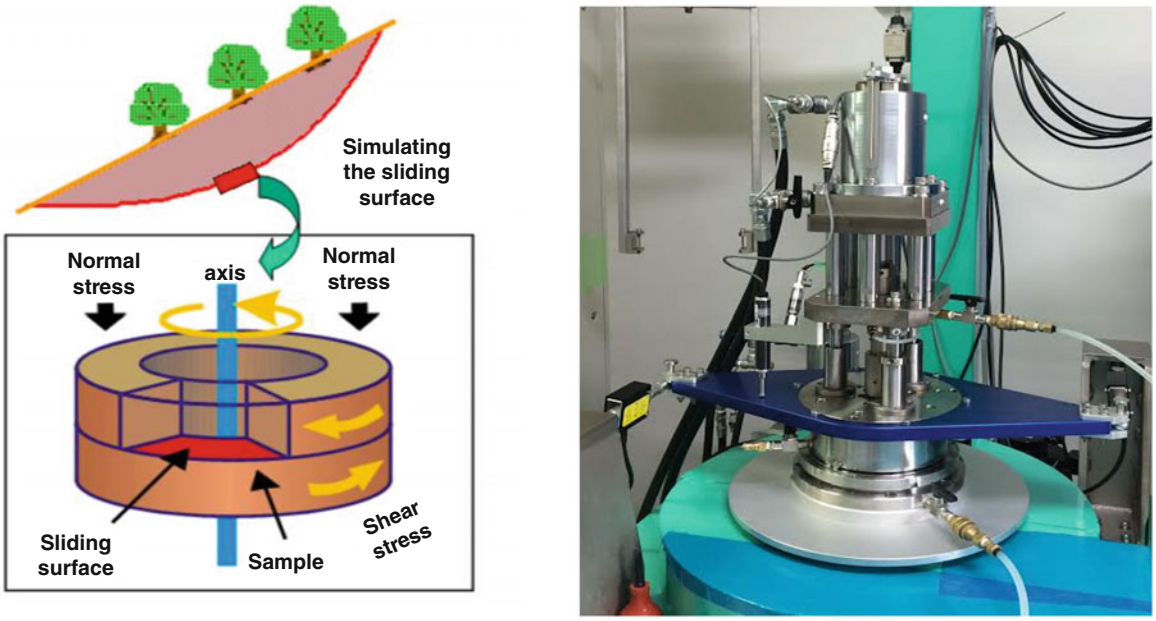

Fig. 12 Shear operation principle (left) and a shear box of Undrained dynamic loading ring shear apparatus ICL-2 (right)

This research applied the undrained dynamic loading ring shear apparatus ICL-2 to drill-core samples from the precursor landslide. Samples for ring shear tests were taken from sandy soil layers of cores found at depths of ~21, ~31, and ~ 50 m, which were considered as possible landslide slip surfaces.

The inclinometer monitoring detected slight movement at about 50 m depth, where the boundary between highly weathered granitic rock and weathered granitic rock was identified. The test was carried out for this in 3 models: Drained Speed Control Test, Undrained Monotonic Stress Control Test, and Pore Water Pressure Control Test (Figs. 13, 14 and 15).

3.2.4 Development of Hazard Assessment Technology for the Precursor Stage of Landslides (Using ICL Result and LS Rapid)

The dynamics of post-failure motion of the Haivan landslides and the development of hazard assessment technology for the precursor stage of landslides have been carried out to predict its influence on the national railway which locates on the toe of the landslide body. After considering the level of risk, the slip surface at the 50-m-depth was selected as the target (Fig. 16).

LS-Rapid is an integrated Landslide Simulation Model, which can simulate the initiation and motion of landslides triggered by earthquakes and rains. Calculations are made using the steady-state shear resistance measured by the undrained ring shear apparatus.

According to Fig. 15, a vertical column is considered within a landslide mass. The model calculated the discharge of X and Y direction (M, N) and the height (h) of soil mass by assuming that the balance of all forces acting on this column (Self-weight (W), Seismic forces, Lateral pressure, Shear resistance including the effect of water pressure) will accelerate the soil mass (m) by acceleration (a) on the horizontal plane(1) and the discharge flowing into the column is the same with the change of the height of soil (2).

The landslide dynamic parameters obtained from the ring shear test of the 50-m-deep sample were used in an integrated numerical simulation model LS-RAPID. The simulation result (Fig. 17) gave the critical pore-pressure ratio for landslide occurrence, the landslide's likely maximum speed, total volume, and depth of landslide debris that could cover the railway. The displacement activation parameters of the sliding block and the predictive model results contribute to the consideration of establishing a railway safety system at Hai Van through monitoring and early warning.

3.3 Monitoring Sensitive Parameters on Landslide Sites and Developing an Early Warning System

3.3.1 Investigation of Active Landslide for Selection of Pilot Monitoring Site

To evaluate risk and develop early warning systems based on landslide monitoring, the selection of a suitable site is very important for study and monitoring equipment setting. With

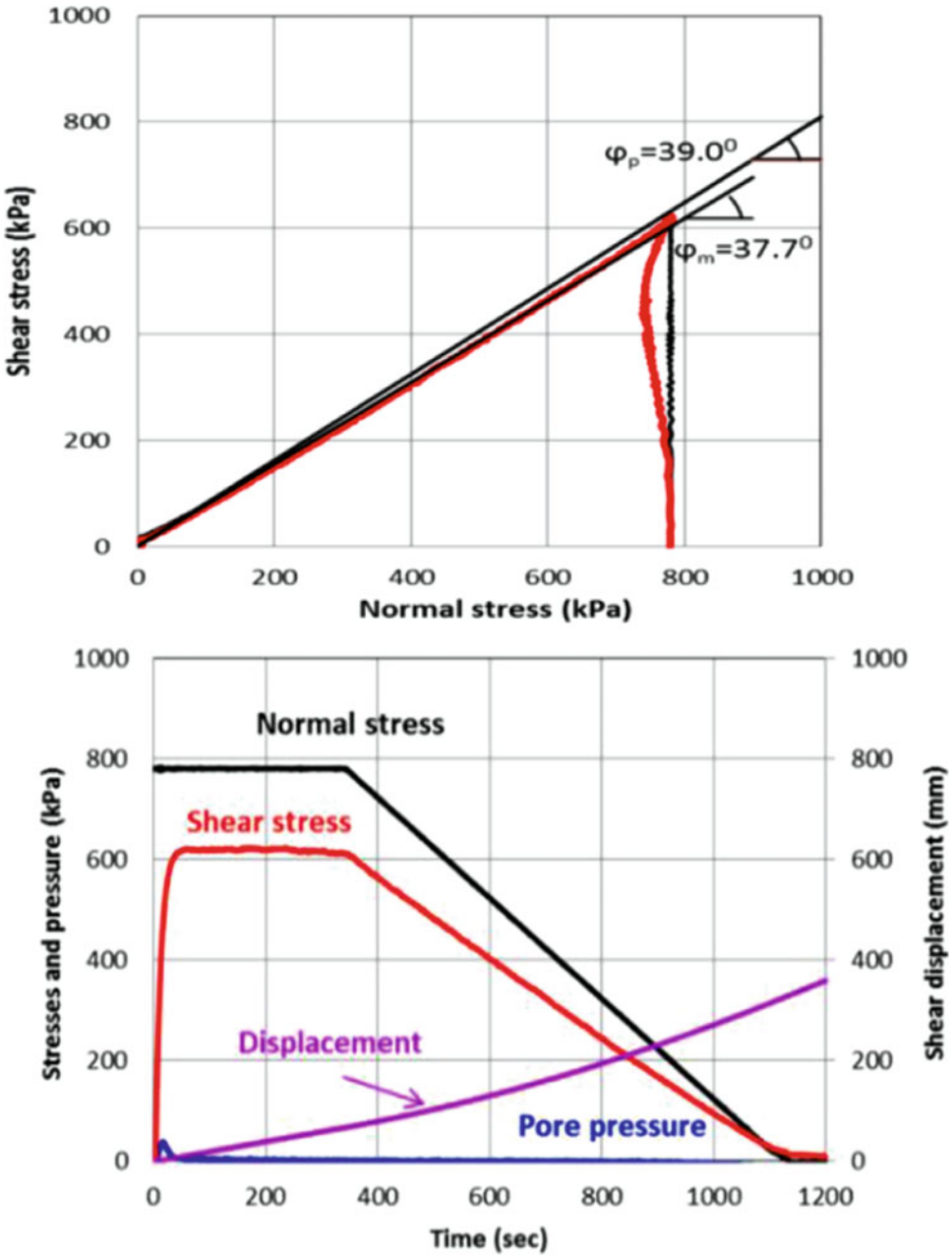

Fig. 13 Model 1 Result—Drained Speed Control Test. Saturated sample, Consolidation to close 780 kPa; the Shear speed at 0.2 cm/s in the drained condition (Quang et al. 2018). After the shear surface reached peak shear resistance, the drained normal stress was reduced to zero at a rate of $\Delta\sigma = 5$ kPa/s. The peak friction angle and friction angle during motion remained = at 39.0°

criteria required for study such as large scale, deep seat, and active landslide, the Haivan landslide had been considered the most suitable site (Fig. 18).

Hai Van is a particularly important area on the North-South railway line, located in the central region. Hai Van railway station is located at a low position on the mountain-side of Bach Ma mountain range overlooking the sea. The site has a particularly complex geological structure with a strongly weathered granite origin. Every year, this location receives a very large amount of rain (over 3000 mm/year). Slope damage has occurred along the railway line through this area, causing significant damage to Vietnam Railways Corporation. The area is still a potentially high-risk area for landslides.

In terms of geomorphology, the ridge area behind Hai Van Railway Station has the topography of a landslide that happened in the past. Over time, with the weathering and erosion, the growth of plants in the area has erased part of the landslide identity. Aerial photo interpretation and topographic maps of the area indicate that the area has a topographical shape of a deep-seat landslide with a wide range (1.5 km width, 1.6 km height). The top of the area has a horseshoe shape with a large main sliding scarp which was divided into 2 sub-scarps.

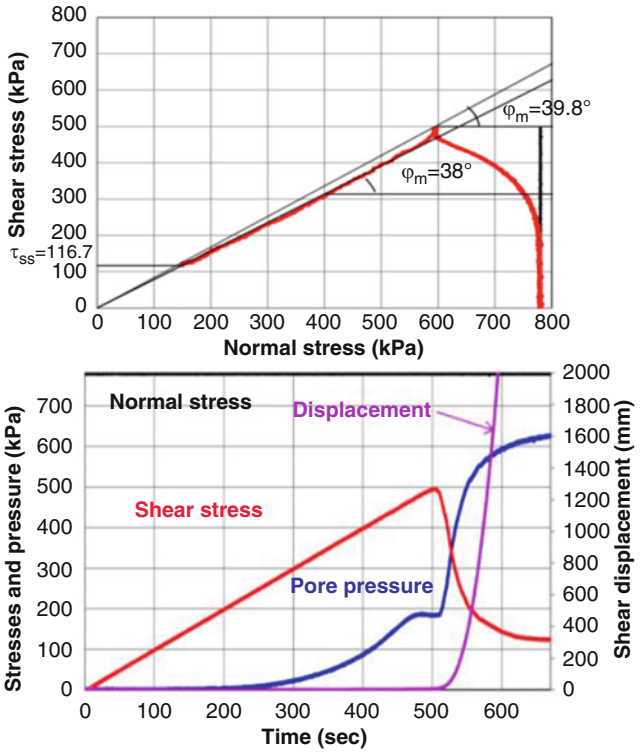

Fig. 14 Model 2 Result—Undrained Monotonic Stress Control Test (Quang et al. 2018). Saturated sample, Consolidation close to 780 kPa; Increase the shear stress value with rate $\Delta\sigma = 1$ kPa/s. The peak friction angle and friction angle during motion remained = at 39,80

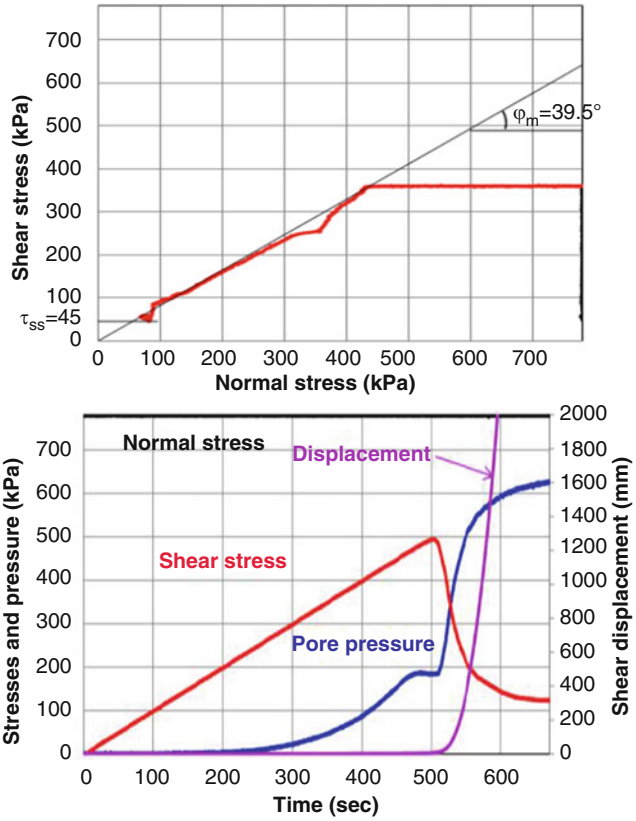

Fig. 15 Model 3 Result: Pore Water Pressure Control Test. Saturated sample; Consolidation to close to: σ:780 kPa, τ = 360 kPa; Increase the pore water pressure value with rate $\Delta\sigma = 1$ kPa/ s. The peak friction angle = friction angle during motion remained = at 39,90. Ru = u/σ = 360/780 = 0,46 (Quang et al. 2018)

The actual site survey results lead to the conclusion that this area has a large sliding block—a product of strongly weathered granite that has moved from the original position of the slope, leaving large and small scarps on the upper slope, and creating a landslide body at the bottom of the slope. The later internal magnetic analysis also confirmed the above statement (Fig. 19).

The landslide body was divided into secondary sliding blocks with widths from 50 m to 100 m. Figure 18 (left) shows a Landslide identification map in the Hai Van area. The Secondary sliding blocks B1, B2, B3, and B4 are located on the body of a deep seat landslide, in which reactive signals such as small deformation cracks were found along sections A-A of the B3 block. The national railway runs through the body deep seat landslide and sliding block body. The surface displacement broke the structure of the protective stone roof protection structure and pushed the railway out of its horizontal position by 20 m in 2007.

Drilling and sampling of the intact coaxial cavity were carried out for the geological survey. At the center of the landslide body, three boreholes were made with a depth of 30, 60, and 80 m. The results of stratigraphic distribution indicate that the main geological products are granite and weathered granite with different degrees of weathering. From a depth of 0 to 51 m, the geology is a gravel-sand mixture caused by strongly weathered granite and unfinished granite cores. Notably, from 0 to 12 m, the degree of weathering is very intense, to which some weathered part easily breaks by pushing it with one's finger.

From 51 to 54 m depth, a layer of weathered fine Granite with white granite composed of feldspar, quartz, muscovite and trace biotite solid with crack was found. From 54 to 80 m, the geology of the area is granite bedrock with the distribution of leucocratic migmatite, granite, gneiss, and melanocratic migmatite rocks respective to the increasing depth.

The experience of landslide identification, the result of site surveying, drilling, and sampling at Hai Van identified the overview of large-scale landslides with a potential depth of slip surface of 51 m and secondary sliding blocks with a potential depth of slip surface of 10–12 m. For risk evaluation, the evidence of the slip surface needs to be made clear before testing its samples for the Elucidation of the initiation mechanism and the dynamics of post-failure motion of the targeted landslides. Hai Van landslide is considered a standard example for surveying to evaluate landslides, especially large-scale landslides in Vietnam.

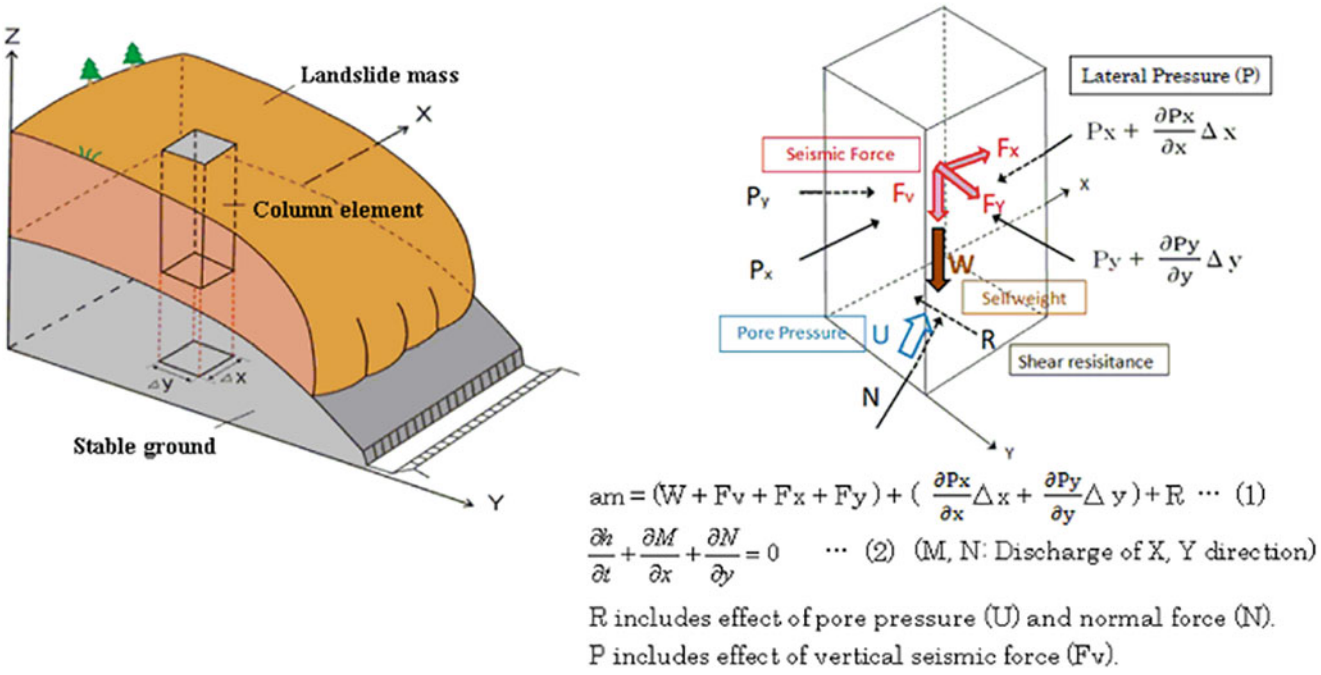

Fig. 16 Integrated Lanslde Simulation Model -LS-rapid. (Sassa and He 2012

3.3.2 SP Drilling Method, Slide Surface Assessment, Measurement of the Groundwater Table

The purpose of the geological survey at Hai Van is not only to collect samples for testing but also to install monitoring devices in the borehole to assess the state of the sliding block, accurately detect the slip surface, and monitor groundwater level.

The Hai Van Landslide area's geological features include deeply weathering rocks, and expectations were that it would be difficult to do drilling work and retrieve high-quality core samples there. The SP method was adopted as it made it possible to do drilling work with the drilling equipment and personnel in Vietnam. The difference from conventional drilling methods is that this drilling method uses sleeve-incorporating double core barrel and diamond bits, which make it possible to extract the core from loose layers as gravel and sand mixed with gravel. At the same time, this technology of drilling was attempted to transfer to Vietnam.

Geological drilling for the sliding surface survey at Hai Van was carried out at the center of the landslide body with a depth of 30, 60, and 80 m. Lithologic description, Drilling samples, and position of drilling holes on the profile section of the Haivan landslide are presented in Fig. 20. The objective of drilling for the sample is to take uniform drilling cores for detecting the depth of slip surface, aquifer, fractured and weathered geological layers as well as bedrock through observation and evaluation of stratigraphic distribution layer from the cores as well as to mechanically test parameters of soil and rock such as grain size, water content, volumetric weight, limit Atterberg, shear strength. Survey drilling results indicate 2 suspected zones at 10–12 m depth, where its uniaxial compressive strength and level weathering change, and at 50–51 m depth, where a weathering boundary between crushed sand and gravel and hard granite bedrock appeared. These zones are believed to have a high potential for locating slips surface of the Haivan landslide.

For determining the slip surface, relying on the results of the geological drilling survey is inadequate. The inclinometer device installed in the 80 m depth borehole to evaluate the horizontal deformation is an effective method to confirm the displacement position of the sliding block in depth.

The inclinometer horizontal displacement measurement results for Hai Van Landslide as an example are presented in Fig. 20, which showed 2 zones in depth (10–12) and (50–51 m) corresponding to the level conversion of weathering from strong to weak weathering and from weaky weathering and hard granite bedrock, respectively. The horizontal displacement results confirm that the slip surface prediction based on the geological core drilling results is reasonable (Fig. 21).

For groundwater level monitoring, the Groundwater pressure gauges were installed in 30 m and 60 m depth boreholes.

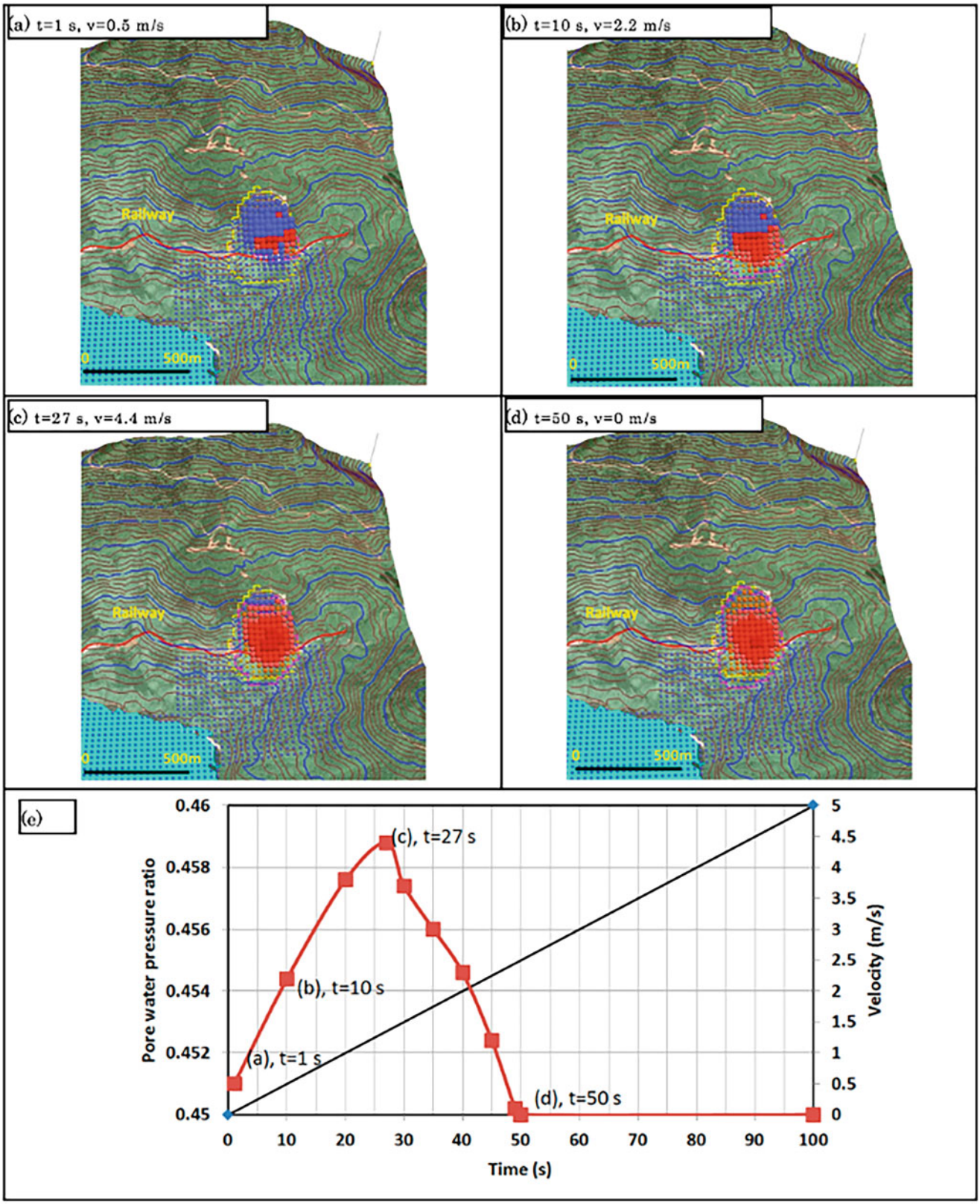

Fig. 17 Simulation integrated results of Time and Velocity displacement and Pore water pressure ratio of the Haivan landslide (Quang et al. 2018)

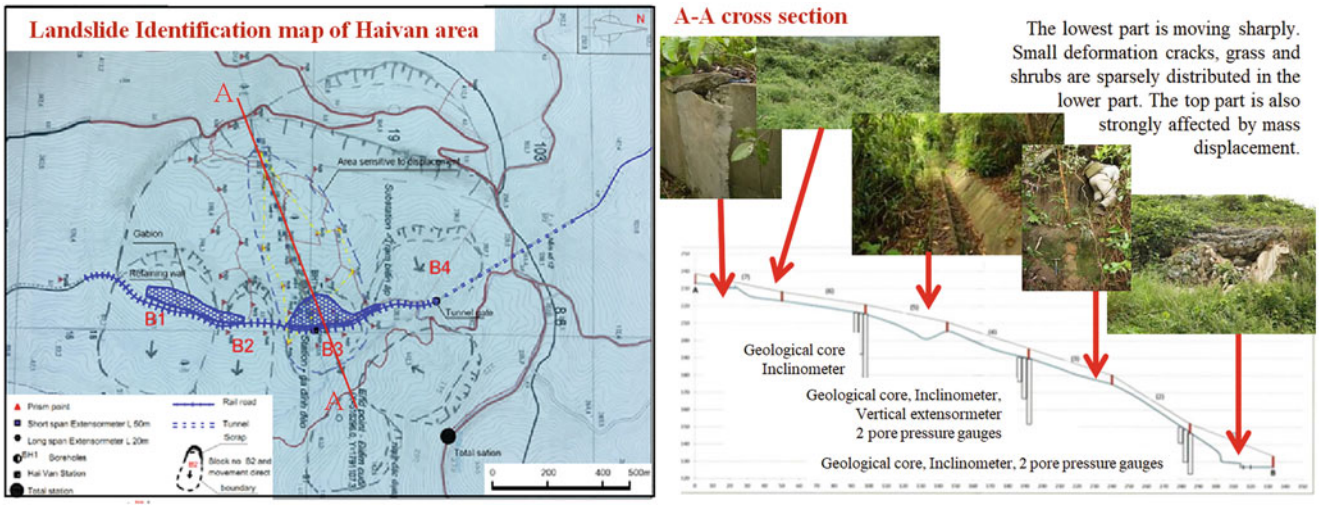

Fig. 18 Landslide identification map in Hai Van area

Monitoring Position of groundwater on the profile section of Haivan landslide and Initial Monitoring data of rainfall, the groundwater table is presented in Fig. 22. Initial Monitoring data showed the sensitive relationship between groundwater table and rainfall, which is considered a potential cause to trigger the landslide movement.

3.3.3 Development of the Integrated Automatic Monitoring System for Rainfall-Groundwater-Slope Movement

For the study of the actual performance of the sliding block, the monitoring system is set up to monitor the movement of the sliding block through representative indicators such as precipitation, surface displacement, displacement within the sliding block, and groundwater level to verify in-room studies and early warning establishment.

In the Hai Van area, an integrated, continuous monitoring system, time synchronization, and automatic data transmission have been established. The location of each device is designed depending on the characteristics of each. Device. The number of devices is shown in Table 2 below. The layout diagram of monitoring equipment of the Long span Extensometer of the monitoring equipment is shown in Fig. 23. The entire system of equipment is powered by a solar battery system. Field monitoring data can be transmitted directly and in real time to the monitoring center in Hanoi.

The results of integrated monitoring between accumulated rainfall, groundwater height, and actual surface displacement are established in Fig. 24. The signs of the increase in

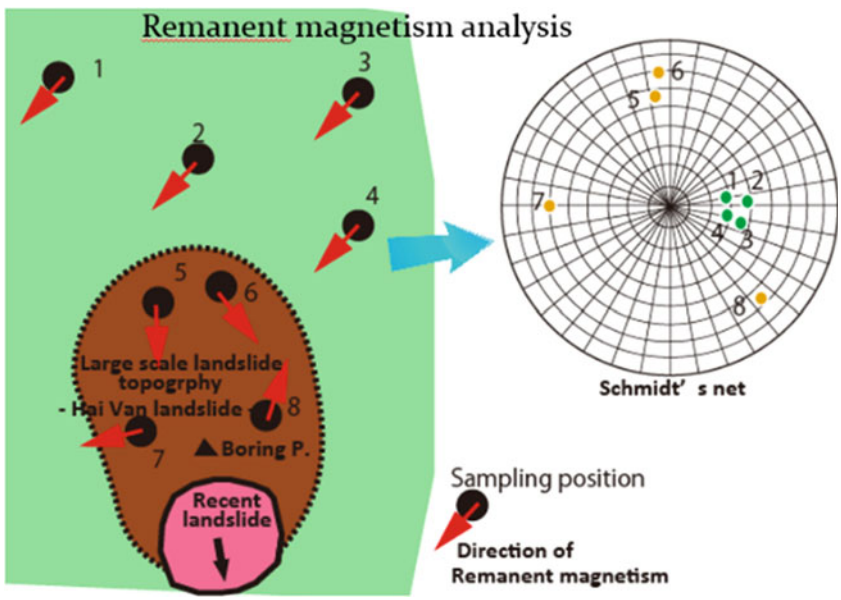

Fig. 19 Results of Remanent magnetism analysis in Hai Van area (Abe et al. 2018)

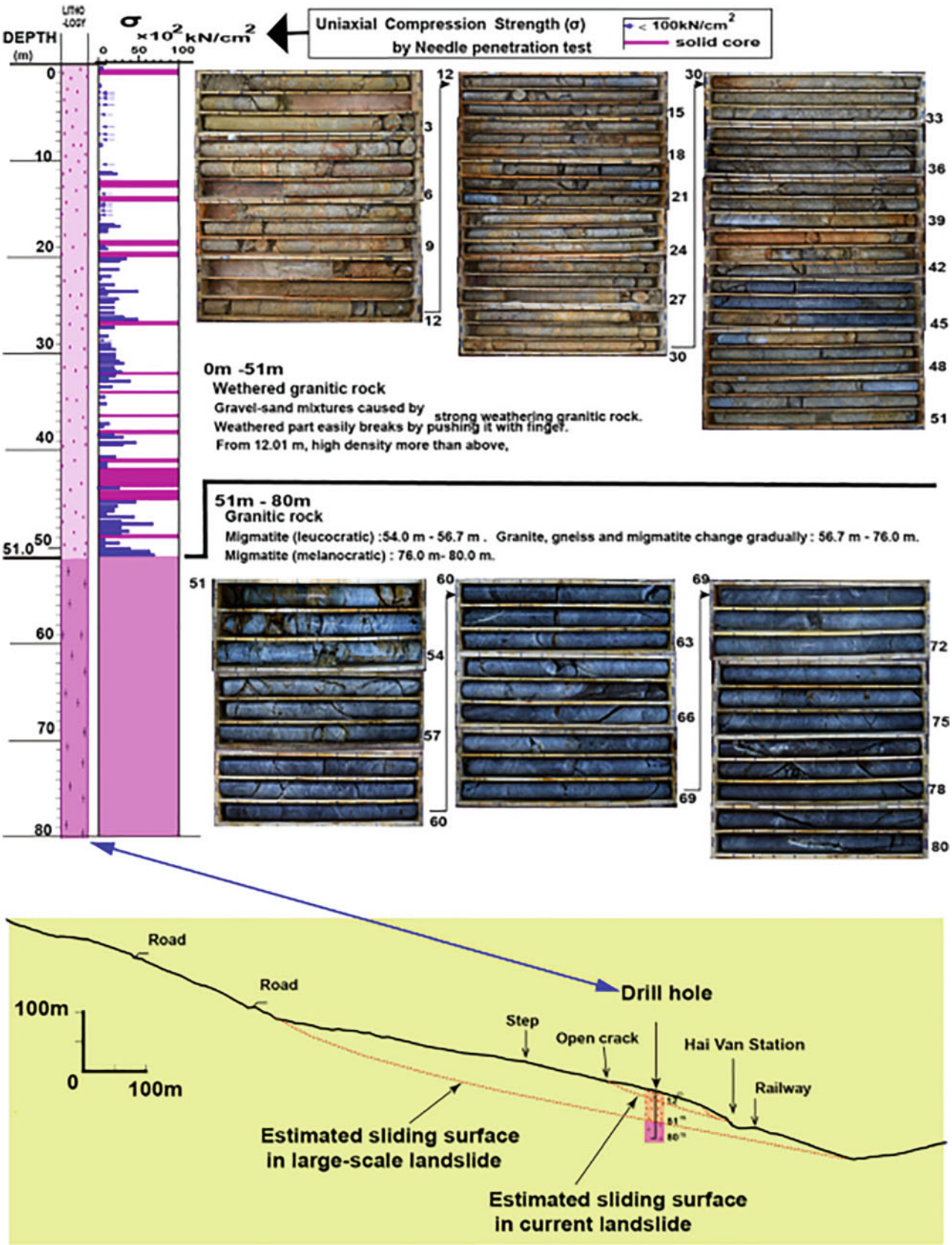

Fig. 20 Geological column, drilling samples, and position of drilling holes on the profile section of the Haivan landslide (Abe et al. 2018)

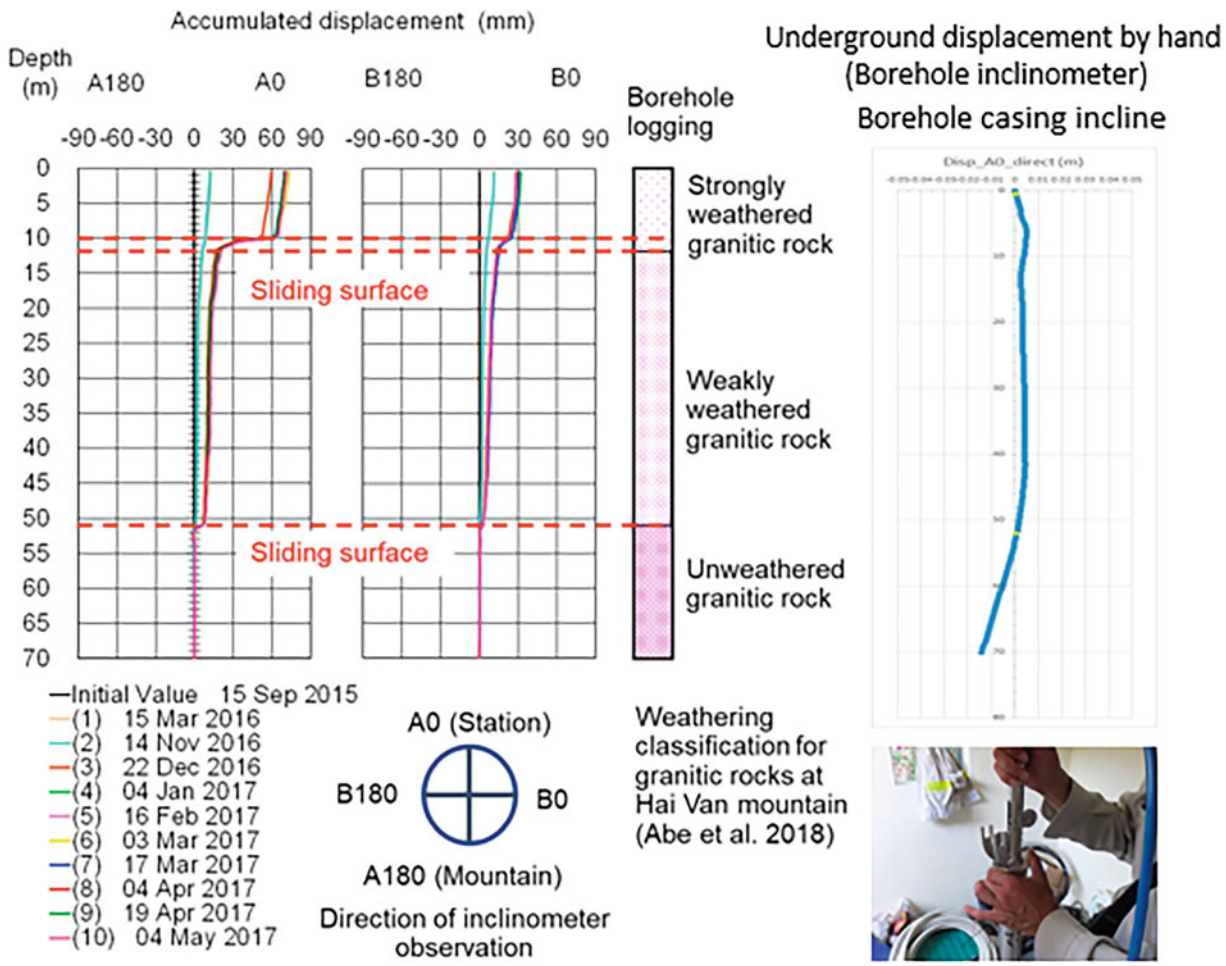

Fig. 21 Monitoring data of borehole inclinometer (Manual –periodical and automatic ones) from September 2015 to May 2017 and borehole logging (Do et al. 2021)

displacement are consistent with the increase in groundwater level which was predicted.

3.3.4 Principle for Landslide Early Warning System Establishment

Landslide early warning is generally understood as the recognition of the beginning of sliding block movement through the values of the predicted motion trigger parameters. To implement early warning effectively, it is necessary to have a reliable landslide forecasting model and the monitoring and measurement of trigger parameters accurately. Depending on the landslide characteristics and forecasting model, the monitoring indicators will be selected and divided into different warning levels such as safe, dangerous, and especially dangerous.

With the advancement of technology, monitoring and measuring with accuracy using modern equipment for relevant parameters such as surface displacement, groundwater level, deformation, and precipitation can be carried out in an integrated and real-time manner. The arrangement of the Hai Van monitoring system is a vivid and complete example of this monitoring system.

The results of topographical, geological and, groundwater surveys at Hai Van have shown that the Hai Van Landslide is a large sliding block with a sliding surface at depth (50–51 m) and its landslide body was divided into 4 secondary blocks with shallow slide surface as (10–12 m). The results of the deformation measurement in the borehole also show signs of displacement at both 51 m and 10 m depths. Therefore, to establish an early warning system, the displacement possibility of both sliding blocks was considered.

To determine the sensitivity parameters to the displacement of large-scale, deep seat landslide, the soil sample of the drilled core at 51 m depth was tested, using ring shear ICL2, and its results were used in the integrated numerical simulation model LS-RAPID.

Results of susceptibility assessment of the precursor stage of a threatening landslide at Haivan Railway Station,

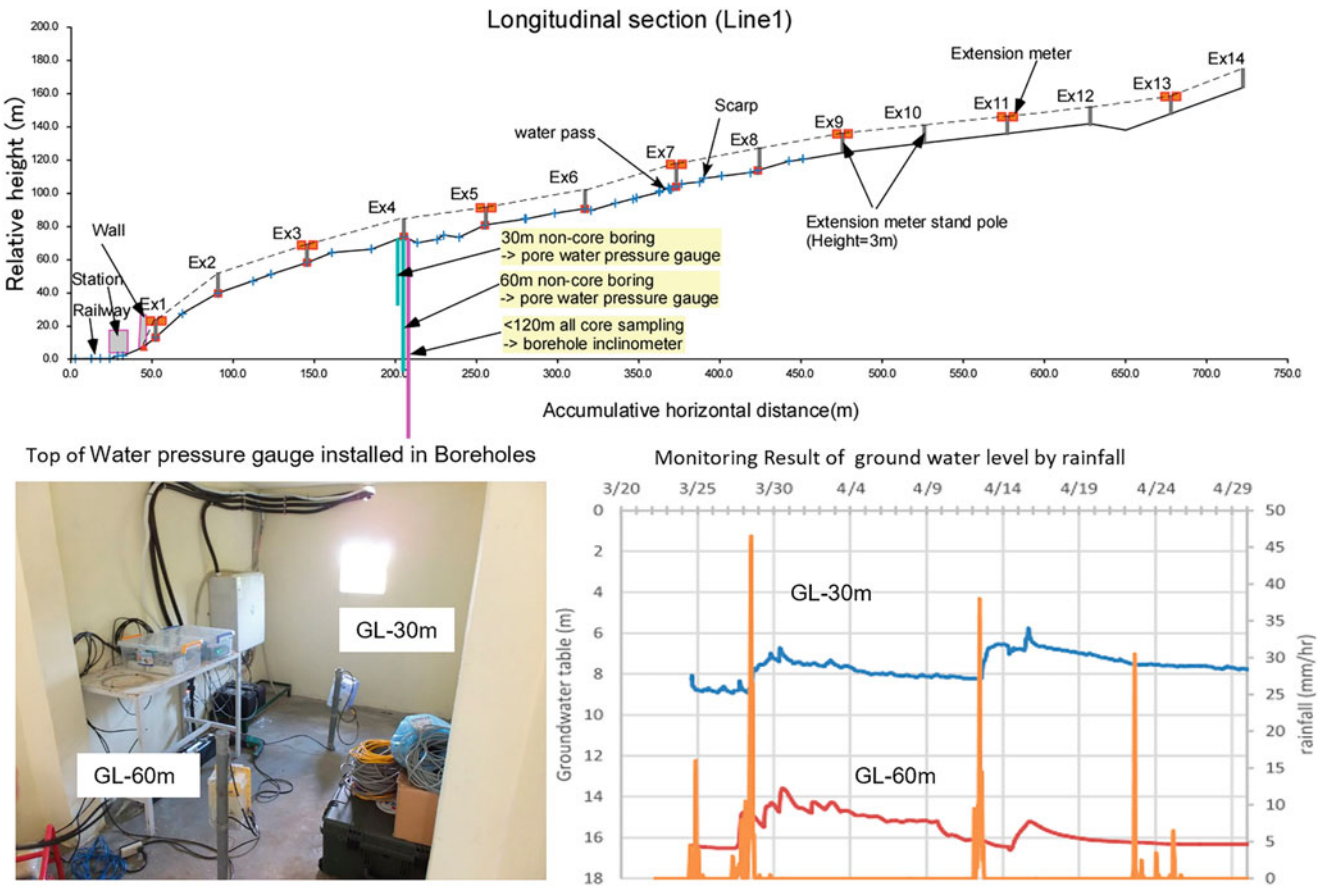

Fig. 22 Monitoring Position of groundwater on the profile section of Haivan landslide and Ini tial Monitoring data of rainfall, groundwater table

Vietnam have shown that the pore-water pressure corresponding to the height of groundwater in the borehole can be used as an important monitoring parameter for early warning (Quang et al. 2018). The value of the height of the groundwater level rising 14 m to the borehole mouth in Fig. 25 is the key value that activates the sliding block to start moving.

Landslide experiments on flume slope with artificial rains and in the lab were conducted to study the displacement mechanism of the shallow sliding block at Hai van, and to predict the sensitivity parameters for the displacement of the sliding block to establish early warning systems.

Soil samples were taken from the body of the large slip block at the site for simulation experiments with different rainfall levels. During the experiment, the relationship between the displacement of the slope surface and the change in groundwater level of the soil layer was continuously monitored and recorded.

Before the slope is demolished, the displacement velocity of the soil mass increases very quickly. The image of the Landslide experiment on natural slopes with artificial rains

Table 2 List of Monitoring Devices Hai van landslide

Monitoring indicators	Monitoring Device	No.
Surface displacement	Electronic total station and prism	40
	GNSS	2
	Long span Extensometer (Lex)	14
	Short span Extensometer (Sex)	5
Hor. Deformation in-depth	Inclination measuring device (Inclinometer)	1
Groundwater table	Groundwater pressure gause	
Vertical deformation	Vertical Extensometer (Vex)	2
Climate	Measure rain, temperature, wind speed, air pressure	1

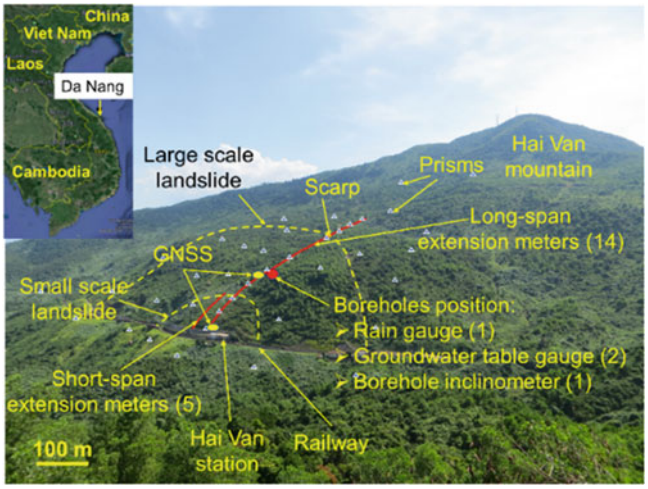

Fig. 23 Monitoring data of long-span extension meters, short-span extension meters, groundwater tables, and rainfall from June 2016 to May 2017 (Do et al. 2021)

from the beginning stage and ending stage of the moving process is presented in Fig. 26. The sliding block gradually changes state from a steady state, with small cracks appearing, to cracks opening, to rapid movement down the slope, and at the end of the movement. The measured displacement velocity is proportional to the precipitation and the slope displacement. Figure 27 presents a result of displacement, accumulated precipitation, and the reverse velocity value over time. For this test, the inverse of displacement velocity by time was created, and accumulated rainfall at the inverse velocity of Zero was used as a sensitive parameter for displacement prediction.

Due to the characteristics of Vietnam's North-South railway going through the affected area of large and secondary landslides, the movement of one or both landslides at the same time will hurt the railway. Under the same triggering conditions due to heavy rain, the hurt in the borehole and accumulated rainfall are used as key parameters for early warning.

3.4 Other Achievements

3.4.1 ITST-ICL Guideline for Landslide Risk Assessement

ITST-ICL guideline for landslide risk assessment is a set of standardized documents intended to guide the survey, assessment, and prediction of landslide risk.

This set of guidelines is the result of the Technical Cooperation Project named "Development of Landslides Risk Assessment Technology along Transport Arteries in Vietnam", which was carried out by cooperation of ICL and ITST.

The Guideline is in both English and Vietnamese, and was published in 3 volumes: Volume 1-Site survey and landslide risk assessment mapping; Volume 2-Testings, simulations, and software for landslide risk assessment and Volume 3-Monitoring and Experiment landslides by flume combined with artificial rain. The content of the integrated set of guidelines for landslide risk assessment is divided into the following 6 sections with 33 guidelines (GLs), including: (1) Site Mapping and Forecasting, (2) Material Testing, (3) Monitoring, (4) Model testing and (5) Software application. Each guideline is coded as GL xx—2016, compiled in the format of Vietnamese national standards with content covering the name of the guide, abstract, the scope of application, terms, definitions, the main body of the guideline, conclusions, and references. The number and name of the guidelines have presented the Table 3 and Fig. 28.

The development of the landslide integrated guideline is not only useful for research and implementation of the project but also serves as an important reference for students and researchers in landslide risk assessment as well as consultants in assessing the risks of landslides and proposing mitigation solutions. The next step of the project dissemination strategy is to upgrade these guidelines to the basic ITST standard and then to become the Vietnam National Standard (TCVN) to strengthen the development of applied technology nationwide for the prevention and mitigation of landslides in Vietnam.

3.4.2 Developing High-Quality Human Resources for Landslide Research through International Cooperation Projects SATREPS Project

The project "Develop Landslide Risk Assessment Technology along Transport Arteries in Vietnam" is the SATREPS project, formed in 2008, within the framework of the program "Science and technology policy" established by the Ministry of Foreign Affairs through the Japan International Cooperation Agency (JICA) and the Ministry of Education, Culture, Sports Science and Technology (MEXT) through the Japan Science and Technology Agency (JST). The project implementation period is 5 years from 2011 and ends at the end of 2016. The overall objective of the project is to socialize the development of landslide risk assessment technology and develop an early warning system that contributes to the safety of the traffic system in particular and the safety and development of the mountainous community in Vietnam. The project is implemented by the Institute of Transport Science and Technology (ITST) and the International Landslide Society (ICL).

The basic research and training achievements of the project include:

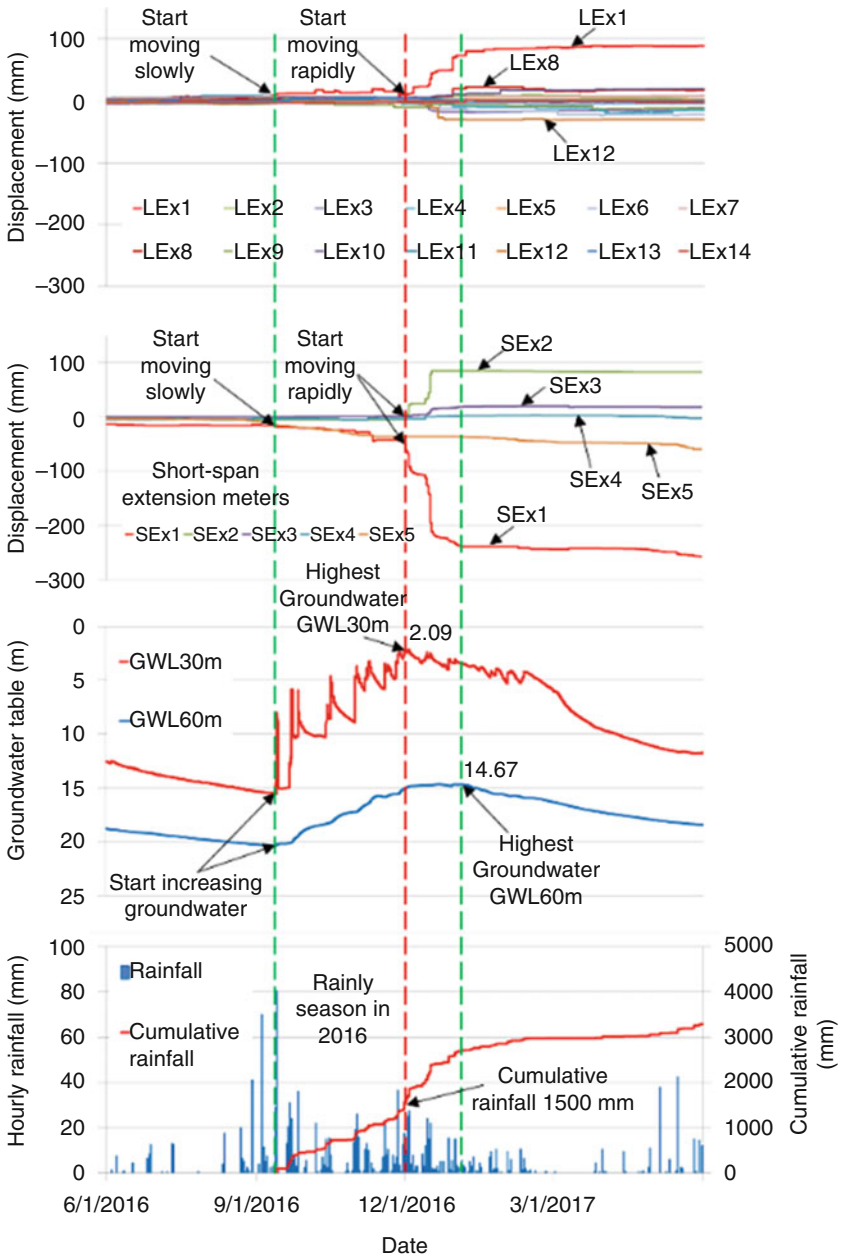

Fig. 24 The results of integrated monitoring in Haivan Landslide (Do et al. 2021)

1. For Human Resource Development for Landslide Research: After finishing the project, 3 PhDs and 5 Masters were trained in Japan and 05 other research students are continuing to study next year.
2. To Landslide risk mapping: Six landslide inventory and risk evaluation maps along Ho Chi Minh road with a length of 60 km, scale (1: 12,000), and Hai Van area map had been established using aerial photo interpretation and site investigation. An evaluation of the sensitivity map for 150 km along the Ho Chi Minh Trail was developed using the AHP method. (Luong et al. 2016; Tien et al. 2016). Aerial photo analysis, combined with pictures taken by UAV to identify landslide spots along Highway 7, (25 kilometers) from Muong Xen to Tam Quang was chosen as the subjects for the setup identifier map (Dung et al. 2016). Recognition conditions of pre-soil through analysis model digital surface (DSM) of the extent of forest cover and others have been developed.
3. To In-room experiment and landslide simulation: to develop investigation and simulation technology of landslide phenomenon, able to apply for slip surface deeper 100 m. (Landslides Magazine—Vol.11, No. 5 in 2014.) The developed ring shear apparatus (ICL II) was revised in 2014–2015 based on the experiences of testing by Vietnamese short-term trainees as well as long- term trainees. (Quang et al. 2018; Tien et al. 2017). Shifting

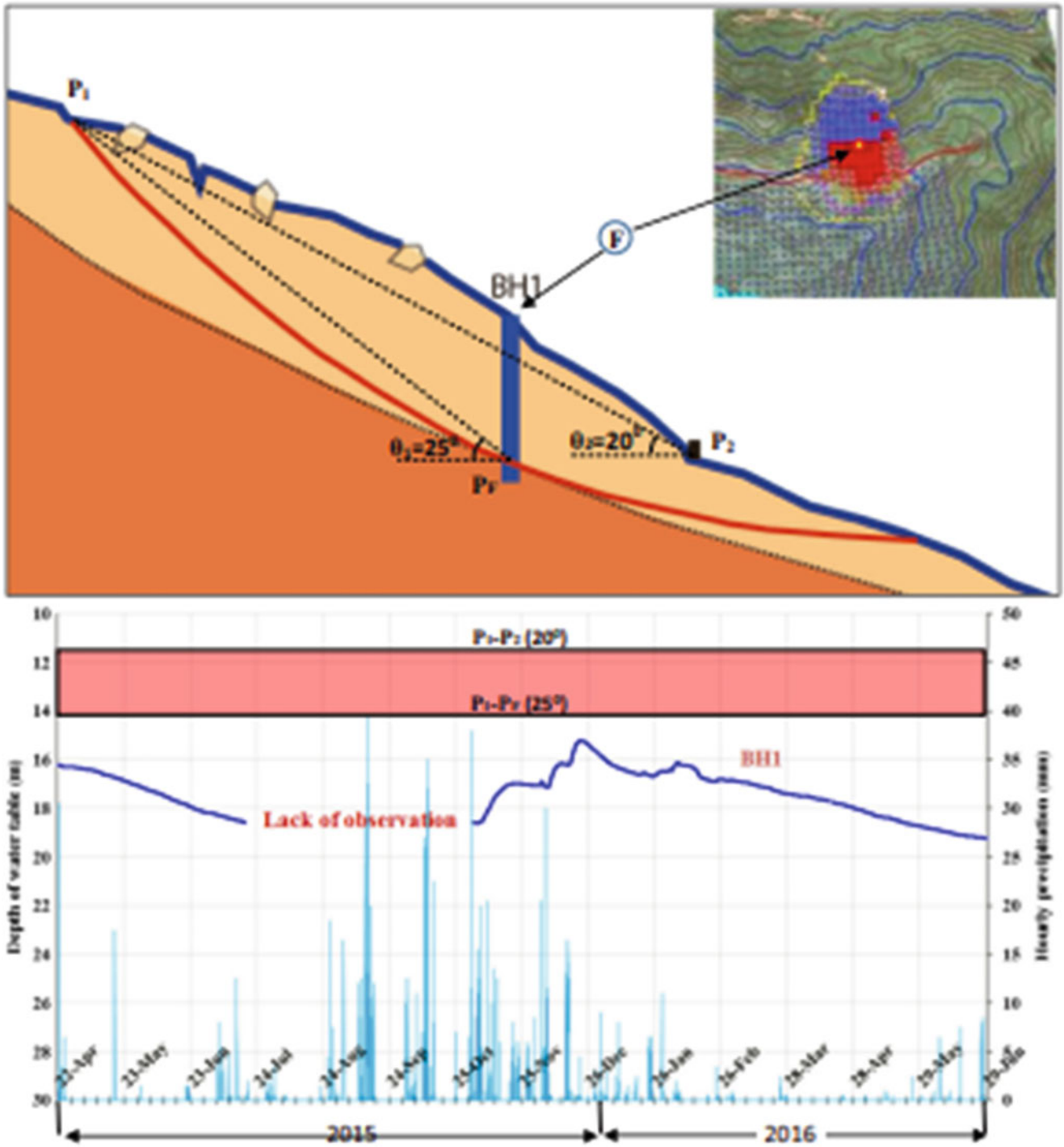

Fig. 25 Result of Forecasting the displacement of the Landslide over time using testing results from ICL2 and LS-rapid model

mechanisms at Hai Van Samples were taken from the ground and the drilled cores at various depths in the Hai van Landslide were tested using ICL-2 and computer simulation was conducted based on the measured parameters by Vietnamese researchers. Adding the function of simulating tsunamis generated by earthquakes is one of the targets of JST research.

4. Setting up an early warning and monitoring system at Hai Van station: Selection Two Landslides and Three boreholes were drilled and sampled in their original form; An integration monitoring system including rain

Fig. 26 The image of the Landslide experiment on a flume slope with artificial rains from the beginning stage and ending stage of the moving process

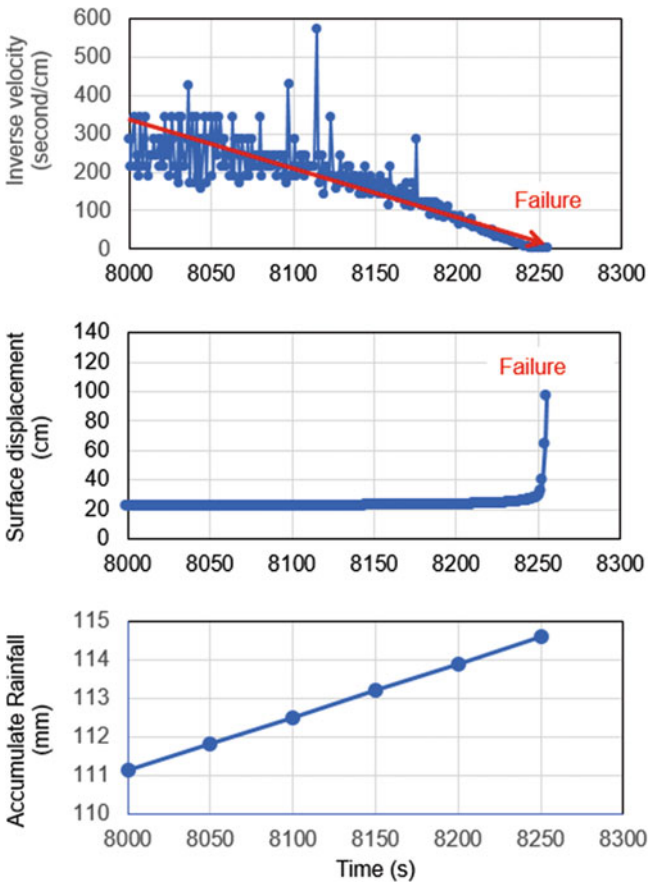

Fig. 27 The result of displacement, precipitation accumulation, and the reverse velocity value over time

gauge, extensometer, inclinometer, total stations, and GNSS are developed here. An automatic data transmission system from Haivan to office projects in ITST and a display system have been set up. This monitoring system can allow monitoring on-site and from real-time remote expressions of sliding blocks.

Landslide chutes, recording systems, and pore water pressure sensors are provided and adapted for ITST experiments. Results of this contribute to the landslide early warning principle.

3.4.3 SAKURA Science Program

The program is implemented by Tohoku Gakuin University and the Institute of Transport Science and Technology under the sponsorship of the Japan Science and Technology Agency (JST). The duration of the program is from 2017 to 2018. The goal of the program is to strengthen the scientific research capacity of young engineers under 40 years old to participate in learning and exchanging Japanese experience and technology on disaster prevention.

Outcomes from the program:

The Sakura Science Program provided young ITST engineers and researchers with initial knowledge and understanding of landslides through attendance at an international symposium, lectures on landslides, and special visits to the typical large-scale landslides in Japan. At the above landslide locations, modern solutions, and new types of works to reduce the impact of landslides on traffic, infrastructure, and people were introduced by Japanese experts. Young researchers from ITST have investigated and collected landslide data by UAV combined with ground control point

Table 3 Name list of landslide assessment set

No	Name of guidelines	Code
I	**Part 1. Mapping and Site Prediction**	
1	Landslide topography mapping through aerial photo interpretation	GL 01: 2016
2	Field Work for Landslide Engineers	GL 02: 2016
3	SFM base DSM establishing	GL 03: 2016
4	Risk Evaluation of occurred landslide using the Analytic Hierarchy Process (AHP)	GL 04: 2016
5	Landslide susceptibility mapping along the Ho Chi Minh route in central Vietnam	GL 05: 2016
6	Hazard zonation for Landslide Risk Reduction	GL 06: 2016
7	Geological Survey for landslide	GL 07: 2016
8	Landslide disaster and mitigation for the region. Guideline for the vulnerability of Landslide mitigation in a humid tropical region	GL OS: 2016
II	**Part 2. Material Tests**	
9	High-Stress Un-drained Ring Shear Apparatus (RSA) Introduction	GL 09: 2016
10	A drained shear speed control test using RSA Ring shear test - Testing method of drained shear speed control test	GL 10: 2016
11	An un-drained shear stress control test using RSA	GL 11: 2016
12	Pore water pressure control test using RSA Ring shear test - Testing method of pore pressure control test	GL 12: 2016
13	A cyclic stress control test using RSA	GL 13: 2016
14	Undrained pore water pressure and seismic loading test using RSA Ring shear test - Testing method of Undrained pore water pressure and seismic loading test	GL 14: 2016
15	Soil shearing test m the lab – Direct shear test	GL 15: 2016
16	Portable Direct shear apparatus and testing	GL 16: 2016
III	**Part 3. Monitoring**	
17	Landslide Monitoring Systems	GL 17: 2016
18	Measurement of slope surface displacement using Robotic total station	GL IS: 2016
19	Measurement of slope surface displacement using Global Navigation Satellite System (GNSS)	GL 19: 2016
20	Measurement of slope surface displacement using Extensometer	GL 20: 2016
21	Measurement of slip surface displacement in the borehole using an Inclinometer	GL 21: 2016
22	Measurement of slip surface displacement in the borehole using a Vertical extensometer	GL 22: 2016
23	Rainfall gauge and other Meteorological equipment	GL 23: 2016
24	Groundwater observation using a water pressure gauge	GL 24: 2016
25	Early warning system	GL 25: 2016
IV	**Part 4. Landslide experiment**	
26	Outline of landslide experiment	GL 26: 2016

(continued)

Table 3 (continued)

No	Name of guidelines	Code
27	Infiltration properties of testing material – for permeameter	GL 27: 2016
28	Testing method (displacement measurement, pore-pressure measurement)	GL 2S: 2016
29	Analysis of measured data (Landslide motion and porewater pressure)	GL 29: 2016
30	Mechanism of landslide initiation	GL 30: 2016
V	**Part5. Software and Simulations**	
31	Alcalc 3D Software	GL 31: 2016
32	Arc View Software - Arc GIS10.1/ Spatial Analysis Software	GL 32: 2016
33	LS rapid	GL 33: 2016

Fig. 28 Picture of landslide assessment covers (volumes 1,2 and 3)

measurement by the GNSS system. 15 young Vietnamese engineers and researchers under the age of 40 participated in the program in Japan for 10 days in 2017 and 2018.

3.4.4 GRASS ROOT Project

Grass Root Project Named "Capacity Building of Local Community for Slope Disaster Risk Reduction (Slope DRR). It was implemented under the cooperation of Kurihara City, Advantechnology Co., Ltd., Lao Cai Province under the support of JICA (Miyagi et al. 2020). The project time is 2019 to 2023. The Institute of Transport science and technology participated in the project as an expert and coordinating agency. Project Purpose is to help residents' disaster prevention organization can carry out disaster prevention and evacuation plan in the pilot commune of Lao Cai province under cooperation with the administration,

The project's output includes:

Basic understanding of the community territory: shares disaster reduction power strengthening-related information, and understands the disaster risk on site.

Support the resident activity: The education program on grasping disaster risk and evacuation drill is carried out by the

collaboration between Japan, Lao Cai DARD, and the local community.

Development of activities in the local community: Management and improvement of the Slope DRR such as maps, manuals, and evacuation drills will be carried out by the leadership of the Lao Cai side.

Cooperation and deployment:Japan, the Lao Cai DARD, and relevant ministries and agencies are provided with the knowledge of this project as an example.

The basic information for disaster risk reduction is established through (1) the map of landslide terrain distribution in a large area, the scale of 1/25000), the landslide risk reduction baseline map slopes for pilot communes and the vicinity of 1/5000, and (2) interactive DRR maps based on UAV images and user manuals were developed with the main contribution of ITST researchers. The above project is a perfect combination of researchers, managers, and local communities for landslide reduction.

4 Conclusions

Landslide risk assessment is one of the fundamental issues in the Vietnamese government's "proactively prevent natural disasters" strategy for natural disaster prevention, response and mitigation solutions for mountainous areas and central highlands. Over the past 10 years, with the efforts of Vietnamese scientists and the support of international cooperation projects and research programs, the Institute of Transport Science and Technology has made important strides in assessing landslide risk.

The overall landslide risk assessment for the area can be done through established and modern landslide identification as well as the development of integrated maps for the classification, distribution, reactivation, and landslide potential assessment. Through the principle of assessment, an application that builds a database on landslides along the roads has been carried out, contributing actively to the management of the road system in mountainous areas.

For landslide risk assessment with specific landslides, especially for deep, large-scale landslides, site topographical and geological surveys define landslide geometrical features. The determination of the slip surface and landslide state can be done by SP drilling and installation borehole inclinometer. Testing samples taken at slip surface by ICL2 ring shear apparatus and application of LS Rapid simulation can assist in the understanding of the initiation mechanism of the Landslide and the dynamics of post-failure motion of the targeted landslides for the prediction. Early warning capabilities can also be realized through synchronous and real-time monitoring systems of the affected parameters using accurate monitoring equipment.

To facilitate the replication and application of research results, an integrated set of guidelines for landslide risk assessment has been developed in Vietnamese. This guideline is gradually being upgraded to a basic standard and national standard.

The achievements for landslide risk assessment are not only useful for natural disaster prevention, response, and mitigation in Vietnam but can also be applied to humid tropical areas with similar conditions.

Acknowledgments This report is a reconstruction, addition, and correction of research results of The project "Develop Landslide Risk Assessment Technology along Transport Arteries in Vietnam", Which had been implemented from 2011 to 2016 and other post-project ones.

References

Abe S, Tien DV, Ha DN, Hoshide T, Nishitani T, Miyagi T (2018) Topography and landslides in weathered granitic rock areas – Hai Van landslide in Central Vietnam. Landslides 15:1675–1689

Carrara A, Cardinali M, Detti R, Guzzetti F, Pasqui V, Reichenbach P (1991). GIS techniques and statistical models in evaluating landslide hazard. In Earth surface processes and landforms, 5, 16 (pp. 427–445). New York: John Wiley & Sons

Do NH, Asano S, Ochiai H, Goto S, Huynh TB, Nguyen KT (2021) Determining the position of the sliding surface of rainfall-induced landslides at Hai Van station, Viet Nam during rainy season in 2016. In: 60th Domestic Conference on Japan Landslide Society, pp 170–171

Dung ND, Miyagi T, Luong LH, Hamasaki E, Hayashi K, Tien DV, Daimaru H, Abe S (2016) Trial of landslide topography mapping using ALOS W3D data – case study along the National Road no. 7 in Central Vietnam –. Trans, Japanese Geomorph. Union 33-1:127–140

Luong LH, Miyagi T, Tien PV (2016) Mapping of large scale landslide topographic area by aerial photograph interpretation and possibilities for application to risk assessment for ho chi Minh route, Viet Nam - trans, Japanese Geomorph. Union 33-1:105–126

Luong LH, Miyagi T, Tien PV, Loi DH, Hamasaki E, Abe S (2017) Landslide evaluation in center provinces of Vietnam – WLF 4

Miyagi T (2013) TXT-tool 1.081–2.1 landslide mapping through the interpretation of aerial photographs

Miyagi T, Prasada GB, Tanavud C, Potichan A, Hamasaki E (2004) Landslide risk evaluation and mapping—manual of landslide topography and risk management. Report of the National Research Institute for Earth Science and Disaster Prevention No. 66, pp 75–137

Miyagi T, Thanh NK, Tien DV, Luong LH, Viet QV (2020) Slope disaster risk reduction map as a communication tool for community-based DRR in Japan & Vietnam

Quang LH, Loi DH, Sassa K, Takara K, Ochiai H, Dang K, Abe S, Asano S, Ha DN (2018) Susceptibility assessment of the precursor stage of a landslide threatening Haivan Railway Station, Vietnam. Landslides 15:309–325

Sassa K, He B (2012) TXT-tool 3.081-1.1 landslide initiation mechanism. In: ICL, landslide teaching tools. ICL, Tokyo, pp 205–214

Thanh NK, Miyagi T, Shinobu S, Tien DV, Luong LH, Ha DN (2020) Developing Recognition and Simple Mapping by UAV/SfM for Local Resident in Mountainous Area in Vietnam—A Case Study in Po Xi Ngai Community, Laocai Province. Understanding and Reducing Landslide Disaster Risk pp 103–109

Tien DV, Miyagi T, Abe S, Hamasaki E, Yoshimatsu H (2016) Landslide susceptibility mapping along the ho chi Minh route in Central Vietnam: AHP approach applied to a humid tropical area-. Trans, Japanese Geomorph. Union 33-1:79–104

Tien DV, Khang NX, Sassa K, Miyagi T, Ochiai H, Vinh HD, Quang LH, Dang K, Asano S (2017) Results of a technical cooperation project to develop landslide risk assessment technology along transport arteries in Vietnam (IPL-175). Workshop on World Landslide Forum - Advancing Culture of Living with Landslides, pp 411–417

Uzielli M (2009) Quantitative Estimation of Vulnerability to Landslides: the VIS framework, International Centre for Geohazards (ICG), Norwegian Geotechnique Institute

Vaners D (1984) Landslide hazard zonation: a review of principles and practice. UNESCO, Paris

Protection and Conservation of Georgian Rupestrian Cultural Heritage Sites: A Review

William Frodella, Giovanni Gigli, Daniele Spizzichino, Claudio Margottini, Mikheil Elashvili, and Nicola Casagli

Abstract

Many of the Georgian cultural heritage sites consist of rupestrian monastic complexes constructed between the sixth and the 12th centuries of exceptional universal value from a historical, cultural, and natural point of view. Many of them are affected by hydrogeological problems and require the planning of an effective risk mitigation strategy. This planning would help not only to preserve invaluable cultural heritage sites but also to enhance Georgia as an important tourist destination and improve the local economy. This paper aims to show an overview on the last decade's activities coordinated by the National Agency for the Preservation of Georgian Cultural Heritage (NAGPCH) for the conservation of Georgian cultural heritage, thanks to the collaboration between national and international centers of research.

Keywords

Landslides · Cultural heritage · Remote sensing · Mitigation

W. Frodella (✉) · G. Gigli · N. Casagli
Department of Earth Sciences, University of Florence, Florence, Italy
e-mail: william.frodella@unifi.it; giovanni.gigli@unifi.it

D. Spizzichino
ISPRA, Higher Institute for Protection and Environmental Research, Rome, Italy
e-mail: daniele.spizzichino@isprambiente.it

C. Margottini
UNESCO Chair on Prevention and Sustainable Management of Geo-Hydrological Hazards, University of Florence, Florence, Italy
e-mail: claudio.margottini@unifi.it

M. Elashvili
Ilia State University, Tbilisi, Georgia
e-mail: mikheil_elashvili@iliauni.edu.ge

1 Introduction

Rock-hewn cultural heritage sites are often developed in slopes formed by weak rocks, such as tuffs or soft sandstones, which are characterized by peculiar lithological, geotechnical, and morpho-structural features. These features lead to an excellent carvability, but at the same time, to weathering, deterioration and landsliding. In this context combining traditional approaches (field surveys and laboratory analyses on rock/soil samples) with close-range non-destructive techniques, can profitably be used for the rapid detection of conservation issues that can lead to slope instability phenomena. These phenomena in particular not only can damage the site, but also put visitors at high risk.

The proposed approach can provide fundamental data to implement a site-specific and inter-disciplinary approach for the sustainable protection and conservation of such fragile cultural heritage sites. This paper presents this methodological approach for several important cultural heritage sites of the UNESCO Tentative List, such as Vardzia, Vanis Kvabebi, Uplistsikhe, and David Gareja (Fig. 1). These are located in mountainous areas, river valleys, and half deserts. The final aim is to provide conservators, practitioners, and local authorities with a useful, versatile, and low-cost methodology, to be profitably used in the protection and conservation strategies of rock-carved sites with similar geomorphological and geological characteristics.

1.1 Vardzia and Vanis Kvabebi

The rock-cut city of Vardzia and the rupestrian monastery of Vanis Kvabebi, dating between the eighth and 12th centuries, are carved in the volcanic tuffs of the Erusheti mountains to the north, and the Javaheti plateau to the south (southern Georgia; Fig. 1b). These sites outcrop along the steep slopes of the Mtkavri river gorge, and are formed by the Goderdzi Formation: an Upper Miocene to Lower Pliocene subaerial

I. Alcántara-Ayala et al. (eds.), *Progress in Landslide Research and Technology, Volume 2 Issue 1, 2023*,
Progress in Landslide Research and Technology, https://doi.org/10.1007/978-3-031-39012-8_14

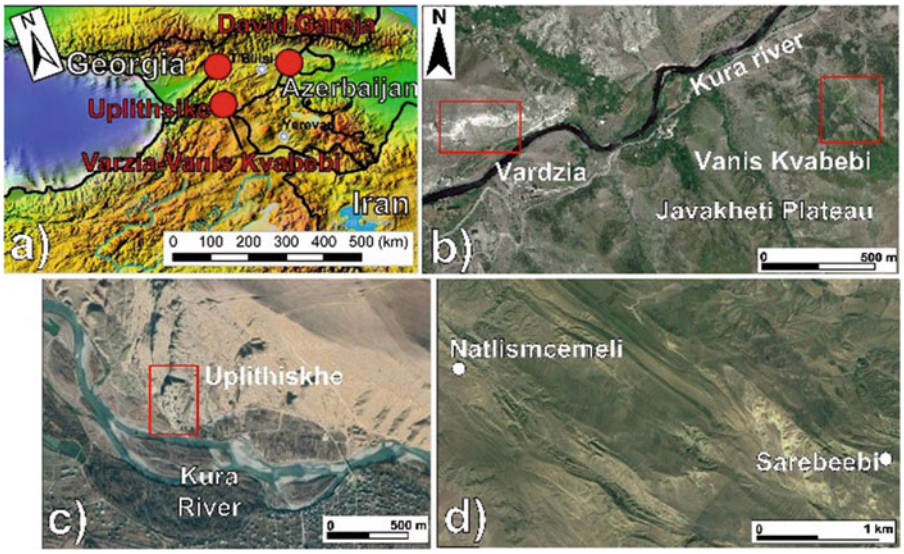

Fig. 1 Map with the location of the analysed rock-carved cultural heritage sites (**a**); locations at a higher scale: (**b**) Vardzia-Vanis Kvabebi; (**c**) Uplithsike; (**d**) David Gareja

volcanogenic–sedimentary sequence, about 1000 m in thickness, composed of volcanic breccias (Layer 1 and 4), and tuffs (Layer 2 and 3) with ashfall deposits (Gudjabidze and Gamkrelidze 2003; Margottini et al. 2015; Okrostsvaridze et al. 2016; Boldini et al. 2018; Frodella et al. 2020a).

1.2 Uplistsikhe

Uplistsikhe is an ancient cave town-fortress located in eastern Georgia about 50 km NW of Tbilisi (Fig. 1c). From a morphological point of view, the complex is located on the left bank of the Kura River on the slopes of the Kvernaqi range. The site develops on top of a rocky terrace bordered to the south-west by a rock cliff up to 40 m high and is completely carved into a thick sequence of Upper Oligocene to lower Miocene quartz coarse sandstones, gently dipping towards SE (Stinghen 2011; Frodella et al. 2021.

1.3 David Gareja

The David Gareja monastery complex is located in Kakheti half-desert region (Eastern Georgia), near the border with Azerbaijan (Fig. 1d). From a geological point of view, the area is formed by a thick sequence of soft sedimentary rocks (Lower Miocene to Pliocene in age) characterized by a monocline "hogback type" structure, with strata dipping SW with low-gentle angles, from very coarse-grained, pebbly thick-bedded sandstones, to coarse-grained soft sandstones, siltstones, and clays (Frodella et al. 2020b, 2021).

2 Materials and Methods

A methodology was implemented integrating field surveys, close-range remote sensing (namely InfraRed Thermography = IRT and Unmanned Aerial Vehicle Digital Photogrammetry = UAV-DP), and laboratory analyses for geotechnical-mineralogical and geological characterization (Fig. 2). The analysis of remote sensing data allowed us to obtain high-resolution slope 3D surfaces and surface temperature maps, while water runoff patterns were mapped in a GIS environment (ESRI 2019). A final phase of data integration and interpretation provided the detection of potential criticalities with respect to weathering, degradation, and slope instability processes.

2.1 Field Surveys and Geotechnical Analysis

Field surveys were aimed at identifying stratigraphic and structural elements representing predisposing factors for land sliding.

Geo-structural data were collected and analyzed with RocScience Dips © software (RocScience 2020) to detect the bedding planes and the main sets of discontinuities. Rock samples were collected in the field for laboratory geotechnical analyses to assess the main physical and mechanical parameters. The following laboratory tests were conducted according to (ISRM 1985): (1) tilt test, (2) point load test, and (3) real unit weight (hydrostatic weighing).

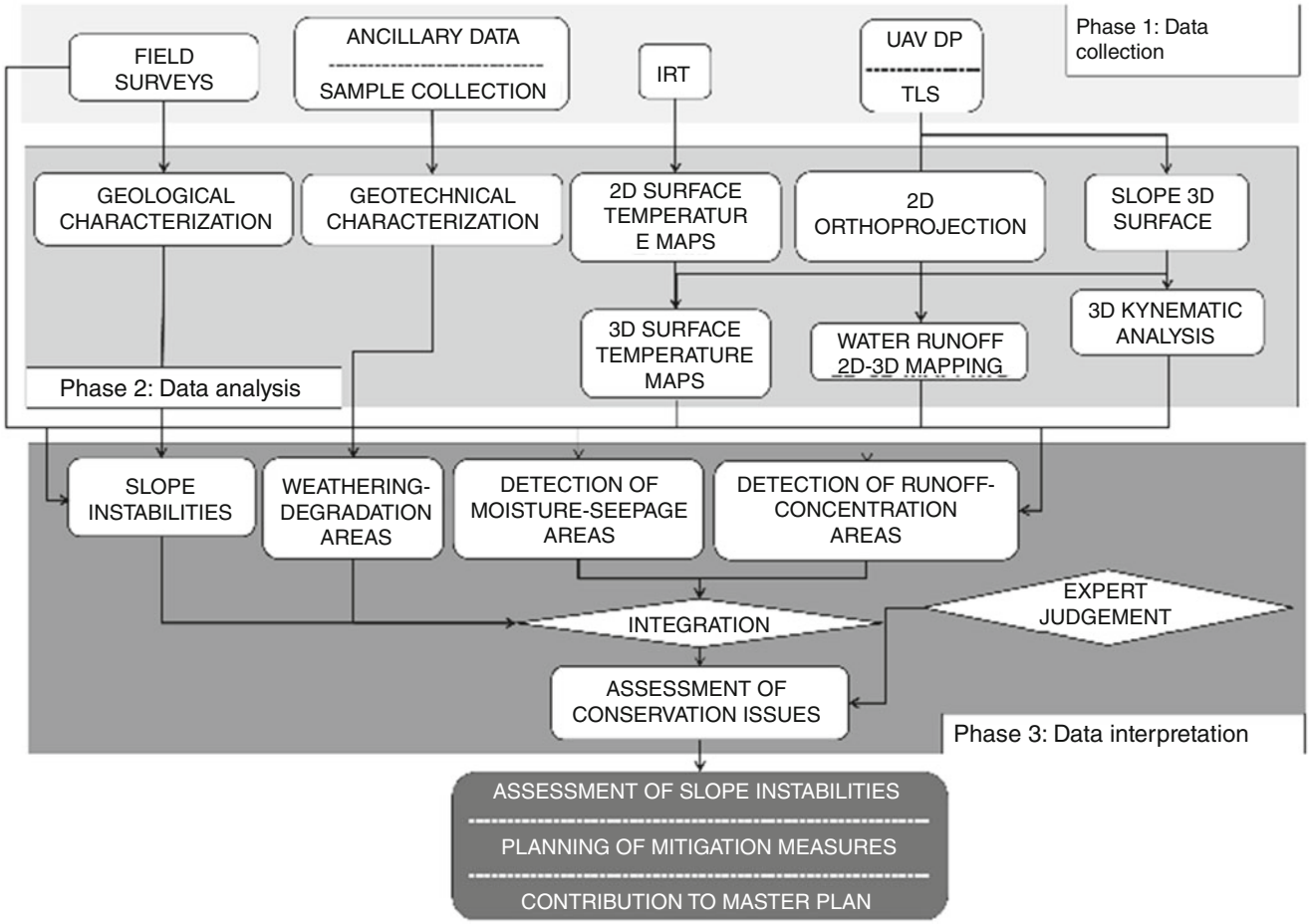

Fig. 2 Work plan of the adopted methodology

2.2 IRT Surveys

Calibrated thermal cameras are used in IRT for the detection and mapping of thermal radiation from the analyzed scenario (Nolesini et al. 2016; Frodella et al. 2017, 2020a, 2021). The IRT array detector acquires a digital image, called a "thermogram" or "thermographic image", which after a calibration procedure is converted by the built-in processor into a ST map (Spampinato et al. 2011).

The IRT surveys were performed with a hand-held FLIR SC620 model thermal camera (FLIR 2009), characterized by a focal plane array microbolometer sensor, a 640 × 480-pixel resolution, and a field of view of 24 × 18 degrees (see Table 1 for further specifications). The IRT surveys were carried out between July and November 2016 in Vardzia, while in the other sites in November 2018. During all the surveys, cloudy skies with low wind proved ideal conditions for the IRT surveys. Thermographic image mosaicking, correction and thermal focusing were carried out using FLIR Tools+ software (FLIR 2015).

2.3 DP-UAV Survey and Surface Runoff Modelling

Digital photogrammetry (DP) is a widely adopted and effective technique for acquiring 3D geometric data from stereoscopic overlaps of photo sequences captured by a calibrated digital camera (Chandler 1999). This technique can provide, in a short time, a detailed spatial representation for the analysis of the geometrical-structural setting and the surface changes of both ground and structures (Zhang et al. 2004). In the past few years, thanks to the rapid techno-logical development of digital cameras and low-cost and small Unmanned Aerial Vehicles (UAV), DP led to new, promising scenarios in cultural heritage applications (Grün et al. 2002; Bolognesi et al. 2014).

UAV-DP surveys were carried out in the analyzed sites with a DJI Phantom 4Pro quadcopter. Agisoft Photoscan software (Agisoft Photoscan 2017) was used for data processing and high-resolution Digital Terrain Model (DTM) construction. Ground control points were fixed using Differential Global Positioning System (DGPS), or

Table 1 IRT survey parameters of the analysed sites

Case study	Slope aspect	Sensor-target distance (m)	Image res. (cm)	Air T (C°) -Rh (%)
Vardzia	S	600	39	28.1;19.5 44.8;52.6
Vanis Kvabebi	W/E	100	6.6	14.4–63.4
Uplistsikhe	SW	100	6.6	21.3–33.6
Natlismcemeli	S	110/20	7.1/1.2	13.4–65.9
Sabereebi	SW	100/20	6.5	22.6–39.8

Table 2 Average values of the collected samples

Case study	Friction angle (°)	Uniaxial compressive strenght (MPa)	Unit weight (KN/m^3)
Vanis Kvabebi	28	2.70	16.76
Uplistsikhe	40	3.55	19.5
Natlismcemeli	27	0.49	16.56
Sabereebi	23	0.52	15.09

Total Station devices to increase the quality of the DTMs. ArcMap (ESRI) Hydrology Tools package was applied using Flow Direction, Accumulation and Stream Order functions to analyze the slope scale drainage system (ESRI 2019). This allowed us to model surficial water runoff trajectories, calculate the corresponding watersheds and categorize the stream order on the DTM.

3 Results

3.1 Geotechnical Data

The laboratory analysis of the samples in Vardzia showed generally high values of primary porosity for the four analyzed layers ($16 < n < 29$). In contrast, the higher values correspond to the tuff layers (with special regard to Layer 3). Also, rock moisture shows higher values in the tuff layers (up to 3.6 in Layer 2 and 3.5 in Layer 3, respectively), while in the volcanic breccia layers, it ranges from 0.6 to 2.6. All these values decrease with depth, showing the action of water infiltration on the weathering from the slope surface (on the contrary, the density increases in depth, as rock gets less weathered). The uniaxial compressive strength UCS for Layer 2 is equal to 9.3 MPa in dry conditions and 2.6 MPa in wet conditions, indicating a strong influence of water content on the material response. A similar effect was detected for the tensile strength σt estimated by the Brazilian tests (925 kPa in dry conditions and 300 kPa in wet conditions). Layer 3 is characterized by very similar physical and mechanical properties. The properties of Layer 1 were investigated by a limited number of tests: point load tests gave an average UCS value of 14.8 MPa in dry conditions. The corresponding values of the cohesion for dry and wet conditions were then calculated from the corresponding UCS values. According to the X-ray phase mineralogical analysis results, the main primary minerals of the rocks are Andesine-Labradorite, Hornblend, Biotite, rare occurrence of quartz, and calcite. Rock-building minerals are cemented by an amorphous phase (volcanic glass). Ca-montmorillonite, occurring in various quantities in all the samples of Vardzia complex rocks, is mainly a product of volcanic glass alteration, while its quantity is determined by the intensity of alteration process. For the sites of Vanis Kvabebi, Uplistsikhe, and David Gareja, all the collected rock samples are characterized by very low strength parameters (many samples were easily broken even by hand), with special regard for the David Gareja samples, showing that these rocks are very weakly cemented (Frodella et al. 2021) (Table 2).

3.2 Field Surveys

3.2.1 Vardzia and Vanis Kvabebi

Two main sets of discontinuities are recognized at Vardzia: (i) high-angle joints dipping SE parallel to the slope face and (ii) subvertical joints oriented NW–SE. These intersect the bedding of the volcanoclastic units along the entire cliff, causing several instability phenomena, such as rock falls, topples, and wedge-planar failures (Cruden and Varnes 1996; Margottini et al. 2015; Boldini et al. 2018; Frodella et al. 2020a). In Vanis Kvabebi Besides the sub-horizontal layer bedding, three main subvertical joint sets were identified (Fig. 3): (1) J1: dipping W and N-S oriented, forming the main slope faces (Fig. 6d); (2) J2: dipping NW and SW-NE oriented, it is responsible for the formation of a master joint intersecting all the upper sections on the eastern rock wall of the complex; (3) J3: dipping SE and trending NW-SE, it represents persistent fractures along which ephemeral creek erosion has caused deep channel cuts in the southern sector of the complex.

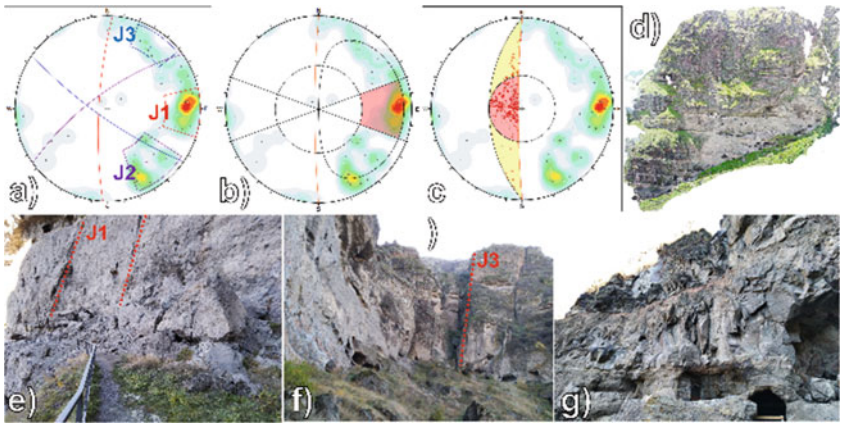

Fig. 3 Structural setting and kinematic analysis: identified sets (**a**); kinematic analysis for planar (**b**) and wedge (**c**) failure; frontal view of the rock cliff from UAV-DP (**d**); 2017 rock fall deposits (**e**); subvertical fracture where creek channel erosion has concentrated (**f**); welded tuff portion affected by wedge failures (**g**)

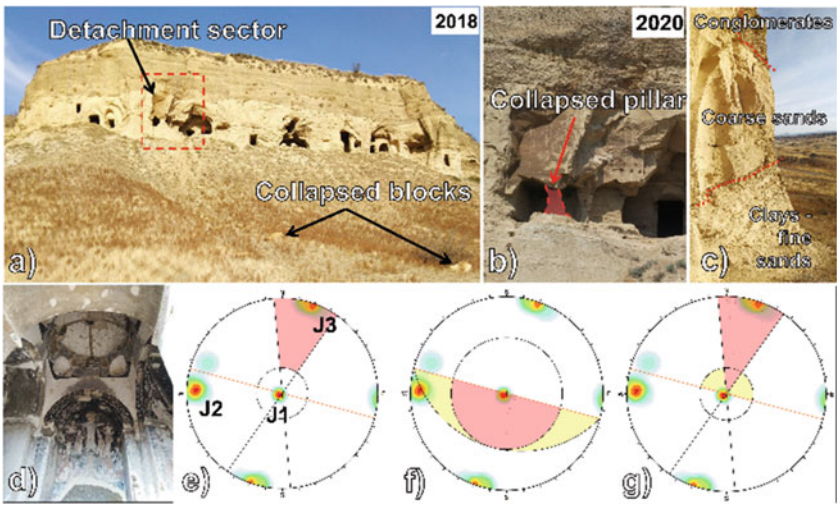

Fig. 4 2D kinematic analysis: Wedge failure mechanism (**a**); Planar failure mechanism (**b**). Field evidence of kinematic mechanisms: wedge failure (**c**) and plane failure (**d**)

3.2.2 Uplistsikhe

Four main identified discontinuity sets were identified in the field: J1 (bedding) dips SE with low angles, J2 joint set dips SW parallel to the slope face with high angles, J3 is a subvertical joint set trending WNW-SSE, and J4 dips NW with mid-high angles (Frodella et al. 2021). The 2D kinematic analysis highlighted two equally predominant instability mechanisms: plane and wedge failures.

3.2.3 David Gareja

In Natlismcemeni the main discontinuities are organized in two main joint sets: J1 is related to the bedding and dips NE against the slope with low angles; J2 is a mainly subvertical set dipping SW along the slope; J3 is a subvertical fracture sparsely cutting the cliff face (Fig. 4) (Frodella et al. 2021).

The performed 2D kinematic analysis allowed us to assess the main instability mechanisms affecting the rock cliff, which are represented by plane failure, followed by wedge failure, and subordinately by toppling and free fall. The latter can be locally predominant in overhanging sectors, such as cave niches, while open fractures parallel to the slope can develop topplings. Very persistent and spaced wide-open fractures enhancing are visible within the monastery caves and can potentially seriously damage the complex.

In Sabereebi, the bedding (J1) dips NE towards the slope with low angles, while two not widely spaced but persistent discontinuity sets cut the slope parallel (J2) and orthogonal (J3) to the cliff face, dipping E and SSW respectively, deeply controlling the stability of the cliff. The 2D kinematic analysis confirms high planar and especially wedge failure indexes along these planes, subordinately toppling.

3.3 Remote Sensing Analysis

3.3.1 Vardzia

The IRT data (Fig. 5) shows lower surface temperatures (ST) in the upper slope sectors (mean value: 23.2 °C during S1 = July and 11.1 °C during S2 = November) than in the lower slope sectors, likely due to the widespread vegetation cover of the former.

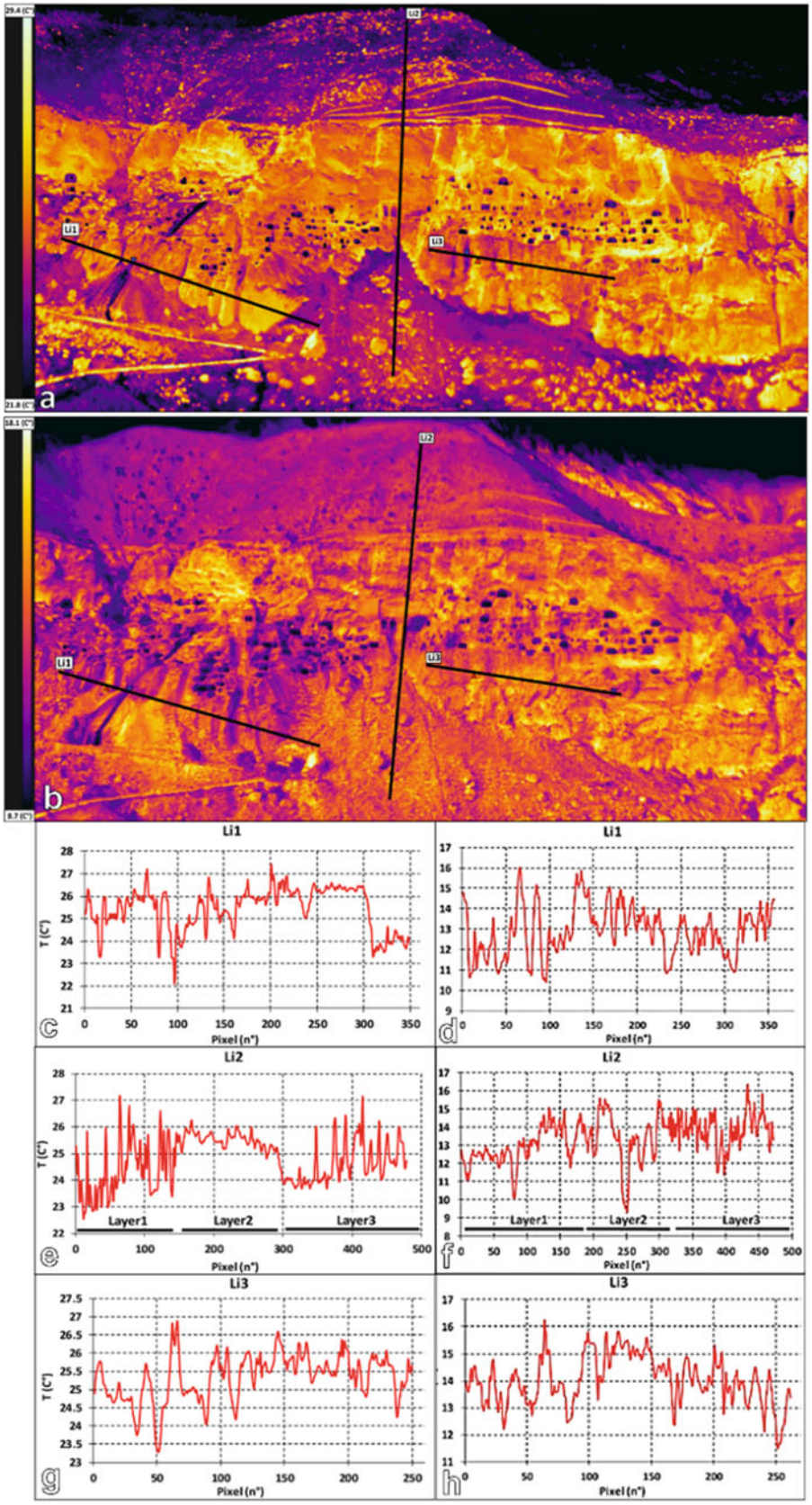

Fig. 5 Vardzia IRT data: (**a**) Mosaicked thermograms acquired on July 16th, 2016, at 19:00 (**a**), on November 20th at 18:40 (**b**). Surface temperature profiles Li1–3 from the IRT data in a (**c**, **e**, **g**) and **b** (**d**, **f**, **h**) (modified after Frodella et al. 2020a)

Some minor warm temperature anomalies (up to 29.4 °C during S1 and 14.7 °C in S2) were observed corresponding to the scattered boulders of the upper breccia, which are isolated from the surrounding finer matrix due to differential erosion. Another widespread vegetated sector is the slope toe, showing slightly higher mean ST values (mean value: 24.1 °C during S1 and 13.4 °C during S2) than the upper slope. Warm temperature anomalies were also detected (up to 29.7 °C during S1 and 17.9 °C) in association with the presence of fallen block deposits that were, in turn, associated with rock cliff face instabilities. The rock cliff shows the highest ST values in the thermal image (mean of 27.8 °C during S1 and 14.1 °C during S2), although several cold thermal anomalies are also present. Based on their spatial patterns, their locations, and interpretation of the corresponding visible-light images, these temperature anomalies can be described as follows: (i) a cave system carved in Levels 2 and 3 (mean ST of 21.1 °C during S1 and 8.9 °C during S2); (ii) vegetated sectors located on both the eastern and western edges (22 °C mean ST during S1 and 9.6 °C during S2); and (iii) near-linear, subvertical anomalies intersecting (21.6 °C mean ST during S1 and 10.2 °C during S2). These subvertical anomalies were detected in both surveys corresponding with open, persistent, subvertical fracture systems orthogonal to the cliff face, that intersect nearly all the layers. Considering their spatial pattern and the continuous rainfall before both surveys, these anomalies were interpreted as moisture areas associated with ephemeral drainage networks. In particular the sharpest of these anomalies, along a slope debris talus, was associated with seepage from a water pipe used for excavation purposes by the local group of archaeologists. Additional cold thermal anomalies were located within the slope toe sector, mostly along the contact of the slope toe with the cliff face; other anomalies exhibited vertical linear shapes representing minor rills.

The hydromodelling allowed us to map the spatial distribution of water runoff within the monastery complex of Vardzia, confirming the insights from the IRT analysis. Streams were categorized by order, and catchments and areas of concentration were identified (Fig. 6). Results of the 2D ortho-projection showed three main catchments in the eastern sector (Streams 1–3) and one located at the western edge of the complex (Stream 4), each showing streams up to the fifth order. At the top of the central slope sector, the hydromodelling showed the effect of runnels and retaining walls on the water runoff. In fact, the runnels effectively channel minor streams toward the two adjacent main-order catchments to the west and the east. However, in some sectors, these runnels have been damaged by the impacts of detached boulders from the uppermost slope sector, so water flows directly along the slope at some points.

The 3D model provides a clear frontal view of the water runoff patterns on the cliff face and on the slope toe (Fig. 6). Four areas of water concentration are present at the slope break between the upper slope and cliff. These are key sites of water runoff concentration, acting as areas of linear erosion, especially in association with Layer 1. From the slope 3D model, it is also evident how the slope morpho-structural setting in the middle–lower cliff sector creates other areas of interest concerning water concentration along large, eroded fractures.

3.3.2 Vanis Kvabebi

In Vanis Kvabebi, the IRT surveys allowed mapping the whole cliff face, highlighting dry conditions corresponding to the collapsed sector. The integrated analysis allowed the detection of other potentially unstable sectors represented by warm thermal anomalies highlighting open-cavernous features (over one meter of fracture aperture; ISRM 1978). These are located along a persistent J2 system master joint intersecting all the basalt flows, which in turn creates a niche at the contact with the underlying more erodible medium-grained tuffs (Fig. 3) (Frodella et al. 2021).

Dry conditions were assessed in the 2017 collapse area (Fig. 7). In the cliff's southern sector, the IRT analysis showed the presence of cold thermal anomalies along the erosional channels developed along the J3 joint system, suggesting the presence of moisture areas (Fig. 7). These warm thermal anomalies also highlight the widespread niches in open features associated with J1 fractures. The hydro-model showed that very low-order ephemeral streams concentrate within J3 fractures within the collapse area. The same discontinuity system is responsible for the water runoff concentration in the slope's southern sector, where streams up to the fifth order are located (Fig. 7). Here, runoff concentrates within wide master joints, generating wide erosional channels cutting deeply into the cliff, as also highlighted by the IRT analysis.

3.3.3 Uplistsikhe

The IRT survey highlighted warm thermal anomalies along persistent joints belonging to J4, where minor rock falls occurred in 2019 (Fig. 8). General dry conditions were assessed along the rock cliff except for the left sector, where a cold thermal anomaly (as well as the presence of vegetation and weathering coating) reveals the presence of an ephemeral stream, which concentrates along J4, the rock cliff most persistent discontinuity set (Fig. 8).

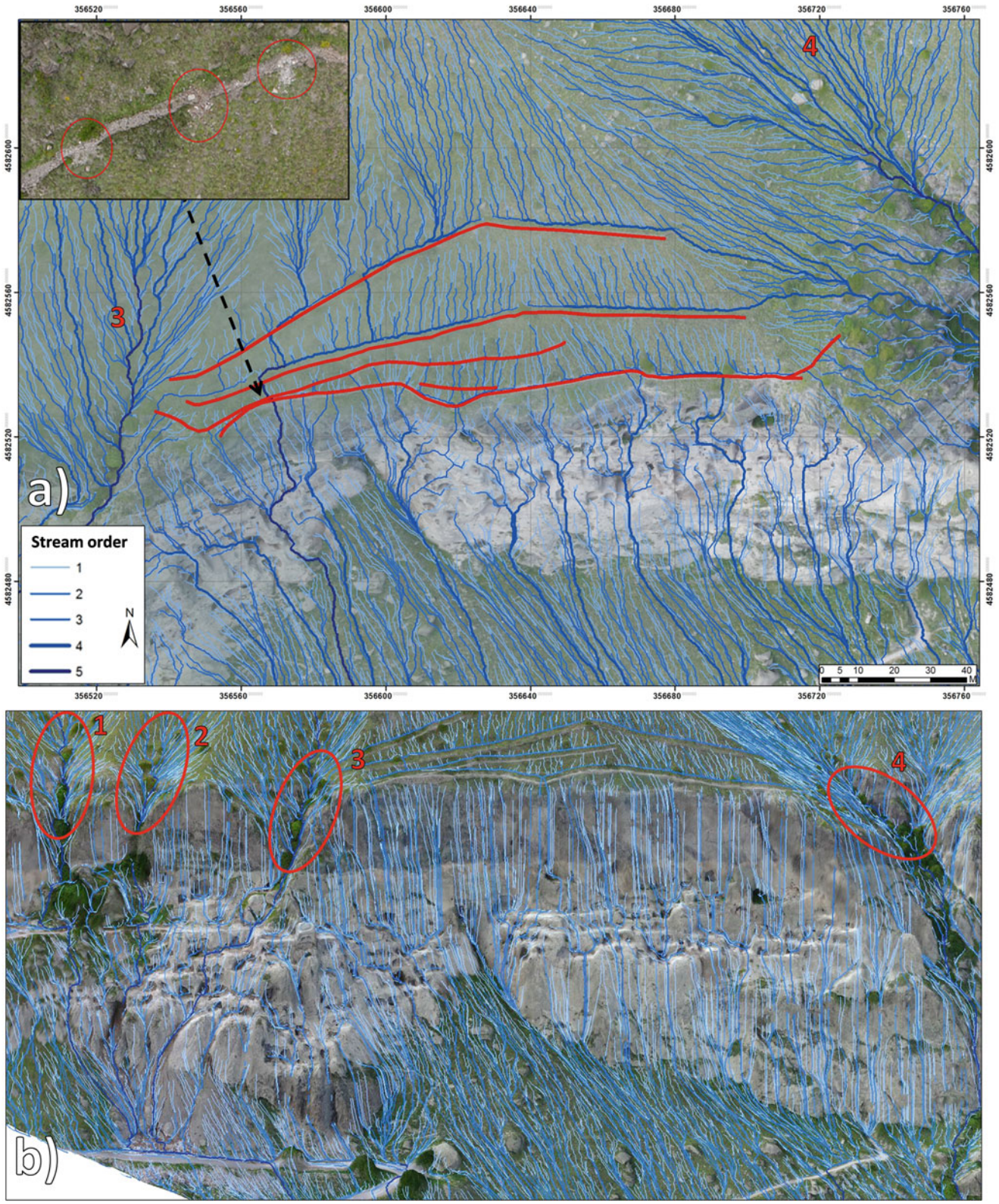

Fig. 6 Unmanned aerial vehicle digital photogrammetry (UAV-DP) products: (**a**) two-dimensional (2D) orthoprojection of Vardzia's hydrographic network on the upper slope sector and cliff face; (**b**) Modeled drainage network for the Vardzia slope's three-dimensional (3D) surface (modified after Frodella et al. 2020a)

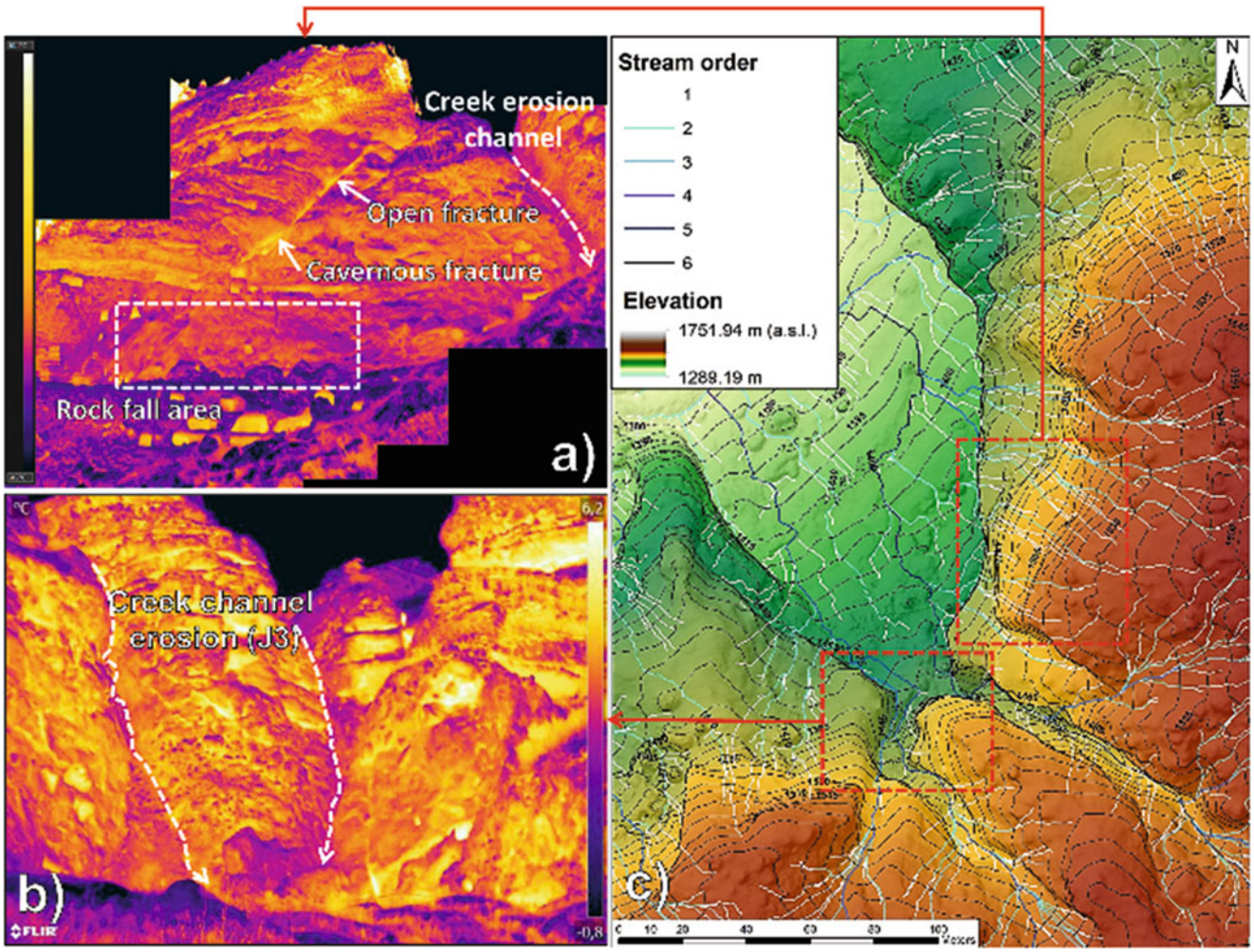

Fig. 7 Vanis Kvabebi IRT data: western main cliff (**a**), and southern rock wall (**b**). Drainage network map (dashed red squares represent areas of interest) (**c**)

This is also confirmed by the hydro-modelling analysis (red arrow in Fig. 8), which also shows how the high-order ephemeral streams concentrate mainly along J3-J2 sets, while low-order ephemeral streams are mainly along J4.

3.3.4 David Gareja

The IRT surveys in Natlismcemeni pointed out that while the rock slope shows average values between 10.2–10.8 C°, warm thermal anomalies (13.8–14.1 C°) were detected both at the top of the thick sandy layer (herein related to J1) and at the topmost sector of the caved accesses, highlighting potentially unstable ledge-niche systems (Fig. 9). Warm thermal anomalies also enhance wide open fractures parallel to the slope (related to J2; Fig. 9). No cold thermal anomalies were detected, therefore dry conditions were assessed. In Sabereebi, IRT analysis showed average temperatures of 26.8 °C of the slope face and warm thermal anomalies (from 31 to 42 C°) in correspondence with the recent collapse sector and the underlying slope talus, where erosion is exposing bare soil (Fig. 10). Sharp cold thermal anomalies (15.4–17.7 °C) highlight a large system of open cracks connected to J3 at the right end of the complex (Fig. 10). As for Natlismcemeni, dry conditions were assessed. The UAV-DP survey and the Hydro-modelling analysis provided a high-resolution DEM, and drainage maps (Fig. 10). This latter showed main cataclinal-type streams draining the hogback of the monoclinal structure to the NE.

In contrast, small anaclinal-type streams erode the debris talus underlying the monastery (as shown by the bare soil sectors highlighted by IRT). This phenomenon could gradually undermine the stability of the cliff.

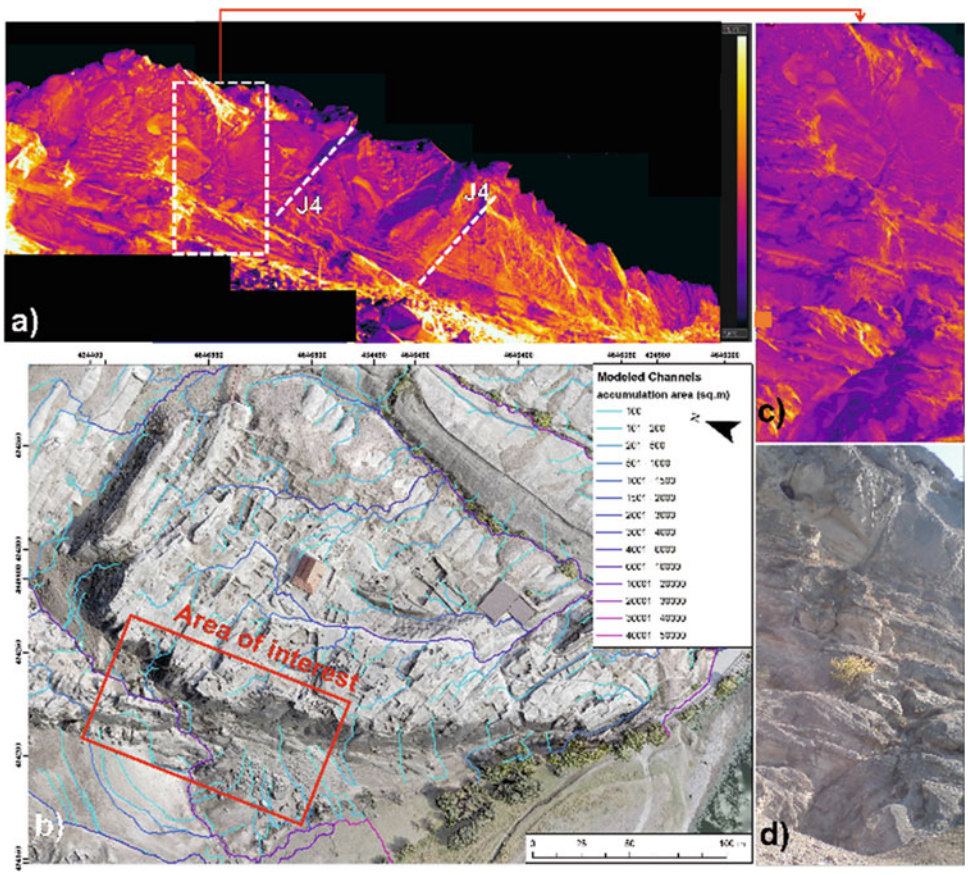

Fig. 8 IRT data of the Uplistsikhe western cliff (mosaicked thermograms with 2800 × 850 pixel) (**a**); modelled ephemeral drainage network of the site (**b**); ephemeral stream IRT and optical image (**c**, **d**), developing along J4 fracture (white dashed rectangle in a)

4 Discussion

In Vardzia, the stratigraphic position and the geomechanical properties of the volcanic breccias play important roles in the current geological structure of the complex. Since this stratum of breccias is located atop the tuffs, their higher density and hardness have protected the softer and weaker tuffs below from erosion (Margottini et al. 2015). Nevertheless, the breccias are currently being deeply cut by stream erosion across the slope's western sector. This phenomenon is responsible for the fast surface weathering of the rock

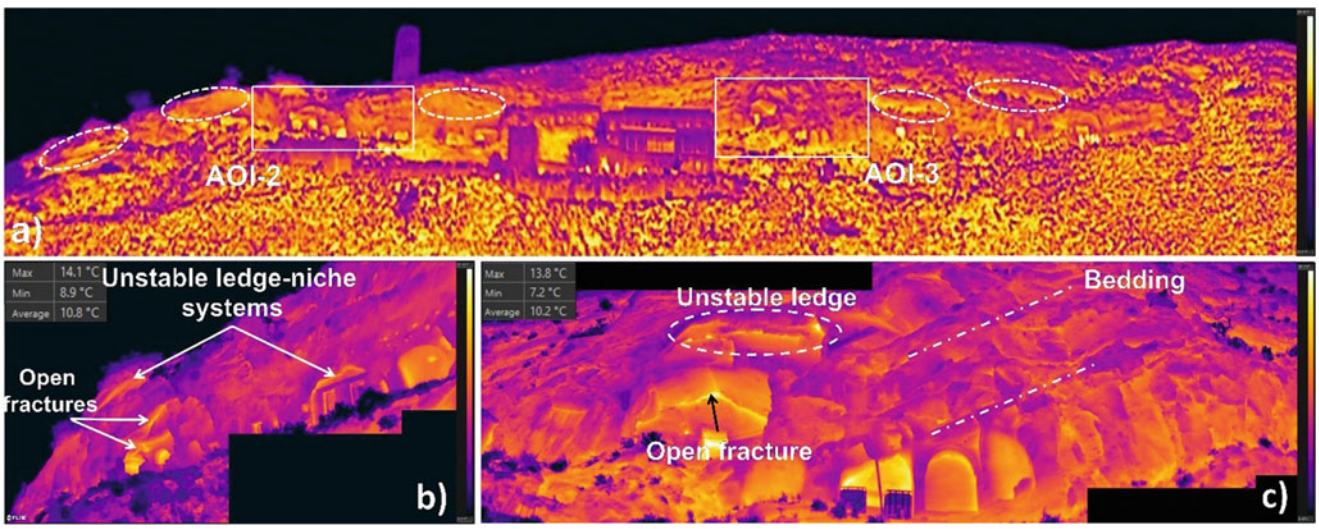

Fig. 9 Outcomes of the IRT surveys of the Natlismcemeni monastery: (**a**) IRT mosaicked image (2075 × 505 pixels with 7.1 cm) showing the AOIs and the warm thermal anomalies (dashed ovals); (**b**) 1160×480 pixels; (**c**) 2120 × 590 pixels

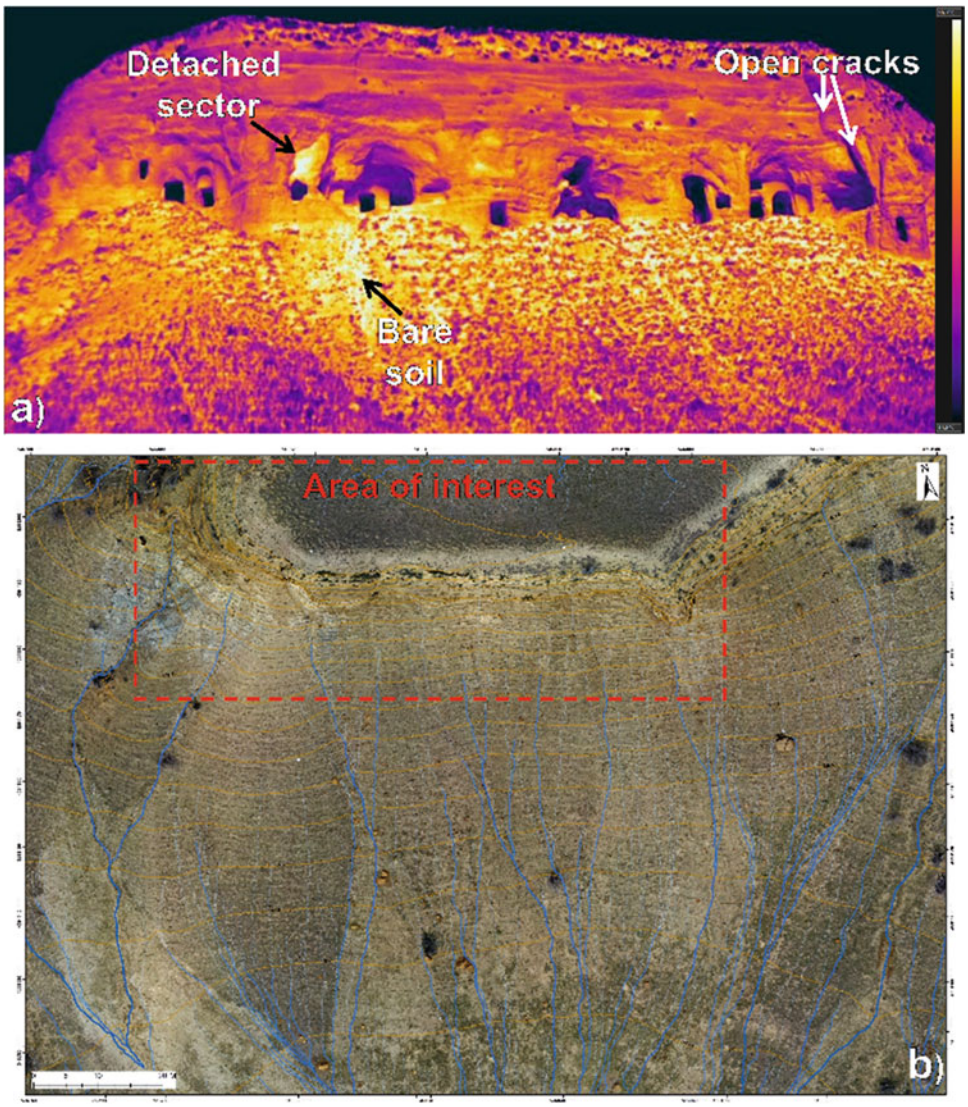

Fig. 10 IRT and UAV-DP data in Sabereebi: mosaicked surface temperature map (950 × 480 pixels with 6.5 cm resolution (**a**). UAV-DP high resolution DEM derived products: drainage pattern map (**b**)

mass. Furthermore, hygric expansion due to water runoff and concentration further exacerbates this scenario since it negatively affects both geotechnical properties and the strength of the discontinuities (Boldini et al. 2018). In Vardzia, the obtained ST maps allowed the mapping of the moisture patterns in correspondence with large subvertical open fractures; these constitute the main ephemeral streams developing along the slope. The association of ST anomalies with moisture demonstrates that the ephemeral drainage pattern is concentrated within the subvertical joint system affecting mostly Layers 1–4 in and 3–4. Rill erosion, in particular, involves the debris talus of the slope. The hydro-modeling analysis on the UAV-DP products confirmed the insights provided by IRT and provided an accurate mapping of the slope ephemeral drainage network. This represents areas of preferential surface erosion and weathering, mainly in Layers 2 and 3. These streams cause moderate mass transport and deposition at the slope toe, creating small taluses. In Vardzia, water runoff and moisture, which often occur in the tuff layers represent an important predisposing factor for instability phenomena.

To mitigate slope instability a new low-cost, low-impact system of runnels and retaining walls should be designed and implemented in the slope's western sector, together with filtering weirs within the creek bed rock cuts (Fig. 11).

In Vanis Kvabebi, the main conservation issues are the following: (i) linear erosion along persistent and open master joints; (ii) slope instabilities due to the combination of the stratigraphy (soft erodible ash layers alternating with tuff layers) and the structural setting. These, in particular, create several unstable protruding and overhanging sectors along the slope. The most relevant instabilities are represented by wedge failure and plane failure. The latter can be locally predominant in overhanging sectors, such as that affected by the 2017 collapse. The adopted methodology supplied insights into the influence of the fracture system with respect

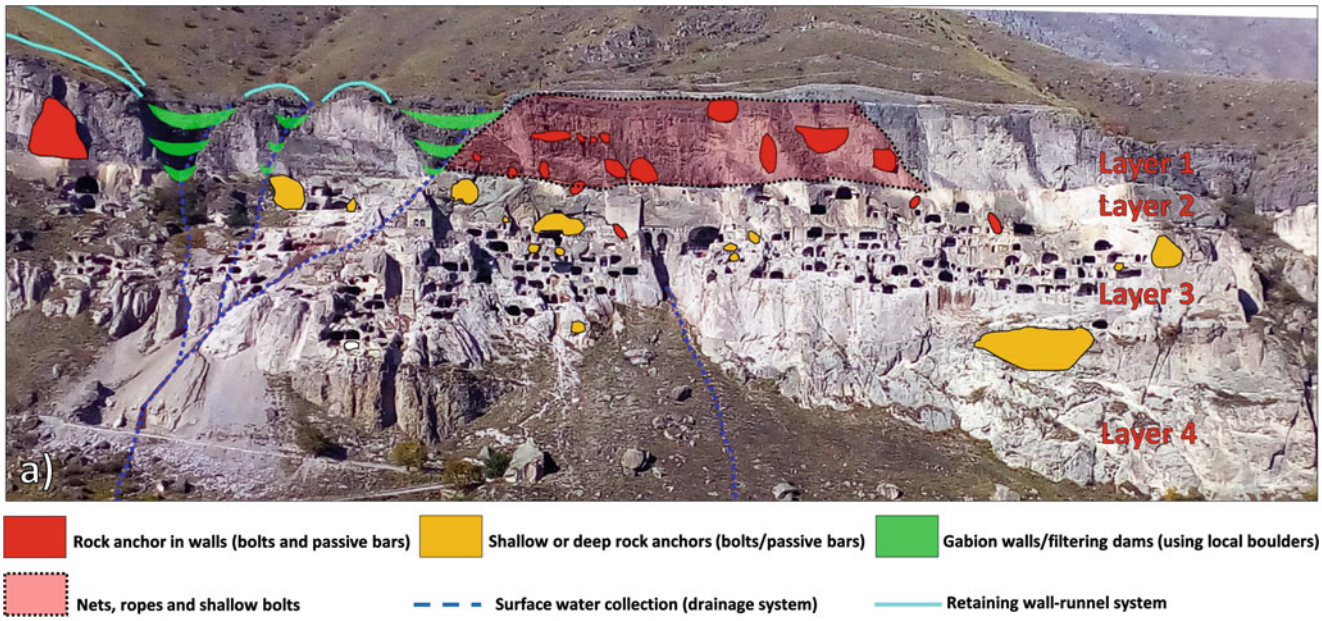

Fig. 11 General master plan for the proposed mitigation measures for the whole Vardzia Monastery

to the hydraulic setting. The collected information was then used as a fundamental input for framing conservation strategies. Furthermore, accurate mapping of open fractures provides useful information for planning a crack meter network for monitoring local deformation. The UAV-DP orthoprojection image granted a useful topographic reference to be used as a starting point for the planning of future conservation works (Fig. 12).

In Uplistsikhe, several critical areas were selected, among which the rockfall-affected areas were selected as the highest priority for the consolidation works. These started from Area 1 by reinforcement of a critical block on the rock cliff using of deep anchoring. A special hanging scaffolding was constructed and fifteen horizontal drillings to depths up to 9 meters were conducted, where the still anchors were fixed and cemented. A water-diverting structure will also be planned in correspondence with the ephemeral stream highlighted in Fig. 8. This first stage of mitigation works will enable the opening of the historical entrance into the Uplistsikhe rock town, located at the bottom of the rock cliff.

In David Gareja, there is generally not a predominant instability process acting in the analyzed sites: they can all be reconducted to rock collapses directly dependent on local structural settings differently interacting with the slope face and stress release. In Natlismcemeni, the performed activities proved to be effective tools in enhancing potentially unstable ledge-niche systems and open fractures, and defining the more landslide-prone sectors as priority areas for sealing/reinforcement.

In Sabereebi, erosional processes caused by an ephemeral stream in the debris talus can undermine the stability of monastery pillars. Future mitigation works to be planned are drainage channels to avoid overland flow on top of the rock slope and erosion of the underlying debris talus. Non-structural mitigation actions, such as the implementation of a monitoring system for the measurement of displacements, such as robotized topographic stations and Ground-based Synthetic Aperture Radar systems, are being implemented. Such action is important for locating the priorities in the areas of intervention, in the framework of the site's preservation, as well as for the safety of local monks, for the staff of rock-climbers which will be operating in reinforcement/conservational tasks in the next future, and for visiting tourists.

5 Conclusions

In all the analyzed sites, the field surveys provided fundamental insights into the acting erosion, weathering, and instability processes affecting the rock cliffs of both sites. Meanwhile, the remote sensing approach provided full coverage of the analyzed slopes, allowing for the detection of slope criticalities in inaccessible or hazardous sectors while granting the safety of the operators. The portability, fast acquisition, and processing times of IRT were profitably applied at both sites for a preliminary mapping of the slope surface moisture sectors associated with ephemeral drainage networks. At the same time, UAV-DP high-resolution

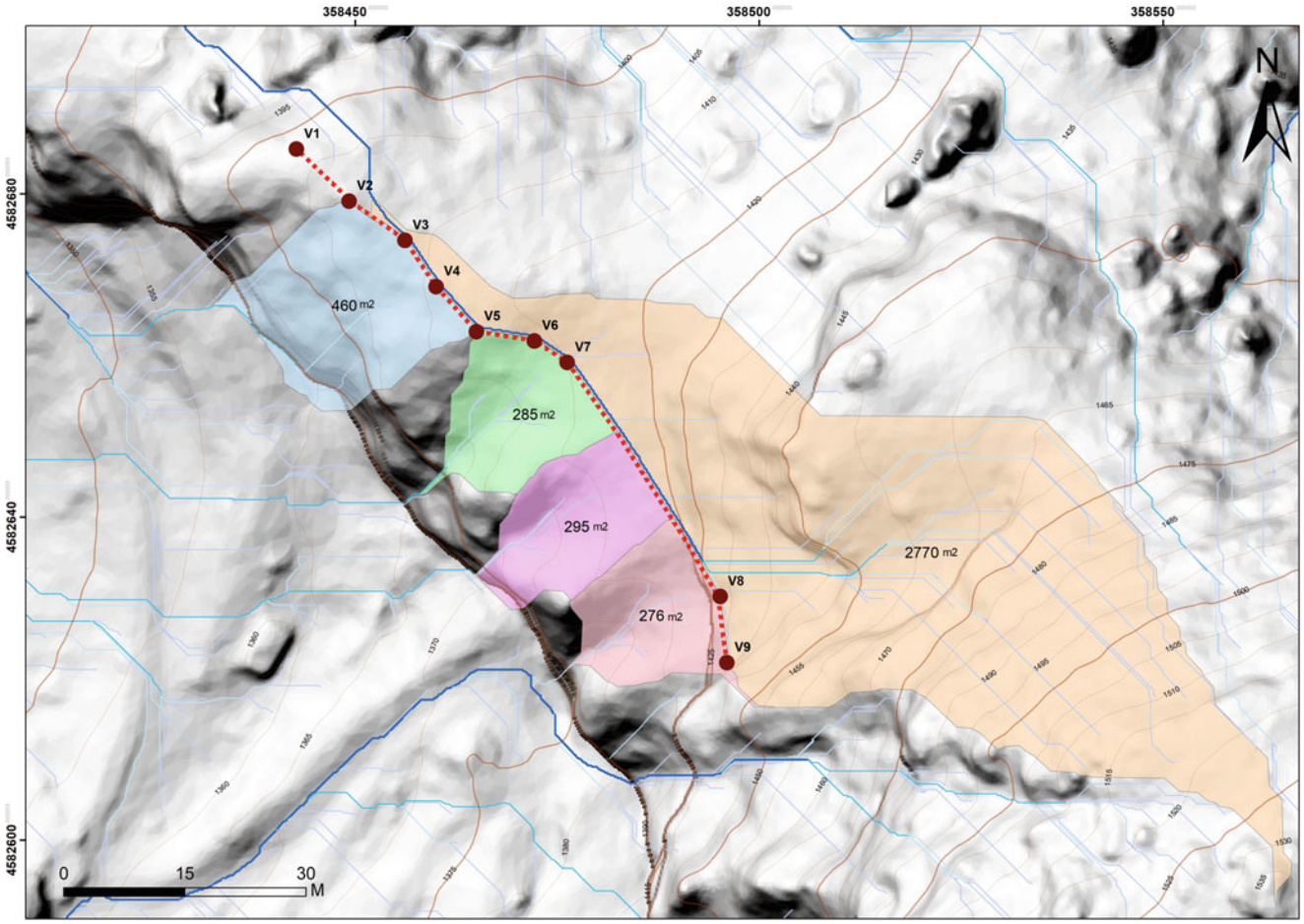

Fig. 12 Hydrographic model of Vanis Kvabebi western cliff showing the watershed surfaces, the area where the water drainage system is planned (the red dashed line shows the planned water diverting wall)

surfaces were useful for performing with high accuracy the hydro-modeling. Generally, the detected ephemeral stream pattern is controlled by the morphological interaction with the main rock slope fractures. This approach served as the basis for proposing the implementation of new drainage channels and retaining walls. Given the possible logistical limitations in the planning of an IRT survey, the timing of the survey and the position of the thermal camera must be carefully considered to obtain both the best image resolution and the widest field of view of the scenario at the same time avoiding the shadowing effects on the slope. Future advancements should include the application of fixed thermal camera installations in remote surveying and monitoring stations for gathering continuous, high-resolution, real-time IRT data. A skilled thermal camera operator is strongly recommended for correct IRT image acquisition, elaboration, and interpretation procedures.

Acknowledgments This work was carried out in the framework of a Bilateral agreement between the Earth Science Department of the University of Florence (Italy) and the Faculty of Natural Sciences and Engineering of Ilia State University (Tbilisi, Georgia). The authors are very grateful to the National Agency for Cultural Heritage Preservation of Georgia (NACHPG) and to all the staff members for their support in the present research.

References

Agisoft Photoscan (2017) datasheet. https://www.agisoft.com/pdf/photoscan-pro_1_4_en.pdf. Last Access December 2019

Boldini D, Guido GL, Margottini C, Spizzichino D (2018) Stability analysis of a large-volume block in the historical rock-cut city of Vardzia (Georgia). Rock Mech Rock Eng 51(1):341–349

Bolognesi M, Furini A, Russo V, Pellegrinelli A, Russo P (2014) Accuracy of cultural heritage 3D models by RPAS and terrestrial photogrammetry. The International Archives of Photogrammetry, Remote Sensing and Spatial Information Sciences 40(5):113–119

Chandler J (1999) Effective application of automated digital photogrammetry for geomorphological research. Earth Surf Process Landf 24: 51–63

Cruden DM, Varnes DJ (1996) Landslide types and processes. In: Turner AK, Schuster RL (eds) Landslides investigation and

mitigation, 1996, special report 247. Transportation Research Board, Washington, D.C, pp 36–75

ESRI (2019) ArcMap 10.6 datasheet. ESRI Inc. https://www.esri.com/content/dam/esrisites/en-us/media/pdf/product/desktop/ArcGIS-10.6-Desktop-ArcMap-Functionality-Matrix.pdf. Last Access October 2019

FLIR (2009) FLIR ThermaCAM SC620 technical specifications. FLIR systems Inc. www.flir.com/cs/emea/en/view/?id=41965. Last Access July 2019

FLIR (2015) FLIR tools+ datasheet. FLIR systems Inc. https://www.infraredcamerawarehouse.com/content/FLIR%20Datasheets/FLIR%20ToolsPlus%20Datasheet.pdf. Last Access September 2019

Frodella W, Gigli G, Morelli S, Lombardi L, Casagli N (2017) Landslide mapping and characterization through infrared thermography (IRT): suggestions for a methodological approach from some case studies. Remote Sens 9(12):1281

Frodella W, Elashvili M, Spizzichino D, Gigli G, Adikashvili L, Vacheishvili N, Kirkitadze G, Nadaraia A, Margottini C, Casagli N (2020a) Combining InfraRed thermography and UAV digital photogrammetry for the protection and conservation of rupestrian cultural heritage sites in Georgia: a methodological application. Remote Sens 12(5):892

Frodella W, Spizzichino D, Gigli G, Elashvili M, Margottini C, Villa A, Frattini P, Crosta G, Casagli N (2020b) Integrating kinematic analysis and infrared thermography for instability processes assessment in the rupestrian monastery complex of David Gareja (Georgia). Understanding and reducing landslide disaster risk. Springer, Cham, pp 457–463

Frodella W, Elashvili M, Spizzichino D, Gigli G, Nadaraia A, Kirkitadze G, Adikashvili L, Margottini C, Antidze NC, N. (2021) Applying close range non-destructive techniques for the detection of conservation problems in rock-carved cultural heritage sites. Remote Sens 13:1040

Grün A, Remondino F, Zhang L (2002) Reconstruction of the great Buddha of Bamiyan, Afghanistan. Int Arch Photogramm Remote Sens 34(5):363–368

Gudjabidze GE, Gamkrelidze IP (2003) Geological map of Georgia 1: 500 000. Georgian State Department of Geology and National Oil Company "Saqnavtobi"

ISRM (1978) Suggested methods for the quantitative description of discontinuities in rock masses. Int J Rock Mech Min Sci Geomech Abs 15(6):319–368

ISRM (1985) Suggested methods for determining point load strength. Int J Rock Mech Min Sci Geomech, Abs 22(2):51–62

Margottini C, Antidze N, Corominas J, Crosta GB, Frattini P, Gigli G, Giordan D, Iwasaky I, Lollino G, Manconi A, Marinos P, Scavia C, Sonnessa A, Spizzichino D, Vacheishvili N (2015) Landslide hazard, monitoring and conservation strategy for the safeguard of Vardzia byzantine monastery complex. Georgia Landslides 12(1): 193–204

Nolesini T, Frodella W, Bianchini S, Casagli N (2016) Detecting slope and urban potential unstable areas by means of multi-platform remote sensing techniques: the Volterra (Italy) case study. Remote Sens 8(9):746

Okrostsvaridze A, Popkhadze N, Bluashvili D, Chang YH, Skhirtladze I (2016) Pliocene Quaternary Samtskhe-Javakheti Volcanic Highland, Lesser Caucasus, as a result of mantle plumes activity. In: Gilbert, A. S., and Yanko-Hombach, Valentina, eds., Proceedings of the Fourth Plenary Conference of IGCP 610 "From the Caspian to Mediterranean: Environmental Change and Human Response during the Quaternary (October 2–9, 2016; Tbilisi, Georgia)". Georgian National Academy of Sciences, Tbilisi, pp 127–131

Rocscience (2020) Dips. v8 graphical and statistical analysis of orientation data. Rocscience Inc., Toronto, Ontario

Spampinato L, Calvari S, Oppenheimer C, Boschi E (2011) Volcano surveillance using infrared cameras. Earth Sci Rev 106:63–91

Stinghen A (2011) Tectonic and geomorphological evolution of the kartalini basin, Georgia, University of Padua, Master's thesis in Geology, p 109

Zhang Z, Zheng S, Zhan Z (2004) Digital terrestrial photogrammetry with photo total station. International Archives of Photogrammetry and Remote Sensing, Istanbul, pp 232–236

Spatial and Temporal Characterization of Landslide Deformation Pattern with Sentinel-1

Francesco Poggi, Roberto Montalti, Emanuele Intrieri, Alessandro Ferretti, Filippo Catani, and Federico Raspini

Abstract

The results of multi-interferometric processing applied to radar images acquired by the European Space Agency (ESA) Sentinel-1 constellation, obtained in the framework of the IPL (International Programme on Landslides) project n.221, are presented in this manuscript. The target area is the Hunza-Nagar River valley, a remote area in northern Pakistan. The Humarri slide, a massive landslide located along the left side of the valley, is the most active phenomenon in the area, and poses a very high risk to the Humarri village built in the lowest part of the landslide, and a threat of damming the Hispar River. The highest deformation rates (with peaks higher than 300 mm/yr) were recorded in the middle and low part of the landslide. Where the Humarri village is located, the velocity values are lower and range between −30 and −80 mm/yr. The analysis of displacement time series, spanning from February 2017 to January 2020, reveal different deformation behaviors and different onset of accelerating behaviors within the landslide body. The global coverage, the wide-area mapping capabilities, and the regular acquisitions planning ensured by the Sentinel-1 constellation, coupled with InSAR ability to deliver very precise and spatially dense information, make it possible to scan wide areas and spot unstable zones, especially where remoteness, vast areal extension, and climatic conditions make it difficult to undertake field activities.

Keywords

Landslides · Sentinel-1 · SAR interferometry · Mapping · Monitoring

1 Introduction

Landslides are ubiquitous phenomena in the mountainous regions of Northern Pakistan (Said 1992; Kamp et al. 2008). Concomitant factors, like geology (the Himalaya represents one of the youngest and most prominent mountain system on the planet), tectonics (frequent and recurrent earthquakes), geomorphology (high relief energy and slope gradient), and environmental conditions (strong weathering processes) make landslide hazard a serious concern for the safety of life and property in the region (Sato et al. 2007; Owen et al. 2008; Khan et al. 2011). Besides earthquakes, heavy rainfall may cause landslides, especially during the monsoon period from July to August when the area receives the bulk of precipitation. Socioeconomic development and related human activities contribute considerably to increase the level of landslide risk. Formation of landslide dams on the streams and rivers is another significant issue in the mountainous areas of Pakistan (Fan et al. 2020). A well-known example is the Hunza lake that formed on 4 January 2010 when the Attabbad landslide blocked the flow of the Hunza River, with a risk for the population downstream in case of sudden out-bursting. However, due to the wide extension, the limited ground-truthing, and remoteness of the area, systematic studies have not been undertaken, while the boundaries and volume of landslide problem remain unknown. A detailed assessment of landslide distribution and characteristics has been advised (Sato et al. 2007).

In this context, satellite Earth Observations (EO) have shown their usefulness in landslide mapping (Sato et al.

F. Poggi · E. Intrieri · F. Raspini (✉)
Department of Earth Sciences, University of Firenze, Florence, Italy
e-mail: francesco.poggi1@unifi.it; emanuele.intrieri@unifi.it; federico.raspini@unifi.it

R. Montalti
TRE Altamira, Barcelona, Spain
e-mail: roberto.montalti@tre-altamira.com

A. Ferretti
TRE Altamira, Milan, Italy
e-mail: alessandro.ferretti@tre-altamira.com

F. Catani
Department of Geosciences, University of Padova, Padova, Italy
e-mail: filippo.catani@unipd.it

I. Alcántara-Ayala et al. (eds.), *Progress in Landslide Research and Technology, Volume 2 Issue 1, 2023*,
Progress in Landslide Research and Technology, https://doi.org/10.1007/978-3-031-39012-8_15

2007). Satellite InSAR (Synthetic Aperture Radar Interferometry), in particular, can give a meaningful contribution thanks to high accuracy, wide-area coverage, the possibility of tracking the history of deformations back to early 90 s, the systematic data sampling, and higher benefit/cost ratio with respect of targeted ground-based monitoring campaigns (Tomás and Li 2017; Cigna 2018). The InSAR algorithm SqueeSAR (Ferretti et al. 2011) can provide accurate information on the possible displacement of a network of radar targets, including man-made structures (e.g., buildings, roads, and bridges) and natural features (e.g., rocky outcrops and bare soils). The SqueeSAR algorithm has been demonstrated to be a reliable technique for landslide investigations over wide areas and in natural terrain (Meisina et al. 2013; Raspini et al. 2016).

Despite more than 20 years of undisputed progress in satellite system imaging capabilities and advancement in processing and analysis of SAR acquisitions, only the launch of the Sentinel-1 constellation opened new possibilities for the operational use of satellite SAR data as a monitoring tool at the regional to national scales (Torres et al. 2012).

In this manuscript, the results obtained in the framework of the IPL project n.221 are presented. The potential of Sentinel-1 is exploited to detect and measure active movements in the Hunza-Nagar valley in North Pakistan. This is a remote area where field investigations need to be driven a by pre-screening phase to minimize efforts and prioritize further activities.

2 Description of the Study Area

The study area is located in the Hunza-Nagar valley of the Gilgit-Baltistan province, in the Karakoram Mountains, in northern Pakistan (Fig. 1). The elevation ranges from 1556 m to 7774 meters above sea level, with an average

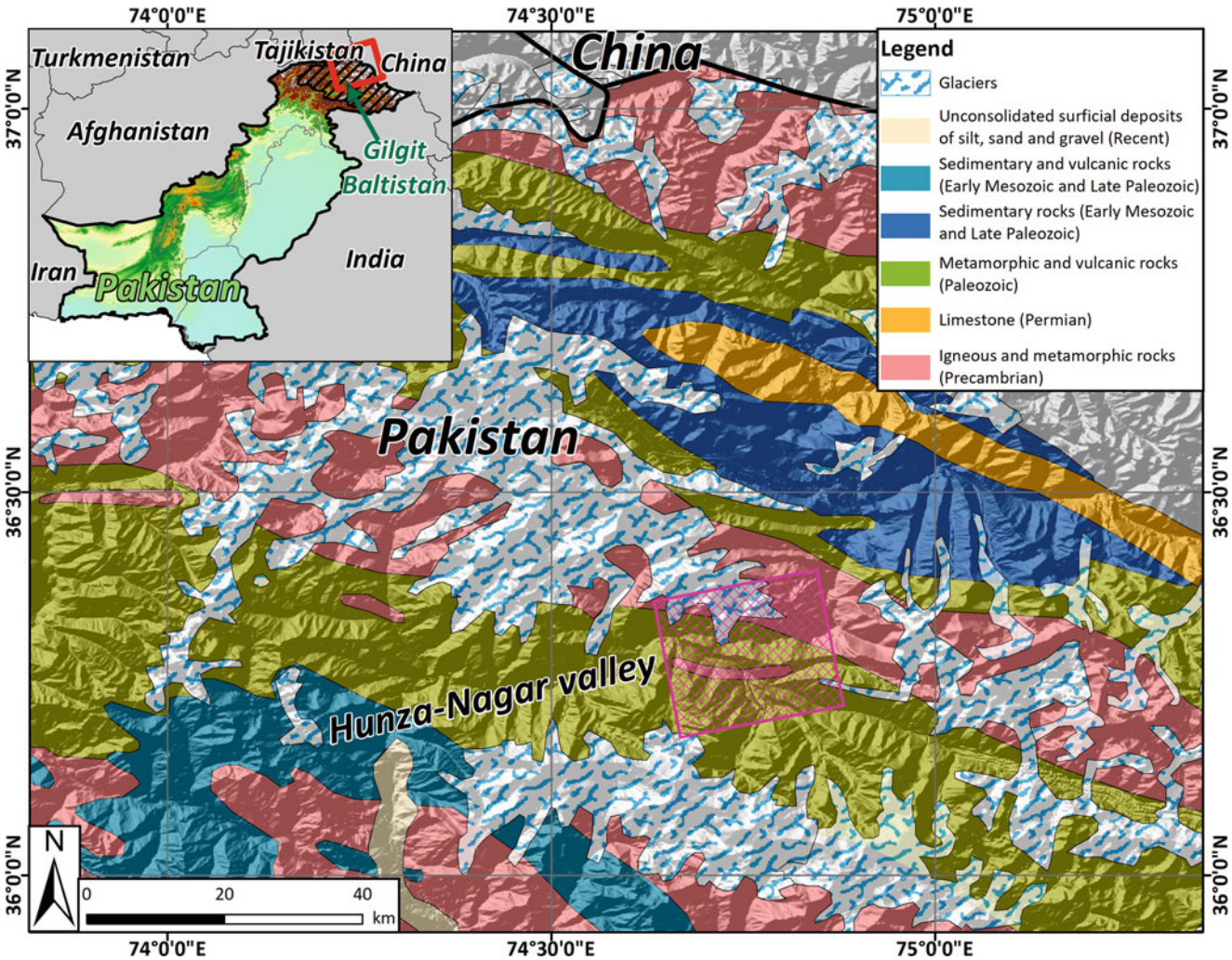

Fig. 1 Location of study area in the Hunza-Nagar valley of the Gilgit-Baltistan province (Northern Pakistan). The pink polygon represents the area processed with Sentinel-1. Redraw of Geological Map of Pakistan (Abu-Bakr and Jackson 1964)

slope of 45°. This region is occupied by the high alpine humid tundra and includes the upper and middle ablation zones. It has an intense snowfall season spanning six to eight months, and a short summer. Glacial and cryogenic processes dominate, with mechanical weathering and rock fragmentation resulting in avalanches, rockfalls, and debris flows (Ali et al. 2019; Ur Rehman et al. 2020).

Tectonically, the site is in the active collision zone of the Indian and Eurasian plates (Searle et al. 1999). Crustal shortening, active faulting, and subduction are continuing with convergence and uplift rates of ~4–5 cm/year (Searle et al. 1999) and ~ 7 mm/year (Zeitler 1985; Coward et al. 1986), respectively. The significant tectonic features responsible for brittle deformation in this area are the Main Karakoram Thrust (MKT) and Karakoram Fault (KF). Due to this brittle deformation, the rock mass is highly fractured and jointed. The MKT is the collision zone of the southern margin of the Eurasian plate, and extends into Baltistan through the Hashupa, Shigar, and Shyok valleys, respectively. MKT is a seismically active thrust fault that has a high angle along which many earthquakes have occurred (Verma and Sekhar 1986). The region has experienced many disastrous earthquakes in the past, about 300 ($M > 5$) and seven ($M > 7$) earthquakes events since 1980 (Kashmir Earthquake October 2005: $M = 7.6$; Afghanistan October 2015: $M = 7.5$) according to the USGS Earthquake Catalog (Ur Rehman et al. 2020). The Hunza-Nagar valley has a series of NE-dipping thrust faults and normal faults, producing foliation and fractures in the rocks.

The geology of the area comprises four formations, namely the Southern Karakoram metamorphic complex (SKm), the Hunza Plutonic Unit (HPU), the Shaksgam Formation (SF) and Quaternary (Q) Deposits (Searle et al. 1999). The SKm consists of paragneiss with interbedded pelites and amphibolites. The Shaksgam Formation is a subsection of northern Karakoram terrain (Searle et al. 1999) and includes Permian massive limestones. The HPU is a subsection of the Karakoram batholith and contains plagioclase, quartz, biotite and hornblende (Searle et al. 1999). Quaternary Deposits consist of alluvium deposits, unconsolidated conglomerate, sandstone, siltstone, and loess (Searle and Kahn 1996).

The geomorphology of the area comprises glaciofluvial fans, terraces, ancient glacial moraines, loose colluviated material on steep scree slopes, debris flows in debris cones, with talus deposits accumulate at the base of high cliffs in deeply dissected mountains (Hewitt 1998). Young, or recent glacial landforms play a significant role in the geomorphological landscape assemblage of the Karakoram Mountains. Lateral moraines consist mainly of supraglacial debris deposited from recent glacier margins, the transfer of englacial debris, or the pushing and redistribution processes of accumulated (pre-glacial) debris. Many active landslides occur in Karakoram ranges, especially in lateral glacial moraine deposits, where they pose severe dangers to roads, house, buildings and community infrastructures. Moraine deposits are unstable glacial landforms, characterized either by discrete shear plane failures due to steep slopes ($> 30°$), or by constant deformation resulting from weak mechanical properties of the ground and moisture (Su et al. 2022). Due to repeated glacier advances, older moraine cores are superimposed by younger supraglacial debris (Kamp and Haserodt 2004). These huge lateral moraines host many villages, and the inhabitants use them extensively for agricultural purposes, e.g., the Humarri village. The Humarri village is situated on the moraine terrace of the formerly glaciated region, and the village is located on the wall of the MKT. High-grade metamorphic rocks of the Karakoram block are exposed above the moraine ridges. The Hispar River flows 300 m below the left side of the hill. A local fault, called Humarri fault, passes near the Humarri Terrace in a NE-SW direction.

Humarri landslide is 2.800 m in length, 1.600 m in width, and about 300 m in maximum thickness. The steepness of the slope varies from 25° to 70°, facing the northeast direction. The sliding body consists of unconsolidated moraine materials, while the bedrock is predominantly ortho- and para-gneiss (Su et al. 2022).

3 Methods

3.1 Generation of Ground Deformation Maps and Time Series

C-band (center frequency 5.405 GHz and wavelength 5.6 cm) images from the ESA Sentinel-1 archive were processed by means of the SqueeSAR algorithm (Ferretti et al. 2011) to obtain the ground deformation map of the study area. A total of 85 images acquired along ascending geometry were used, covering the interval from February 2017 to January 2020.

The SqueeSAR algorithm represents the evolution of the Permanent Scatterer SAR Interferometry (PSInSAR) (Ferretti et al. 2001). The process is aimed at identifying radiometrically stable reflectors called Permanent Scatterers (PS) and exploiting whole stacks of SAR images. Every PS represents a pixel of a SAR image with high signal coherence, mainly corresponding to bedrock outcrops and man-made objects. The main drawback of this technique is the low density of PS that could be obtained in agricultural, natural and peri-urban areas (< 10 PS/km^2 using C-band radar images), compared to the PS density in urban areas (> 100PS/km^2 using C-band radar images).

The SqueeSAR algorithm was designed to overcome this limitation, defining a new type of PS points: the Distributed Scatterers (DSs), thus maximizing the spatial density of measurement points. A DS is a target corresponding to an area,

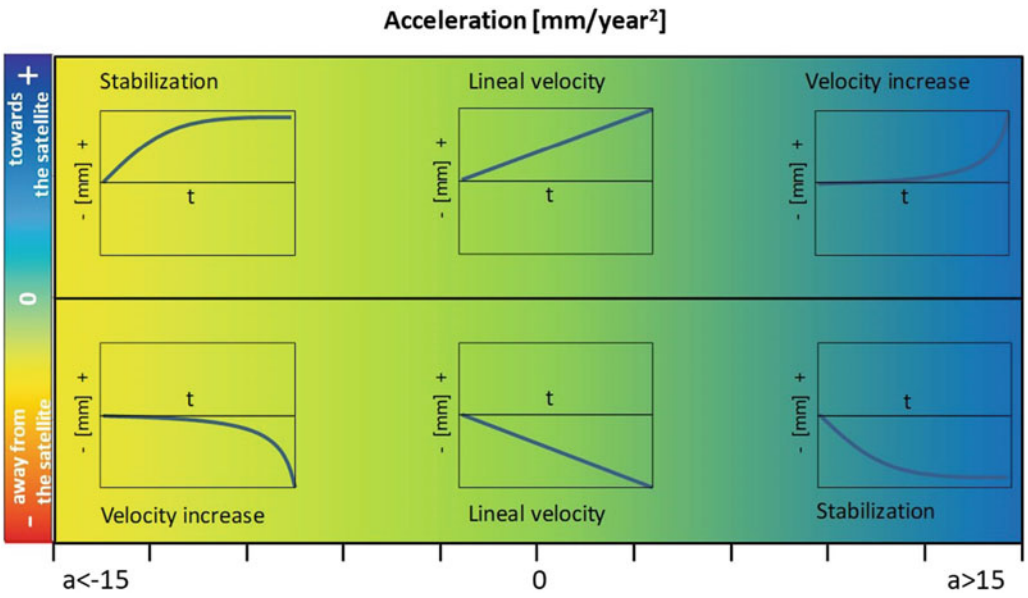

Fig. 2 Screening and classification of displacement time series with respect to absence or presence of velocity variation

where a certain number of neighboring pixels share similar reflectivity values and moderate interferometric coherence. By combining and merging the signal of these pixels, it is possible to extract a point-like feature with high interferometric coherence. DSs typically match with homogeneous areas such as deserts, debris, or uncultivated areas. The SqueeSAR approach jointly process PS and DS and considers their different statistical behaviors. This is possible through space adaptive filtering with DespecKS (Ferretti et al. 2011), which statistically averages homogeneous pixels (SHP) while preserving pointwise information associated with point targets. A filter based on the Kolmogorov-Smirnov statistical test (Stephens 1970; Kvam and Vidakovic 2007), was applied to all pixels within a certain estimation window, centred on the pixel under analysis (Ferretti et al. 2011). After that, it was possible to: (1) despeckle amplitude data; (2) filter interferometric phase values; and (3) estimate coherence values properly. The SqueeSAR analysis was designed to identify a dense grid of measurement points (MPs), either PS or DS, for which it would be possible to estimate the mean deformation velocity (usually measured in mm/yr) and the displacement time series (TS) (cf. Ferretti et al. 2011). Both of these parameters were estimated with millimeter accuracy (Colesanti et al. 2003) along the satellite Line of Sight (LOS).

3.2 Generation of Acceleration Maps

TS represent the most advanced SqueeSAR product, providing a deformation history over the analyzed time interval. As such, TS are basic tools for studying the kinematics of a given phenomenon, highlighting any potential changes occurred during the monitoring period (Zhang et al. 2018), such as sudden accelerations prior to a landslide failure (Intrieri et al. 2018; Carlà et al. 2019). More recently, TS were successfully exploited to set up a continuous monitoring system at the regional scale based on systematic imagery processing (Raspini et al. 2018) and identification of anomalies of movement (Raspini et al. 2019), *i.e.*, points where a change in the dynamic of motion is occurring.

To fully exploit information contained within SqueeSAR outputs for the Humarri landslide, TS of each measurement point were analysed to identify any change in the deformation pattern. Displacement TS were analyzed year by year, to highlight kinematic variations (acceleration or deceleration, Fig. 2). This action reproduced, automatically, the manual process of identifying anomalous movement during visual inspection by radar interpreters.

4 Results

Figure 3 shows the deformation map of the area of interest exploiting the 85 Sentinel-1 ascending images, processed by the SqueeSAR algorithm. Each point on the map is classified according to its mean deformation velocity along the satellite LOS. Green colors indicate null to very low LOS deformation rates, usually between +2.0 and − 2.0 mm/yr (*i.e.*, close to the sensitivity of the SqueeSAR technique), and reflects motionless areas. Point with LOS velocities < -2.0 mm/yr indicate surface deformation motion away from the satellite, while LOS deformation rates $>$ +2.0 mm/yr reflect

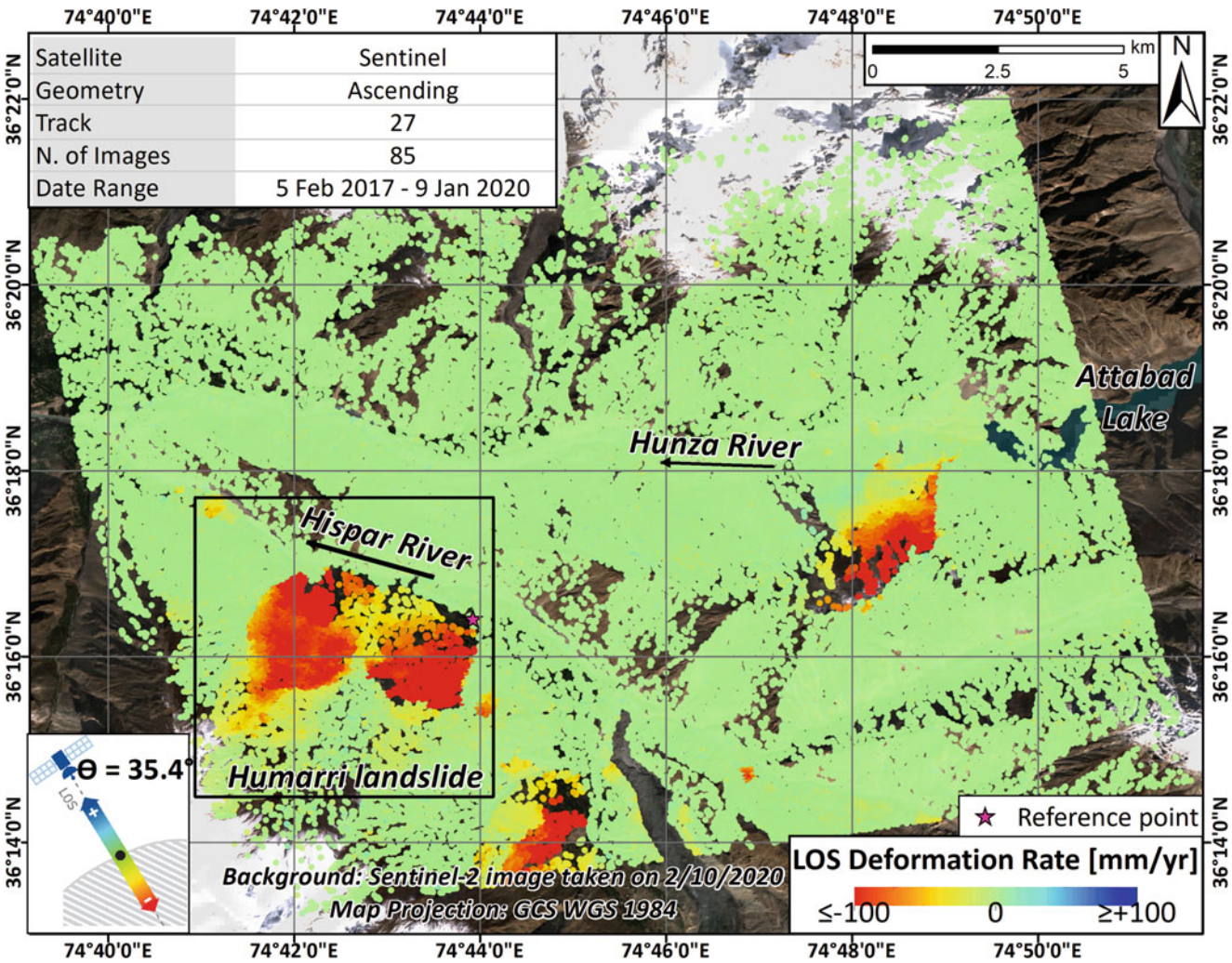

Fig. 3 Ground deformation map for the wide area of the Humarri landslide

movements towards the satellite. The color scale gradations from yellow to dark red, and from light blue to violet represent increasing deformation rates.

With almost seventy-one thousand points covering an area of approximately 200 km^2, this map includes a wealth of information that can be exploited to scan wide areas, to spot unstable zones, and to reconstruct the deformation history of the observed scene back to 2017. This aspect is particularly relevant for inaccessible places where field inspection would be difficult, and for remote areas where ground-based monitoring is not unfeasible. SqueeSAR results indicate the presence of areas affected by active movements within the narrow and deep valleys incised by the Hunza River and its left tributary, the Hispar River. These movements are clearly related to slope instability phenomena, and as a consequence of scant to absent vegetation, the extent of the moving areas can be successfully depicted. Only the presence of snow cover and glaciers hinders the density of MPs.

The Humarri landslide (Ur Rehman et al. 2020) is situated along the left bank of the Hispar River and it is well depicted by the SqueeSAR results (Fig. 4) and by large fractures in the crown area, clearly visible within mid-resolution satellite imagery. Outside the landslide body stable points exhibit random oscillations of displacement values around zero, reflecting the absence of appreciable movements. A total of 7778 measure points (MPs) is extracted from within the landslide area, with a density of 463 MP/km^2, and a mean velocity of −110 mm/year. The highest deformation rates (dark red points in Fig. 4) are located in the middle and lower part of the landslide where velocities higher than 300 mm/yr are recorded. Where the Humarri village is located, the velocity values are lower and range between −30 and −80 mm/yr.

Considering the acquisition geometry and the slope orientation, this landslide is moving towards north-east, *i.e.*, towards the Humarri village and Hispar River valley, thus

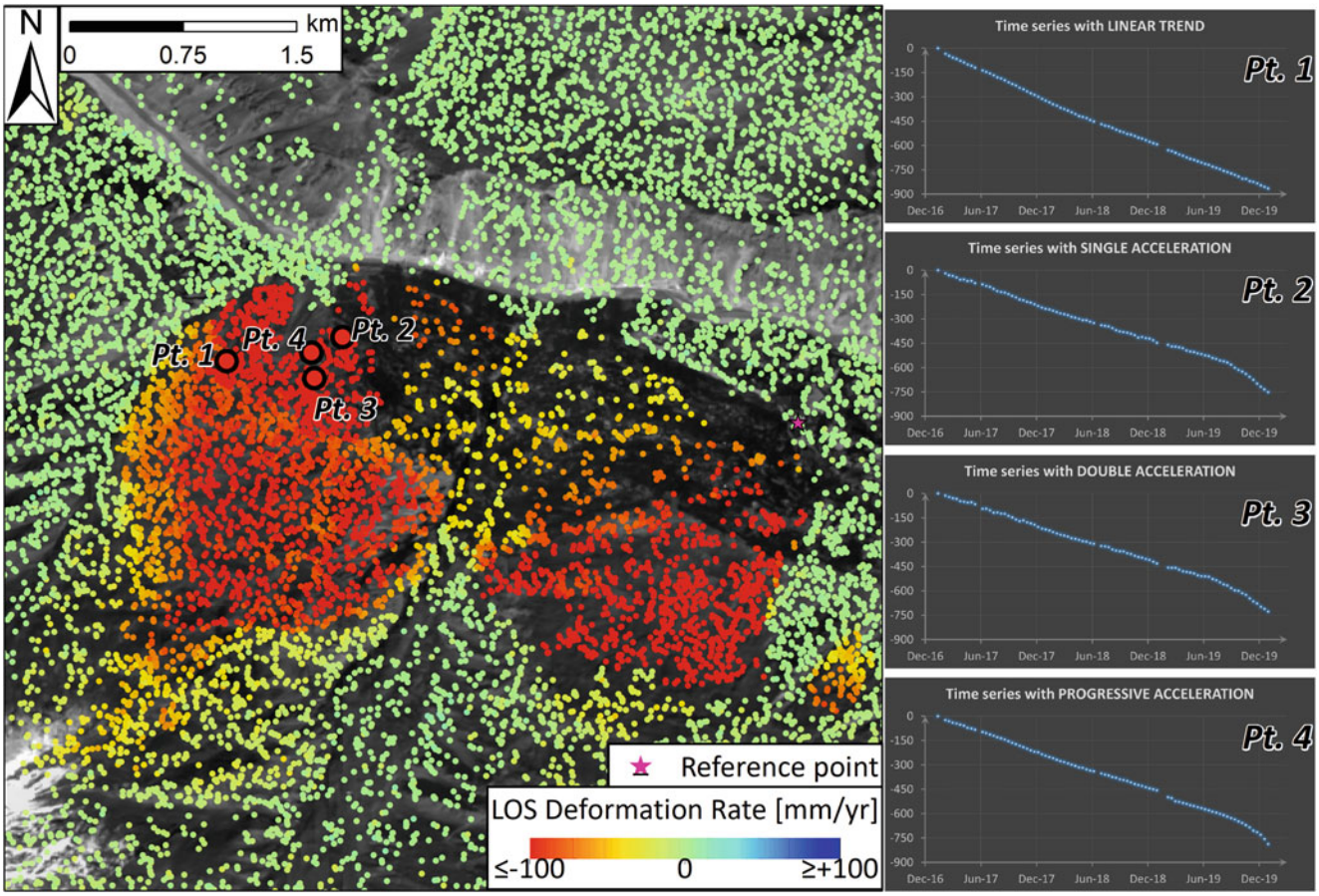

Fig. 4 Ground deformation map for the Humarri landslide. On the right displacement time series, representative of different styles of motion have been selected and plotted

posing a very high risk for inhabitants, and a potential risk of a failure leading to the damming of the river. Different velocity patterns are identified for the different sectors of the landslide. The high variability of landslide kinematics, highlighted by different spatial patterns of deformation, is confirmed by the TS analysis of displacement, with measurement points exhibiting different temporal behavior even at a short distance (TS included on the right of Fig. 4). Despite a certain level of variability, TS within the Humarri landslide can be classified according four different styles of motion. A linear trend of deformation characterizes those points that have a constant rate of deformation and do not register any velocity variation during the monitored period (Pt. 1 in Fig. 4). Conversely, TS affected by trend changes denote a clear variation of their temporal behavior: Pt 2 and Pt 3 in Fig. 4 exhibit a single, or double acceleration during the monitored period that corresponds to slope instability with increasing displacement rate. Finally, Pt. 4 in Fig. 4 appears to indicate a progressive acceleration, contributing to an increasing strain rate in soil on the slope.

The early detection of accelerating areas, with particular attention to increasing strain rate, is the main purpose of any landslide monitoring system. As such, they can indicate a slope instability potentially leading to future landslide failure.

For this reason, to enhance information provided by SqueeSAR analysis following the manual inspection of the TS, displacement TS were automatically analyzed to determine the occurrence and magnitude of accelerations over the monitored period (2017–2019). This analysis uncovered further details, and extends spatially the results obtained with manual analysis, recognizing, year by year, those points with deformation rates higher than expected. For each area affected by accelerations during 2017 and 2019, a representative point has been selected and plotted (Fig. 5).

5 Discussion and Conclusions

The current focus of research is to exploit the maximum potential of Sentinel-1 to scan, detect, and quantify active movements in the Hunza-Nagar valley in North Pakistan.

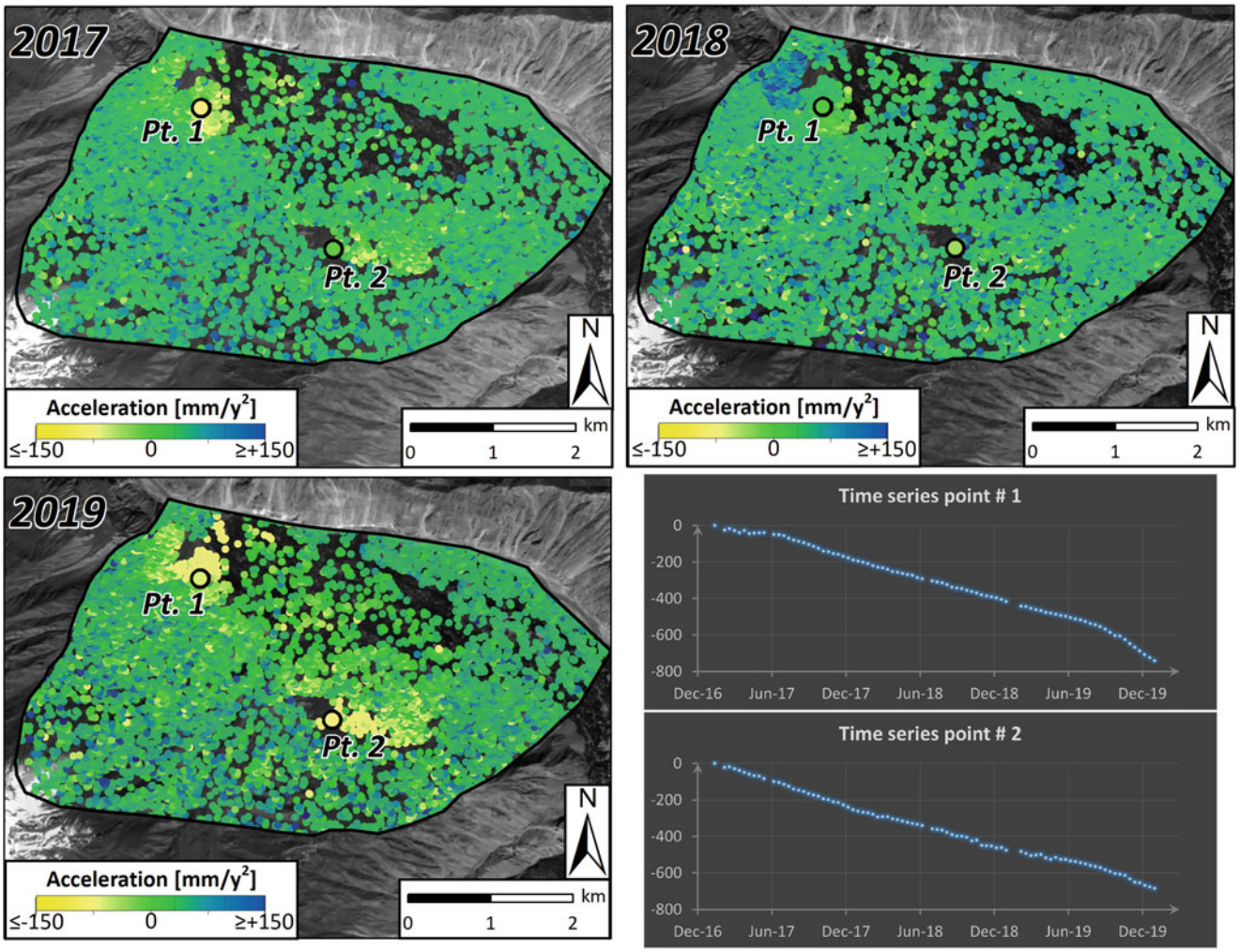

Fig. 5 Acceleration maps for the Humarri landslide. On the right displacement time series are plotted: point 1 shows a double acceleration in 2017 and 2019, while point 2 a single acceleration in 2019

This is a remote area where field investigations require a pre-screening phase to minimize efforts and prioritize further activities.

The SqueeSAR algorithm applied to Sentinel-1 radar images successfully identified the active movements in the Hunza-Nagar valley. The advantage of Sentinel-1 images lies in its open access policy, the global coverage, and covering a time span of several years. The deformation map (Fig. 3) captures three main areas of deformation, detected in the narrow and deep valleys incised by the Hunza River and its left tributary, the Hispar River. In this pre-screening phase, priority for investigation are the lowest parts of the landslide on which the Humarri village is built. This landslide poses a very high risk for the inhabitants with a potential risk of river damming during failure.

The SqueeSAR results depict the body of Humarri landslide. Considering the acquisition geometry and the slope orientation, this landslide is moving towards the north-east. The density of measurement points is high due to the scarcity of vegetation on the slope. The highest deformation rates (over 300 mm/yr) are recorded in the middle and lower part of the landslide. Different velocity patterns are identified for different sectors of the landslide (Fig. 4). The analysis of displacement TS highlights the variability of landslide kinematics, with measurement points showing different temporal behavior, even at a short distance. Linear deformation trends, single or double acceleration, and progressive acceleration were all observed in the Sentinel-1 time series data. To determine the magnitude of accelerations within the monitored time period, we find that the manual inspection of displacement TS enhances the information provided by SqueeSAR analysis. For the Humarri landslide, we identified two main areas affected by accelerations. The former (Pt. 1 Fig. 5) was characterized by double acceleration in July 2017, and between July and August 2019. The latter (Pt. 2 Fig. 5) shows an acceleration between in September

2019. As expected, acceleration events correspond to the monsoon period (from July to August), when the area receives the bulk of the annual precipitation. The combination of slope steepness, scarce vegetation and heavy rains favors slope instability.

The successful application of InSAR analysis, coupled with the global coverage, and regular acquisition planning ensured by the Sentinel-1 constellation, allowed to deliver very precise and spatially dense information on ground motion. These qualities make it possible to scan wide areas, and to identify unstable zones, especially where remoteness, vastness, and climatic conditions make it difficult to perform field activities. We demonstrate the effectiveness of InSAR in the Hunza-Nagar valley in North Pakistan. Here, we identify all possible ground deformation with potential to directly impact on the community and we localize areas within the landslide where ground deformation is more intense for prioritized further investigations.

Acknowledgments The results presented in this paper have been obtained in the framework of the IPL (International Programme on Landslides) project n.221 "*PS continuous streaming for landslide monitoring and mapping*" led by Federico Raspini.

References

Abu-Bakr AM, Jackson RC (1964) Geological map of Pakistan. Government of Pakistan and United States Agency for International Development

Ali S, Biermanns P, Haider R, Reicherter K (2019) Landslide susceptibility mapping by using a geographic information system (GIS) along the China–Pakistan Economic Corridor (Karakoram Highway), Pakistan. Nat Hazards Earth Syst Sci 19(5):999–1022. https://doi.org/10.5194/nhess-19-999-2019

Carlà T, Intrieri E, Raspini F, Bardi F, Farina P, Ferretti A, Casagli N (2019) Perspectives on the prediction of catastrophic slope failures from satellite InSAR. Sci Rep 9(1):1–9. https://doi.org/10.1038/s41598-019-50792-y

Cigna F (2018) Observing geohazards from space. Geosciences 8(2):59. https://doi.org/10.3390/geosciences8020059

Colesanti C, Ferretti A, Locatelli R, Novali F, Savio G (2003) Permanent scatterers: precision assessment and multi-platform analysis. In: IGARSS 2003. 2003 IEEE international geoscience and remote sensing symposium. Proceedings, July 2003. (IEEE cat. No. 03CH37477). Toulouse, France Vol. 2, pp. 1193–1195. https://doi.org/10.1109/IGARSS.2003.1294055

Coward MP, Rex DC, Asif Khan M, Windley BF, Broughton RD, Luff IW, Pudsey CJ (1986) Collision tectonics in the NW Himalayas. Geol Soc Lond, Spec Publ 19(1):203–219. https://doi.org/10.1144/GSL.SP.1986.019.01.11

Fan X, Dufresne A, Subramanian SS, Strom A, Hermanns R, Stefanelli CT, Xu Q (2020) The formation and impact of landslide dams–state of the art. Earth Sci Rev 203:103116. https://doi.org/10.1016/j.earscirev.2020.103116

Ferretti A, Prati C, Rocca F (2001) Permanent scatterers in SAR interferometry. IEEE Trans Geosci Remote Sens 39(1):8–20. https://doi.org/10.1109/36.898661

Ferretti A, Fumagalli A, Novali F, Prati C, Rocca F, Rucci A (2011) A new algorithm for processing interferometric data-stacks: SqueeSAR. IEEE Trans Geosci Remote Sens 49(9):3460–3470. https://doi.org/10.1109/TGRS.2011.2124465

Hewitt K (1998) Catastrophic landslides and their effects on the upper Indus streams, Karakoram Himalaya, northern Pakistan. Geomorphology 26(1–3):47–80. https://doi.org/10.1016/S0169-555X(98)00051-8

Intrieri E, Raspini F, Fumagalli A, Lu P, Del Conte S, Farina P, Casagli N (2018) The Maoxian landslide as seen from space: detecting precursors of failure with Sentinel-1 data. Landslides 15(1):123–133. https://doi.org/10.1007/s10346-017-0915-7

Kamp U, Haserodt K (2004) Quaternary glaciations in the high mountains of northern Pakistan. Dev Quat Sci 2:293–311. https://doi.org/10.1016/S1571-0866(04)80135-0

Kamp U, Growley BJ, Khattak GA, Owen LA (2008) GIS-based landslide susceptibility mapping for the 2005 Kashmir earthquake region. Geomorphology 101(4):631–642. https://doi.org/10.1016/j.geomorph.2008.03.003

Khan AN, Collins AE, Qazi F (2011) Causes and extent of environmental impacts of landslide hazard in the Himalayan region: a case study of Murree. Pakistan Natural Hazards 57(2):413–434. https://doi.org/10.1007/s11069-010-9621-7

Kvam PH, Vidakovic B (2007) Nonparametric statistics with applications to science and engineering. John Wiley & Sons, Hoboken. (ISBN 978-047008147-1)., p 429. https://doi.org/10.1002/9780470168707

Meisina C, Notti D, Zucca F, Ceriani M, Colombo A, Poggi F, Zaccone A (2013) The use of PSInSAR™ and SqueeSAR™ techniques for updating landslide inventories. Landslide science and practice. Springer, Berlin, pp 81–87. https://doi.org/10.1007/978-3-642-31325-7_10

Owen LA, Kamp U, Khattak GA, Harp E, Keefer DK, Bauer M (2008) Landslides triggered by the October 8, 2005, Kashmir earthquake. Geomorphology 94:1–9. https://doi.org/10.1016/j.geomorph.2007.04.007

Raspini F, Ciampalini A, Bianchini S, Bardi F, Di Traglia F, Basile G, Moretti S (2016) Updated landslide inventory of the area between the Furiano and Rosmarino creeks (Sicily, Italy). J Maps 12(5):1010–1019. https://doi.org/10.1080/17445647.2015.1114975

Raspini F, Bianchini S, Ciampalini A, Del Soldato M, Solari L, Novali F, Casagli N (2018) Continuous, semi-automatic monitoring of ground deformation using Sentinel-1 satellites. Sci Rep 8(1):1–11. https://doi.org/10.1038/s41598-018-25369-w

Raspini F, Bianchini S, Ciampalini A, Del Soldato M, Montalti R, Solari L, Casagli N (2019) Persistent Scatterers continuous streaming for landslide monitoring and mapping: the case of the Tuscany region (Italy). Landslides 16(10):2033–2044. https://doi.org/10.1007/s10346-019-01249-w

Said M (1992) Natural hazards of the Hunza valley. Proceedings of the national seminar on progress of geography in Pakistan, 1992, Pakistan, pp 75–83

Sato HP, Hasegawa H, Fujiwara S, Tobita M, Koarai M, Une H, Iwahashi J (2007) Interpretation of landslide distribution triggered by the 2005 northern Pakistan earthquake using SPOT 5 imagery. Landslides 4(2):113–122. https://doi.org/10.1007/s10346-006-0069-5

Searle MP, Kahn MA (eds) (1996) Geological map of North Pakistan and adjacent areas of northern Ladakh and Western Tibet (Western Himalaya, salt ranges, Kohistan, Karakoram, Hindu Kush), 1:650 000. Oxford University, Oxford

Searle MP, Khan MA, Fraser JE, Gough SJ, Jan MQ (1999) The tectonic evolution of the Kohistan-Karakoram collision belt along the Karakoram highway transect, North Pakistan. Tectonics 18(6):929–949. https://doi.org/10.1029/1999TC900042

Stephens MA (1970) Use of the Kolmogorov-Smirnov, Cramér-Von Mises and related statistics without extensive tables. J R Stat Soc

Series B (Methodological) 32:115–122. https://doi.org/10.1111/j.2517-6161.1970.tb00821.x

Su LJ, Ullah F, Ali S, Cheng L, Ur Rehman M, Alam M (2022) Experimental observation and geophysical modeling of the hydrological effects on Pleistocene glaciation deposits susceptible to landslide. Int J Environ Sci Technol 1-14:1699–1712. https://doi.org/10.1007/s13762-022-04103-0

Tomás R, Li Z (2017) Earth observations for geohazards: present and future challenges. Remote Sens 9(3):194. https://doi.org/10.3390/rs9030194

Torres R, Snoeij P, Geudtner D, Bibby D, Davidson M, Attema E, Potin P, Rommen B, Floury N, Brown M, Rostan F (2012) GMES Sentinel-1 mission. Remote Sens Environ 120:9–24. https://doi.org/10.1016/j.rse.2011.05.028

Ur Rehman M, Zhang Y, Meng X, Su X, Catani F, Rehman G, Ahmad I (2020) Analysis of landslide movements using interferometric synthetic aperture radar: a case study in Hunza-Nagar Valley, Pakistan. Remote Sensing 12(12):2054. https://doi.org/10.3390/rs12122054

Verma RK, Sekhar CC (1986) Focal mechanism solutions and nature of plate movements in Pakistan. J Geodyn 5(3–4):331–351. https://doi.org/10.1016/0264-3707(86)90013-X

Zeitler PK (1985) Cooling history of the NW Himalaya, Pakistan. Tectonics 4(1):127–151. https://doi.org/10.1029/TC004i001p00127

Zhang Y, Meng X, Jordan C, Novellino A, Dijkstra T, Chen G (2018) Investigating slow-moving landslides in the Zhouqu region of China using InSAR time series. Landslides 15(7):1299–1315. https://doi.org/10.1007/s10346-018-0954-8

Lessons from 2019–2020 Landslide Risk Assessment in an Urban Area of Volcanic Soils in Pereira-Colombia

Diego Ríos and Guillermo Ávila

Abstract

The city of Pereira is in the central-western region of Colombia, in the valley of the Otún River in the Central Cordillera of the Colombian Andes, whose soils are mostly composed of volcanic ash and Lahar flows. On June 11, 2019, after intense rains, a landslide of about 13,000 m^3 was triggered. This landslide killed 4 people, interrupted the traffic on an important national road, and endangered the airport runway. Just after the event, it was necessary to evacuate 100 homes, located in the upper part of the slope and 234 in the following days. A second landslide occurred on July 24, 2020, mobilizing 52,000 m^3 and affecting 33 of the previously evacuated houses, then there were about 20 more small landslides. A zone of about 2.300 m long and 300 m wide (69 ha) was identified to be susceptible to new landslides that may affect more than 15.000 people. Identification of landslide triggering factors, failure, post-failure behavior, and the retrogressive landslide advance are reviewed because they are key factors for an effective hazard evaluation and risk governance. The landslide event was also used to calibrate a general methodological guide for landslide risk assessment, developed by the Colombian Geological Service and the National University of Colombia (Ávila et al. 2016) that has been extensively applied for the inclusion of risk evaluation in the land use planning, as required by the Colombian legislation.

Keywords

Landslide evolution · Volcanic tropical soils · Retrogressive advance · Risk management

D. Ríos (✉) · G. Ávila
Universidad Nacional de Colombia, Department of Civil and Agricultural Engineering, Bogotá, Colombia
e-mail: dariosa@unal.edu.co; geavilaa@unal.edu.co

1 Introduction

Landslide events in volcanic materials triggered by intensive rain periods tend to generate flow-type movements during post failure and as stated by Picarelli et al. (2020) this behavior strongly affects displacements and run out, as it was evident in two landslides that occurred in an urban area in the city of Pereira (Colombia) on June 11, 2019, and on July 24, 2020. The stress reduction caused by the first landslide produced a retrogressive advance, evidenced by the presence of soil cracks in which water accumulated during rain periods, the accumulated water, together with the water absorbed by the volcanic soils, gave the second landslide great mobility and its travel distance was much higher than that estimated with empirical correlations. This article describes the landslide evolution, the significant retrogressive process, the application of a methodological guide developed by the Colombian Geological Service for landslide risk evaluation (Ávila et al. 2016), and the risk management after the emergency caused by the first landslide in a densely populated area.

2 Description and Evolution of the Instability Process

The city of Pereira is located in the Central Cordillera of the Colombian Andes. This mountain range is characterized by having an important volcanic chain, for which many of the cities are founded on lahar deposits and soils derived from volcanic ashes. Figure 1 shows the general site location of the study area and Fig. 2 shows an aerial photograph of the landslide that occurred on June 11, 2019 (the first landslide).

Multitemporal analysis, starting with an aerial photograph of the year 1946 (Fig. 3), which, although it does not have a very good resolution, allows us to see the construction process of the airport runway and the presence of the railway line (built in 1927). In this image also some incipient features of

I. Alcántara-Ayala et al. (eds.), *Progress in Landslide Research and Technology, Volume 2 Issue 1, 2023*,
Progress in Landslide Research and Technology, https://doi.org/10.1007/978-3-031-39012-8_16

Fig. 1 General location of the study area

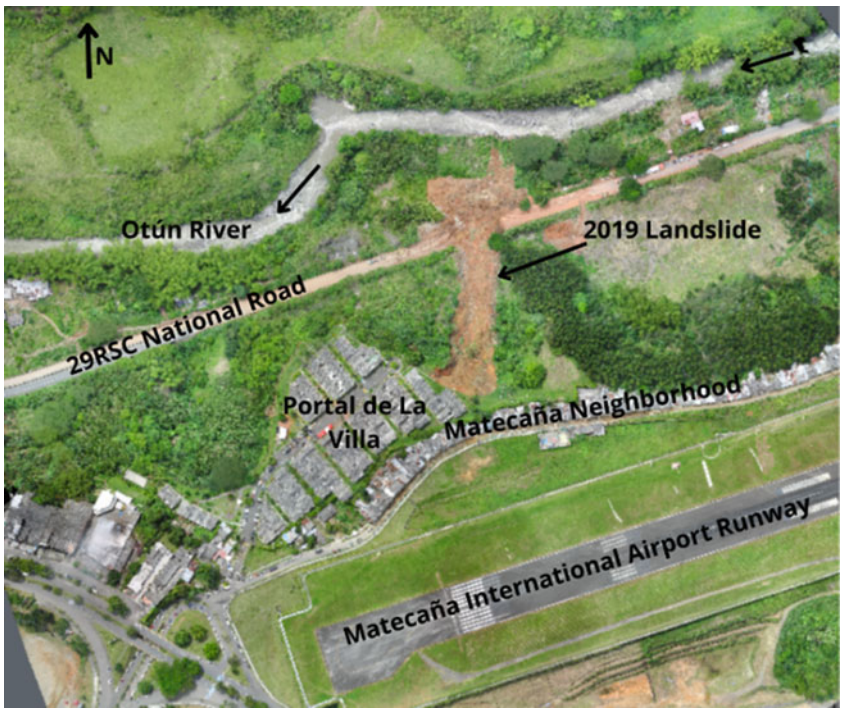

Fig. 2 Aerial photograph of the 2019 Pereira landslide

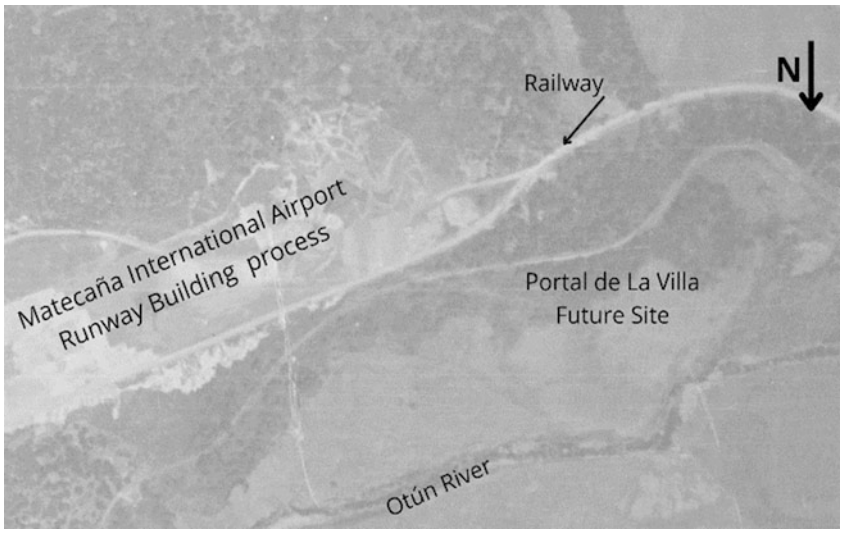

Fig. 3 1946 image: construction of the airport runway. The railroad was constructed in 1927. Some incipient landslide scarps may be identified (Image IGAC, 1946)

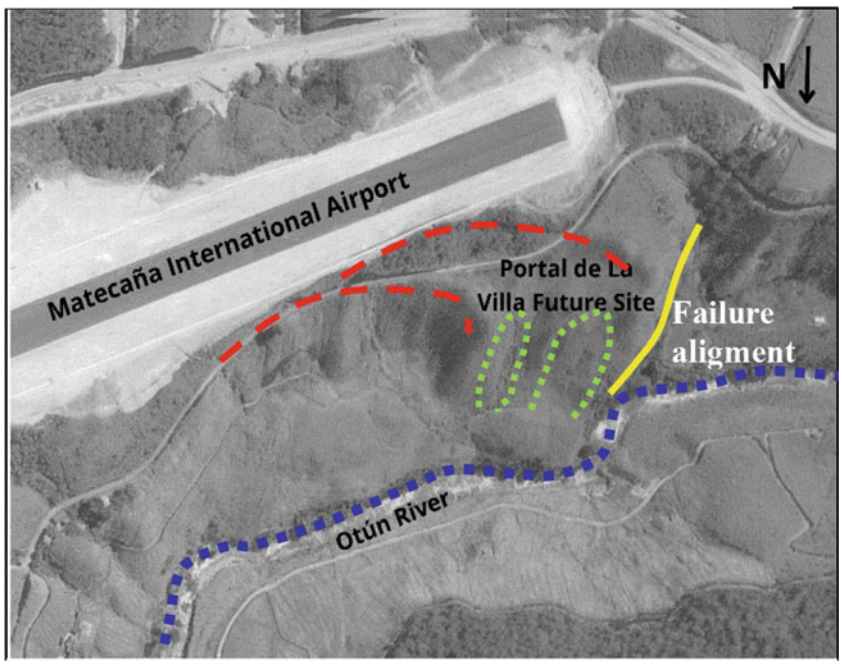

Fig. 4 1969 image: No signs of increased instability but some dispersed constructions block up intermittent water courses. Normal operation of the railroad and the airport

instability can be identified, such as small escarps. A second aerial image from 1969 (Fig. 4) shows geomorphological evidence of ancient scarp surfaces (dashed lines) but no evidence of any significant sign of instability of the slope. A geological fault alignment is also indicated in the image. At that moment the airport and the railroad had normal operation, and some dispersed constructions may be observed. The third image is from 2005 (Fig. 5) and shows the construction process of the Portal de la Villa neighborhood for what was necessary to make significant slope cuts and conformation fills. The National Road 29RSC can be observed in this image. The area remained relatively stable until July 11, 2019, when the first landslide occurred (Fig. 2). This landslide killed 4 people, affected many of the houses located on the top slope (Portal de La Villa and Matecaña, neighborhood) and the 29RSC national road. The instability process continued and on July 24, 2020, a second landslide event, larger than the previous one, was triggered. This new event destroyed 33 houses (previously evacuated), produced partial damming of the Otún river, caused the closure of the national road for almost 20 days, and came close to affecting the airport runway (Fig. 6).

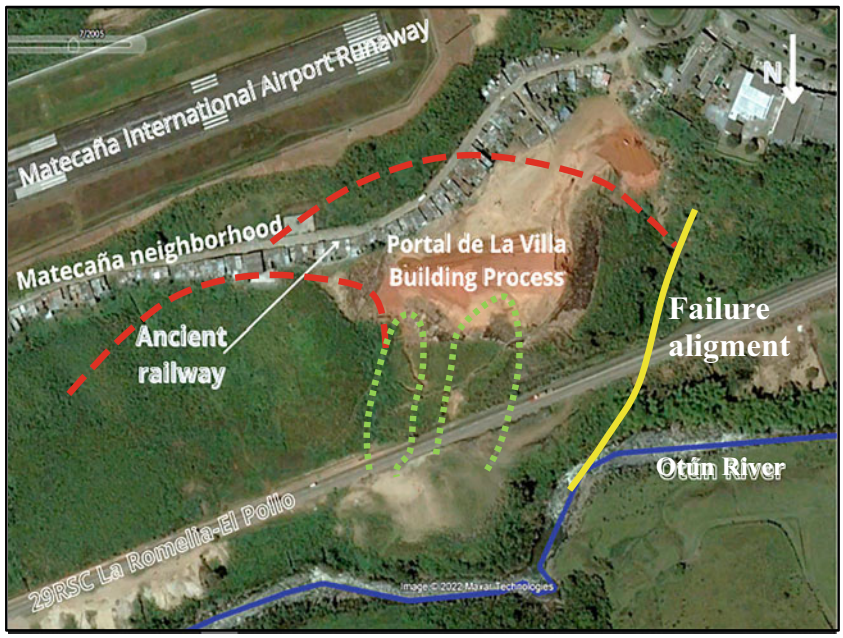

Fig. 5 2005 image: explanations for the construction of the Portal de la Villa neighborhood. (Google Earth, 2005)

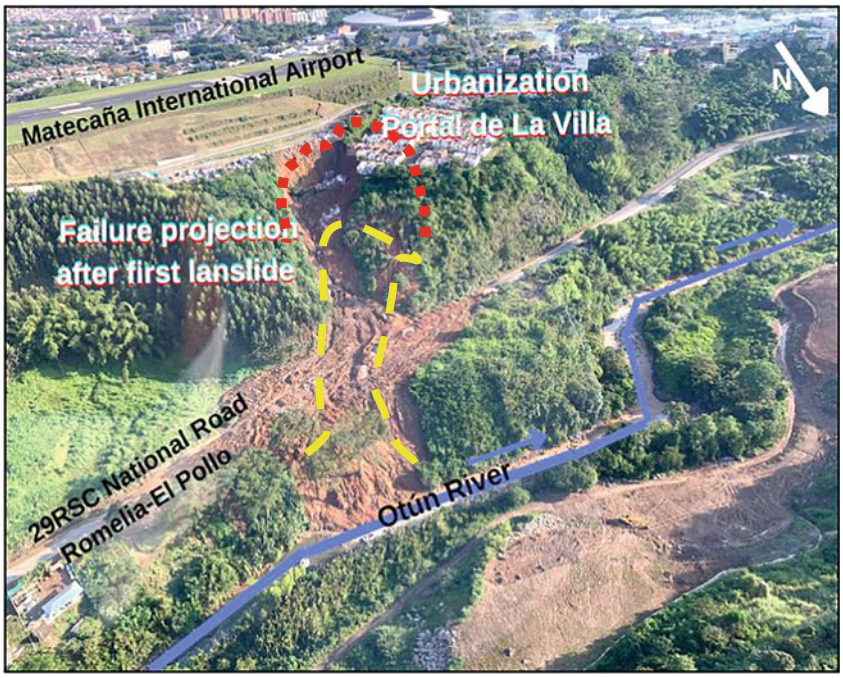

Fig. 6 Second landslide occurred on July 21, 2020, affecting a greater area in the upper and lower sectors

3 Site Characterization

After the 2019 landslide, a detailed geological and geotechnical site characterization was carried out. This characterization included geological and geomorphological surveys, geophysical exploration, mechanical drilling, sampling, laboratory tests, and a detailed topographic survey. All this information permitted us to obtain a digital elevation model and detailed geological and geotechnical characteristics. A synthetic geological and geotechnical profile is shown in Fig. 7. Table 1 presents the mean water content and Atterberg limits of the surface soils, which are predominantly high-plasticity sandy silts (MH).

4 Alert Signs and Damage Evolution

One of the most important aspects of landslide risk management is to opportunely identify the instability signs that permit alert people and take mitigation actions. Reports from the local emergency office, show that instability signs

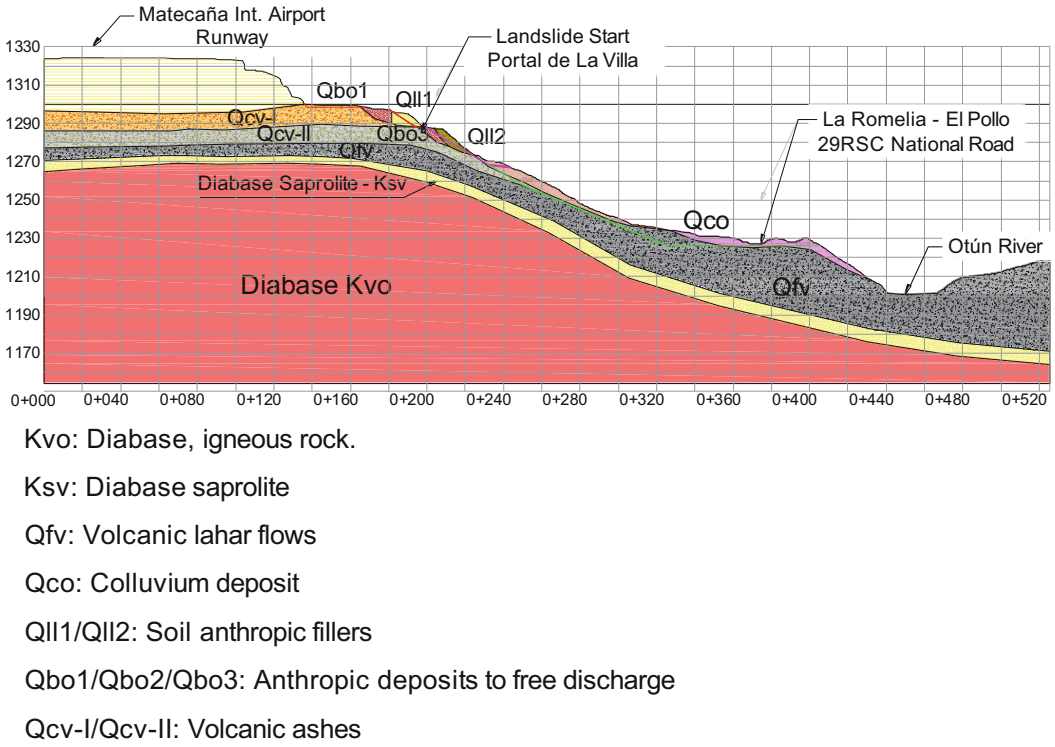

Fig. 7 General geological profile of the landslide and the influence areas

were occurring since 2011 (there are reports in 2011, 2015, 2017, and 2019). On tenth July 2019 (one day before the first great landslide) a scarp was observed in the upper part of the slope (Fig. 8) and it was covered by plastic. However, the next day a landslide occurred as shown in Fig. 9, killing 4 people.

Signs of imminent instability are common in most landslides, for example, Hancox (2008), indicated that the Abbotsford Landslide in New Zealand that occurred on 8 August 1979 showed minor cracking and damage on one house located 60 m from the landslide of almost 11 years before the landslide occurrence (1968–1972) due to a graben. Xian et al. (2022) reported crack and small landslide evolution from 2005 to 2019, revealing a significant increase in crack number as in crack length as the instability increased. These warning signs, such as small cracks, small landslides punctual soil deformations, water emanations from the subsoil, etc., should not go unnoticed since, if they are corrected in time, they can allow long-term stability to be achieved and with relatively lower costs. Stabilization measures that are taken very close to the imminent failure (as those shown in Fig. 8) can be dangerous since the speed of the landslide tends to be fast and there is no time to escape. In these cases, the most convenient procedure is to carry out a quick and organized evacuation of the people who are within the possible landslide influence area.

Ávila et al. (2016) published for the Colombian Geological Service a technical guide to performing landslide risk analysis at a detailed scale which has been extensively used for consulting firms to actualize land use planning in several Colombian municipalities. In this guide four main sectors are defined in a landslide profile, in order to define vulnerability

Table 1 Water content and Atterberg limits

Soil Layer	Water content (%)	Liquid limit (%)	Plasticity index (%)
Qcv-I	75.0	90.0	36.0
Qcv-II	53.0	59.0	21.0
Qbo-1-2	52.8	76.6	26.9
Qbo-3	36.2	69.7	27.8
Qll-1	53.0	70.1	21.3
Qll-2	47.0	71.9	29.0

Fig. 8 Scarp evidence one day before landslide 2019

and hazard areas to take effective mitigation actions, these sectors are shown in Fig. 10. Zones 2 and 3 are those directly affected by the landslide and all exposed elements located in these areas may result strongly affected or destroyed. The limit between zones 1 and 2 is controlled by geological and geomorphological conditions but not always is easy to define it. Normally it is necessary to estimate how far from the landslide scarp the soil may present cracks or deformations.

Fig. 9 Landslide principal scarp on Jun 11, 2019

Numerical models, considering multiple slip surfaces and lateral stress relaxation may be applied for this kind of estimation but, real observations are necessary for calibration.

For the Pereira Landslide, the limit between Zone 1 and Zone 2 extended as far as 80 m, from the main scarp, as shown in the aerial photograph of Fig. 11 and in detail, in the photograph of Fig. 12. Another important element in the risk attention process is to have a reasonable estimation of the time evolution of the retrogressive landslide progress, for which, documentation of previous cases, under particular geological and geotechnical conditions, is very useful as a calibration measure. Once the first landslide occurred, a significant crack opening and new cracks were observed after 20 days. Also, the damage in houses was evident, as shown in Fig. 13. for what people had to be evacuated. Figure 14 shows the situation after the second landslide, which occurred on July 21, 2020, one year and 10 days after the first landslide. The previous cracks had converted now.

The Limit between Zones 3 and 4 of Fig. 10 may be estimated according to different empirical procedures of landslide travel distance as reported by Corominas (1996) or Hungr et al. (2005).

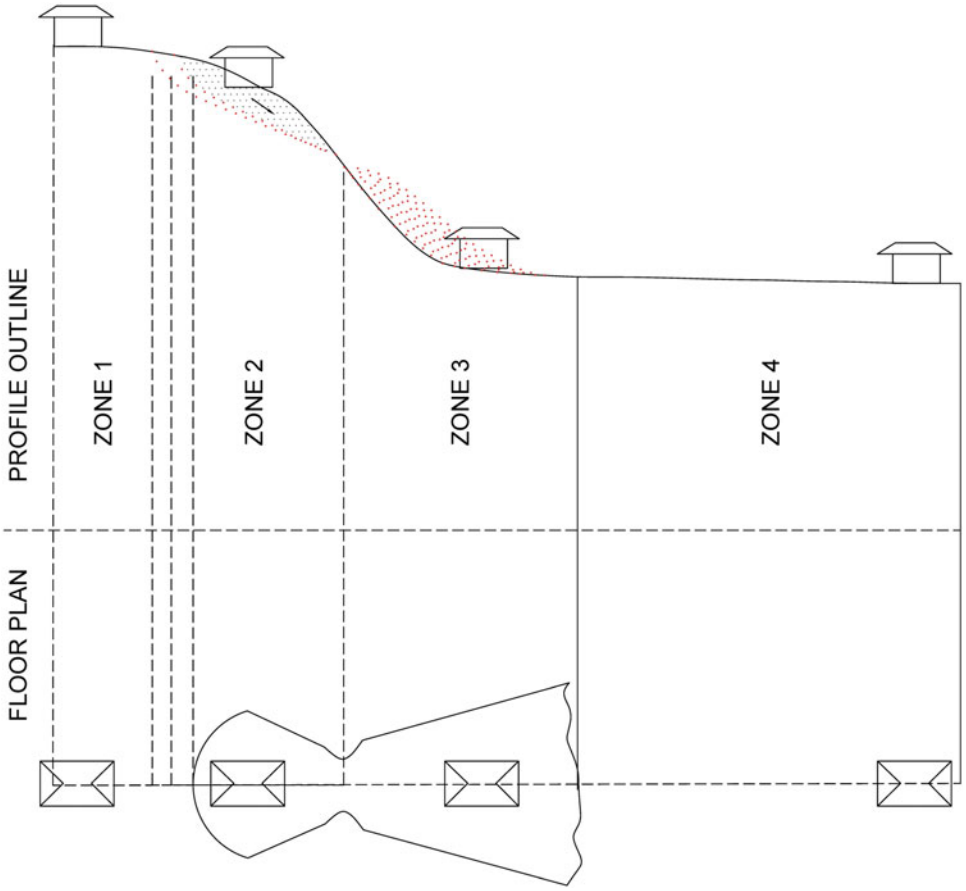

Fig. 10 Landslide exposure zones (Ávila et al. 2016)

5 Rainfall Behavior Previous to the Landslides

Figure 15 shows the mean monthly rainfall histogram from Matecaña Airport Station (IDEAM 2022). A bimodal regime is observed with a first pick in May (250 mm) and the second pick in October and November (250 mm).

The first landslide (June 11, 2019) occurred just after the first monthly rain pick and it was triggered by an intense rain day (93.7 mm), as shown in Fig. 16.

The second main landslide (July 21, 2020) did not occur during the strong rainy season, as can be observed in Fig. 17, however, due to the intense soil cracking and the rains of the previous months, part of that water could have accumulated, especially in the ancient natural watercourses that were filled

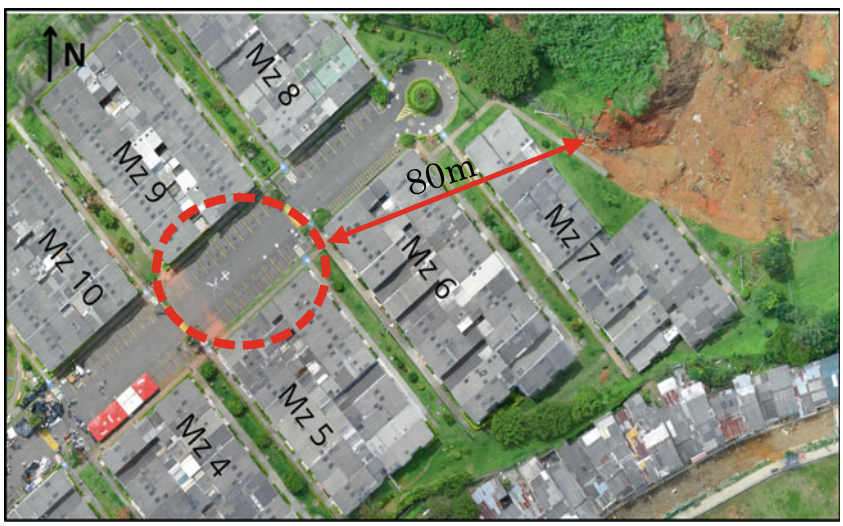

Fig. 11 Aerial image of the Portal de la Villa on June 12 (one day after the landslide). The distance from the scarp to the initial cracks is about 80 m

Fig. 12 First cracks appeared on June 12, 2019 (One day after the landslide) in block Mz5, 80 m far from the main scarp, as indicated in Fig. 11

during the construction process and this, in turn, generated the flow-type landslide, of high mobility, capable of reaching a long distance. The situation of general instability of the area between the first and the second landslides made it difficult to build emergency drainage systems, in order to reduce the water accumulation, and the emergency actions concentrated on evacuation and periodical monitoring of land deformations.

6 Travel Distance, Velocity, and Mobilized Volume

Comparative values of calculated and measured travel distances and mobilized volumes of the 2019 and 2020 events are shown in Table 2. Using the methodology of

Fig. 13 Crack evolution on July 1st (20 days after the landslide

Fig. 14 Total damage observed in block Mz 5 on July 21, the same day of occurrence of the second landslide

Hungr et (Hungr et al. 2005), the calculated travel distance for both events was 125 m. For the 2019 event, this result is of the same order as the measured value, however, for the 2020 event, the calculated value of 125 m resulted much lower than the real value of 290 m. The significant difference in travel distance, in this case, may be attributed to the great amount of water present in the soil cracks and internally, in the volcanic soil mass, converting the landslide into a flow-type process.

The calculated volume of the 2019 event was 50.000 m^3 but the real volume was only 13.000 m^3. Similarly, for the 2020 event, the calculated volume was 71.000 m^3 but the measured volume was only 52.000 m^3. The difference is due to the presence of a lithological control that did not permit a deep failure surface as initially assumed.

Direct landslide velocity (V) was measured from a video taken by local people. The approximate velocity was 12 m/s. Using the sliding block model, the landslide velocity may be estimated by the fallowing equation:

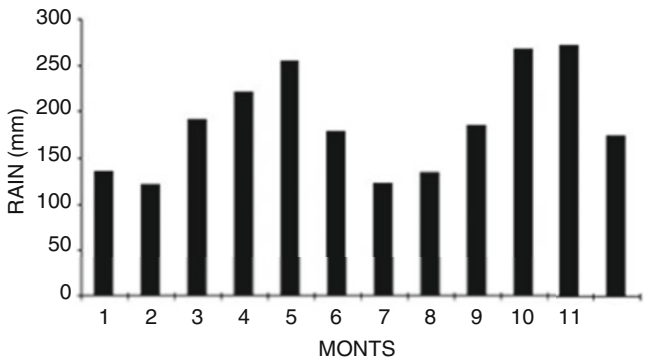

Fig. 15 Mean monthly rainfall histogram from the Matecaña Airport (adapted from IDEAM 2022)

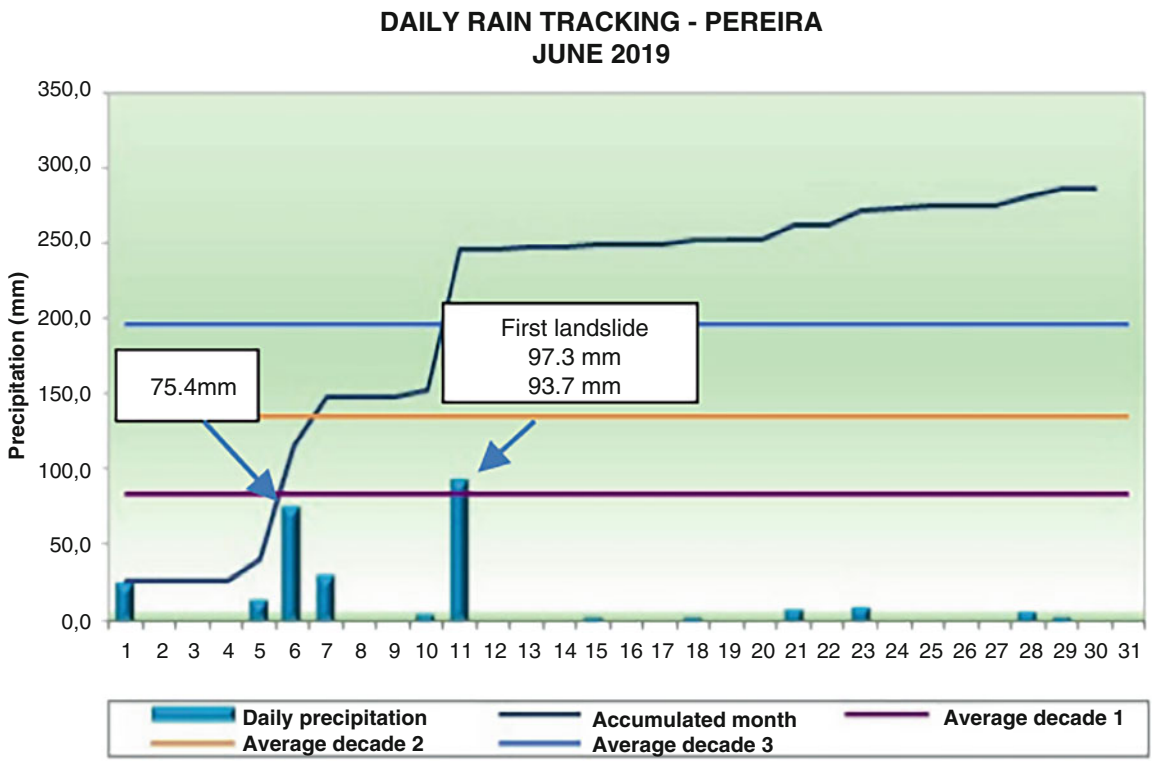

Fig. 16 Daily rain previous to the first landslide (IDEAM 2022)

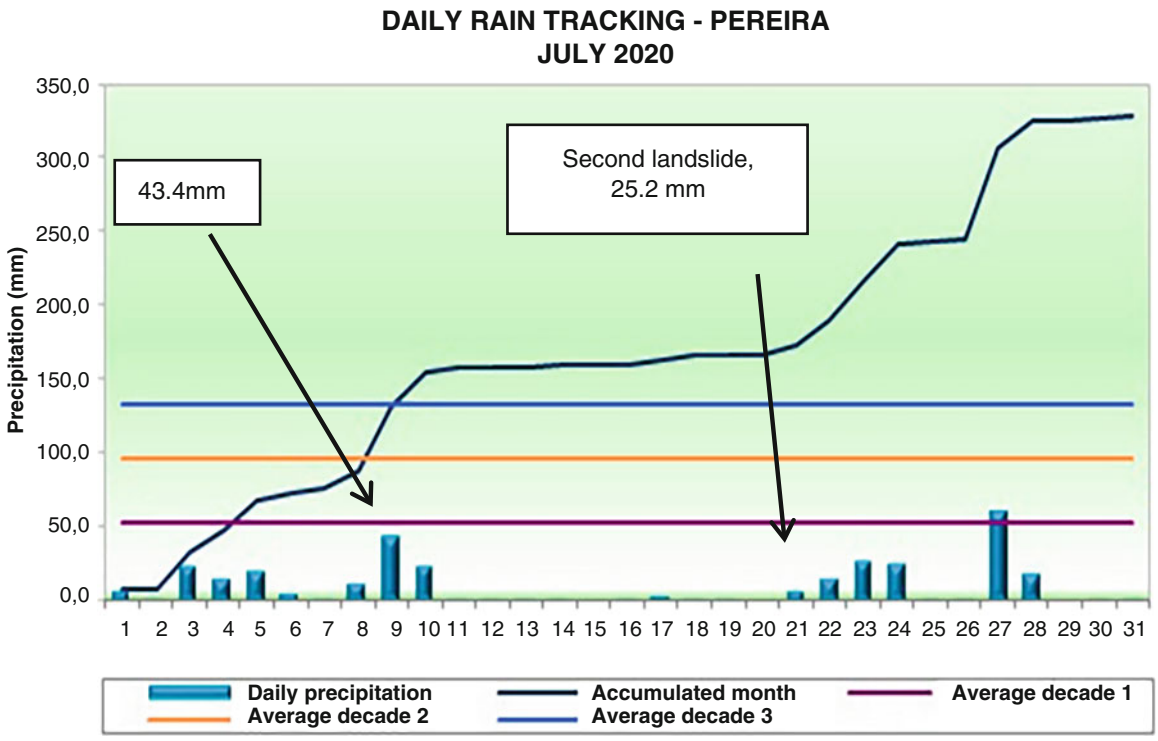

Fig. 17 Daily rain previous to the second landslide (IDEAM 2022)

Table 2 Comparison between calculated and real travel distance and mobilized volume for the 2019 and 2020 events

Event -Type of evaluation	Travel distance (m)	Mobilized volume (m^3)
2019 landslide—Hungr et al. (2005)	125	52.000
2019 landslide—Measured	130	13.000
2020 landslide—Hungr et al. (2005)	125	71.000
2020 landslide—Measured	290	52.000

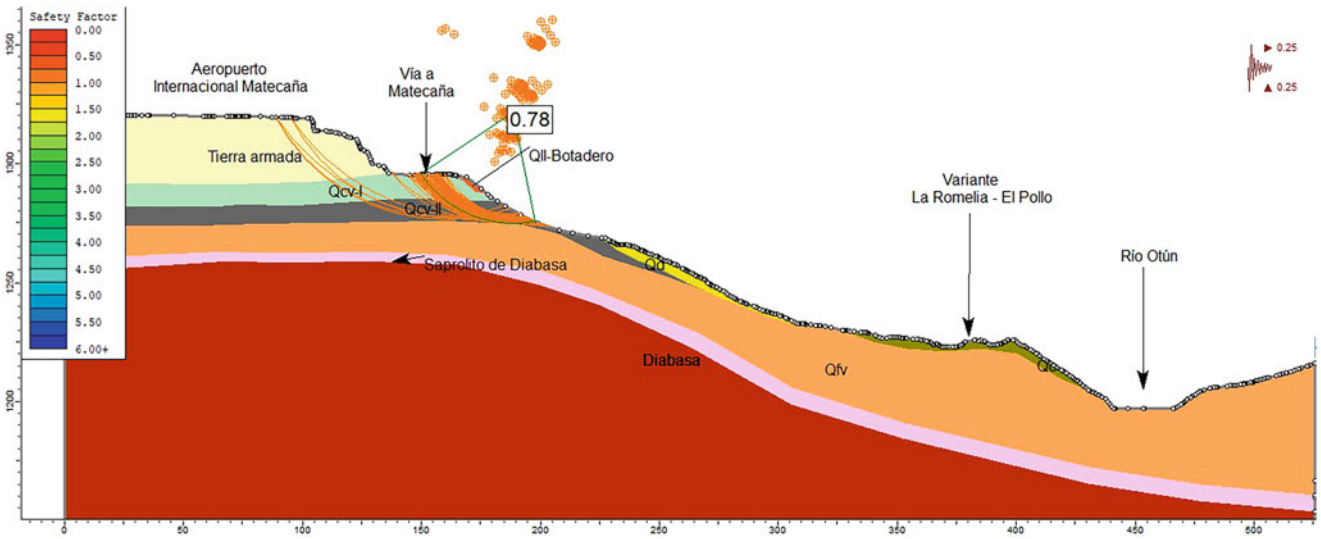

Fig. 18 Limit equilibrium analysis for hazard modelling

$$V = \sqrt{2gH\left(1 - \frac{\tan\varphi}{\tan\beta}\right)}$$

Were:
H landslide height
ϕ internal friction angle
β slope angle
g acceleration of gravity

In this case, H = 70 m, β = 30°, and the internal friction angle results to be 27.3°. This value corresponds to the residual strength and is in the range reported for this type of residual volcanic soil in other tropical countries (i.e., Rigo et al. 2006; Wesley 1992).

7 Hazard Assessment

Two elements should be considered in hazard assessment: the possible failure conditions and the reach distance of the potential landslide. Failure conditions were evaluated based on the limit equilibrium method. The modeled circular failure surfaces (Fig. 18) were in general similar to those observed in the field (Fig. 9), while, as previously mentioned, travel distances had good prediction in the 2019 event but large underprediction in the 2020 event.

A hazard map was constructed based on the factor of safety (FS) obtained for different terrain profiles and the corresponding computed travel distances. In this case FS < 1.1 was classified as a high hazard level, FS between 1.1 and 1.5 was a medium hazard level and FS > 1.5 was a low hazard level. Although the calculated travel distances represented lower values than those that actually occurred, this possible effect was previously estimated based on the morphological characteristics and on the high saturation observed in the intensely cracked soils, as a result of which a safety corridor was left that finally allowed the construction of a conservative hazard map, as shown in Fig. 19. This map showed good agreement with the 2020 event.

8 Vulnerability Assessment

The previously mentioned methodological guide for landslide risk assessment developed by the Colombian Geological Service (Ávila et al. 2016) presents a detailed procedure

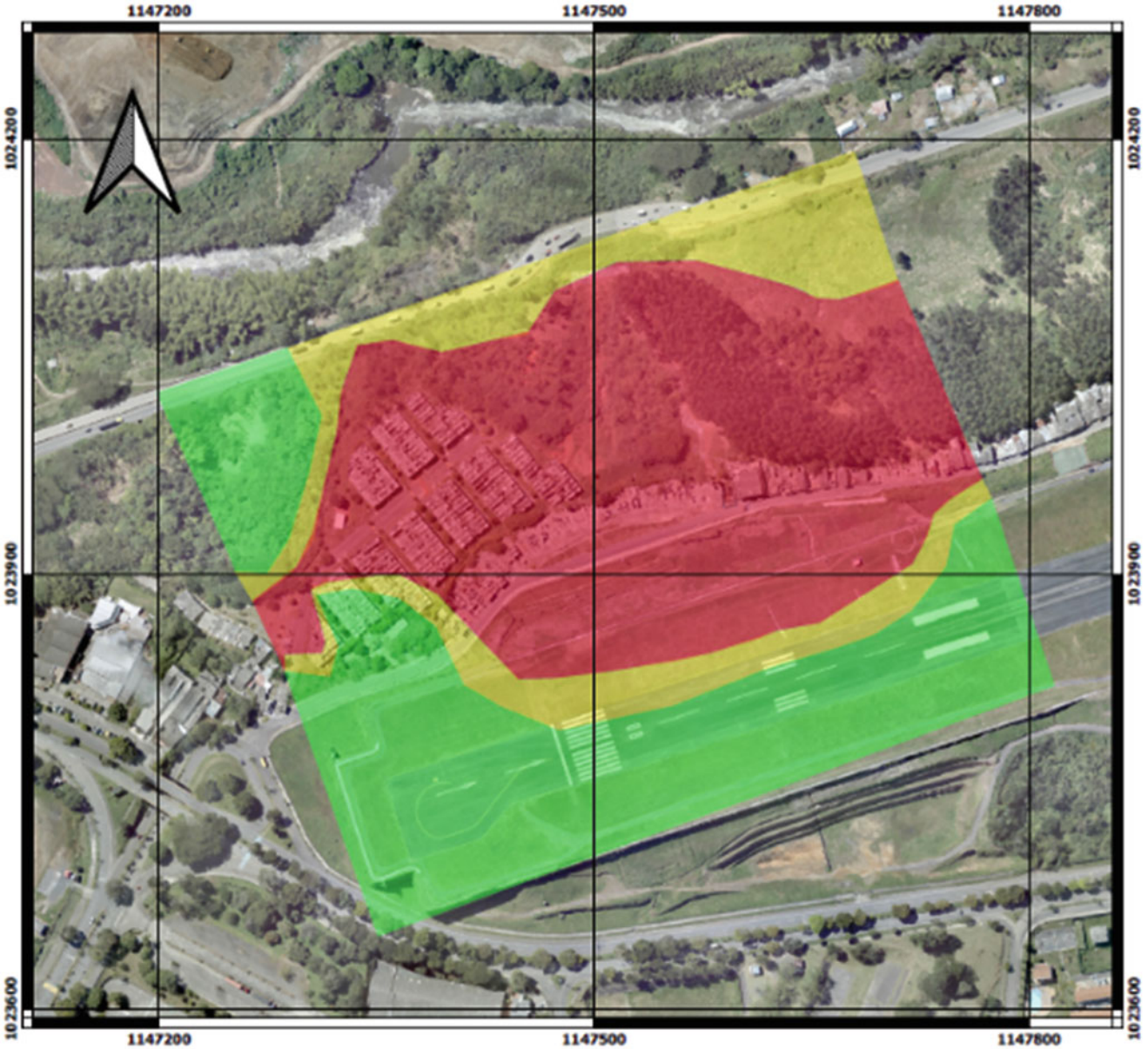

Fig. 19 Hazard map constructed just after the 2019 event

for vulnerability evaluation, based on the postulates of Uzielli et al. (2008), Li et al. (2009) and Du et al. (2013). The general steps required for vulnerability assessment are:

- Identification and location of exposed elements.
- Evaluation of structural fragility.
- Calculation of the intensity factor and.
- Evaluation and zoning of vulnerability.

Exposed elements were classified into two main groups: physical elements (buildings, lifelines, and transportation infrastructure) and persons. The typology of buildings was based on 7 possible classifications, according to the structural construction system. Exposed elements were clearly identified on the base map with respect to the landslide exposure zones. Structural fragility was calculated considering the typology of the building, its number of floors, the state of conservation, and the age of the constructions.

The intensity factor is related to the potential energy of the landslide, therefore, it is necessary to identify, firstly, to which vulnerability scenario is referred (rock fall, rapid landslides, or slow landslides) and secondly, what is the position of the exposed elements in relation to the landslide. In this case, a rapid landslide is the adopted scenario (according to Cruden and Varnes (1996) when velocity is higher than 5 m/s, as in this case, the landslide is classified as

very rapid), and the exposition is based on the location of the elements, as shown in Fig. 10.

According to Du et al. (2013), the vulnerability of the exposed elements (V) may be expressed by:

$$V = \frac{1}{2}\left(\frac{I}{1-S}\right)^2 \text{ if } I \leq 1 - S \text{ or}$$

$$V = 1 - \frac{1}{2}\left(\frac{1-I}{S}\right)^2 \text{ if } I > 1 - S$$

Where:
I Intensity factor
S Structural fragility

For structures, a vulnerability value of 1 means the complete destruction of the property, and a vulnerability value of 0 indicates no damage. Values between 1 and 0 represent a proportion of expected structural damages. In people, a vulnerability value equal to 1 means loss of life, and values less than 1 are considered as the corresponding probability of loss of life. A vulnerability value equal to zero means no loss of life is expected. Table 3, presents the vulnerability parameters for each type of structure that could potentially be involved in the landslide.

Based on this procedure, in the Matecaña neighborhood, 49 houses were classified as vulnerable equal to 1. For the Portal de la Villa neighborhood two main susceptibility areas were identified: one with S = 0.69 (187 houses) and the other with S = 1 (63 houses), however, due to the high-intensity factor, in both cases, vulnerability is equal to 1 and therefore consequences will be catastrophic for both, structures and people. For lifelines and transportation fragility the intensity factors were also evaluated and, as in buildings, their vulnerability factors were equal to 1.

Once the previously described factors have been analyzed, a zoning map was obtained (Fig. 20). The Portal de la Villa neighborhood, the Matecaña neighborhood and the 29RSC road were classified as highly vulnerable (red), while the Matecaña International Airport was classified as medium vulnerability (yellow). The rest of the studied area was classified as low vulnerability.

9 Risk Assessment

Vulnerability maps and hazard maps may be used to take decisions on-site about risk management; however, a risk map is better because it takes into account both, hazard and vulnerability. Classical risk calculations are based on the product of the probability of occurrence of event times the expected consequences, expressed in cost or adversity derived from that event (Beacher and Christian 2003). However, when circumstances require rapid and safe decisions, related to evacuation processes or suspension of a high-traffic road, a simplified method of risk assessment may be a good alternative. In this case, a risk matrix method was used, based on the combination of the hazard map and the vulnerability map as shown in Fig. 21.

The risk map constructed after the 2019 event is shown in Fig. 22. This map was very effective at that moment for the risk management and the evacuation process because it was clear and easy to explain to local authorities and to the affected community. In the 2020 event, people had already been evacuated from the impact area and for this reason, there were no deaths or injuries, showing the effectiveness of the procedure. A formal risk analysis and a clear risk map undoubtedly represent a fundamental tool for risk governance.

Table 3 Vulnerability parameters

Exposed elements	S	Intensity factor	Vulnerability factor
Budlings			
Matecaña	1	1	1
Portal villa—1	0.69	1	1
Portal villa—2	1	1	1
Lifelines			
Aqueduct	0.44	1	1
Sewerage	0.5	1	1
Electrical	0.9	1	1
Communications	0.9	1	1
Transportation			
Internal roads	0.4	1	1
National Road (La Romelia—El Pollo)	0.2	1	1

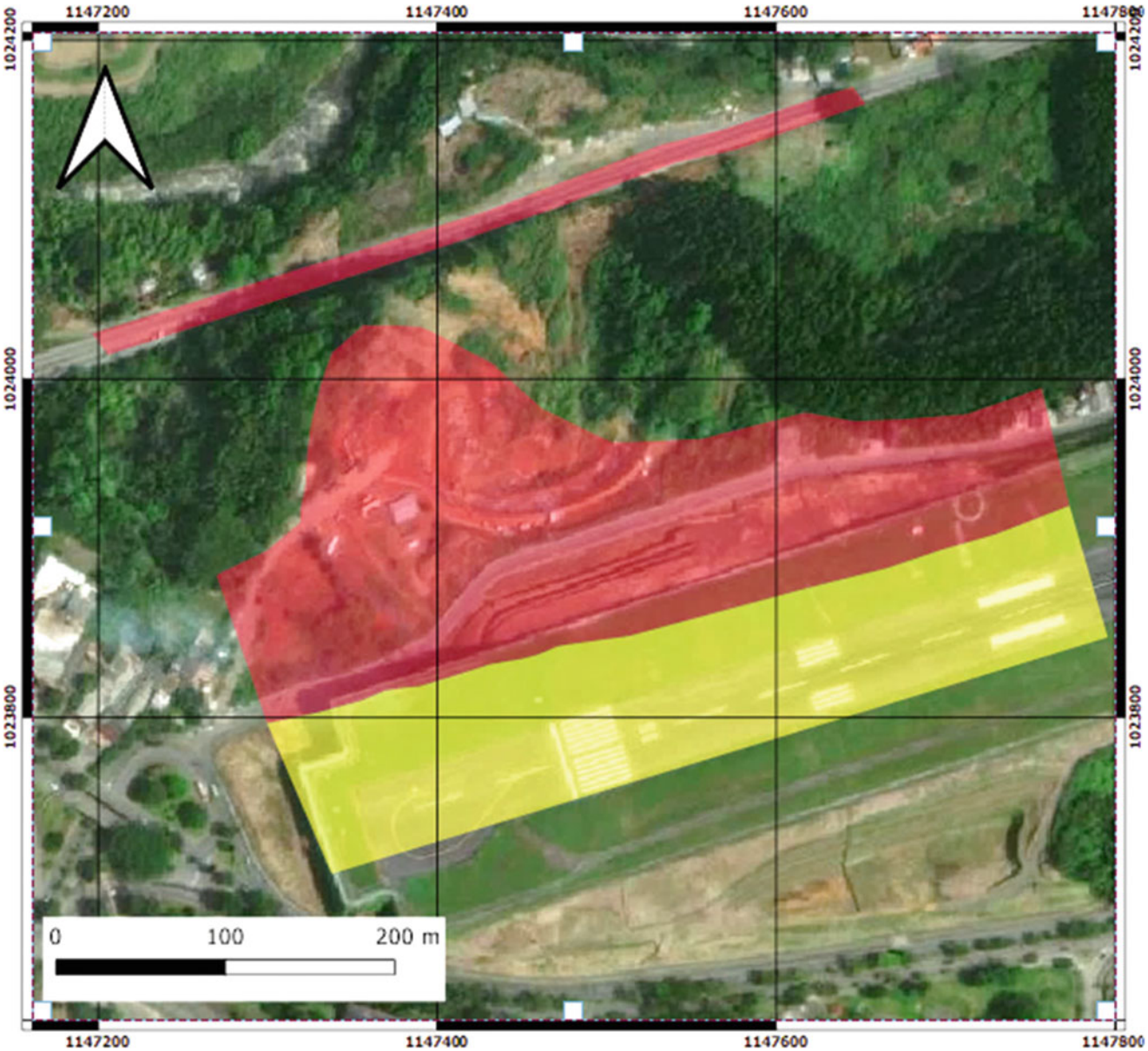

Fig. 20 Vulnerability map prepared just after the 2019 event

RISK LEVEL			
VULNERABILITY	HAZARD		
	HIGH	MEDIUM	LOW
HIGH	HIGH	HIGH	MEDIUM
MEDIUM	HIGH	MEDIUM	LOW
LOW	MEDIUM	LOW	LOW

Fig. 21 Risk matrix based on hazard and vulnerability maps

10 Conclusions

When landslides occur in highly populated urban areas with critical public services and transportation infrastructure, efficient risk management is required in order to save people's lives and keep local governance. The methodological landslide risk assessment guide, developed by the Colombian Geological Service (Ávila et al. 2016) showed to be a practical and effective tool to apply in these cases.

The application of this systematic methodology requires detailed geological and geotechnical data and a precise digital elevation model. Gathering this information may require

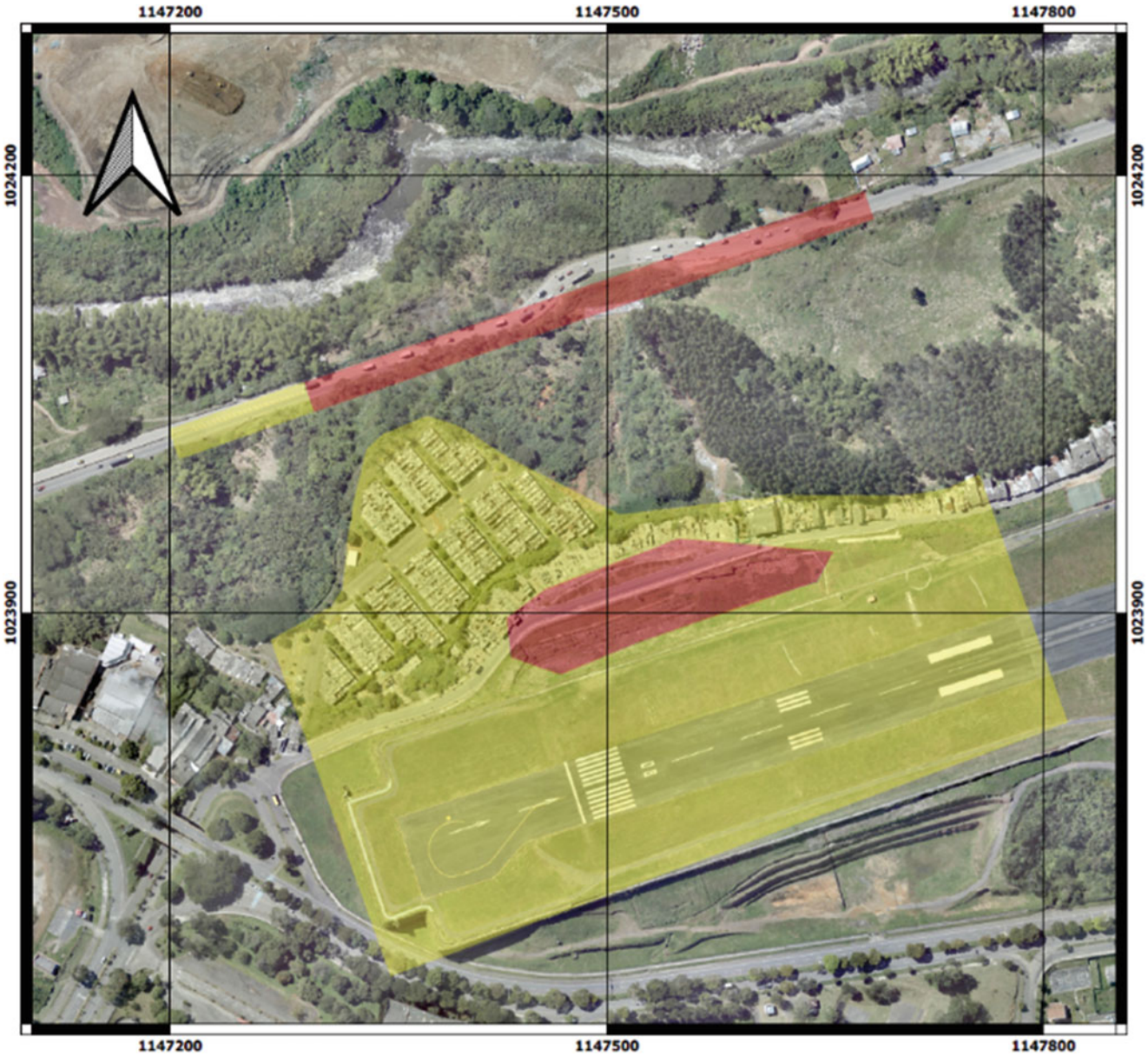

Fig. 22 Risk map constructed after the 2019 landslide

some time (time is a critical factor in these conditions) but it is essential for safe decision-making, based on objective parameters.

Landslide travel distances based on empirical correlations resulted in good agreement with the first landslide (2019 landside), however, a significant underestimation of the travel distance was observed during the second landslide (2020 landslide). This can be explained by the presence of a large amount of water in the cracks that were formed in the upper part of the landslide and the high moisture content of the shallow volcanic soils. These two factors reduced soil resistance and produced a high-mobility flow-type landslide.

In many tropical regions, urban developments are carried out in hillside areas of volcanic soils, for which land cuts and fillings are required. This procedure often obstructs the natural water channels and if efficient drainage is not implemented, long-term instability processes may develop.

When initial instability signals are observed (surface cracks land deformations or water flows) it is necessary to act immediately, to take appropriate corrective measures. If not, the problem can become uncontrollable, as in the case of the Pereira landslide.

References

Ávila G, Cubillos C, Granados A, Mediana E, Rodríguez E, Rodrigue C, Ruiz, G (2016) Guía metodológica para estudios de amenaza, vulnerabilidad y riesgo por movimientos en masa. Convenio Servicio Geológico Colombiano-Universidad Nacional de Colombia. Bogotá D.C. Imrenta Nacional de Colombia. (ISBN 978-958-99528-5-6). p 179

Beacher B, Christian J (2003) Reliability and statistics in geotrechnical engineering. (ISBN 0-471-49833-5). Wiley, p 605

Corominas J (1996) The angle of reach as a mobility index for small and large landslides. Can Geotech J 33:260–271

Cruden DM, Varnes DJ (1996) Landslide types and processes. Transportation Research Board, U.S. National Academy of Sciences, Special Report 247:36–75

Du J Yin K, Lacasse S, Nadim F (2013) Quantitative vulnerability estimation for individual landslides. Proceedings of the 18th international conference on soil mechanics and geotechnical engineering, Paris

Hancox G (2008) The 1979 Abbotsford landslide, Dunedin, New Zealand: a retrospective look at its nature and causes. Landslides 5:177–188

Hungr O, Corominas J, Eberhardt E (2005) State of the art paper # 4. Estimating landslide motion mechanism, travel distance and velocity. Landslides Risk Management Proceedings. Vancouver, Canada

IDEAM (2022) Cartas climatológicas medias mensuales. Aeropuerto Matecaña (Pereira). http://bart.ideam.gov.co/cliciu/pereira/precipitacion.htm. Last Accessed 3 Sept 2022

Li Z, Nadim F, Huang H, Uzielli M, Lacasse S (2009) Quantitative vulnerability estimation for scenario-based landslide hazards. Landslides 7(2):125–134

Picarelli L, Olivares L, Daminano E, Darban R, Santo A (2020) The effects of extreme precipitations on landslide hazard in the pyroclastic deposits of Campania region: a review. Landslides 2020(17): 2343–2358

Rigo ML, Pineiro RJB, Bressani LA, Bica ABD, da Sileira RM (2006) The residual shear strength of tropical soils. Can Geotech J 43:431–447. https://doi.org/10.1139/T06-015

Uzielli M, Nadim F, Lacasse S, Kaynia AM (2008) A conceptual framework for quantitative estimation of physical vulnerability to landslides. Eng Geol 102:251–256

Wesley LD (1992) Some residual strength measurements on New Zealand soils. In proceedings of the 6th Australia – New Zealand conference on Geomechanics, Christchurch, New Zealand. New Zealand Geomechanics Society, Christchurch, pp 381–385

Xian Y, Zhou H, Chen N, Lui F, Sun H (2022) Snowmwlt-triggered reactivation of a loess landslide in Yili, Xinjiangang, China: mode and mechanism. Landslides 2022(19):1849–1860

Part IV

ICL Landslide Teaching Tools

Zonation of Landslide Susceptibility in the Gipuzkoa Province (Spain): An Application of LAND-SUITE

Txomin Bornaetxea, Mauro Rossi, and Paola Reichenbach

Abstract

In the past 50 years, a large variety of statistically based models and methods for landslide susceptibility zonation have been proposed in the literature. The numerous methods, applicable to a large range of spatial scales, use several input thematic data, different model combinations and various approaches to evaluate the model performance. In the literature, only few articles describe tools that apply statistically based approaches for the susceptibility evaluation. This paper describes and illustrates, through an example in the Gipuzkoa province (Spain), the use of LAND-SUITE, a tool for the statistically based landslide susceptibility zonation. The application aims to show how LAND-SUITE provides utilities to: (i) support the user for the input data preparation; (ii) perform preliminary and exploratory analysis of the available data; (iii) test different combinations of variables and select the optimal thematic/explanatory set; (iv) test different model types and their combinations; and (v) evaluate the model performance and uncertainty. The suite showed high flexibility and allowed to perform different susceptibility applications, with diversified training/validation datasets partitions and validation tests. Given its specifications, LAND-SUITE can be easily applied elsewhere to perform similar studies but also to explore other landslide susceptibility applications.

Keywords

Landslide · Open-source tool · Statistically based susceptibility

T. Bornaetxea (✉)
Geology Department of the University of the Basque Country (UPV/EHU), Leioa, Spain
e-mail: txomin.bornaetxea@ehu.eus

M. Rossi · P. Reichenbach
Istituto di Ricerca per la Protezione Idrogeologica, Consiglio Nazionale delle Ricerche (CNR IRPI), Perugia, Italy
e-mail: mauro.rossi@irpi.cnr.it; paola.reichenbach@irpi.cnr.it

1 Introduction

Landslide susceptibility measures the degree to which a terrain can be affected by future slope movements and provides an estimate of where landslides are likely to occur (Chacón et al. 2006; Guzzetti et al. 2005). A wide variety of statistically based models and methods for landslide susceptibility mapping and zonation have been proposed in the literature in the past 50 years (Reichenbach et al. 2018). Statistically based susceptibility models are applied to identify the functional (statistical) relationship between instability factors, described by sets of geo-environmental (independent) variables, and the known distribution of landslides, taken as the dependent model variable. In the literature, several articles introduce and describe tools that apply physically based models to forecast shallow landslides (as for example, SHALSTAB, SINMAP, GEOtop-FS, HIRESSS, TRIGRS, r.slope.stability, etc), but few propose software for statistically based susceptibility zonation (as for example, Brenning 2008; Osna et al. 2014; Bragagnolo et al. 2020; Sahin et al. 2020).

To facilitate the landslide susceptibility assessment process, Rossi et al. (2022) have implemented the LAND-SUITE software (LANDslide—SUsceptibility Inferential Tool Evaluator). The tool was designed to provide the user with the possibility to perform more easily, more flexible, and more informed statistically based landslide susceptibility zonation, and includes the possibility to: (i) facilitate the data preparation; (ii) perform preliminary and exploratory analyses of the available data; (iii) test different combinations of variables and select the optimal thematic/explanatory variable set; (iv) test different model types and their combinations; and (v) evaluate the models performance and uncertainty.

This article describes with an example in the Gipuzkoa province (Spain) some functionalities offered by LAND-SUITE and provides guidance for its use in different study areas.

I. Alcántara-Ayala et al. (eds.), *Progress in Landslide Research and Technology, Volume 2 Issue 1, 2023*,
Progress in Landslide Research and Technology, https://doi.org/10.1007/978-3-031-39012-8_17

2 General Description of the Tool

LAND-SUITE is a suite of R (R Core Team 2021) scripts aimed to support the landslide susceptibility inference process. A detailed description of the tool functionalities can be found in Rossi et al. (2022).

LAND-SUITE is composed by three modules:

- LAND-SIP: LANDslide—Susceptibility Input Preparation
- LAND-SVA: LANDslide—Susceptibility Variable Analysis
- LAND-SE: LANDslide—Susceptibility Evaluation

The three modules are coded as separate R script files and can be executed under different operating systems. The common LAND-SUITE run starts with LAND-SIP, which can execute in cascade LAND-SVA and successively LAND-SE. Alternatively, only one of these last two modules can be executed after LAND-SIP, depending on the user needs and on the type of susceptibility application. The three modules can also be executed separately if the user provides the appropriate data input.

LAND-SUITE can use data in raster (GeoTiff) or vector (ESRI shapefile) format, depending on the type of application. The input data can be provided with different resolutions (for rasters) and attributes (for vectors) and using different reference systems. The software can accept data stored in a local system folder, or alternatively, the data can be stored and imported from a GRASS GIS Mapset. The use of GRASS GIS Mapset is preferred for large datasets because it facilitates the massive code execution via command line interface.

A prerequisite for the execution of LAND-SUITE, is the availability of two main input data: (i) a landslide inventory map to be used as a dependent variable in the susceptibility analysis, and (ii) a set of thematic maps to be used as independent explanatory variables. To execute the tool in raster mode, the user needs to provide all the inputs as raster layers, while in the vector mode the software requires a vector layer (e.g., a polygon-based slope unit partition layer) with the attribute table containing both the dependent (i.e., derived from the landslide inventory map) and the independent variables (i.e., the thematic information).

The selection and the preparation of model inputs is an important preliminary phase for the landslide susceptibility assessment and for the execution of LAND-SUITE. The different types of inventory maps (e.g., historical, geomorphological, event and multi-temporal landslide inventories) are usually chosen to derive landslide information used as a dependent variable in the modelling (Reichenbach et al. 2018). Inventory data are used to classify the mapping units as 0 or 1, a largely accepted method to indicate the absence or presence of landslides respectively. This classification is also used in LAND-SUITE to describe the dependent or grouping variable.

The independent variables for the modelling are the numerous thematic variables, which can be either continuous (e.g., slope, elevation, etc.) or categorical (e.g., lithology, land use, etc.). Depending on data types, to be properly used in the statistical models, thematic variables require different pre-processing phases. In particular, the continuous variables can be used directly in the analyses implemented in LAND-SUITE, while the categorical need to be converted into dummy variables. Dummy variables represent categorical data using distinct numerical categories and can be derived using different approaches (Rossi et al. 2022).

Another common data pre-elaboration step in multivariate statistics is the variable scaling (Becker et al. 1988; Han et al. 2011). The data scaling may hold a strong statistical meaning, particularly in the case of normally distributed variables (i.e., following a Gaussian distribution), transforming their distribution into a standard normal distribution (i.e., with mean value equal to 0 and standard deviation equal to 1). In all the other cases, such transformation chiefly aims at making variable values ranging on a similar scale, improving their comparability. In many cases, the scaling does not lead to significantly different susceptibility results, but in some conditions, it may avoid problems on numerical model convergence. LAND-SUITE includes a specific option to perform scaling, but this preliminary transformation can also be done in a GIS or other computational environments.

The maximum extension of the study area and the relative calculation times are strongly controlled by the data size and resolution and by the hardware characteristics, chiefly the RAM size and CPU speed. The software, which is composed essentially by different R scripts, is executed in memory. During the execution and computations, the data are converted in a tabular format and stored in the filesystem at intermediate software execution steps, in the binary RDATA format.

During the software execution, LAND-SUITE provides outputs of specific analyses and evaluations in textual and graphical formats. At the end of the modelling computation, maps are also available as output in the classical GIS geographical formats.

3 Description of the Example Area and Available Data

To illustrate the LAND-SUITE functionalities, we have selected the Oria river basin, located in the Gipuzkoa Province, in the northern part of the Iberian Peninsula. The application provides examples of the susceptibility analysis

outputs, including plots and maps. The critical evaluation of the results and their scientific relevance is out of the scope of this article and requires dedicated analysis, such as those described by Bornaetxea et al. (2018) and Rossi et al. (2021).

The Oria river basin has an extension of 882 km^2 with elevation ranging from the sea level to 1528 meters (Fig. 1). The basin is characterized by two main geological units: the Basque Arc with Mesozoic and Cenozoic marine sedimentary materials in the southwestern portion of the basin, and the Palaeozoic Massif of Cinco Villas in the northeaster sector (EVE 2010). The head of the basin is dominated by marls, limestones and calcarenites with some alternating detrital rock outcrops. In the middle part there are strata of marls, limestone, ophiolites, clays, gypsum, and thick detrital grain materials (Campos and García-Dueñas 1972; Campos et al. 1983). The basin is mainly covered by forest plantations, natural forests, and meadows. The area is characterized by an Atlantic climate, with average annual precipitation of about 1600 mm (González Hidalgo et al. 2011) concentrated in the winter season, with November, December and January commonly exceeding 150 mm of rain.

The landslide inventory map, the first input required by LAND-SUITE, was prepared by an experienced geomorphologist during field surveys. Figure 1 shows the location of the landslides mostly classified as shallow slides and stored digitally in polygon format.

For the area, a total of 14 environmental data layers in raster format were used as explanatory variables. Morphometric variables, such as elevation, slope, sinusoidal slope (Santacana Quintas 2001; Amorim 2012), aspect, surface area ratio (SAR), terrain wetness index (TWI), curvature, planar curvature, and profile curvature, were derived from a DEM with a 5 m × 5 m spatial resolution. In addition, lithology, permeability, regolith thickness, land use and vegetation were downloaded from the official spatial data repository of the Basque Country (GeoEuskadi). The latter maps together with the reclassified aspect are considered as categorical variables and the relative landslide incidence, by means of the Frequency Ratio (Bonham-Carter 1994; Lee et al. 2002), was used to assign a numerical value to each category (i.e., obtaining dummy variables).

4 Input Preparation and Description of the Applied Approach

In this application we have chosen to organize the input data in a GRASS Location/Mapset. The 14 thematic variables described before were imported as raster layers, with the same spatial resolution and grid dimension. The landslide map was first converted in raster format and then imported in the GRASS Mapset. Such map has values equal to 1 in landslide areas and 0 in the rest of the area, which we assume to be free of failures. Additionally, a mask layer was prepared to constrain the LAND-SUITE analyses in a specific areal extension. To avoid execution errors, it is very important to verify that within the mask, all the pixels of the input layers have "non-null" values.

The input preparation is a relevant phase for the susceptibility analysis because the training and validation datasets are prepared automatically by the LAND-SIP module, based on the input configuration. In addition, the training and validation datasets will be used in tabular format within R by the other two modules (i.e., LAND-SVA and LAND-SE).

The training and validation dataset partition is customized by the user, that can (i) select the type of the mapping unit (i.e., raster or polygons); (ii) choose the appropriate combination of variables; (iii) define the extent (i.e., using a mask) of the training and the validation areas; and (iv) choose the output types.

LAND-SIP allows the user to select different functionalities and criteria to partition the training and validation datasets (for more detail see Rossi et al. 2022).

The flexibility of the choices in the configuration phase allows the user to draw and execute many diversified susceptibility applications. It is out of the scope of this paper, if not impossible, to identify all the possible potential software applications. However, in the following, five possibilities (i.e., hereafter referred to as "Cases") are listed and discussed, with the purpose of explaining how LAND-SIP, and in turn LAND-SUITE, can be used for executing the most common susceptibility investigations (Fig. 2).

Case A: The susceptibility modelling is performed applying a regular cross validation approach. A balanced random sampling is used to select the grouping variable mapping units following the "pixels sampling" selection criteria, with the size of training and validation datasets (e.g., 70% training and 30% validation) selected by the user (Fig. 2 Case A). This configuration is usually applied for exploratory analysis focused on the preliminary evaluation of the explanatory variables, and of the statistical performance of the model. This execution can be performed by the user to select, add, or remove explanatory variables before the application of the trained model to the entire study area (Fig. 2 Case C).

Case B: This application considers a cross validation approach similar to Case A, but the training and validation datasets partition uses the "landslides sampling" selection criteria. As before, a balanced random sampling and a specific size of the training and validation datasets (e.g., 70% training and 30% validation) are chosen (Fig. 2 Case B). As in Case A, it can be used to analyse the explanatory variables and to test the modelling results as well as its dependency from the selection of different landslide samples.

Case C: The training configuration can be similar either to Case A or B, but the validation is applied to the entire study area. This case should be applied when the definitive set of

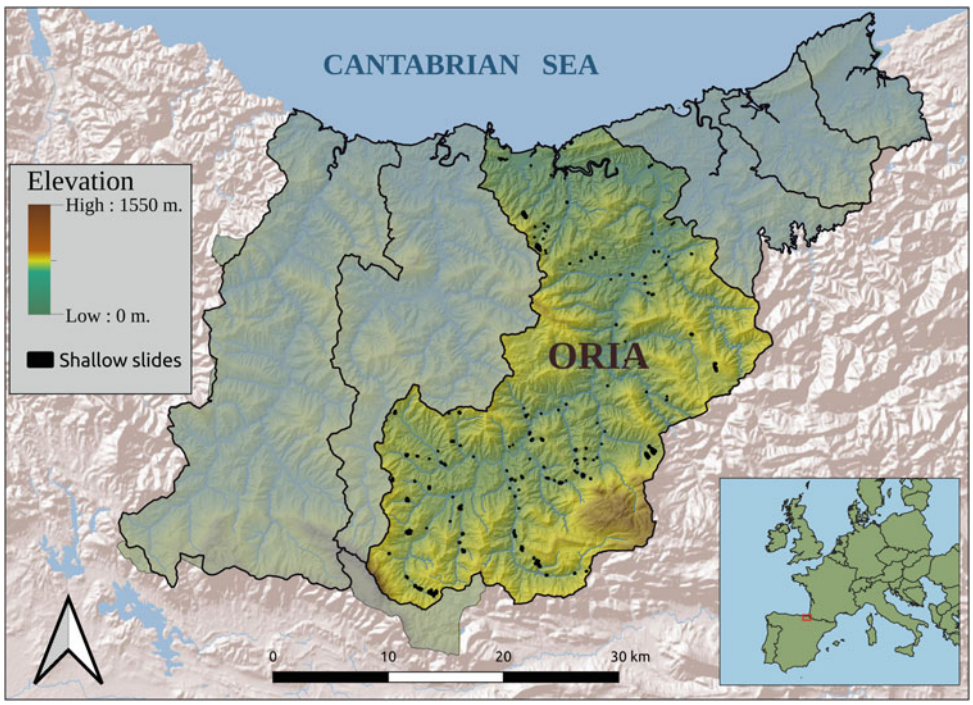

Fig. 1 Elevation map of the Oria river basin (Gipuzkoa Province, Spain). Black polygons show shallow slides

explanatory variables is selected, and the statistical performance of the model is satisfactory and acceptable. The validation map will show the susceptibility zonation for the entire extent of the study area (Fig. 2 Case C).

Case D: This case performs a temporal validation, applicable when a geomorphological/historical inventory map is available to train the model and an event (or a successive) landslide inventory map is used for validation. In such a case the landslide event map used for the model validation may cover only a portion of the study area, with a spatial extent different from the inventory map used for the calibration (Fig. 2 Case D). This configuration requires two different mask files, one covering the entire study area for the training and the other only the area affected by the event for the

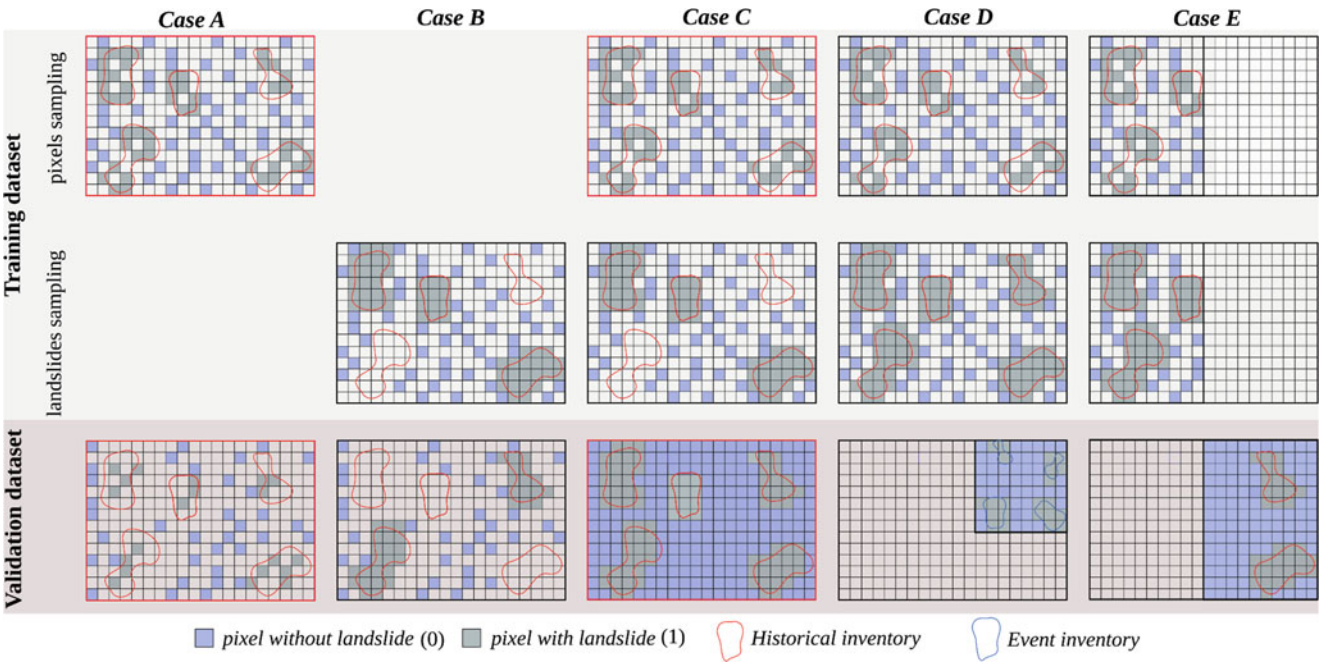

Fig. 2 Simplified representations of five LAND-SUITE applications, referred to as "Cases" in the figures and text, representing common susceptibility investigations. Red boxes highlight the cases described as example

validation. The selection of the explanatory variables and the preliminary evaluation of the model can be performed applying Case A or B. The temporal validation may also cover the entire study area, but only when an event inventory is available for its total extent.

Case E: This case performs a spatial validation, with the model calibration performed in a given region of the study area and the validation in a different one. For example, the model training and validation can be performed in two contiguous but not overlapping river basins. In such a case, the variable selection and the preliminary model testing could be performed only in one of the two basins similarly to Case A or B. In this case the explanatory variables and landslide inventory map should be available in the two regions with the same characteristics (Fig. 2 Case E). This configuration requires two different landslide inventory maps, two mask files and two explanatory variables datasets, respectively for the calibration and validation region.

5 Example Procedure

In the following section we provide results of the example of LAND-SUITE application in the Oria river basin to illustrate a common procedure to prepare landslide susceptibility zonation using data in raster format. Among all the possible LAND-SUITE applications, we have selected the cross-validation approach with pixel sampling method (Case A) applying the balanced random sampling criteria to select the same number of pixels with and without landslides, for both the training (70%) and validation datasets (30%).

In the first step we have performed a preliminary evaluation of all the available explanatory variables, using the LAND-SVA module. Then, we have selected the most significant explanatory variables, and we have evaluated the statistical performance of the calibrated model with the inspection of the susceptibility outputs produced by LAND-SE. At the final step, we have applied Case C (Fig. 2) to obtain a susceptibility zonation for the entire study area.

5.1 Step 1: Susceptibility Variable Analysis

To carry out the variable analysis, we set up the LAND-SUITE options as specified in the first column of Table 1 (First run, Case A). Using this set of parameters, we run only LAND-SVA, which is designed for the explorative analysis of the training and validation input datasets supporting the user for the selection of the optimal set of variables. LAND-SVA automatically detects continuous or dummy variables (i.e., derived from categorical data and normally represented with numerical discrete values) and chooses the type of analysis accordingly.

In the example, we have decided to scale the variables, applying the option jointly to the training and validation datasets, to guarantee the comparability and applicability of the trained susceptibility model to the validation datasets.

LAND-SVA produces the following outputs that provides statistical descriptive information about all the continuous or categorical input variables:

- **Density plots** (Fig. 3) are applied to the continuous variables and show the distribution of the values of numeric variables, stratified by the corresponding grouping variable value (0 and 1). Such plots use a kernel density estimator to show the probability density function of the variable. It corresponds to a smoothed version of a histogram plot and can be interpreted similarly. In Fig. 3 we can observe that Curvature, Curvature Planar, Curvature Profile and SAR show hardly distinguishable distributions between the presence and absence of landslides.
- **Conditional density plots** (Fig. 3) are also applied to the continuous variables, and they examine the proportion of the grouping variable values (0 and 1) against the variation of a given continuous variable. The shapes of the plots displayed in Fig. 3 for Curvature, Curvature Planar, Curvature Profile and SAR indicate a dramatic oscillation of the proportions, together with some slight data lacking portions.
- **Histogram plots** (Fig. 4) show, similarly to density plots, the distribution of the values of categorical variables stratified by the corresponding grouping variable value (0 and 1). These plots use a normalized histogram counting to estimate the probability density function.
- **Mosaic plots** (Fig. 4) show, the proportion of the grouping variable values (0 and 1) for different categorical variables. According to our examples in Fig. 4, Permeability shows almost the same proportion of presence and absence of landslides in all the categories except in one.

The examination of the density and histogram plots, allow to identify significant numerical and categorical variables when the distribution of the values corresponding to the grouping variable categories (0 or 1) are significantly different (i.e., different shapes and lack of overlapping). Only under these circumstances, a variable may have a high significance in the modelling. In addition, conditional density and mosaic plots need to be interpreted considering the variation and trend of the proportion of the grouping variable categories (i.e., the proportion of 0 or 1 along the vertical axis) along with the variable value (i.e., along the horizontal axis). A distinct increase or decrease of such proportion, along with a reduced oscillation of it, and without lack of

Table 1 Parameters' values specified in LAND-SIP to run the cases described in the article, with raster selected as mapping unit

	Type	First run (Case A)	Second run (Case A*)	Third run (Case C)
executing_LAND_SVA	*logic*	TRUE	TRUE	FALSE
LAND_SVA_script_version	*string*	LAND-SVA.R	LAND-SVA.R	LAND-SVA.R
executing_LAND_SE	*logic*	FALSE	TRUE	TRUE
LAND_SE_script_version	*string*	LAND-SE.R	LAND-SE.R	LAND-SE.R
export_shapefiles	*logic*	FALSE	FALSE	TRUE
export_txtfiles	*logic*	FALSE	FALSE	TRUE
mapping_unit_type	*string*	"Raster"	"Raster"	"Raster"
enable_grass_import	*logic*	TRUE	TRUE	TRUE
use_mask	*logic*	TRUE	TRUE	TRUE
use_separate_raster_validation_files	*logic*	FALSE	FALSE	FALSE
use_separate_raster_validation_dependent	*logic*	FALSE	FALSE	FALSE
generate_random_validation_dependent	*logic*	FALSE	FALSE	FALSE
use_mask_validation	*logic*	FALSE	FALSE	FALSE
execute_multiple_validation	*logic*	FALSE	FALSE	FALSE
names_multiple_validation_layers	*string*	–	–	–
original_data_training	*logic*	FALSE	FALSE	FALSE
validation_dim	*value*	30	30	30
change_dependent_proportion	*logic*	TRUE	TRUE	TRUE
nodependent_percentage	*value*	50	50	50
validation_entire_area	*logic*	FALSE	FALSE	TRUE
reducing_sample_size	*logic*	FALSE	FALSE	FALSE

The type *string* refers to character strings that should be written in the script within double quotes. The type *logic* can be either TRUE or FALSE. The type *value* is a numerical value. The complete list of options can be found in the LAND-SUITE User Guide reported as supplementary material of the article by Rossi et al. (2022)

data, is the expected behaviour to identify a variable contributing significantly to the susceptibility zonation. Under these circumstances, an independent explanatory variable may have an unambiguous effect on the dependent grouping variable used in the modelling (i.e., the presence or absence of landslides in the mapping unit). Following these considerations and the outputs in Figs. 3 and 4, we can conclude that for the Orio basin area, the Curvature, Curvature Planar, Curvature Profile and SAR variable are not potentially beneficial for the modelling.

LAND-SVA provides the following results to evaluate the inter-related role of the variables in the modelling.

- The **pairwise correlation analysis** (Fig. 5) provides a correlation matrix that shows pairwise correlation statistics among the different explanatory variables. The correlogram shows: in the upper triangular matrix, the values of the Pearson correlation coefficient for each pair of variables (i.e.; R coefficient ranging between −1 and 1, respectively for a perfect negative and positive correlation); in the lower triangular matrix, a graphical representation of the level of correlation (i.e.; flattened negatively and positively oriented ellipses, respectively for a negative and positive correlation); in the diagonal, the R value for the correlation of a variable with itself (R = 1). Colours indicate different levels of correlation (i.e., white for no correlation, red and blue respectively for negative and positive correlations).
- A **multicollinearity table** (Belsley et al. 1980) is prepared to identify multicollinearity among the explanatory variables. The test calculate the condition index statistics used to detect multicollinearity, which exists whenever a variable is highly correlated with one or more of the other variables and represents a problem undermining the statistical significance of the independent variables. Multicollinearity implies that one variable in a multiple regression model can be linearly predicted from the others, with a substantial degree of accuracy.

The pairwise correlation analysis and multicollinearity test are easier to interpret. When a significant high correlation is detected among two or more variables, one or more of the correlated variables should be excluded from the analysis. Highly correlated variables are those with a Pearson R values in the correlogram matrix close to +1 or − 1 (Fig. 5). Instead, multicollinearity is detected when the test statistic (i.e., the condition index in Table 1) is greater than 30 (Belsley 1991). When a large condition index (rows with condition index >30) is associated with two or more variables with large variance decomposition proportions (values corresponding to variables >0.5), these variables may cause collinearity problems. And this is relevant for the following reasons:

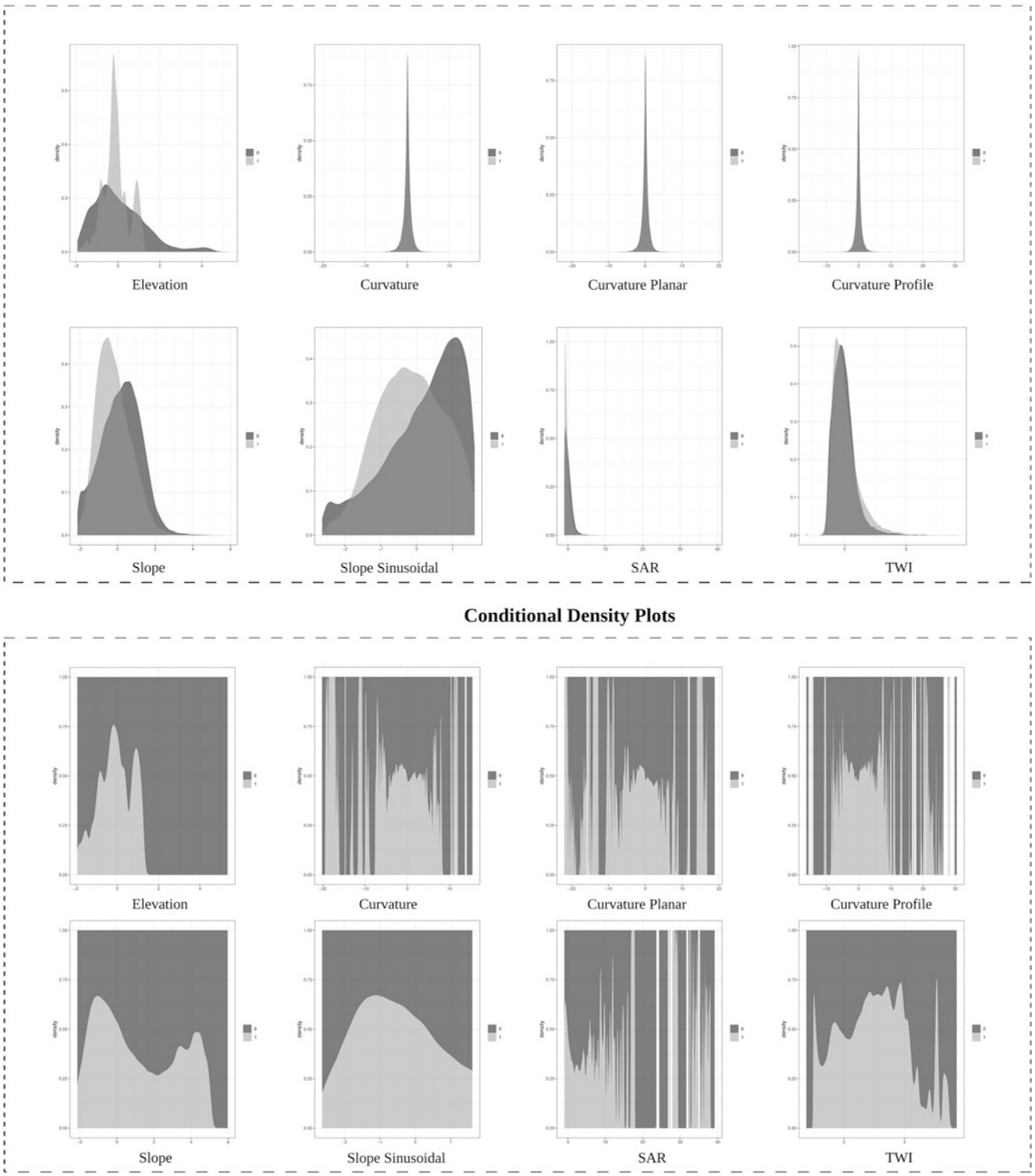

Fig. 3 LAND-SVA output: density plots and conditional density plots for the continuous explanatory variables

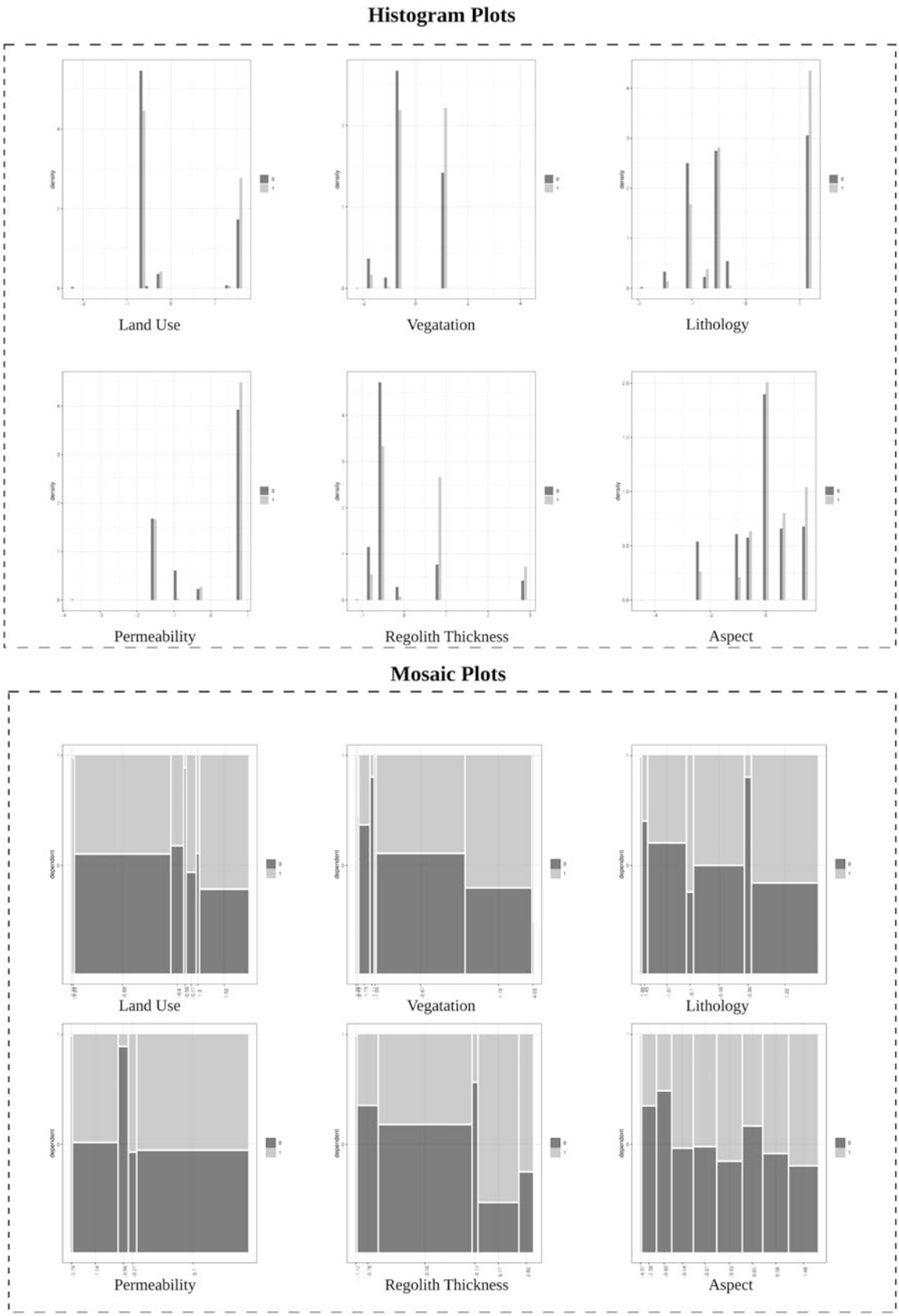

Fig. 4 LAND-SVA output: histogram plots and mosaic plots for the categorical explanatory variables

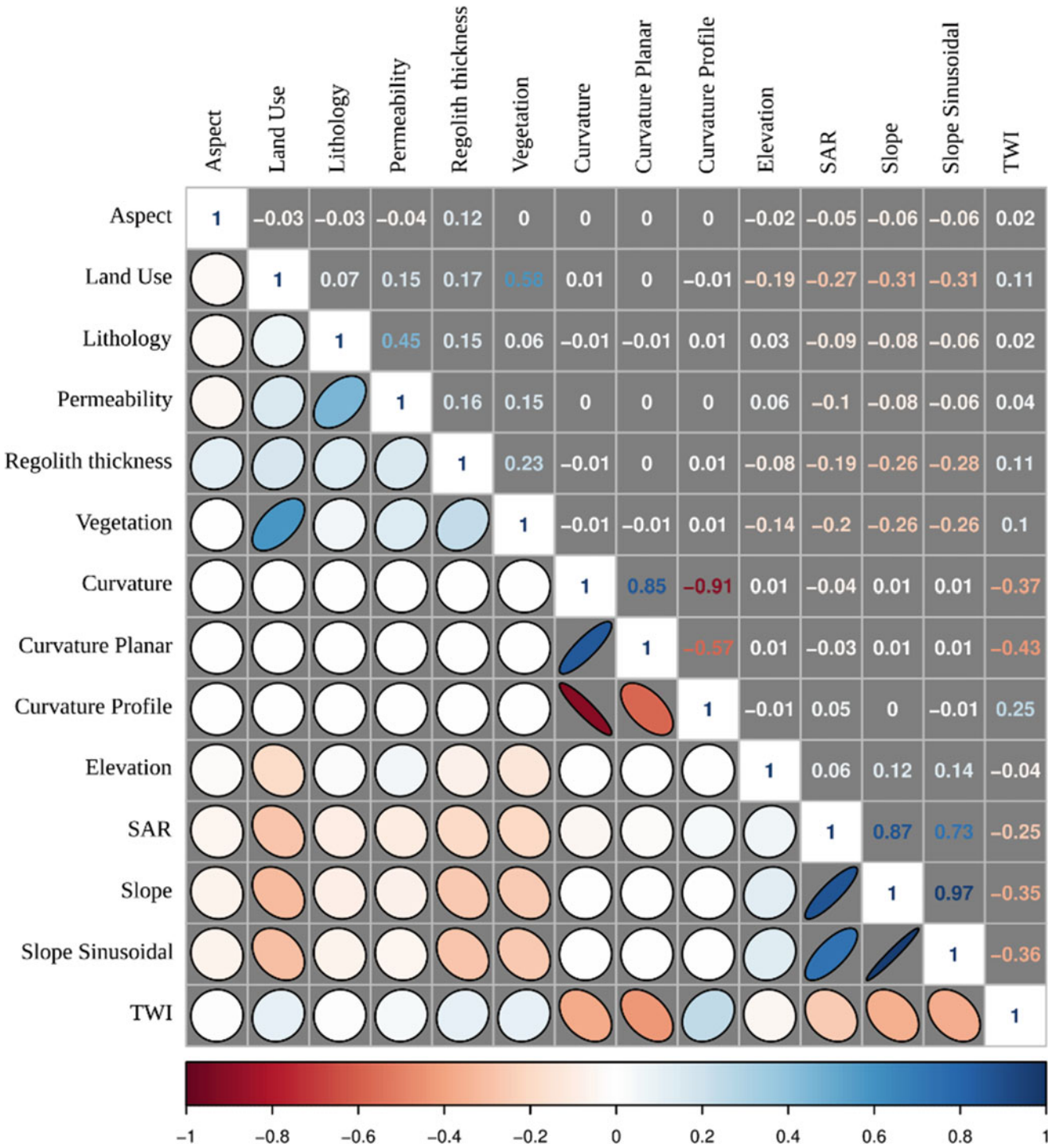

Fig. 5 LAND-SVA output: the correlogram for the complete set of variables available for the Oria river basin (Case A)

- the joint use of two or more correlated variables does not introduce a significant advance for the multivariate modelling;
- generally, multivariate models assume independence among explanatory variables and when correlation exists, the independence assumption is not verified;
- when the degree of correlation among variables is high, it can introduce problems during the model fitting and for the interpretation of the model results;
- multicollinearity can introduce two main types of problems: (i) the coefficient estimates can vary largely depending on the other independent variables considered

Table 2 LAND-SVA output: multicollinearity table for the Oria river basin

Condition index	*intercept*	Aspect	Landuse	Litology	Permeability	Regolith_ thickness	Vegetation	Cuvature	Curvature_ planar	Curvature _profil	Elevation	Sar	Slope	Slope_ sinusoidal	Twi
1.000	.	.	.	.	.	.	.	.	.	.	.	.	.	.	.
1.116	.	.	.	.	.	.	.	.	.	.	.	.	.	.	.
1.488	.	.	.	.	.	.	.	.	.	.	.	.	.	.	.
1.615	.	.	.	.	.	.	.	.	.	.	.	.	.	.	.
1.794	.	0.664	.	.	.	.	.	.	.	.	.	.	.	.	.
1.844	0.999	.	.	.	.	.	.	.	.	.	.	.	.	.	.
1.947	.	.	.	.	.	.	.	.	.	.	0.799	.	.	.	.
2.085	.	.	.	.	.	0.728	.	.	.	.	.	.	.	.	.
2.186	.	.	.	.	.	.	.	.	.	.	.	.	.	.	0.654
2.529	.	.	.	0.672	0.726	.	.	.	.	.	.	.	.	.	.
2.892	.	.	0.752	.	.	.	0.717	.	.	.	.	.	.	.	.
3.002	.	.	.	.	.	.	.	.	.	.	.	.	.	.	.
3.654	.	.	.	.	.	.	.	.	.	.	.	.	.	.	.
29.660	.	.	.	.	.	.	.	.	.	.	.	0.888	0.998	0.981	.
314802.234	.	.	.	.	.	.	.	1.000	1.000	1.000	.	.	.	.	.

in the model, with such coefficients' values becoming very sensitive to small model changes; (ii) multicollinearity may reduce the precision of the estimated coefficients, weakening the statistical significance of the model, leading to a limited p-values reliability when identifying statistically significant independent variables;
- when collinearity occurs, the model coefficient values and their signs may change significantly depending on the specific variables included in the model, leading to difficulties to evaluate the results. Slightly different models may lead to different conclusions, making the actual contribution of variables impossible to understand.

Based on the above considerations, for the Oria river basin, the multicollinearity table (Table 2) shows one condition index larger than 30 and one close (29.660), with variance decomposition proportion values larger than 0.5. Thereby, the test detected two groups of variables (group I: Curvature, Curvature Planar, and Curvature Profile; group II: SAR, Slope, Sinusoidal slope) with multicollinearity problems. Inspection of the correlogram (Fig. 5) confirmed the pairwise correlations within groups I and II and highlights an additional correlation between Vegetation and Land use, assuming a Pearson R absolute value of 0.5 as thresholds for detecting correlations.

To obtain additional information on the highly correlated continuous variables, the relation of each explanatory layer with the dependent variable can be analysed through the density plots and conditional density plots reported in Fig. 3. Similarly, we checked the histogram plots and mosaic plots (Fig. 4) to analyse the categorical variables. Therefore, the evaluation of LAND-SVA outputs allowed:

- the removal of all the variables in group I, due to high correlation and to the lack of relevant differences between 1 and 0 in the density plots and conditional plots;
- the selection of Slope in group II, based on the better distribution separation and trend shown in the density and conditional plots;
- the selection of Land use, and exclusion of the Vegetation, due to their weak correlation confirmed by their Pearson R value;
- the exclusion of Permeability because of the poor differences in the presence and absence of landslides in the most part of its categories observed in the mosaic plot.

In the example, we have decided to scale the variables, applying the option jointly to the training and validation datasets, to guarantee the comparability and applicability of the trained susceptibility model to the validation datasets.

5.2 Step 2: Susceptibility Evaluation

Inspection of the results produced by LAND-SVA, allowed to select the final set of explanatory variables (i.e., Aspect, Land use, Lithology, Elevation, Slope, and TWI) used to run the second step. The parameters' configuration chosen in this run are specified in the second column of Table 1.

In this second step, we also run LAND-SE that is the module for landslide susceptibility modelling and zonation, described in detail in Rossi and Reichenbach (2016). LAND-SE holds on to the possibility to perform and combine different statistical susceptibility modelling methods, evaluate the results, and estimate the associated uncertainty. In particular, it allows for: (i) the selection of different multivariate approaches (currently Linear Discriminant Analysis, Quadratic Discriminant Analysis, Logistic Regression and Neural Network) and the combinations between them (Combined Model's Function); (ii) the evaluation of the model prediction skills and performances using success contingency matrices and plots, ROC curve and prediction rate curves; (iii) the estimation of the associated uncertainty and errors; (iv) the production of results in standard geographical formats (shapefiles, geotiff); and (v) the usage of additional computational parameters to tune the calculation procedure for the analysis of large data sets.

The basic LAND-SE execution flow involves the following steps:

- the single susceptibility models' executions and zonation production;
- the combination of the single susceptibility models using a logistic regression approach;
- the evaluation of the single and combined susceptibility models;
- the estimation of the uncertainty of the single and combined susceptibility models.

For the example, the same training set was used to prepare the four single landslide susceptibility models and the combined model (see maps in Fig. 7). In Fig. 6 we show the ROC plot, contingency or fourfold plot, success rate plot, and the variability plot for both training and validation data sets corresponding to the combined models. This set of outputs, produced by LAND-SE, is commonly used for the verification and analysis of the susceptibility zonation obtained by LAND-SUITE.

In both training and validation datasets ROC curves and Success/Prediction rate curves look very similar. The area under the ROC curve is 0.825 for training and 0.827 for validation, which suggests the absence of model overfitting.

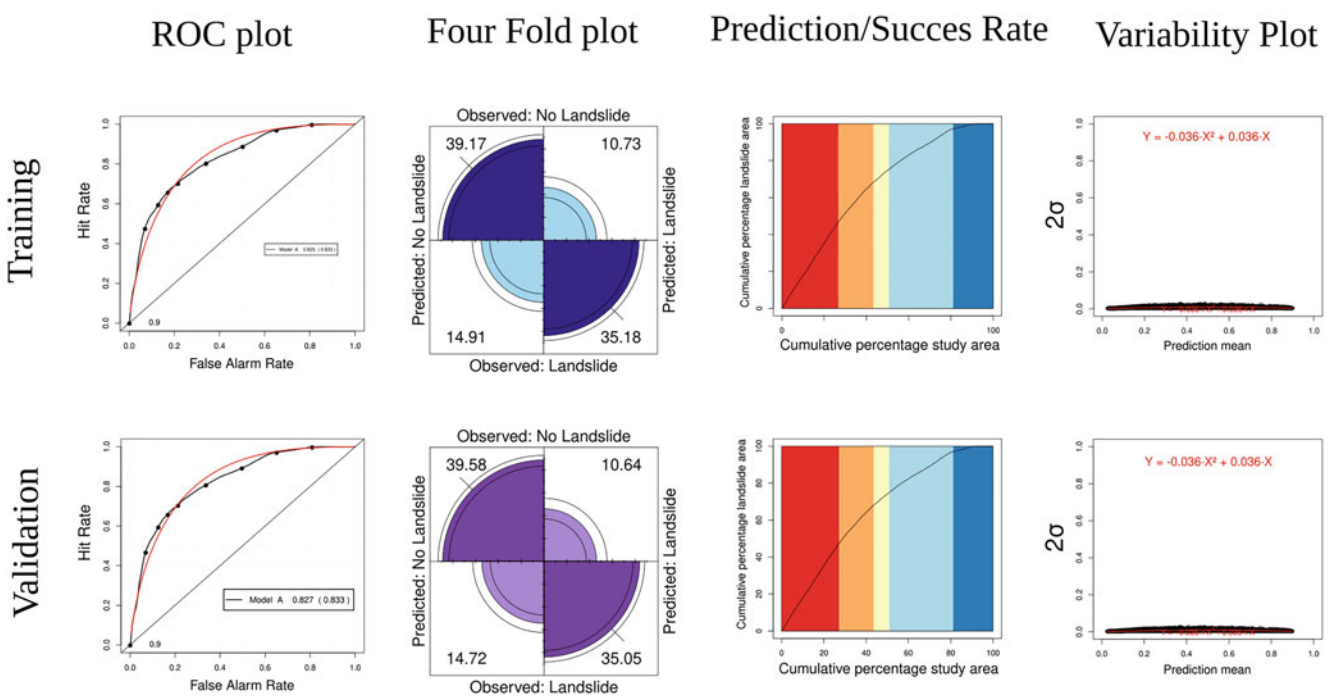

Fig. 6 LAND-SE output: graphs showing the training and the validation models performance for the Oria river basin

Similar conclusion can be obtained from the four-fold plots, where 74.35% and 74.63% of the observations were classified as true positive or true negative for training and validation respectively.

LAND-SE also evaluates and quantifies the uncertainty adopting a "bootstrapping" approach. Bootstrapping is a resampling technique for estimating the distributions of statistics based on independent observation (Efron 1979; Davison and Hinkley 2006). In the training phase, 100 runs are performed varying the selected data set. Then descriptive statistics for the probability (susceptibility) estimates, including the mean (μ) and the standard deviation (σ), are obtained from this ensemble of model runs. Such information is portrayed in variability plots showing estimates for the model uncertainty in each mapping unit (Fig. 6). The results in the Oria river basin show a flattened variability curves in both training and validation plots, which indicates that the estimated susceptibility was stable and did not suffer from high uncertainty.

Additional details on the LAND-SE tool specifications, configuration, functioning, and the scientific assumption can be found in Rossi and Reichenbach (2016), Rossi et al. (2010, 2022).

5.3 Step 3: Final Susceptibility Maps

As a final step, we set up the LAND-SUITE parameters to perform the susceptibility zonation in the entire area, instead of in the validation subsample only (see the tool configuration in the third column of Table 1). The purpose of this step is to obtain the susceptibility maps for each single model and for their combination. In Fig. 7a is possible to recognize significant differences in the four single models that should be analysed in more detail. The map in Fig. 7b1 shows the susceptibility zonation derived from the four single models. The map in Fig. 7b2 shows the geographical distribution of the uncertainty, which can provide additional and relevant information to the decision makers for the use of LS zonation in environmental, management and planning evaluations.

6 Final Remarks

LAND-SUITE is a suite of tools for statistically based landslide susceptibility zonation implemented in R and released with an open-source license. The tool was developed to support the landslide susceptibility inference process. LAND-SUITE was not designed to substitute the geomorphological/geological experience and competence of the operator, but to facilitate the preparation and the selection of the variables/data required for a reliable statistical analysis. LAND-SUITE can be used to test diversified geomorphological hypotheses allowing to verify and discuss initial assumptions and to prepare less subjective statistically based susceptibility zonation. Few initial skills are required to run the software, but the learning curve is not steep. A user

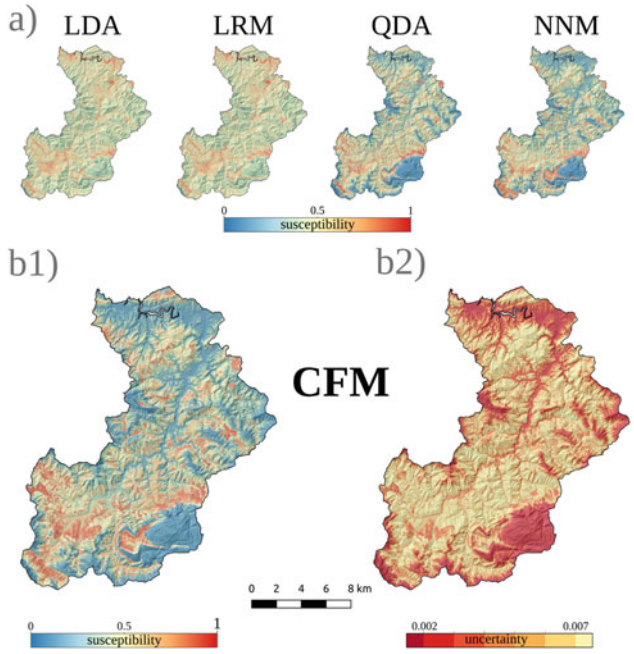

Fig. 7 LAND-SE output: results of the susceptibility zonation for the Oria river basin obtained using different models. (**a**) maps derived from single susceptibility models (*LDA* Linear discriminant analysis, *LRM* Logistic regression model, *QDA* Quadratic discriminant analysis, *NNM* Neural network analysis). (**b1**) the map shows the result of the combined model (CFM). (**b2**) the map shows the geographical distribution of the uncertainty

with a good knowledge of LAND-SUITE can run different models changing options, configurations, and data.

A key step for a reliable landslide susceptibility modelling, is the preparation of robust and unbiased input data, which largely depends on the user's skill and experience. In many cases, the data classification approaches, reliability and representativeness of the thematic information are more important than the statistical methods and tools used for the landslide susceptibility estimation. Low quality output and errors derive often from incomplete or not significant data. The tool has the ambition to help the preparation of statistically correct and robust models, allowing to apply classical and standard statistical procedures (e.g., random sampling, data scaling, use of common machine learning approaches and standard evaluation metrics).

Moreover, LAND-SUITE can be applied using different mapping units (e.g., pixel, slope units, administrative units, etc.), with distinct configurations and data resolution at diverse spatial scales. The tool uses standard geographical formats in input and output and can facilitate the massive code execution via command line interface.

The suite has high flexibility and allows to perform different partitions of the training/validation dataset and diversified validation tests (e.g., temporal, spatial, cross validation, etc.), as discussed in the example of zonation in the Oria river basin, presented in this article.

LAND-SUITE can be also used to model and evaluate the spatial probability of the occurrence of other types of natural phenomena, such as floods, forest fires, rock falls source areas (Rossi et al. 2021). Indeed, as an open-source tool, LAND-SUITE can be easily modified by a R programming skilled user and adapted to any specific needs.

7 Code Availability and Licence

LAND-SUITE is composed of three modules (LAND-SIP, LAND-SVA, LAND-SE) coded as separate. R script files and can be executed under different operating systems. The software was mainly tested under WindowsOS and LinuxOS, with the version of R-4.1.1 (64bit). Some code functionalities of LAND-SIP require GRASS GIS binding. We tested the script using GRASS GIS version 7 under WindowsOS and LinuxOS. We recommend LinuxOS, due to the better software integration at a bash scripting level.

LAND-SUITE is free software; it can be redistributed or modified under the terms of the GNU General Public (either version 2 of the license, or any later version) as published by the Free Software Foundation. The program is distributed in the hope that it will be useful, but without any warranty, without even the implied warranty of merchantability or fitness for a particular purpose. See the GNU General Public License for more details.

LAND-SUITE V1.0 is archived in ZENODO repository with the DOI: 10.5281/zenodo.5650810.

Acknowledgments Txomin Bornaetxea was financially supported by the postdoctoral fellowship program of the Basque Government (grant numbers POS_2020_2_0010) in the framework of a scientific collaboration with the Geological Survey of Canada and the Geomorphological Group of the Research Institute for the Geo-Hydrological Protection in Perugia, Italian National Research Council (CNR-IRPI).

References

Amorim SF (2012) Estudio comparativo de métodos para la evaluación de la susceptibilidad del terreno a la formación de deslizamientos superficiales: Aplicación al Pirineo Oriental. PhD thesis, Universidad Politécnica de Catalunya, Barcelona, Spain

Becker RA, Chambers JM, Wilks AR (1988) The new S language. Wadsworth & Brooks, Cole

Belsley DA (1991) A guide to using the collinearity diagnostics. Comput Sci Econ Manage 4(1):33–50

Belsley DA, Kuh E, Welsch RE (1980) Regression Diagnostics. John Wiley & Sons, New York

Bonham-Carter GF (1994) Geographic information systems for geoscientists-modeling with GIS. Comput Methods Geosci 13:398

Bornaetxea T, Rossi M, Marchesini I, Alvioli M (2018) Effective surveyed area and its role in statistical landslide susceptibility

assessments. Nat Hazards Earth Syst Sci 18(9):2455–2469. https://doi.org/10.5194/nhess-18-2455-2018

Bragagnolo L, Da Silva RV, Grzybowski JMV (2020) Landslide susceptibility mapping with r.landslide: a free open-source GIS-integrated tool based on artificial neural networks. Environ Model Softw 123:104565. https://doi.org/10.1016/j.envsoft.2019.104565

Brenning A (2008) Statistical geocomputing combining R and SAGA: The example of landslide susceptibility analysis with generalized additive models. In: SAGA–Seconds Out, Hamburger Beiträge Zur Physischen Geographie und Landschaftsökologie. Böhner, J, Blaschke, T, Montanarella, L. (eds). 19: 23–32

Campos J, García-Dueñas V (1972) Mapa Geológico de España escala 1:50.000. 2ª Serie (MAGNA), Hoja de San Sebastián. IGME. Servicio de Publicaciones Ministerio de Industria, Madrid

Campos J, Olivé A, Ramírez JI, Solé J, Villalobos L (1983) Mapa Geológico de España escala 1:50.000. 2ª Serie (MAGNA), Hoja de Tolosa. IGME. Servicio de Publicaciones Ministerio de Industria, Madrid

Chacón J, Irigaray C, Fernandez T, El Hamdouni R (2006) Engineering geology maps: landslides and geographical information systems. Bull Eng Geol Environ 65(4):341–411

Davison AC, Hinkley D (2006) Bootstrap methods and their applications, 8th edn., Cambridge Series in Statistical and Probabilistic Mathematics,. Cambridge University Press, Cambridge

Efron B (1979) Bootstrap methods: another look at the jack knife. Annals Statistics 7:1–26

EVE (2010) Mapa Geológico del País Vasco 1:100.000. Ente Vasco de la Energía, Bizkaia

González Hidalgo JC, Brunetti M, De Luis M (2011) A new tool for monthly precipitation analysis in Spain: MOPREDAS database (monthly precipitation trends December 1945–November 2005). Int J Climatol 31(5):715–731

Guzzetti F, Reichenbach P, Cardinali M, Galli M, Ardizzone F (2005) Probabilistic landslide hazard assessment at the basin scale. Geomorphology 72:272–299

Han J, Pei J, Kamber M (2011) Data mining: concepts and techniques. Elsevier, Amsterdam

Lee S, Chwae U, Min K (2002) Landslide susceptibility mapping by correlation between topography and geological structure: the Janghung area, Korea. Geomorphology 46(3–4):149–162

Osna T, Sezer EA, Akgun A (2014) GeoFIS: an integrated tool for the assessment of landslide susceptibility. Comput Geosci 66:20–30

R Core Team (2021) R: A language and environment for statistical computing. R Foundation for Statistical Computing, Vienna, Austria, available at: https://www.R-project.org/. Last access: 20 Sep 2021

Reichenbach P, Rossi M, Malamud BD, Mihir M, Guzzetti F (2018) A review of statistically based landslide susceptibility models. Earth Sci Rev 180:60–91

Rossi M, Reichenbach P (2016) LAND-SE: a software for statistically based landslide susceptibility zonation, version 1.0. Geosci Model Dev 9(10):3533–3543. https://doi.org/10.5194/gmd-9-3533-2016

Rossi M, Guzzetti F, Reichenbach P, Mondini AC, Peruccacci S (2010) Optimal landslide susceptibility zonation based on multiple forecasts. Geomorphology 114:129–142

Rossi M, Sarro R, Reichenbach P, Mateos RM (2021) Probabilistic identification of rockfall source areas at regional scale in El Hierro (Canary Islands, Spain). Geomorphology 381:107661

Rossi M, Bornaetxea T, Reichenbach P (2022) LAND-SUITE V1.0: a suite of tools for statistically based landslide susceptibility zonation. Geosci Model Dev 15(14):5651–5666

Sahin EK, Colkesen I, Acmali SS, Akgun A, Aydinoglu AC (2020) Developing comprehensive geocomputation tools for landslide susceptibility mapping: LSM tool pack. Comput Geosci 144:104592

Santacana Quintas N (2001) Análisis de la susceptibilidad del terreno a la formación de deslizamientos superficiales y grandes deslizamientos mediante el uso de sistemas de información geográfica, Aplicación a la cuenca alta del río Llobregat. PhD thesis, Universitat Politècnica de Catalunya, Barcelona, Spain

Landslide and Soil Erosion Inventory Mapping Based on High-Resolution Remote Sensing Data: A Case Study from Istria (Croatia)

Sanja Bernat Gazibara, Petra Jagodnik, Hrvoje Lukačić, Marko Sinčić, Martin Krkač, Gabrijela Šarić, Željko Arbanas, and Snježana Mihalić Arbanas

Abstract

The central part of the Istrian Peninsula (Croatia) is the area of the Eocene flysch basin, i.e. "Gray Istria, which is prone to weathering and active geomorphological processes. The high erodibility of the Istrian marls led to the formation of steep barren slopes and badlands exceptionally susceptible to slope movements. This research presents the application of high-resolution remote sensing data, i.e., Light Detection and Ranging (LiDAR) data and orthophoto images, for landform mapping at a large scale (1:500). Visual interpretation of remote sensing data was done for the pilot area (20 km^2) near City of Buzet to produce detailed inventory maps for implementation in the spatial planning system. There is a lack of detailed inventory maps because systematic mapping was not performed for any part of Istria until the scientific research project *LandSlidePlan* (HRZZ IP-2019-04-9900), funded by the Croatian Science Foundation. After preliminary visual interpretation of LiDAR DTM and field verifications, it was concluded that four types of landforms could be mapped, i.e. badlands, gully and combined erosion, unstable slopes and landslides. The research objective is to show the representative examples and potential of direct and unambiguous identification and mapping of small and shallow landslides and soil erosion processes based on the visual interpretation of high-resolution remote sensing data in flysch-type rock.

Keywords

Landslides · Soil erosion · Inventory mapping · LiDAR

S. Bernat Gazibara (✉) · H. Lukačić · M. Sinčić · M. Krkač · G. Šarić · S. Mihalić Arbanas
University of Zagreb Faculty of Mining, Geology and Petroleum Engineering, Zagreb, Croatia
e-mail: sanja.bernat@rgn.unizg.hr

P. Jagodnik · Ž. Arbanas
University of Rijeka Faculty of Civil Engineering, Rijeka, Croatia

1 Introduction

Inventory mapping of slope processes presents essential input parameters for multiple spatial analyses such as landslide or erosion susceptibility, hazard, and risk assessment (Guzzetti et al. 2000; van Westen et al. 2006), especially in the case of large-scale hazard zoning (Sinčić et al. 2022). However, the traditional landslide and erosional inventory mapping methods include field mapping and interpretation of aerial photos and satellite images, which produces a limited amount of data in case of an inaccessible and overgrown area. Therefore, the LiDAR data is the only appropriate remote sensing tool for landslide and soil erosion mapping in a forest or densely vegetated areas. The landslide maps obtained through the visual analysis of LiDAR-derived DTMs have better landslide area statistics and completeness than the inventories obtained through field mapping or the interpretation of aerial photographs (Eeckhaut et al. 2007).

One of the priorities for an action plan in the Sendai Framework for Disaster Risk Reduction 2015–2030 (UN 2015) is understanding disaster risk in all its dimensions and disseminating location-based information to decision-makers, the general public, and at-risk communities. Therefore, the most critical risk reduction measure and mitigation of the geohazards' consequences is creating inventory and prognostic maps that should be implemented into the spatial planning system for defining building conditions or restricting development in erosion or landslide-prone areas. The scientific research project *Methodology development for landslide susceptibility assessment for land-use planning based on LiDAR technology* (LandSlidePlan, HRZZ IP-2019-04-9900), funded by the Croatian Science Foundation (Bernat Gazibara et al. 2022), deals with inventory mapping of small and shallow landslides and presents innovative approaches to scientific research of landslide susceptibility assessment using LiDAR technology. Among other study areas, selected based on geological settings and degree

I. Alcántara-Ayala et al. (eds.), *Progress in Landslide Research and Technology, Volume 2 Issue 1, 2023*,
Progress in Landslide Research and Technology, https://doi.org/10.1007/978-3-031-39012-8_18

of urbanisation, the landslide maps will be developed for the pilot area in the central part of the Istrian Peninsula (Croatia).

2 Study Area

The Istrian peninsula is a geomorphological unit separated from the interior by the limestone mountains of the Ćićarija Mt. Istria is geomorphologically composed of a hilly northern edge (White Istria), lower flysch hills (Gray Istria) and low limestone plateaus (Red Istria). "Gray Istria" is in the inland of the Istrian peninsula, where a more continental and humid climate prevails. Based on the precipitation data recorded at the Lanišće weather station (NE border of the Istrian flysch basin) for the past 49 years (from 1961 to 2010), this area received mean annual precipitation (MAP) of 1774.3 mm.

The study area (19.96 km^2) is located in the northern part of Istrian County, in Gray Istria, and it includes the part of the City of Buzet between the valley of the river Mirna in the north and the accumulation Butoniga in the south. From the geomorphological standpoint, it is a predominantly hilly area with most terrain steeper than 12°. Approximately 2.6% of the study area has slope angles less than 2°, 9.7% between 2–5°, 25.5% between 5–12°, 45.5% between 12–32°, 16.1% between 32–55° and 1.1% steeper than 55° (Fig. 1a).

According to the Basic geological map of Croatia with a scale of 1:100,000, most of the study area is composed of Middle Eocene sediments (Fig. 1b). Those are represented by the alteration of sandstones and marls, also known as flysch deposits, with thicknesses ranging from 0.3–7 m (Pleničar et al. 1969). Bergant et al. (2003) state that Flysch deposits can be divided into upper and lower parts. The lower part of the flysch complex is mainly composed of the interbedding of marls and carbonate lithological members with occasional carbonate megalayers. On the other hand, the upper part of the Flysch complex is mainly composed of carbonate turbidite sediments which appear in very thin layers. Alongside the Middle Eocene sediments study area comprises Alluvium deposits as the youngest lithological member and Nummulitic and Foraminifera Limestones as the oldest lithological member.

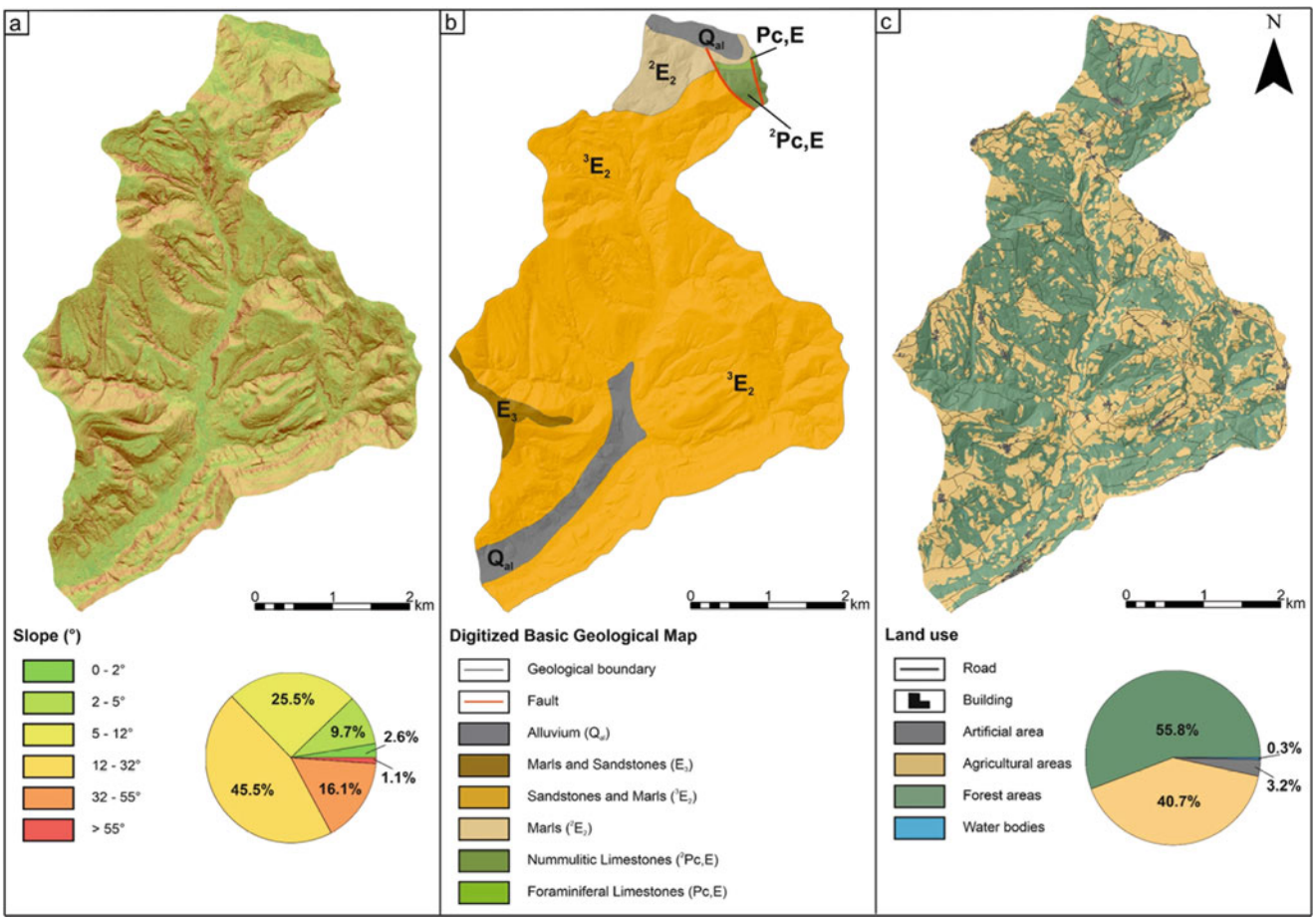

Fig. 1 Study area location and characteristics: (**a**) slope distribution; (**b**) geology; (**c**) land-use

In Sinčić et al. (2022), a detailed land use classification based on high-resolution orthophoto images was performed for the study area. As shown in Fig. 1c, 55.8% of the study area is covered by forests, 40,7% is an agricultural area, 3.2% is artificial (urban), and 0.3% represents water bodies. Although the population density is low, the revitalisation of old and abundant villages and construction outside of the areas defined in the spatial plans due to tourism development is present in the interior parts of the Istrian peninsula.

The central part of Istria is characterised by moderate dissection (100–300 m), which is a consequence of the high erodibility and low durability of flysch sediments and the reason for the frequent occurrence of intense exogenetic processes, such as sliding (Arbanas et al. 1999; Dugonjić Jovančević and Arbanas 2012; Arbanas et al. 2014), gully erosion and badland formation (Gulam et al. 2014.). In addition, more intensive weathering and selective erosion of less-durable marls compared with sandstones enable the development of deeper weathering profiles with up to 10 m of weathered rock mass (Vivoda Prodan and Arbanas 2016).

Sliding is most often in weathered Eocene flysch-like deposits and on contacts between weathered and fresh flysch-type rock, especially at places of concentrated flows of superficial water (e.g., near roads), which typically cause small and shallow landslides (Dugonjić Jovančević and Arbanas 2012). Also, block translational landslides are possible (Arbanas et al. 2010; Mihalić et al. 2011). Landslides are mostly small to medium-sized (Fig. 2a, b), with sliding surfaces at depths of several meters to a maximum of 15 m triggered mostly by precipitations and human activity. Dugonjić Jovančević et al. analysed 19 landslides recorded as singular phenomena that occurred from 1979 through 2010, and the general conclusion is that long rainfall periods are crucial for initiating landslides. In contrast, short rainfalls have a significant influence on erosion. Moreover, debris flows (Arbanas et al. 2006), rock falls, and toppling (Fig. 2c, d) also become active under the influence of heavy rainfall and superficial flows.

Since 2008, the landslide database for the "Gray Istria" was conducted by the Department of Hydrotechnics and Geotechnics, Faculty of Civil Engineering, University of Rijeka, using documentation collected from the department's archives and the archives of the Istrian County Roads Office and the Civil Engineering Institute of Croatia. The collected data for the studied landslides contain basic information about the location, type, dimensions and time of occurrence and other data from geological and geotechnical studies, laboratory test reports, remediation designs, etc. However, there is a lack of detailed landslide inventories because systematic inventory mapping was not performed for any part of Istria until today.

Badland formations (Fig. 3) in the central part of Istria are predefined by the combination of specific lithology, i.e. Eocene flysch deposits, and climate. However, according to Gulam et al. (2014), the most important factor in badland development and formation is the close contact of the channel flow with the accumulated material at the badland slope foot. Also, badlands in central Istria are very small, susceptible to slope movements and characterised by sparse or no vegetation. The most extensive single badland area has an area of 0.08 km^2, according to the badland inventory map made by Gulam et al. (2014), based on visual identification and mapping of the orthophoto images on a scale of 1:5.000. Existing inventory covers approx. 500 km^2 in the central part of Istria, and the badland area covers 2.2% of the total research area. However, there is a lack of previous investigations on other soil erosion processes in the central part of Istria, such as gully or sheet erosion, and these processes were never systematically mapped.

3 Remote Sensing Data

Remote sensing data for the study area were acquired in the framework of the project *"Methodology development for landslide susceptibility assessment for land-use planning based on LiDAR technology (LandSlidePlan IP-2019-04-9900)"* funded by the Croatian Science Foundation (Bernat Gazibara et al. 2022).

LiDAR scanning using an Airborne laser scanning system (ALS) was undertaken in March 2020 using Reigl LMS-Q780 long-range airborne laser scanner coupled with a high-resolution Hasselblad camera at the average altitude of 700 m a.s.l.. LiDAR system used in this study acquires data at the pulse rate of 400 kHz and horizontal surface accuracy of 3 cm (XY plane) and vertical accuracy of 4 cm (Z-direction). Final Point Cloud has approx. 623 million points, with an average point density of 16,09 pt./m^2 resulting in average point spacing of 0.18 cm. Additionally, the final Point Cloud was classified into four distinct classes: (i) default unclassified points, (ii) ground bare earth points, (iii)vegetation, and (iv) noise. Based on the classified Point Cloud bare-earth DEM was generated using kriging interpolation method resulting in a spatial resolution of 30 cm.

For the purpose of landslide and soil erosion inventory mapping morphometric derivative maps were derived from a 30 cm resolution digital terrain model (DTM) using ArcGIS 10.8. software. A total of four types of morphometric derivatives were used; (i) hillshade map, (ii) slope map, (iii) roughness map (Surface/Area Ratio, SAR), and (iv) stream power index map (SPI).

Hillshade map represents a pseudo-three-dimensional visualisation of the terrain surface used for the visual

Fig. 2 Badlands in the Istrian flysch area

interpretation of morphological terrain characteristics (Guzzetti et al. 2012). The map was derived using ArcGIS 10.8. Spatial Analyst extension Hillshade by simulating the illumination conditions that are defined by the azimuth of the light source (0° to 360°) and the angle of incidence of light rays (0° to 90°). The resulting map has the value of surface brightness for each cell ranging from 0 to 254, depending on the illumination conditions (Jenness 2007). The final hillshade map was derived using illumination parameters 315°/45° and 45°/45°.

Slope map represents the spatial distribution of the terrain slope angle (gradient or steepness) ranging from 0°-90°. As well as the hillshade map the slope map enables the identification of characteristic geomorphological elements such as landslide and erosion boundaries (Ardizzone et al. 2007). The map was derived using ArcGIS 10.8. Spatial Analyst extension Slope which calculates the average slope angle value using a 3 by 3 cell moving window to process the data for the same (central) pixel and the eight surrounding pixels' angle.

Terrain roughness map represents the local variability in the slope angle, terrain elevation, and slope orientation. For the purpose of the landslide and erosion inventory mapping Surface/Area Ratio (SAR) map proposed by Berry (2002)

Fig. 3 Landslides activated in December 2020 in the Istrian flysch area

was used. The map represents the ratio between 2D and 3D terrain maps using the following expression (Berry 2002):

$$\mathrm{SAR} = \frac{c^2}{\cos\left(slp\left(\frac{\pi}{180}\right)\right)} \tag{1}$$

where c is the DTM cell size, slp is the slope map in degrees derived from the LiDAR DTM. The final SAR map was classified into two categories using the quantile classification method.

Stream power index (SPI) map represents the erosive power of the surface water runoff (Moore et al. 1991). For the calculation of the SPI, it is necessary to derive a flow accumulation map and slope angle map. The flow accumulation map represents accumulated flow as the accumulated weight of all cells flowing into each downslope cell in the output raster. The stream power index map was derived using the Raster calculator implemented in ArcGIS 10.8. following the equation proposed by Moore et al. (1991):

$$\mathrm{SPI} = \ln(\text{flow accumulation}) \times \frac{slp}{100} \tag{2}$$

where flow accumulation is the value of each cell on the flow accumulation map and, slp is the slope map in degrees derived from the LiDAR DTM. The final SPI map was classified into four categories using the quantile classification method.

High-resolution digital orthophoto images of 0.5 m resolution for different periods are available via Web Map

Service (WMS) on The Geoportal of the State Geodetic Administration (SGA). Orthophoto images used for interpretation of badland areas and verification of visual interpretated landslides based on LiDAR data is from 2020.

4 Results

Visual identification and mapping of landform features were made on the study area (20 km^2) at a large scale (1:500) to produce detailed landslide and erosion inventory maps for implementation in the spatial planning system. After a preliminary visual interpretation of LiDAR DTM and field verifications, it was concluded that four types of landforms could be mapped, i.e. badlands, gully and combined erosion, unstable slopes, and landslides.

4.1 Badlands

Badlands were identified and mapped starting from the orthophoto images (year 2020, resolution 0.5 m) available for the territory of the Republic of Croatia on the State Geodetic Administration website. The badland areas were identified as landforms with sparse or no vegetation in the surrounding areas. In addition, most of the badlands in the study area are characterised by a sandstone cap, representing an erosive base level. The boundary of the badland-affected slope was additionally mapped in detail on the LiDAR DTM derivatives, i.e. a combination of hillshade map, 65% transparent slope map and 1 m contour map. Differences between orthophoto and LiDAR interpretation were significant (Fig. 4), on some locations, the difference was up to 20 m. The unique ID, type of badlands and the total area covered by the erosion process were associated with each mapped landform. There are three morphological types of badland areas in the study area, following the classification developed by Moretti and Rodolfi (2000). Type "A" develops because of the action of concentrated water runoff and results in sharp and dissected landforms, very dense drainage patterns and deep V-shaped channels. Type "B" is mainly due to superficial slides of soil or regolith on the unweathered substratum, resulting in gentler slopes and less dense drainage patterns, i.e. it represents a natural evaluation of type A badlands due to landform smoothing and vegetation growth (Ciccacci et al. 2008). Type "AB" is an intermediate landform between Type A, where the dominant process is vertical erosion, and Type B, where superficial sliding prevails. Classification of each mapped badlands area was performed based on LiDAR data derivatives because shadows on orthophoto images disabled the possibility of identifying the degree of landform dissection and drainage network density.

4.2 Gully and Combined Erosion

Based on the LiDAR DTM derivatives, the identification and detailed mapping of different types of soil erosion processes is widely used (Vanmaercke et al. 2021). The whole methodology for the identification and mapping of a gully, combined, and sheet erosion using the visual interpretation of high-resolution LiDAR DTM is presented in Đomlija et al. (2019) and Jagodnik et al. (2020). Furthermore, Đomlija et al. (2019) proved that only gully and combined erosion phenomena could be mapped with a high geographical and thematic accuracy using LiDAR data. Sheet erosion, however, can only be indirectly identified on certain LiDAR DTM derivatives based on the recognition of colluvial deposits accumulated at the foot of the eroded slopes. Considering the potential of high-resolution LiDAR data for soil erosion mapping, only gully and combined erosion were mapped in the study area. Gullies with a width of more than 3 m and wider areas affected by combined erosion were mapped by a single polygon (Fig. 5).

Gully erosion was easily recognised due to the elongated or branchy shape of gully channels on hillshade, slope and SPI maps. The SPI approximates the potential locations and magnitude of the gully formation, and higher values of the SPI indicate a high erosional capacity, while lower values indicate ridges. The wider area affected by combined erosion can be precisely delineated based on the disturbed slope surface appearance on the hillshade map, the small-sized drainage networks on the SPI map and the rough surface on the SAR maps. Furthermore, all areas identified as combined erosion are located within the relief concavities, with gullies formed in their central parts. The rough texture of the affected areas (Fig. 5b) distinguishes the soil erosion area from the surroundings, while the highest values are assigned to badland areas. A high level of precision in mapping the gully and combined erosion phenomena was achieved by drawing the separate portions of polygons based on the visual analysis of different LiDAR DTM derivatives and subsequent merging of drawn lines into a unique polygon while mapping.

4.3 Unstable Slopes

Unstable slopes were categorised as areas with different types of landslide mechanisms on the artificial slopes (Fig. 6). During intense rainfall events, there are a large number of slope movement processes on the artificial slopes along the roads, including superficial sliding, falling and toppling. Examples of slope movements on unstable slopes along the roads after extreme rainfall events in December 2020 are shown in Fig. 2c, d. Furthermore, most of these slope instabilities have a small volume that can be removed quickly

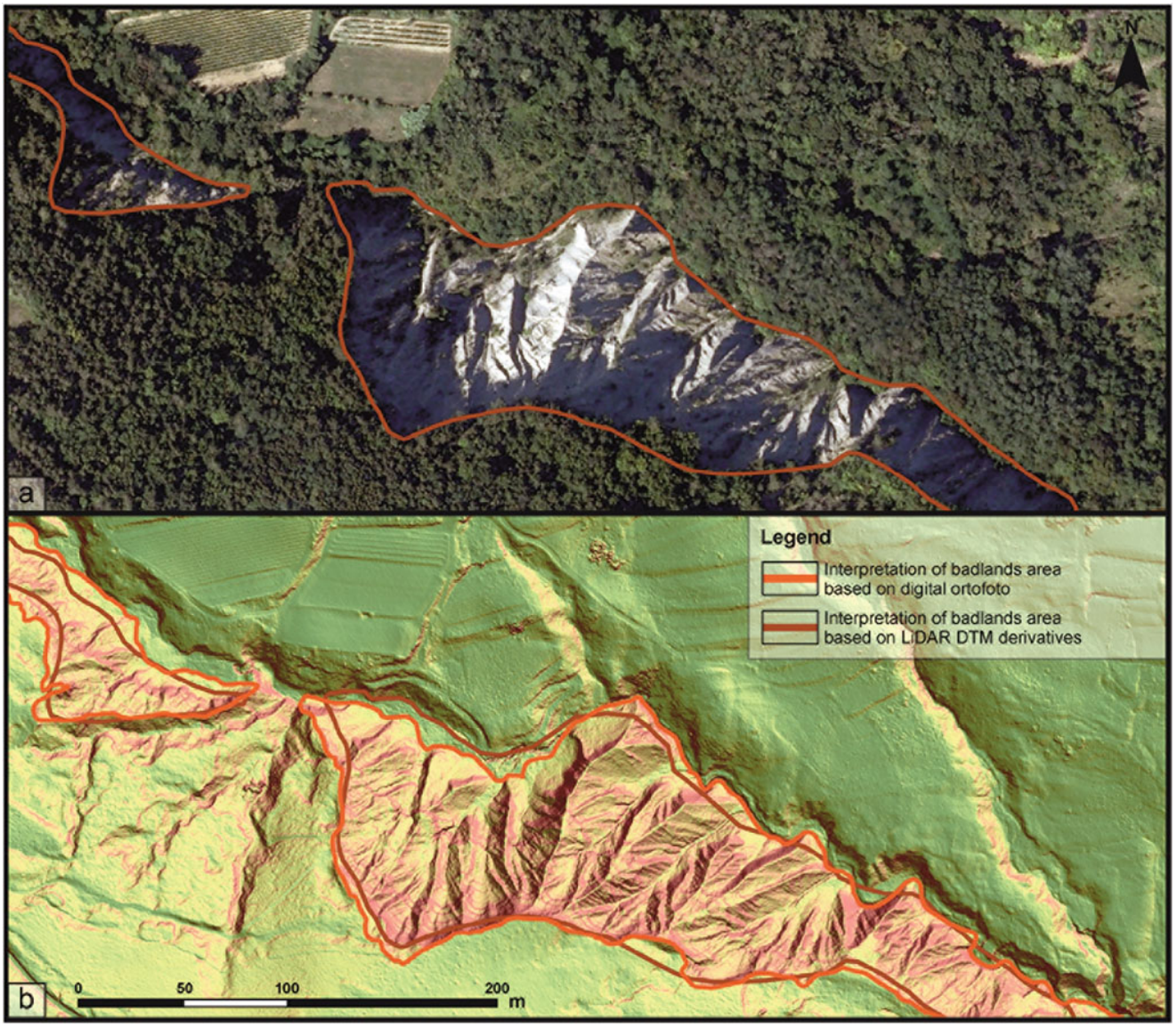

Fig. 4 Badland inventory mapping: (**a**) interpretation based on digital orthophoto map; (**b**) interpretation based on LiDAR DTM derivatives

after initiation during emergency road maintenance. Considering the removal of colluvium from the roads, most of the landslide phenomena on artificial slopes will not be visible on LiDAR DTM derivatives unless laser scanning is recorded immediately after the landslide event. Furthermore, if visible on the LiDAR DTM derivatives, the exact landslide boundaries could not be mapped due to the coalescence of superficial landslides or poor contrast between affected and unaffected areas due to the intense erosion.

4.4 Landslides

Landslide identification on the LIDAR DTM morphometric derivatives (Fig. 7) is based on recognising landslide features (e.g., concave main scarps, hummocky landslide bodies and convex landslide toes). A digital orthophoto map from 2020 (Fig. 7a) was used during landslide identification to check the morphological forms along roads and houses, such as artificial fills and cuts, which can have a similar appearance to landslides on DTM derivatives. Each mapped landslide polygon was assigned with the landslide type and certainty of

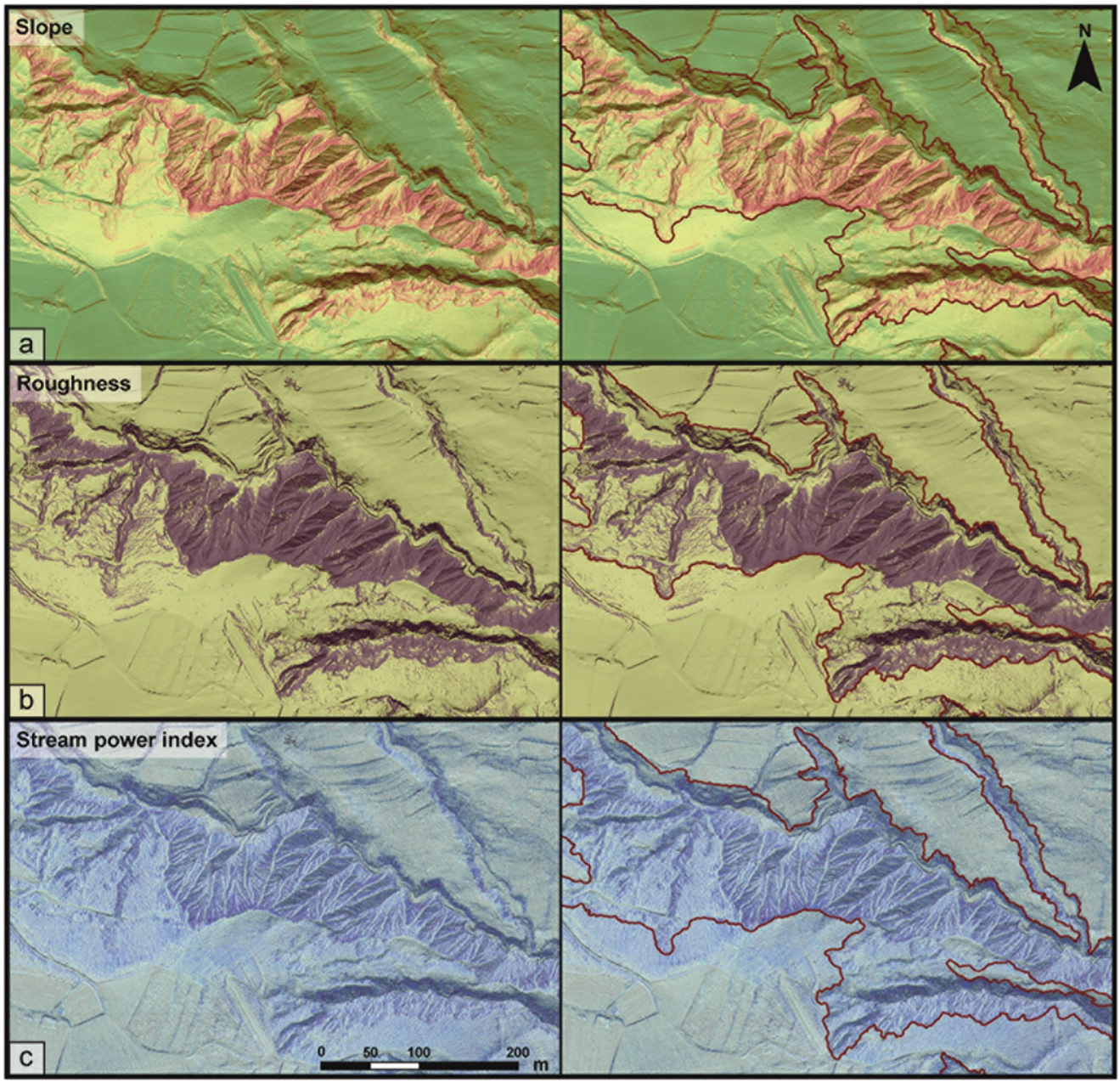

Fig. 5 Gully and combined erosion inventory mapping: (**a**) interpretation on transparent slope map over hillshade map; (**b**) interpretation on transparent SAR map; (**c**) interpretation on transparent SPI map

mapping, e.g., accuracy and precision. The certainty of landslide identification was expressed as 'high certainty' where the landslide parts and morphology are clearly visible and easy to identify and 'low certainty' where the landslide parts are not clearly visible or are missing, and the landslide morphology is unclear, i.e., landslide identification is not with high reliability. The precision of mapping was expressed as 'high precision' where the landslide boundaries (crown, flanks, and toe) are clearly visible, and landslide mapping can be performed with high spatial accuracy; and 'low precision' where the landslide boundaries are smooth and unclear, i.e. where landslides are assumed based on a zone of depression/ accumulation and landslide boundary mapping is with low spatial accuracy.

At the beginning of the landslide inventory mapping process, Lukačić et al. 2022 conducted research in which seven landslide researchers interpreted landslides on LiDAR data on a small part of the study area (0.3 km^2). Landslide researchers had different levels of LiDAR mapping experience and knowledge of the study area. The results were

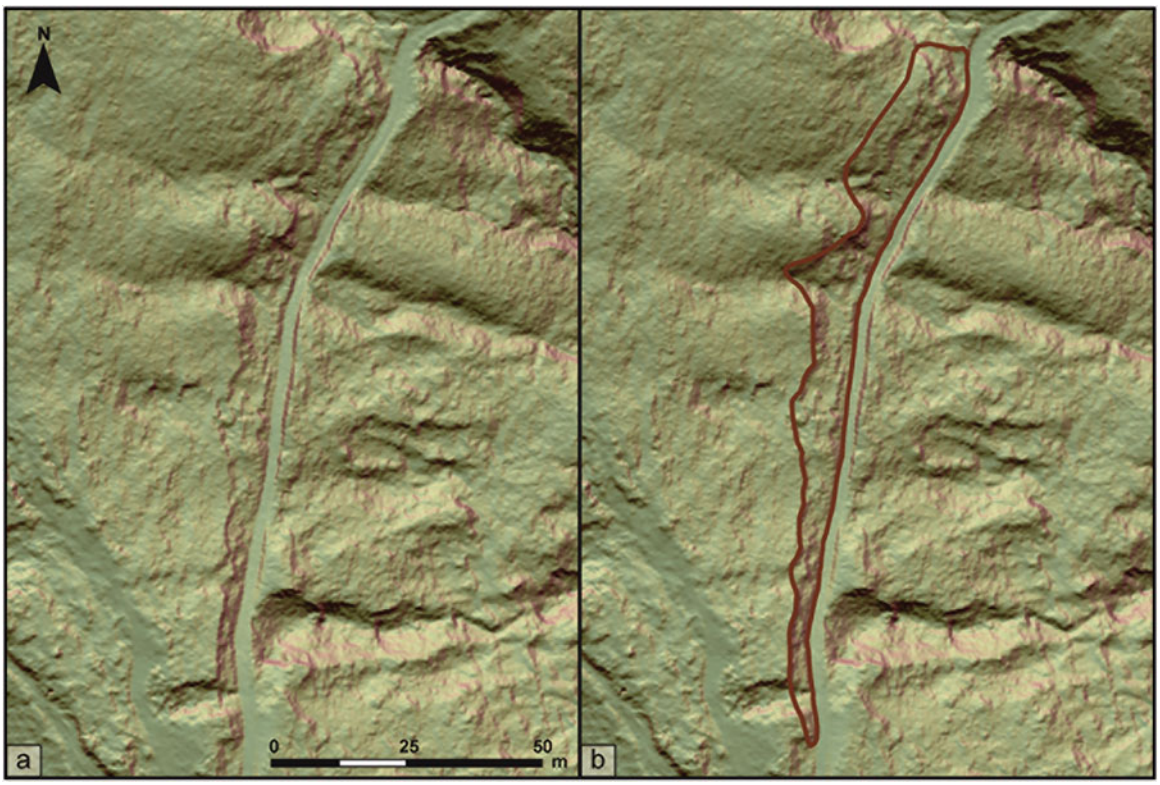

Fig. 6 Interpretation of unstable slopes based on LiDAR DTM derivatives, i.e. hillshade and slope map

significant differences in LiDAR interpretation among landslide experts (Fig. 8), which did not depend on previous knowledge of the study area, but on the experience and skill of interpreting LiDAR data. The final matching of landslide inventories produced by eight experts was less than 30%. Furthermore, obtained results show that the same pilot area must be mapped multiple times to accomplish a high-accuracy landslide inventory map (Lukačić et al. 2022). Landslide inventory mapping was back and forth between LiDAR interpretation in the cabinet and field verification because it was necessary to calibrate mapping skills in the Istrian flysch terrains. During the field verification, the number of unconfirmed and confirmed landslides with modified landslide boundaries indicated that the common recommendation about verifying 10% of landslides in the landslide inventory (Galli et al. 2008) is not sufficient in the pilot area with complex geology settings and multi-hazard processes. Therefore, to ensure the accuracy of the landslide inventory map, it is necessary to increase the ratio of field-verified and confirmed landslides related to the total number of landslides in an inventory map (Lukačić et al. 2022).

The biggest challenge was landslide identification and mapping in the affected by gully and combined erosion and badland areas (Fig. 9). Every inch of erosion-affected area is disturbed due to the slope processes, and because of that, it was very hard to distinguish sliding from erosion processes on LIDAR DTM derivatives. Furthermore, due to the higher certainty of the final landslide inventory, only landslides with clearly visible depression and accumulation zones were mapped in soil erosion areas.

5 Application in the Spatial Planning System

Detailed landslide and soil erosion inventory maps (M 1:500) of the study area (20 km^2) in Istrian flysch-type rocks consist of four types of landforms, i.e. badlands, gully and combined erosion, unstable slopes, and landslides (Fig. 10a). Potential users of landslide and soil erosion inventory data and information differ widely (Wold et al. 1989), although they can be divided in four general categories are (1) scientists and engineers who use the information directly; (2) planners and decision-makers who consider landslide hazards among other land-use and development criteria; (3) developers, builders, and financial and insuring organisations; and (4) interested citizens, educators, and others with little or no technical experience. The main purpose of derived inventories is an implementation in the spatial planning system and application in further large-scale landslide

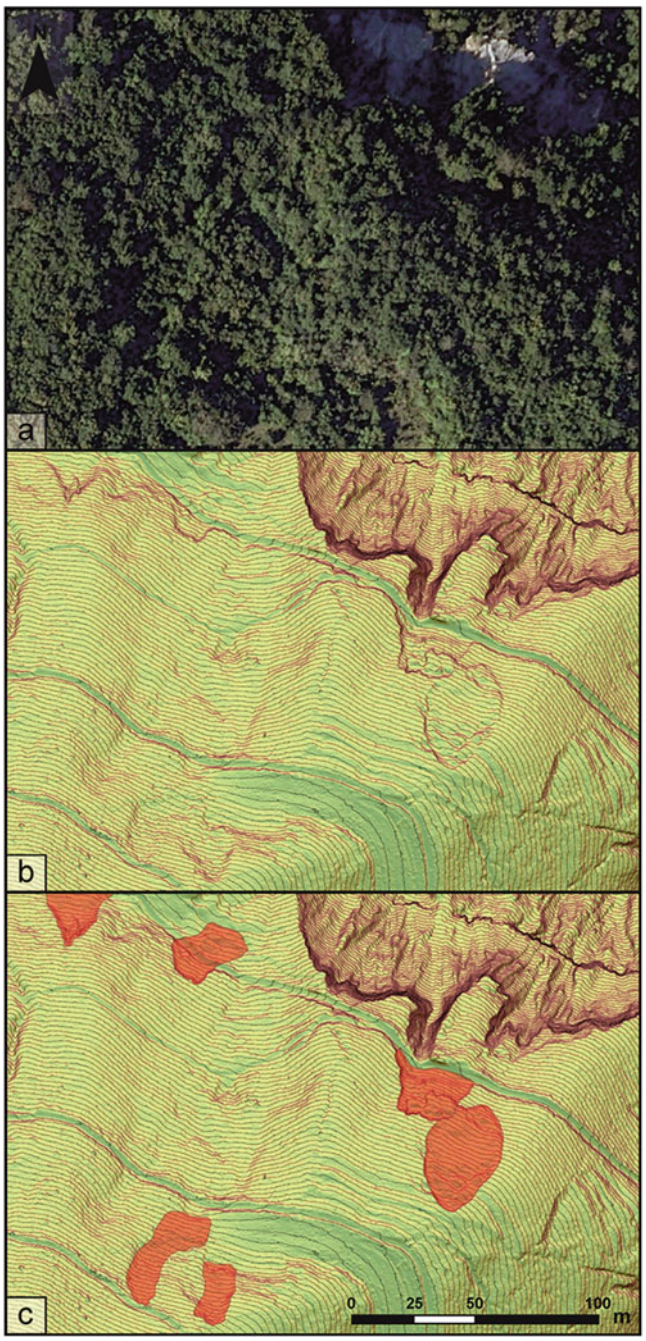

Fig. 7 Landslide inventory mapping based on LiDAR DTM derivatives, i.e. hillshade, slope and contour map

susceptibility assessment. Inventory maps could be used to manage landslide and soil erosion hazards in populated areas by excluding development or by proposing requirements for minimum on-site geotechnical investigations in the frame of slope stability assessment before constructing in areas endangered by registered landslides or soil erosion processes. The approach of avoiding erosion and landslide-prone areas is rarely feasible, and it is neither possible nor desirable to proscribe development in any urbanised area. However, the USGS proposal for a national landslide hazards mitigation strategy (Spiker and Gori 2000) summarises the major mitigation approaches, including: (1) restricting development in landslide-prone areas; (2) enforcing codes for excavation, construction, and grading; (3) engineering for slope stability; (4) deploying monitoring and warning systems; and (5) providing landslide insurance.

Based on the USGS strategy, we defined two zones with measures applicable to spatial plans at the local level. The first zone was determined based on the extent of badland areas and includes restricting development, i.e., a ban on expanding construction areas in the badlands areas. The second zone includes areas affected by gully and combined erosion and shallow landslides, in which a spatial plan measure enforces codes for excavation and construction. In Fig. 10b it is shown an example of zoning based on the close-up extent of derived landslide and erosional landslide inventory.

Regardless of restricting development in badland areas, several badlands areas in central Istria have a large potential as geoturisam sites because of their often great esthetical value or picturesque nature. Furthermore, if well managed, gullies can become productive and biodiverse hotspots that play a key role as ecological corridors (Romero-Díaz et al. 2019).

6 Discussion and Conclusion

The findings of this study inform which LiDAR-based morphometric maps are the most effective in providing geomorphological clues and which landslide and erosion processes can be identified and mapped with high geographical and thematic accuracy using high-resolution remote sensing data. Furthermore, the proposed methodology for accurately identifying and detailed inventory mapping of badlands, gully and combined erosion, unstable slopes and landslides on a large scale can be used as guidance in future studies in areas with similar geological settings and degree of urbanisation.

Although the visual interpretation of LiDAR DTM derivatives and manual mapping of landslide and soil erosion landforms is time-consuming, it is considered that the same quality of the results could not be obtained by using the conventional geomorphological mapping methods, given the specific topographic characteristics of the studied area, i.e. inaccessible and densely vegetated area. Furthermore, the possibilities of using the automated landslide and soil erosion mapping methods are limited regarding the numerous artificial traces on the affected surface that are not topographic signatures of geomorphological processes. However, the possibilities of visual recognition of landslide and soil erosion phenomena, and thus the quality of the mapping results,

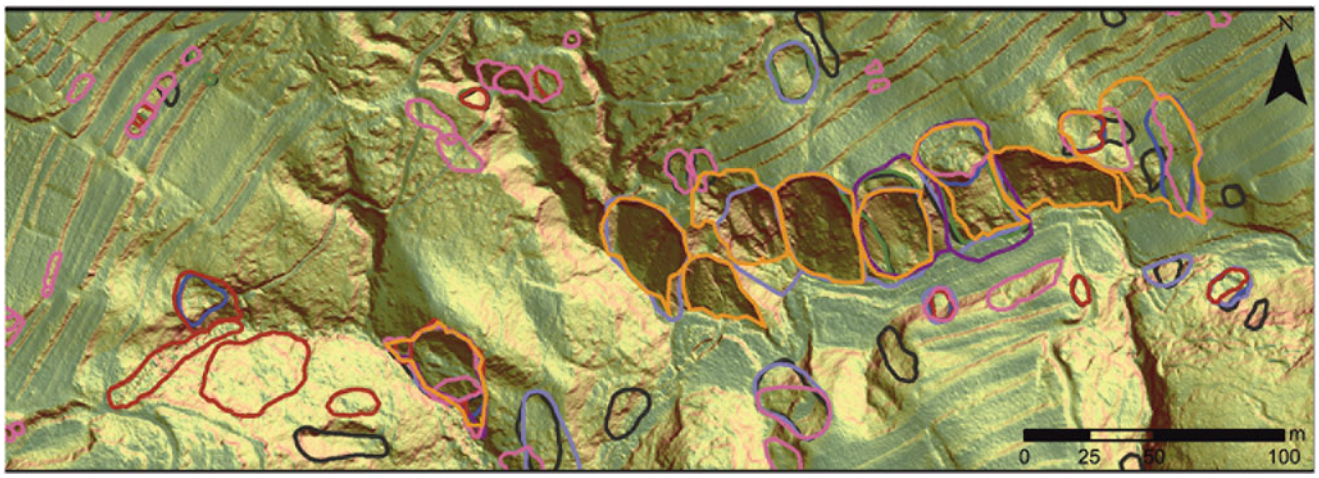

Fig. 8 Result of visual landslide interpretation carried out by seven landslide experts with different LiDAR mapping experience and knowledge of the study area

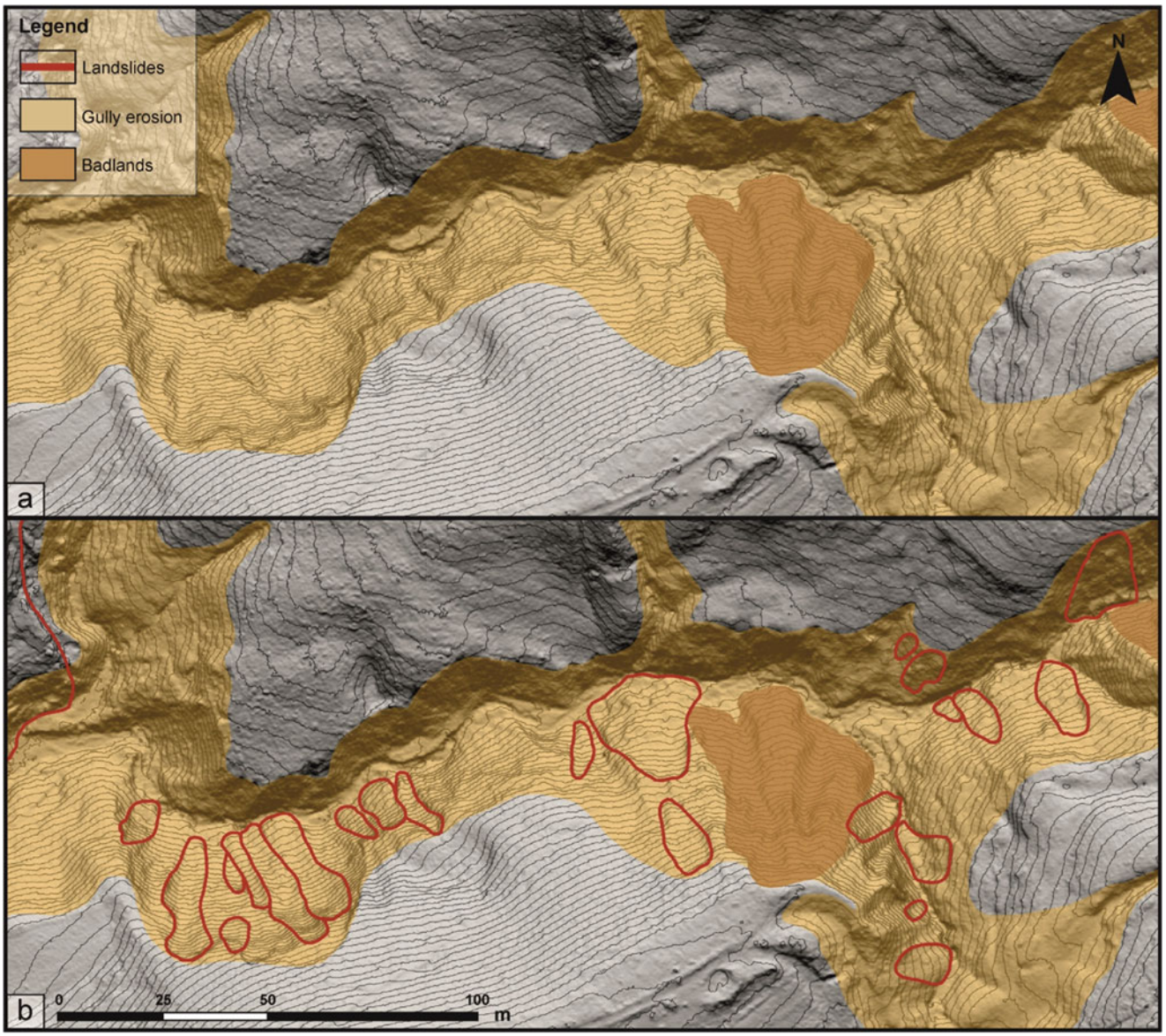

Fig. 9 Example of landslide mapping in areas affected by gully and combined erosion on LiDAR DTM derivatives

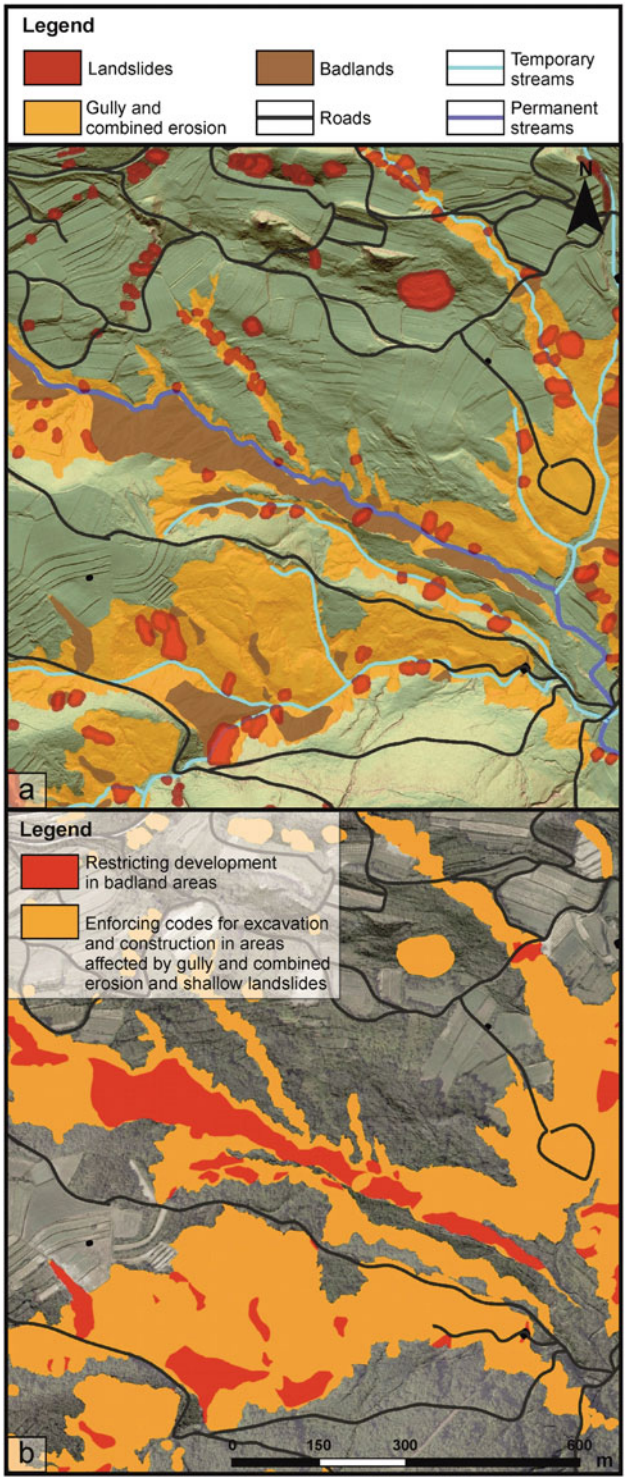

Fig. 10 Application of landslide and soil erosion inventory maps in the spatial planning system: (**a**) close-up extent of final inventory map; (**b**) derived map with defined spatial plan measures

strongly depends on the spatial resolution of used remote sensing data and researcher experience in interpreting LiDAR DTM derivatives because accurate and precise delineating of the landforms can be complex mapping challenge. By analysing inventory completeness and size of mapped landforms, we can estimate the quality of LiDAR-derived inventory maps (Bernat Gazibara et al. 2019a, b). Therefore, the LiDAR-base landslide and erosion inventory maps prepared using the proposed mapping procedure are usually considered sustainably complete for future applications, such as landslide and erosion susceptibility assessment or estimating temporal changes in gully erosion. Furthermore, a detailed inventory map derived based on visual interpretation of high-resolution remote sensing data, combined with landslide and soil erosion susceptibility maps, provides appropriately detailed input data for defining measures in local-level spatial plans. Derived inventory maps can be used to manage landslide and soil erosion hazards in populated areas by restricting development in badland areas or enforcing codes for excavation and construction in areas endangered by registered landslides or gully and combined erosion processes.

Acknowledgments This research has been fully supported by the Croatian Science Foundation under the project methodology development for landslide susceptibility assessment for and use planning based on LiDAR technology, LandSlidePlan (HRZZ IP-2019-04-9900, HRZZ DOK-2020-01-2432).

References

Arbanas Ž, Benac Č, Jardas B (1999) Small landslides on the flysch of Istria. In: Proceedings of the 3rd conference of Slovenian geotechnical society. SloGeD, Ljubljana, pp 81–88

Arbanas Ž, Benac Č, Jurak V (2006) Causes of debris flow formation in flysch area of North Istria, Croatia. In: Monitoring, simulation, prevention and remediation of dense and debris flows. WIT Press, Rhodes, pp 283–292

Arbanas Ž, Mihalić S, Grošić M et al (2010) Brus Landslide, translational block sliding in flysch rock mass. In: Zhao J, Labiouse V, Dudt J-P, Mathier J-F (eds) Proceedings of the European rock mechanics symposium (Eurock 2010). CRC Press/Balkema, Laussane, London, pp 635–638

Arbanas Ž, Jovančević SD, Vivoda M, Arbanas SM (2014) Study of landslides in flysch deposits of North Istria, Croatia: landslide data collection and recent landslide occurrences. In: Sassa K, Canuti P, Yin Y (eds) Landslide science for a safer Geoenvironment. Springer International Publishing, Cham, pp 89–94

Ardizzone F, Cardinali M, Galli M et al (2007) Identification and mapping of recent rainfall-induced landslides using elevation data collected by airborne Lidar. Nat Hazards Earth Syst Sci 7:637–650. https://doi.org/10.5194/nhess-7-637-2007

Bergant S, Tišljar J, Šparica M (2003) Eocene Carbonates and Flysch Deposits of the Pazin Basin. In: Vlahović I, Tišljar J (eds) Field trip guidebook: evolution of depositional environments from the palaeozoic to the quaternary in the Karst Dinarides and the Pannonian Basin. Institut za geološka istraživanja, Opatija, Zagreb, pp 57–64

Bernat Gazibara S, Krkač M, Mihalić Arbanas S (2019a) Verification of historical landslide inventory maps for the Podsljeme area in the City of Zagreb using LiDAR-based landslide inventory. Rudarsko-geološko-naftni zbornik 34(1):45–58. https://doi.org/10.17794/rgn.2019.1.5

Bernat Gazibara S, Krkač M, Mihalić Arbanas S (2019b) Landslide inventory mapping using LiDAR data in the City of Zagreb (Croatia). J Maps 15:773–779. https://doi.org/10.1080/17445647.2019.1671906

Bernat Gazibara S, Mihalić Arbanas S, Sinčić M, et al (2022) LandSlidePlan -scientific research project on landslide susceptibility assessment in large scale. In: Proceedings of the 5th regional symposium on landslides in Adriatic-Balkan region. Faculty of Civil Engineering, University of Rijeka and Faculty of mining, geology and petroleum engineering, University of Zagreb, Rijeka, Croatia

Berry JK (2002) Use surface area for realistic calculations. Geoworld 15(9):1–20

Ciccacci S, Galiano M, Roma MA, Salvatore MC (2008) Morphological analysis and erosion rate evaluation in badlands of Radicofani area (southern Tuscany — Italy). Catena 74:87–97. https://doi.org/10.1016/j.catena.2008.03.012

Đomlija P, Bernat Gazibara S, Arbanas Ž, Mihalić Arbanas S (2019) Identification and mapping of soil erosion processes using the visual interpretation of LiDAR imagery. IJGI 8:438. https://doi.org/10.3390/ijgi8100438

Dugonjić Jovančević S, Arbanas Ž (2012) Recent landslides on the Istrian peninsula, Croatia. Nat Hazards 62:1323–1338. https://doi.org/10.1007/s11069-012-0150-4

Eeckhaut MVD, Poesen J, Verstraeten G et al (2007) Use of LIDAR-derived images for mapping old landslides under forest. Earth Surf Process Landforms 32:754–769. https://doi.org/10.1002/esp.1417

Galli M, Ardizzone F, Cardinali M et al (2008) Comparing landslide inventory maps. Geomorphology 94:268–289. https://doi.org/10.1016/j.geomorph.2006.09.023

Gulam V, Pollak D, Podolszki L (2014) The analysis of the flysch badlands inventory in Central Istria, Croatia. Geol Cro 67:1–15. https://doi.org/10.4154/GC.2014.01

Guzzetti F, Cardinali M, Reichenbach P, Carrara A (2000) Comparing landslide maps: a case study in the upper Tiber River basin, Central Italy. Environ Manag 25:247–263. https://doi.org/10.1007/s002679910020

Guzzetti F, Mondini AC, Cardinali M et al (2012) Landslide inventory maps: new tools for an old problem. Earth Sci Rev 112:42–66. https://doi.org/10.1016/j.earscirev.2012.02.001

Jagodnik P, Bernat Gazibara S, Arbanas Ž, Mihalić Arbanas S (2020) Engineering geological mapping using airborne LiDAR datasets – an example from the Vinodol Valley, Croatia. J Maps 16:855–866. https://doi.org/10.1080/17445647.2020.1831980

Jenness J (2007) Some thoughts on analyzing topographic habitat characteristics

Lukačić H, Bernat Gazibara S, Sinčić M, et al (2022) Influence of expert knowledge on completeness and accuracy of landslide inventory maps – example from Istria, Croatia. In: Proceedings of the 5th regional symposium on landslides in Adriatic-Balkan region. Faculty of Civil Engineering, University of Rijeka and Faculty of mining, geology and petroleum engineering, University of Zagreb, Rijeka, Croatia

Mihalić S, Arbanas Ž, Krkač M, Dugonjić S (2011) Analysis of sliding hazard in wider area of Brus landslide. In: Anagnostopoulos A, Pachakis M, Tsatsanifos C (eds) Proccedings of the XV European conference on soil mechanics and geotechnical engineering. IOS Press, Atena, Amsterdam, pp 1377–1382

Moore ID, Grayson RB, Ladson AR (1991) Digital terrain modelling: a review of hydrological, geomorphological, and biological applications. Hydrol Process 5:3–30. https://doi.org/10.1002/hyp.3360050103

Moretti S, Rodolfi G (2000) A typical "calanchi" landscape on the eastern Apennine margin (Atri, Central Italy): geomorphological features and evolution. Catena 40:217–228. https://doi.org/10.1016/S0341-8162(99)00086-7

Pleničar M, Polšak A, Šikić D (1969) Basic geological map, scale 1: 100,000, Trst, Sheet 33–88

Romero-Díaz A, Díaz-Pereira E, De Vente J (2019) Ecosystem services provision by gully control. A review. CIG 45:333–366. https://doi.org/10.18172/cig.3552

Sinčić M, Bernat Gazibara S, Krkač M et al (2022) The use of high-resolution remote sensing data in preparation of input data for large-scale landslide Hazard assessments. Land 11:1360. https://doi.org/10.3390/land11081360

Spiker EC, Gori PL (2000) National Landslide Hazards Mitigation Strategy: a framework for loss reduction. U.S. Dept. of the Interior, U.S. Geological Survey

UN (2015) Sendai framework for disaster risk reduction 2015–2030. UN, Geneva

van Westen CJ, van Asch TWJ, Soeters R (2006) Landslide hazard and risk zonation—why is it still so difficult? Bull Eng Geol Environ 65:167–184. https://doi.org/10.1007/s10064-005-0023-0

Vanmaercke M, Panagos P, Vanwalleghem T et al (2021) Measuring, modelling and managing gully erosion at large scales: a state of the art. Earth Sci Rev 218:103637. https://doi.org/10.1016/j.earscirev.2021.103637

Vivoda Prodan M, Arbanas Ž (2016) Weathering influence on properties of siltstones from Istria, Croatia. Adv Mater Sci Eng 2016:1–15. https://doi.org/10.1155/2016/3073202

Wold RL, Jochim CL, Agency USFEM, Survey CG (1989) Landslide loss reduction: a guide for state and local government planning. Federal Emergency Management Agency, Washington, DC

Part V

Technical Notes and Case Studies

Landslide Monitoring with RADARSAT Constellation Mission InSAR, RPAS-Derived Point-Clouds and RTK-GNSS Time-Series in the Thompson River Valley, British Columbia, Canada

David Huntley, Drew Rotheram-Clarke, Roger MacLeod, Robert Cocking, Jamel Joseph, and Philip LeSueur

Abstract

In this paper, we evaluate the effectiveness of four land-deformation measurement techniques for monitoring slow-moving landslides along a high-risk section of the national railway corridor traversing the Thompson River valley, British Columbia, Canada. The geomorphically active North Slide acts as an ideal field laboratory for testing and evaluating novel monitoring techniques and methods. We compare differential processing of Structure from Motion (SfM) products such as point-cloud elevation models and orthophotos derived from Remotely Piloted Aircraft Systems (RPAS), along with satellite based Interferometric Synthetic Aperture Radar (InSAR) deformation measurements derived from RADARSAT Constellation Mission (RCM). These results are ground-truthed with periodic real-time kinematic (RTK) global navigation satellite system (GNSS) measurements. We evaluate point-cloud comparison techniques, including the multi-scale model-to-model cloud comparison (M3C2) algorithm and digital ortho image correlation techniques. Multi-temporal RCM InSAR deformation measurements are processed using a semi-automated processing system for interferogram generation and unwrapping. Manual processing of small baseline subsets (SBAS) leads to the recovery of 1-dimensional line-of-sight (LoS) and 2-dimensional deformation measurements. Lastly, we discuss the strengths and limitations of these techniques, considerations for interpreting their outputs, and considerations for direct comparisons between InSAR, RPAS and RTK-GNSS deformation measurements.

Keywords

Landslides · Railway infrastructure · Remote piloted aircraft system · Satellite synthetic aperture radar interferometry · Real-time kinematic global navigation satellite systems

1 Introduction

The Thompson River valley in south-central British Columbia (BC), Canada (Fig. 1a) serves as a field laboratory for testing and comparing the reliability and effectiveness of different static, dynamic, and real-time landslide monitoring technologies along a strategically important section of the national railway network (Huntley et al. 2017; Huntley et al. 2019a, b; Huntley et al. 2021a). In this paper, we present research at the North Slide (Fig. 1b) undertaken as part of International Consortium on Landslides (ICL) International Programme on Landslides (IPL) Project 202. The economic importance of the Thompson valley transportation corridor, along with the need to understand and manage the safety risk related to the landslides that threaten the national railway network, mandate the North Slide (Fig. 1b) a research priority for Natural Resources Canada (NRCAN) and the Geological Survey of Canada (GSC). Following the approach outlined in Huntley et al. (Huntley et al. 2022a, b), here, we compare differential processing of Structure from Motion (SfM) products, such as point-cloud digital elevation models (DEM) and orthophotos derived from Remotely Piloted Aircraft Systems (RPAS), with satellite based Interferometric Synthetic Aperture Radar (InSAR) deformation measurements derived from RADARSAT Constellation Mission (RCM). These results are ground-truthed with periodic real-time kinematic (RTK) global navigation satellite system (GNSS) measurements (cf. Huntley et al. 2022b).

D. Huntley (✉) · D. Rotheram-Clarke · R. Cocking · J. Joseph · P. LeSueur
Geological Survey of Canada, Vancouver, BC, Canada
e-mail: david.huntley@nrcan-rncan.gc.ca; drew.rotheram-clarke@nrcan-rncan.gc.ca; robert.cocking@nrcan-rncan.gc.ca; jamel.joseph@nrcan-rncan.gc.ca; philip.lesueur@nrcan-rncan.gc.ca

R. MacLeod
Geological Survey of Canada, Sidney, BC, Canada
e-mail: roger.macleod@nrcan-rncan.gc.ca

I. Alcántara-Ayala et al. (eds.), *Progress in Landslide Research and Technology, Volume 2 Issue 1, 2023*,
Progress in Landslide Research and Technology, https://doi.org/10.1007/978-3-031-39012-8_19

RPAS, satellite InSAR, and other geospatial and temporal datasets will help stakeholders develop a more resilient railway national transportation network able to meet Canada's future socioeconomic needs, while ensuring protection of the environment and resource-based communities from natural disasters related to extreme weather events and climate change.

2 Study Site: North Slide

The North Slide is located approximately 6 km south of Ashcroft on the east bank of the Thompson River (Fig. 1a). Around 9 pm on October 14, 1880, an ancient landslide (Fig. 1b) reactivated as a sudden onset, rapid retrogressive rotational-translational flow-slide (Stanton 1898; Evans 1984; Clague and Evans 2003). In common with other nineteenth Century landslides in the valley, the slope failed rapidly after months of intensive summer irrigation and while the toe slope was being excavated during railway construction.

Exposures across the slide main body and head scarp reveal glaciolacustrine sandy silt and sandy gravel outwash unconformably overlying silty till and glaciolacustrine silt and clay (Fig. 1c). A toe slope bulge on the river floodplain exposes back-tilted rhythmically interbedded layers of soft brown clay, stiff, highly plastic dark grey clay, and grey silt overlying bedrock (Huntley et al. 2021b). Borehole piezometer and inclinometer monitoring reveal preferential shearing of soft brown clay beds, with rupture zones at 264 and 269 m above sea level (asl): equivalent to 25 m and 30 m below the CP rail grade, and 5 m to 10 m below the riverbed. Piezometer data indicate hydrostatic conditions at depth below the track, and an upward groundwater gradient in the landslide toe (Porter et al. 2002).

2.1 Landslide Hazards and Railway Infrastructure

Thompson River is a major control on landslide form and function (Eshraghian et al. 2007; Eshraghian et al. 2008). Riverbed incision is contributing to changes in toe slope geometry, with 5 m-deep scour pools likely intersecting rupture zones. Air photos from 1928 and 1997 suggest historical channel-bank erosion rates averaging 70 cm $yr.^{-1}$ (Porter et al. 2002). Reactivation of the North Slide toe slope began in October 2000 along a 150 m section of riverbank (the "Solar Slump"), with 5 cm to 15 cm of settlement at the CP grade. Peak observed surface movement rates were approximately 15 cm $yr.^{-1}$, with an average rate of 3 cm $yr.^{-1}$ (Porter et al. 2002). Displacement along the shallow rupture surface ranged from 5 cm to 11 cm $yr.^{-1}$; while on the deeper slide surface, borehole inclinometers recorded a movement rate of 3 cm to 4.5 cm $yr.^{-1}$ (Porter et al. 2002). RADARSAT 2 (RS2) and SENTINEL-1 (S1) persistent scatterer interferometry showed the slide toe remained active between 2013 and 2015, with displacement of coherent targets indicating line-of-sight (LoS) deformation rates in excess of 5 cm $yr.^{-1}$ (Huntley et al. 2017; Journault et al. 2018; Huntley et al. 2021b).

Instrumental and operational measures are in place to reduce the risk of train derailment due to landslide activity. Mercury switch tip-over posts linked to rail signals were installed in 2001 to detect ground displacement. Small, incremental surface displacements contribute to minor track misalignment requiring continuous remote monitoring and short-term (seasonal) reorganization of train schedules to allow ground crews to safely add ballast and adjust the track positions. By contrast, infrequent, rapid, large and widespread ground movements are a concern for railway companies, government agencies, and local communities because they cause major track misalignment, train derailment, and considerable local environmental damage. Substantial channel and slope remediation following a major retrogressive failure will require costly reorganization of transportation and shipping schedules, leading to national socioeconomic losses.

3 Methods and Results

3.1 RPAS Surveying

Periodic RPAS surveys were flown using a DJI Phantom 4. This RPAS (Fig. 2) was equipped with a 12.4 M pixel FC330 outputting 3000 × 4000-pixel images (Huntley et al. 2022b). These images were geotagged by the onboard GPS. However, since no real-time or post-processing corrections were applied to the GPS tags, manual RTK-GNSS ground control was required.

Digital optical imagery was processed using Pix4D to produce optical orthophotos at 2 cm ground sample distance (GSD), an elevation point-cloud, and a digital surface model (DSM) with a 5 cm ground sample distance. To mitigate seasonal effects while allowing movement to accumulate to detectable levels, two surveys separated by approximately two years (September 19, 2019, and September 28, 2021) were undertaken. Two post-processing techniques for calculating deformation from these datasets were evaluated: M3C2, and a combination of digital image correlation and DSM of difference.

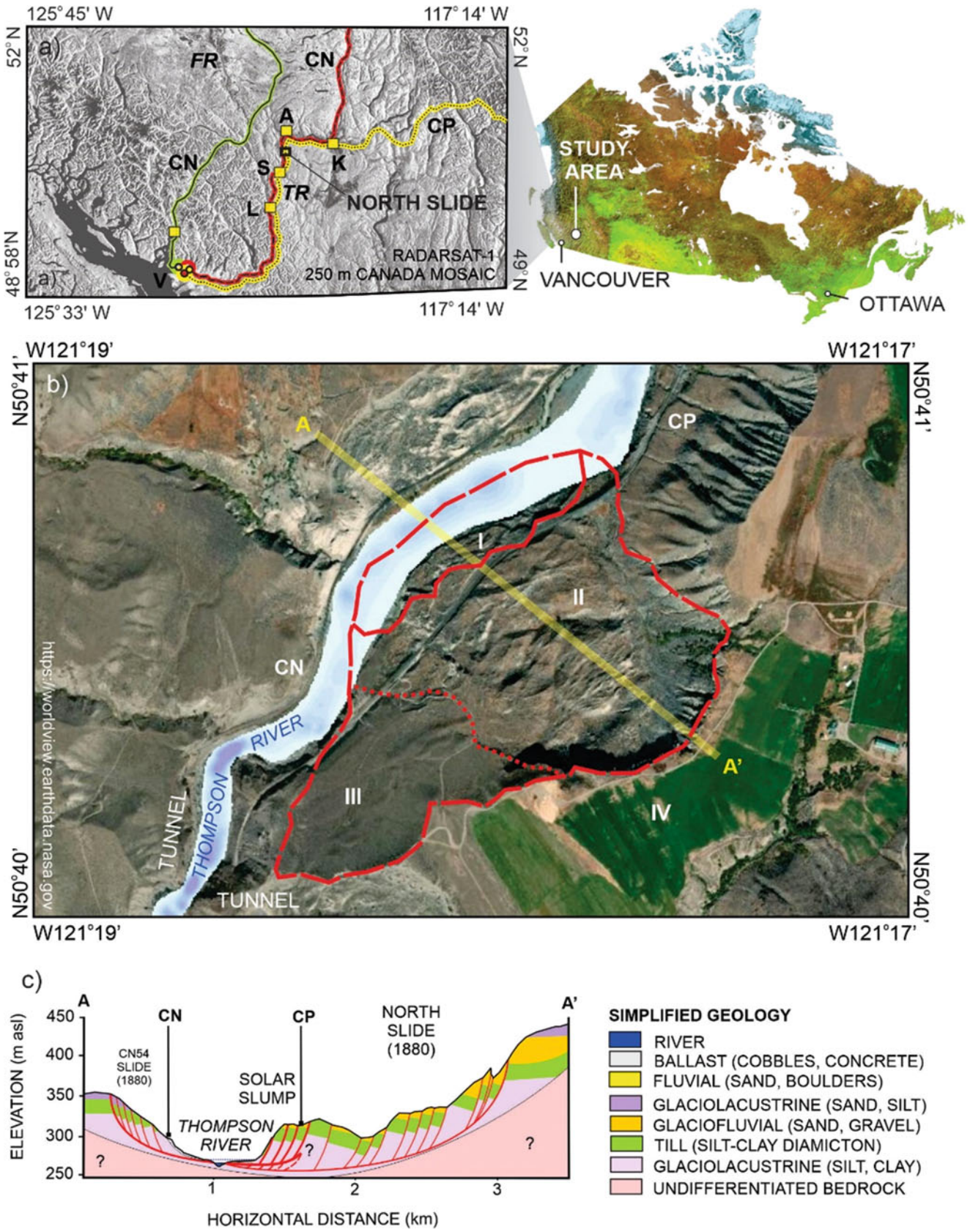

Fig. 1 Location of the ICL-IPL Project 202 study area: (**a**) southwestern British Columbia showing major railway corridors. *CN* Canadian National Railways, *CP* Canadian Pacific Railways, *A* Ashcroft, *K* Kamloops, *L* Lytton, *S* Spences Bridge, *V* Vancouver, *FR* Fraser River, *TR* Thompson River. (**b**) The North Slide showing geomorphic extent in red. I—active slide toe (0.08 km^2)—the "Solar Slump"; II—

Fig. 2 DJI Phantom 4 RPAS (NRCAN Photo 2020–845)

3.2 M3C2 Point Cloud Comparison

The Multiscale Model to Model Cloud Comparison (M3C2) algorithm was introduced to fill a perceived gap in time-series point-cloud comparison (Lague et al. 2013). This algorithm had three relevant characteristics: (a) it operated directly on point-clouds without the need to grid or mesh one, or both point-clouds; (b) it calculated displacement along a vector normal to the local surface topography; and (c) it estimated confidence intervals for these measurements.

The algorithm functioned with two steps. A surface normal was first calculated at each point by considering a neighbourhood of surrounding points controlled by user-defined parameters. Secondly, two neighbourhoods surrounding each point, often a subset of the points, were used to define the surface normal and calculate the average distance between these points along the surface normal vector.

This algorithm was well suited for complex topographic situations such as steep or rough surfaces. Simpler methods like DEM differencing cannot accurately capture complex deformation in steep and/or rough topographic settings such as rock falls, or toppling of vertical and sub-vertical rock faces. A fundamental assumption of the M3C2 algorithm was that deformation occurs on a vector normal to the ground surface. This may be reasonable for measurements of sediment erosion and deposition. However, the algorithm may dramatically underestimate displacement where ground movement is parallel to the surface (Fig. 3), a situation common in earthflows and translational slides (Fig. 4; Rotheram-Clarke et al. 2022).

3.3 Digital Image Correlation

Photogrammetric processing and 3D reconstruction was completed using Micmac, a free and open-source software package distributed by The National Institute of Geographic and Forest Information (IGN) (Rupnik et al. 2017). The digital image correlation functions in Micmac were used to calculate subpixel offsets between precisely co-registered imagery (cf. Rosu et al. 2015; Galland et al. 2016). This was tested on both RPAS orthophotos and hill-shaded Digital Surface Models (DSMs) from the SfM results. Significantly, it was determined that hill-shaded DSMs produced less noisy outputs. This is likely a result of uniform input images containing few differences in dynamic range and surface texture due to earth materials and vegetation cover (Rotheram-Clarke et al. 2022). Combining these results with a simple DEM difference image was the only method tested capable of recovering the full 3D deformation vector with wide coverage (Fig. 5).

3.4 RTK-GNSS Surveying

Campaign RTK surveys were completed using a Spectra SP80 GNSS system. At a designated survey base station approximately 1 km south of the study site, a piece of rebar approximately 60 cm in length was driven into stable ground and marked precisely with a 2 mm punch. This site was occupied for 24 hours and the GNSS observations processed using the NRCAN PPP service (cf. Huntley et al. 2021a). Subsequent surveys reoccupied this known reference point. Large, heavy boulders embedded in the landslide blocks were marked with a cross pattern typical of airphoto ground control point (GCP) surveys, using orange survey paint that was visible in RPAS imagery (Fig. 6). The centres of these patterns were scored with a rock drill to ensure exact repeat occupation. These RTK-GNSS measurements constrained the RPAS SfM measurements, and benchmarked deformation measurements derived from RPAS and InSAR measurements.

Fig. 1 (Continued) inactive (1880) slide main body and headscarp (0.55 km^2); III—inactive (early Holocene) slide body (0.37 km^2); IV—stable postglacial slopes and terraces. (**c**) Cross-section A to A' across the North Slide modelled as a rotational-translational landslide in glacial deposits confined to a bedrock paleochannel or basin (after Huntley et al. 2021b)

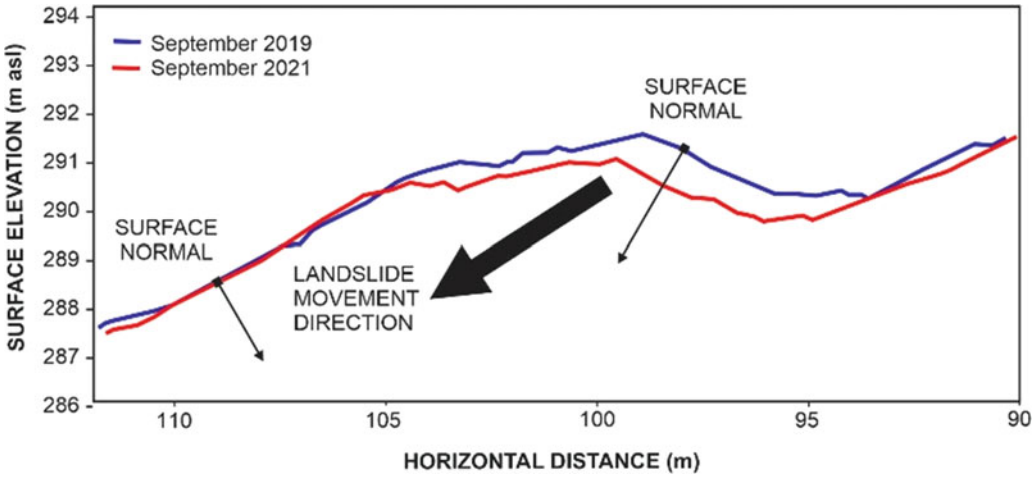

Fig. 3 Conceptual diagram of how M3C2 calculates displacement along surface normals (vectors). Note the insensitivity to surface parallel displacement

3.5 RCM InSAR Analysis

A stack of 3 m RCM descending images were tasked and acquired by the Canadian Space Agency (CSA). The SAR Toolbox in the Earth Observation Data Management System (EODMS) was used to generate interferometric pairs that were then corrected for spatial atmospheric errors, unwrapped, and masked for low coherence (cf. Dudley and Samsonov 2020). The network of unwrapped phase measurements was then manually examined. InSAR pairs that had obvious unwrapping errors or significant decorrelation noise were removed. A free SBAS processing package developed and distributed by NRCAN (MsBASv3, Samsonov 2019) was used to recover the deformation time-series history for the period of InSAR observation (Fig. 7).

4 Discussion

4.1 Comparing Displacement Measurements

Individually, each landslide displacement monitoring approach has limitations that must be considered when comparing to other methods. Measurements vary in terms of directional sensitivities, frequency of observations, temporal coverage, and absolute–vs-differential measurements.

Two methods of comparison across datasets are employed in this study. First, RTK-GNSS measurements and 3D RPAS displacement are projected onto the RCM InSAR LoS, then time-series profiles of all three measurement techniques are compared at all GCP positions. This method only considers a small subset of point available to both the wide area RPAS and InSAR methods. The second comparison method leverages the broad spatial coverage of both the 3D RPAS

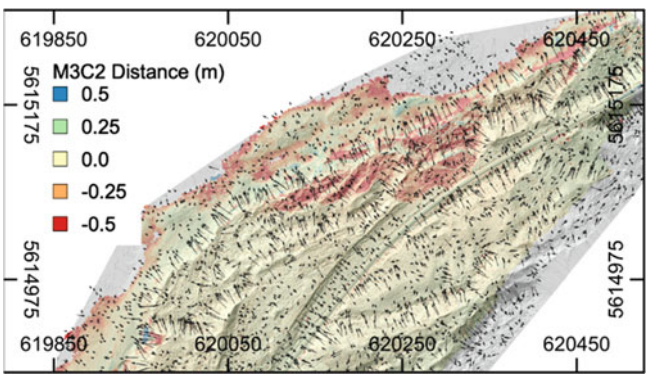

Fig. 4 Horizontal projection of the M3C2 surface normals (vectors) over M3C2 horizontal distance (raster). Hill-shade transparency is applied for context. All M3C2 surface normals are unit vectors, so shorter vectors have a larger vertical component, while longer vectors have a larger horizontal component

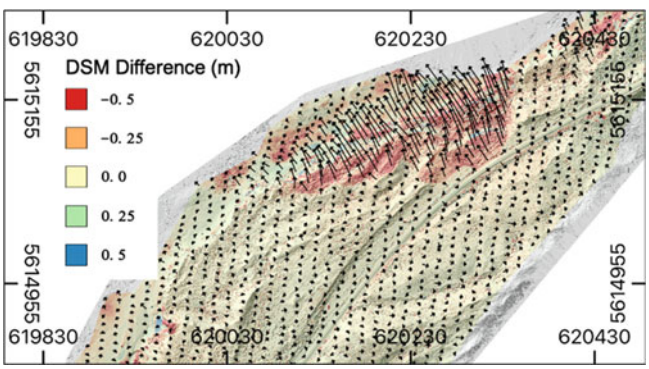

Fig. 5 3D RPAS deformation over North Slide between 2019-09-19 and 2021-09-28. Vectors indicate horizontal deformation from MicMac digital image correlation and colour scale represents difference in DSMs. Hill-shade transparency is applied for context

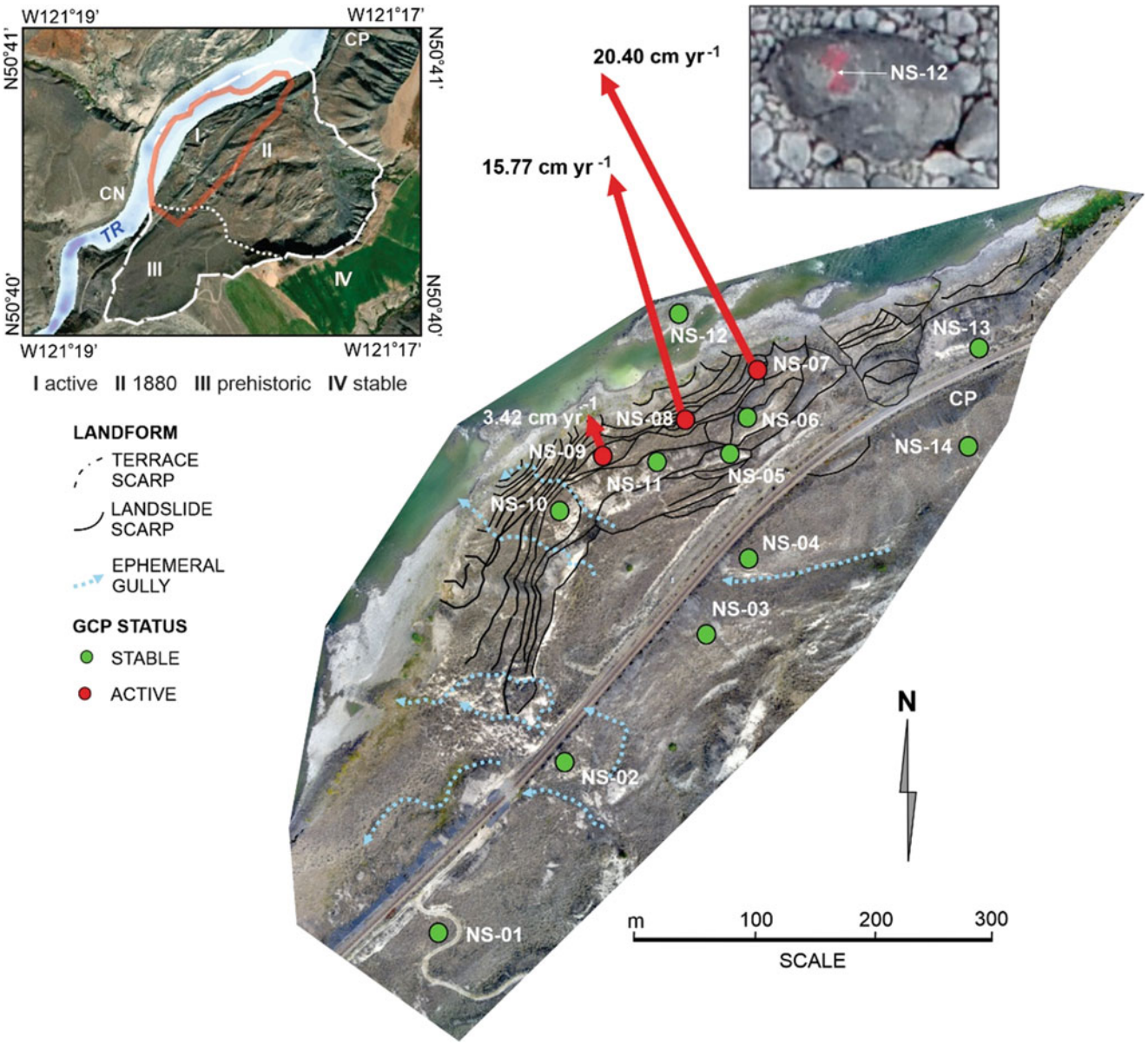

Fig. 6 RTK-GNSS GCP measurements, showing scaled horizontal movement vectors plotted on annotated RPAS digital orthomosaic image. Location of DSM highlighted in red on inset map of North Slide

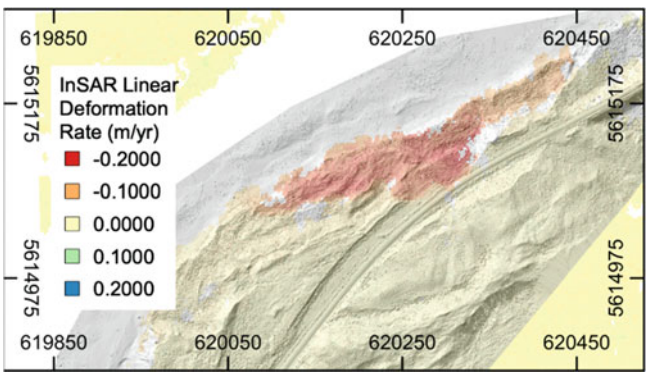

Fig. 7 InSAR-derived ground surface velocities mapped with semi-transparent hill-shade applied for context

measurements and InSAR by estimating an annual deformation rate of both datasets and comparing all collocated points.

Of the four deformation-measurement techniques presented, only the M3C2 algorithm is able to calculate deformation along a vector normal to the ground surface. The result is that the direction of deformation is highly variable. It is likely that M3C2 generally underestimates deformation of the "Solar Slump" to a degree that varies with how the movement vector and surface normal are aligned (cf. Fig. 3). The M3C2 algorithm can be expected to output nearly accurate estimates of ground deformation on surfaces perpendicular to the ground movement. At worst,

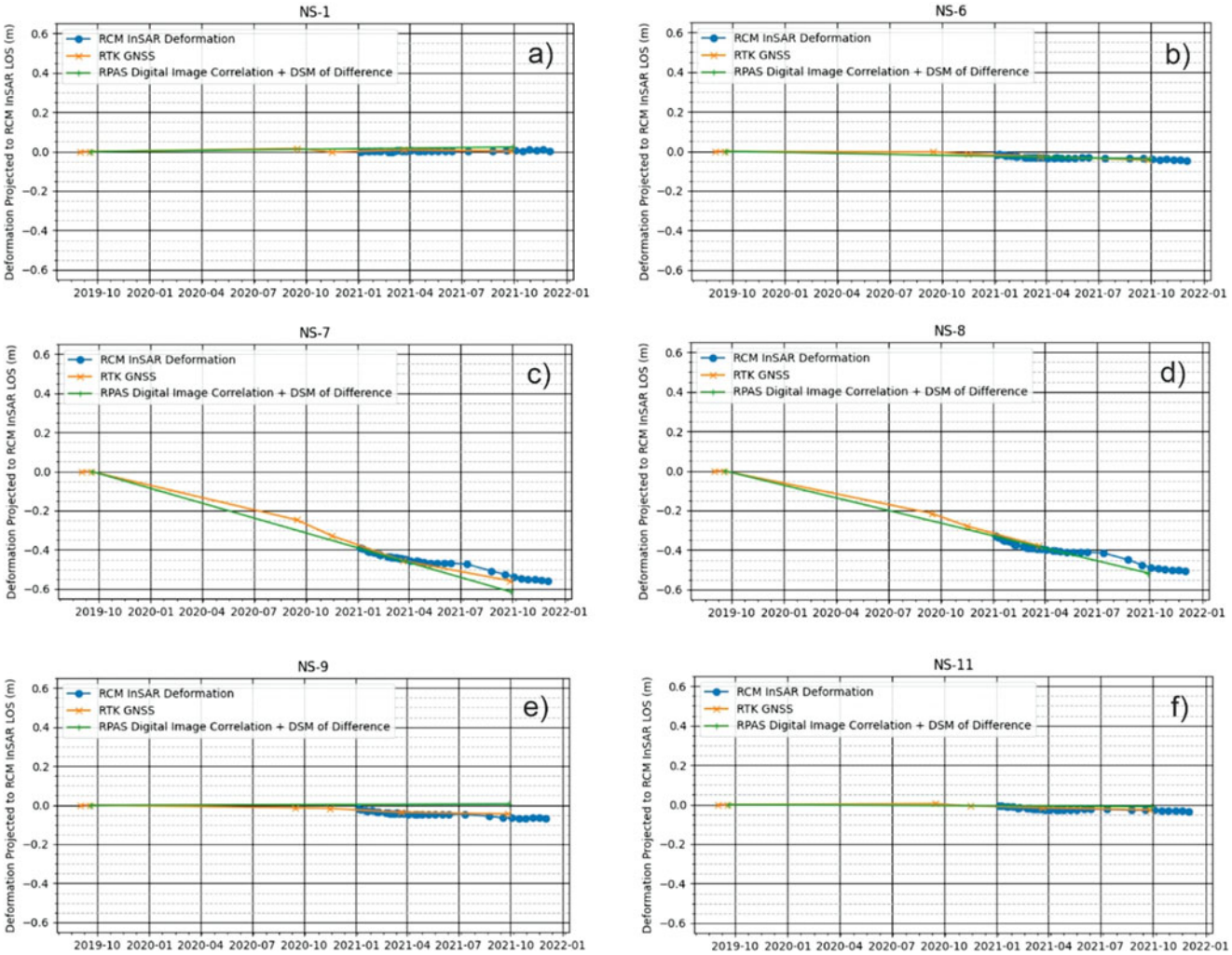

Fig. 8 (**a–f**) Selected RCM, RTK-GNSS and RPAS deformation time-series, projected to RCM LoS. See Fig. 6 for location of GCPs (after Rotheram-Clarke et al. 2022)

M3C2 is insensitive to surface parallel movement. Although it would be possible to project normal vectors into the InSAR LoS vector or decompose the deformation vectors into their Cartesian components, comparisons would not be meaningful since InSAR can be insensitive to movement along a particular orientation. M3C2 has the added complexity that this orientation is highly variable, and can change dramatically in rough topography.

4.2 Comparing RTK–InSAR–RPAS Point-Clouds

Full InSAR time-series and cumulative RPAS deformation measurements were extracted for points locations at each of the 11 GCPs where InSAR measurements were available (Rotheram-Clarke et al. 2022). Differences in the RTK-GNSS positions were calculated to construct a displacement time-series. Displacements in X, Y and Z were projected to the RCM LoS for both the RTK-GNSS and RPAS to create an accurate basis for comparison. Coincidental time-series profiles for key GCPs across the "Solar Slump" are shown in Fig. 8a–f.

Merged orthophoto mosaics and DSMs (Figs. 4, 5 and 6) capture the baseline surface condition of the North Slide "Solar Slump", along with the extent of bare earth and vegetation growth (e.g., grasses, shrubs and trees). Metre-scale anthropogenic features (e.g., train tracks, signals bungalow, solar panel array) are resolvable in the orthophoto mosaic and DSM.

Geomorphic features visible include: terraces graded to 300 m and 340 m asl, with steep river-cut scarps; ephemeral gullies draining the inactive nineteenth Century slide surface; active slide blocks, scarps and tension cracks across the

"Solar Slump"; and a toe bulge in the active floodplain of Thompson River (Fig. 6).

The pattern of cumulative deformation in 2021 derived from RCM data is very similar to that seen in the RPAS-generated imagery. In Fig. 7, the colour stretch is +/−5 cm, indicating measurement of 5 cm to 6 cm of LoS deformation at GCPs NS-07 and NS-08 (Fig. 8c, d). There is also uplift between NS-07 and NS-12 where back-tilted clay-silt beds are exposed in the active floodplain (Huntley et al. 2021b). Future research efforts will be directed at comparing the two time-series and converting satellite LoS displacements to correspond with movement vectors derived from UAV and RTK-GNSS datasets.

4.3 Comparing Wide Area InSAR-RPAS

To examine a statistically significant number of points, 3D RPAS deformation measurements were projected to the InSAR LoS vector. This raster was then down-sampled and aligned to match perfectly the pixel geometry of the InSAR results. Only spatially coincident pixels present in both the RPAS results and the InSAR were considered, resulting in 20,843 points of comparison. The RPAS deformation represented a 2-year cumulative measurement without intermediate points in the time-series, while the InSAR data represented a temporally dense set of measurements over a one-year period.

For a scatter-plot analysis, the RPAS cumulative deformation measurements were plotted against the InSAR annual rate map with the axes scaled 2:1 and a trend line scaled to match (Fig. 9). Due to conflicts with other RCM users, the longest period between sequential InSAR pairs was 44 days. With the relatively small spatial footprint of this landslide, unwrapped phase values beyond 1 phase cycle were considered unreliable. This placed an upper bound for robust measurements of deformation rate. For this study, the bound was deemed to be 2.8 cm/44 days, or approximately 24 cm yr.$^{-1}$. This limit can be improved with a higher revisit frequency, and is not as much of a limitation when the spatial extents of the movement zone are larger and vary gradually. Figure 9 distinguishes points in excess of this rate by colour.

Figure 9 reveals a clear agreement between the RPAS and InSAR deformation trends. The cluster of points around the origin represents most of the surveyed area where the surface is relatively stable, and displays a spread in RPAS points that is approximately an order of magnitude larger than the spread of the InSAR. For deforming points, a general agreement in rate is observed up to nearly 20 cm yr.$^{-1}$. At higher movement rates, InSAR underestimates displacement when compared the RPAS deformation rates. This may be due to a combination of factors such as phase aliasing of rapid deformation, or a tendency for SBAS to smooth transient higher velocity deformation events. An imperfect comparison might also result from temporal overlaps between the two datasets. This is explained by a higher average rate in the period preceding the InSAR time-series, a lower average rate in the period following the final RPAS survey date, or a combination of both.

To arrive at the closest estimate of an annual rate given the sampling frequency, a histogram was constructed by scaling the 2-year cumulative RPAS deformation by half (Fig. 10). These points were differenced with the InSAR annual rate at each coincident point to create a difference metric. Across

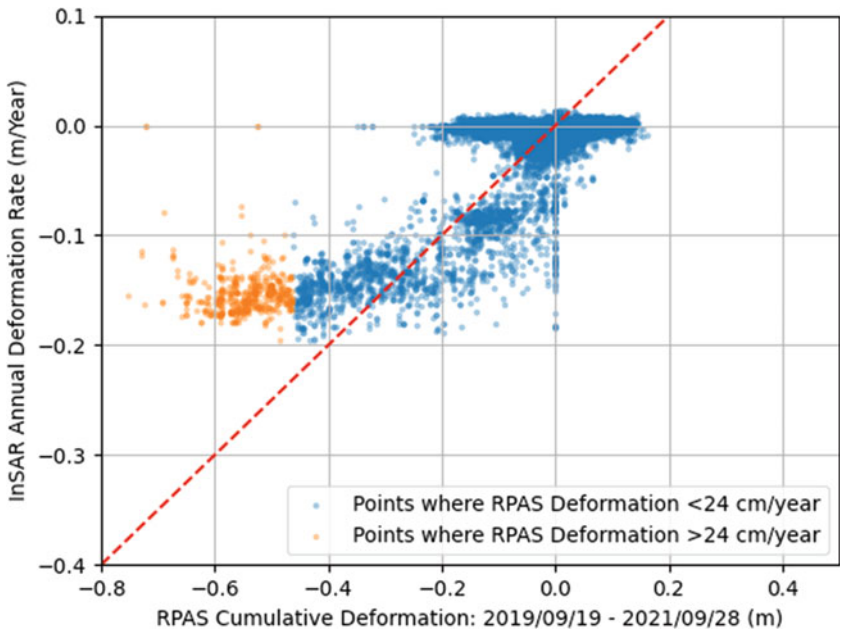

Fig. 9 Wide area direct comparison of co-located InSAR and RPAS deformation. InSAR measurements represent a best-fit annual rate, while RPAS measurements represent 2 years of cumulative deformation. Note the 2:1 scaling to account for the difference in temporal periods (after Rotheram-Clarke et al. 2022)

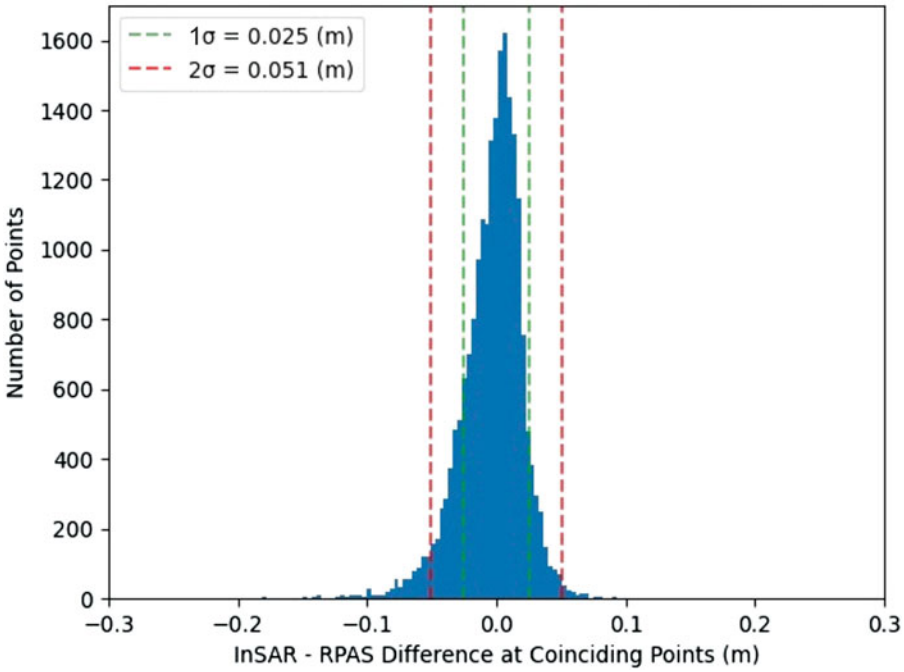

Fig. 10 Histogram distribution of differences in collocated InSAR and RPAS deformation rates (after Rotheram-Clarke et al. 2022)

20,843 points, the 1σ and 2σ were 0.025 m yr.$^{-1}$ and 0.051 m yr.$^{-1}$ respectively. As in the scatter plot analysis, this is an imperfect comparison because the temporal overlap of the two datasets is not consistent.

5 Conclusions and Evaluation

The four landslide change-detection methods evaluated in this study have their individual strengths and limitations when applied to mapping slow-moving rotational-translational landslides. RTK-GNSS surveying is well accepted as being both accurate and precise. However, collecting data is laborious, and achieving wide area measurement coverage similar to InSAR or RPAS surveying, even at small sites, is impractical.

M3C2 is a simple and accessible algorithm to run. It is free and open source. By operating directly on point-clouds, the complexity of intermediate processing steps is greatly reduced. The displacement magnitude of the M3C2 output may appear simple to interpret, but the variability in measurement direction, and the insensitivity to surface parallel movement are major limitations for rotational and translational landslides. Since variation in movement direction is only measured on surface normals, M3C2 is the only measurement technique that cannot be directly compared with other methods.

InSAR is the only method not requiring physical site visits. RCM data acquisitions allowed for a set of measurements that were not only broad in spatial coverage, but also dense in temporal measurements. These data provided a level of insight into the seasonal dynamics of landslide movement not possible with other methods. The LoS limitation of InSAR added complexity to interpretation and satellite tasking.

Generally, we found good agreement between our InSAR and 3D RPAS methodologies for stationary and lower deformation rates. However, in parts of the landslide where the deformation rate approached approximately 20 cm yr.$^{-1}$, InSAR measurements typically reported lower rates than the 3D RPAS method. This may have been a result of an imperfect comparison of datasets with different measurement periods.

Combining RPAS digital image correlation with the DSM of difference was the only method able to provide a full 3D movement vector for each point with broad coverage across the landslide. Compared to M3C2, the processing requires more complexity and familiarity with a number of open source tools. However, the outputs are more directly interpretable, and capable of providing better insights into the landslide dynamics.

Acknowledgments The Government of Canada, through the Ministry of Transport and Ministry of Natural Resources, funds field-based landslide research in the Thompson River valley, BC, and elsewhere across Canada.

References

Clague J, Evans S (2003) Geologic framework for large historic landslides in Thompson River valley, British Columbia. Environ Eng Geosci 9:201–212

Dudley J, Samsonov S (2020) The Government of Canada automated processing system for change detection and ground deformation analysis from RADARSAT-2 and RADARSAT constellation Mission synthetic aperture radar data: description and user guide, Geomatics Canada. Open File 63:65

Eshraghian A, Martin C, Cruden D (2007) Complex earth slides in the Thompson River valley, Ashcroft, British Columbia. Environ Eng Geosci XIII:161–181

Eshraghian A, Martin C, Morgenstern N (2008) Movement triggers and mechanisms of two earth slides in the Thompson River valley, British Columbia, Canada. Can Geotech J 45:1189–1209

Evans S (1984) The 1880 landslide dam on Thompson River, near Ashcroft, British Columbia. Geological Survey of Canada, Current Research, Part A, Paper 84-1A, pp 655–658, https://doi.org/10.4095/119628

Galland O, Bertelsen H, Guldstrand F, Girod L, Johannessen R, Bjugger F, Burchardt S, Mair K (2016) Application of open-source photogrammetric software MicMac for monitoring surface deformation in laboratory models. J Geophys Res Solid Earth 121:2852–2872

Huntley D, Bobrowsky P, Zhang Q, Zhang X, Lv Z (2017) Fibre Bragg grating and Brillouin optical time domain reflectometry monitoring manual for the Ripley landslide, near Ashcroft, British Columbia. GSC Open File 8258:66

Huntley D, Bobrowsky P, Hendry M, Macciotta R, Best M (2019a) Multi-technique geophysical investigation of a very slow-moving landslide near Ashcroft, British Columbia, Canada. J Environ Eng Geophys 24(1):85–108. https://doi.org/10.2113/JEEG24.1.87

Huntley D, Bobrowsky P, Hendry M, Macciotta R, Elwood D, Sattler K, Chambers J, Meldrum P (2019b) Application of multi-dimensional electrical resistivity tomography datasets to investigate a very slow-moving landslide near Ashcroft, British Columbia, Canada. Landslides 16:1033–1042. https://doi.org/10.1007/s10346-019-01147-1

Huntley D, Bobrowsky P, MacLeod R, Cocking R, Joseph J, Rotheram-Clarke D (2021a) Ensuring resilient socio-economic infrastructure: field testing innovative differential GNSS-InSAR-UAV monitoring technologies in mountainous terrain near Ashcroft, British Columbia, Canada. J Mountain Sci 18(1):1–20. https://doi.org/10.1007/s11629-020-6552-y

Huntley D, Rotheram-Clarke D, Pon A, Tomaszewicz A, Leighton J, Cocking R, Joseph J (2021b) Benchmarked RADARSAT-2, SENTINEL-1 and RADARSAT constellation Mission change detection monitoring at north slide, Thompson River valley, British Columbia: implications for a landslide-resilient national railway network. Can J Remote Sens 47(4):635–656. https://doi.org/10.1080/07038992.2021.1937968

Huntley D, Bobrowsky P, MacLeod R, Rotheram-Clarke D, Cocking R, Joseph J, Holmes J, Sattler K, Chambers J, Meldrum P, Wilkinson P, Donohue S, Elwood D (2022a) IPL project 202: landslide monitoring best practices for climate-resilient railway transportation corridors in southwestern British Columbia, Canada. Prog Landslide Res Technol 1(1):18

Huntley D, Rotheram-Clarke D, MacLeod R, Cocking R, LeSueur P, Lakeland B, Wilson A (2022b) Scalable platform for UAV flight operations, data capture, cloud processing and image rendering of landslide hazards and surface change detection for disaster-risk reduction. Prog Landslide Res Technol 1(2):15

Journault J, Macciotta R, Hendry M, Charbonneau F, Huntley D, Bobrowsky P (2018) Measuring displacements of the Thompson River valley landslides, south of Ashcroft, B.C., Canada, using satellite InSAR. Landslides 15(4):621–636. https://doi.org/10.1007/s10346-017-0900-1

Lague D, Brodu N, Leroux J (2013) Accurate 3D comparison of complex topography with terrestrial laser scanner: application to the Rangitikei canyon (N-Z). ISPRS J Photogramm Remote Sens 82:10–26

Porter M, Savigny K, Keegan T, Bunce C, MacKay C (2002) Controls on stability of the Thompson River landslides. Canadian Geotechnical Society, Ground and Water – Theory to Practice, Proceedings of the 55th Canadian Geotechnical Conference, pp 1393–1400

Rosu A, Pierrot-Deseilligny M, Delorme A, Binet R, Klinger Y (2015) Measurement of ground displacement from optical satellite image correlation using the free open-source software MicMac. ISPRS J Photogramm Remote Sens 100:48–59

Rotheram-Clarke, D, Huntley, D, LeSueur, P, Cocking R, Joseph, J and MacLeod, R (2022) Direct comparison of RADARSAT constellation Mission InSAR, UAV derived point-cloud comparison and RTK-GNSS deformation monitoring at north slide, Thompson River Valley, British Columbia. GeoCalgary 2022, p 9

Rupnik E, Daakir M, Pierrot-Deseilligny M (2017) MicMac – a free, open-source solution for photogrammetry. Open Geospat Data Softw Stand 2:14

Samsonov S (2019) User manual, source code, and test set for MSBASv3 (multidimensional small baseline subset version 3) for one- and two-dimensional deformation analysis. Geomatics Canada, Open File

Stanton R (1898) The great land-slides on the Canadian Pacific railway in British Columbia. Proc Civil Eng 132:1–48

Digital Terrain Models Derived from Unmanned Aerial Vehicles and Landslide Susceptibility

Gabriel Legorreta Paulín, Jean-François Parrot, Rutilio Castro-Miguel, Lilia Arana-Salinas, and Fernando Aceves Quesada

Abstract

Digital Terrain Models (DTMs) are among the most important spatial information tools used in geomorphological landslide assessment because they allow the extraction of crucial attributes, such as landslide geometry, slope, terrain curvature, etc. However, at a local scale, the assessment of remote volcanic terrains is difficult because the DTMs have poor spatial and temporal representation. Worldwide, geomorphological analysis of landslides processes in mountainous terrains with difficult access has benefited with virtual topography representations using high-resolution Digital Surface Models (DSMs) generated by imagery captured by unmanned aerial vehicles (UAV). These DSMs include not only the ground topography, but also other landscape elements such as vegetation, buildings, cars, etc. These natural and anthropogenic elements are considered as non-relevant information or noise to obtain only the ground information. Photogrammetric post-processing of the DSM is required to derive a DTM that represent only ground topography. This research uses a Canopy Height Model (CHM), an altimetric selection mask, weights, a low-pass filter, and specific algorithms to generate a DTM from a high-resolution DSM derived from the UAVs and a DTM of a 1:50,000 map. With the DTM thus obtained, landslide susceptibility assessment was then conducted. The assessment completed by means of multiple logistic regression (MLR) in the study area. The Cerro de la Miel in Tepoztlán, State of Morelos, Mexico, is selected to exemplify this method. The study area was affected by rockfalls and shallow landslides during the earthquake on September 19, 2017. The results show an adequate representation of the ground topography, and eliminating most of the noise coming from the high-resolution DSM allowed us to define the landslide susceptibility. For the calculated landslide susceptibility, there is a 76% match between the model and the landslide inventory.

Keywords

Digital terrain models · UAV · Landslide susceptibly · Multiple logistic regression · GIS

1 Introduction

Landslides are significant natural hazards that cause damage to human settlements and their economic activities, especially in mountainous areas where abrupt relief, rainfall and/or earthquakes trigger gravitational processes (Sim et al. 2022). Worldwide, geomorphological cartography is used as a valuable tool to assess the landslide susceptibility. It provides concrete and precise information of distribution, frequency, size, origin, and chronological sequences of landslides (Jasiewicz and Stepinski 2013). The elaboration of geomorphologic maps requires high quality materials, such as topographic cartography, aerial photographs, and digital terrain models to analyze the landscape and its relationship with geological, structural, lithological, tectonic, morphometric, morphographic, weathering, and human factors (Knight et al. 2011). At regional scale, these materials are obtained by satellite and aerial remote sensing techniques that use multispectral sensors, LiDAR, synthetic aperture radars (SAR), and digital cameras (Francioni et al. 2018).

However, at local scale the geomorphologic evaluation of landslide processes is difficult not only because the small-

G. L. Paulín (✉) · J.-F. Parrot · F. A. Quesada
Instituto de Geografía, Universidad Nacional Autónoma de México, Circuito Exterior, Ciudad Universitaria, Ciudad de México, Mexico
e-mail: parrot@igg.unam.mx

R. Castro-Miguel
Escuela Nacional de Ciencias de la Tierra, Universidad Nacional Autonoma de Mexico, Ciudad Universitaria, Ciudad de Mexico, Mexico
e-mail: rutilio.castro@encit.unam.mx

L. Arana-Salinas
Universidad Autónoma de la Ciudad de México, Colegio de Ciencias y Humanidades, Academia de la Licenciatura Protección Civil y Gestión de Riesgos, Ciudad de México, Mexico

I. Alcántara-Ayala et al. (eds.), *Progress in Landslide Research and Technology, Volume 2 Issue 1, 2023*,
Progress in Landslide Research and Technology, https://doi.org/10.1007/978-3-031-39012-8_20

scale cartography, but also due to other natural and technical problems. The complexity concomitant of these natural and technical problems affects and compromises the landslide susceptibility assessment (Haneberg 2005). To mitigate these problems, intensive fieldwork improves landslide data collection, as well as knowledge of an area, but does not guarantee an exhaustive representation of gravitational processes (Van Den Eeckhaut et al. 2005). Also, its application is limited when researchers want to monitor short-term changes in an area due to the costs and effort required. To solve this situation, high spatial and temporal resolution aerial photos and DTMs are essential for the interpretation, detection, measurement, and modeling of small landslides.

In recent years, with the advent of Unmanned Aerial Vehicles (UAVs), or drones, and their products (aerial photos, orthophotos, dispersed or dense point clouds, and Digital Elevation Models (DEM)) a new opportunity has emerged to satisfy researcher needs (Annis et al. 2020). However, because this technology relatively new, there is still no robust methodology for acquiring and processing images derived from UAVs. The methodology depends highly on the used software, and has a significant influence on the resulting accuracy (Colomina and Molina 2014). For example, the DEMs derived from the UAVs do not separate the different return levels of the laser detection and measurement signals as does LiDAR. Therefore, UAVs produce Digital Surface Models (DSM) with a zenith vision in which the surface corresponds to the elements present on the earth's surface (vegetation, buildings, cars, etc.) and locally, if no obstacle, to the ground. In contrast, LiDAR, by separating the different return levels of the laser detection and measurement signals, allows both creation of DSM and Digital Terrain Models (DTM, to virtually represent terrain topography without artifacts) (Dubbini et al. 2016). Limitations of DSM derived from the UAVs to create a DTM are partially resolved during post-processing that eliminates other elements not corresponding to ground data (called "noise") by using specialized photogrammetry programs (Dubbini et al. 2016).

Governmental and academic institutions use commercial programs specialized in photogrammetric processes to eliminate the noise and to produce high-resolution DSMs and DTMs. DTMs are obtained by post-processing the DSM semi-automatically or automatically. The semi-automatically procedure eliminates the noise by manually enclosing and erased with selection polygons vegetation, buildings, cars, etc. The program then interpolates the ground elevation to fill the gaps left by the elimination of the noise to produce the DTM. For an automatic procedure, the user defines the best parameters (such as angles, distances, minimum heights from which a point must not be considered as a ground, the average slope of the terrain, concavity, etc.) to reclassify the elevation point cloud in two classes (points representing the ground, and the remainder) (Anderson and Gaston 2013; Dubbini et al. 2016; Escobar-Villanueva et al. 2017).

Although the use of this new technologies is Mexico is very promising as a tool for the rapid acquisition of aerial photos, orthophotos, and 3D data to map and assess remote landslide areas, there is a lack of non-commercial programs and methods to facilitate post-processing of point cloud datasets from UAVs to produce DTM at low cost, and in an acceptable manner. Also, little work has been done to obtain the landslide susceptibility in areas with difficult access and scarce or small-scale cartographic and geomorphologic information.

The present study develops algorithms, applications, and an alternative method to eliminate the existing noise in an UAV-derived DSM which allow an adequate DTM (referred as a moderate-resolution DTM) to be obtained for landslide susceptibility evaluation. The method uses a 50 cm-pixel resolution DSM derived from an UAV, a DTM derived from a map with 10 m topographic contour lines (referred herein as low-resolution DTM), a Canopy Height Model (CHM), altimetric selection mask, interpolation, weights, and a low-pass filter to obtain a 50 cm moderate-resolution DTM.

The moderate-resolution DTM is the foundation to assess the landslide susceptibility by using Multiple Logistic Regression (MLR) in the study area. The study area is the Cerro de la Miel, in the Municipality of Tepoztlán, State of Morelos, Mexico (Fig. 1). In the area, rockfalls and shallow landslides were triggered by an Earthquake (magnitude 7.1) on September 19, 2017 and are used to evaluate the method and its landslide susceptibility. In this study, MLR is selected to assess landslide susceptibility because it avoids problems of non-linear relationships between dependent and independent variables. Also, MLR landslide probability prediction is fairly successful in identifying current and potential landslide areas (Field 2014; Legorreta et al. 2016; Castro-Miguel et al. 2022). Three topographic variables derived from the moderate-resolution DTM (altimetry, slope, and terrain curvature) are used as the input for MLR analysis. The results illustrate that although the moderate-resolution DTM shows a vertical error of ~ <=1.5 m, the method allows elimination of much of the DSM inherent noise. The resulting DTM has a fair topographic representation that permits calculation of the landslide susceptibility. The calculated landslide susceptibility has a moderate match between the inventory map and the model (76.91%). The landslide model validation is performed by the model's accuracies obtained from a cross table between models and landslide inventory and with the Receiver Operating Characteristic (ROC) curve.

2 Study Area

The Cerro de la Miel is at 18° 59′ 13.920″-18° 59′ 20.1048″ N and 99° 6′ 45.2889″-99° 6′ 38.7957″ W, within the municipality of Tepoztlán, State of Morelos, Mexico (Fig. 1). The study area belongs to the Tepoztlán Formation, which is composed of reworked volcanoclastic deposits caused by mud flows or lahars (Lenhardt et al. 2010). The Cerro de la Miel is affected sporadically, but importantly, by gravitational processes. Rockfall and shallow landslides are triggered constantly due to the combination of several factors, such as high precipitation, land use changes caused by human settlements, a high degree of weathered bedrock located at high elevations with steep slopes, and earthquakes.

The study area covers 3.63 ha with an elevation range from 1789 to 1875 m a.s.l., and hillslopes from 3° to 35° (in the piedmont zone) and > 35° (in mountainous terrain). The deposits of the Tepoztlán Formation contain angular and subangular dacitic clasts 20 cm to >2 m in diameter. These clasts vary in resistance from strong (rock specimens are broken with a single hammer stroke) to weak (the rock specimens are fragmented under firm a hammer stroke) (Dackombe and Gardiner 1983). These clasts are bound in a matrix composed of silt and sand.

The instability situation is exacerbated by an heterogeneous sets of fractures, predominantly vertical and with a NE-SW trend. These fractures allow the infiltration of water, which in turn creates alteration planes that weaken the contact between the blocks and facilitates their fall. The average annual rainfall is 1592 mm/year. Most of the rain fall occurs as seasonal storms during the wet season between May and November (CLICOM 2018). Access to the upper part is difficult due to the abundant low deciduous forest vegetation (CONANP 2017).

On September 19 2017, at 13:14:40 local time, an intense earthquake with a magnitude of 7.1 on the Momentum Magnitude (Mw) scale struck the country. The epicenter was located 12 km from Axochiapan (Morelos), according to the preliminary special report of the National Seismological Service of Mexico (Servicio Sismológico Nacional 2017). This earthquake generated an estimated economic loss between US $ 4000 and US $ 8000 million (Capraro et al. 2018). During this seismic event, a rock fragment of approximately 3.1 m long × 2.8 wide × 1.7 m high detached from a height of 57 m. The rock impacted a house located on the SW flank of the Cerro de la Miel, but not human lost were reported.

3 Method

The method encompasses four main stages to obtain a moderate-resolution DTM, and for modeling, mapping, and validating landslide susceptibility in the study area. *Stage 1*: Planning, fieldwork, and post-processing of products derived from a UAV to obtain a high-resolution DSM (50 cm pixel size) (stage 1 in Fig. 2); *Stage 2*: Obtaining and standardizing a DTM derived from altimetric curves (stage 2, Fig. 2); *Stage 3*: Obtaining the canopy height model and altimetric mask to create the final moderate-resolution DTM by using weights and filters (stage 3, Fig. 2), and *Stage 4*: Create the landslide susceptibility map and assess the performance of the MLR model (stage 4, Fig. 2).

Although the first stage described how the ASCII or LAS (Long ASCII Standard) file was obtained with X, Y, and Z

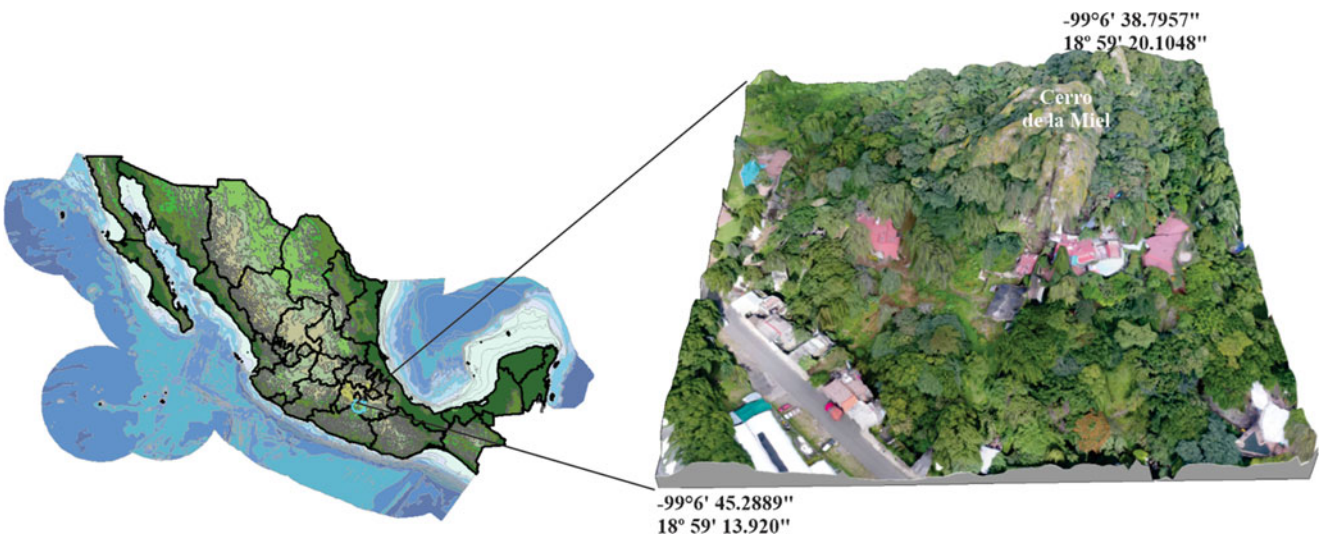

Fig. 1 Study area, Cerro de la Miel, Tepoztlán, State of Morelos, Mexico

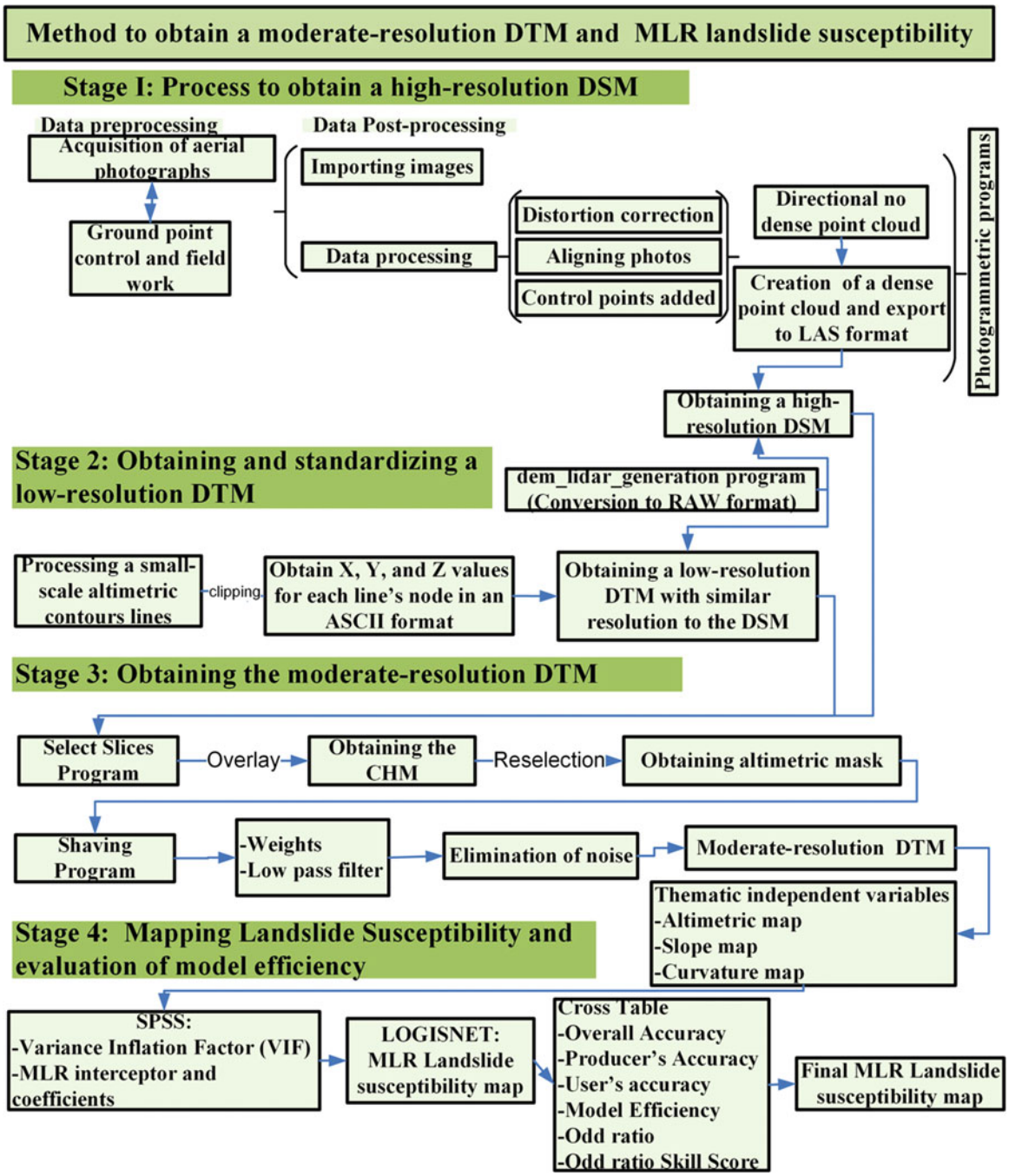

Fig. 2 General method to obtain a DTM and the landslide susceptibility

coordinates in this research, the focus of this work is the post-processing of the ASCII or LAS file, regardless the photogrammetric process or programs used (for example, Argisoft PhotoScan, Pix4D, VisualSFM, Accute3D, etc.) to obtain them.

For the first stage, used a Phantom 4 Pro quadrocopter, designed and built by Da-Jiang Innovation (DJI) with a camera with CMOS sensor of 1″ providing 20 megapixels of resolution. The flight capture planning was carried out using the Pix4D capture program (Pix4D 2022). With a photogrammetric double-mesh flight capture pattern, 103 aerial images were acquired with two flights, approximately 20 minutes in duration. The average height of the flights was approximately 100 m, and at a speed of 1.5 m/s. The front and lateral overlap between each aerial photograph was 80%.

Along with the flight planning, some ground control points (GPCs) were defined in the area to georeference the

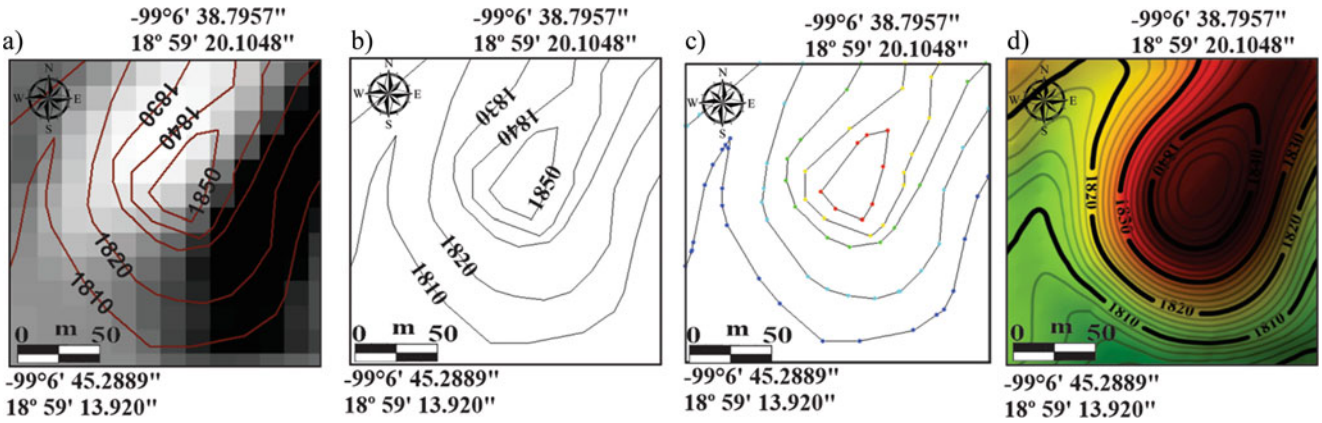

Fig. 3 Procedure to obtain a DTM from a low-resolution map: (**a**) 15 m resolution DTM; (**b**) 10 m equidistance altimetric contour lines; (**c**) extraction of points with X, Y, and Z from the nodes of altimetric contour lines; (**d**) interpolated low-resolution DTM (50 cm in pixel size)

aerial photographs. Unfortunately, a large part of the study area was private property, and was difficult to access. Therefore, to help with the georeferencing process, four GPC were captured using a geodetic dual frequency differential GPS. To palliate this, Google Earth images were used to establish a large number of control points, and to georeference the images. The horizontal coordinates were referenced to the UTM 14 N zone using the WGS84 ellipsoid.

Image post-processing was accomplished using the photogrammetric software Argisoft PhotoScan (Agisoft 2014). Post-processing included alignment of aerial photographs, creating an orthophoto, and generating a dense point cloud with X, Y, and Z values. The dense point cloud was exported as an ASCII X, Y, and Z file, from which a standard high-resolution DSM was generated by using the dem_lidar_generation program (Parrot 2011). A resolution of 50 cm per pixel is established. Furthermore, a DTM of the area was obtained from the Instituto Nacional de Geografía y Estadística (Fig. 3a) (INEGI 1998a). However, it was not suitable for topographic representation and landslide susceptibility analysis due to its low resolution (15 m per pixel). As a result, in the second stage, the derivation of a more suitable low-resolution DTM was obtained from a topographic map at a scale 1:50,000 by using altimetric curves with a 10 m equidistance (INEGI 1998b). From each altimetric curve's node, the X, Y, and Z values were extracted. Due to the sparse distribution of contour lines in the study area, the nodes were interpolated by a multidirectional linear interpolation (Parrot 2012; Parrot 2016; Šiljeg et al. 2019) (Fig. 3b and c). A low-resolution DTM of 50 cm resolution was generated for the two subsequent stages (Fig. 3d).

In the third stage, the moderate-resolution DTM was created by using the software Select Slices (Parrot 2018a), and the developed program Shaving (Parrot 2018b). The software Select Slices allows the user to create a CHM and derive binary images to use as masks that correspond to height difference of various vegetation, representing the vertical distance between the ground and the top of trees. With Shaving, templated vegetation height ranges were used to perform analyses. The CHM was created with a pixel size of 50 cm by subtracting the low-resolution DTM (derived from topographic curves) from the high-resolution DSM (derived from the UAV).

The different masks of vegetation created by the Shaving program were used to remove the noise according to vegetation height by applying a selective subtraction. Height differences were subtracted only from the area framed within the mask to the DSM. Figure 4, shows the results obtained using three different masks. One mask with noise heights ranges from 10 m to 25 m (Fig. 4d, g, j), another with heights from 10 cm to 25 m (Fig. 4e, h, k), and the last one from 0 m to 25 m (Fig. 4f, i, l).

This last mask was selected and used to obtain the pre-final moderate-resolution DTM. With the selected mask, the Shaving program (Parrot 2018b) was used to eliminate full ranges of height differences. If the low-resolution DTM was used to subtract the full ranges of height differences, the resulting map would have the same spatial characteristics as the low-resolution DTM, and the potential advantages obtained with the UAV are lost (Fig. 4f, i, l). To reduce this problem, we proceeded in an heuristic way.

First, the distribution of height differences in the CHM was evaluated with a histogram and then weighted. In this study, the height differences were weighted by 4%. For example, if there were in a pixel with a height difference of 5 m, by weighted 4%, the Shaving program would subtract 4.80 m rather than of 5 m. The resulting DTM still presented altimetric jumps (Fig. 5), for that, a low-pass filter was applied to obtain the final moderate-resolution DTM. With this procedure, a maximum error was estimated for the study area between 0 and 1.5 m.

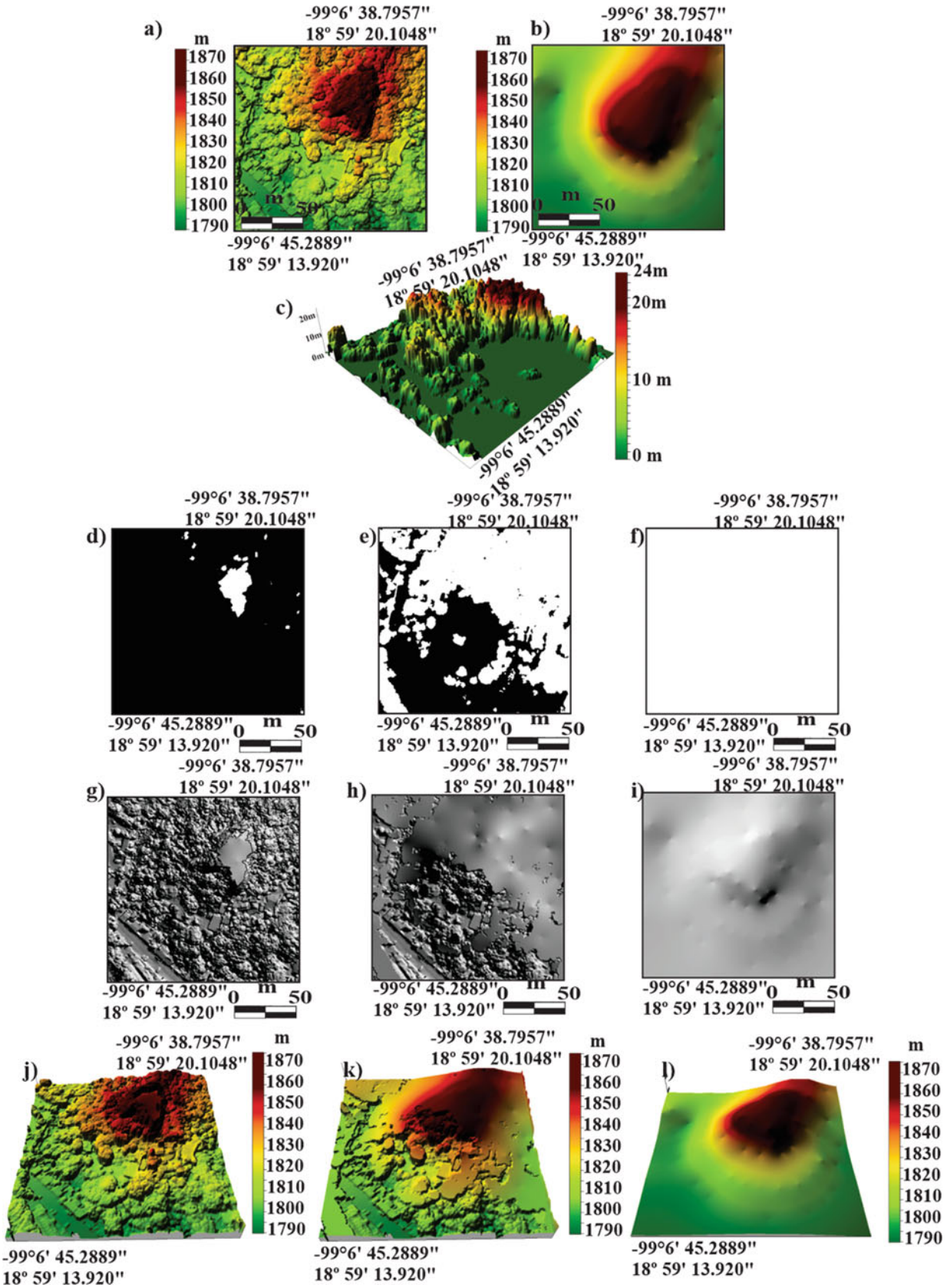

Fig. 4 Example of using Select Slices and Shaving programs (**a**) DSM derived from the UAV; (**b**) DTM derived from a topographic 1: 50,000 map; (**c**) CHM created from the algebraic subtraction of (**a**, **b**; **d**) Altimetric mask (in white color) from 10 m to 25 m; (**e**) Altimetric mask (in white color) from 10 cm to 25 m; (**f**) Altimetric mask (in white color) from 0 m to 25 m; (**g**, **h**, **i**, **j**, **k**, **l**) Resulting DTMs

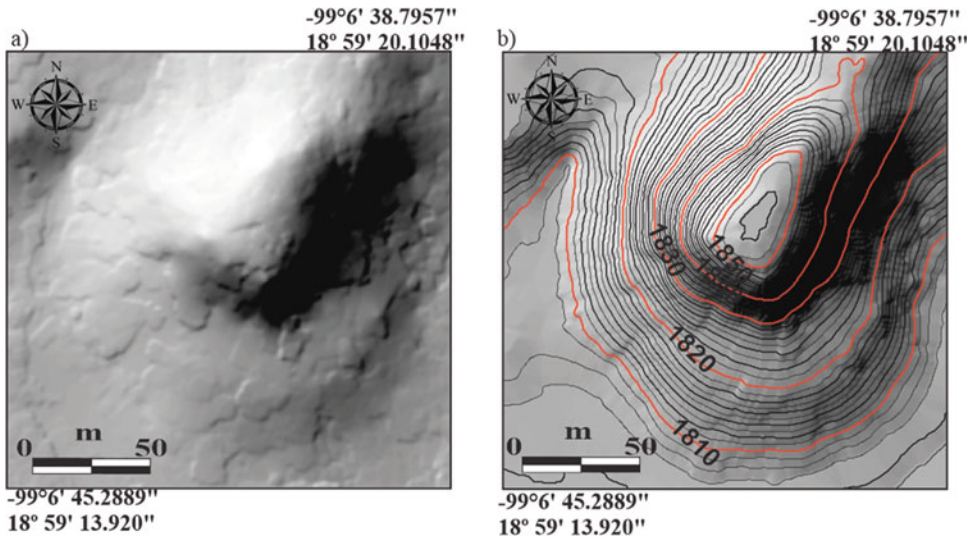

Fig. 5 (**a**) pre-weighted and filtered DTM; (**b**) Final weighted and filtered moderate-resolution DTM

In the fourth stage, slope angles and slope curvature were derived from the final moderate-resolution DTM. These two independent variables together with the altimetric elevation were used to feed the MLR model for landslide susceptibility assessment. The probability of landslide triggering was calculated by use of a random sample from non-landslide and landslide areas for the three independent variables. The landslide analysis excluded evacuation zones and deposits. The total number of landslide pixels on the landslide inventory was 96 pixels (24 m^2). The landslide area included the head scarps of shallow slides and rockfalls. The same number of sampled pixels (96 pixels) was sampled in non-landslide areas. With the total number of sampled pixels, the three independent variables were tested for multi-collinearity using the Variance Inflation Factor (VIF) (Pallant 2013). The VIF values in Table 1 shows no serious multicollinearity problem (Field 2014). However, the analysis of backward Multiple Logistic Regression discarded slope curvature. Based on the logit form, landslide susceptibility was mapped using a 10-classification probability scheme in the GIS (Table 1, Fig. 7a).

To evaluate the model prediction, LOGISNET under ArcInfo GIS software (Legorreta and Bursik 2008), and the Statistical Package for the Social Sciences (SPSS) were used. The gauge of how well the model predicted reality was assessed by the percentage of overlay between the model map and inventory map (Table 2). In LOGISNET, a two-classification scheme (landslide and non-landslide) was used for the inventory and model maps to facilitate the comparison in a contingency table. The contingency table was used to summarize the error and success in landslide and non-landslide area (overall accuracy), the degree of

Table 1 Coefficients, logit form, and statistical test of MLR

MLR								
						95% C.I. for EXP(B)		
Variable	Coefficient	S.E.	Wald	df	Exp(B)	Lower	Upper	Collinearity statistics
Interceptor	74.087	14.724	25.316	1	1.4992E32			VIF
Altimetry	−0.041	0.008	25.884	1	0.959322	0.944	0.974	1.374
Slope	0.071	0.009	54.633	1	1.074084	1.053	1.094	1.365
Slope curvature								1.009
Logit form	1/1 + Exp-(74.087 + Altimetric map (−0.041) + slope area map (0.071)							

Table 2 ROC, accuracies, and model efficiency

	MLR model
Area under the ROC curve	64.1%
Overall accuracy	66.51
	Landslide area
Producer's accuracies	76.91
User's accuracies	63.79
Model efficiency	0.33

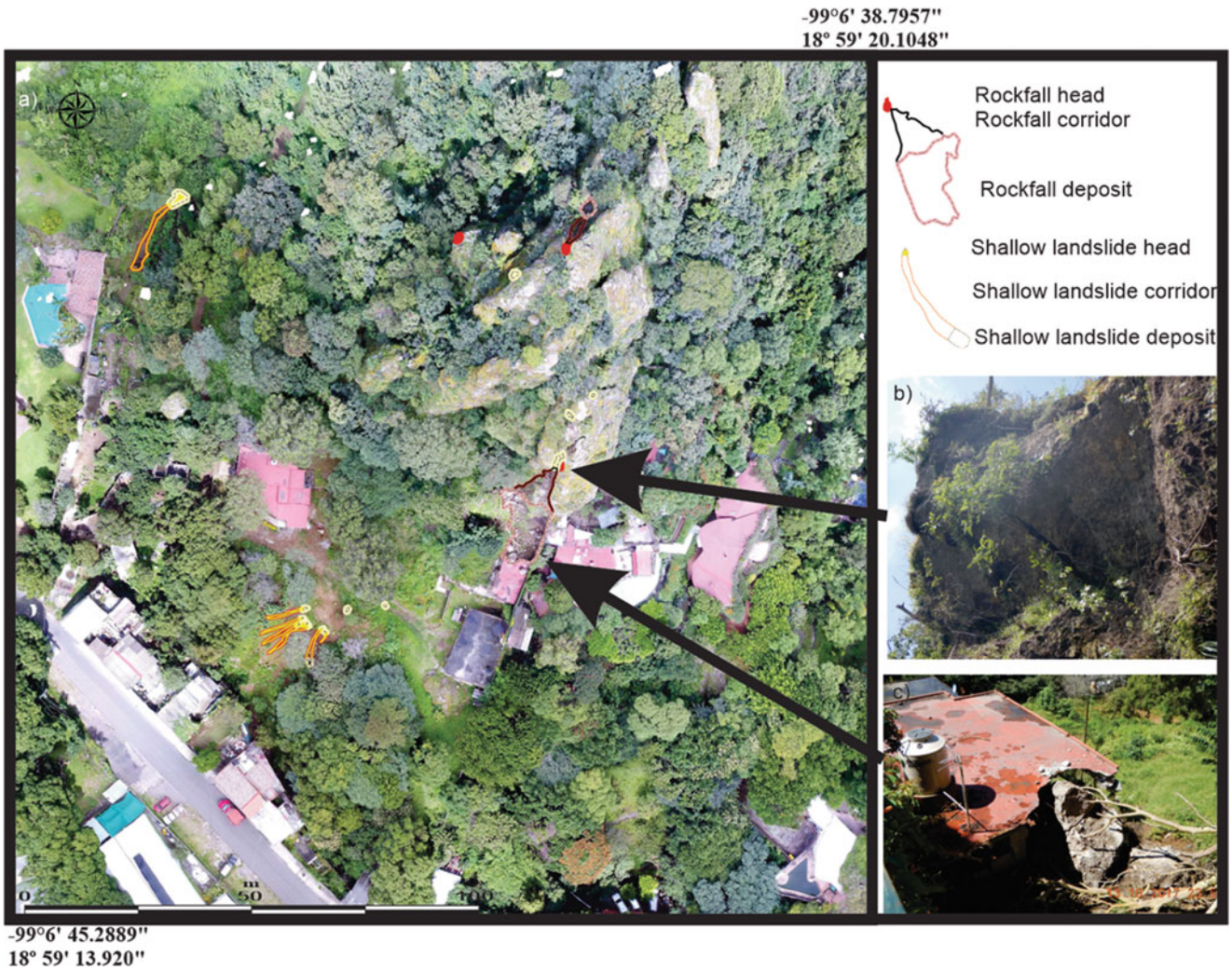

Fig. 6 (**a**) Landslide inventory map; (**b**) Rock fall detachment zone; (**c**) House destroyed by a ~ 15 m^2 bold

coincidence between the model and inventory (producer's accuracy), the degree of model over-prediction or under-prediction, and model efficiency (user's accuracy and model efficiency). In SPSS, the model accuracy was evaluated with the area under the ROC curve (AUC) (Legorreta et al. 2016). When the model predicted all correctly, the statistics derived from the contingency table and the AUC had a maximum value of 1 or 100%. Model efficiency went from 1 (a perfect model) to negative values when the number of pixels incorrectly indicated landslides were larger than the correct ones (Legorreta et al. 2016).

4 Results

Following the September 2017 assessment of triggers was included in the landslide inventory for Cerro de la Miel (Fig. 6). The landslide inventory shows that in the study area, small shallow landslides (including debris slides and debris flows) are, by number, the predominant type (23), followed rockfalls (7). They affect an area of 244.73 m^2. About 78% of the shallow landslides are located along the piedmont with slopes between 8–35°, while rockfalls are the predominant process along the contact between the relative flat hilltops and hillslopes >35°.

Although there is a relatively small number of large rockfalls, these are the main hazard in the study area. For example, Fig. 6 shows a rockfall triggered by the Earthquake. The corridor and deposit have blocks ranging from small cobbles to large boulders ~15 m^3 in volume. The blocks were channelized toward the house by a structural fracture. Based on *in situ* observations, the detached rock block lost support during the Earthquake by the formation of a shallow landslide at its base.

Landslide susceptibility assessment is not suitable with a low resolution DTM for small areas and, or with unprocessed

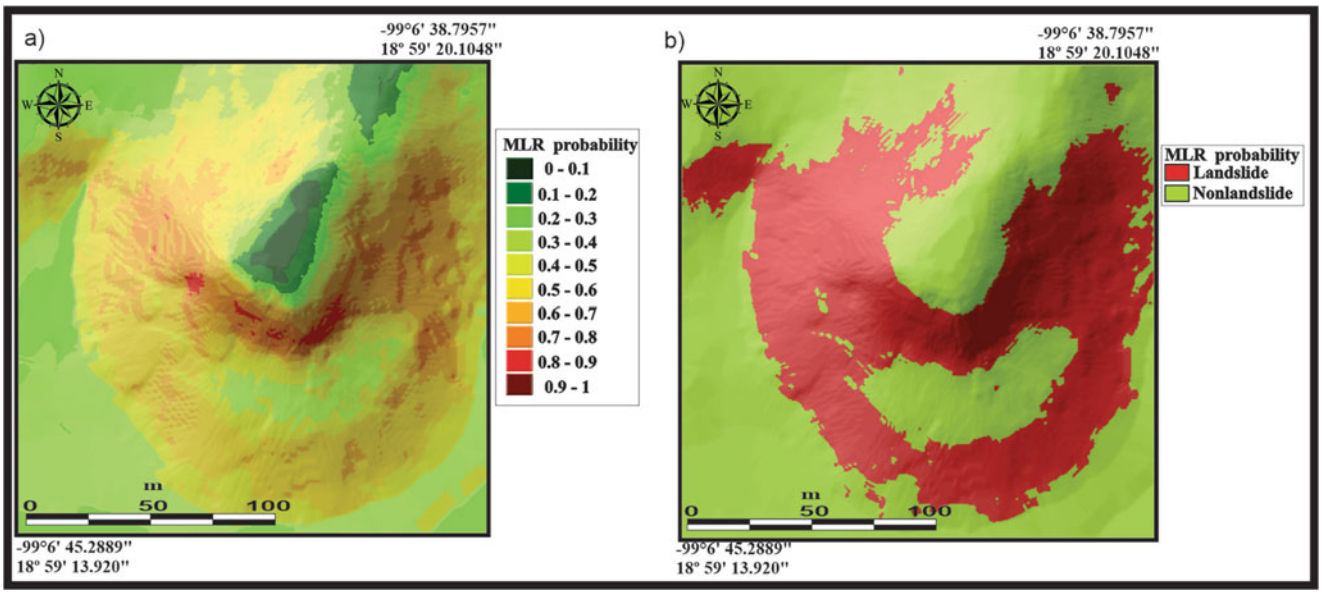

Fig. 7 (**a**) MLR model with a ten-classification scheme. (**b**) MLR model with a two-classification scheme used for inventory vs. model comparison

high-resolution UAV-created DSM. With our method, most landscape elements are considered as non-relevant information, or noise and are eliminated to obtain a fair topographic (bare earth) representation (Fig. 5). The processed moderate-resolution DTM is suitable for modeling landslide susceptibility with MLR. The landslide susceptibility map is categorized into 10 and 2 probability zones for description and evaluation purposes (Fig. 7). The model shows moderate coincidence with observations in the inventory and from the field. The heads of larger triggered boulders are located in non-landslide predicted zones (with probability values between 4.7 to 5). However, shallow landslides at the base of these large boulders were triggered by the Earthquake. High potential probability (>80%) of fall areas are located on the cemented flows of conglomerates with steep walls >35°. In the field it was not possible to detect landslides triggered by the Earthquake in these areas. However, some neighbors have reported damage to their properties by detachments from this wall during the rainy season.

The AUC and overall accuracy (Table 2), also shows moderate performance of the models by using only altimetry and slope variables. The Producer's accuracy shows that the models have >76% of coincidence with the landslide inventory map. The model tends to under-predict as it shows the moderate percentage (>66%) of user's accuracy and low value in the model efficiency.

5 Conclusions

Landslide susceptibility is difficult to model due to the continuous changes in the topography by landslides, land use changes, and environmental conditions in remote volcanic areas with difficult access. Mapping and modeling landslide susceptibility are not suitable with a low-resolution DTM and/or with unprocessed high-resolution DSM created from a UAV. This is because the former has a poor spatial and temporal landslide representation in the topography, while and the latter includes not only the ground topography, but also other landscape elements considered as noise.

This study briefly presents a method that allows landslide specialist and other applier and users to obtain a moderate-resolution DTM from which landslide susceptibility can be evaluated. The implementation of this method at Cerro de la Miel in Tepoztlán is an attempt to produce a standardized procedure for landslide susceptibility studies in the volcanic areas of Mexico that lack high-resolution topographic information. Our method uses and adapts a governmental low-resolution DTM and a high-resolution DSM created from a UAV to obtain the moderate-resolution DSM for landslide modeling.

We emphasize that the starting point for the method is a non-pre-processing ASCII or LAS file, independent of any photogrammetric program treatment. We also acknowledge the technical limitation of using a low-resolution DTM. When a low-resolution DTM is used as a reference for the initial topography, compensations using an heuristic

approach (employing mask selections, weights, and filters) are needed to eliminate most of the noise. In this research, a trade-off between a maximum topography vertical error of ~1.5 m and the selected mask, 4% of weighted, and the use of a low-pass filter was acceptable to model landslide susceptibility.

Landslide susceptibility was modeled by using three topographic variables in MLR model. The model was able to have a moderate success of landslide prediction using only slope and altimetry variables. It will be possible to improve the model if other thematic variables are used. However, in Mexico coverage of those thematic variables are temporally and spatially poor in many remote areas.

Despite these limitations, the programs developed, and analysis presented in this work are the basis of an integral methodology to obtain a UAV-derived DTM, and for slope instability prognosis.

Acknowledgments The authors thank authorities from the International Consortium on Landslides (ICL) and the International Programme on Landslides (IPL) for their approval and help.
This research was supported by the Programa de Apoyo a Proyectos de Investigación e Innovación Tecnológica (PAPIIT), UNAM. # IN100223.

Source Code https://github.com/jfparrot/gullies.git

Declarations of Interest The authors declare no competing interests.

References

Agisoft LLC (2014) Agisoft PhotoScan user manual: professional edition. St Petersburg, Russia: Agisoft LLC. Online: https://www.agisoft.com/pdf/photoscan-pro_1_4_en.pdf. Last Accessed 15 Nov 2022

Anderson K, Gaston KJ (2013) Lightweight unmanned aerial vehicles will revolutionize spatial ecology. Front Ecol Environ 11(3): 138–146

Annis A, Nardi F, Petroselli A, Apollonio C, Arcangeletti E, Tauro F, Grimaldi S (2020) UAV-DEMs for small-scale flood hazard mapping. Water 12(6):1717

Capraro S, Ortiz S, Valencia R (2018) Los efectos económicos de los sismos de septiembre. Accessed March 28, 2019. Online: http://www.economia.unam.mx/assets/pdfs/econinfo/408/02CapraroOrtizValencia.pdf. Last Accessed 15 Nov 2022

Castro-Miguel R Legorreta-Paulín G, Bonifaz-Alfonzo R, Aceves-Quesada J F, Castillo-Santiago M Á (2022) Modeling spatial landslide susceptibility in volcanic terrains through continuous neighborhood spatial analysis and multiple logistic regression in La Ciénega watershed, Nevado de Toluca, Mexico Natural Hazards, 1–22

CLICOM, (2018) Base de datos meteorológica nacional. http://clicom-mex.cicese.mx/ Last Accessed: 15 Nov 2022

Colomina I, Molina P (2014) Unmanned aerial systems for photogrammetry and remote sensing: a review. ISPRS J Photogramm Remote Sens 92:79–97

Comisión Nacional de Áreas Naturales Protegidas (CONANP). Dirección Regional Centro y Eje Neovolcánico, (2017) Opinión sobre la situación que presenta el cerro del Tepozteco y camino de ascenso a la zona arqueológica del mismo cerro, en el municipio de Tepoztlán Morelos, debido al sismo ocurrido el 19 de septiembre de 2017, pp 1–17

Dackombe RV, Gardiner V (1983) Geomorphological field manual. Allen & Unwin, London

Dubbini M, Curzio LI, Campedelli A (2016) Digital elevation models from unmanned aerial vehicle surveys for archaeological interpretation of terrain anomalies: case study of the Roman castrum of Burnum (Croatia). J Archaeol Sci Rep 8:121–134

Escobar-Villanueva J, Parrot JF, Ramírez-Núñez C (2017) Propuesta metodológica para la generación de un DTM a partir de datos provenientes de RPAS, parámetros morfológicos e interpolación multidireccional como apoyo para la simulación de inundaciones en zonas urbanas. Ejemplo de la ciudad de Riohacha. Colombia. Primer Congreso Centroamericano de Ciencias de la Tierra y el Mar. Universidad Nacional, Costa Rica

Field A (2014) Discovering statistics using IBM SPSS. Sage Publications, Thousand Oaks, CA, p 916

Francioni M, Coggan J, Eyre M, Stead D (2018) A combined field/remote sensing approach for characterizing landslide risk in coastal areas. Int J Appl Earth Obs Geoinf 67:79–95

Haneberg WC (2005) New quantitative landslide hazard assessment tools for planners.Landslide hazards and planning. Plan Advis Serv Rep 533/534:76–84

INEGI (1998a) Modelo Digital de Elevación, Escala 1:50,000, México

INEGI (1998b) Carta topográfica Cuernavaca, Escala 1:50,000, México

Jasiewicz J, Stepinski T (2013) Geomorphons—a pattern recognition approach to classification and mapping landforms. Geomorphology 182:147–156

Knight J, Mitchell WA, Rose J (2011) Geomorphological field mapping. In: Developments in earth surface processes, vol 15. Elsevier, Amsterdam, pp 151–187

Legorreta PG, Bursik M (2008) Logisnet: a tool for multimethod, multiple soil layers slope stability analysis. Comput Geosci 35: 1007–1016. https://doi.org/10.1016/j.cageo.2008.04.003

Legorreta PG, Pouget S, Bursik M, Quesada FA, Contreras T (2016) Comparing landslide susceptibility models in the Río El Estado watershed on the SW flank of Pico de Orizaba volcano. Mexico. Natural Hazards 80(1):127–139

Lenhardt N, Böhnel H, Wemmer K, Torres-Alvarado IS, Hornung J, Hinderer M (2010) Petrology, magnetostratigraphy and geochronology of the Miocene volcaniclastic Tepoztlán formation: implications for the initiation of the Transmexican Volcanic Belt (Central Mexico). Bull Volcanol 72(7):817–832

Pallant J (2013) SPSS survival manual: a step by step guide to data analysis using SPSS for windows (version 12). Open University Press, Buckingham, p 319

Parrot JF (2011) Dem_lidar_generation. Módulo ejecutable MS-DOS, Inédito

Parrot JF (2012) Software DEMONIO (Digital Elevation Models Obtained by Numerical Interpolating Operations) Copyright INDA (Instituto Nacional de Derecho de Autor): 03-2012-120612205000-01

Parrot JF (2016) Generación de MDE a partir de datos vectoriales. Paquete de Módulos Ejecutables desarrollados en C++. Copyright INDA (Instituto Nacional de Derecho de Autor): 03-2016-103110072200-01

Parrot JF (2018a) Software Select Slices. Copyright INDA (Instituto Nacional de Derecho de Autor): 03-2018-011109492800-01

Parrot JF (2018b) Shaving, V 1.0, Módulo ejecutable MS-DOS. Inédito

Pix4D (2022) Getting Started - PIX4Dcapture/User manual/Special Install. Website. https://support.pix4d.com/hc/en-us/articles/202557269-Getting-Started-PIX4Dcapture. Last Accessed 15 Nov 2022

Servicio Sismológico Nacional. UNAM (2017) Sismo del día 19 de septiembre de 2017, Puebla-Morelos (M 7.1). http://www.ssn.unam.mx/sismicidad/reportesespeciales/2017/SSNMX_rep_esp_20170919_Puebla-Morelos_M71.pdf) (pdf). Last Accessed 19 Sep 2017

Šiljeg A, Barada M, Marić I, Roland V (2019) The effect of user defined parameters on DTM accuracy – development of hybrid model. Applied Geomatics 11(1):81–96

Sim KB, Lee ML, Wong SY (2022) A review of landslide acceptable risk and tolerable risk. Geoenvironmental Disasters 9(1):1–17

Van Den Eeckhaut M, Poesen J, Verstraeten G, Vanacker V, Moeyersons J, Nyssen J, Van Beek LPH (2005) The effectiveness of hillshade maps and expert knowledge in mapping old deep-seated landslides. Geomorphology 67(3–4):351–363

Use of GIS to Assess Susceptibility per Landform Unit to Gravitational Processes and their Volume

Gabriel Legorreta Paulín, Rocío Marisol Alanís-Anaya, Lilia Arana-Salinas, Jean-François Parrot, and Rutilio Castro-Miguel

Abstract

Landslide susceptibility per landform unit and its potential contribution of material was calculated for a 105 km^2 watershed on the south flank of Pico de Orizaba volcano, Mexico. More than six hundred landslides were mapped and grouped into landform units. Fifteen landform units were derived from fieldwork, aerial photo interpretation, land use, and morphometric parameters. For each landform, landslide susceptibility was calculated from the area and frequency of landslides. Volume calculation used a surface area-volume power law from geometric values of shallow landslides. Support by Geographic Information Systems created a comprehensive method. Although most landslides were in volcanic landform units, those in sedimentary units contributed more sediment per square kilometer. The study shows that landform units can be used to explain the predisposition and variability of landslide sediment production for a large and complex geological watershed.

Keywords

Gravitational processes susceptibility · Landform · Landslide volume · GIS

G. L. Paulín (✉) · J.-F. Parrot
Instituto de Geografía, Universidad Nacional Autónoma de México, Circuito Exterior, Ciudad Universitaria, Ciudad de México, Mexico
e-mail: parrot@igg.unam.mx

R. M. Alanís-Anaya
Colegío de Geografía. Facultad de Filosofía y Letras, Universidad Nacional Autónoma de México, Ciudad de México, Mexico
e-mail: ammonite@ciencias.unam.mx

L. Arana-Salinas
Universidad Autónoma de la Ciudad de México, Colegio de Ciencias y Humanidades, Academia de la Licenciatura Protección Civil y Gestión de Riesgos, Ciudad de México, Mexico

R. Castro-Miguel
Escuela Nacional de Ciencias de la Tierra, Universidad Nacional Autonoma de Mexico, Ciudad Universitaria, Ciudad de Mexico, Mexico
e-mail: rutilio.castro@encit.unam.mx

1 Introduction

In mountainous volcanic terrains, shallow and deep-seated landslides represent a major natural hazard for human settlements and their economic activities (Sim et al. 2022). Such is the case for Pico de Orizaba volcano (5675 m a.s.l.), the highest dormant stratovolcano in Mexico. This study refers in more detail to shallow landslides, including debris flows and debris slides, that affect the Río Chiquito-Barranca del Muerto watershed on the south flank of Pico de Orizaba. In the area, steep slopes, heavy rainfall, and changes in land use from forests to subsistence agriculture contribute to the potential mobilization of landslides and debris flows. This creates a dangerous situation for inhabitants of cities on the southern flanks of the volcano. In 2003 and 2011, landslides delivered material and increased the destructive power of the debris flows, which caused fatalities and disrupted economic activity in Balastrera, a town at the mouth of the watershed (Legorreta-Paulín et al. 2013). Despite the importance of assessing such processes, there are few landslide inventory maps and few evaluations of the sediment budget and sediment availability connected to landslides in the area.

Worldwide studies of susceptibility in an area to gravitational processes (called landslide susceptibility hereinafter) consider the distribution, frequency, and size of landslides in relation to homogeneous areas, called landform units (Washington State Department of Natural Resources, Forest Practices Division 2006; Bachri et al. 2020). The use of these landform units allows a better understanding of landslide susceptibility and the volume of material displaced by a landslide in a watershed with complex geology and geomorphology (Broeckx et al. 2016). Techniques for calculating the landslide volume may be based on the geometric shape of the current physical form of a landslide, and on analytical methods for resolution (Šíma and Seidlová 2014; Tang et al. 2018). The physical form of the landslide and landform units are obtained by using detailed Digital Elevation Models (DEMs) through the use of differential GPS and digital

I. Alcántara-Ayala et al. (eds.), *Progress in Landslide Research and Technology, Volume 2 Issue 1, 2023*,
Progress in Landslide Research and Technology, https://doi.org/10.1007/978-3-031-39012-8_21

cameras, multispectral sensors, Light Detecting and Ranging (LiDAR) instruments and Synthetic Aperture Radars (SAR) carried by airplanes or unmanned aerial vehicles (UAVs) (Young 2015; Ray et al. 2020). To determine the volume of landslide materials in large, affected areas, empirical relationships are established by use of a power-law function that links geometric measurements of landslide area to landslide volume (Guzzetti et al. 2009; Wenkey et al. 2011).

In Mexico, few works refer to landslide susceptibility per landform unit (Legorreta-Paulín et al. 2014; Alanis-Anaya 2017) and landslide volume (Muñoz-Salinas et al. 2009; Legorreta-Paulín et al. 2017). For Pico de Orizaba, a map of landslide susceptibility within the watershed was created by use of multiple logistic regression (MLR), SINMAP, and multicriteria evaluation (Legorreta-Paulín et al. 2016). To address landslide sediment production per landform unit with more detail than previous works, we improve the landslide inventory map and the geomorphologic landforms. The study divides the watershed into 15 geomorphologic landform units. Each landform unit is derived by aerial photo interpretation, geological fieldwork, land use, and morphometric parameters (hypsometry, drainage density, vertical erosion, and slope). For each landform unit, the area and the spatial-temporal distribution of landslides are used to determine the landslide susceptibility.

The landslide geometry and volume of a representative sample of landslides are obtained by a UAV to establish a power law model for volume calculation.

2 Study Area

The study area lies on the south flank of the volcano Pico de Orizaba, which rises at the junction of Puebla and Veracruz states (Fig. 1a). Pico de Orizaba is a dormant stratovolcano in the eastern part of the Neogene-Quaternary Transmexican Volcanic Belt physiographic province (Macías 2005). Its lavas, pyroclastic flows, and fall deposits are affected by hydrothermal alteration and they overlie a weathered and highly dissected, folded and faulted, Cretaceous basement of limestone and shale. This geological setting could potentially trigger shallow landslides (Concha-Dimas et al. 2005). The present study refers in more detail to the Rio Chiquito-Barranca del Muerto watershed on the south flank of Pico de Orizaba and to shallow landslides triggered by rain events. The area covers approximately 105 km^2 of rugged terrain, ranging from 1280 to 5675 m a.s.l, and with the slope angle generally increasing with elevation (from ~5° to ~65°). Rio Chiquito-Barranca del Muerto is a fourth-order watershed (Strahler's method) with a radial sub-parallel and dendritic pattern which flows into the Gulf of Mexico. Andesitic and dacitic Tertiary and Quaternary volcanic rocks form the main rock types in the study area followed by Cretaceous limestone and shales. Sedimentary landform units represent almost 30% of the total watershed area. Rainfall in the study area is concentrated mainly from May to November. The maximum mean annual rainfall in a period of ~20 years is ~1100 mm, mostly concentrated in the mountain area at >4000 m a.s.l. The minimum precipitation is recorded in the lower parts of the watershed where annual rainfall is ~927 mm/yr. (CLICOM 2014). The study area is naturally prone to landslides due to the erosive effects of high precipitation on steep and weathered volcanic and sedimentary terrains, exacerbated by deforestation and agricultural activities. Within a period of nine years (2003 to 2012) changes in land use have been significant. Forested areas (2.64 km^2) have been lost in favor of urban, pastural, and agricultural areas. Deforestation and modification of the slopes in favor of human activities have left the main river and its tributaries with a buffer of only 50 –100 m of forest along the hillsides (Alanis-Anaya 2017). Such massive destruction of the forest has accelerated erosive and gravitational processes in sedimentary and volcanic deposits.

3 Method

We obtained the landslide susceptibility and landslide volume per geomorphologic landform unit in the study area by the following four steps:

Step 1: Incidence of gravitational processes was mapped; the inventory was obtained through compiling data from an existing landslide geo-database and with a landslide map that identified 442 gravitational processes (Legorreta-Paulín et al. 2013). This landslide inventory map uses the Landslide Hazard Zonation Protocol (LHZP) (Washington State Department of Natural Resources, Forest Practices Division 2006) to classify landslides into shallow landslides, debris flows, debris slide flows, deep-seated landslides, earthflows, and rockfalls. The same approach was followed to develop a new landslide inventory (Fig. 1b). It incorporates 165 newly identified landslides mapped on the basis of analog aerial photographs (scale 1:20,000 from 1994 and 1: 10,000 from 2008) and panchromatic SPOT satellite imagery (from 2003 and 2012), and by local field surveys. Landslide head scarp, evacuation zone, and deposit (these last two were not always visible) were mapped into the GIS. The interpretation with aerial photographs for landslide mapping was aided by field work. Three sessions of field work per year were conducted from 2012 to 2017 along the main and secondary rivers, for data validation, landslide and landform mapping, verification, and landslide volume measurements. For the mapping, landslides that were substantially reforested and estimated to have been covered by vegetation for more

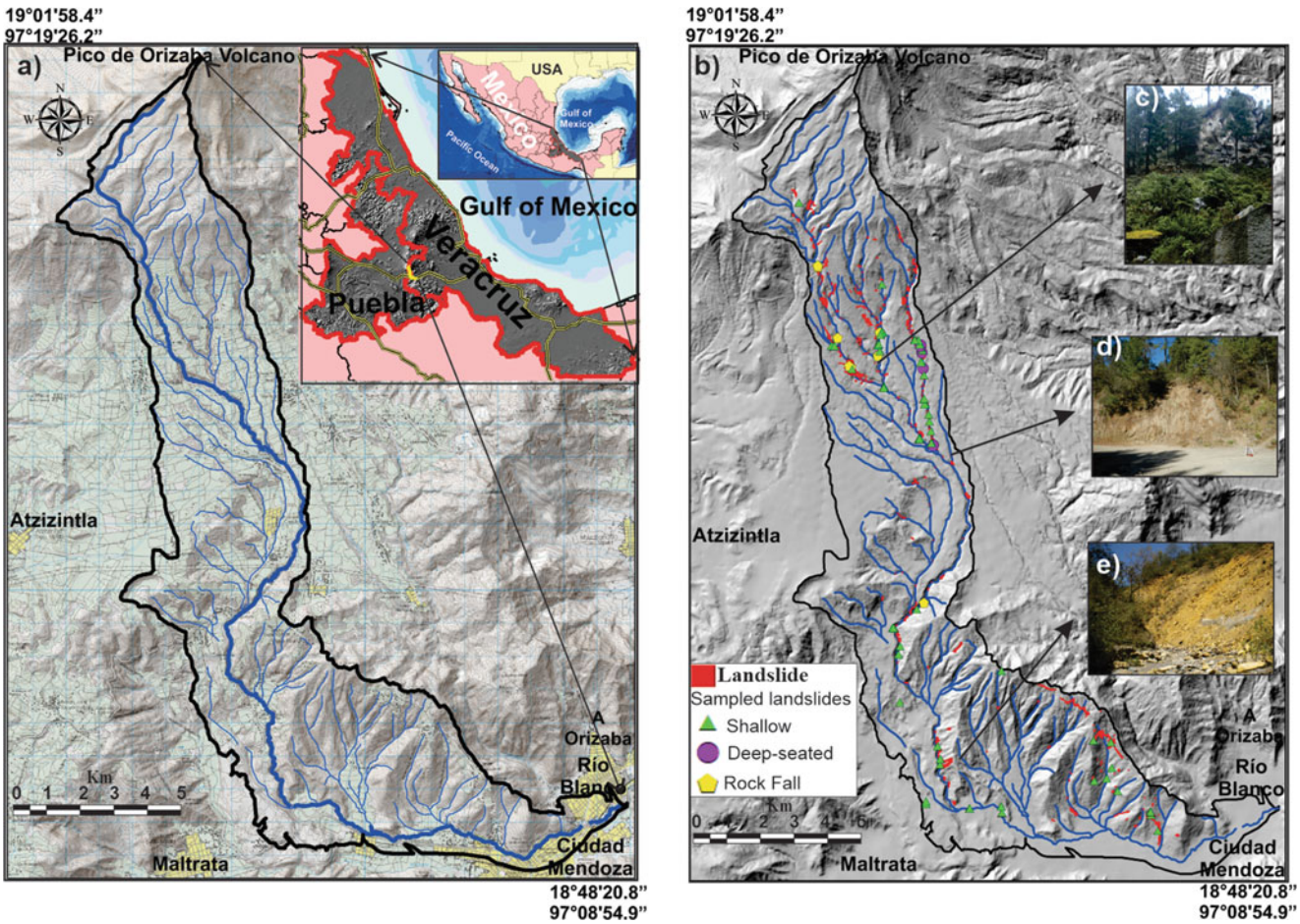

Fig. 1 (**a**) Río Chiquito-Barranca del Muerto study area; (**b**) Landslide inventory map and the 61 sampled landslides; (**c**) Rockfalls along a lava flow front; (**d**) Debris slide on volcanic terrain; (**e**) Debris slide on sedimentary terrain

than 22 years (the span of this study, from the 1994 aerial photographs to 2016) were not included in the inventory or in the evaluation of volume.

Step 2: A landform map was produced; the landform units map was the result of combination and interpretation of thematic maps according to geomorphological criteria and field evaluation (Demeck 1972). The method for mapping landform units was defined by geomorphologic rules adopted by the WSDNR to address landslide hazards (Washington State Department of Natural Resources, Forest Practices Division 2006) and adapted after Legorreta-Paulín et al. (2014). To define landform units, we used more specific criteria that included photointerpretation, field geology, land use, hypsometry, slope, drainage density, and the vertical erosion (Fig. 2). Drainage density was calculated by dividing the study area into 1 km^2 grids, and the total talweg length was obtained for each square kilometer. Vertical erosion was calculated by dividing the study area into 1 km^2 grids, and the maximum vertical distance was obtained for each square kilometer. The values obtained were interpolated (Zamorano-Orozco 1990; Lugo-Hubp 1991). Field recognition with ninety-six control points per landform unit was used to verify the units.

Step 3: A landform units susceptibility map was produced; to produce a landslide susceptibility map we followed the LHZP of WSDNR (Washington State Department of Natural Resources, Forest Practices Division 2006). The guidelines of the LHZP are based on a semiquantitative approach to determine the landslide susceptibility in each landform unit. First, the number of landslides and their accumulative area in acres per landform unit was obtained by using the GIS landslide inventory map. Both values, the number of landslides and their cumulative area per landform unit were divided by the period of time spanned in the study (in our case 22 years), and the landform unit area. These values were then heuristically multiplied by one million and rounded for easier interpretation (Powell 2007) to obtain the landslide frequency rate (LFR) and the landslide area rate (LAR). The LFR represents the number of landslide events registered in the reference landform unit in a time period, and the LAR represents the spatial area impacted by landslides in the reference landform unit in a time period. After the LFR and

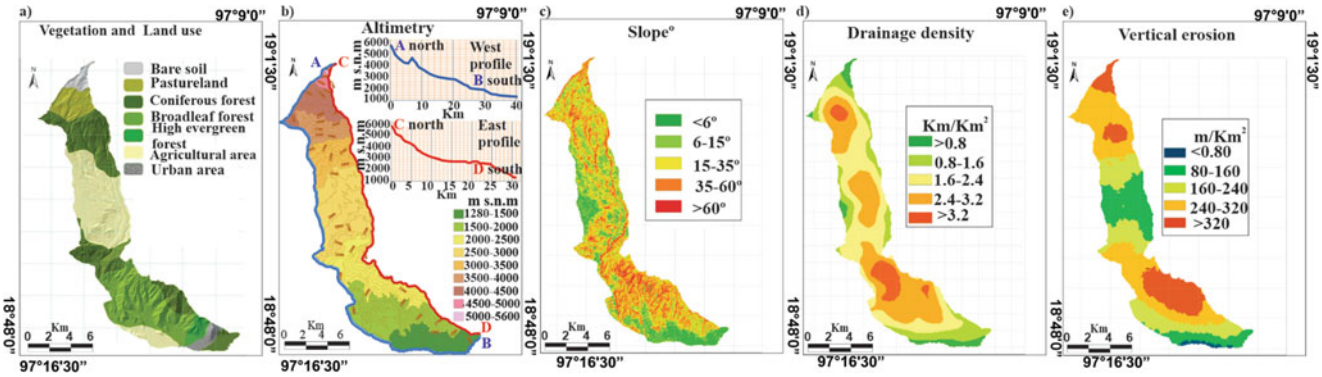

Fig. 2 (**a**) Vegetation and land use map; (**b**) Altimetric map; (**c**) Slope map; (**d**) Drainage density; (**e**) Vertical erosion

LAR values had been determined, each was classified into Low, Moderate, High or Very High rating (Table 1). The qualitative LFR and LAR values were then entered into a matrix (Table 2) in order to determine the overall susceptibility rating for each landform (Washington State Department of Natural Resources, Forest Practices Division 2006). For instance, the landform known as the pyroclastic ramp unit has a LFR value of 815 (15 landslides/815 acres/22 years * 1000000) and a LAR value of 258 (4.6 acres/815 acres/22 years * 1000000). Each of these values is classified as High (Table 1). According to the juxtaposition of these two qualitative values into Table 2, this landform has a high landslide susceptibility.

For the landslide susceptibility analysis, the fluvial valley landform unit is not taken into account because this landform unit is contained in the remaining 14 landform units. Instead, the area of fluvial valleys that affects each landform unit is given in the Results section.

Step 4: We estimated the landslide volume per unit. Sixty-one landslides (~10%) from the new landslide inventory (encompassing 607 landslides) were verified in the field for calculation of their area and volume. The area and volume of the landslide head scarp were measured with a UAV. We excluded the volume and area of the deposits and the slip evacuation area. Geometrical measurement of the 61 landslides used a Phantom 4 Pro quadcopter with a camera with 20 megapixels resolution and a CMOS sensor of 1″. Flight planning used the Pix4D capture program. Aerial images were acquired with an average flight height of 100 m and at a speed of 1.5 m/s. The front and side overlaps between aerial photographs was 80%. To georeference the photographs during the post-processing, the cost and effort required to establish GPS ground control points in remote areas with difficult access restricted our use of these points to between 1 (90% of the sampled landslides) and 4 (one at each extreme corner of the landslides).

The post-processing of the images used Agisoft PhotoScan photogrammetric software. We followed a standard post-processing work flow adapted after Ouédraogo et al. (2014). The work flow in PhotoScan was as follows. (1) Selection and addition of all captured photos for each landslide. (2) Alignment of the loaded aerial photographs. (3) Addition of markers that represent GCP. (4) Construction of a cloud of dense point values. (5) Reclassification of the dense point cloud values into ground and the other elements (vegetation, buildings etc.). (6) Creation of a DEM, and (7) Creation of an orthophotograph. DEMs at 50 cm per pixel were obtained.

In ArcMap, the post-sliding topography and the reconstructed pre-sliding topography were created. This pre-sliding topography was set heuristically by field observation and reconstruction of the original topography from the post-sliding topography generated by the UAV. The nodes from polygons that represent the current landslide headscarp boundary were used to create a point file which in turn was used to extract the elevation data from the DEM for the topography of the landslide. The nodes were interpolated to create the interpolated pre-sliding topography. No internal topographic relics were observed in the field that could be used to improve representation. It was considered that the reconstructed pre-sliding topography in general gives an adequate representation of topographic geometry, subsequently modified to varying degrees by gravitational and erosive processes. If exogenous forms such as valleys or sliding surfaces were removed from the topographic map, an approximation to the original relief could be obtained by interpolations (Lugo-Hubp 1991).

Table 1 Qualitative rating for the landslide frequency and landslide area rates

	Low	Moderate	High	Very high
LFR	<100	100 to 199	200 to 999	>999
LAR	<76	76 to 150	151 to 799	>799

Table 2 Classification for overall landslide susceptibility based on LFR and LAR

Overall landslide susceptibility per landform unit		Landslide Frequency Rate			
		Low	Moderate	High	Very High
Landslide area rate	Low	Low	Low	Low	Low
	Moderate	Low	Low	Moderate	High
	High	Moderate	High	High	Very high
	Very high	High	High	Very high	Very high

The landslide volume was calculated from the algebraic difference between the reconstructed pre-sliding topography and the actual topography (Fig. 3), multiplied by the area of the pixel.

Selection for sampling landslides was based on field reconnaissance of the landslide process and the accessibility to the sites. Data limitation included lack of sampling; also, statistical validity was precluded by the wide dispersion in a scatter plot of area against volume for deep-seated landslides (only 48% (R^2) of the volume was explained by the area of landslides). Owing to such limitations, the empirical relationship between area and volume was calculated only for shallow landslides (51 of the 61 sampled landslides). From these 51 shallow landslides (including debris flows and debris slides), a validation subsample of 10 was used to test the power law model. The remaining 41 shallow landslides with narrow scatter plot dispersion (97% (R^2) of the volume is explained by the area of landslides) were used to determine the empirical relationship. The area (A) and volume (V) of these 41 shallow landslides were used to determine a power law of $V = 0.93239514 * A^{1.0480}$. With the landslide inventory map and related geo-database, the planimetric area of the remaining 465 shallow landslides was obtained. The planimetric area was the input for the empirical relationship area-volume in the power law. Finally, we added the calculated volumes of all shallow landslides to estimate the potential total volume that landslides can contribute per landform unit to the stream system.

4 Results

The 607 landslides in the inventory could be assigned to 6 types: 295 shallow landslides (48.6%), 126 debris flows (20.8%), 85 debris slides (14%), 77 rockfalls (12.7%), 19 deep-seated landslides (3.1%), and 5 earthflows (0.8%). In this watershed, the abundance and types of landslides are determined by geomorphological conditions in conjunction with land use change: 405 (66.7%) are in volcanic terrain from which 249 (61.48%) landslides are located in pyroclastic deposits where the land use has changed from forest activities to agriculture and 202 (33.3%) are in sedimentary terrain (mostly in folded and faulted Cretaceous limestones covered by broad-leaf and coniferous forest); of the 202 landslides in the sedimentary soils, 123 (60.9%) are in areas that have experienced land use changes.

During the assessment of the watershed, 15 homogeneous landform units were identified as well as the landslide susceptibility associated with each one and their contribution in terms of volume (Fig. 4 and Table 3). These landform units are:

1. The relict of volcanic collapse. This is an eroded, fractured, and weathered andesitic collapse structure of the ancestral Pico de Orizaba volcano (0.25 Ma) (Höskuldsson 1992; Macías 2005). No landslides have been mapped in this landform unit. It is not affected by the fluvial valley landform unit since it has high permeability.

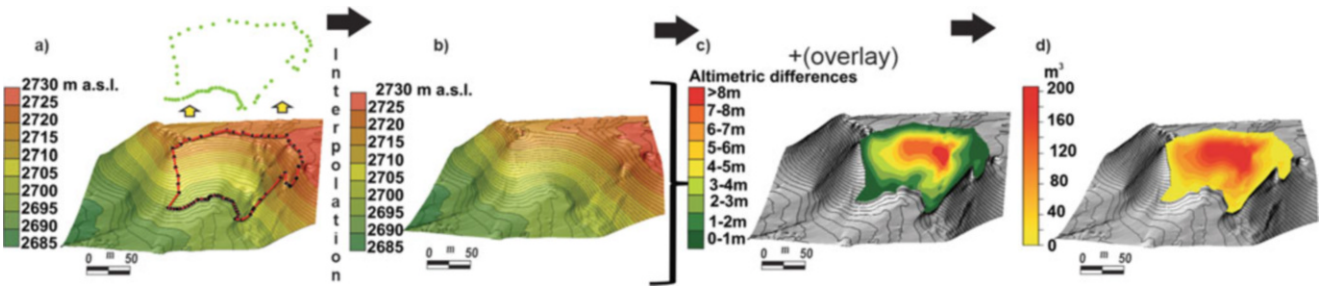

Fig. 3 General procedure to create the DEM and calculate the landslide volume. (**a**) DEM generated with the UAV topographic survey of a landslide. From the inventory map, the headscarp polygon is extracted and overlaid to the DEM (red line). Then the nodes (black dots) from the polygon are extracted to create a point shapefile (green dots) which in turn is used to obtain the elevation data from the DEM. (**b**) DEM of the reconstructed pre-sliding topography generated by interpolation of point shapefile. (**c**) Altimetric changes between pre- and post-sliding surfaces. (**d**) Landslide volume map. The landslide altimetric change is then multiplied by the pixel size to derive the volume

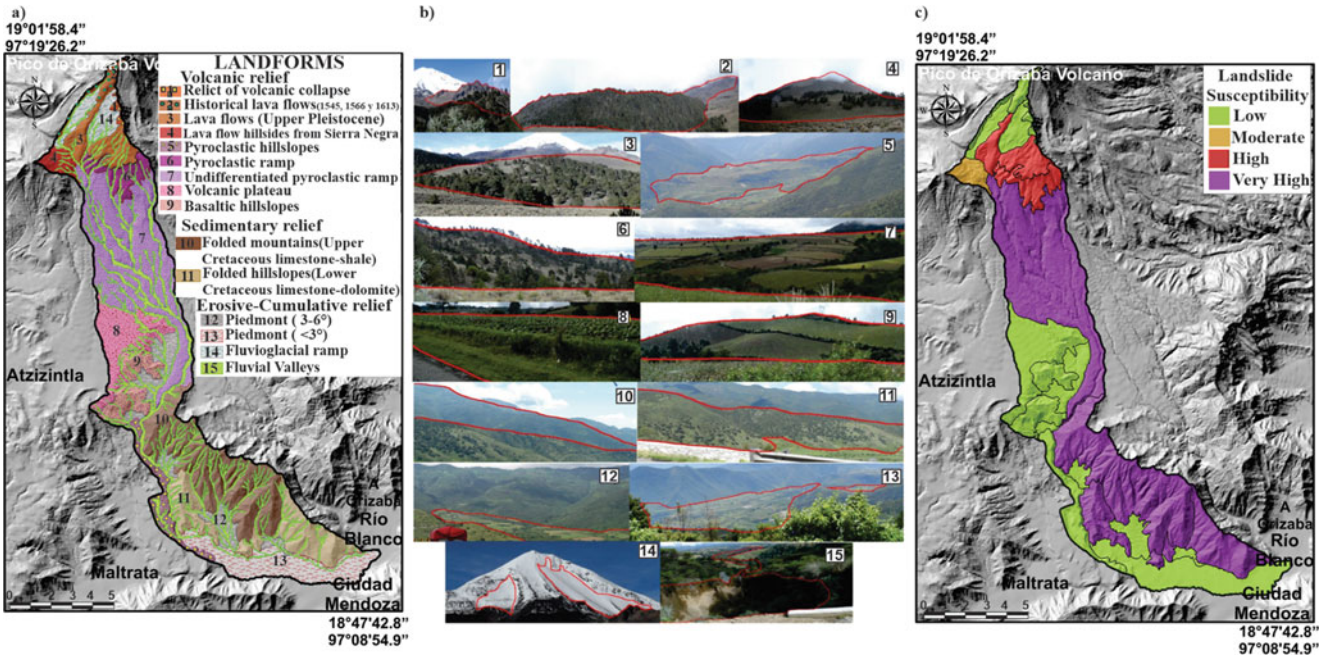

Fig. 4 (**a**) Landform units distribution; (**b**) Example of landform units; (**c**) Landslide susceptibility per landform unit

Table 3 Characteristics of landform units

Landform unit	Landslide susceptibility	Total area of landform unit (km^2)	No. of landslides in landform	Landslide area (m^2)	Volume delivered by landslides in landform (m^3)	Landslide density (per km^2)	Volume density (m^3/km^2)
1. Relict of volcanic collapse	Low	0.4	0	0	0	0	0
2. Historical lava flows (1545, 1566 and 1613)	Low	1.5	0	0	0	0	0
3. Lava flows (upper Pleistocene)	High	4.7	13	21537.7	30092.5	2.8	6430.0
4. Lava flow hillsides from sierra Negra (Pleistocene)	Moderate	1.8	2	3378.6	4531.7	1.1	2555.5
5. Pyroclastic hillslopes	Low	4.0	0	0	0	0	0
6. Pyroclastic ramp	High	3.3	15	18724.8	25126.3	4.6	7675.1
7. Undifferentiated pyroclastic ramp	Very high	25.8	356	389303.2	550369.2	13.8	21322.8
8. Volcanic plateau	Low	8.1	12	9860.7	13335.0	1.5	1653.2
9. Basaltic hillslopes	Low	4.9	7	3573.2	4654.4	1.4	950.3
10. Folded mountains (upper cretaceous limestone-shale)	Very high	19.5	111	99673.7	134936.7	5.7	6921.0
11. Folded hillslopes (lower cretaceous limestone-dolomite)	Very high	11.2	91	192000.8	274908.4	8.1	24572.9
12. Piedmont (3–6°)	Low	6.7	0	0	0	0	0
13. Piedmont (<3°)	Low	10.1	0	0	0	0	0
14. Fluvioglacial ramp	Low	3.6	0	0	0	0	0
Totals		105.4	607	738052.6	1037954.2		

2. The historical lava flows (1545, 1566 and 1613). These andesitic and dacitic lava flows are associated with the end of the effusive period of the present Pico de Orizaba volcano (Höskuldsson 1992; Macías 2005). No landslides have been mapped in this landform unit. Seasonal fluvial valleys affect 3.4% of its area.
3. The lava flows (Upper Pleistocene). These andesitic and dacitic lava flows (0.09–0.15 Ma) are associated with the second constructional stage of Pico de Orizaba volcano (Höskuldsson 1992; Macías 2005). This unit includes 2.1% of the mapped landslides, which contribute 2.9% of the sediments that are delivered to the stream system. The fluvial landform unit dissects this unit and covers 11.4% of its area. Five of its 13 landslides are along the stream system.
4. The lava flow hillsides from Sierra Negra (Pleistocene) are andesitic and dacitic lava flows from the Sierra Negra volcano. These flows were emplaced before those of the ancestral Pico de Orizaba volcano (Höskuldsson 1992; Macías 2005). This unit includes 0.3% of the mapped landslides, which contribute 0.4% of the sediments delivered to the stream system. The fluvial landform unit dissects this unit and covers 11.4% of its area. Of the two landslides in this unit, one lies along the stream system.
5. The pyroclastic hillslopes unit is correlated with the eruptive sequence of ash and blocks from Loma Grande (8200 ± 120 yr. B.P.) that have been re-deposited along the highest regions of the watershed (Höskuldsson 1992; Macías 2005). No landslides have been mapped in this landform unit. Fluvial valleys affect 20.9% of its area.
6. The pyroclastic ramp landform unit is a volcanic depositional surface with slope less than 15° (Lugo-Hubp 2011). The unit is formed by andesitic-basaltic lava that is overlaid by andesitic blocks, lava, breccia, lahars, and tephra (Lower Pleistocene) (Höskuldsson 1992; Macías 2005). It includes 2.5% of the mapped landslides, which contribute 2.4% of the sediments delivered to the stream system. The fluvial landform unit dissects this unit and covers 14.1% of its area. Five of its 15 landslides are along the stream system.
7. The undifferentiated pyroclastic ramp landform unit is formed by diverse deposits (pyroclastic, scoria, and pumice flows) originating from the successive eruptive phases of Pico de Orizaba volcano (Höskuldsson 1992; Macías 2005). This landform unit includes 58.6% of the mapped landslides, which contribute 53% of the sediments delivered to the stream system. The fluvial landform unit dissects this unit and covers 18.3% of its area. Of its 356 landslides, 266 are along the stream system.
8. The volcanic plateau landform unit is formed by a sequence of pyroclastic flows with andesitic-dacitic blocks and ashes dated between the years 1860 and 1910 (Höskuldsson 1992; Macías 2005). It includes 2% of the mapped landslides, which contribute 1.3% of the sediments delivered to the stream system. The fluvial landform unit dissects this unit and covers 10.9% of its area. Ten of its 12 landslides are along the stream system.
9. The basaltic hillslopes landform unit is formed by a sequence of Pliocene and Early Pleistocene basaltic lava flows associated with small cinder cones (Höskuldsson 1992; Macías 2005). It includes 1.2% of the mapped landslides, which contribute 0.4% of the sediments delivered to the stream system. The fluvial landform unit dissects this unit and covers 10.8% of its area. Six of its 7 landslides are along the stream system.
10. The folded mountains (Upper Cretaceous limestone-shale) landform unit is formed by a sequence of limestones and shales that were formed from Upper Cretaceous reefs (Höskuldsson 1992; Macías 2005; Alanis-Anaya 2017). It includes 18.3% of the mapped landslides, which contribute 13.9% of the sediments delivered to the stream system. The fluvial landform unit dissects this unit and covers 13% of its area. Of its 111 landslides, 41 are along the stream system.
11. The folded hillslopes (Lower Cretaceous limestone-dolomite) unit comprises a sequence of limestones and dolomite that were formed from the Lower Cretaceous reefs (Höskuldsson 1992; Macías 2005; Alanis-Anaya 2017). It includes 15% of the mapped landslides, which contribute 26.5% of the sediments delivered to the stream system. The fluvial landform unit cuts across this unit and covers 11% of its area. Of its 91 landslides, 19 are along the stream system.
12. The piedmont (3–6°) comprises a sequence of reworked deposits along the base of the highest region of the watershed. No landslide has been mapped in this landform unit. The fluvial landform unit cuts across this unit and covers 23% of its area (Alanis-Anaya 2017).
13. The piedmont (<3°) comprises a sequence of reworked sedimentary and volcanic deposits along the base of the highest region of the watershed. No landslide has been mapped in this landform unit. The fluvial landform unit cuts across this unit and covers 6.1% of its area (Alanis-Anaya 2017).
14. The fluvioglacial ramp unit comprises a sequence of moraine and reworked fluvial deposits. No landslide has been mapped in this landform unit. The fluvial landform unit cuts across this unit and covers 13.3% of its area (Alanis-Anaya 2017).
15. The fluvial valleys unit is distributed throughout the watershed and is found in 13 of the other 14 landform

units (Fig. 4a, b). It is characterized by intermittent rivers with a dendritic pattern that form fluvial deposits. This landform unit covers an area of 14.78 km^2. If it had been taken into account for the landslide susceptibility analysis, the landform would have shown very high landslide susceptibility. The landform unit would cover 14% of the watershed area and would include 58.2% (353) of the mapped landslides, which would contribute 48.7% of the sediments. This landform unit is seriously affected by logging, leaving a small buffer of 50—100 m of vegetation along the hillsides (Alanis-Anaya 2017).

Landslide susceptibility is very high for one volcanic and two sedimentary landform units (Fig. 4c, Table 3). Volcanic landform units cover 54.4 km^2, of which 47.4% has very high landslide susceptibility (undifferentiated pyroclastic ramp), 14.6% has high susceptibility, 3.3% has moderate susceptibility, and 34.7% has low susceptibility. The remaining 51 km^2 is covered by sedimentary landform units; of this area, 60.2% has very high landslide susceptibility and the remaining 39.8% has low susceptibility.

Dispersion of data in the scatter plot shows that 97.8% (R^2) of the volume is explained by the area for shallow landslides, whereas only 48.1% (R^2) is explained for deep-seated landslides. That leads to a potential total shallow landslide volume of 1,037,954.2 m^3.

5 Discussion

The present study shows that in the study area, some two-thirds of landslides occur in volcanic terrain, and that instability is highest in steep sedimentary followed by steep volcanic hills and valleys. These results agree with landslide distribution and landslide susceptibility tendencies reported with more quantitative techniques (e.g. Legorreta-Paulín et al. 2013). The present study defines 15 landform units to represent volcanic and sedimentary landscape units. Our analysis shows that one volcanic landform unit and two sedimentary units contribute the most sediment per square kilometer and have the highest landslide susceptibility. Among the landforms, the fluvial valley unit covers 14% of the watershed and encompasses more than one-half of the landslides. However, since this landform unit is embedded in the other landform units, it is not taken into account for the landslide susceptibility analysis. Also, the result suggests that the combined effect of land use changes, the geological and geomorphological conditions, and the size of the study area covered by very highly susceptible landform units can explain the predisposition and variability of landslide sediment production. For example, among the sedimentary terrains, the folded mountains (Upper Cretaceous limestone-shale) and the folded hillslopes (Lower Cretaceous limestone-dolomite) units had the highest landslide susceptibility. Both have high-density drainage, vertical erosion, and clay-rich soils, but there is a difference in the amount of sediment delivered, due in part to having been exposed to different lengths of weathering conditions. This is reflected in the fact that 26.5% of the sediments delivered to the stream system come from the folded hillslopes unit compared to 13.9% of the sediments delivered from the folded mountain landform unit. Another example is the undifferentiated pyroclastic ramp landform unit. In Table 3, the landslide density (ratio between number of landslides and the landform area) shows that this landform unit has the highest number of landslides per kilometer (13.8). This landform unit, originally covered by forest, has fertile weathered and unconsolidated soils that have favored a change to large agricultural areas; however, unsuitable treatment of the remaining forest has triggered the high incidence of gravitational processes and erosion. The volume density or normalized volume (ratio between volume delivered by landslides and the landform area) shows that this landform unit contributes 29.6% of the total volume of sediments in the watershed, or 21,322.8 m^3/km^2; of this contribution, almost 75% is derived from landslides along the fluvial valley that cuts across this pyroclastic ramp landform. Even though the area of the undifferentiated pyroclastic ramp is ~4 and 2 times larger than that of the sedimentary Cretaceous mountains and hillslopes respectively, the sedimentary units rival the volcanic areas in number of landslides per square kilometer. The contribution of sediments from the folded hillslopes (Lower Cretaceous limestone-dolomite) unit is the highest in the watershed (24,572.9 m^3/km^2 or 34.1%), and the folded Cretaceous mountains (Lower Cretaceous limestone-shale) unit contributes 6921 m^3/km^2 or 9.6%; hence, the sedimentary landform units contribute 43.7% of the sediments by volume whereas the volcanic landform units contribute 56.3%.

It is stressed that calculated sediments delivered per landform unit reflect only a potential sediment volume, because not all of them are incorporated into the streams in one event. During fieldwork, it was observed that some landslide deposits were eroded by more than one subsequent rainfall event. Displacement distance and volume storage is determined by local conditions of precipitation, stream slope, landslide volume, and junction angle. Although local conditions are not considered in this analysis, it is observed that in volcanic landforms at high elevations (>4000 m a.s.l,) with steep topography and resistant materials (volcanic plateau landform and basaltic hillslopes landform unit) the small first-order streams have larger junction angles (>65°); as the vertical erosion decreases, streams are nearly parallel downstream with small junction angles. Streams along volcanic landforms have a sub-parallel pattern that cuts deep into loose material across lithologic contacts with a N-S slope trend. In

these volcanic areas, landslide deposits are remobilized more frequently. Along the folded Cretaceous sedimentary units, streams show a dendritic NE-SW pattern that may follow fractures parallel to normal faults that affect Cretaceous rocks (Concha-Dimas et al. 2005).

Our analyses also reveal that although no landslides were mapped in 5 volcanic and 3 sedimentary landform units, some units have the potential to develop shallow landslides, deep-seated landslides, and rockfalls due to their steep gradients and loose weathered material.

Although there is a more generic and rapid approach to the definition and classification of landform units based on hillslope gradient and shape, rock type, and landslide density (Washington State Department of Natural Resources, Forest Practices Division 2006; Legorreta-Paulín et al. 2014), the geomorphological method used here was preferable; its focus on geomorphological detail allowed specific volcanic and sedimentary terrains of Pico de Orizaba volcano to be characterized.

We acknowledge that the production of morphometric maps is time consuming and requires expert knowledge in geomorphology. Also, that the subjective evaluation of field conditions by the researcher will influence the delineation of landform borders. Nevertheless, the resulting landslide susceptibility classes allow comparison between landforms because their semi-quantitative value is normalized by the landform size. The landform units and the susceptibility classification can also be related with the volume delivered and may be useful in the quantification, assessment, and modeling of debris flows in the near future.

In this study, geometry and volume of 61 landslides were determined by fieldwork and use of a UAV. These measurements made it possible to establish an empirical area-volume relationship, expressed as a power law to calculate the volume of landslides for the entire landslide inventory.

The power law obtained is in general agreement with existing relationships published in the literature (Martin et al. 2012; Guzzetti et al. 2009); however, several caveats and practical challenges need to be considered for further studies. First, generation of the DEMs used terrain data collected from the UAV that were not error free. Few GCPs were obtained for georeferencing photographs, and this is a source of potential errors in the volume calculation. Topographic displacement errors could lead to miscalculation of volumes, especially for long-term landslide studies where the post-sliding and pre-sliding topography are surveyed in the field. In our case the pre-sliding topography was derived (reconstructed) exclusively from the post-sliding topography and not from two specific periods of time. This decreases the potential topographic displacement. The power law relationship was used to calculate the volume of the 465 landslides not selected for field measurements. The total landslide volume was calculated for each landform unit (excluding the fluvial valley landform unit) and for the entire watershed (Table 3 and Fig. 4c). Overall, the landslides represented a potential contribution of 1,037,954.2 m^3 of material to the main valley. The validation subsample shows that the calculated power law sub-predicts the total volume by 2.3%. On the other hand, use of the 61 sampled landslides (including deep-seated and rockfall) obtains a power law of $V = 0.70242506 * A^{1.1263}$, and this leads to a total volume of 1,547,656.6 m^3; however, owing to the high dispersion of data in the scatter plot, only 48.1% (R^2) of the volume is explained by the area of landslides. Our study is in agreement with Broeckx et al. (2016) in showing a significant correlation between landslide sediment production and landslide susceptibility. However, we consider that the landslide volume calculation underpredicts the volumes delivered because the power law was calculated and applied only for shallow landslides and it does not include deep-seated slides, rockfalls, and earthflows or potential landslide areas predicted by a model (e.g. MLR model); hence, the calculated volume of sediment is well below the total potential volume that landslides can deliver to the main stream in extraordinary precipitation events. This is in agreement with previous work that shows that the relation area-volume differs significantly for very large landslides (Martin et al. 2012; Guzzetti et al. 2009). A large number of samples of rockfalls, deep-seated slides and earthflows are needed to improve the power law and decrease the sub-prediction of landslide volumes.

6 Conclusions

For large, remote watersheds that are difficult to reach, it is difficult to model landslide susceptibility and the potential volume of material that gravitational processes can deliver, since the topography is continuously undergoing change by landslides, local land use, and environmental conditions. The main aim of this study was to model and assess landslide susceptibility and landslide volume in terms of landform units. The approach uses and adapts the LHZP of WSDNR to map landslides, and to define landform units. It also uses aerial photographs and DEMs acquired with UAV surveys and geomorphological evaluation to establish the post-sliding and reconstructed pre-sliding topography of shallow landslides, from which a power law is established to calculate potential total landslide volume.

The results indicate that the landform units and the susceptibility classification can be related with the landslide volume delivered and may be useful in the quantification, assessment, and modeling of landslides and debris flows in the future. The homogeneous units allow comparison of the

intensity with which they trigger landslide sediment production.

In addition, these analyses have demonstrated how the predisposition of certain areas to shallow landslides has been influenced by geological, geomorphological, and anthropic conditions. The most susceptible areas were, in fact, located in 3 of the 15 landform units that encompassed 79.9% of the watershed area. Although volcanic landform units accounted for 2/3 of the landslides that contributed with 56.3% of volume, the Folded Cretaceous Hillslopes (Cretaceous limestone) landform contributes the most in the watershed (34.1%). However, a large number of landslides will need to be sampled in future work to fine-tune the power law calculation for shallow landslides. Another power law may need to be calculated for the potential landslide volume from other types of landslides. Regardless of drawbacks and limitations, the use of specific landform units allows a better understanding of landslide susceptibility and the potential sediment delivery from landslides in a watershed. While small-scale maps and high-resolution topographic data from LiDAR remain limited for remote areas, the use of UAV and photogrammetric programs for the generation of DEMs and the calculation of landslide volumes are options. Despite the above-mentioned caveats and practical challenges, the study of potential minimum landslide volume per landform unit presented here forms the basis of an integral methodology to estimate landslide sediment production in areas of Mexico that lack of high-resolution topographic information.

Acknowledgments The authors thank authorities from the International Consortium on Landslides (ICL) and the International Programme on Landslides (IPL) for their approval and help. This research was supported by the Programa de Apoyo a Proyectos de Investigación e Innovación Tecnológica (PAPIIT), UNAM, #IN100223.

Declarations of Interest The authors declare no competing interests.

References

Alanis-Anaya RM (2017) Influencia del cambio de uso de suelo en la inestabilidad de la ladera en la subcuenca del Río Chiquito-Barranca del Muerto, volcán Pico de Orizaba. Tesis. Facultad de Filosofía y Letras, UNAM

Bachri S, Shrestha RP, Yulianto F, Sumarmi S, Utomo KSB, Aldianto YE (2020) Mapping landform and landslide susceptibility using remote sensing, gis and field observation in the southern cross road, Malang regency, East Java, Indonesia. Geosciences 11(1):4

Broeckx J, Vanmaercke M, Bălteanu D, Chendeş V, Sima M, Enciu P, Poesen J (2016) Linking landslide susceptibility to sediment yield at regional scale: application to Romania. Geomorphology 268:222–232

CLICOM (2014) National climatological database. (http://clicommex.cicese.mx/, Accessed on 2017-11-05). (In Spanish)

Concha-Dimas A, Cerca M, Rodríguez SR, Watters RJ (2005) Geomorphological evidence of the influence of pre-volcanic basement structure on emplacement and deformation of volcanic edifices at the Cofre de Perote–Pico de Orizaba chain and implications for avalanche generation. Geomorphology 72(1–4):19–39

Demeck J (ed) (1972) Manual of detailed geomorphological mapping. Academia, Praga

Guzzetti F, Ardizzone F, Cardinali M, Rossi M (2009) Landslide volumes and landslide mobilization rates in Umbria, Central Italy. Earth Planet Sci Lett 279:22–229

Höskuldsson A (1992) Le complexe volcanique Pico de Orizaba-Sierra Negra-Cerro Las Cumbres (sud-est mexicain): structure, dymamismes eruptifs et evaluations del areas: Clermont-Ferrand, Francia, Université Blaise Pascal, Tesis doctoral, 210 p

Legorreta-Paulín G, Bursik M, Ramírez-Herrera MT, Contreras T, Polenz M, Lugo-Hubp J, Paredes-Mejía LM, Arana-Salinas L (2013) Landslide inventory mapping and landslide susceptibility modeling assessment on the SW flank of Pico de Orizaba volcano, Puebla-Veracruz, Mexico. Zeitschrift für Geomorphologie 57(3): 371–385

Legorreta-Paulín G, Bursik M, Lugo-Hubp J, Paredes-Mejía LM, Aceves-Quesada JF (2014) A GIS method for landslide inventory and susceptibility mapping in the Río El Estado watershed, Pico de Orizaba volcano, México. Natural Hazards Journal 71(1):229–241

Legorreta-Paulín G, Pouget S, Bursik M, Aceves Quesada F, Contreras T (2016) Comparing landslide susceptibility models in the Río El Estado watershed on the SW flank of Pico de Orizaba volcano, Mexico. Natural Hazards 80(1):127–139

Legorreta-Paulín G, Bursik M, Zamorano-Orozco J J, Lugo Hubp J, Martinez-Hackert B, Bajo Sánchez J V, (2017) Estimación del volumen de los depósitos asociados a deslizamientos a través de geoformas, en el flanco SW del volcán Pico de Orizaba, Puebla-Veracruz Investigaciones geográficas, (92), 0–0

Lugo-Hubp J (1991) Elementos de Geomorfología Aplicada, métodos cartográficos. Instituto de Geografía, Universidad Nacional Autónoma de México

Lugo-Hubp J (2011) Diccionario Geomorfológico. Instituto de Geografía, UNAM, México

Macías JL (2005) Geología e historia eruptiva de algunos de los grandes volcanes activos de México. Bol Soc Geol Mex 57(3):379–424

Martin Y, Rood K, Schwab JW, Church M (2012) Sediment transfer by shallow landsliding in the queen Charlotte Islands, British Columbia. Can J Earth Sci 39(2):189–205

Muñoz-Salinas E, Renschler CS, Palacios D (2009) A GIS-based method to determine the volume of lahars: Popocatepetl volcano, Mexico. Geomorphology 111(1–2):61–69

Ouédraogo MM, Degré A, Debouche C, Lisein J (2014) The evaluation of unmanned aerial system-based photogrammetry and terrestrial laser scanning to generate DEMs of agricultural watersheds. Geomorphology 214:339–355

Powell L (2007) Mass wasting assessment: landslide Hazard zonation project Major Creek/Bingin watershed, Klickitat County, Washington, 43 p. with plates

Ray RL, Lazzari M, Olutimehin T (2020) Remote sensing approaches and related techniques to map and study landslides. Landslides-Investig Monit 2:1–25

Sim KB, Lee ML, Wong SY (2022) A review of landslide acceptable risk and tolerable risk. Geoenvironmental Disasters 9(1):1–17

Šíma J, Seidlová A (2014) The comparison of the calculation of the volume of the foundation pit. Procedia Engineering 91:328–333

Tang C, Tanyas H, van Westen CJ, Tang C, Fan X, Jetten VG (2018) Analysing post-earthquake mass movement volume dynamics with multi-source DEMs. Eng Geol 248:89–101

Washington State Department of Natural Resources, Forest Practices Division (2006) Landslide Hazard Zonation (LHZ) Mapping Protocol, version 2.1, accessed at: http://www.dnr.wa.gov/Publications/fp_lhz_protocol_v2_1_final.pdf

Wenkey D, Jen CH, Böse M, Lin JC (2011) Assessment of sediment delivery from successive erosion on stream-coupled hillslopes via a

time series of topographic surveys in the central high mountain range of Taiwan. Quat Int 263:14–25. https://doi.org/10.1016/j.quaint.2011.02.018

Young AP (2015) Recent deep-seated coastal landsliding at San Onofre State Beach, California. Geomorphology 228:200–212

Zamorano-Orozco JJ (1990) Análisis ingeniero-geomorfológico de la cuenca de México (Doctoral thesis (Geomorphology), Faculty of Geography, Lomonosov Moscow State University, Russia), p 225

KLC2020 Official Promoters

The Kyoto Landslide Commitment 2020 (KLC2020)

Kyoto 2020 Commitment for Global Promotion of Understanding and Reducing Landslide Disaster Risk
A Commitment to the Sendai Landslide Partnerships 2015–2025, the Sendai Framework for Disaster Risk Reduction 2015–2030, the 2030 Agenda Sustainable Development Goals, the New Urban Agenda and the Paris Climate Agreement

KLC2020 Official promoters are public and private organizations who promote the Kyoto Landslide Commitment 2020 and provide financial support for the implementation of the KLC2020 activities including the Open Access Book Series "Progress in Landslide Research and Technology."

Host organization
International Consortium on Landslides (ICL)/Nicola Casagli.

Public sectors: KLC2020 Official Promoters-public
International Unions/Associations, Governmental organizations, Universities and Research institutes

- The International Union of Geological Sciences (IUGS)/John Ludden
- The International Union of Geodesy and Geophysics (IUGG)/Kathy Whaler
- The International Association for the Engineering Geology and the Environment/Rafig Azzam
- International Geosynthetics Society (IGS)/John Kraus
- Geological Survey of Canada, Natural Resources Canada, Canada/Daniel Lebel
- Faculty of Civil and Geodetic Engineering, University of Ljubljana, Slovenia/Matjaž Mikoš
- China University of Geosciences, Wuhan, China/Huiming Tang
- Department of Civil Engineering, National Taiwan University, Chinese Taipei/Shang-Hsien Hsien
- Institute of Rock Structure and Mechanics, the Czech Academy of Sciences/Josef Stemberk
- Institute of Cold Regions Science and Engineering, Northeast Forestry University/Wei shan.

Private sectors: KLC2020 Official Promoters-private
Companies and corporation.

- Marui & Co. Ltd., Japan
- Nippon Koei Co., Ltd., Japan
- Ellegi srl, Italy
- IDS GeoRadar s.r.l., Italy
- Chuo Kaihatsu Corporation, Japan
- Godai Corporation, Japan
- Kiso-Jiban Consultants Co., Ltd., Japan
- Kokusai Kogyo Co., Ltd., Japan
- OSASI Technos, Inc., Japan.

I. Alcántara-Ayala et al. (eds.), *Progress in Landslide Research and Technology, Volume 2 Issue 1, 2023*,
Progress in Landslide Research and Technology, https://doi.org/10.1007/978-3-031-39012-8

Geological Survey of Canada, Natural Resources Canada

GSC-Pacific Division

Geological Survey of Canada: Who we Are

The Geological Survey of Canada (GSC) is part of the Earth Sciences Sector of Natural Resources Canada. The GSC is Canada's oldest scientific agency and one of its first government organizations. It was founded in 1842 to help develop a viable Canadian mineral industry by establishing the general geological base on which the industry could plan detailed investigations. Throughout its long and colourful history, the GSC has played a leading role in exploring the nation.

Today, the GSC is Canada's national organization for geoscientific information and research. Its world-class expertise focuses on the sustainable development of Canada's mineral, energy and water resources; stewardship of Canada's environment; management of natural geological and related hazards; and technology innovation (Fig. A.1).

The GSC celebrated its 175th anniversary in 2017 which coincided with Canada's 150th anniversary of Confederation. The GSC co-leads the Canada-Nunavut Geoscience Office and works with dozens of universities and research institutes, industry organizations, other federal departments, provinces, territories and municipalities in Canada and across the world. In particular, we work closely with other geological survey organizations in Canada through the unique Intergovernmental Geoscience Accord.

Every year, we publish hundreds of maps, Open Files, peer-reviewed papers and other reports. Our scientists are recognized worldwide and sought after for their expert advice on locating mineral, energy and groundwater resources, reducing risk from natural hazards and reviewing environmental assessments.

Strategic Priorities

The GSC has attempted to plot a course through this changing, uncertain world.

First, we identify three core areas of persistent scientific endeavour, which reflect stable, long-term needs of society:

- **Geological knowledge for Canada's onshore and offshore lands**
- **Geoscience for sustainable development**
- **Geoscience for keeping Canada safe.**

Next, we outline a new, fourth area of endeavour, Geoscience for society, which is the need to address the uncertainties of the changing world by expanding the reach and impact of geoscience knowledge in land-use decision making and in efforts to reduce the risk of disasters.

Finally, we recognize that our strength lies in a fifth area of endeavour, Our people, Our science, which we need to nurture to maintain a high-performing workforce capable of world leading innovative geoscience for the benefit of Canada.

(a) Geological knowledge for Canada's onshore and offshore lands

Geoscientific knowledge is fundamental to managing our onshore and offshore lands and their abundant resources. With its ten million km^2 of onshore land and an additional seven million km^2 of ocean estate, Canada is a vast country and a core mission of the GSC is to map and understand the land and its resources. Our Geo-mapping for Energy and Minerals (GEM) program continues to advance our knowledge of the North and by 2020 will complete a first mapping of surface geology at a coarse scale.

In the offshore lands, our geoscience knowledge also serves to confirm the farthest extents of the Canadian territory. Our joint program with Global Affairs Canada and Fisheries and Oceans Canada to delineate the outer limits of the continental shelf in the Atlantic and Arctic Oceans will reach a critical milestone in 2019. The program will file its

GSC-Pacific Division
Vancouver, BC, Canada
e-mail: David.Huntley@nrcan-rncan.gc.ca

I. Alcántara-Ayala et al. (eds.), *Progress in Landslide Research and Technology, Volume 2 Issue 1, 2023*,
Progress in Landslide Research and Technology, https://doi.org/10.1007/978-3-031-39012-8

Fig. A.1 Paleotsunami investigations in order to understand regional earthquake cycles and submarine landslide hazards

Fig. A.2 The GSC studies the sea floor of the Arctic to understand its geology and geohazards. Here a small craft surveys the bottom of Southwind Fjord (Baffin Island, N Nunavut)

Arctic submission under the United Nations Convention on the Law of the Sea (UNCLOS) (Fig. A.2).

(b) **Geoscience for sustainable development**

Finding new resources remains a major challenge. Many near-surface deposits have been discovered in Canada, but significant mineral resources remain to be found in less accessible regions and at depths below the surface. Finding new resources requires systematic, intensive and innovative methods to assess the mineral potential in remote locations.

It requires searching beneath overburden cover, imaging the 3-D structure of the earth and understanding the geological processes that lead to concentration of minerals in certain locations (Fig. A.3).

For the Energy sector, the greatest challenge is in the transition to a low-carbon economy. Although global fossil fuel use is likely to continue to grow over the foreseeable future, the trend will likely be at a decreasing rate. Canada

Fig. A.3 GSC geologists near the Heiberg Formation in northern Ellesmere Island (NU) as part of the geo-mapping for energy and minerals program. This formation is the primary host of major gas accumulations in the Canadian High Arctic

Fig. A.4 The GSC conducts climate change studies, here documenting the effects of fast melting permafrost leading to extreme coastal erosion on Pelly Island, NT

has an abundant supply of conventional and unconventional (oil sands and shale) oil and gas, so development in frontier areas is likely to be slow. In addition, the government has placed a moratorium on exploration activity in the Arctic offshore lands.

(c) **Geoscience for keeping Canada safe**

The GSC will continue to work on understanding how landscapes will change, how infrastructure will be affected and how resilience to climate change can be built into new infrastructure. Climate change will likely have a significant impact on the water cycle. GSC research will shed light on the risk to potable water supplies, hydroelectric power generation, and hazards from floods and drought (Fig. A.4).

(d) **Geoscience for society**

The scientific knowledge required to assess cumulative effects is broad. The complex interactions between land use, water management and waste management require an integrated approach at a landscape scale. The GSC is a national provider

Fig. A.5 The GSC conducts geohazard studies to reduce risks to people and infrastructure, here installing equipment to monitor landslide activity above a critical railway corridor in central BC

Fig. A.6 Among many celebratory activities for the GSC's 175th anniversary in 2017, the GSC held a Rock and Fossil Exhibit, at its site at the Bedford Institute of Oceanography (Dartmouth, NS), as part of a two-day open-house event, where more than 20,000 visitors participated

of information on both land (surficial and solid geology) and water, including the integration of surface water and groundwater into the complete water cycle (Fig. A.5).

The GSC recognizes that this area of endeavour involves inherent complexities and that our goals in this area will be to some degree aspirational. However, we will investigate new ways of planning our programs, undertaking our fieldwork, interacting with key stakeholders, and communicating our expert knowledge in ways that contribute positively to decision making about resource development.

(e) **Our people, Our science**

As a science organization within the federal government, the GSC's mandate is to conduct world-class science to inform public decision making. The Canadian government has articulated and adopted the principle of evidence-based decision making and reaffirmed the need for government science to be objective and non-partisan.

To remain at the leading edge, our scientists need to work with a variety of partners. We need to reinforce the central role that the GSC plays in the Canadian geoscience community by building networks of collaboration, fully participating in national geoscience initiatives, and advocating for Canadian geoscience at the international level (Fig. A.6).

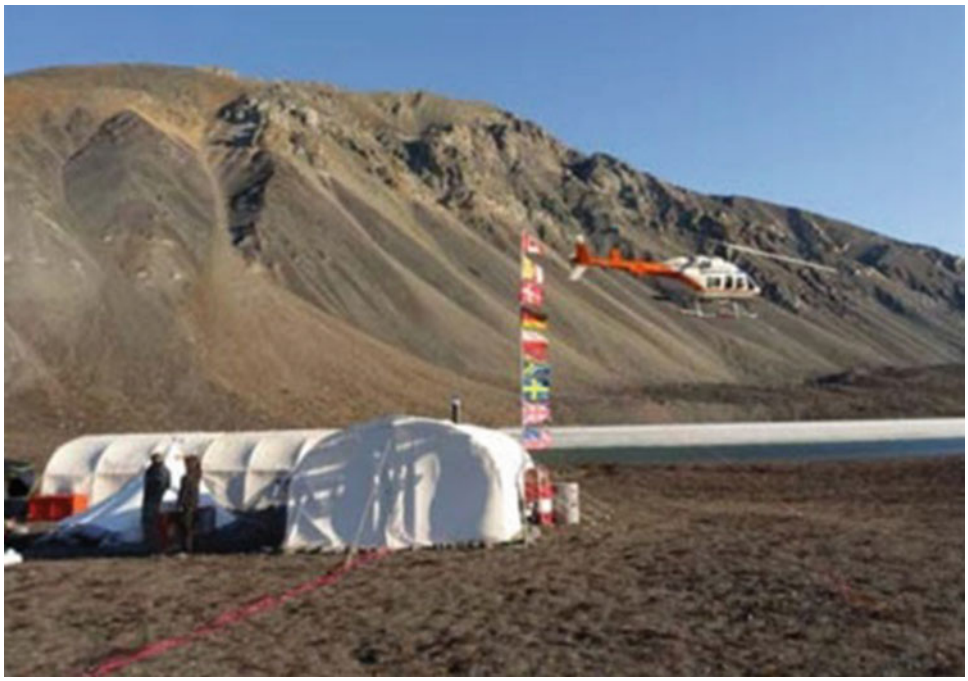

Fig. A.7 Joint Canadian/German (GSC/BGR) field mapping camp on northern Ellesmere Island, looking west as the fog covered sea ice of Yelverton Inlet, 2017

Moving Forward

Some of the objectives and goals that the GSC has set represent familiar territory for a national geoscience organization, but many others will pull us out of our comfort zone. We will take the time to better understand the challenges of delivering objective, nonpartisan science to support evidence-based decision making in Canada at a time of great technological and social change.

We will not be able to do this alone, so we look forward to strengthening our ties to other federal departments, provinces and territories, universities, Indigenous organizations, the private sector and civil society as a whole.

We ask all our stakeholders to contact us, to challenge us and, most importantly, to join with us to assure the future of Canada through thoughtful, respectful dialogue about the land we live on, its resources and its future (Fig. A.7).

Exploring Canada

Through its history, the GSC has been responsible for mapping the land mass of Canada, which supported the integration of the western provinces and northern territories into the country that we have today. The limit of Canada's offshore territory is still being extended today though surveys conducted by the GSC and the Canadian Hydrographic Service.

In more recent years, the GSC helped find the first economic diamond deposit in the Northwest Territories, leading to the expansion of diamond mining in Canada. These are only a few of the key GSC achievements that have built our knowledge of Canada's lands and provided the building blocks of its natural resource economy.

Today, exploration of this vast land is still reaping its natural resource rewards. The search for natural resources is difficult, akin to looking for a needle in a haystack.

The GSC's GEM program is exploring vast tracts of Canada's North, a land mass roughly equivalent to the combined areas of Quebec, Ontario and Manitoba, to find the "haystacks" with resource potential. This information is shared with the provinces and territories, as well as the private sector, so that the search for the "needles" can continue. The information is also critical to inform land-use planning.

In November 2016, the Royal Canadian Geographical Society (RCGS) awarded its prestigious Gold Medal to the GSC in recognition of the Survey's outstanding contribution to the development of Canada on the occasion of it's 175th anniversary.

Faculty of Civil and Geodetic Engineering, University of Ljubljana

Matjaž Mikoš

Summary

The Faculty of Civil and Geodetic Engineering of the University of Ljubljana (UL FGG) covering engineering disciplines, including water science and technology, has been involved in landslide risk reduction activities at the national level in Slovenia (former Yugoslavia, until 1991) for decades. In 2008, UL FGG became an ICL Full Member and has gradually developed its ICL engagement. UL FGG has been awarded the title of the World Centre of Excellence (WCoE) in Landslide Risk Reduction for 5 consecutive periods (2008–2011, 2011–2014, 2014–2017, 2017–2020, 2020–2023). Together with the Geological Survey of Slovenia, UL FGG hosted in 2017 the fourth World Landslide Forum in Ljubljana, Slovenia.

UL FGG strongly supports diverse activities of the International Consortium on Landslides, Kyoto, Japan, and thus contributes to the 2030 Agenda for Sustainable Development, as well as to the Sendai Framework for Disaster Risk Reduction 2015–2030 (SF DDR). UL FGG was a signatory of the Sendai Landslide Partnerships 2015–2030, and is a dedicated official promoter of the Kyoto Landslide Commitment 2020, a SF DRR voluntary commitment by ICL.

In 2016, UL FGG started to host the University of Ljubljana UNESCO Chair on Water-related Disaster Risk Reduction (WRDRR), being still the only UNESCO Chair at this university, and one of a few in Slovenia. Among different activities, in 2022 the WRDRR Chair supported the launching of the regional platform called Resili- Enhance for enhancing the resilience to disasters for sustainable development. UL FGG also supports activities of the Slovenian National Committee for UNESCO Intergovernmental Hydrological Programme (IHP), now working on the IHP-IX programme (2022–2029).

UL FGG is actively involved in numerous international (bilateral) and national research projects in the field of hydrology and hydraulic engineering, including topics such as landslide research, landslide risk mitigation, natural risk dialogue, and capacity building for society resilience.

In the field of capacity building, UL FGG offers several courses for graduate and postgraduate students in landslide mechanics and dynamics, landslide stabilization and landslide risk mitigation. In this article, a short overview of the past and current activities of UL FGG as ICL Full Member and KLC2020 Official Promoter is shown.

World Centre of Excellence on Landslide Risk Reduction and IPL Projects

WCoE Activities

The title of World Centre of Excellence (WCoE) on Landslide Risk Reduction is given to a governmental or non-governmental entity, which contributes to the landslide disaster risk reduction at a regional and/or global level in a specific unique field of expertise, as well as helps promoting International Programme on Landslides (IPL) and landslide research intellectually, practically and financially (https://www.landslides.org/ipl-info/world-centre-of-excellence/). UL FGG was granted the title of WCoE five consecutive times:

- WCoE 2008–2011 & 2011–2014: Mechanisms of landslides in over -consolidated clays and flysch.
- WCoE 2014–2017: Mechanisms of landslides and creep in over-consolidated clays and flysch.
- WCoE 2017–2020: Landslides in Weathered Flysch: from activation to deposition.
- WCoE 2020–2023: Landslides in Weathered Heterogenous Sedimentary Rock Masses such as Flysch.

M. Mikoš
Faculty of Civil and Geodetic Engineering, University of Ljubljana, Ljubljana, Slovenia
e-mail: matjaz.mikos@fgg.uni-lj.si

I. Alcántara-Ayala et al. (eds.), *Progress in Landslide Research and Technology, Volume 2 Issue 1, 2023*,
Progress in Landslide Research and Technology, https://doi.org/10.1007/978-3-031-39012-8

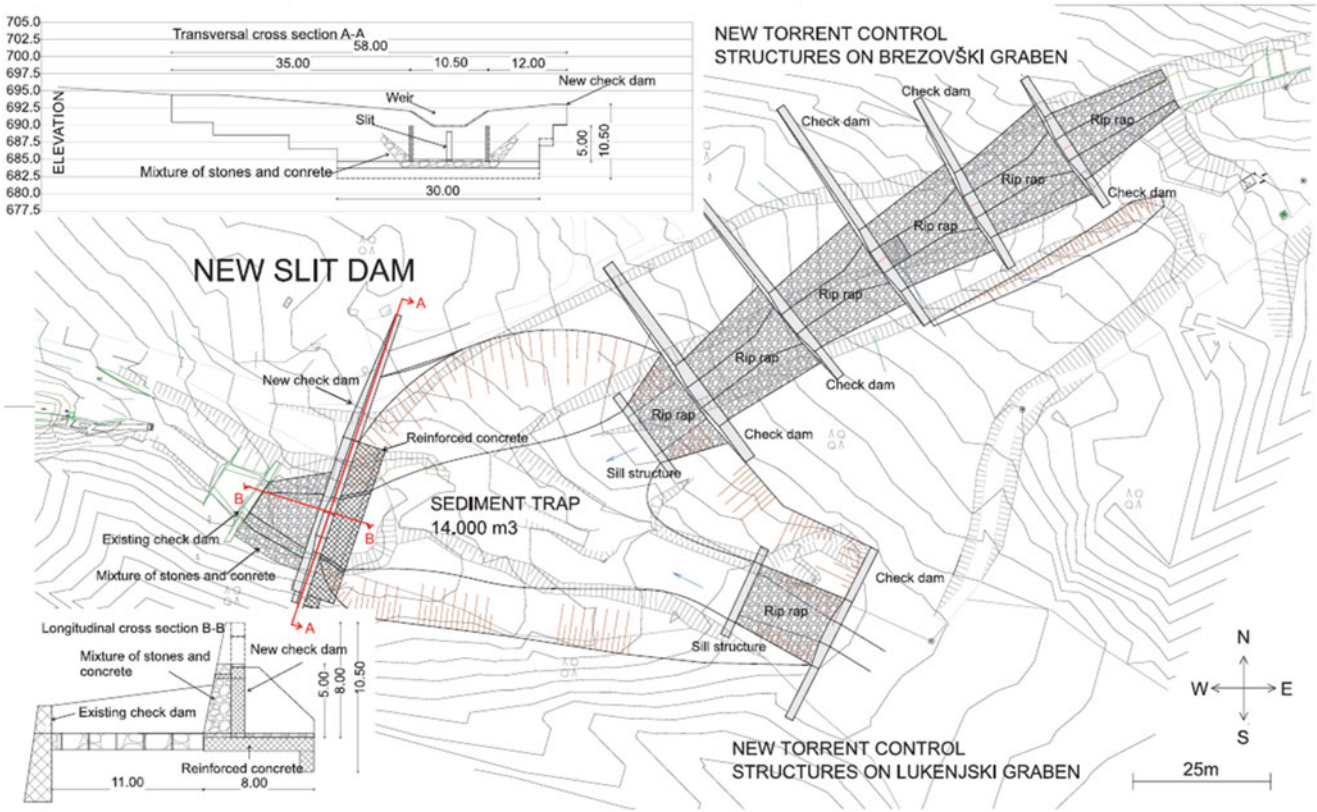

Fig. A.8 Technical countermeasures for future debris floods threatening the cabin station of the Krvavec ski area in N Slovenia: An extreme May 2018 debris flood case study in northern Slovenia: analysis, modelling, and mitigation. Landslides 17: 2373–2383, DOI 10.1007/s10346-019-01325-1)

The research efforts at UL FGG were focused on:

- Mechanisms of triggering such landslides (mud flows), estimation of debris-flow magnitudes triggered as shallow or deep-seated landslides (debris slides), and triggering of shallow rainfall-induced landslides using advanced statistical methods.
- Field and laboratory investigations of suction in over-consolidated clays and flysch, such as to improve the understanding of softening in stiff over–consolidated clays and marls, using soil matrix suction as an indicator for mudflow occurrence, and executing suction long-term monitoring of the Slano Blato landslide.
- Laboratory investigations of coarse debris-flow rheological parameters and soil–water characteristic curve of residual soil from a flysch rock mass.
- Mathematical modelling of debris flows (hazard assessment in deposition areas), using different numerical models and different digital terrain models.

The WCoE activities were financially supported by the Slovenian Research Agency through the Research Programme P2–0180 "Water Science and Technology, and Geotechnical Engineering: Tools and Methods for Process Analyses and Simulations, and Development of Technologies," as well as by several national (Fig. A.8) and international (bilateral) research projects.

UL FGG and the Geological Survey of Slovenia jointly organized fourth World Landslide Forum (WLF4), in Ljubljana between May 29 and June 2, 2017. With over 600 participants from 49 countries and 5 international organizations, WLF4 was promoting the culture of living with natural hazards.

IPL Projects

An important ICL activity is IPL projects (https://www.landslides.org/projects/ipl-projects/). The IPL Evaluation Committee examines the submitted proposals of ICL members by carefully reading the written proposals and by listening to their presentations at annual ICL conferences. The initially accepted proposals by the IPL Evaluation Committee are discussed and then approved at the annual Board of Representatives meeting of ICL members (Annual Assembly). Finally, the IPL projects are approved annually by the

Global Promotion Committee IPL-KLC. UL FGG has successfully submitted several proposals for IPL projects and has been so far actively involved in the following ones:

- IPL-151 Soil matrix suction in active landslides in flysch—the Slano Blato landslide case (2010–2012).
- IPL-225 Recognition of potentially hazardous torrential fans using geomorphometric methods and simulating fan formation (2017–2020).
- IPL-226 Studying landslide movements from source areas to the zone of deposition using a deterministic approach (2017–2020)—coordinated by the Geological Survey of Slovenia.
- IPL-261 World-wide-web-based Landslide Observatory (W3bLO) (2022–2024)

ICL Thematic and Regional Networks

Following the ICL Strategic Plan 2012–2021, several thematic networks and regional networks have been established (for an overview, see https://www.landslides.org/projects/icl-networks/).

Landslide Monitoring and Warning Thematic Network: LaMaWaTheN

In 2012, UL FGG proposed the ICL landslide monitoring and warning thematic network—almost 10 ICL members joined the initiative. The general objective of the proposed network was to compare experiences in the field of landslide monitoring and installed early warning systems for active landslides in various regions of the world. Lately, we contributed to the network activities by preparing practice guidelines on monitoring and warning technology for debris flows.

The idea of the network was partially taken over by the web database ICL World Report on Landslides (https://www.landslides.org/projects/world-report-on-landslides/), created to be a platform to share landslide case studies among the global landslide community, with monitoring and warning systems being a part of the platform.

ICL Adriatic-Balkan Network: ICL ABN

Jointly with other ICL members from Croatia and Serbia, in 2013, UL FGG proposed to establish an ICL Adriatic-Balkan Regional Network. Various network activities were proposed, the most active being the organization of biennial regional symposia on landslide risk reduction in the Adriatic-Balkan Region (called ReSyLAB). UL FGG supported the first Symposium in Zagreb (Croatia, 2013), second in Belgrade (Serbia, 2015), third in Ljubljana (Slovenia, 2017), 4th (Sarajevo, 2019), and fifth in Rijeka (Croatia, 2022).

In the last decade, UL FGG has signed bilateral research projects with the ICL members in the region: "Adriatic-Balkan Regional Network: Landslide Risk Mitigation for Society and Environment" (2012–13 with University of Belgrade, Serbia), "Study of landslides in flysch deposits: sliding mechanisms and geotechnical properties for landslide modelling and landslide mitigation SoLiFlyD" (2014–15 with University of Rijeka, Croatia), and "Laboratory investigations and numerical modelling of landslides in flysch deposits in Croatia and Slovenia" (2016–17 with the University of Rijeka, Croatia). This joint research has helped strengthen regional cooperation within the ICL ABN regional network.

Other ICL-Related International Activities

UL FGG served the ICL by taking different leading roles in the Consortium, i. e. UL FGG member served as Chair of IPL Evaluation Committee, twice as ICL Vice President, and was elected to Co-Chair and in 2021 to Chair of the IPL-KLC (https://www.landslides.org/ipl-info/ipl-klc-globalpromotion-committee/).

UL FGG has been strongly supporting the journal *Landslides*: Journal of the International Consortium on Landslides, published by Springer Nature (https://link.springer.com/journal/10346) since its launch in 2004. UL FGG works for the journal in the roles of reviewers and an associate editor, and regularly publishes its top research results in the journal, as well as disseminates information important for capacity building in landslide risk reduction—such as results of bibliometric studies on the journal *Landslides* and ICL books.

UL FGG also contributed to the two-volume set of Landslide Dynamics: ISDR-ICL Landslide Interactive Teaching Tools (LITT), namely to Vol. 1: Fundamentals, Mapping and Monitoring by practice guidelines on monitoring and warning technology for debris flows (https://www.springer.com/gp/book/9783319577739), and to Vol. 2: Testing, Risk Management and Country Practices (https://www.springer.com/gp/book/9783319577760) by a state-of-the-art overview on landslide disaster risk reduction in Slovenia, a study on two-dimensional debris-flow modelling and topographic data, and by study on intensity duration frequency curves for rainfall-induced shallow landslides and debris flows using copula functions.

UL FGG also contributed to the open-access book series "Progress in Landslide Research and Technology" Vol. 1 by a review article on the history of the International Programme on Landslides (IPL) (https://doi.org/10.1007/978-3-031-16898-7_3), an original article on the natural-hazard-related web observatory as a sustainable development tool (https://doi.org/10.1007/978-3-031-16898-7_5), and an original

article on landslide research and technology in patent documents (https://doi.org/10.1007/978-3-031-18471-0_3).

*U*niversity of Ljubljana UNESCO Chair on Water-Related Disaster Risk Reduction (2016–2020 & 2020–2024)

Experiences and knowledge accumulated in the past decades at the Chair on Hydrology and Hydraulic Engineering at UL FGG in the field of (applied) hydrology in experimental basins, hydraulic engineering, landslide research, landslide risk reduction, and flood risk management, culminated in 2016 in the establishment of the UNESCO Chair on Water-related Disaster Risk Reduction (WRDRR Chair; www.unesco-floods.eu) at the University of Ljubljana. The UNESCO WRDRR Chair was positively evaluated by UNESCO in 2020 and prolonged for another 4 years (2020–2024). The Chair is associated to the university twinning and networking UNITWIN UNESCO—Kyoto University—ICL on "Landslide and Water-Related Disaster Risk Management".

The UNESCO WRDRR Chair is involved into numerous international (bilateral) and national research projects. Their results are timely reported in scientific literature (https://www.unesco-floods.eu/category/publications/).

In 2022, the UNESCO Chair supported launching of the ResiliEnhance Program for enhancing the resilience to disasters for sustainable development (https://unescochair-sprint.uniud.it/en/resilienhance-program/). The program is at the moment focused to Central and Eastern Europe, and supported by the Central Europe Initiative (CEI).

In 2022, the UNESCO Chair started to lead the University of Ljubljana project on Sustainable Development (2022–2025; www.unesco-floods.eu/ultra-pilot-projects/)to modernize university professional study programmes, especially in civil engineering, to increase students' competences for sustainable development, including disaster risk reduction and resilience building.

UL FGG supports activities of the Slovenian National Committee for UNESCO Intergovernmental Hydrological Programme (www.ncihp.si)—focus of the activities is the development of the IHP-IX Programme (2022–2029).

Conclusions

UL FGG as one of World Centres of Excellence in Landslide Risk Reduction, hosts the UNESCO Chair on Water-related Disaster Risk Reduction. UL FGG strongly supports ISDR-ICL Sendai Partnerships 2015–2025 for global promotion of understanding and reducing landslide disaster risk, and its extension to 2030 and beyond: the Kyoto 2020 Commitment for Global Promotion of Understanding and Reducing Landslide Disaster Risk that that was signed in November 2020. UL FGG is proud to be its Official Promoter, and will specifically work for its Actions 2, 5, 6, 9 and 10.

This review article is intentionally written without a list of references to described activities. For this purpose, listed websites and links may be used.

The author wants to thank colleagues from UL FGG and University of Ljubljana, and from the ICL community for the past and long-lasting excellent cooperation with a joint vision to reduce landslide disaster risk.

China University of Geosciences, Wuhan

Huiming Tang, Changdong Li, and Qinwen Tan

Introduction

China University of Geosciences, Wuhan (CUG), founded in 1952, is a key national university affiliated with the Ministry of Education. It is also listed in the National "211 Project", the "985 Innovation Platform for Advantageous Disciplines," and the "Double First-class Plan". CUG, featuring geosciences, is a comprehensive university that also offers a variety of degree programs in science, engineering, literature, management, economics, law, education, and arts. Its Geology and Geological Resources & Engineering have both been ranked as the national number one disciplines.

CUG has two campuses in Wuhan. The main campus is the Nanwang Mountain Campus, located in the heart of the Wuhan East Lake National Innovation Demonstration Zone, which is popularly known as China Optics Valley. The Future City Campus is located in the east of Wuhan and is 27 km from the main campus. These two picturesque campuses cover a combined area of 1,474,353 m2. They are ideal places to study, work, and enjoy life. CUG owns a 4A-Level tourist attraction— the Yifu Museum. CUG also boasts four field training centers: Zhoukoudian in Beijing, Beidaihe in Hebei Province, Zigui in Hubei Province, and Badong in Hubei Province.

CUG has established a complete education system. As of December 2020, 30,239 full-time students, including 18,080 undergraduate students, 9302 master's students, 1916 doctoral students, and 941 international students, have enrolled in its subsidiary 23 schools and 86 research institutes. CUG currently has a faculty of 1858 full-time teachers, among which there are 539 professors (11 of which are members of the Chinese Academy of Sciences) and 984 associate professors.

CUG is focused on fostering high-quality talent. Among its over 300,000 graduates, many have gone on to become scientific and technological elites, statesmen, business leaders and athletes. And they have made great contributions to the nation and society, represented by former Premier WEN Jiabao and 39 members of the Chinese Academy of Sciences and Chinese Academy of Engineering.

CUG has strengthened exchanges and cooperation with international universities. It has signed friendly cooperation agreements with more than 100 universities from the United States, France, Australia, Russia, and other countries. CUG has actively carried out academic, scientific, and cultural exchanges with universities around the world. There are about 1000 international students from more than 100 countries studying at CUG. It also sponsors more than 900 teachers and students to study abroad or conduct international exchanges and invites more than 400 international experts to visit, lecture, and teach at CUG every year. In 2012, CUG initiated and co-established the International University Consortium in Earth Science (IUCES) with 11 other world-renowned universities. IUCES is committed to promoting the common development of geosciences education and scientific research through resource sharing, exchange, and cooperation among its member institutions. In addition, CUG has partnered with Bryant University from the USA, Alfred University from the USA, and Veliko Turnovo University from Bulgaria in establishing three Confucius institutes on their campuses (Fig. A.9).

H. Tang · C. Li · Q. Tan
China University of Geosciences, Wuhan, People's Republic of China
e-mail: tanghm@cug.edu.cn

I. Alcántara-Ayala et al. (eds.), *Progress in Landslide Research and Technology, Volume 2 Issue 1, 2023*,
Progress in Landslide Research and Technology, https://doi.org/10.1007/978-3-031-39012-8

Fig. A.9 Strategic plan of building a world-renowned research university in earth science

Strategic Plan of Building a World-Renowned Research University in Earth Sciences: A Beautiful China and a Habitable Earth—Towards 2030

CUG reviewed and approved Strategic Plan of Building a World-Renowned Research University in Earth Sciences on December 25 of 2019.

Themed "A Beautiful China & A Habitable Earth", the Plan depicts the blueprint of the second goal of the "three-step strategic goals", which is to build a world-renowned research university in Earth Sciences by 2030 based on the attained goal of developing CUG into a "high-level university with first-class Earth Sciences and coordinated development of multi-disciplines".

According to the Plan, our education missions are: Remaining true to CUG's core value of "seeking harmonious development between man and nature" we are committed to cultivating innovative talents who have lofty morality, solid foundation, and profound expertise and who pursue the unity of knowing and doing. We should provide personnel support and endeavor to innovate, apply and spread knowledge in order to provide theories, technologies, and approaches for the construction of a Beautiful China and a Habitable Earth. We should strive to optimize governance, reform culture, and fully invigorate the vitality of running a university. We should provide our service to the construction of an innovative country and to the promotion of a harmonious co-existence between man and nature. We should provide our service to the people and the governance of China. We should provide our service to the consolidation and development of the system of socialism with Chinese characteristics. We should provide our service to the reform and opening up and to the construction of socialist modernization.

According to the Plan, our endeavoring goals are: By 2030, we will have built a world-renowned research university in Earth Sciences, whose main indexes will have reached or nearly reached the level of other world-class universities. To upgrade CUG into a world-class university, we will endeavor to make the discipline of Earth Sciences rank top in the world and forge boldly ahead in competition to improve the quality of other disciplines of CUG. We will assemble a contingent of teachers and researchers with international competitiveness and influences to build a university with Chinese characteristics and superiority. We will build a world-class university that will be fully engaged in international exchange and cooperation and that will achieve educational, academic, cultural, and administrative excellence.

Outstanding Recent Achievements

In recent years, CUG has achieved significant progress in the research fields of geohazards, water resource, geochemistry, paleontology, geodetic surveying and lunar exploration program, etc. To keep to the theme of KLC2020, recent achievements on geohazards researches of CUG are focused and introduced.

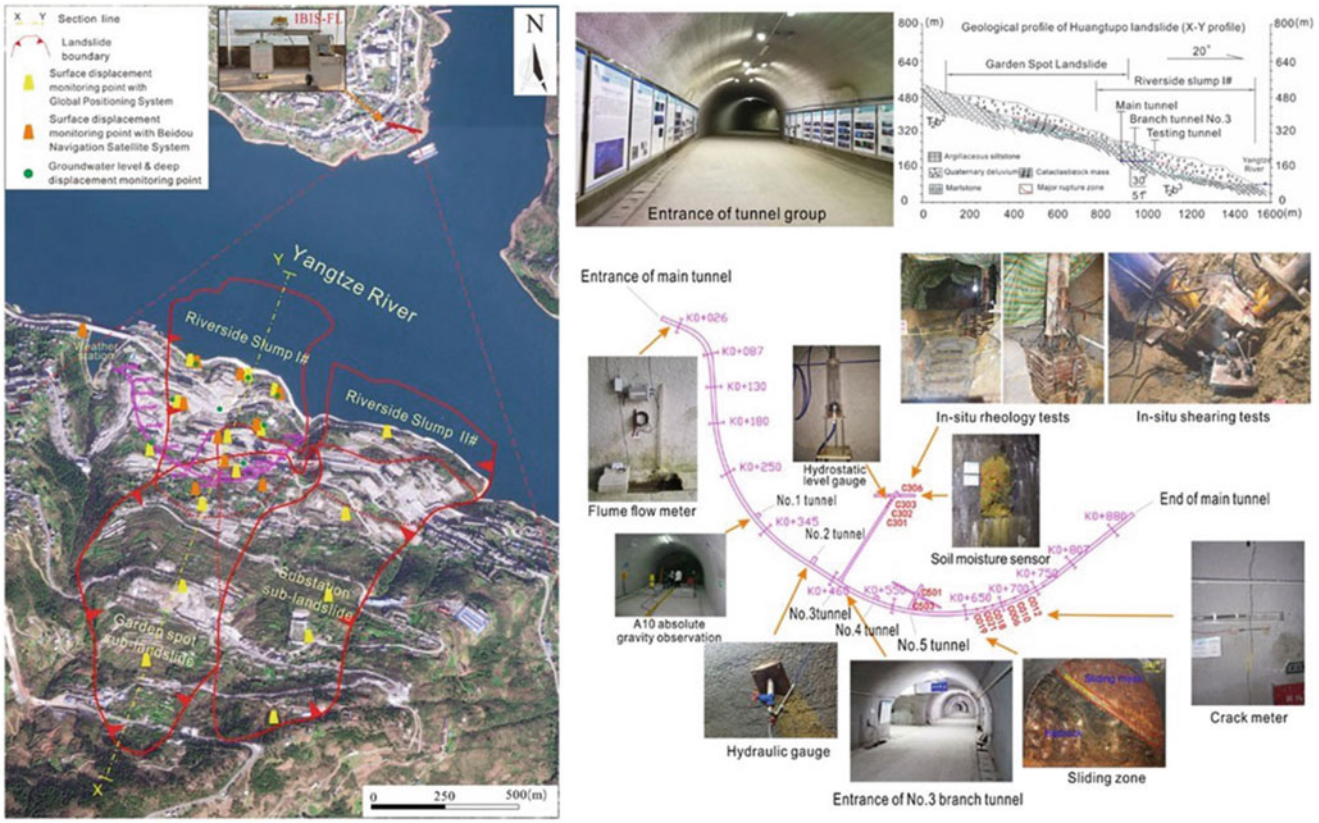

Fig. A.10 Badong in-situ large-scale experimental station of the National Observation and Research Station for Geohazards in the Three Gorges Reservoir Area, Hubei

(a) **Approval of National Observation and Research Station for Geohazards in the Three Gorges Reservoir Area, Hubei**

CUG was newly approved **National Observation and Research Station for Geohazards in the Three Gorges Reservoir Area, Hubei**. This station, founded and administrated by Prof. Huiming Tang, is responsible to carry out field observations and scientific research on geohazards in condition of reservoir operation.

The central site of the station is located in Badong County of the Three Gorges Reservoir area (hereinafter abbreviated as the TGR area), and a larger monitoring network of multiple sites has been established, including the geohazard field test site for the Majiagou landslide, Zigui County, and systematic geophysical monitoring station for the whole TGR area, etc.

The Badong field site (also named Badong in-situ large-scale experimental station) is located in the Huangtupo landslide area, which has been recognized the largest reservoir landslide by volume in the TGR area. The field site consists of a tunnel complex and a series of monitoring systems (Fig. A.10). The tunnel complex, built in the Huangtupo riverside sliding mass #1, consists of a main tunnel with a length of 908 m and a width of 5 m, five branch tunnels (5 m to 145 m long, 3.5 m wide), two test tunnels, and 35 observation windows. The test tunnels exposed the sliding zones of the landslide, facilitating their direct observation and the execution of scientific experiments, such as large-scale in-situ mechanical tests and deep deformation monitoring. The monitoring systems measure deformation as well as hydrologic, meteorological and hydro-chemical variables. The deformation system is composed of a slope surface displacement measurement unit and an underground displacement measurement unit. The slope surface displacement unit includes a number of GPS (Global Positioning System) and BDS (BeiDou Navigation Satellite System) measurement points, as well as an IBIS-FL (Interferometric Radar) monitoring system (Fig. A.10). The underground displacement unit includes nine deep inclinometer boreholes, a number of crack meters installed on the ground and the walls of tunnels, and many hydrostatic level gauges that measure the settlement of the tunnels in the sliding mass. The hydrologic system includes a number of devices that allow for observation of the water level of the Yangtze River, the ground water level and water discharge of the tunnels (Fig. A.10). A small meteorological station is located on the landslide and provides rainfall data. So far, multiple and massive data have been collected for the landslide area since the year 2012, when the field site was constructed; over 10,000 people with a variety of geology-related backgrounds from >20 countries have visited this experimental station.

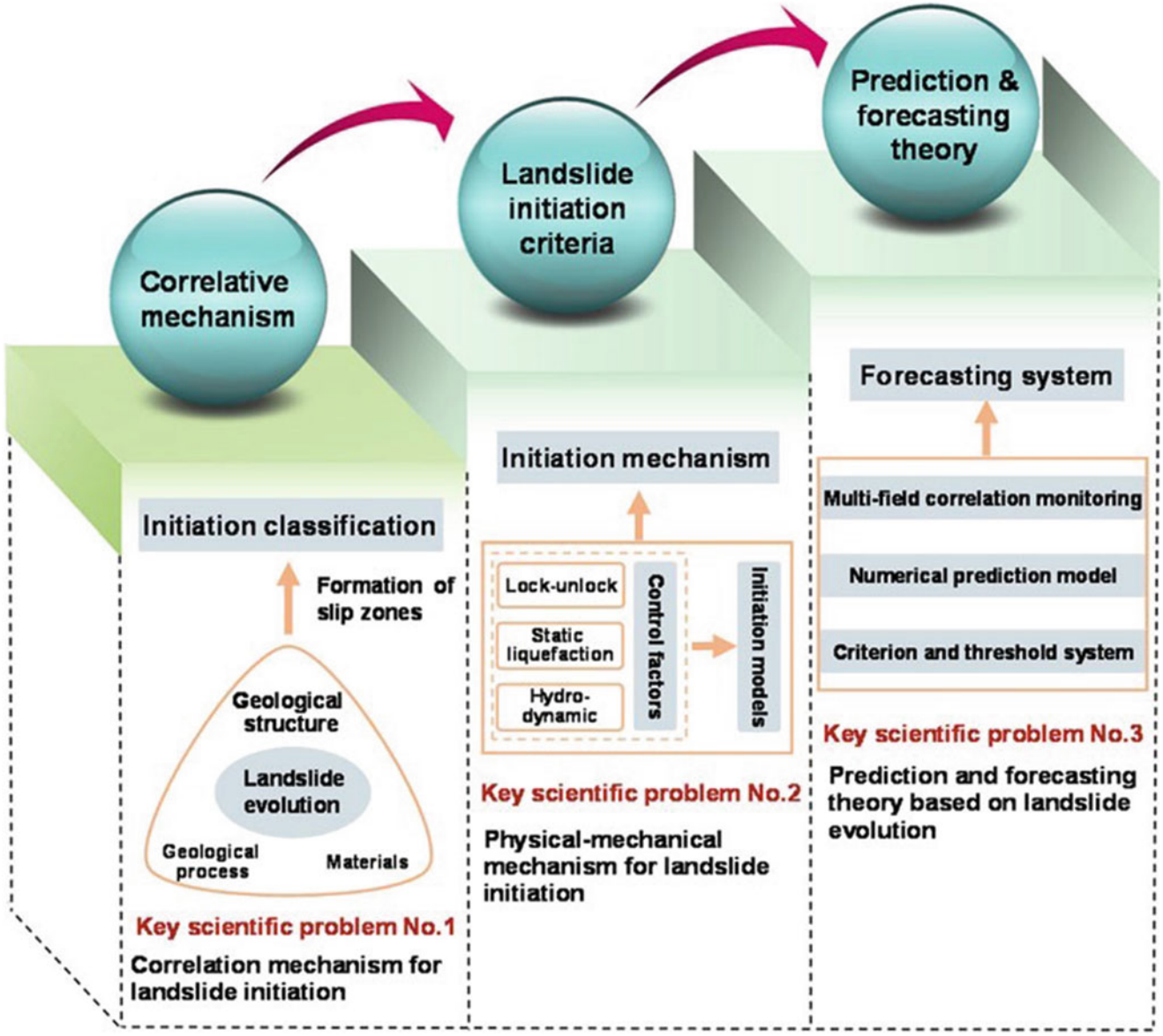

Fig. A.11 Scientific thought for the implement of research

(b) **Approval of the Basic research on the prediction and forecasting of major landslides program supported by the Major Program of NSFC**

CUG was approved the **Basic research on the prediction and forecasting of major landslides program** (2021–2025), supported by the Major Program of the National Natural Science Foundation of China. The program was designed for the prediction and forecasting of major landslides, with the concentration on the core scientific problems of landslide evolution process and physical-mechanical mechanism. Three key scientific problems, including correlation mechanism for landslide initiation, physical-mechanical mechanism for landslide initiation, and prediction and forecasting theory based on landslide evolution were proposed.

Five topics were set up to achieving those objectives. Topic 1 was proposing the initiation classification of major landslides based on large field test platform, with the adoption of field prototype test and other technical means. Topics 2–4 aimed to reveal the physical and mechanical mechanism of locked-segment dominated landslide, static liquefaction loess landslide and hydrodynamic pressure-driven landslide, and to establish the corresponding landslide initiation criteria, respectively. Topic 5 was responsible to established the prediction mode and real-time forecasting system. Ultimately, the landslide prediction and forecasting theory based on the evolution process and physical-mechanical mechanism would be put forward. The scientific thought for the implement of research is exhibited in Fig. A.11.

The implementation of the research is respected to lay the geological, mechanical and physical foundation for the above

Fig. A.12 Photo of old Badong County, showing the populated area built on the Huangtupo landslide (Tang et al., 2015a)

three types of landslide prediction, and to substantially promote the research on landslide prediction.

Figure A.12 shows the old Badong county, situated in the Huangtupo landslide area, and the exposures of the main rupture zones are now more than 50 m below the water surface of the Three Gorges Reservoir (Tang et al., 2015a). During the second relocation from 1982 to 2003, the county moved from Xinling town to the Huangtupo landslide area (Gong et al., 2021). A series of investigations were conducted during that period, and the new county area was further confirmed to be on the site of an ancient landslide then (Gong et al., 2021). Huangtupo landslide is developed in the Middle Triassic Badong Formation strata, within which interbedded strata structures are often observed, and many geohazards developed. The material composition of the Huangtupo landslide includes mudstone, pelitic siltstone, and argillaceous limestone (Tang et al., 2015b). Multiple slumps formed the complex mass at least 4000 years ago (Tang et al., 2015b). The elevation of the crown of the landslide is about 600 m asl., while its toe varies from 50 to 90 m, submerged in the Yangtze River. The composite landslide covers an area of 1.35 km2, and its volume of nearly 70 million m3 makes it the largest reservoir landslide in China (Tang et al., 2015b). Considering the risk of landslide reactivation by long-term reservoir operation and human activities, the drainage system and the anchored defense structures along its leading edge were constructed to control the landslide. Huangtupo demonstration base was designed and constructed in 2012, during the third relocation period from 2007 to 2017 (Gong et al., 2021). At that time, some Badong county residents still lived in the Huangtupo area, facing the unsure threat. The old giant landslide is in need of further research to ensure its safety as well as provide access for landslide hazard study. The demonstration base was in great request. With the building and development of the demonstration base, Over 10,000 people with various geology-related backgrounds from more than 20 countries have visited. A national observation station was also settled rely on the base in 2020.

Gong W, Juang CH, Wasowski J (2021) Geohazards and human settlements: lessons learned from multiple relocation events in Badong, China – engineering geologist's perspective [J]. Eng Geol 285:106051

Tang H, Li C, Hu X, Wang L, Criss R, Su A, Wu Y, Xiong C (2015a) Deformation response of the Huangtupo landslide to rainfall and the changing levels of the three gorges reservoir. Bull Eng Geol Environ 74(3):933–942

Tang H, Li C, Hu X, Su A, Wang L, Wu Y, Criss R, Xiong C, Li Y (2015b) Evolution characteristics of the Huangtupo landslide based on in situ tunneling and monitoring. Landslides 12(3):511–521

Department of Civil Engineering, National Taiwan University

Department of Civil Engineering, National Taiwan University

Introduction

National Taiwan University (NTU) was originally established in 1928, when Taiwan was under Japanese rule, as Taihoku Imperial University. The current name dates back to 1945. As Taiwan's oldest and most prestigious university, we are also the largest comprehensive higher education institution (HEI) in the country. The academic freedom that we cherish and our excellent faculties attract both domestic and international students. Throughout our 90-year history, we have nurtured many talents, including leading academics and leaders in the public and private sectors. Our campus is vast, and spans across multiple locations, including Taipei, Yilan, Hsinchu, Yunlin, and mountainous areas in central Taiwan—accounting for nearly 1% of Taiwan's total land area. This provides teachers and students with an environment rich in biological and ecological diversity.

As the leading university in Taiwan, we are strongly committed to social responsibility as we strive to drive sustainable development and influence positive change in society. This was also reflected in the first University Impact Rankings launched in 2019 by Times Higher Education (THE), which measure the contributions of HEIs to the United Nations' Sustainable Development Goals (SDGs). We were ranked 70th in the world overall, and first in the world for SDG16: Peace, Justice, and Strong Institutions. Starting from creating a sustainable culture on campus, we aim awareness about sustainability throughout the university, through innovative teaching and research, environmental protection and recycling efforts, and a school administration that supports equality and wellbeing. Our sustainability efforts extend beyond our campus through industry-academia collaborations and service teams deployed to remote areas. In the near future, we will continue to reinforce the spirit of innovation and sustainability thinking among all faculty members and students. We will also continue our efforts to address economic, environmental, and social challenges through interdisciplinary collaboration, as we create connections between the local and the international community. The Department of Civil Engineering (Fig. A.13) can be regarded as the root of The College of Engineering. The early civil engineering education covers a wide range of professions. With the development and differentiation of various social industries, some fields have gradually separated and established specialized departments. We have also moved on, combining different fields and top-notch technology to remain as the leader of the tide.

Civil engineering is inseparable from the development of human civilization. From the beginning of civilization, all man-made structures have enchased and highlighted the value of civil engineering. NTU Civil Engineering is no exception. From the Department of Civil Engineering of the Imperial College of Taipei to the National Taiwan University Department of Civil Engineering today, the majority of Taiwan's significant constructions is and will always be our finest gallery.

In National Taiwan University, you will obtain high-quality guidance in and out of the classroom. Academic resources in the classroom and sports culture clubs, various student activities throughout the year, will bind you together with peers of the same dream. These friends may also be partners that can help you in future careers. If you are willing to take civil engineering as a career and take on the challenges and step forward as a team, then listen to your inner call, join us, and let us stride ahead hand in hand (Fig. A.14).

Department of Civil Engineering, National Taiwan University
Department of Civil Engineering, National Taiwan University, Taipei, Taiwan
e-mail: louisge@ntu.edu.tw

I. Alcántara-Ayala et al. (eds.), *Progress in Landslide Research and Technology, Volume 2 Issue 1, 2023*,
Progress in Landslide Research and Technology, https://doi.org/10.1007/978-3-031-39012-8

Fig. A.13 Quick facts of the Department of Civil Engineering

Fig. A.14 Life beyond Classroom

Outstanding Recent Achievements

Mitigating the Impacts of Natural Disasters Via Cutting Edge Technology

Taiwan is located in the Circum-Pacific seismic belt, with many active faults and frequent typhoons. Due to the effects of climate change, extreme rainfall events that used to occur once in a century are now becoming more frequent, exacerbating the threat of landslides and debris flows. The prevention and mitigation of natural disasters such as earthquakes and flooding have therefore become a priority for the twenty-first century.

(a) **Earthquake Early Warning Systems: Gain Valuable Response Time**

For most natural disasters, potential losses to life and property can be mitigated through early warning and prevention. After the earthquake disaster of September 21st, 1999, building safety inspections needed to be conducted all across Taiwan. Our faculty and students with expertise in civil engineering and geology were quick to respond to this urgency, working closely with the National Center for Research on Earthquake Engineering to help the government improve the earthquake resistance standards and test specifications. Moreover, they proposed a more elaborate system for earthquake damage and liquefaction assessment,

Fig. A.15 Taiwan Earthquake Loss Estimation System (TELES)

and conducted a complete review and classification of the earthquake risk tolerance for all areas in Taiwan. The team also developed new disaster prevention technologies. One of the most significant contributions was to assist the public high (vocational) schools around Taiwan with assessments of the earthquake resistance and reinforcement needs of old buildings. In the numerous earthquakes that have since occurred, the effect of these reinforcements has become apparent. The stronger earthquake resistance of these buildings has improved safety for 2.65 million teachers and students around Taiwan (Fig. A.15).

Our school has also developed technology to monitor the status of bridges with high traffic volumes. This optical fiber monitoring system will emit a warning whenever poor conditions are recorded, prompting an early response from management that can prevent a disaster from happening. When bridges in remote areas are damaged, a lightweight bridge developed by NTU out of composite materials can be assembled by residents in short time. In this way, access to affected areas can be quickly restored, and disaster relief provided more efficiently. In the event of an earthquake, Taiwan's citizens will immediately receive an emergency alert by text message. This warning system, which was developed by Professor Wu, Yih-Min at our Department of Geosciences, analyzes the properties of a P-wave within three seconds after detecting the wave so that it can issue an alert to citizens more than 10 seconds before the S-wave, which is most likely to cause damage arrives. This early warning system is accurate and fast, giving people valuable seconds to escape to safety. Because it is also much cheaper to manufacture network of multiple sites has been established, including the geohazard field test site for the Majiagou landslide, Zigui County, and systematic geophysical monitoring station for the whole TGR area, etc. than previous seismographs, it could be rapidly rolled out to several hundred elementary and junior high schools, ensuring better protection of our country's younger generation. Moreover, this system has been successfully introduced in other earthquake-threatened countries, such as Indonesia, India, Vietnam, Nepal, and Mexico.

(b) **After the Flood: Rapid Mobilization and Improved Ability to Provide Relief**

Another critical area is flood disaster prevention. Also here, our faculty and students are actively involved in key activities ranging from early warning and response during the disaster, to raising the awareness of, and capability for, disaster prevention among citizens more generally. Our Center for Weather Climate and Disaster Research comprises experts in meteorology, hydrology, bioenvironmental engineering, and geology etc. This center helped New Taipei City and Keelung City establish an extreme weather and flood monitoring & warning system. Other projects include combining advanced deep learning with the analysis of radar data, which allows for closer monitoring of rainfall data in hydrologically sensitive areas. The improvement of flood models increases the accuracy of flood warnings and pro- vides disaster prevention units with valuable information for them to rapidly

formulate response strategies. From past experiences outside of Taiwan, we know that self-help and mutual support account for the largest share of the relief effort (90%) in the event of a disaster. In other words, even if flood warnings are effective, people in the affected area still need to be able to take own measures to protect themselves. At NTU, we actively participate in the community-level disaster relief preparations around the country, as well as in the training of disaster relief officers. Our experts provide citizens with the most up-to-date knowledge in disaster prevention, operate independent disaster relief systems, and evaluate the safety of shelters. These efforts contribute to the resilience and ability of local communities to mitigate impact, helping them recover more quickly. A plan for how to improve the disaster relief ability in the country proposed by our experts is another example of how we help make sure that the best disaster response capacity is in place. After improving the ability to respond to disasters, NTU's team also contributed to disaster prevention infrastructure around Taiwan, such as seismic isolation technology for buildings and equipment, or detention ponds in communities at risk. Our work and efforts in these areas help protect lives and property. As climate change continues to impact the world, we hope to leverage our technologies and expertise in these domains even further, and help strengthen the capacity to prevent and withstand natural disasters throughout the world.

Institute of Cold Regions Science and Engineering, Northeast Forestry University

Wei Shan and Ying Guo

Introduction

Institute of Cold Regions Science and Engineering of Northeast Forestry University (ICRSE-NEFU) is committed to the environmental geology and engineering geology of high latitude permafrost region and deep seasonal frozen area under the background of climate change, and attaches importance to the combination of basic research and applied research. With undergraduate, master, doctor, postdoctoral professional training system and standards, ICRSE-NEFU initiated "Geological environment risk research plan for permafrost degraded areas in Northeast China (GERRP)". With the support of the Chinese government, "Field scientific observation and research station of the Ministry of Education—Geological environment system of permafrost area in Northeast China (FSSE-PFNEC)" was established. Its observation stations cover all kinds of permafrost areas in Northeast China. At the same time, in order to develop and transfer technologies related to environmental governance and infrastructure construction in permafrost regions, "Provincial Collaborative Innovation Centre, Environment and road construction & maintenance in permafrost area of Northeast China (PCIC-PFER)" was established. Over the years, ICRSE-NEFU have continuously established cooperation with academic institutions and organizations at home and abroad, held various academic exchanges and regularly held "Academic Seminar on Engineering Geology and Environmental Geology in the Permafrost Along the Sino-Russian-Mongolian Economic Corridor", edited and published research cases of geoenvironmental disasters in permafrost regions in Northeast China, and shared the research results of GERRP. At present, the research results of GERRP are gradually enriched, some of them have highly academic value, and have been put into engineering practice. ICRSE-NEFU has gradually shown its unique research charm since it became an ICL member in 2003 2002. In 2012, ICRSE-NEFU established a landslide research network in cold regions (ICL-CRLN), and then Research Center of Cold Regions Landslide was built.

Permafrost as one of the elements of the cryosphere, the change of thermodynamic stability of permafrost will directly affect the changes of hydrosphere, biosphere and lithosphere. Under the trend of global warming, the frequency and intensity of environmental and engineering geological disasters caused by permafrost degradation are getting higher and higher (Figs. A.16 and A.17). Taking the cold area in the southern boundary of the permafrost zone in Northeast China as study area, disasters such as ground subsidence, slope icing, landslides and other disasters caused by permafrost melting were studied. At the same time, we found melting permafrost also leads to seasonally high concentrations of greenhouse gases, triggering wildfires that may further accelerate permafrost degradation and environ- mental changes of terrestrial ecosystems and roads.

W. Shan · Y. Guo
Institute of Cold Regions Science and Engineering Northeast Forestry University, Harbin, China
e-mail: shanwei456@163.com

I. Alcántara-Ayala et al. (eds.), *Progress in Landslide Research and Technology, Volume 2 Issue 1, 2023*,
Progress in Landslide Research and Technology, https://doi.org/10.1007/978-3-031-39012-8

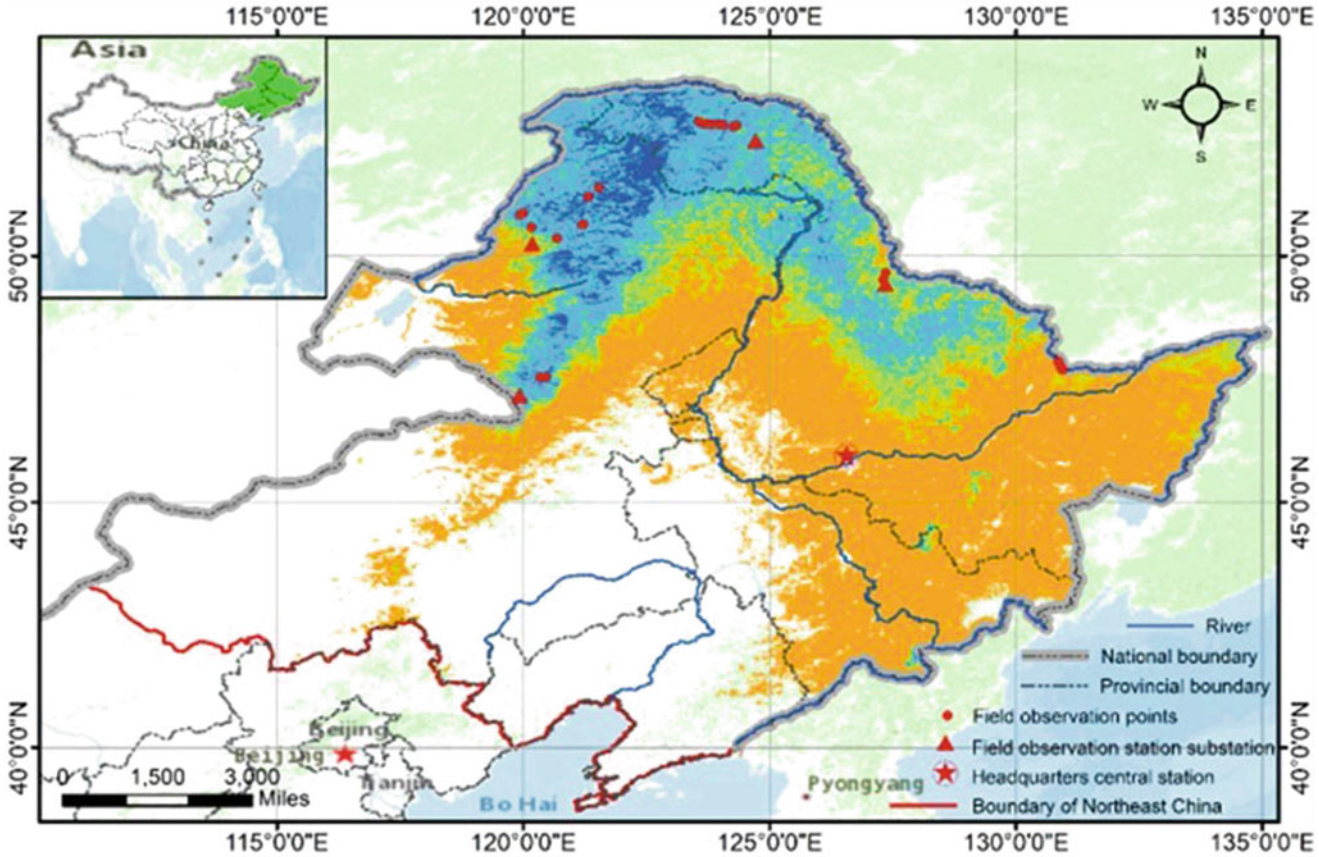

Fig. A.16 Permafrost distribution in NE of China (2014–2019)

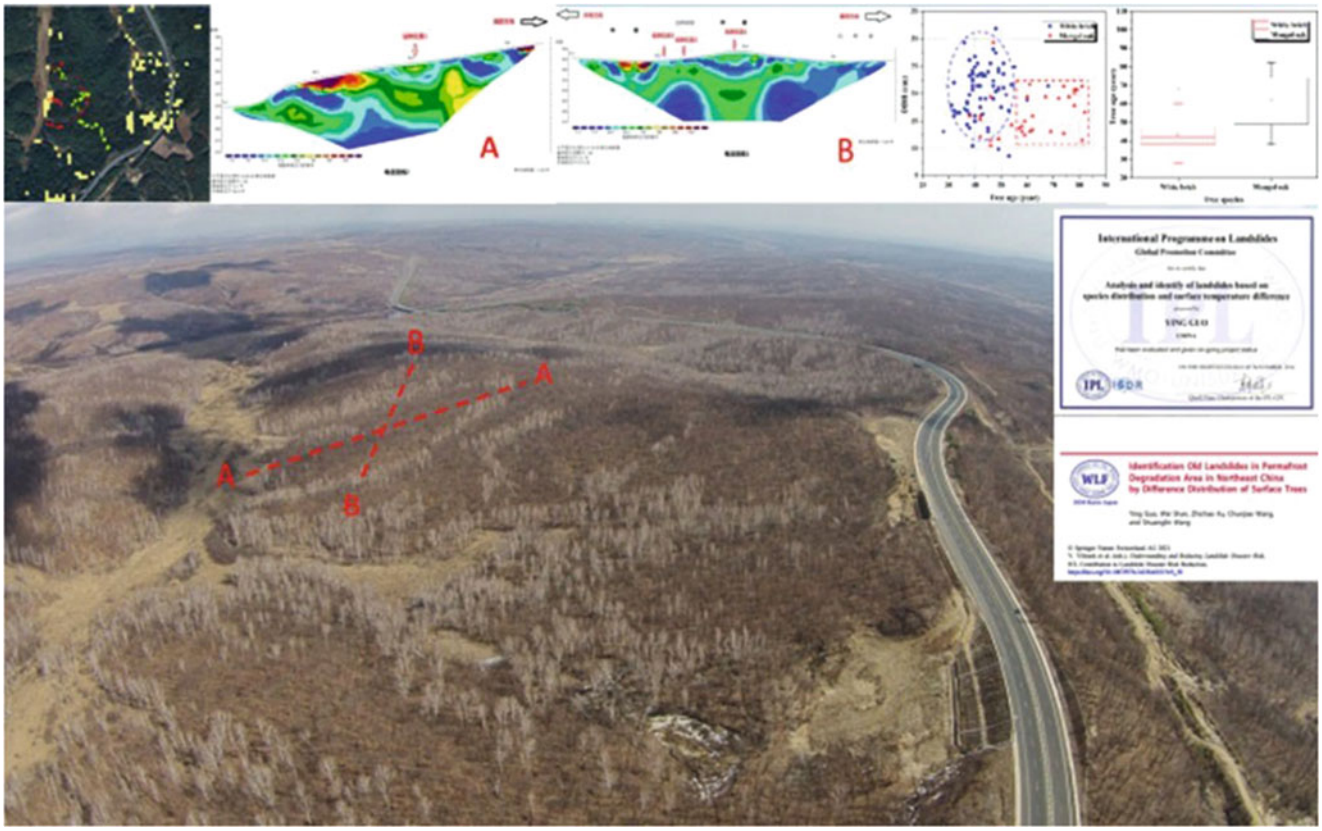

Fig. A.17 Different tree species and ages in the landslide area caused by permafrost degradation

Marui & Co. Ltd.

Taketoshi Marui and Yuji Ikari

Introduction

Marui & Co. Ltd. celebrated its 100th anniversary in 2020. Marui, as one of the leading manufacturers of testing apparatuses in Japan, has constantly been striving further to improve its service since its foundation in 1920, thus contributing to the sustainable development of our nation and society. Our main products cover various destructive and non-destructive testing apparatuses in geotechnical engineering, concrete engineering (mortar, aggregates, etc.), and ceramic engineering (Fig. A.18). Of particular note is that Marui has been helping manufacture ring-shear apparatuses (Fig. A.19) for the past half-century based on the leading-edge idea of Dr. Kyoji Sassa, Professor Emeritus at Kyoto University. Marui has delivered seven ring-shear apparatuses to the Disaster Prevention Research Institute, Kyoto University, and two to the International Consortium on Landslides. Also, the apparatuses were exported to the United States of America, China, Croatia, and Vietnam.

Since 2002, Marui has been a supporter of the International Consortium on Landslides (ICL) and has gradually been intensifying its contribution to the ICL's worldwide efforts for landslide risk reduction and international promotion of landslide research. According to NASA, more frequent and intense rainfall events due to climate change have been causing frequent landslides, particularly in mountains of Asian regions, including Japan, where waters can be stored in various ways. Summer monsoon rains, snow and glacier melt waters can destabilize steep mountainsides, triggering landslides, which are down-slope movements of rocks, soils, water, trees, etc. Marui, as an engineering supporter, commits deeply to various activities of research, particularly on triggering mechanisms of landslides.

In addition to the ring-shear apparatuses mentioned above, our company develops and sells soil and ground testing equipment. For example, our standard cyclic triaxial testing machine (Fig. A.20) is used by geological consultants, research laboratories, and educational institutions such as universities and technical colleges. Ground destruction phenomena, which often occur concurrently with earthquakes, significantly affect the seismic resistance of superstructures. Cyclic triaxial tests are used to determine the constants required to judge the liquefaction potential and to determine the cyclic deformation characteristics of the ground required for seismic response analysis.

This equipment can perform not only liquefaction and deformation tests, but also static triaxial tests, isotropic consolidation tests, and anisotropic consolidation tests.

In addition, control and data recording can be processed entirely on a personal computer.

Marui & Co. Ltd. takes great pleasure in developing, manufacturing, and providing new products of high value, sharing the sense of s achievement with our customers and thus contributing to social development. The entire staff of Marui is determined to devote ceaseless effort to keep its organization optimized for its speedy and high-quality services, by the motto "Creativity and Revolution," and strive hard to take a step further as a leading manufacturer of testing apparatuses, to answer our customer's expectations for the twenty-second century to come.

Marui continuously contributes to the 2030 Agenda for Sustainable Development and the Sendai Framework for Disaster Risk Reduction 2015–2030. In line with this, Marui signed KLC2020 in 2019 and will strongly support its actions, especially KCL2020 Actions 3,4,5, and 9.

T. Marui · Y. Ikari
Marui & Co. Ltd., Osaka, Japan
e-mail: hp-mail@marui-group.co.jp; http://marui-group.co.jp/en/index.html

I. Alcántara-Ayala et al. (eds.), *Progress in Landslide Research and Technology, Volume 2 Issue 1, 2023*,
Progress in Landslide Research and Technology, https://doi.org/10.1007/978-3-031-39012-8

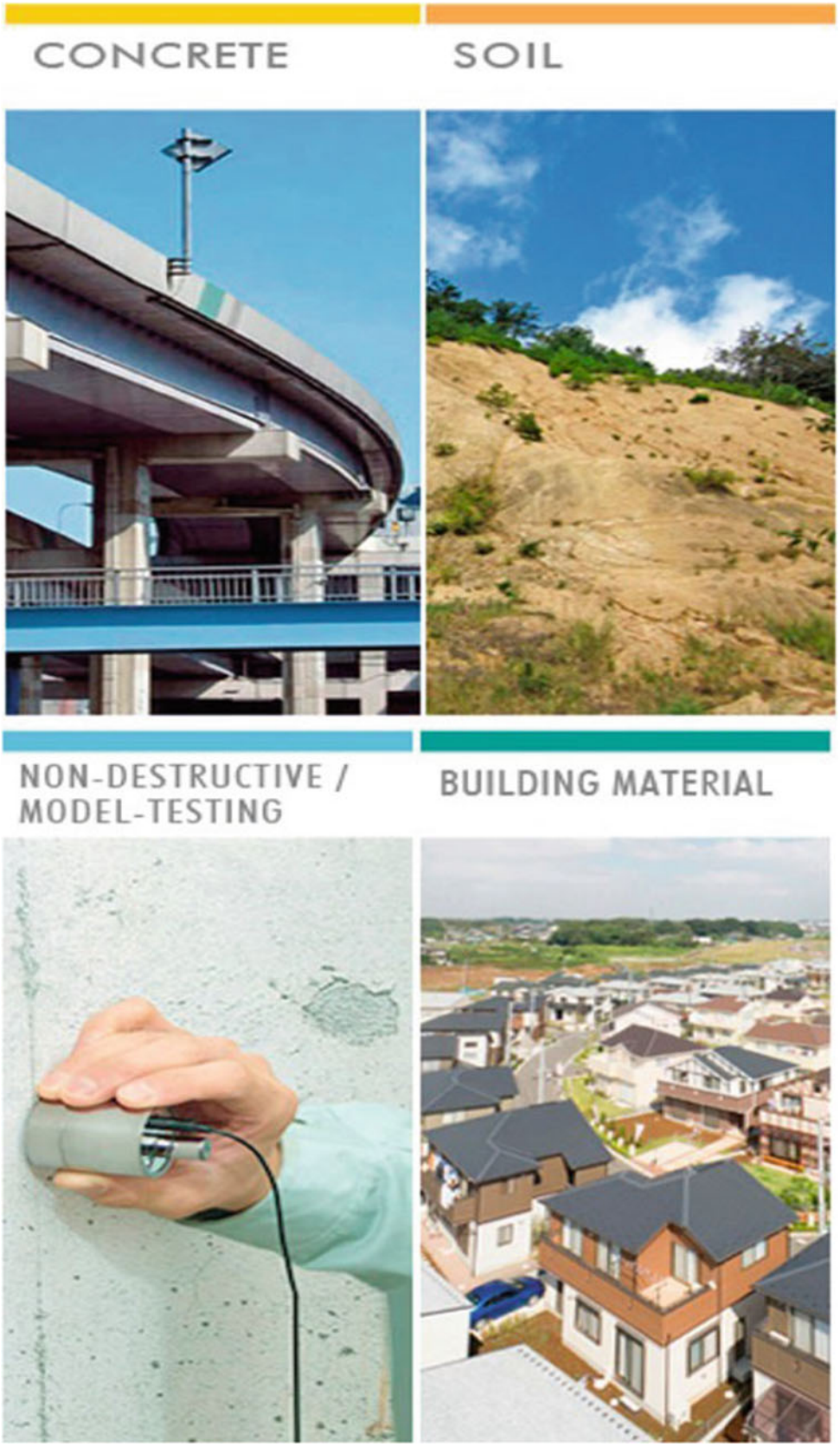

Fig. A.18 Products of testing apparatus such as non-destructive/model-testing for measuring intensity, physical property, durability, etc. for concrete, soil, building material, etc.

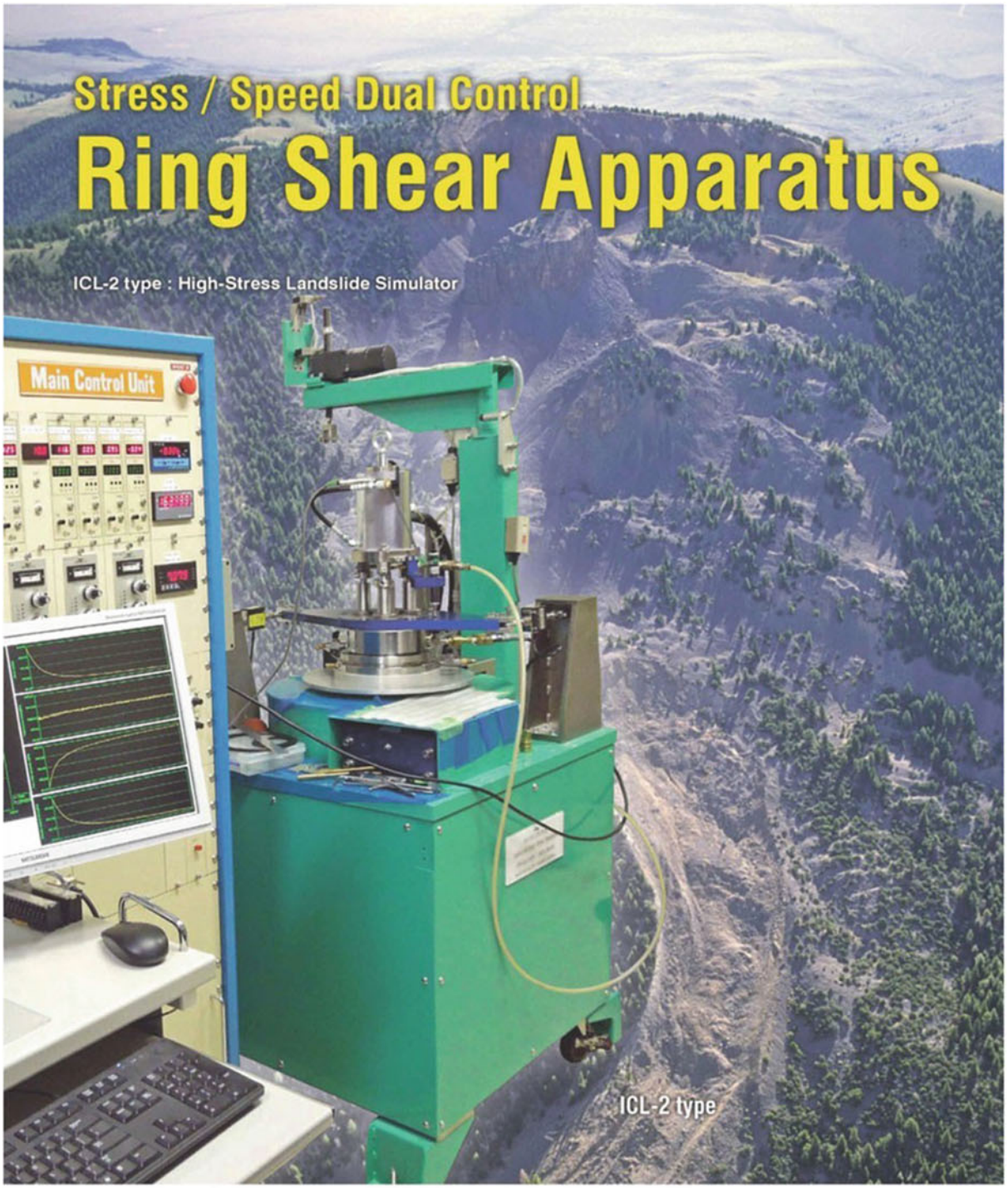

MARUI & CO., LTD.

Web site : https://www.marui-group.co.jp/en/
E-mail : hp-mail@marui-group.co.jp
Address : 1-9-17 Goryo, Daito City,
Osaka Prefecture,
574-0064, Japan
Phone : 81-72-869-3201
F a x : 81-72-869-3205

Fig. A.19 High-stress landslide simulator

Compliant standards	JGS 0541 / JGS 0542
Dynamic vertical load	Pneumatic servo system: 1 kN
Static vertical load	Servo motor method: 5 kN
Side pressure load	Air regulator method: 1 MPa
Back pressure load	Air regulator method: 0.5 MPa
Dynamic control method	Load/displacement control: 0.05 to 1.0 Hz
Static control method	Displacement control: 0.005 to 5.0 mm/min
Three-axis room	• Three-pillar fixed system • Specimen size: φ50 × H 100 mm
Measurement	• Axial pressure (external): 5 kN • Axial pressure (internal): 1 kN • External displacement: 25 mm • Internal displacement: ± 2 mm x 2 • Side pressure: 1 MPa • Pore pressure: 1 MPa • Volume change: 50 cc

Fig. A.20 Cyclic triaxial testing machine

NIPPON KOEI Nippon Koei Co., Ltd., Geohazard Management Division

Hiroaki Tauchi

Introduction

The Nippon Koei Group (NK) has been a leading international consultant providing engineering consulting services to over 5500 multi-disciplinary infrastructure and development projects in 160 countries worldwide. The landslide prevention specialist team (now called Geohazard Management Division) was established in 1966 to provide countermeasures against sediment disasters. Over the last 50 years, we have significantly improved the capacity of countries to respond and reduce risk from debris flows, slope instabilities, landslides, avalanches, and rock falls due to torrential rains, large-scale earthquakes, and volcanic eruptions that threaten a country's vital economic infrastructure lifelines, especially the road networks. At present, approximately 160 engineers provide a variety of technical consulting services to protect communities from disasters, as shown in Fig. A.21.

During disasters, we utilize remote sensing technologies such as 3D point clouds and interferometric SAR to create 3D models and gather surface and damage information to conduct a broad area survey, as shown in Fig. A.22. Based on this information, we provide experienced professional engineers to assess risk quickly and promptly respond with engineering design analyses and emergency and permanent measures based on our extensive experience and know-how. In order to efficiently plan and design disaster countermeasure works, we have implemented the automated design using visual programming, as shown in Fig. A.23. This automated design enables us to perform the 3D design of countermeasures quickly and calculate project costs, streamlining the overall process. Organizing design and construction information in 3D facilitates the construction process and allows for permanent maintenance by passing it on to the maintenance management phase as BIM (Building Information Modeling). As a result, the information necessary for effective maintenance is readily available and can be utilized throughout the project's lifespan.

To maximize the effectiveness of infrastructures, we address efficient countermeasure plans, design, and research regarding cost reduction and cost-effectiveness using various numerical analyses such as the finite element method (FEM) and discrete element method (DEM), etc.

In Japan, we have worked hard to restore and recover from sediment-related disasters caused by earthquakes and heavy rainfalls that have frequently occurred in recent years (the 2011 Great East Japan Earthquake, the Northern Kyushu Flood in 2017, etc.). We have received letters of appreciation from national and local governments for our efforts.

Our major international projects include "The Project for Countermeasure Construction Against the Landslides on Sindhuli Road Sect. II, Nepal," "The project for the rehabilitation of Sindhuli road affected by the 2015 Gorkha Earthquake, Nepal," and "The project for landslide prevention for National Road 6 in Honduras"; all funded by the Japan International Cooperation Agency (JICA) grantsin-aid. Through these projects, we are contributing to the socioeconomic development of each country by improving vulnerable locations in road networks against sediment disasters, promoting traffic safety, and providing logistics assistance for road users. In particular, the first of the three NK's projects mentioned above won the "third JAPAN Construction International Award" from the Ministry of Land, Infrastructure, Transport and Tourism as the project that has realized "high-quality infrastructures" through its excellent know-how, technical capabilities, and project management capabilities.

NK is an ICL member using its technology to reduce geohazard risk. Through various projects, NK continuously contributes to the 2030 Agenda for Sustainable Development and the Sendai Framework for Disaster Reduction 2015–2030. Using our full capability with abundant experiences in Japan and Asia prone to natural disasters, we hope to contribute much more to reducing global sediment disasters, including landslides (Fig. A.24). In line with this, NK has signed the KLC 2020 and will strongly support its actions.

H. Tauchi
Geohazard Management Division, Nippon Koei Co., Ltd., Tokyo, Japan

I. Alcántara-Ayala et al. (eds.), *Progress in Landslide Research and Technology, Volume 2 Issue 1, 2023*,
Progress in Landslide Research and Technology, https://doi.org/10.1007/978-3-031-39012-8

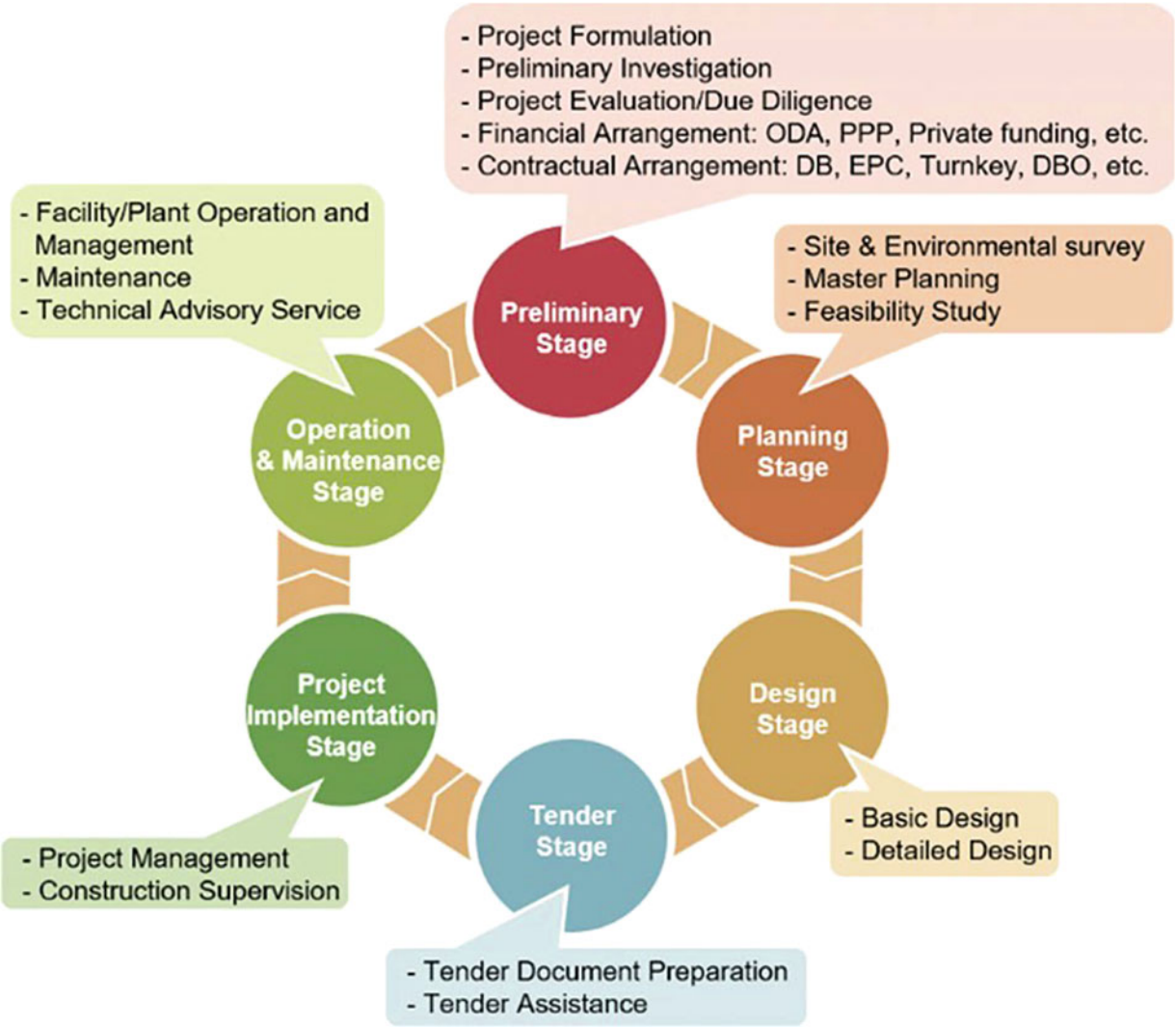

Fig. A.21 Our service for geohazard management

Fig. A.22 (left) a Landslide site, (right) 3D Point Clouds

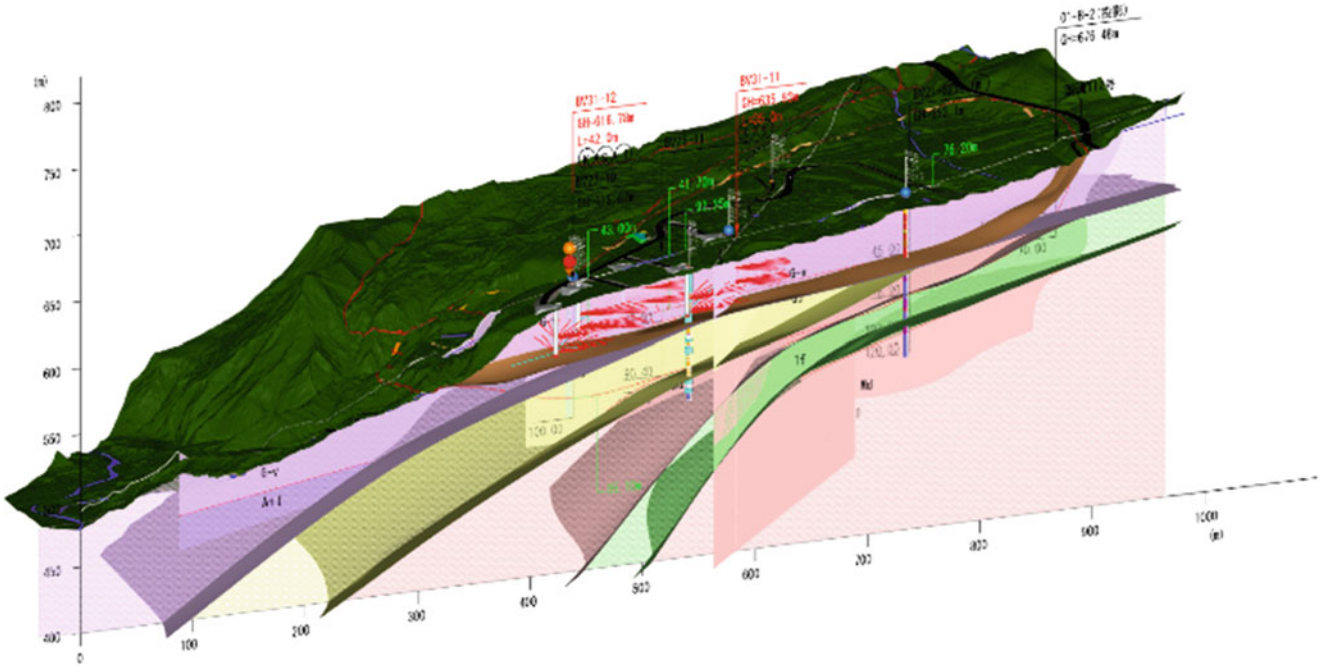

Fig. A.23 Visual programming and Automated design

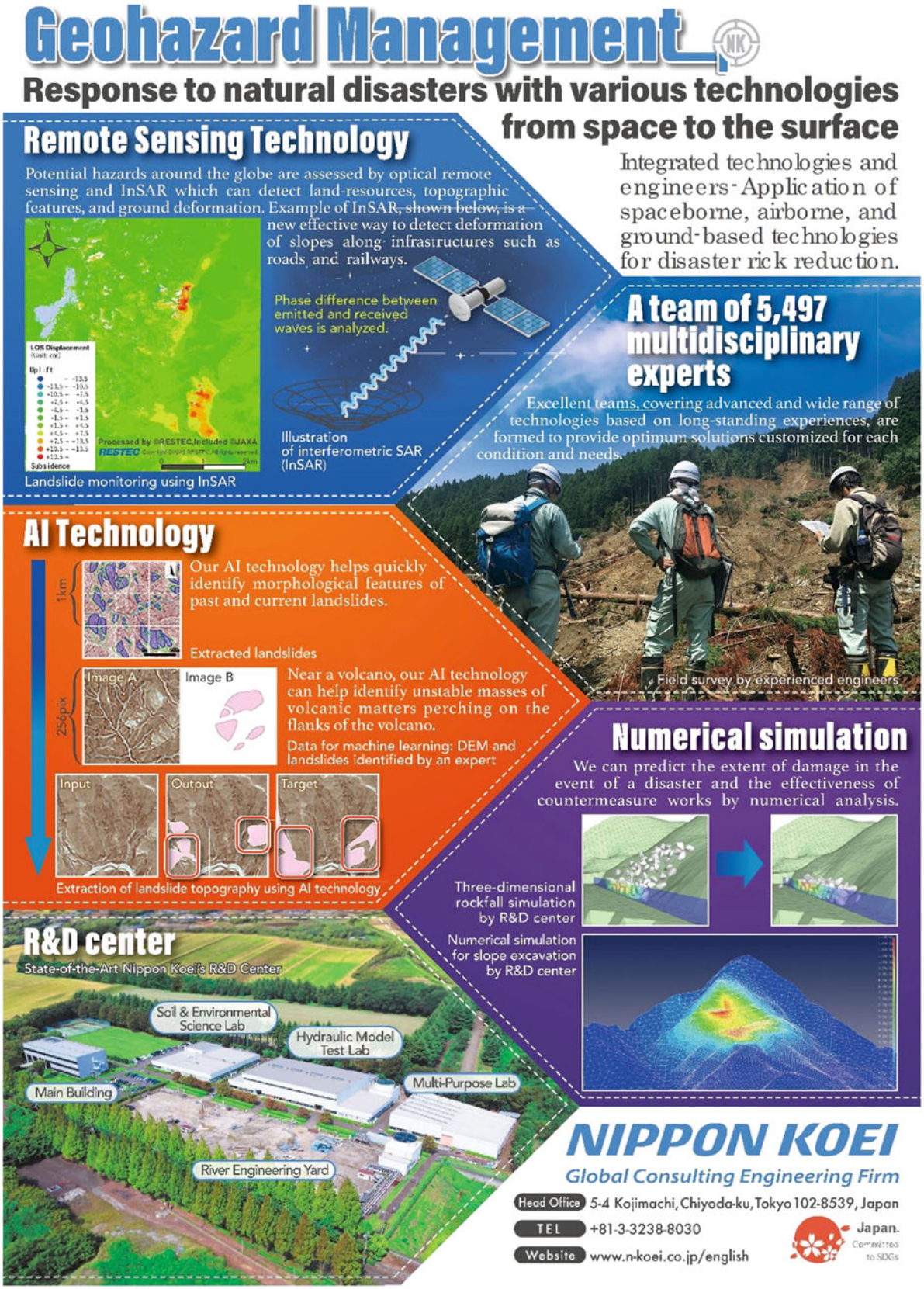

Fig. A.24 Introduction of our survey analysis technology for geohazard

Ellegi Srl

Ellegi Srl

Introduction

Ellegi srl provides worldwide monitoring services and produces Ground Based synthetic aperture radar (GBInsAR) for remote measurement of displacements and deformations on natural hazards and manmade buildings using its own designed and patented LiSALab system.

Its activities started in 2003 as a spin off project to exploit commercially the Ground Based Linear Synthetic Aperture Radars technology developed by European Commission's Ispra Joint Research Centre and based on the results of more than 10 years of research. Since then, Ellegi has industrialized and developed the core technology of the LiSALab system and latest LiSAmobile system represents the fifth generation of development.

In 2003 it was the first commercial company in the world to provide GBInSAR measurements of natural hazards and structure (Figs. A.25 and A.26).

Ellegi srl offers:

- Displacement fields measurement, control and monitoring of the deformation caused by natural hazards, like landslides, rockslides, sinkhole, volcanic deformation in every operative condition, including emergencies,
- Structural strain fields measurement, control, monitoring and diagnosis of the deformation affecting buildings, bridges, viaducts, dams.
- GBInSAR monitoring systems, installation, management and maintenance in order to provide information about natural hazards or anthropic activity, that can generate or cause slopes failures or buildings instabilities.

In all the above-mentioned activities Ellegi srl uses the GBInSAR LiSALab technology that represents a real "break-through".

E. Srl
Como, Italy

I. Alcántara-Ayala et al. (eds.), *Progress in Landslide Research and Technology, Volume 2 Issue 1, 2023*,
Progress in Landslide Research and Technology, https://doi.org/10.1007/978-3-031-39012-8

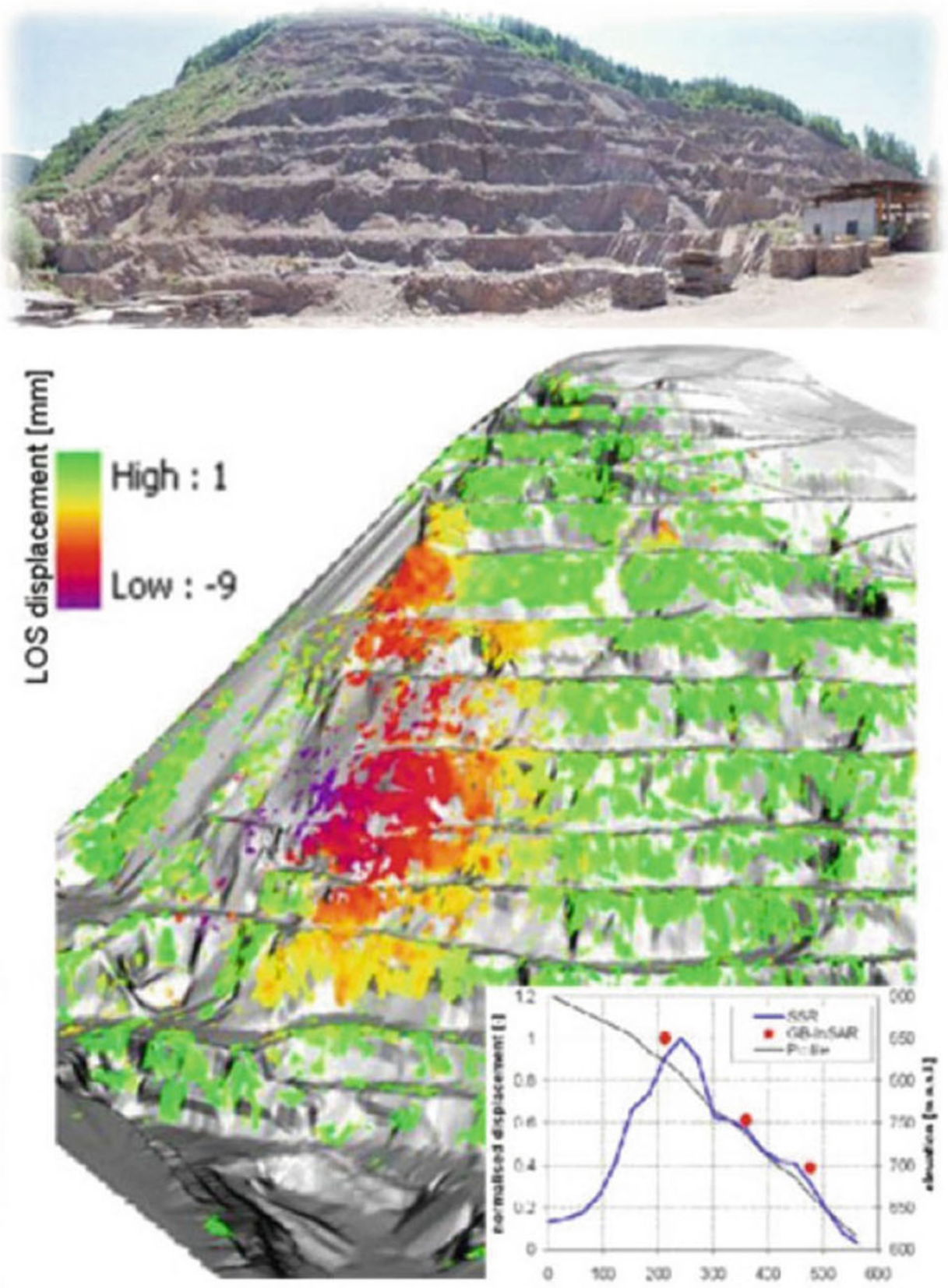

Fig. A.25 GBInSAR LiSALab technology quarry monitoring example and displacements' field comparison between the GBInSAR measurement and FEM model results

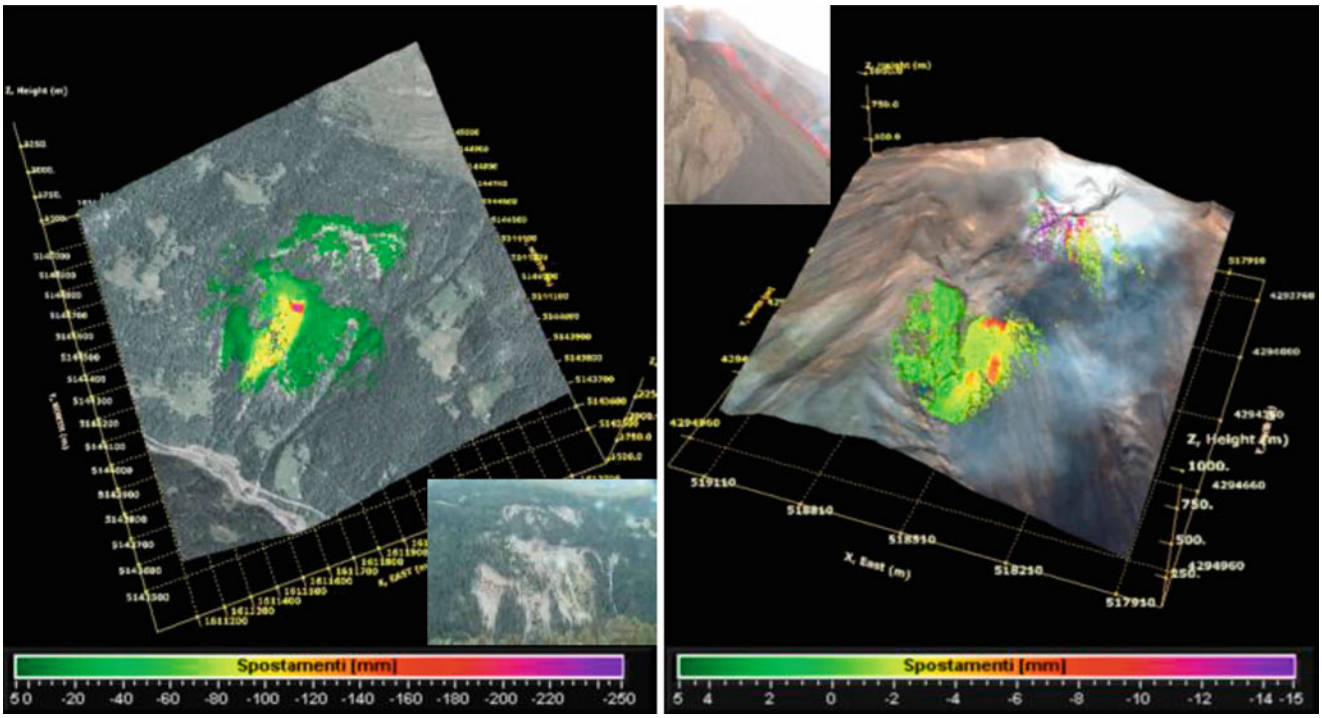

Fig. A.26 GBInSAR LiSALab technology result in monitoring a slope affected by a landslide (left) and a volcanic slope affected by deformation (right). Landslide or moving area mapping and boundaries identification is made easy by GBInSAR LiSALab technology

IDS GeoRadar s.r.l.

IDS GeoRadar s.r.l.

Introduction

IDS GeoRadar, part of Hexagon, provides products and solutions, based on radar technology, for monitoring applications including landslides, rockfalls, complex structures, mining and civil engineering. The company is a leading provider of Ground Penetrating Radar (GPR) and Interferometric Radar solutions worldwide.

IDS GeoRadar is committed to delivering best-in-class performance solutions and to the pursuit of product excellence, through the creation of application-specific, innovative and cost-efficient systems for a wide range of applications:

- Utility mapping and detection
- Civil engineering
- Railway and road engineering
- Geology and environment management
- Archaelogy
- Forensics
- Landslide monitoring
- Mining safety

Natural Hazard Monitoring Solution

The use of slope monitoring radar is now the standard practice for the active monitoring of slope in open pit mines and for safety critical landslide monitoring with the aim of providing alerts in the event of progressive movements which could potentially lead to slope failure and assessing worker safety. The unique IBIS-FM EVO radar system accurately monitors multiple scales of displacements in real time, from early detection of slow movements to fast accelerations associated with slope collapse. The great operative range, up to 5000 m, allows to safely deploying the system in comfortably accessible areas, without exposing people and equipment to hazardous zones.

IDS GeoRadar cooperate with TRE ALTAMIRA, the worldwide leader in ground monitoring services using satellite InSAR offer a comprehensive solution—InSAR Service—to fulfill all mine stability needs, ranging from monitoring large-scale mining operations over hundreds of square kilometers, to specific movements at the pit scale. With the large spatial coverage of satellite data, mining engineers can identify unstable areas over wide areas, also with the ability to extend the analysis of deformation back in time. All mining assets can be monitored regularly and precisely for deformation (Figs. A.27 and A.28).

IDS GeoRadar s.r.l.
Pisa, Italy

I. Alcántara-Ayala et al. (eds.), *Progress in Landslide Research and Technology, Volume 2 Issue 1, 2023*,
Progress in Landslide Research and Technology, https://doi.org/10.1007/978-3-031-39012-8

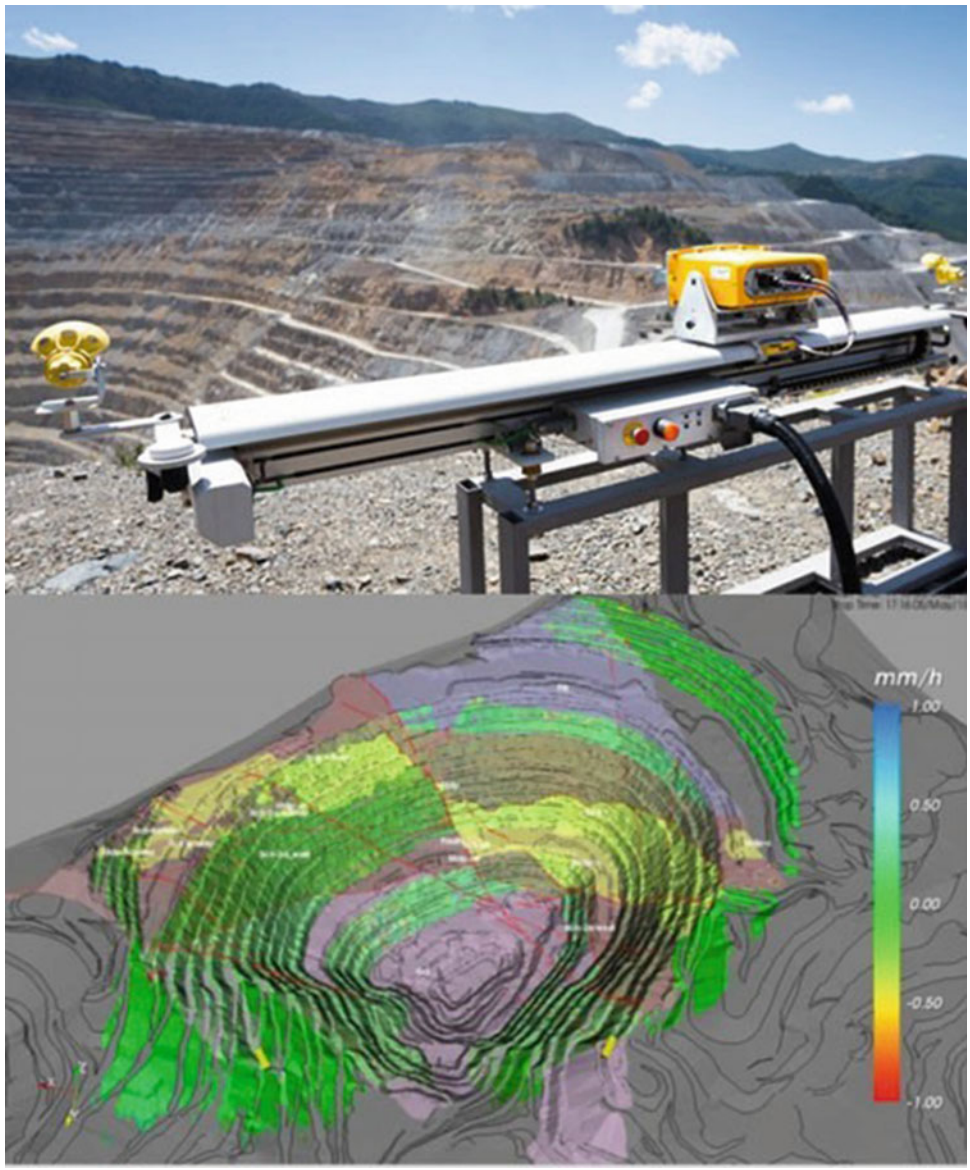

Fig. A.27 IDS GeoRadar: innovative interferometric radar for mining, environmental and civil engineering

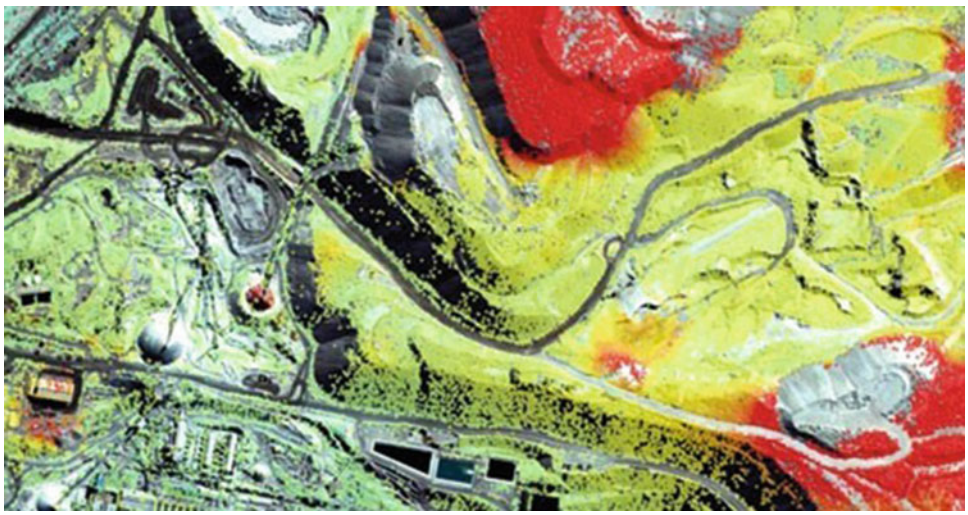

Fig. A.28 InSAR service—ground motion monitoring for mining operations

Chuo Kaihatsu Corporation

Lin Wang

Introduction

Chuo Kaihatsu Corporation (CKC) was founded in 1946, and has been aiming to become the "Only One" consultant for our customers. We engage in the hands-on work that will "Remain with the earth, Remain in people's hearts, and Lead to a prosperous future". We focus on road, river and dam engineering to flesh out industrial infrastructures specifically by means of geophysical/geotechnical/geological investigations, civil engineering surveys and project implementations. In recent years, we make significant efforts on earthquake disaster mitigation, sediment disaster prevention/mitigation and ICT information services. Many achievements of ours have already contributed to the mitigation of natural disasters such as landslides, earthquakes and slope failures in Japan, Asia and the Pacific Region. We aim to provide technological contributions so that a sustainable society will continue to develop in the future (Figs. A.29, A.30, A.31 and A.32).

Fig. A.29 Design for various structures

L. Wang
Chuo Kaihatsu Corporation, Tokyo, Japan
e-mail: wang@ckcnet.co.jp; https://www.ckcnet.co.jp/global/; https://www.ckcnet.co.jp/contactus/

I. Alcántara-Ayala et al. (eds.), *Progress in Landslide Research and Technology, Volume 2 Issue 1, 2023*,
Progress in Landslide Research and Technology, https://doi.org/10.1007/978-3-031-39012-8

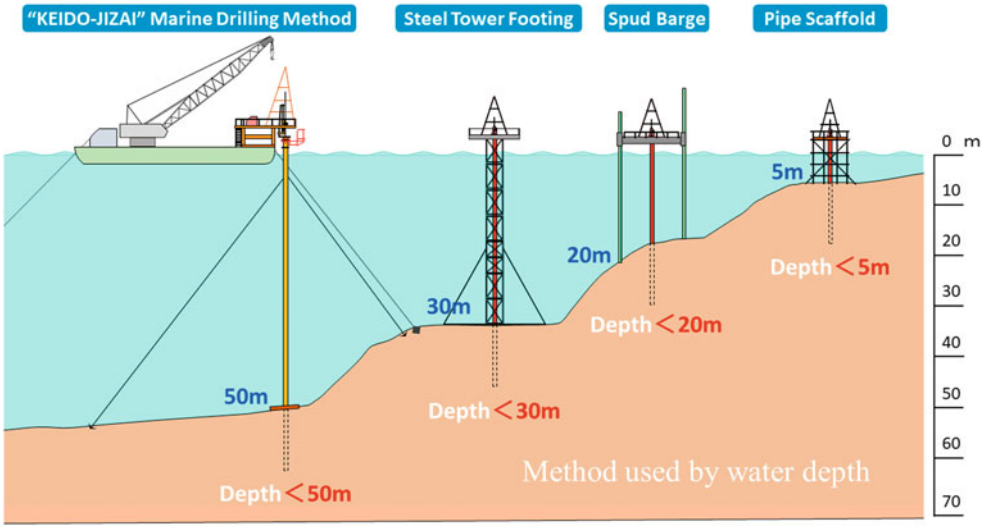

Fig. A.30 Deepwater drilling surveys

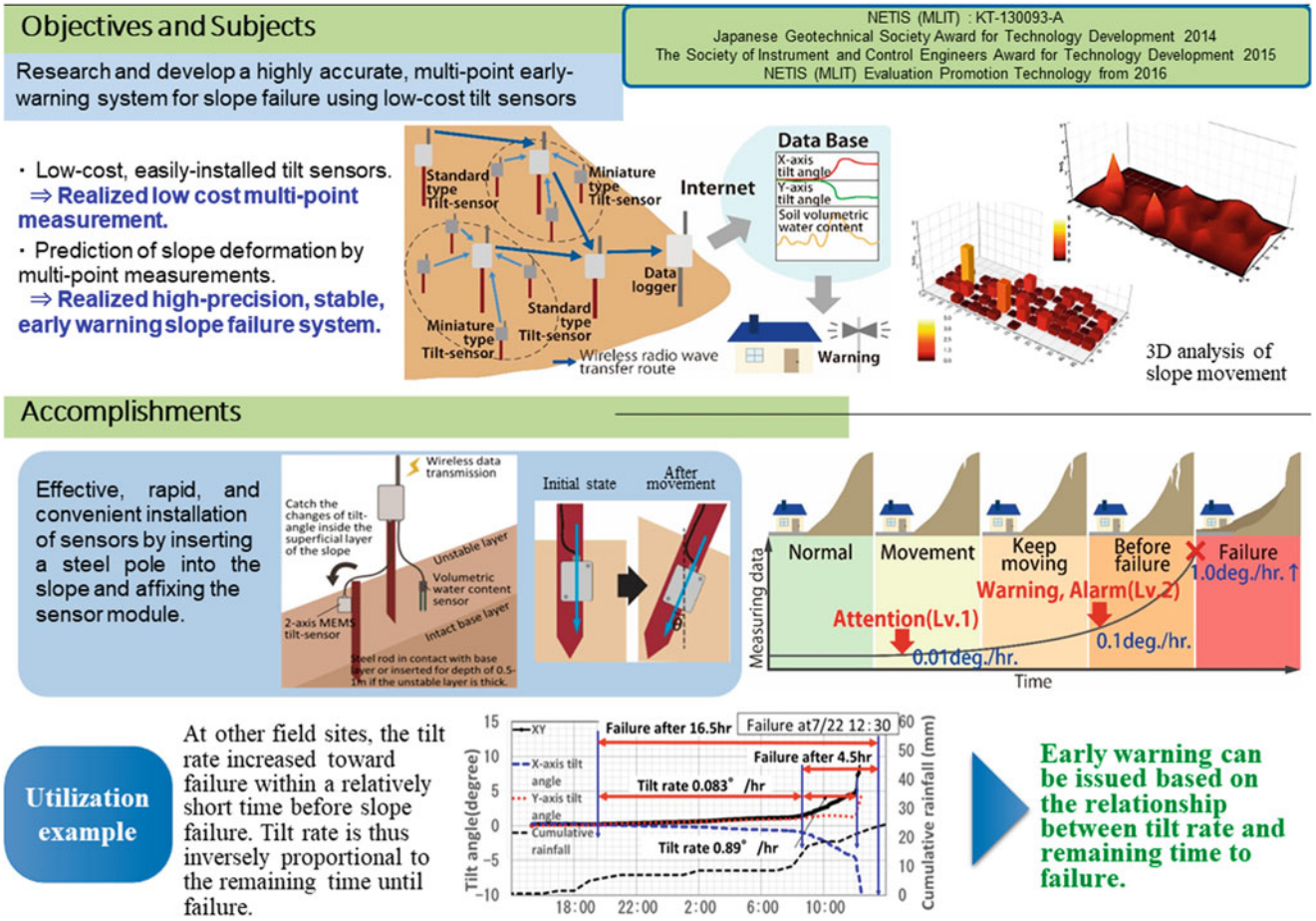

Fig. A.31 The early warning monitoring system of slope failure using multi-point tilt change and volumetric water content

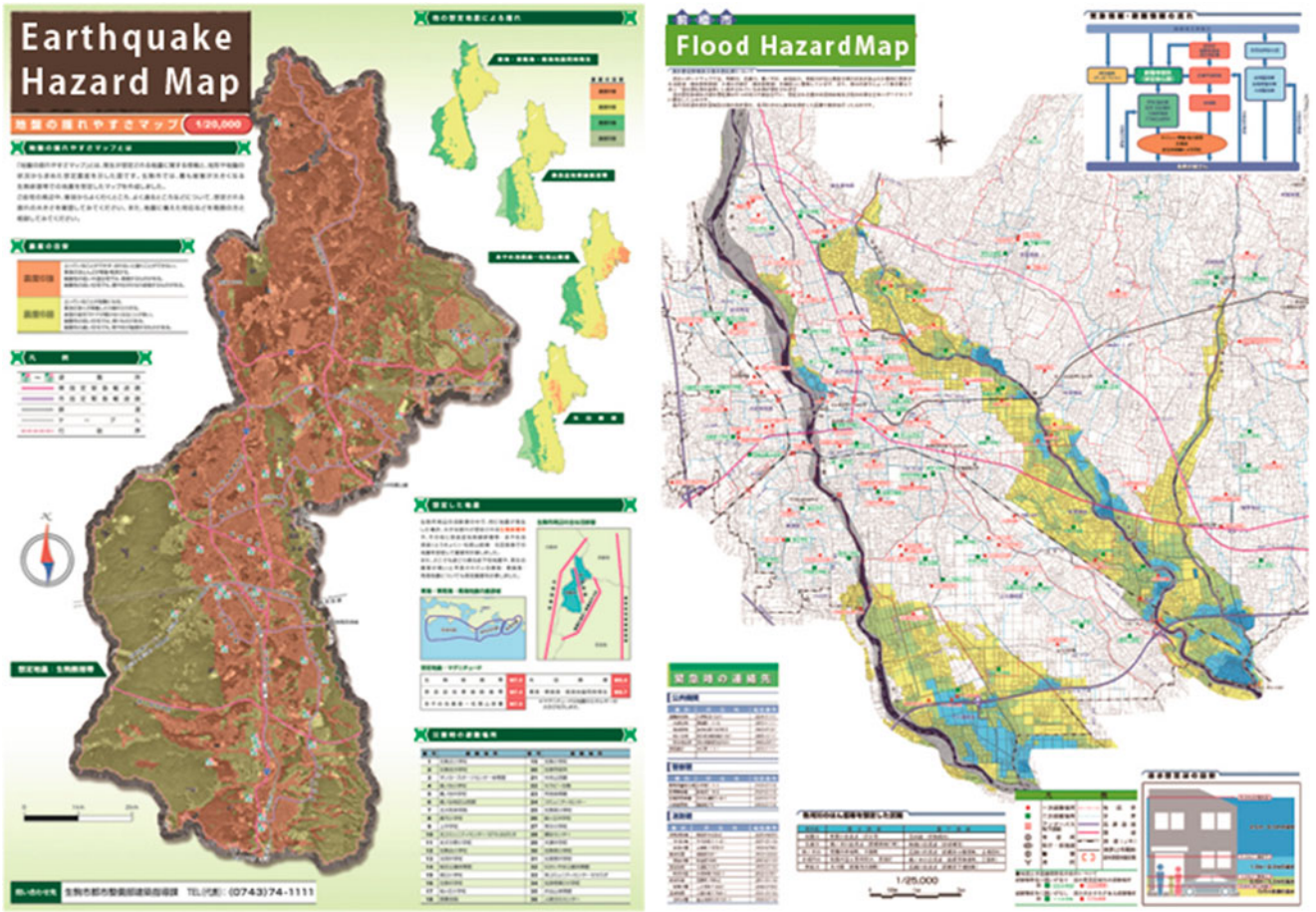

Fig. A.32 Making hazard map for sediment disaster, tsunami, flood, earthquake, liquefaction, etc.. . .

Godai Corporation

Godai Corporation

Introduction

Ever since its foundation in 1965, Godai Kaihatsu Co. Ltd. a civil engineering consulting firm, has long been providing a variety of software and measures particularly for natural disaster mitigation. With its rich expertise in both civil engineering and information technology (IT), the company has its primary goal to address real-world needs of disaster mitigation. All the staff of Godai Kaihatsu Co. Ltd. feels it more than happy that their cutting-edge technologies help mitigate natural disasters (Figs. A.33, A.34, A.35 and A.36).

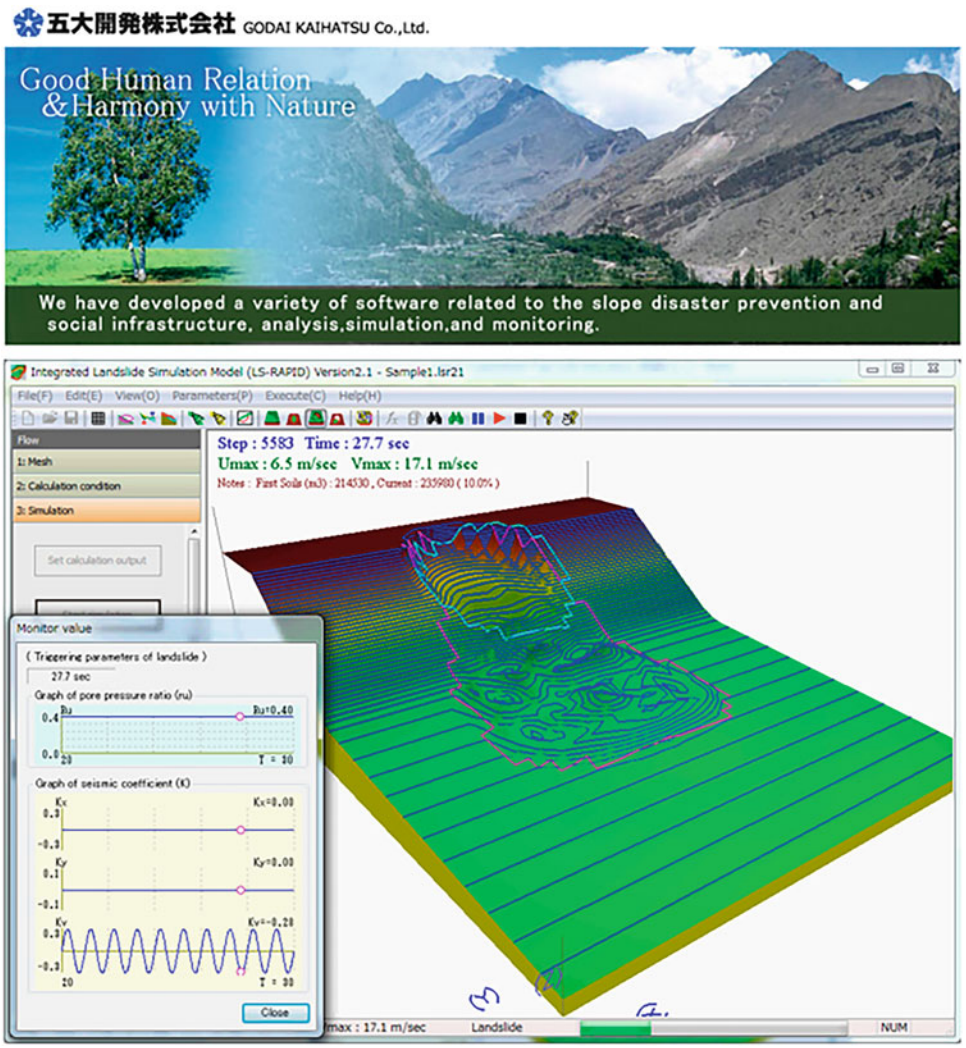

Fig. A.33 Integrated model simulating of earthquake & rain induced rapid landslides (LS-RAPID)

I. Alcántara-Ayala et al. (eds.), *Progress in Landslide Research and Technology, Volume 2 Issue 1, 2023*,
Progress in Landslide Research and Technology, https://doi.org/10.1007/978-3-031-39012-8

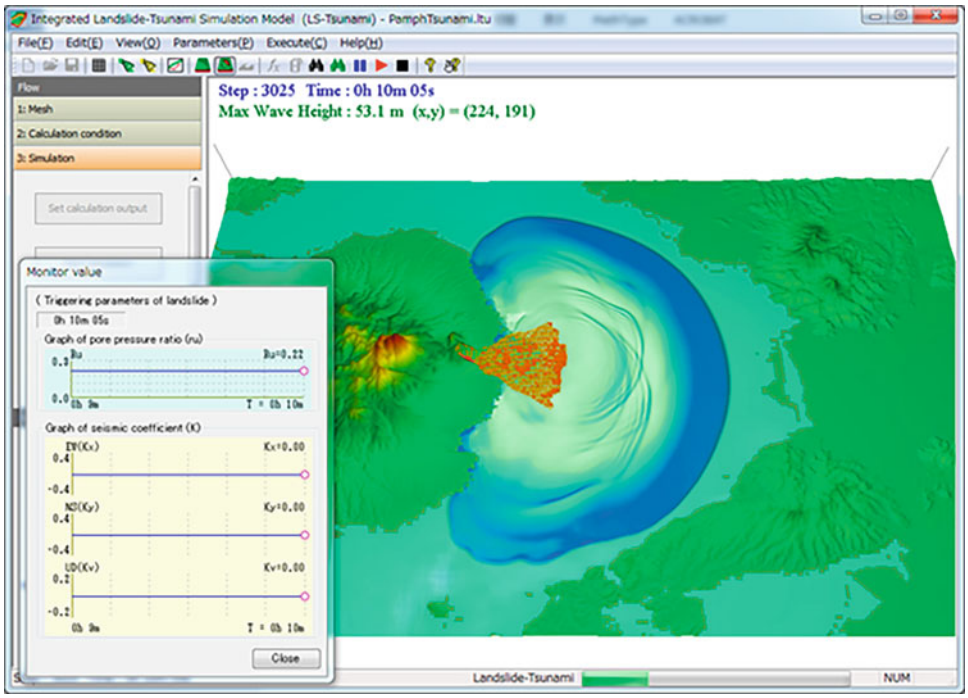

Fig. A.34 Tsunami model (LS-Tsunami)

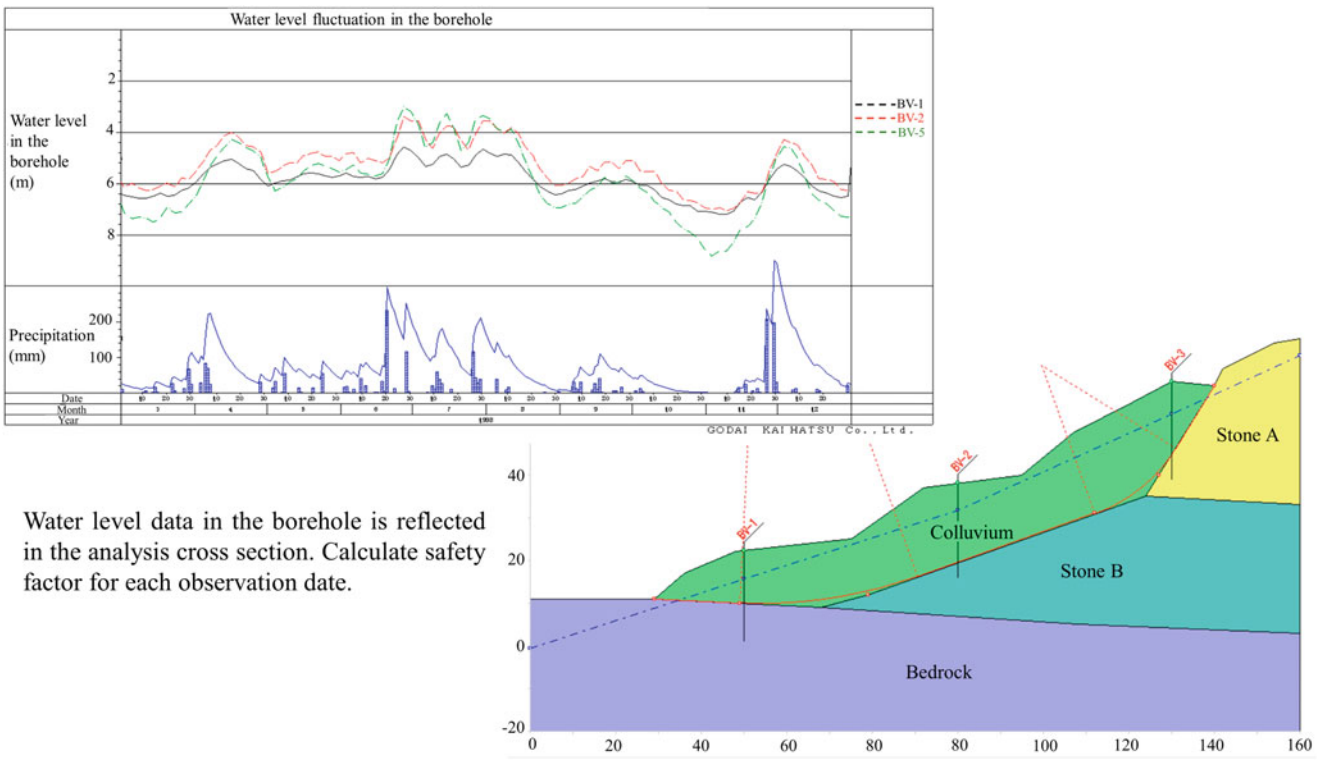

Fig. A.35 Power SSA PRO-Two-dimensional slope stability calculation of earthquake and rain induced landslide

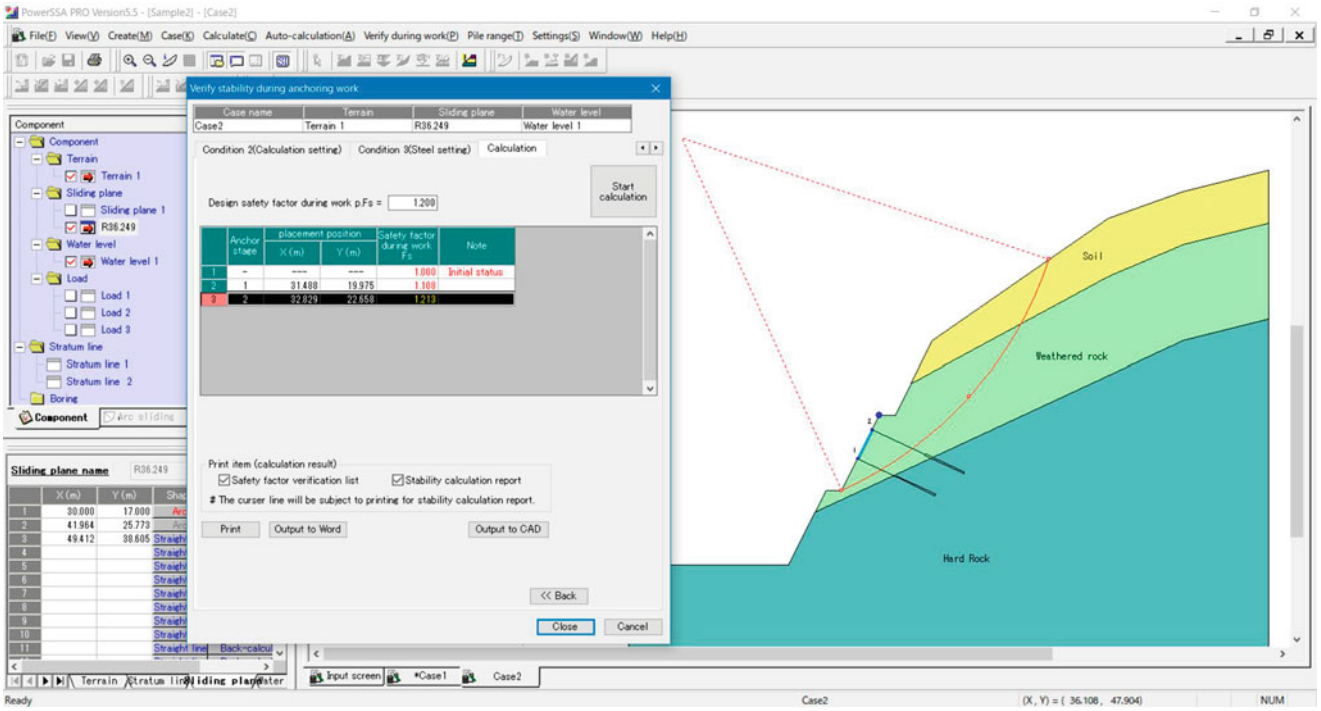

Fig. A.36 Anchor software-slope stability analysis for ground ancho

Kiso-Jiban Consultants Co. Ltd

Kaoru Hanai and Junichiro Odaka

Introduction

Since its establishment in 1953, Kiso-Jiban has been contributing on the development of social infrastructure as a "comprehensive construction consultant with strong geotechnical capabilities" in various situations, such as ground investigation, laboratory testing, analysis, civil structure design, etc. Kiso-Jiban has been working on the technological development for disaster prevention and mitigation against the recent exacerbation of natural disasters.

InSAR (Interferometric Synthetic Aperture Radar)

SAR is a technique that utilizes interference of radio waves for precise determination of distance. Kiso-Jiban has succeeded in estimation of both extent and rate of landslide movements by combining the topography interpretation and InSAR analysis.

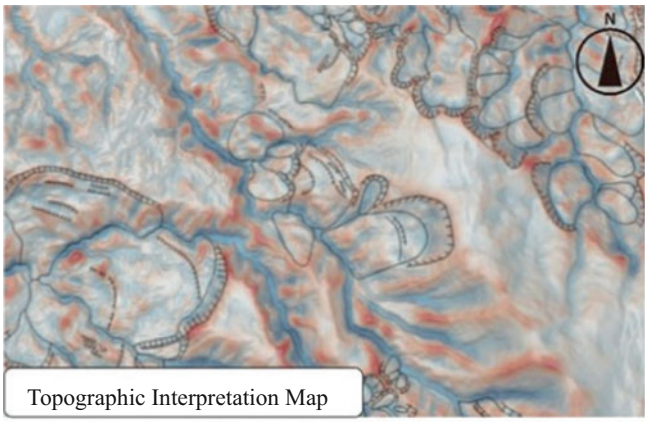

Topographic Interpretation Map

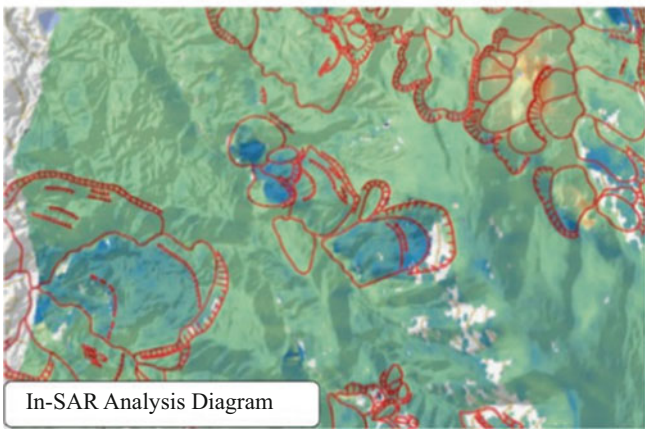

In-SAR Analysis Diagram

GP (Gel-Push) Sampling

GP Sampling can collect gravelly soil, etc., which is difficult to be collected by conventional samplers, by using a highly-concentrated water-soluble polymeric gel. GP Sampling was introduced in ISO 22475-1: 2021 revised in October 2021 as Category A, which provides the highest quality soil samples.

K. Hanai · J. Odaka
Kiso-Jiban Consultants Co. Ltd., Tokyo, Japan
e-mail: kisojiban-contactus@kiso.co.jp; https://www.kisojiban.com/

I. Alcántara-Ayala et al. (eds.), *Progress in Landslide Research and Technology, Volume 2 Issue 1, 2023*,
Progress in Landslide Research and Technology, https://doi.org/10.1007/978-3-031-39012-8

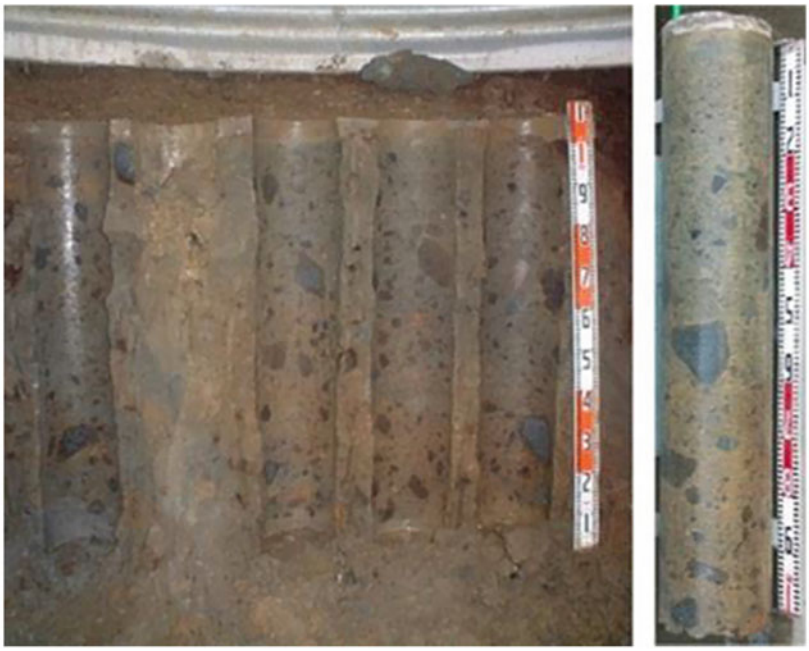

GP Sampling was performed in the disturbed soil mass right above the landslide surface (left) and the soil sample collected (right)

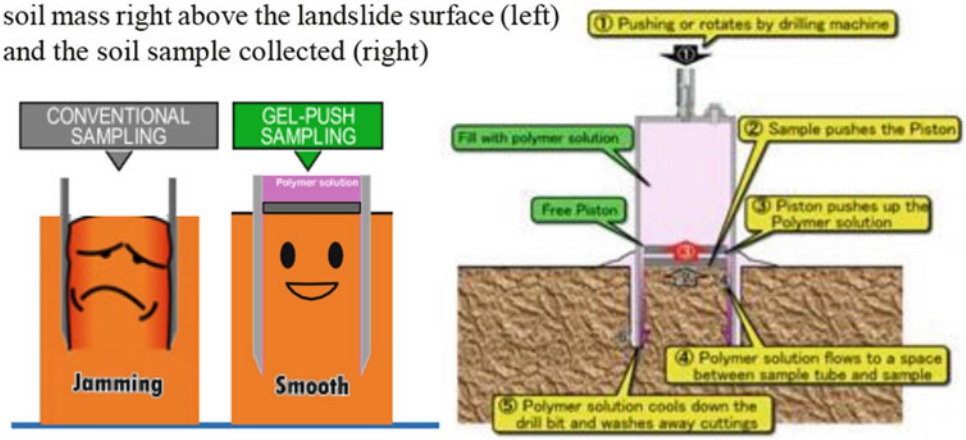

Slope Stability Analysis and Evaluation

Kiso-Jiban provides a wide range of numerical analyses related to slope stability evaluation. We have a wide range of analysis methods, from general two-dimensional limit equilibrium analysis to finite element analysis and analysis of rock masses with discontinuities, and we are challenging on the analysis that considers variability of ground and modelling uncertainty.

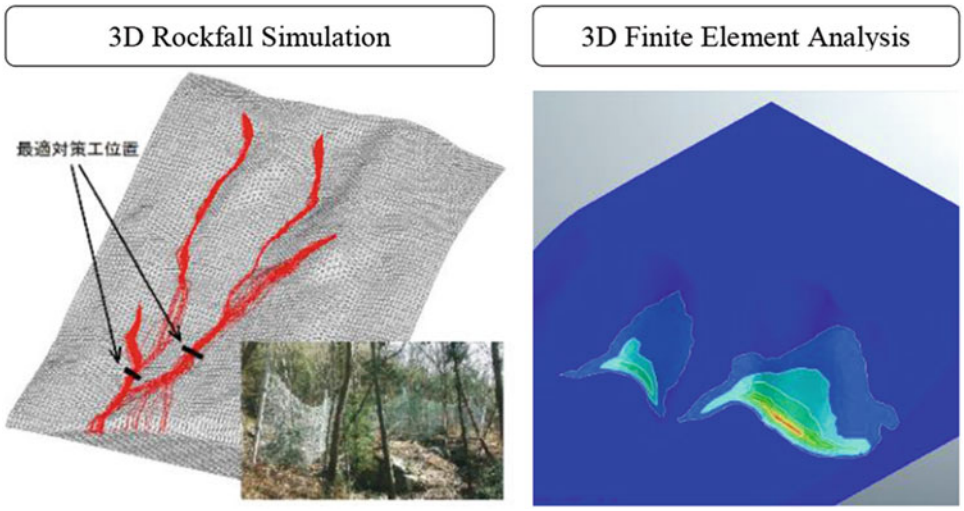

Inspection Technique for Disaster Danger Spots Using Mixed Reality (MR) Technology

MR (Mixed reality) is a technology that blends physical and digital worlds by superimposing 3D data and digital information on the real world as computer graphics.

Dangerous slopes with rockfall sources are spots where many unstable bedrocks and floating rocks exist. In many cases, approaching the inspection point on an outcrop is a difficult and dangerous task for investigators. Using MR technology makes it possible to realistically reproduce the outcrop situation at the site as a hologram. The outcrop situation can be safely inspected and confirmed without going to the site.

Kokusai Kogyo Co. Ltd

Kokusai Kogyo Co. Ltd.

Introduction

Kokusai Kogyo Co. Ltd. as a leading company of geospatial information technologies has long been providing public services with its comprehensive expertise to address real-world needs and cutting-edge measurement technologies. Kokusai Kogyo Co. Ltd. helps rebuild "Green Communities," which has been of our great concern in terms of "environment and energy," "disaster risk reduction" and "asset management". Kokusai Kogyo Co. Ltd. offers advanced and comprehensive analyses of geospatial information for developing new government policies, maintaining and operating social infrastructures safe and secure, and implementing low-carbon measures in cities. Influenced by the recent global climate change, extreme rainfall events have become more frequent worldwide and resultant hydro-meteorological hazards are creating more deaths and devastations particularly in many developing countries where effective advanced countermeasures are not readily available. Kokusai Kogyo Co. Ltd. is proud of its achievements in establishing resilient infrastructure systems and implementing effective monitoring/early warning systems in developing countries, which have long been helping reduce the risks from natural hazards (Figs. A.37, A.38, A.39 and A.40).

I. Alcántara-Ayala et al. (eds.), *Progress in Landslide Research and Technology, Volume 2 Issue 1, 2023*,
Progress in Landslide Research and Technology, https://doi.org/10.1007/978-3-031-39012-8

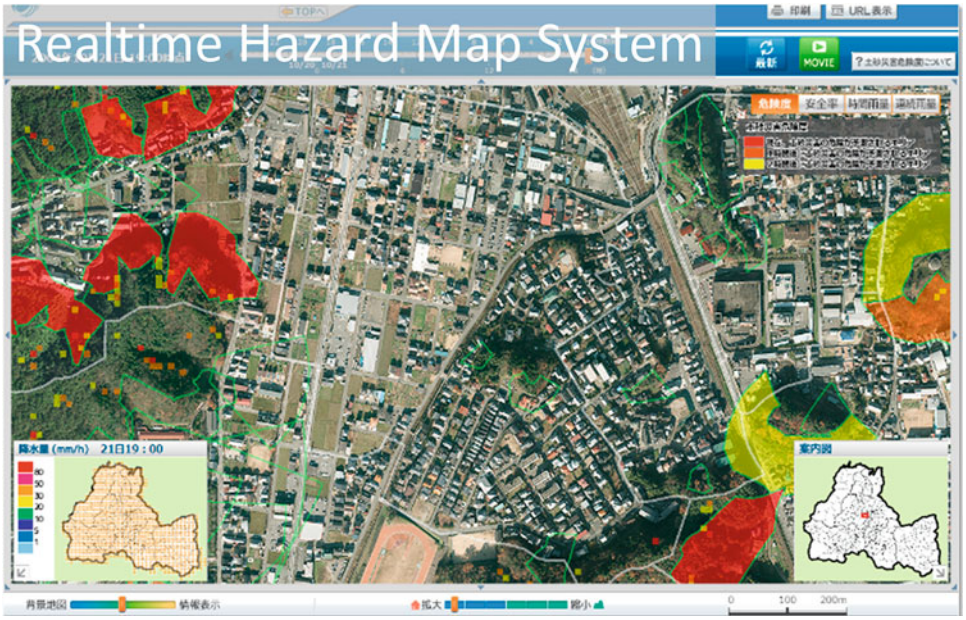

Fig. A.37 Our realtime hazard map reflects up-to-date information of soil natures and precipitations at landslide hazard sites, etc. that can constantly be changing, and evaluates area-wide hazard risk in real-time

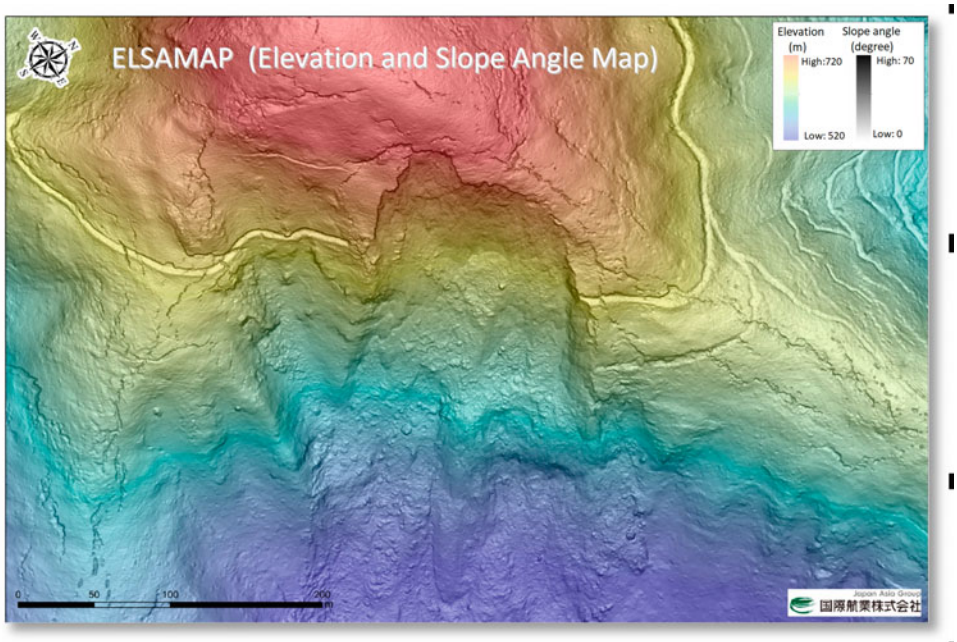

Fig. A.38 ELSAMAP is our cutting-edge 3D terrain visualization method allowing great geomorphological details to be visualized in one glance with gray-scaled slope inclinations and colored altitudes. ELSAMAP has been used to interpret micro-topographies, landslides and some other things

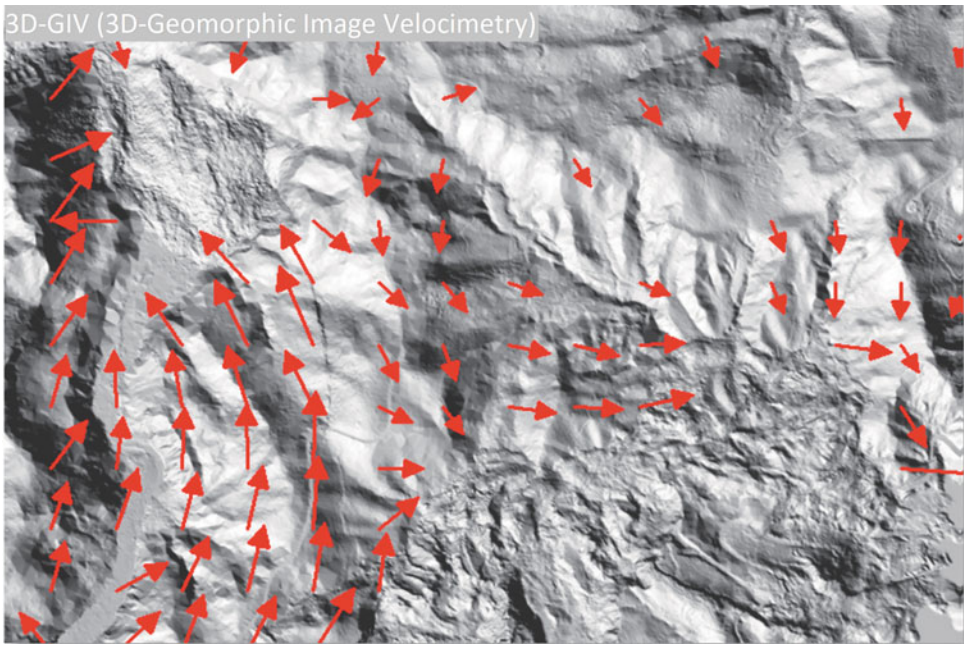

Fig. A.39 3D-GIV can help grasp the ground surface displacement caused by natural phenomena such as landslide by analyzing differences between digital geomorphic images obtained through ad hoc Airborne Laser Surveys

Fig. A.40 "Shamen-net" is a total monitoring system integrating GNSS and other monitoring device (Measurement precision: ± mm, on a real time basis)

OSASI Technos, Inc.

OSASI Technos, Inc.

Introduction

OSASI Technos, Inc. has been making its best efforts to develop its cutting-edge technologies for landslide early warning. Its unique compact and lightweight sensors making up the Landslide Early Warning System enable long-term monitoring of unstable landslide mass movements, precipitations, porewater pressure buildups, etc. in a remote mountainous area where commercial power is often unavailable. OSASI Technos, Inc. is also proud of its advanced technology to transfer observed data even in areas with poor telecom environments as proven in the successful implementations in South Asia. All staff members of OSASI Technos work together for mitigation of landslide disasters worldwide (Figs. A.41, A.42, A.43 and A.44).

OSASI Technos, Inc.
OSASI Technos, Inc., Kochi, Japan

I. Alcántara-Ayala et al. (eds.), *Progress in Landslide Research and Technology, Volume 2 Issue 1, 2023*,
Progress in Landslide Research and Technology, https://doi.org/10.1007/978-3-031-39012-8

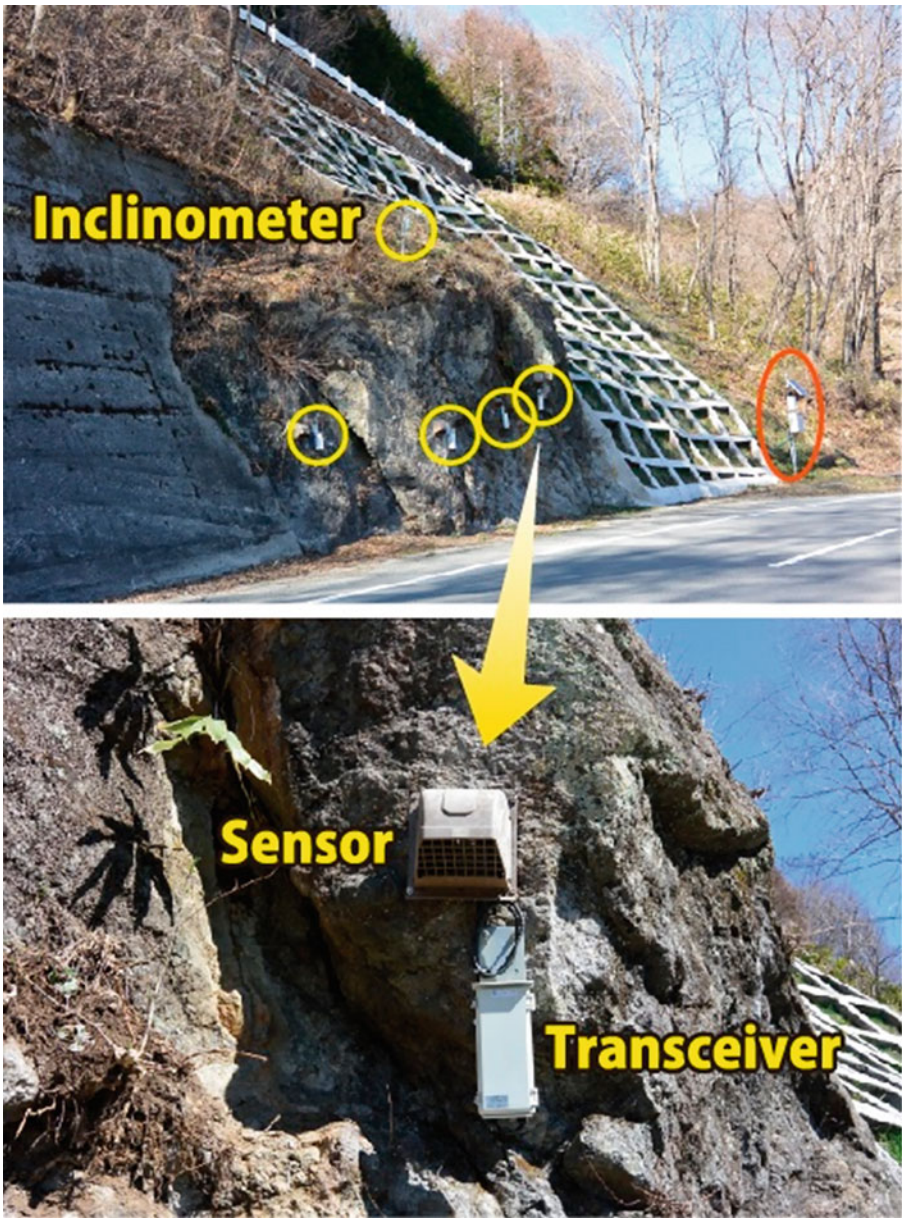

Fig. A.41 Bedrock slope monitoring (maintenance control)

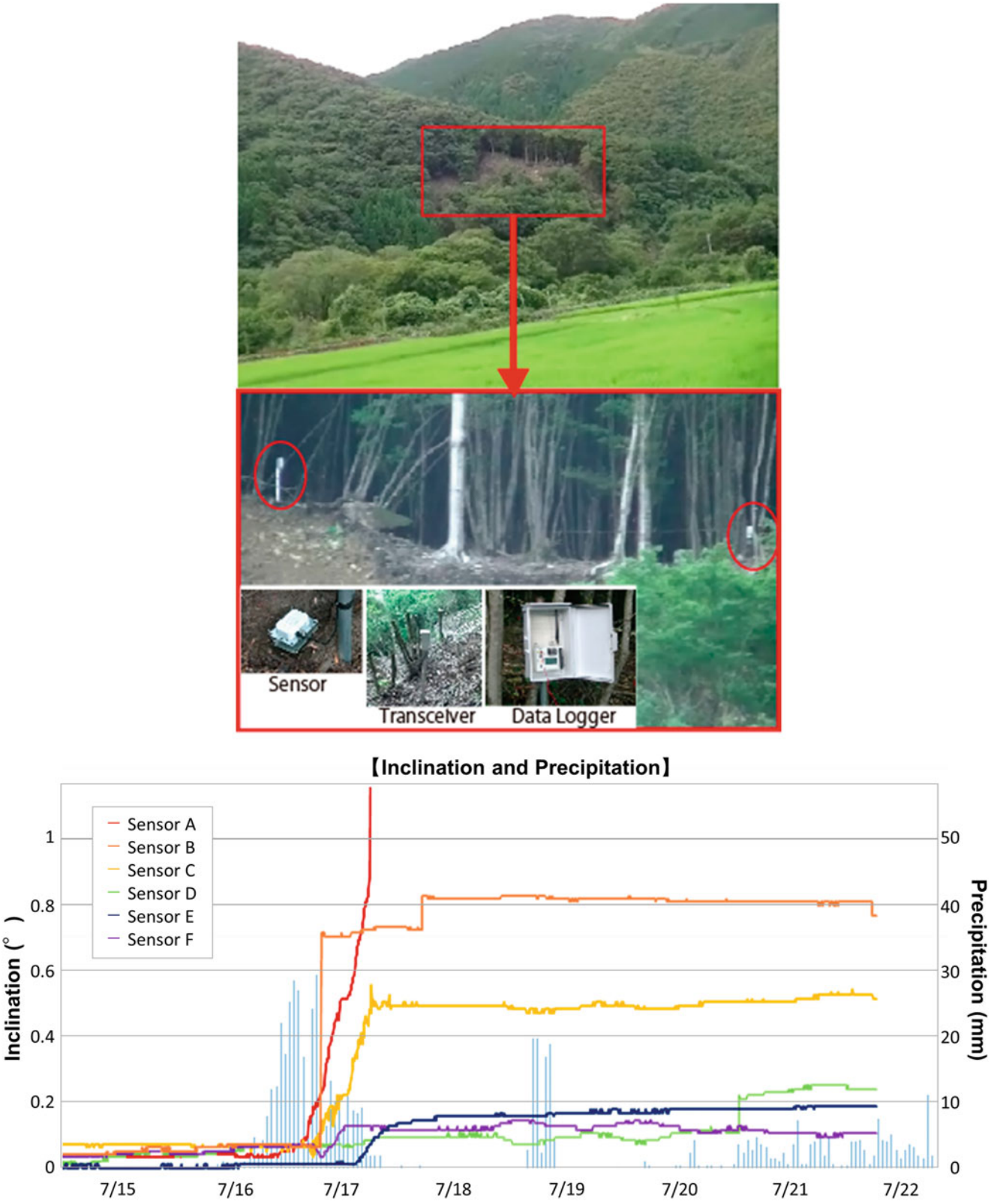

Fig. A.42 Measurement of the dynamic state of landslide using inclinometers with a wireless function

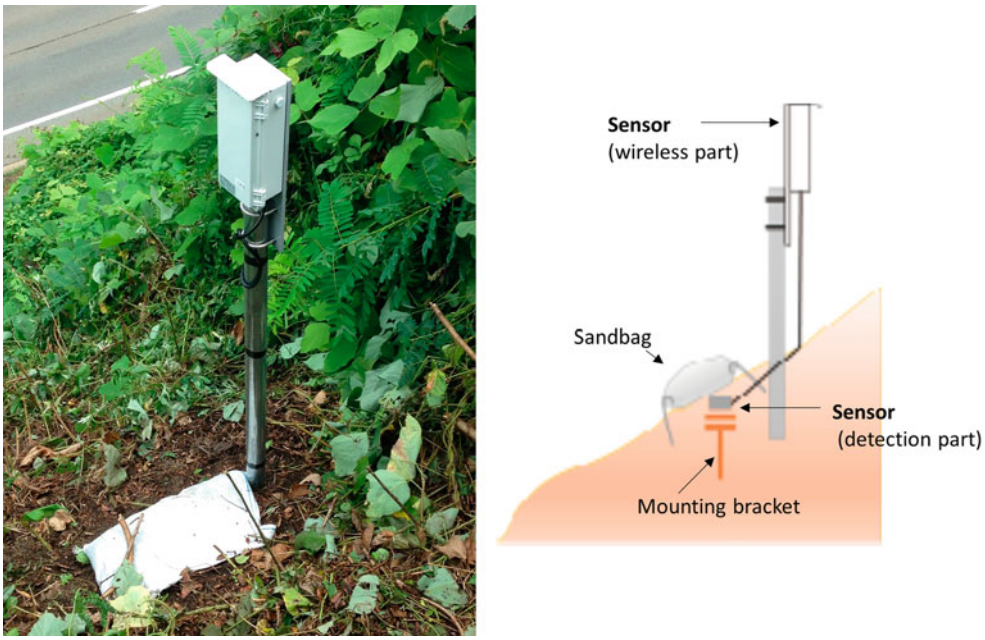

Fig. A.43 Example of sensor installation

Fig. A.44 Compact alarm device to alert local people to landslide risk

List of ICL Members

International Consortium on Landslides

An international non-government and non-profit scientific organization promoting landslide research and capacity building for the benefit of society and the environment.

President: Nicola Casagi (University Florence, Italy)

Vice Presidents: Peter Bobrowsky (Geological Survey of Canada. Canada), Zeljko Arbanas (University of Rijeka, Croatia), Binod Tiwari (California State University, USA), Faisal Fathani (University of Gadjah Mada, Indonesia), Veronica Tofani (University of Florence, Italy), Vit Vilimek (Charles University, Czech Republic) Executive Director: Kaoru Takara (National Research Institute for Earth Science and Disaster Resilience, Japan), Treasurer: Kyoji Sassa (Prof. Emeritus, Kyoto University, Japan)

Country/Region	**ICL Full member**
Bosnia and Herzegovina	The Geotechnical Society of Bosnia and Herzegovina
Brazil	Center for Scientific Support in Disasters—Federal University of Parana
Canada	Geological Survey of Canada
Canada	University of Alberta
China	Northeast Forestry University, Institute of Cold Regions Science and Engineering
	China University of Geosciences
	Chinese Academy of Sciences, Institute of Mountain Hazards and Environment
	Tongji University, College of Surveying and Geo-Informatics
	Shanghai Jiao Tong University
	Tsinghua University
	Civil Engineering and Development Department, Geotechnical Engineering Office, Hong Kong
	The Hong Kong University of Science and Technology
	The University of Hong Kong
Colombia	Universidad Nacional de Colombia
Croatia	Croatian Landslide Group from Faculty of Civil Engineering University of Rijeka and Faculty of Mining, Geology and Petroleum University of Zagreb
Czech Republic	Charles University, Faculty of Science
	Institute of Rock Structure and Mechanics, Department of Engineering Geology
Egypt	The American University in Cairo
Germany	Technische Universitat Darmstadt, Institute and Laboratory of Geotechnics
Georgia	Department of Geology of National Environmental Agency of Georgia
Honduras	Universidad Nacional Autónoma de Honduras (UNAH)
India	Amrita Vishwa Vidyapeetham, Amrita University
	National Institute of Disaster Management, New Delhi
Indonesia	Gadjah Mada University, Center for Disaster Mitigation and Technological Innovation (GAMA-InaTEK)
	Parahyangan Catholic University
	Agency for Meteorology, Climatology, and Geophysics of the Republic of Indonesia (BMKG Indonesia)
Iran	Building & Housing Research Center
Italy	UNESCO Chair for the prevention and the sustainable management of geo-hydrological hazards—University of Florence

(continued)

I. Alcántara-Ayala et al. (eds.), *Progress in Landslide Research and Technology, Volume 2 Issue 1, 2023*,
Progress in Landslide Research and Technology, https://doi.org/10.1007/978-3-031-39012-8

	ISPRA-Italian Institute form Environmental Protection and Research
	University of Calabria, DIMES, CAMILAB
	Istituto di Ricerca per la Protezione Idrogeologica (IRPI), of the Italian National Research Council (CNR)
	Universita di Torino, Department of Earth science
	Centro di Ricerca CERI—Sapienza Università di Roma
	National Institute of Oceanography and Applied Geophysics—OGS, Italy
Japan	Kyoto University, Disaster Prevention Research Institute
	Japan Landslide Society
	International Consortium on Geo-disaster Reduction
Korea	Korean Society of Forest Engineering
	National Institute of Forest Science
	Korea Authority of Land & Infrastructure Safety
	Korea Institute of Civil Engineering and Building Technology
Mexico	Institute of Geography, National Autonomous University of Mexico (UNAM)
Nepal	International Centre for Integrated Mountain Development (ICIMOD)
Russia	Moscow State University, Department of Engineering and Ecological Geology
	JSC "Hydroproject Institute"
Serbia	University of Belgrade, Faculty of Mining and Geology
Slovakia	Comenius University, Faculty of Natural Sciences, Department of Engineering Geology
Slovenia	University of Ljubljana, Faculty of Civil and Geodetic Engineering (ULFGG)
	Geological Survey of Slovenia
Sri Lanka	Central Engineering Consultancy Bureau (CECB)
	National Building Research Organization
Chinese Taipei	Landslide group in National Central University from Graduate Institute of Applied Geology, Department of Civil Engineering, Center for Environmental Studies
	National Taiwan University, Department of Civil Engineering
Thailand	Ministry of Agriculture and Cooperatives, Land Development Department
	Asian Disaster Preparedness Center (ADPC)
Ukraine	Institute of Telecommunication and Global Information Space
United Kingdom	British Geological Survey
USA & Nepal	California State University, Fullerton & Tribhuvan University, Institute of Engineering
Viet Nam	Institute of Transport Science and Technology
	Vietnam Institute of Geosciences and Mineral Resources (VIGMR)
Country/Region	**ICL Associate member**
Belgium	Liege University, Georisk and Environment (G&E) group
China	State Key Laboratory of Geohazard Prevention and Geoenvironment Protection (Chengdu University of Technology)
	State Key Laboratory of Plateau Ecology and Agriculture (Qinghai University)
Czech Republic	Czech Geological Survey
	Brown Coal Research Institute
Italy	Department of Earth and Environmental Sciences, University Aldo Moro, Bari
	University of Sannio, Department of Sciences and Technologies
	Geotechnical Engineering Group (GEG), University of Salerno
	Department of Earth and Environmental Sciences—University of Pavia
	University of Chieti-Pescara, Department of Engineering and Geology
	Federico II University of Naples, Department of Earth, Environmental and Resource Sciences
	DIA—Università degli Studi di Parma
	University of Urbino "Carlo Bo", Department of Pure and Applied Sciences
Japan	Ehime University, Center for Disaster Management Informatics Research
	Kochi University
	National Institute of Maritime, Port and Aviation Technology
Kyrgyzstan	Tian-Shan Geological Society
North Macedonia	Macedonian Association for Geotechnics
Russia	Russian State Geological Prospecting University n.a. Sergo Ordzhonikidze (MGRI-RSGPU)
Slovenia	University of Ljubljana, Faculty of Natural Sciences and Engineering (UL NTF)

(continued)

Switzerland	Institute of Earth Sciences, Faculty of Geoscience and Environment/University of Lausanne	
USA	Iowa State University	
Country/Region	**ICL Supporter**	
Italy	IDS GeoRadar s.r.l.	
Japan	Marui & Co., Ltd., Osaka	Okuyama Boring Co., Ltd., Yokote
	Ohta Geo-Research Co., Ltd., Nishinomiya	Japan Conservation Engineers Co., Ltd., Tokyo
	Sabo Technical Center, Tokyo	GODAI Development Corp., Kanazawa
	OYO Corporation, Tokyo	Kokusai Kogyo Co., Ltd., Tokyo
	OSASI Technos Inc., Kochi	NIPPON KOEI CO., LTD.
Chinese Taipei	Sinotech Engineering Consultants, Inc	

ICL Secretariat
Secretary General: Kyoji Sassa
International Consortium on Landslides, 138-1 Tanaka Asukai-cho, Sakyo-ku, Kyoto, 606-8226, Japan
Web: https://www.landslides.org/ E-mail: secretariat@landslides.org
Tel:+81 (75) 723 0640, Fax:+81(75) 950 0910

Index

I. Alcántara-Ayala et al. (eds.), *Progress in Landslide Research and Technology, Volume 2 Issue 1, 2023*,
Progress in Landslide Research and Technology, https://doi.org/10.1007/978-3-031-39012-8